FLUID FLOW AND HEAT TRANSFER in Wellbores

Second Edition

Rashid Hasan and Shah Kabir

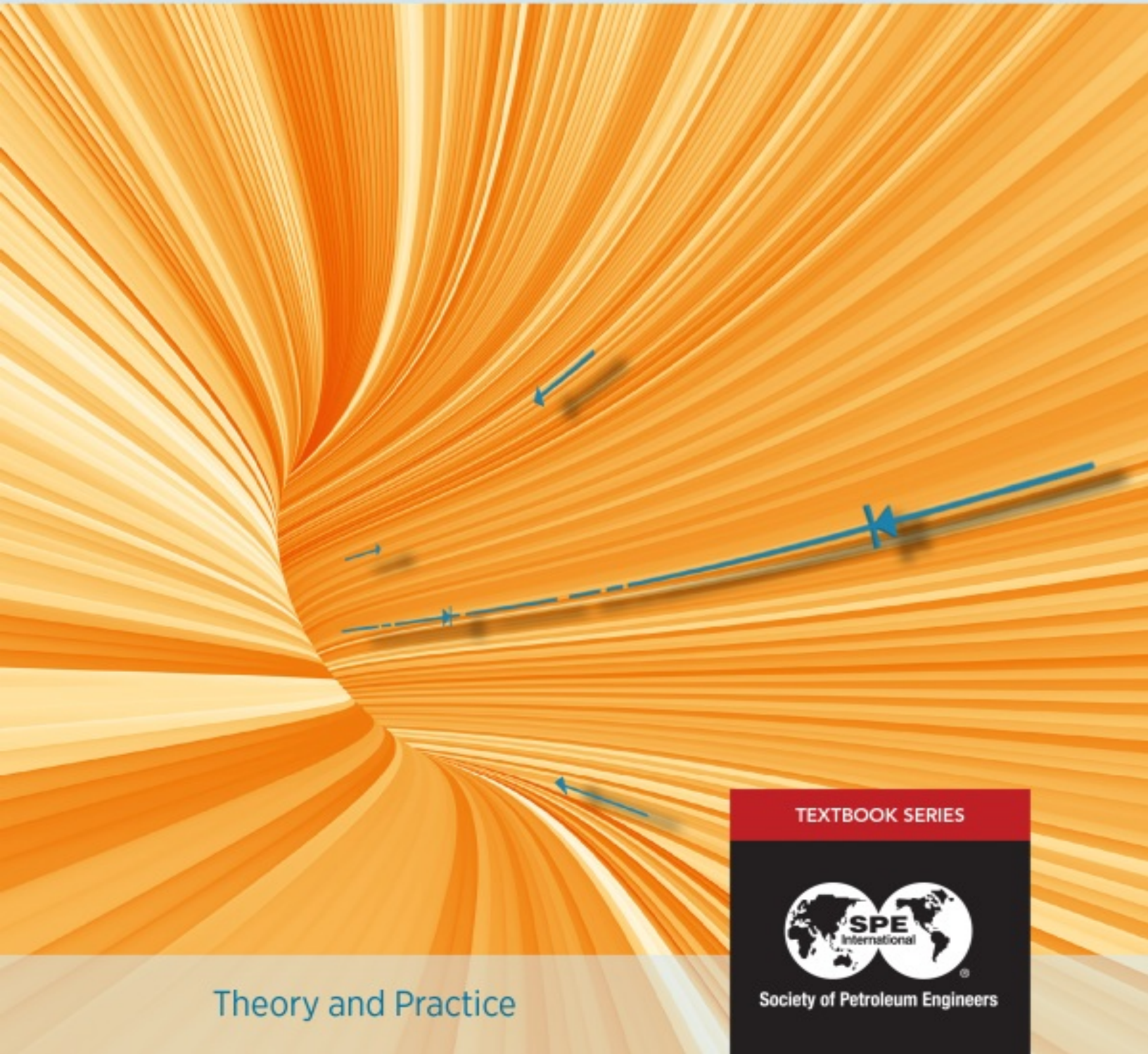

Theory and Practice

TEXTBOOK SERIES

SPE International

Society of Petroleum Engineers

Fluid Flow and Heat Transfers in Wellbores

Second Edition

Fluid Flow and Heat Transfers in Wellbores

Second Edition

Rashid Hasan

Professor, Larry A. Cress ’76 Faculty Fellow

Harold Vance

Department of Petroleum Engineering, Texas A&M University

Shah Kabir

Adjunct Faculty Member

Department of Petroleum Engineering, University of Houston

Society of Petroleum Engineers

© Copyright 2018 Society of Petroleum Engineers

All rights reserved. No portion of this book may be reproduced in any form or by any means, including electronic storage and retrieval systems, except by explicit, prior written permission of the publisher except for brief passages excerpted for review and critical purposes.

Printed in the United States of America.

Disclaimer

This book was prepared by members of the Society of Petroleum Engineers and their well-qualified colleagues from material published in the recognized technical literature and from their own individual experience and expertise. While the material presented is believed to be based on sound technical knowledge, neither the Society of Petroleum Engineers nor any of the authors or editors herein provide a warranty either expressed or implied in its application. Correspondingly, the discussion of materials, methods, or techniques that may be covered by letters patents implies no freedom to use such materials, methods, or techniques without permission through appropriate licensing. Nothing described within this book should be construed to lessen the need to apply sound engineering judgment nor to carefully apply accepted engineering practices in the design, implementation, or application of the techniques described herein.

ISBN 978-1-61399-545-7

Second Edition 2018

Society of Petroleum Engineers
222 Palisades Creek Drive
Richardson, TX 75080-2040 USA

http://www.spe.org/store

service@spe.org
1.972.952.9393

About the Authors

A. Rashid Hasan is a professor of petroleum engineering at Texas A&M University (TAMU). Before joining TAMU, he headed the Chemical Engineering Departments at University of Minnesota, Duluth and University of North Dakota (UND), Grand Forks, and directed UND's doctoral program in energy engineering. Hasan has also worked with NASA Glenn on various aspects of multiphase flow and thermohydraulic transients. He is an expert in the areas of production engineering, focusing on modeling complex transport processes in various elements of petroleum production systems. Hasan is one of the pioneers in modeling steady and transient transport of heat and momentum in wellbores. He applies heat-and fluid-flow modeling to the analyses of production safety, wellbore integrity, flow assurance, flow metering, and some aspects of pressure-transient testing. Hasan holds a PhD degree (1979) from the University of Waterloo, Canada. He has published extensively and has served on various SPE committees. Hasan was the recipient of the 2011 SPE Production and Operations Award and the 2015 SPE Distinguished Membership Award.

C. Shah Kabir is the proprietor of CS Kabir Consulting in Houston. With more than 40 years of experience in the ol and gas industry with Dome, Arco, Schlumberger, Chevron, and Hess, he has expertise in pressure- and ratetransient analysis, wellbore fluid- and heat-flow modeling, many aspects of reservoir engineering, and testing and performance forecasting in unconventional reservoirs. Kabir has published more than 140 papers and two books, and contributed to the SPE monograph *Transient Well Testing*. His experience includes knowledge of major oil provinces, including those in North America, North Sea, Middle East, and Far East. He holds a master's degree (1976) in chemical engineering from University of Calgary, Canada. Kabir has served SPE in many capacities, including as an associate editor for *SPE Production & Operations, SPE Reservoir Evaluation & Engineering*, and *SPE Journal*, and as an SPE Distinguished Lecturer during the 2006–2007 season. His major SPE awards include Honorary Membership (2016), Reservoir Description and Dynamics Award (2010), and Distinguished Membership (2008).

Dedicated to Nilufar and Kumkum

Preface

Fluid flow in wellbores occurs during various phases of a well's life. Our ability to optimize each flow process depends largely on grasping the underlying physics so that we can mathematically describe the process involved. At a well's inception, drilling operations require mud circulation, causing considerable heat exchange between the colder fluid and the warmer formation. In the event of a blowout, because of lost circulation or unexpected overpressured zone, we encounter transient two-phase flow as the formation interacts with the wellbore prematurely. When we initiate flow from the formation by design, such as in a drillstem or production test, flow of either a single-phase or a multiphase fluid occurs. As the fluids ascend the wellbore, the warm formation fluid begins to exchange heat with the colder formation above it. Therefore, heat flow is always coupled with fluid flow in actual wellbores.

In this book, we attempt to address the coupled fluid/heat flow issue as encountered in many practical production/operation problems, including in drilling. Both steady- and unsteady-state transport problems are considered. Even when steady fluid flow is maintained during circulation, injection, or production modes, unsteady heat transport in the formation occurs nonetheless. Fluid circulation during drilling and workover operations and injection of annular gas in a gas lift operation are cases in point. We also examine fully transient processes of fluid and heat flows, such as those in drillstem or production testing.

Before we undertake a detailed analysis of each operational problem, we introduce the reader to some basic concepts, starting with the rudiments of single-phase flow (Chapter 1) and moving to more-complex issues of two-phase flow modeling (Chapters 2, 3, and 4). Chapter 5 is a new addition to encapsulate the lessons learned from application of the models in various field settings discussed in earlier chapters. Then, the principles of heat conduction in the formation, as well as the elements of fluid flow and the associated heat flow, are discussed in Chapter 6, followed by a new Chapter 7 showing various applications in coupled fluid/heat flow problems.

Chapter 8 introduces analytical models in various bundled-tube settings, where production and/or injection occurs in multitubing configurations. Chapter 9 presents aspects of modeling transient fluid and heat flow problems. Well integrity issues pertaining to annular pressure buildup, sustained casing pressure, and gas lift valves form the cornerstone of Chapter 10; both appropriate models and field examples exemplify the lessons learned from coupled fluid/heat flow modeling. Along with Chapters 5 and 7, Chapter 10 is new to this edition of the book.

Chapter 11 presents various analytical models pertaining to drilling operations. Here, simple analytical tools attempt to capture the evolution of wellbore temperature profiles in various operational settings, followed by an estimation of the static formation temperature, leading to determination of the geothermal gradient.

Thereafter, estimating the spilled volume in uncontrolled wells is pursued for both gas and oil wells in a probabilistic framework.

Chapter 12 attempts to capture various aspects of production operations with surveillance data. In this context, production of organic solids, such as paraffins and asphaltenes, is addressed. Two field studies involving coupled modeling of reservoir/wellbore/surface network emphasize the lessons learned from a holistic approach. Finally, Chapter 13 discusses some aspects of production logging; flowmeter and temperature responses are the essence of this discussion.

Besides introducing three new chapters (Chapters 5, 7, and 10), this new edition of the book has updated all others wherever appropriate. Our expectation is that the three new chapters illuminate application of diverse flow problems that can be tackled with the basic principles learned. This edition is expected to serve a variety of readers, from advanced senior and graduate students to researchers and practicing engineers. The overall philosophy is to show not just how to solve a given problem but also why the recommended approach is preferred. Illustrative examples presented at the end of each major section reinforce the principles learned. In other words, striking a balance between theory and practice has led us to the avoidance of a proverbial cookbook approach.

Although over the last seven decades hundreds of papers have been written on the topics of multiphase flow and heat transfer, here we have attempted to present only those that pertain to solving some of the wellbore flow problems. Therefore, this book does not treat either topic in great depth, but attempts to acquaint the reader with enough information so that practical oilfield flow problems can be tackled. In presenting various approaches to solving a problem, we have favored physical models, which have been verified with either laboratory or field data, or with both, over purely empirical correlations. However, in choosing mechanistic models, we have leaned toward a simpler approach, rather than delving into complex but rigorous solutions. Here, the motivation was to retain simplicity and engineering accuracy. In this context, we must point out that we have drawn heavily from our experience, both academic and applied, to present this material. In this compilation effort, our familiarity with our own material has taken precedence, notwithstanding objectivity. The citations mostly included accessible peer-reviewed papers, although hard-to-find classic papers required mention, given their seminal contributions.

We have not attempted to solve *all* the coupled fluid/heat flow problems in production operations. This second edition of the book is simply an attempt to capture a few more problems than those investigated earlier. Our ardent hope is that the presented material gives both the foundation and the tools for tackling a new class of problems.

Acknowledgments

In our quest to grasp various aspects of production operations as practiced in the oil field, we learned from others through personal interaction and through published work. Our colleagues, in both academia and the industry, have enriched our knowledge over the years. We are indebted to them all.

We would like to recognize a few who have made the real difference in our learning and the eventual compilation of the second edition of this book. Three noted practitioners reviewed three new chapters in this edition of the book. Specifically, we are indebted to Janvier Lissanon of BHP Billiton for reviewing Chapter 5, U. B. Sathuvalli of Blade Energy for scrutinizing Chapter 10, and Suri Suryanarayana, also of Blade Energy, for providing useful feedback on Chapter 7. We remain grateful to Cem Sarica of Tulsa University for reviewing the manuscript of the book's first edition. We express our sincere gratitude to our respective organizations, the University of North Dakota, Texas A&M University, and Chevron and Hess, for aiding our pursuit. SPE book editor Jane Eden's stewardship is much appreciated. We are immensely grateful to Harry Butler for doing a thorough painstaking job during the copy-editing phase of this project.

We are indebted to many graduate students who have made direct contributions to the book's cause over the years. Most notably, Xiaowei Wang and Dongqing Lin at the University of North Dakota contributed a great deal in developing many models presented in several chapters. We acknowledge the contributions of Bulent Izgec of Texas A&M University and Chevron to modeling thermal effects influencing pressure gauge response and annular pressure buildup. More recently, two Texas A&M University graduate students gave invaluable help: Tony Rocha-Valadez contributed to the modeling of sustained casing pressure and integrity of gas lift valves, and Ruochen Liu helped develop blowout models for gas and oil wells. A current Texas A&M University student, Gibran Hashmi, assisted in developing models for rate estimation from temperature or pressure data. Many field examples were drawn from hands-on experience that one of us (C. S. Kabir) has had in fields across many basins.

Several academics helped shape our understanding of this technology through their exemplary leadership. Graham Wallis of Dartmouth College formalized the drift-flux approach for two-phase flow modeling. The late Abraham Dukler of the University of Houston and the late Hank Ramey Jr. of Stanford University laid the foundation for mechanistic modeling of two-phase flow and wellbore heat transfer, respectively. We were inspired by the body of work that James Brill of the University of Tulsa and Khalid Aziz of Stanford University had contributed to the field.

Last, our family members, especially our spouses, deserve particular mention for their encouragement and fortitude. Their extraordinary understanding allowed us to steal countless hours from family time so that we could complete this edition of the

book. Finally, our parents taught us values that inspired us to compile this material. To this end, we hope the reader finds this text stimulating and useful.

Rashid Hasan
Shah Kabir

Table of Contents

About the Authors

Dedication

Preface

Acknowledgments

Chapter 1 – Overview

1.1 Single-Phase Flow
1.2 Flow in Nonisothermal Systems
1.3 Flow in Annulus
1.4 Flow in Horizontal Wells
Summary
Nomenclature

Chapter 2 – Multiphase Flow: Introduction

2.1 Introduction
2.2 Concepts and Definitions
2.3 Method of Analysis
2.4 Homogeneous Flow Models
2.5 Separated Flow Models
Summary
Nomenclature

Chapter 3 – Multiphase Flow: Mechanistic Models for Vertical Wells

3.1 Introduction
3.2 Flow Pattern Delineation
3.3 Liquid Holdup and Pressure Drop
3.4 Discussion
Summary
Nomenclature

Chapter 4 – Multiphase Flow: Deviated and Horizontal Wells and Other Systems

4.1 Introduction
4.2 Flow in Deviated Wells
4.3 Flow in Horizontal Pipes and Wells

4.4 Modeling Flow in Nonconventional Situations
Summary
Nomenclature

Chapter 5 – Multiphase Flow: Field Applications

5.1 Overall Modeling Approach in Gas/Liquid Flow
5.2 Two-Phase Flow in Oil Wells
5.3 Two-Phase Flow in Gas/Condensate Wells
5.4 Liquid Loading in Gas Wells
5.5 Estimating Flow Rates With Multiphase Choke Correlations
Summary
Nomenclature

Chapter 6 – Wellbore Heat Transport

6.1 Introduction
6.2 Formation Temperature Distribution
6.3 Energy Balance for Wellbore Fluid
6.4 Wellbore Fluid Temperature
Summary
Nomenclature
Appendix 6-A Heat-Transfer Coefficients for Wellbores

Chapter 7 – Heat Transport: Field Applications

7.1 Introduction
7.2 Rate Estimation With Steady- and Unsteady-State Temperature/Pressure Data
7.3 Thermal Effects Influencing Pressure Response in Off-Bottom Gauges
7.4 Geothermal Well Modeling
7.5 Transient Temperature in Oil Reservoirs With Large Drawdowns
Summary
Nomenclature
Appendix 7-A Flow Rate Estimation From Temperature Data
Appendix 7-B Depth-Dependent Fluid Temperature With Superposition
Appendix 7-C Flow Rate Estimation for Slug and Closed-Chamber Tests
Appendix 7-D Transient Temperature Model During Water Injection
Appendix 7-E Example Bottomhole Pressure Calculations for a Geothermal Well
Appendix 7-F Comprehensive Energy Balance for Transient Temperature in Oil Reservoirs

Appendix 7-G Input Data for Model Validation

Chapter 8 – Wellbore Temperature Profiles in Multiple Strings

8.1 Introduction

8.2 Production Through the Tubing and Annulus

8.3 Production Through Two Tubing Strings

8.4 Production and Injection Through a Common Wellbore

Summary

Nomenclature

Appendix 8-A Working Equations for Multiple-String Completions

Chapter 9 – Transient Fluid and Heat Flows in Wellbores

9.1 Introduction

9.2 Modeling Single-Phase Gas Flow

9.3 Modeling Single-Phase Oil Flow

9.4 Modeling Two-Phase Gas/Oil Flow

9.5 Analytical Wellbore Transient Temperature Modeling

Summary

Nomenclature

Appendix 9-A Finite-Difference Equations for Wellbore Fluid Temperature

Appendix 9-B Derivation of Analytical Transient Fluid Temperature Models

Chapter 10 – Applications of Transient Heat Flows in Assessing Well Integrity

10.1 Introduction

10.2 Annular Pressure Buildup

10.3 Sustained Casing Pressure in an Annulus

10.4 Integrity Testing of Gas Lift Valves

Summary

Nomenclature

Appendix 10-A Annular Pressure Buildup Formulation in Multiple Annuli

Appendix 10-B Solution of Transient Formulation for Annular Pressure Buildup

Appendix 10-C Sustained Casing Pressure Model Derivation and Analytical Solution

Chapter 11 – Drilling Operations

11.1 Fluid Circulation Temperature

11.2 Static Formation Temperature

11.3 Well Blowout

Summary

Nomenclature
Appendix 11-A Models Related to Drilling Operations
Appendix 11-B Constants for the Variable Heat-Flux Model
Appendix 11-C Transient Heat Transfer From Mud to Formation
Appendix 11-D Oil PVT Properties for Estimating Maximum Discharge

Chapter 12 – Production Operations and Flow Assurance

12.1 Systems Analysis
12.2 Temperature Profiles in Gas Lift Wells
12.3 Wellbore Steam/Water Flow and Surface Metering
12.4 Combating Wellbore Solids Deposition
Summary
Nomenclature
Appendix 12-A Derivation of Superposition Equations
Appendix 12-B Solution of Equation 12.14 in Gas Lift
Appendix 12-C Solids Deposition Models

Chapter 13 – Production Logging

13.1 Introduction
13.2 Spinner Flowmeter Production Log Interpretation
13.3 Flow Pattern Maps for Production Log Analysis
13.4 Rate Estimation From Temperature Surveys
13.5 Discussion
Summary
Nomenclature

References

Index

Chapter 1

Overview

1.1 Single-Phase Flow

Fluid flow, in a variety of forms and complexities, is a basic entity that must be dealt with in the production of hydrocarbons. In its rudiments, single-phase gas or oil production and water injection form the core of all flow problems. Therefore, Chapter 1 discusses the mechanical energy balance equation, which relates pressure drop to its various components for single-phase flow. Next, the components of total pressure drop—static, kinetic, and frictional—are discussed. In addition, flows in tubing/casing annuli and horizontal wells, which are of particular interest to petroleum engineers, are briefly discussed.

1.1.1 Mechanical Energy Balance. A simple one-dimensional (1D) analysis of single-phase gas or liquid flow is best made with the aid of a schematic, as shown in **Fig. 1.1.** The channel, inclined at an arbitrary angle α with the horizontal, shows upward flow of the fluid. We use the industry convention that the vertical axis z is positive in the downward direction. For the present, we consider only the steady-state case and assume that pressure, at any point in the cross-sectional plane normal to flow, remains the same. With these simplifications, we derive the momentum balance equation.

Conservation of Momentum. The sum of forces acting on the fluid element, shown in Fig. 1.1, equals the change of momentum of the fluid. The forces acting on the fluid element are those owing to pressure p, friction F, and gravity. Referring to the differential length dz of Fig. 1.1, we write

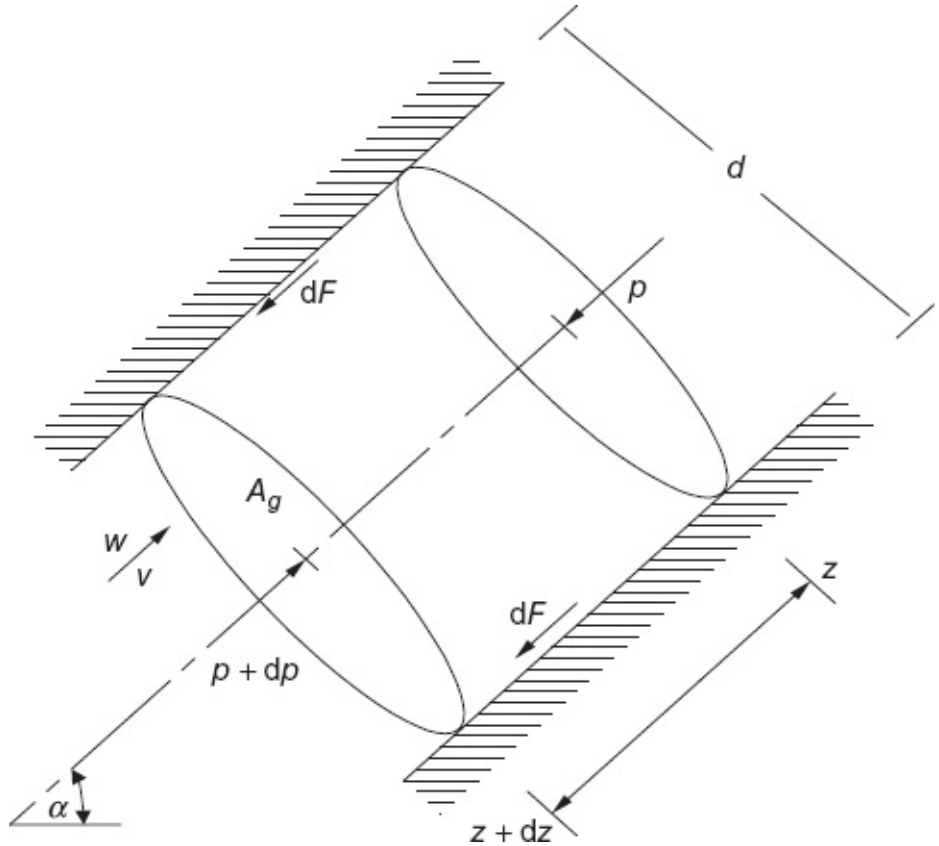

Fig. 1.1—Momentum balance for a fluid element.

$$pA - (p + \mathrm{d}p)A + \mathrm{d}F + A\,(\mathrm{d}z)\,g\,\rho\,\sin\alpha = \text{change of fluid momentum.} \quad (1.1a)$$

If the fluid mass flow rate is *w* and its velocity is *v*, then its momentum equals *wv*. For the general case of transient flow, when both flow rate and velocity change along the flow direction, fluid momentum change is given by (*w* + *dw*) (*v* + *dv*) –*wv*. Therefore,

$$pA - (p + \mathrm{d}p)\,A + \mathrm{d}F + A\,(\mathrm{d}z)\,g\,\rho\,\sin\alpha = (w + \mathrm{d}w)\,(v + \mathrm{d}v) - wv. \quad (1.1b)$$

Simplifying, we obtain

$$-A\mathrm{d}p + \mathrm{d}F + A\,(\mathrm{d}z)\,g\,\rho\,\sin\alpha = w\mathrm{d}v + v\mathrm{d}w. \quad (1.2)$$

Usually, the mass flow rate is invariant; that is, *dw* = 0, leading to

$$-A\mathrm{d}p + \mathrm{d}F + A\,(\mathrm{d}z)\,g\,\rho\,\sin\alpha = w\mathrm{d}v. \quad (1.3)$$

Dividing both sides of Eq. 1.3 by A*dz*, we obtain

$$-(\mathrm{d}p/\mathrm{d}z) + (\mathrm{d}p/\mathrm{d}z)_F + g\rho\,\sin\alpha - (w/A)\,\mathrm{d}v/\mathrm{d}z = 0 \quad (1.4)$$

or

$$(\mathrm{d}p/\mathrm{d}z) = (\mathrm{d}p/\mathrm{d}z)_F + (\mathrm{d}p/\mathrm{d}z)_H + (\mathrm{d}p/\mathrm{d}z)_A, \quad (1.5)$$

where

$$-(dp/dz)_H = -g\,\rho\,\sin\alpha \quad (1.6)$$

and

$$-(dp/dz)_A = (w/A)\,d(v)/dz = \rho\,v\,d(v)/dz. \quad (1.7)$$

1.1.2 Components of Pressure Gradient. Eq. 1.5 shows the total pressure gradient is the sum of the frictional gradient $(\mathbf{dp}/dz)_F$, the hydrostatic gradient $(dp/dz)_H$, and the accelerational gradient $(dp/dz)_A$. Of these three terms, perhaps the static gradient is the easiest to estimate because it only requires knowledge of the fluid density and well-deviation angle. Because gas density depends on pressure, the static term will vary along the well for gas wells. Usually such variation is small, and relatively simple equations of state can be used to account for it. To some extent, even for single-phase oil production, oil-density variation with well depth, owing to temperature and dissolved gases, must be taken into account. The same comments apply to the estimation procedure for the kinetic head (Eq. 1.7).

For incompressible flow (gases at very high pressures and liquids) in a straight pipe with no change in cross-sectional area, the change in fluid velocity with axial distance (dv/dz) is generally negligible. However, for gases at moderate and low pressures, and especially at high velocities, the kinetic energy loss can be a significant portion of the total pressure loss and must be accounted for properly. Computational complications that arise for gas flow have led to a number of correlations for calculating pressure drop in a wellbore. We recommend the widely used Cullender and Smith (1956) method for computing pressure drop in a gas well, when the accelerational component becomes negligible.

The frictional pressure gradient is generally represented by

$$(dp/dz)_F = fv^2\rho/(2g_c d). \quad (1.8)$$

In this book, we are using the Moody friction factor because of its popularity in the oil industry. The alternative is to use the Fanning friction factor, which is one-quarter the value of the Moody friction factor. In that case, Eq. 1.8 will change to $(dp/dz)_F = 2fv^2\rho/(g_c d)$, reflecting the lower value of the Fanning friction factor. Friction factor f depends on fluid turbulence and pipe roughness. The friction factor is usually expressed as a function of Reynolds number

$$\mathrm{Re} = dv\rho/\mu \quad (1.9)$$

and roughness factor ε/d. The chart for friction factor as a function of Reynolds number with pipe roughness as a parameter is shown in **Fig. 1.2,** whereas **Fig. 1.3** presents the chart for estimating relative roughness. Note, ε/d represents the relative roughness in both figures.

At low Reynolds numbers (Re < 2,100), the flowing-fluid elements do not interact

with each other, and the flow is called laminar. For laminar flow in either rough or smooth pipes, friction factor is inversely related to Reynolds number,

$$f = \frac{64}{\mathrm{Re}} = \frac{64\mu}{dv\rho}, \qquad (1.10a)$$

when

$$\mathrm{Re} < 2{,}100. \qquad (1.10b)$$

At high Reynolds numbers (Re > 4,000), the flow is termed turbulent. During turbulent flow, the friction factor depends on both Reynolds number and pipe roughness. For smooth pipes, such as plastic pipes and tubulars coated with polyvinyl chloride lining, friction factor can be estimated reliably from the Blasius equation,

$$f = 0.32\,(\mathrm{Re})^{-0.25}, \qquad (1.11)$$

when

$$\mathrm{Re} > 2{,}100. \qquad (1.12)$$

For very high Reynolds numbers (Re > 50,000), Eq. 1.11 is slightly modified as $f = 0.184\,(\mathrm{Re})^{-0.2}$.

Eq. 1.11, of course, is invalid for rough pipes, which need the use of a chart, such as that in Fig. 1.2. Although a chart is useful for all types of pipe roughness, chart reading is tedious and is not easily amenable to computer calculations. A number of equations, relating friction factor to Reynolds number and pipe roughness, have been proposed over the years and are in fair agreement with the original friction factor charts. We recommend the following expression proposed by Chen (1979), modified to yield Moody friction factor

$$f = \frac{4}{\left[4\log\left(\frac{\varepsilon/d}{3.7065} - \frac{5.0452}{\mathrm{Re}}\log\Lambda\right)\right]^2}, \qquad (1.13)$$

where ε is pipe roughness and the dimensionless parameter Λ is given by

$$\Lambda = \frac{(\varepsilon/d)^{1.1098}}{2.8257} + \left(\frac{7.149}{\mathrm{Re}}\right)^{0.8981} \qquad (1.14)$$

Unlike many other expressions, which require iterative solutions for the friction factor, Eq. 1.13 is explicit and, therefore, computationally efficient. de Nevers (2004, p.187) suggested a simpler explicit formulation, with somewhat lesser accuracy, given by

$$f = 0.0055\left\{1+\left[20{,}000\left(\frac{\varepsilon}{d}\right)+\frac{10^6}{\mathrm{Re}}\right]^{1/3}\right\} \quad (1.15)$$

More recently, Ghanbari et al. (2011) have presented a similar explicit formulation with improved accuracy, given by

$$f = 4\left\{-1.52\log\left[\left(\frac{\varepsilon / D}{7.21}\right)^{1.042}\right]+\left(\frac{2.731}{\mathrm{Re}}\right)^{0.9152}\right\}^{-2.169} \quad (1.16)$$

Note that Eqs. 1.15 and 1.16 have been modified to represent Moody friction factor. The evaluation of various terms in Eq. 1.13 is relatively easier for flow of single-phase fluids, even for gases, than for two-phase mixtures. In the latter case, estimating the average density and friction factor can be challenging because these are complex functions of fluid properties and flow conditions. Chapter 2 discusses various approaches taken to evaluate these entities in two-phase flow.

1.2 Flow in Nonisothermal Systems

Fluid temperature in the wellbore often varies significantly with depth, and sometimes with time. Many of the fluid properties that influence pressure drop, such as density and viscosity, are greatly influenced by the fluid temperature. Therefore, we cannot overemphasize the importance of accurate fluid temperature estimation as a function of well depth and production or injection time. This calculation can be performed by a proper energy balance on the fluid/wellbore system, as shown in Chapter 6. For single-phase liquid flow, the expression for fluid temperature, T_f, may be simplified with minimal inaccuracy to

$$T_f = T_{ei} + \left(1 - e^{-zL_R}\right) g_G \sin\alpha / L_R, \quad (1.17)$$

where the parameter L_R, which is a function of wellbore heat-transfer coefficient U and formation heat conductivity k_e, is defined by

$$L_R = \frac{2\pi}{c_P w}\left[\frac{rUk_e}{k_e + \left(rUT_D\right)}\right] \quad (1.18)$$

In Eq. 1.18, T_D represents dimensionless temperature, which is a function of dimensionless producing time, $t_D = \alpha t / r_{wb}^2$.

$$T_D = \ln\left[e^{-0.3t_D} + \left(1.5 - 0.3719e^{-t_D}\right)\sqrt{t_D}\right] \quad (1.19)$$

For a complete discussion of Eqs. 1.17 through 1.19, please refer to Chapter 6.

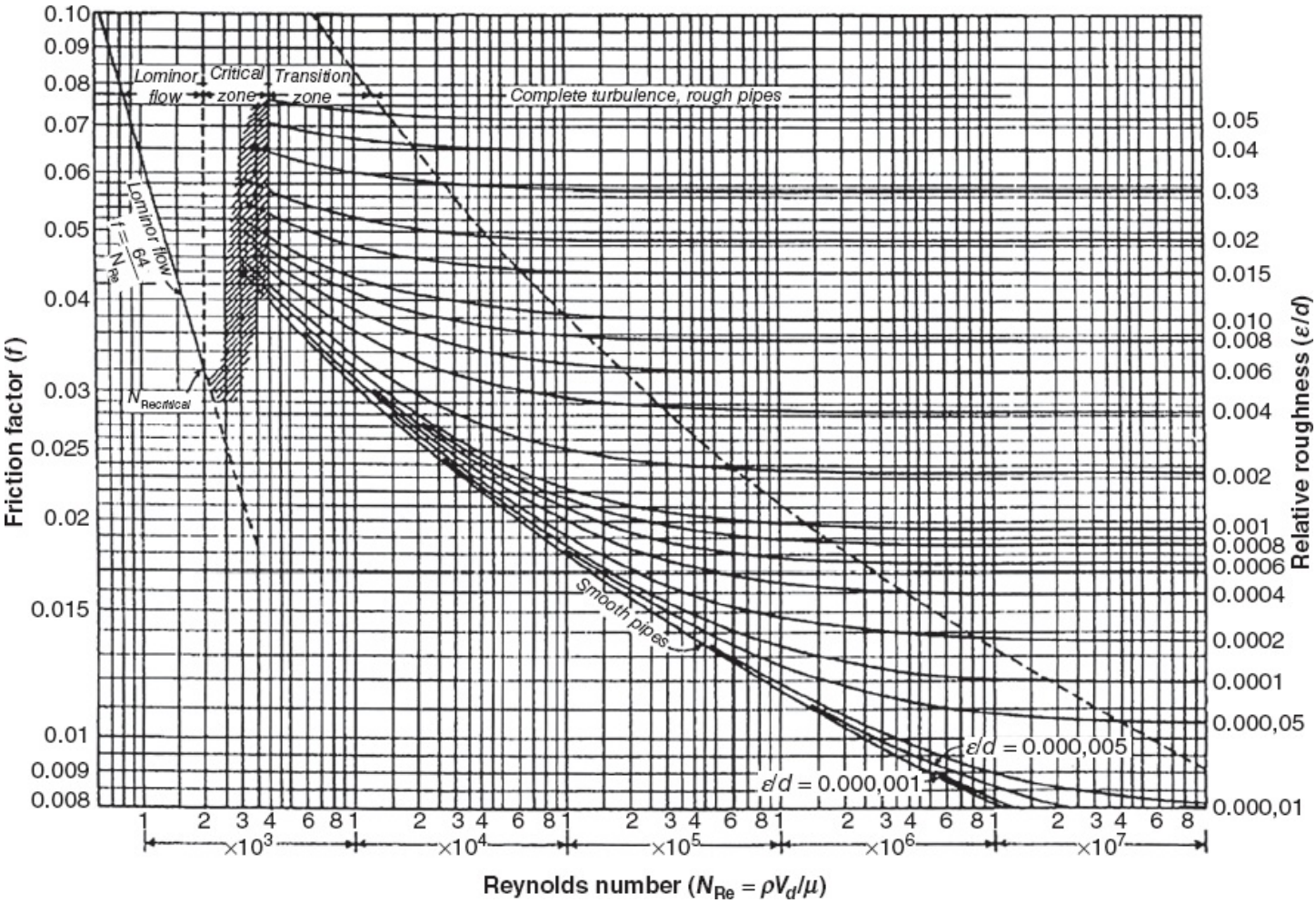

Fig. 1.2—Moody friction factor chart for turbulent flow (Moody 1944).

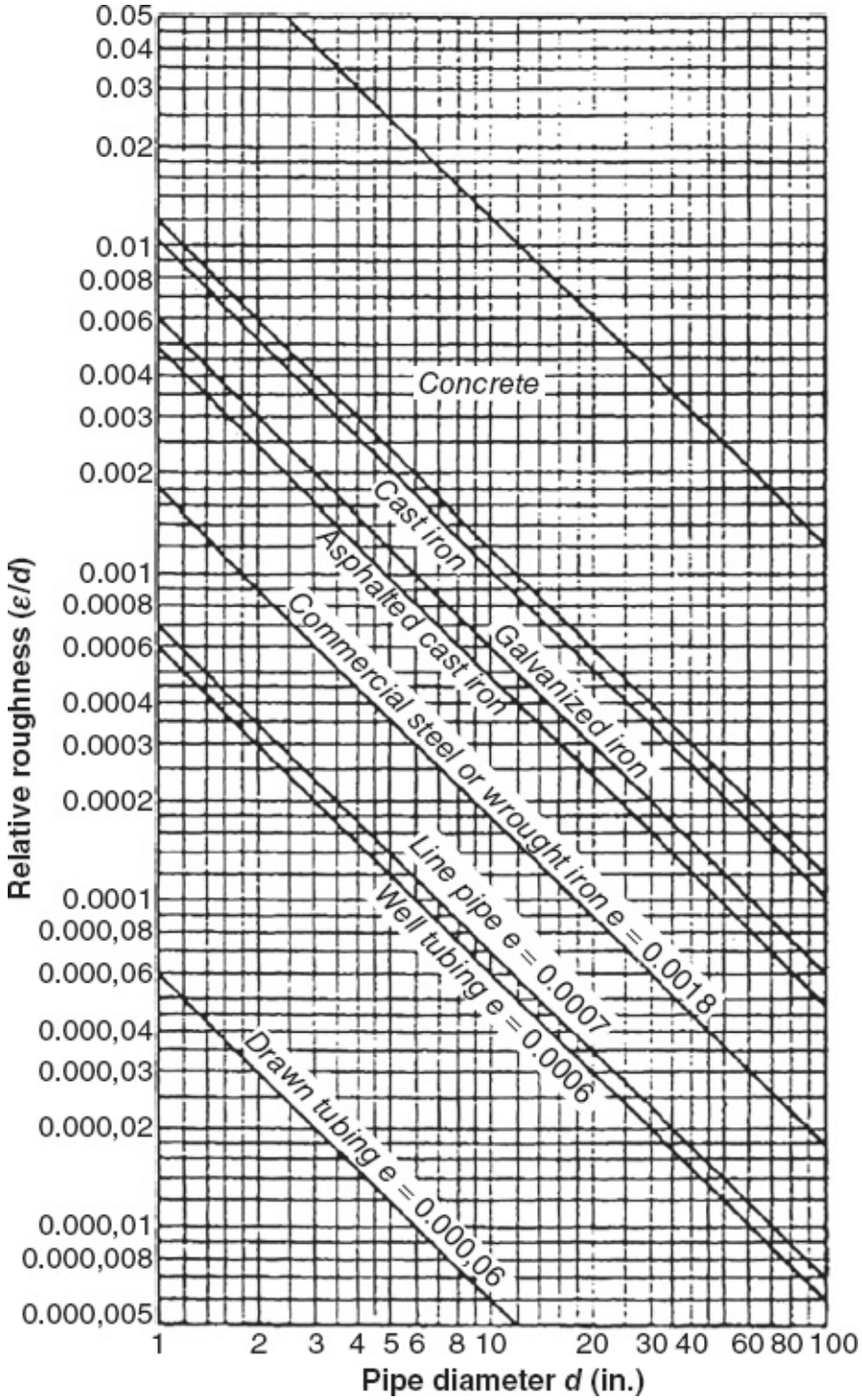

Fig. 1.3—Relative roughness of pipes (Moody 1944).

1.3 Flow in Annulus

Although flow through a tubing string is the most common configuration, drilling, as well as many completions, dictates modeling for flow up the tubing/casing annulus. The presence of two walls makes flow through an annulus different from that through ordinary circular strings. The classical work of Bird et al. (2002) shows that Eq. 1.8 is also applicable for such geometry, although the correlation for friction factor must be modified to reflect greater wall shear. For laminar flow in a concentric annulus, the

Moody friction factor f_{CA} is given by Bird et al. (2002) as

$$f_{CA} = \frac{64}{\mathrm{Re}} \frac{(1-K)^2}{\left[\frac{1-K^4}{1-K^2} - \frac{1-K^2}{\ln(1/K)}\right]}, \quad (1.20)$$

where K is the diameter ratio, d_t/d_c. Following the studies of Gunn and Darling (1963) and Caetano et al. (1992a), we recommend expressing turbulent flow in a concentric annulus as

$$\frac{1}{\left\{ f_{CA} \left(\frac{F_p}{F_{CA}} \right)^{0.45\exp\left[-(\mathrm{Re}-3000)/10^6\right]} \right\}^{0.5}}$$

$$= 4\log\left(\mathrm{Re} \left\{ f_{CA} \left(\frac{F_p}{F_{CA}} \right)^{0.45\exp\left[-(\mathrm{Re}-3000)/10^6\right]} \right\}^{0.5} \right) - 0.4, \quad (1.21)$$

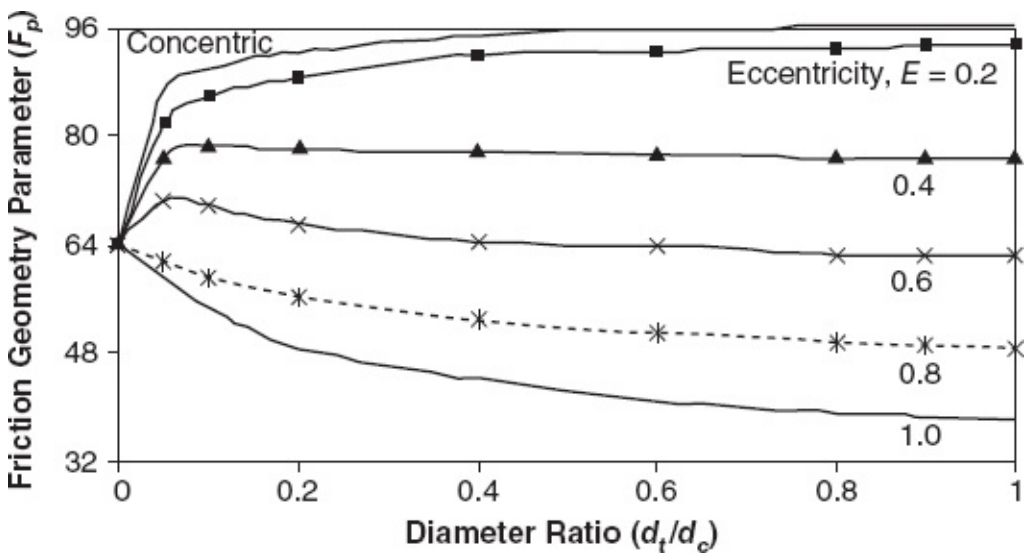

Fig. 1.4—Friction geometry parameter for concentric and eccentric annuli.

where F_p is the laminar-flow friction factor geometry parameter and F_{CA} is the ratio of friction factor for the annulus to that of a circular channel with the same d_c. Therefore, from Eq. 1.21, F_p for a concentric annulus is given by

$$F_P = \frac{(1-K)^2}{\left[\frac{1-K^4}{1-K^2} - \frac{1-K^2}{\ln(1/K)}\right]}. \quad (1.22)$$

Understanding mud flow behavior in horizontal and near-horizontal drilling requires

fluid flow through eccentric annuli. For such flows, eccentricity (E) is defined as

$$E = D / (d_c - d_t), \quad (1.23)$$

where D is the distance between the pipe centers. The values of F_p, as a function of K and E, are shown in **Fig. 1.4.** For an eccentric annulus, the friction factor equation is similar to Eq. 1.20:

$$f_{ECA} = \frac{4}{\mathrm{Re}} \frac{4(1-K)^2}{\xi \sinh^4 \eta_o}. \quad (1.24)$$

In Eq. 1.24, η_o incorporates the effect of eccentricity factor E, and ξ is a function of η_o. A complete treatment of flow through eccentric annuli is beyond the scope of this book; for further details, the reader is directed to Caetano et al. (1992a). Chapter 4 discusses two-phase flow in an annular geometry.

1.4 Flow in Horizontal Wells

The interest in horizontal wells stems from significant increases in productivity and ultimate recovery in certain cases, such as unconventional reservoirs. Initial efforts by Dikken (1990) and Novy (1995) to couple the wellbore with the reservoir using analytic approaches considered frictional effects only. In other words, fluid ingress along the well length leading to momentum and related effects was ignored in those formulations.

Estimating pressure drop in horizontal wells presents a number of difficulties. First, pipe-surface roughness is a difficult entity to discern because of perforations along the well length in a cased borehole. Because most completions occur openhole, complexity increases significantly to ascribe a friction factor for an ill-defined surface —that is, the formation. The second factor revolves around fluid influx or changes in momentum that occur along the well length.

Experimental studies of Asheim et al. (1992), Ouyang et al. (1998), and Yuan et al. (1999) in perforated horizontal pipes, allowing fluid ingress along the well length, led to the development of several friction factor correlations. Of these, the results of Ouyang et al. (1998) and Yuan et al. (1999) are noteworthy.

Ouyang et al. (1998) presented the following Moody friction factor correlations for laminar and turbulent flows, respectively.

$$f = \frac{64}{\mathrm{Re}}\left(1 + 0.04304\,\mathrm{Re}_w^{\,0.6142}\right) \quad (1.25)$$

and

$$f = f_o\left(1 - 0.0153\,\mathrm{Re}_w^{\,0.3978}\right), \quad (1.26)$$

where f_o is the no-wall-flow friction factor, which can be estimated from Eq. 1.13.

Note, Re_w represents the wall Reynolds number, which is based on the pipe inner diameter (ID) and equivalent inflow velocity per unit wellbore length.

A somewhat different approach led Yuan et al. (1999) to obtain the following expression for the total or apparent friction factor, f_T (Moody friction factor), for fluid ingress along the borehole.

$$f_T = a\,\mathrm{Re}^{-b} + C_n 2d\phi \frac{q_i}{q_a}, \qquad (1.27)$$

where

$$a = 10219.5\phi - 3.25\frac{q_i}{q_a} - 8.87\times10^{-4}\phi^2 + 5.37\times10^{-2}\phi - 0.075 \qquad (1.28)$$

and

$$b = \left(-1.24\times10^{5}\phi^{-3.075} + 42.4\right)\left(\frac{q_i}{q_a}\right)^2 + 1.577\times10^{3}\phi^{-2.63}\frac{q_i}{q_a} - 5\times10^{-4}\phi^2 + 2.31\times10^{-2}\phi + 0.085. \qquad (1.29)$$

For $(q_i/q_a) < 0.02$, $C_n = 2.3$, and for $(q_i/q_a) > 0.02$, C_n is given by

$$C_n = 4.25\left(\frac{q_i}{q_a}\right)^{-0.099}. \qquad (1.30)$$

Experience shows that pressure drop in horizontal wells becomes important in high-transmissivity reservoirs, where the pressure drop in the wellbore becomes comparable to that in the formation. When the wellbore pressure drop becomes important, in most cases, the frictional component becomes the dominant mechanism. Chapter 4 discusses two-phase flow in horizontal wells.

Summary

The objective of this introductory chapter is to acquaint the reader with the rudiments of single-phase flow, which forms the backbone for understanding the mechanics of two-phase flow. Here, we attempted to capture some elements of fluid flow through conduits of various complexities, such as annuli and horizontal wells, and when fluid flow is accompanied by heat flow. Subsequent chapters discuss these elements in detail.

Nomenclature

a = parameter defined by Eq. 1.28, dimensionless

A = cross-sectional area for fluid flow, ft^2

A_g, A_t = cross-sectional area available for gas or liquid to flow, ft_2

b = parameter defined by Eq. 1.29, dimensionless

c_p = heat capacity, Btu/(lbm-°F)

C_n = parameter defined by Eq. 1.27, dimensionless

d = pipe or well diameter, in.

d_c, d_t = casing or tubing diameter, in.

D = distance between pipe centers in Eq. 1.23, ft

E = eccentricity factor, dimensionless

f = friction factor, dimensionless

f_o = no-wall friction factor, dimensionless

f_{CA} = friction factor of concentric annulus, dimensionless

f_{ECA} = friction factor of eccentric annulus, dimensionless

f_T = apparent friction factor, dimensionless

F = force, lbf

F_p = friction geometry parameter, dimensionless

g = acceleration because of gravity, ft/sec^2

g_c = conversion factor, 32.17 lbm-ft/lbf-sec^2

g_G = geothermal gradient, °F/ft

H = fluid enthalpy, Btu/lbm

k = formation permeability, md

k_e = earth conductivity, Btu/(hr-ft-°F)

K = annulus/tubing diameter ratio, dimensionless

L_R = relaxation distance parameter, ft^{-1}

p = pressure, psi

(dp/dz) = pressure gradient, psi/ft

$(dp/dz)_A$ = accelerational (kinetic) pressure gradient, psi/ft

$(dp/dz)_F$ = frictional pressure gradient, psi/ft

$(dp/dz)_H$ = static pressure gradient, psi/ft

q_a = average flow rate over incremental length, ft^3/hr

q_i = influx rate from each perforation, ft^3/hr

r_{wb} = wellbore radius, ft

r_{to} = outside tubing radius, ft

Re = Reynolds number (= $dv\rho/\mu$), dimensionless

Re_g, Re_L = Reynolds number for gas (= $\rho_g v_g d/\mu_g$) or liquid phase (= $\rho_L v_L/\mu_L$), dimensionless

Re_m = Reynolds number for mixture (= $\rho_m v_m d/\mu_m$), dimensionless

Re_w = wall Reynolds number, dimensionless

t = production, injection, or circulation (mud) time, hours

t_D = dimensionless time, $\hat{\alpha} t / r_w^2$ (= $2.64 \times 10^{-4} kt/\phi\mu c_t r_w^2$)

T_{ei}, T_e = formation temperature at initial condition or at any radial distance, °F

T_f = fluid temperature, °F

T_D = dimensionless temperature = $(2\pi k_e)(T_{wb} - T_{ei})/Q$

T_{wb} = wellbore fluid temperature, °F

U = overall-heat-transfer coefficient, Btu/(hr-°F-ft)

v = fluid velocity, ft/hr

w = mass flow rate of fluid, lbm/hr

z = any vertical well depth, ft

Z = gas-law deviation factor, dimensionless

α = wellbore inclination with horizontal, degrees

Λ = parameter given by Eq. 1.14, dimensionless

μ = oil viscosity, cp

ε = pipe roughness factor, ft

ϕ = perforation density, 1/ft

ρ = density, lbm/ft^3

λ = parameter for Baker flow pattern map, dimensionless

η = parameter used in Eq. 1.24

Subscripts

c = casing

o = oil

t = tubing

to = tubing outside

wb = wellbore

Chapter 2

Multiphase Flow: Introduction

2.1 Introduction

Most installations for petroleum production and testing involve concurrent flow of gas and liquid. A schematic of the overall production system is shown in **Fig. 2.1.** The reservoir fluid, entering the wellbore, may contain all three phases (gas, oil, and water), in which case, multiphase flow starts at the perforations. However, gas often enters the wellbore in solution with the oil. Gas comes out as a separate phase only when fluid moves up enough for the pressure to drop below the bubblepoint pressure, thus leading to gas/liquid two-phase flow. In a favorable system, the entire fluid mixture may flow freely to the wellhead through a vertical or directional wellbore and then onto the separator through a horizontal or near-horizontal flowline.

Artificial lift is required in low-energy environments and/or when oil production is accompanied by water. When the artificial lift is provided by gas injection (gas lift) through the annulus, the production becomes two- or three-phase flow after the point of gas injection. Similarly, when a sucker rod or an electrical submersible pump is used for the lift, only liquid is produced through the tubing to sustain high pump efficiency, while gas is vented through the annulus. Even in this case, a substantial portion of the tubing may experience gas/liquid flow as well as three-phase flow. Some production facilities have to contend with the simultaneous flow of solids (sand), liquids (water and oil), and gases (injected and in solution).

Interest in multiphase flow is not restricted to the oil industry. Nuclear, geothermal, and chemical processing plants routinely encounter two-phase flow problems. The diverse interest explains the large number of publications in this area. At the same time, the plethora of publications indicates that the basics of multiphase flow are not completely understood. Often, correlations are published that have no general applicability to any situation other than the specific conditions under which they were developed.

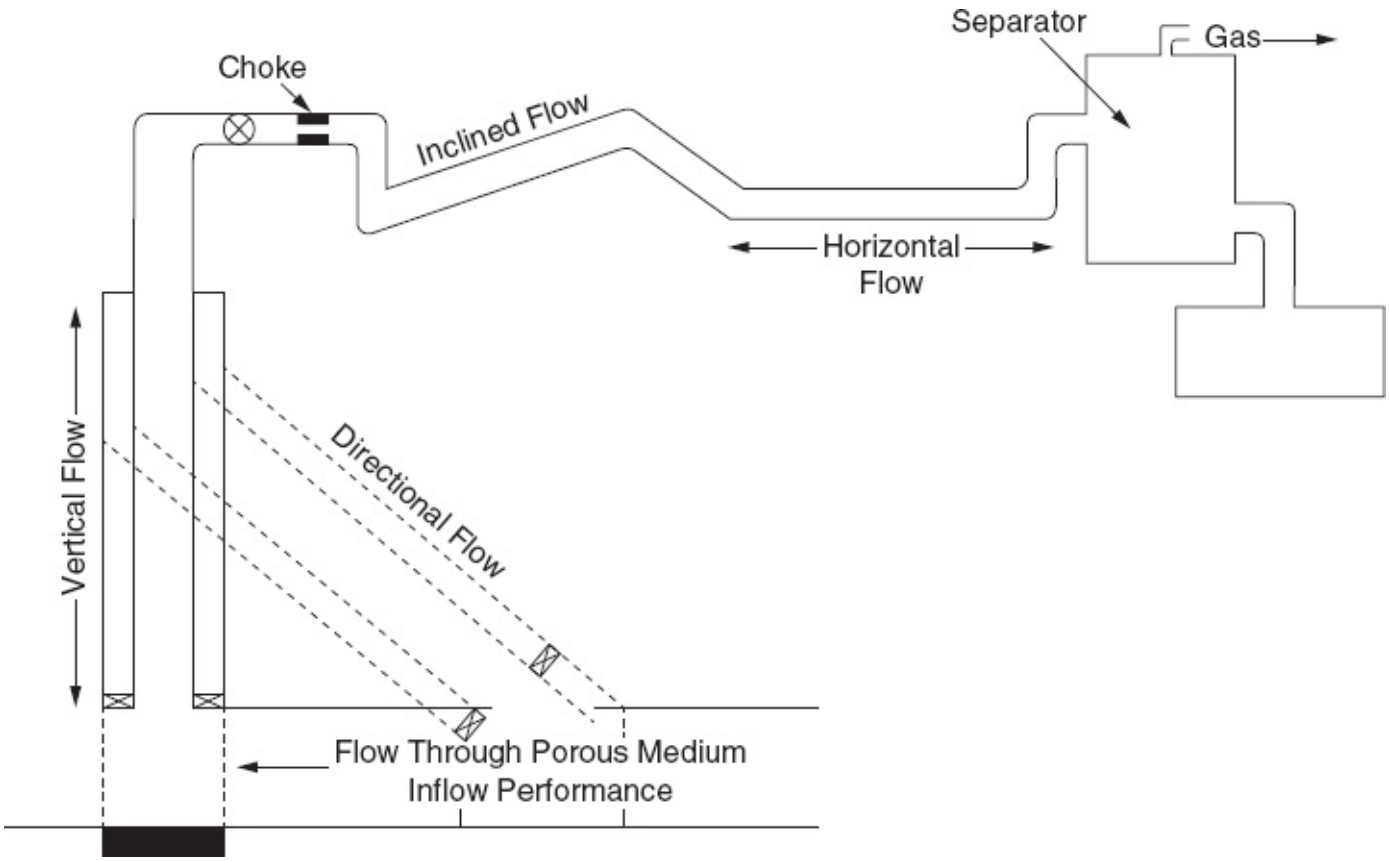

Fig. 2.1—Schematic of a production system (after Brown 1984).

One of the reasons multiphase flow is more complicated than single-phase flow is that two or more fluids compete for the available flow area. To model flow behavior, one needs to know how the flow cross section is occupied by each fluid phase. Therefore, understanding physics of multiphase flow demands grasping important concepts, such as flow patterns, in-situ velocity, and volume fractions. In these and subsequent discussions, we focus on systems containing only two phases, gas and liquid. Many of these concepts may be extended to systems experiencing three-phase flow.

2.2 Concepts and Definitions

2.2.1 Flow Pattern. During flow of two or more immiscible fluids, deformable interfaces present complications. Shape and distribution of these interfaces greatly influence flow characteristics. These interfaces tend to be spherical at low relative velocities, owing to surface tension effects. However, at higher relative velocities of the lighter fluid, the bubbles begin to elongate and coalesce, gradually changing into a different flow pattern or flow regime. Thus, bubbly flow, with small bubbles distribute uniformly across the flow channel, changes to slug flow, with large bubbles that fill the entire channel cross section with slugs of liquid between them. At extremely high gas rates, all the gas may flow through the core of the channel, while the liquid flows

through the annulus formed by the gas core and pipe wall. This flow pattern is called annular flow. Therefore, multiphase flow can be categorized into a number of flow patterns or regimes, the dynamics of which differ from each other. The existence of these flow patterns is influenced by many parameters, including fluid velocities, fluid properties, channel geometry, and channel orientation. These flow patterns, their transition from one to another, and their effect on pressure drop will be discussed later in more detail in Chapters 3 and 4.

2.2.2 Superficial and In-Situ Velocities. Superficial velocity of any phase is the volumetric flow rate of that phase, divided by the total cross-sectional area of the channel. Thus, the superficial liquid velocity v_{sL} is given in terms of the volumetric liquid flow rate q_L and the cross-sectional area A of the pipe by

$$v_{sL} = q_L / A \qquad (2.1)$$

Similarly,

$$v_{sg} = q_g / A \qquad (2.2)$$

The superficial velocity of the total mixture of gas and liquid v_m is as important as the individual phase velocities in modeling multiphase flow. We define v_m as the total volumetric flow rate divided by the total flow cross-sectional area. Therefore, for two-phase gas/liquid flow, we have

$$v_m = \left(q_g + q_L\right) / A = v_{sL} + v_{sg} \qquad (2.3)$$

Note that superficial velocity is a quantity averaged over the flow cross section. Even for single-phase flow, fluid velocity varies along the radial direction; elements of fluid flowing close to the wall have much lower velocity than those flowing near the channel center.

As mentioned before, neither phase occupies the entire pipe flow cross section. In other words, the actual velocity of the liquid phase—which can be observed by injecting a colored dye into the channel—will be considerably higher than its superficial velocity, given by Eq. 2.1. The actual velocity of any phase is called in-situ velocity and is defined as

$$v_L = q_L / A_L, v_g = q_g / A_g, \qquad (2.4)$$

where A_g and A_L are crosssectional areas available for gas and liquid phases to flow, respectively. Obviously, if these are the only two phases flowing, then $A_g + A_L = A$, or $A_L = A - A_g$. Unfortunately, while the pipe cross-sectional area is usually evident, the area (A_g or A_L) in which each phase flows is usually unknown.

2.2.3 Volume Fraction, Mass Fraction, and Mass Flux. The relative amount of

each phase in the wellbore may be expressed in many ways. We may wish to express the volumetric flow of the gas or liquid phase as a fraction of the total volumetric flow. This volume fraction, calculated from the known flow rates, is different from the in-situ volume fraction discussed in Section 2.2.4. The gas volume fraction, C_g, can be calculated from superficial phase velocities as

$$C_g = q_g / (q_g + q_L) = v_{sg} / v_m \quad (2.5)$$

Similarly, we can define flowing gas mass fraction, x, (called quality in steam/water flow) in terms of the mass flow rates, w_g and w_L, as

$$x = \frac{w_g}{w_g + w_l} = \frac{q_g \rho_g}{q_g \rho_g + q_L \rho_L} = \frac{v_{sg} \rho_g}{v_{sg} \rho_g + v_{sL} \rho_L} \quad (2.6)$$

Of course, volume and mass fraction for the liquid phase can be described similarly.

Mass flux, G, is the mass flow rate per unit area and is also known as mass velocity. Therefore, for the two-phase mixture, the mixture mass flux, G_m, is given by

$$G_m = \frac{w_L + w_g}{A} = \frac{\rho_L v_{sL} + \rho_g v_{sg}}{A} \quad (2.7)$$

Similarly, for the liquid and gas phases,

$$G_L = \frac{w_L}{A} = \frac{(1-x) w_m}{A} = (1-x) G_m, \; G_g = x G_m \quad (2.8)$$

2.2.4 Slip, Gas Volume Fraction, and Liquid Holdup. During two-phase flow, the actual or in-situ velocities of the phases are unknown, but the superficial velocities v_{sg} and v_{sL} are easily estimated from the volumetric rate. In addition, the in-situ velocity of the gas phase is different from that of the liquid phase, even when the volumetric flow rates of the phases are equal. Indeed, in upflow, the lighter gas phase moves faster than the liquid phase, especially in vertical and near-vertical systems. This difference in in-situ velocities is called slip and is defined as

$$v_s = v_g - v_L \quad (2.9)$$

We can relate in-situ velocity to superficial velocity by

$$v_g = q_g / A_g = \frac{q_g}{A} \frac{A}{A_g} \quad (2.10)$$

Gas in-situ volume fraction (also known as void fraction, f_g) is defined as the fraction of the total cross-sectional area through which gas flows.

$$f_g = A_g / A \quad (2.11)$$

By combining Eqs. 2.10 and 2.11, we obtain

$$v_g = \frac{v_{sg}}{f_g} \quad \text{(2.12)}$$

Because cross-sectional area is volume per unit length, f_g may be defined as the fraction of the channel volume occupied by the gas. Similarly, we can define a liquid (or the heavier phase) in-situ volume fraction, f_L, as

$$f_L = A_L/A = (A - A_g)/A,$$
$$v_L = v_{sL}/(A_L/A) = v_{sL}/f_L, \quad \text{(2.13)}$$

and

$$f_L = 1 - f_g \quad \text{(2.14)}$$

Fig. 2.2 depicts the in-situ volumetric fractions of the two phases in a pipe's cross-sectional area of flow. The figure attempts to illustrate the relative portions of the two phases on segregation if a sample is drawn from a given portion of the pipe. The liquid in-situ velocity is generally less than that of the gas phase, which means the liquid is held up. This is why in the petroleum industry f_L is known as the liquid holdup. However, gas is not held up during two-phase flow, and the term "gas holdup" is a misnomer.

Note that if either slip velocity or in-situ volume fraction is known, the other can be calculated from superficial velocities. Thus,

$$v_s = v_g - v_L = \frac{v_{sg}}{1 - f_L} - \frac{v_{sL}}{f_L} \quad \text{(2.15)}$$

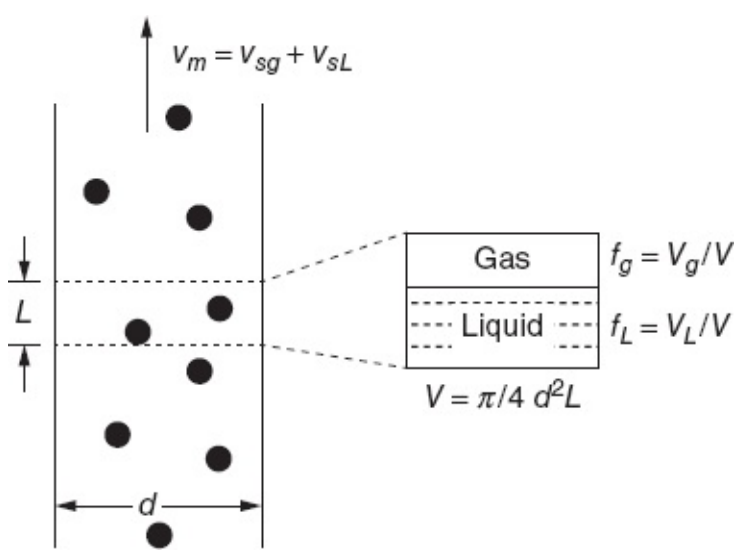

Fig. 2.2—Schematic of in-situ gas and liquid volume fractions in two-phase flow.

There are other ways of expressing the slip (or void fraction) phenomenon, such as

holdup ratio. These definitions are no longer widely used; therefore, they will not be discussed in this text.

2.3 Method of Analysis

The analysis of two-phase flow closely follows that of the well-established method for single-phase flow. Eq. 1.5, derived for single-phase flow, applies to two-phase systems with appropriate definition for average properties for the mixture.

$$dp/dz = (dp/dz)_F + (dp/dz)_H + (dp/dz)_A, \quad (1.5)$$

$$-(dp/dz)_F = \frac{f_m v_m^2 \rho_m}{2 g_c d}, \quad (2.16)$$

$$-(dp/dz)_H = \rho_m g \sin\alpha / g_c, \quad (2.17)$$

and

$$-(dp/dz)_A = \rho_m v_m (dv_m/dz)/g_c \quad (2.18)$$

Therefore,

$$-\frac{dp}{dz} = \frac{f_m v_m^2 \rho_m}{2 g_c d} + \frac{g \sin\alpha}{g_c}\rho_m + \frac{\rho_m v_m}{g_c}\frac{dv_m}{dz} \quad (2.19)$$

The symbol f is widely used for friction factor by engineers of all disciplines. We use the same symbol, subscripted with m (f_m), to represent the Moody friction factor for the mixture in Eqs. 2.16 and 2.19 and in subsequent parts of this book. When viewed in the appropriate context, there should be no confusion with the usage of f for friction and f_L and f_g for in-situ volume fraction of the phases.

By definition, mixture density is the mass of gas and liquid in a unit volume of the mixture. Of course, in a cubic foot of the mixture, there is f_L ft^3 of liquid and $(1 - f_L)$ ft^3 of gas. Therefore, in-situ density of the two-phase mixture, ρ_m, is determined based on the in-situ volume fraction of each phase and is given by

$$\rho_m = f_L \rho_L + (1 - f_L)\rho_g \quad (2.20)$$

Estimating density (or liquid holdup) and friction factor for the fluid mixture becomes complicated for two-phase flow because mixture properties need to be estimated. Two different approaches, generalized and flow pattern based, may be taken to express frictional, accelerational, and potential pressure gradient during multiphase flow. The simpler of the two—the generalized approach—attempts to develop methods for computing pressure drop and liquid holdup that will be applicable to all types of flow geometry and patterns. Within the generalized approach, two types of flow models can be used: homogeneous flow and separated flow.

The homogeneous flow model is the simplest. The model assumes that the multiphase mixture behaves much like a homogeneous single-phase fluid, with property values that are some type of average of the constituent phases. Once one decides the kind of averaging procedure to use (e.g., mass- or volume-weighted average), the computation problem becomes identical to that of a single-phase system. The assumption of homogeneity presupposes a condition of no slip; that is, all the phases move with the proportionate in-situ velocities. Consequently, in-situ liquid fraction or liquid holdup f_L is the same as the input fraction C_L.

In contrast, the separated flow model recognizes that the phases are segregated and that they move with unequal velocities. Therefore, the slip between the phases (or liquid holdup) needs to be known in addition to the frictional interaction of the phases with the wall and among themselves. In the simpler versions of the separated flow model, the frictional interactions among the phases are ignored. Consequently, even for the simplest model in this category, empirical correlations for computing liquid holdup and wall shear are needed, unlike the homogeneous model, in which only wall shear is required.

In the flow pattern approach, an attempt is made to develop a mathematical model consistent with the observed physical phenomena for each flow regime. While modeling, only the most dominant processes are recognized, and unimportant effects, which do not add significantly to the solution accuracy, are neglected. Because flow patterns are somewhat different for horizontal, vertical, and inclined flows, pipe orientations are usually treated separately. Various flow patterns arise because of different hydrodynamic conditions. The consensus is that this approach leads to the development of accurate working equations, which are much more suitable for extrapolation and interpolation than the generalized approach. However, this method requires determining all relevant flow patterns beforehand. In most oil industry applications, the flow pattern visualization is either impossible or uncertain; therefore, the pattern must be inferred from measured data, thereby introducing a possible source of error. A number of empirical or semitheoretical correlations or maps are available for flow pattern delineation. Much progress has been made recently to model flow pattern transition.

To summarize, the homogeneous model requiring the input of only one entity (the wall friction) is the simplest of all models and yields reasonable estimates of pressure drop under favorable conditions. However, the model is unrealistic for vertical and near-vertical flow of gas/liquid mixtures. The separated flow model, requiring estimates of friction and liquid holdup, is more sophisticated and usually more accurate than the homogeneous model. This model, however, is more complex and time consuming from a computational standpoint than the homogeneous model. The flow pattern approach is the most sophisticated of all models and is generally recognized as the most accurate method. The method requires estimating flow pattern, wall friction, and liquid holdup. This chapter discusses the homogeneous and the separated flow models. A detailed exposition of the flow pattern approach will be given in Chapters 3 and 4.

2.4 Homogeneous Flow Models

As the name implies, the homogeneous flow model assumes fluids in the system to be perfectly mixed, forming a homogeneous mixture with no slip between the phases. The no-slip assumption treats the two-phase mixture essentially as a single-phase fluid. In general, earlier attempts to compute pressure loss in wellbores (e.g., Poettmann and Carpenter 1952) used this simplifying assumption to estimate mixture density and friction factor.

Because the model assumes no slip between the phases, $v_s = 0$, and Eq. 2.15 yields

$$\frac{v_{sg}}{v_{sL}} = \frac{1 - f_L}{f_L} \qquad (2.21)$$

Adding unity to both sides, we obtain $v_m/v_{sL} = 1/f_L$. Therefore, the homogeneous model allows us to calculate liquid holdup from

$$f_L = \frac{q_L}{q_g + q_L} = \frac{v_{sL}}{v_m} = C_L \qquad (2.22)$$

Similarly,

$$f_g = \frac{q_g}{q_g + q_L} = \frac{v_{sg}}{v_m} = C_g \qquad (2.23)$$

The mixture density ρ_m can be computed from Eq. 2.20, and f_L and f_g, using Eqs. 2.22 and 2.23, respectively. Those equations, in turn, allow us to express the mixture density in terms of gas mass fraction and the density of the individual phases by

$$\frac{1}{\rho_m} = \frac{x}{\rho_g} + \frac{1 - x}{\rho_l} \qquad (2.24)$$

With known mixture density, an expression for mixture friction factor is all that is needed to compute pressure drop in two-phase flow. Poettmann and Carpenter (1952), in their classical work, presented a graph of friction factor vs. pseudo-Reynolds number, defined as $dv_m\rho_m$. They developed the friction factor chart based on field data, collected from 49 vertical wells. During formulation, they subtracted the static head, calculated with Eq. 2.17 from the measured total pressure drop and with the rest attributed to the frictional head. Using Eq. 2.16, they then calculated friction factor, which was in turn correlated to the pseudo-Reynolds number. The exclusion of fluid viscosity from friction factor correlation makes this method theoretically deficient, leading to unreliable pressure-drop estimation. For instance, data gathered by Baxendell and Thomas (1961) deviate significantly from the Poettmann-Carpenter correlation. Fancher and Brown (1963) modified the Poettmann-Carpenter correlation to account for the effect of gas/liquid ratio (GLR) on mixture friction factor, which was

evident from the extensive data they gathered from an 8,000-ft well. Their data indicate a decrease in f_m with an increase in the GLR. Hagedorn and Brown (1965) also noted a similar trend in f_m with GLR.

The effect of GLR and liquid viscosity on two-phase friction factor is explained by noting that the gas has much lower viscosity than the liquid. Thus, the actual mixture viscosity decreases with increasing GLR, especially when the liquid is a highly viscous crude. Consequently, the actual (not the pseudo) Reynolds number of the mixture increases with an increase in the GLR, accounting for the lower value of f_m. Therefore, a two-phase average mixture viscosity is needed to correlate the two-phase friction factor properly. A number of researchers have defined such mixture viscosity using various averaging approaches. Definitions proposed by Cicchitti et al. (1960), Dukler et al. (1964), and McAdams et al. (1942) are presented below.

$$\mu_m = x\mu_g + (1-x)\mu_L \qquad \text{(Cicchitti)}, \qquad (2.25)$$

$$\mu_m = \rho_m \left[\frac{x\mu_g}{\rho_g} + \frac{(1-x)\mu_L}{\rho_L} \right] \qquad \text{(Dukler)}, \qquad (2.26)$$

and

$$\frac{1}{\mu_m} = \frac{x}{\mu_g} + \frac{(1-x)}{\mu_L} \qquad \text{(McAdams)}. \qquad (2.27)$$

Any of the three methods presented in Eqs. 2.25 through 2.27 will work better than the Poettmann and Carpenter (1952) approach. We recommend the Cicchitti et al. (1960) correlation (Eq. 2.25) because of its simplicity.

Apart from the problem of defining a proper two-phase viscosity or a two-phase Reynolds number, the homogeneous model also suffers from the unrealistic assumption regarding slip and liquid holdup. As stated earlier, the no-slip assumption for vertical and near-vertical systems can lead to significant underestimation of the liquid holdup because the in-situ velocity of the liquid phase is much lower than that of the gas phase. This fact implies that the actual liquid holdup f_L is higher than the input volume fraction C_L of the liquid phase. Therefore, the actual static head is higher than that when calculated using the homogeneous model. The Poettmann-Carpenter (1952) and related correlations were developed using data from vertical wells. They computed static head using the homogeneous model, leading to its underestimation. Therefore, their friction factor correlation, obtained by subtracting these low static-head values from the total pressure drop, was too high. In other words, these correlations compensate one error by the other; consequently, caution should be taken when contemplating their application.

2.5 Separated Flow Models

Unlike the homogeneous models, the separated flow model makes a more realistic assumption in that the two phases are segregated and flow at different velocities. As with the homogeneous model, Eq. 2.20 gives the density of the mixture, but liquid holdup, f_L, cannot be assumed to be given by Eq. 2.22 and must be estimated. The estimation of the two important parameters (f_L and Moody friction factor, f_m) has led to the development of many correlations. Three useful correlations are discussed in this section.

2.5.1 Lockhart-Martinelli Correlation. In the Lockhart-Martinelli correlation (Lockhart and Martinelli 1949), the frictional component of the pressure gradient is expressed in terms of a two-phase friction multiplier ϕ_L^2 and the single-phase (generally liquid-phase) frictional pressure gradient, which will be obtained if that (liquid) phase is flowing alone in the channel. In other words,

$$-\left(\frac{dp}{dz}\right)_F = -\left[\left(\frac{dp}{dz}\right)_F\right]_L \phi_L^2 = \frac{f\rho_L v_{sL}^2}{2g_c d}\phi_L^2 \quad (2.28)$$

One may use a gas-phase friction multiplier ϕ_g^2 with a gas-phase frictional pressure gradient, instead of ϕ_L^2. In Eq. 2.28, the term $\rho_L v^2_{sL}$ can be replaced by $G^2_m(1 - x)^2/\rho_L$ or (G^2_L/ρ_L).

Calculating frictional pressure gradient using Eq. 2.28 requires estimating the two-phase friction multiplier, ϕ_L^2. Inaddition, liquid holdup estimates are needed to calculate the static head. Lockhart and Martinelli (1949) proposed a generalized method to compute the values of the two-phase friction multiplier and liquid holdup for isothermal two-component flow. They defined a parameter X^2 as the ratio of liquid-phase/gas-phase frictional pressure drop, given by

$$X^2 = \left[\left(\frac{dp}{dz}\right)_F\right]_L \Big/ \left[\left(\frac{dp}{dz}\right)_F\right]_g, \quad (2.29)$$

and correlated ϕ_L and ϕ_g as unique functions of X. When both phases are flowing in a turbulent manner, which is often the case in most wells, a simple expression for the parameter X may be derived by writing the single-phase frictional pressure gradients and using the Blasius equation, as follows:

$$X^2 = \left(\frac{1-x}{x}\right)^{1.8} \frac{\rho_g}{\rho_L}\left(\frac{\mu_L}{\mu_g}\right)^{0.2} \quad (2.30)$$

Lockhart and Martinelli expressed their findings as four distinct curves for ϕ_L vs. X, depending on the viscous (laminar) or turbulent nature of the gas and liquid flows, and a single curve for f_L vs. X. These curves are reproduced in **Fig. 2.3,** where the first subscript of ϕ represents the turbulent or viscous nature of the liquid phase, and the

second one denotes the same for the gas phase. For example, ϕ_{tt} represents turbulent liquid/turbulent gas flow—note that $Re_L = G\ d\ (1 - x) / \mu_L > 1{,}000$ indicates turbulent liquid flow—while ϕ_{vt} represents viscous (laminar, $Re_L < 1{,}000$) liquid/turbulent gas flow. These curves can be represented by the following expression:

$$\phi_L^2 = 1 + \frac{C}{X} + \frac{1}{X^2}, \qquad (2.31)$$

where the value of C varies: $C_{tt} = 20$, $C_{vt} = 12$, $C_{tv} = 10$, and $C_{vv} = 5$. Their volume fraction correlation may be represented at low pressures and low values of the LockhartMartinelli parameter X ($X < 10$), by

$$f_L = 1 - f_g = 1 - \left(1 + X^{0.8}\right)^2 \qquad (2.32)$$

Subsequently, Gregory (1974, 1975) showed that the liquid holdup, computed by the Lockhart-Martinelli correlation, agreed with his data quite well. The Lockhart-Martinelli correlation is specifically derived for horizontal flow without significant acceleration. Its application to other situations, where frictional gradient is comparatively small (e.g., vertical systems), can lead to errors. One aspect of the Lockhart-Martinelli correlation is that it skirts the flow pattern issue. This simplification has the advantage of avoiding the flow pattern discontinuities at the transition boundaries, although at a cost of model performance. Another well-known deficiency of the model is its unsatisfactory representation of the effects of system variables, in particular flow rate. The effect of flow rate on the curves of ϕ_L vs. X, originally not considered in the Lockhart-Martinelli correlation, was reported by some investigators (e.g., Gregory 1974, 1975; Hasan and Rhodes 1984).

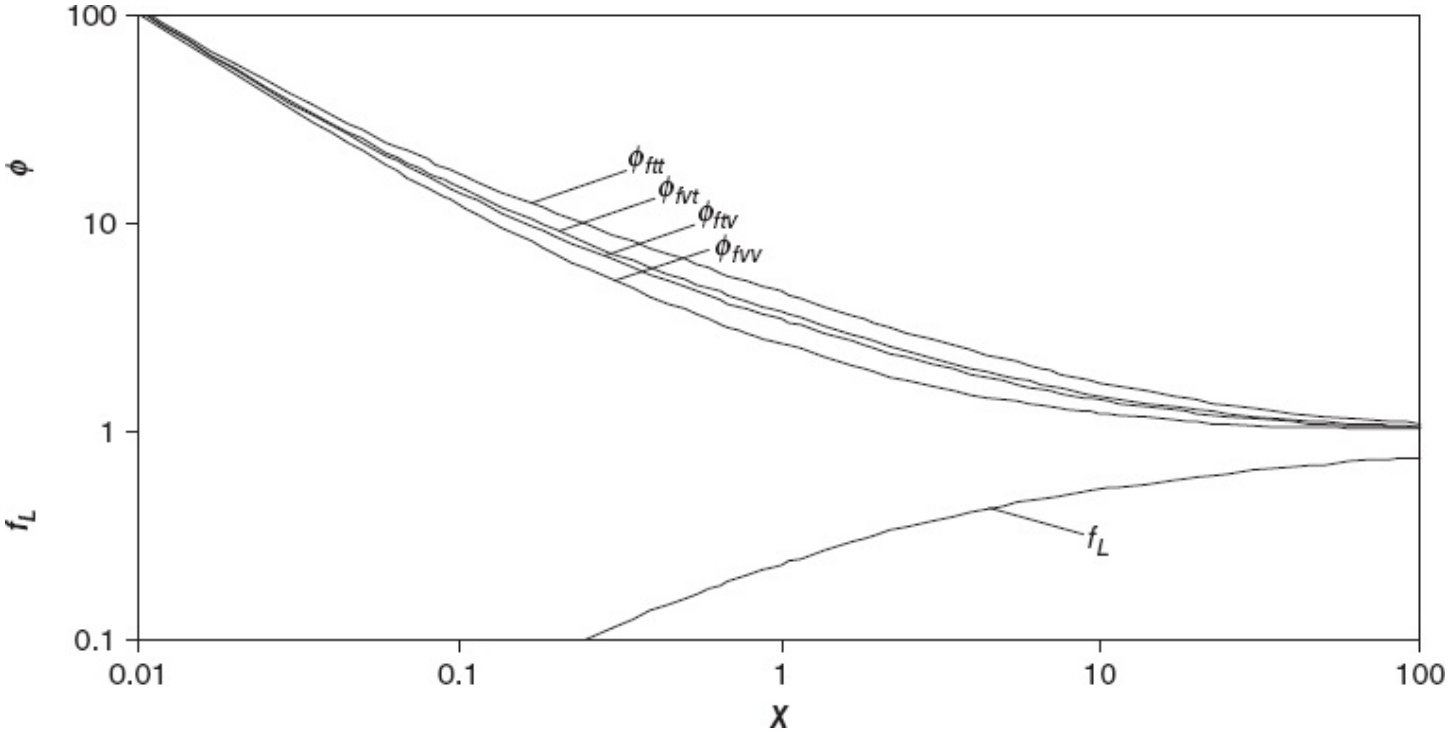

Fig. 2.3—Lockhart-Martinelli correlation for ϕ_L and f_L.

Despite some limitations of the original formulation, Chisholm (1967b) provided a theoretical basis for the Lockhart-Martinelli correlation. The extensive comparison, made by Idsinga et al. (1977) against a large data bank, shows that the Lockhart-Martinelli correlation is quite reliable in computing pressure drop in channels of various orientations if modification for mass effect is made. Even the unmodified correlation is preferable to the homogenous model in vertical and near-vertical systems.

2.5.2 Duns-Ros Correlation. In the early 1960s, Ros (1960) and Duns and Ros (1963) developed an empirical correlation from a large set of laboratory data. Their method does not strictly fall in the generalized correlation category because they defined four different flow regimes and assigned individual correlations for slip between the phases for each regime. However, the flow regimes they defined are quite different from those that are understood today.

They defined Region I as the flow regime in which the liquid is the continuous phase and therefore includes bubble, froth (presumably dispersed bubbly), plug, and some slug flow. Region II covers situations in which neither phase is continuous and hence includes the rest of the slug and froth flows, as well as heading or pulsating flow. When gas becomes the continuous phase, as in annular flow, it is termed Region III. Duns and Ros also included a transition region (probably corresponding to churn flow) between Region II and Region III.

The Duns and Ros flow regime map is based on the gas velocity number, $v_{gd} = v_{sg}(\rho_L/g\sigma)^{1/4}$; the liquid velocity number, $v_{Ld} = v_{gd}(v_{sL}/v_{sg})$; the liquid viscosity number, $N_L = (\mu_l)(1/\rho_l\sigma^3)^{0.25}$; and the pipe diameter number, $N_d = d(\rho_L g/\sigma)^{1/2}$. **Table 2.1** shows

the transition criteria for the various regions.

Note that the gas and liquid velocity numbers, v_{gd} and v_{Ld}, are phase superficial velocities made dimensionless by dividing with the bubble rise velocity, v_∞, because v_∞ is proportional to $(g\sigma/\rho_L)^{1/4}$.

Duns and Ros defined a slip velocity number, $N_s = S\ (\rho_L/g\sigma)^{1/4}$, to estimate liquid holdup in any region. Once N_s and the slip are determined, the liquid holdup can be calculated. The correlation for N_s, however, is different in each region. For example, for Region I,

$$N_s = F_1 + F_2 v_{Ld} + F_3' \left[\frac{N_s}{1+N_s} \right]^2, \qquad (2.33)$$

where

$$F_3' = F_3 - \frac{F_4}{N_d}, \qquad (2.33a)$$

The factors F_1, F_2, F_3, and F_4 are given as functions of the liquid viscosity number, $N_L = \mu_L(g/\rho_L s^3)^{1/4}$. The frictional pressure gradient is calculated in the following manner.

$$-\left(\frac{dp}{dz}\right)_F = \frac{2 f_m v_{sg}^2 \rho_g}{g_c d}\left(1 + \frac{v_{sL}}{v_{sg}}\right), \qquad (2.34)$$

The twophase friction factor f_m is estimated with the expression

$$f_m = f_1 f_2 / f_3, \qquad (2.35)$$

Region	Limit	Parameters
I	$V_{gd} < L_1 + L_2\ V_{Ld}$	L_1 and L_2 are functions of pipe diameter number, $N_d = d(\rho_L g/\sigma)^{1/2}$
II	$V_{gd} > L_1 + L_2\ V_{Ld}$ and $V_{gd} < L_S$	$L_S = 50 + 36\ v_{Ld}$
Transition	$L_M > v_{gd} > L_S$	$L_M = 75 + 84\ v_{Ld}^{3/4}$
III	$v_{gd} > L_M$	

Table 2.1—Transition boundaries of the Duns-Ros model.

where f_1 is the conventional single-phase friction factor determined based on the Reynolds number, calculated from the superficial liquid velocity and liquid properties. The friction-factor/Reynolds-number relationship is slightly modified in the transition range, $700 < \mathrm{Re}_{sL} < 3{,}000$. The factors f_2 and f_3 are intended to correct for the effect of holdup. The factor f_2 is correlated in terms of f_L, v_{sg}/v_{sL}, and the diameter number, N_d. The factor f_3 is a secondary correction factor for high-viscosity (μ_L/ρ_L > 50 cSt)

liquids and is given by

$$f_3 = 1 + f_1 \sqrt{\frac{v_{sg}}{50 v_{sL}}} \quad (2.36)$$

For Region II, Duns and Ros proposed the correlation for the slip velocity number as

$$N_s = (1 + F_5) \frac{v_{gd}^{0.982} + F_{6'}}{(1 + F_7 v_{Ld})^2}, \quad (2.37)$$

Where $F' = 0.029N_d + F_6$

The factors F_5, F_6, and F_7 are functions of the liquid viscosity number N_L. The frictional pressure drop in Region II mimics the approach of Region I, and Regions I and II neglect the accelerational pressure loss.

For the transition region, Duns and Ros (1963) suggested that the average fluid density and the frictional gradient be calculated by linear interpolation between Region II and Region III boundaries with respect to v_{gd}. Therefore,

$$\rho_m = \frac{L_M - v_{gd}}{L_M - L_S} (\rho_m)_{\mathrm{II}} + \frac{v_{gd} - L_S}{L_M - L_S} (\rho_m)_{\mathrm{III}}. \quad (2.38)$$

A similar expression can be written for the frictional pressure gradient.

For Region III, slip is assumed to be zero and the liquid holdup is estimated from $f_L = v_{sL}/v_m$. The frictional loss is calculated from

$$-\left(\frac{\mathrm{d}p}{\mathrm{d}z}\right)_F = \frac{f_m v_g^2 \rho_g}{2 g_c d}, \quad (2.39)$$

where the friction factor f_m is calculated from the total Reynolds number (= $dv_m\rho_L/\mu_L$) and a roughness factor, ε/d. Duns and Ros gave the correlation for the roughness factor as

$$\frac{\varepsilon}{d} = \frac{34\sigma}{\rho_g v_g^2 d} \; if \; N_w < 0.005$$
$$\frac{\varepsilon}{d} = 174 \frac{\sigma N_w^{0.302}}{\rho_g v_g^2 d} \; if \; N_w > 0.005 \quad (2.39a)$$

where

$$N_w = 4.52 \times 10^{-7} \left(\frac{v_g \mu_L}{\sigma}\right)^2 \left(\frac{\rho_g}{\rho_L}\right). \quad (2.40)$$

Duns and Ros limit the value of ε/d to be no smaller than 0.001 and no greater than 0.50. Friction factor is estimated from the ε/d value calculated from Eq. 2.39a and

using a standard friction factor chart for single-phase flow, as shown in Chapter 1. When the calculated ε/d is outside the limits, the limiting value is used.

2.5.3 Hagedorn-Brown Method. Hagedorn and Brown (1965) and Brown et al. (1982) recognized that for vertical and near-vertical systems, the static-head loss accounts for most of the total pressure drop and that any reasonable estimate of the frictional component would suffice as long as the liquid holdup is estimated accurately. They assumed that the friction-factor/Reynolds-number relationship for two-phase flow is the same as for the single-phase flow and arbitrarily defined the two-phase viscosity as

$$\mu_m = \left(\mu_L^{f_L}\right)\left(\mu_g^{f_g}\right), \qquad (2.41)$$

where f_L and f_g are liquid holdup and gas volume fraction, respectively.

Hagedorn and Brown (1965) developed their correlation for effective liquid holdup with data obtained from a 1,500-ft vertical experimental well that used air as the gas phase and four different liquids. They subtracted the frictional component, calculated it with Eq. 2.16 in combination with Eq. 2.40, and attributed the rest to the static head. The effective liquid holdup f_L so calculated was then related to the dimensionless numbers proposed by Duns and Ros (1963) (v_{Ld}, v_{gd}, N_D, and N_L) and pressure ratio, p/p_a.

Hagedorn and Brown (1965) crossplotted various dimensionless parameters as shown in **Figs. 2.4 through 2.6** for ease of use. These curves can be represented as equations that are used in the example problem that follows.

Over the years, modifications have been proposed to the original Hagedorn-Brown correlation to overcome some of its deficiencies. The most serious of these problems is that the correlation sometimes estimates lower liquid holdup (f_L) than the no-slip holdup value (C_L). This outcome suggests that liquid slips past the gas phase—a physical impossibility during two-phase upflow. In those situations, when the computed f_L is greater than C_L, the procedure should be set to $f_L = C_L = v_{sL}/v_m$. Another recommendation is to use the Orkiszewski (1967) correlation for bubbly flow in that region. A third proposal is to use the Duns-Ros method for computing pressure gradient, but only if Regime III is prevalent, to account for accelerational effects.

Economides et al. (2012) presented very useful expressions to represent the curves presented in Figs. 2.4 through 2.6, as follows:

$$C_{NL} = \frac{0.0019 + 0.0322N_L - 0.6642N_L^2 + 4.9951N_L^3}{1 - 10.014N_L + 33.8696N_L^2 + 277.281N_L^3} \qquad (2.42)$$

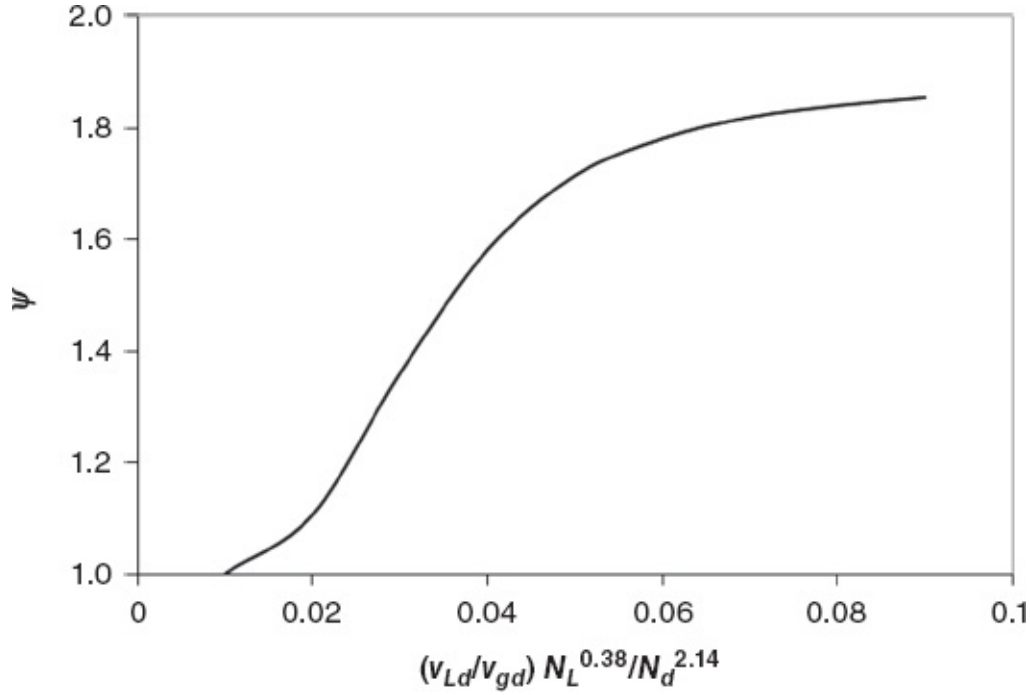

Fig. 2.4—Hagedorn-Brown correlation for ψ.

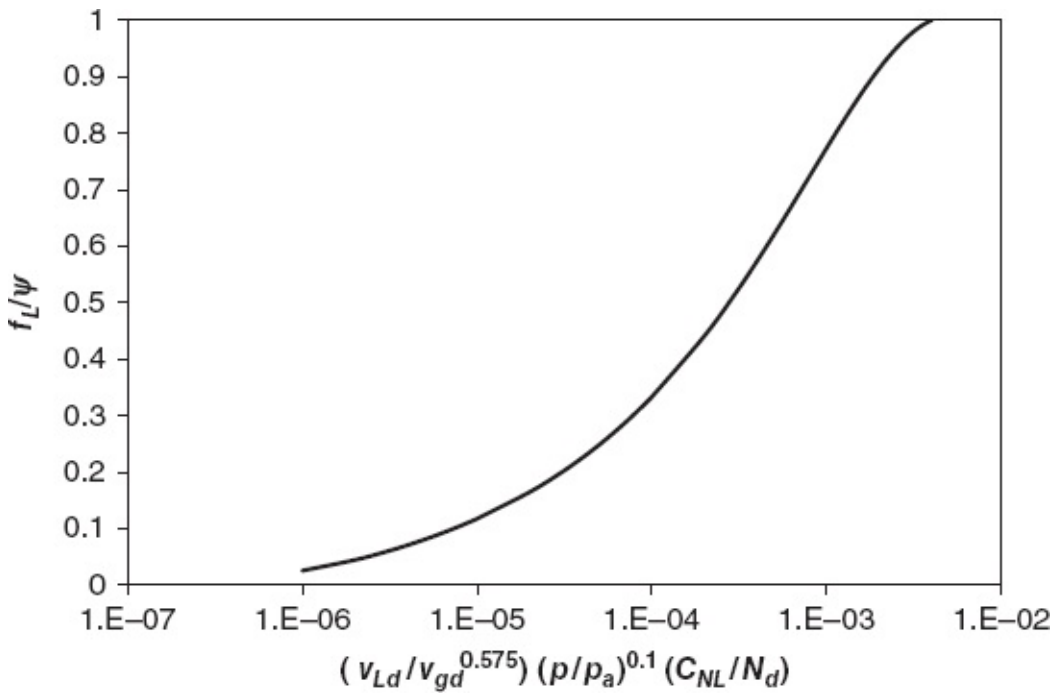

Fig. 2.5—Hagedorn-Brown correlation for f_L/ψ.

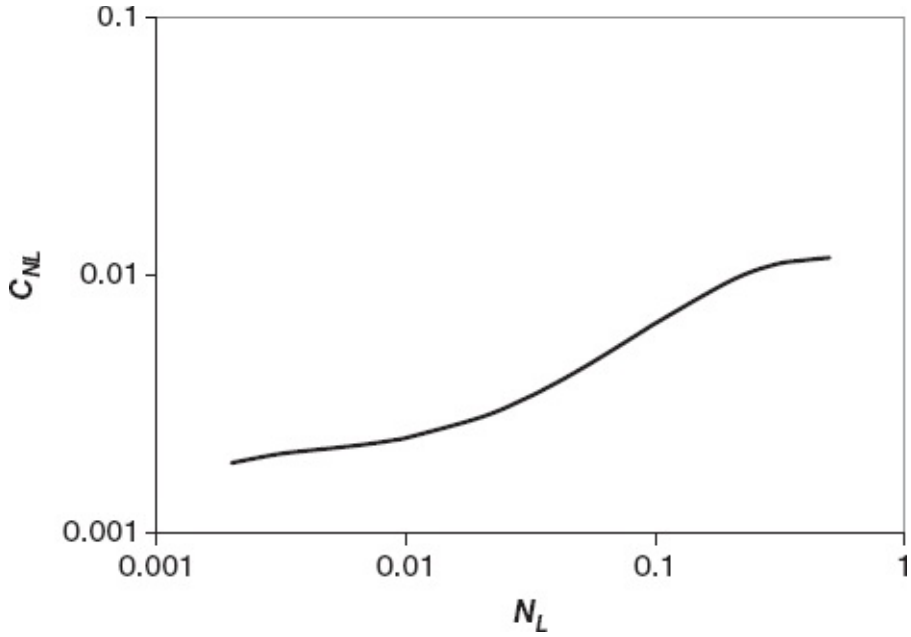

Fig. 2.6—Hagedorn-Brown correlation for C_{NL}.

$$\frac{f_L}{\psi} = \left(\frac{0.0047 + 1123.32H + 729489.64H^2}{1 + 1097.1566H + 722153.95H^2} \right)^{1/2} \quad (2.43)$$

$$\psi = \frac{1.0886 - 69.9473B + 2334.3497B^2 - 12896.683B^3}{1 - 53.4401B + 1517.9369B^2 - 8419.8115B^3} \quad (2.44)$$

$$B = \frac{N_{vg} N_L^{0.38}}{N_D^{2.14}} \quad (2.45)$$

Example 2.1. Estimating Pressure Gradient. A 5,151-ft vertical well produces 23 °API dry oil at 1,140 STB/D through a 2.99-in.-ID tubing. The gas/oil ratio (GOR) is 450 scf/STB, and the gas gravity is 0.8. The following property values and computed fluid parameters are available at the wellhead:

v_{sL} = 1.601 ft/sec
μ_L = 13.09 cp
p = 505 psig
v_{sg} = 2.84 ft/sec
μ_g = 0.019 cp
d = 2.99 in. = 0.25 ft
ρ_L = 55.042 lbm/ft^3
σ = 31.6 dynes/cm = 0.06966 lbm/sec^2
ρ_g = 2.17 lbm/ft^3

Calculate the pressure gradient at this point.

The Hagedorn-Brown Correlation.

$v_{Ld} = (v_{sl})(\rho_l/g\sigma)^{0.25} = 1.60(55.04/32.2/0.0697)^{0.25} = 3.564.$

$v_{gd} = (v_{sg})(\rho_l/g\sigma)^{0.25} = 2.84(54.04/32.2/0.0697)^{0.25} = 6.335.$

$N_d = (d)(g\rho_l/\sigma_l)^{0.5} = (0.25)(55.04 \times 32.2/0.044)^{0.5} = 39.78.$

$N_L = (m_l)(1/\rho_l\sigma^3)^{0.25} = [13.09 \times 0.000672 \text{ lbm/(ft-sec)}][1/(55.04 \times 0.06966^3)]^{0.25} = 0.0567.$

$B = (v_{gd})(N_L)^{0.38}/(N_d)^{2.14} = (6.335)(0.0567)^{0.38}/(39.78)^{2.14} = 8.03 \times 10^{-4}.$

C_{NL} from Eq. 2.42 = 0.0042.

$$H = \frac{v_{ld}\, p^{0.1}(CN_L)}{v_{gd}^{0.575}\, p_a^{0.1} N_d} = 1.87 \times 10^{-4}$$

For $B < 0.01$, as Fig. 2.6 shows, $\psi = 1.0$:

$$\psi = \frac{1.0886 - 69.9473B + 2334.3497B^2 - 12896.683B^3}{1 - 53.4401B + 1517.9369B^2 - 8419.8115B^3} = 1.0.$$

$$f_L = \psi\left(\frac{0.0047 + 1123.32H + 729489.64H^2}{1 + 1097.1566H + 722153.95H^2}\right)^{1/2} = 0.442.$$

$\rho_m = \rho_L f_L + (1 - f_L)\rho_g = 55.04\ (0.0.442) + (1 - 0.442)^{2.25} = 25.54 \text{ lbm/ft}^3.$

$\mu_m = \left(\mu_L^{f_L}\right)\left(\mu_g^{f_g}\right) = (13.09)^{0.446}\ (0.019)^{(1-0.446)} = 0.37$ cp.

$q_g = v_{sg}A = (2.75)[(\pi/4)\ (0.25)^2] = 4.932 \text{ ft}^3\text{/sec}.$

$q_l = v_{sl}A = (1.71)[(\pi/4)\ (0.25)^2] = 0.078 \text{ ft}^3\text{/sec}.$

$v_m = v_{sL} + v_{sg} = 4.445$ ft/sec.

$\text{Re} = (\rho_m)(v_m)(d)/(\mu_m) = (25.54)(4.445)(0.25)/(0.37 \times 0.000672) = 113{,}927.$

$f = 0.32(\text{Re})^{-0.25} = 0.32(92{,}426)^{-0.25} = 0.0174.$

– $(dp/dz)_F = (f)(\rho_{nm})(v_m)^2/[2(g_c)(d)] = (0.0174)(25.54)(4.445)^2/[2(32.2)(0.25)]$

$= 0.378$ psf/ft.

– $(dp/dz)_H = \rho_m\ g/g_c = 25.54$ psf/ft.

– dp/dz = 0.378 + 25.54 = 26.92 psf/ft = 0.181 psi/ft total pressure gradient at wellhead.

The Lockhart-Martinelli Correlation.

$$-\left(\frac{dp}{dz}\right)_F = -\left[\left(\frac{dp}{dz}\right)_F\right]_L \phi_L^2 = \frac{f\rho_L v_{sL}^2}{2g_c d}\phi_L^2.$$

$G_m = v_{sg}\ \rho g + vs_L\ \rho_l = 94.28 \text{ lbm/ft}^2\text{-sec}.$

$x = (v_{sg}\ \rho g)/\ G_m = 0.066.$

$X^2 = [(1 - x)/x]^{1.8}\ (\rho_g/\rho_l)(\mu_L/\mu_g)^{0.2}$

$= [(1–0.066)/0.066]^{18}\ (2.17/54.04)\ (13.04\ /0.019)^{0.2} = 17.41.$

$f_g = (1+X^{0.8})^{-0.378} = 0.58.$

$\rho_m = \rho_g f_g + f_L\rho_l = 24.13 \text{ lbm/ft}^3$ $\qquad C_{tt} = 20.$

$\phi_L{}^2 = 1 + C/X + 1/X^2 = 5.85.$

$\text{Re}_L = (dv_{sL}\rho_L/\mu_L) = [(0.25 \times 1.6 \times 55.04)/\ (13.09 \times 0.000672)] = 2{,}495.5.$

$f = 0.32(\mathrm{Re}_L)^{-0.25} = 0.0453$.

– $(dp/dz)_F = \{[f\rho_L\ (G_m)^2(1-x)^2\phi_L{}^2\ /[2(\rho_L)(g_c)(d)\} = 2.33$ psf/ft = 0.0162 psi/ft.

Or, $-(dp/dz)_F = [f\rho_L\ v_{sL}{}^2\phi L^2]/[2g_c d] = 0.0162$ psi/ft.

– $(dp/dz)H = (\rho_g f_g + \rho_L f_L)\ g/g_c = 24.14$ psf/ft = 0.168 psi/ft.

– $dp/dz = 0.0162 + 0.168 = 0.184$ psi/ft total pressure gradient at wellhead.

The Homogenous Model.

$\mu_m = \mu_L\ (1-x) + \rho_g\ x = 13.04\ (1–0.066) + 0.0139\ (0.066) = 12.2$ cp.

$f_g = v_{sg}/v_m = 0.64$.

$\rho m = 21.2$.

Or, $1/\rho_m = [(1-x)/\rho_L] + [x/\rho_g] = (0.934/55.04) + (0.066/2.25)$

$= 0.0472;\ \rho_m = 21.2$ lbm/ft^3.

$\mathrm{Re} = G_m d/\mu m = 94.28\ (0.25)/(12.2 \times 0.000672) = 2{,}858$.

$f_m = 0.32(\mathrm{Re})^{-0.25} = 0.0438$.

– $(dp/dz)_F = f_m\ (v_m)^2\rho_m\ /[2(g_c)(d)] = 1.144$ psf/ft = 0.0079 psi/ft.

– $(dp/dz)_H = \rho_m\ g/g_c = 21.22$ psf/ft = 0.1474 psi/ft.

– $dp/dz = 0.\ 1553$ psi/ft total pressure gradient at wellhead.

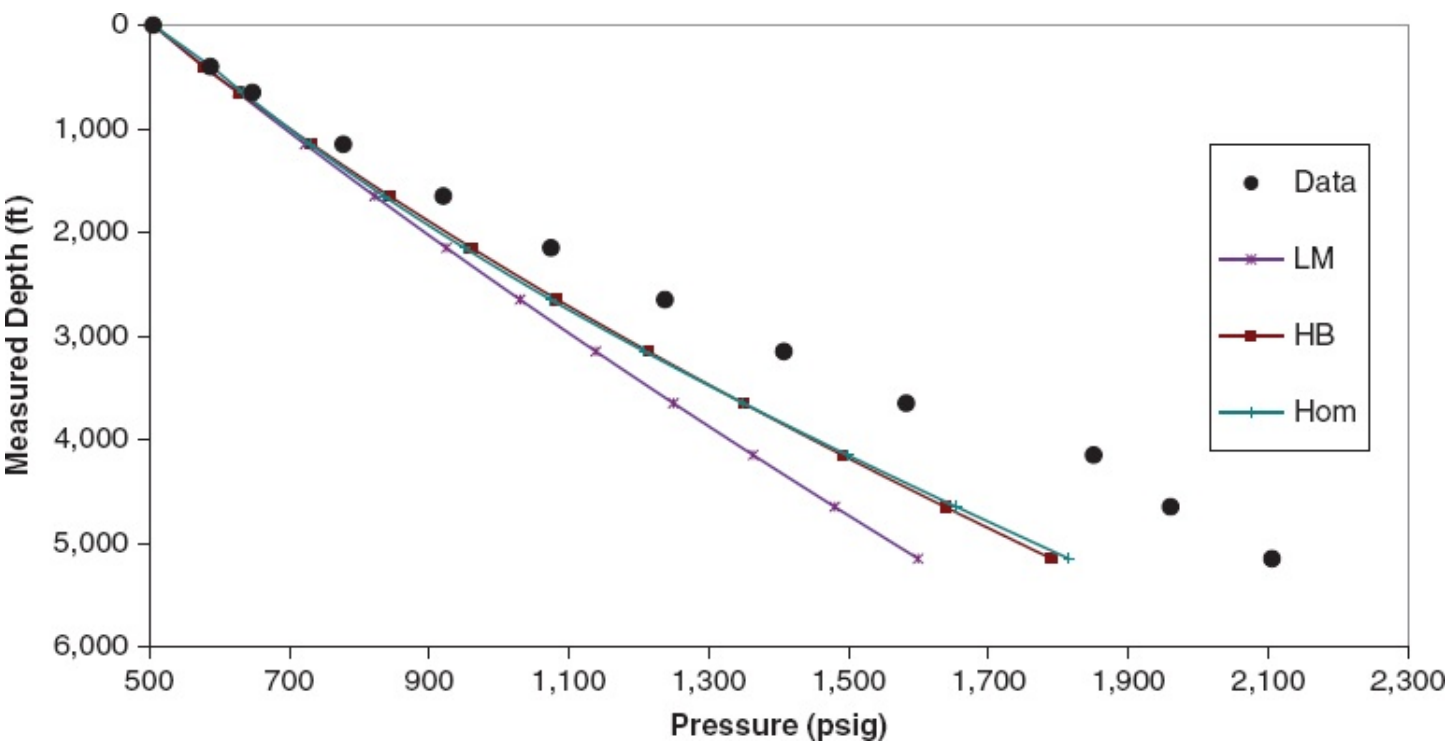

Fig. 2.7—Performance comparison of the Lockhart-Martinelli (LM), Hagedorn-Brown (HB), and homogeneous (Hom) correlations.

Although the estimated pressure gradient at the wellhead is approximately the same for all three methods shown in Example 2.1, **Fig. 2.7** shows that the Lockhart-Martinelli method becomes unreliable with increasing depth. Our experience with data from other sources reinforces that the Lockhart-Martinelli method for vertical and near-vertical oil wells is unreliable. We introduced that method because we make

appropriate reference to it in Chapter 4. By contrast, the Hagedorn-Brown and homogeneous models provide a reasonable agreement with field data, yielding a bottomhole pressure of 1,790 psig and 1,815 psig, respectively, compared with the measured bottomhole pressure of 2,105 psig. As Chapter 3 discusses, the success of the latter two methods stems largely from the high flow rates involved in this problem. For a low-rate well, performance of the homogeneous model tends to be poorer than Example 2.1 indicates.

Summary

This chapter provides ingredients for understanding the fundamentals of two-phase flow. For instance, concepts of superficial and in-situ velocities, in-situ and input volume fractions, and slip between phases were explored. To model flow behavior, we discussed three approaches: homogeneous, separated flow, and flow pattern based. Here, we addressed the first two types. Chapters 3 and 4 will discuss the modern flow pattern approach.

Among the correlations presented, we strongly recommend the Hagedorn-Brown method with the modifications mentioned. Developed for the oil industry, the modified Hagedorn-Brown method is more appropriate than the Lockhart-Martinelli method. The method is also less complicated than the Duns-Ros correlation. Perhaps more important, a comprehensive study by Ansari et al. (1994) showed that when the above modifications are incorporated, the Hagedorn-Brown correlation mimics data from several sources very well. Indeed, the performance of the modified correlation appears to be better than most available correlations.

Nomenclature

A = cross-sectional area for fluid flow, ft^2

A_g, A_L = cross-sectional area available for gas or liquid flow, ft^2

C = constant in Lockhart-Martinelli parameter, dimensionless

C_g = input volume fraction of gas phase, dimensionless

C_L = input volume fraction of liquid phase, dimensionless

C_{NL} = parameter in Hagedorn-Brown method for dimensionless viscosity number, N_L, dimensionless

C_{tt} = constant in Lockhart-Martinelli parameter, C, for turbulent gas/turbulent liquid flow, dimensionless

C_{tv} = constant in Lockhart-Martinelli parameter, C, for turbulent gas/viscous (laminar) liquid flow, dimensionless

C_{vt} = constant in Lockhart-Martinelli parameter, C, for viscous gas/turbulent liquid flow, dimensionless

C_{vv} = constant in Lockhart-Martinelli parameter, C, for viscous gas/viscous liquid flow, dimensionless

d = pipe or well diameter, in.

F = force, lbf

f = friction factor, dimensionless

f_g = gas in-situ volume fraction (void fraction), dimensionless

f_L = liquid holdup/in-situ volume fraction, dimensionless

f_m = mixture friction factor, dimensionless

g = acceleration because of gravity, ft/sec^2

G = mass flux, mass flow rate per unit area, ρv, lbm/(hr-ft^2)

g_c = conversion factor, 32.17 (lbm-ft)/(lbf/sec^2)

G_m = mixture mass flux, $\rho_m v_m$, lbm/(hr-ft^2)

L = total vertical well depth, ft

L_M = parameter in Duns-Ros regime transition criteria, dimensionless

L_S = parameter in Duns-Ros regime transition criteria, dimensionless

L_s = total length of cell in slug flow, ft

N_d = diameter number, dimensionless

N_f = inverse viscosity number [= $gd^3\rho_L(\rho_L - \rho_g)]^2/\mu_L$], dimensionless

N_L = liquid viscosity number [= $\mu_L(g/\rho_L\sigma^3)$], dimensionless

N_s = Duns-Ros slip velocity [= $S(\rho_L/g\sigma)^{1/4}$], dimensionless

N_w = parameter in Duns-Ros correlation for calculating roughness factor, dimensionless

p = pressure, psi

dp/dz = pressure gradient, psi/ft

(dp/dz)$_A$ = accelerational (kinetic) pressure gradient, psi/ft

(dp/dz)$_F$ = frictional pressure gradient, psi/ft

(dp/dz)$_H$ = static pressure gradient, psi/ft

q_g, q_L = gas or liquid flow rate at standard conditions, MMscf/D or STB/D

Re$_g$, Re$_L$ = Reynolds number for the gas (= $\rho_g v_g d/\mu_g$) or liquid phase (= $\rho_L v_L d/\mu_L$), dimensionless

S = slip between phases [= v_g-v_L], ft/sec

V = volume, ft^3

V_g = volume of gas, ft^3

V_L = volume of liquid, ft^3

v = fluid velocity, ft/sec

v_∞, $v_{\infty T}$ = terminal rise velocity of bubbles in bubbly flow/Taylor bubble in slug flow, ft/sec

v_g, v_L = gas or liquid in-situ velocity, ft/sec

v_{gd}, v_{Ld} = dimensionless phase velocities

v_m = mixture velocity, ft/sec

v_s = slip velocity, ft/sec

v_{sg}, v_{sL} = superficial gas or liquid in-situ velocity, ft/sec

w= mass flow rate of fluid, lbm/sec

w_m = mixture mass flow rate, lbm/sec

x = gas mass fraction in tubing fluid mixture, dimensionless

X = Lockhart-Martinelli parameter, dimensionless

z = any vertical well depth, ft

ε = pipe roughness factor, ft

μ = oil viscosity, cp

μ_m = mixture viscosity, cp

ρ = density, lbm/ft^3

ρ_g, ρ_L = gas- or liquid-phase density, lbm/ft^3

ρ_m = density of gas/liquid mixture, lbm/ft^3

ρ_L = liquid density, lbm/ft^3

ρ_n = mixture density assuming no slip between phases, lbm/ft^3

ϕ_g, ϕ_L = friction multiplier in the Lockhart-Martinelli correlation, based on gas or liquid flowing alone in the channel, dimensionless

ϕ_{tt} = friction multiplier in the Lockhart-Martinelli correlation for turbulent gas/turbulent liquid flow, dimensionless

ϕ_{vt} = friction multiplier in the Lockhart-Martinelli correlation for viscous gas/turbulent liquid flow, dimensionless

σ = surface tension, lbm/sec^2

σ_L = surface tension of the liquid phase, lbm/sec^2

Ψ = Hagedorn-Brown flow parameter, dimensionless

Chapter 3

Multiphase Flow: Mechanistic Models for Vertical Wells

3.1 Introduction

The methods described in Chapter 2 for calculating liquid holdup and pressure drop during two-phase flow are largely empirical. Empirical approaches can potentially give inaccurate results when applied to situations different from the database from which they are derived. A more satisfactory approach models flow mechanics and develops governing equations, which are then tested against laboratory and field data.

Gas flowing simultaneously with a liquid can take many configurations or patterns. Sometimes, when liquid flows as the continuous medium, the gas flows as discrete bubbles of various shapes and sizes. In other cases, the gas may flow through the channel core as the continuous medium, carrying liquid droplets along with it. Dynamics of each flow pattern are unique and generally require individual treatment.

This chapter examines the mechanistic models used to estimate in-situ phase volume fractions and pressure drop. Major flow pattern characteristics are then discussed, followed by the procedures that determine flow regimes. Hydrodynamic models for each flow regime allow estimation of liquid holdup and pressure drop. Flow pattern during multiphase flow is strongly influenced by channel orientation. Chapter 3 presents the vertical cocurrent upflow of gas and liquid. A discussion of flow in deviated wellbores follows in Chapter 4. Effects of other flow variables and geometry, such as flow through annuli and three-phase flow, will also be discussed in Chapter 4. Chapter 5 collates the findings from Chapters 3 and 4 and presents a work flow for pressure-traverse calculation using a unified approach.

3.1.1 Flow Patterns in Vertical Cocurrent Systems. Various techniques exist to study flow patterns in heated and isothermal channels. Distinguishing flow patterns by direct observation is feasible at low velocities in transparent pipes. When flow patterns become indistinct at higher velocities, still and video cameras become necessary. However, reflection and refraction at multiple interfaces often make the interpretation of visual observations and photographs open to considerable uncertainty. This observation is particularly true at high flow rates. Other ingenious observation techniques have emerged, such as looking down the axis of a tube containing a two-phase mixture, to examine flow patterns in boiling systems at high pressures. Various probes, such as electrical, hotwire, pressure, and optical allow study of flow structure. Signals from these probes provide indirect information, which leads to the identification of flow patterns.

Because the name given to a flow pattern is somewhat subjective, a multitude of terms have evolved to describe the various possible phase distributions. In this text, we consider the four major flow patterns—bubbly, slug, churn, and annular. These flow patterns are clearly distinguishable and are generally recognized by all researchers. However, subdivisions do exist, but transitions between these subpatterns are seldom well-defined. The flow patterns encountered in vertical upward cocurrent flow are shown schematically in **Fig. 3.1.**

Bubbly Flow. In bubbly flow, the gas or vapor phase is distributed as discrete bubbles in a continuous liquid medium. At one extreme, the bubbles may be small and spherical, and on the other, they may be large with a spherical cap and a flat tail. In the latter state, although the size of bubbles does not approach the diameter of the pipe, potential for confusion with slug flow exists. In vertical bubbly flow, bubbles are uniformly distributed throughout the liquid at low gas velocities. Boiling water in a beaker or a kettle provides an example of everyday occurrence of bubbly flow. In general, bubbly flow occurs at low gas flow rates.

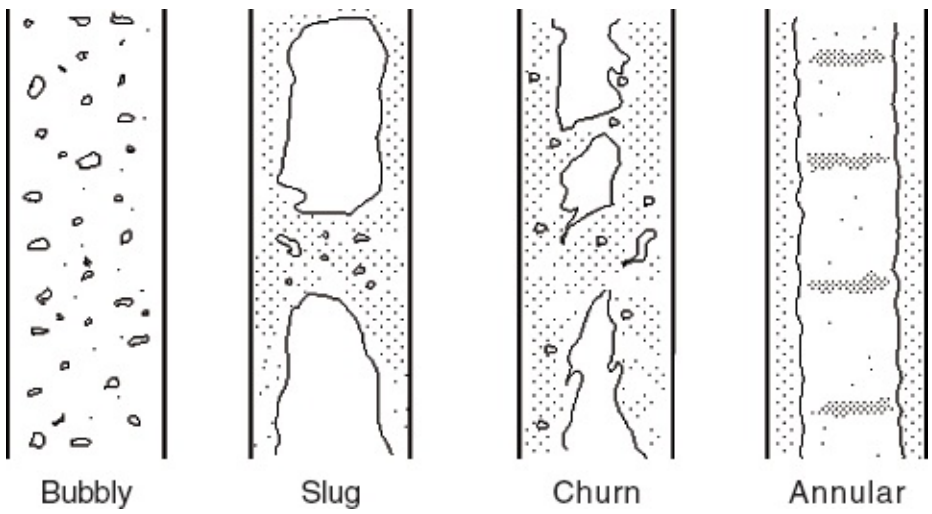

Fig. 3.1—Flow patterns in vertical upward flow (after Taitel et al. 1980).

Slug Flow. In slug flow, the dominant gas or vapor bubbles have approximately the same diameter as the channel and are known as Taylor bubbles. The nose of the Taylor bubble has a characteristic hemispherical shape, and the gas in the bubble is separated from the pipe wall by a slowly descending thin film of liquid. The primary liquid flow is contained in liquid slugs that separate successive gas bubbles. These slugs often contain smaller entrained gas bubbles, carried in the wake of a large Taylor bubble. The length of the main gas (Taylor) bubble, as well as the liquid slug, can vary considerably. Some designate this pattern as plug or piston flow (low flow rates with well-defined gas/liquid boundaries) and as slug flow (higher flow rates with less clear boundaries). Slug flow can sometimes be observed while pouring liquid from a large bottle, for example. Slug flow usually occurs when gas flow rate is higher than that in bubbly flow, causing small bubbles to agglomerate and form large Taylor bubbles.

***Churn Flow*.** Churn flow forms by the breakdown of Taylor bubbles in slug flow, generally requiring higher gas flow rate than that needed for slug flow. The gas or vapor flows in a chaotic manner through the liquid, which is mainly displaced to the channel wall. The flow has an oscillatory or time-varying character; hence, the descriptive name—churn flow. This region is also sometimes referred to as semiannular flow, annular-to-slug transition flow, or froth flow.

***Annular Flow*.** At very high flow rates, the gas phase may flow through the core of the channel, forming a continuous phase; this pattern is called annular flow. The liquid phase is dragged along the pipe wall and appears to flow through the annulus formed by the channel wall and the vapor core. The gas core generally carries entrained liquid droplets along with it. Large, amplitude-coherent waves are usually present on the surface of the liquid film, and the continuous breakup of these waves forms a source for droplet entrainment. Droplet entrainment occurs in varying amounts in the central gas core. The droplets can be separated or agglomerated and appear as irregular filaments or wisps. Because strong drag forces are needed to maintain liquid droplets in suspension, annular flow occurs only at high gas rates.

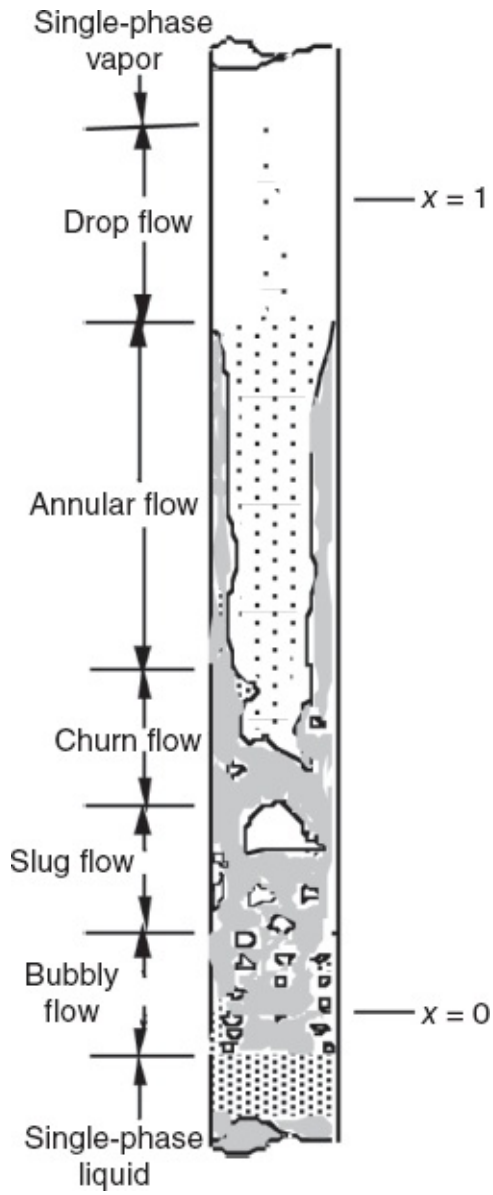

Fig. 3.2—Flow patterns in a wellbore (after Collier 1981).

3.1.2 Flow Patterns in Wellbores. Large variations in pressure and temperature along a wellbore suggest that different flow patterns can exist at various depths. For example, near the well bottom, we may only have the liquid phase or two liquid phases consisting of oil and water. Because the hydrocarbon crude is a mixture of a large number of components, the liquid phase usually contains a significant amount of dissolved gases—chiefly methane and ethane. As the fluid moves upward, the pressure on it gradually decreases. At a point where the pressure becomes less than the bubblepoint pressure, the gas starts to come out of solution, resulting in bubbly flow. As pressure decreases further with upward movement of fluids, more gas comes out of solution, and the whole range of flow patterns may be visible **(Fig. 3.2).** However, in oil wells, gas flow is rarely high enough for annular flow to exist. Indeed, most multiphase flow patterns in oil wells are limited to bubbly, slug, and churn flow. Therefore, these three flow patterns are important for oil wells.

Gas production may also involve flow of more than one phase, because of coproduction of condensate or water or both. The gas flow rate is generally high enough to sustain annular flow. In the lower flow rate limit, liquid unloading becomes a real practical issue, which we address later. Annular flow is also prevalent in geothermal wells producing saturated water and steam.

3.2 Flow Pattern Delineation

Determining the type of flow that will occur under a given flow situation is essential for mechanistic modeling of multiphase flow. A completely satisfactory general method to correctly establish a flow pattern for a specified local condition is yet to be developed. One reason for this difficulty is the lack of agreement in describing and classifying flow patterns. The flow is often chaotic and difficult to describe, allowing room for individual judgment and interpretation.

Primary variables determining the pattern of flow are the velocities of the individual phases and their in-situ volume fractions. Besides the dominating influences of phase velocities and volume fractions, secondary variables contribute to the subjective flow pattern classification. These variables include the method of formation of two-phase flow, the amount of departure from local hydrodynamic equilibrium, and the presence of trace contaminants in the system. One example is the formation of bubbly flow by injecting air through a porous wall into water. Close to the injector, bubbly flow will exist up to relatively high gas volume fractions. Downstream of the injector, in relatively pure tap water, coalescence of bubbles will result in bubbly-slug or slug flow. In water containing trace amounts of a surface-active agent, this coalescence may be inhibited.

Despite these deficiencies, many methods have been proposed to delineate flow pattern during gas/liquid two-phase flow. Some of these methods can be extended to liquid/liquid systems, with lesser accuracy. One method of representing various transitions is in the form of flow pattern maps. We may represent individual patterns as areas on a two-dimensional (2D) graph, on which coordinates are the actual superficial phase velocities (v_{sL}, v_{sg}) or generalized parameters containing these velocities. Obviously, the influence of secondary variables cannot be represented easily on a 2D map. In the second approach, efforts are directed toward modeling mechanisms that cause one type of flow pattern to change into another. Therefore, modeling flow pattern transition implies defining individual transition criteria. In the next section, we will present these two approaches to flow pattern delineation: flow regime maps and individual transition criteria.

3.2.1 Flow Pattern Maps. A number of flow pattern maps, using superficial phase velocities as primary variables, have been proposed over the last few decades, some of which are quite accurate and have found wide usage in the industry. Most of these works attempt to generalize the map by choosing parameters that will represent the effect of some secondary variables influencing pattern transitions. **Fig. 3.3** shows the

flow pattern map of Hewitt and Roberts (1969), who have used superficial momentum fluxes ($v_{sL}^2\rho_L$ and $v_{sg}^2\rho_g$) of the two phases for the axes. The momentum fluxes may also be expressed in terms of total mass flux and mass fraction of the phases (e.g., $\rho_L v_{sL}^2 = G^2(1 - x)^2/\rho_L$ and $\rho_g v_{sg}^2 = G^2x^2/\rho_g$). The map is based on low-pressure air/water and high-pressure steam/water data from small-diameter (1- to 3-cm) tubes. Inclusion of fluid density, instead of merely superficial velocities, in the axes of the map appears to allow for the effect of pressure on flow pattern transition quite well. However, because the map was developed from air/water and steam/water data, the effect of fluid properties in an oil well may not be captured very well. The small-diameter pipe used to gather the data also makes the map less appealing for gas/oil flow, particularly because of the influence of pipe diameter on bubbly and slug flows.

Fig. 3.4 shows the generalized map of Govier and Aziz (2008, p.337). Axes used are the modified superficial phase velocities, Yv_{sL} and Xv_{sg}, where

$$Y = (\rho_L\sigma_{wA} / \rho_w\sigma)^{1/4},$$

and

$$X = Y(\rho_g / \rho_A)^{1/3} \quad (3.1)$$

In Eq. 3.1, σ represents surface tension and ρ represents fluid density. Subscripts L, g, w, and A represent liquid, gas, water, and air, respectively, at standard conditions. The curves for various transitions may be represented by the following equations:

$$Yv_{sL} = 0.01\ (1.96\ Xv_{sg})^{5.81} \text{ (bubbly-slug)},$$

$$Yv_{sL} = 0.263\ (Xv_{sg} - 8.61) \text{ (slug-froth/churn)},$$

$$Xv_{sg} = 26.5 \text{ (slug-annular)},$$

and

$$Yv_{sL} = 0.01\ (Xv_{sg} / 70)^{-6.17} \text{ (froth-annular)}. \quad (3.2)$$

Fig. 3.4 is based on air/oil and air/water data and may predict pattern transition in hydrocarbon systems better. However, the effect of pressure, which is extremely important for application to wellbores, may be poorly represented on this map.

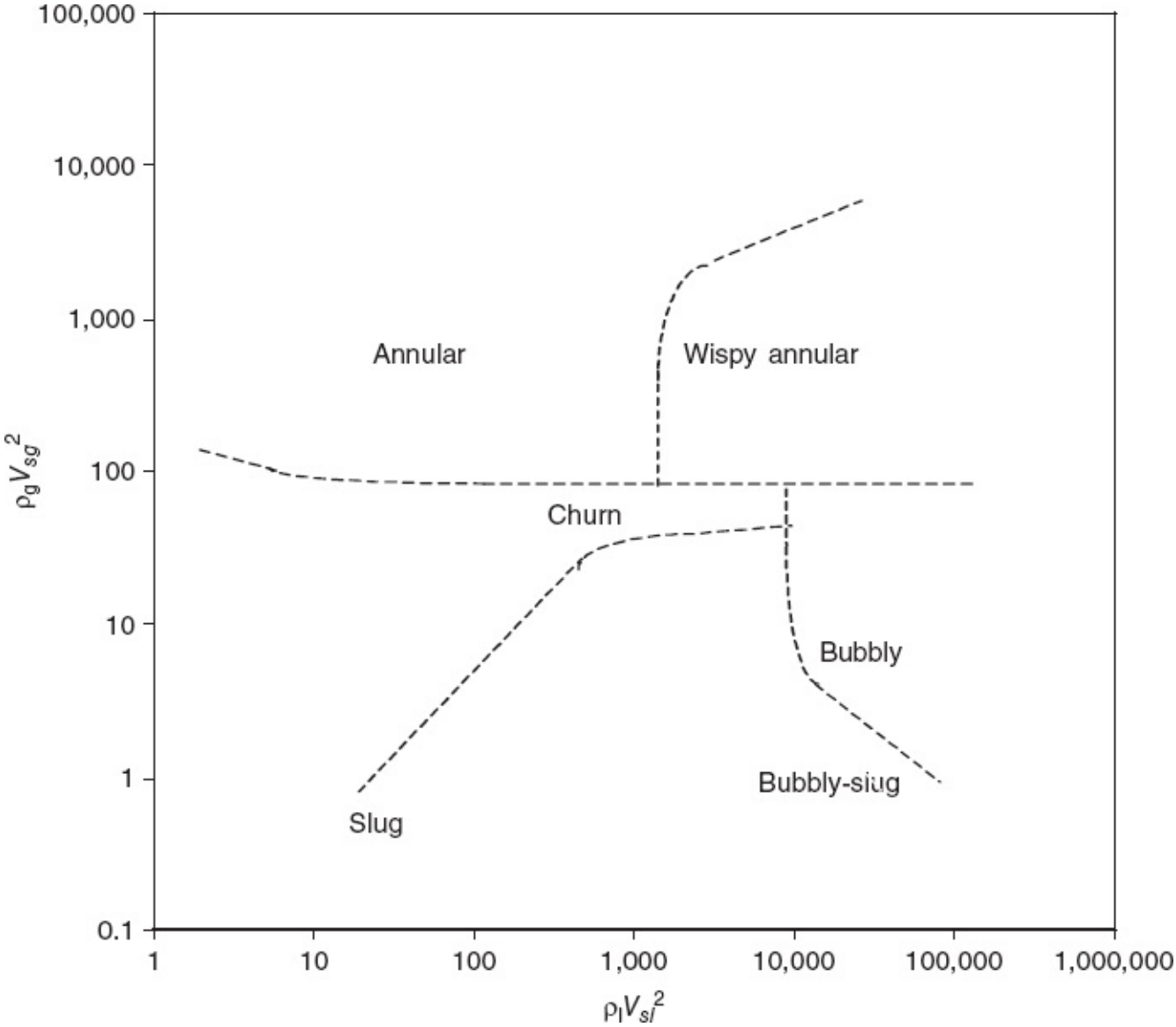

Fig. 3.3—Flow pattern map of Hewitt and Roberts (1969).

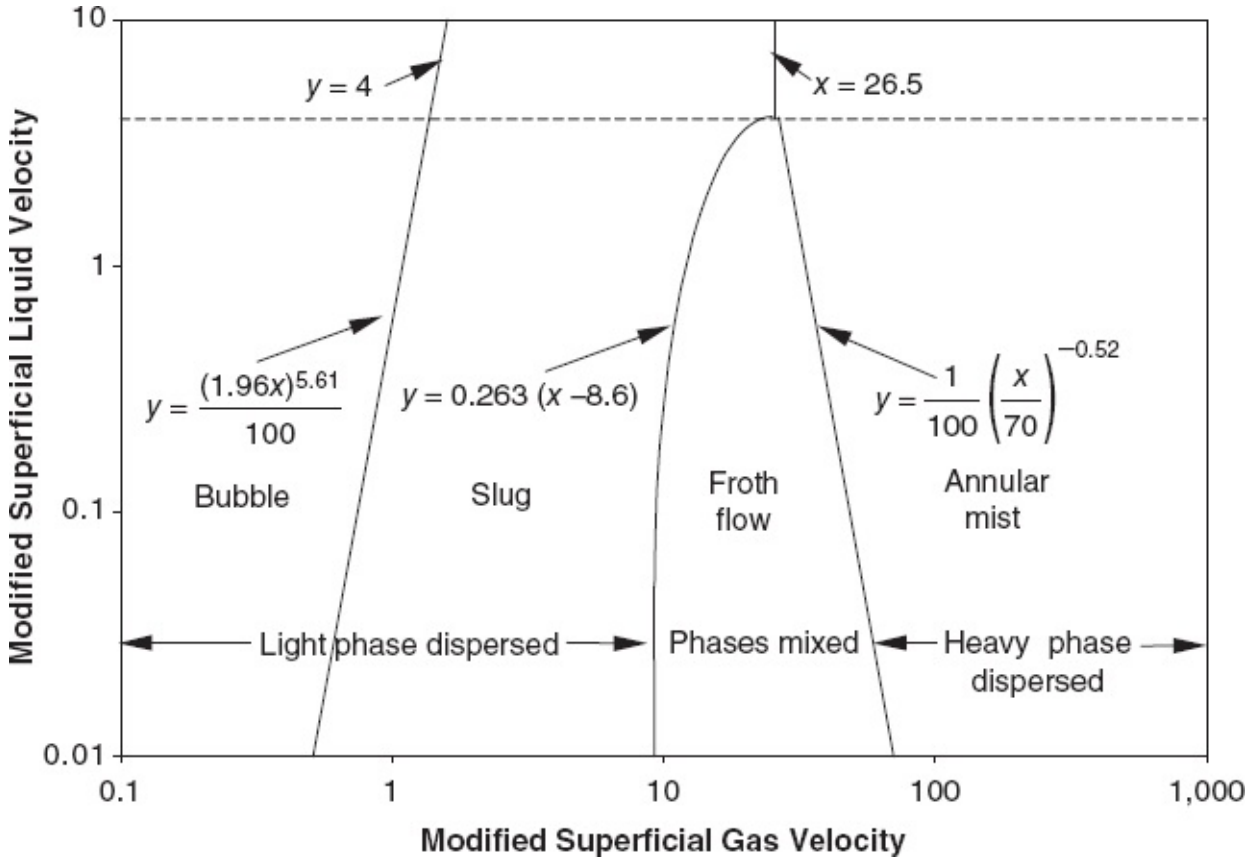

Fig. 3.4—Flow pattern map of Govier and Aziz (2008).

A number of sophisticated flow pattern maps have appeared in recent years. For example, Weisman and Kang (1981), among others, proposed a generalized map for vertical and inclined systems. The axes of their map contain property groups, reflecting the influence of pipe orientation, flow direction, and other parameters. We defer this discussion until the next chapter because of its use in inclined systems, although it is applicable to vertical systems as well. The Taitel et al. (1980) flow pattern map, based on physics of individual pattern transition, is discussed in Section 3.2.2.

Limitations in representing all flow pattern transitions arise in maps because of the influence of secondary variables, which cannot easily be represented on a 2D graph. The use of superficial phase velocities for the axes of the map restricts its application to a particular situation. Any attempt to generalize the map requires choosing adequate parameters that represent various flow pattern transitions. Because differing hydrodynamic conditions and balance of forces govern different transitions, a truly generalized map is very difficult to construct.

3.2.2 Flow Pattern Transition Criteria. An alternative and more flexible approach to empirical flow pattern maps is to examine each pattern transition and develop criteria valid for that specific transition. In the last few years, this approach has made enormous progress. Because examining specific transitions allows physical modeling of individual flow patterns, this is probably the most reliable approach available today.

We will now discuss transition criteria based on this approach, with special emphasis given to bubbly flow/slug flow transition because of its importance to the petroleum industry.

***Bubbly Flow/Slug Flow Transition*.** Transition from bubbly flow to slug flow requires the small, dispersed bubbles to agglomerate or coalesce to become large enough to fill the entire pipe cross section. Except for the very small ones, most bubbles follow a zigzag path when rising through a liquid. This movement results in collisions among bubbles, with consequent bubble agglomeration and formation of larger bubbles. Obviously, collision frequency and bubble agglomeration increases with increasing gas flow rate. At gas volume fractions higher than 0.25 (i.e., liquid holdup $f_L < 0.75$), the collision frequency becomes extremely high and transition to slug flow becomes highly likely, as shown by Radovicich and Moissis (1962). Experimental verification that the transition to slug flow occurs at a volume fraction of approximately 0.25 has been offered by many (Zuber and Findlay 1965; Hasan et al. 1988; among others). Hasan et al. (1988) also found the transition to take place at a volume fraction of approximately 0.25, even when the flow occurs in tubing/casing annuli.

Therefore, $f_g = 0.25$ ($f_L = 0.75$) may be taken as the criterion for transition between bubbly and slug flow. We can express the transition criterion of $f_g = 0.25$ in terms of such measured variables as superficial velocities using an expression for the gas volume fraction. The expression for volume fraction in bubbly flow (to be developed later) is given by

$$f_g \equiv 1 - f_L = \frac{v_{sg}}{C_o v_m + v_\infty}. \qquad (3.3)$$

By rearranging Eq. 3.3, one can obtain a linear relationship, $v_{sg}/f_g = C_o v_m + v_\infty$, between the in-situ gas velocity and its superficial velocity. **Fig. 3.5** captures the v_g – v_{sg} linear behavior, which also shows transition to slug flow. Because $f_g = 0.25$ for this transition, Eq. 3.3 yields

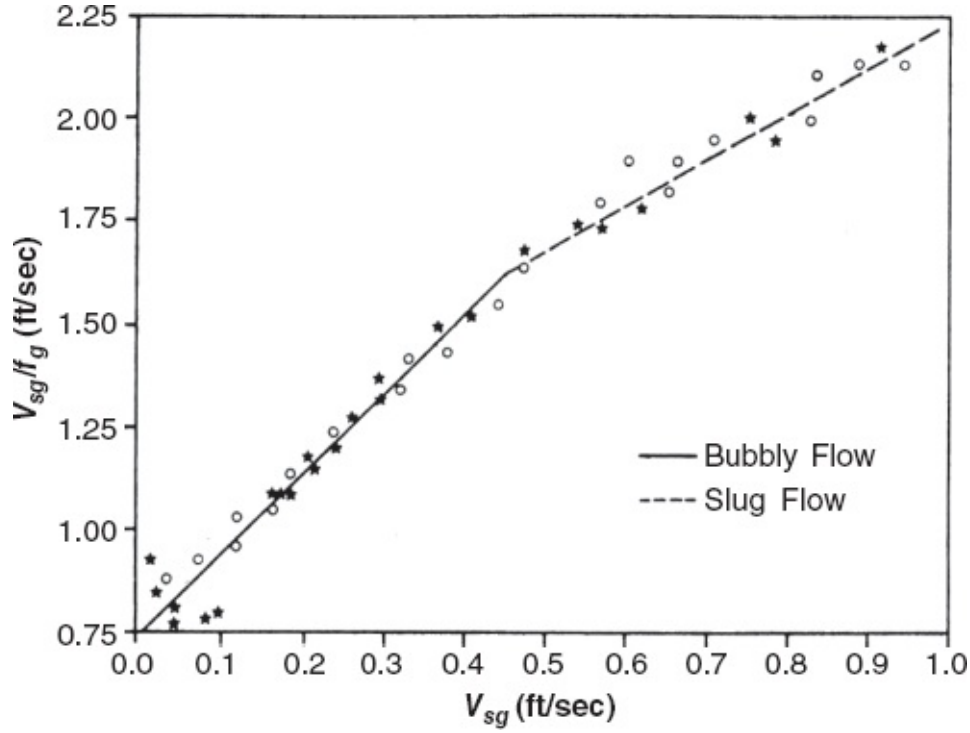

Fig. 3.5—Gas in-situ and superficial velocities bear a linear relationship in bubbly and slug flow (after Hasan and Kabir 1988b).

$$v_{sg} = \frac{C_o v_{sL} + v_\infty}{4 - C_o} \quad \text{(3.4)}$$

By using a value of 1.2 for the flow parameter C_o as suggested by many (Zuber and Findlay 1965; Hasan and Kabir 1988b; Ansari et al. 1994; among others), we obtain

$$v_{sg} = 0.429 v_{sL} + 0.357 v_\infty. \quad \text{(3.5)}$$

We recommend the use of the Harmathy (1960) equation for estimating single-bubble terminal rise velocity, v_∞.

$$v_\infty = 1.53 \left[g(\rho_L - \rho_g)\sigma / \rho_L^2 \right]^{1/4} \quad \text{(3.6)}$$

For an air/water system at room temperature, Eq. 3.6 calculates a terminal rise velocity of approximately 0.80 ft/sec (for oil with ρ_L = 1 g/cm^3 and σ = 20 dynes/cm, $v_\infty \approx$ 0.60 ft/sec ≈ 0.18 m/s). Therefore, Eq. 3.5 suggests that for a stagnant water column, slug flow will occur whenever superficial air velocity exceeds 0.29 ft/sec (0.088 m/s).

Taitel et al. (1980) arrived at the following expression for transition to slug flow, assuming that the slip between the phases equals v_∞:

$$v_{sg} = 0.33 v_{sL} + 0.25 v_\infty. \quad \text{(3.7)}$$

Although Eq. 3.7 was adopted by Ansari et al. (1994), we recommend the use of Eq. 3.5 for bubble-to-slug pattern transition because slip between the phases does not generally equal terminal rise velocity. However, differences in the results of Eqs. 3.5 and 3.7 are small, particularly at low phase velocities characteristic of this pattern transition. Various uncertainties involved in the transition from bubbly to slug flow probably overshadow that difference. In addition, the bubbly-to-slug transition is gradual. Therefore, applicability of the holdup relationship for bubbly flow, up to the point of transition—implicit in deriving Eq. 3.5—is unlikely. If the expression for holdup for slug flow is assumed at the transition point, the terminal rise velocity, v_∞, for small bubbles will have to be replaced by the Taylor bubble rise velocity, $v_{\infty T}$, in Eq. 3.5. However, the difference in the rise velocities of a small bubble and a Taylor bubble is usually small, and Eq. 3.5 is quite adequate in representing the transition between bubbly and slug flow.

Fig. 3.6 shows the bubbly-to-slug transition data from a number of sources. The agreement between Eq. 3.5 with these data appears good. Of particular interest are the data reported by Sadatomi et al. (1982) for circular-annular and rectangular channels. The excellent agreement of these data with Eq. 3.5 indicates the applicability of this transition criterion for noncircular geometry. We explore this point further in Chapter 4.

If the pipe diameter is very small or if the fluid velocities are very high, the transition criterion given by Eq. 3.5 (or Eq. 3.7) may not apply. These two exceptions are discussed next.

Pipe-Diameter Effect. An interesting aspect of the channel diameter in the transition between bubbly and slug flows was pointed out by Taitel et al. (1980). They observed that the terminal rise velocity of small bubbles, given by Eq. 3.6, is unaffected by the channel diameter. In contrast, the rise velocity of a Taylor bubble, $v_{\infty T}$, is strongly dependent on pipe diameter, as shown by the expression for $v_{\infty T}$ (Govier and Aziz 2008, p.396):

$$v_{\infty T} = 0.35\sqrt{gd\left(\rho_L - \rho_g\right)/\rho_L} \qquad (3.8)$$

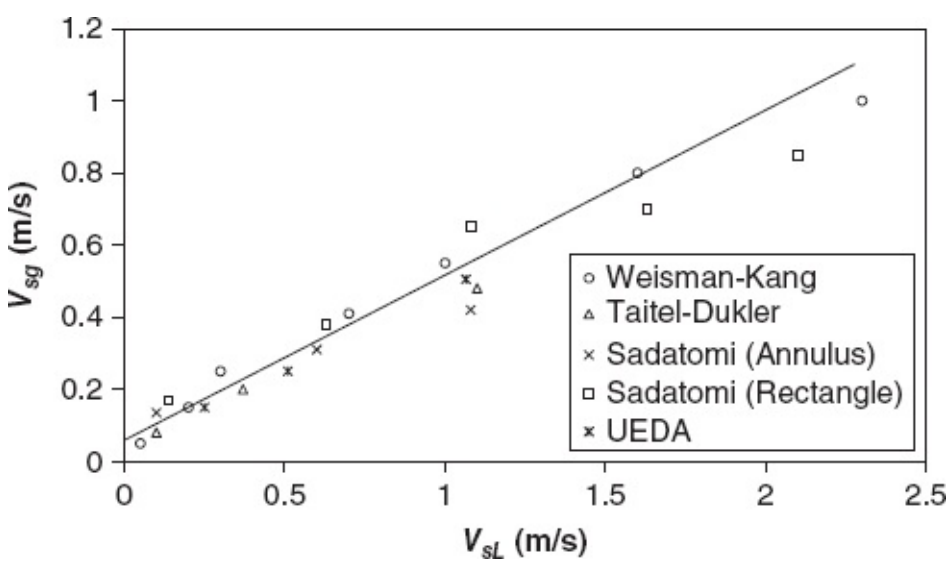

Fig. 3.6—Eq. 3.5 represents bubbly-to-slug transition data from several sources.

When $v_{\infty T}$ is greater than v_∞, the nose of the any existing Taylor bubble will sweep the smaller bubbles ahead of it. But, when $v_{\infty T}$ is less than v_∞, which is possible in small pipes, the rising smaller bubbles approach the back of the Taylor bubble, coalesce with it, increase its size, and ultimately cause a transition to slug flow. Taitel et al. (1980) claimed that bubbly flow cannot exist under the condition $v_{\infty T} < v_\infty$; that is, when

$$1.53\left[g\left(\rho_L-\rho_g\right)\sigma/\rho_L^2\right]^{1/4} > 0.35\sqrt{gd\left(\rho_L-\rho_g\right)/\rho_L}$$

or

$$d < 19.1\sqrt{\sigma_L/g\left(\rho_L-\rho_g\right)} \quad \text{(3.9)}$$

This fact is also evident from the Hewitt and Roberts (1969) map. Here, data were gathered with 10- to 25-mm-inner-diameter ((ID) tubes for which $v_{\infty T}$ is smaller than v_∞. Bubbly flow cannot exist at low liquid rates in the Hewitt and Roberts (1969) map, supporting the Taitel et al. (1980) contention.

Dispersed Bubbly Flow. At higher flow rates, shear stress caused by turbulence tends to break up the larger bubbles. Such breakups of larger bubbles may inhibit transition to slug flow even when gas volume fraction exceeds 0.25. This type of bubbly flow resulting from the breakdown and dispersion of larger bubbles in the liquid is known as dispersed bubbly flow. Mechanics of dispersed bubbly flow were analyzed by Taitel et al. (1980) and Shoham (1982). Based on maximum bubble diameter analysis, which is possible under highly turbulent conditions, they arrived at the following implicit expression for the onset of dispersed bubbly flow:

$$2v_m^{1.2}\left(\frac{f}{2d}\right)^{0.4}\left(\frac{\rho_L}{\sigma}\right)^{0.6}\sqrt{\frac{0.4\sigma}{g(\rho_L-\rho_g)}} = 0.725+4.15\sqrt{\frac{v_{sg}}{v_m}} \quad \text{(3.10)}$$

Therefore, if the actual mixture velocity is greater than the velocity calculated with Eq. 3.10, bubbly flow will persist, even when $f_g > 0.25$. However, Taitel et al. (1980) showed that even for small gas bubbles, the gas volume fraction could be 0.52, at most. At higher volume fractions, transition to slug or churn flow must take place, even though v_m exceeds that when calculated with Eq. 3.10.

We note that for air/water systems at 25°C in a 2-in. (50.8-mm) pipe, one computes a mixture velocity of approximately 12 ft/sec (3.6 m/s) (≈ 4,000 B/D or 609 m^3/d) with Eq. 3.10, above which bubbly flow will only persist up to $f_g = 0.52$. For 100-cp oil under similar conditions, the mixture velocity must exceed 8.5 ft/sec (2.6 m/s). Also, at least half of this volumetric rate must be owing to the liquid phase

because bubbly flow can exist only when $f_g < 0.52$. Such high velocities are not usual in oil wells, and the transition to slug flow usually takes place when v_{sg} exceeds the value given by Eq. 3.5. However, geothermal wells, producing saturated water at high rates, as well as high-rate offshore wells, offer the potential for occurrence of dispersed bubbly flow.

Slug Flow to Churn Flow Transition. In slug flow, Taylor bubbles, formed by the agglomeration of smaller bubbles, occupy most of the pipe cross-sectional area. A liquid slug, in which small bubbles are dispersed axially, separates the Taylor bubbles. The liquid confined by the Taylor bubble and the tube wall flows around the bubble as a falling film. With an increasing flow rate, the interaction between the falling film and the rising Taylor bubble increases. The upper limit of the slug flow occurs when the interaction becomes high enough to break up the long bubbles, thus causing the transition to churn flow. This breakup of Taylor bubbles is similar to the phenomenon of flooding during countercurrent flow of gas and liquid.

Many investigators have examined slug/churn transition with empirical (Barnea 1987), semitheoretical (Weisman and Kang 1981), and theoretical (Hasan 1988) analysis. However, none appears satisfactory for oilwell applications. The most promising model for this transition is probably the one proposed by Brauner and Barnea (1986). They analyzed the condition of the liquid slug following the Taylor bubble just before transition to churn flow occurs. If the mixture velocity is high enough for dispersed bubbly flow to occur, the local in-situ gas volume fraction in the liquid slug can attain a maximum value of 52%. In other words, for transition to churn flow, the mixture velocity v_m must be higher than that predicted by Eq. 3.10, and the gas velocity must be high enough so that the gas volume fraction is greater than 52%. In addition, they noted that at high flow rates, characteristic of this flow regime, the in-situ volume fraction may be approximated by the no-slip volume fraction, so $f_g = v_{sg}/v_m$. Therefore, for transition to churn flow,

$$\frac{v_{sg}}{v_{sg}+v_{sL}} > 0.52 \qquad (3.11a)$$

or

$$v_{sg} > 1.08\, v_{sL} \qquad (3.11b)$$

Brauner and Barnea (1986) presented data that lend support to the equation they proposed. They also show how this criterion can be modified for inclined two-phase flow. Ansari et al. (1994) recommended a higher value of 0.76 for the limiting gas volume fraction proposed by Scott and Kouba (1990), which leads $v_{sg} > 3.17\, v_{sL}$ for the superficial gas velocity needed for the transition to churn flow. Performance of Eq. 3.11 may be improved by noting that the gas volume fraction may be better represented by Eq. 3.3, $f_g = v_{sg}/(C_o v_m + v_\infty)$. For example, Hasan and Kabir (1988b) proposed that the flow parameters for dispersed bubbly flow, C_o and v_∞, have the

same values as those for ordinary bubbly flow. Subsequently, Kaya et al. (2001) recommended an even higher limiting void fraction of 0.78 for the existence of slug flow. Using $f_g = v_{sg} /(1.2v_{sL} + v_{\infty T})$, as proposed by Hasan and Kabir (1988b), they showed that when v_{sg} exceeds 12.9 v_{sL}, transition from slug to churn flow should occur. Their proposed method, with appropriate modification for rise velocity, is also applicable for deviated wells and is discussed in Chapter 4. Note that in any case, for churn flow to take place, v_m must exceed the value given by Eq. 3.10.

Despite these efforts to characterize churn flow, uncertainties remain. For instance, Mao and Dukler (1993), deriving support from their experimental measurements, concluded that churn flow is really a manifestation of slug flow and that it may not exist as a separate entity. However, Hewitt and Jayanti (1993), citing their earlier work (Jayanti and Hewitt 1992), contended that flooding waves are formed within the Taylor bubbles in slug flow as the churn flow transition is approached. Our experience shows that churn flow can be treated much like slug flow for oilfield applications, as we discuss later.

Transition to Annular Flow. At high gas flow rates, transition from churn or slug flow to annular flow takes place. The liquid flows upward along the tube wall, while the gas flows through the center of the tube. The liquid film on the wall has a wavy interface, part of which can be broken by the gas and carried away as entrained droplets.

The transition between churn (or slug) and annular flow can be understood by visualizing a long vertical tube with a porous section at the middle. If the liquid is fed through the porous section at the middle and gas from the bottom, then at low gas flow rates, the liquid will flow down the tube as a film. However, at high gas flow rates, the shear force of the gas on the liquid will pull it upward, just as in the case of annular flow. Wallis (1969, p.93), among others, proposed criteria for transition to annular flow on the basis of the minimum gas velocity needed for reversal in the direction of the liquid flow.

Taitel et al. (1980) adopted a different physical model and examined the drag force needed to keep the entrained liquid droplets in suspension. They suggested that when the gas velocity is not sufficient to keep the liquid drop-lets in suspension, the droplets will fall back, accumulate, and form a bridge, leading to churn or slug flow. The minimum velocity required to keep a droplet with an average diameter *d* in suspension can be determined from a balance of the drag force on the droplet and the gravitational force acting on it. This analysis leads to the following expression for gas velocity, beyond which annular flow is expected:

$$v_{sg} > 3.1\left[g\sigma\left(\rho_L - \rho_g\right)/\rho_g^2\right]^{1/4} \qquad (3.12)$$

Taitel et al. (1980) presented data from various sources that appear to agree with the results of Eq. 3.12 quite well. Note that both Eq. 3.12 and the Hewitt-Roberts (1969) map suggest that the transition to annular flow is not affected by the liquid flow rate. For an air/water system at standard conditions, Eq. 3.12 predicts a gas

velocity of approximately 50 ft/sec (15 m/s), above which annular flow exists, whereas the Hewitt and Roberts map suggests a gas velocity of approximately 35 ft/sec. In practical applications, such high gas flow rates occur only in gas/condensate and geothermal wells.

More recently, pipe flow experiments in the laboratory have offered considerable insights into transition from annular flow that leads to liquid loading. Veeken et al. (2010) suggested that film flow reversal is responsible for liquid loading by modeling the process with a transient multiphase-flow simulator. Alamu (2012) conducted laboratory experiments and concluded that the film flow reversal occurs at the transition between mist and annular flows during cocurrent annular flow. Sarica et al. (2013) conducted multiphase flow experiments for the vertical and deviated pipes and made similar observations. They concluded that flow pattern transition from fully cocurrent annular flow to partially cocurrent annular flow triggers the initiation of film flow reversal for vertical and deviated wellbores. Therefore, the studies by these authors suggest that liquid loading is tied to film flow reversal as opposed to the droplet flow reversal. These insights are further discussed in Chapter 5; this chapter uses the simpler approach represented by Eq. 3.12.

Transition to or from annular flow is very important in understanding liquid loading in gas wells. Continued production from a gas reservoir may cause its pressure to drop so much that production rate and gas velocity fall below what is needed to sustain annular two-phase flow. When transition from annular to churn (or slug) flow occurs, liquid holdup increases, which promotes the formation of a growing liquid column at the well bottom. Increased liquid loading, in turn, causes greater pressure drop in the well when the annular pattern existed throughout the wellbore. Greater pressure loss in the well causes increased bottomhole pressure (for the same surface line pressure), thereby promoting further decrease in production rate. This process becomes a vicious circle with decreased production causing increased liquid loading and pressure loss in the well. Chapter 5 presents details of liquid loading and approaches to physically modeling the process.

When the liquid film at the wall is thick and a significant amount of liquid is entrained in the gas, the liquid might bridge the gas core. Barnea (1987) proposed the following correlation for f_{LF}, the maximum liquid holdup beyond which annular flow cannot exist, even if v_{sg} is higher than that given by Eq. 3.12.

$$\left[f_{LF} + (E_{Lc} A_c / A)\right] > 0.12. \qquad (3.13)$$

From geometrical considerations,

$$f_{LF} = 4\,\underline{\delta}(1-\underline{\delta}). \qquad (3.14)$$

In Eq. 3.14, the dimensionless liquid-film thickness $\underline{\delta}$ equals δ/d, where δ is the actual film thickness. In addition, E_{Lc} represents the fraction of flowing liquid that is entrained in the gas core, and A_c is the average cross-sectional area of the gas core.

The liquid holdup f_{LF} depends on the combined momentum equation,

$$Y_M = \frac{f_i / f_c}{(1 - f_{LF})^{2.5} f_{LF}} - \frac{X_M^2}{f_{LF}^3} \quad (3.15)$$

In Eq. 3.15, the dimensionless parameter Y_M represents the ratio of static/frictional pressure gradient in the gas core.

$$Y_M = \frac{g \sin\alpha (\rho_L - \rho_c)}{(dp/dz)_c} \quad (3.16)$$

Note that X_M represents the Lockhart-Martinelli parameter defined in Chapter 2, modified here to reflect the fact that the liquid flow rate in the film is reduced by the liquid entrained in the gas core.

$$X_M = \sqrt{(1-E)^2 (f_F / f_{sL}) \frac{(dp/dz)_{fL}}{(dp/dz)_c}} \quad (3.17)$$

The procedure for calculating interfacial friction factor, $f_{c,}$, fraction of liquid entrained, E, and core cross-sectional area, *Ac*, is discussed later.

***Flow Pattern Map in an Oil Well*.** The individual transition criteria discussed so far are presented in the form of two flow pattern maps in **Figs. 3.7a and 3.7b** for a 30 °API oil flowing in a 3-in.-ID pipe. The fluid properties used are γ_g = 0.75, ρ_L = 54.67 lbm/ft³, σ = 0.0685 lbm/sec² (31 dynes/cm), and μ_g = 0.0103 cp. Fig. 3.7a shows the map at the standard (14.7 psia and 60°F) conditions. Note that the dispersed bubbly flow pattern is represented by two transition lines. The segment represented by AB is given by Eq. 3.10, while the BC segment is based on Eq. 3.11. The segment BD, representing the slug/churn transition, is a continuation of the line AB. As mentioned earlier, the line BD is the locus of constant mixture velocity for a given set of fluid properties. On the right of the BD line, mixture velocity is high enough for dispersed bubbly flow, but the in-situ gas volume fraction is higher (below line BC) than 0.52; therefore, churn flow results.

Fig. 3.7b represents a condition likely to be prevalent in an oil well with a pressure of 1,000 psia and a temperature of 100°F in which the following property values were used: ρ_g = 3.77 lbm/ft³, ρ_L = 54 lbm/ft³, σ = 0.0316 lbm/sec², and μ_g = 0.0127 cp. At this higher pressure, the gas density is significant; therefore, transition to annular flow occurs at a much lower superficial gas velocity of 6.8 ft/sec, compared to 44.4 ft/sec at standard conditions. Note also that the bubbly flow area shrinks and the churn flow regime vanishes entirely.

***Pattern Transition Computation Approach*.** Using any of the flow pattern based models requires determining the existing flow pattern at any location in the well. In applying these pattern transition criteria, we find it simpler to first check for bubbly flow (with Eq. 3.5) and annular flow (with Eq. 3.12) because existence of either one

precludes need for further checking. When those two tests fail, the pattern must be slug, churn, or dispersed bubbly. If the actual mixture velocity v_m is less than that given by Eq. 3.10, we know that slug flow pattern should prevail. If, however, v_m is greater than that computed by Eq. 3.10, then we have churn flow if $v_{sg} > 1.08\ v_{sL}$ (Eq. 3.11b) or else dispersed bubbly flow. The example problem at the end of this chapter shows this calculation approach.

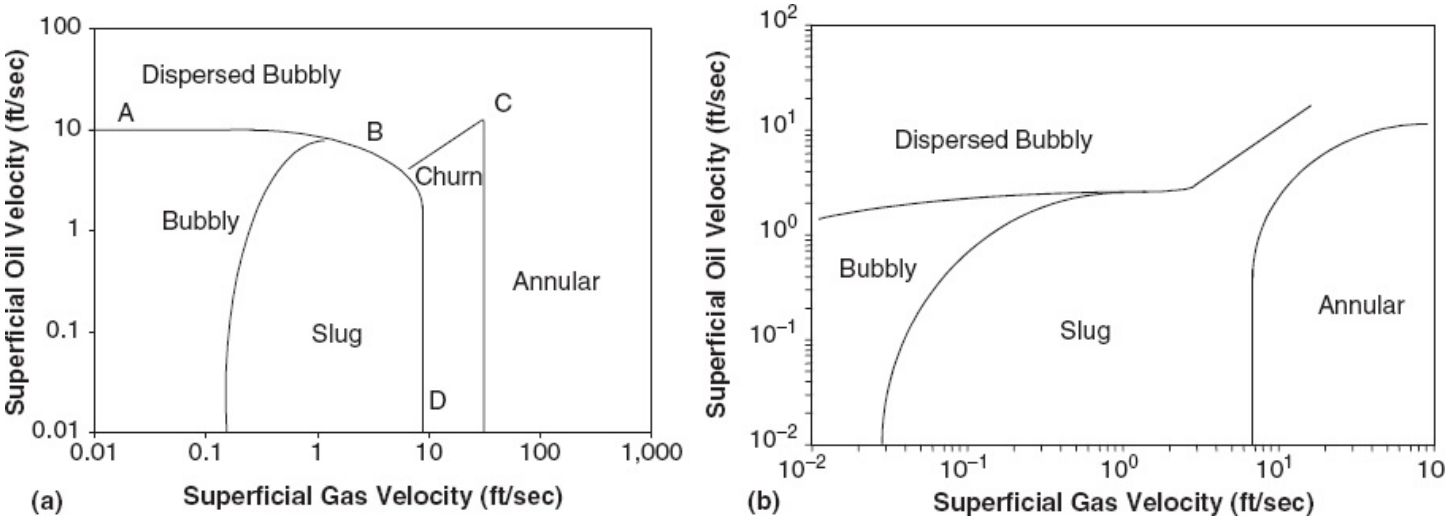

Fig. 3.7—Flow pattern map at standard conditions (a) and at 1,000 psi (b).

3.3 Liquid Holdup and Pressure Drop

In the analysis of multiphase flow in vertical and near-vertical systems, the estimation of static head becomes extremely important. In most vertical flow situations, the static head is the major contributor to the total pressure gradient and can account for more than 90% of the total pressure drop. Because the mixture density and, therefore, the static head are directly dependent on the liquid holdup, f_L, an accurate estimation of liquid holdup is of paramount importance.

The success of the flow pattern based approach stems from the fact that slip between the phases depends on the buoyancy of the lighter phase and its tendency to flow through the center of the channel. The effect of buoyancy and the channeling tendency of the gas phase depend, in turn, on the particular flow pattern that exists under the given conditions of flow, pressure, and channel geometry. One may surmise that the dynamics of flow are different for each flow regime and that individual modeling for each regime should lead to better insights into flow behavior and, therefore, more-reliable computational tools. We will now discuss the modeling approach for each of those four regimes.

3.3.1 Bubbly Flow. In bubbly flow, gas bubbles tend to flow mostly through the center of the channel. At the channel center, the mixture velocity is significantly higher than the cross-sectional average velocity, which means that gas bubbles are moving faster than the average velocity of the mixture, v_m. In addition, the density difference

between the phases gives rise to a drift flux, v_d, which adds a velocity, v_d/f_g, to the lighter phase.

Holdup. If we assume that the velocity at the channel center is C_o times the cross-sectional average velocity, we can write the expression for in-situ gas velocity, v_g, as

$$v_g = C_o v_m + v_d / f_g. \quad (3.18)$$

Because in-situ velocity is equal to the superficial velocity v_{sg} divided by the gas volume fraction f_g, we have a simple relationship between volume fraction and phase velocities, given by

$$f_g = \frac{v_{sg}}{C_o v_m + \left(v_d / f_g\right)}. \quad (3.19)$$

Eq. 3.19 expresses gas volume fraction in an implicit form and requires an expression for drift flux, v_d. For upward vertical flow of small bubbles or particles in liquids, Zuber and Findlay (1965) and Wallis (1969) suggested the following semitheoretical expression for drift flux in terms of the volume fraction f_g and the terminal rise velocity v_∞:

$$v_d = v_\infty f_g \left(1 - f_g\right)^n. \quad (3.20)$$

For gas/liquid flow in vertical pipes, we recommend a value of zero for the exponent n, as noted by some researchers (Zuber and Findlay 1965; Hasan and Kabir 1988b; among others). Therefore, for gas/liquid flow, the expression for drift flux simplifies to $v_d = v_\infty f_g$, and Eq. 3.19 can be rewritten as

$$f_g = \frac{v_{sg}}{C_o v_m + v_\infty}. \quad (3.21)$$

Therefore, the liquid holdup f_L (= 1 − f_g) is given by

$$f_L = 1 - \frac{v_{sg}}{C_o v_m + v_\infty}. \quad (3.22)$$

Eq. 3.21 can be recast in the form

$$v_g \equiv v_{sg} / f_g = v_{sg} / (1 - f_L) = C_o v_m + v_\infty. \quad (3.23)$$

Eq. 3.23 shows that the in-situ gas velocity varies linearly with the mixture velocity with a slope, C_o, and an intercept, v_∞. Stated differently, in-situ gas velocity equals the fluid velocity at the channel center plus the bubble's terminal rise velocity.

Ansari et al. (1994) used a value of 0.5 for the exponent n in Eq. 3.20, which leads to the implicit expression for liquid holdup,

$$f_L = 1 - \frac{v_{sg}}{C_o v_m + v_\infty f_L^{0.5}} \quad (3.24)$$

The use of either Eq. 3.22 or Eq. 3.24 requires estimates of the flow parameter C_o and the terminal rise velocity v_∞. Next, we discuss the values of these parameters.

Terminal Rise Velocity, v_∞. A single gas bubble rising through an infinite liquid medium soon attains a constant rise velocity v_∞ owing to the balance of drag and buoyancy forces on it. We have found the expression for v_∞, developed by Harmathy (1960) to be simple and accurate, and therefore we use it in this book. We point out that the bubble rise velocity can be significantly lower if the bubble diameter approaches that of the pipe wall.

Many researchers have used Eq. 3.23 to correlate their holdup data without gathering independent rise-velocity data. In such cases, the value used for v_∞ is essentially a correlating parameter for the data and is often slightly different from the value estimated from the Harmathy equation. We recommend the use of Eq. 3.6.

Flow Parameter C_o. Analysis of velocity and bubble concentration profiles may allow estimation of C_o. For a vast majority of multiphase flow applications, the flow can be assumed turbulent, so the maximum velocity at the channel axis is 1.2 times the average velocity. In addition, the velocity profile is quite flat for a portion of the central section of the pipe. Although not all bubbles flow through the channel center because a few flow close to the wall, 1.2 has been found to be a reasonable value for C_o. The classical study of Zuber and Findlay (1965) established a value of C_o = 1.2 for an air/water system in a 2-in. pipe. Many studies, in a variety of systems since then, have firmly established this value of C_o.

An exception to this C_o value occurs for bubbly flow in large-diameter pipes (>100 mm) with stagnant-liquid columns. The upward motion of gas bubbles through the central portion of the channel causes the liquid surrounding them to move upward. Because net liquid movement is zero in a stagnant-liquid column, backflow of liquid occurs along the channel wall. The resulting liquid recirculation in a stagnant column leads to a significantly higher ratio of maximum-to-average velocity, resulting in a higher value of the flow parameter in such cases.

Analyzing holdup data with Eq. 3.23, Rahman (1984) reported a C_o value of 2.0 for a stagnant-liquid column in a 127-mm vertical pipe. Earlier, some investigators, Zahradnik and Kast Nek (1979), for example, determined C_o to be 1.95 for large-diameter (>127-mm) bubble columns. Our work (Kabir and Hasan 1994) also suggested that *Co* = 2.0 is appropriate, not only for stagnant-liquid columns but also for very low liquid rates (v_{sL} < 3.0 mm/s). Similarly, data from a 5.5-in. (140-mm)-ID tube at moderate liquid velocities show a value of 1.6 for C_o.

Therefore, a *Co* value of 2.0 is applicable for large-diameter pipes in stagnant or near-stagnant liquid systems. However, C_o = 1.2 appears to be well-established for bubbly flow in small-diameter pipes, even with stagnant liquid columns. Unfortunately, the precise pipe size at which the change in value for *Co* occurs has not been

investigated, nor do we know if the transition is gradual or abrupt. Clearly, the dependence of *Co* on liquid velocity in near-stagnant, large-diameter columns needs investigation.

Eq. 3.21 reproduces bubbly flow data quite well, such as that shown in Hasan and Kabir (1988b); **Fig. 3.8** provides the testimony. The figure also shows that the simplified slug flow model, given by Eq. 3.26, is capable of reproducing laboratory data satisfactorily.

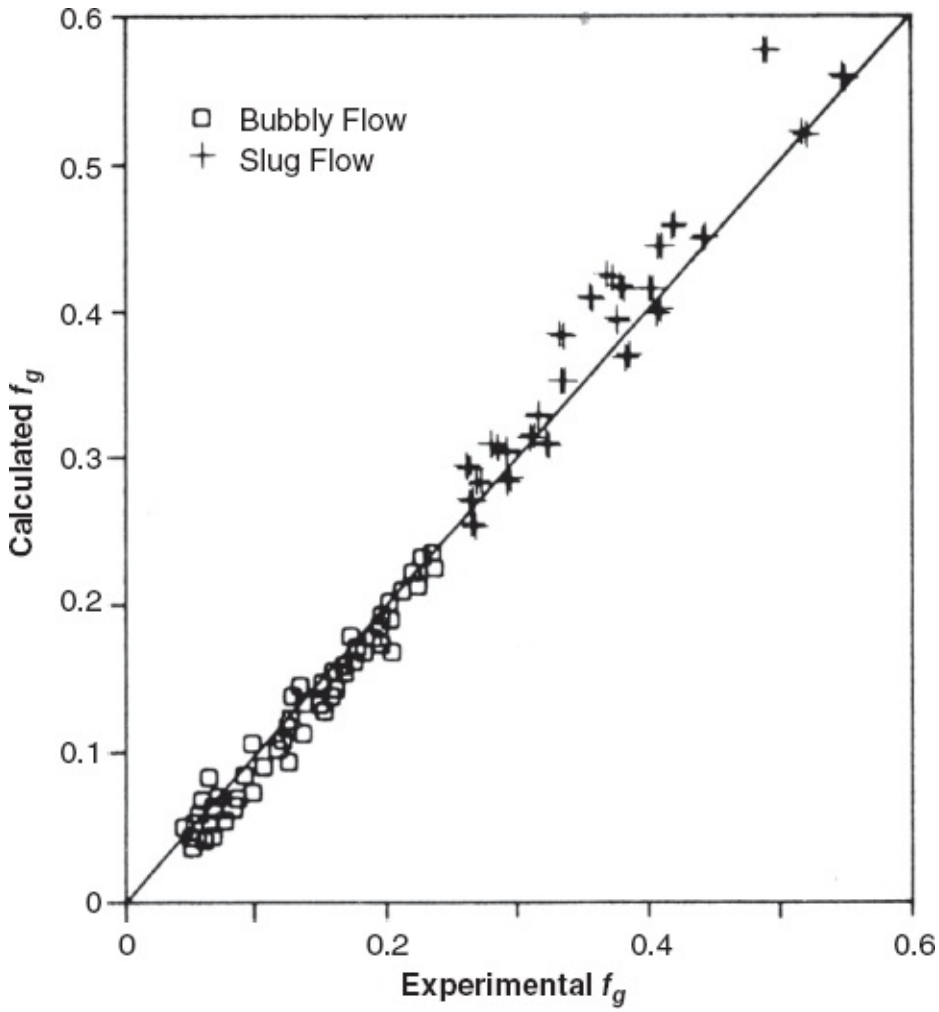

Fig. 3.8—Eqs. 3.21 and 3.26 mimic laboratory data (after Hasan and Kabir 1988b).

For estimating holdup in dispersed bubbly flow, we propose to use Eq. 3.22 with C_o = 1.2 and v_∞ as given by the Harmathy (1960) equation. Dispersed bubbly flow is therefore treated similar to ordinary bubbly flow. Many researchers, including Ansari et al. (1994), have used a homogeneous flow approach in calculating holdup and pressure drop in a dispersed bubbly flow regime. However, we think that large superficial velocities, involved in dispersed bubbly flow, make the fluids more homogeneous but do not necessarily lead to a no-slip condition. In other words, the gas phase still flows mostly through the channel center at a velocity higher than the average mixture velocity.

Pressure Drop. As mentioned in Chapter 2, the general expression for total pressure gradient during two-phase flow is given by

$$-\frac{dp}{dz} = \frac{g}{g_c}\rho_m + \frac{f_m v_m^2 \rho_m}{2 g_c d} + \frac{\rho_m v_m}{g_c}\frac{dv_m}{dz}, \quad (2.19)$$

where the average mixture density ρ_m is given by

$$\rho_m = \rho_L f_L + \rho_g (1 - f_L), \quad (2.20)$$

and the liquid holdup f_L is given by Eq. 3.22 or Eq. 3.24.

Wall friction contributes a small fraction of the total pressure drop during vertical bubbly flow. Using the homogeneous model for estimating frictional pressure drop reduces calculation complexity without introducing any significant inaccuracy. The well may be assumed to be smooth, allowing one to use the simple Blasius equation presented in Chapter 1 (Eq. 1.11) for estimating the friction factor. However, we recommend the Chen (1979) correlation presented in Chapter 1 (Eq. 1.13).

One may use any of the three methods (Eqs. 2.21 through 2.23) suggested in Chapter 2 to estimate mixture average viscosity, μ_m. Considering the insignificance of the friction term, Govier and Aziz (2008, p387) suggested the use of liquid density and viscosity values, instead of the mixture property values, for estimating f_m, as

$$f_m = 0.32\left(d v_m \rho_L / \mu_L\right)^{-0.25} \quad (3.25)$$

Fluid acceleration during bubbly flow is quite small, and the last term in Eq. 2.15 is often neglected. A good estimate of this term can be obtained by taking the difference in mixture velocity over a finite depth of the well to calculate the mixture velocity gradient, dv_m/dz. **Fig. 3.9** exhibits the quality of match obtained, when pressure gradients were computed for both bubbly and slug flows.

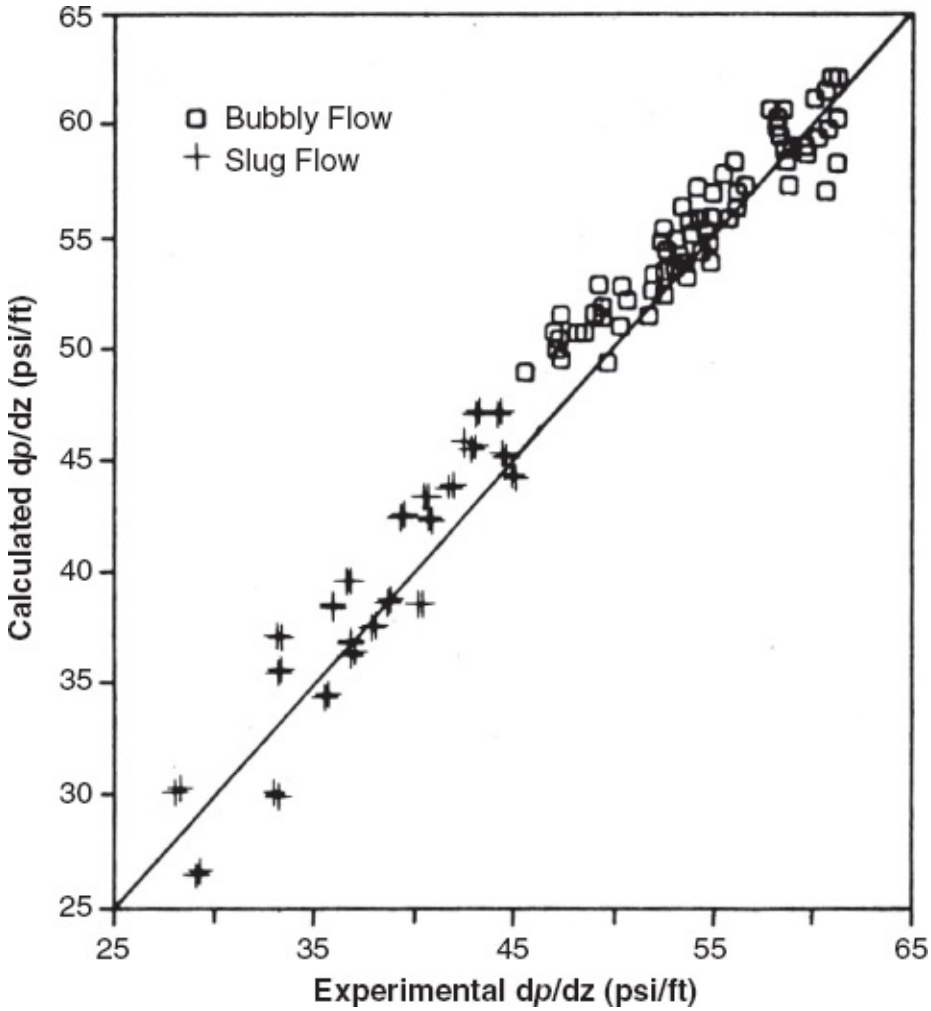

Fig. 3.9—Laboratory data lend support to pressure-gradient calculations in bubbly and slug flows (after Hasan and Kabir 1988b).

3.3.2 Slug Flow. Fluid configuration in slug flow is quite different from that in bubbly flow. As **Fig. 3.10** illustrates, there are two distinct zones during slug flow: one dominated by the large Taylor bubble, and the other consisting of small bubbles dispersed in the liquid slug. The Taylor bubble rises up against a falling liquid film at a velocity generally much higher than that of the small bubbles in the liquid slug. This difference in drift velocities makes it difficult to apply the simple drift-flux model developed for bubbly flow to slug flow. One can still develop a simple expression for liquid holdup in slug flow by neglecting these differences in drift velocities.

Holdup. Assuming differences in these drift velocities to be negligible, one can derive the following expression (Hasan and Kabir 1988b) for holdup using $v_{\infty T}$ for the rise velocity of a Taylor bubble:

$$f_L = 1 - \frac{v_{sg}}{C_o v_m + v_{\infty T}}. \qquad (3.26)$$

If the gas content in the liquid slug is a small fraction of the total gas phase and the difference in drift velocities between the slug and the Taylor bubble is not large, Eq.

3.26 estimates f_g with good accuracy.

However, in many instances of slug flow, the liquid slug might be quite large compared to the Taylor bubble, casting doubt on the accuracy of Eq. 3.26. One simple way to account for different drift velocities in slug flow is to use some type of an average rise velocity for all gas bubbles, large and small, in the system. Therefore, for estimating in-situ gas volume fraction during slug flow, we modify Eq. 3.26 as

$$f_L = 1 - \frac{v_{sg}}{C_o v_m + \overline{v}_\infty} \quad (3.27)$$

The average rise velocity is expressed in terms of the Taylor bubble rise velocity, small-bubble rise velocity, and bubbly-to-slug transition velocity as

$$\overline{v}_\infty = v_\infty \left(1 - e^{-0.1 v_t/(v_{sg} - v_t)}\right) + v_{\infty T} e^{-0.1 v_t/(v_{sg} - v_t)} \quad (3.28)$$

where the superficial gas velocity for transition to slug flow is given by Eq. 3.5, v_t = 0.429 v_{sL} + 0.357 v_∞. This approach was used successfully to compute laboratory liquid holdup data during countercurrent slug flow (Hasan et al. 1994).

In addition to simplifying the computation procedure, an advantage of using this average rise velocity becomes apparent when we consider the calculated values of liquid holdup and pressure drop in bubbly and slug flow regimes near the transition zone. Use of separate rise velocities in the two flow regimes results in different values of the holdup and pressure gradient, even if the same fluid velocities are used. This approach causes an abrupt change in the computed pressure gradient in a well as the flow regime changes from bubbly to slug flow. The continuous nature of Eq. 3.28 avoids this problem, thereby conforming to the measured wellbore pressure profiles.

However, the contrast in rise velocities is not the only difference between the two zones—Taylor bubble and liquid slug—of the slug unit. The velocity profile and, therefore, the flow parameter in the two zones can also differ. To rigorously account for these differences between the liquid slug and the Taylor bubble, a few hydrodynamic models for vertical circular pipes have appeared, as shown by Fernandes et al. (1983) and Sylvester (1987). Fig. 3.10 shows a model cell of length L consisting of a Taylor bubble of length L_{TB} and a liquid slug of length L_{sB}.

The average gas volume fraction in the cell is the sum of volume fraction in the Taylor bubble and that in the liquid slug. Denoting the in-situ gas fraction in the Taylor bubble portion by f_T and that in the liquid slug portion by f_s, we arrive at the expression for the average gas volume fraction for the cell, which is written as

$$f_g = \beta\, f_T + (1 - \beta)\, f_s, \quad (3.29)$$

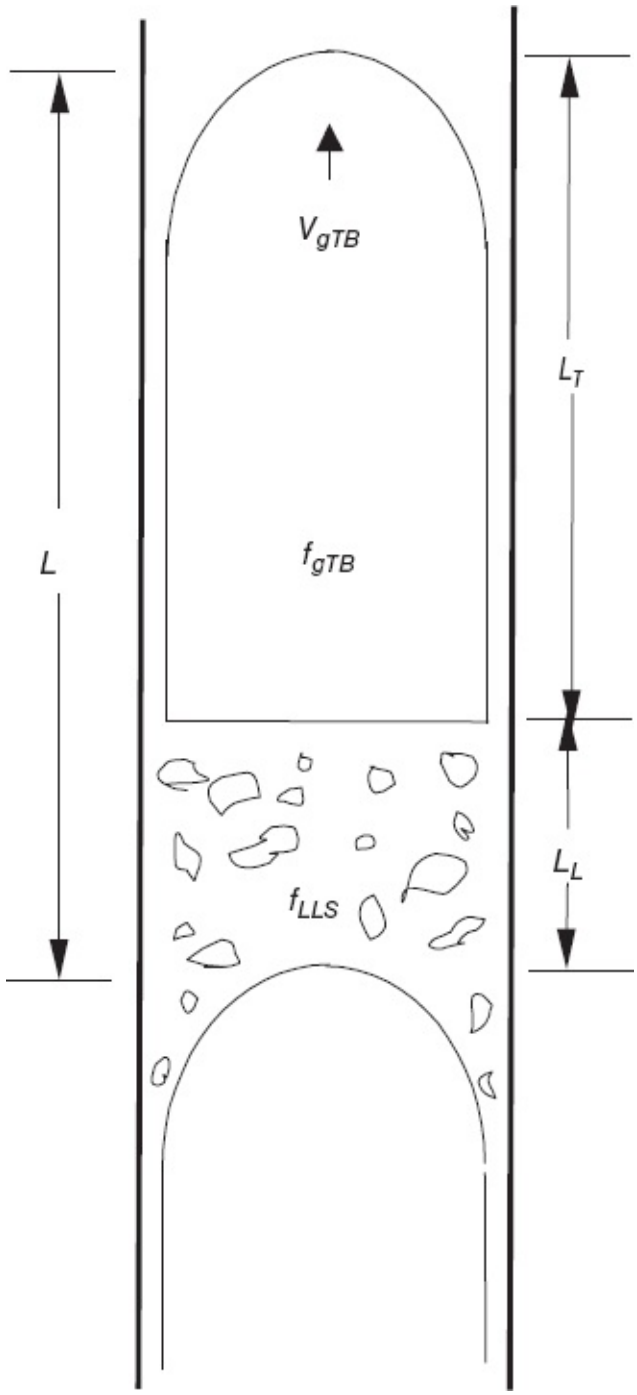

Fig. 3.10—A model cell in slug flow.

where β is the fraction of the cell that is the Taylor bubble portion and is equal to L_T/L. Eq. 3.29 requires estimates of gas volume fraction in the Taylor bubble zone and in the liquid slug, besides requiring an estimate of β. Fernandes et al. (1983) and Sylvester (1987) have suggested estimating the liquid slug volume fraction and other parameters required for the model. Caetano et al. (1992b) successfully extended this approach to a vertical annular channel. Hasan and Kabir (1992) presented a simplified cellular approach using data and correlations from the literature to estimate β. However, the model presented by Ansari et al. (1994) is perhaps the best known. In the following, we present their analysis.

The Ansari et al. (1994) model is based on a material balance for the liquid and the gas in the Taylor bubble zone, denoted by the subscript $_{TB}$, and the liquid slug zone, denoted by the subscript $_{LS}$. Density of the individual phases is assumed to remain constant in the cell, thereby allowing us to write the balance in volumetric flow terms. We need to account for gas velocity in both the Taylor bubble and the liquid slug. The gas velocity in the Taylor bubble segment can be obtained by multiplying the in-situ gas velocity v_{gTB} by the gas volume fraction, $(1 - f_{LTB})$, and by the volume fraction of the Taylor bubble segment, β. A similar rationale follows for estimating gas velocity in the liquid slug segment. Accordingly, superficial gas and liquid velocities, v_{sg} and v_{sL}, can be written as follows:

$$v_{sg} = \beta v_{gTB}(1 - f_{LTB}) + (1 - \beta) v_{gLS}(1 - f_{LLS}), \qquad (3.30)$$

and

$$v_{sL} = (1 - \beta) v_{LLS} f_{LLS} - \beta v_{LTB} f_{LTB}. \qquad (3.31)$$

The difference in velocities between the Taylor bubble and liquid film, and between the bubble and the wall, will cause liquid to flow downward from the Taylor bubble section into the liquid slug. The Taylor bubble is assumed to have an in-situ velocity, v_{TB}, which is given by the sum of the channel center velocity and rise velocity (analogous to that given by Eq. 3.23) as

$$v_{TB} = 1.2 v_m + v_{\infty T}. \qquad (3.32)$$

We defer discussion on estimation procedure for the rise velocity of a Taylor bubble, $v_{\infty T}$. The volumetric rate of liquid moving into the slug is $(v_{TB} + v_{LTB}) f_{LTB}$, where f_{LTB} is the fraction of a Taylor bubble section volume that is liquid. This rate must equal the increase in the flow rate of the liquid slug; that is,

$$\left(v_{TB} + v_{LTB}\right) f_{LTB} = \left(v_{TB} - v_{LLS}\right) f_{LLS}. \qquad (3.33)$$

A similar equation is written for the gas-phase mass balance:

$$\left(v_{TB} - v_{gTB}\right)(1 - f_{LTB}) = \left(1.2 v_m + v_{\infty T} - v_{gLS}\right)(1 - f_{LLS}).$$

Using Eq. 3.32, and noting 1 – = $f_{LLS} = f_{gLS}$,

$$\left(v_{TB} - v_{gTB}\right)(1 - f_{LTB}) = \left(v_{TB} - v_{gLS}\right)(1 - f_{LLS}),$$

so that

$$v_{gTB} = v_{TB} - \left(v_{TB} - v_{gLS}\right) \frac{f_{gLS}}{1 - f_{LLS}}. \qquad (3.34)$$

For the in-situ velocity of the gas phase in the liquid slug v_{gLS}, Ansari et al. (1994) used

$$v_{gLS} = 1.2v_m + v_\infty f_{LLS}^{1/2}, \quad (3.35)$$

where v_∞ is the small-bubble rise velocity estimated with the Harmathy (1960) correlation. For the falling liquid-film velocity v_{LTB}, they used

$$v_{LTB} = 9.916\left[gd\left(1-\sqrt{f_{gTB}}\right)\right]^{1/2}. \quad (3.36)$$

Ansari et al. (1994) calculated the liquid holdup in the liquid slug, $f_{gLS} = 1 - f_{LLS}$, on the basis of the correlation of Schmidt (1977) data, as follows:

$$f_{gLS} = \frac{v_{sg}}{2.65v_m + 0.425}, \quad (3.37)$$

where the velocities are in SI units (m/s); 0.425 m/s will have to be replaced by 1.394 ft/sec if the other velocities are in ft/sec. By combining Eqs. 3.29 through 3.35, one obtains

$$\left(9.916\sqrt{gd}\right)\left(1-\sqrt{f_{gTB}}\right)^{1/2} f_{LTB} + \overline{A} = v_{TB}\left(1-f_{LTB}\right), \quad (3.38)$$

where

$$\overline{A} = v_{TB}f_{gLS} + (1-f_{gLS})\left\{v_m - f_{gLS}\left[v_\infty(1-f_{gLS})^{1/2}\right]\right\}. \quad (3.39)$$

The solution procedure is detailed in Brill and Mukherjee (1999). To solve for f_{LTB} using a successive iterative approach, we can rewrite Eq. 3.36 as

$$v_{LTB}f_{LTB} + v_{TB}f_{LTB} = v_{TB} - \overline{A}.$$

That is,

$$f_{LTB} = \frac{v_{TB} - \overline{A}}{v_{LTB} + v_{TB}}. \quad (3.40)$$

Estimating liquid holdup using this approach requires simultaneous solution of Eqs. 3.32 through 3.40. Shoham (2006, 153) shows a way to combine these equations into one and solve it using the Newton-Raphson method. We show the application of the model with an example problem at the end of this chapter.

Ansari et al. (1994) also used the presence of a developing slug flow zone, where the Taylor bubble has a cap that is a very large fraction of its total length. For detail of the delineation of this zone and estimating various flow parameters for it, the reader is referred to Ansari et al. (1994) and/or Brill and Mukherjee (1999).

***Taylor Bubble Rise Velocity*.** Following the classical work of Davies and Taylor (1949), the Taylor bubble rise velocity in vertical circular channels $v_{\infty T}$ in slug flow is written as

$$v_{\infty T} = C_2 \sqrt{gd\left(\rho_L - \rho_g\right)/\rho_L}. \qquad (3.41)$$

Analyses and data presented by a number of researchers show that the constant C_2 is influenced by the forces of inertia, viscosity, and surface tension. Wallis (1969) showed that

$$C_2 = 0.35\left(1 - e^{-0.029\mathrm{N_f}}\right)\left[1 - e^{(3.37 - 0.029\mathrm{E_o})/m}\right]. \qquad (3.42)$$

where N_f is the inverse viscosity number and E_o represents the Eotvos number. Thus,

$$\mathrm{N_f} = \sqrt{d^3 g\left(\rho_L - \rho_g\right)\rho_L/\mu_L^2} \qquad (3.43)$$

and

$$\mathrm{E_o} = d^2 g\left(\rho_L - \rho_g\right)/\sigma. \qquad (3.44)$$

The value of the parameter m depends on N_f.

$$\begin{aligned} m &= 10, && \text{for} \quad \mathrm{N_f} > 250 \\ &= 69\mathrm{N_f}^{-0.35}, && \text{for} \quad 18 < \mathrm{N_f} < 250. \\ &= 25, && \text{for} \quad 18 < \mathrm{N_f} \end{aligned} \qquad (3.45)$$

For large values of N_f (>300) and E_o (>100), Eq. 3.41 reduces to C_2 = 0.345.

For air/water flow through a 2-in. pipe at standard conditions, N_f = 35,000 and E_o = 322. For a 100-cp oil under similar conditions (with σ = 30 dynes/cm), N_f = 350 and E_o = 817. Therefore, for most practical purposes, $C_2 \approx 0.35$ and Eq. 3.41 for Taylor bubble rise velocity becomes

$$v_{\infty T} = 0.35\sqrt{gd\left(\rho_L - \rho_g\right)/\rho_L}. \qquad (3.46)$$

Often $\rho_L >> \rho_g$, in which case Eq. 3.46 further simplifies to $v_{\infty T} = 0.35\sqrt{gd}$.

***Pressure Gradient*.** The total pressure gradient during slug flow can be obtained by adding the three components as shown in Eq. 2.19, making use of Eq. 3.27 to estimate holdup. Because accelerational and frictional contribution to the total pressure drop is small, the homogeneous model may be used to estimate these two components, as in the case of bubbly flow.

Ansari et al. (1994) and Collier (1981, p.11) suggested that the wall shear stress around a Taylor bubble can be ignored. That is because some liquid flows downward as a film against the Taylor bubble, while most of the liquid flows upward in the liquid

slugs. Therefore, they recommended that the frictional pressure drop for the liquid slug, using the mixture density of the slug, ρ_{LS}, and its length, $(1-\beta)_z$, be used to calculate frictional pressure loss for the entire cell. For estimating the static-head component, Ansari et al. (1994) suggested that we assume that the entire Taylor bubble section is 100% gas, while the liquid slug contains f_{gLS} fraction gas. Therefore, in their model, the liquid slug density, ρ_{LS}, the static head, $(dp/dz)_H$, and the friction head, $(dp/dz)_F$, are given by

$$\rho_{LS} = \rho_L f_{LLS} + \rho_g (1 - f_{LLS}), \quad (3.47)$$

$$\left(\frac{dp}{dz}\right)_H = \frac{g}{g_c}\left[\rho_{LS}(1-\beta) + \beta\rho_g\right], \quad (3.48)$$

and

$$\left(\frac{dp}{dz}\right)_F = \frac{f_{LS}\rho_{LS}(1-\beta)v_m^2}{2d\,g_c}. \quad (3.49)$$

Ansari et al. (1994) neglected acceleration in this flow regime. Note that because $\rho_{LS}(1-\beta)$ is approximately equal to ρ_m, the frictional component estimated with Eq. 3.49 is not very different from that using Eq. 2.16.

3.3.3 Churn Flow. The chaotic nature of churn flow causes difficulty not only in delineating this flow regime but also in modeling it. Consequently, this flow pattern has not been investigated extensively. However, a number of investigators (Govier and Aziz 2008; Hasan et al. 1988; Hasan and Kabir 1988b; among others) suggested that the drift-flux model may be applied to the churn flow pattern. Specifically, Govier and Aziz (2008) recommended that the equations developed for slug flow be used for the churn flow regime. This approach is also suggested by Fernandes et al. (1983) for circular channels and by Kelessidis and Dukler (1989) and Caetano et al. (1992b) for annuli. Subsequent experimental observations of Mao and Dukler (1993) also lend credence to this suggestion. Kaya et al. (2001) used a modification of this approach in vertical and deviated wells.

Although the bubble shape during churn flow is quite different from that in slug flow, the rise velocities in these two regimes are probably not much different. In addition, because the mixture velocity is much higher than the bubble rise velocity during churn flow, a small error in estimating v_{tT} does not significantly affect holdup estimation. However, an accurate estimation of the flow parameter, C_o, is important for computing holdup in churn flow. The bubble concentration profile is likely to be different from that in slug flow because of the characteristic churning motion of this flow regime, which tends to make the mixture velocity and gas concentration profiles flat. This argument leads to a C_o value lower than 1.2. We recommend a value of 1.15 for C_o in churn flow.

3.3.4 Annular Flow. In annular flow, gas flows through the central core of the pipe, while liquid flows along the wall as a film. Therefore, the system can be viewed as single-phase flow of gas through a pipe, in which its walls are formed by the liquid film. If we assume that no liquid is being carried as droplets in the gas phase and that the gas/liquid interface is smooth, then the problem reduces to estimating pressure drop in single-phase gas flow. For such an ideal annular flow, we do not need to estimate holdup, given that we are modeling a true single-phase flow, except that the pipe diameter must be reduced somewhat. The liquid-film thickness is typically less than 10% of the pipe diameter, thus introducing a negligible error.

Unfortunately, annular flow is rarely ideal. Usually, a certain fraction of the liquid is carried as droplets in the gas stream. Often, the amount of entrained liquid is a substantial portion of the total liquid flow. The existence of liquid droplets in the gas core requires the core fluid density to properly account for the droplets. More important, the gas/liquid interface is usually wavy, thereby causing difficulty while establishing an appropriate friction factor. Frictional loss constitutes a very large fraction of the total pressure gradient in annular two-phase flow; consequently, an accurate estimation of the friction factor becomes highly important.

Consider the gas core, as shown in **Fig. 3.11,** and assume the liquid droplet velocity to be equal to that of the gas in the core. Using v_c for the core fluid in-situ velocity and v_g for the gas in-situ velocity, we can write the equation for the total pressure gradient during annular flow as

$$-\frac{dp}{dz} = \frac{1}{g_c}\left[g\rho_c + \frac{f_c v_c^2 \rho_c}{2d(1-2\delta)} + \rho_c v_g \frac{dv_g}{dz}\right]. \qquad (3.50)$$

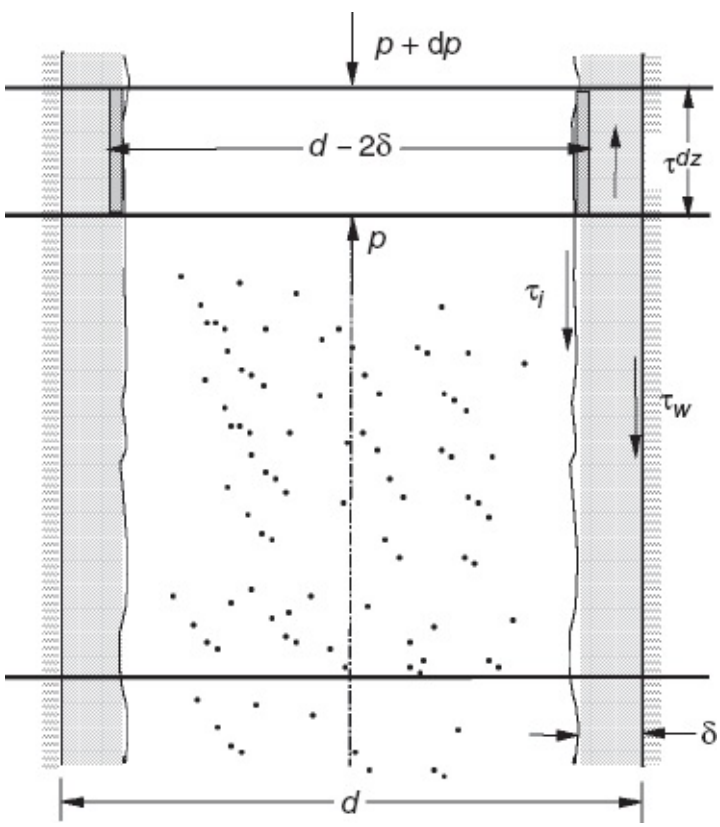

Fig. 3.11—Vertical annular flow.

The differential, dv_g/dz, in the acceleration term may be rewritten as $-v_g(dp/dz)$ using the gas law, which results in the expression for pressure gradient,

$$-\frac{dp}{dz} = \frac{1}{g_c}\frac{g\rho_c + \left\{f_c v_c^2 \rho_c / \left[2(1-\underline{\delta})d\right]\right\}}{1-\left(\rho_c v_c^2\right)/\left(pg_c\right)} \quad (3.51)$$

The problem then reduces to that of estimating the density of the fluid in the core, ρ_c; the friction factor, f_c, for gas flowing through a rough pipe; and the liquid-film thickness, δ.

Entrainment Estimation. To determine the density of the fluid flowing through the core, we must estimate the fraction of total liquid that is entrained in the gas core. Entrainment is defined as the fraction, E, of the input liquid that is entrained in the vapor core. Entrainment increases with increased gas velocity. We recommend the following correlation that Wallis (1969, p.396) presented for E, as a function of critical gas velocity, v_{sgc}.

$$E = 1 - e^{-0.125(v_{sgc}-1.5)}, \quad (3.52)$$

where critical gas velocity is a dimensionless number that depends on the superficial gas velocity, fluid densities, gas viscosity, and surface tension. The following expression presents the critical gas velocity:

$$v_{sgc} = \frac{10^4 v_{sg}\mu_g}{\sigma}\sqrt{\rho_g / \rho_L} \quad (3.53)$$

Note that entrainment varies between zero and unity. Therefore, when Eq. 3.52 calculates a negative value for E, it should be set to zero, while a value greater than unity should be set equal to unity. Once entrainment is estimated, the core fluid density is determined by considering the gas core as the system. In that case, the superficial gas velocity remains equal to v_{sg}, but the superficial liquid velocity becomes Ev_{sL} because only the entrained fraction of the liquid is in this system. Therefore, we define superficial core fluid velocity, v_{sc}; in-situ core fluid velocity, v_c; and core fluid density, ρ_c as

$$v_{sc} = v_{sg} + Ev_{sL}, \quad (3.54)$$

and

$$\rho_c = \left(\rho_L E v_{sL} / v_{sc}\right) + \left(\rho_g v_{sg} / v_{sc}\right). \quad (3.55)$$

The in-situ core velocity v_c is needed for calculating frictional pressure loss. The in-situ core velocity is obtained by dividing the core superficial velocity by the cross-

sectional area of the gas core. With reference to Fig. 3.11, the gas core area equals $\pi(d - 2\delta)^2/4$, where δ is the liquid-film thickness. Therefore, in terms of dimensionless liquid-film thickness, $\underline{\delta} = (\delta/d)$, v_c is given by

$$v_c = v_{sc} / (1 - 2\underline{\delta})^2. \quad (3.56)$$

Film Friction Factor. There are a number of correlations available for estimating the liquid-film roughness or film friction factor, f_c. Probably the best correlation is the one proposed by Wallis (1969, p.320), which relates the film friction factor to the wall friction factor f and the dimensionless liquid-film thickness, $\underline{\delta}$ (= δ/d). The wall friction factor is the one that will experience gas flowing through a smooth pipe. The equation for this correlation is written as

$$f_c = f\left(1 + 300\underline{\delta}\right). \quad (3.57)$$

From geometrical considerations, $4\underline{\delta}$ equals liquid holdup, f_L. Thus, Eq. 3.57 is rewritten as

$$f_c = f\left(1 + 75 f_L\right), \quad (3.58)$$

where f is estimated with the Blasius equation for smooth pipes, $f = 0.32/\mathrm{Re}_c^{0.25}$. Ansari et al. (1994) pointed out that the expression for f_c proposed by Whalley and Hewitt (1978) is more accurate when entrainment, E, is smaller than 0.9. Thus

$$f_c = f\left[1 + 24\underline{\delta}\left(\rho_L / \rho_g\right)^{1/3}\right] \text{ if } E < 0.9. \quad (3.59)$$

An accurate estimation of the liquid-film thickness δ or the liquid holdup f_L is needed because the core friction factor is extremely sensitive to this entity. For this purpose, f_L can be computed with the separated flow model, as described in Chapter 2 (Eq. 2.32). To estimate f_L with Eq. 2.32, the effective liquid and gas mass fluxes must be used.

Several rigorous models for annular flow have been developed in recent years. These models incorporate velocity profiles in the liquid film and the gas core in an attempt to better relate the interfacial friction. Although complex, some of these models are two-dimensional in nature, which allows a better description of physics of flow. In the following, we describe the model proposed by Ansari et al. (1994).

The method proposed by Ansari et al. (1994) is similar to the one previously described (Eq. 3.50), although the researchers neglected the accelerational component. They wrote the expression for pressure gradient for the gas core as

$$-\left(\frac{\mathrm{d}p}{\mathrm{d}z}\right)_c = \frac{g\rho_c}{g_c} + \frac{f_c v_c^2 \rho_c}{2 d g_c (1 - 2\underline{\delta})}. \quad (3.60)$$

For estimating core density, they use Eq. 3.55, along with Eq. 3.52. For friction factor

computation, they recommended the use of Eq. 3.57 when $E > 0.9$, and Eq. 3.59 when $E \leq 0.9$. To calculate the liquid-film thickness, Ansari et al. (1994) noted that the pressure gradient for the gas core must be equal to that for the liquid film. Analogous to Eq. 3.60, they wrote the expression for $(dp/dz)_L$ as

$$-\left(\frac{dp}{dz}\right)_L = \frac{g\rho_L}{g_c} + \frac{2f_{LF}v_{sL}^2(1-E)^2\rho_L}{64g_c d\underline{\delta}^3(1-2\underline{\delta})^3} - \frac{f_c v_c^2(1-2\underline{\delta})\rho_c}{2g_c d\underline{\delta}(1-\underline{\delta})} \quad (3.61)$$

Equating $(dp/dz)_L$ and $(dp/dz)_c$, Ansari et al. (1994) arrived at the expression

$$\frac{f_c v_c^2 \rho_c}{2g_c d\underline{\delta}(1-\underline{\delta})(1-2\underline{\delta})} = \frac{g(\rho_L-\rho_c)}{g_c} + \frac{2f_{LF}v_{sL}^2(1-E)^2\rho_L}{64g_c d\underline{\delta}^3(1-2\underline{\delta})^3} \quad (3.62)$$

Eq. 3.62 is solved iteratively for the single unknown, $\underline{\delta}$.

Gomez et al. (2000) and Xiao et al. (1990) proposed similar methods on the basis of the two-fluid approach. Because the authors claim the model to be applicable at all inclination angles, we discuss it under horizontal annular flow in Chapter 4.

Figs. 3.12 and 3.13 show that the simple mechanistic approach used by Hasan and Kabir (1988b) (Eqs. 3.23, 3.26, and 3.57) estimates the liquid holdup and pressure drop data in all four flow regimes within engineering accuracy. The newer and rigorous mechanistic models perform even better, as discussed earlier in this section.

***Simplified Annular Flow Model*.** The mechanistic model for annular flow presented above is complicated; requires complex algorithms for computation of various elements in the model, especially the liquid-film thickness; and requires empirical closure relations. Our experience shows that at the high phase velocities involved in annular flow, the simple homogeneous model performs quite well in estimating pressure loss and liquid holdup. This contention is evident in **Fig. 3.14,** as shown in Hasan et al. (2010b).

3.4 Discussion

In this chapter, our emphasis has been on mechanistic modeling. We have presented models to determine flow pattern that exists under the given flow condition and offered expressions for estimating liquid holdup and pressure drop for that particular flow pattern. An example problem is solved to show the computational procedure that is applied. Mechanistic modeling, besides being accurate over a variety of situations, provides insights into mechanics of flow while solving field problems. Chapter 5 will make this point amply clear. Nonetheless, which approach is most suitable to solve a given problem remains in question. Unfortunately, there is no single answer. Although our preference is to recommend the use of a mechanistic model to solve all flow problems, the Hagedorn-Brown empirical correlation and its modifications appear to work quite well in many field settings.

Because some models (Xiao et al. 1990; Kaya et al. 2001) are applicable to wells

of any deviation angle, we discuss them in Chapter 4. However, the overall performance of various methods, such as those of Hagedorn and Brown (1965), Aziz et al. (1972), Duns and Ros (1963), Ansari et al. (1994), and Hasan and Kabir (1988b), are comparable. When annular flow is encountered, such as in gas wells producing gas and liquids (condensate and/or water), the Ansari et al. model appears to perform better than others. However, Hasan and Kabir (2007) have shown that the simple homogeneous model performs just as well in estimating pressure gradient in annular two-phase flow.

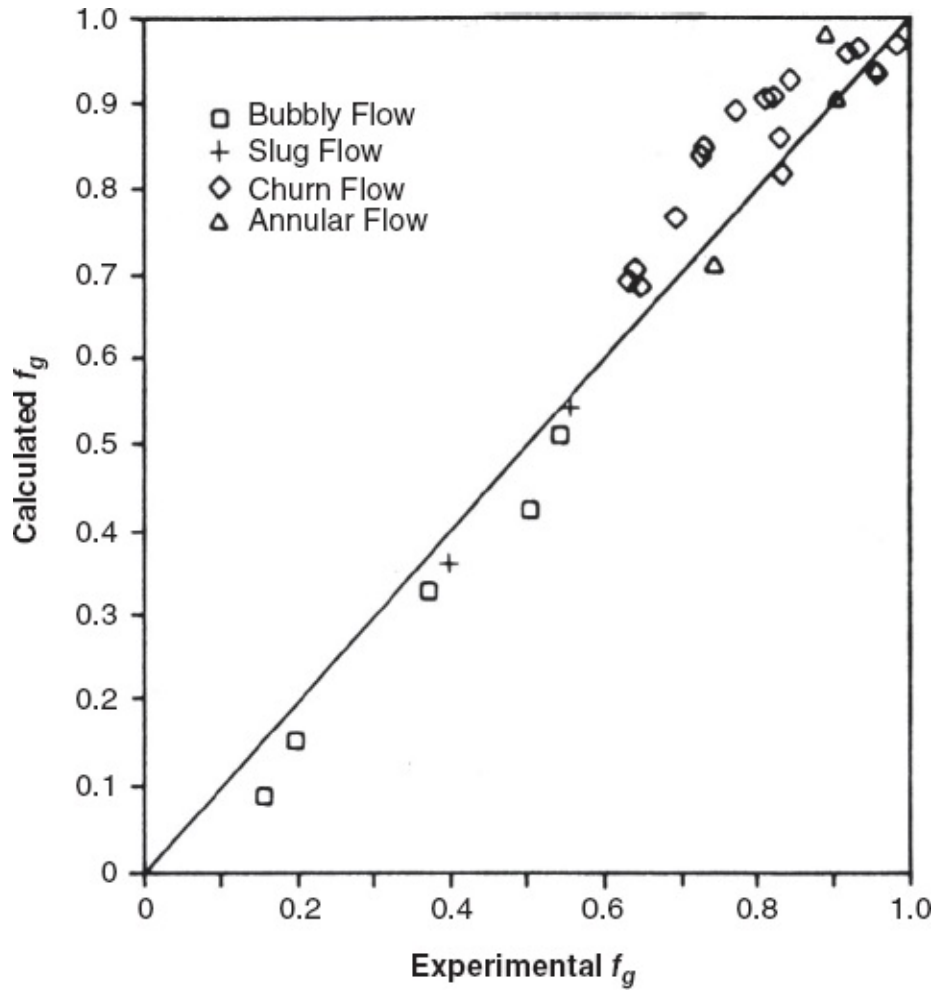

Fig. 3.12—Laboratory data show good agreement with calculations in all flow regimes (after Hasan and Kabir 1988b).

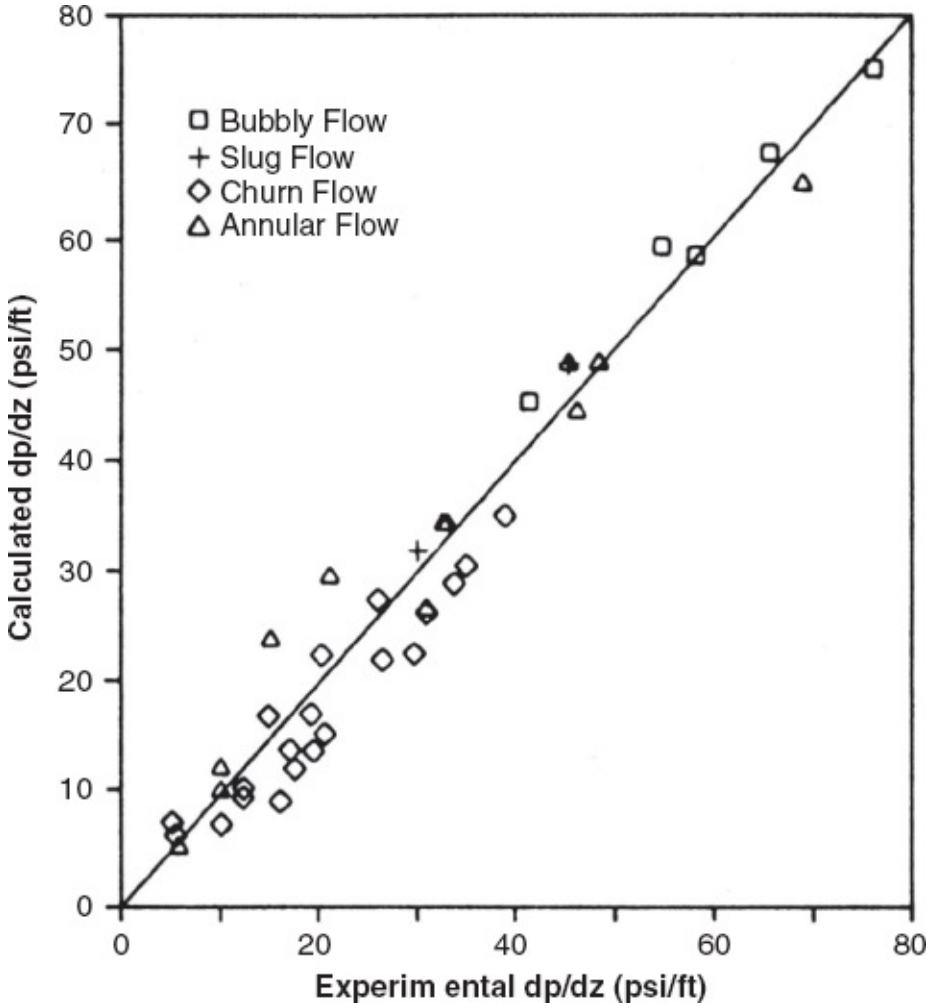

Fig. 3.13—Laboratory data lend support to pressure-gradient calculations in all flow regimes (after Hasan and Kabir 1988b).

In slug flow, the Hagedorn-Brown correlation has a slight edge over all others. Note that this correlation owes its success to the large database used in its development and the subsequent modifications that it has undergone (Brill and Mukherjee 1999). A comparative study by Pucknell et al. (1993) involving eight North Sea fields showed that mechanistic models provided overall superior results in both oil and gas wells. Similar success was reported by Gomez et al. (2000) while testing their mechanistic model with field data. Note that Pucknell et al. (1993) reported that the Hasan-Kabir model provided the smoothest transition, even before the introduction of Eq. 3.28. We find that the differences in predictive accuracy in most of the recent models are minimal; Hasan et al. (2010b) makes this point with high-quality field data.

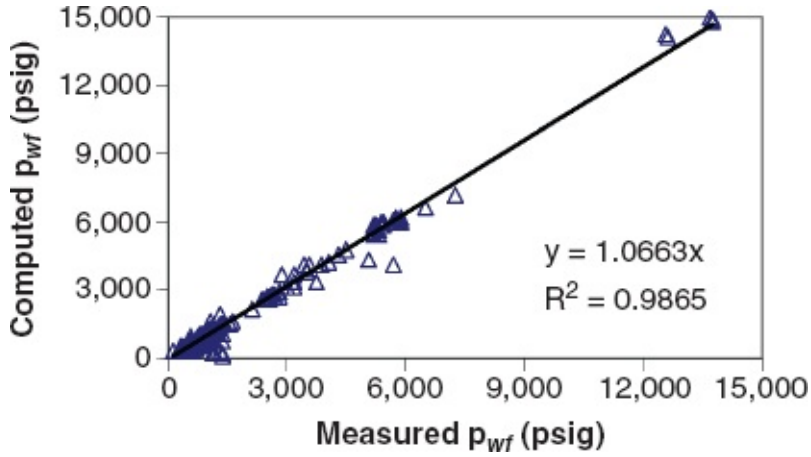

Fig. 3.14—Agreement of the homogeneous model with field data (Hasan, A. R., Kabir, C. S., and Sayarpour, M. 2010b. Courtesy Elsevier).

One problem, common to most methods, is the lack of smooth transition from one flow regime to another. Abrupt transitions cause discontinuities, which may appear in wellbore pressure profiles and may also precipitate problems while solving transient flow situations. They are discussed in Chapter 9. To alleviate this awkward flow regime transition problem, we presented Eq. 3.28 to address the bubbly-to-slug flow transition. The sudden change in the value of C_o for transition from slug to churn flow and from churn to annular flow can be smoothed empirically; Chapter 5 discusses this approach.

Throughout this chapter and the next, we present a simple, yet accurate model for two-phase flow in wellbores with various configurations and flow directions. Chapter 5 presents a summary of this unified model.

Field Example 3.1. A 5,151-ft vertical well produces 23 °API dry oil at 1,140 STB/D through a 2.99-in.-ID tubing. The gas/oil ratio is 450 scf/STB, and the gas gravity is 0.80. The following property values and computed fluid parameters are available at the wellhead, where pressure is 505 psig:

v_{sL} = 1.601 ft/sec

μ_L = 13.09 cp

v_{sg} = 2.784 ft/sec

μ_g = 0.019 cp

ρ_L = 55.042 lbm/ft^3

σ = 31.6 dynes/cm = 0.0696 lbm/sec^2

ρ_g = 2.17 lbm/ft^3

Calculate the pressure gradient at this point.

Solution: Flow Pattern. The transition criteria to consider begin with Eqs. 3.6 and 3.8.

Eq. 3.6: $v_\infty = 1.53\,[g\sigma(\rho_L - \rho_g)/\rho_L{}^2]^{0.25}$

$= 1.53\,[(32.2)(0.0696)(52.79/55.042)^2]^{0.25} = 0.680$ ft/sec.

Eq. 3.8: $v_{\infty T} = 0.35\,[gd\,(\rho_L - \rho_g)/\rho_L]^{0.5}$

$= 0.35\,[(32.2)(0.25)(52.87)/55.042]^{0.5} = 0.971$ ft/sec.

Because $v_{\infty T} > v_\infty$, Eq. 3.5 would apply for transition from bubbly to slug flow.

Eq. 3.5: $v_t = 0.429\,v_{sL} + 0.357\,v_\infty$

$= (0.429)(1.601) + (0.357)(0.680) = 0.930$ ft/sec.

Because the actual $v_{sg} > 0.93$ ft/sec, the flow pattern is *not* bubbly. Let us now check for annular flow using Eq. 3.12

Eq. 3.12: $v_{sg} = 3.1\,[(32.2)(0.0696)(52.85)/2.17^2]^{1/4} = 6.939$ ft/sec.

Eq. 3.12 shows the required superficial gas velocity for annular flow to be 6.939 ft/sec, while the actual v_{sg} is 2.784 ft/sec. Thus, flow is *not* annular.

The flow pattern, therefore, must be slug, churn, or dispersed bubbly. For slug flow to exist, the mixture velocity must be less than that given by Eq. 3.10, repeated below. Note that the actual mixture velocity is $v_{sg} + v_{sL} = 4.446$ ft/sec. Eq. 3.10 requires an estimate of the friction factor. We use a value of $f = 0.04$; its computation will be shown later.

$$2v_m^{1.2}\left(\frac{f}{2d}\right)^{0.4}\left(\frac{\rho_L}{\sigma}\right)^{0.6}\sqrt{\frac{0.4\sigma}{g(\rho_L-\rho_g)}} = 0.725 + 4.15\sqrt{\frac{v_{sg}}{v_m}}.$$

The left-hand side (LHS) of Eq. 3.10 is $2(4.446)^{1.2}\,(0.04/0.5)^{0.4}\,(55.042/0.0696)^{0.6}$ $\{0.4(0.0696)/[(32.2)(52.87)]\}^{0.5} = 0.9677$. The right-hand side (RHS) of Eq. 3.10 is $0.725 + 4.15\,(2.824/4.425)^{0.5} = 4.0405$. Therefore, the mixture velocity is too low (LHS is too low compared to the RHS) to support dispersed bubbly flow. This test also implies that the flow pattern is *not* churn. This process of elimination leads us to slug flow occurring at the wellhead.

Solution: Gas Volume Fraction and Pressure Gradient. The Hasan-Kabir (1988) and Ansari et al. (1994) models can be used to determine the gas volume fraction and the pressure gradient.

The Hasan-Kabir (1988) Model.

Gas Volume Fraction:

$x = v_{sg}\rho_g/(v_{sg}\rho_g + v_{sl}\rho_l) = (2.845)(2.17)/[(2.845)(2.17) + (1.601)(55.042)] = 0.066.$

Eq. 3.28: $\bar{v}_\infty = 0.68\,[1 - e^{-0.93/2.845}] + 0.971e^{-0.93/2.845} = 0.89$ ft/sec.

Eq. 3.27: $f_g = 2.845/[1.2(4.445) + 0.89] = 0.457$. Holdup: $f_L = 0.543$.

Pressure Gradient:

Eq. 2.19: $\rho_m = 55.042\,(0.543) + 2.17\,(0.457) = 30.9$ lbm/ft^3.

Eq. 2.17: $(dp/dz)_H = \rho_m\, g/g_c = 30.9$ psf/ft $= 0.2146$ psi/ft.

Eq. 2.25: $\mu_m = 0.934(13.09) + 0.066(0.019) = 12.2$ cp.

$Re_m = (0.25)(4.445)(30.44)/(12.796 \times 0.000672) = 3{,}903$.

Eq. 1.11: $f_m = 0.032\ (3{,}903)^{-0.25} = 0.04$.

Eq. 2.16: $(dp/dz)_F = (0.04)(4.445)^2(30.9)/[2(32.2)(0.25)]$

$= 1.517$ psf/ft $= 0.0105$ psi/ft.

Eq. 2.19: $dp/dz = 0.2146 + 0.\ 0105 = 0.221$ psi/ft = total pressure gradient at wellhead.

To perform pressure-traverse calculations, we can now use this pressure gradient to remain constant for the next few hundred feet of measured depth (MD) and estimate pressure at that point. For example, pressure increase for a 400-ft section will be 88.4 psig (= 400 ft × 0.221 psi/ft). Therefore, pressure at 400 ft below the wellhead amounts to 593.4 psig (= 505 + 88.4). Now that we have a reasonable estimate of pressure at MD = 400 ft, we can compute pressure gradient here. The computed gradient at this depth will be higher because of reduced volume of free gas and lower volume fraction of that gas. Therefore, pressure gradient here will be slightly higher; we calculated that to be 0.269 psi/ft. We can now take the average of these two pressure gradients—0.245 psi/ft—and recalculate the pressure at MD = 400 ft, which turns out to be 598 psig (505 + 0.245 × 400).

The Ansari et al. (1994) Model.

Gas Volume Fraction:

Eq. 3.37: $f_{gLS} = 2.845/[2.65(4.445) + (1.394)] = 0.216$;

$f_{LLS} = 1 - 0.216 = 0.784$.

Eq. 3.35: $v_{gLS} = 1.2(4.445) + (0.68)(0.784)^{0.5} = 5.94$ ft/sec;

$v_{TB} = 1.2(4.445) + 0.971 = 6.31$ ft/sec.

Eq. 3.39: $\overline{A} = (6.31)(0.216) + (0.784)\{4.445 - 0.216[0.68(0.784)^{0.5}]\}$

$= 4.75$ ft/sec.

Eq. 3.36: $v_{LTB} = 9.916\ [32.2(0.25)\ (1-\sqrt{f_{gTB}})]_{0.5} = 28.13\ (1-\sqrt{f_{gTB}})_{0.5}$.

Eq. 3.40: $f_{LTB} = [6.31 - 4.75]/[6.31 + v_{LTB}]$.

Note, however, that $f_{LTB} = 1 - f_{gTB}$, requiring simultaneous solutions of Eqs. 3.36 and 3.40. Then, trial and error gives $f_{LTB} = 0.118$; $v_{LTB} = 6.94$ ft/sec.

Eq. 3.33: $(6.28 + 6.93)\ (0.118) = (6.28 - v_{LLS})\ (0.784)$; hence, $v_{LLS} = 4.30$ ft/sec.

Eq. 3.34: $(6.28 - v_{gTB})\ (1-0.118) = (6.28 - v_{gLS})\ (0.216)$; $v_{gTB} = 6.19$ ft/sec.

Eq. 3.30: $2.824 = \beta(6.19)(1 - 0.118) + (1 - \beta)(5.912)(1 - 0.785) = >\beta = 0.37$.

Pressure Gradient:

Eq. 3.47: $\rho_{LS} = 55.042\ (0.784) + 2.17\ (0.216) = 43.6$ lbm/ft^3.

Eq. 3.48: $(dp/dz)_H = [\rho_{LS}\ (1 - b) + \rho_g\beta]g/g_c = 28.21$ psf/ft $= 0.196$ psi/ft.

$\mu_{LS} = \mu_g f_{gLS} + \mu_L\ (1-f_{gLS}) = 10.27$ cp.

$Re_{LS} = dv_m\rho_{LS}/\mu_{LS} = 7004$; $f_{LS} = 0.0313$.

Eq. 3.49: $(dp/dz)_F = (0.0316)(4.425)^2(43.7)(1 - 0.37)/[2(32.2)(0.25)]$

$= 1.06$ psf/ft $= 0.00734$ psi/ft.

Eq. 2.15: $dp/dz = 0.196 + 0.00734 = 0.203$ psi/ft = total pressure gradient at wellhead.

Calculations shown in Field Example 3.1 for the two mechanistic models were performed for the conditions prevailing at the wellhead of an actual well. **Table 3.1** presents the results of pressure-traverse calculations, and **Fig. 3.15** compares the same information with measured data. This example is a continuation of the example discussed in Chapter 2, where we compared the solutions of models without considering flow pattern maps.

Note that because the computation was performed top-down, discrepancy occurs at the well bottom. Experience shows that when computations are performed along the direction of flow—that is, bottom-up—errors decrease significantly. In this example, we wanted to show the complex computations involved for the slug flow pattern existing at the wellhead condition. To compare the results from all models and correlations at this point, we decided on a top-down calculation. The use of fluid property correlations inevitably influences the computed results. In all examples in this book, presenting simplified spreadsheet calculations, we used the Standing (1981) correlation for bubblepoint pressure and formation volume factor, Dranchuk and Abou-Kassem (1975) correlation for gas-law deviation factor (*z*-factor), Beggs and Robinson (1975) correlation for dead- and live-oil viscosity, and Baker and Swerdloff (1956) correlation for oil surface tension.

Note that friction factors and frictional pressure gradients calculated by the two approaches are quite different on a percentage basis. However, because friction contributes only a small fraction to the total pressure drop, the differences in the pressure profiles computed by the two models depend almost totally on the computed static heads. This observation reinforces our belief that great sophistication for calculating frictional pressure drop is unwarranted for most vertical and near-vertical wells.

	Pressure (psig)		
Depth (ft)	Data	Hasan and Kabir (1988)	Ansari et al. (1994)
0	505	505	505
400	587	598	590
650	647	660	647
1,150	777	790	768
1,650	920	937	899
2,150	1,074	1,077	1,039
2,650	1,237	1,231	1,186
3,150	1,407	1,391	1,341
3,650	1,582	1,557	1,502
4,150	1,850	1,726	1,668
4,650	1,960	1,899	1,836
5,151	2,105	2,075	2,007

Table 3.1—Pressure-traverse calculation.

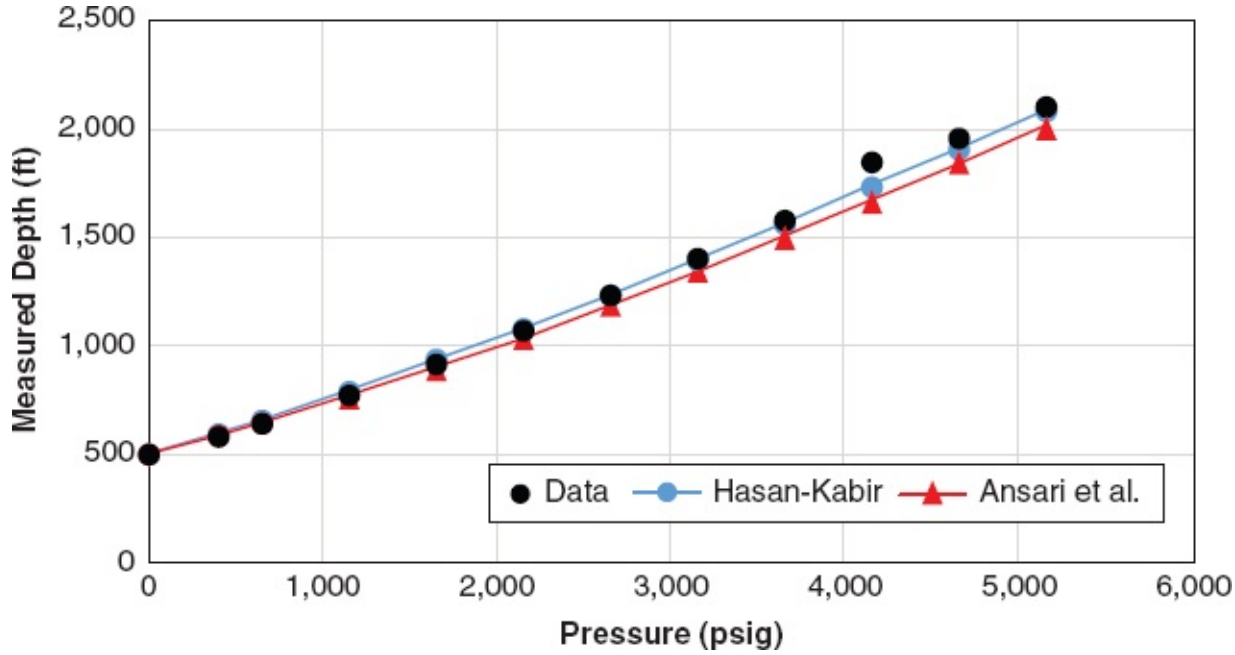

Fig. 3.15—Comparison of mechanistic models with field data.

Summary

In this chapter, we have presented a mechanistic approach for two-phase flow modeling in vertical systems. Models have been developed for all four major flow regimes—bubbly, slug, churn, and annular. These models use flow pattern maps and individual transition criteria for discerning flow regimes.

The slip between the phases is modeled by noting the effect of buoyancy and the tendency of the gas phase to flow through the channel center. The flowing mixture densities, calculated from these expressions, are useful for pressure-gradient calculations. Note that the static head $g\rho_m/g_c$ is quite often the major contributor to the total head loss for vertical two-phase flow in wellbores. A number of researchers are in good agreement with the performance of the models presented in this chapter, showing data from both the laboratory (Ansari et al. 1994) and the field (Pucknell et al. 1993; Kabir and Hasan 1990; Hasan et al. 2010b). We did not make strong recommendation for any particular model, nor did we present an overall approach for pressure-traverse calculation. For a summary of the approach for pressure-traverse calculation, the reader is referred to Chapter 5.

Nomenclature

(dp/dz) = pressure gradient, psi/ft

$(dp/dz)_c$ = pressure gradient for the core fluid, psi/ft

$(dp/dz)_F$ = frictional pressure gradient, psi/ft

$(dp/dz)_{fL}$ = pressure gradient for the liquid film, psi/ft

$(dp/dz)_H$ = static pressure gradient, psi/ft

$(dp/dz)_L$ = pressure gradient for liquid flowing alone in the channel, psi/ft

A = cross-sectional area for fluid flow, ft^2

A_c = core cross-sectional area

C = constant in Lockhart-Martinelli parameter, dimensionless

C_o = flow parameter in bubbly flow, dimensionless

d = pipe or well diameter, in.

E = entrainment

Eo = Eotvos number [= $gd^2(\rho_L-\rho_g)/s$], dimensionless

f = friction factor, dimensionless

f_c = film friction factor for gas core in annular flow, dimensionless

f_g = gas in-situ volume fraction (void fraction), dimensionless

f_{gLs} = gas in-situ volume fraction in liquid slug portion of cell, dimensionless

f_{gTB} = gas in-situ volume fraction in Taylor bubble portion of cell, dimensionless

f_i = interfacial friction factor, dimensionless

f_L = liquid holdup or in-situ volume fraction, dimensionless

f_{LF} = friction factor for the liquid film, dimensionless

f_{LLS} = liquid holdup in liquid slug portion of cell, dimensionless

f_{LTB} = liquid holdup in Taylor bubble portion of cell, dimensionless

f_m = two-phase mixture friction factor, dimensionless

f_s = in-situ gas volume fraction in liquid slug during slug flow, dimensionless

f_T = in-situ gas volume fraction in Taylor bubble during slug flow, dimensionless

G = mass flux = mass flow rate per unit area, lbm/ft^2

g = acceleration because of gravity, ft/sec^2

g_c = conversion factor, 32.17 lbm-ft/lbf-sec^2

L = length, ft

L_s, L_T = length of liquid slug or Taylor bubble in slug flow, ft

L_{sB} = length of liquid slug

L_{TB} = length of a Taylor bubble

m = mass of fluid in a control volume, lbm

m = parameter defined by Eq. 3.45, dimensionless

N_f = inverse viscosity number [= $gd^3\rho_L(\rho_l-\rho_g)]^2/\mu_l$], dimensionless

p = pressure, psi

Re_m = Reynolds number for mixture (= $\rho_m v_m d/\mu_m$), dimensionless

v = fluid velocity, ft/hr

v_∞, $v_{\infty T}$ terminal rise velocity of bubbles in bubbly flow or a Taylor bubble in slug flow, ft/hr

v_c = core fluid velocity, ft/hr

v_d = drift velocity of the lighter phase, ft/hr

v_g, v_L = gas or liquid in-situ velocity, ft/hr

v_{gd}, v_{Ld} = dimensionless phase velocities

v_{gls} = in-situ gas velocity in liquid slug portion of cell, ft/hr

v_{gTB} = in-situ gas velocity in Taylor bubble portion of cell, ft/hr

v_{LLS} = in-situ liquid velocity in liquid slug portion of cell, ft/hr

v_{LTB} = in-situ liquid velocity in Taylor bubble portion of cell, ft/hr

v_m = two-phase mixture velocity, ft/hr

v_∞ = terminal rise velocity of single bubble, ft/hr

$\bar{v}_\infty$ = average rise velocity of small bubbles, ft/hr

v_{sg}, v_{sL} = superficial gas or liquid in-situ velocity, ft/hr

v_{sgc} = critical superficial gas velocity given by Eq. 3.53

v_t superficial gas velocity needed for transition from bubbly to slug flow, ft/sec

v_{TB} = in-situ velocity of Taylor bubble, ft/hr

$v_{\infty T}$ = rise velocity of Taylor bubbles, ft/hr

X = Lockhart-Martinelli parameter, dimensionless

X_M modified Lockhart-Martinelli parameter for annular flow defined by Eq. 3.17, dimensionless

Y_M = ratio of gravitational to gas-phase frictional gradient, dimensionless

z = any vertical well depth, ft

α = well inclination from horizontal, degrees

δ = liquid-film thickness, ft

$\underline{\delta}$ = dimensionless liquid-film thickness (= δ/d)

μ_L = liquid-phase viscosity, cp

μ_m = two-phase mixture viscosity, cp

μ_g = gas viscosity, cp

β = ratio of length of Taylor bubble to total cell, L_T/L, dimensionless

ρ = density, lbm/ft^3

ρ_w = water density, lbm/ft^3

ρ_A = air density, lbm/ft^3

ρ_c, ρ_e = core fluid or earth (formation) density, lbm/ft^3

ρ_g, ρ_L = gas- or liquid-phase density, lbm/ft^3

ρ_{LS} = density of the fluid in liquid slug, lbm/ft^3

ρ_m = two-phase mixture density, lbm/ft^3

σ = surface tension, lbf/sec^2

σ_{wA} = surface tension between air and water, lbf/sec^2

γ_g = gas specific gravity

Subscripts

A	=	air
g	=	gas
L	=	liquid
w	=	water

Superscripts

n = exponent used in Eq. 3.20, dimensionless

Chapter 4

Multiphase Flow: Deviated and Horizontal Wells and Other Systems

4.1 Introduction

Increased offshore production over the last few decades makes multiphase flow from deviated wells a common occurrence. Advances in horizontal and multilateral well technology demand understanding of multiphase flow in complex well architectures. Besides flow in wellbores, pipeline transportation of produced fluids in an undulating terrain, either on the seabed or at the surface, clearly presents significant challenges in understanding the fluid and heat transport behavior for optimal design.

The models and correlations developed for flow in vertical wells are not always applicable for inclined or horizontal flow. Wellbore deviation adds another dimension to the already complex flow phenomena generally observed in vertical wells. Modeling flow pattern transitions and pressure drop in deviated and horizontal wells requires that we account for the effect of well deviation.

Modeling flow behavior also becomes necessary for many other flow geometry and pipe orientations. For example, transient testing of a sucker-rod-pumping well requires holdup and pressure-drop estimates for multiphase fluid in the tubing/casing annulus of a well. Similarly, steam injection and the design of gas anchors often require understanding two-phase behavior when flow occurs downward. Modeling of phase redistribution during shut-in tests might require understanding bubble migration in countercurrent two-phase flow. In addition, flow of oil/water is encountered in many mature oil reservoirs where production-logging diagnosis is required for water management.

In this chapter, we first present empirical correlations and mechanistic models for computing flow patterns and pressure drop in deviated wells. Multiphase flow in horizontal wells is discussed thereafter. We then present models for multiphase flow behavior in annuli, downward direction, and countercurrent flow. The last section discusses two-phase flow of oil and water in vertical and deviated wells.

4.2 Flow in Deviated Wells

Flow of multiphase fluids in vertical pipes is now reasonably well-understood. As described in Chapter 3, a number of models, which allow delineation of flow patterns at any position in the well, are available. Following the flow pattern delineation, estimation of holdup and pressure drop, using models appropriate for the given flow regime, becomes possible. In contrast, understanding multiphase flow behavior in

deviated wells has not matured to the level of its vertical counterpart. Correlations available to determine flow pattern transitions and to estimate holdup and pressure gradient in inclined pipes are largely empirical. Recently, a few mechanistic models for computing flow regime, holdup, and pressure drop have emerged for multiphase flow in deviated wells. In Section 4.2.1, we discuss flow patterns and their determination, using both maps and modeling.

4.2.1 Flow Patterns in Upwardly Inclined Systems. Flow patterns observed in upward-inclined flow are quite similar to those observed in vertical upward flow, especially for near-vertical systems. In other words, we observe bubbly and dispersed bubbly, slug, churn, and annular flow in deviated wells. These flow patterns are shown in **Fig. 4.1.** Slug and churn flows are often lumped together and are called intermittent flow because they behave in a similar manner and are difficult to distinguish. For systems deviated by more than 20° from vertical, churn flow is rarely observed. For near-horizontal systems, the bubbly flow pattern is sometimes absent. Indeed, Taitel et al. (1978) contended that for systems deviated by more than 50° from vertical, bubbly flow never occurs. In addition, for near-horizontal systems, stratified flow is observed.

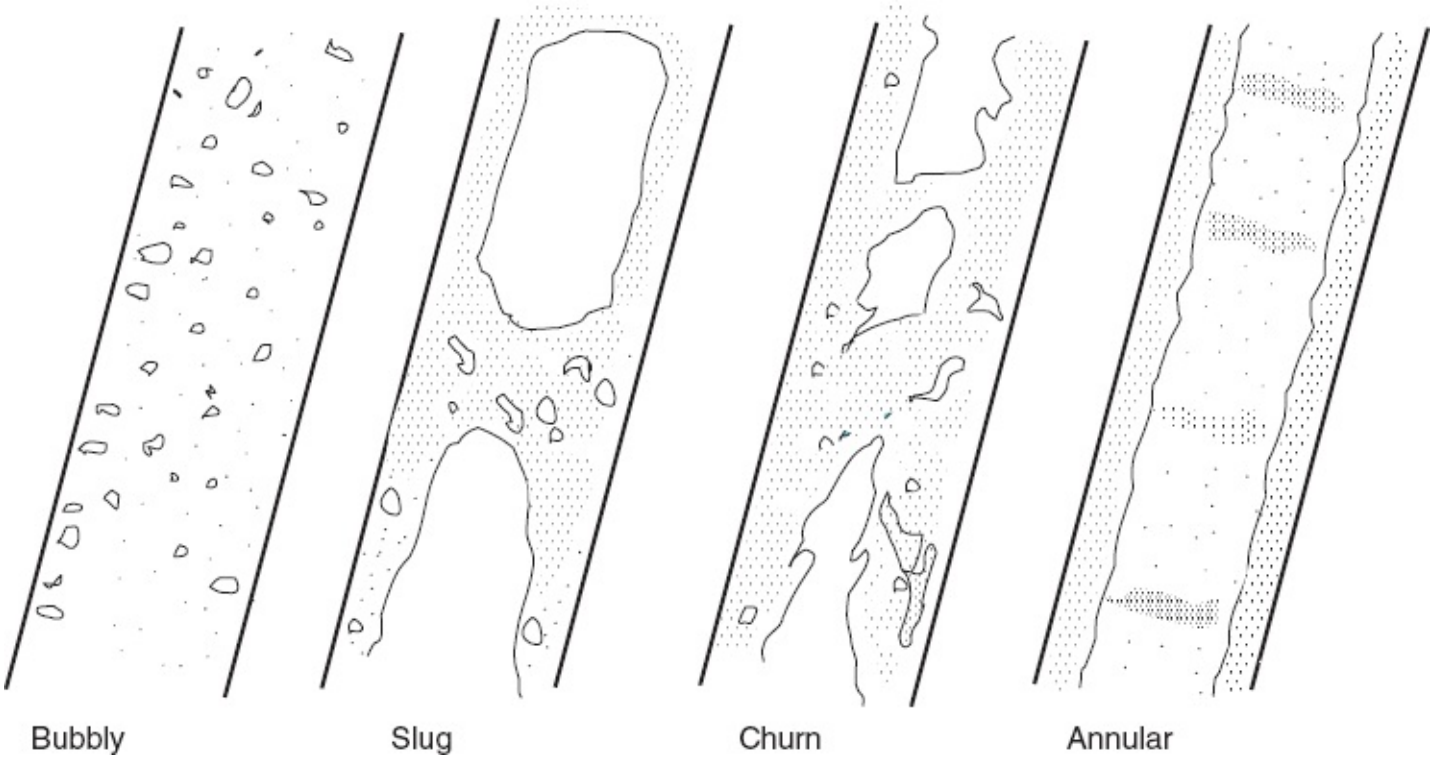

Fig. 4.1—Flow patterns for cocurrent gas/liquid flow in inclined pipes.

One distinction between flow patterns in vertical and inclined systems becomes evident when we examine Fig. 4.1. Because of buoyancy, more of the gas phase tends to flow along the upper wall of the pipe than the lower wall. This gas segregation is particularly true for flow patterns in which phase velocities are

generally small, as with bubbly and slug flow. In these two flow regimes, gravity effect dominates, and bubbles tend to favor the upper portion of the channel. For annular flow, and to some extent for churn and dispersed bubbly flow, strong fluid shear force counteracts gravity, and much of the gas phase tends to flow through the central portion of the channel, as in a vertical system.

Another distinction between vertical and inclined flow is the influence of channel inclination on the shape of the bubbles. The increased radial pressure on the bubbles tends to make them sharper than their counterpart in vertical systems. This observation is particularly true of Taylor bubbles in slug flow. In vertical flow, the Taylor bubbles have been shown, both theoretically and experimentally, to have a symmetrical, hemispherical top. In inclined flow, the top of the Taylor bubble is shaped much more like an ellipsoid than a hemisphere and is no longer symmetrical about the bubble axis. The effect of this shape change on the bubble's rise velocity and holdup is discussed later.

4.2.2 Pattern Transition Criteria. There are very few data sets or correlations available for flow pattern transition in inclined systems. Physical modeling of such systems is even scarcer. The empirical work by Weisman and Kang (1981) on flow pattern transition is a major contribution in this area and is presented first. Modeling approach to pattern transition is then presented with data and analysis from various authors (Taitel et al. 1978, 1980; Weisman and Kang 1981; Barnea et al. 1985; Hasan and Kabir 1988a).

Flow Pattern Maps. The major premise of Weisman and Kang (1981) is that the boundaries of flow patterns existing at very high flow rates are usually unaffected by well deviation. For instance, they found that the transitions to annular flow and dispersed bubbly flow are unaffected by a pipe's inclination angle. This observation, according to Weisman and Kang (1981), extends all the way from vertical to horizontal flow. Their simplified correlation for transition to annular flow, for all inclination angles, is given by

$$(\mathrm{Fr}_{sg})\ (\mathrm{Ku}_{sg}) = 25 \left(\frac{v_{sg}}{v_{sL}} \right)^{0.625}, \qquad (4.1)$$

where the Froude number, Fr_{sg} (= v_{sg}^2/gd), and the Kutadelaze number, Ku_{sg}, are both based on superficial gas velocity, v_{sg}.

$$\mathrm{Ku}_{sg} = \frac{v_{sg}\rho_g}{[g(\rho_L - \rho_g)\sigma]^{0.25}} \qquad (4.2)$$

We should note that unlike Weisman and Kang (1981), Taitel et al. (1978) found the transition to annular flow to be independent of liquid velocity and pipe diameter. Otherwise, however, the two correlations generally indicate similar dependency of the gas velocity at transition on liquid and gas densities and surface tension.

Weisman and Kang (1981) proposed that the following condition must prevail for transition to dispersed bubbly flow for all angles of inclination to occur:

$$\left[\frac{(-\mathrm{d}p/\mathrm{d}z)_L}{g(\rho_L-\rho_g)}\right]^{0.5}\left[\frac{g(\rho_L-\rho_g)d^2}{\sigma}\right]^{0.25} \geq 9.7, \quad (4.3)$$

where $(\mathrm{d}p/\mathrm{d}z)_L$ is the frictional pressure gradient of liquid flowing alone through the pipe. Estimates of the Weisman-Kang correlation for the transition to dispersed bubbly flow are also similar to those of Taitel et al. (1978) in vertical flow (Eq. 3.10). Both correlations suggest a mixture velocity of approximately 10 ft/sec (3.05 m/s) for air/water systems at standard conditions before transition to dispersed bubbly flow occurs. However, the Weisman-Kang correlation indicates independence of this transition to gas velocity, whereas the Taitel et al. (1978) model does not.

Unlike the Barnea et al. (1985) approach for horizontal and slightly inclined systems, Weisman and Kang did not distinguish churn from slug flow but lumped these two flow patterns together as intermittent flow. Their approach to delineate the transition between bubbly and intermittent flow uses Froude numbers, based on v_{sg} and v_m, as the correlating parameters. Their transition expression is given by

$$\frac{v_{sg}^2}{gd} = 0.2\left(\frac{v_m}{gd}\right)^{1.56}(1-0.65\cos\alpha)^2. \quad (4.4)$$

The last term, $(1 - 0.65 \cos\alpha)^2$, where α is inclination from horizontal, accounts for the effect of inclination. Weisman and Kang (1981) showed good agreement between the transition condition calculated with Eq. 4.4, and the bubbly/intermittent transition data for systems inclined at various angles from the horizontal, 2.75 to 90°.

Fig. 4.2 presents the flow pattern map of Weisman and Kang (1981). The basic map, with v_{sg} and v_{sL} as the axes, is for two-phase flow in a horizontal system with particular (standard) values of fluid properties and system dimensions. The parameters ϕ_1 and ϕ_2 are used to make the map general, not only for all fluids but also for inclination angles. The expressions for ϕ_1 and ϕ_2, as reported by Weisman and Kang, are reproduced in **Table 4.1.**

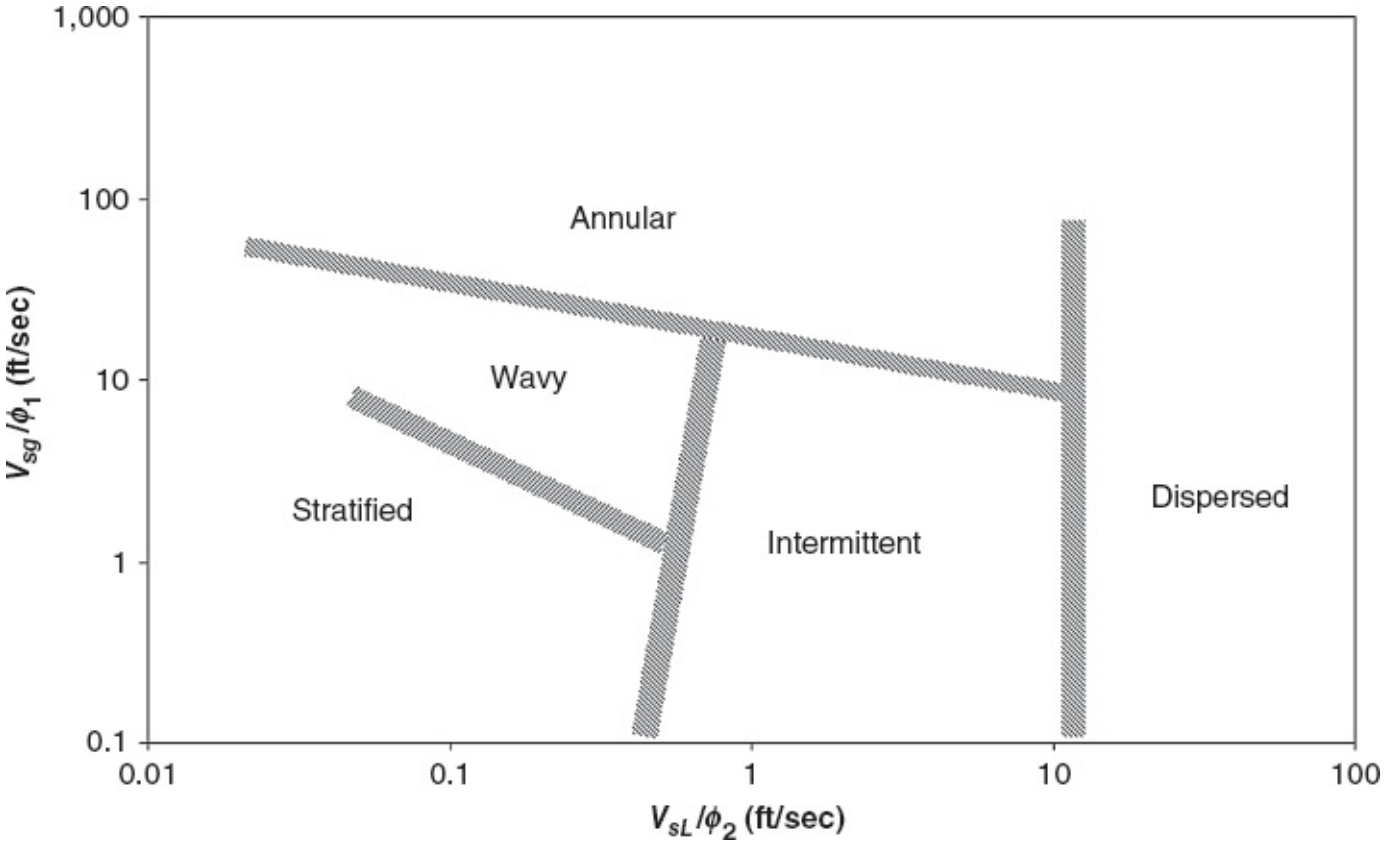

Fig. 4.2—Generalized flow pattern map of Weisman and Kang (1981).

Flow Orientation	Transition To	ϕ_1	ϕ_2
Horizontal, vertical, and inclined	Dispersed flow	1.0	$(\rho_L/\rho_{sL})^{-0.33}\,(d/d_s)^{0.16}\,(\mu_{sL}/\mu_L)^{0.09}\,(\sigma/\sigma s)^{0.24}$
	Annular flow	$(\rho_{sg}/\rho_g)^{0.23}\,(\Delta\rho/\Delta\rho_s)^{0.11}\,(\sigma/\sigma_s)^{0.11}(d/d_s)^{0.415}$	1.0
Vertical and inclined	Bubbly/intermittent	$(d/d_s)^n\,(1 - 0.65\cos\alpha)$	1.0
		$n = 0.26e^{-0.17 v_{sL}/v_{ssL}}$	

Key: s denotes standard conditions, d_s = 1.0 in., ρ_{sg} = 0.0013 kg/L, ρ_{sL} = 1 kg/L, σ_s = 70 dynes/cm, v_{ssL} = 1.0 ft/sec

Table 4.1—Parameters for the Weisman and Kang (1981) flow pattern map.

Individual Transition Criteria. Physical analysis for the transition from bubbly to slug flow, presented by Hasan (1988) and Hasan and Kabir (1988a), follows the approach discussed for vertical systems. Recall that for vertical systems, when the gas volume fraction exceeds 0.25, transition from bubbly flow generally occurs. However, in an inclined pipe, the gas phase tends to flow along the upper wall. This preferential flow increases the actual in-situ gas fraction near the upper wall. Therefore, near the upper wall the in-situ gas fraction may exceed the value of 0.25,

even when the cross-sectional average is much lower. As a result, collisions among the bubbles increase sharply, forming Taylor bubbles, and the transition to slug flow occurs at a cross-sectional average volume fraction lower than 0.25.

We can apply Eq. 3.3 for holdup in vertical systems to an inclined pipe if the actual superficial velocity of the gas phase at the upper section of the pipe is used rather than the cross-sectional average. In an inclined pipe, we assume that the actual cross-sectional area available for the gas to flow is the projection of the area on a horizontal plane. Thus, if A is the pipe cross-sectional area, then the area available for gas flow through a pipe inclined at an angle, α, to the horizontal is $A \sin\alpha$. Therefore, the actual superficial velocity, $(v_{sg})_a$ of the gas phase is

$$\left(v_{sg}\right)_a = \frac{q_g}{A \sin\alpha} = \frac{v_{sg}}{\sin\alpha}. \qquad (4.5)$$

By substituting $(v_{sg})_a$ in place of v_{sg} in Eq. 3.3, we obtain the local in-situ gas fraction, f_{gL}, near the upper wall.

$$f_{gL} = \frac{\left(v_{sg}/\sin\alpha\right)}{C_0\left(v_{sL} + v_{sg}/\sin\alpha\right) + v_\infty}. \qquad (4.6)$$

By rearranging and using f_{gL} = 0.25 at transition,

$$\begin{aligned} v_{sg} &= \left(\frac{C_0 f_g}{1 - C_0 f_g} v_{sL} + \frac{C_0 f_g}{1 - C_0 f_g} v_\infty\right)\sin\alpha \\ &= \left(0.43 v_{sL} + 0.357 v_\infty\right)\sin\alpha \end{aligned} \qquad (4.7)$$

For an inclined system, the bubble rise velocity v_∞, determined by the balance of the buoyancy and drag forces, can differ from that for a vertical system. The buoyancy force obviously decreases as the pipe is deviated from the vertical system, which tends to reduce the bubble rise velocity. However, as mentioned earlier, deviation from the vertical system also causes a shape change, generally making the bubble nose sharper. A sharper bubble nose causes a decrease in the drag force on it. Therefore, the overall effect of pipe inclination on these two forces can cancel out, and the influence of pipe inclination on the terminal rise velocity of the bubble can be negligible. Limited data of Hasan and Kabir (1988a) indicate that the terminal rise velocity of small bubbles is not appreciably affected by the inclination angle. Therefore, the Harmathy (1960) correlation for v_∞ (Eq. 3.6) can be used in Eq. 4.7. Patel's (1988) data corroborate this contention.

Barnea et al. (1985) also extended their analysis for transition in vertical systems, presented in Chapter 3, to inclined systems by replacing the terminal rise velocity of the bubble with $v_\infty \sin\alpha$. For example, they suggested that transition from bubbly flow occurs when v_{sg} is greater than $0.33 v_{sL}$ + 0.25 $\sin\alpha$ v_∞. However, this criterion is doubtful because as we indicated earlier, the rise velocity of small bubbles does not

appear to decrease with deviation from vertical systems. For most systems with low superficial liquid velocity, the difference is negligible. Hasan and Kabir (1988a) showed good agreement of Eq. 4.7 with the data of Barnea et al. (1985) and those of Weisman and Kang (1981).

Barnea et al. (1985) also pointed out that preferential migration of bubbles to the upper part of a deviated pipe leads to a limiting inclination angle beyond which bubbly flow cannot exist. By equating buoyancy to lift forces, they proposed that when well inclination (from horizontal) is less than that given by the expression

$$\frac{\cos\alpha}{\sin^2\alpha} = \frac{3}{4}\cos 45^\circ \frac{v_\infty}{g}\left(\frac{C_L\gamma^2}{d}\right), \qquad (4.8)$$

bubbly flow cannot exist. For the lift coefficient C_L in Eq. 4.8, Barnea et al. (1985) recommended a value of 0.8, and the distortion coefficient γ varies between 1.1 and 1.5. For air/water flow through a 2-in.-inside-diameter (ID) pipe at standard conditions, Eq. 4.8 suggests that the maximum well inclination for bubbly flow is approximately 55 to 70°.

In addition to deviation, well diameter also imposes a restriction on the occurrence of bubbly flow. The diameter of the well must be large enough to satisfy the condition that the Taylor bubble rise velocity is greater than that for the small bubbles; that is, $v_{\infty T} > v_\infty$. For vertical flow, this condition results in a well diameter that must exceed the value given by Eq. 3.8. Barnea et al. (1985) and Kaya et al. (2001) suggested the same expression for deviated wells. However, the differences in Taylor bubble rise velocity in deviated wells may need to be taken into account.

Transition to Churn Flow. As mentioned earlier, the chaotic nature of churn flow pattern makes modeling the dynamics of this flow regime quite difficult. The analysis presented in Chapter 3 for vertical systems might apply. Kaya et al. (2001) presented an analysis that appears promising and is well-supported by data. They noted that the transition to churn flow occurs when the gas volume fraction exceeds 0.78. They also argued that the average f_g in this flow regime may be approximated, following the drift-flux approach, as given by

$$f_g = \frac{v_{sg}}{C_o v_m + v_{\infty T\alpha}}. \qquad (4.9)$$

With the transition f_g of 0.78 and C_o = 1.2, they arrived at the following expression for v_{sg} in which churn flow occurs:

$$v_{sg} = 12.19\left(1.2 v_{sL} + v_{\infty T\alpha}\right). \qquad (4.10)$$

Note that if we followed the Hasan-Kabir suggestion that the value of C_o is 1.15 for churn flow, the required gas velocity for the transition will be much smaller; that is, $v_{sg} = 7.57(1.2v_m + v_{\infty T\alpha})$. However, Kaya et al. (2001) showed data from a number of sources in support of Eq. 4.10. Note that Eq. 4.10 indicates dependence of this

transition on the Taylor bubble rise velocity, which, in turn, depends on well deviation.

Transition to Dispersed Bubbly Flow. Barnea et al. (1985) suggested that the criteria developed for vertical systems (Eq. 3.10) also apply to deviated wells.

Transition to Annular Flow. Following the approach of Taitel et al. (1980), Barnea et al. (1985) presented an analysis that results in the expression for transition to annular flow, which is written as

$$v_{sg} = 3.1\,(\sin\alpha)^{1/4}\left[\,g\sigma(\rho_L - \rho_g)/\rho_g^2\,\right]^{1/4} \qquad (4.11)$$

Eq. 4.11 shows that superficial gas velocity, needed for transition to annular flow, depends on the one-fourth power of the sine of the inclination angle.

The work of Weisman and Kang (1981) shows that, with the exception of bubbly-to-slug flow transition, the transition criteria established for vertical systems are apparently applicable to inclined systems. Because the criteria established in Chapter 3 are based on sound physical modeling, they are preferable to the ones proposed by Weisman and Kang. However, the criterion proposed by Kaya et al. (2001) for transition to churn flow indicates slight dependence of this transition on well deviation. The work of Barnea et al. (1985) also shows that the transition to annular flow is mildly affected by the pipe inclination angle. Yet, because of the support provided by the Weisman-Kang work and for the sake of simplicity, one may ignore the influence of pipe inclination angle on flow pattern transition in any regime other than bubbly flow.

4.2.3 Holdup and Pressure Drop in Deviated Wells: Empirical Correlations. We now present empirical methods available for computing holdup and pressure drop in inclined two-phase flow. The most extensive experimental study on inclined two-phase flow was reported by Beggs (1972) and by Beggs and Brill (1973). While a number of other significant works have since been performed, most notably by Mukherjee and Brill (1983), the Beggs and Brill (1973) method remains perhaps the most accurate and certainly the best-known.

***The Beggs and Brill Correlation*.** The Beggs and Brill (1973) correlation is based on the data they gathered in 90-ft pipes with pipe IDs of 1.0 and 1.5 in. These pipes were inclined at various angles between zero and 90° in both upward and downward directions.

We first briefly describe the Beggs and Brill method for horizontal systems because their correlation for inclined systems is based on the modification of their horizontal system correlation. They divided the flow patterns observed in horizontal systems into four categories. The first is segregated flow, which includes smooth and wavy stratified flow and annular flow. The intermittent flow pattern encompasses slug and plug flow. The transition flow regime (Regime IV) includes regions between intermittent and stratified flow patterns, and the distributed flow pattern (Regime III) comprises bubbly and mist flows.

Beggs and Brill based their horizontal flow pattern map on the input liquid volume

fraction C_L (= v_{sL}/v_m) and the mixture Froude number ($Fr_m = v_m^2/gd$). They defined the four transition parameters L_1 through L_4 that relate to liquid fraction C_L as exponential functions. On a log-log plot, therefore, these four parameters plot as a straight line, as shown in **Fig. 4.3.**

$$L_1 = 316\, C_L^{0.302}, \quad L_2 = 0.0009252\, C_L^{-2.4684};$$
$$L_3 = 0.1\, C_L^{-1.4516}, \quad \text{and} \quad L_4 = 0.5\, C_L^{-6.738}. \qquad (4.12)$$

As Fig. 4.3 shows, when the Froude number is greater than $0.1/C_L^{1.4516}$ (points over line L_3), the flow regime is distributed (Regime III) as long as the volumetric liquid flow rate is less than 40% (C_L < 0.4). The area bounded by L_1 and L_2 has segregated flow (Regime I), while that bounded by L_2 and L_3 is the transition region (Regime IV). Intermittent flow (Regime II) is bounded by L_1, L_3, and L_4. The following inequalities can be used to determine flow patterns.

Segregated (Regime I):	$C_L < 0.01$ and $Fr < L_1$, or
	$C_L > 0.01$ and $Fr < L_2$;
Intermittent (Regime II):	$0.01 < C_L > 0.4$ and $L_3 < Fr < L_1$, or
	$C_L > 0.4$ and $L_3 < Fr < L_4$;
Distributed (Regime III):	$C_L < 0.4$ and $Fr > L_1$, or
	$C_L > 0.4$ and $Fr > L_4$;
and	
Transition (Regime IV):	$C_L > 0.01$ and $L_2 < Fr < L_3$.

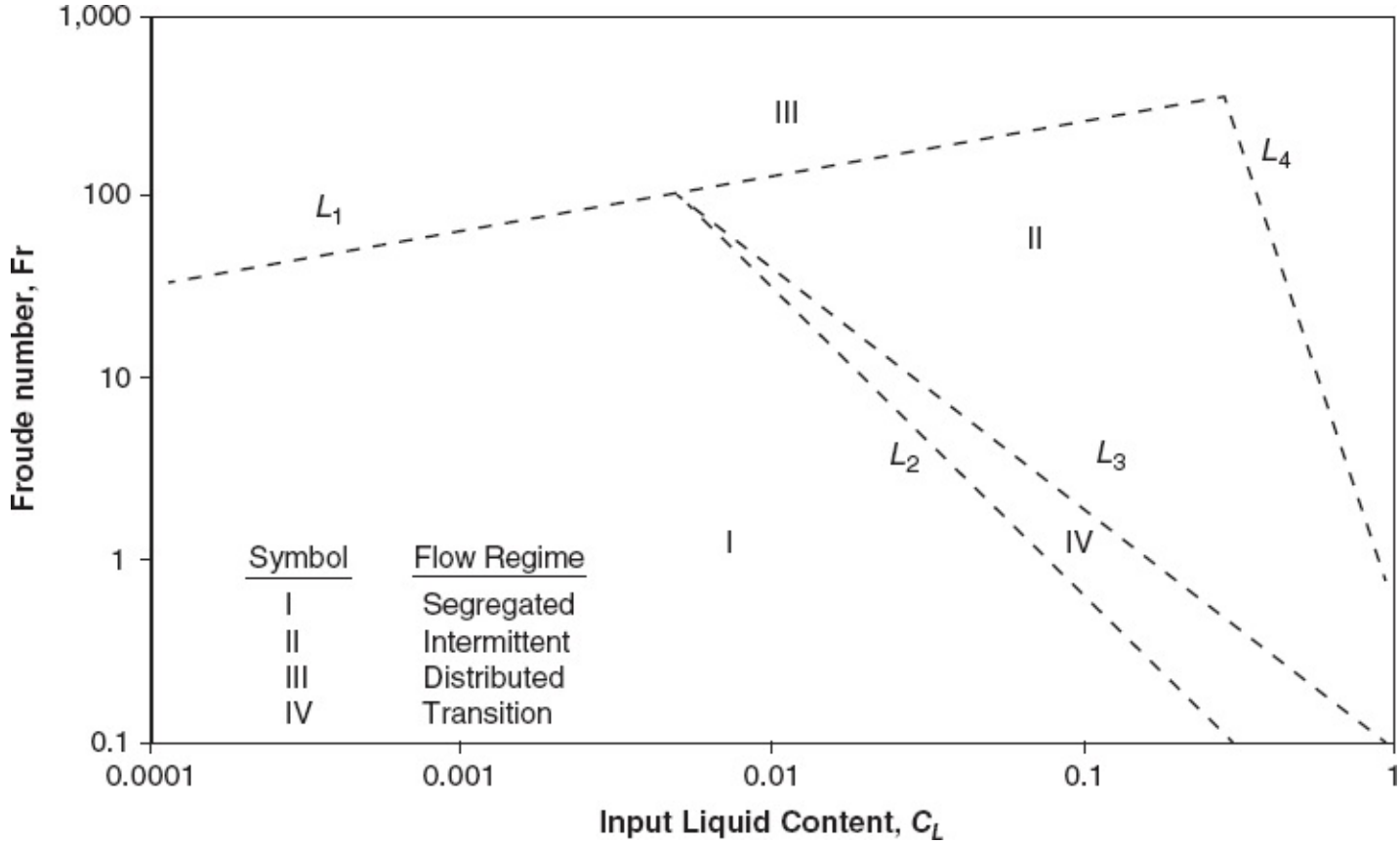

Fig. 4.3—Beggs and Brill (1973) flow pattern map for horizontal systems.

The flow pattern map on log/log coordinates with the transition parameters is shown in Fig. 4.3.

They proposed the correlation for liquid holdup, f_L (=1–f_g), for horizontal (zero-degree inclination) systems as

$$f_{L(0)} = a\,C_L^b / \mathrm{Fr}^c. \qquad (4.13)$$

The following are the values of parameters a, b, and c, which depend on specific flow patterns.

	a	*b*	*c*
Segregated	0.980	0.4846	0.0868
Intermittent	0.845	0.5351	0.0173
Distributed	1.065	0.5824	0.0609

Beggs and Brill suggested that when the flow regime falls in the transition zone, f_L should be estimated from a linear interpolation of f_L values calculated for the segregated and intermittent flow regimes. Thus, they computed frictional pressure gradient using an expression similar to Eq. 2.16,

$$f_{L,\text{tran}} = \left[\frac{(L_3 - \text{Fr})}{(L_3 - L_2)}\right] f_{L,\text{seg}} + \left[\frac{(\text{Fr} - L_2)}{(L_3 - L_2)}\right] f_{L,\text{int}}, \quad (4.14)$$

where the gradient depends on the mixture density, velocity, channel diameter, and a friction factor and is given by

$$\left(-\frac{\mathrm{d}p}{\mathrm{d}z}\right)_F = \frac{2 f_m \rho_n v_m^2}{g_c d}. \quad (4.15)$$

However, the density used in Eq. 4.15, ρ_n, is the no-slip (homogeneous) mixture density, $\rho_n = \rho_L C_L + \rho_g C_g$. The mixture friction factor f_m is also related to the no-slip, two-phase friction factor f_n and a multiplier, e^s. Therefore, two-phase friction factor f_m is written as

$$f_m = f_n e^s. \quad (4.16)$$

The no-slip friction factor f_n is based on the no-slip Reynolds number, $\text{Re}_n = dv_m\rho_n/\mu_n$. The mixture viscosity, μ_n, is also a no-slip property, $\mu_n = \mu_L C_L + \mu_g C_g$. To calculate the exponent s needed to determine the two-phase friction factor, Beggs and Brill (1973) defined a parameter y in terms of C_L and holdup as

$$y \equiv C_L / f_{L(\alpha)}^2. \quad (4.17)$$

The exponent s is empirically related to the parameter y when $y > 1.2$, and it is written as

$$s = \frac{\ln y}{-0.0523 + 3.182(\ln y) - 0.8725(\ln y)^2 + 0.01853(\ln y)^4}. \quad (4.18)$$

For a value of y between 1.0 and 1.2, s is given by

$$s = \ln(2.2y - 1.2), \qquad 1 < y < 1.2. \quad (4.19)$$

Thus, frictional pressure gradient is dependent on the flow regime because y depends on $f_{L(\alpha)}$, which, in turn, depends on the flow regime, as well as on the inclination angle.

For estimating liquid holdup in inclined systems, Beggs and Brill (1973) used their holdup correlation for the horizontal system (Eq. 4.13) along with a correction factor for well inclination, $F(\alpha)$. The flow regime that would exist if the system were horizontal is first determined using the criteria previously discussed. Holdup is then calculated with Eq. 4.13. Thereafter, it is multiplied by the correction factor $F(\alpha)$ to estimate the holdup for the actual inclined system. In other words,

$$f_{L(\alpha)} = f_{L(0)} F(\alpha). \quad (4.20)$$

The correction factor $F(\alpha)$ depends on the inclination angle and parameter Z,

$$F(\alpha) = 1 + Z\left[\sin(1.8\alpha) - \sin^3(1.8\alpha)\right] \quad (4.21)$$

The parameter Z depends on the no-slip liquid volume fraction C_L, dimensionless velocity v_{Ld}, and Froude number F_r, and is given by

$$Z = (1 - C_L)\ \ln\left(d\, C_L^e\, v_{Ld}^f\, \mathrm{Fr}^g\right), \quad (4.22)$$

and

$$v_{Ld} = v_{sL} \sqrt[4]{\rho_L / g\sigma} \quad (4.23)$$

Parameters *d, e, f*, and *g* depend on the flow pattern that was determined with an equivalent horizontal system. The following are the specific flow patterns with parameter values:

	d	*e*	*f*	*g*
Segregated uphill	0.011	–3.768	3.539	–1.614
Intermittent uphill	2.96	0.305	–0.4473	0.0978
Distributed uphill	No correction, $F(\alpha) = 1.0$			
All flow regimes downhill	4.70	–0.3692	0.1244	–0.5056

Beggs and Brill (1973) did not suggest any specific method for calculating the accelerational component. Where it is significant, the accelerational gradient can be calculated with either the separated or the homogeneous flow approach, and ρ_m can be estimated with the Beggs and Brill method. The total pressure gradient is given by

$$-\frac{\mathrm{d}p}{\mathrm{d}z} = \frac{g \sin\alpha}{g_c}\left(\rho_L f_L + \rho_g f_g\right) + \frac{f_m\, v_m^2\, \rho_n}{2\, g_c\, d} + \frac{\rho_m v_m}{g_c}\frac{\mathrm{d}v_m}{\mathrm{d}z}. \quad (4.24)$$

Other Correlations. Several other methods have been proposed for computing flow behavior using a flow pattern approach. For instance, Singh and Griffith (1969), Bonnecaze et al. (1971), Mattar and Gregory (1974), and Asheim (1986) have proposed correlations for estimating holdup in slug flow, which are very similar to the expression for f_{gT}, given by Eq. 4.9. In fact, on the basis of data from pipes inclined at 5, 10, and 15° from horizontal, Singh and Griffith suggested that holdup in inclined slug flow can be represented by $f_g = v_{sg} / (0.95\, v_m + 1.15)$. The correlation makes the simplifying assumption that the Taylor bubble may represent the drift flux for the entire gas flow. In addition, comparison of this equation with its counterpart for vertical systems indicates that Singh and Griffith found the Taylor bubble rise velocity in inclined pipes to be independent of not only pipe diameter but also inclination angle. As discussed earlier, Beggs and Brill (1973) found holdup to be a strong function of pipe deviation. The data reported by Wallis (1969, 304–305) also show holdup to be a strong function of inclination angle during inclined slug flow. Therefore, the

procedure presented in this text is preferred to correlations similar to those proposed by Singh and Griffith (1969).

Most of these studies, however, appear to agree that the liquid holdup for intermittent flow in a well slightly deviated from vertical is usually higher than that calculated under conditions similar to vertical flow. Indeed, the data of Beggs and Brill (1973) suggest that liquid holdup becomes a maximum at an angle of +50° from the horizontal.

4.2.4 Holdup and Pressure Drop in Deviated Wells: Mechanistic Models. There are few mechanistic models for computing holdup and pressure drop in deviated systems. Hasan (1988), Hasan and Kabir (1988a), Kaya et al. (2001), and Gomez et al. (2000) have proposed comprehensive models for deviated wells. Recent studies of Zhang et al. (2003a, b) and Zhang and Sarica (2006) have added greater sophistication and accuracy. We present the major developments of these models, emphasizing the simpler approaches.

The Hasan-Kabir model uses the flow pattern approach for vertical systems, discussed in Chapter 3, with modifications for the system's deviation from vertical orientation. Hasan and Kabir (1988a), Kaya et al. (2001), and Shoham (2006, p.185) noted that for annular and dispersed bubbly flow, the flow rates are very high. Consequently, the influence of buoyancy is small, and the effect of pipe inclination is negligible. Thus, for those flow regimes, the relationships developed for vertical systems can be used without any modifications. We therefore address only the bubbly and intermittent flow patterns.

***Bubbly Flow*.** For vertical systems, Hasan and Kabir (1988a) postulated that the in-situ velocity, v_g, of the gas phase is the sum of the terminal rise velocity v_∞ and the mixture velocity v_m, multiplied by the flow parameter, C_o. Therefore, $v_g = v_{sg}/f_g = C_o v_m + v_\infty$. This analysis should also hold for deviated wells. Thus, as in Eq. 3.21, holdup is given by

$$f_L \equiv 1 - f_g = 1 - \frac{v_{sg}}{C_o v_m + v_\infty}. \qquad (4.25)$$

Kaya et al. (2001) and Gomez et al. (2000), following the approach of Ansari et al. (1994) for vertical systems, arrived at a slightly different expression, which is given by

$$f_L \equiv 1 - f_g = 1 - \frac{v_{sg}}{C_o v_m + v_\infty \sqrt{f_L \sin\alpha}}. \qquad (4.26)$$

Therefore, the procedure for estimating holdup and pressure drop in deviated wells will be similar to those discussed for vertical systems. One will, however, need values for the flow parameter C_o and the bubble rise velocity v_∞ in an inclined system.

Flow Parameter and Bubble Rise Velocity. For vertical systems, we were able to reason that the value of the flow parameter C_o should be 1.2 because the flow is turbulent and the bubbles ride the central portion of the channel, where the mixture

velocity is 1.2 times the cross-sectional average value. The bubble concentration profile is likely to be affected by the pipe's deviation. Intuitively then, one can expect C_o to be influenced by well deviation, which has led Gomez et al. (2000) to use C_o = 1.15.

However, the effect of pipe inclination on C_o appears negligible. This trend is observed in the data of Patel (1988) for pipes deviated up to 32° from vertical. Even for the case of elongated bubble flow through horizontal pipes, the value of C_o has been generally found to be 1.2 (Hughmark 1965; Gregory and Scott 1969). Consequently, Hasan and Kabir (1988a) and Kaya et al. (2001) proposed a value of 1.2 for C_o in Eqs. 4.25 or 4.26. As discussed earlier, the bubble rise velocity may be assumed to remain unchanged with pipe inclination. Therefore, the same expression, with the identical values of parameters used in vertical flow, can be used to estimate holdup in deviated wells. The only difference between bubbly flow in deviated wells and that in vertical wells is the transition to slug flow.

Once holdup is estimated, the total pressure gradient may be calculated by adding the frictional and accelerational components to the static head. The contribution of these components, which are extremely small, may be estimated with the method applicable to vertical systems (Eq. 2.19). The static head for an inclined system, of course, is equal to $\rho_m \sin\alpha$. Therefore,

$$-\frac{\mathrm{d}p}{\mathrm{d}z} = \frac{g\sin\alpha}{g_c}\left(\rho_L f_L + \rho_g f_g\right) + \frac{f_m\, v_m^2\, \rho_m}{2\, g_c\, d} + \frac{\rho_m v_m}{g_c}\frac{\mathrm{d}v_m}{\mathrm{d}z} \qquad (4.27)$$

Slug Flow. Application of the simple drift-flux model, developed for bubbly flow, to slug flow becomes difficult. This difficulty stems from the difference in drift velocities between the small and the Taylor bubbles and the asymmetric nature of the distribution and shape of the bubbles. As discussed in Chapter 3, one simple way to account for different drift velocities in slug flow is to use some type of an average rise velocity for all gas bubbles—large and small—in the system. Therefore, for estimating in-situ gas volume fraction during slug flow, we use Eq. 3.26, reproduced here for convenience.

$$f_L \equiv 1 - f_g = 1 - \frac{v_{sg}}{C_o\, v_m + \overline{v}_{\infty\alpha}}. \qquad (4.28)$$

As in the case of vertical flow, the average rise velocity is expressed in terms of the Taylor bubble rise velocity in a deviated well, small-bubble rise velocity, and bubbly/slug transition velocity as

$$\overline{v}_{\infty\alpha} = v_\infty\left(1 - e^{-0.1 v_t/(v_{sg} - v_t)}\right) + v_{\infty T\alpha}\, e^{-0.1 v_t/(v_{sg} - v_t)}, \qquad (4.29)$$

where v_t, the superficial gas velocity for transition to intermittent flow, is given by Eq. 4.7.

If further rigor is desired, one can take the cellular approach, as performed in

Chapter 3 for vertical systems, and model the dynamics of the Taylor bubble and liquid slug portions of the cell. Unfortunately, for deviated systems, the asymmetric nature of the Taylor bubble, liquid film, and bubble distribution in the channel makes such an analysis extremely difficult. The effort of Kaya et al. (2001) and Gomez et al. (2000) to adapt the Ansari et al. (1994) vertical flow model for this regime, with modifications for well deviation, is an auspicious beginning. The next section presents these adaptations for flow in near-horizontal systems.

Flow Parameter C_o. As discussed in bubbly flow, the flow parameter may be affected by channel inclination angle. However, data, gathered by Lau (1972) and Patel (1988), show that the value of the flow parameter remains constant at 1.2, irrespective of the channel inclination. This finding makes the estimation procedure simple. Both Hasan and Kabir (1988a) and Kaya et al. (2001) used this value of the flow parameter. We note, though, that data supporting a constant value of C_o = 1.2 for all inclinations are limited and are derived from small-diameter pipes.

Taylor Bubble Rise Velocity, $v_{\infty T\alpha}$. Unlike the flow parameter in inclined flow, the terminal rise velocity of a Taylor bubble is strongly influenced by pipe inclination. The high Eotvos number data from Wallis (1969) clearly show strong variation in Taylor bubble rise velocity with pipe inclination. Note that for most practical systems, the inverse viscosity number is very high (>30,000; refer to material on slug flow in Chapter 3). In such cases, the Wallis (1969) data indicate that the Taylor bubble rise velocity increases with increasing deviation of the pipe from the vertical system until a maximum is reached for a deviation angle of approximately 50°. The rise velocity then gradually decreases with increasing deviations and finally becomes zero for horizontal systems. The data of Patel (1988), among others, also led to a similar conclusion. This observation is of great significance because for most practical systems the Eotvos number is large.

Balancing the buoyancy force against the drag force, experienced by a rising bubble, leads to the following expression for the rise velocity of a bubble of volume V_B and projected area A_P:

$$V_B g \sin\alpha \left(\rho_L - \rho_g\right) = \frac{1}{2} C_{D\alpha}\, v_{\infty T\alpha}^2\, \rho_L\, A_{P\alpha}. \qquad (4.30)$$

In Eq. 4.30, $C_{D\alpha}$ is the drag coefficient for the bubble and $v_{\infty T\alpha}$ is its rise velocity in a pipe, inclined to the horizontal by an angle, α. A similar expression can be written for a vertical system. Taking the ratio of these two expressions leads to the following:

$$\frac{v_{\infty T\alpha}}{v_{\infty T}} = \sqrt{\sin\alpha\, \frac{(C_D A_P)_{90}}{C_{D\alpha} A_{P\alpha}}}. \qquad (4.31)$$

If the product of the drag coefficient and projected area of the bubble were the same for vertical and inclined systems—that is, if $(C_D A_P)_{90}$ / $(C_{D\alpha} A_{P\alpha})$ = 1—then Eq. 4.31 suggests that the rise velocity of the bubble will gradually decrease as the deviation

of the pipe increases. However, in inclined flow, the Taylor bubble has a sharper nose, compared to that in vertical systems, with a consequent lower drag coefficient. This lowering of the drag coefficient increases as the pipe deviates from the vertical. In addition, the projected area in a deviated well is also smaller. The net effect is that the ratio, $(C_D A_P)_{90} / (C_{D\alpha} A_{P\alpha})$, becomes greater than 1.0. Consequently, an increase in the terminal rise velocity with pipe deviation occurs when the deviation is small, with a consequent increase in liquid holdup, compared with that for a vertical system.

At large deviations from vertical, the buoyancy force begins to decrease much faster than the drag force and the bubble rise velocity begins to decrease with further deviation from the vertical. The variation in the $C_D A_{P\alpha}$ product with inclination angle may be approximated by $(C_D\ A_P)_{\ 90}\ (1 + \cos\alpha)^n$.

$$v_{\infty T\alpha} = v_{\infty T} \sqrt{\sin\alpha\ (1+\cos\alpha)^n} \qquad (4.32)$$

The data of Runge and Wallis, as reported by Wallis (1969), is well-represented by Eq. 4.32 if n = 2.4 is used, as shown in **Fig. 4.4.** With this value of n (and using the Taylor bubble rise velocity for vertical flow, Eq. 3.46), the bubble's terminal rise velocity in intermittent flow becomes

$$v_{\infty T\alpha} = 0.35 \sqrt{gd\left(\rho_L - \rho_g\right)/\rho_L}\ (1+\cos\alpha)^{1.2} \sqrt{\sin\alpha} \qquad (4.33)$$

Combining Eq. 4.33 with Eqs. 4.28 and 4.29 will yield liquid holdup and, therefore, the mixture density. The total pressure gradient can then be evaluated with the method developed for vertical flow (Eq. 2.19 or Eq. 4.24). Eq. 4.33 shows that at small deviation angles, liquid holdup increases with increasing deviation of the pipe from the vertical system, reaching a maximum value at deviation angles of approximately 50°. This observation is consistent with the findings of Beggs and Brill (1973).

A different approach was adapted by Bendiksen (1984), who proposed the following expression for $v_{\infty T\alpha}$:

$$v_{\infty T\alpha} = (0.35\sin\alpha + 0.54\cos\alpha) \sqrt{gd\left(\rho_L - \rho_g\right)/\rho_L} \qquad (4.34)$$

Eq. 4.34, which has been adapted by many researchers, including Zhang et al. (2003b), Kaya et al. (2001), and Gomez et al. (2000), calculates nonzero rise velocity for a Taylor bubble in a horizontal system.

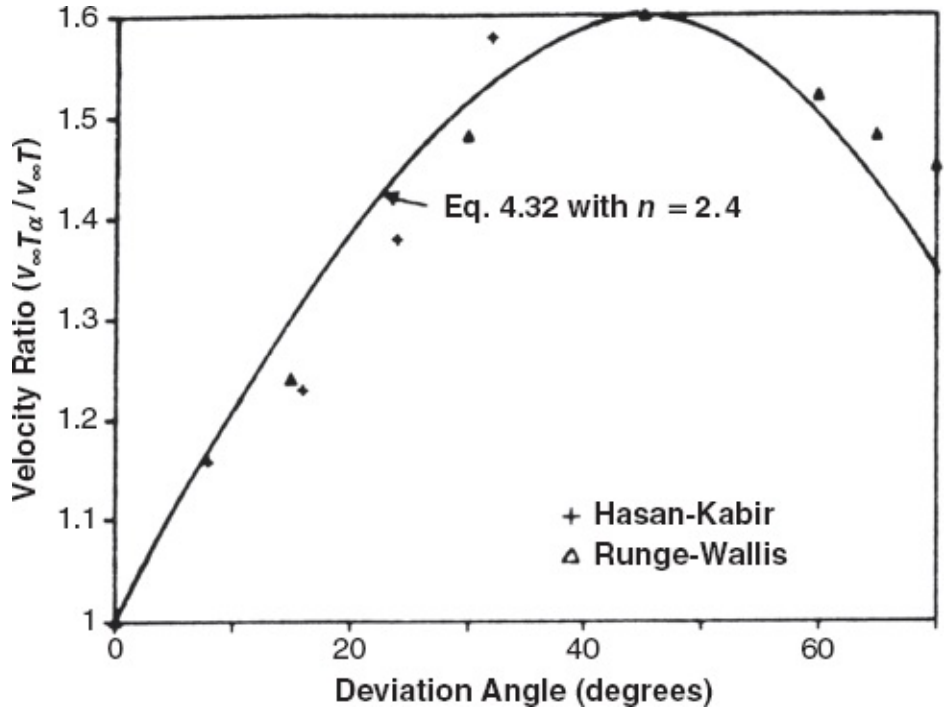

Fig. 4.4—Correlating Taylor bubble rise velocity ratio with well deviation angle, Eq. 4.32 (after Hasan and Kabir 1988a).

The goodness of the simplified slug flow model's performance, which we discussed, can be observed by inspecting **Figs. 4.5 and 4.6,** which display in-situ gas volume fraction and pressure-gradient data, respectively. Earlier, Hasan and Kabir (1988a) presented these figures. In the same study, they showed that the simplified mechanistic model performs satisfactorily in representing the Beggs and Brill (1973) data, encompassing all four flow regimes. **Figs. 4.7 and 4.8** compare the gas volume fraction and pressure-gradient data, respectively.

Rigorous approaches for modeling two-phase flow in deviated wells have been completed in recent years at the University of Tulsa by Wang et al. (2013, 2014) and Zhang et al. (2003a, b), and at Stanford University by Shi et al. (2005a, b), among other organizations. Specifically, Zhang et al. (2003a, b) presented a unified approach that models flow pattern transitions, pressure gradient, liquid holdup, and slug characteristics at all inclination angles. The model is based on the dynamics of slug flow, which shares transition boundaries with all the other flow patterns. Researchers modeled the momentum exchange between the slug body and the film zone by using the entire film zone as the control volume. The combined momentum equation of slug flow facilitates calculation of slug characteristics and predict transitions from slug to other flow patterns.

The models discussed so far generally assume that the viscosity of the liquid phase, which influences frictional pressure drop, has minimal effect on the overall pressure gradient. However, recent work by Wang et al. (2013, 2014) pointed out that for very viscous oil, the liquid phase, particularly the liquid slug in slug flow, may be in a laminar state. They also showed that the laminar nature of the liquid slug may

in some cases significantly influence the flow dynamics and total pressure gradient.

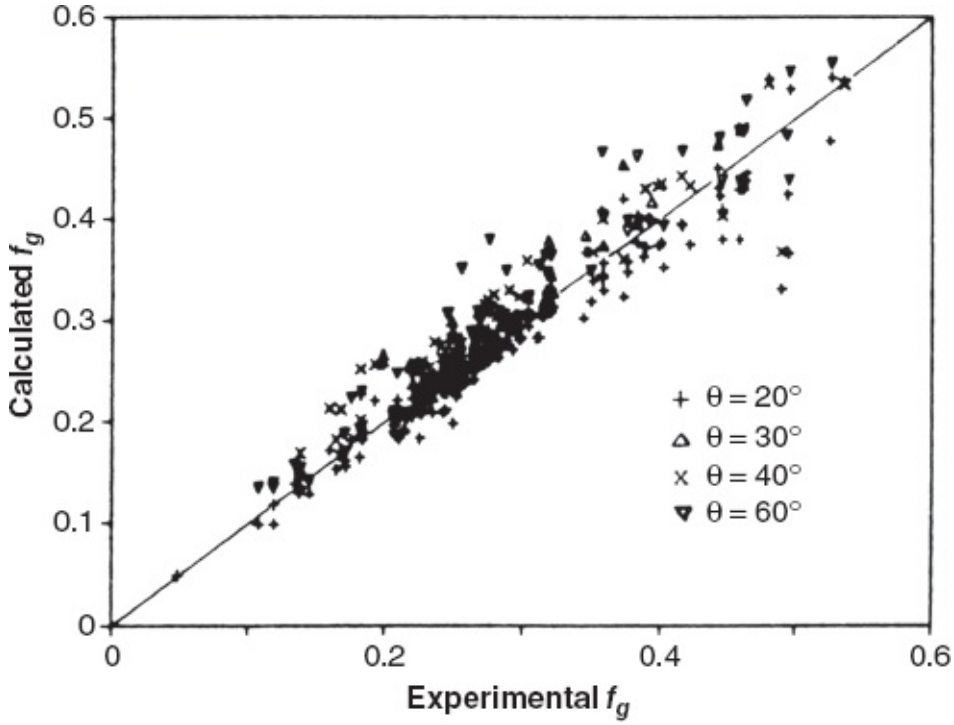

Fig. 4.5—Laboratory data support slug flow model, Eq. 4.28 (after Hasan and Kabir 1988a).

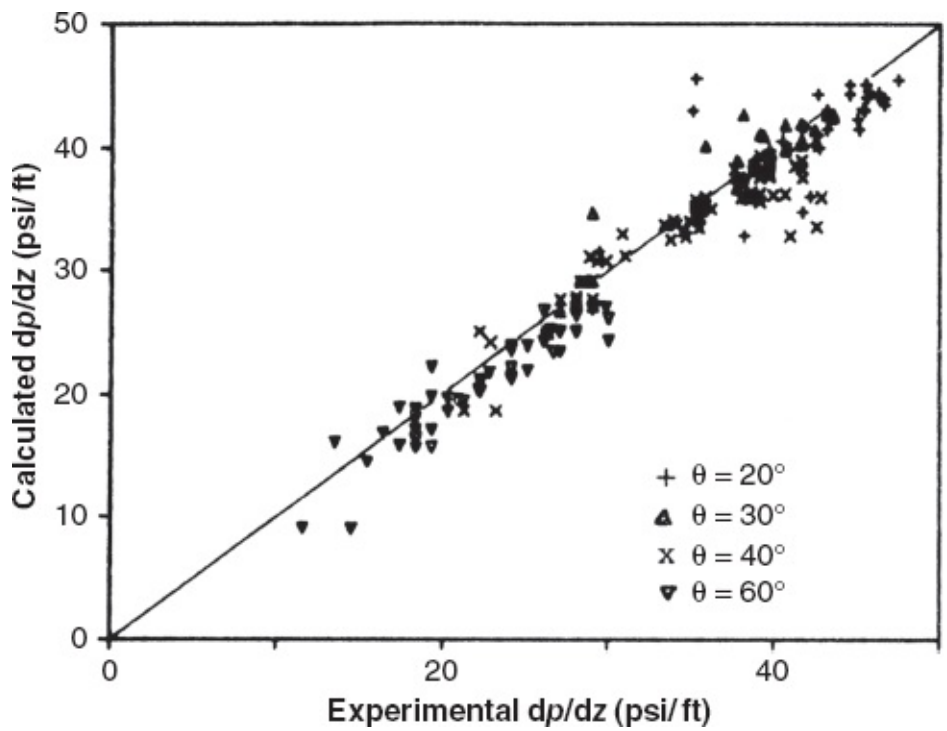

Fig. 4.6—Laboratory data lend support to pressure-gradient calculations in slug flow (after Hasan and Kabir 1988a).

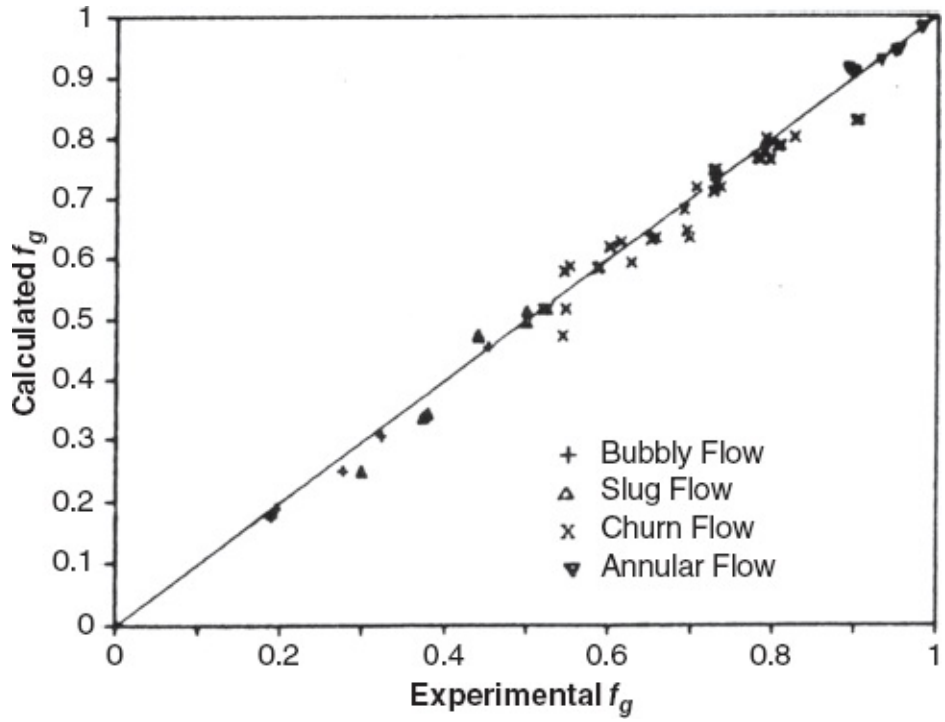

Fig. 4.7—Laboratory data lend support to fg calculations in all flow regimes (after Hasan and Kabir 1988a).

Field Example 4.1. A 17.5° deviated well (inclined at 72.5° from horizontal) has a measured depth of 6,241 ft. The well produces 33 °API oil at 2,922 STB/D with 20% water cut through a 2.435-in. (0.203 ft)-ID tube. The gas/oil ratio (GOR) is 447 scf/STB, and the gas gravity is 0.6. The following property values and computed fluid parameters are available at the wellhead, where the pressure is 361 psig.

v_{so} = 6.2233 ft/sec

ρ_o = 51.04 lbm/ft^3

μ_L = 0.6 cp

Z = 0.923

v_{sw} = 1.468 ft/sec

ρ_w = 63.32

μ_g = 0.014 cp

v_{sL} = 7.691 ft/sec

ρ_L = 53.3 lbm/ft^3

σ = 29 dynes/cm = 0.064 lbm/sec^2

v_{sg} = 17.62 ft/sec

ρ_g = 1.08 lbm/ft^3

Calculate the pressure gradient at this point.

Solution. This problem involves two liquid (oil and water) phases and one gas phase. For most cases of flow of two liquids and one gas, our experience indicates that the two liquid phases are well-mixed and that their fluid-dynamic behavior is like that of a single homogeneous liquid. We therefore combine the two liquids to form a single liquid phase with average mixture properties. We then apply the principles of two-phase flow to this *homogeneous* liquid and the gas phase. Thus, for this problem, we have

$v_{sL} = v_{so} + v_{sw}$ = 7.691 ft/sec $\rho_L = (\rho_o v_{so} + \rho_w v_{sw})/(v_{so} + v_{sw})$ = 53.38 lbm/ft^3.

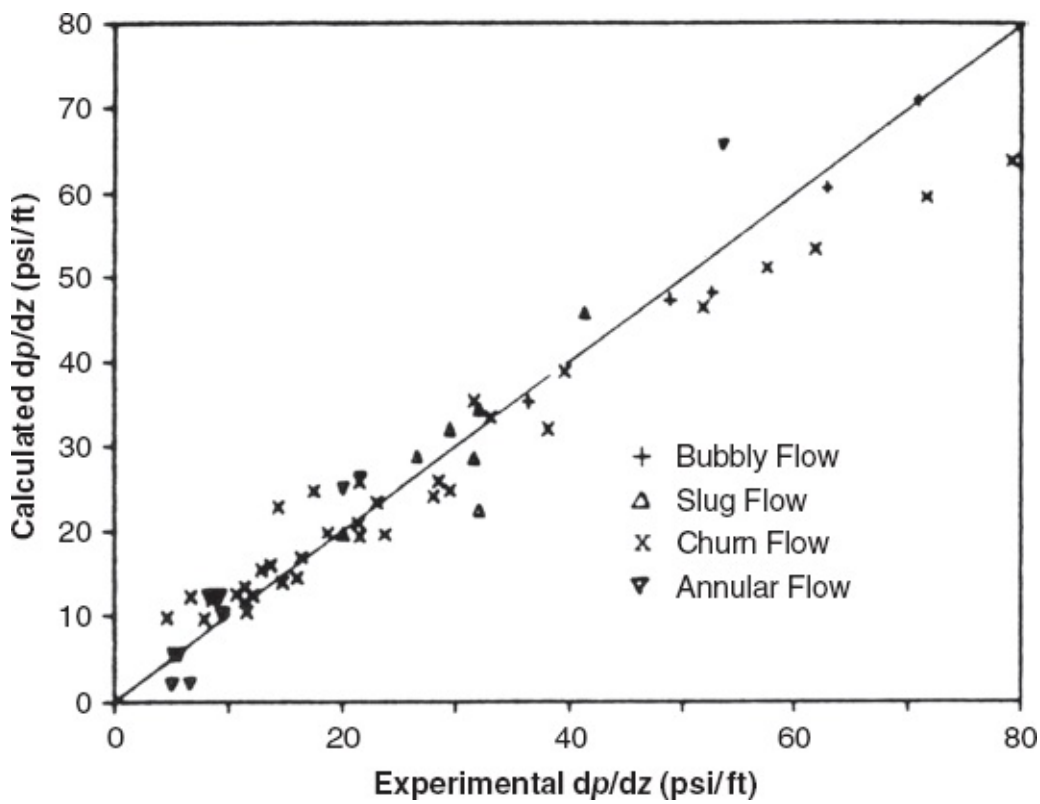

Fig. 4.8—Laboratory data lend support to pressure-gradient calculations in all flow regimes (after Hasan and Kabir 1988a).

Flow Pattern and Transition Criteria. For flow pattern and transition criteria, begin with Eqs. 3.6 and 4.33.

Eq. 3.6: $v_\infty = 1.53\,[g\sigma(\rho_L - \rho_g)/\rho_L{}^2]^{0.25}$

$= 1.53\,[(32.2)(0.108)(52.05)/53.13^2]^{0.25} = 0.675$ ft/sec.

Eq. 4.33: $v_{\infty T\alpha} = 0.35\,[gd\,(\rho_L - \rho_g)/\rho_L]^{0.5}\,[(\sin\alpha)^{1/2}\,(1 + \cos\alpha)^{1.2}]$

$= 0.35\,[(32.2)(0.203)(52.05)/53.13]^{0.5}\,(1.208) = 1.125$ ft/sec.

Because $v_{\infty T} > v_\infty$, Eq. 4.7 would apply for transition from bubbly to slug flow.

Eq. 4.7: $v_t = (0.429\, v_{sL} + 0.357\, v_\infty)(\sin 72.5)$

$= [(0.429)(7.512) + (0.357)(0.675)]\,(0.9537) = 3.38$ ft/sec.

Because the actual $v_{sg} > 3.38$ ft/sec, the pattern is not bubbly. Test each flow regime before moving forward with any calculations. First, use Eq. 3.10 to compute the minimum mixture velocity needed for the dispersed bubbly flow to exist. Note that the actual mixture velocity is $v_{sg} + v_{sL} = 25.3$ ft/sec. Eq. 3.10 requires an estimate of the friction factor. Use a value of $f = 0.0148$, the computation of which will be shown later.

The left-hand side (LHS) of Eq. 3.10 is $2(25.31)^{1.2}\,(0.0147/0.406)^{0.4}\,(53.3/0.064)^{0.6}\,\{0.4(0.064)/[(32.2)\,(52.33)]\}^{0.5} = 5.64$. The right-hand side (RHS) of Eq. 3.9 is $0.725 + 4.15\,(17.62/25.31)^{0.5} = 4.19$. Therefore, the mixture velocity (LHS) is high enough (compared to the RHS) to support either dispersed bubbly or churn flow. Using Eq. 3.11 ($v_{sg} = 1.08 v_{sL}$), we conclude that because actual v_{sg} is greater than ($1.08 v_{sL}$ =) 8.11 ft/sec, dispersed bubbly flow cannot be sustained; so, churn flow is the likely pattern. However, we have to check whether this high gas velocity could cause annular flow to exist.

Transition to Annular Flow. We use Eq. 3.12 to estimate the minimum gas velocity needed to sustain annular flow. In Eq. 3.12, $v_{sg} = 3.1\,[(32.2)(0.064)(52.33)/1.08^2]^{1/4} = 9.595$ ft/sec. Although the actual superficial gas velocity is higher than that estimated with Eq. 3.12 for annular flow, the calculated in-situ gas volume fraction, f_g of 0.587, as shown later, is too low to sustain annular flow. Barnea et al. (1985) indicated that when f_g is less than 0.85, the liquid phase often bridges the entire flow channel, causing the pattern to be either slug or churn. Therefore, the flow pattern at the wellhead in this example is deemed to be *churn flow*.

Gas Volume Fraction and Pressure Gradient. The Hasan and Kabir (1988a) and Ansari et al. (1994) models and the Beggs and Brill (1973) correlation can be used to determine gas volume fraction and pressure gradient.

The Hasan-Kabir Model. The value parameters for the Hasan-Kabir model include

$v_{sL} = 7.691$ ft/sec

$\mu_L = 0.6$ cp

$v_\infty = 0.675$ ft/sec

$v_{sg} = 17.62$ ft/sec

$\mu_g = 0.014$ cp

$v_{\infty T\alpha} = 1.125$ ft/sec (Eq. 4.33)

$\rho_L = 53.3$ lbm/ft^3

σ = 29 dynes/cm = 0.064 lbm/sec^2

ρ_g = 1.08 lbm/ft^3

v_t = 3.38 ft/sec

Gas Volume Fraction:

$x = v_{sg}\ \rho_g\ /(v_{sg}\ \rho_g + v_{sL}\ \rho_L)$ = (17.62)(1.08)/[(17.62 × 1.08) + (7.691)(53.3)] = 0.044.

Eq. 4.29: $\overline{v}_\infty = 0.675\ (e^{-0.0675./14.24}) + 1.125\ (1-e^{-0.0675./14.24})$ = 1.04 ft/sec.

Eq. 4.28: f_g = 17.62/[1.15(25.3) + 1.04] = 0.583. Holdup, f_L = 0.417.

Pressure Gradient:

Eq. 2.20: ρ_m = 53.3 (0.417) + 1.08 (0.583) = 22.89 lbm/ft^3.

Eq. 2.17: $(dp/dz)_H = \rho_m\ g \sin\alpha/g_c$ = 21.83 psf/ft = 0.1516 psi/ft.

Eq. 2.25: μ_m = 0.954(0.6) + 0.046(0.014) = 0.57 cp

Re_m = (0.203)(25.3)(22.89)/(0.57 × 0.000672) = 304,872.

Eq. 1.11: $f = 0.184\ (304{,}872)^{-0.2}$ = 0.0147.

Eq. 2.16: $(dp/dz)_F = (0.0147)(25.3)^2(22.89)/[2(32.2)(0.203)]$ = 16.517 psf/ft = 0.1147 psi/ft.

Eq. 2.19: dp/dz = 0.1516 + 0. 1147 = 0.2673 psi/ft = total pressure gradient at wellhead.

The Ansari et al. Model.

Gas Volume Fraction:

Eq. 3.37: f_{gLS} = 17.62/[2.65(25.13) + (0.425/0.3048)] = 0.259, and f_{LLS} = 1 – 0.259 = 0.741.

Eq. 3.35: $v_{gLS} = 1.2(25.13) + (0.675)(0.741)^{0.5}$ = 30.7 ft/sec. v_{TB} = 1.2(25.13) + 1.125 = 31.05 ft/sec.

Eq. 3.39: $\overline{A}$ = (31.05)(0.259) + (0.741){25.13 – 0.675[0.675(0.741)$^{0.5}$]} = 26.6 ft/sec.

Eq. 3.36: $v_{LTB} = 9.916\ \{32.2(0.203)\ [1-\sqrt{f_{gTB}}]\}_{0.5} = 25.3\ (1-\sqrt{f_{gTB}})_{0.5}$.

Eq. 3.40: f_{LTB} = (31.05 – 26.6)/(31.05 + v_{LTB}). However, $f_{LTB} = 1 - f_{gTB}$, requiring simultaneous solutions of Eqs. 3.36 and 3.40. Trial and error gives f_{LTB} = 0.12, and v_{LTB} = 6.31 ft/sec.

Eq. 3.33: (31.05 + 6.31) (0.12) = (31.05 – v_{LLS}) (0.741), so v_{LLS} = 25 ft/sec.

Eq. 3.34: (31.05 – v_{gTB}) (1 – 0.12) = (30.16 + 1.125 – 30.7) (0.259), so v_{gTB} = 30.96 ft/sec.

Eq. 3.30: 17.62 = β(30.96)(1 – 0.12) + (1–β)(30.7)(1 – 0.741), and β = 0.501.

Pressure Gradient:

Eq. 3.47: ρ_{LS} = 53.3 (0.741) + 1.08 (0.259) = 39.6 lbm/ft^3.

Eq. $(dp/dz)_H = [\rho_{LS}\ (1-\beta) + \rho_g\beta]g \sin\alpha/g_c$ = 19.39 psf/ft = 0.1346 psi/ft, $\mu_{LS} = \mu_g f_{gLS} + \mu_L\ (1 - f_{gLS})$ = 4.5 cp,

3.48: $Re_{LS} = dv_m\rho_{LS}/\mu_{LS}$ = 671,462, and f_{LS} = 0

Eq. 3.49: $(dp/dz)_F = (0.0126)(25.3)^2(39.6)(1 – 0.501)/[2(32.2)(0.203)]$
= 12.034 psf/ft = 0.0836 psi/ft.

Eq. 2.19: p/dz = 0.1346 + 0.0836 = 0.2191 psi/ft = total pressure gradient at wellhead.

The Beggs and Brill Correlation.
$C_L = v_{sL}/v_m$ = 0.307, and Fr = v_m^2/gd = 61.2.
$L_1 = 316\ C_L^{0.302}$ = 221.3, and $L_2 = 0.0009252\ C_L^{-2.4684}$ = 0.017.
$L_3 = 0.1\ C_L^{-1.4516}$ = 0.5754, and $L_4 = 0.5\ C_L^{-6.738}$ = 1,416.

Note that Fr is less than both L_1 and L_4 but greater than L_3. Therefore, the flow pattern is intermittent, and the following are the applicable parameter values.

a = 0.845

b = 0.5351

c = 0.0173

d = 2.96

e = 0.305

f = –0.4473

g = 0.0978

Pressure Gradient:

Eq. 4.13: $f_{L(0)} = a\ C_L^b/\mathrm{Fr}^c = 0.845(0.307)^{0.5351}/(61.2)^{0.0173} = 0.4146$.

Eq. 4.22: $Z = (1 – C_L)\ \ln(dC_L^e v_{dl}^f\ \mathrm{Fr}^g) = –0.034$, and

Eq. 4.21: $F(\alpha) = 1 + Z[\sin(1.8\alpha) – \sin^3(1.8\alpha)] = 0.984$.

Eq. 4.20: $f_L = f_{L(0)} \times F(\alpha) = 0.412$.

Pressure Gradient:

ρ_m = 53.3 (0.412) + 1.08 (0.588) = 22.82 lbm/ft^3.

$(dp/dz)_H = \rho_m\ g\ \sin\alpha/g_c$ = 21.79 psf/ft = 0.151 psi/ft.

Eq. 2.21: $\mu_n = \mu_L C_L + \mu_g(1 – C_L)$ = 0.19 cp,
$\rho_n = r_L C_L + \rho_g(1 – C_L)$ = 17.308 lbm/ft^3, and
$Re_n = dv_m\rho_n/\mu_n = (0.203)(25.3)(17.308)/(0.19 \times 0.000672) = 538{,}772$.

Eq. 1.11: $f_n = 0.182\ (667{,}872)^{-0.2} = 0.0131$.

Eq. 4.17: $y = C_L\ /\ f_L^2 = 1.81$.

Eq. 4.18: $s = \ln(1.81)/[–0.0523 + 3.182(\ln y) – 0.8725(\ln y)^2 + 0.01853(\ln y)^3] = 0.39$.

Eq. 4.16: $f_m = f_n\ e^s = 0.019$.

Eq. 4.15: $(dp/dz)_F = (0.0189)(25.3)^2(17.308)/[2(32.2)(0.203)]$

= 10.27 psf/ft = 0.071 psi/ft.

Eq. 2.15: d*p*/d*z* = 0.151 + 0.071 = 0.223 psi/ft = total pressure gradient at wellhead.

We note that Ansari et al. (1994) did not suggest applicability of their model for deviated wells. Nonetheless, we showed calculations for the Ansari et al. model using Eq. 4.34 for the Taylor bubble rise velocity. One can also use Eq. 4.33 with minute changes in estimated holdup and pressure gradient for this example.

Calculations presented in the field example are for the wellhead condition of an actual well. The computed values show that our model estimated somewhat higher values for liquid holdup and pressure gradient than the other two methods. Note that the estimated frictional loss by all three methods is approximately 40% of the total pressure loss at the wellhead, much higher than the example presented in Chapter 3. This is because the velocities, particularly gas velocity, are extremely high and the frictional gradient is nearly proportional to the square of the mixture velocity. Contribution of the frictional component drops to a much lower value of approximately 8% of the total at the well bottom. More important, at the well bottom the gas velocity is approximately 1/30 of that at the wellhead and the mixture velocity is one-third of that at the wellhead; high pressure promoting gas solubility and compression triggers this outcome.

An interesting point to note is that *F(a)* for the Beggs and Brill method is less than unity for this case, suggesting that liquid holdup for this slightly deviated well is approximately 4% lower than for flow in a vertical well under similar conditions. In practice, liquid holdup is rarely lower for wells deviated by less than 50° than that in vertical wells. Therefore, this particular example shows that computations using even the most robust of empirical correlations can sometimes lead to nonphysical results.

Note that in this example, as well as the one in Chapter 3, we ignored kinetic energy losses. That is because rigorous calculations showed that the pressure drop owing to kinetic energy losses amounted to less than 0.07% of the total pressure drop. **Table 4.2** presents the results of pressure-traverse calculations, and **Fig. 4.9** compares the same information with measured data. Calculations showed that bubbly flow exists at the well bottom. Because the computation was performed top-down so that results could be compared directly at the wellhead condition, discrepancy occurs at the well bottom. As mentioned in the example in Chapter 3, experience shows that when computations are performed along the direction of flow—bottom-up—errors decrease.

	Pressure (psig)			
Depth (ft)	Measured Data	Hasan-Kabir (1988a)	Ansari et al. (1994)	Beggs-Brill (1973)
0	361	361	361	361
1,000	611	635	576	595
2,000	876	920	840	850

3,000	1,161	1,221	1,116	1,145
4,000	1,473	1,540	1,414	1,458
5,250	1,875	1,959	1,831	1,867
5,750	2,084	2,132	2,001	2.034
6,000	2,189	2,219	2,083	2,118
6,241	2,238	2,304	2,166	2,199

Table 4.2—Pressure-traverse calculations.

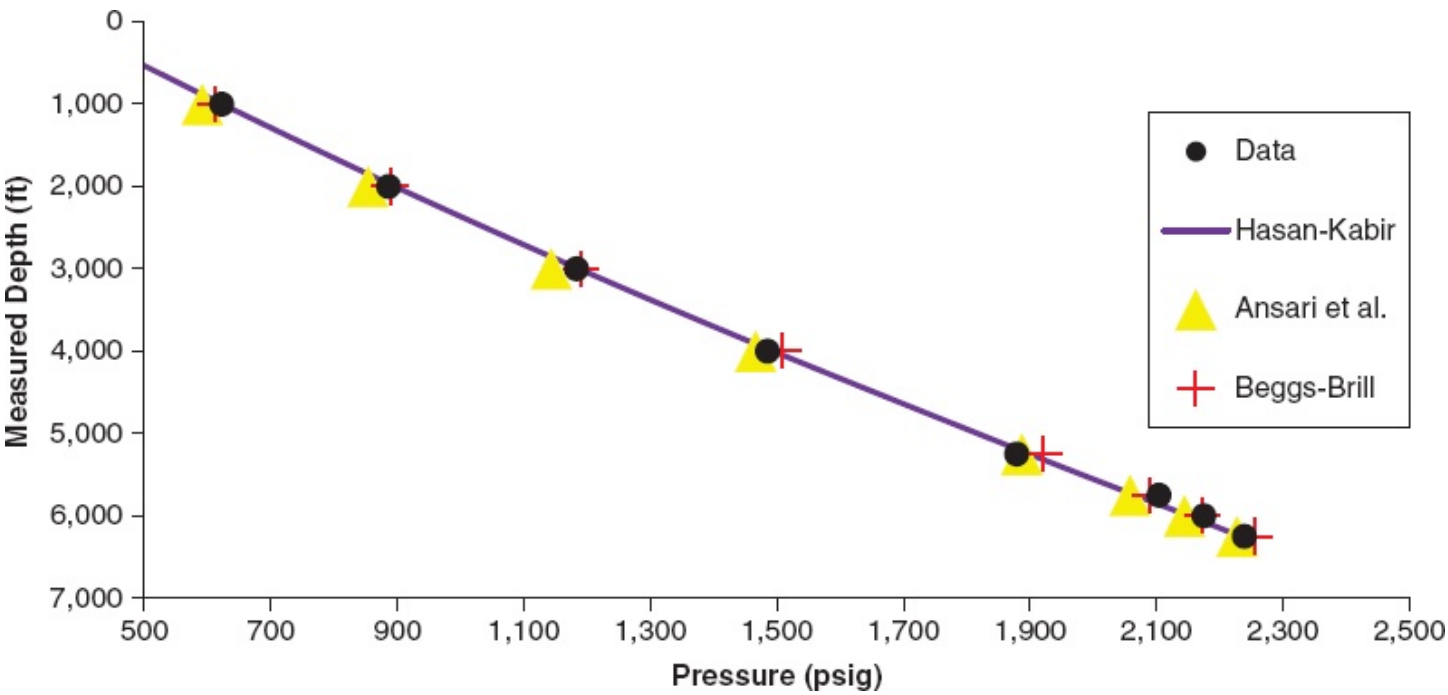

Fig. 4.9—Comparison of model performance with field data.

4.3 Flow in Horizontal Pipes and Wells

Over the last decade the tremendous importance of and interest in horizontal and multilateral wells have presented a challenge for improved understanding of two-phase flow behavior in horizontal and near-horizontal systems. Analysis of horizontal multiphase flow behavior can be adapted for slightly inclined systems. Besides wellbores, transportation of petroleum fluids demands modeling of multiphase flow in horizontal and slightly inclined systems, leading to pipeline design over flat or hilly terrain.

4.3.1 Flow Patterns in Horizontal Flow. Flow patterns that occur during two-phase flow through horizontal pipes are in many ways similar to those observed during vertical flow. However, there are some important differences, arising mainly from the differential effects of gravity on lighter and heavier phases. Except at high flow rates, distribution of the phases tends to be asymmetrical, with the gas phase concentrating toward the upper wall. As in vertical flow, subjective judgment in designating flow

patterns causes difficulty in presenting a general discussion on various flow regimes and transition from one regime to another. Here, we will follow the discussion of Taitel and Dukler (1976) and Taitel et al. (1978), which is in general agreement with most of the other studies in the area (Hewitt and Hall-Taylor 1970, p.6-7; Baker 1954). Taitel et al. (1978) described six distinct flow regimes in horizontal two-phase flow, five of which are shown in **Fig. 4.10**.

***Stratified Smooth Flow*.** At very low flow rates of the phases, particularly of the gas phase, the liquid flows through the bottom portion of the pipe, while the gas flows at the top. The two phases are thereby stratified, and the interface between them is smooth. This is known as stratified smooth flow.

***Stratified Wavy Flow*.** At somewhat higher gas flow rates than needed for stratified smooth flow, the liquid and the gas phases are still separated, as before, but the interface becomes wavy in what is known as stratified wavy flow.

***Plug (or Elongated Bubbly) Flow*.** At somewhat lower gas flow rates but higher liquid rates than needed for stratified wavy flow, the liquid could fill the entire pipe and flow as plugs. In that case, the gas flows as elongated bubbles near the top of the pipe. Thus, this type of flow is called plug (or elongated bubbly) flow.

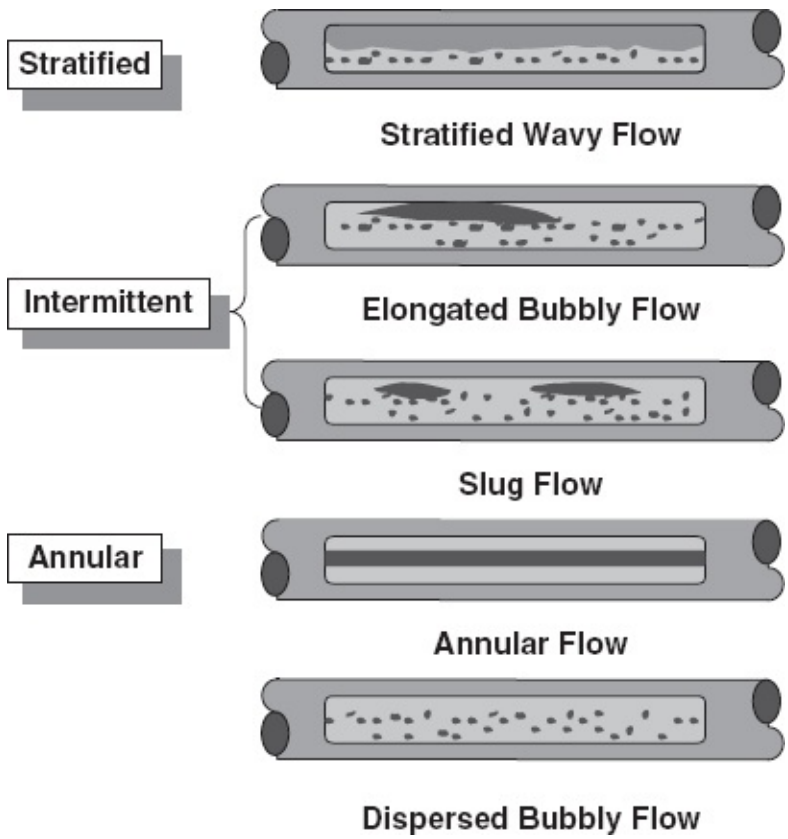

Fig. 4.10—Flow patterns in horizontal systems (after Taitel et al. 1978).

***Slug Flow*.** At higher gas flow rates the bubbles become large, filling up a substantial portion (but not entirely, as in vertical slug flow) of the flow cross section. The liquid slugs in between move violently downstream and are usually aerated by small bubbles. This is slug flow. The distinction between plug and slug flow is difficult

to establish and becomes subjective because of similar appearances. Indeed, Taitel et al. (1978) combined these two patterns into one and called it intermittent flow.

***Annular Flow*.** At high rates, the gas flows through the center of the pipe and the liquid flows along the tube wall, forming an annulus. This flow pattern, called annular flow, is quite similar to its counterpart in vertical flow, except that the liquid film is thicker at the bottom than at the top because of gravity in horizontal flow. Annular flow may be visualized to form from slug flow when the aeration in the slug becomes sufficient to form a continuous phase. It forms from stratified flow when the liquid flow rate is low and the gas flow rate is high enough to spread the liquid around the tube.

***Dispersed Bubbly Flow*.** At very high liquid rates, the gas phase may become dispersed as small bubbles in a continuous liquid phase. Similar to its counterpart in vertical flow, the shear energy of the turbulent liquid phase reduces the effect of gravity, causing the gas bubbles to be distributed more or less uniformly across the flow channel. The bubble concentration profile in this dispersed bubbly flow is still asymmetrical, with the peak occurring at some point above the pipe axis.

4.3.2 Flow Pattern Maps and Transition Criteria. As in vertical flow, a number of flow pattern maps in two-dimensional (2D) coordinates have appeared to represent flow regime transitions in horizontal systems. In some cases, attempts have been made to make the maps general by incorporating dimensionless groups (usually property groups) in the axes of the maps. One of the most durable maps is that of Baker (1954), which is often used in the petrochemical industry and is shown in **Fig. 4.11.** Along with including the gas and liquid mass fluxes, the map uses the dimensionless parameters, λ and ψ, which are defined in Eqs. 4.35 and 4.36.

$$\lambda = \sqrt{(\rho_g / \rho_A)/(\rho_L / \rho_w)}. \qquad (4.35)$$

$$\psi = (\sigma_w / \sigma)\sqrt[3]{(\mu_L / \mu_w)/(\rho_w / \rho_L)^2}. \qquad (4.36)$$

The subscripts *A* and *w* refer to values of the physical properties of air and water at standard conditions (atmospheric pressure and 60°F).

As pointed out for the case of vertical flow, representation of the effect of all secondary variables in a 2D map is impossible. However, we cannot expect one pair of dimensionless variables to generalize the transitions for all the flow regimes either. Analysis of transitions for the individual patterns, on the basis of a sound physical model and verified by experimental data, is therefore likely to be more accurate. We now present such an analysis for a near-horizontal system.

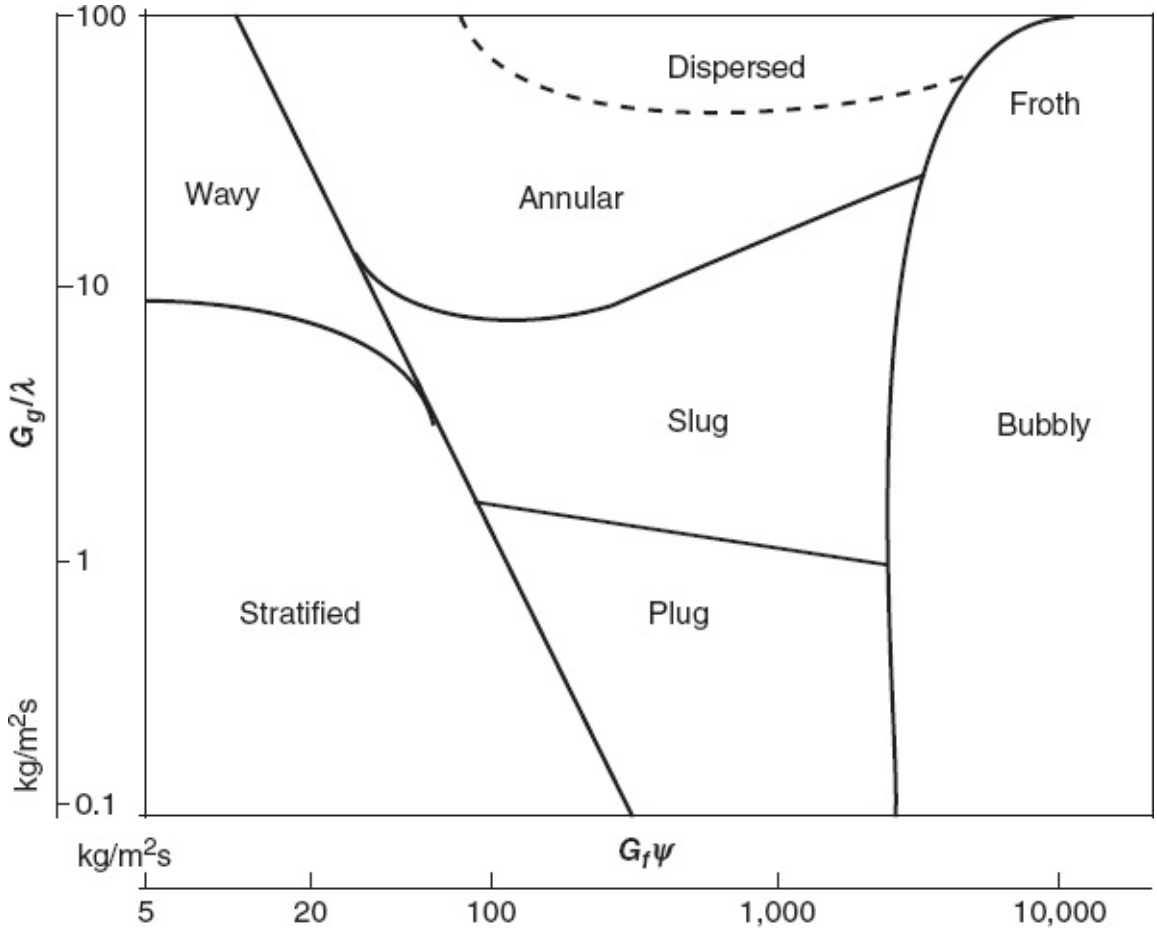

Fig. 4.11—Horizontal flow pattern map of Baker (1954).

Transition Between Stratified and Intermittent or Annular Flow. We follow the analysis presented by Taitel et al. (1978) for the transition between stratified (both smooth and wavy) and intermittent (slug and plug) flows and between stratified and annular flows in a system inclined by an angle, α, from a horizontal plane. The analysis depends on the fact that the pressure gradient in the liquid and the gas phase at any point in the channel must be equal. **Fig. 4.12** schematically represents smooth stratified flow in a circular channel. The liquid film occupies an area A_L over a height h with an in-situ velocity of v_L. The gas phase has an in-situ velocity of v_g and occupies an area A_g, which leads to $f_L = A_L/A$. The equilibrium in stratified flow will be disturbed if the gas flow rate is high enough to create an unstable wave. By analyzing the stability of a finite wave, Taitel et al. (1978) derived a relationship for the gas velocity at which the transition from stratified to either intermittent or annular flow takes place.

$$v_g > [1-(h/d)]\left[\frac{g\cos\alpha\,(\rho_L-\rho_g)A_g}{\rho_g(\mathrm{d}A_L/\mathrm{d}h)}\right]^{0.5} \qquad (4.37)$$

To estimate the important parameter, h/d, the momentum balances for the gas and liquid phases are used. The analysis presented below is similar to the one presented

for single-phase flow in Chapter 1 (Eqs. 1.1 through 1.3), except that one set of momentum balance is written for each phase here. The analysis yields

$$-A_g \mathrm{d}P - \tau_{wg}\mathrm{d}zS_g - \tau_i \mathrm{d}zS_i - \rho_g A_g g\mathrm{d}z\sin\alpha = W_g \mathrm{d}v_g + v_g \mathrm{d}W_g + \mathrm{d}W_L v_L, \quad (4.38)$$

and

$$-A_L \mathrm{d}P - \tau_{wL}\mathrm{d}zS_L - \tau_i \mathrm{d}zS_i - \rho_L A_L g\mathrm{d}z\sin\alpha = W_L \mathrm{d}v_L. \quad (4.39)$$

In Eqs. 4.38 and 4.39, shear stresses between the phases and between the channel wall and each phase are expressed in terms of the interface perimeters S, with appropriate subscripts. Therefore, S_g and S_L are used to calculated shear stress for the gas and liquid phases with the wall, while S_i is used to calculate shear stress between the phases. Neglecting the accelerational component (RHS of Eqs. 4.38 and 4.39) and equating the pressure gradient in each phase, one obtains

$$\tau_{wg}\frac{S_g}{A_g} - \tau_{wL}\frac{S_L}{A_L} + \tau_i S_i\left(\frac{1}{A_L} + \frac{1}{A_g}\right) - \left(\rho_L - \rho_g\right) g\sin\alpha = 0. \quad (4.40)$$

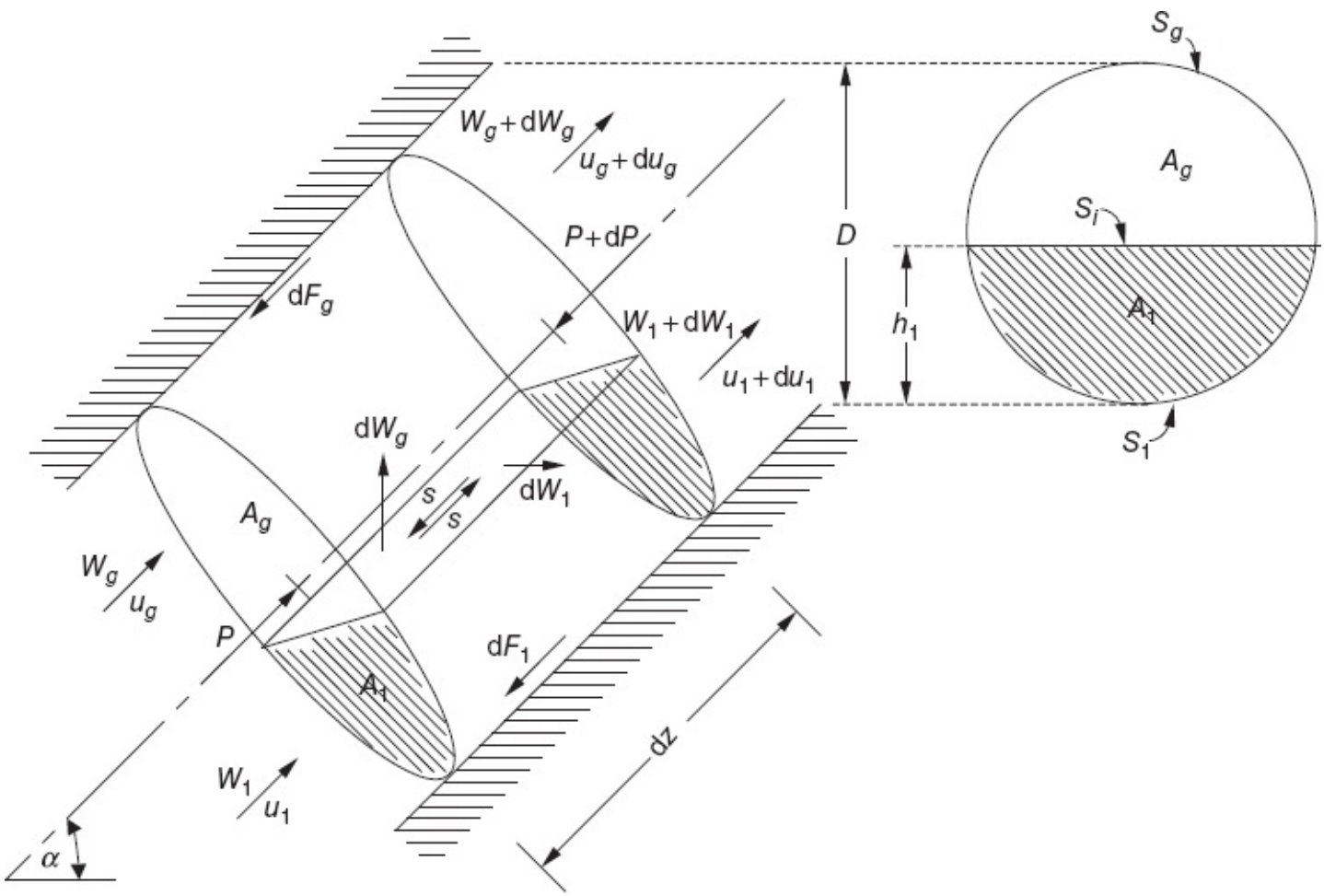

Fig. 4.12—Stratified two-phase flow in a slightly inclined system (after Taitel et al. 1978).

We evaluate shear stress in the usual manner, $\tau_{wg} = f_g\rho_g v_g^2/8$, $\tau_{wL} = f_l\rho_L v_L^2/8$, and so on, where friction factors for both phases are estimated with a Blasius-type equation, $f = C(Dv\rho/\mu)^{-m}$. To transform this equation into a dimensionless form, Taitel et al. (1978) divided the length dimension (h) by the pipe diameter d, and the areas (A_L) by d^2. This process yields dimensionless variables denoted by overbars ($\bar{h} = h/d$). Superficial velocities, v_{sg} (= $W_g/\rho_g A$) and v_{sL} (= $W_L/\rho_L A$), are used to render velocities (e.g., v_L) dimensionless (e.g., $\bar{v}_L = v_L/v_{sL}$). Therefore, Eq. 4.40 becomes

$$X^2\left[\left(\bar{v}_L\bar{d}_L\right)^{-n}\bar{v}_L^2\frac{\bar{S}_L}{\bar{A}_L}\right]-\left[\left(\bar{v}_g\bar{d}_g\right)^{-m}\bar{v}_g^2\left(\frac{\bar{S}_g}{\bar{A}_g}+\frac{\bar{S}_i}{\bar{A}_L}+\frac{\bar{S}_i}{\bar{A}_g}\right)\right]=4Y, \quad (4.41)$$

where X is the Lockhart-Martinelli (1949) parameter discussed in Chapter 2, which is given by

$$X^2=\left[\left(\frac{\mathrm{d}p}{\mathrm{d}z}\right)_F\right]_L\Big/\left[\left(\frac{\mathrm{d}p}{\mathrm{d}z}\right)_F\right]_g. \quad (2.26)$$

In Eq. 4.41, Y represents the ratio of gas-phase gravitational-to-frictional gradient and is given by

$$Y=\frac{(\rho_l-\rho_g)g\sin\alpha}{2(C/d)(v_{sg}d\rho_g/\mu_g)^{-m}\rho_g v_{sg}^2}=\frac{(\rho_l-\rho_g)g\sin\alpha}{\left|(\mathrm{d}p/\mathrm{d}z)_{sg}\right|}. \quad (4.42)$$

The X/Y relationship is shown in graphical form in **Fig. 4.13.** Note that when α equals zero, Y = zero. Note also that Eq. 4.41 represents the relationship between X and Y for a horizontal system.

Application of Eq. 4.41 requires expressions for various dimensions, such as S_L, S_i, A_L, in terms of the single variable liquid height h. For a circular geometry, the cross-sectional area for liquid flow A_L, and its variation, $\mathrm{d}A_L/\mathrm{d}h$, is related to the liquid height h by

$$A_L=\left(d^2/4\right)[\pi-\cos^{-1}\xi+\xi\sqrt{(1-\xi^2)}], \quad (4.43)$$

and

$$\frac{\mathrm{d}A_L}{\mathrm{d}h}=d\sqrt{1-\xi^2}, \quad (4.44)$$

where $\xi = 2(h/d) - 1$. Similarly, the wetted liquid perimeter S_L and the interface perimeter S_i are

$$S_L=d(\pi-\cos^{-1}\xi), \quad \text{and} \quad S_i=d\sqrt{(1-\xi^2)}. \quad (4.45)$$

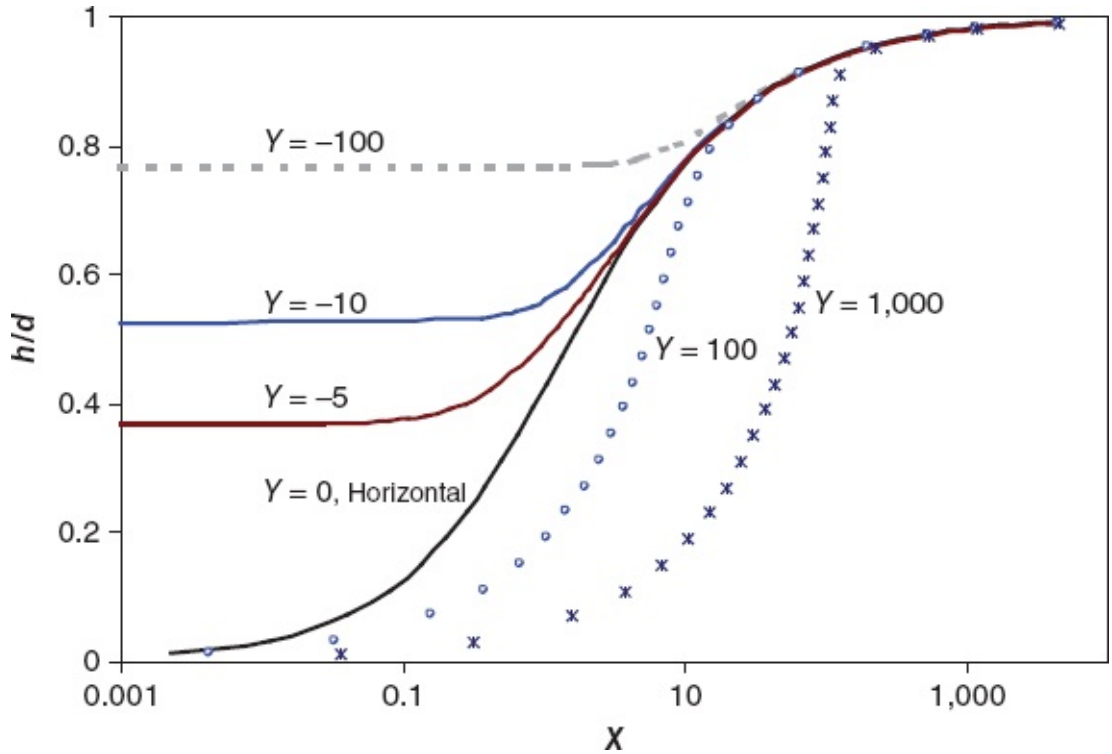

Fig. 4.13—Dimensionless liquid level as a function of *X* and *Y* (after Taitel et al. 1978)

Note that the in-situ velocities needed in Eq. 4.41 can be calculated from the superficial velocities once A_L and A_g (= 1 – A_L) are known.

Therefore, the transition from stratified flow to intermittent or annular flow is determined by the liquid level h for a given gas velocity v_g, as represented by Eq. 4.37. However, although Eq. 4.37 gives the gas velocity at which stratified flow changes, it does not indicate whether this change is to the annular or to the intermittent flow pattern. When the liquid level is high enough to maintain a liquid slug (i.e., a complete bridge), a stable slug can form; this will transition to intermittent flow. However, if the liquid level is below the center line, $h/d < 0.5$, a complete bridge of liquid between the top and the bottom of the pipe cannot be maintained. In such a case, the waves formed on the liquid surface will be swept around the tube, resulting in annular flow. Note that this reasoning also applies to the transition from dispersed bubbly to annular flow.

Transition to annular flow takes place when the gas velocity exceeds that given by Eq. 4.37 and h/d is less than 0.5. For horizontal flow, this value of h/d corresponds to 1.6 for the Lockhart-Martinelli (1949) parameter X, as shown in Fig. 4.13. When v_g exceeds that given by Eq. 4.37 and $h/d > 0.5$, transition to intermittent flow occurs.

Barnea et al. (1985) pointed out that a value of $h/d < 0.5$ is probably insufficient for transition to annular flow because the liquid slugs always carry some gas bubbles. Therefore, even when the calculated liquid level in the pipe is below the midpoint, a complete liquid bridge may be possible. If a gas holdup of approximately 35% is assumed in the liquid slugs, then transition to annular flow will occur when $h/d < 0.35$. However, all the liquid being available to form the slugs is an improbable scenario

because the gas bubbles are not likely to fill up the entire pipe cross section. Consequently, the transition to annular flow probably occurs when the *h*/*d* ratio falls below 0.40 to 0.45. For horizontal flow, this *h*/*d* ratio corresponds to a value of approximately 1.0 for the Lockhart-Martinelli (1949) parameter *X*.

Transition Between Smooth and Wavy Stratified Flows. Transition between smooth and wavy stratified flows is difficult to determine because it depends on the judgment as to when waves have formed. Taitel et al. (1978) offered an analysis based on the phenomenon of wave formation and some simplifying assumptions, such as the assumption that wave propagation velocity is much smaller than the gas in-situ velocity and that the sheltering coefficient is 0.01. Their analysis suggests that the flow pattern changes from smooth to wavy stratified flow when the in-situ gas velocity exceeds that given by

$$v_g > \sqrt{\frac{400\mu_L(\rho_L - \rho_g)g\cos\alpha}{\rho_L\rho_g v_L}} \qquad (4.46)$$

Transition Between Intermittent and Dispersed Bubbly Flow. At high liquid and low gas velocities, the turbulent fluctuations of the liquid cause the gas to disperse as bubbles throughout the channel, resulting in bubbly flow. As the liquid velocity decreases, buoyant forces tend to push the gas bubbles upward, allowing agglomeration and, finally, transition to slug or plug flow. Thus, a balance between the buoyant forces expressed as

$$F_B = g\cos\alpha(\rho_L - \rho_g)A_g, \qquad (4.47)$$

and the force owing to turbulent fluctuation expressed as

$$F_t = 0.25\,\rho_L\, v_L^2\, f_L\, S_i / 4, \qquad (4.48)$$

And Eqs. 4.47 and 4.48 should establish the transition between bubbly and intermittent flow. Taitel et al. (1978) took this approach and arrived at the criterion for the transition from intermittent to bubbly flow, which is written as

$$v_L = \sqrt{\frac{4A_g g\cos\alpha}{S_i f_L}\left(\frac{\rho_L - \rho_g}{\rho_L}\right)} \qquad (4.49)$$

The liquid friction factor f_L can be determined from the Blasius equation in which the Reynolds number is calculated using the hydraulic diameter (= $4A_L/S_L$), liquid viscosity, liquid density, and the in-situ liquid velocity. The terms in Eq. 4.49 depend only on *h*/*d*, which can be evaluated from the Lockhart-Martinelli parameter *X* and the inclination angle *α* using Fig 4.13.

Taitel and Dukler (1976) expressed these transition equations in terms of the Lockhart-Martinelli parameter *X* and three other dimensionless parameters, such as *F*, *K*, and *T*. These parameters are shown on the flow pattern map **(Fig. 4.14).** Note

that α is zero for horizontal flow.

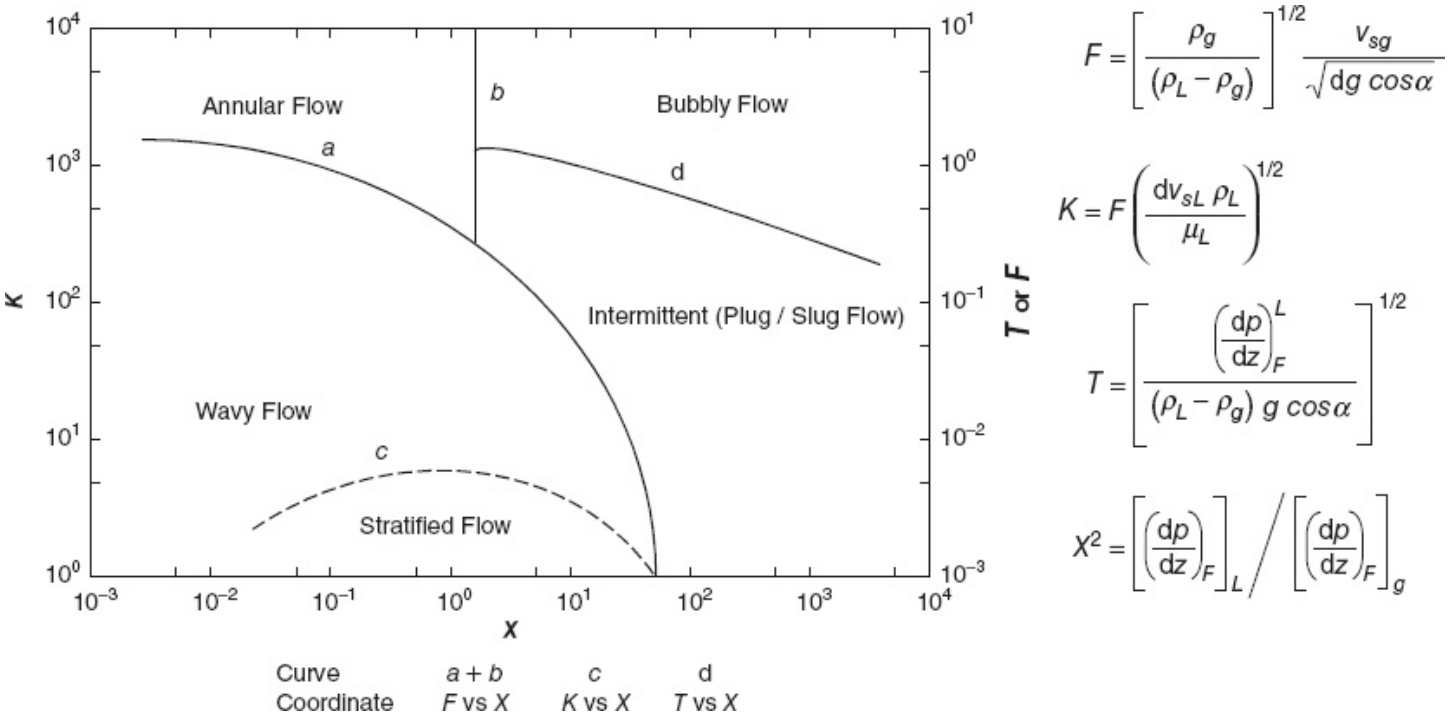

$$F = \left[\frac{\rho_g}{(\rho_L - \rho_g)}\right]^{1/2} \frac{v_{sg}}{\sqrt{dg\cos\alpha}}$$

$$K = F\left(\frac{dv_{sL}\,\rho_L}{\mu_L}\right)^{1/2}$$

$$T = \left[\frac{\left(\frac{dp}{dz}\right)_F^L}{(\rho_L - \rho_g)\,g\cos\alpha}\right]^{1/2}$$

$$X^2 = \left[\left(\frac{dp}{dz}\right)_F\right]_L \Big/ \left[\left(\frac{dp}{dz}\right)_F\right]_g$$

Fig. 4.14—Horizontal flow pattern map of Taitel and Dukler (1976).

Taitel and Dukler (1976) also converted this horizontal flow pattern map for air/water systems at standard conditions and showed its excellent agreement with the map of Mandhane et al. (1974). This is especially true when the differences in definitions for bubbly and annular flow by Mandhane et al. (1974) and Taitel and Dukler (1976) are taken into account. If the transition to annular flow is assumed to take place for $X < 1.0$ and the gas velocity is high enough so that Eq. 4.37 is satisfied, the agreement between the Mandhane et al. data and the Taitel et al. map becomes slightly better at low flow rates and somewhat worse at high flow rates. The Taitel et al. transition equations and the horizontal flow map derived from it, shown in Fig. 4.14, appear to be based on a sound physical model and are supported by experimental data. Another attractive feature of the model is that it appears to be applicable in a somewhat modified form for slightly inclined flow as well.

4.3.3 Holdup and Pressure Drop in Near-Horizontal Flow. The static pressure gradient is absent in horizontal two-phase flow and is small for near-horizontal systems. In addition, the contribution of the accelerational component also tends to be small because the total pressure change, causing variation in ρ_g, is usually small. Consequently, the estimation of the frictional pressure gradient becomes very important. This reasoning obviously reduces the importance of slip between phases. Therefore, in this section, we will not concern ourselves with an accurate correlation for holdup in any flow regime. We recommend the Lockhart-Martinelli correlation for calculating holdup in all flow regimes unless a simpler and more accurate correlation

is available in any given regime.

Estimating friction factor and, hence, the frictional pressure gradient is usually entirely empirical in nature. In other words, useful models for near-horizontal systems are few. Nonetheless, a number of modeling efforts appear quite promising, as articulated by Gomez et al. (2000) and Xiao et al. (1990).

Stratified Wavy/Smooth Flow. The stratified wavy flow regime is difficult to analyze because of waves on the liquid surface. The characteristics of these waves vary with varying gas and liquid properties and flow rates, making it difficult to predict the frictional resistance offered by the waves. The Lockhart-Martinelli method is probably as good as (and simpler than) any of the few other methods available for pressure-drop computation in this flow regime. Govier and Aziz (2008, pp.562–563) also suggested a simple method, which requires estimating the gas flow rates at which transitions from wavy flow to smooth flow and annular flow take place at the given liquid flow rate. The pressure gradients at those two flow rates are then calculated using correlations specific to the smooth stratified flow and annular flow regimes. A log-linear interpolation for the given gas flow rate is then made by making a log-log plot of pressure gradient vs. gas flow rate. The holdup can also be estimated in a similar manner by log-linear interpolation. Of course, the Lockhart-Martinelli method can also be applied.

The stratified smooth flow regime is the simplest to analyze theoretically because of the simple geometry of the interface. However, this flow pattern is also the least likely to occur in practice. There are, therefore, very few field or experimental data available for this flow regime. Although we suggested the use of the method of Lockhart and Martinelli (1949), we note that for liquid/liquid flow, the Lockhart-Martinelli method significantly overestimates the frictional pressure gradient. Baker (1954) also indicated significant differences between Lockhart-Martinelli predictions and his data. Baker's empirical correlation for ϕ_g, the gas-phase friction multiplier (see Chapter 2, Section 2.51, Eq. 2.23) for a smooth stratified flow regime, is given by

$$\phi_g = \frac{15,400\,X}{\left(\rho_L v_{sL}\right)^{0.8}} \qquad (4.50)$$

Note that this expression is another way of accounting for the effect of mass flux on a friction multiplier, as discussed in Chapter 2. One can also calculate a liquid-phase friction factor with the Blasius equation. The hydraulic diameter needed to calculate the Reynolds number can be determined from 4 A_L/S_L, as described in the discussion of Eq. 4.49.

The liquid holdup and pressure gradient in stratified smooth and stratified wavy regions can be calculated in the manner suggested by Taitel et al. (1978) and discussed in the last section. Both Gomez et al. (2000) and Xiao et al. (1990) adapted this approach and suggested using Eq. 4.40 for estimating pressure gradient in both smooth and wavy stratified flows. Xiao et al. proposed using the Moody

friction factor chart (or Eq. 1.12) for f_L and f_g, although they noted that f_L, calculated in this manner, is often inaccurate because of the presence of interfacial waves. For interfacial-friction factor f_i in small-diameter pipes ($d \leq$ ½ in.), they recommended using $f_i = f_g$ when

$$v_{sg} \leq v_{sgt}, \qquad (4.51)$$

where

$$v_{sgt} = 5(p_s/p)^{0.5}, \qquad (4.52)$$

where p_s is standard atmospheric pressure (14.7 psi) expressed in the same units as p. When $d \leq 0.5$ in. and $v_{sg} \geq v_{sgt}$, they suggested

$$f_i = f_g\left[1 + 15 v_{sgt}(v_{sg} - v_{sgt})\sqrt{h/d}\,\right]. \qquad (4.53)$$

For pipes with diameters larger than ½ in., they recommended using equivalent roughness factors for use with the Moody friction factor chart or equations.

$$\varepsilon = \frac{34\sigma}{\rho_g v_L^2}, \qquad (4.54)$$

when

$$\frac{\rho_g v_L^2 \varepsilon}{\sigma}\frac{\mu_L^2}{\sigma \rho_L \varepsilon} > 0.005. \qquad (4.55)$$

Otherwise, for $d \geq$ ½ in., they recommended

$$\varepsilon = \frac{170\sigma}{\rho_g v_L^2}\left(\frac{\rho_g v_L^2 \varepsilon}{\sigma}\frac{\mu_L^2}{\sigma \rho_L \varepsilon}\right)^{0.3}. \qquad (4.56)$$

Gomez et al. (2000) followed the Xiao et al. (1990) method for calculating f_i and agreed with their suggestion that f_g be calculated with the Moody friction factor chart (or Eq. 1.12). However, for f_L they suggested the following correlation:

$$f_L = \frac{1.629}{\mathrm{Re}_L^{0.5161}}\left(v_{sg}/v_{sL}\right)^{0.0926}. \qquad (4.57)$$

Intermittent Flow. For the intermittent (slug and plug) flow pattern, the drift-flux approach to flow modeling may be taken. In horizontal and near-horizontal systems, the drift velocity of the bubbles is low, and so the single drift velocity, that of the Taylor bubble, may be used for the entire cell. Therefore, the holdup is given by

$$f_L \equiv 1 - f_g = 1 - \frac{v_{sg}}{C_o v_m + v_{\infty T\alpha}} \quad (4.58)$$

Taylor bubble rise velocity may be estimated with either Eq. 4.33 or Eq. 4.34. The value of the parameter C_o depends on the velocity profile and the distribution of the bubbles across the flow channel. For laminar flow, or ($dv_m\rho_L/\mu_L$ < 1,000), the value of C_o has been found to be 2.0. The local velocity at the pipe axis during laminar flow is twice that of the average velocity in the pipe, which suggests that the bubbles occupy the central portion of the flow channel. While this conclusion is obviously not true for horizontal flow, it is safe to use a value of 2.0 for C_o. For highly turbulent flow ($dv_m\rho_L/\mu_L$ > 200,000), C_o is found to be between 1.2 and 1.35, as shown by Hughmark (1965) and Gregory and Scott (1969). Their work suggested that the bubbles occupy the pipe center, which is likely to occur during highly turbulent flow. For the intermediate region, the data of Hughmark may be approximated by C_o = 3.04 – 0.151 ln ($dv_m\rho_L/\mu_L$).

Gomez et al. (2000) and Kaya et al. (2001) extended the vertical slug flow model of Ansari et al. (1994) (see Chapter 3, Section 3.3.2) for inclined and horizontal systems. They assumed that the liquid film surrounding the Taylor bubble has a uniform thickness. Using an approach similar to that for stratified flow, they suggested that an equivalent form of Eq. 4.40 can be solved iteratively for the area occupied by the Taylor bubble, A_g, and the area for the liquid film, A_L, thereby allowing the computation of the liquid-film thickness.

Gomez et al. (2000) used the following correlation for liquid holdup in the slug body, f_{LLS}:

$$f_{LLS} = e^{-(0.45\alpha_R + 2.48\times10^{-6}\,\mathrm{Re}_{LS})} \quad (4.59)$$

Gomez et al. claimed that α_R, the well inclination from horizontal in radians, makes the method applicable to all inclination angles. In Eq. 4.59, the slug body Reynolds number Re_{LS} is given as

$$\mathrm{Re}_{LS} = \rho_L v_m d/\mu_L. \quad (4.60)$$

For calculating frictional gradient during slug flow, Hughmark (1965) suggested that the corresponding single-phase equation can be used with in-situ liquid velocity and liquid properties; that is,

$$\left(\frac{dp}{dz}\right)_F = \frac{2 f_{fL} \rho_L v_L^2}{g_c\, d}. \quad (4.61)$$

In Eq. 4.61, f_{fL} is the single-phase friction factor calculated with the liquid-phase Reynolds number, $dv_L\rho_L/\mu_L$. Gregory and Scott (1969) found the Hughmark correlation to be quite satisfactory. Gomez et al. (2000) recommended calculating frictional losses for the various parts of the cell unit, the liquid slug, the liquid film, and

the interface between the liquid film and the Taylor bubble. This calculation procedure for slug flow should be applicable for the entire intermittent flow regime. As indicated earlier, Taitel et al. (1978) did not consider the slug and plug flows as two distinct flow patterns.

***Dispersed Bubbly Flow*.** The dispersed bubbly flow pattern is particularly amenable to modeling by the driftflux approach. As in the case of intermittent flow, the drift velocity between the phases may be neglected. Because of the high liquid flow rate, the bubble concentration profile is more symmetrical around the tube axis, and so a value of 1.2 for C_o may give good results. Therefore, holdup can be correlated with the equation

$$f_L \equiv 1 - f_g = 1 - \frac{v_{sg}}{1.2\, v_m}. \qquad (4.62)$$

The frictional pressure gradient may be estimated from

$$\left(\frac{\mathrm{d}p}{\mathrm{d}z}\right)_F = \frac{2 f_m \rho_m v_m^2}{g_c\, d}, \qquad (4.63)$$

where f_{fm} is estimated from the single-phase correlation using mixture density $\rho_m = f_L\rho_L + f_g\rho_g$ and mixture viscosity $\mu_m = f_L\mu_l + f_g\mu_g$.

***Annular Flow*.** The annular flow pattern is similar to its counterpart in vertical flow because the high flow rates make the effect of gravity small. Therefore, the methods for computing holdup and pressure drop valid for vertical flow may also be applied to horizontal flow. Following the approach used in stratified flow, Gomez et al. (2000) presented a rigorous method to write separate momentum balances for the liquid film and the gas core. The resulting expression is similar to Eq. 4.40, except that the term involving gas wall shear stress is absent.

$$-\tau_{wL}\frac{S_L}{A_L} + \tau_i S_i\left(\frac{1}{A_L} + \frac{1}{A_g}\right) - \left(\rho_L - \rho_g\right) g \sin\alpha = 0. \qquad (4.64)$$

Note that neglecting kinetic energy losses, required to arrive at Eq. 4.62, could lead to inaccuracy. Gomez et al. extended the approach they used for vertical systems (see Chapter 3, Section 3.3.4) to express the interfacial friction factor f_{fi} in terms of the friction factor that the core fluid would experience when flowing alone in the channel f and the inclination factor, I. Therefore,

$$f_{fi} = If, \qquad (4.65)$$

where for vertical systems the inclination factor I_v is given by

$$I_V = (1 + 300\delta/d). \qquad (4.66)$$

For horizontal systems, Gomez et al. (2000) adopted the correlation proposed by Henstock and Hanratty (1976) to represent the inclination factor I_H.

$$I_H = (1+800)\frac{\left[(0.707\,\mathrm{Re}_{sL}^{0.5})^{2.5} + \left(0.0379\,\mathrm{Re}_{sL}^{0.9}\right)^{2.5}\right]^{0.4}}{\mathrm{Re}_{sg}^{0.9}}\frac{v_L}{v_g}\sqrt{\rho_L/\rho_g}. \quad (4.67)$$

For an inclined system, Gomez et al. proposed the relationship as

$$I_\alpha = I_H \cos^2\alpha + I_V \sin^2\alpha. \quad (4.68)$$

They used Eq. 3.53 for estimating entrainment in annular flow for all angles of inclination.

The models and correlations discussed in Sections 3.1 through 3.3 assume that the flow rate in the channel remains constant. In a horizontal well, this assumption is untrue; fluid influx along the wellbore makes flow rate in the well continually increase from the toe to the heel. The next subsection explores this point further.

4.3.4 Flow in Horizontal Wells. An important aspect of horizontal wells is that fluid influx may occur through almost the entire horizontal section of the well. This recurrent fluid influx means that the mass flow rate increases in the direction of flow during production and decreases in the flow direction during injection. The continual change of fluid flow rate along the wellbore inhibits the full development of classical flow patterns. In addition, modifying the pipe roughness characteristics in the well may change the pipe friction factor. Furthermore, fluid inlet/exit through a perforation may cause significant changes in its kinetic energy. In openhole completions, the uneven formation surface and wellbore diameter present further complications.

In horizontal wells, gravity plays a negligible role, making estimation of accurate frictional pressure gradient of utmost importance. In addition, horizontal wells are rarely truly horizontal, causing terrain-generated slug flow to occur. Modeling two-phase flow in such wells to account for all these factors presents a serious challenge.

Ihara et al. (1994) conducted experimental research and found that flow through perforations increases the apparent friction factor. Dikken (1990) presented an interesting model for predicting pressure drop in horizontal wells. He ignored the effect of changes in kinetic energy and extra friction caused by flow through perforations. Results from his analysis, shown in **Fig. 4.15,** present dimensionless production as a function of dimensionless distance and the exponent of the Blasius friction factor *a*.

Note that $\alpha = 0$ for a completely rough pipe, and $\alpha = 0.25$ for a fully smooth pipe. His analysis showed that increasing turbulence limits production gains from lengthening a well beyond a certain critical length.

Ouyang and Aziz (2000) presented a comprehensive study for fluid ingress in horizontal pipes. They gathered data from 100-ft-long pipes of various diameters with perforations at various positions. They noted that all available models underestimated

the pressure-drop data. They postulated that kinetic energy loss owing to flow through perforations is highly significant in such systems and that ignoring the loss causes the present models to underestimate pressure loss. Ouyang and Aziz proposed a homogeneous model with an extra accelerational pressure loss term, $(dp/dz)_{AW}$, to account for fluid influx through perforations. Therefore, similar to Eq. 1.5, they proposed that the total pressure gradient is given by

$$(dp/dz) = (dp/dz)_F + (dp/dz)_H + (dp/dz)_A + (dp/dz)_{AW}. \quad (4.69)$$

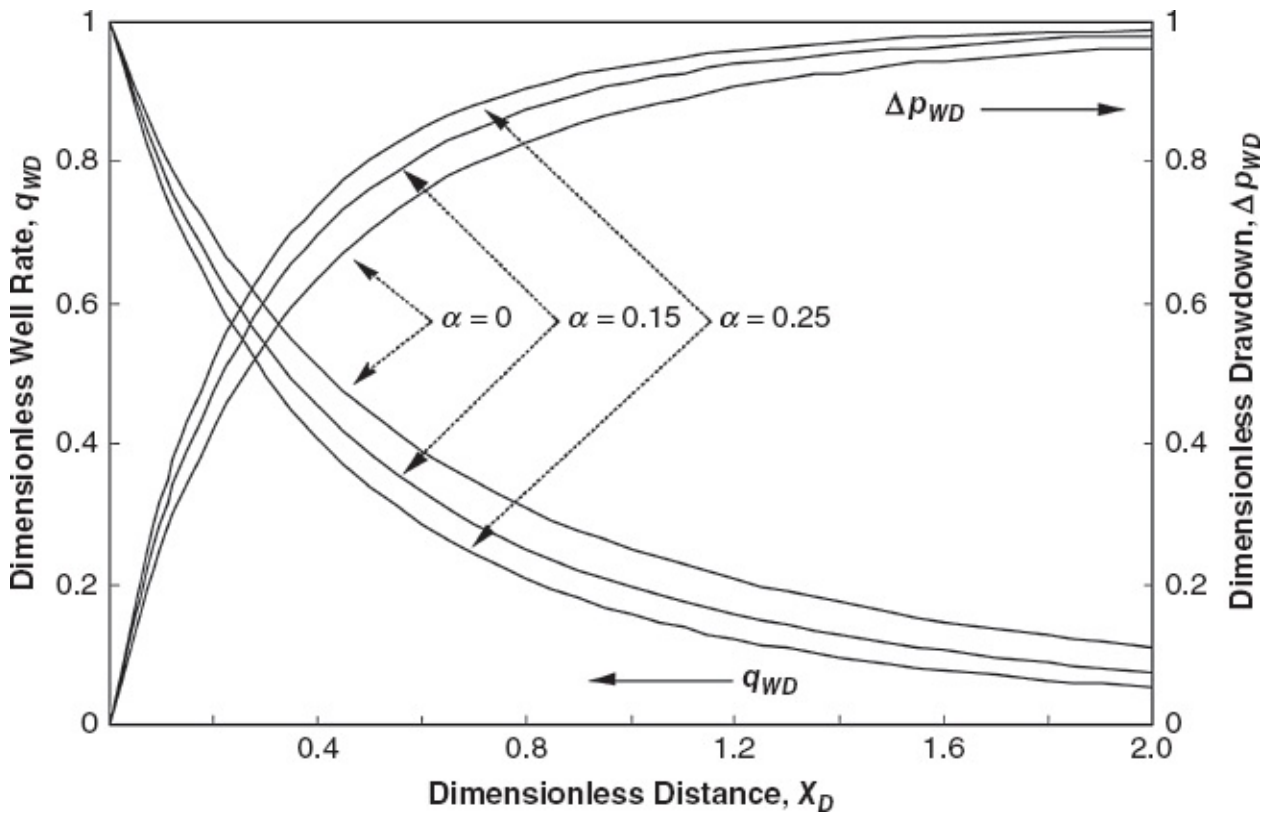

Fig. 4.15—Diminishing influx with increasing well length (after Dikken 1990).

The first two terms on the right side of Eq. 4.69 are the same as those for the homogeneous models discussed in Chapter 2, Section 2.4. They expressed the acceleration terms, $(dp/dz)_A$ and $(dp/dz)_{AW}$, as

$$\left(\frac{dp}{dz}\right)_A = \frac{\beta}{1-\beta}\left[-(\tau_w S/A) - \rho_{tp} g \sin\theta + (dp/dz)_{AW}\right], \quad (4.70)$$

and

$$\left(\frac{dp}{dz}\right)_{AW} = -\frac{\rho_m}{A}\left[\omega\left(v_m q_{Itp} + v_{tp} q_{Im}\right) + 2(1-\omega) v_{tp} q_{Itp}\right]. \quad (4.71)$$

The volumetric expansion coefficient β is given by $(\rho_m\ v_m\ v_{sg})/\rho$, and the weighting

factor ω has an empirically determined value of 0.8. Ouyang and Aziz (2000) used two types of velocities, v_m and v_{tp}. The mixture velocity v_m is the same one used in this book; that is, $v_m = v_{sL} + v_{sg}$. The two-phase flow velocity v_{tp} is defined as

$$v_{tp} = v_{sL}\,(\rho_L/\rho_m) + v_{sg}\,(\rho_g/\rho_m), \qquad (4.72)$$

where ρ_m is the usual two-phase homogeneous mixture density, $\rho_m = (v_{sL}/v_m)\rho_L + (v_{sg}/v_m)\rho_g$. In a similar manner, they defined two volumetric influx rates.

$$q_{Im} = q_{IL} + q_{Ig} \qquad (4.73)$$

and

$$q_{Itp} = q_{IL}\,(\rho_L/\rho_m) + q_{Ig}\,(\rho_g/\rho_m). \qquad (4.74)$$

Note that q_{IL} and q_{Ig} are the liquid and gas inflow (or outflow) rates per unit wellbore length.

Ouyang and Aziz (2000) proposed two correlations for the two-phase mixture friction factor for injection wells and three for producing wells, depending on the laminar or turbulent nature of flow. Their laboratory data lend credence to the correlations. The reader is advised to consult the original paper for details of the experiments and the model.

Discussion. The mechanistic approach to modeling flow in deviated wells presented in Section 4.2.4 appears promising because of its theoretical basis. The models, however, are still being improved. There are disagreements, especially regarding the expression for bubble terminal rise velocity in both bubbly and slug flows. Our data suggest that inclination angles have an insignificant influence on v_∞, but others have assumed that it varies with $\sin\alpha$. Similarly, the Taylor bubble rise velocity data of Lau (1972) is better represented by $n = 4$ rather than $n = 2.4$, as Hasan and Kabir (1988a) proposed originally. In addition, $v_{\infty T\alpha}$ values, evaluated using our model, are quite different from that proposed by Bendiksen (1984) for near-horizontal systems. Another difficulty arises from the use of a constant value of the flow parameter C_o for all inclination angles, proposed by both Hasan and Kabir (1988a) and Kaya et al. (2001). Further data, especially from large-diameter pipes, are needed to fully establish the value of the flow parameter. The churn flow regime, which has been lumped with the slug flow regime, may require separate values of the parameters (C_o = 1.15). Unfortunately, no reliable method exists for distinguishing churn from slug flow at present.

In spite of these difficulties, the models advanced by Hasan and Kabir (1988a), Kaya et al. (2001), Gomez et al. (2000), and Zhang et al. (2003a, b) appear sound. They presented good agreement of their models with holdup and pressure-drop data from several sources. In particular, the model of Gomez et al. appears to perform very well for both vertical and deviated wells. Nonetheless, much of the data (Beggs 1972; Beggs and Brill 1973; Mukherjee and Brill 1983) against which these models

were validated are from 1- to 2-in.-ID pipes. This fact leaves some doubt as to the value of the flow parameter in large-diameter pipes.

For computing holdup and pressure drop in inclined systems, the Beggs and Brill (1973) correlation is the most comprehensive empirical method available at present. On the surface, the correlation appears to account for the prevailing flow pattern in inclined flow. However, the flow pattern determined by this method is applicable only for a horizontal system. For an inclined system, the flow pattern discerned might not correspond to the actual pattern observed in the system but is used by Beggs and Brill as a correlating parameter only. Complications involved in the calculation procedure and the method's exclusive reliance on empiricism make it less than completely satisfactory. Nonetheless, performance of the Beggs and Brill correlation is usually quite good.

For horizontal and near-horizontal systems, the Taitel et al. (1978) model has become well-established for determining flow patterns. In addition, the Taitel et al. model is useful in estimating holdup in stratified flow regimes. For estimating pressure gradient and holdup in horizontal/near-horizontal systems, the correlation of Lockhart and Martinelli (1949) for all flow regimes may also be used. For estimating frictional pressure gradient in horizontal wellbores, we recommend the Ouyang and Aziz (2000) correlations. As mentioned earlier, Zhang et al. (2003a, b) and Zhang and Sarica (2006) models are applicable to all angles of inclination. Note, however, that many horizontal wells are completed open hole and no simple solution exists.

4.4 Modeling Flow in Nonconventional Situations

Upward multiphase flow in vertical and deviated circular wellbores is the norm in petroleum production. However, exceptions occur in many applications. Some examples include these:

- Performing a transient test in a sucker-rod-pumping well requires holdup and pressure-drop estimations in the tubing/casing annulus.
- Designing steam injection and gas anchors demands understanding downward two-phase flow.
- Modeling phase redistribution during shut-in tests requires understanding bubble migration in countercurrent two-phase flow.

These situations add complexity to already complex flow phenomena. Models and correlations developed for vertical and deviated wells are not always directly applicable, although they form a basis for analyzing these systems.

In the rest of this chapter, we discuss two-phase gas/liquid flow in an annulus, downward direction flow, and countercurrent flow. The last section discusses two-phase, oil/water flow in vertical and deviated wells.

4.4.1 Two-Phase Flow in an Annulus. Two-phase flow patterns observed in an annular channel are similar to those observed in vertical and inclined upward flow; that is, bubbly and dispersed bubbly, slug, churn, and annular flow. As in the case of flow in inclined systems, slug and churn flow are combined and called intermittent flow. Another similarity between flow in deviated wells and flow in annular channels is the influence of geometry on the shape of bubbles and, therefore, on their rise velocities.

Very little work is available on two-phase flow in an annulus. The early studies of Godbey and Dimon (1977) and Hasan and Kabir (1992) involved stagnant liquid columns while estimating bottomhole pressure in sucker-rod-pumping wells. Caetano et al. (1992b) presented a mechanistic model for two-phase flow in annuli. Hasan and Kabir (1992) presented a simplified approach to estimate liquid holdup and pressure gradient on the basis of the models for vertical and deviated wellbores discussed earlier. Because of its simplicity and accuracy, we present this work here.

The approach adapted for deviated circular channels appears to work well for vertical and deviated annuli. For bubbly flow in vertical or deviated annuli, Hasan and Kabir (1992) found that holdup may be estimated using Eq. 3.20 (or Eq. 4.25) with C_o = 1.2 and v_∞ given by the Harmathy (1960) correlation (Eq. 3.6). Therefore, no modification in the estimation procedure of a vertical circular channel is needed. Indeed, as in circular channels, the transition from bubbly to slug flow occurs in an annulus when the gas volume fraction exceeds 25%. Thus, we used Eq. 4.7 [$v_{sg} > (0.43\ v_{sL} + 0.357\ v_\infty)\ \sin\alpha$] as the criterion for this transition in vertical and deviated annuli.

Similarly, for intermittent flow, we can use Eqs. 4.23 [$f_g = v_{sg}/(C_o v_m + \bar{v}_\infty$] and 4.24 (for average rise velocity) to estimate holdup. We noted that a value of 1.2 for C_o worked well for both vertical and deviated annuli. However, we found the rise velocity of Taylor bubbles to be influenced by both pipe inclination and the inside to outside-diameter ratio of the annulus. The expression for estimating the Taylor bubble rise velocity in an annulus is written as

$$v_{\infty T\alpha} = \left[\ 0.35 + 0.1\left(d_i / d_o\right)\right]\left(1+\cos\alpha\right)^{1.2}\sqrt{\sin\alpha}\,\sqrt{g d_o\left(\rho_L - \rho_g\right)/\rho_L}\,, \qquad (4.75)$$

where d_i is the diameter of the inner tubing [tubing outer diameter (OD)] and d_o is that of the outer tubing (casing ID). Yu et al. (2010) also found Eq. 4.75 to be applicable for two-phase flow in vertical annuli. Note that for a circular channel, when there is no inner tubing, d_i is zero, and Eq. 4.75 collapses to Eq. 4.32, which in turn reduces to Eq. 3.7 (Nicklin equation) for vertical systems in which cosa is zero and sinα = 1.0.

Using Caetano et al. (1992b) data, among others, Hasan and Kabir (1992) showed that the volume-fraction data of three flow regimes can be modeled quite satisfactorily. **Figs. 4.16 through 4.18** provide the model's validation. Note that slug and churn flow patterns, presented as intermittent flow in this text, were treated separately.

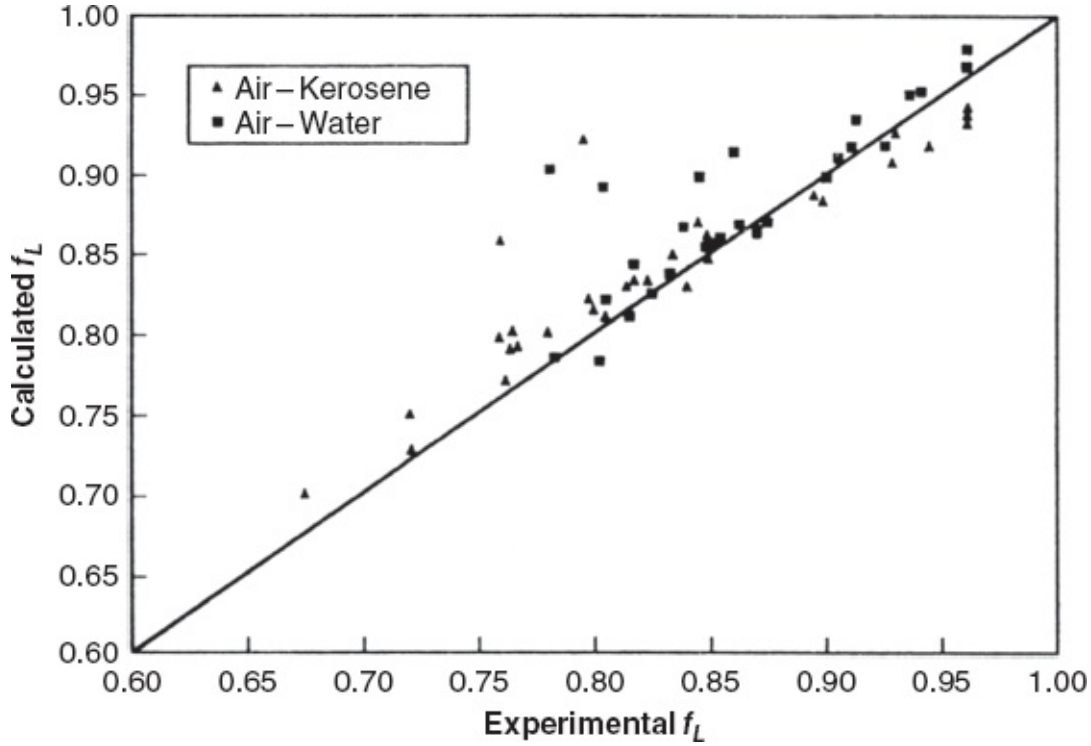

Fig. 4.16—Model mimics bubbly flow data of Caetano et al. (after Hasan and Kabir 1992).

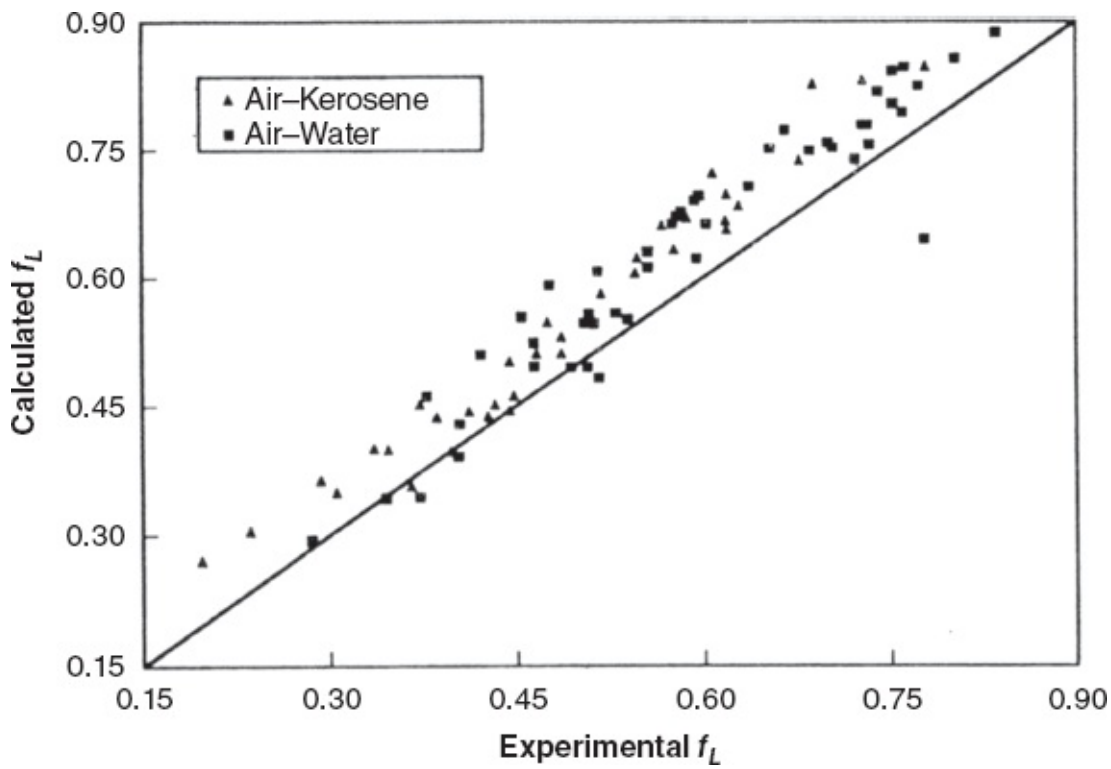

Fig. 4.17—Model mimics slug flow data of Caetano et al. (after Hasan and Kabir 1992).

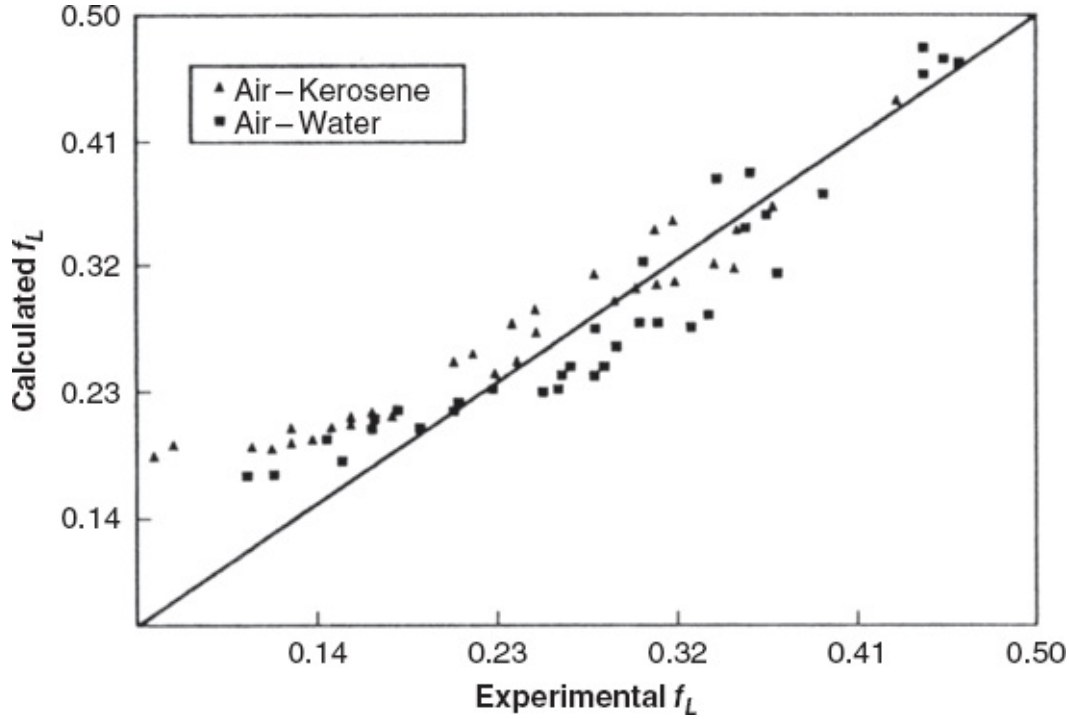

Fig. 4.18—Model mimics churn flow data of Caetano et al. (after Hasan and Kabir 1992).

We recommend Eq. 3.11 for transition to annular flow in an annulus. That is because neither the pipe geometry nor its inclination affects this transition significantly. In addition, as in the case of annular two-phase flow in vertical and deviated wells, we recommend that liquid holdup in this regime be calculated on the basis of a no-slip approach; that is, $fL = v_{sL}/v_m$.

Once holdup is estimated, pressure gradient in bubbly and intermittent flow regimes may be calculated with the usual approach, which is

$$-\frac{dp}{dz} = \frac{g \sin\alpha}{g_c}\left(\rho_L f_L + \rho_g f_g\right) + \frac{f_m v_m^2 \rho_m}{2 g_c d} + \frac{\rho_m v_m}{g_c}\frac{dv_m}{dz} \quad (4.27)$$

For a rigorous and complete analysis of two-phase flow in annuli, refer to the study of Caetano et al. (1992b). Their estimations of liquid holdup and pressure drop match reasonably well with the estimates of the simplified model presented above. A somewhat similar approach was taken by Lage and Time (2002) to model flow pattern transition and pressure-drop estimation in vertical concentric annuli. Their flow pattern model adopted the pattern transition criteria proposed by Taitel et al. (1980), and their holdup and pressure estimation modeling followed the work by Papadimitriou and Shoham (1991). Yu et al. (2010) presented a rigorous model of two-phase flow in concentric and eccentric annuli. An important conclusion of the Yu et al. study is that annulus eccentricity has minimal impact on two-phase flow behavior. Cavalcanti et al. (2014) also arrived at the same conclusion. Both Yu et al. and Cavalcanti et al. noted that the shape of the Taylor bubble for an eccentric annulus differs from that for a concentric annulus.

A pressure-buildup test in a sucker-rod-pumping well presents an essentially nonfrictional pressure-drop calculation situation. That is because the low velocity of the annular fluids, whose movement is monitored by acoustic pulses, suggests hydrostatic head as the major contributor to the total pressure. **Fig. 4.19,** taken from Kabir and Hasan (1994), compares the performance of various f_g models in computation of bottomhole pressures.

4.4.2 Downward Two-Phase Flow. Downward simultaneous flow of gas and liquid, although rare, is important in the chemical process industry and also in petroleum production. An example of two-phase downflow is the injection of wet steam in thermal recovery. Gas anchor design in pumped wells provides another example.

As mentioned earlier, the Beggs and Brill (1973) correlation allows holdup and pressure-drop computation for all inclination angles, including when flow occurs in the downward direction. Mukherjee and Brill (1983) also presented extensive data and a correlation for downward twophase flow. Both correlations are quite robust. However, they are less reliable at low liquid rates because of their parametric dependence on input liquid fraction.

Barnea (1986) proposed a unified model for flow pattern transitions in both upward and downward flows. Crawford et al. (1986a) presented data and an empirical method for estimating pattern transitions in downflow by modifying the Weisman and Kang (1981) approach for pattern transition in inclined upflow. Crawford et al. (1986b) also proposed a simplified driftflux approach to compute the gas volume fraction in downward bubbly and slug flow.

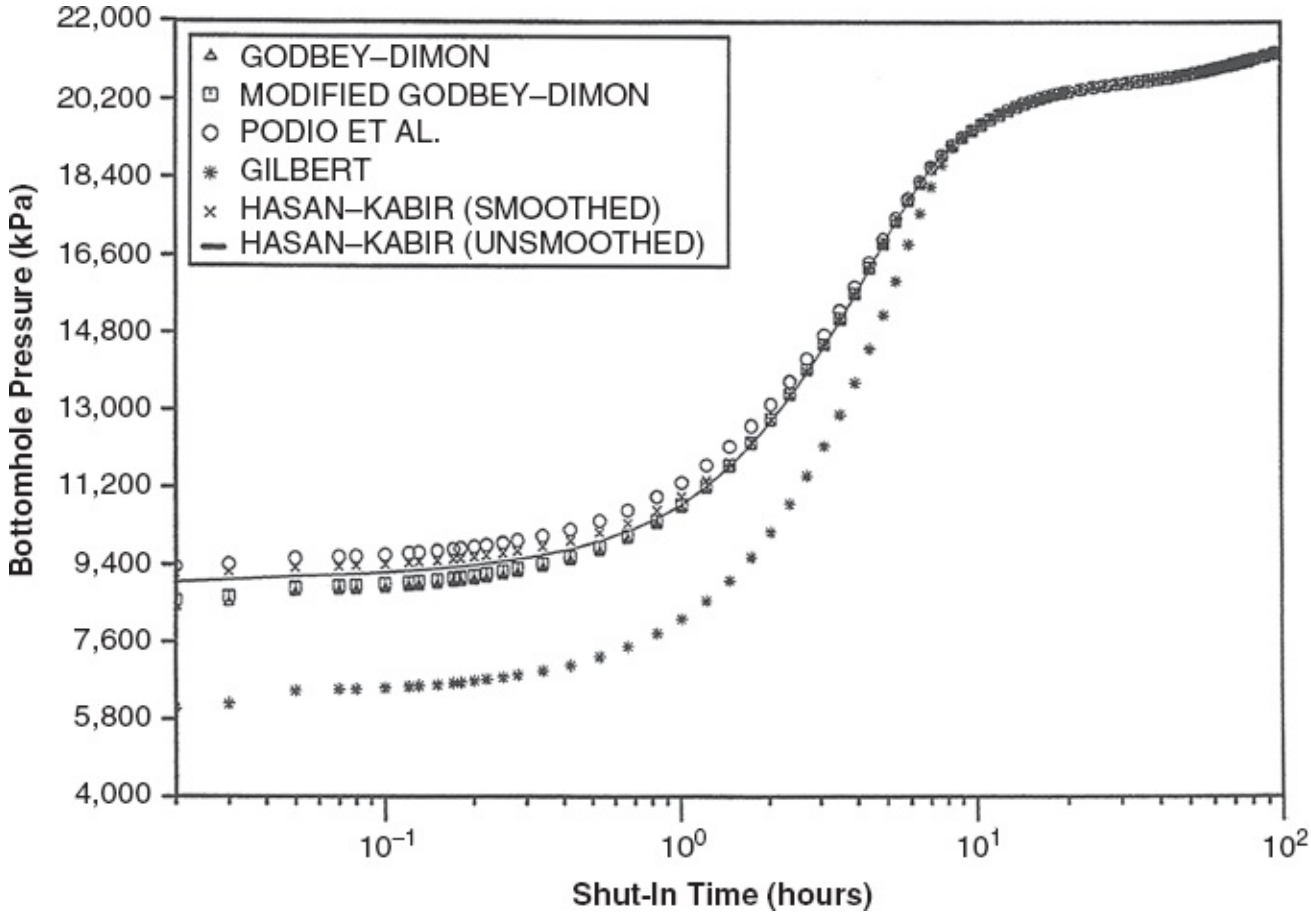

Fig. 4.19—Computing bottomhole pressures in a buildup test using *fg* models (after Kabir and Hasan 1994).

Based on the drift-flux approach, which has worked well for vertical and deviated upflow, Hasan (1995) presented a model for estimating holdup in downward bubbly and intermittent two-phase flow. We present the essence of that study in the following. Here, we assume that the behavior of vertical and inclined downward two-phase flow will be similar to that of their counterpart in upflow, except that buoyancy will oppose the flow of the gas phase in downflow. Following Eq. 3.22 for upflow, we express the in-situ gas velocity v_g during downflow at all inclinations as $C_o v_m - v_\infty$. Therefore, the model expresses liquid holdup in these two flow regimes as

$$f_L \equiv 1 - f_g = 1 - \frac{v_{sg}}{C_o v_m - v_\infty}. \qquad (4.76)$$

The effect of buoyancy (i.e., the value of v_∞) and bubble distribution across the channel (i.e., the value of C_o) will depend on the existing flow pattern. Analysis of inclined downflow data, from diverse sources, shows that Eq. 4.76 can be used for bubbly flow with a value of 1.2 for C_o and that the Harmathy (1960) equation can estimate the rise velocity of bubbles for all inclination angles. Therefore, the only difference in computing liquid holdup during bubbly flow in the downward direction, compared to that for upflow (Eq. 4.21), is the negative sign in front of the terminal rise velocity v_∞ in Eq. 4.50.

For slug or intermittent flow, the approach used for deviated upflow can be extended to inclined downflow (Eq. 4.28), with a negative sign for the average rise velocity, $\bar{v}_{\infty\alpha}$; that is,

$$f_L \equiv 1 - f_g = 1 - \frac{v_{sg}}{C_o v_m - \bar{v}_{\infty\alpha}}, \quad \ldots\ldots (4.77)$$

where, as in upflow,

$$\bar{v}_{\infty\alpha} = v_\infty \left(1 - e^{-0.1 v_t/(v_{sg} - v_t)}\right) + v_{\infty T\alpha} e^{-0.1 v_t/(v_{sg} - v_t)}, \quad \ldots\ldots (4.29)$$

Analysis of slug flow holdup data suggests that Eq. 4.77 applies when a slightly lower value of 1.12 is used for C_o, instead of using 1.2 in upflow.

As in the case of upflow, a gas volume fraction of 25% (holdup of 75%) can be used as the transition criterion between bubbly and intermittent flow. This criterion also applies to deviated wells if the actual superficial velocity of the gas phase at the upper section of the pipe is used, as shown earlier. Thus, we recommend using

$$v_{sg} = \left(0.43 v_{sL} - 0.357 v_\infty\right) \sin\alpha \quad \ldots\ldots (4.78)$$

to allow for the opposing effect of buoyancy. Transition data from various sources lend credence to Eq. 4.78. Note that Eq. 4.58 indicates a minimum required v_{sL} value below which v_{sg} becomes negative; that is, the system becomes unstable—a fact noted by Crawford et al. (1986a). **Fig. 4.20** provides testimony to the benefits of the recommended approach.

4.4.3 Countercurrent Two-Phase Flow. Countercurrent two-phase flow, in which liquid flows downward and the gas phase moves upward, may occur during oil production, transient testing, and well-control operations. Transient tests that are performed by shutting the well at the surface often lead to interpretation problems when high gas/liquid productions occur. The preferential upward movement of the gas may cause severe segregation, resulting in anomalous wellbore pressure increase. The increased pressure can cause the liquid to flow back into the formation, while the gas phase moves in the upward direction. Similarly, oil production often requires separating gas by reversing the direction of liquid flow to maintain high pump efficiency. Countercurrent flow is also prevalent in the chemical industry in equipment such as absorption columns and bubble-column reactors.

Very few works exist in the petroleum literature that examine countercurrent two-phase flow. The work of Shah et al. (1978), among others, is essentially empirical in nature. Taitel and Barnea (1983) were the first to report the existence of three flow regimes—bubbly, slug, and annular—and presented a map delineating the boundaries. The existence of annular flow regime during countercurrent flow, however, is likely to be limited because of the opposing flow direction of the phases.

The behavior of countercurrent flow may be viewed as a combination of

simultaneous flow of two phases in the upward and downward directions. Indeed, Hasan et al. (1994) proposed that the drift-flux approach can be used to estimate holdup and pressure drop during bubbly and slug flow, with appropriate signs for the flow velocities. Therefore, for bubbly flow, noting that v_m in the upward direction is given by $v_{sg} - v_{sL}$, we write

$$f_L \equiv 1 - f_g = 1 - \frac{v_{sg}}{C_o(v_{sg} - v_{sL}) + v_\infty} \quad (4.79)$$

As in cocurrent flow, we recommend the use of the Harmathy correlation (Eq. 3.6) for estimating v_∞. For single bubbles rising against downward liquid flow, the velocity data of Hasan et al. (1994) agree well with those estimated with Eq. 3.6. Unlike the case of cocurrent flow, where C_o = 1.2, the holdup data suggest a higher value of 2.0 for the flow parameter C_o in countercurrent bubbly flow. Fluid recirculation causes the velocity profile to be sharper with a much higher maximum velocity at the channel center than in the case of cocurrent turbulent flow. Consequently, the value of C_o is higher than in cocurrent flow.

Similarly, for slug or intermittent flow, we suggest an average rise velocity approach to estimate holdup.

$$f_L \equiv 1 - f_g = 1 - \frac{v_{sg}}{C_o(v_{sg} - v_{sL}) + \overline{v}_{\infty\alpha}}, \quad (4.80)$$

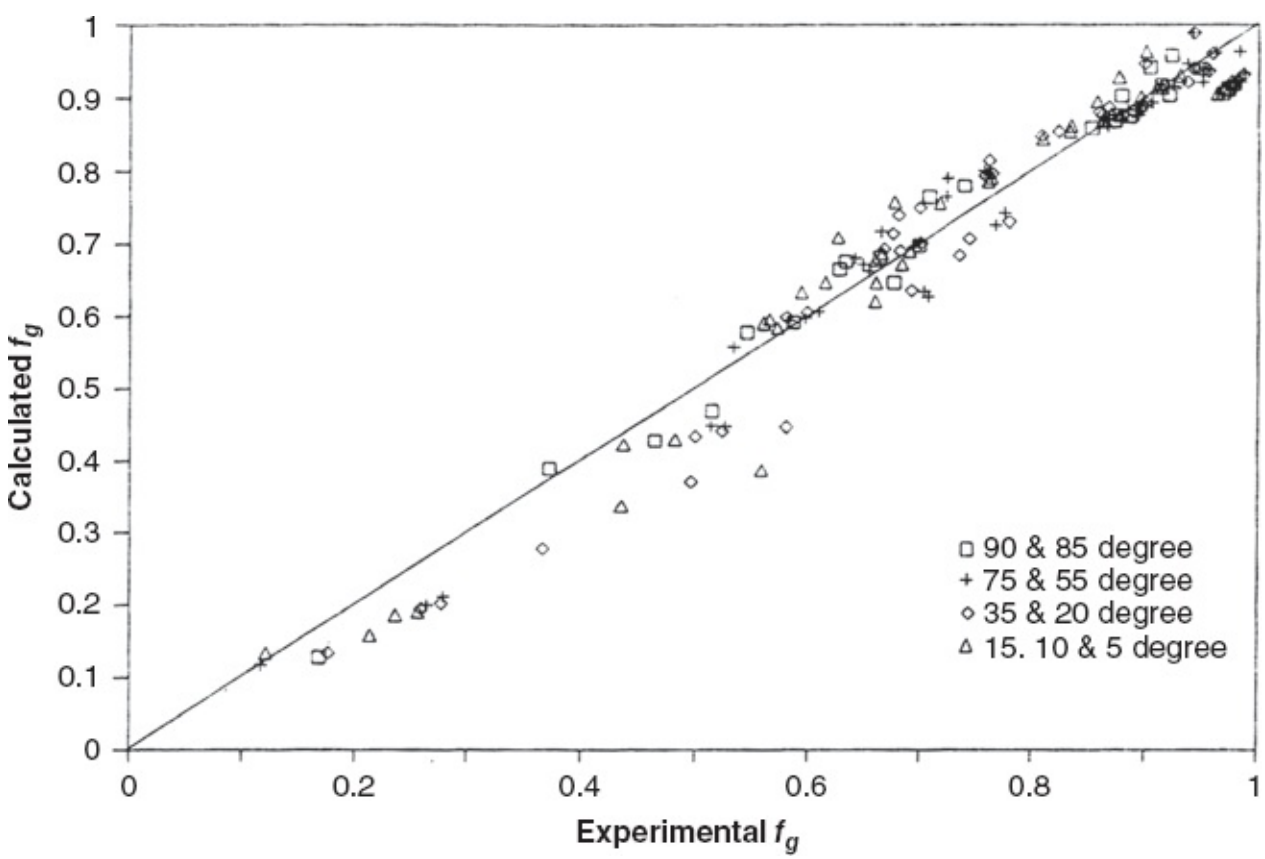

Fig. 4.20—Model mimics bubbly and intermittent flow data for various pipe angles (after Hasan 1995).

where, as in upflow, $\bar{v}_{\infty\alpha}$ is calculated from Eq. 4.28, with the Taylor bubble rise velocity estimated from Eq. 3.7 for vertical systems. In this case, a value of C_o = 1.2 agrees very well with countercurrent slug flow data from several sources. **Fig. 4.21** shows the data of Hasan et al. (1994) and those of the model presented by Eqs. 4.59 and 4.60.

As in the case of cocurrent flow, we found that the transition from bubbly to slug flow occurs at f_g of approximately 25% (f_L = 75%). Using Eq. 4.79 with C_o = 2.0, we can express the superficial gas velocity needed for the bubbly/slug flow transition in countercurrent flow as

$$v_{sg} = 0.5v_{\infty} - v_{sL}. \quad (4.81)$$

No work has been reported for estimating holdup in deviated wells for countercurrent flow. We conjecture that the approach used for inclined cocurrent flow will apply to countercurrent flow. Therefore, Eq. 4.79 will be applicable to bubbly flow without modifications in deviated wells. Similarly, Eq. 4.80 may apply to countercurrent intermittent flow in deviated wells when the Taylor bubble rise velocity $v_{\infty Ta}$ is estimated with Eq. 4.29.

Firouzi et al. (2015) presented an interesting work for countercurrent, two-phase slug flow in a vertical annulus. They used the Taitel and Barnea (1983) countercurrent model for delineating the slug flow regime from bubbly and annular flow, and the Caetano et al. (1992b) model for liquid holdup and pressure-drop estimation in annuli.

4.4.4 Oil/Water Two-Phase Flow. As oil fields mature, coproduction of water with oil generally increases with time. Consequently, wellbore two-phase oil/water flow is encountered in most operations. A reliable holdup model that allows interpretation of spinner logs measures the mixture velocity, not the individual phase velocities. Controlling water production is one of the key elements in reservoir management. Therefore, any downhole remedial actions for water control are critically dependent on the accuracy of the model used in analysis of production logs. Liquid/liquid flow is also encountered when a power fluid, such as in a jet pump, is used to assist the lift. Despite diverse needs, only a handful of investigations attempt to explain the simultaneous flow of two immiscible liquids.

Flores et al. (1999) presented a comprehensive study of oil/water flow patterns in vertical and deviated pipes. An important finding of their study is characterization of flow patterns into oil- and water-dominated regimes. Significant slippage occurs between the oil and water phases in water-dominated flow, whereas slippage is negligible in oil-dominated flow. Their study also shows that while the behavior of oil/water flow has many similarities with gas/liquid flow, important differences remain. One significant difference is that the formation of a Taylor-like bubble is not evident in oil/water flow, although pseudoslug flow can be observed. Pseudoslugs are characterized by the oil droplets that tend to move as a packet, interrupted by water breaks. Even in churn flow, the oil droplets tend to maintain their individual identity,

although some irregular-shaped oil droplets can be observed visually.

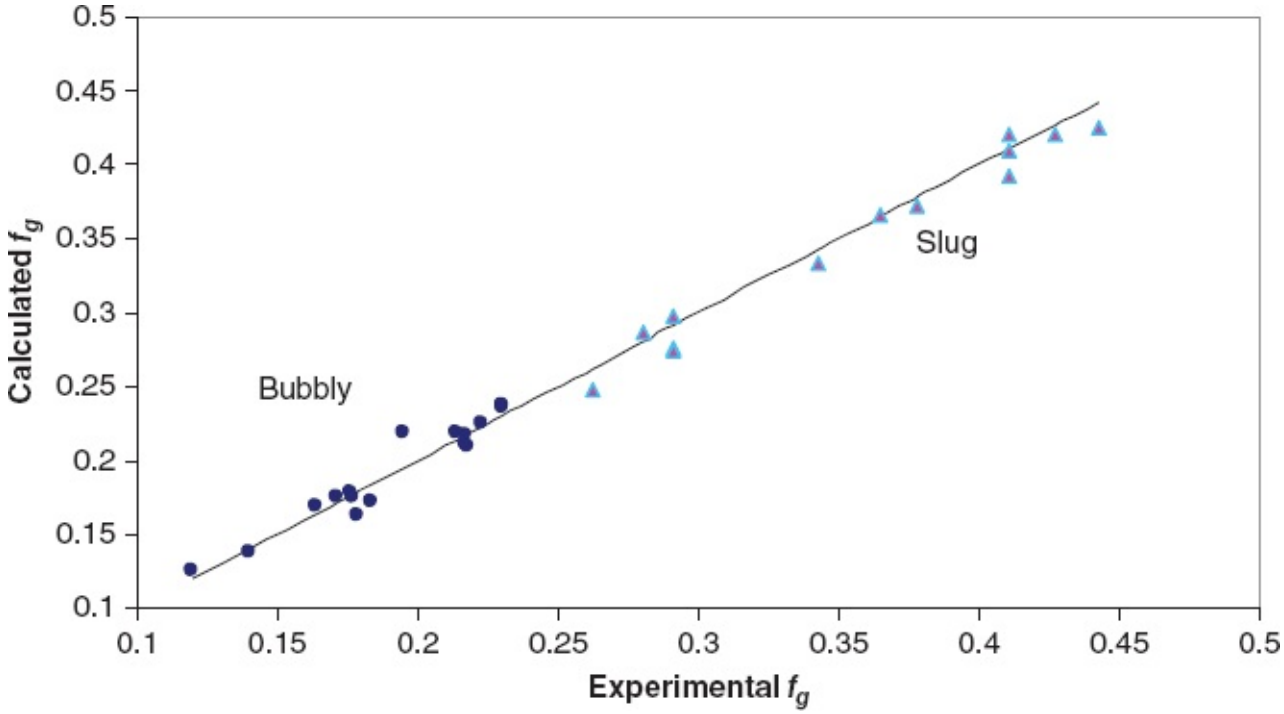

Fig. 4.21—Model explains countercurrent bubbly and slug flow data (after Hasan et al. 1994).

Hasan and Kabir (1990b, 1999) and Flores et al. (1998) proposed semimechanistic models on the basis of the drift-flux approach for estimating in-situ oil fraction f_o and pressure gradient for oil/water two-phase flow in vertical and deviated wells. Similar in nature, the models propose that the slip between the phases is negligible for oil-dominated flows, which occur when in-situ oil fraction is greater than 70%,—that is, when $f_o > 0.7$ (or $f_w < 0.3$). In terms of superficial oil and water velocities, v_{so} and v_{sw}, respectively, we have

$$f_o \equiv 1 - f_w = \frac{v_{so}}{v_m}. \qquad (4.82)$$

For all water-dominated flow regimes ($f_o < 0.7$) and well deviations less than 70°, Hasan and Kabir (1999) recommended the following expression for the in-situ oil volume fraction f_o:

$$f_o \equiv 1 - f_w = \frac{v_{so}}{1.2 v_m + v_{\infty\theta} f_w^2}. \qquad (4.83)$$

Note the similarity between Eq. 4.83 for in-situ oil volume fraction and Eq. 4.28 for in-situ gas volume fraction in deviated wells. A constant value of 1.2 for the flow parameter is used in both oil/water and liquid/gas systems for all deviations < 70°. The presence of the water-holdup term in the denominator of the right side of Eq. 4.83, recommended by both Hasan and Kabir (1999) and Flores et al. (1998),

reduces the effective rise velocity of oil bubbles. Therefore, the in-situ fraction calculated with Eq. 4.83 is higher than that of Eq. 4.28. Note that Eq. 4.83, implicit in holdup, requires a root solver, such as the secant-bisection method, or an iterative procedure for its evaluation.

For rise velocity of oil bubbles in vertical systems, Hasan and Kabir (1990b, 1999) recommended the use of the Harmathy correlation. Using Nicolas and Witterholt (1972) data for a number of liquid/liquid systems with varying densities (1000 to 773 kg/m^3) and interfacial tensions (18 to 43 dynes/cm), we showed a good agreement between the bubble-rise-velocity data and the Harmathy correlation. For deviated wells, Hasan and Kabir (1999) proposed an expression similar to Eq. 4.33.

$$v_{\infty\alpha} = v_{\infty}\sqrt{\sin\alpha}\,(1+\cos\alpha)^2 = 1.53\sqrt[4]{g\sigma(\rho_w-\rho_o)/\rho_w^2}\,\sqrt{\sin\alpha}\,(1+\cos\alpha)^2 \quad (4.84)$$

Note, however, that we used the Harmathy correlation for bubble rise velocity for a vertical well for all flow regimes and that the factor accounting for well inclination has a slightly different exponent than does Eq. 4.33. In contrast, Flores et al. (1998) used a Nicklin-type correlation with an empirically determined constant for bubble rise velocity in churn flow, $v_{\infty T}$.

$$v_{\infty T} = 0.25\sqrt{gd(\rho_w-\rho_o)/\rho_w}. \quad (4.85)$$

We presented data from a number of sources that lend strong support to Eqs. 4.82 through 4.84. For estimating frictional pressure head in oil/water flow, the no-slip approach is recommended because the frictional pressure gradient is expected to be small in all but near-horizontal systems. However, for greater accuracy, especially for near-horizontal systems, refer to Flores et al. (1998), who proposed the following expression for the mixture friction factor f_{fm}, in terms of the Reynolds number:

$$f_{fm} = C\,\mathrm{Re}_m^{-n} = C\left(\rho v_m d/\mu\right)^{-n}. \quad (4.86)$$

The values of the properties (density and viscosity) and the constants (C and n) depend on the phase that is continuous. For example, when water is the continuous phase, C = 63.8 and n = 0.84, and for continuous oil phase, C = 207.3 and n = 1.27.

To show robustness of the recommended modeling approach, we present data from our work (Hasan and Kabir 1999) in **Figs. 4.22 and 4.23.**

Subsequently, Zhang and Sarica (2006) presented a more sophisticated approach by modeling three-phase flow of gas, oil, and water. The approach is based on the basic two-phase model of Zhang et al. (2003a, b), with additional closure relationships for the extra liquid phase.

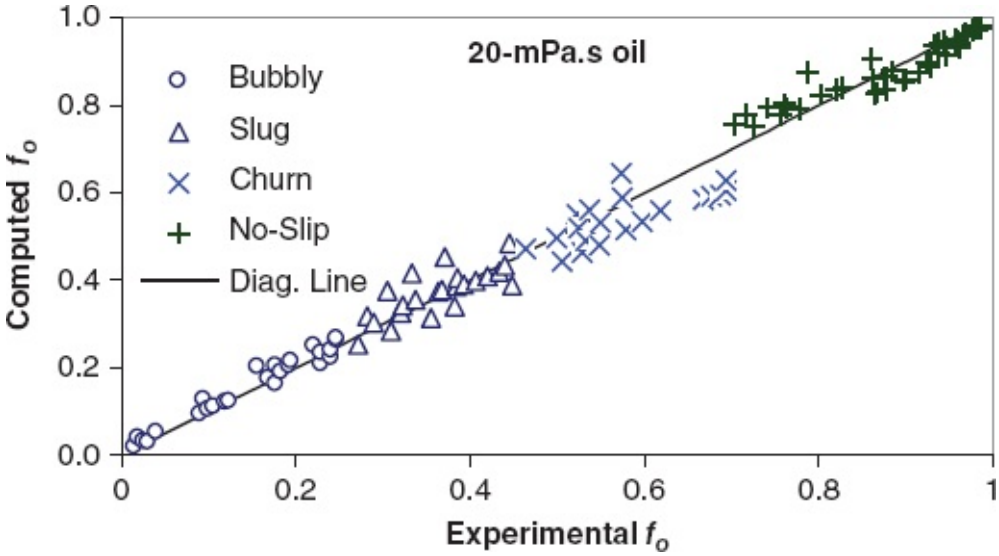

Fig. 4.22—Model mimics data in a 1.06-in.-ID pipe (after Hasan and Kabir 1999).

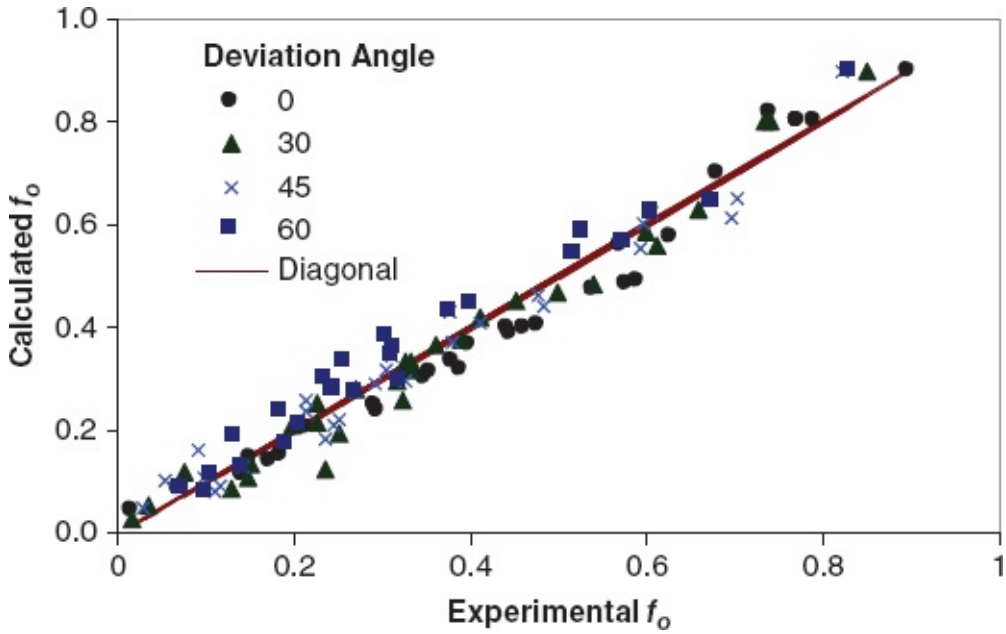

Fig. 4.23—Model mimics data in a 6.5-in.-ID pipe (after Hasan and Kabir 1999).

Summary

In petroleum production, two-phase flow occurs in a variety of situations other than the conventional upward flow of gas and liquid. In cases where flow occurs in deviated wells, in vertical and inclined annuli, moves in downward directions, or is counter to other flows, we show that the drift-flux approach provides a good estimation of holdup. The same is also true when two immiscible liquid phases, such as oil and water, are involved in vertical or deviated wells. The method's simplicity and engineering accuracy are appealing.

A summary of the model, showing the unification of these concepts, is presented in Chapter 5. Chapter 5 also presents a number of applications of the model. Additional

applications of the model are made elsewhere in the book. For instance, Chapter 12 discusses downward flow of wet steam, and Chapter 13 shows how oil/water flow modeling is used in production log interpretation.

Nomenclature

a = factor used in Beggs-Brill holdup equation, Eq. 4.13

A = cross-sectional area for fluid flow, ft^2

A_g, A_L = cross-sectional area available for gas or liquid flow, ft^2

C = constant in Lockhart-Martinelli parameter, dimensionless

C_2 = constant for Taylor bubble rise velocity in slug flow, dimensionless

$C_{D\alpha}$ = bubble drag coefficient for inclined channel, dimensionless

C_o = flow parameter in bubbly flow, dimensionless

d = flow-string diameter, ft

d_c, d_t = casing or tubing diameter, ft

E = fraction of liquid phase entrained in gas core, dimensionless

Eo = Eotvos number, $gd^2(\rho_L-\rho_g)/\sigma$, dimensionless

f = friction factor, dimensionless

f_c = film friction factor for gas core in annular flow, dimensionless

f_g = in-situ gas volume fraction (void fraction), dimensionless

f_{gL} = local in-situ gas volume fraction (void fraction), dimensionless

f_{gLS} = in-situ gas volume fraction in liquid slug portion of cell, dimensionless

f_{gTB} = in-situ gas volume fraction in Taylor bubble portion of cell, dimensionless

f_{fL} = single-phase liquid friction factor, used in Eq. 4.61, dimensionless

f_i = friction factor at the gas/liquid interface, dimensionless

f_L = liquid holdup, (in-situ liquid volume fraction), dimensionless

f_{LLS} = liquid holdup in liquid slug portion of cell, dimensionless

f_{LTB} = liquid holdup in Taylor bubble portion of cell, dimensionless

f_m = friction factor for two-phase mixture, dimensionless

f_n = friction factor calculated assuming no slip between phases, dimensionless

f_w = water holdup, (in-situ water volume fraction), dimensionless

F = parameter in Taitel et al. horizontal flow pattern map, dimensionless

F_B, F_T = force caused by buoyancy or turbulent fluctuation, lbf

F_p = friction geometry parameter, dimensionless

Fr = Froude number, v^2/gd, dimensionless

$F(\alpha)$ = parameter used by Beggs and Brill, defined by Eq. 4.21, dimensionless

g = acceleration caused by gravity, ft/sec^2

=

g_c conversion factor, 32.17 (lbm-ft)/lbf-sec^2

G_m = mixture mass flux, $\rho_m v_m$, lbm/hr-ft^2

G_g, G_L = gas or liquid mass flux, $\rho_g v_{sg} = G_m x$, or $\rho_L v_{sL} = G_m(1 - x)$, lbm/hr-ft^2

h = liquid height in horizontal/near-horizontal flow, ft

I = Gomez et al. inclination factor, dimensionless

I_H, I_V = Gomez et al. inclination factor for horizontal or vertical systems, dimensionless

K = parameter in Taitel et al. horizontal flow pattern map, dimensionless

Ku_{sg} = Kutadelaze number, = $v_{sg}\rho_g/[g(\rho_L - \rho_g)\,\sigma]^{0.25}$, dimensionless

L = total vertical well depth, ft; also total length of a cell in slug flow, ft

L_R = relaxation distance, 1/ft

L_s, L_T = length of liquid slug or Taylor bubble in slug flow, ft.

N_f = inverse viscosity number, $[gd^3\rho_L(\rho_L - \rho_g)]^2/\mu_L$, dimensionless

p = pressure, psi

$(\mathrm{d}p/\mathrm{d}z)$ = total pressure gradient, psi/ft

$(\mathrm{d}p/\mathrm{d}z)_A$ = accelerational (kinetic) pressure gradient, psi/ft

$(\mathrm{d}p/\mathrm{d}z)_F$ = frictional pressure gradient, psi/ft

$(\mathrm{d}p/\mathrm{d}z)_H$ = static pressure gradient, psi/ft

p_{wf} = flowing bottomhole pressure, psi

Pr = Prandtl number, $c_p\mu/k$, dimensionless

q = fluid flow rate at standard conditions, STB/D or MMscf/D

q_g, q_L = gas or liquid flow rate at standard conditions, MMscf/D or STB/D

q_{wh} = wellhead rate, STB/D or MMscf/D

Q = heat-transfer rate per unit length of wellbore, Btu/hr-ft

r_w = wellbore radius, ft

r_D = dimensionless radial distance, r/r_w, dimensionless

Re = Reynolds number, $dv\rho/\mu$, dimensionless

Re_m = Reynolds number for mixture, $\rho_m v_m d/\mu_m$, dimensionless

Re_g, Re_L = Reynolds number for gas ($\rho_g v_g d/\mu_g$) or liquid phase ($r_L v_L d/\mu_L$), dimensionless

R_s = solution gas/oil ratio, scf/STB

s = parameter used by Beggs and Brill, defined by Eqs. 4.18 and 4.19, dimensionless

S_g = wetted-gas perimeter, ft

S_i = gas/liquid interface perimeter, ft

S_L = wetted-liquid perimeter, ft

T = parameter in Taitel et al. horizontal flow pattern map, dimensionless

V_B = bubble volume, ft^3

v = fluid velocity, ft/sec

v_c = core fluid velocity, ft/sec

v_d = drift velocity of lighter phase, ft/sec

v_g, v_L = gas or liquid in-situ velocity, ft/sec

v_{gd}, v_{Ld} = dimensionless phase velocities, dimensionless

v_{gTB} = in-situ gas velocity in Taylor bubble portion of cell, ft/sec

v_{sg}, v_{sL} = superficial gas or liquid in-situ velocity, ft/sec

$(v_{sg})_a$ = superficial gas velocity at bubbly-to-slug transition zone, ft/sec

v_t = superficial gas velocity at bubbly-to-slug transition zone, ft/sec

v_{TB} = in-situ velocity of Taylor bubble, ft/sec

v_{gLS} = in-situ gas velocity in liquid slug portion of cell, ft/sec

v_∞, $v_{\infty T}$ = terminal rise velocity of bubbles in bubbly flow or a Taylor bubble in slug flow, ft/sec

$v_{\infty Ta}$ = terminal rise velocity of Taylor bubble in horizontal well inclined by α degrees,ft/sec

w = mass flow rate of fluid, lbm/sec

x = gas mass fraction in tubing fluid mixture, dimensionless.

X = Lockhart-Martinelli parameter, dimensionless

y = parameter used by Beggs and Brill, defined by Eq. 4.17, dimensionless

Y = ratio of gravitational gradient/gas-phase frictional gradient, dimensionless

z = vertical well depth (measured from wellhead), ft

α = horizontal wellbore inclination, degrees

β = ratio of length of Taylor bubble to total cell, L_T/L, dimensionless

δ = film thickness, ft

$\underline{\delta}$ = dimensionless film thickness

μ = oil viscosity, cp

ε = pipe roughness factor, ft

ϕ_g, ϕ_L = friction multiplier of gas or liquid flowing alone in the channel, Lockhart–Martinelli correlation, dimensionless

ϕ_1, ϕ_2 = parameters for the Weisman-Kang inclined flow pattern map, dimensionless

ρ = density, lbm/ft^3

ρ_g, ρ_L = gas- or liquid-phase density, lbm/ft^3

ρ_c, ρ_e = core fluid or earth (formation) density, lbm/ft^3

λ = parameter for Baker flow pattern map, Eq. 4.35, dimensionless

σ = surface tension, lbm/sec^2

ψ = parameter for Baker flow pattern map, Eq. 4.36, dimensionless

γ = distortion coefficient used in Eq. 4.8, dimensionless

τ = shear stress, psi

ω = empirical constant in Eq. 4.71

Subscripts

a = annulus

A = air

c	=	casing
g	=	gas
L	=	liquid
LS	=	liquid slug
o	=	oil
P	=	projected (area of a bubble)
s	=	standard conditions for Weisman-Kang map
T	=	Taylor bubble
w	=	water

Chapter 5

Multiphase Flow: Field Applications

The last three chapters presented various ways of estimating pressure loss during two-phase flow, from completely empirical to nearly mechanistic modeling approaches of varying complexity. This chapter presents field application of these models in vertical and deviated wells. In presenting these applications, we rely heavily on our own experience and those of our colleagues. We begin this chapter with an overall modeling approach that is grounded in simple physics and yet is quite general in applications, as presented earlier in Chapters 3 and 4. Therefore, this chapter may be viewed as a summary of our model. We show the modeling approach with specific applications to oil wells, gas/condensate wells, and liquid loading in gas wells. Last, the chapter addresses two-phase flow metering across surface chokes. Note that in three-phase flow we simply lump the two liquid phases, but discerning the physical properties of the oil/water mixture presents a challenge while estimating viscosity, interfacial tension, and other factors.

5.1 Overall Modeling Approach in Gas/Liquid Flow

The accuracy of model estimates depends not only on how closely a model represents reality but also on the data fed to the model. Therefore, in calculating pressure traverse during multiphase flow, fluid properties—especially gas in solution—are as important as the choice of the model. With that in mind, we present an overall modeling approach that is generally applicable to all situations, is physically sound, and is computationally simple. Although various components of this model have already been presented in the last two chapters and in some recent papers, we present them here in a generalized form. Hasan et al. (2010b) present much of the discourse presented in this section. We emphasize that data integrity and pressure/volume/temperature (PVT) properties play key roles before any modeling is attempted.

Expression for the total pressure gradient during steady two-phase-flow has been presented as the sum of the friction, static, and kinetic gradients by Eq. 2.19 in Chapter 2. The friction factor f_m in the frictional component [$= f_m v_m^2/(2d)$] is calculated using Eq. 1.12 for turbulent flow or Eq. 1.11 for laminar flow, for all flow patterns. The mixture Reynolds number needed in Eq. 1.11 and Eq. 1.12 is calculated using mixture average properties, $\mathrm{Re}_m = dv_m\ \rho_m/\mu_m$. The mixture viscosity μ_m needed for Re_m is calculated using Eq. 2.25, $\mu_m = x\mu_g + (1 - x)\mu_L$. The mixture density ρ_m in Re_m and in Eq. 2.19 is the in-situ volumetric weighted average density of the two phases, ρ_L and ρ_g, and is given by Eq. 2.20.

5.1.1 Volume Fraction. For vertical and near-vertical systems, the static head often represents more than 80% of the total pressure gradient, making estimation of liquid holdup, f_L (= 1 – f_g), extremely important. We estimate liquid holdup using the following expression based on a drift-flux approach for all flow regimes:

$$f_L = 1 - f_g = 1 - \frac{v_{sg}}{C_o v_m \pm v_\infty} \quad (5.1)$$

For cocurrent upflow, the mixture velocity, v_m, is the sum of the gas and liquid superficial velocities, $v_m = v_{sg} + v_{sL}$. However, during countercurrent flow, when the liquid flows downward as gas flows up, the appropriate mixture velocity is given by $v_m = v_{sg} - v_{sL}$. Similarly, when both the phases flow downward, buoyancy acts in the direction opposite to the flow; for this condition, the rise velocity v_∞ is subtracted from $C_o v_m$ to obtain the gas in-situ velocity v_g and, therefore, liquid holdup f_L.

	Flow parameter (C_o)			
Flow Pattern	Upward Cocurrent	Upward Countercurrent	Downward	Rise Velocity (v_∞)
Bubbly or disp. bubbly	1.2	2.0	1.2	$v_{\infty b} = 1.53\left[g\sigma\left(\rho_L - \rho_g\right)\right]^{0.25}$
Slug	1.2	1.2	1.12	$\bar{v}_\infty$
Churn	1.15	1.15	1.12	$\bar{v}_\infty$
Annular	1.0	1.0	1.0	0

Table 5.1—Parameters for flow type and flow pattern.

5.1.2 Model Parameter Values. Although the form of the expression for liquid holdup remains the same, the values of the flow parameter C_o and the rise velocity v_∞ depend on the flow pattern, well deviation, flow direction (upward or downward, cocurrent or countercurrent), and flowing phases (gas/liquid, liquid/liquid). **Table 5.1** summarizes values of the flow parameters and the rise-velocity relationships under various flow conditions. Note that Table 5.1 implies that the *homogeneous* model applies for estimating pressure gradient in annular two-phase flow, meaning that there is no difference in the velocity of the gas and liquid phases. The rationale for this recommendation is discussed in the next section on gas/condensate wells, in which the flow is almost entirely dominated by annular two-phase flow. Table 5.1 also implies that well deviation and annulus dimensions (for flow through annuli) influence the bubble rise velocity in slug and churn flow, but not in bubbly or annular flow.

The rise velocity of Taylor bubbles, characteristic of slug flow, is estimated from Eq. 4.75, recast here as a generalized expression:

$$v_{\infty T\alpha} = 0.35\sqrt{gd\left(\rho_L - \rho_g\right)/\rho_L}\; F_\alpha F_a. \quad (5.2)$$

In Eq. 5.2, the well deviation factor F_α, in terms of inclination angle from horizontal α, is given by

$$F_\alpha = (1+\cos\alpha)^{1.2}\sqrt{\sin\alpha} \quad (5.3)$$

We need to emphasize that θ is the angle of deviation of the well from vertical, which is different from $\alpha(= 90 - \theta)$, the angle of inclination from horizontal. These two angles are related by the expression $\cos\theta = \sin\alpha$. For oil/water flow, the exponent of the first term in Eq. 5.3 is 2; that is, $F_\alpha = (\sin\alpha)^{0.5}(1 + \cos\alpha)^2$. For flow in annuli, the annulus factor F_a, expressed below in terms of the inner and outer diameters d_i and d_o of the annulus, allows Eq. 5.2 (with d replaced by d_o) to be used for flow through an annulus. Note that d_i is the annulus inside diameter; that is, the tubing outside diameter d_{to}. Similarly, d_o is the annulus outside diameter; that is, $d_o = d_{ci}$, the casing inside diameter. Therefore, F_a is written as

$$F_a = 1 + 0.286(d_i / d_o). \quad (5.4)$$

In slug flow, liquid slugs that separate the Taylor bubbles also contain small bubbles, whose rise velocities are best estimated with Eq. 3.6. Therefore, for slug flow we need a rise velocity that is an average of bubble rise velocities represented by Eq. 3.6 and Eq. 5.2. We use the following averaging process that depends on the magnitude of the superficial gas velocity compared to that needed for transition from bubbly to slug flow:

$$\overline{v}_{\infty\alpha} = v_\infty\left(1 - e^{-0.1 v_t/(v_{sg}-v_t)}\right) + v_{\infty T\alpha} e^{-0.1 v_t/(v_{sg}-v_t)}, \quad (5.5)$$

Although empirical, Eq. 5.5 provides a smooth transition in the values of void fraction and pressure gradient when bubbly flow gradually transforms into slug flow.

5.1.3 Pattern Transition Criteria. Chapters 3 and 4 discussed criteria for pattern transition from one flow regime to another. In presenting these criteria in a unified form in **Table 5.2,** we have made some assumptions in annular and dispersed bubbly flows. For example, in these flow patterns the gravitational force plays an unimportant role; as a result of well orientation, geometry, and flow direction do not affect the transition criteria. However, neglecting well deviation on transition boundary for dispersed bubbly and annular flow may lead to errors in highly deviated wells. Eq. 5.6, in Table 5.2, implies that the negative sign for v_∞ is applicable for countercurrent flow for transition from bubbly to slug flow. In addition, the absolute value of inclination from horizontal, α must be used for downward flow.

Bubbly to slug	v_{sg}	>	$\dfrac{C_o v_{sL} \pm v_\infty}{4 - C_o}\sin\alpha$	(5.6)
Slug to churn				

	$2v_m^{1.2}\left(\frac{f}{2d}\right)^{0.4}\left(\frac{\rho_L}{\sigma}\right)^{0.6}\sqrt{\frac{0.4\sigma}{g(\rho_L-\rho_g)}} > 0.725+4.15\sqrt{\frac{v_{sg}}{v_m}}$, ... (3.10)
	and $v_{sg} > 1.08v_{sL}$. ..... (3.11b)
Slug/churn to annular	$v_{sg} > 3.1\left[g\sigma(\rho_L-\rho_g)/\rho_g^2\right]^{0.25}$. ..... (3.12)

Table 5.2—Flow pattern transition criteria.

5.1.4 Pattern Transition Smoothing. For C_o in bubbly flow, we use the values reported in Table 5.1. Therefore, for either upward or downward cocurrent bubbly flow, C_o = 1.2; however, its value is 2.0 for countercurrent bubbly flow. For all other flow patterns, we use an exponential weighted average value of C_o derived from the fully developed C_o values of the adjoining flow regimes. Therefore, for slug flow close to the bubbly/slug flow transition boundary, we can write

$$C_o = 1.2\left(1-e^{-0.1v_t/(v_{sg}-v_t)}\right)+1.2\left(e^{-0.1v_t/(v_{sg}-v_t)}\right). \quad (5.7)$$

where v_t is the superficial gas velocity, given by Eq. 4.7, at which the bubbly-to-slug flow transition occurs, $v_t = (0.43\ v_{sL} + 0.357v_\infty)\ \sin\alpha$. The constants 1.2 in Eq. 5.7 represent the value of C_o for bubbly and slug flows in vertical systems. Note that their magnitude will change for countercurrent and downward flows.

Similarly, for upward cocurrent or countercurrent churn flow near the slug/churn transition boundary, C_o is given by the following expression:

$$C_o = C_{os}\left[1-e^{-0.1v_{ms}/(v_{sg}-v_{ms})}\right]+C_{oc}\left[e^{-0.1v_{ms}/(v_{sg}-v_{ms})}\right]. \quad (5.8)$$

In Eq. 5.8, v_{ms} represents the mixture velocity, given by Eq. 3.10, when transition from slug to churn flow occurs. Similarly, for cocurrent and countercurrent annular flow, we have

$$C_o = C_{oc}\left[1-e^{-0.1v_{gc}/(v_{sg}-v_{ms})}\right]+C_{oa}\left[e^{-0.1v_{gc}/(v_{sg}-v_{ms})}\right]. \quad (5.9)$$

In Eq. 5.9, v_{gc} is the superficial gas velocity needed for transition to annular flow, given by Eq. 3.12. Note that Eqs. 5.7, 5.8, and 5.9 express values of C_o for the entire slug, churn, or annular flow regime, respectively, not just near the transition boundary. When the fluid velocities are high enough for a flow regime to be fully developed, the exponential nature of the expressions tends to allow the parameter value to asymptotically approach the “stabilized” value.

5.1.5 Computational Approach for Pattern Transition. Based on the discussion in Chapter 3, let us summarize an approach to determining the existing flow patterns for a given flow problem in a well cell. Because the existence for bubbly and annular

flows can be determined by one equation each, these flow patterns should be checked first. Therefore, we first use Eq. 5.6 to check if a bubbly flow pattern exists; if it does, no further calculation is necessary. If not, we check for the existence of annular flow with Eq. 3.12. If annular flow exists, no further checking is necessary. When both of these checks fail, we conclude that the existing flow pattern must be either slug or churn, or dispersed bubbly. To discern among these three flow patterns, we first use Eq. 3.10. If the actual mixture velocity is less than that given by Eq. 3.10, the flow pattern has to be slug. If all these three conditions fail, the flow pattern is either churn or dispersed bubbly. We conclude that the existing flow pattern is churn if the actual v_{sg} is greater than that given by Eq. 3.11; otherwise, the pattern is dispersed bubbly. Earlier, this approach was used in solving the example problem in Chapter 3.

Variable	Maximum	Minimum
Liquid rate, STB/D	27,760	100
Gas/liquid ratio, scf/STB	5,615	104
Water cut, %	98	0
Measured depth, ft	30,650	1,635
Bottomhole pressure, psig	13,755	108
Wellhead pressure, psig	10,218	90

Table 5.3—Range of variables used in the comparative study.

5.2 Two-Phase Flow in Oil Wells

We used a small but high-quality data set from 212 flowing wells to compare and contrast performance of various models commonly used. These wells are instrumented with permanent downhole pressure sensors with periodic surface rate measurements. **Table 5.3** summarizes the range of variables used in this section. These models include those of Hagedorn and Brown (H-B) (1965), PE-2 (*Prosper User's Manual* 2015), steady-state OLGA (Bendiksen et al. 1991), Ansari et al. (1994), Gomez et al. (2000), and the one just discussed in the previous section, designated as the Hasan-Kabir (H-K) model. The content presented here is a summary of findings reported earlier by Hasan et al. (2010b).

5.2.1 Comparative Study of Six Models. Overall, all the models behaved similarly. For instance, **Figs. 5.1a and 5.1b,** respectively, show that the data are well correlated by both the popular H-B method and the H-K model. Stated differently, when we crossplot computed bottomhole pressures between different models, good correlations are apparent; **Figs. 5.2a and 5.2b** are cases in point.

To put the performance of various models in proper perspective, we resorted to statistical analyses. **Table 5.4,** showing correlation coefficients of 212 test points,

suggest that all the models are highly correlated with data. In fact, the significance of the correlation coefficient *r* is presented in terms of the *t* values (shown in the penultimate row), given by the following expression (Blalock 1972, 400):

$$t = \left[r\sqrt{(n-2)} \right] / \sqrt{(1-r^2)}, \quad (5.10)$$

where *n* indicates the number of data points. We point out that for any of the models to assure existence of correlation with data, we needed a *t* value of only 2.6 within the 99% confidence interval. As the penultimate row shows, all the *t* values are well over 100, thereby indirectly suggesting that sufficient data points exist for all these models to apply equally within the confidence interval. Similarly, the *F*-test values displayed in the last row exceed the critical value of 6.63, thereby attesting to the *t*-test results.

To explore the level of similarity among the models, we performed another statistical *t*-test in accord with the following relationship (Blalock 1972, p.407):

$$t_{xz} = (r_{xy} - r_{zy})\sqrt{\left\{\left[(n-3)(1+r_{xz})\right] / \left[2\left(1 - r_{xy}^2 - r_{xz}^2 - r_{zy}^2 + 2r_{xy}r_{xz}r_{zy}\right)\right]\right\}}. \quad (5.11)$$

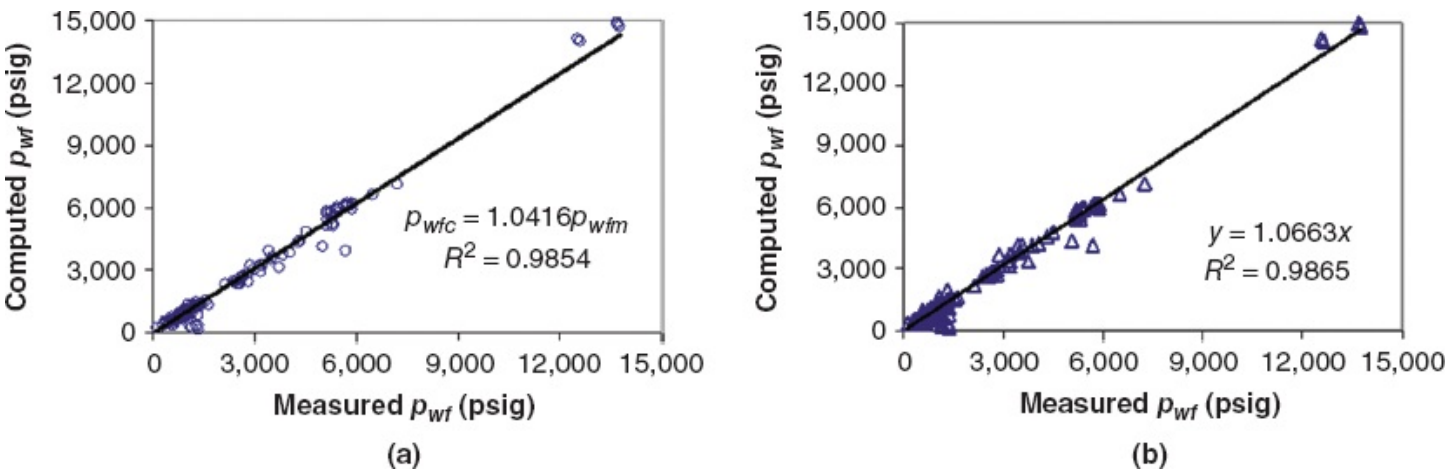

Fig. 5.1—Performance of H-B correlation (a) and H-K model (b).

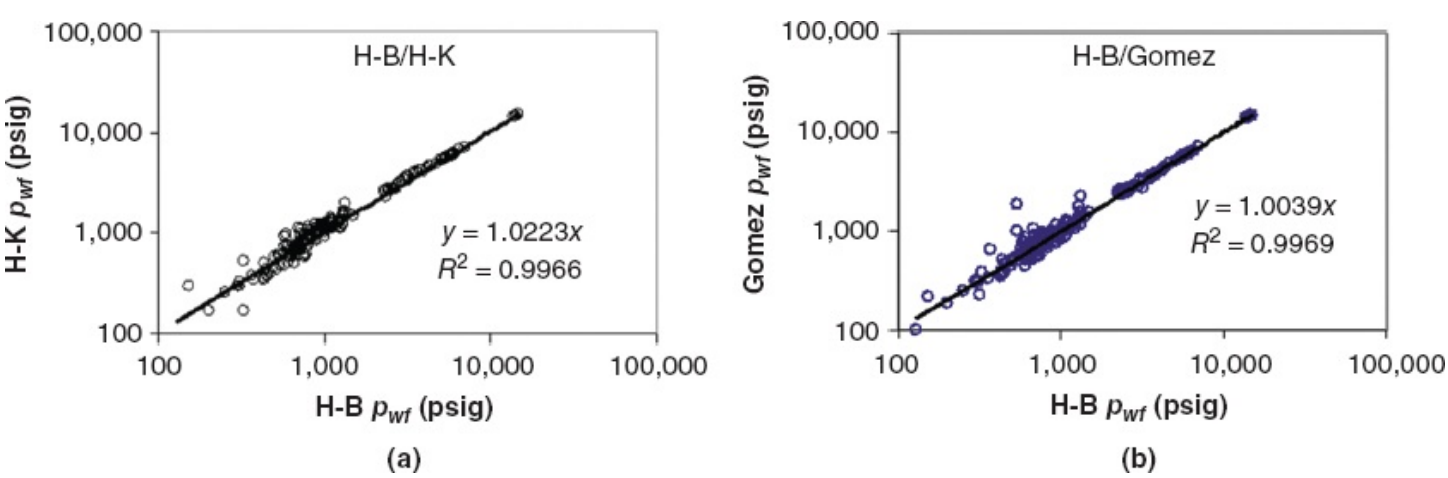

Fig. 5.2—Performance comparison shows good agreement between H-B and H-K models (a) and H-B and

Gomez models (b).

In Eq. 5.11, *y* is the data-set array and *x* and *z* represent the model estimation arrays. **Table 5.5** compares t-test values between the correlations to show likelihood of similarity between any model pairs for the same data set. Those values colored in blue suggest that no significant differentiation between the performances of the model pair can be made because they are below the *t* value of 2.6 within the confidence interval of 99%. For those model pairs shown in black, we conclude that the models are significantly different from, but not necessarily inferior to, others because the previous test showed their reliability. Stated differently, four of the models correlate with each other better than the other two.

5.2.2 Uncertainty Analysis. Over the years, many authors (Aggour and Al-Yousef 1996; Ansari et al. 1994; Pucknell et al. 1993; Kabir and Hasan 1990, to name a few) have attempted comparative studies to discern the reliability of two-phase flow models for diverse applications. However, no model has emerged as the single, most-reliable tool for routine applications, although the H-B and PE-2 models enjoy widespread popularity. On the basis of the data analysis of the previous subsection, we hypothesize that reliability of input data, entering typical top-down pressure-traverse calculations, perhaps plays a larger role in any comparative study. Let us explore this point.

Consider a highly deviated 31,000-ft well from our data set producing at 6,394 STB/D. **Fig. 5.3a** shows that the computed pressures from all the six models are clustered together and suggest pressures higher than that measured downhole with a permanent sensor. Domination of single-phase liquid and bubbly flow explains why all the models behave so similarly. The reported gas/oil ratio (GOR) of 703 scf/STB translates to a maximum spread of only 73 psi or 1.27% of the minimum pressure of 5,717 psig, obtained from the H-B model.

r	H-B	PE-2	OLGA	Ansari	Gomez	H-K
H-B	1	0.9998	0.9998	0.9994	0.9984	0.9986
PE-2	0.9998	1	0.9998	0.9990	0.9980	0.9989
OLGA	0.9998	0.9998	1	0.9993	0.9983	0.9992
Ansari	0.9994	0.9990	0.9993	1	0.9994	0.9982
Gomez	0.9984	0.9980	0.9983	0.9994	1	0.9973
H-K	0.9986	0.9989	0.9992	0.9982	0.9973	1
Data	0.9941	0.9941	0.9939	0.9931	0.9922	0.9937
t	132.52	132.87	130.75	122.42	114.98	128.42
F	24,849	26,738	26,323	21,961	19,657	27,722

Table 5.4—Correlation coefficient for different models.

t	H-B	PE-2	OLGA	Ansari	Gomez	H-K
H-B	NA	0.211	0.965	3.938	4.570	0.975
PE-2	0.211	NA	1.192	3.161	4.076	1.195
OLGA	0.965	1.192	NA	2.924	3.980	0.740
Ansari	3.938	3.161	2.924	NA	3.247	1.362
Gomez	4.570	4.076	3.980	3.247	NA	2.735
H-K	0.975	1.195	0.740	1.362	2.735	NA

Table 5.5—The t-test values for different models.

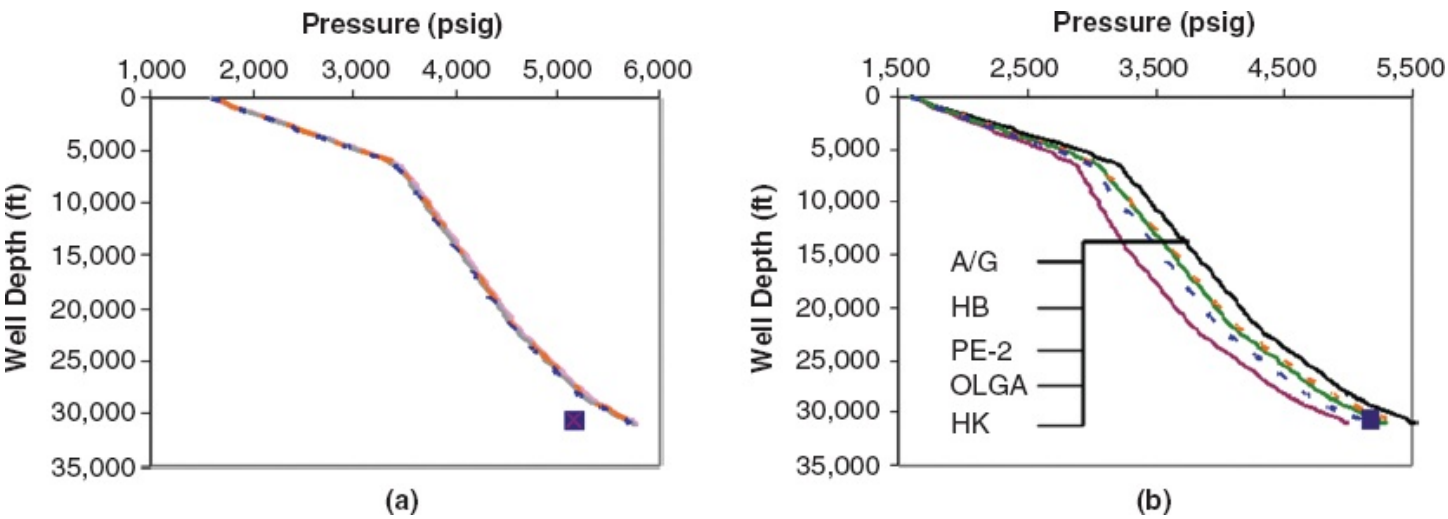

Fig. 5.3—Higher p_{wf} calculation of all models suggests suspect data (a). Good performance of all models after GOR correction (b).

However, a test reported 4 days later suggested a considerable increase in GOR. The new GOR value of 1,250 scf/STB is consistent with breakthrough of free gas from the reservoir. When the new GOR was used, we observed an acceptable match, as Fig. 5.3b suggests. In Fig. 5.3b, A/G implies model results of Ansari et al. and Gomez et al., which are indistinguishable traces for the scale used. Both dispersed bubbly, owing to high liquid velocity, and slug flow dominated the results in this increased-GOR scenario. We surmise that misreporting of GOR triggered the earlier mismatch, because failure of all models is highly unlikely. No attempt was made to seek corrections of this nature in the database. This example merely highlights the uncertainty of input parameters in routine calculations even in a well-instrumented environment.

Let us explore how measurement errors may potentially cause significant uncertainty in p_{wf} estimation. Consider a well exhibiting all four flow regimes from this data set. **Table 5.6** presents the uncertainty values, which are assigned relative to those presented in the last row, displaying the true values. For instance, we assumed the oil rate measurement uncertainty to be ±10%, GOR to be ±15%, and so on.

Fig. 5.4 displays the Pareto chart summarizing the results of the four-variable

Plackett and Burman (1946) design of experiments. The positive sign associated with each independent variable suggests that any increase is reflected as an increase in the dependent variable, while the opposite is true for those associated with negative values. Note that nonlinearity in this comparative picture is small, as signified by the small curvature value. Here, the dependent variable is error, defined as the difference in pressure with respect to the true value, corresponding to the input values of the last column of Table 5.6. We note that GOR is the largest contributor to error, followed by the oil rate itself. Because gas is flared in many field settings, the measurement accuracy suffers; the same remark holds for water-cut measurements. Of course, the impact of uncertainty of each independent variable on the dependent variable (error) is case specific; this example is intended for illustrative purpose only.

Oil Rate q_o (STB/D)	Water Cut f_w	GOR R_{go} (scf/STB)	Oil Gravity γ (°API)	Error Δp (psi)
21,764	14.45	732	36	–143
21,764	19.6	732	32	–231
21,764	19.6	990	32	–28
17,807	19.6	990	36	145
21,764	14.45	990	36	41
17,807	19.6	732	36	–88
17,807	14.45	990	32	157
17,807	14.45	732	32	–68
19,786	17	861	34.5	0

Table 5.6—Uncertainty variables for Plackett and Burman (1946) design.

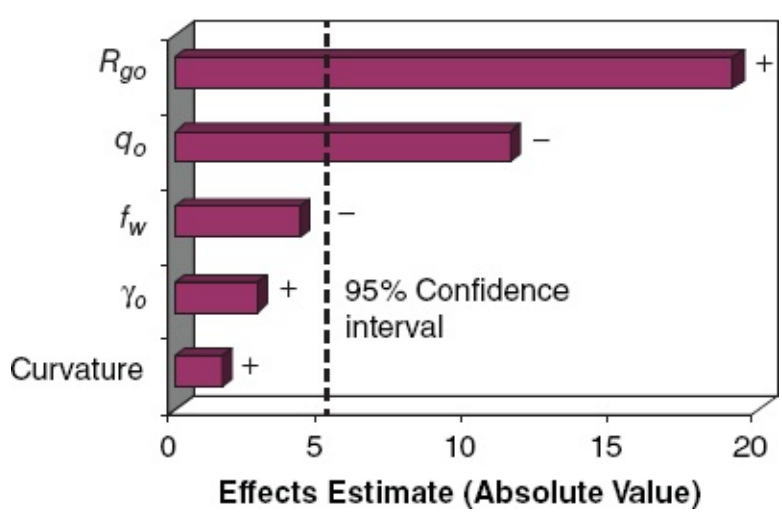

Fig. 5.4—Pareto chart shows dominance of GOR and oil rate on p_{wf} error estimation.

5.2.3 Lessons Learned. Tables 5.1 and 5.2 consolidated two-phase flow models that appeared in Chapters 3 and 4, using the drift-flux approach. This unified approach applies to a variety of well orientation, geometry, and fluids with minimal

changes in parameter values. We think that this simplified, transparent approach allows for ease of imple-mentation and understanding of mechanics of flow.

While seeking to compare the H-K model with others, we learned that their collective performance is comparable in a statistical sense. Perhaps this outcome owes largely to the high-quality data set that we used. Even in this set, data were far from perfect; **Fig. 5.5** illuminates this point. Our view is that improvement in two-phase flow modeling has probably reached a point of diminishing returns. Focusing on data gathering and quality control will perhaps pay greater dividends than improving the models. To that end, the current practice of production rate validation through real-time integrated asset modeling is a step in the right direction.

Uncertainty in input data stems from allocated oil rates and low-quality measurements of the gas and water phases. Changes in oil properties also occur because of changes in reservoir pressure and compositional grading, particularly in thick-oil columns. Therefore, periodic calibration of oil properties with a PVT model is definitely required while attempting pressure-traverse computations.

We also note that common practice is to use a single, overall-heat-transfer coefficient in pressure-drop calculations. Although this approach often produces satisfactory p_{wf} estimation, the resultant temperature profile may not necessarily reflect the reality, especially in deepwater and high-pressure/high-temperature environments. In other words, good accuracy in p_{wf} calculations does not guarantee the same in the temperature profile, as discussed elsewhere (Hasan et al. 2009). The implication is that simplified heat-transfer modeling may provide a temperature trace that is not worthy of use for combating production of thermodynamic solids, such as hydrates, paraffins, and asphaltenes. Solids buildup or corrosion may also significantly contribute to the uncertainty of pipe inner diameter (ID), thereby affecting results.

5.3 Two-Phase Flow in Gas/Condensate Wells

Production from gas/condensate and geothermal wells is dominated by annular two-phase flow. Oil wells also experience the same during high-GOR production. As mentioned in Chapter 3, a number of sophisticated models are available that attempt to describe physics of annular two-phase flow accurately. However, we recommend the homogeneous model for annular flow regime. The reason for this adoption is that in spite of being the simplest of the approaches, its accuracy in estimating pressure gradient is comparable to that of the more rigorous models. Details of this section can be found in Kabir and Hasan (2006).

In the subsequent materials in this section, we offer analyses of field data from various sources in support of the homogeneous model's comparative accuracy. This section points out some of the practical difficulties that limit the potential of the more sophisticated models because these require an accurate estimate of the liquid-film thickness δ riding up along the wall.

The difficulties in obtaining an accurate film thickness estimate are (1) the wavy

nature of the film and its thinness (often δ is < 5% of channel diameter), (2) the need for accurate values of a number of parameters to estimate δ, and (3) the need to solve a fifth-order polynomial equation for δ that is very sensitive to various parameters in the equation. Among the input parameters needed to estimate δ are (1) fraction of total liquid entrained in the gas core, (2) liquid-film friction factor that depends on δ, (3) gas/liquid interface friction gradient that depends on gas and liquid velocities at the gas/liquid interface, and (4) the core fluid velocity that also depends on δ.

In short, the homogeneous model for annular two-phase flow shows comparable accuracy with existing mechanistic models, thereby retaining simplicity and transparency.

5.3.1 Computational Approach and Field Applications. Independent gas/condensate data from three different sources comprising 167 wells constituted the basis of this analysis. The methods used involved the homogeneous approach of Gray (User's Manual for API 14B 1978), Aziz et al. (1972), and Ansari et al. (1994); steady-state OLGA; and the wet-gas approach advanced by Peffer et al. (1988). The accelerational term, in addition to friction and hydrostatic head, is implicit in all methods, although the original wet-gas approach excludes this term.

These three data sets come from drillstem tests in West Africa (Kabir and Hasan 2006), as well as from two others reported by Govier and Fogarasi (1975) and by Peffer et al. (1988). We discuss the results of the Texas Railroad Commission (TRRC) data set (Peffer et al. 1988) to illustrate the lessons learned, and we show the final results from the other two data sets.

The TRRC data set lends itself to an in-depth study because of large variations in GOR (5,180 to 780,000 scf/STB), wellhead pressure (WHP) (3,107 to 12,313 psig), and bottomhole pressure (BHP) (4,125 to 11,250 psig). When graphing the percent error compared with those estimated with the homogeneous model in BHP with GOR, WHP, and rate, we did not observe any particular trend. **Figs. 5.5 and 5.6** show that random errors abound. Perhaps uncertainty in rate measurements is responsible for the lack of a trend. Nonetheless, the overall error is rather small, as testified by **Fig. 5.7. Table 5.7** presents the error analysis for this data set, showing comparable performance among the methods used.

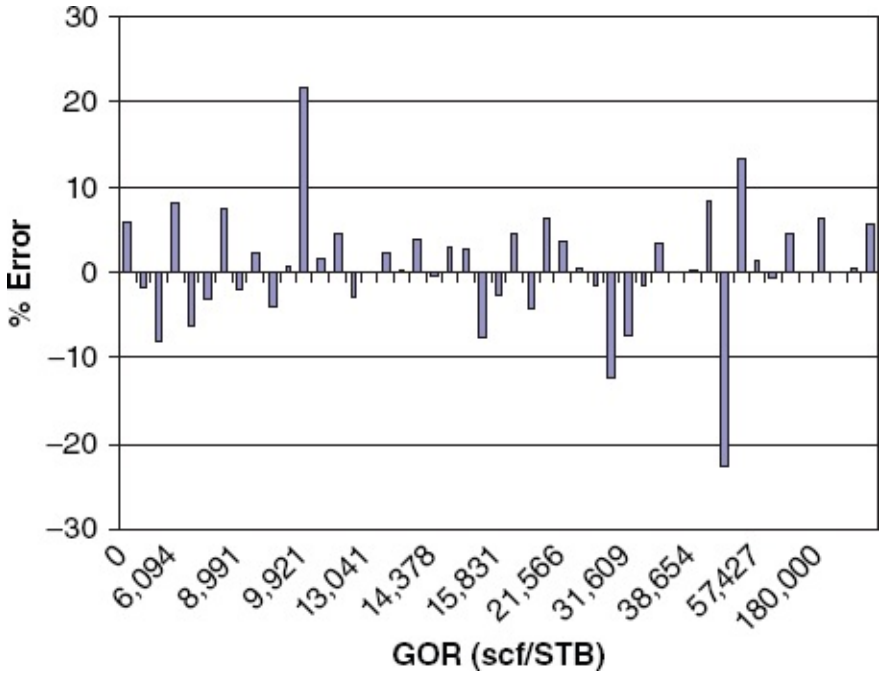

Fig. 5.5—Error bears no correlation with GOR, TRRC data.

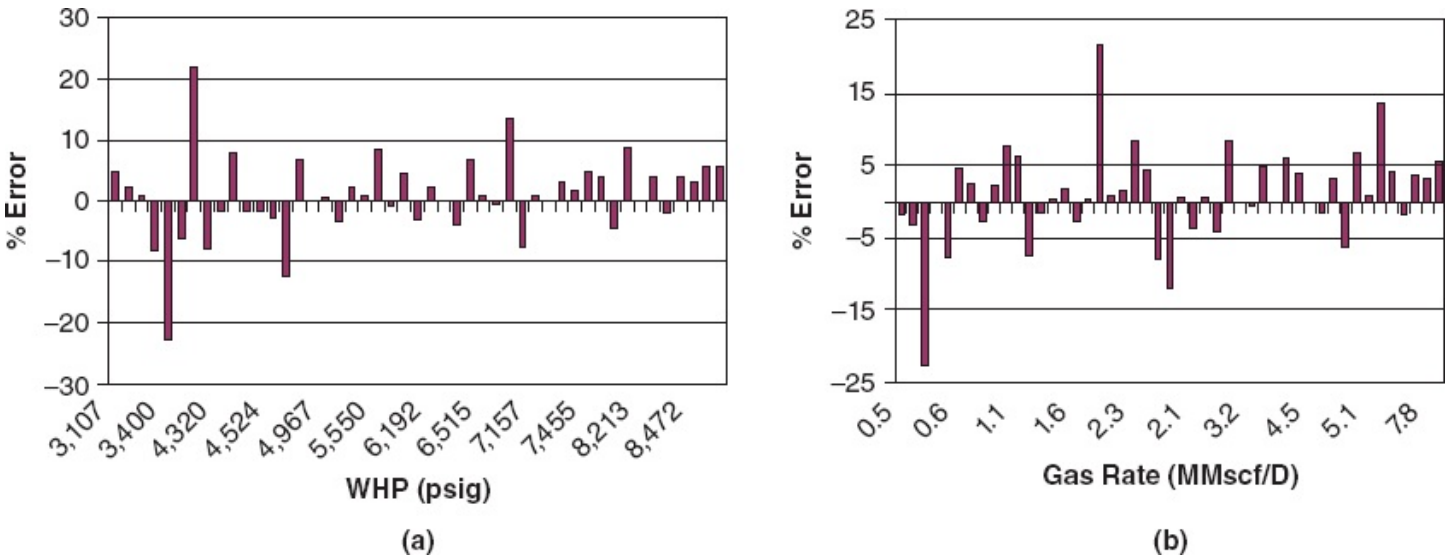

Fig. 5.6—Error bears no correlation with WHP (a) and rate (b), TRRC data.

Parameter	Gray (User's Manual for API 14B 1978)	Aziz et al. (1972)	Homo	Ansari et al. (1994)	OLGA	Wet Gas
Avg. % error	3.92	26.03	–0.228	1.37	4.25	5.60
Abs. avg. % error	13.89	31.98	12.16	12.82	13.47	17.33
% Standard deviation	7.60	331.88	0.094	0.99	8.90	15.73
Abs. avg. error, psi	254.61	500.07	236.44	241.25	249.43	99.91
Avg. error, psi	27.72	366.92	47.13	18.13	42.10	356.3

Table 5.7—Error analysis, TRRC data set.

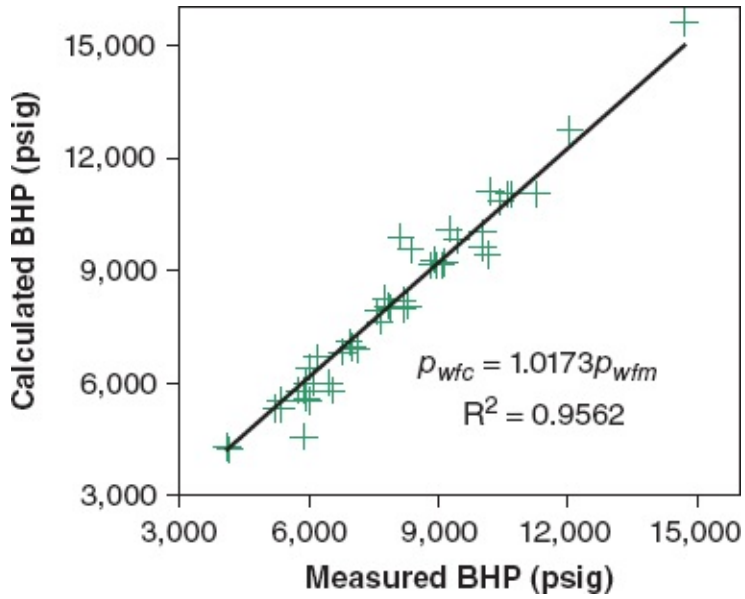

Fig. 5.7—Comparison of measured and homogeneous-model performance, TRRC data.

Two other independent data sets, as shown in **Fig. 5.8,** corroborate our contention that the simplified, homogeneous modeling approach works very well under diverse conditions of annular two-phase flow.

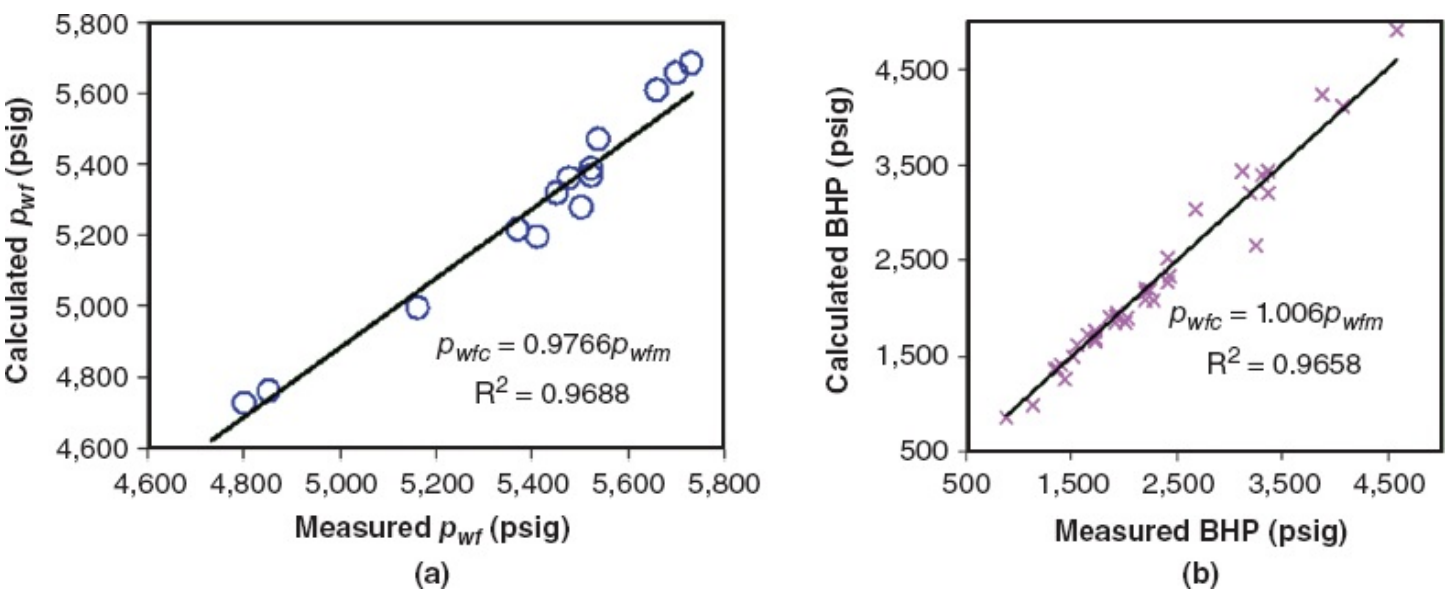

Fig. 5.8—Comparison of measured and computed data with homogeneous model, N. Apoi field (a), and Govier-Fogarasi (1975) data set (b).

5.3.2 Uncertainty of Input Data for Bottomhole-Pressure Calculations.

Various issues can potentially affect the outcome of otherwise routine estimation of BHP from WHP. In this section, we explore issues pertaining to gauge accuracy, flow rates of individual phases, fluid composition, and wall roughness. The West Africa data set, mentioned earlier, was used in these analyses.

Absolute Accuracy of Two Gauges. Any pressure-traverse computation

presupposes that the wellhead gauge has the same characteristics as the one placed downhole, especially with regard to absolute accuracy. In practice, this condition is rarely satisfied. Typically, the downhole gauge is of the quartz crystal variety with good accuracy and resolution. In contrast, in the past, the one at the wellhead has been of the bourdon-tube variety, with far less accuracy. Their relative performance was rarely checked before conducting a test. Given this reality, close agreement between a model and measurement may be hard to achieve when old data sets are examined.

***Liquid Rate or Condensate/Gas Ratio Trend and Separator Efficiency*.** Liquid production is relatively small in a typical gas/condensate well. Consequently, separation of this liquid from large volumes of produced gas may not be efficient. Issues with collecting representative fluid samples are well-known and are discussed by McCain and Alexander (1992).

Let us examine this issue for wells producing moderate amounts of condensate during a transient test. **Fig. 5.9** shows that liquid rate measurement and/or separation of phases introduces uncertainty. Increasing condensate/gas ratio (CGR) signifies issues with the liquid rate measurements because of its instability, unlike the stable gas rate at each choke setting. Note that the BHP stabilizes rapidly in concert with the gas rate behavior while the WHP does not. **Fig. 5.10** makes this point amply clear. The increasing-WHP trend is expected to occur owing to thermal storage (Hasan et al. 2005), and is not an anomaly. We think inadequate separation and/or shearing of liquid at low rates owing to excessive choking causes opposing trends when the two fluid streams are measured at the separator.

We ensured that all the reported rates were above the critical unloading rate for the West Africa data set. The use of the Li et al. (2002) model shows the critical rate varying between 1.77 and 2.61 MMscf/D, thereby leaving no doubt about continuous lift of the condensate. These tests produced only trace amounts of water, with the lowest rate being 5 MMscf/D.

***Condensate Gravity Range*.** Moses (1986) reported that condensate liquid gravity should range from 40 to 60 °API. Others have suggested 70 °API as the upper limit. But the reported values from the field may not adhere to this range. For instance, of the 102 tests, Govier and Fogarasi (1975) reported 56 tests that had °API greater than 70 and five tests lower than 40.

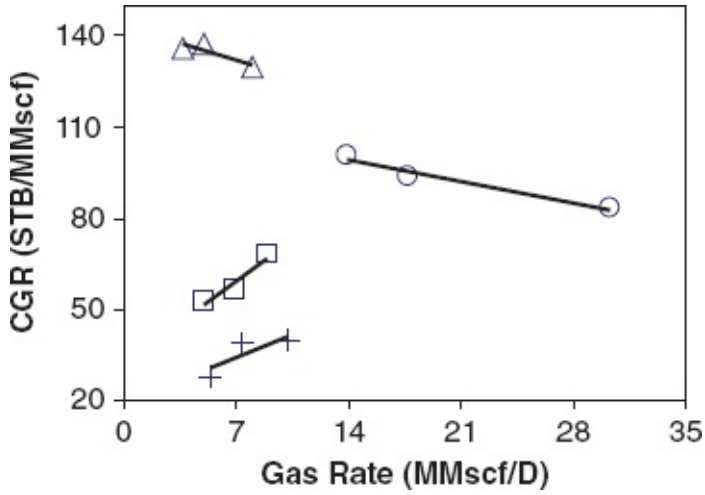

Fig. 5.9—CGR trends underscore the difficulty of obtaining quality rate data, West Africa data.

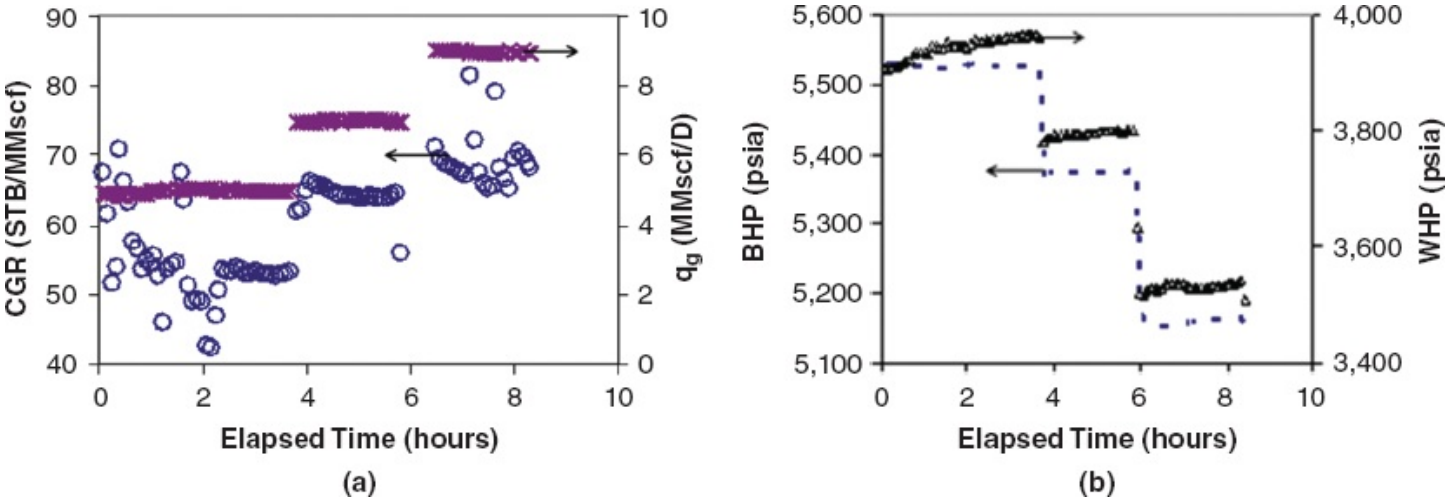

Fig. 5.10—Difficulty with liquid rate measurement is apparent during a transient test (a), but BHP response shows stable flow during a transient test (b), West Africa data.

We surmise that fluid contamination is responsible for this anomalous reporting. Presence of dissolved gas at conditions other than stock-tank conditions will lighten the liquid. By contrast, production of some liquids from the associated oil rim will make the condensate heavier than the lower limit of approximately 40 °API.

Clearly, contamination can be a major source of density error if density is used literally, particularly in the wetgas approach in which densities are used explicitly. For our computations, we set the gravity values to the upper and lower limits when they were violated. In contrast to this data set, the other two did not have this issue.

Wall Roughness. Wall roughness is another potential source for error. We used 0.0018-in. pipe wall roughness for all wells reported here. In so doing, we presupposed all tubulars were made of smooth commercial steel with no provisions for corrosion or in-line coating. This assumption is very good for the new wells in the West Africa data set, but wells in the other two data sets have unknown character.

5.3.3 Justification of Homogeneous Modeling Approach. As mentioned in the introduction to Section 5.3, we recommend using the homogeneous model when annular flow pattern is encountered. The results presented clearly show that the estimates of the simple homogeneous model are comparable with those obtained from the more complicated models of Ansari et al., Gray, OLGA, and Aziz et al. To further explain the performance of the homogeneous model vs. the sophisticated models, let us explore the significance of various terms in these models.

Comparison With Gray Correlation. The Gray correlation uses a pseudohomogeneous approach for computing frictional, static, and accelerational head losses. Gray noted, however, that even for condensate wells, the liquid droplets may not be moving as fast as the gas phase; that is, there is some liquid holdup. To account for the holdup, Gray proposed the following expression for in-situ gas volume fraction, f_g:

$$f_g = \left\{1 - e^{-2.314\left[N_v\left(1+\frac{205}{N_d}\right)\right]B}\right\}\left(\frac{v_{sg}}{v_m}\right), \quad (5.12)$$

where

$$B = 0.0814\left[1 - 0.0554\ln\left(1 + \frac{730 v_{sL} / v_{sg}}{1 + v_{sL} / v_{sg}}\right)\right] \quad (5.13)$$

and N_v and N_d are dimensionless velocity and diameter numbers defined in the Nomenclature section. Note that for the homogeneous model, $f_g = v_{sg} / v_m$. In other words, Gray's correlation becomes identical to the homogeneous model when the exponential term in Eq. 5.12 vanishes. Perhaps the physical explanation may lay in the fact that the gas mass dominates the bulk flow and that near-critical fluids have low interfacial tension between them, leading to minimum slip. Our computations on the field examples showed that the exponential term in Eq. 5.12 varies between 0.004 and 0.01. Therefore, one can logically conclude that the Gray correlation collapses into the homogeneous model for most gas/condensate wells. **Fig. 5.11a** illustrates this point by showing data from two wells with high and medium CGRs. Fig. 5.11b compares performance of the Gray correlation with the homogeneous model for all three data sets used in this study. The excellent correlation between the two methods suggest that the Gray correlation can be extended beyond its original bounds and also sheds light on its popularity.

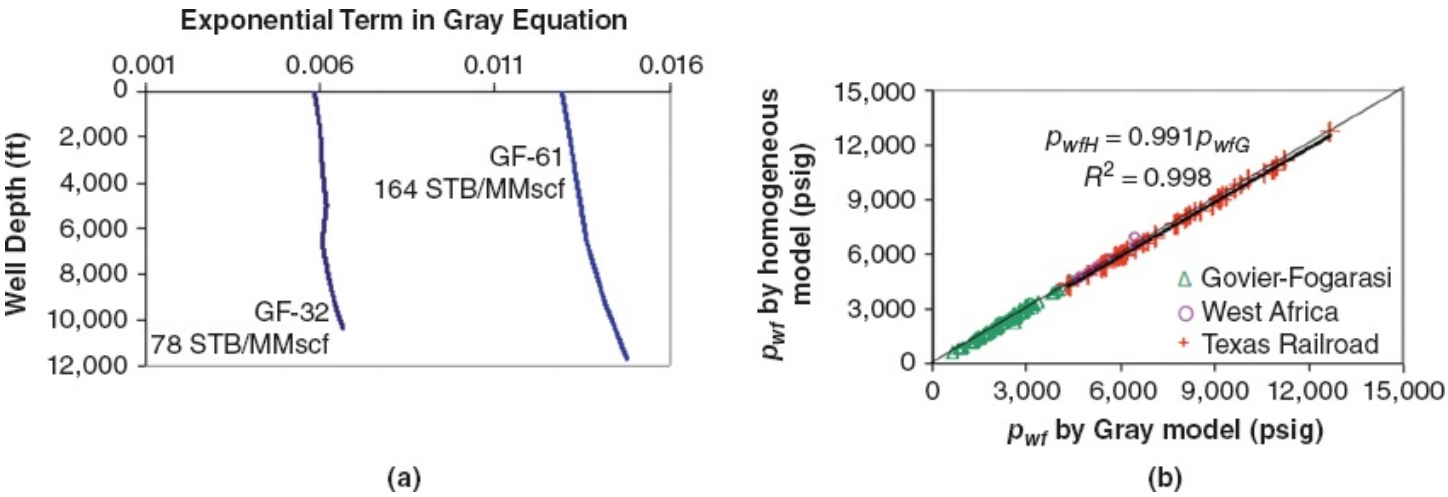

Fig. 5.11—Minimal departure of Gray correlation from the homogeneous model for medium- and high-CGR wells (a); overall correlation reaffirms the same point for three data sets (b).

Comparison With the Ansari et al. Model. In annular flow, the primary difference between the Ansari et al. (1994) and homogeneous models is in the way friction factor is computed. In the Ansari et al. model, friction factor for the gas phase f_{fg}, flowing alone in the well, is initially computed from the usual Reynolds number ($dv_{sg}\rho_g/\mu_g$) friction factor relationship. Thereafter, following the suggestion of Wallis (1969), this friction factor is multiplied by a factor accounting for roughness, which the gas phase experiences in flowing against a wavy film of liquid along the wall of a pipe. This multiplier depends on $\underline{\delta}$, the dimensionless thickness of the liquid film—film thickness/well ID—and is given by (1 + 300$\underline{\delta}$). In other words,

$$f_{fgA} = (1+300\,\underline{\delta}). \qquad (5.14)$$

Ansari et al. proposed a method for estimating film thickness by equating shear forces acting on the liquid film and the gas phase. However, we chose the simpler Lockhart-Martinelli (L-M) approach (Lockhart and Martinelli 1949) to estimate film thickness because it is expected to be extremely small for most gas/condensate wells. An example calculation is shown at the end of this section.

Our computations show that $\underline{\delta}$ is less than 0.015 for the field examples. Nonetheless, the Ansari et al. method computes a friction factor that is slightly higher than the one obtained from using the f_{fg} alone. Note that the homogeneous model uses average mixture property values of the gas and liquid phases to calculate a Reynolds number, which is lower than $dv_{sg}\rho/\mu$. Therefore, the calculated friction factor for the homogeneous model is similar to that of the Ansari et al. model. In fact, the difference in the calculated p_{wf} from the two methods rarely exceeded 1 psi.

Fig. 5.12a presents computational results of δ for two wells producing at different CGRs; a detailed discussion on the film thickness issue can be found elsewhere (Hasan and Kabir 2007). The near-perfect agreement between the Ansari et al. model and the homogeneous model, as shown in Fig. 5.12b, establishes their

equivalence in mist flow. This agreement is owing largely to negligible liquid-film thickness even for condensate-rich wells. That a part of the well may experience single-phase flow becomes a nonissue as long as the friction calculations are performed appropriately in a gas-flow-dominated system.

5.3.4 Lessons Learned. We have demonstrated that applications of the homogeneous model are reliable for pressure-drop computation in wellbores for gas/condensate systems over a wide range of operating conditions. Note that the condition of homogeneity improves with time as a condensate system becomes leaner. Therefore, the use of a homogeneous model in an integrated model involving a reservoir/wellbore/pipe network is extremely appealing because of its simplicity and robustness.

Comparison of performance of the homogeneous model with others suggests that it is a reliable tool. Indeed, both the Gray and Ansari et al. models converge to a homogeneous model when mist flow occurs in gas/condensate systems. Occurrence of mist flow—a condition of quasihomogeneity of the two phases—appears to hold for a wide range of BHP, CGR, well depth, and flow rate for the three independent data sets. **Fig. 5.13** exhibits a very good correlation between the homogeneous model and the measured data. Despite the uncertainty in various elements of field data discussed earlier, we think that this agreement is remarkable.

One may wonder about the applicability of the homogeneous model in diverse field conditions.

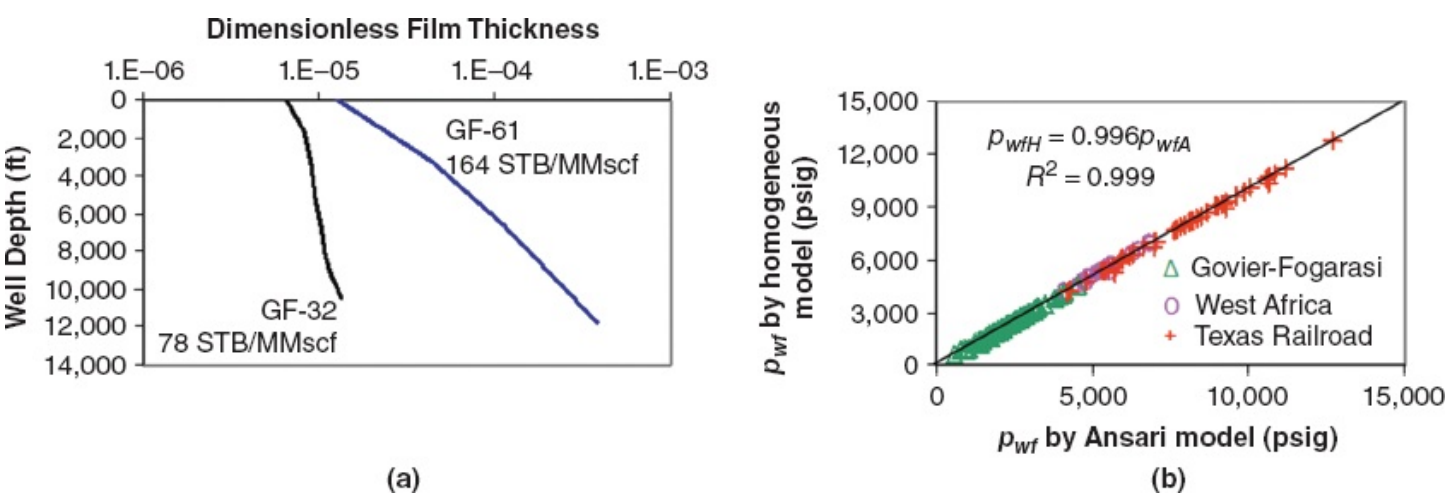

Fig. 5.12—The L-M model shows negligible film thickness in high- and medium-CGR wells (a), and the homogeneous model correlates well with the Ansari et al. (1994) model (b).

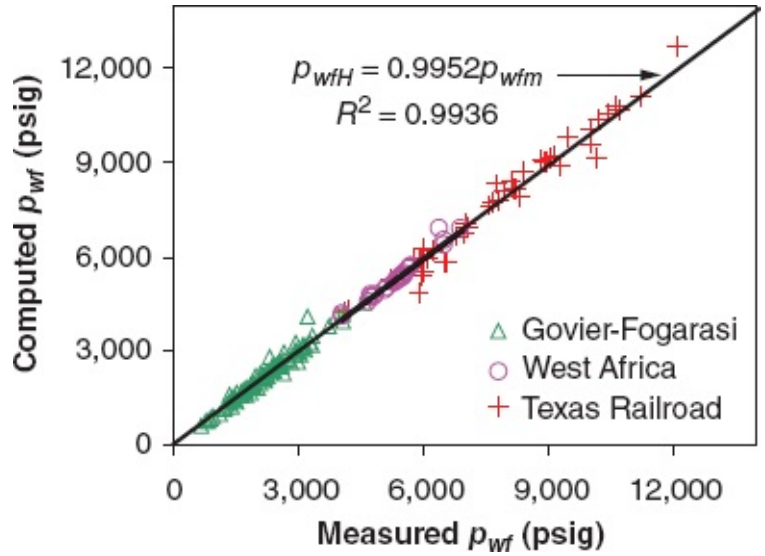

Fig. 5.13–Overall performance of the homogeneous model.

Data Set	*p_{wh} (psig)*	*p_{wf} (psig)*	*Well Depth (ft)*	*q_g (MMscf/D)*	*CGR (STB/MMscf)*
TRRC	3,107–10,190	4,125–12,045	7,676–15,676	0.53–24.9	1.4–256
Govier-Fogarasi (1975)	450–2,815	65–4,579	5,939–12,073	0.67–27.4	1.3–194
West Africa	2,062–4,900	4,076–6,889	9,454–13,800	3.71–30.24	28–131

Table 5.8—Range of variables in three data sets.

Table 5.8 presents the range of some key input variables for the three data sets. In terms of BHP or WHP, the Govier-Fogarasi data set has the low range, followed by the West Africa data set in the middle range, with the TRRC data set having the highest range. Figs. 5.11a, 5.12b, and 5.13 graphically show this trend. In this respect, these data sets are complementary. Perhaps most important, the homogeneous model does a fine job for the entire range of CGR typically encountered in gas/condensate wells.

Motivated by the ease of calculation before the computer era, some authors—Cullender and Smith (1956), for example—chose not to include accelerational gradient ($\rho v_m dv_m/dz$) in the overall pressure-drop calculations. This assumption is often quite reasonable in many cases. However, our experience shows that neglecting this component is imprudent in high-rate wells with multiple downhole changes in internal diameter resulting from restrictions because of large range of $(dv_m/dz)_A$, as **Fig. 5.14** suggests.

5.3.5 Example Calculation. We use the data for Well 61 in the Govier-Fogarasi (1975) data set to show computation procedures for the homogeneous model, the Gray correlation, and the Ansari model. The well was producing 70 **°API dry oil at 635 STB/D through a 2.992-in**.-ID tubing. The GOR is 6,100 scf/STB, and the gas gravity is 0.712. The following property values and computed fluid parameters are available at the wellhead, where pressure is 1,169 psig:

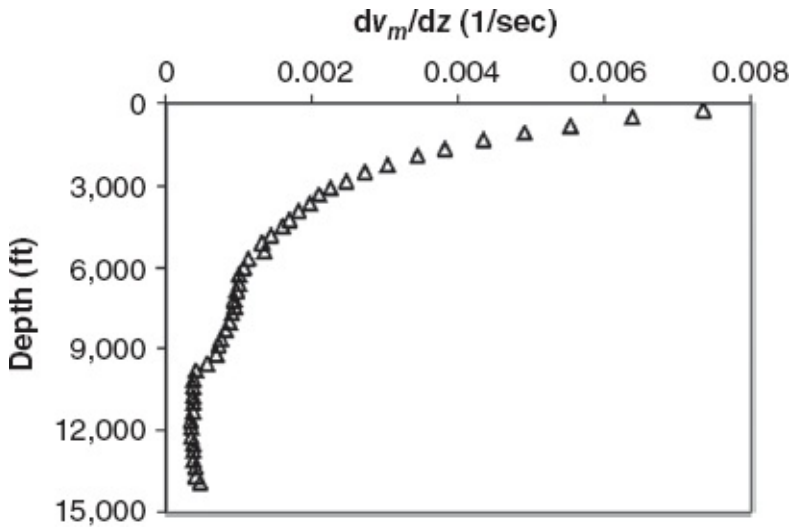

Fig. 5.14—Velocity gradient in Sonam J-02 well.

v_{sL} = 1.08 ft/sec, v_{sg} = 10.4 ft/sec

$v_m = v_{sL} + v_{sg}$ = 11.48 ft/sec d = 0.25 ft

ρ_L = 44.12 lbm/ft^3, ρ_g = 4.0 lbm/ft^3

μ_L = 1.0 cp, μ_g = 0.0135 cp, σ = 15.68 dynes/cm = 0.0346 lbm/sec^2

Quality, $x = [v_{sg}\,\rho_g/(v_{sg}\rho_g + v_{sL}\rho_L)] = 0.465$

Gas volume fraction = $v_{sg}/v_m = 0.906 = 1/(R+1)$

Mixture density, $\rho_m = 0.906\rho_g + 0.094\rho_L$ = 7.793 lbm/ft^3

***The Gray Correlation (User's Manual for API 14B 1978*).** Let us evaluate the dimensionless numbers:

$N_v = [v_m 4\rho_m{}^2/[(g\sigma)(\rho_L - \rho_g)]\} = [(11.48)^4\,(7.793)^2/(32.2 \times 0.0346 \times 40.04)] = 23{,}381$

$N_d = [d^2 g(\rho_L - \rho_g)/\rho] = (0.252 \times 32.2 \times 40.04)/(0.0346) = 2{,}318$

$$C = \text{in}\left(1 + \frac{730R}{R+1}\right) = 4.2468$$

$B = 0.0814(1–0.0554C) = 0.0622$

Correction to homogeneous gas volume fraction yields

$$\xi = \exp\left\{-2.314\left[N_v\left(1 + \frac{205}{N_d}\right)\right]^B\right\} = 0.01293,$$

where f_g (the two-phase gas volume fraction) is given by

$$f_g = \frac{1-\xi}{R+1} = f_{g\,\mathrm{homo}}\left(1-\xi\right).$$

Therefore, for this particular case, the two-phase gas volume fraction is approximately 1.3% less than the one calculated using the homogeneous model.

The Ansari et al. (1994) Model. To calculate liquid-film thickness δ, Ansari et al. noted that the pressure gradient for the gas core must equal that for the liquid film. They wrote the expressions for these two gradients in terms of liquid-film thickness and solved for δ by equating the two expressions. The expression for δ so generated is an implicit one, requiring iterative solution. We use a simple approach to estimating δ by noting that geometrical considerations allow us to write $\delta = (1 - f_g)/4$. To estimate gas volume fraction, f_g, we used the well-known L-M correlation (Lockhart and Martinelli 1949) for the annular flow regime, as follows:

L-M Parameter: $X^2 = [(1 - x)/x]^{1.8}(\rho_g/\rho_L)^{0.2}$.

The value of x (quality) to be used in this expression is the mass fraction of the vapor phase. Because we are interested in estimating the film thickness of the liquid on the channel wall, the liquid droplets flowing as an entrained phase along with the gas core need to be counted as part of the core vapor phase. This calculation step requires an estimate of the fraction, f_E, of the total liquid that is flowing as entrained droplets, which is given by

$$f_E = 1 - \exp\left[-0.125\left(v_{sgc} - 1.5\right)\right].$$

The critical gas velocity is given by

$$v_{sgc} = 10^4\, v_{sg}\mu_g \frac{\sqrt{\rho_g / \rho_L}}{\sigma} = 7.89.$$

Therefore, $f_E = 0.55$.

The modified quality for this case, then, is

$$x_{\mathrm{mod}} = [(v_{sg}\,\rho_g + f_E \times v_{sL}\rho_L)/(v_{sg}\rho_g + v_{sL}\rho_L)] = 0.759.$$

The L-M parameter: $X^2 = [(1 - x_{\mathrm{mod}})/x_{\mathrm{mod}}]^{1.8}(\rho_g/\rho_L)\ (\mu_L/\mu_g)^{0.2} = [(1 - 0.\ 0.759)/\ 0.759]^{1.8}\ (4.0/44.12)\ (1/0.0135)^{0.2} = 0.0182$.

Therefore, $f_g = (1 + X^{0.8})^{-0.378} = 0.933$ and $\delta/d = (1 - f_g)/4 = 0.01675$.

5.4 Liquid Loading in Gas Wells

Liquid loading is the inability of a producing gas well to remove its coproduced liquids from the wellbore. The liquid flowing as droplets or film accumulates at the well bottom, thereby imposing backpressure at the sand-face and triggering increasingly higher pressure loss in the wellbore. The problem initiated by liquid loading is manifested in terms of loss in well deliverability, causing the WHP to decline significantly, which, in turn, leads to the cessation of gas production. Accordingly, the liquid-loading issue reduces the ultimate recovery of a gas well.

Both the droplet flow reversal and liquid-film flow reversal have been postulated to be the underlying mechanism for liquid loading. Both mechanisms are predominantly premised on diagnosing the problem at the wellhead flow conditions. This section presents the deliquefication issue in a gas well by fluid and heat flow modeling of the entire wellbore for a variety of flow situations in gas and gas/condensate reservoirs, as detailed in Riza et al. (2016).

5.4.1 Understanding Liquid-Loading Mechanism. This section attempts to underscore our understanding of various critical velocity models and initiation of the liquid-loading process.

- ***Critical Liquid-Loading Velocity Model*.** Liquid loading is initiated when gas velocity in the well declines to such a low value that it cannot drag up the liquid being coproduced. This minimum velocity of the gas phase needed to coproduce liquid is termed the critical liquid-loading velocity. Researchers agree that in an annular two-phase flow pattern the characteristic high velocity in the gas core enables all liquid to be produced up the tubing. However, when the gas velocity becomes low enough for churn flow to exist, the gas loses its ability to drag all the liquid up, leading to liquid loading. Consequently, most researchers use the transition from annular to churn flow as the *initiation* of liquid loading.
- We used the transition from slug or churn to annular flow as discussed by Taitel et al. (1980). This criterion is used widely in many two-phase flow models. We note that Turner et al. (1969) started with the same criterion, but the constant was adjusted to match their field data. In fact, when Coleman et al. (1991a, b) pursued their study they reverted to the original Turner et al. criterion. To summarize, the transition from churn to annular flow occurs if v_{sg} is higher than the critical velocity, which is given by the original Taitel et al. model (without the 20% correction) and used by many as

$$v_{gc} = 3.1\left[\frac{g\left(\rho_l - \rho_g\right)\sigma}{\rho_g^{\,2}}\right]^{0.25} \qquad (5.15)$$

We note that some authors have used various forms of Eq. 5.15, which may

confuse some readers because of use of field units and/or lumping of the quarter root of gravitational acceleration with the constant 3.1. Eq. 5.15 appears in many papers in field units as v_{gc} = 1.594 $[(\rho_L-\rho_g)\sigma/\rho_g^2]^{0.25}$, where σ is in dynes/cm and g is taken out of the parentheses and combined with the constant. In arriving at Eq. 5.15, Turner et al. (1969) used various assumptions, including average liquid droplet size, which introduces possible inaccuracy to the estimated critical velocity. In addition, in field applications, the value of the interfacial tension σ is rarely known with sufficient accuracy. Consequently, v_{gc} estimated with Eq. 5.15 must be assumed to have some uncertainty associated with it.

Some researchers (van't Westende et al. 2008; Waltrich et al. 2013) considered the Wallis (1969) approach of delineating churn-to-annular transition using the liquid-film flow reversal principle. According to Wallis, film flow reversal occurs when the following condition is satisfied:

$$v_{sg}=\left[\frac{\rho_g}{gd(\rho_L-\rho_g)}\right]^{\frac{1}{2}}+mv_{sL}\left[\frac{\rho_L}{gd(\rho_L-\rho_g)}\right]^{\frac{1}{2}}=C \qquad (5.16)$$

Wallis observed that m = 1.0 for the usual case of turbulent flow. He also noted that the value of C varies between 0.88 and 1.0. Therefore, Eq. 8 is usually used with the values of both m and C equal to 1.0. Generally, $v_{sL}\rho_L$ is much smaller than $v_{sg}\rho_g$, which led Waltrich et al. (2013) to suggest the following simpler expression for the film flow reversal criterion:

$$v_{sg}=\left[\frac{\rho_g}{gd(\rho_L-\rho_g)}\right]^{\frac{1}{2}}=1 \qquad (5.17)$$

Although Eqs. 5.15 and 5.17 may appear different, they both embody the same force (gravitational and drag) balances and usually lead to similar estimation for the pattern transition. The analyses that we present and the conclusions derived use Eq. 5.15 for the transition criterion; however, similar conclusions will result by using Eq. 5.17.

Example Calculations. The following example calculation explains the transition criterion used in Eqs. 5.15 through 5.17. For estimating critical velocity for an air/water system, let us consider v_{sL} = 0.5 ft/sec, well ID = 3 in., p = 40 psia, and ρ_L = 62.4 lbm/ft^3. At this pressure, air may be assumed ideal with a density of ρ_g = 0.207 lbm/ft^3.

The Taitel et al. (1980) criterion or the Coleman et al. (1991a, b) approach, given by Eq. 5.15, yields a critical superficial gas velocity of 30.44 ft/sec, irrespective of superficial liquid velocity:

$$v_{gc}=3.1\left[\frac{g(\rho_l-\rho_g)\sigma}{\rho_g^{\,2}}\right]^{0.25}=3.1\left[\frac{32.2(62.2)0.2}{0.207^2}\right]^{0.25}=30.44\,ft/\sec.$$

The simplified film flow reversal model, Eq. 5.17, yields a critical superficial gas velocity of 40.17 ft/sec, for all superficial liquid velocities as follows:

$$v_{sg} = \left[\frac{gd(\rho_l - \rho_g)}{\rho_g}\right]^{\frac{1}{2}} = \left[\frac{32.2 \times 0.167(62.2)}{0.27}\right]^{\frac{1}{2}} = 40.17 \text{ft / sec}.$$

Finally, the complete film flow reversal model, as presented in Eq. 5.16, with both *m* and *C* equal to 1.0, gives a critical superficial gas velocity of 31.49 ft/sec for a v_{sL} of 0.5 ft/sec:

$$v_{sg} = \left[\frac{gd(\rho_L - \rho_g)}{\rho_g}\right]^{\frac{1}{2}} = v_{sL}\left[\frac{gd(\rho_L - \rho_g}{\rho_L}\right]^{\frac{1}{2}} = \left[\frac{32.2x0.167(62.2)}{0.27}\right]^{\frac{1}{2}} - 0.5\left(\frac{62.4}{0.2}\right)^{\frac{1}{2}} = 31.49 \text{ft / sec}.$$

For a clear perspective, let us consider Fig. 5.15, which compares various models for the annular/churn transition boundary for the flow problem at hand. The transition criterion of Taitel et al. (1980) used by Coleman et al. (1991a, b) is on the left, and the conservative criteria of Barnea (1986, 1987) as used by Luo et al. (2014) and those of Alamu (2012) are on the right. A conservative criterion is one that implies that liquid loading is initiated at high superficial gas velocities or earlier in well life than modeled by Taitel et al. The Alamu criteria are based on laboratory experimental data involving granularities of annular flow pattern transitions by considering the film flow reversal mechanism.

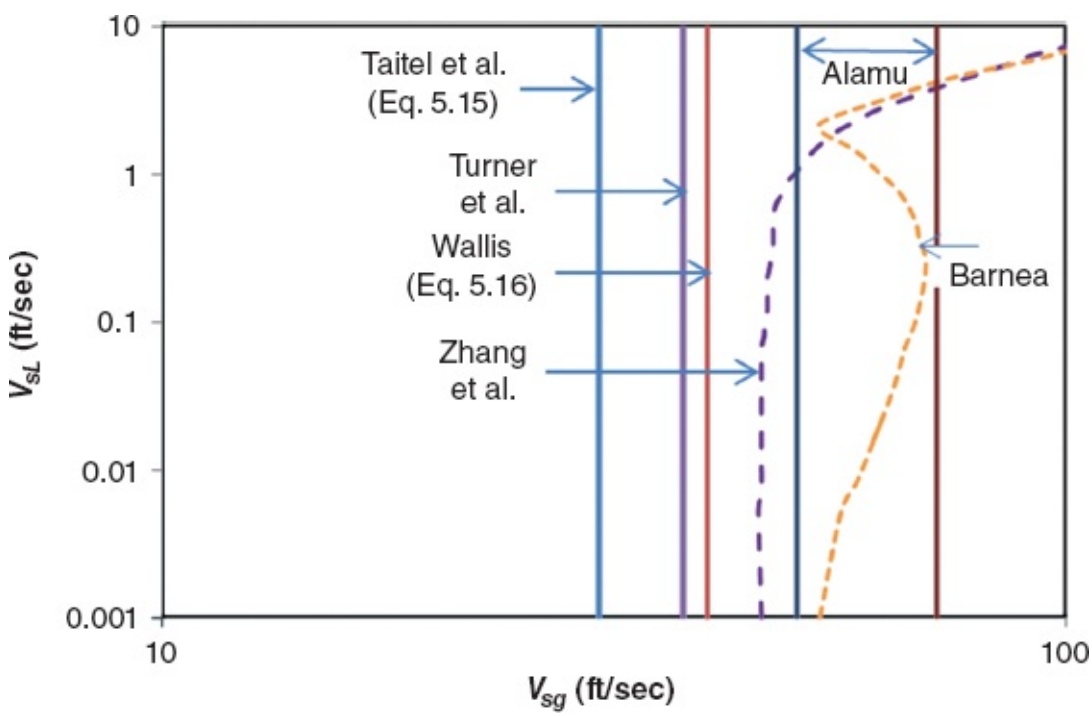

Fig. 5.15—Various models show transition to an annular flow pattern.

Because of computational difficulties at that time, Turner et al. (1969) used Eq.

5.15 and its modification at the wellhead conditions and were able to match 66 out of 90 field data points in their study. Sutton et al. (2010), among others, observed that using wellhead data to calculate critical loading rate could sometimes be misleading and suggested that using bottomhole conditions would give more-accurate predictions. In this context, we think that the entire wellbore must be in the annular flow pattern for a well to be free from liquid loading. The occurrence of slug or churn flow anywhere in the wellbore will indicate that the well is undergoing liquid loading. Because pressure is highest at the well bottom, the gas velocity is expected to be the lowest, meaning transition from annular flow is most likely to occur at the bottom of the hole first, as Sutton et al. (2010) surmised.

Accordingly, liquid-loading problem should be approached by investigating the two-phase flow pattern in the entire wellbore. Development of either a churn or a slug flow pattern is expected at the bottom of the hole first, while the rest of the wellbore experiences annular flow. When churn or slug flow develops at the bottom of the hole, liquid loading is initiated; eventually, the well dies without intervention. Liquid loading occurs when there is insufficient energy to carry the gas/liquid mixture to surface. Because of the reduced mixture velocity in the tubing, one way to address this lift problem lies in installing “velocity strings,” meaning tubing with smaller ID that helps stabilize the flow by increasing the velocity and, therefore, the frictional pressure drop. In most cases, a suitable artificial-lift system is installed, such as plunger lift, gas lift, electrical submersible pump, or rod pump, to extend the well’s producing life. In economically challenged unconventional wells, intermittent production is becoming an increasingly viable production strategy, where the well is shut in for a few days or weeks until the pressure builds up sufficiently and the well produces in cyclical fashion.

***Analysis of Well Performance With Simulated Data*.** To gain insights into well performance, solutions were generated with a simplified wellbore/reservoir model, as detailed in Riza et al. (2015). **Fig. 5.16** depicts the simulated gas flow rate and the predicted wellhead pressure for a reservoir with an initial in-situ gas of 6.11 Bscf. As shown, all five production cycles involve liquid loading. Each cycle starts with a gas production rate higher than the critical rate with a specific p_{wf} that is held constant. Production rate gradually decreases and goes below the critical rate and ends when the wellhead pressure falls below the minimum tubinghead pressure of 250 psia. The wellhead pressure shows a similar trend, starting with a high value and then gradually decreasing to a minimum specified value of 250 psia. At that point, p_{wf} is decreased by 200 psia, thereby allowing more reservoir-fluid influx and starting a new cycle with a higher wellhead pressure. Eventually, after 703 days, the well cannot maintain the minimum wellhead pressure, and the well dies after cumulative production (G_p) of 3.12 Bscf. Because of simplified reservoir modeling, the results should be viewed as directional only and not in the absolute sense.

Let us explore the evolving nature of the liquid-loading process that underlies Fig. 5.16. For clarity we used three (2 through 4) of the five cycles to help understand the transition process by comparing liquid holdup at the wellhead (WH in **Fig 5.17**) and

the bottom of the hole, as Fig. 5.17 shows. Initialization of data at zero time for each cycle lasting 150 days allows direct comparison. In each cycle the liquid holdup at two points (the wellhead and the bottom of the wellbore) begins to diverge. We term this point initiation of liquid loading, indicating either churn or slug instead of annular flow at some point near the well bottom.

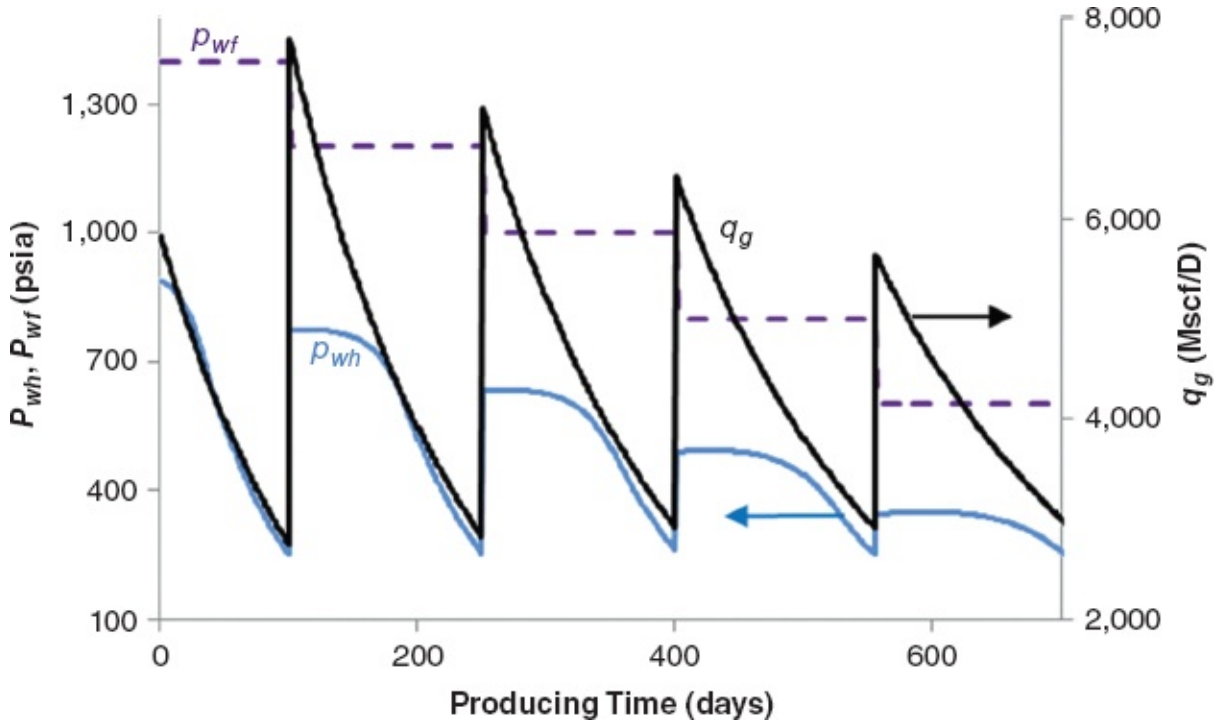

Fig. 5.16—Five production periods at constant p_{wf} in each cycle.

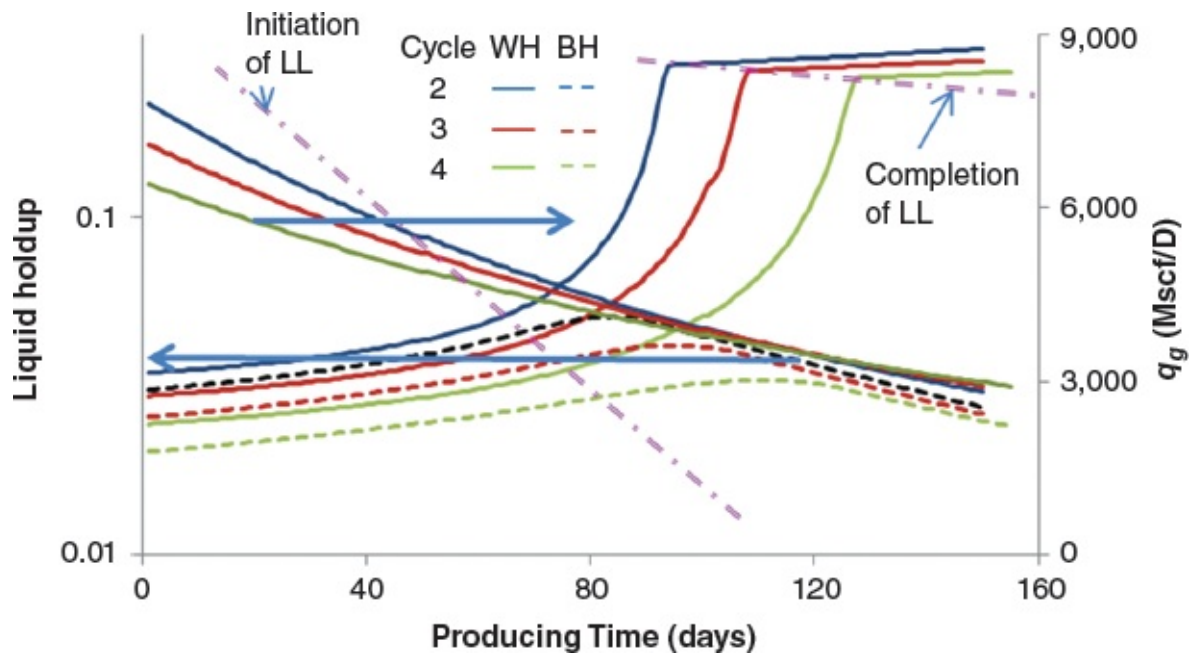

Fig. 5.17—Transition of liquid loading (LL) is identified by examining liquid holdup at WH and BH.

Eventually, the sharp change in the holdup slope signifies that the *entire* wellbore

has transitioned from the annular to churn or slug flow. This point in time is termed completion of the liquid-loading process. As expected, duration of this transition depends on the flow rate: A low rate will lengthen the process compared with high rates. Depending on the reservoir pressure, a well can continue production long after the initiation of liquid loading. However, in a low-pressure reservoir, the well can kill itself when the backpressure becomes larger than p_{wf} within a few days of initiation of liquid loading. Because liquid loading may be viewed as a result of imbalance between gravity and friction, it can occur at any depth in the wellbore, not just at the wellhead. The lack of stability in fluid motion may disappear or get worse; this challenge is also faced in riser slugging.

Initiation of liquid loading may also be discerned from the combined reservoir/wellbore response. **Fig. 18a** illustrates this point with a plot of wellhead pressure with rate for four constant p_{wf} cycles shown in Fig. 5.16. Earlier, Kabir and Izgec (2009) introduced this p/q plot for diagnosing reservoir flow condition in rate-transient analysis, as shown in Fig. 18b. Note that the connotation of time is from right to left during constant-p_{wf} production and pseudosteady-state flow on the p/q plot. In our simulations, constant-p_{wf} production occurred during each cycle as shown in Fig. 5.18a. Therefore, any deviation from the expected flat response on the p/q plot signifies a wellbore event because pressure at the wellhead is expected to remain the same when p_{wf} is held constant during steady-state flow in the wellbore. Initiation of this wellbore event is tied to liquid loading, which triggers declining p_{wh}.

5.4.2 Application of the Diagnostic Approach. Turner et al. (1969), Coleman et al. (1991a), and Veeken et al. (2010) published extensive data sets while investigating liquid loading. We verified the critical loading rate calculation using the proposed computational approach and compared the results with those previously published. The liquid-loading rate q_c is observed and approximated using the bottomhole condition. We define the critical liquid-loading rate as the rate at which slug or churn flow begins developing at any place in the well, which is characterized by Eq. 5.15. Because most investigators used the wellhead condition to calculate the critical liquid-loading rate, we performed the top-down pressure and heat-loss calculations as well as flow pattern identification to determine liquid loading using the proposed diagnostic approach.

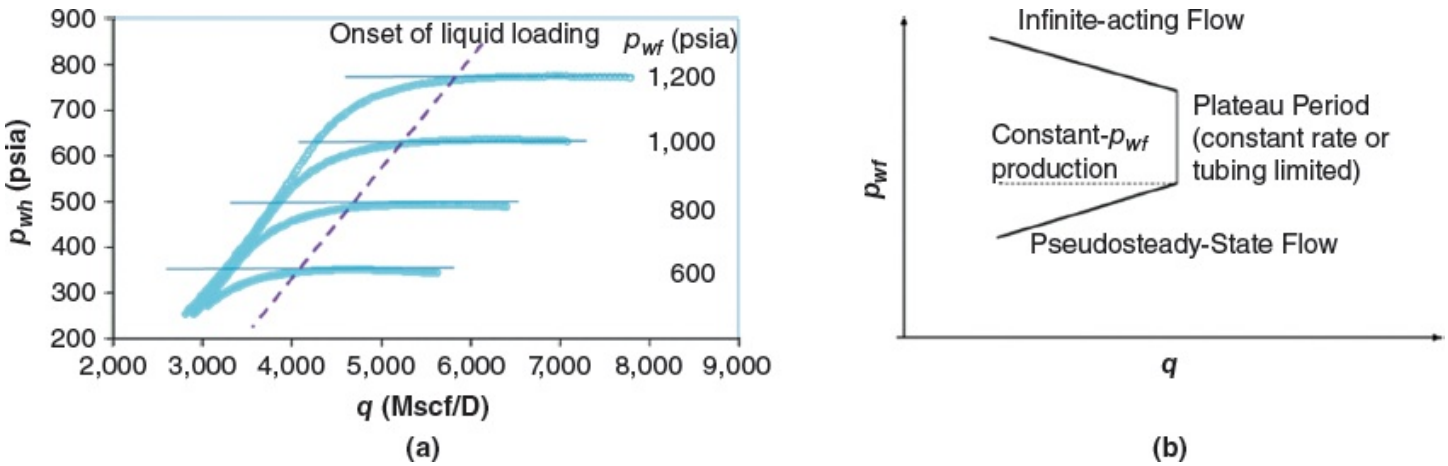

Fig. 5.18—Onset of liquid loading is identified by deviation from the horizontal line on the pwh − q plot (a). Diagnostic p/q plot represents the coupled wellbore/reservoir performance (b).

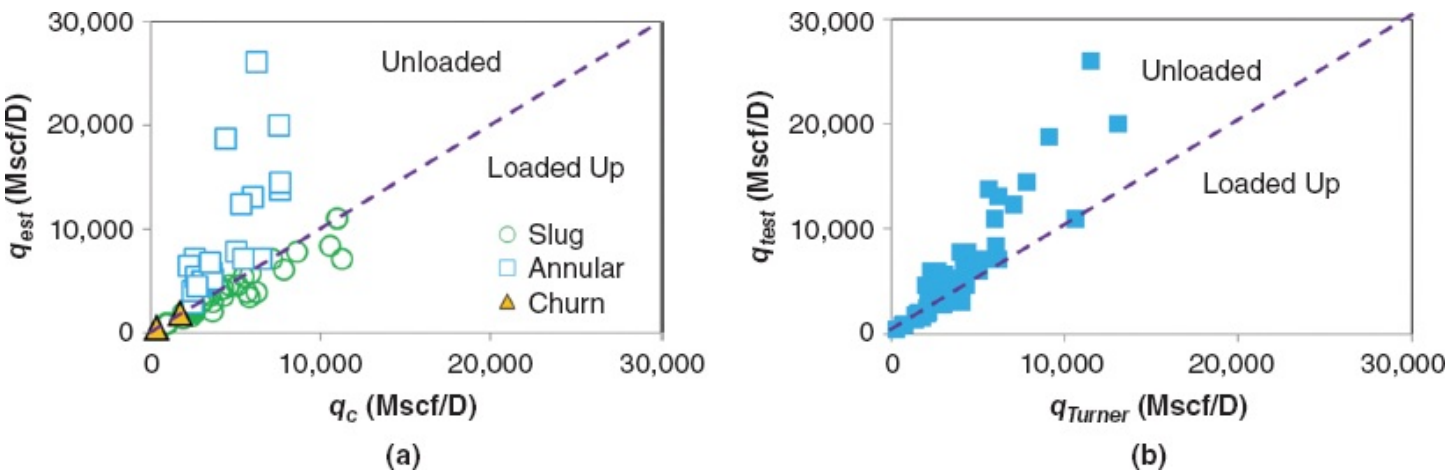

Fig. 5.19—Actual liquid-loading rate q_{test} vs. critical annular-to-churn transition rate q_c indicates wells exhibiting annular flow and those with slug flow (a), whereas the Turner method suggests very few wells with the loading issue (b).

***Veeken et al. Data Set*.** Veeken et al. (2010) published data from offshore liquid-loaded gas wells with substantial wellbore and reservoir information. However, several important parameters needed to calculate liquid-loading rate went unreported, such as the gas/liquid ratios and gas and liquid densities. The absence of data about gas/liquid ratio and fluid properties, complex trajectory of the well, and tubular sizes contributes to the error in liquid-loading rate calculations. The deviation of the wellbore might also affect the increasing critical loading velocity calculation as suggested by Belfroid et al. (2008). Nevertheless, the proposed method makes an important point in understanding the liquid-loading issue compared with the modified-droplet model of Turner et al. (1969), as shown in **Figs. 5.19a and 5.19b.**

***Coleman et al. Data Set*.** We validated the proposed critical liquid-loading gas rate calculation with the data set published by Coleman et al. (1991a) that included 55 wells, all liquid loaded. Using the given information in this data set, we matched the calculated bottomhole pressure with the measured static bottomhole pressure by

adjusting the liquid density and liquid/gas ratio parameters; these data were not reported by Coleman et al.

Coleman et al. used the original Turner droplet velocity expression (Eq. 5.15) to calculate the critical loading velocity for low wellhead pressure and low-rate gas wells. **Figs. 5.20a** (entire wellbore approach) and **5.20b** (applied at wellhead) depict the relationship between the critical liquid-loading rates vs. the actual liquid-loading gas rate, q_{test}. We identified 51 out of 55 liquid-loaded gas wells with slug or churn flow starting to develop at the bottom of the hole. The four data points that the proposed approach missed are actually quite close to the critical churn-to-annular transition line. Therefore, the proposed method correlates well with the Coleman et al. data set.

The primary reason for the proposed approach to outperform the Coleman et al. method, though both applied the same critical velocity model (Eq. 5.15), is that most of these wells experienced liquid-loading initiation at the well bottom. When Eq. 5.15 is used for the entire wellbore, liquid loading became apparent that was missed at times when the evaluation was based on the wellhead condition only.

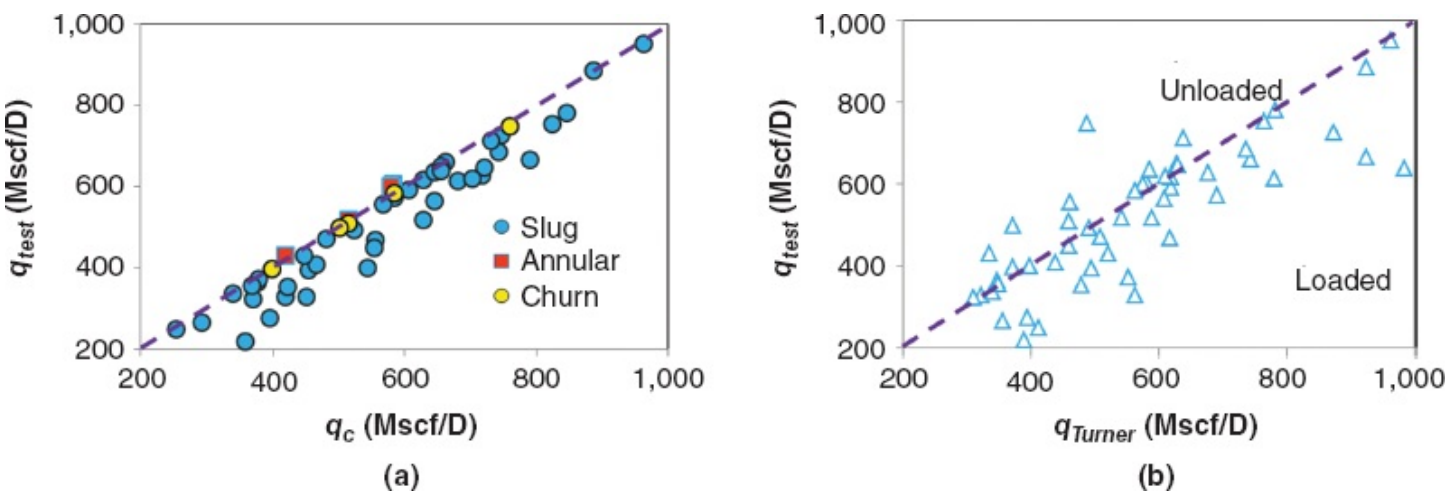

Fig. 5.20—The relationship of actual loading rate (q_{test}) with critical annular-to-churn transition rate (q_c) correlates well with the entire-wellbore diagnostic approach (a); Coleman et al. (1991a, b) also suggested the same for these liquid-loaded wells (b).

Case	PI (MScf/D-psi^2)	WGR (STB/Mscf)	CGR (STB/MMscf)	Tubing ID (in.)
Low	0.005	10	10	4
Medium	0.010	80	50	4.28
High	0.020	550	80	4.35

Table 5.9—Independent variables influencing critical liquid-loading rate.

5.4.3 Parameters Influencing Liquid Loading. This section explores the influence of various independent variables on the dependent variable—the critical liquid-loading rate. **Table 5.9** identifies the four variables of interest: well productivity index (PI), water/gas ratio (WGR), CGR, and tubing ID. The Pareto chart in **Fig.**

5.21a summarizes the results of a two-level Plackett and Burman (1946) analysis of statistical design of experiments (DoE). In this first experiment with DoE analysis, the critical liquid-loading rate is the dependent variable, whereas pipe ID, well PI, CGR, and WGR constituted the four independent variables. The positive sign associated with any independent variable on the Pareto chart suggests that an increase of the independent variable will result in an increase of the dependent variable, whereas the opposite applies to those with negative values. The Pareto chart does not imply that variables with absolute t-test value below 95% confidence level are not influencing the critical loading rate; rather, the chart shows that they are statistically insignificant within the 95% confidence interval.

Fig. 5.21b suggests that the well PI dominates the onset of liquid loading. Wells with smaller PI experience liquid loading later than wells with higher PI because the critical liquid-loading rate of a given well will be lower, as previously explained. In addition, wells with small tubing ID would have a lower critical gas rate than wells with a larger tubing ID; thus, the well can produce longer before experiencing the liquid-loading problem.

5.4.4 Lessons Learned. We have presented a methodology for understanding a well's liquid-load-free life. To that end, the section focused on fluid flow from reservoir to surface as a seamless process. In this context, fluid flow modeling in the reservoir involved single-phase gas flow to gain clarity of the holistic flow problem up front. In reality, numerical reservoir models (e.g., Limpasurat et al. 2015) need incorporating.

We learned that transition from annular flow at any point in the wellbore triggers the onset of liquid loading. Because the lowest gas velocity is at or near the bottom of the hole, the transition from annular two-phase flow is much more likely there than at higher elevations in the wellbore. Both multiphase flow and the attendant heattransfer modeling in the entire wellbore are implicit in this approach. Although we used the Taitel et al. (1980) model for transition from annular flow, this methodology is independent of transition criteria (such as those shown in Fig. 5.15) to simulate fluid flow from the reservoir to surface for determining the initiation of liquid loading.

Initiation of liquid loading foretells that eventually the well will die, but we cannot readily predict the timeline for that outcome. Disappearance of the annular flow pattern entirely from the wellbore signifies completion of the liquid-loading process from the point of initiation. Whereas a low production rate will lengthen the transition process compared to high rates, high reservoir pressure (such as is found in overpressured systems) can sustain production for a very long time.

Clearly, both initiation of liquid loading and its remaining life are a case-specific problem. Only flow simulations for the coupled-flow problem at hand—that is, the reservoir/wellbore system along with the wellhead operating conditions—enable one to estimate a well's remaining productive life. The holistic approach discussed here attempts to diagnose the problem at hand as correctly as possible before the coupled-system modeling is leveraged to find a pragmatic solution. Some of the solutions include installing a plunger lift system or a jet pump, initiating an intermittent

production cycle, installing smaller-diameter tubing, and using compression to lower wellhead pressure.

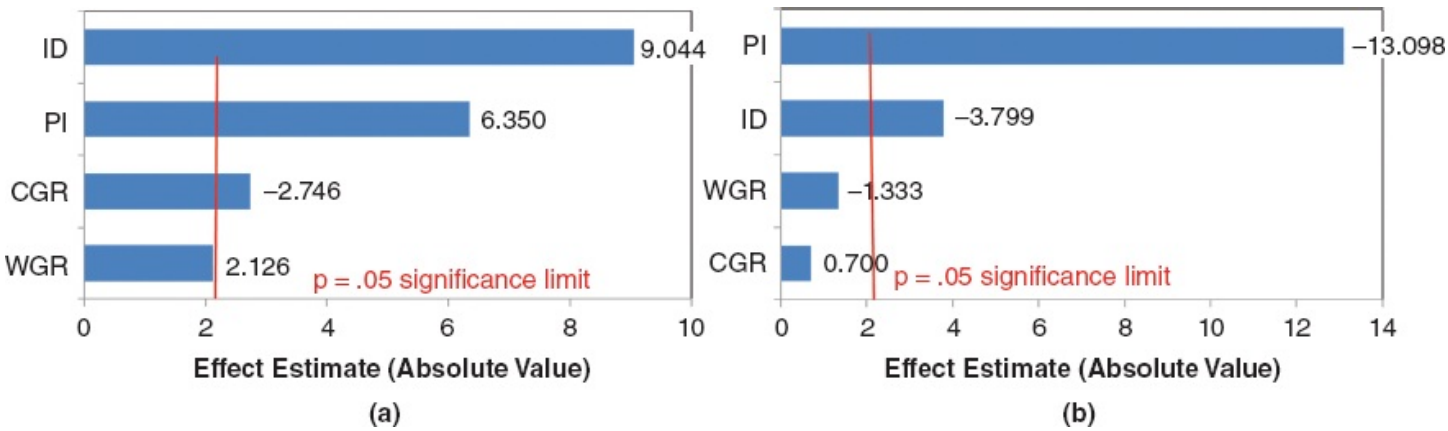

Fig. 5.21—Pipe ID and well PI dominate the critical liquid-loading rate (a) and the onset of liquid loading (b).

5.5 Estimating Flow Rates With Multiphase Choke Correlations

Surface chokes at the wellhead serve a multitude of purposes for flow control. The need for well-specific flow control arises from dampening large pressure fluctuations to combat slugging, minimizing risk of excessive pressure drawdown at the sandface for maintaining completion integrity, and managing solids production, among others. In short, controlling flow rates in daily field operations is the norm in most settings.

Motivated by various needs, empirical correlations have emerged since the 1950s for modeling two-phase flow through chokes. However, physical modeling has taken root with the publication of Sachdeva et al. (1986) to improve prediction performance. This section provides a brief account of the physical modeling first, before discussing a few empirical correlations.

5.5.1 Modeling Approach. The wellhead choke, which can also serve as a metering device, is a primary tool for controlling a well's flow rate. **Fig. 5.22** presents a choke schematic.

When single-phase fluid flows through a choke or any other restriction, the reduced flow area causes increased fluid velocity. For a horizontal system with negligible friction, this kinetic energy change can be related to the pressure differential created. The following expression presents a relationship between the velocity through the choke and pressure difference across it:

$$q = A_2 v_2 = C_D A_2 \sqrt{\frac{p_1 - p_2}{\rho\left(1-(A_2/A_1)^2\right)}} \quad \text{(5.18)}$$

In Eq. 5.18, subscripts1 and 2 represent the upstream and downstream conditions, respectively, and C_D is a fraction that accounts for the frictional loss. Rooted in Bernoulli's principle, Eq. 5.18 is also used in the chemical process industry for

flowmetering.

Eq. 5.18 implies that flow rate increases with the increase in pressure drop across the choke. However, this is true only until the velocity at the choke reaches sonic velocity through the fluid. After sonic velocity, also called critical velocity, has been reached, no further increase in v_2 can be achieved by decreasing p_2. Note that this critical or sonic velocity should not be confused with that in liquid loading, discussed in the previous section. Therefore, using a small enough choke—known as a flow prover—so that sonic velocity is achieved, flow rate can be determined by measuring only p_1, because the sonic velocity is known for most fluids. For example, gas wells lend themselves to this approach to rate metering. Sonic velocity for an ideal gas is given by

$$v_c = \sqrt{\lambda RT / M}, \quad (5.19)$$

where $\lambda = c_p/c_v$, the ratio of specific heat of gas at constant pressure to that at constant volume, and M is the molecular weight of gas. For many gases, λ has a value between 1.2 and 1.4. Therefore, for air with $\lambda = 1.4$, the sonic velocity at standard conditions turns out to be 1,120 ft/sec or 760 miles/hr. Sonic velocity for liquids is usually much higher and is calculated from $v_c = \sqrt{(B/p)}$, where B is the bulk elastic modulus of the liquid. For example, velocity of sound in water with B = 314,000 lbf/in.^{2}, is approximately 4,830 ft/sec.

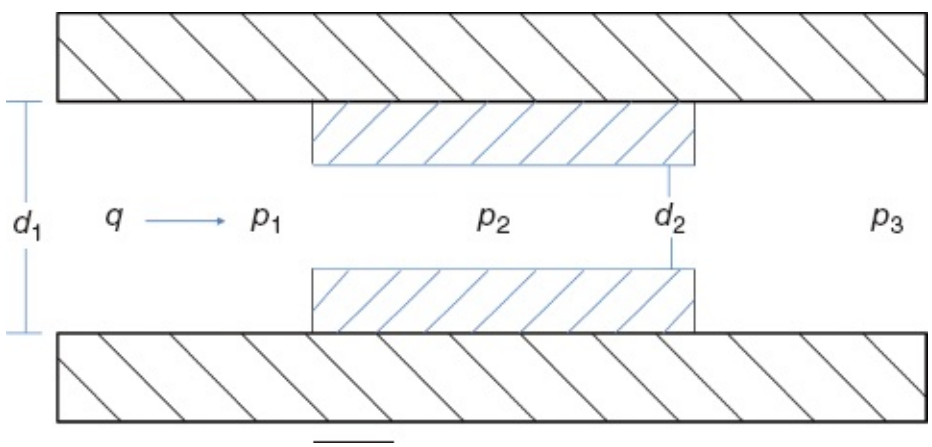

Fig. 5.22—A choke schematic identifies model elements.

The critical pressure ratio for an ideal gas, $y_c = (p_2/p_1)_c$, is given by

$$y_c = \left(\frac{p_2}{p_1}\right)_c = \left(\frac{2}{\lambda+1}\right)^{\frac{\lambda}{\lambda-1}}. \quad (5.20)$$

For $\lambda = 1.4$, the value of $y_c = (p_2/p_1)_c = 0.53$. In other words, most gas wells discharging into the atmosphere through a choke achieve sonic velocity. To give a clear perspective, **Fig. 5.23** illustrates the critical/subcritical flow boundary.

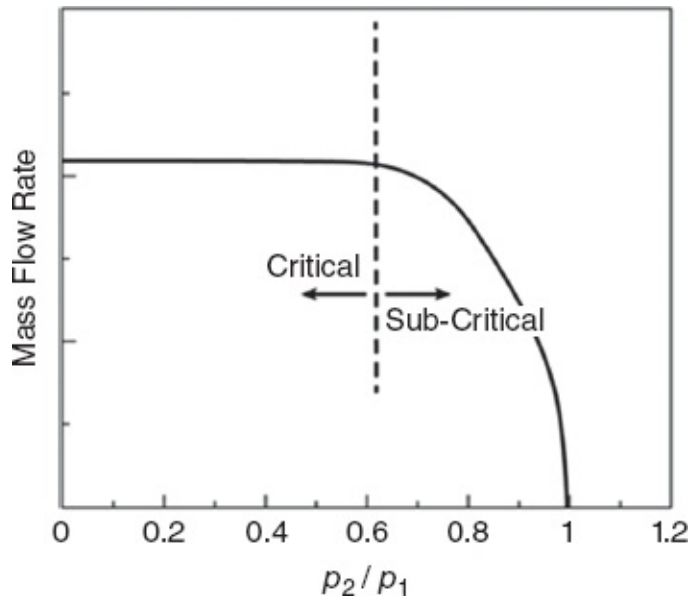

Fig. 5.23—Understanding critical and subcritical flow regimes.

5.5.2. Two-Phase Flow Through Chokes. Note that Eqs. 5.18 through 5.20 are inapplicable to two-phase flow for both critical and subcritical flows. The interaction between the phases, the differences in their sonic velocities, and the cross-sectional area each phase occupies are the likely causes for these equations' inapplicability to two-phase flow. Many studies have endeavored to estimate flow rate q and critical/subcritical boundary y_c for two-phase flows. Let us discuss work that is based on sound thermodynamic principles and supported by laboratory data (Sachdeva et al. 1986; Perkins 1993; Al-Safran and Kelkar 2009). Thereafter, we present a brief account of the empirical models of Gilbert (1954), Ros (1960), and others that were developed from field data.

***Thermodynamic Modeling*.** One of the earliest models of two-phase flow through chokes was offered by Sachdeva et al. (1986). They started with the basic flow expression shown in Eq. 5.18 and assumed isentropic (frictionless, adiabatic) expansion of the gas phase to relate p_1 to p_2. Assuming that there was no slip between the phases (that is, $R = v_g/v_L = 1.0$), they derived a simple thermodynamic model for both critical/subcritical boundary and total mass flow rate through a choke. Their method determines the location of the critical flow boundary through an iterative use of the following implicit expression for the pressure ratio, $y = p_2/p_1$:

$$(y) = \frac{\dfrac{\lambda}{\lambda-1} + \dfrac{(1-x_1)(1-y)\rho_{g1}}{x_1\rho_L}}{\dfrac{\lambda}{\lambda-1} + \dfrac{n}{2} + \dfrac{n(1-x_1)\rho_{g2}}{x_1\rho_L} + \dfrac{n}{2}\left[\dfrac{(1-x_1)\rho_{g2}}{x_1\rho_L}\right]^2}. \quad \ldots\ldots (5.21)$$

When y on one side of Eq. 5.21 equals the y on the other side, it becomes the critical pressure ratio, y_c. If actual $p_2/p_1 < y_c$, the flow is subcritical. Note that x_1 is the

upstream gas mass fraction, which is assumed to remain constant; that is, $x_1 = x_2 = x$.

Sachdeva et al. (1986) assumed isentropic gas expansion in parts of their model development, but also attempted to allow for the polytropic expansion (i.e., less than ideal expansion) of the two phases. They used the expression for the coefficient n (a parameter similar to l) for fluid expansion during two-phase flow suggested by Ros (1960), given by

$$n = \frac{x\lambda c_v + (1-x)c_L}{xc_v + (1-x)c_L} \quad (5.22)$$

In Eq. 5.22, x is the mass fraction of the gas phase; $x = (\rho_g v_{sg})/(\rho_g v_{sg} + \rho_L v_{sL})$.

Sachdeva et al. (1986) developed the expression for mass flow rate, w (lbm/sec), in terms of the homogeneous mixture density at the choke, ρ_{m2}, as

$$w^2 = (9270) C_D^2 A_2^2 \rho_{m2}^2 p_1 \left[\frac{(1-x)(1-y)}{\rho_L} + \frac{x\lambda}{\lambda - 1}\left(\frac{1}{\rho_{g1}} - \frac{y}{\rho_{g2}} \right) \right] \quad (5.23)$$

Subsequent investigation of Perkins (1993) closely follows the work of Sachdeva et al. (1986). He noted that liquid fraction flowing through the choke is generally composed of oil and water and that proper accounting of fractional water production is needed. In addition, Perkins noted that pressure measurement at Point 3 in Fig. 5.22 (p_3) is usually available, rather than at p_2; that is, pressure inside the choke. In general, however, the discharge coefficient C_D takes this difference into account.

More recently, Al-Safran and Kelkar (2009) proposed a model for estimating both subcritical and critical flow rates and their boundary using an approach similar to that proposed by Sachdeva et al. (1986). The model proposes that the pressure ratio for the critical flow rate, $y_c = (p_2/p_1)_c$, is given by

$$(y_c)^{[(n-1)/n]} = \frac{\alpha(1-y_c) + n/(n-1)}{n/(n-1) + \frac{n}{2}\left(1 + \alpha y_c^{1/n}\right)} \quad (5.24)$$

Also similar to Sachdeva et al., Al-Safran and Kelkar used Eq. 5.21 for the polytropic expansion parameter, n. They used the following expression for the parameter α:

$$\alpha = \frac{R_c(1-x)\rho_{g1}}{x\rho_L} \quad (5.25)$$

Their expression for total critical or subcritical mass flow rate w (lbm/sec) is given by

$$w^2 = (9{,}270) C_D^2 A_2^2 p_1 \frac{\alpha(1-y) + \frac{n}{(n-1)}\left[1 - y^{(n-1)/n}\right]}{(x/\rho_{g1})\left(y^{-1/n} + \alpha\right)^2 \left[x + \frac{1}{R_c}(1-x)\right]} \quad (5.26)$$

In Eq. 5.26, y_c replaces y for critical flow, and the constant 9,270 (= 2 × 144 × g_c) includes the conversion factor for using p_1 in field units (psi). For the slip ratio during critical flow R_c, Al-Safran and Kelkar proposed the use of the Schuller et al. (2006) model.

Unlike Sachdeva et al. and Perkins, Al-Safran and Kelkar (2009) assumed that the gas slips past the liquid phase. Therefore, their expressions for mass flow rate w and parameter α include the slip ratio, R_s (= v_g/v_L). For critical flow, they used the expression proposed by Schuller et al. (2006) for R_c as follows:

$$R_c = \sqrt{1 + x\left(\frac{\rho_L}{\rho_g} - 1\right)}\left(1 + 0.6/e^{5x}\right). \quad (5.27)$$

For subcritical flow, they recommend using the Grolmes and Leung (1985) correlation, given by

$$R_{sc} = \left(\frac{1-x}{x}\right)^{(a_1-1)} \left(\frac{\rho_L}{\rho_g}\right)^{(a_2+1)} \left(\frac{\mu_L}{\mu_g}\right)^{a_3}. \quad (5.28)$$

The values of the parameters a_1, a_2, and a_3 used in Eq. 5.28 reduce it to a simple expression given by

$$R_{sc} = \left(\frac{\rho_L}{\rho_g}\right)^{(0.17)} \quad (5.29)$$

Given that thermodynamic principles underlie both methods, the similarities between the Al-Safran and Kelkar (2009) and Sachdeva et al. (1986) models for estimating the critical boundary and flow rate are not surprising. Indeed, Al-Safran and Kelkar (2009) showed that their model collapses into the simpler Sachdeva et al. (1986) model when R is set equal to 1.0, and a few reasonable assumptions are made about gas expansion. More recently, Zhou (2017) explored the merits of various correlations and found that the Fortunati (1972) correlation outperformed others primarily because it honored the critical/subcritical flow boundary, unlike all others (see Fig 5.24).

Empirical Correlations. The complexity of high-velocity flow of two phases through a restriction and the need for making many assumptions have led many investigators in this area to take an empirical approach of gathering data and correlating them to a few significant variables. Indeed, most of the early studies in this area fall into this category and include those of Gilbert (1954), Ros (1960),

Achong (1961), and Pilehvari (1981), among many others. The correlations these researchers used to express liquid rate q_L may be written as the general expression

$$q_L = A(R_{GL})^B d_{64}^C p_1^D \quad (5.30)$$

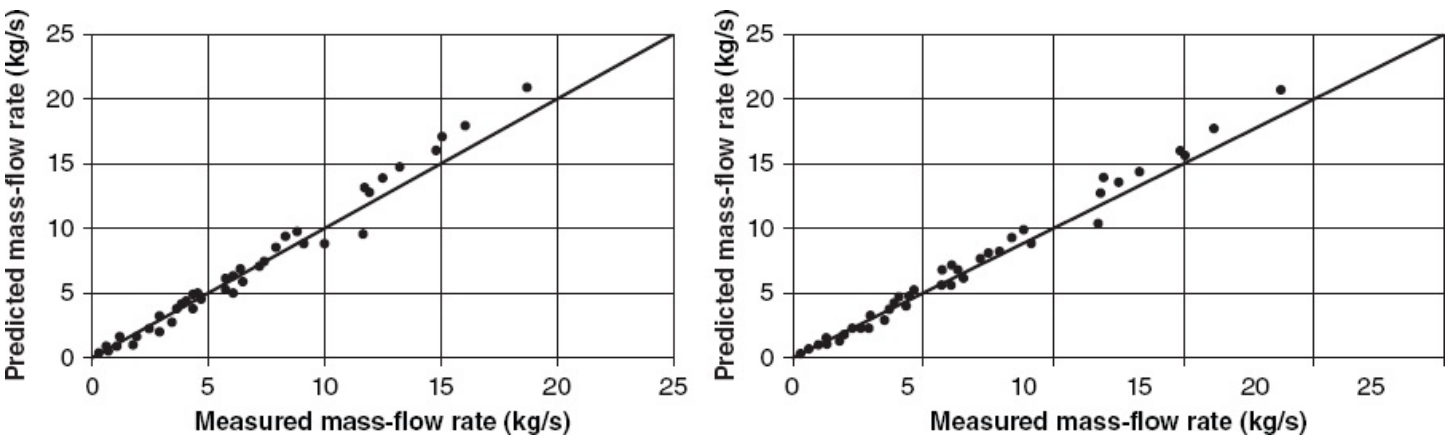

Fig. 5.24—Validation of models with field data: (a) Al-Safran and Kelkar (2009) model; (b) Perkins (1993) model (after Al-Safran and Kelkar 2009).

Correlation	*A*	*B*	*C*	*D*
Gilbert (1954)	0.1	–0.546	1.89	1
Ros (1960)	0.0574	–0.5	2.00	1
Achong (1961)	0.2618	–0.65	1.88	1
Beiranvand and Khorzoughi (2012)	1	–0.1	1.5	0.5

Table 5.10—Proposed parameters for Eq. 5.30.

The industry practice is to use Eq. 5.30 in field units: q_L in (STB/D); d_{64} in bean size (in.); gas/liquid ratio, R_{GL}, in scf/STB; and upstream pressure, p_1, in psi. **Table 5.10** shows the values of the parameters proposed by various investigators.

An important difference between the empirical models and those anchored in thermodynamics is the dependence of rate on upstream pressure. All correlations reported in Table 5.10, except that of Beiranvand and Khorzoughi (2012), express a linear relationship between liquid rate and upstream pressure, whereas the thermodynamic models imply a square-root relationship. As expected, various studies have shown that all correlations show large errors compared to their thermodynamic counterpart in matching field data. More recently, Zhou (2017) explored the merits of various correlations and found that the Fortunati (1972) correlation outperformed others primarily because it honored the critical/subcritical flow boundary, unlike all others.

5.5.3 Application of Models. To apply either thermodynamic models or the empirical correlations presented above, one needs to be aware of the need for some data and

for unit conversions. Because a two-phase flow problem needs solving, a single equation, such as Eq. 5.23 or Eq. 5.36, is inadequate. In general, the gas mass fraction x requires input of GOR and other field data. Using the following procedure, the gas mass flow rate can be calculated from the volume of free gas multiplied by gas density. On the basis of one barrel of liquid that contains f_o and f_w volume fractions of oil and water, the total mass m in lbm is written as

$$m = 0.0764\gamma_g(R_{GL} - R_s) + 5.615\left(f_o B_o \rho_o + f_w B_w \rho_w\right). \quad (5.31)$$

In Eq. 5.31, γ_g is the gas gravity, R_s is the gas in solution (scf/STB), and 0.0764 is the density of air at standard conditions in lbm/ft^3. Therefore, the gas mass fraction is given by

$$x = \left[\frac{0.0764\gamma_g(R_{GL} - R_s)}{0.0764\gamma_g(R_{GL} - R_s) + 5.615\left(f_o B_o \rho_o + f_w B_w \rho_w\right)}\right]. \quad (5.32)$$

To calculate liquid flow rate from Eq. 5.30 (or Eq. 5.23 or Eq. 5.26), we can recast it in terms of barrels per day of liquid production from total lbm/sec of fluid produced. With appropriate unit conversions, Eq. 5.23 can be rewritten as

$$q_L = \frac{0.525\, C_D d_2^2 \rho_{m2} \sqrt{p_1}}{C_m}\left[\frac{(1-x)(1-y)}{\rho_L} + \frac{x\lambda}{\lambda - 1}\left(\frac{1}{\rho_{g1}} - \frac{y}{\rho_{g2}}\right)\right]^{0.5}, \quad (5.33)$$

where C_m is given by Beggs (1991) as

$$C_m = \left(8.84 \times 10^{-7}\right)\gamma_g(R_{GL} - R_s) + \left(6.5 \times 10^{-5}\right)\left(f_o B_o \rho_o + f_w B_w \rho_w\right). \quad (5.34)$$

Eq. 5.33 is dimensional with choke diameter d_2 being in inches and upstream pressure p_1 in psia.

5.5.4 Lessons Learned. Two types of models have emerged for estimating rates during flow through surface chokes. The number of empirical models is far greater than the number of models based on the physical principles of thermodynamics and two-phase flow. Each succeeding correlation intended to improve those that preceded them. The lessons learned from wellbore flow modeling suggests that the integrity of input data may simply outweigh some of the perceived improvements in empirical correlations.

Our contention is that uncertainties of many input parameters in any correlation or model may largely affect the solution outcome. Some of the inherent uncertainties stem from inaccuracies in rate metering, integrity of choke diameter from erosion when solids production is prevalent, pressure-dependent fluid properties with increasing production time, and production of organic solids (wax, hydrates, asphaltenes), to name but a few factors. In heavy-oil settings, foam and emulsion

offer additional challenges. Our recommendation is to use thermodynamics-based models with careful data input for ensuring quality solutions. In fact, Zhou's recent thesis (2017) sheds further light on the importance of working with Sachdeva et al. model for its simplicity and foundation on thermodynamic principles.

Summary

This chapter has presented a simplified two-phase flow model encompassing various types of fluid (oil/gas, oil/water) and flow direction (cocurrent, countercurrent, and downflow). Sophisticated models based on rigorous physical principles appear to offer no improved accuracy over the simplified approach summarized in section 5.1 or the widely used Hagedorn and Brown (1965) and PE-2 correlations. Input-data accuracy is the key to a model's performance. Uncertainty stemming from rate measurements and PVT parameters has significant influence on the performance of one or a group of two-phase flow models.

In gas/condensate wells, mist flow supporting the no-slip flow condition appears pertinent in the entire wellbore. Consequently, homogeneous modeling is robust for a wide range of well-operating conditions. This approach is therefore suitable for long-term reservoir performance prediction when integrated reservoir/wellbore/flowline network modeling is sought. The mechanistic model of Ansari et al. (1994) and the empirical correlation of Gray (User's Manual for API 14B 1978) converge to homogeneous-model formulation because mist flow occurs with marginal liquid-film thickness on the pipe wall. These methods provide accurate solutions. Just as in oil wells, no single method provided consistent superiority over any other for the three data sets presented here.

We addressed the critical liquid-loading determination by assuming that the unloaded well experiences annular two-phase flow throughout the wellbore. The transition from annular to churn or slug flow triggers the film flow reversal, thereby initiating liquid loading at the well bottom. Because this transition from annular to churn or slug flow in the entire wellbore takes time, coupled wellbore/reservoir flow modeling is prudent. Forward modeling suggests that the tubing ID and the well PI are the most important variables in determining the critical liquid-loading rate and the onset of liquid loading.

We endeavored to use simplified models for handling gas/oil and gas/condensate fluids in wellbores; however, this simplification was not at the expense of sacrificing underlying physics. The same modeling principle applies while considering two-phase flow through chokes. In this case, our observation is that models based on thermodynamics principles are preferred over those with empirical roots. Perhaps the following nuggets are helpful while pursuing analysis of field data:

- Check PVT data (°API, GOR, gas gravity, viscosity): Laboratory PVT data are generally more reliable than those measured at field separators.
- Note that process data (GOR and gravities) are path dependent. This reality

implies that even if the reservoir pressure remains above the saturation pressure, the GOR will change if the separation conditions (number of separators, pressure, and temperature) change.

- Honor mass balance: Surface mass must equal downhole mass. This condition is often violated when GOR and °API are altered randomly.
- Assess well-test reliability: Stable well-operating conditions and calibrated metering devices are the key.
- Use rate data validation using redundancy techniques; surface choke calculations can cross validate the overall data trend.

Nomenclature

A_x = cross-sectional area for flow, ft^2

a_1, a_2, a_3 = parameters used in Beggs-Brill holdup equation, Eq. 5.28

A_1 = tubing cross-sectional area for fluid flow, ft^2

A_2 = choke cross-sectional area for fluid flow, ft^2

B = factor used in Gray correlation, dimensionless

c_p = fluid specific heat at constant pressure, Btu/(lbm-°F)

c_v = fluid specific heat at constant volume, Btu/(lbm-°F)

C_o = flow parameter, dimensionless

C_{ob} = flow parameter for fully developed bubbly flow, dimensionless

C_{os} = flow parameter for fully developed slug flow, dimensionless

d = tubing ID, ft

d_1, d_2 = tubing and choke diameters, respectively, ft

C_D = choke coefficient, dimensionless

f_m = Moody friction factor, dimensionless

f_g = in-situ gas volume fraction, dimensionless

f_L = liquid holdup, dimensionless

f_o = in-situ oil volume fraction, dimensionless

F_a = annulus factor, given by Eq. 5.4, dimensionless

F_θ = well-deviation factor, given by Eq. 5.3, dimensionless

g = gravitational acceleration, ft/sec^2

g_c = conversion factor, 32.17 (lbm-ft)/lbf/sec^2

n = number of data points, dimensionless

N_d = dimensionless diameter number [$= g(\rho_L - \rho_g)d^2/\sigma_L$]

N_v = dimensionless velocity number [$= \rho_n{}^2 v_m{}^4/g\ \sigma_L\ (\rho_L - \rho_g)$]

N_{vg} = Duns-Ros dimensionless gas velocity number [$= v_{sg}(\rho_L/g\ \sigma_L)^{1/4}$]

N_{vL} = Duns-Ros dimensionless liquid velocity number [= $v_{sL}(\rho_L/g\,\sigma_L)^{1/4}$]

p = pressure, psig

p_{wh} = flowing wellhead pressure, psig

p_{wf} = flowing bottomhole pressure, psig

p_{wfc} = computed flowing BHP, psig

p_{wfm} = measured flowing BHP, psig

dv_m/d_z = velocity gradient of mixture, ft/sec

$-\,dp/dz$ = total pressure gradient, psi/ft

$-\,(dp/dz)_A$ = accelerational pressure gradient, psi/ft

$-\,(dp/dz)_F$ = frictional pressure gradient, psi/ft

$-\,(dp/dz)_{fl}$ = hydrostatic pressure gradient, psi/ft

q or q_g = gas rate, MMscf/D

q_o = oil or condensate rate, STB/D

r = correlation coefficient, dimensionless

r_{xy} = correlation coefficient between data and Model 1, dimensionless

r_{xz} = correlation coefficient between Model 1 and Model 2, dimensionless

r_{zy} = correlation coefficient between data and Model 2, dimensionless

R_g = gas/oil ratio, scf/STB

R_{GL} = gas/liquid ratio, scf/STB

R_s = solution gas/oil ratio, scf/STB

R_w = gas/water ratio, scf/STB

Re_m = mixture Reynolds number, dimensionless

t = statistical measure for model comparison, dimensionless

T = absolute fluid temperature, °R

v_{bs} = superficial gas velocity needed for transition from bubbly to slug flow,

v_{bs} = $(0.43\,v_{sL} + 0.357 v_\infty)\,\sin\alpha$, ft/sec

v = fluid velocity, ft/sec

v_c = critical (sonic) fluid velocity, ft/sec

v_{gc} = superficial gas velocity needed for transition to annular flow, given by Eq. 3.12, ft/sec

v_{gc} = superficial gas velocity needed for transition from churn to annular flow, ft/sec

v_m = velocity of gas/liquid mixture, ft/sec

v_{ms} = mixture velocity, given by Eq. 3.10, when transition from slug to churn flow occurs, ft/sec

v_g = in-situ velocity of gas, ft/sec

v_{ot} = superficial oil velocity needed for transition to oil-dominated flow, ft/sec

v_{sL} = superficial velocity of liquid, ft/sec

v_{sg} = superficial velocity of gas, ft/sec

v_t = superficial gas velocity needed for transition from bubbly to slug flow, ft/sec

$v_{\infty b}$ = small-bubble rise velocity, ft/sec

$v_{\infty T}$ = Taylor bubble rise velocity, ft/sec

dv/dz = velocity gradient, ft/sec

x = gas mass fraction [= $v_{sg}\rho_g/(v_{sg}\rho_g = v_{sL}\rho_L)$]

y = ratio of upstream to downstream pressures, $y = p_1/p_2$, dimensionless

z = vertical well depth, ft

Z = gas-law deviation factor, dimensionless

α = parameter used in Eq. 5.24, dimensionless

γ_g = gas gravity (air = 1)

ρ_n = no-slip mixture density, lbm/ft^3

Λ = parameter for friction factor calculation, dimensionless

ε = pipe roughness factor, ft

ρ_g = gas density, lbm/ft^3

ρ_L = liquid density, lbm/ft^3

ρ_m = mixture density, lbm/ft^3

γ_g = dry-gas gravity (air = 1.0)

γ_o = condensate gravity (water = 1.0)

γ_{wg} = wet-gas gravity (air = 1.0)

μ_L = liquid viscosity, cp

μ_m = mixture viscosity, cp

μ_g = gas viscosity, cp

σ = surface tension, lbm/sec^2

θ = well inclination with horizontal, degrees

δ = dimensionless thickness of the liquid film (= film thickness/well ID)

λ = gas specific-heat ratio = c_p/c_v, dimensionless

Subscripts

c	=	critical
g	=	gas
L	=	liquid

Chapter 6

Wellbore Heat Transport

6.1 Introduction

Hydrocarbon production or fluid injection inevitably involves significant heat exchange between the wellbore fluid and its surroundings. Presence of seawater and air in the riser adds complexity to the heat-transfer process in an offshore environment. During production, the hot fluid continues to lose heat to the increasingly cold surroundings as it ascends the borehole. In contrast, the injected fluid may either gain (cold water) or lose (steam or hot water) heat on descent.

The heat-transfer process just described affects fluid properties and, in turn, the dynamics of fluid flow. Consequently, the coupled nature of momentum and energy transport may require simultaneous solutions for both processes. Whereas steady-state flow modeling is adequate for designing tubular hardware en route to optimal wellhead production, pressure-transient testing may demand rigorous treatment of the coupled and transient nature of momentum, fluid, and heat flows. Similar treatment may be required when shut-in passes are made during production logging runs. This chapter presents a model for estimating the flowing-fluid temperature for the simplest case—that is, when steady-state wellbore fluid and heat flows occur. Chapter 9 discusses transient fluid and heat flow models, followed by their field applications in Chapter 10.

When oil is produced, its sandface temperature is approximately the same as that of the formation. Only very large drawdown will precipitate a temperature increase, owing to the Joule-Thomson (J-T) effect. By contrast, the gas may exhibit cooling for the same reason. In either case, fluid temperature at the sandface may be estimated from the knowledge of formation temperature and the J-T effect. However, as the fluid rises up the well, its temperature becomes higher than the surrounding earth because of the decline in earth temperature with decreasing depth. A wellbore fluid temperature profile and a static (undisturbed) earth temperature profile for an oil well are shown in **Fig. 6.1.**

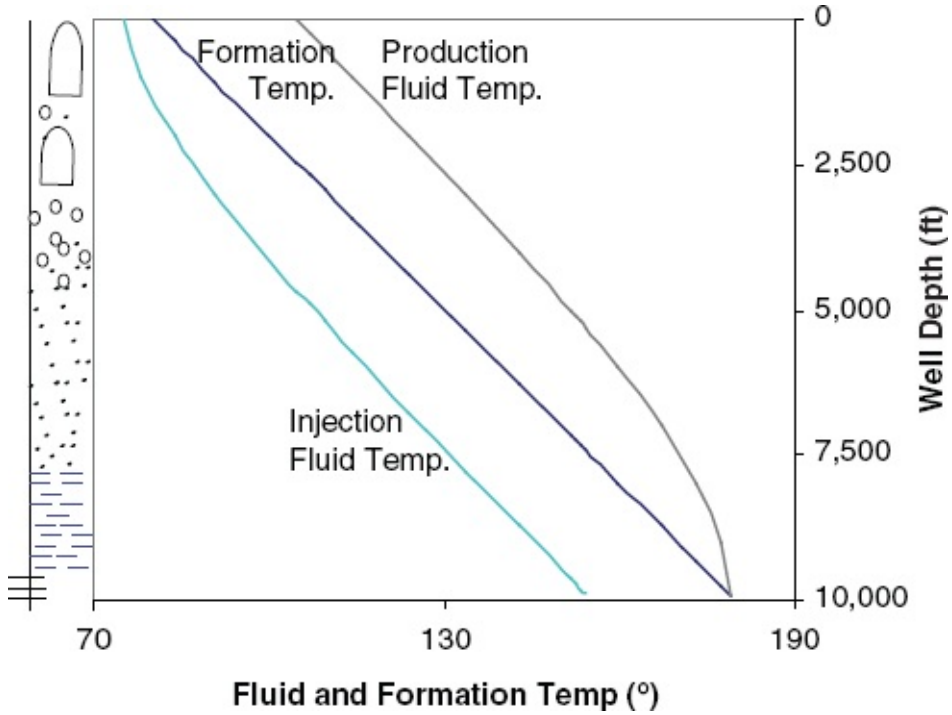

Fig. 6.1—Fluid and formation temperature profiles during production and injection.

The temperature difference between the wellbore fluid and the formation causes transfer of heat from the fluid to its surroundings. As Fig. 6.1 shows, the temperature difference increases with decreasing depth, causing greater heat transfer and lower fluid temperature as the fluid rises up the wellbore. At any given depth, the formation temperature will vary with radial distance from the well. The near-wellbore formation temperature also varies somewhat with production or injection time. Therefore, heat loss from the producing fluid decreases with time. Fig. 5.1 also depicts the increase in the injected-fluid temperature with well depth.

The importance of various aspects of heat transfer between a wellbore fluid and the formation has generated rich literature on the subject. For instance, the usefulness of measuring wellbore fluid temperature was pointed out as early as 1937 by Schlumberger et al. (1937). Perhaps the earliest application of the heat-transfer principle was the use of temperature logs for estimating water and gas injection profiles in the 1950s (Bird 1954; Lesem et al. 1957). However, a lack of complete understanding of the physics of heat flow led to a few problems in the field in the early days. Thermal stress failure of casings in steam injection wells is a case in point.

A theoretical model for estimating fluid temperature as a function of well depth and production or injection time was first presented by Ramey (1962). Ramey's pioneering work spawned a number of applications. Some of these applications include heat-loss estimation in steam injection and geothermal wells, production log interpretation, and estimation of fluid circulation temperature and static formation temperature.

Although Ramey's method gave us a much-needed impetus for further

development, the method does have a few limitations. For example, the effects of kinetic energy and friction are neglected, and flow of only a single-phase fluid can be handled. Equally important, Ramey assumed the well radius—that is, the line-source well—to be vanishingly small. This assumption can prove untenable in many instances. However, the work of Carslaw and Jaeger (1986) may be adapted to remove the restrictive line-source approximation. Methods have also been proposed to handle two-phase flow (Satter 1965; Shiu and Beggs 1980; Sagar et al. 1991; Alves et al. 1992), thereby removing the other assumption. The work of Hasan and Kabir (1994a) shows how both assumptions can be removed for the general case of steady-state, wellbore two-phase flow.

As mentioned earlier, the temperature difference between the wellbore fluid and the formation is the driving force for heat transfer. Because the formation temperature varies with both depth and radial distance from the wellbore, the nature of temperature distribution in the formation needs to be determined first. In the following sections, we first model the formation temperature distribution. We then present the energy balance for the wellbore fluid as it exchanges heat with the surrounding earth. In Section 6.4, we develop expressions for wellbore fluid temperature for both production and injection wells. Our development closely follows the work of Hasan and Kabir (1994a).

6.2 Formation Temperature Distribution

6.2.1 Diffusivity Equation. During production, the hot wellbore fluid provides a source of heat to the formation, whereas during fluid injection, the wellbore acts as a heat sink. To model heat flow and the resulting temperature distribution in such systems, we treat the formation as a homogeneous solid. Assuming symmetry around the well simplifies the three-dimensional (3D) problem to a two-dimensional (2D) one. In addition, heat diffusion in the vertical direction may be ignored, owing to small vertical temperature gradients. Neglecting vertical heat flow reduces the system to a one-dimensional (1D) heat-diffusion problem. This approach, adopted by Hasan and Kabir (1994a) and others, introduces very little error and allows an analytical solution for the problem. The analytic approach is often preferred to the alternative numerical solutions, which may prove tedious and time consuming.

An energy balance on the formation then leads to the partial-differential equation, derived in cylindrical coordinates, for the variation of formation temperature with radial distance from the well and production time,

$$\frac{\partial^2 T_e}{\partial r^2} + \frac{1}{r}\frac{\partial T_e}{\partial r} = \frac{c_e \rho_e}{k_e}\frac{\partial T_e}{\partial t}. \qquad (6.1)$$

In Eq. 6.1, T_e is the formation temperature at an arbitrary depth at time, t, and distance, r, measured from the center of the wellbore. Heat capacity, density, and

thermal conductivity of formation are given by c_e, ρ_e, and k_e, respectively. The thermal diffusivity equation is analogous to that used in pressure diffusion while solving pressure-transient problems.

The three boundary conditions needed for the solution of Eq. 6.1 can be obtained from the examination of the physical system. **Fig. 6.2** is a schematic of the temperature distribution in the formation around a producing well at a given depth. At very early times, the formation temperature retains its initial value (T_{ei}) except near the wellbore, as shown by the inner curve. Thus, initially (t = 0), we assume T_e equals T_{ei} everywhere in the formation.

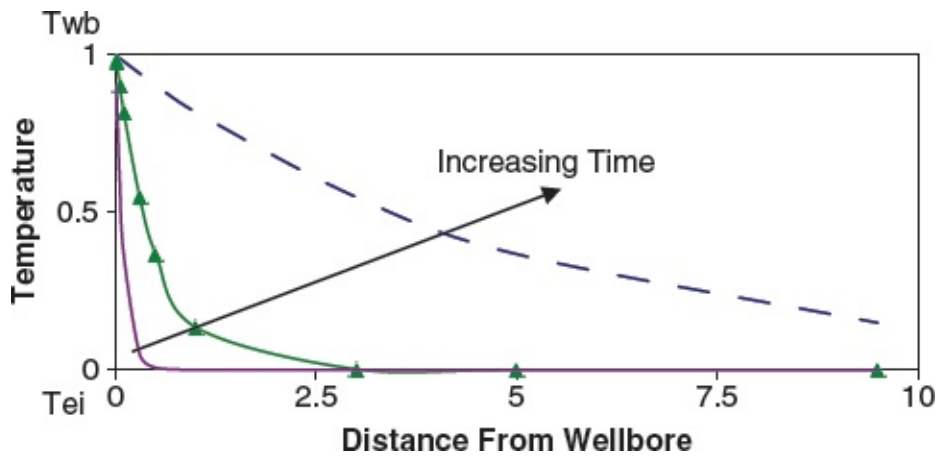

Fig. 6.2—Formation temperature profile at a given depth around the wellbore.

As time increases, heat, transferred from the warm wellbore fluid will raise the formation temperature in its vicinity. The formation temperature profile at such a time will look somewhat like the middle curve shown in Fig. 6.2. However, at the outer boundary, formation temperature does not change with radial distance; that is, the slope is zero, or $\partial T/\partial r$ = 0. Finally, the heat flow rate at the wellbore/formation interface is governed by Fourier's law of heat conduction. Therefore, one can write the three boundary conditions as

$$\lim_{t\to 0} T_e = T_{ei}, \qquad (6.2)$$

$$Q = 2\pi k_e \left.\frac{r\,\partial T_e}{\partial r}\right|_{r=r_{wb}}, \qquad (6.3)$$

and

$$\lim_{r\to\infty} \frac{T_e}{\partial r} = 0. \qquad (6.4)$$

In Eq. 6.3, Q is the heat flow rate from the formation to the well per unit length of the well, and r_{wb} is the outer radius of the wellbore.

As production continues, heat transfer from the wellbore causes a gradual rise in

the temperature of the surrounding formation, which in turn causes a slow decrease in the rate of heat flow. Ameen (1992) and Hashmi et al. (2015) used the superposition principle to account for changing heat flow rate using a numerical approach. Their solutions show that the assumption of constant heat flow rate introduced very little inaccuracy; in this chapter, we will assume heat flux to remain constant.

6.2.2 Solution of Diffusivity Equation. Eq. 6.1 is generally solved in terms of dimensionless variables r_D (dimensionless radial distance = r/r_{wb}), $\hat{\alpha}$ (thermal diffusivity = $k_e/\rho_e c_e$), and t_D (dimensionless time = $\hat{\alpha}/r_{wb}^2$). Hasan and Kabir (1994a) solved the resulting equation with the Laplace transform, following the approach suggested by van Everdingen and Hurst (1949) for a similar set of equations used for pressure transients. They presented the expression for formation temperature as a function of radial distance and time. For estimating flowing-fluid temperature, the formation temperature and its spatial derivative at the wellbore/formation interface (r_D = 1) are needed. We can write the expression for the temperature at the wellbore/formation interface as

$$T_{wb} = T_{ei} + \frac{Q}{\pi^2 k_e} I, \quad (6.5)$$

where

$$I = \int_0^\infty \frac{1-e^{-u^2 t_D}}{u^2} \frac{Y_1(u)J_0(u) - J_1(u)Y_0(u)}{J_1^2(u) + Y_1^2(u)} \mathrm{d}u \quad (6.6)$$

Analogous to the dimensionless pressure, p_D, used in pressure-transient analysis, we define dimensionless temperature, T_D, as

$$T_D \equiv -\frac{2\pi k_e}{Q}\left(T_{wb} - T_{ei}\right). \quad (6.7)$$

Therefore, $T_D = -2I/\pi$. Note that T_D is always positive and that it represents heat flow from the formation toward a well. For the more usual case of fluid production, T_{wb} is greater than T_{ei}, causing the computed value of Q to be negative, meaning that the wellbore fluid loses heat to its surroundings. Computations using Eqs. 6.5 through 6.7 require tedious evaluation of an integral involving modified Bessel functions of zero order and first order over the limits of zero and infinity. Hasan and Kabir (1994a) found the following algebraic expressions for dimensionless temperature T_D in terms of dimensionless time t_D to represent the solutions quite accurately.

$$T_D = \left(0.4063 + \frac{1}{2}\ln t_D\right)\left(1 + \frac{0.6}{t_D}\right), \quad \text{if } t_D > 1.5, \quad (6.8)$$

and

$$T_D = 1.1281\sqrt{t_D}\left(1 - 0.3\sqrt{t_D}\right), \quad \text{if } t_D \le 1.5 \qquad (6.9)$$

Eqs. 6.8 and 6.9 are discontinuous at t_D = 1.5. The continuous expression for T_D may be more suitable in some applications and is written as

$$T_D = \ln\left[e^{-0.2t_D} + \left(1.5 - 0.3719e^{-t_D}\right)\sqrt{t_D}\right] \qquad (6.10)$$

At large times, Eqs. 6.9 and 6.10 both reduce to the following expression:

$$T_D = 0.4063 + \frac{1}{2}\ln t_D \qquad (6.11)$$

The log-linear representation of T_D, given by Eq. 6.11, was first used by Ramey (1962) and Edwardson et al. (1962). Eq. 6.11 is valid for wells of small diameters (diameter approaching zero) at all times and for all diameters at long times—that is, t approaching infinity. Therefore, the expressions proposed by Hasan and Kabir (1994a) and Ramey (1962) are equivalent at late times, although differences may occur at early times for finite-diameter wells.

Solution of Eq. 6.1 needs three initial/boundary conditions. We used constant heat transfer between the wellbore and formation, represented by Eq. 6.2, as one of those conditions. Ramey (1962) and Hagoort (2004) pointed out that a few other conditions can be used: (1) constant temperature at the wellbore/formation interface T_{wb}, (2) convective heat loss, and (3) radiative heat loss. Ramey presented various dimensionless temperature solutions resulting from these boundary conditions as a chart, as shown in **Fig. 6.3.** Note that Ramey used the symbol $f(t)$ for dimensionless temperature, which is the same as T_D used in this book. As Fig. 6.3 shows, all solutions converge to a single curve for t_D greater than approximately 200. Ramey pointed out that for many reservoirs, t_D > 200 implies approximately a week, meaning when Eq. 6.11 may be used for estimating T_D. For computing T_D, we consistently use Eq. 6.10, represented by the lowest curve in Fig. 6.3. Other studies, as discussed in Chapter 7, indicate that Eq. 6.10 appears to work well for all field settings and better than do the other models shown in Fig. 6.3.

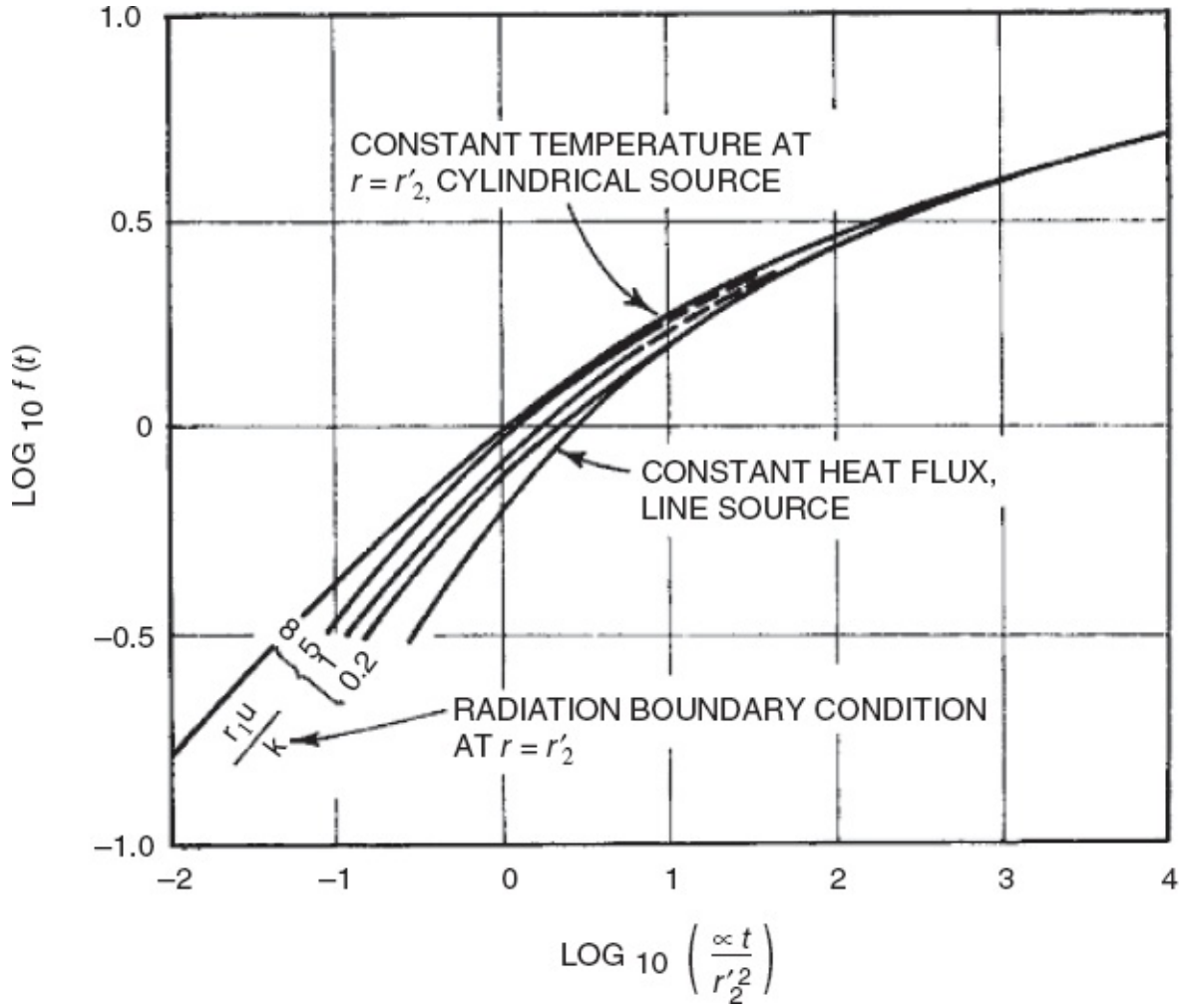

Fig. 6.3—Different T_D [= $f(t)$] values for various boundary conditions (from Ramey 1962).

Eq. 6.7 is a convenient expression that relates heat flow to the temperature-difference driving force, (T_{wb} – T_{ei}), and allows heat-transfer computation with Eqs. 6.8 through 6.11. However, the temperature at the wellbore/formation interface T_{wb} is unknown and must be replaced by the wellbore fluid temperature. This substitution of T_{wb} by T_f is accomplished by using an energy balance for the wellbore fluid.

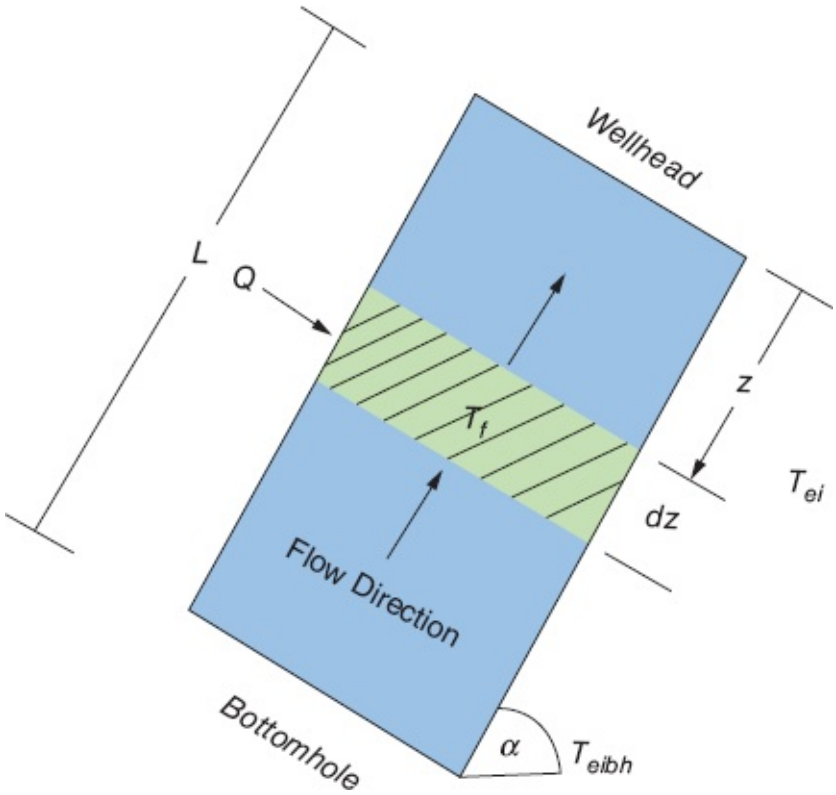

Fig. 6.4—Energy balance for wellbore fluid.

6.3 Energy Balance for Wellbore Fluid

Temperature difference between the wellbore fluid and the surrounding formation results in energy exchange. An energy balance for the fluid may be performed following any standard text on thermodynamics. Ramey (1962) made an energy balance for the fluid by assuming single-phase flow. A general energy balance (Hasan and Kabir 1994a) for either a single- or two-phase system is presented here.

Fig. 6.4 shows a production system using single tubing, inclined at an angle, α, to the horizontal. Consider a control volume of length dz at a distance z from the wellhead in this system, where the distance coordinate, z, is positive in the downward direction, representing measured (not true vertical) depth. The amount of heat ($wH|_{z+dz}$) enters the element at ($z + dz$) by convection, while conduction from the formation adds Q to the element. Similarly, ($wH|_z$) heat leaves the element at z by convection. Adding potential and kinetic energies to the heat energy of the fluid, we obtain

$$wH|_{z+\mathrm{d}z} + \frac{(L-z-\mathrm{d}z)wg\sin\alpha}{Jg_c} + \frac{wv^2|_{z+\mathrm{d}z}}{2Jg_c} + Q\mathrm{d}z = wH|_z + \frac{(L-z)wg\sin\alpha}{Jg_c} + \frac{wv^2|_z}{2Jg_c} \quad \ldots\ldots\ldots\ldots\ldots\ldots (6.12)$$

During injection, every term except Q in Eq. 6.12 changes sign. We can generalize the energy balance equation for both production and injection systems as

$$\frac{dH}{dz} - \frac{g\sin\alpha}{Jg_c} + \frac{v}{Jg_c}\frac{dv}{dz} = \mp\frac{Q}{w}. \quad (6.13)$$

In Eq. 6.13 the negative sign on the right side applies to production and the positive sign to injection. The second and third terms of Eq. 6.13 use factors g_c and J and convert lbm to lbf and ft-lbf to Btu (these are defined in the Nomenclature section). For a fluid undergoing no phase change—that is, when heat effects owing to evaporation/condensation, solution, and mixing are negligible—enthalpy is a function of pressure and temperature and is given by

$$dH = \left(\frac{\partial H}{\partial T}\right)_p dT + \left(\frac{\partial H}{\partial p}\right)_T dp = c_p dT - C_J c_p dp, \quad (6.14)$$

where C_J represents the J-T coefficient and c_p is the mean heat capacity of the fluid at constant pressure. Note that because of significant evaporation/condensation during steam injection, Eq. 6.14 is inapplicable. We discuss issues related to steam injection or geothermal production in Chapter 7, Section 7.4, as well as in Chapter 12. Using Eq. 6.14, we can write the expression for the wellbore fluid temperature as a function of depth as

$$\frac{dT_f}{dz} = C_J\frac{dp}{dz} + \frac{1}{c_p}\left(\mp\frac{Q}{w} + \frac{g\sin\alpha}{Jg_c} - \frac{v}{Jg_c}\frac{dv}{dz}\right). \quad (6.15)$$

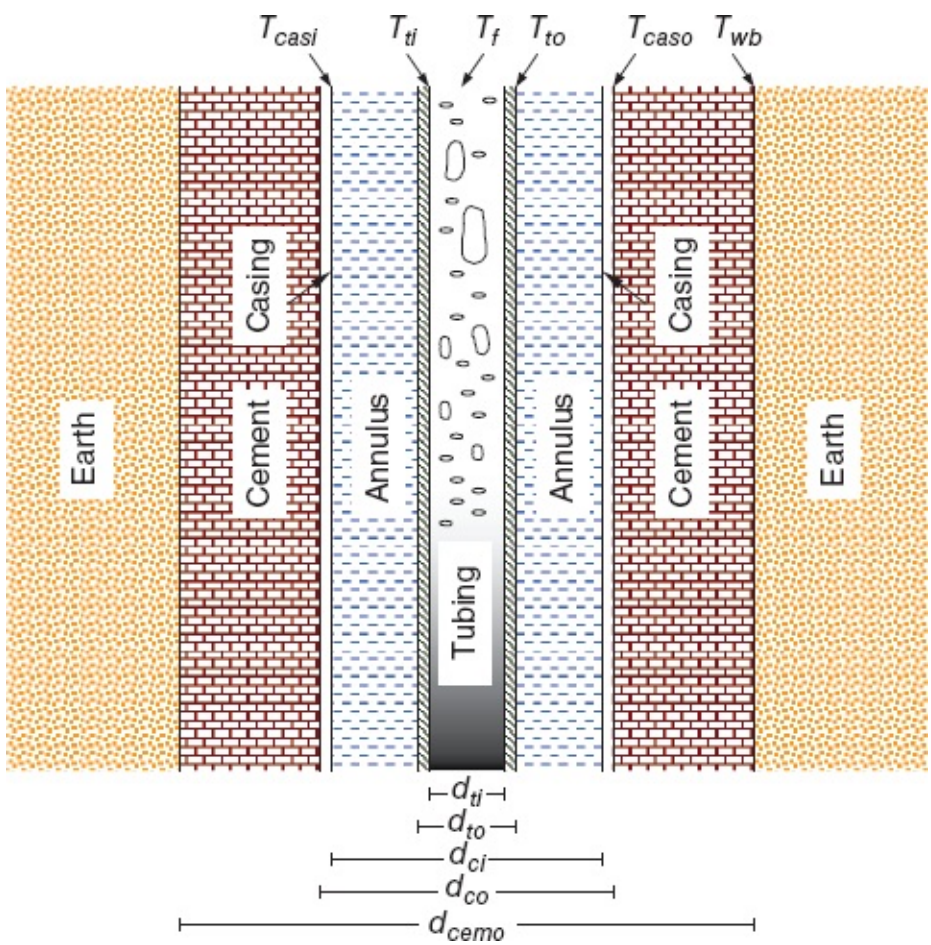

Fig. 6.5—Resistances to heat flow in a wellbore.

Combining Eq. 6.15 with Eqs. 6.7 and 6.10, one can arrive at an expression for T_f. However, to eliminate T_{wb} from the resultant expression, one must use the overall-heat-transfer coefficient for the wellbore.

6.3.1 Overall-Heat-Transfer Coefficient for Wellbores. Radial heat transfer occurs between the wellbore fluid and the earth, overcoming resistances offered by the tubing wall, tubing/casing annulus, casing wall, and cement, as shown in **Fig. 6.5.** These resistances are in series, and except for the annulus, the only energy transport mechanism is conductive heat transfer. At steady state, the rate of heat flow, through a wellbore per unit length of the well, Q, can be expressed as

$$Q = -2\pi r_{to} U_{to} \left(T_f - T_{wb}\right). \qquad (6.16)$$

In Eq. 6.16, U_{to} is defined as the overall-heat-transfer coefficient, based on the tubing outside surface area, $2pr_{to}$, and the temperature difference between the wellbore fluid and wellbore/formation interface, $(T_f - T_{wb})$. Thus, the overall-heat-transfer coefficient for a given well is an extremely important parameter. Discussion on this topic has been presented by a number of authors (Hasan and Kabir 1994a; Willhite 1967) and is summarized in Appendix 6-A.

When heat transfer occurs at steady state, heat flowing through each of the elements (see Fig. 6.5) must be the same. Steady-state heat transfer allows us to derive the expression for the overall-heat-transfer coefficient (Hasan and Kabir 1994a; Willhite 1967), given by

$$\frac{1}{U_{to}} = \frac{r_{to}}{r_{ti}\, h_{to}} + \frac{r_{to} \ln\left(r_{to} / r_{ti}\right)}{k_t} + \frac{1}{h_a} + \frac{r_{to} \ln\left(r_{co} / r_{ci}\right)}{k_c} + \frac{r_{to} \ln\left(r_{wb} / r_{co}\right)}{k_{cem}}. \qquad (6.17)$$

Most of the terms in Eq. 6.17 are easily computed. However, the resistance to heat transfer, offered by the annulus, represented by $1/h_a$ in Eq. 6.17, is somewhat difficult to estimate. In case of steam injection or geothermal production, the large temperature difference between the tubing and the annular fluids may cause both radiation and natural convection. Details of radiative and natural convective heat-transfer mechanisms are also discussed in Appendix 6-A.

6.3.2 Heat Loss to the Formation. We may rewrite the expression for T_D (Eq. 6.7) in terms of heat transfer from the formation to the wellbore/formation interface as

$$Q \equiv -\frac{2\pi k_e}{T_D}\left(T_{wb} - T_{ei}\right). \qquad (6.18)$$

Combining Eqs. 6.16 and 6.18 and eliminating T_{wb}, we obtain

$$Q \equiv -L_R w c_p \left(T_f - T_{ei}\right) = -\frac{w c_p}{A}\left(T_f - T_{ei}\right), \quad (6.19)$$

where L_R is the relaxation length parameter defined as

$$L_R \equiv \frac{2\pi}{c_p w}\left[\frac{r_{to} U_{to} k_e}{k_e + \left(r_{to} U_{to} T_D\right)}\right]. \quad (6.20)$$

Note that the relaxation parameter, L_R, is inverse of the parameter, A, used by Ramey (1962); that is, $A = 1/L_R$.

6.3.3 Relaxation Parameter, L_R (1/A). Eq. 6.20 shows that the heat loss (or gain) by the fluid in the wellbore to the formation is directly proportional to ($T_f - T_{ei}$) and the parameter, L_R. Thus, L_R may be viewed as a type of overall-heat-transfer coefficient for the formation/wellbore system having the units of reciprocal length, ft^{-1} or m^{-1}. Note that the expression for L_R contains thermal properties of both the formation and the wellbore. It also includes the dimensionless temperature function T_D, which varies with time. However, T_D is a weak function of time, especially at late times. Therefore, the constant-L_R assumption works well in most practical applications.

The overall-heat-transfer coefficient for the wellbore system may vary with well depth because of the changing well configuration. In addition, as Eq. 6.17 suggests, natural convection in the annulus can contribute significantly to the value of U. Temperature difference, driving natural convection, varies with well depth, causing L_R to be a function of depth. However, variation of L_R with depth is usually small and generally neglected because U_{to} appears in both the numerator and the denominator of Eq. 6.20. The assumption of constant L_R has important consequences for the solution of the differential equation representing wellbore fluid temperature, which is discussed in Section 6.4.

6.3.4 Heat Transport in Offshore Riser. Computing wellbore fluid temperature in an offshore environment is a demanding task. That is because energy transport between cold seawater (and air) and the flowing fluid must be accounted for in an offshore riser. Depending on riser length and water temperature, the wellbore fluid temperature may be affected significantly; **Fig. 6.6** illustrates such a case.

For the submerged section of the production system, a tubing/casing configuration without the cement sheath is assumed. The heat-transfer rate, Q, through successive layers of cylindrical resistances is given by

$$Q = -2\pi r_{to} U_{to}\left(T_f - T_{ei}\right), \quad (6.21)$$

where T_{ei} represents the static seawater temperature far away from the well at a given depth. The variation in seawater temperature with depth is needed to apply Eq. 6.22. In most cases, the water temperature decreases with increasing depth, but in a

nonlinear fashion. Fig. 6.6 illustrates measured sea current and temperature profiles. The overall-heat-transfer coefficient U_{toc}, based on the tubing outside surface area, is given by

$$\frac{1}{U_{to}} = \frac{r_{to}}{r_{ti}\,h_t} + \frac{r_{to}\ln\left(r_{to}/r_{ti}\right)}{k_t} + \frac{1}{h_a} + \frac{r_{to}\ln\left(r_{co}/r_{ci}\right)}{k_c} + \frac{r_{to}}{r_{co}h_c}, \quad (6.22)$$

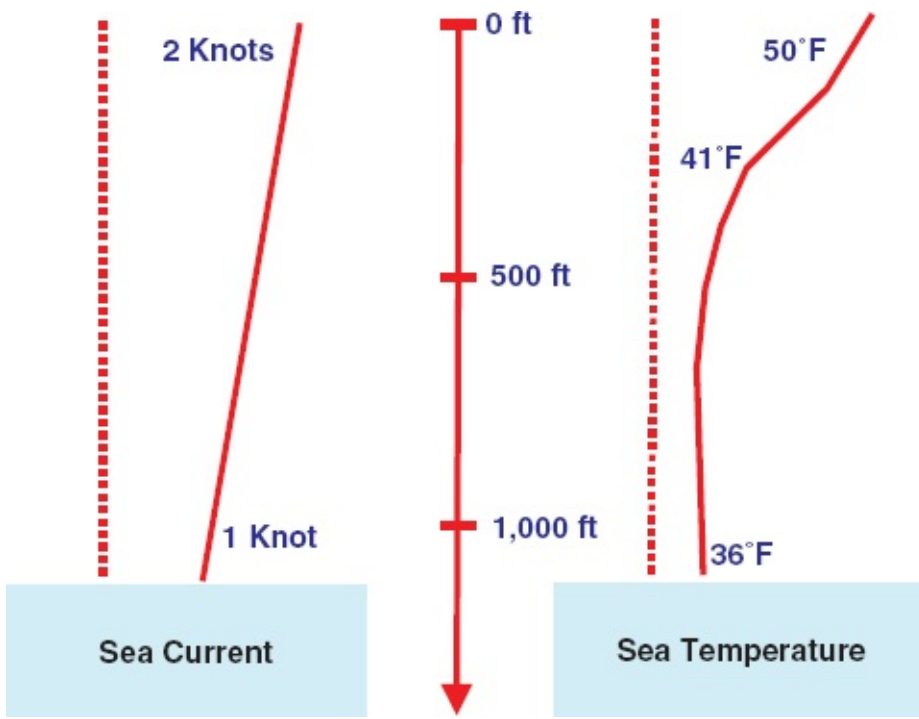

Fig. 6.6—Measured seawater temperature and velocity profiles (after Romero and Touboul 1998).

where h_c represents the heat-transfer coefficient applicable to seawater. Eq. 6.22 may be recast in the same form as Eq. 6.19. Comparing these two equations for the case of production/injection through submerged tubulars, we derived the expression for relaxation parameter L_{Rc} as

$$L_{Rc} = \frac{2\pi r_{to} U_{toc}}{c_p w}. \quad (6.23)$$

During production through the submerged section, natural current will make forced convection the most likely mode of heat transfer, especially near the air/water interface. Appendix 6-A presents the available correlations for estimating h_c.

6.4 Wellbore Fluid Temperature

We relate fluid temperature to well depth by substituting the expression for heat loss to the formation, Q, (Eq. 6.19) into the energy balance equation (Eq. 6.15).

$$\frac{dT_f}{dz} = \pm\left(T_f - T_{ei}\right)L_R + \frac{g\sin\alpha}{c_p J g_c} - \frac{v}{c_p J g_c}\frac{dv}{dz} + C_J\frac{dp}{dz}, \quad (6.24)$$

where the plus (+) sign applies to production, and the minus (–) sign applies to injection. We assume that the undisturbed formation temperature, T_{ei}, varies linearly with depth. Therefore, one can write an expression for T_{ei} for a deviated well of length, L, as

$$T_{ei} = T_{eibh} - (L - z)g_G \sin\alpha, \quad (6.25)$$

where g_G represents the geothermal gradient in terms of vertical depth and T_{eibh} is the static earth temperature at the bottom of the hole. Note that z is positive in the downward direction. Even when the earth temperature is not linear with depth, it may be reasonably well-represented by a few linear equations. Eq. 6.24 may be written as

$$\frac{dT_f}{dz} = \pm L_R(T_f - T_{ei}) + \frac{g\sin\alpha}{c_p J g_c} + \phi, \quad (6.26)$$

where

$$\phi = -\frac{v}{c_p J g_c}\frac{dv}{dz} + C_J\frac{dp}{dz}. \quad (6.27)$$

As expected, Eq. 6.26 shows that the change in fluid temperature with depth depends on the difference in temperature between the wellbore fluid and the surrounding formation. During production when $T_f > T_{ei}$, the fluid temperature decreases as the fluid moves up (Δz negative) the wellbore.

6.4.1 Producing-Fluid Temperature. If we assume that φ and L_R are independent of well depth, Eq. 6.26 becomes a first-order linear differential equation. The solution to Eq. 6.26 becomes

$$T_f = T_{ei} + \frac{1}{L_R}\left(g_G \sin\alpha + \phi + \frac{g\sin\alpha}{c_p J g_c}\right) + ICe^{(z-L)L_R}, \quad (6.28)$$

where IC, representing the integration constant, is evaluated by noting that at the bottom of the hole ($z = L$), the fluid temperature is equal to the formation temperature; that is, $T_f = T_{eibh}$. Therefore,

$$T_f = T_{ei} + \frac{1 - e^{(z-L)L_R}}{L_R}\left(g_G \sin\alpha + \phi + \frac{g\sin\alpha}{c_p J g_c}\right). \quad (6.29)$$

In high-production systems, fluid entering the bottom of the hole could be at a

different temperature, T_{fo}, than the bottomhole formation temperature, T_{eibh}. As explained in Section 6.4.3. (Eq. 6.45), in such a case, the right side of Eq. 6.29 will have an additional term, $(T_{fo} - T_{eibh})$.

Single-Phase Liquid Flow. Given that liquids are essentially incompressible, Eq. 6.29 may be simplified for single-phase oil or water flow. For example, fluid velocity changes with depth, *dv/dz*, and becomes negligible. In addition, because liquid density variation with pressure is usually quite small, one can write

$$\mathrm{d}H = \mathrm{d}E + \mathrm{d}(pV) = c\mathrm{d}T + V\mathrm{d}p, \quad (6.30)$$

and

$$C_J \equiv \frac{-1}{c_p}\left(\frac{\partial H}{\partial p}\right)_T \approx -\frac{V}{c_p} = -\frac{1}{\rho c_p}. \quad (6.31)$$

Therefore, for liquids,

$$\varphi \equiv -\frac{v}{c_p J g_c}\frac{\mathrm{d}v}{\mathrm{d}z} + C_J\frac{\mathrm{d}p}{\mathrm{d}z} = \frac{-1}{c_p\rho}\frac{\mathrm{d}p}{\mathrm{d}z}. \quad (6.32)$$

However, for single-phase liquid flow, the static-head loss nearly equals the total pressure gradient. In othe words, $\mathrm{d}p/\mathrm{d}z \approx \rho\,(g/g_c)\sin\alpha$. Therefore, Eq. 6.28 reduces to

$$\begin{aligned} T_f &= T_{ei} + g_G \sin\alpha\left[1 - e^{(z-L)L_R}\right]/L_R \\ &= T_{eibh} - g_G \sin\alpha\left\{(L-z) - \left[1 - e^{(z-L)L_R}\right]/L_R\right\} \end{aligned} \quad (6.33)$$

We can also arrive at Eq. 6.33 by noting that for liquids, the energy balance (Eq. 6.13) may be simplified to $c_p\,\mathrm{d}T/\mathrm{d}z = -Q/w = (T_f - T_{ei})\,L_R$. Eq. 6.32 shows that the fluid temperature decreases exponentially from the bottom of the hole (z = L) to the wellhead. It also shows that whereas the temperature of the fluid and the formation are the same at the bottom of the hole, the fluid temperature is higher than the formation temperature at any other location in the well. The difference in temperature between the wellbore fluid and the formation gradually increases as the fluid ascends the well. However, greater temperature difference between the fluid and its surrounding increases heat loss from the fluid. Eventually, for very deep wells, fluid heat loss by conduction will equal heat gained by convection, so the temperature difference between the fluid and surrounding, $T_f - T_{ei}$, becomes constant.

For deep wells, $(z - L)L_R$ may become a large negative number, thereby making $e^{(z-L)LR}$ a negligible entity. In this case, Eq. 6.33 becomes

$$T_f - T_{ei} = g_G \sin\alpha / L_R \quad (6.34)$$

Eqs. 6.33 and 6.34 show that for deep wells, the temperature difference $(T_f - T_{ei})$

may asymptotically approach a constant value. The magnitude of this temperature difference depends on the value of L_R. Therefore, if the asymptotic approach holds, temperature logs may be used to estimate the value of L_R. When thermal properties needed to calculate L_R (Eq. 6.20) are available, one may use temperature logs to calculate flow rates from various producing zones, as was proposed by Curtis and Witterholt (1973). This estimation is possible because L_R is inversely proportional to the mass flow rate. However, various assumptions inherent in this approach often render such estimates approximate.

Single-Phase Gas Flow. Gas wells present more complication than oil wells because the static head is not canceled by the ϕ term. However, for gases at low pressures, ϕ is usually small and may be neglected. In that case, the following expression for fluid temperature may be derived from Eq. 6.29.

$$T_f = T_{ei} + \frac{1-e^{(z-L)L_R}}{L_R}\left(g_G \sin\alpha + \frac{g\sin\alpha}{c_p J g_c}\right). \quad (6.35)$$

Because gas in most wells is rarely ideal, we do not recommend the use of Eq. 6.35.

6.4.2. Estimation of Joule-Thomson Coefficient and ϕ. To use Eq. 6.29 for calculating the flowing-fluid temperature, we need to estimate the parameter, ϕ. Based on laboratory and field flowing-fluid temperature data, Sagar et al. (1991) developed an empirical correlation for ϕ. Their correlation has been used by many, including Hasan and Kabir (1994a). For production rates less than 5 lbm/sec (18,000 lbm/hr), ϕ (in °F) is given by the fol-lowing expression:

$$\begin{aligned}\phi = &-0.002978 + 1.006x10^{-6} p_{wh} + 1.906x10^{-4} w \\ &- 1.047x10^{-6} GLR + 3.229\times10^{-5} API + 0.004009\gamma_g - 0.3551 g_G.\end{aligned} \quad (6.36)$$

For flow rates higher than 5 lbm/sec, Sagar et al. (1991) set $\phi = 0$.

The completely empirical nature of Eq. 6.36 makes its applicability to diverse production/operation situations doubtful. Because Eq. 6.36 was developed for two-phase production, we do not recommend its use for either single-phase gas and oil production or injection.

Instead of using Eq. 6.36, we recommend estimating ϕ from its two components, shown in Eq. 6.27. The kinetic energy component can be calculated from an estimate of $\Delta v/\Delta z$; the contribution of this term is small, its accurate estimation unwarranted. The major part of ϕ is the J-T effect, $C_J c_p dp/dz$. To estimate C_J, we note that, by definition, $c_p C_J \equiv (\partial H/\partial p)_T$. From the Maxwell equations, $(\partial H/\partial p)_T = V + T(\partial S/\partial p)_T$ and $(\partial S/\partial p)_T = -(\partial V/\partial T)_p$. In other words, C_J can be expressed in terms of the temperature derivative of fluid volume, $dH = c_p dT + [V - T(\partial V/\partial T)_P]dp$ and $c_P C_J = -[V - T(\partial V/\partial T)_p]$. We now present calculation procedures for C_J for single-phase liquid, single-phase gas, and two-phase systems. In these expressions, V is specific

volume, with units in ft^3/lbm; that is, $V = 1/\rho$.

Single-Phase Liquid. Using volume expansivity, $\beta \equiv (1/V)(\partial V/\partial T)_p$, $\equiv (-1/\rho)(\partial \rho/\partial T)_p$, we write

$$dH = c_p dT + V(1 - \beta T)dp \text{ and } c_P C_J = -V(1 - T\beta). \quad (6.37)$$

Note that for a truly incompressible liquid, $\beta = 0$ and $C_J = -1/(\rho c_p)$, as pointed out in Eq. 6.31. For oil, V increases with T, so β is positive. In general, β is small enough so that $1 - T\beta$ is positive for liquids, making $-V(1 - T\beta)$ and C_J negative quantities for liquids. This is why for oil production, as pressure decreases, its temperature tends to increase.

Single-Phase Gas. Expressing the volume of a real gas in terms of Z-factor, $V \equiv ZRT/p$,

$$(\partial V/\partial T)_p = (ZR/p) + (RT/p)(\partial Z/\partial T)_p = (V/T) + (V/Z)(\partial Z/\partial T)_p. \quad (6.38)$$

Therefore,

$$c_p C_J = -[V - V - (VT/Z)(\partial Z/\partial T)_p] = (VT/Z)(\partial Z/\partial T)_p. \quad (6.39)$$

For gases at low-to-medium pressures (up to 4,000 psia), Z increases with T; that is, $(\partial Z/\partial T)_p$ is positive. This means that C_J is positive. Therefore, when pressure decreases, temperature of a gas at moderate pressures also decreases. However, at higher pressures, the opposite is true.

Two-Phase Fluid. For two-phase flow, the fluid mixture enthalpy, consisting of x mass fraction gas and $(1 - x)$ mass fraction liquid, can be expressed as the weighted mass average of the liquid and gas enthalpies, given by

$$\begin{aligned} dH &= x dH^v + (1 - x) dH^l \\ &= \left[x c_{pg} + (1 - x) c_{pL}\right] dT - dp\left[(x V^v T/Z)(\partial Z/\partial T)_p - (1 - x) V^L (1 - T\beta)\right], \end{aligned} \quad (6.40)$$

$$dH = c_{p_{mg}} dT - \left[\frac{x V^v T}{Z}\left(\frac{\partial Z}{\partial T}\right)_P - (1 - x) V^L (1 - T\beta)\right] dp = c_{p_{mg}} dT - C_J c_P dp, \quad (6.41)$$

and

$$C_J c_p = \left[\frac{xT}{Z\rho_g}\left(\frac{\partial Z}{\partial T}\right)_p - \frac{(1 - x)(1 - T\beta)}{\rho_L}\right]. \quad (6.42)$$

The units of $c_p C_J$ ($c_p C_J \equiv V \equiv$ ft^3/lbm) are those of volume; therefore, $dp(c_p C_J)$ has the units of ft-lbf/lbm. Pressure in the oil field is generally reported in psi (lbf/in.^{2}); therefore, $dp(c_p C_J)$ may need to be multiplied by (144 in.^{2}/ft^2) for proper unit conversion. In addition, for temperature calculations, ft-lbf must be converted to Btu by noting that 778 ft-lbf is equal to 1 Btu.

No matter which equation is used, estimated values of ϕ tend to be a very small fraction. This small magnitude of the parameter may tempt one to ignore it completely; however, doing so will introduce error. In **Fig. 6.7,** we show the estimated values of fluid temperature for a field example using three different values of ϕ (Hasan et al. 2009). The average value of ϕ for this case was calculated to be 0.00212 using Eq. 6.42 that matched the reported wellhead temperature of 201°F. Using a value of ϕ = 0 leads to a much lower wellhead temperature estimate of approximately 170°F. In contrast, using ϕ =0.0038, estimated from Eq. 6.36, results in a higher wellhead temperature of 215°F.

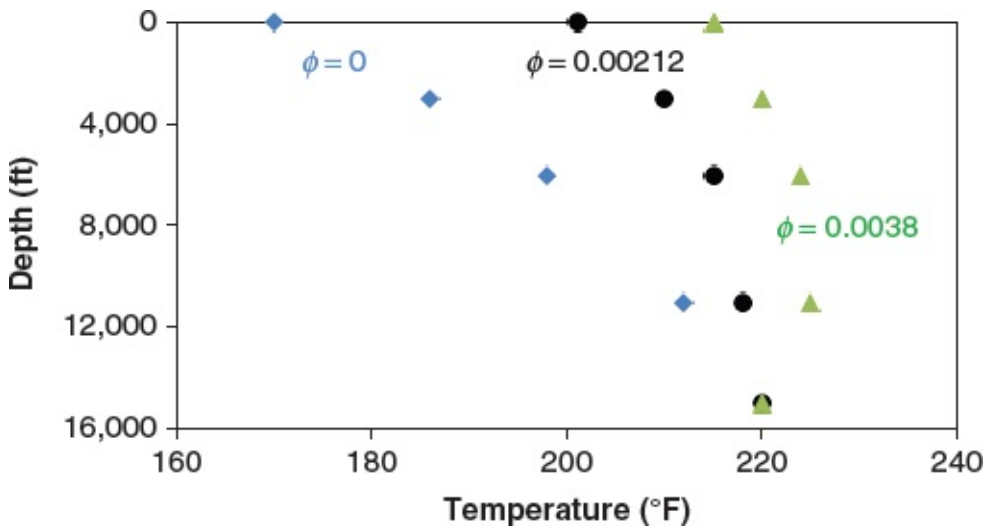

Fig. 6.7—Effect of ϕ on estimated fluid temperature.

6.4.3 Fluid Temperature in Injection Wells. Injection wells are common occurrences in oilfield operations. Sometimes part of the produced water or gas is injected back into the formation for pressure maintenance. Secondary and tertiary recovery schemes also demand fluid injection. Injecting live steam into the formation often helps reduce reservoir fluid viscosity by raising its temperature. In these and other applications, one must be able to calculate the injection fluid temperature as it flows down the wellbore.

The differential equation describing flowing-fluid temperature in wellbores, Eq. 6.26 with the negative sign, is valid for injection wells without evaporation/condensation. Eq. 6.26 is integrated for an injection well with the wellhead fluid temperature, T_{fwh}, and surface earth temperatures, T_{es}, used as boundary conditions to yield

$$T_f = T_{ei} - \frac{1-e^{-zL_R}}{L_R}\left[g_G \sin\alpha + \phi - \frac{g\sin\alpha}{c_p J g_c}\right] + e^{-zL_R}\left(T_{fwh} - T_{es}\right) \quad (6.43)$$

Condensable systems are treated in Chapter 9, Section 9.3.

6.4.4 Temperature in Complex Wells. For a well with multiple changes in inclination

angle α and/or geothermal gradient g_G, as shown in **Fig. 6.8,** Eq. 6.28 cannot represent flowing-fluid temperature for the entire well. In such a case, the differential equation, Eq. 6.26, may be integrated by dividing the well into a number of intervals with constant geothermal gradients and other properties applied to each interval. The fluid temperature calculated at the end of the interval is used as the entrance fluid temperature for the next interval. Of course, changing geothermal temperature, as well as other parameters, needs to be properly accounted for. The appropriate expression for T_{ei} under such changing conditions is written in terms of T_{ei} just before this interval as

$$T_{ei} = T_{ei_j} - (z_j - z) g_{G_j} \sin\alpha_j. \qquad (6.44)$$

Therefore, Eq. 6.26 is rewritten as

$$\frac{\mathrm{d}T_f}{\mathrm{d}z} = \pm L_R \left(T_f - z g_{Gi} \sin\alpha_i\right) \mp z_R (T_{ei_j} - z_j g_{Gj} \sin\alpha_j) + \frac{g \sin\alpha_i}{c_P J g_c} + \phi. \qquad (6.45)$$

Note that T_{ei} without the subscript is a variable, being a linear function of z, whereas T_{eij} is a constant and is the value of the undisturbed formation temperature at the position z_j. Eq. 6.45 can be solved to obtain

$$T_f = T_{ei} + \frac{1 - e^{(z - z_j) L_R}}{L_R} \left(g_{Gj} \sin\alpha_j + \phi + \frac{g \sin\alpha}{c_p} \right) + e^{(z - z_j) L_R} \left(T_{f_j} - T_{eij} \right) \qquad (6.46)$$

Eq. 6.46 uses the boundary condition that the fluid temperature at the measured distance, z_j, (the “entrance” to the interval) is known and is T_{fj}. The values of the parameters T_{ei}, g_G, ϕ, and α to be used in Eq. 6.46 are those that apply to this interval. When inclination angle, geothermal gradient, and the like do not change with depth, $T_{fj} = T_{eibh}$ at $z = L$ and Eq. 6.46 collapses into Eq. 6.29 for a simple well. On the other hand, for such a simple well, if bottomhole fluid temperature, T_{fo}, is different from bottomhole formation temperature, T_{eibh}, one need only add ($T_{fo} - T_{eibh}$) to the right side of Eq. 6.46 to obtain T_f.

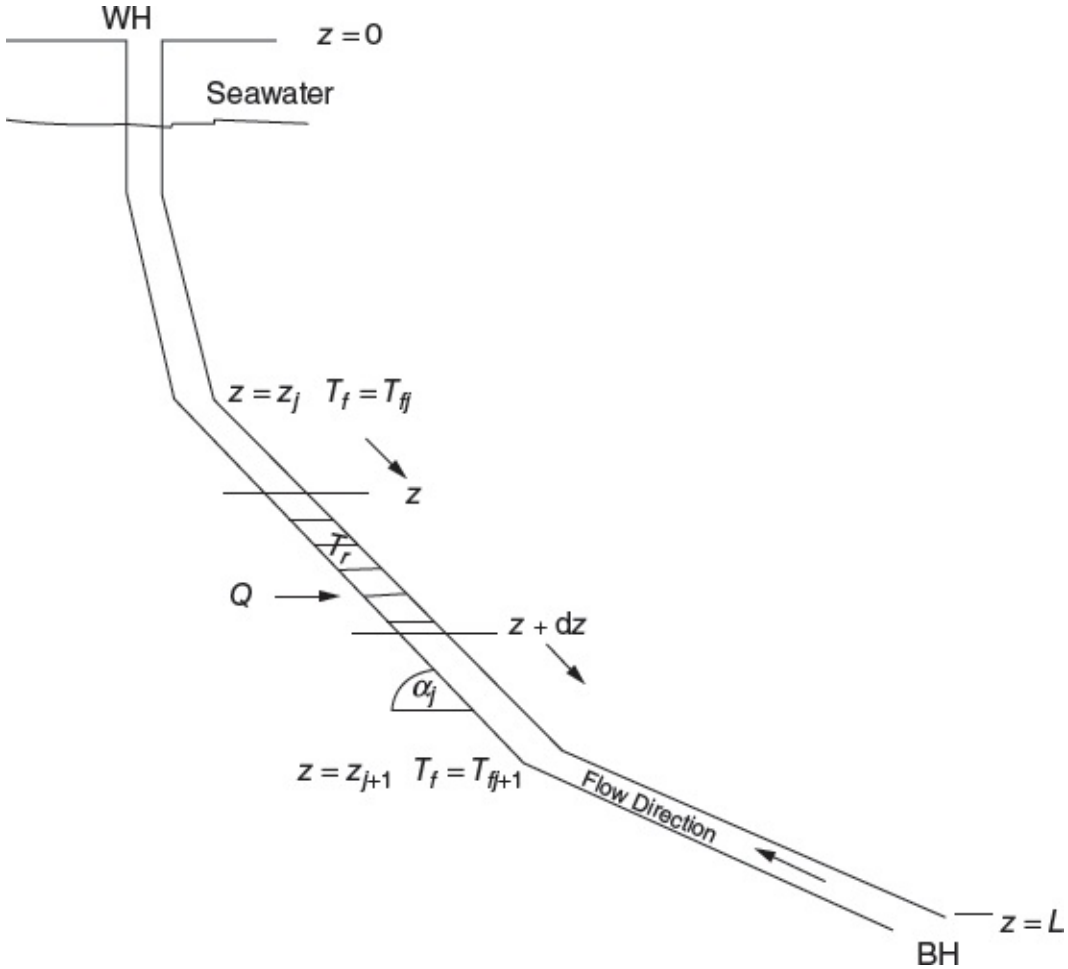

Fig. 6.8—Schematic of a complex well, from wellhead (WH) to the bottom of the hole (BH).

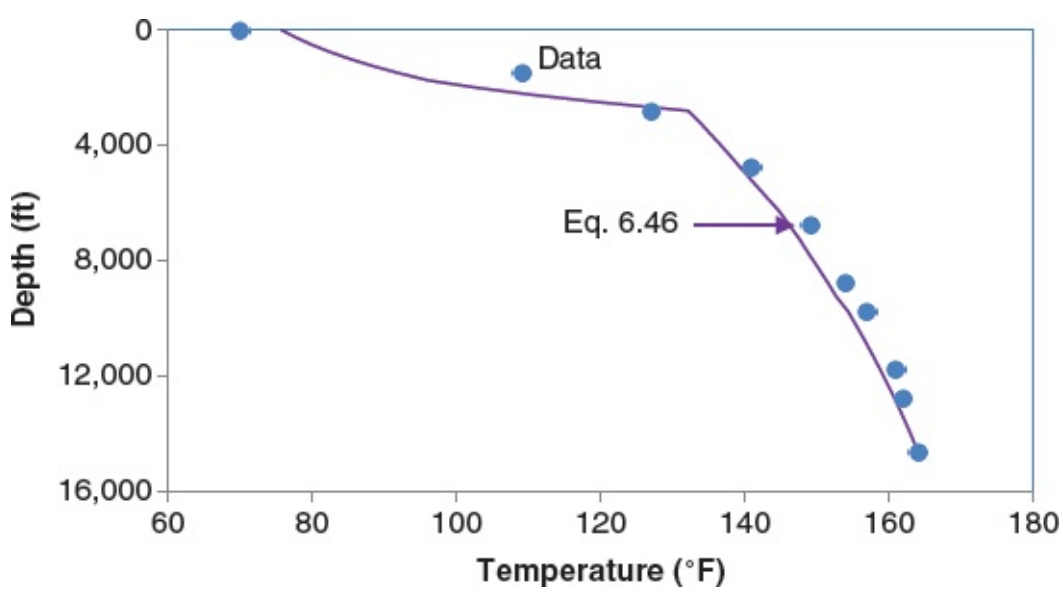

Fig. 6.9-Estimated fluid temperature using Eq. 6.46 agrees with data from an offshore well.

For a system with variable geothermal properties and changing well configuration, such as that represented by Fig. 6.7, Eq. 6.46 must be used instead of Eq. 6.29. An obvious use of Eq. 6.46 will be to estimate flowing-fluid temperature for an offshore

well with a significant section submerged in water, as shown in **Fig. 6.9,** in which the circles represent fluid temperature data from an offshore well. The solid line represents data estimated with Eq. 6.46 (Hasan et al. 2009).

Field Example

Data reported by Sagar et al. (1991) from a vertical flowing well are used to show the procedure for calculating fluid temperature in a producing well. The flow rates and well dimensions are

q_o = 59 STB/D

γ_o = 34.3 °API

d_{ti} = 2.875 in.

d_{ci} = 6.46 in.

q_w = 542 STB/D

γ_w = 1.01

d_{to} = 3.00 in.

d_{co} = 7.00 in.

q_g = 41 MScf/D

γ_g = 1.04

d_{wb} = 9.00 in.

p_{wh} = 113 psig

depth = 5,355 ft

T_{ewh} = 76°F

t_p = 158 hours

T_{eibh} = 108°F = T_{fbh}

The following typical values for the thermal properties of the various elements are used:

k_e = 1.40

c_p = 0.947 Btu/lbm-°F

k_{cem} = 4.021

μ_a = 2.0 cp

k_a = 0.2

μ_t = 1.0 cp

k_f = 0.1 Btu/hr-ft-°F

$\hat{\alpha}$ = 0.04 ft^2/hr

Solution. To calculate the various resistances to heat transfer, in the process of calculating the overall-heattransfer coefficient, we need to make a few assumptions. For example, the heat-transfer coefficient for the tubing fluid requires calculation of Reynolds number for the produced fluid. This step also requires mixture velocity, density, and viscosity. This is a three-phase mixture whose gas fraction changes with depth because of gas coming out of solution. However, this resistance is quite small, and an average value for the entire wellbore should suffice. Because we know the wellhead pressure and can approximate the fluid temperature there to be near 90°F, we can calculate approximate gas, oil, and water velocities at the wellhead to be approximately 2.25 ft/sec. We take this as the mixture velocity for the entire well, use an average viscosity of 1 cp (= 2.54 lbm/ft/hr) and average density of 53.25 lbm/ft^3. These input parameters lead to Re ≈ 40,500, Pr = 24, and h_t = 133 Btu/(hr-ft-°F). We show later that a 20% different value of h_t will not affect the fluid temperature in a significant way. Using tubing and casing material conductivities of 26 Btu/hr-ft-°F, other components of the total resistance in Btu/(hr-ft-°F) are given by

$rt_o/(r_{ti}h_{to})$

0.0075

$rt_o\ln(r_{to}/r_{ti})/k_t$

0.00020

$rt_o\ln(r_{co}/r_{ci})/k_t$

0.00037

$rt_o\ln(r_{wb}/r_{co})/k_{cem}$

0.0075

Calculating the overall-heat-transfer coefficient with Eq. 6.17 requires estimating h_a

with the Dropkin and Sommerscales (1965) correlation (see Eq. 6-A-22 in Appendix 6-A). This step requires calculating annular fluid Grashof number using Eq. 6-A-23, which requires temperature difference across the annular fluid, $T_{to} - T_{ci}$. Because calculation of ΔT (= $T_{to} - T_{ci}$) requires an estimate of U_{to}, an iterative approach is called for at each depth location of the well. Therefore, for the wellhead conditions, we assume ΔT = 10 and calculate these values (first trial):

Gr = 124,880

L_R = 3.22 × 10^{-4} ft^{-1} (A = 3,108 ft)

h_a = 12.5

Btu/hr-ft^2-°F

T_f (Eq. 6.28) = 89.58°F

U_{to} = 15.44

Btu/hr-ft^2-°F

Note that these values of U and A (=1/L_R) differ considerably from those computed by Sagar et al. (1991) (4.57 Btu/hr-ft^2-°F and 5,000 ft, respectively) because they neglected natural convection in the annulus. In this example, instead of using the Sagar et al. correlation (Eq. 6.35) to evaluate ϕ, we estimated it for the three-phase mixture as –0.002. This consideration results in the wellhead fluid temperature to be 90.32°F, compared with a measured value of 88°F. Note that the resistance to heat transfer offered by the annular fluid, even after natural convection has been accounted for, is more than two orders of magnitude higher than any other resistance. Therefore, accurate estimation of h_a is highly important. In this context, note that the first edition of this book recommended that fractional value of h_a calculated by Eq. 6-A-22 be used. Our experience since then indicates that the full value of h_a calculated by Eq. 22 offers better accuracy.

However, this value of h_a was calculated using ΔT = 10, which requires validation. We calculate heat loss by the fluid to the formation with Eq. 6.19, yielding $Q = L_R\, wc_p\, (T_f - T_{ei})$ = 37.3 Btu/(hr-ft). Therefore, ΔT from Eq. 6-A-11 = 3.19°F; this is not close to our assumed value of 10°F. We can now get a better estimate of h_a using this ΔT of 3.19 (better to use a value between 3.19 and 10), which will yield a value higher than 3.19. This iterative process continues until two successive values of ΔT are very close to each other. Finally, ΔT converged to 4.15°F, leading to the following computed values:

Gr = 94,952

$L_R = 2.94 \times 10^{-4}$ ft^{-1}

h_a = 11.55 Btu/hr-ft^2-°F

T_f (Eq. 6.28) = 90.3°F

U_{to} = 9.79 Btu/hr-ft^2-°F

If we use the approximate expression in Eq. 6-A-17 for estimating the overall-heat-transfer coefficient, the values will be U_{to} = 10.7, $L_R = 3.0 \times 10^{-4}$, and T_f = 90.1°F.

Fig. 6.10 and **Table 6.1** report the flowing-fluid temperature calculation done at various depths and compare these estimates against the measured data.

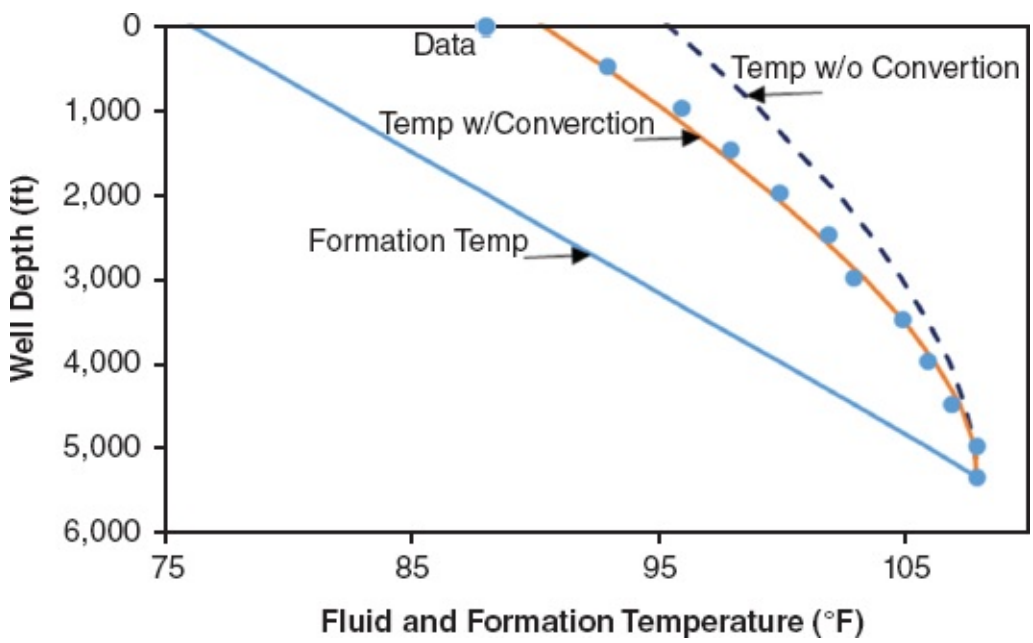

Fig. 6.10—A field example of wellbore fluid temperature profile.

Depth (ft)	h_a (Btu/hr-ft^2-°F)	U (Btu/hr-ft^2-°F)	1000 L_R (ft^{-1})	Formation Temp. (°F)	Calculated Fluid Temp. (°F)	Measured Fluid Temp. (°F)
0	11.55	9.791	0.294	76	**90.2**	88
500	11.45	9.723	0.294	79	**92.8**	93
1,000	11.31	9.617	0.293	82	**95.1**	96
1,500	11.13	9.49	0.291	85	**97.3**	98
2,000	10.92	9.332	0.289	88	**99.4**	100
2,500	10.65	9.136	0.287	91	**101.3**	102
3,000	10.31	8.885	0.284	94	**103.1**	103
3,500	9.87	8.557	0.281	97	**104.6**	105
4,000	9.278	8.109	0.275	100	**105.9**	106
4,500	8.428	7.452	0.266	103	**107.0**	107
5,000	7.019	6.328	0.248	106	**107.7**	108

5,355	0.346	1.451	0.099	108	**108.0**	108

Table 6.1—Fluid temperature and other data for the field example

The agreement of the computed fluid temperatures (bottom-heavy curve) with the measured values (filled circles) appears quite good. Our experience with these and other field data show that Eq. 6-A-22 works well in practice. Computations suggest that a higher value for k_e near the wellhead, when compared to the rest of the formation, provides a better agreement for this example. The top curve in Fig. 6.10 shows flowing-fluid temperature that would result in absence of annular convection. Note that Table 6.1 does not report the temperature values without convection simply because its exclusion is imprudent in practice.

Table 6.1 shows that the overall-heat-transfer coefficient, U_{to}, is much smaller at the bottom of the hole than at the wellhead. The marked variation in the U_{to} values with well depth is a direct result of the contribution of the natural convective heat-transfer coefficient of the annular fluid to the overall-heat-transfer coefficient. Because of small temperature differences between the tubing fluid and the earth near the bottom of the hole, temperature difference across the annulus (that is, $T_{to} - T_{ci}$) is small, and so is h_a. This low h_a value leads to a smaller value for U_{to}. At the wellhead, the reverse is true, resulting in a much larger overall-heat-transfer coefficient. Of course, the annulus may not be filled with liquid up to the wellhead; sometimes gas occupies parts of the annulus. In such cases, computations must be performed in segments, allowing for variable h_a with well depth, thereby honoring fluid composition in the annulus.

Summary

Estimating fluid temperature in a production or injection well is a challenging task owing to complex interaction of wellbore fluid with its surroundings. A part of the complexity arises from the transient nature of heat dissipation in the formation, even when wellbore fluid flow occurs at steady state. In this chapter, we presented simplified relations for the dimensionless temperature representing heat flow from formation toward wellbore. Performing energy balance for the wellbore fluid and coupling it with that in the formation develops relationships for wellbore fluid temperature. Using simplifying assumptions, we arrived at desired fluid-temperature expressions for flow of single-phase liquid, single-phase gas, and two-phase gas/liquid mixture. Please note that the sign in front of the term g (sinα), used in various equations, such as Eqs. 6.13, 6.15, and 6.29, was reversed in the first edition of the book as a result of inconsistent use of positive direction for the z-coordinate.

Usually, appropriate sign reversal accounts for flow in the opposite direction for injection wells. The treatment also includes offshore wells where both seawater and air are encountered in the riser. Experiences show that convective heat transport

through the annular fluid is important and should be included in all cases. The material in this chapter is designed for flow of noncondensable fluids. Issues related to steam injection and geothermal production are discussed in Chapter 7.

Nomenclature

c_e = formation heat capacity, Btu/lbm-°F

c_p = heat capacity at constant pressure, Btu/lbm-°F

c_{pa} = heat capacity of annular fluid, Btu/lbm-°F

c_{pm} = heat capacity of wellbore fluid mixture, Btu/lbm-°F

c_{pa}, c_{pt} = heat capacity of annular or tubing fluid, Btu/lbm-°F

c_t = total system compressibility, 1/psi

C_J = Joule-Thomson coefficient, °F/psi

d = pipe or well diameter, in.

d_c, d_t = casing or tubing diameter, in.

E = internal energy, Btu/lbm

f = friction factor, dimensionless

g = acceleration owing to gravity, ft/sec2

g_c = conversion factor, 32.17 (lbm-ft)/lbf-sec2

g_G = geothermal gradient, °F/ft

Gr = Grashof number (defined by Eq. 6-A-23), dimensionless

h = formation thickness, ft

h_c = convective heat-transfer coefficient, Btu/°F-hr-ft

h_a, h_t = convective heat-transfer coefficient for annular or tubing fluid, Btu/°F-hr-ft

H = fluid enthalpy, Btu/lbm

I = integral defined by Eq. 6.6, dimensionless

J = conversion factor, 778 (ft-lbf)/Btu

J_o, J_1 = Bessel functions of first kind of order zero and one, dimensionless

k_a = conductivity of annular fluid, Btu/hr-ft-°F

k_c = conductivity of casing material, Btu/hr-ft-°F

k_{cem} = conductivity of cement, Btu/hr-ft-°F

k_e = conductivity of earth or formation, Btu/hr-ft-°F

L = total well measured depth, ft

L_R = relaxation-distance parameter, 1/ft

m = mass of fluid in a control volume, lbm

Nu = Nusselt number (= hd/k), dimensionless

p = pressure, psi.

p_{wf} = flowing bottomhole pressure, psi

Pr = Prandtl number (= $c_p\mu/k$), dimensionless

q = fluid flow rate at standard conditions, STB/D or MMscf/D

q_{wh} = wellhead rate, STB/D or MMscf/D

Q = heat-transfer rate per unit length of wellbore, Btu/hr-ft

r = radius, ft

r_w = wellbore radius, ft

r_D = dimensionless radial distance (= r/r_w), dimensionless

Re = Reynolds number (= $dv\rho/\mu$), dimensionless

Re_m = Reynolds number for mixture (= $\rho_m v_m d/\mu_m$), dimensionless

Re_g, Re_L = Reynolds number for gas (= $\rho_g v_g d/\mu_g$) or liquid phase (= $\rho_L v_L d/\mu_L$), dimensionless

t = production or injection time, hours

t_D = dimensionless time, $\hat{\alpha}\, t/r_w^2 (= 2.64 \times 10^{-4} kt/\phi\mu c_t r_w^2)$

T = temperature, °F

T_a, T_t = temperature of annulus or tubing fluid, °F

T_{ai}, T_{ti} = inlet temperature of annular or tubing fluid, °F

T_{ci} = casing inside temperature, °F

T_D = dimensionless temperature = $(27\pi k_e)\,(T_{wb} - T_{ei})/Q$

T_{ei}, T_e = formation temperature at initial condition or at any radial distance, °F

T_{eij} = formation temperature at z_j, °F

T_{eibh}, T_{ew} = static formation temperature at bottom of the hole or wellhead °F

T_f = fluid temperature, °F

T_{ins} = insulation temperature, °F

T_{wb} = temperature at wellbore/formation interface, °F

U = overall-heat-transfer coefficient, Btu/hr-ft^2-°F

v = fluid velocity, ft/sec

w = mass flow rate of fluid, lbm/hr

x = gas mass fraction in tubing fluid mixture, dimensionless

Y_0, Y_1 = Bessel functions of the second kind of zero and one order

z_j specific well depth from surface at which formation property change occurs, ft

z = variable well depth from surface, ft

α = wellbore inclination with horizontal, degrees

$\hat{\alpha}$ = heat diffusivity of formation (= $k_e/c_e\rho_e$), ft^2/hr

β = fluid thermal expansion coefficient, 1/°F

ϕ = lumped parameter defined by Eq. 6.27, °F/ft

μ = oil viscosity, cp

ρ = density, lbm/ft^3

ρ_g, ρ_L = gas- or liquid-phase density, lbm/ft^3

ρ_c, ρ_e = core fluid or earth (formation) density, lbm/ft^3

σ = surface tension, lbm/sec^2

γ_g = gas gravity (air = 1)

γ_o = oil gravity, °API

Subscripts

a = annulus

c = casing

c = properties applicable to seawater

ccm = cement

ins = insulation

g = gas

L = liquid

o = oil

t = tubing

ta = tubing to annulus for heat-transfer coefficient

ti = tubing inside

to = tubing outside

w = water

wb = wellbore

Appendix 6-A

Heat-Transfer Coefficients for Wellbores

In this appendix we present approaches to estimating various parameters needed to use the fluid temperature expressions developed in Chapter 6. For example, to use Eq. 6.33, we need to calculate L_R, which, in turn, requires estimation of the overall-heat-transfer coefficient, U. As Eq. 6.17 shows, calculation of U requires estimations of h_{to} and h_a. Correlations needed for these and other parameters appear in this appendix. However, before those correlations are presented, we discuss some basic concepts of heat transfer that could be useful to some readers.

6-A.1. Basic Heat Transfer. Heat flows spontaneously from a high-temperature body toward a low-temperature one. Three basic mechanisms—radiation, conduction, and convection—allow flow of heat. Let us discuss these items as they pertain to wellbores.

***Radiation*.** Radiative heat transfer does not require any medium through which to flow. Stated simply, when we stand in the sun, we feel its warmth even though there is vast nothingness between us and the sun. Radiative heat transfer depends on the fourth power of absolute temperature. Eq. 6-A-1 can be used to calculate the radiative heat-transfer rate Q in terms of the area of transfer A and the hot and cold body temperatures, T_h and T_c (in K or °R), as follows:

$$Q = -Ah_r\left(T_h^4 - T_c^4\right). \qquad \text{(6-A-1)}$$

The radiative-heat-transfer coefficient h_r is obtained from the following expression:

$$h_r = \frac{\sigma\left(T_h^2 + T_c^2\right)\left(T_h + T_c\right)}{\dfrac{1}{\varepsilon_h} + \dfrac{r_{\text{ins}}}{r_{ci}}\left(\dfrac{1}{\varepsilon_c} - 1\right)}, \qquad \text{(6-A-2)}$$

where σ represents the Stefan-Boltzmann constant with a value of 1.713×10^{-9}/ft^{2}hr °R^4, and ε_h and ε_c are the emissivities of the hot and cold surfaces. Difficulties exist for obtaining accurate values of emissivities because of their dependence on surface finish and view factor, among other variables. In addition, an iterative solution procedure becomes necessary. In most cases of petroleum production, the temperature difference between surfaces and, therefore, h_r are usually negligible.

***Conduction*.** Conductive heat transfer occurs within solids or very viscous

(immovable) liquids. **Fig. 6-A-1** is useful in explaining 1D conductive-heat-transfer mechanism, in which heat flows only in the *x*-direction. With reference to the upper part of Fig. 6-A-1, conductive heat transfer rate is given by

$$Q = -kA\mathrm{d}T / \mathrm{d}x = kA\left(T_h - T_c\right) / \left(x_1 - x_2\right). \quad \text{(6-A-3)}$$

In Eq. 6-A-3, k, the conductivity is a property of the material and *A* is the cross-sectional area through which heat is flowing from x_1 to x_2. The lower part of Fig. 6-A-1 shows a situation in which there are two separate bodies through which a quantity, *Q*, of heat flows. If the system is at steady-state condition, then the amount of heat flowing through both bodies must be the same. In that case, we can write the same *Q* for both the bodies as follows:

$$Q = k_1 A\left(T_1 - T_2\right) / \left(x_1 - x_2\right) = k_2 A\left(T_2 - T_3\right) / \left(x_2 - x_3\right), \quad \text{(6-A-4)}$$

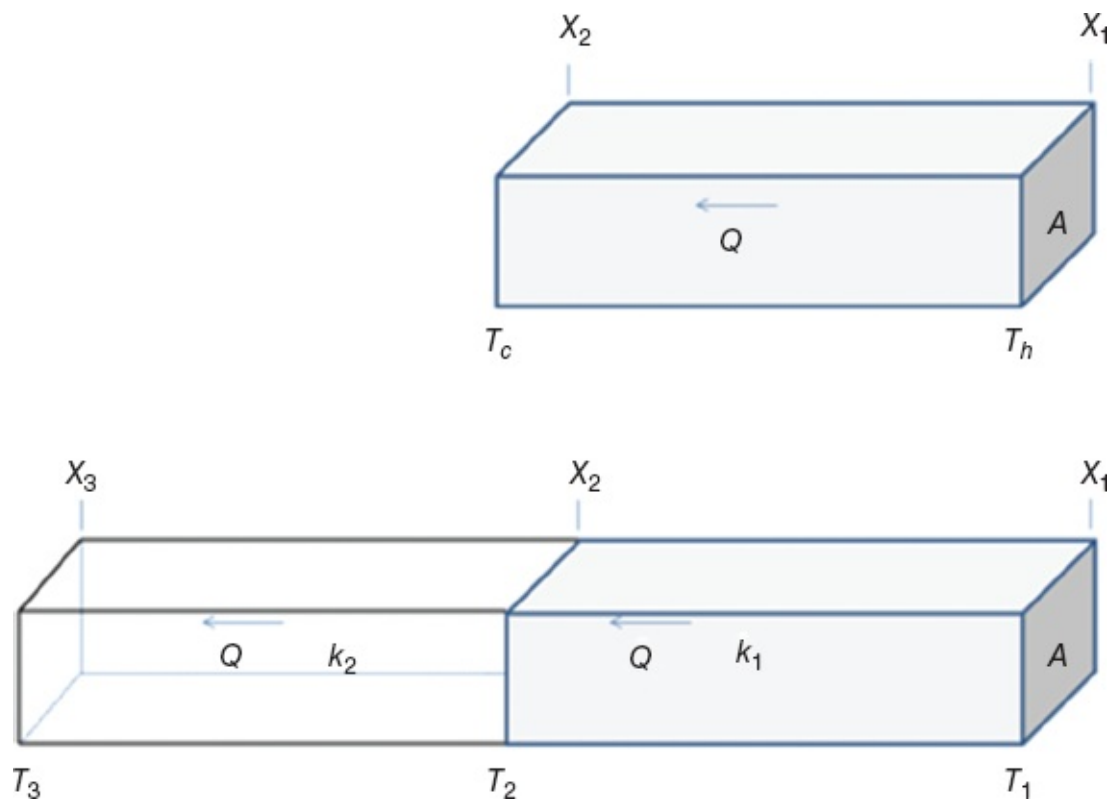

Fig. 6-A-1—Schematic of 1D heat flow.

or

$$\left(T_1 - T_2\right) / Q = \left(x_1 - x_2\right) / \left(k_1 A\right) = R_1, \text{ and } \left(T_2 - T_3\right) / Q = \left(x_2 - x_3\right) / \left(k_2 A\right) = R_2, \quad \text{(6-A-5)}$$

where R_1 and R_2 are the conductive resistances of the two solid blocks, respectively. We can add the two resistances and obtain the following expression:

$$\left(T_1 - T_3\right) / Q = R_1 + R_2. \quad \text{(6-A-6)}$$

For any number of such solid bodies in series, we can write similar expressions for resistances such that $Q = (T_n - T_{n+1})/R_n$. Adding these resistances in series yields

$$(T_1 - T_n)/Q = R_1 + R_2 + ... + R_n = R. \quad \text{(6-A-7)}$$

and

$$Q = R(T_1 - T_n) = R\Delta T. \quad \text{(6-A-8)}$$

In other words, when we have a series of different materials, we can calculate an overall resistance R of all the materials, and calculate the heat flow from one end to the other using the two temperatures at the extremities, without calculating the intermediate temperatures. We show the use of Eq. 6-A-7 with two simple examples.

Example 6-A-1. The wall of a room facing the outside is 10 ft high and 20 ft wide, and it is made of 6-in.-thick material with thermal conductivity of 1 Btu/(hr-ft^2-°F). If the outside temperature is 40°F and the room needs to be maintained at 70°F, how much heat must a furnace supply this room on a daily basis?

Solution. $Q = kA\Delta T/\Delta x$ = [1 Btu/(hr-ft^2-°F)(20 × 10 ft^2)(70 – 40°F)/(0.5 ft)] = 12,000 Btu/hr = 288,000 Btu/D.

Example 6-A-2. Let us calculate the required heating when a 3-in. insulating material (that is, 10 × 20 × 0.25) with a conductivity of 0.1 Btu/(hr-ft^2-°F) is added to the problem in Example 6-A-1.

Solution. $R_1 = (x_1 - x_2)/(k_1A)$ = (0.5 ft)/[200 Btu/(hr-°F)] = 0.0025 (hr-°F)/Btu
R_2 = (0.25 ft)/[200 × 0.1 Btu/(hr-°F)] = 0.0125 (hr-°F)/Btu
$R = R_1 + R_2$ = 0.015 (hr-°F)/Btu
$Q = (T - T_2)/R$ = (70 – 40 °F)/[0.015 (hr-°F)/Btu] = 2,000 Btu/hr = 48,000 Btu/D

Therefore, the 3-in. insulation saves approximately 240,000 Btu/D, which is equivalent to approximately 240 scf/D of natural gas.

Convection. Convective heat transfer occurs within a fluid when its movement (convection) in one direction causes mixing in the direction perpendicular to that flow. For production or injection in a well, the fluid movement in the vertical direction will cause many of the elements of the fluid to mix with each other in the radial direction, enhancing *radial* direction heat flow. With reference to Fig. 6.5, fluid flow in the tubing will cause heat from the bulk of the fluid (in and around the tubing center) to flow toward the tubing wall. This convective heat-transfer rate is expressed in terms of a heat-transfer coefficient h, for the tubing fluid and the temperature difference between the bulk fluid T_f and the inside of the tubing wall T_{ti}, as follows:

$$Q = Ah_t(T_f - T_{ti}). \quad \text{(6-A-9)}$$

Based on a unit length of the tubing, when $A = 2\pi r_{ti}$, heat flowing *toward* the fluid from the tubing wall is given by

$$Q = -2\pi r_{ti} h_t \left(T_f - T_{ti}\right). \quad \text{(6-A-10)}$$

Similarly, heat flowing from the casing toward the tubing through the "natural convective" fluid in the annulus, in terms of the annular fluid's convective heat-transfer coefficient h_a, is given by

$$Q = -2\pi r_{to} h_a \left(T_{ci} - T_{to}\right). \quad \text{(6-A-11)}$$

Correlations to estimate h_t, h_a, and the like, will be discussed in a later section. In the following subsection, we discuss the concept of an overall-heat-transfer coefficient U, which is the inverse of overall-heat-transfer resistance R.

6-A.2. Conductive/Convective Heat Transfer in Cylindrical Geometry. Resistance to heat transfer offered by individual elements of rectangular solid blocks in a series of resistances, given by Eq. 6-A-5, can be added together to obtain a total resistance, given by Eq. 6-A-7. However, a similar approach for a wellbore is somewhat complicated because heat transfer occurs through a cross-sectional area that increases as the radial distance increases. In that case, the differential form of the conduction equation, Eq. 6-A-3, can be used (for unit well length, refer to Fig. 6.5). Thus,

$$Q = -kA\mathrm{d}T / \mathrm{d}r = k2\pi r\mathrm{d}T / \mathrm{d}r. \quad \text{(6-A-12)}$$

Rearranging Eq. 6-A-12 to separate the variables ($2k\pi \mathrm{d}T/Q = \mathrm{d}r/r$) and integrating, we obtain

$$\left(T_{ti} - T_{to}\right) = -\frac{Q}{2\pi k}\ln\left(r_{to} / r_{ti}\right). \quad \text{(6-A-13)}$$

We can similarly write expressions for temperature differences across other elements in terms of the element's conductivity, k; or heat-transfer coefficient, h; the inner and outer radii; and heat flow, Q. For example, the temperature difference for the cement sheath is given by $(T_{co} - T_{wb}) = (-Q/2\pi k) \ln(r_{wb}/r_{co})$. Because of the nature of the transport mechanism, convective heat transfer is written in terms of a single radius, not the radial distance, as shown by Eq. 6-A-11 for natural convective heat transfer in the annulus.

We can add these temperature differences across each element to obtain the total temperature difference, $\Delta T = (T_f - T_{wb})$, and a total resistance, analogous to Eq. 6-A-7, as

$$T_f - T_{wb} = -\frac{Q}{2\pi}\left[\frac{1}{r_{ti}\,h_t} + \frac{\ln(r_{to}/r_{ti})}{k_t} + \frac{1}{h_a} + \frac{\ln(r_{co}/r_{ci})}{k_c} + \frac{\ln(r_{wb}/r_{co})}{k_{cem}}\right], \quad \text{(6-A-14)}$$

or

$$T_f - T_{wb} = -\frac{Q}{2\pi r_{to} U_{to}}. \quad \text{(6-A-15)}$$

Eq. 6-A-15 is another form of Eq. 6.16, in which U_{to}, the inverse of total resistance, is given by

$$\frac{1}{U_{to}} = \frac{r_{to}}{r_{ti}\,h_t} + \frac{r_{to}\ln(r_{to}/r_{ti})}{k_t} + \frac{1}{h_a} + \frac{r_{to}\ln(r_{co}/r_{ci})}{k_c} + \frac{r_{to}\ln(r_{wb}/r_{co})}{k_{cem}}. \quad \text{(6-A-16)}$$

Not all the components shown in Fig. 6.5 are present in all well configurations, and some elements offer negligible resistance to heat flow even when they are present. One may assume that the fluid heat-transfer coefficient is so high that T_f may be assumed to be equal to T_{ti}. The high values of conductivity of metals, coupled with relatively thin tubing and casing walls, allow us to make the assumption that temperature differential across the tubing and casing walls may be neglected; that is, $T_{ti} = T_{to}$, and $T_{ci} = T_{co}$. Therefore, U_{to} for a typical well may be approximated by

$$\frac{1}{U_{to}} = \frac{1}{h_a} + \frac{r_{to}\ln(r_{wb}/r_{co})}{k_{cem}}. \quad \text{(6-A-17)}$$

The resistance to heat transfer offered by the annulus, represented by the first term on the right side of Eq. 6-A-17, may involve radiative and natural convective heat-transfer mechanisms.

6-A.3 Convective Heat-Transfer Coefficient Estimation. ***Forced Convection*.** Convective heat transfer, caused by fluid movement, can be either “forced” or “natural.” Forced convection occurs because of fluid flow resulting from a pressure differential, such as when oil production occurs from a reservoir through a wellbore. For pipe flow, forced convective heat-transfer coefficient is often calculated using the Dittus and Boelter (1930) correlation. The correlation relates three dimensionless numbers—Nusselt number, Reynolds number, and Prandtl number—as follows:

$$\mathrm{Nu} = 0.023(\mathrm{Re})^{0.8}(\mathrm{Pr})^{1/3}, \quad \text{(6-A-18)}$$

where

$$\mathrm{Nu} = \frac{hd}{k}, \quad \mathrm{Re} = \frac{dv\rho}{\mu}, \quad \mathrm{Pr} = \frac{c_p\mu}{k}. \quad \text{(6-A-19)}$$

During production in an offshore environment, the submerged section of a well will

be subjected to cold sea-water flowing across it. Fishenden and Saunders (1950) have studied forced convection and recommend the following correlation for flow *across* long vertical pipes:

$$\mathrm{Nu} = 0.26(\mathrm{Re})^{0.6}(\mathrm{Pr})^{0.3}, \qquad (6\text{-A-}20)$$

where Nusselt, Reynolds, and Prandtl numbers are given in terms of seawater properties by Nu = $h_c d_{co}/k_c$, Re = $\rho_c v_c d_{co}/\mu_c$, and Pr = $c_{pc}\mu_c/k_c$. Gebhart (1971, p.272) presents a slightly different correlation for *crossflow* given by

$$\mathrm{Nu} = \left[0.35 + 0.56(\mathrm{Re})^{0.52}\right](\mathrm{Pr})^{0.3}. \qquad (6\text{-A-}21)$$

In the range of parameter values of interest, Eqs. 6-A-20 and 6-A-21 yield similar results. Note that these expressions are also applicable to the wellbore exposed to air currents.

Natural Convection. When a fluid at a given temperature is in contact with a surface at a different temperature, heat transfer takes place primarily because of a phenomenon known as natural convection. Natural convection arises because fluid density depends on its temperature. The temperature difference, and therefore the density difference, between the bulk fluid and fluid close to the surface causes fluid circulation, which, in turn, enhances heat transfer. Thus, heat transfer from the tubing outer wall to the casing inner wall does *not* take place through conduction—that is, $Q \neq k_a A\mathrm{d}T/\mathrm{d}r$). Instead, it is given by the convective heat-transfer expression $Q = Ah_a(T_{ci} - T_{to})$, shown in Eq. 6-A-11.

Unfortunately, very little work on natural convection in vertical annular geometry is reported in the literature. Willhite (1967) and Hasan and Kabir (1994a) adapted the correlation proposed by Dropkin and Sommerscales (1965) for heat-transfer coefficients for natural convection in fluids between *two vertical plates*. Their correlation for h_a, expressed for cylindrical geometry, is

$$h_a = \frac{0.049(\mathrm{Gr}\,\mathrm{Pr})^{0.333}\,\mathrm{Pr}^{0.074}\,k_a}{r_{to}\ln\left(r_{ci}/r_{to}\right)}. \qquad (6\text{-A-}22)$$

The Grashof number Gr in Eq. 6-A-22 is defined as

$$\mathrm{Gr} = \left(r_{ci} - r_{to}\right)^3 g\rho_a^2\beta\left(T_{to} - T_{ci}\right)/\mu_a^2 \qquad (6\text{-A-}23)$$

and reflects the extent of motion of the annular fluid owing to the natural convection. The density of the heated fluid next to the insulation layer is less than that next to the casing, creating a buoyancy force. The viscous force, working against the buoyancy, generates a circular motion of the fluid in the annulus. In Eq. 6-A-22, Prandtl number, Pr, defined as $c_p\mu_a/k_a$, is a measure of the interaction between the hydrodynamic boundary layer and the thermal boundary layer. For gases, the value of the Prandtl number is usually close to 1.0 (1.06 for steam and 0.69 for air); typical values for

liquids range from unity to 10.

Another correlation for the annuli Nusselt number was presented by Fishenden and Saunders (1950) in a graphical form, in terms of Grashof and Prandtl numbers and the annular diameter ratio, d_{ci}/d_{to}. The following equation can be used to represent those curves (Hasan and Kabir 1994a).

$$\mathrm{Nu} \equiv \frac{hd}{k} = 0.10\left(\frac{d_{ci}}{d_{to}}\right)^{0.15}(\mathrm{GrPr})^{0.3}, \qquad (6\text{-A-}24)$$

where Pr is defined the same way as before. However, Nu and Gr are defined in terms of the annular inner diameter d_{to} giving the correlation for h_a, which is written as

$$h_a = 0.10\left(d_{ci}/d_{to}\right)^{0.15}\left[\frac{\rho_a^2\beta g(T_{to}-T_{ci})}{\mu_a^2}\right]^{0.3} k_a d_{to}^{-0.1}(\mathrm{Pr})^{0.3} \qquad (6\text{-A-}25)$$

Eq. 6-A-25 shows a slight dependence of h_a on the pipe inner diameter, whereas Eq. 6-A-22 does not. Eq. 6-A-25 also generally yields much lower h_a values than Eq. 6-A-22.

Eq. 6-A-25 and Eq. 6-A-22 were developed from short tubes in laboratories, and direct application of either equation to wells that are orders of magnitude taller needs further investigation. Indeed, attempts have been made to incorporate an *L/d* ratio in correlating annular natural convective heat-transfer data (Sheriff 1966), which is given by

$$\mathrm{Nu} = a\,\mathrm{Gr}^b\,\mathrm{Pr}^c\,(L/d)^{-n}. \qquad (6\text{-A-}26)$$

Sheriff used a value of n = ¼ to express Nu data that he gathered with carbon dioxide in short vertical annuli. Unfortunately, such an approach is inapplicable in wells with very large values of *L/d*.

Chapter 7

Heat Transport: Field Applications

7.1 Introduction

Individual well rates enter into a variety of engineering calculations; surprisingly, the industry has struggled to meter this entity with decent accuracy unless the field is well-instrumented. In fact, accuracy in flow metering has not kept pace with pressure and temperature measurements. Ordinarily, allocation algorithms are used to assign individual well rates from total production unless a well is instrumented with a flowmeter. The lack of rigor of these allocation routines poses significant challenges during history matching of reservoir performance, particularly those routines involving rapidly changing events, such as coning or cresting of gas or water. In this context, test separators do not necessarily alleviate the metering issue simply because of inadequate flow time for large distances between a well and the point of separation, coupled with low test frequency. To compound the matter further, the industry has lacked motivations for accurate metering of nonessential entities, such as water, and to a large extent of gas because of its flaring in many field operations.

In Chapter 6, we introduced the basic concepts of wellbore heat transport in the presence of single- and two-phase fluid flow. This chapter presents applications of some of those principles in various field operations. Specifically, we present (1) estimation of gas or oil flow rates with wellbore temperature and/or pressure measurements and of rate inversion resulting from the Joule-Thomson (1853) (J-T) effect, (2) challenges in translating offbottom pressure-transient data to that at the datum depth in both gas and oil producers and in water injectors, and (3) pressure-traverse computation during steam/water flow in geothermal wells.

7.2 Rate Estimation With Steady- and Unsteady-State Temperature/Pressure Data

To enhance the quality of rate measurements at the individual wells, dedicated metering has evolved over the past 2 decades. However, direct metering of multiphase fluid flow in a pipe is a difficult proposition because volume fractions and the individual phase velocities must be ascertained. Accordingly, flowmeters have been developed to handle complete, partial, and no separation of phases. Because gas volume fraction increases with decreasing pressure, downhole metering at higher pressures can largely mitigate handling of the gas phase. Venturi-type flowmeters, requiring no separation of phases, have gained wide acceptance both downhole (Webster et al. 2006; Tibold et al. 2000; Brodie et al. 1995) and at surface (Warren et al. 2001, 2003; Retnanto et al. 2001; Pinguet et al. 2006). A Venturi-type

flowmeter appears to have performed well in a comparative study reported by Busaidi and Bhaskaran (2003). Like the Venturi, a downhole fiber-optic flowmeter is another nonintrusive device that has undergone considerable field testing (Kragas et al. 2002, 2003). Gas/liquid cylindrical cyclone (GLCC) technology (Kouba et al. 2006) separates gas from the liquid phases to facilitate ease of measurement at surface. The liquids are metered on the basis of mass using the Coriolis principle (Liu et al. 1988). Oglesby et al. (2006) reported their field experiences with GLCC while testing high-water-cut wells.

More recently, the increasing use of distributed temperature sensing or DTS has led to profiling flow across different producing intervals (Ouyang and Belanger 2006; Johnson et al. 2006; Wang et al. 2008; and Kabir et al. 2012b). Knowledge of independent total rate at the wellhead allows appropriate zonal allocation of rate in accord with flow fraction. This section presents a method for estimating rates from temperature data, independent of flow sensing. The intrinsic idea is to provide engineering tools to check on measurement quality and fill in the information void created when infrequent measurements are being made, such as in a brownfield environment.

7.2.1 Rate Estimation With Temperature Data. Estimation of flow rate from fluid temperature relies on the pseudosteady-state, flowing-fluid temperature expression developed in Chapter 6, reproduced below for convenience.

$$T_f = T_{ei} + \frac{1-e^{(z-L)L_R}}{L_R}\left(g_G \sin\alpha + \phi + \frac{g\sin\alpha}{c_p J g_c}\right) \quad (6.29)$$

In Eq. 6.29 the parameter L_R relates the mass flow rate w (lbm/hr) to thermal properties of the fluid and the formation and is given by

$$L_R \equiv \frac{2\pi}{c_p w}\left[\frac{r_{to}U_{to}k_e}{k_e + \left(r_{to}U_{to}T_D\right)}\right] \quad (6.20)$$

In Chapter 6, the known flow rate w allowed calculation of L_R using Eq. 6.20, which, in turn, was used with Eq. 6.29 to calculate the fluid temperature. In this chapter, we show how to estimate rate by calculating L_R from known fluid temperatures. Often, fluid temperatures are available at the wellhead and at the bottom of the hole. In such cases, calculating the rate from Eq. 6.20 in combination with 6.29 is reasonably straightforward, but this calculation is tedious because of the nonlinear relationship between the fluid temperature and L_R. Example 1 discusses such a simple case, though it involves temperature data from seven stations. When flowing-fluid temperature data are available at multiple depths and for multiple rates, the computational approach must be modified to account for these multiple data and associated uncertainties. Later examples discuss those cases, and Appendix 7-A presents a robust mathematical approach for performing such computations.

Example 1. The first example in this section comes from a 7,000-ft dry-gas well that is vertical for the first 2,500 ft and deviates thereafter by 50° from vertical, terminating at a true vertical depth (TVD) of 5,412 ft. At a reported production rate of 50 MMscf/D, the wellhead temperature (WHT) and bottomhole temperature (BHT) are 129 and 150°F, respectively. A production log was also run, thereby providing us with a distributed temperature profile throughout the wellbore. The model estimated a rate of 49.7 MMscf/D, which is in good agreement with the data. **Fig. 7.1** depicts the temperature-profile match obtained during history matching.

Example 2. This example is from a deepwater asset in West Australia producing essentially dry gas (Kabir et al. 2014). During drillstem testing of this just-completed well, the acoustic surface-readout technology was used to transmit pressure and temperature measurements from downhole gauges to the surface in real time. This telemetry required acoustic repeater units to be installed onto the outside of the test string, approximately every 1,500 ft below the mudline, to allow communication with the tools downhole. These acoustic repeater stations also measured and recorded temperatures at various depths. These temperature sensors have a resolution of 0.03125°C. **Fig. 7.2** presents a composite picture of the data set from Well 3.

As discussed in subsequent sections, this distributed temperature data set formed the backbone of this approach. As expected, the smallest response occurs near the well bottom, whereas the largest excursion is noted near the mudline. The temperature transients at each depth collectively became the necessary ingredients for ascertaining both the static geothermal gradient and the flowing gradient to aid in casing design and in establishing safe operable limits. The difference between the static formation temperature and the flowing-fluid temperature drives heat exchange between the wellbore fluid and the formation. All four wells in this study had long (approximately 100-hr) shut-in periods during their last buildup; these data provided us with an opportunity to obtain the static formation temperature (T_{ei}) at each depth in the system. We present static formation temperature estimation from transient data in Chapter 11. This section presents computation of flow rate from temperature data after steady-state flow is attained.

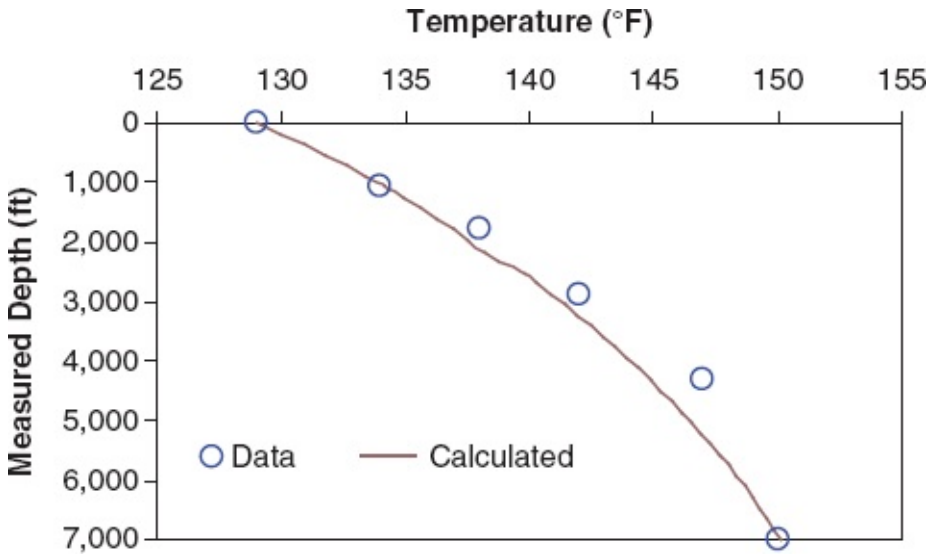

Fig. 7.1—Wellbore temperature profile match obtained as part of the rate-estimation process.

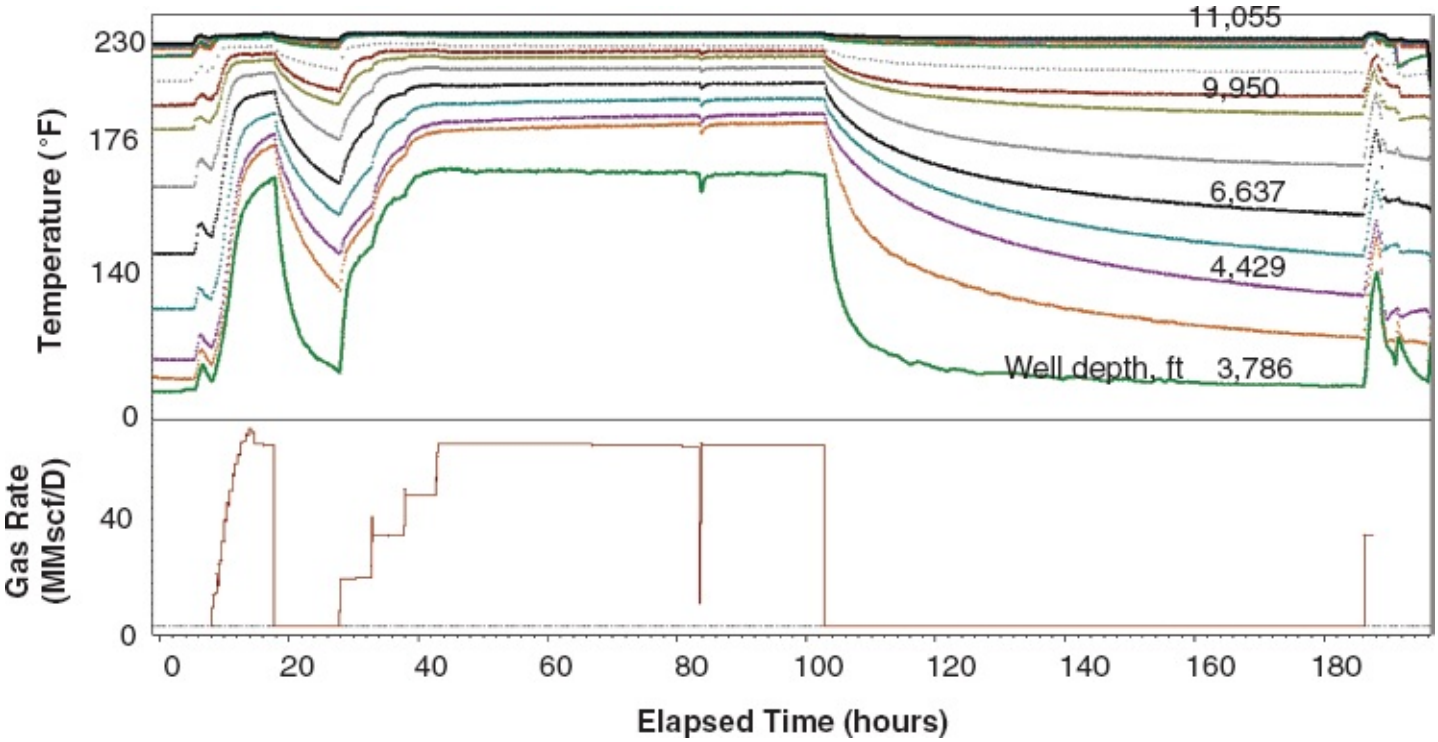

Fig. 7.2—Depth-dependent measurements of transient temperature in Well 3.

7.2.2 Estimating Flow Rate From Multistation Temperature Data. The computational algorithm for flow rate estimation from wells that had multiple sensor stations is largely made on the basis of the recent studies of Izgec et al. (2010), Ismadi et al. (2012), and Hashmi et al. (2015).

Intrinsically, rates are estimated between the point of fluid entry and the temperature-sensor station at a higher elevation; Appendix 7-A details the computational approach. The computation proceeds by marching up the well column from the point of fluid entry until the terminal point is reached near the mudline. As

expected, the solution grows increasingly robust with the increase in fidelity of temperature response, which occurs at shallower depths. We sought an overall match by honoring discrete temperature data at the end of each flow period.

Although the computation was extended from the dry-tree to the mudline segment, uncertainty in the heattransfer parameters in the wet section and also convective heat loss at the wellhead precipitated by the variable wind speed and other factors collectively demand a large entry of accurate information for credible solutions. Given the number of discrete points of temperature measurements up to the mudline and considering the overall well depth, we think that the rate computation approach as outlined here suffices.

***Well 2 Example*.** The depth-dependent temperature response for a given flow rate became the cornerstone of history matching. This modeling approach considered the last data point from each flow period by recognizing that the transient nature of temperature response requires a considerable period before stabilization occurs. The results turned out to be quite satisfactory in spite of this assumption.

Fig. 7.3a presents the history-matching effort of the temperature profiles, whereas Fig. 7.3b shows the same results by crossplotting temperature vs. rate at various depths. Note that only one set of input parameters enabled obtaining this quality history match for the entire time and depth domain. **Table 7.1** presents the error analysis and suggests that the solutions were obtained with reasonable accuracy when compared with the sophisticated multiphase flow metering. The stated resolution and repeatability of the multiphase flowmeter is 0.1 and 1% of the total mass rate, respectively, provided that calibration is performed with the fluids metered. We also note that J-T cooling sets in at higher rates, as **Fig. 7.4** exhibits. The implication of this observation is that if the test rates were such that the flat portion of the temperature response were to prevail, the quality of rate solution would likely suffer because of loss of fidelity. This point is further explored in the next section.

***Well 3 Example*.** The same solution approach discussed earlier was adopted for Well 3. Similar to the previous case, the match was predicated on honoring the last temperature data point (to satisfy the steady temperature assumption) for a given flow rate at each depth. **Fig. 7.5a** presents the history-matched temperature profiles, and Fig. 7.5b exhibits the temperature rate signatures at various depths. Predictably, the match quality suffers at the lowest gauge depth because of the low-resolution temperature response but improves at shallower depths with the increase in signal fidelity. **Table 7.2** presents the error analysis.

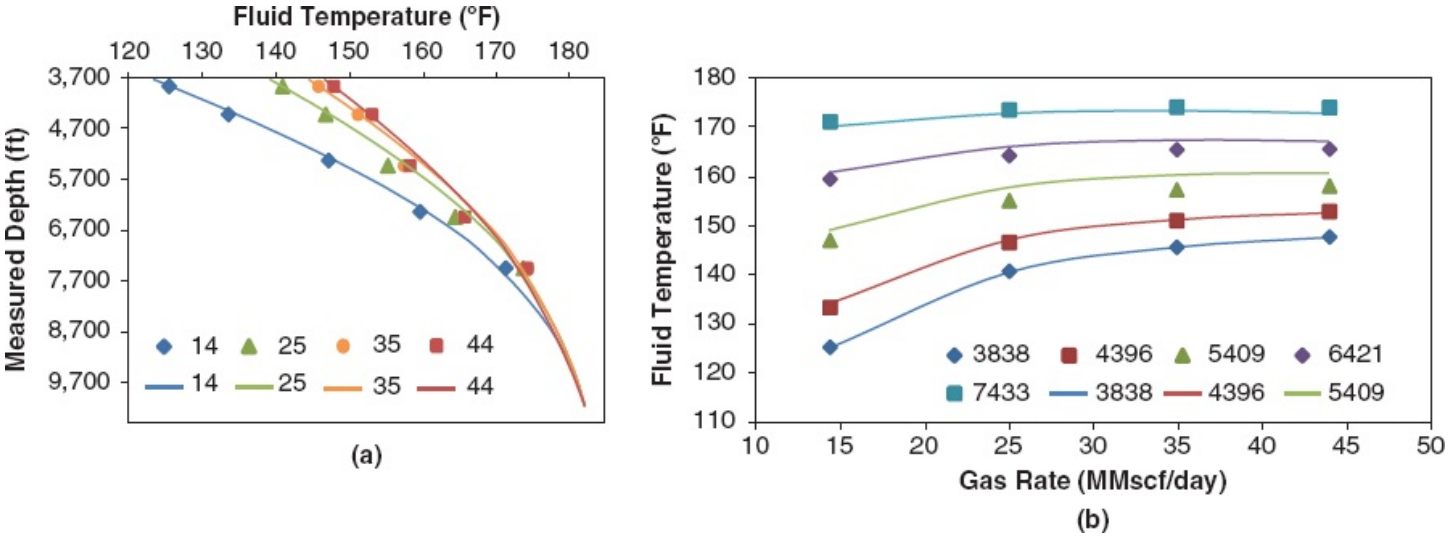

Fig. 7.3—History-matching time-lapse temperature profiles at various rates (a) and depth-dependent temperatures at various rates (b), Well 2. TVDSS = TVD subsea.

	Flow Rate (MMscf/D)			
	Rate 1	Rate 2	Rate 3	Rate 4
Computed	14.9	25.0	33.2	49.7
Measured	14.40	25.02	34.95	44.00
Error, %	3.29	0.00	–5.11	12.91

Table 7.1—Error estimation in computed rates, Well 2.

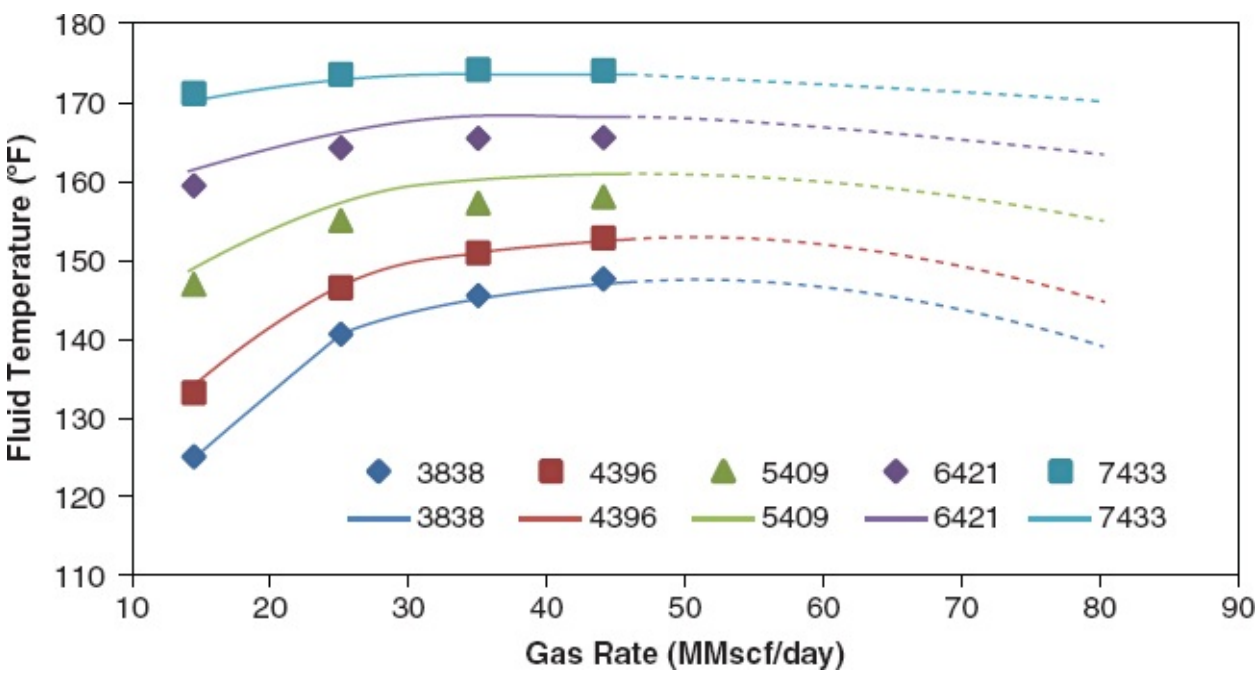

Fig. 7.4—The gas exhibits J-T cooling at higher rates, Well 2.

7.2.3 Rate Estimation With Unsteady-State Temperature Data. When production is initiated or when the production rate is changed, thermal transients set in that take much longer to stabilize than the pressure counterpart. The flow rate becomes stable soon after its initiation or change from one rate to another. However, corresponding temperature changes take a much longer time to attain stability; Fig. 7.2 illustrates this point for the time periods between 10 to 40 hours and between 100 to 120 hours. Although rates become steady almost instantaneously, temperature transients persist for quite some time. Obviously, Eq. 6.29 cannot be applied to temperature data for these periods.

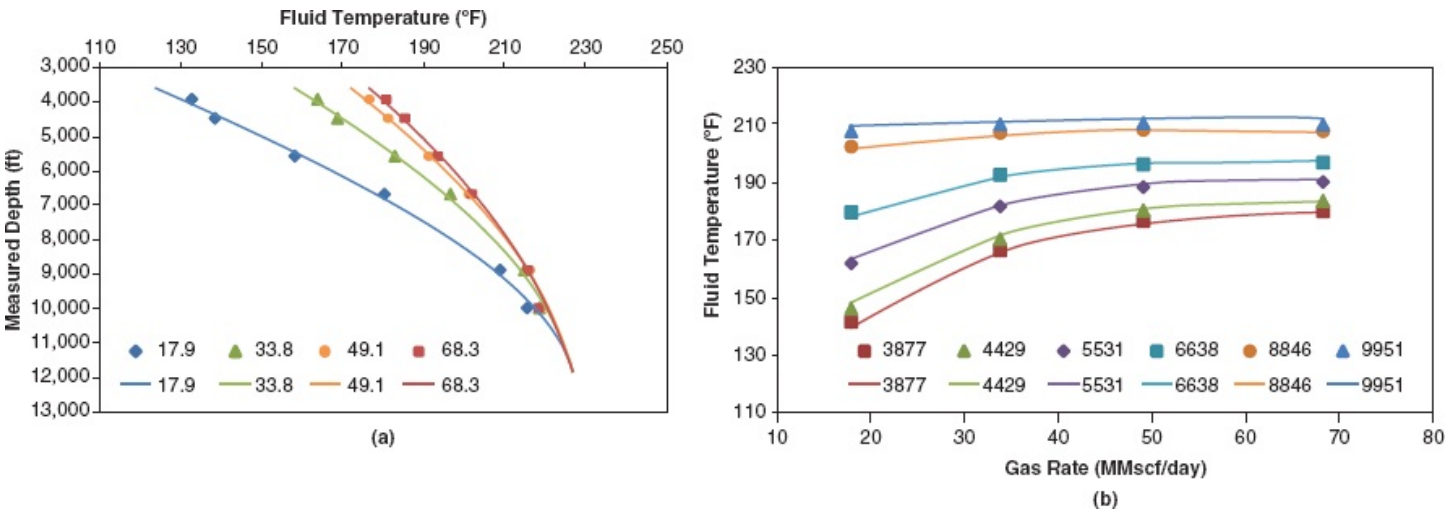

Fig. 7.5—History-matching time-lapse temperature profiles at various rates (a) and depth-dependent temperatures at various rates (b), Well 3.

	Flow Rate (MMscf/D)			
	Rate 1	Rate 2	Rate 3	Rate 4
Computed	15.4	31.8	49.1	77.1
Measured	17.89	33.80	49.10	68.30
Error, %	–13.1	–5.9	–0.06	12.91

Table 7.2—Error estimation in computed rates, Well 3.

We account for the effect of variable heat flux at any discrete time by adding ξ, which represents the superposition term, as shown in Appendix 7-B. Therefore, the following expression presents the transient flowing-fluid temperature:

$$T_f = T_{ei} + \frac{\left(1-e^{-at}\right)\left[1-e^{(z-L)L_R}\right]}{L_R}\left(\psi+\xi\right)+\left(T_{fi}-T_{ei}\right)e^{-at}, \quad (7.1)$$

where

$$\psi = g_G \sin\alpha + \phi + \frac{g\sin\alpha}{c_p J g_c} \quad (7.2)$$

and

$$\xi = -T_D\left(t_D - t_{D,n-1}\right)\frac{L_{Rn}Q_{n-1}}{2\pi k_e} + \frac{L_{Rn}}{2\pi k_e}\sum_{n-1} \quad \ldots\ldots (7.3)$$

Note that Eq. 7.1 differs from Eq. 6.29 in that it includes the exponentially decaying time function, $(1 - e^{-at})$; ~~so~~ meaning at very long time, the two equations become the same. In Eq. 7.1, L_R is given by Eq. 6.20 and the system constant *a* represents thermal storage for both the fluid and the tubulars; Appendix 7-B presents the details. The computational approach is similar to that used in the earlier section except that temperature at any depth is calculated using Eq. 7.1. Computation starts with a known pressure and temperature at the well bottom. A rate is assumed, and pressure and temperature are calculated for the next depth segment. We minimize the standard deviation in estimated temperature to estimate mass rate. This computation continues until the desired depth is reached for a given timestep. Next, we divide the flow period into time segments and compute similar temperature and pressure profiles at each timestep, thereby ensuring that the previous history is accounted for, as given in Eq. 7.1.

We then compare the final calculated temperature with those measured at different depth intervals. As expected, the solution becomes increasingly robust with the increase in fidelity of temperature response that occurs at shallower depths. The overall match provides flow rates by honoring the discrete temperature data at the end of each flow period. We also show the results for a case wherein only one shallow interval constituted the option for rate estimation even when data from discrete, stable rate intervals are available. Exploring this option has considerable merit in that in most instances the distributed-temperature profile is an exception rather than the norm.

***Well 4 Example*.** As discussed in the previous examples, we have multistation temperature and rate data for more than 100 hours from three different wells situated in a formation off the coast of West Australia. Temperature sensors embedded in the acoustic telemetry system at 11 depth locations approximately 1,500 ft apart in each well provided the distributed-temperature data over the entire test period with rates varying from zero to approximately 55 MMscf/D. Unlike the other two examples, this one illustrates application of the transient-temperature model for handling distributed-temperature data, as shown in **Fig. 7.6.**

As Fig. 7.6 indicates, formation of hydrates occurred in the wellbore during the flow period, as characterized by the dips in gas rates. Methanol injection mitigated this problem. However, the benefit of using temperature measurements for flow rate estimation becomes more evident here because the fluid temperature captured this anomaly. **Fig. 7.7** demonstrates that the model and the commercial simulator both successfully reproduced this signature.

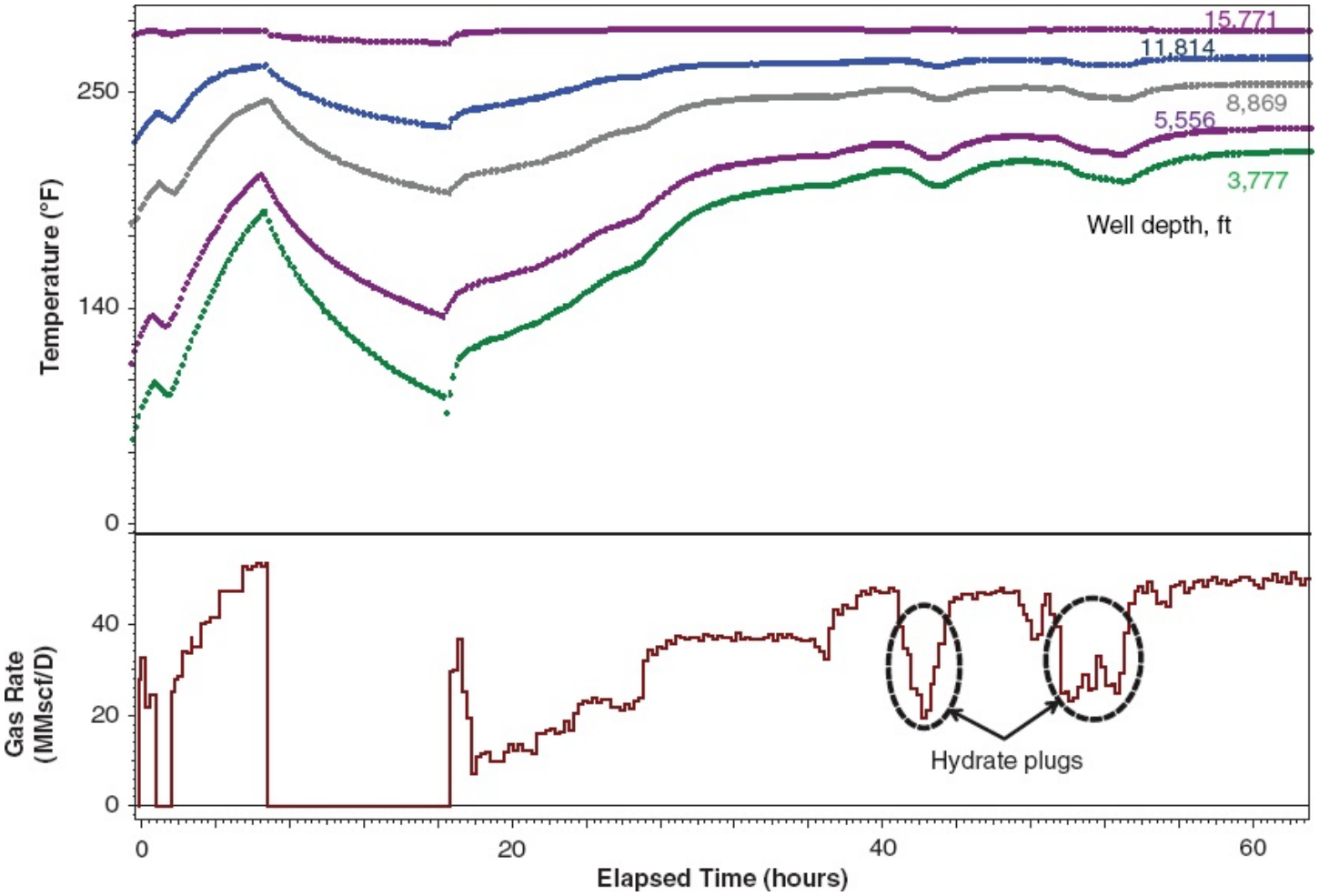

Fig. 7.6—Depth-dependent measurements of transient temperature in Well 4.

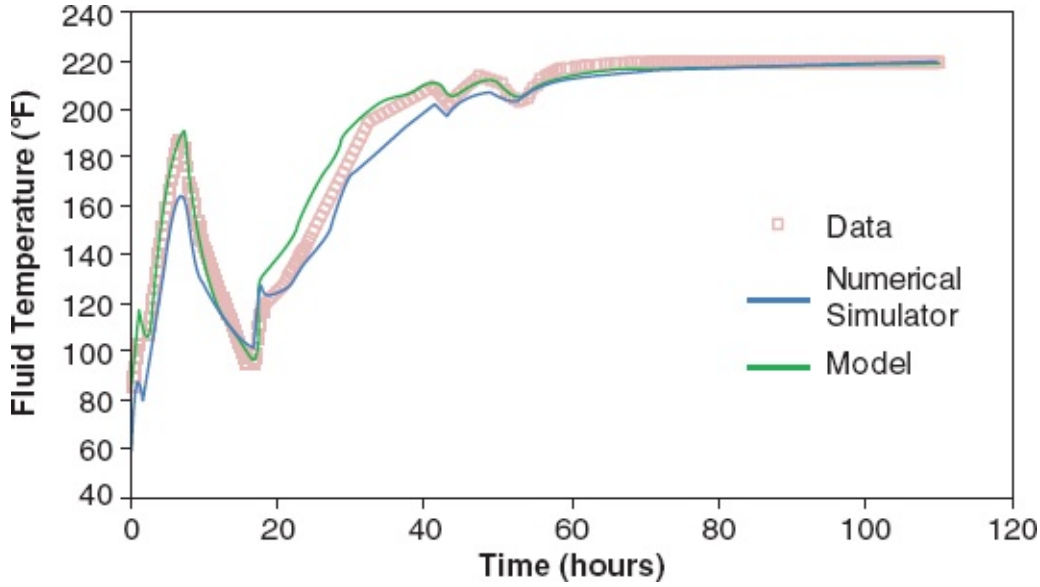

Fig. 7.7—History-matching transient-temperature profiles, Well 4.

Fig. 7.8a shows the history match of transient temperature profiles done at various depths. For clarity of presentation, only three depths are shown, but in reality we

have had 10 depths (each 1,500 ft apart) to anchor the model solution. As expected, the fidelity of the temperature response decreases with increasing depth. Yet, the decrease in flow rate is captured at greater depths as well. Such spatial data help in accurate estimation of the fluid flow rates because multiple data sets constrain the problem at hand. Fig. 7.8b presents the rate history related to temperature matches at various depths. As shown in Fig. 7.8b, the predicted rates closely follow those recorded with the multiphase flowmeter. The model's sensitivity enabled us to capture the flow rate restrictions around 42 and 52 hours.

A problem that often occurs during inverse modeling is solution nonuniqueness, which may originate from underdefining the problem. However, temperature data at multiple depths make up for the lack of underdefined parameters. That said, we cannot ignore that more often than not, such a wealth of data is unavailable in most test settings. Usually the temperature data are limited to the wellhead and bottomhole conditions. Therefore, we employed the same methodology discussed earlier on temperature data from just one depth nearest the mudline, which is construed as most appropriate for the analysis because of the largest temperature response.

Fig. 7.9a offers the results for the history matching of temperature estimates, and **Fig. 7.9b** presents the rate estimated on the basis of the match shown in Fig. 7.9a. As shown, the match quality for the temperature is not much different; however, the rate quality suffers slightly. This observation suggests that the model should be calibrated and anchored for a known rate to achieve more confidence in the prediction when using data from a single location.

Overall temperature match at various depths by honoring discrete temperature data at the end of each flow period allows rate estimation. **Fig. 7.10a** depicts the temperature data and estimates using the rigorous transient model (Eq. 7.1) for the early cleanup phase of Well 4. An important observation in **Fig. 7.10b** is that the smooth nature of the temperature profile may lead one to think that the rise in temperature resulted from the production period alone. That notion, however, is inaccurate. In fact, the cleanup-fluid flow rate changed significantly and irregularly over time. Fig. 7.10b provides a comparison between the estimated rates using the described methodology and the measured rates during the early cleanup phase in Well 4. As Fig. 7.10b points out, the transient temperature modeling allows for the determination of rate, and those rate fluctuations are captured effectively despite the steady overall increase of temperature.

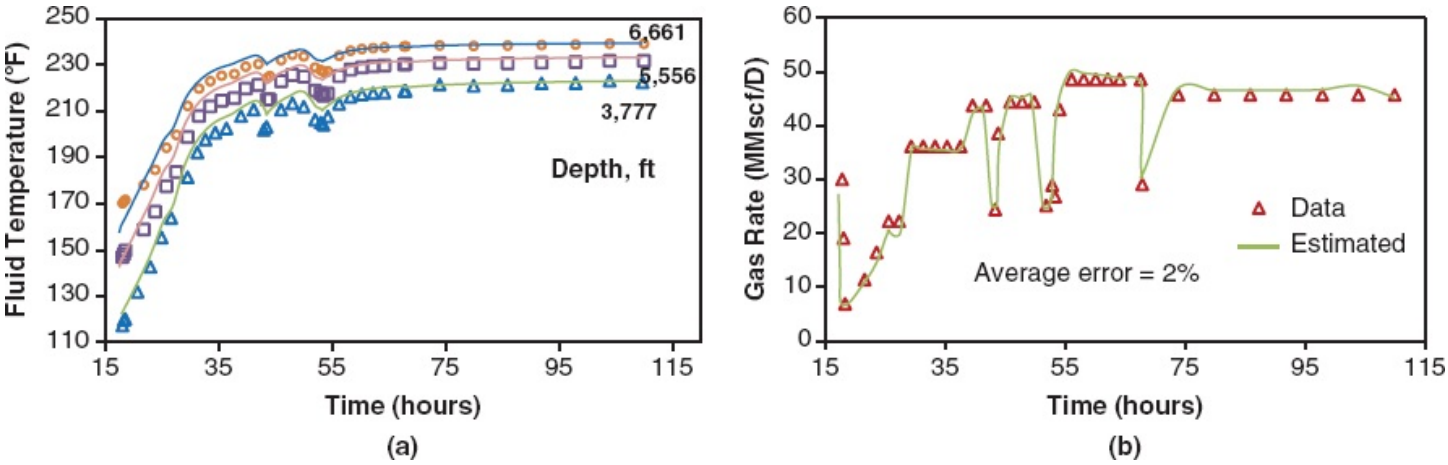

Fig. 7.8—History-matching transient-temperature profiles (a) and rate profile (b) using data at different depths, Well 4.

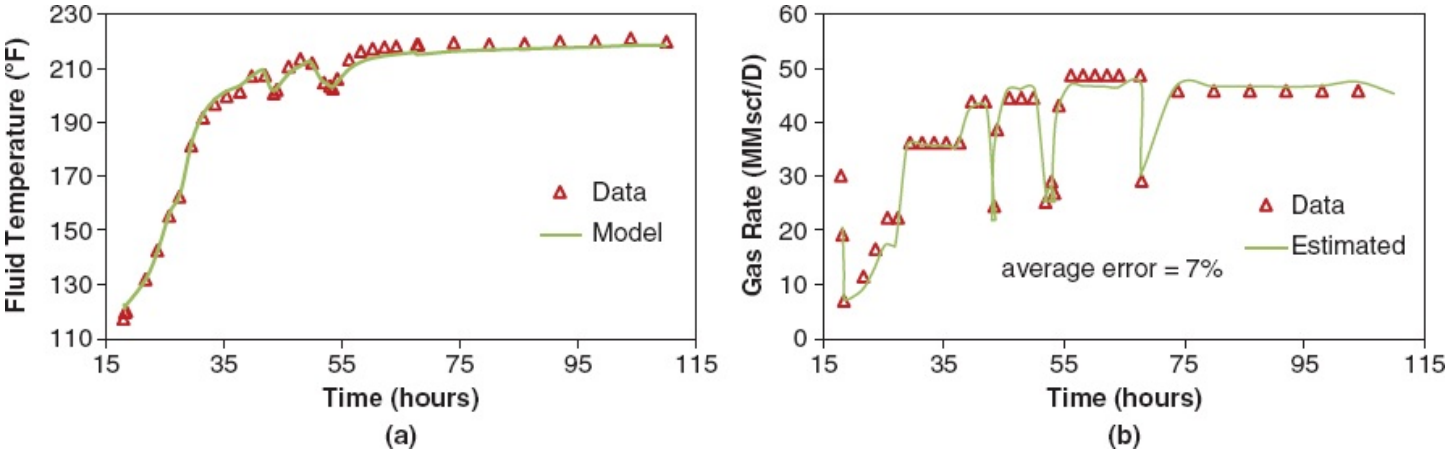

Fig. 7.9—History-matching transient-temperature profile (a) and rate profile (b) using data at the wellhead, Well 4.

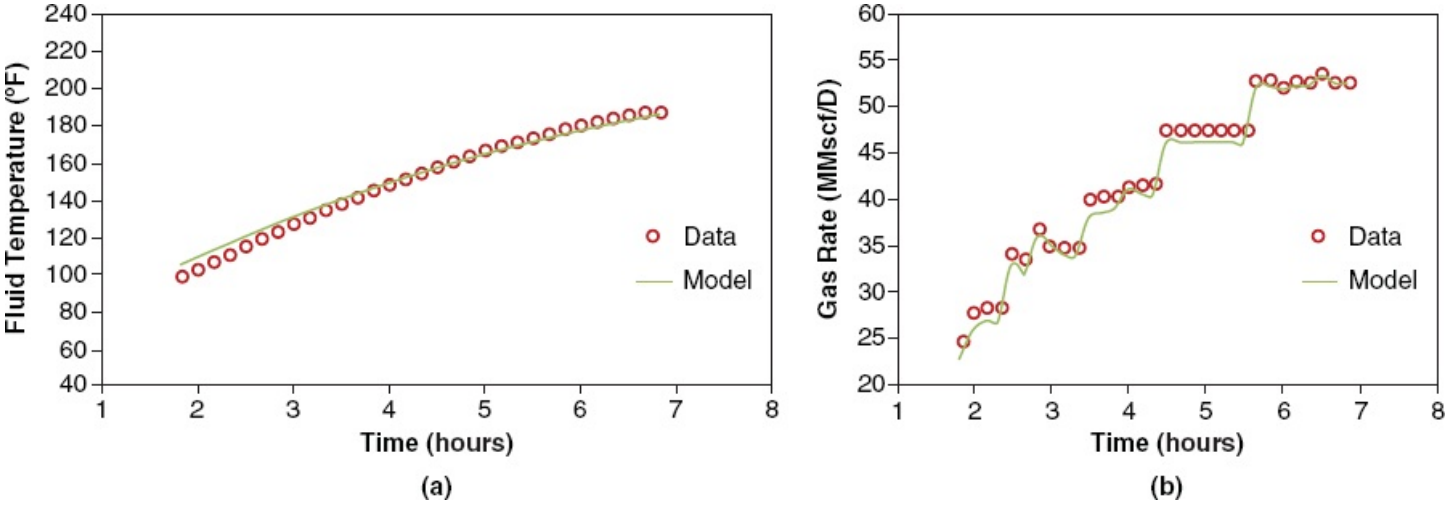

Fig. 7.10—Temperature history matching using a transient model (a) and comparison of measured and estimated rates during the cleanup phase (b), Well 4.

7.2.4 Rate Inversion: Joule-Thomson Effect. The previous sections discussed

methods for rate computation with measured pressure and temperature. **Fig. 7.11** shows another example of rate estimated from pressure and temperature data to point out an important phenomenon. This data set comes from a dry-gas field, discussed in Ismadi et al. (2012).

Fig. 7.11 also shows that rate increases slowly with WHT at lower temperatures, the WHT enabling accurate rate estimation. However, rate increases much more sharply with WHT at higher temperatures, causing estimation accuracy to suffer. For example, at a WHT of 145°F, an error of 1°F will translate into an error of approximately 0.25 MMscf/D in rate. However, at approximately 175°F WHT, an error of 1°F in the WHT will mean approximately 1.3 MMscf/D of error in rate estimation. Another way of looking at this temperature phenomenon is to note that at high production rates, the WHT is high and an increase in rate causes only a marginal increase in WHT.

A logical corollary of this observation is that at very high WHTs, the temperature derivative of rate will approach infinity and a solution for rate for a given WHT will be impossible. This point is made clear in **Fig. 7.12,** which has been constructed by estimating WHTs for a broad range of rates for the same well, as shown in Fig. 7.9. For a WHT of approximately 180°F, $dq/dT \approx \infty$ and estimating q from WHT becomes infeasible. For this well, WHT can never exceed 180°F. Fig. 7.12 also shows that for production rates above 55 MMscf/D, increased rates actually result in decreased WHT.

Note that the data for Fig. 7.12 were generated by estimating WHT given a flow rate, not by estimating the rate given the WHT. This distinction is important because an examination of the nature of Eq. 7-A-1 shows that given a rate, only one fluid temperature can be computed. However, the reverse is not true. That is, a given WHT may be satisfied by two very different rates, everything else remaining the same. This point is illustrated with **Fig. 7.13** for Field Example 1. Here, the WHT for a production rate of 20 MMscf/D is approximately the same as that for 35 MMscf/D. We term this phenomenon of rate reversal WHT reversal. Note that our model estimates these temperatures (given rates) with good accuracy. It is difficult to estimate rates when two rates can satisfy the same temperature data, however; in this circumstance, obviously, another piece of information is needed. If wellhead pressure (WHP) and bottomhole pressure (BHP) are both available, along with temperatures, these data can be used as the needed additional information to estimate the existing rate. For example, pressure drop for 35 MMscf/D flow rate is approximately twice as much as that for the 20-MMscf/D case, thereby allowing one to assign the correct rate, given the WHT. The difficulty with using this approach is that for near-vertical wells, pressure-drop variation with rate can be too small to allow accurate rate estimation.

Increasing WHT with increasing rate is intuitively understood. As the hot fluid from the well bottom moves up the wellbore, it loses heat to the surrounding formation. Heat loss from the fluid to the formation during production does not change much with rate. However, total energy carried with the fluid is higher at higher rates than at

lower rates. Therefore, temperature change from well bottom to wellhead is higher at lower flow rates than at higher rates. However, fluid temperature is also affected by J-T expansion. For gas wells at low pressures, J-T expansion leads to cooling that is proportional to the pressure gradient. Thus, at high flow rates, J-T cooling could be so high as to cause a decrease in fluid temperature with increasing rate, as shown in Fig. 7.13. A priori prediction of WHT reversal for any given well cannot be made without performing elaborate computations. However, because it occurs as a result of J-T cooling, which itself depends on J-T coefficient and pressure gradient, WHT reversal is more likely to occur in small-diameter rough pipes at low pressures and at high rates. Section 7.5 details a new analytical model dealing with J-T heating in oil reservoirs.

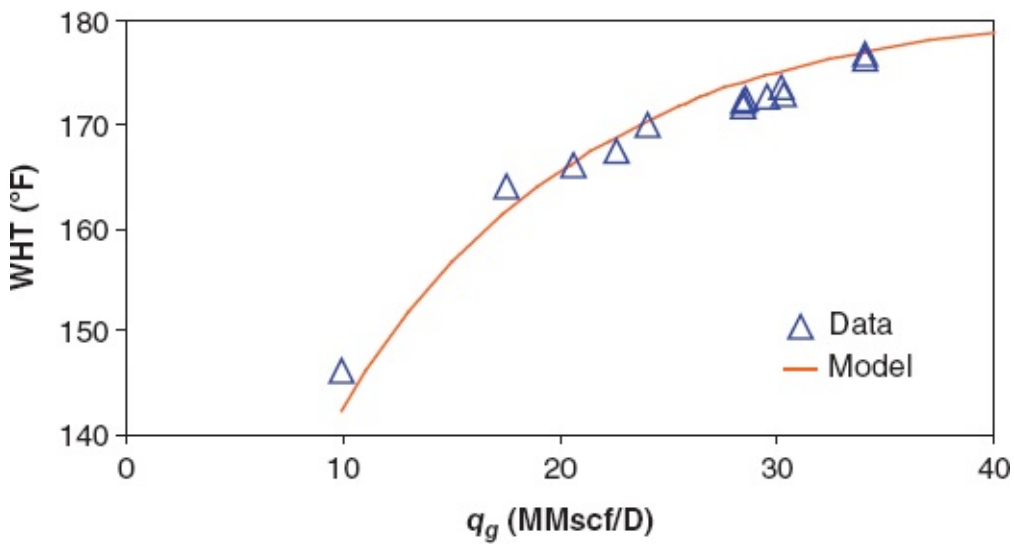

Fig. 7.11—Computed rates are in good agreement with measurement, Field Example 1.

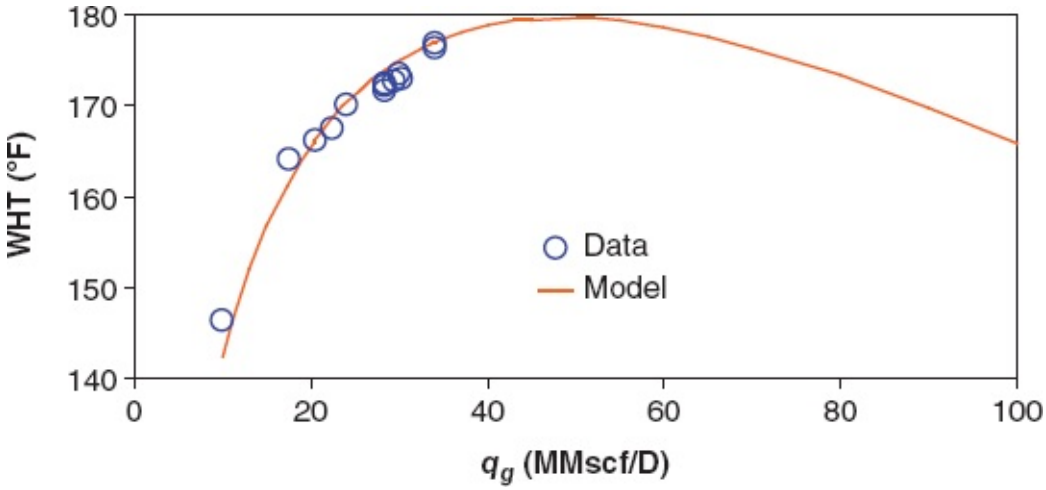

Fig. 7.12—Estimated WHT for a large range of flow rates, Feld Example 1.

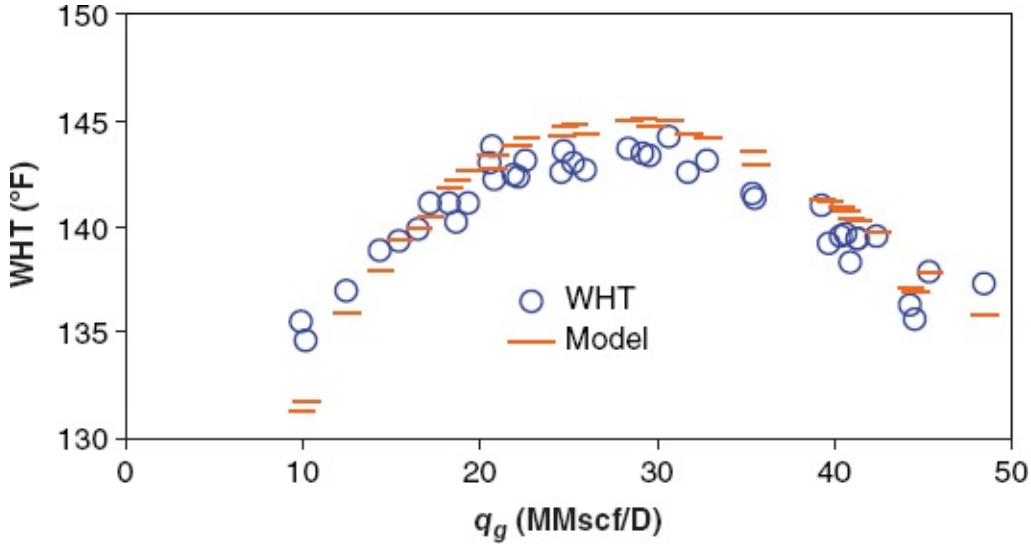

Fig. 7.13—Computing reliable rates despite temperature reversal, Field Example 1.

7.2.5 Rate Estimation During Initiation of Flow at Well's Inception. This section discusses the feasibility of conducting short-term transient tests at a well's inception to evaluate reservoir parameters that can aid in long-term testing if needed. As discussed by Hashmi et al. (2016), the design tool or the forward model allows for the generation of pressure and flow data for a given set of reservoir and wellbore parameters. Similar to conventional tests, pressure and flow rates are both required for test interpretation. Most published studies are intended for test analysis and are not conducive to design calculations or forward simulations. In contrast to previous studies, this one presents a simple model based on a mechanistic approach to design these short-term tests. Although simple, the model comprehensively accounts for the pressure drop in both the wellbore and the reservoir.

Wellbore/reservoir coupling is implicit in this modeling approach. The wellbore model includes the gravitational, frictional, and kinetic effects to allow estimation of rate from pressure data. The kinetic effects are often insignificant for liquids. However, frictional effects are very significant because of high initial flow rates. Most existing models for short-term tests neglect frictional effects. The reservoir model assumes infinite-acting radial flow, which works well considering the short duration of the test. Convolution of rate and pressure constitutes the main part of analysis, although short-term pressure analysis, considering just the total accumulated fluid before shut-in (Soliman 1986), is also used for comparison.

***Slug Model*.** The slug model is ideal for underpressured reservoirs in which the fluid will not reach the surface without supplementary techniques, such as artificial lift. At the inception of such a well, the well is perforated and the tester valve opened. The consequent liquid influx inside the wellbore continues until the static head equalizes the reservoir pressure. Such a test can be designed easily with the use of static and other pressure-drop components in the wellbore and the flow equation in the reservoir. The model accounts for all fluids inside the wellbore, calculating the pressure at bottomhole, p_{wf}, at each timestep. The BHP is then matched with the flow

equation, thereby estimating rate, given reservoir parameters. Note that the BHP is the sum of the gas pressure in the chamber, p_g, plus the pressure exerted by any water column present in the wellbore, p_w, and the pressure exerted by reservoir fluid coming into the wellbore, p_{rf}. The following expression was used to calculate the BHP in the wellbore:

$$p_{wf} = p_g + p_w + p_{rf} \quad (7.4)$$

Appendix 7-C provides details about the components of Eq. 7.4. The reservoir flow equation used includes the rate superposition effects with the infinite-acting radial flow model. Any reservoir model can be substituted for the problem; however, given the short duration of the test, this approach appears prudent. The following expression allows computation of sandface pressure:

$$p_{wf} = p_i - q_n m' \left\{ \sum_{j=1}^{n} \left[\left(\frac{q_j - q_{j-1}}{q_n} \right) log\left(t_n - t_{j-1}\right) \right] + A \right\}, \quad (7.5)$$

where

$$m' = \frac{162.6\mu}{kh} \quad (7.6)$$

and

$$A = log \frac{k}{\phi \mu c_t r_w^2} - 3.23 + 0.869s \quad (7.7)$$

The two pressure relationships, shown in Eqs. 7.4 and 7.5, allow estimation of the bottomhole flow rate.

Computation starts with a known fluid level in the wellbore or with a known BHP at the start of the test. Thereafter, pressure components for each timestep are calculated using the different pressure components in the wellbore. Next, the BHP is calculated using the design parameters of the reservoir—such as permeability, porosity, and compressibility—and the reservoir flow equation. Equating the two sources of pressure yields the desired flow rate. This computation is repeated at each timestep, resulting in the desired time-dependent pressure and rate profiles.

Figs. 7.14a and 7.14b present the schematics for a slug and a closed-chamber test, respectively. With the rise in the fluid level in Fig. 7.14a, the BHP increases. This pressure rise, in turn, reduces the drawdown with time and brings about a consequent decline in flow rate. Eventually, the accumulated fluid in the wellbore kills the relatively underpressured reservoir, leading to a cessation of flow.

Figs. 7.15a and 7.15b illustrate the typical responses for slug and closed-chamber tests. As in Figs. 7.14a and 7.14b, with the rise in the fluid level the BHP increases, which reduces the drawdown with time and results in a declining flow rate. In the case of a slug test, the accumulated fluid in the wellbore kills the

underpressured system, whereas in the case of a closed-chamber test, the chamber pressure increases dramatically along with the rise in static fluid pressure, thereby generating a spike in the BHP.

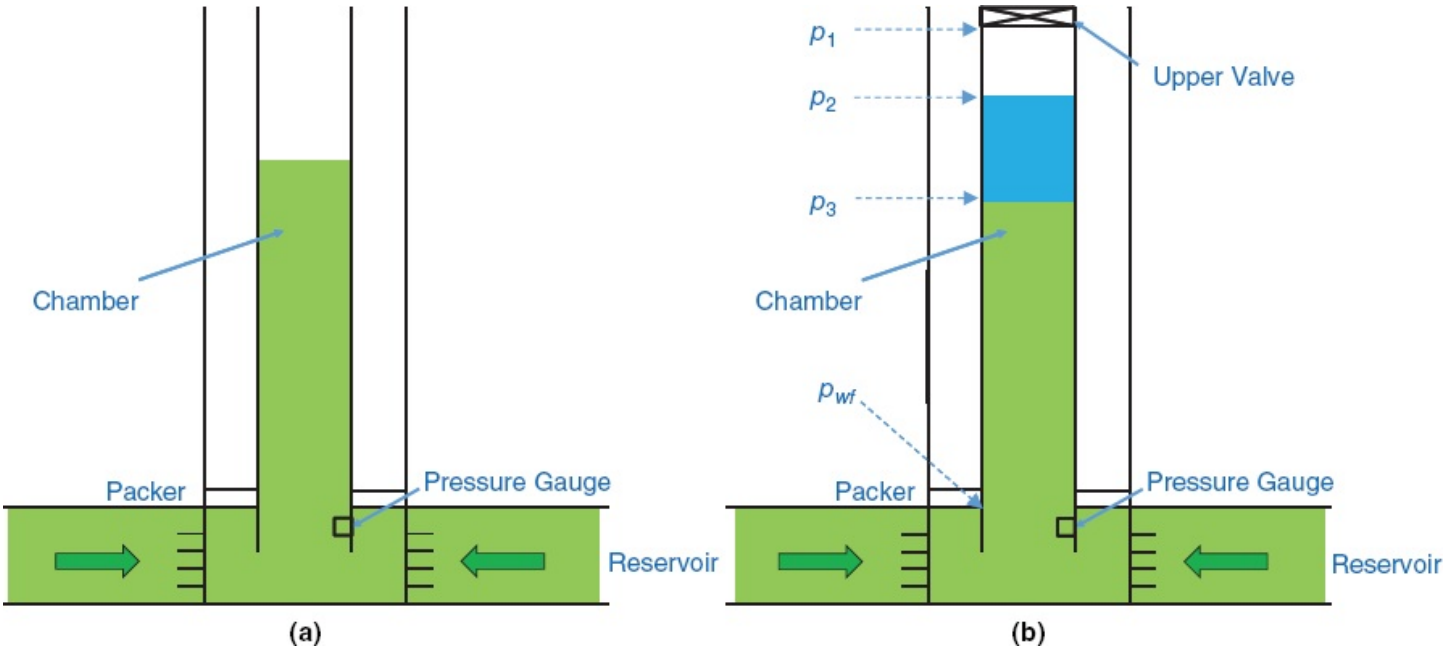

Fig. 7.14—Schematic for slug (a) and closed-chamber (b) tests.

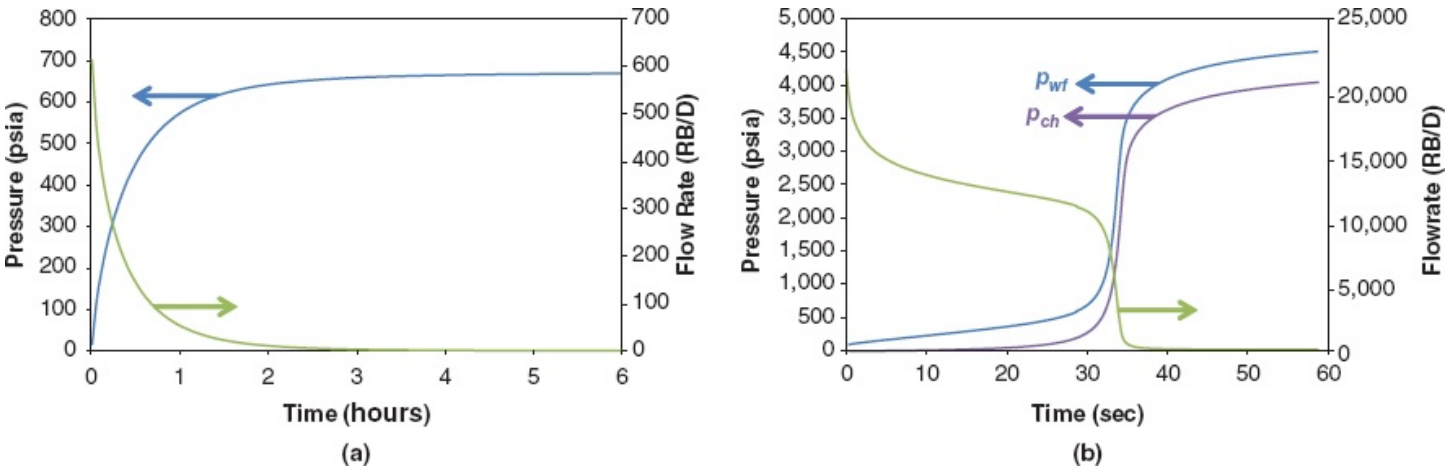

Fig. 7.15—Typical pressure/rate responses for slug (a) and closed-chamber (b) tests.

***Closed-Chamber Model*.** Our closed-chamber model is similar to the slug model. However, in this model, the well is shut in either at surface or at a specific depth in the wellbore, hence the term "closed-chamber." Fig. 7.14b illustrates the physical mechanism for a closed-chamber test in which fluid enters the wellbore after perforation, thereby increasing the BHP. However, in this case because the well is shut in at the head (or some other appropriate location), the gas between the rising-fluid column and the valve becomes trapped. Consequently, this chamber of gas is compressed with the increase in fluid level, causing a dramatic increase in pressure and a corresponding decline in flow rate.

This closed system allows handling of reservoirs with diverse geopressure gradients. Intrinsically, the closed-chamber system demands a different treatment for wellbore pressure computation. For instance, gas compression in the chamber largely influences the static pressure component in the wellbore, which, in turn, increases the chamber pressure and BHP. Appendix 7-C provides details of these calculations. Computation proceeds as it would in a slug test. However, in a closed-chamber test, the pressure stabilization takes place after the chamber pressure has stabilized. Just as in the slug test model, this model also allows for forward design calculations to assess various design variables, such as the chamber length and static backpressure at the start of test. Test design calculations are critical to closed-chamber tests because significant gas compression in the chamber can compress the test duration to seconds in highly conductive formations. This ability to design any test by forward modeling is one of the strengths of this simple yet accurate model.

7.3 Thermal Effects Influencing Pressure Response in Off-Bottom Gauges

A buildup test, in which a producing well is shut in and transient BHP data are analyzed, allows estimation of formation parameters such as permeability, static and non-Darcy skin, and average formation pressure. Similar information may be obtained by running a pressure drawdown test whereby a previously shut-in well is suddenly started. In either case, pressure-transient data are needed at the sandface.

Although near-sandface pressure measurements become a necessity for unambiguous interpretation, placement of permanent downhole sensors is often dictated by completion hardware and other logistical issues. As a consequence, a pressure gauge is often placed hundreds of feet away from the point of fluid entry, requiring estimation of gauge pressure to sandface condition. Translation of pressure at a given point in the well to some other place is nontrivial because with time, temperature transients change fluid properties, especially density and viscosity. Whether pressure data collected in this way are free of wellbore thermal effects remains in question. From a transient-pressure analysis standpoint, flow rate for a given gauge location plays the most dominant role in distorting pressure response. In other words, the larger the rate, the larger the thermally induced distortion. Consequences of potentially inaccurate pressure data can be significant for both pressure- and rate-transient analyses.

Studies dealing with thermally induced pressure distortion are very few. Kabir and Hasan (1998) showed how off-bottom gauge measurements can induce significant errors in pressures, thereby posing serious interpretation difficulties. In other words, when temperature diffusion dominates pressure diffusion, pressure may decline during a shut-in test and increase during a flow test. Consequently, standard interpretation techniques cannot be used. Both forward and reverse simulations with a coupled wellbore/reservoir simulator accounting for energy transport in the wellbore appear to be the most prudent approach.

Advances in coupled wellbore/reservoir modeling have been reported with the introduction of a semianalytical energy transport equation in the wellbore (Hasan et al. 2005; Izgec et al. 2007). Significant gain in computational speed results when efficient coupling of finite-difference forms of mass and momentum equations occurs with the semianalytical energy equation. Transient-temperature model development is presented in Chapter 9; we use the results from that chapter in the following.

This section attempts to address the gauge placement issue, permanent or otherwise, in a difficult environment, such as in deep water. The intrinsic issue is significant heat transfer potentially distorting pressures in off-bottom gauges, thereby yielding moderate-to-large errors while conducting conventional transient analysis. We probed both oil and gas flow problems in a systematic way to arrive at simple design tools for rapid evaluation of acceptable gauge depth. In this context, the role of a secondary gauge located at the mudline is also examined.

7.3.1 Model Validation With Field Example. Tahiti Field sits in more than 4,000 ft of water in the Gulf of Mexico and is a three-way anticlinal structure trapped against salt. The primary pays are Miocene turbidite sheet sands at depths ranging from 24,000 to 27,000 ft TVD. The field was discovered in April 2002 by the GC 640 #1 and appraised in 2003–2004 with the drilling of two additional wells, both with major sidetracks. In addition, a surface flow test was conducted in the original discovery well over a 7-day period in August 2004. The flow test data from Izgec et al. (2009) were used to verify the simulation model.

Fig. 7.16 presents raw pressure/rate data for the entire test, including the cleanup period. As shown, multiple drawdown tests were conducted in a decreasing-rate sequence before the final buildup occurred. The rigorous approach of tackling both downhole and off-bottom pressure and temperature matching is detailed in the next subsection.

***Modeling Field Data*.** The 26,500-ft well is represented by 46 grid cells in the simulator, each of which is approximately 650 ft long. Reservoir pressure is 19,530 psi, and reservoir temperature is 200°F. The geothermal gradient and seawater temperature profiles used in the model are given by **Fig. 7.17.**

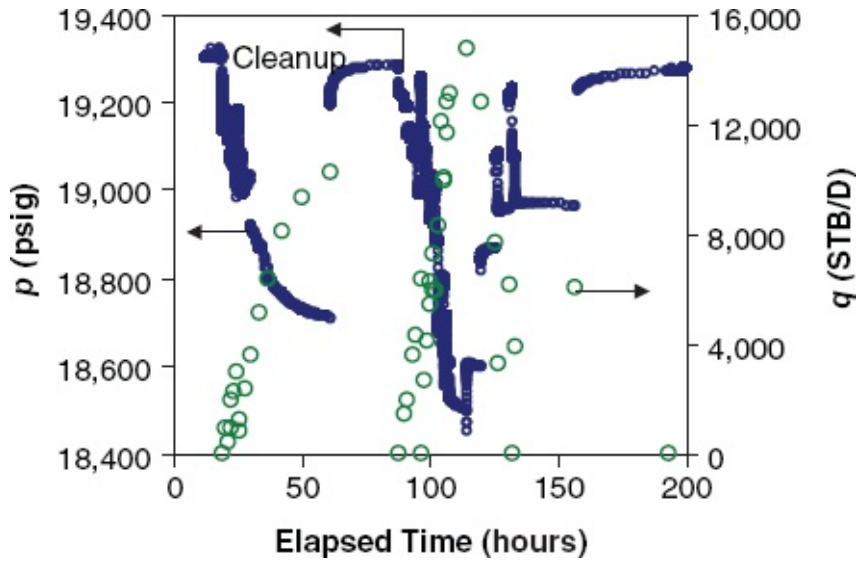

Fig. 7.16—Test history showing cleanup period.

The seawater temperature profile is linear from 40°F at the mudline to 75°F at the surface. The mudline of the well is located at approximately 4,000-ft water depth. This water column acts as a heat sink, and the produced fluid will cool considerably while passing through this region, regardless of the producing rate.

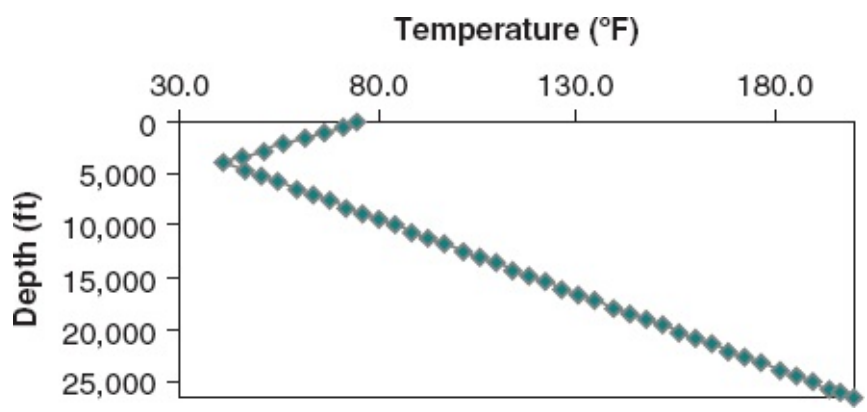

Fig. 7.17—Geothermal gradient and seawater temperature profile.

This well also passes through 10,500 ft of salt layer. A vacuum-insulated tubing section is installed to prevent annulus pressure buildup owing to thermal expansion of fluids. The vacuum-insulating tube has been accounted for in the simulation model for accurate heat-transfer calculations. Beyond the cleanup period, data collected during the 60-hour test period were sandface pressure, surface WHP and WHT, and flow rates. **Fig. 7.18a** shows the measured and input production rates. The "surface" WHP/WHT measurements occur at 9,625 ft from the surface, at roughly the midpoint of the flow string. Fig. 7.18b compares the measured and simulated BHPs for the 60-hour multirate test.

Fig. 7.19a compares the measured and calculated temperature response. The temperature data were collected at the midpoint of the flow string. The initial

discrepancy between the measured and calculated temperature profiles is the result of another flow period and subsequent shut-in period that were not simulated. As shown in Fig. 7.16, a cleanup period involving flow and shut-in lasted approximately 42 hours. Consequently, the wellbore fluid temperature distorted the thermal equilibrium between the formation and the wellbore. No attempt was made to match the cleanup period because predominantly completion fluids were produced. Fig. 7.19b shows the pressure match at the same location but does not reveal any serious issues even though we ignored the cleanup period. Overall, our ability to reproduce pressure response at the bottom of the well and at the wellbore midpoint and the temperature at the wellbore midpoint instilled a great deal of confidence to move forward with parametric studies.

Optimal Location of Permanent Downhole Gauge. Ideally, pressure gauges should be placed as close to perforations as possible to ensure that data remain unaffected by thermal effects, friction in the tubing between the perforations, and the gauge and phase segregation during shut-ins. In addition, restrictions in internal diameter of the tubing string associated with downhole equipment may add to pressure drop at high rates. For most types of downhole pressure gauge installations without sand control, one can place a mandrel with pressure gauges near the perforated zone using a feed-through packer, as depicted on the right side of Fig. 7.20. In a set of stacked completions without sand control, the gauges can be run in the specific producing zone by using multiple feed-through retrievable production packers.

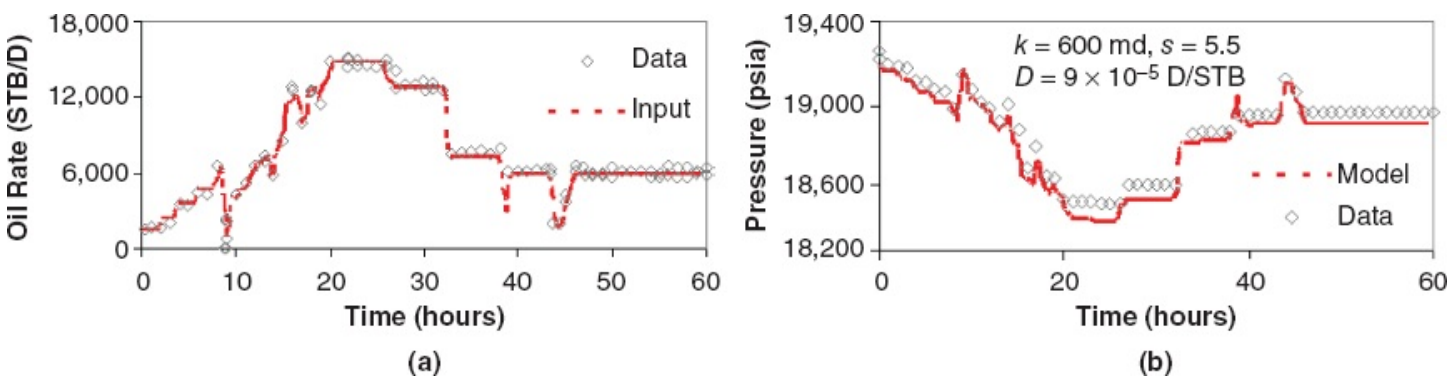

Fig. 7.18—Mimicking oil production rate input (a) and matching BHP (b).

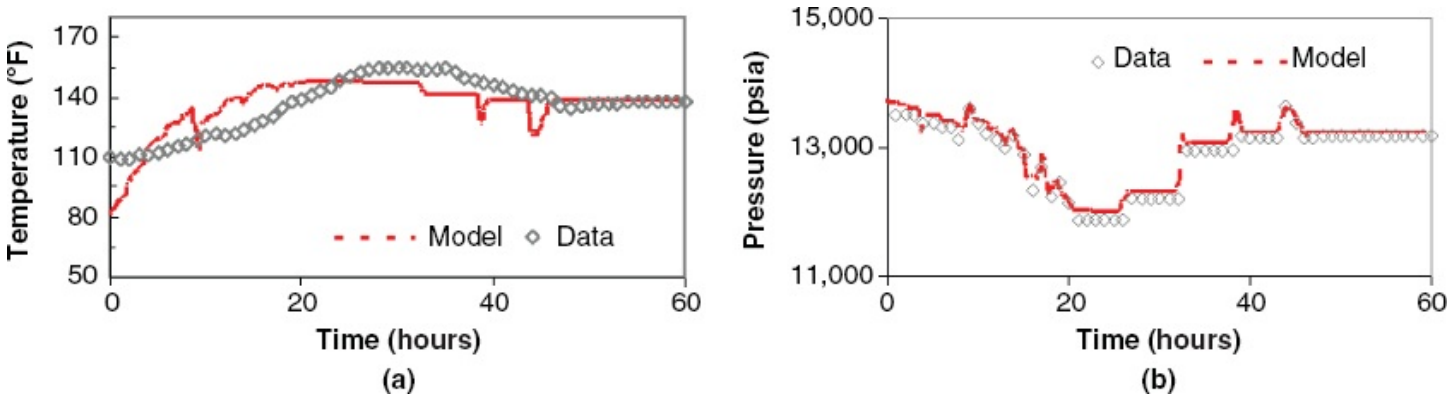

Fig. 7.19—Matching temperature (a) and pressure (b) at the midpoint of the flow string.

Getting gauges close to the perforations in a frac-pack well is challenging in that a service packer below the retrievable production packer does not allow feed-through applications. The location of the service packer below the retrievable production packer dictates the depth of the bottom-most downhole pressure gauge, as shown on the left side of Fig. 7.20.

There are some circumstances for which a feed-through packer system may be unavailable (e.g., the Tahiti example above) and some operational conditions for which a simpler and robust equipment design may be chosen—for example, in a very deep, high-pressure/high-temperature environment. The same is true in deepwater exploratory-well testing. A temporary downhole gauge system may be run with control lines to provide surface readout instead of running wireline in the hole. For these installations, the decision may be made to place the gauge mandrel above the packer to maximize reliability in a high-profile operation.

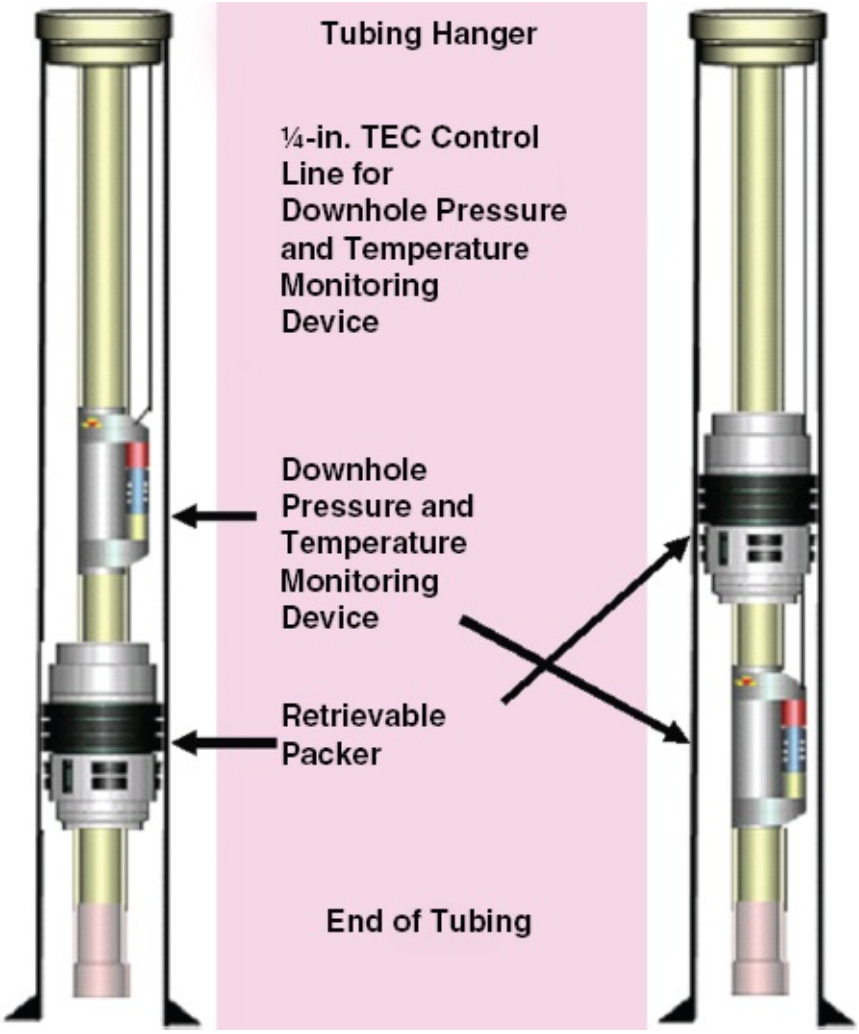

Fig. 7.20—Downhole gauge placement configurations.

In all these cases, the value of better-quality data must be weighed against the

practicality of the completion design, the increase in risk with additional completion complexity, and the cost incurred. The simple correlations for design of gauge placement developed in this paper should prove useful when planning a new completion or when attempting to cope with the effect of offset gauge placement on analysis results.

Drawdown Response in Oil Wells. A well model similar to the Tahiti offshore well with 4,000 ft of water depth is used for drawdown and buildup simulations. We investigated the effect of gauge location on calculated formation parameters by analyzing pressure data at increasing distances away from the sandface.

Continuously changing flowing-fluid temperature during both drawdown and shut-in affects the wellbore density profile. **Fig. 7.21a** shows fluid temperature and density profile when the well was producing at 5,000 STB/D. As the produced fluid approaches the mudline, a significant amount of heat is lost to the seabed, leading to changes in flowing-fluid properties. Fig. 7.21b shows the increasing viscosity profile around the mudline in relation to the decreasing fluid temperature. The combined effects of increased density and viscosity around the mudline cause some fluctuations, even in a steady-state flow profile. As a consequence of thermal effects, the rate of pressure change at any point in the wellbore does not necessarily reflect the same at the sandface for single-phase oil. Therefore, we cannot readily use pressures at any point of the column to extract formation parameters at all times.

For single-phase oil experiencing drawdown, we demonstrate this point by plotting the changes in semilog slope as the virtual gauge moves up in the wellbore. **Fig 7.22** shows the calculated error in semilog slope as a function of depth. The percentage error in the slope increases with decreasing depth and reaches its maximum near the mudline. Thereafter, the error remains constant. For this particular case, it was possible to identify the radial flow region on the derivative plot up to the mudline, unlike some of the buildup runs, as we discuss later.

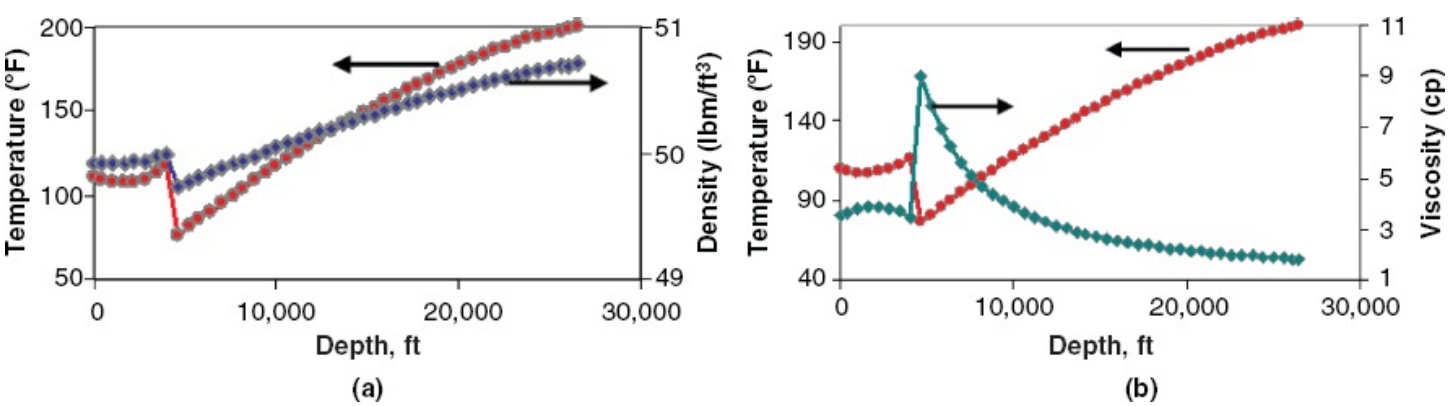

Fig. 7.21—Temperature and density (a) and viscosity (b) profiles in the wellbore.

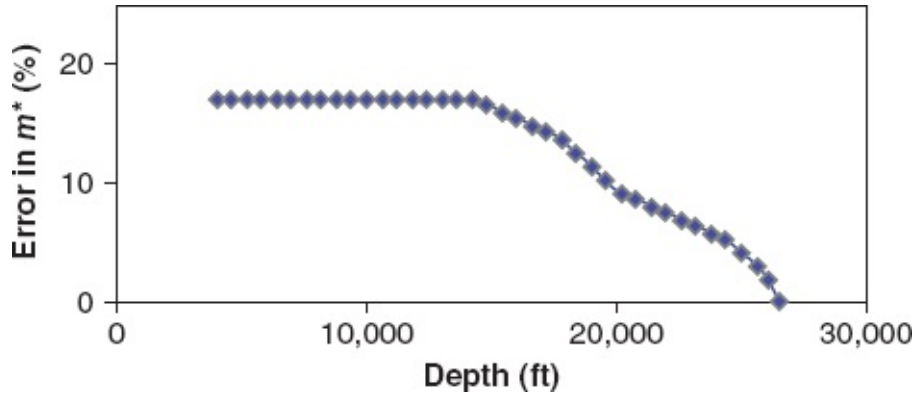

Fig. 7.22—Error in semilog slope as a function of depth.

Variable	p-10	p-50	p-90
kh, md-ft	50 × 250	80 × 250	600 × 200
q, STB/D	5,000	10,000	25,000
Y_o	25	30	32
D_G, ft	20,000	1,500	400
k_{an}, Btu/hr-ft-°F	0.1	0.2	0.3
g_T, °F/ft	1	1.2	1.4
θ, degrees	45	30	0

Table 7.3—Range of sensitivity variables for design of experiments

We used experimental design to investigate the effect of different variables on the semilog slope. The variables used in experimental design are perforation-to-gauge distance (D_G), permeability-thickness product (*kh*), geothermal gradient (g_G), flow rate (*q*), oil gravity (γ_o), deviation angle (θ), and thermal conductivity of annular fluid (k_a). **Table 7.3** provides the range of variables used to generate the experimental design table. This table attempts to capture the reservoir properties generally encountered in the Gulf of Mexico. Note that the entire range of variables cannot be encapsulated because nonphysical reservoir/wellbore models are generated that do not lend themselves to a solution.

Fig. 7.23 displays the Pareto chart for drawdown using the Plackett and Burman (1946) statistical design of experiments. A similar approach is described by Hasan et al. (2005). The Pareto chart shows that perforation-to-gauge distance (D_G) has the biggest effect on percent error in semilog slope, followed by permeability-thickness product (*kh*) and deviation angle (θ). Note that the vertical line signifies the 95% confidence interval. In other words, one can develop a simple linear correlation with the first three variables influencing the semilog slope, *m**.

Nonetheless, the following correlation includes all the variables studied, for completeness:

$$E_{m*} = -2.521 - 3.759\times10^{-4}\times q + 8.301\times10^{-4}\times D_G + 7.706\times10^{-5}\times kh + 0.039\times g_T + 0.234\times\gamma_o + 14.302\times k_{an} + 0.177\times\theta \quad (7.8)$$

As long as radial flow can be identified on the derivative plot, one can calculate the error on the semilog slope by using this correlation for the variable range presented in Table 7.3. One can easily show that the error in slope estimated with Eq. 7.8 may be translated into permeability using the following relationship:

$$k = \frac{162.6qB\mu(100 - E_{m*})}{100hm*} \quad (7.9)$$

Let us illustrate applications of Eqs. 7.8 and 7.9. Consider a drawdown test for a well with an off-bottom gauge for which a slope of 14 psi/log cycle was estimated corresponding to the production rate of 5,000 STB/D. Fluid and formation properties are B_o = 1.2, μ = 2.6, and h = 218 ft. Using Eq. 7.8, we estimated an error of 15% for this flow problem. The corresponding permeability from Eq. 7.9 turns out to be 706 md, which compares favorably with the input value of 700 md. However, if one were to estimate permeability directly with the thermally distorted slope of 14 psi/log cycle, 831 md would result.

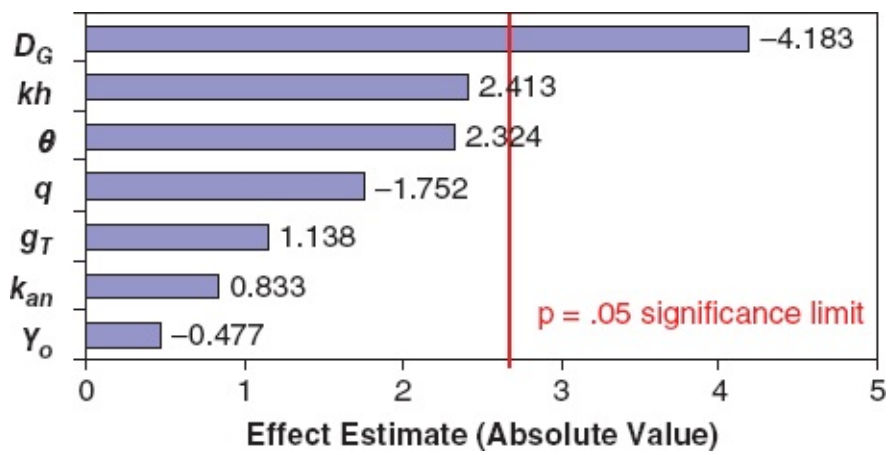

Fig. 7.23—Pareto chart for oilwell drawdown for the dependent variable E_{m*}.

Buildup Response in Oil Wells. In buildup simulations, we observed that the radial flow regime becomes difficult to identify as pressure is gathered at increasing distances from the sandface. The reason for this behavior is twofold. After the valve at the mudline is completely closed, the mass flow rate at the upper parts of the wellbore diminishes rapidly. By contrast, the incoming flow at the sandface maintains a velocity profile up to certain depth, thereby creating a fully transient profile throughout the wellbore. Once mass flow rate ceases, the temperature of the wellbore fluid decreases rapidly, especially around the mudline, thereby triggering rapid changes in fluid properties.

For a buildup test, continual changes in fluid properties combined with afterflow may mask the radial flow regime or lead to an erroneous interpretation on a log-log plot. Presence of gas, such as in two- or three-phase flow, makes the situation even more complicated. **Fig. 7.24a** presents the percent error on a semilog slope for a buildup test conducted at different locations in the wellbore. Also, the error on slope from a drawdown run, as shown in Fig. 7.24a, is included for comparison. Notice that the error curve for the buildup tests disappears after reaching a certain depth. That is because radial flow cannot be identified beyond 3,000 ft from the sandface, implying that no meaningful information can be extracted. Fig. 7.24b shows the derivative plot generated at 3,000 ft away from the sandface. Duration of the buildup test would not change the signature on the log-log plot in this case because at the end of the run the BHP is only 1 psia lower than the initial reservoir pressure.

Fig. 7.25 presents a Pareto chart for buildup tests using the Plackett and Burman (1946) design, with the same variables identified earlier in Table 7.3. Note that only the upper limit for perforation-to-gauge distance needed to be adjusted because radial flow did not develop beyond 3,000 ft.

For the buildup runs, the most-influential variables affecting the dependent variable m^* are the perforation-to-gauge distance and permeability-thickness product, as signified by the 95% confidence limit. However, the third important variable for buildup runs turned out to be the production rate just before the shut-in as opposed to deviation angle in drawdown runs.

Drawdown and Buildup Responses in Gas Wells. For the single-phase gas simulations, we used an offshore wellbore model with the same water depth to investigate mudline issues during gas production. **Table 7.4** presents the range of variables considered in this study. Flow and shut-in periods of 30 and 20 hours, respectively, were used for all simulation runs.

Because gas pressure/volume/temperature properties are much more sensitive to changes in temperature, flow and shut-in periods both exhibited trend reversals during simulations at increasing distances from the sandface. Because gases have intrinsically much lower heat capacity and, therefore, lower enthalpy than a liquid, heat dissipation occurs much faster, leading to trend reversal of pressure. **Fig. 7.26a** compares the BHP and mudline pressure for flow and shut-in periods.

During drawdown, pressure at the mudline *increases* even though the BHP declines in accord with normal behavior. Conversely, during a shut-in period, pressure at the mudline *declines* continuously. This trend reversal at the mudline is a direct consequence of temperature response, which eliminates the possibility of extracting any formation parameters with conventional pressure-transient analysis. Similarly, this inverted pressure behavior precludes one from doing wellhead-to-well-bottom pressure conversion or reverse simulation. Fig. 7.26b shows the derivative plot for the shut-in period generated with pressure data collected at 3,000 ft away from the sandface. Here, the radial flow is hard to discern.

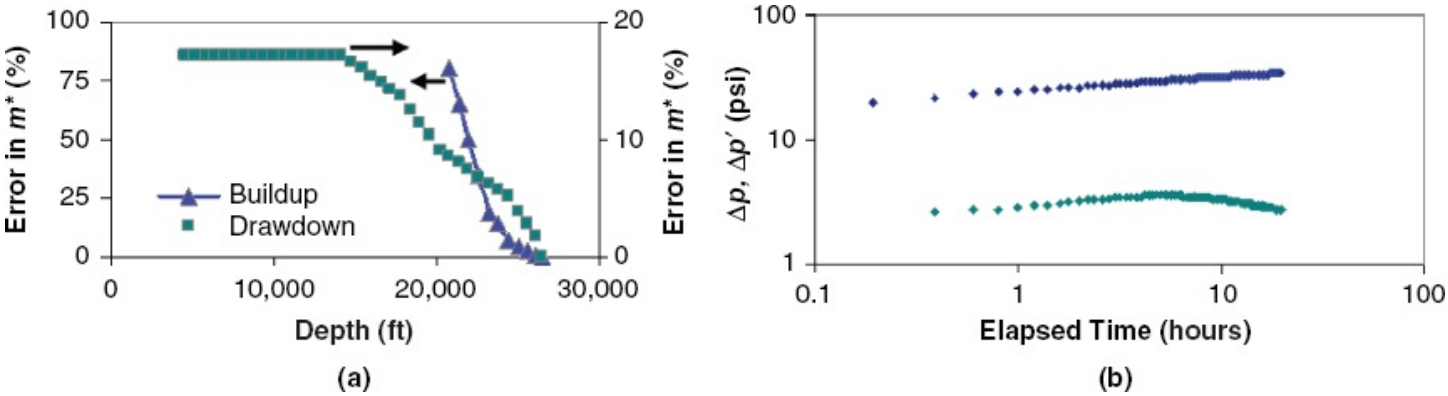

Fig. 7.24—Error in semilog slope for drawdown and buildup as a function of depth (a) and log-log response for a drawdown in an oil well (b).

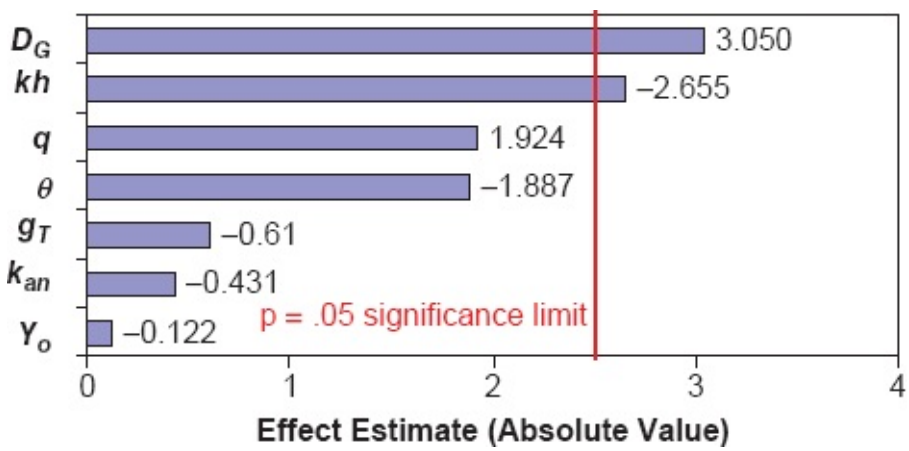

Fig. 7.25—Pareto chart for oilwell buildup for the dependent variable E_{m*}.

Variable	p-10	p-50	p-90
kh, md-ft	10 × 250	80 × 250	600 × 200
q, MMscf/D	10	25	50
Y_g	25	30	32
D_G, ft	20,000	1,500	400
k_{an}, Btu/hr-ft-°F	0.1	0.2	0.3
g_T, °F/ft	1	1.2	1.4
θ, degrees	45	30	0

Table 7.4—Range of sensitivity variables for design of experiments.

Fig. 7.27a shows the changes in mudline pressure in relation to temperature. The similarity in pressure and temperature trends clearly demonstrates the strong connection between the two responses, as one may surmise intuitively from the real-gas law. One consequence of this gas-well behavior is that significant heat loss not only occurs at the seabed, but its effect is transmitted thousands of feet below the mudline. Fig. 7.27b shows the temperature and pressure profiles during gas

production at 2,000 ft below the mudline.

We found that the trend reversal for drawdown pressure is a strong function of gas production rate and duration of the production period. The initial pressure trend reversal takes place regardless of the production rate. However, duration of this reverse-trend period depends on the rate, and with continued production the trend gradually begins to mimic that of the BHP. Again, placing the gauge close to the sandface is the only way to ensure data quality. As with the oil flow problem, we generated the Pareto chart with the data presented in Table 7.4. **Fig. 7.28** presents the chart.

7.3.2 Wellhead Pressure Conversion in Shut-In and Flowing Conditions. Let us illustrate issues with a buildup test in an onshore gas field to underscore some of the points made in the previous subsection with an example from Ismadi et al. (2010). **Fig. 7.29a** displays a declining WHP trend during well shut-in condition. Besides the inevitable pressure decline, periodic noise of the WHP response is of interest. This apparent noise is induced by the ambient day-and-night temperature cycle. Unfortunately, this noise is carried over to the converted BHP, as Fig. 7.29b testifies. In other words, literal translation of WHP retains the periodic event, which does not appear in the bottomhole measurement. Clearly, any attempt to discern reservoir character in this complex system will be futile when the derivative is taken of the distorted BHP, as **Fig. 7.30** illustrates. Whereas pressure buildups at the wellhead present a significant challenge, this issue can be sidestepped completely in the well flowing condition, as we discuss next.

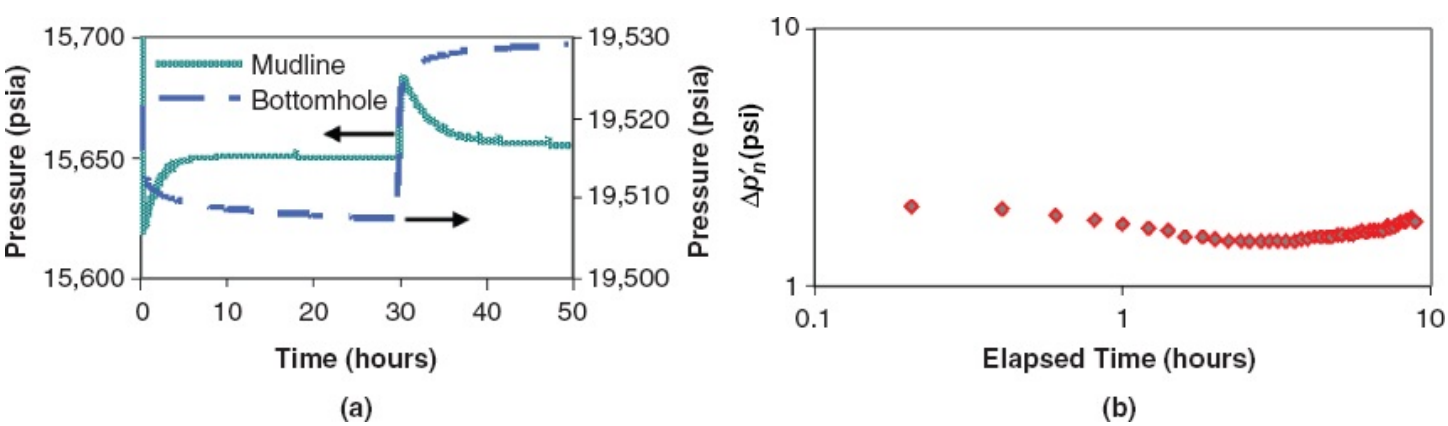

Fig. 7.26—Pressure at the mudline and well bottom for a deepwater gas well (a); diagnosis of gas-well buildup for a gauge at 3,000 ft away from sandface (b).

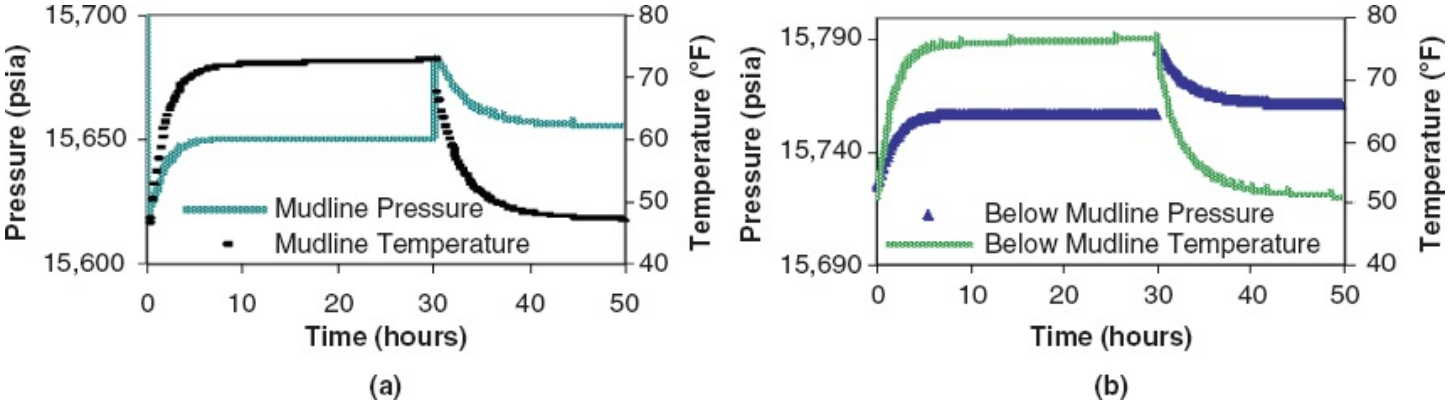

Fig. 7.27—Pressure/temperature behavior at the mudline (a) and 2,000 ft below the mudline (b).

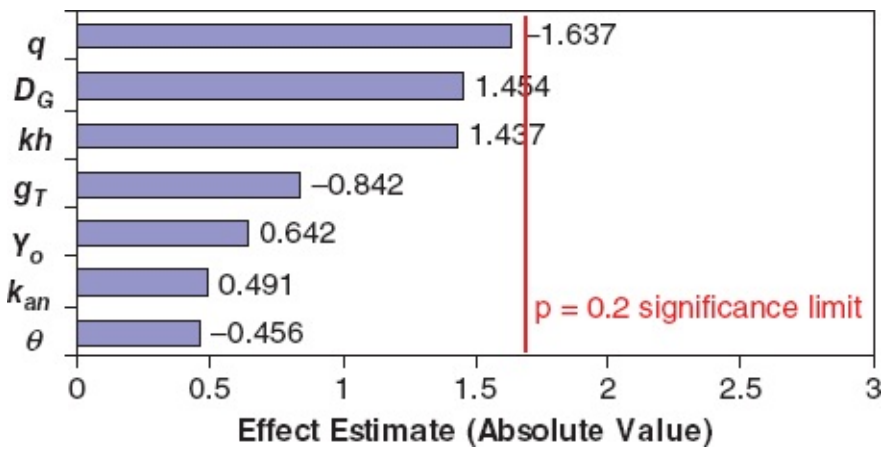

Fig. 7.28—Pareto chart for gas-well drawdown for the dependent variable E_{m*}.

In many assets, measurement of pressure and rate at the wellhead is the norm. Therefore, verification of both entities instills a great deal of confidence in data analysis. In particular, issues with data noise and accuracy may often cloud the material balance calculation picture in light of the difficulties arising from delineating the start of the pseudosteady-state flow period. Differential reservoir volumes in a layered system and various well/reservoir configurations in a drainage pattern precipitate this issue.

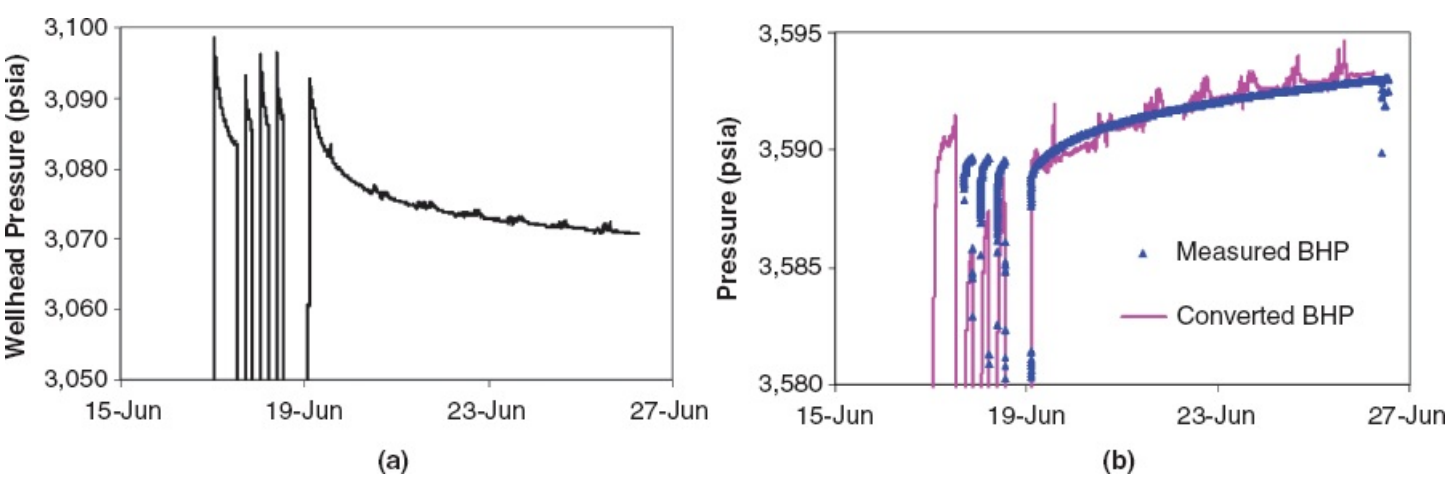

Fig. 7.29—WHP response during shut-ins (a); converted BHPs show the difficulty of pressure conversion (b).

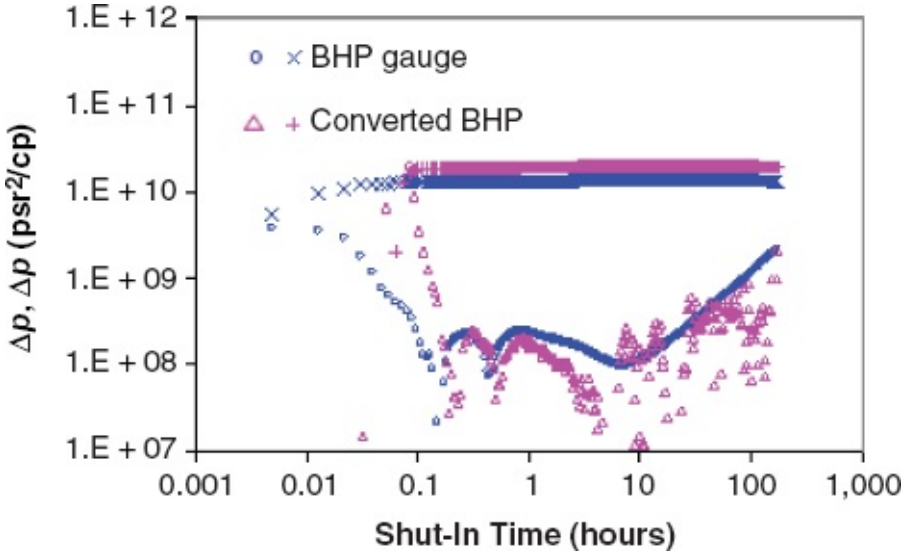

Fig. 7.30—Comparison of derivative signatures of measured and converted BHP.

As discussed by Ismadi et al. (2010), periodic downhole production logging and buildup tests allow verification of WHP conversion; **Fig. 7.31** presents such a case. Overall, the error bar is within 1.5%. In fact, both field examples are subject to this type of error bounds.

Let us explore the impact of J-T cooling at various rates experienced at the sandface for pressure conversion. Although J-T expansion influences fluid temperature significantly, especially at higher rates, the effect of this altered temperature on pressure estimates is minimal. This outcome is a direct consequence of minimal changes in gas properties of density and viscosity, leading to minimal changes in the pressure profile. For example, we calculated pressure/temperature profiles for seven flow rates ranging between 20 and 46 MMscf/D for this case, with and without accounting for J-T expansion. The estimated pressure drop for the well differed for the two cases by no more than 0.5%, as **Fig. 7.32** testifies.

7.3.3 Wellhead- and Bottomhole-Pressure Conversion in Water Injection Wells During Diagnostic Fracture Injection Testing. Diagnostic fracture injection testing entails inducing a hydraulic fracture by injecting a small volume of fluid into the formation and shutting the well in for a long-duration falloff. Typically, this type of test allows estimation of p_{fb}, p_{fc}, initial reservoir pressure (p_i), the leakoff type, and some measure of formation conductivity. The injection period leads to the determination of p_{fb}, whereas the falloff analysis yields the remaining parameters.

The use of BHP is implicit in all interpretation methods. However, the economic reality in field operations suggests the use of WHPs in most settings. Whether the WHP data lend themselves to transient interpretation without rigorous wellbore modeling, given significant changes in water density and compressibility as a function

of shut-in time, remains in question. Although compressibility of water is much lower than that of hydrocarbons, this question merits thorough vetting, as Section 7.3.2 addressing the gauge placement issue in conventional gas and oil reservoirs has suggested. Here, we present an analytical fluid-temperature model as a rigorous determination of BHP.

The pressure-computation algorithm entails two steps. First, we evaluate the temperature as a function of time at various depths throughout the wellbore. As expected, the temperature at the well bottom (BHT) will exhibit the largest excursion. Second, the fluid properties of density and compressibility are evaluated at each depth step corresponding to the temperature profile, leading to the BHP estimation at a given timestep. Let us illustrate the computational approach with a field example.

Fig. 7.33a presents the falloff data measured during a test, discussed earlier by Nojabaei et al. (2014). The rapid rise in temperature over the first 10 hours suggests potentially large changes in compressibility and density of water. Therefore, if the fracture closure occurs within this time period, uncertainty in BHP estimation may affect analysis. Fig. 7.33b shows the quality of match obtained for temperature data with the square-root-of-time model. As detailed in Appendix 7-D, the expression in Eq. 7.10 presents the model.

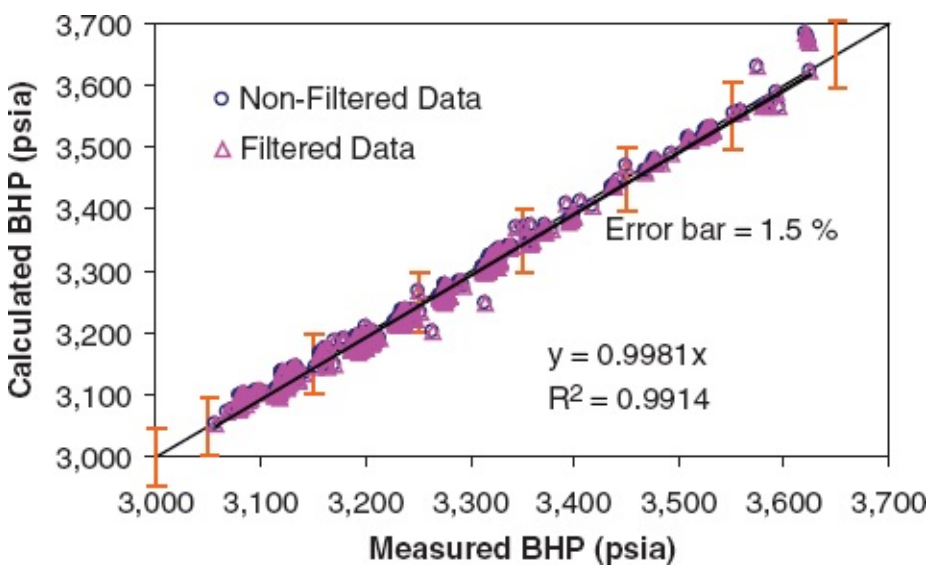

Fig. 7.31—Good correlation between the measured and converted BHP.

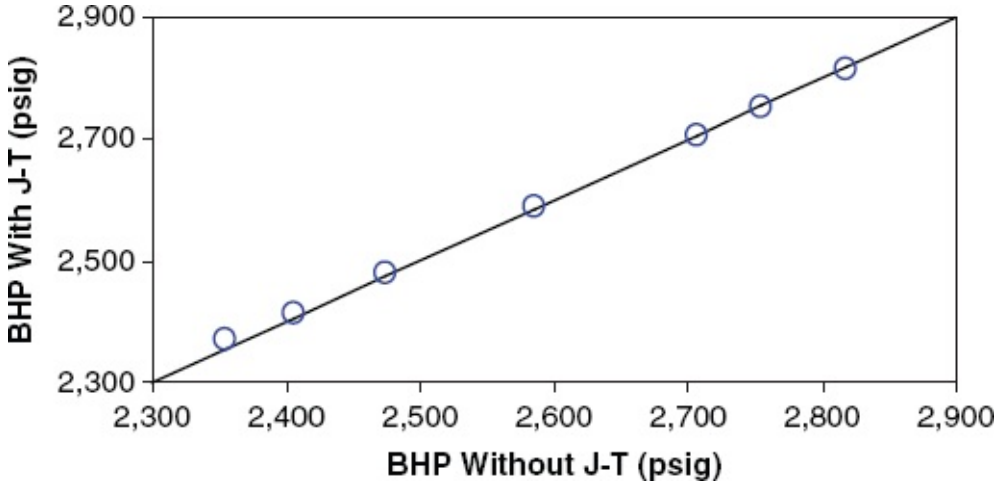

Fig. 7.32—Minimal J-T effect on pressure conversion.

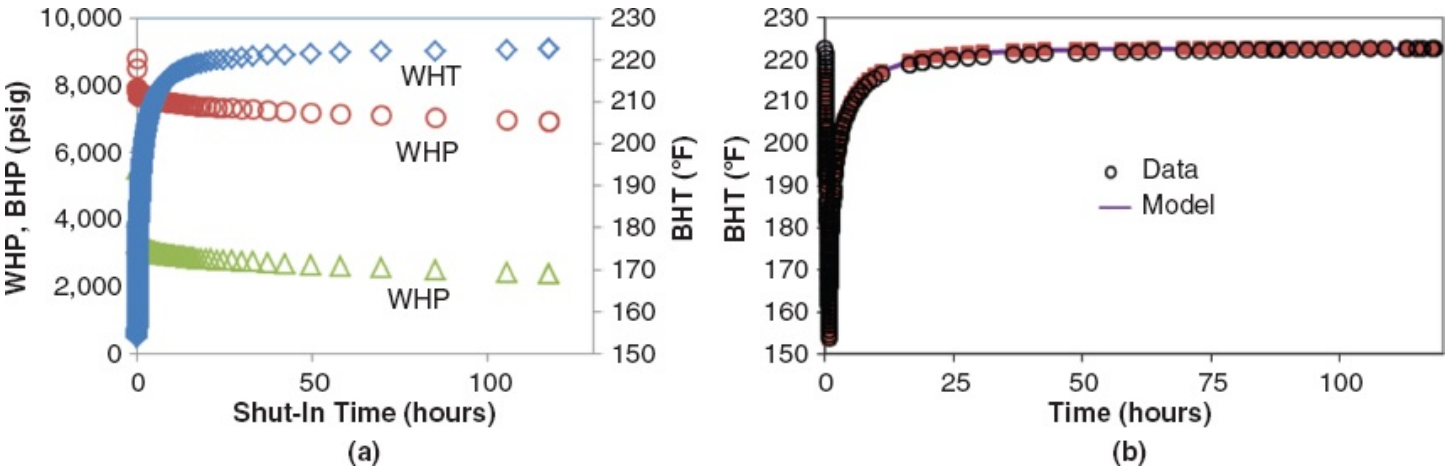

Fig. 7.33—BHP, BHT, and WHP data gathered during a falloff test (a), showing good agreement of temperature data with Eq. 7.4 (b).

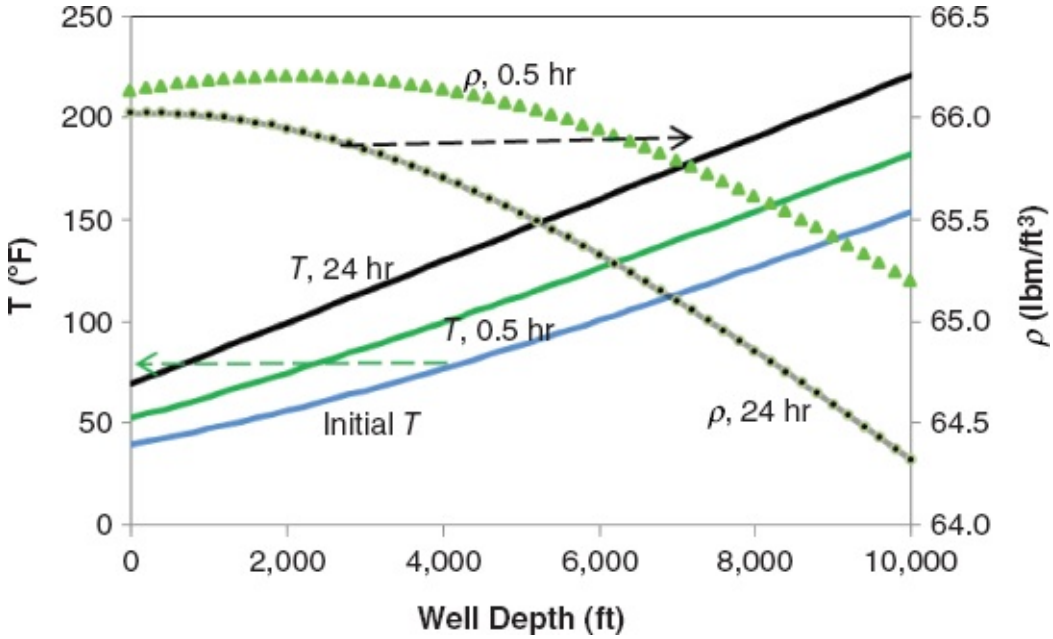

Fig. 7.34—Time-dependent temperature gradient affects wellbore fluid density.

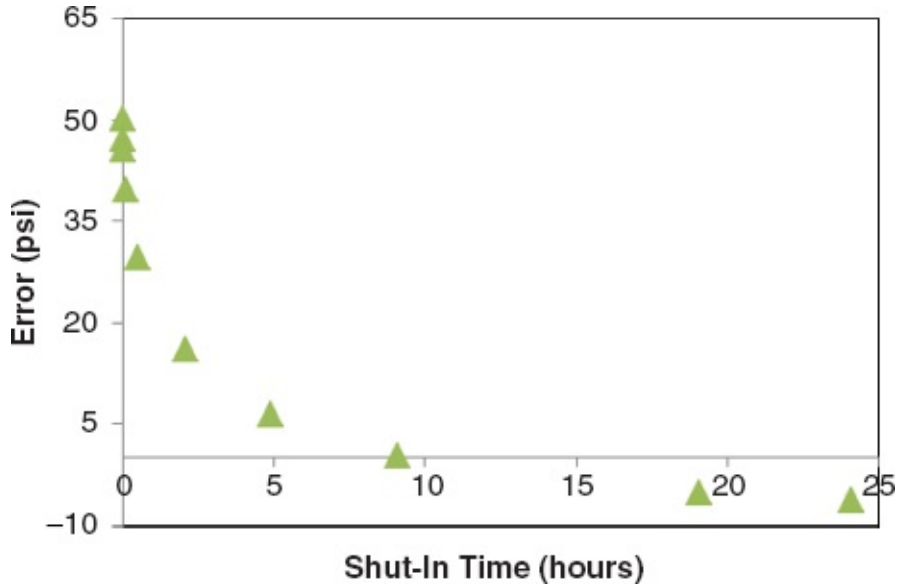

Fig. 7.35—Nonlinear correction of pressure data with increasing shut-in time.

$$T_f = T_{ei} + \left(T_{fo} - T_{ei}\right) e^{-a'\sqrt{t}} \quad (7.10)$$

Establishing time-dependent temperature profiles with Eq. 7.10 is a first step toward computing BHP from WHP. Thereafter, the fluid's expansivity and compressibility are estimated as outlined in Appendix 7-D. **Fig. 7.34** displays the temperature and density profiles. Note that the error between the corrected and the uncorrected pressures begins to diminish with time because the change in density or expansivity is counteracted by the fluid's compressibility, as shown in **Fig. 7.35.**

7.4 Geothermal Well Modeling

Historically, pressure-traverse computation in geothermal wellbores followed a trend similar to that in wells producing hydrocarbons. This similarity is appreciated by noting that all the principal flow regimes, bubbly, slug, churn, and annular, are common to both systems. Some authors of early studies adopted a hybrid approach; that is, they computed the slip between the steam and water phases with a different model in each flow regime. One potential difficulty of this approach is that the transition between the flow regimes may not be smooth, thereby triggering discontinuity. A few authors, such as Upadhyay et al. (1977), used different models in their entirety to find the one most reliable. The Orkiszewski (1967) correlation appeared to have an edge in their study. Subsequently, Acuña and Arcedera (2005) expressed a similar sentiment while discussing one field example. However, this view is not universal, as Tanaka and Nishi (1988) showed in a study with 16 wells containing varying amounts of carbon dioxide.

Despite reporting as comparative studies, most studies dealt with a very few wells, thereby posing an important question: Is the number of field tests sufficient to draw statistically significant conclusions with regard to the superiority of one model

over any other? To compound the problem, the data sets were incomplete; that is, both BHT and geothermal gradient often went unreported. Any comparative study involving models' relative performance is akin to the one used extensively in the petroleum literature. However, the number of wells in the petroleum industry dwarfs the number available in geothermal production, thereby posing challenges in identifying reliable models for pressure-traverse computation.

More recently, Garg et al. (2004a, b) reported successful application of a method that is based largely on the Duns and Ros (1963) flow pattern map and Hughmark's (1963) correlation for pressure-drop calculations, with parameters optimized to best represent the field data. Their data set (Garg et al. 2004b) appears complete, unlike the data sets presented earlier. As expected, absence of BHT and the geothermal gradient make any heat-transfer computation a rather challenging proposition. Because of significant changes in steam/water-phase behavior, accurate heat-transfer modeling for pressure-traverse calculation in geothermal wells is much more important than in oil wells. While Garg et al. model most two-phase flow largely on the basis of previous models meant for oil wells, they modeled heat transfer with a constant overall-heat-transfer coefficient (U_t). Using Garg et al. data, Hasan and Kabir (2010) showed that heat-transfer modeling can be improved when U_t is allowed to vary with changes in tubular diameters and thermal properties. Overall, statistical analyses of a reliable data set comprising 36 wells show that no model emerged as a clear winner.

The next subsection presents a model for both fluid and heat flows in geothermal wells, followed by illustration with field examples.

7.4.1 Modeling Approach. Pressure-drop calculations in the wellbore follow the same logic as presented in Chapters 3 and 5. For completeness, let us provide a brief account of the approach adopted here.

***Momentum Transport*.** Total pressure gradient during fluid flow is the sum of the static, friction, and kinetic gradients, which is written as

$$-\frac{dp}{dz} = g\rho_m \sin\theta + \frac{f v_m^2 \rho_m}{2d} + \rho_m v_g \frac{dv_m}{dz} \quad (7.11)$$

Mixture density, ρ_m, is calculated from the in-situ volume fraction of the two phases; therefore, $\rho_m = f_g\rho_g + (1 - f_g)\rho_L$. As explained in Chapters 3 and 5, f_g is given by

$$f_g = \frac{v_{sg}}{C_o v_m \pm v_\infty} \quad (7.12)$$

For most geothermal wells, which are vertical or near-vertical, the static-head component dominates. Because the static head depends directly on the volume average-mixture density, for geothermal wells, two-phase flow modeling amounts to estimating density of the fluid mixture or gas volume fraction. While Eq. 7.12 is general in its application, the values of the flow parameter C_o and rise velocity v_∞ are

dependent on the type of flow and flow pattern. Chapters 3 and 5 presented these values.

***Energy Transport*.** Production or injection of steam/water mixtures inevitably involves significant heat exchange between the wellbore fluid and its surroundings. During production, the hot fluid continues to lose heat to the increasingly cold surroundings on its ascent up the wellbore. In contrast, the injected fluid may either gain (cold water) or lose (steam or hot water) heat on its descent.

Wellbore heat transfer affects fluid properties and, in turn, the dynamics of fluid flow. Consequently, the coupled nature of momentum and energy transport may require simultaneous solutions for both processes. A general energy balance for the wellbore fluid is given in Chapter 6 (Eq. 6.13) and is reproduced here:

$$\frac{\mathrm{d}H}{\mathrm{d}z} - \frac{g\sin\alpha}{Jg_c} + \frac{v}{Jg_c}\frac{\mathrm{d}v}{\mathrm{d}z} = \mp\frac{Q}{w} \qquad (6.13)$$

In Eq. 6.13, Q represents the rate of heat transfer between the fluid and the surrounding formation per unit depth of the wellbore; the negative sign applies to fluid production, and the positive sign applies to fluid injection. As shown in Chapter 6, this heat loss from the fluid to the formation is modeled in two steps: that of loss from fluid to the wellbore/formation interface and that from this interface to the formation. In other words,

$$Q \equiv -L_R w c_p \left(T_f - T_{ei}\right) \qquad (6.19)$$

For a wellbore surrounded by formation, L_R is given by

$$L_R \equiv \frac{2\pi}{c_P w}\left[\frac{r_{to}U_{to}k_e}{k_e + \left(r_{to}U_{to}T_D\right)}\right] \qquad (6.20)$$

When fluid in oil and/or gas production undergoes no significant phase change, enthalpy is expressed as a function of pressure and temperature, and Eq. 6.13 is solved to obtain an expression for fluid temperature as a function of well depth. However, for geothermal wells, where water evaporates or condenses, application of such a procedure becomes infeasible. Consequently, Eq. 6.13 must be discretized and solved numerically with a known boundary condition. In the simplest case, when pressure and enthalpy are known at a position, Eqs. 6.13 and 6.19 are solved numerically to obtain pressure and enthalpy of the fluid in the next position in the well. Fluid enthalpy and pressure are then be used to estimate steam mass fraction or quality, x, with the following expression:

$$x = \frac{H - H_l^{\mathrm{sat}}}{H_{lg}} \qquad (7.13)$$

In Eq. 7.13, H_l^{sat} and H_{lg} are the liquid saturation enthalpy and heat of vaporization,

respectively, and are dependent on fluid pressure. Therefore, the computed quality at the new location depends on the fluid pressure at that location. However, as Eq. 7.11 shows, fluid pressure, in turn, depends on vapor velocity and, hence, the quality. This coupled nature of the transport processes demands a robust iterative-solution technique. Note that although the fluid loses heat to the surroundings as it moves up the well, its quality x can actually increase because of depressurization.

7.4.2 Analysis of Field Data. Most studies in the past provided a substantially limited data set, often with incomplete information. Absent, for example, was information about the geothermal gradient and reservoir temperature, the lack of which becomes a serious impediment to performing an objective analysis. In contrast, the data provided by Garg et al. (2004a) is exemplary, and so Hasan and Kabir (2010) used the Garg et al. data from 36 wells for their study.

Pressure-Drop and Pressure-Traverse Calculations. Two approaches to the statistical analysis with five independent two-phase flow models form the cornerstone of this subsection. The models include the homogeneous approach and those of Orkiszewski (1967), Hagedorn and Brown (H-B) (1965), Ansari et al. (1994), and Hasan-Kabir (H-K), as discussed in Chapters 2 and 3. For comparison, the results of Garg et al. (2004a, b) are also included in a limited form. The two statistical approaches involved the total pressure-drop consideration ($p_{wf} - p_{wh}$) and each measured pressure point or the pressure profile in the wellbore. Measured pressure profiles enriched this data set immensely, and we treated each depth-dependent value as an independent measurement.

Table 7.5 summarizes the statistical results involving the total wellbore pressure drop. The Garg et al. (2004a, b) results are made on the basis of their reported p_{wh} values for their best-fit correlation. As Table 7.5 shows, the Garg et al. results appear to be an improvement over others in all statistical measures. However, we note that their empirical model optimized certain parameters to best fit the data; that the Garg et al. correlation works better than others for this data set is not a surprise. For a proper evaluation of the Garg et al. correlation, one needs to compare its performance against other independent data sets.

In Table 7.5, the average percent error reflects the trend in performance relative to the measurement, the absolute average error indicates how large the errors are, the percent standard deviation suggests scattering of errors about their average value, the average error is a measure of overall trend independent of measurement, the average absolute error mirrors the magnitude of average error, and the standard deviation is simply scattering of results independent of measured pressure drop.

In their computations, Garg et al. (2004a, b) assumed a smooth pipe by setting the roughness ratio, ε/d, to zero. However, we think that the notion of zero pipe roughness is difficult to defend in geothermal wells, where scaling would lead to rough pipe surfaces. Our computation showed that all the models showed poorer fit for some wells, but better for others with $\varepsilon/d = 0$.

Each well in this study had approximately 17 independent measured pressure

points along the wellbore, digitized from the charts. **Table 7.6,** showing correlation coefficients of 576 test points, suggests that all the models are highly correlated with the data. In fact, the significance of the correlation coefficient, *r*, is presented in terms of the *t* values, given by the following expression (Blalock 1972, p.400):

	Orkiszewski	H-B	Homogeneous	Ansari	H-K	Garg
Avg. % error	–6.983	–0.710	–12.852	–12.301	–1.294	–1.437
Abs. avg. % error	16.119	13.007	15.079	19.846	10.175	2.343
% Standard deviation	42.067	4.280	77.423	74.107	7.793	1.463
Avg. error	–0.318	0.036	–0.966	–0.865	0.185	–0.155
Abs. avg. error	1.687	1.389	1.464	2.356	1.245	0.297
Standard deviation	10.630	8.427	7.615	12.878	7.513	1.916

Table 7.5—Statistical analysis of wellbore total pressure drop, $\varepsilon = 2.5 \times 10^{-5}$.

$$t = \left[r\sqrt{(n-2)} \right] / \sqrt{(1-r^2)}, \quad (7.14)$$

where *n* indicates the number of data points. For any of the models to assure existence of correlation with data, we needed a *t* value of only 2.6 within the 99% confidence interval. Obviously, each model met this criterion with ease. As with the previous analysis, no clear performance winner is apparent. No measures of the Garg et al. model are presented because their model was not part of this evaluation.

Table 7.7 reports the repeat of some of the statistical measures presented earlier in Table 7.5, but with the 576 data points. Here, pressure difference at each depth is simply the difference between the measured value and the value generated by the corresponding model. This larger data set is a better indicator of a model's performance because the entire pressure traverse is treated rather than each well's individual overall pressure drop. The inherent advantage of comparing and contrasting the entire pressure profile is that the heat-transfer considerations are implicitly accounted for. As indicated elsewhere, the variable-U_t modeling, as espoused here, is superior to the constant-U_t approach used in the past.

Figs. 7.36 through 7.38 compare the results of the five models with field data. Good correlation of all models with field data is readily apparent. The success of the homogeneous model should not be too surprising because many wells exhibited annular flow. As discussed in Chapter 5, the homogeneous model is quite appropriate for annular flow. Overall, the analyses lead to the inevitable conclusion that all the models behave similarly and none really stands out; this outcome is unsurprising, given the data quality. Chapter 5, discussing modeling experiences in gas and oil wells, suggests that modeling two-phase flow and the attendant heat transfer probably amounts to using a reasonable approach and paying attention to the data set. Stated differently, lack of data quality cannot be compensated for by a model, regardless of its sophistication.

Heat-Transfer Calculations. As stated earlier, heat-transfer calculations are implicit in any pressure-traverse algorithm. In particular, such computation becomes more important in a geothermal well, which has much higher energy dissipation than its oil counterpart. Most studies in the past reported the use of the constant-U_t approach with the Ramey (1962) heat-transfer model. Although the intrinsic approach of using Ramey's model is correct, the lack of granularity in U_t may have adversely contributed to the match quality of pressure-drop calculations.

Two issues are important while evaluating U_t in any flow situation. First, we need to honor the convective heat-transfer coefficient in the tubing/casing annulus, the controlling resistance over the depth interval of interest; and second, any change in flow cross-sectional area should be accounted for. Let us illustrate both points with example calculations.

Fig. 7.39a shows the pressure profile calculated by the five models for the KE1-22 well. This particular example was chosen because it exhibited multiple flow regimes, starting with single-phase water flow at the bottom of the hole and ending with annular two-phase flow at the wellhead. Therefore, the homogeneous model was not expected to perform well in estimating pressures in the entire wellbore. For instance, in slug flow, the homogeneous model significantly underestimates liquid holdup, and consequently the static head, leading to 26% lower pressure-gradient estimation compared to the Hasan-Kabir (Chapter 5) model. In the accompanying heat-transfer calculations, U_t varied from 7.4 Btu/hr-ft^2-°F at the bottom to approximately 10 Btu/hr-ft^2-°F at the top. Fig. 7.39b presents the U_t variation along with the estimated fluid temperature. Stepwise calculations for this well are shown in Appendix 7-E for two stations, each depicting a different flow regime.

	Orkiszewski	H-B	Homogeneous	Ansari	H-K
r	0.9879	0.9889	0.9875	0.9714	0.9848
t-test	150.712	157.363	148.438	96.817	134.305

Table 7.6—Correlation with measured wellbore pressure profile, Garg et al. (2004a, b) data.

	Orkiszewski	H-B	Homogeneous	Ansari	H-K
Avg. error	–0.624	–0.274	–0.819	–0.736	–0.091
Abs. avg. error	1.041	0.873	1.110	1.528	0.927
Standard deviation	22.093	20.656	22.091	33.273	21.595

Table 7.7—Statistical analysis of measured wellbore pressure profile, Garg et al. (2004a, b) data.

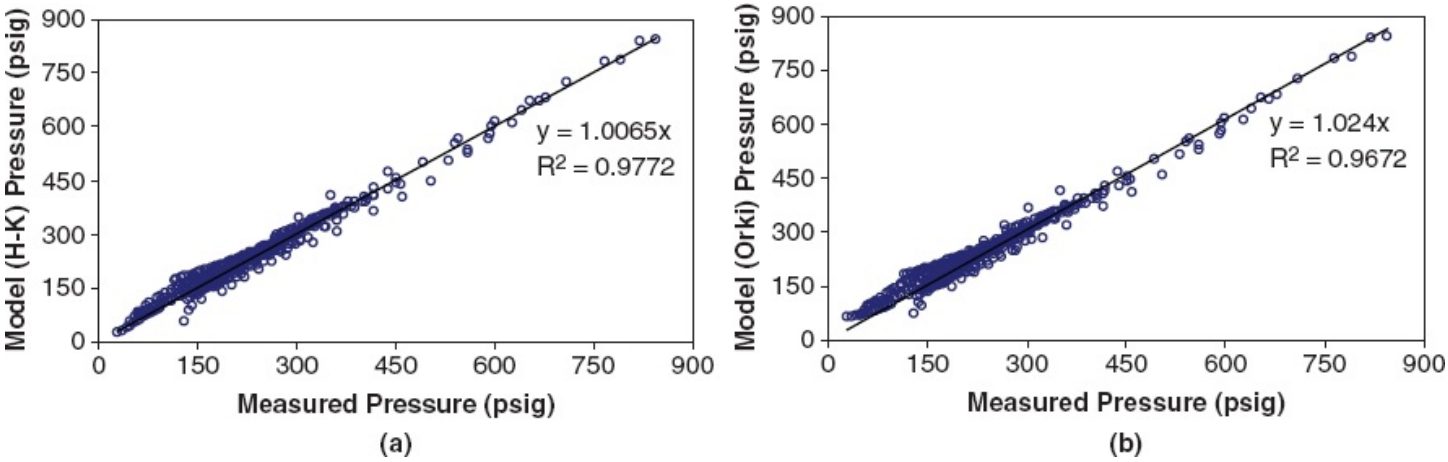

Fig. 7.36—Good correlation of model responses with field data: (a) Hasan-Kabir and (b) Orkiszewski.

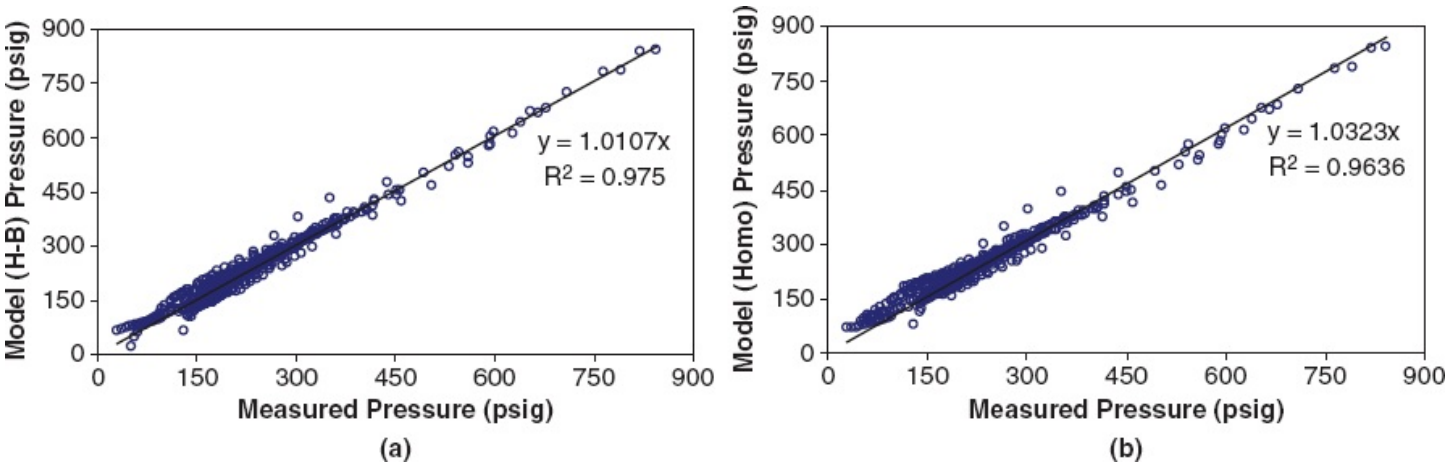

Fig. 7.37—Good correlation of model responses with field data: (a) Hagedorn-Brown (H-B) and (b) homogeneous.

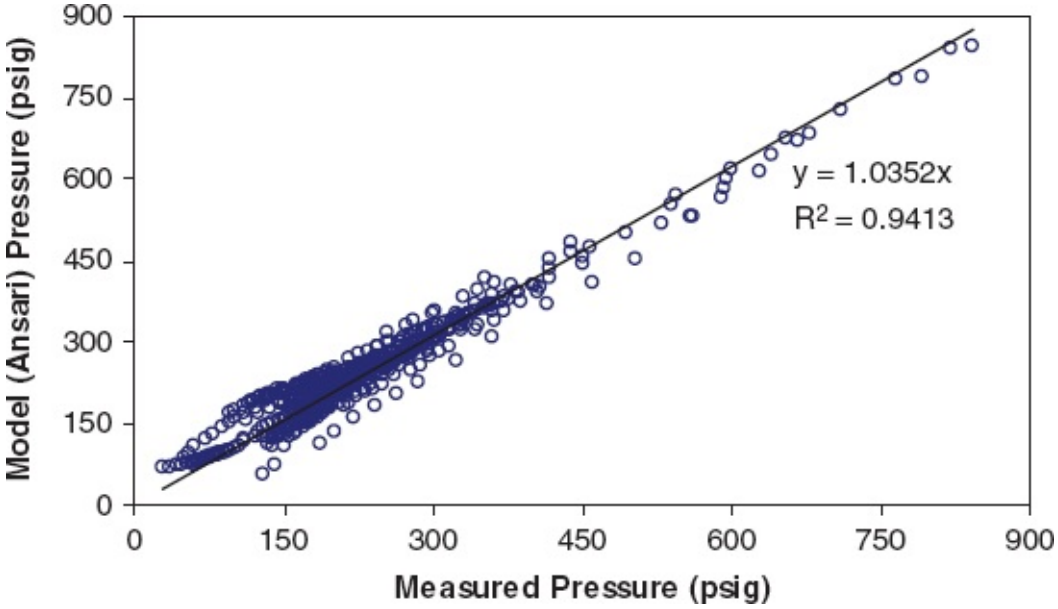

Fig. 7.38—Model pressures from Ansari et al. correlate well with field data.

Although the Ansari et al. model's results in this flow regime nearly match those of the Hasan-Kabir model, the cumulative effect of this slight (≈ 4%) difference results in a significant difference in the estimated WHP. The calculated pressure drop for annular flow with the Ansari et al. model is extremely sensitive to the estimation of the liquid-film thickness, which explains the difference in the estimated WHP. Just like the Ansari et al. model, the Hagedorn-Brown (1965) and Orkiszewski (1967) methods estimate somewhat lower liquid holdup. Consequently, the cumulative effect of the bottom-up computational approach translates into a significantly lower pressure loss, with a consequent higher WHP than the reported value. That the Hasan-Kabir model outperformed others in this particular case is probably fortuitous and should not be construed as the norm.

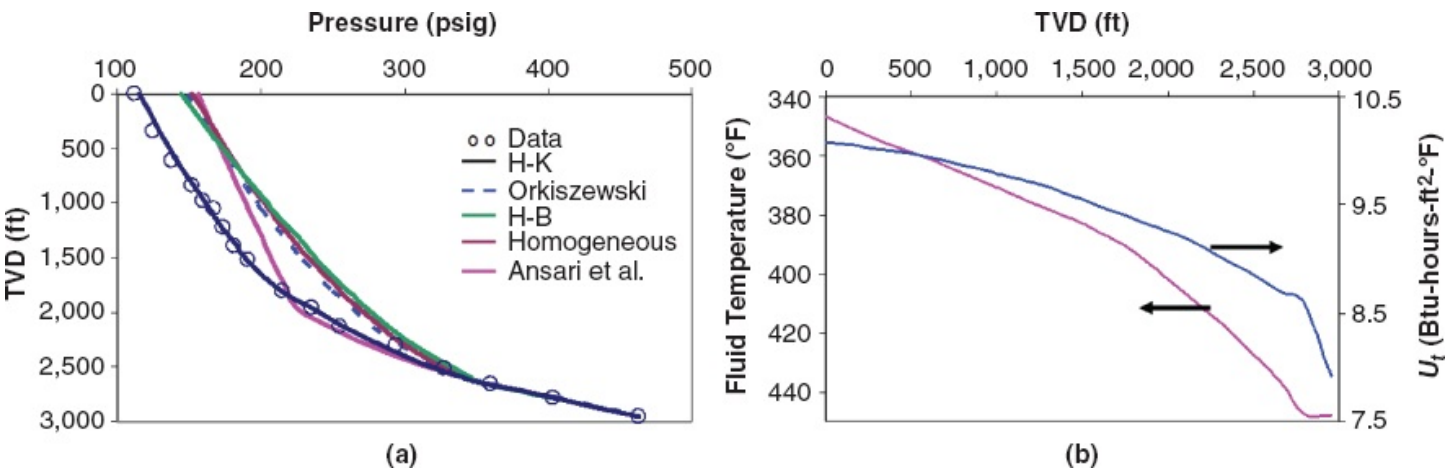

Fig. 7.39—Pressure-traverse computation with five models (a) and variable-U_t and fluid temperature profiles (b), Well KE1-22.

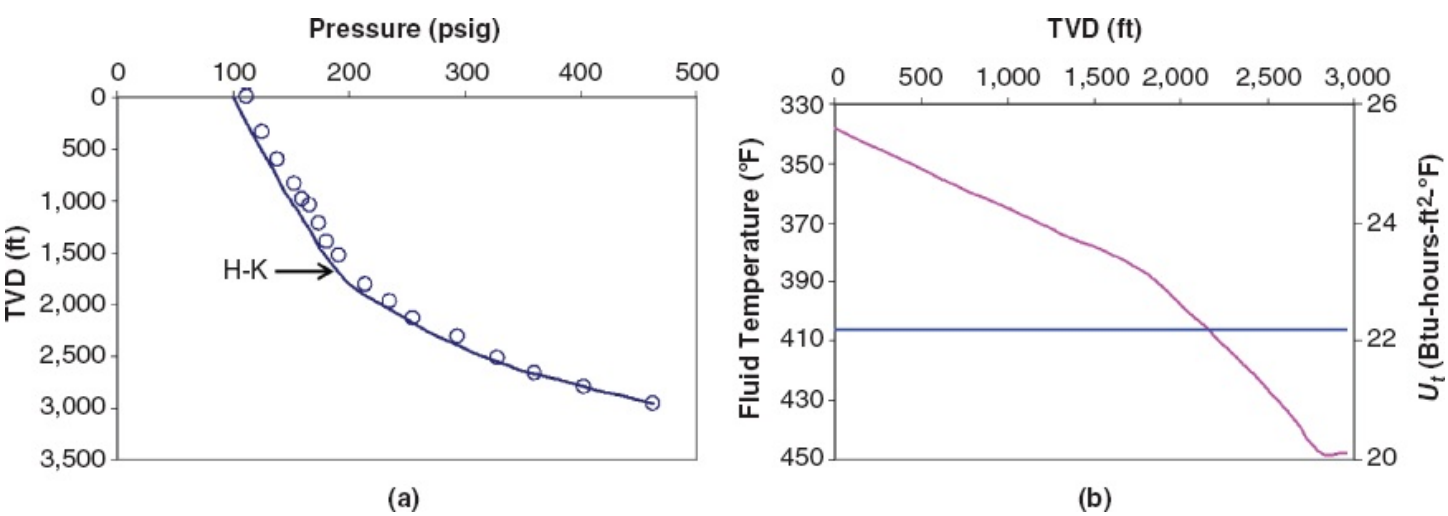

Fig. 7.40—Pressure-traverse computation with 33-in. casing (a) and constant-U_t and fluid temperature profiles (b), Well KE1-22.

As indicated earlier, investigators often used a constant value for the overall-heat-transfer coefficient for the entire wellbore. Although convenient, this approach can

lead to errors in both pressure-drop and heat-loss estimation simply because a well configuration (diameter, annular cross-sectional area, and so on) can change significantly with depth. To illustrate this point, let us recalculate the pressure profile for the KE1-22 well for a larger casing diameter (33 in. compared to 26.8 in.) and allow the full effect of natural convective heat transfer in the annulus, as shown in Chapter 6. A change in tubing diameter is consistent with deposition of scale, as pointed out by Goyal et al. (1980), among others.

Fig. 7.40a shows the increased pressure loss with the proposed model, leading to a lowered WHP. The increased heat transfer, as indicated by the increased U_t in Fig. 7.40b, is directly responsible for the decreased WHP. As one would expect, increased heat transfer leads to a lower wellhead enthalpy and the consequent lower steam quality, 0.072 compared to 0.09. Lower steam quality, in turn, leads to a higher fluid density and higher pressure loss resulting in 13.7 psi or 3.9% lower WHP for the proposed model. Note that the greater heat loss may not necessarily lead to a higher pressure loss. In cases where the frictional pressure loss predominates, such as when the steam quality is very high, greater heat loss leading to lowering of quality can reduce the frictional loss much more than would be compensated by an increased static-head loss. Therefore, rigorous heat-transfer computation, along with proper pressure-loss estimation, is essential for modeling geothermal wells.

7.5 Transient Temperature in Oil Reservoirs With Large Drawdowns

Modern downhole temperature measurements indicate that bottomhole fluid temperature can be significantly higher or lower than the original reservoir temperature, especially in reservoirs where high pressure drawdown is expected during production. These observations contradict the isothermal fluid flow assumption originally made for routine calculations. In a high pressure drawdown environment, the J-T phenomenon plays an important role in fluid temperature alteration in the reservoir. This section presents a robust analytical model to estimate the flowing-fluid temperature distribution in a reservoir that accounts for the J-T heating or cooling effect on the basis of the Chevarunotai et al. (2015) study. All significant heat-transfer mechanisms for fluid flow in the reservoir, including heat transfer from convection, J-T phenomenon, and heat transfer from over- and underburden formations, are incorporated. The results of this model are validated with those from a rigorous numerical simulator (App 2010) using field data.

Early attempts to establish fluid temperature were mainly for heavy-oil reservoir management in thermal recovery operations. One of the earliest models for estimating temperature distribution during steam injection was presented by Lauwerier (1955). Subsequent models followed treated heat conduction and convection as main heat-transfer mechanisms in the reservoir; however, fluid temperature change resulting from the J-T effect remained unaccounted for. The J-T effect is caused by an immediate expansion of fluid (i.e., fluid pressure drop along the reservoir and into the wellbore) at constant enthalpy without any work or heat transfer

to surroundings. Duru and Horne (2010) developed a semianalytical solution for the same problem, taking into account viscous dissipation (J-T heating or cooling), as well as heat conduction and convection. They also coupled the reservoirtemperature model with the analytical wellbore temperature model of Izgec et al. (2007) for fluid temperature analysis in the entire production system.

High pressure drawdown is normally required to produce from challenging reservoirs, such as those in deep, tight, and overpressured systems in an offshore environment. In some cases, the J-T effect may trigger fluid temperature increase of 20 to 30°F higher than the initial reservoir condition. Yoshioka et al. (2005, 2006) introduced a coupled reservoir/wellbore analytical temperature model for horizontal well production in a single-phase reservoir, assuming steady-state conditions. An extended version of Yoshioka et al.'s work was presented by Dawkrajai et al. (2006). They developed a finite-difference solution for the coupled reservoir/wellbore system to estimate fluid temperature distribution in the reservoir for two-phase production in horizontal wells. Their numerical solution removes the steady-state assumption and allows variation of reservoir and fluid properties in space and time.

Recently, App and Yoshioka (2013) offered an analytical solution for steady-state fluid temperature change as a function of producing rate, reservoir permeability, and drawdown, among other variables. They used Péclet number ($P_e = ur/\alpha$) to combine production rate and formation thermal conductivity to emphasize the effect of P_e on fluid temperature change. Their study clearly shows that for high reservoir thermal conductivity when $P_e < 1$, fluid temperature change is strongly influenced by P_e However, for $P_e > 3$, the influence of P_e on steady-state fluid temperature is negligible. The study also shows that fluid temperature changes minimally at very low P_e (< 0.1), which appears quite reasonable. The rationale for high formation thermal conductivity characteristic at low P_e implies that any heat generated (or dissipated) because of fluid expansion is quickly conducted through the formation.

7.5.1 Analytical Model. The reservoir system considered in this study is a one-dimensional (1D) radial reservoir where fluid flow occurs only in the radial direction; Chevarunotai et al. (2015) provides the model details. The only flowing fluid in the reservoir is oil; there is no free gas in the system, and connate water remains immobile. **Fig. 7.41** shows a schematic of the reservoir system used. We note that fluid flow in the idealized circular reservoir occurs in the "negative" *r* direction.

The principle for estimation of fluid temperature distribution in the reservoir is conservation of energy in the system, which includes reservoir fluid and rock. Conservation of mass for reservoir fluids facilitates deriving a comprehensive energy balance equation of the system. We also assume that the reservoir is perfectly horizontal; therefore, gravitational effect (change in fluid potential energy) is negligible.

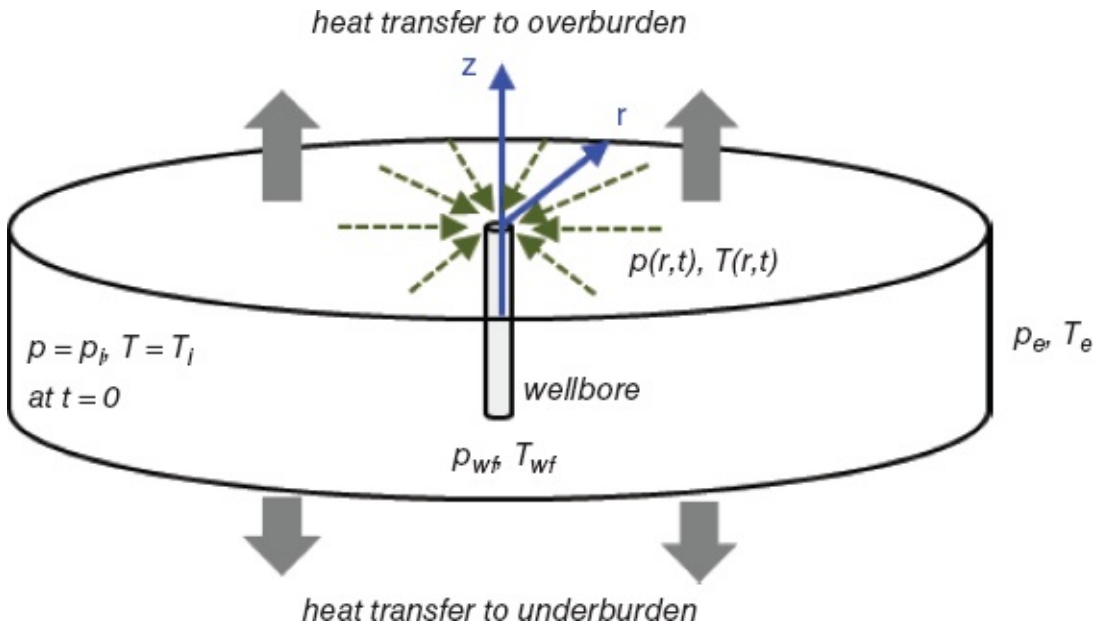

Fig. 7.41—A schematic of the wellbore/reservoir system configuration.

The general form of thermal energy balance in terms of the equation of change for internal energy (Bird et al. 2002, p.336) can be written as

$$\frac{\partial}{\partial t}\rho\hat{U} = -\left(\nabla\cdot\rho\hat{U}\bar{u}\right)-\left(\nabla\cdot\bar{q}\right)-p\left(\nabla\cdot\bar{u}\right)-\left(\bar{\tau}:\nabla\bar{u}\right)+\dot{Q}, \quad (7.15)$$

where $\hat{U}$ is fluid internal energy, ρ is fluid and/or rock density, and $\bar{u}$ is fluid local velocity. The ∇. term generally represents the net input rate of energy per unit volume of the system. The first term on the left side of Eq. 7.15 represents the total rate of internal energy increase in the system. The first and second terms on the right side are net input rate of internal energy to the system caused by convective transport and heat conduction, respectively. The third term represents the net reversible rate of internal energy increase from fluid compression (pressure difference), while the fourth term is the net irreversible rate of internal energy increase caused by fluid viscous dissipation. In this study, the fourth term is also referred to as J-T effect.

In addition to heat conduction, convection, and the J-T phenomenon caused by fluid flow in the reservoir, energy transfer from the surroundings (over- and underburden formations) to the system (reservoir fluids and formation) is considered in this model. Therefore, a term representing the net energy transfer rate between the system and its surroundings, $\dot{Q}$, is added to the energy balance equation as the last term in Eq. 7.15.

By using principles of rock and fluid enthalpy, Fourier's law of conduction, Newton's law of cooling, conservation of mass, and Darcy's law, Eq. 7.15 can be rearranged and rewritten as

$$\left[\phi s_o \rho_o c_{po} + \phi s_w \rho_w c_{pw} + (1-\phi)\rho_f c_{pf}\right]\frac{\partial T}{\partial t} + \rho_o u_r c_{po}\frac{\partial T}{\partial t} + \rho_o u_r \sigma_o \frac{\partial p}{\partial r}$$
$$+\left(\phi s_o \rho_o \sigma_o + \phi s_w \rho_w \sigma_w - 1\right)\frac{\partial p}{\partial t} = \frac{1}{r}\frac{\partial}{\partial r}\left(\lambda r \frac{\partial T}{\partial r}\right) + \dot{Q} \quad \ldots\ldots (7.16)$$

Eq. 7.16 is considered a comprehensive energy balance equation for our system. The first term on the left side of Eq. 7.16 contains the heat capacity of oil, water, and rock, which collectively represent energy change because of the temperature transient. Similarly, the second term represents convective heat transport. The third term is energy change resulting from the J-T effect, and the fourth term represents energy change because of the pressure transient in the reservoir. The first term on right side is energy change from radial heat conduction, and the last term represents rate of heat transfer across system boundary (to over- and underburden formations). Appendix 7-F presents the relevant assumptions and details of the comprehensive energy balance equation.

We rearranged the comprehensive energy balance equation of the system by applying all the assumptions described above. The energy balance equation can be reduced to a first-order, partial-differential equation. Thus,

$$\frac{\partial T}{\partial t} - \frac{B}{Ar}\frac{\partial T}{\partial r} - \frac{C}{Ar^2} = -\frac{D}{A}T + \frac{E}{A} \quad \ldots\ldots (7.17)$$

The method of characteristics was used to solve the partial-differential equation to arrive at a final form of the proposed analytical solution, which is given as

$$T(r,t) = T_i + \frac{C}{2B}e^{\frac{H\left(Ar^2+2Bt\right)}{2B}}Ei\left[-\frac{H\left(Ar^2+2Bt\right)}{2B}\right] - \frac{C}{2B}e^{\frac{HAr^2}{2B}}Ei\left(-\frac{HAr^2}{2B}\right) \quad \ldots\ldots (7.18)$$

Appendix 7-F presents the details of derivation of Eq. 7.18. Note that although Eq. 7.18 was solved assuming fluid property variation to be negligible, temperature computation with Eq. 7.18 does allow variation of fluid properties with fluid pressure and temperature. For this purpose, the reservoir was divided into 100 radial segments using logarithmic scale. Calculation initiates at the reservoir boundary with known pressure and temperature and progresses toward the wellbore. Let us illustrate this concept with a field example.

7.5.2 Model Validation With a Field Example. The App (2010) field data, which he validated with his numerical model, formed the cornerstone of model validation. Appendix 7-F presents the relevant reservoir and heat-transfer parameters. In this example, the flowing-fluid temperature distribution is calculated for five different constant production rates: 970, 2,050, 3,270, 4,650, and 6,200 STB/D. **Fig. 7.42** compares the temperature estimates generated with Eq. 7.20 with those of App. The solid lines represent the solutions of the analytical model, and the dashed lines do the same for those of App. Each profile represents distribution of the flowing-fluid

temperature in the reservoir at different production rates, after 50 days of continuous production at a constant rate. One observes that the estimated temperatures with the proposed model are extremely close to App's rigorous numerical solutions.

Fig. 7.43 compares the analytical solutions (solid lines) with those of App (dashed lines). This figure reveals the evolution of flowing-fluid temperature at the sandface with time for the same constant-rate production scenarios as before. This figure instills confidence in that the simplified analytical model yields quite reasonable estimations of BHT for different production rate scenarios.

Section Summary. This section has presented an analytical model for flowing-fluid temperature estimation in a single-phase oil reservoir. The analytical model provides reservoir-temperature estimation comparable to that of the rigorous numerical simulator developed by App (2010), which is anchored in actual field data. Calculations of Péclet numbers in Appendix 7-G suggests that ignoring conductive heat transport appears reasonable for field production rates. The advantage of this analytical model over other analytical solutions for reservoir-temperature estimation is that heat transfer from/to over- and underburden formations $\dot{Q}$ is included. Accounting for viscosity variation with temperature and pressure enhances the accuracy of temperature estimation.

These model results show that fluid temperature in the near-wellbore region can be significantly different from the original reservoir temperature. An accurate estimation of the reservoir fluid temperature from the analytical formulations can yield a better estimation of well productivity index, which is useful in production optimization and well development planning. A reasonable estimation of the bottomhole flowing-fluid temperature is also advantageous in well design from the standpoints of equipment selection and management of annular pressure buildup, discussed in Chapter 10.

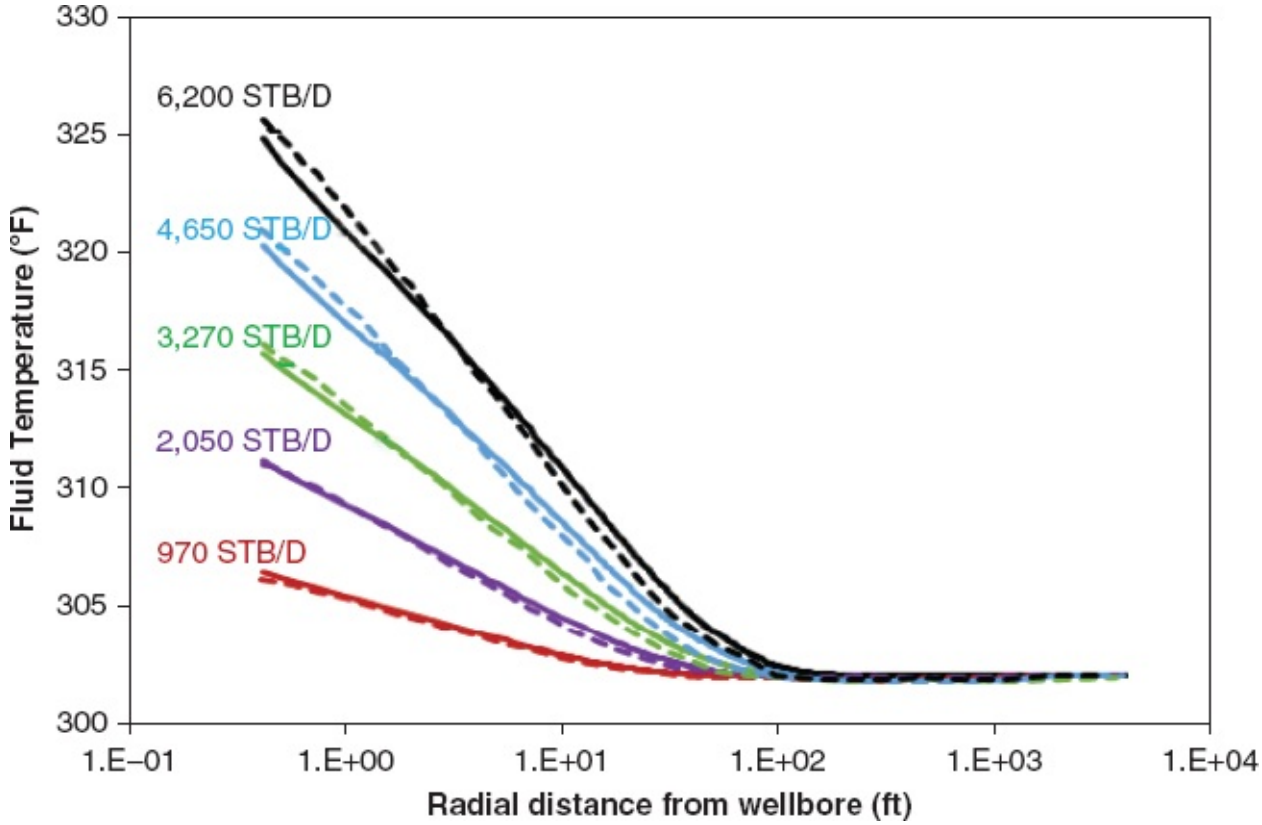

Fig. 7.42—Analytical model's temperature estimates at different rates compare favorably with those of the App (2010) numerical model.

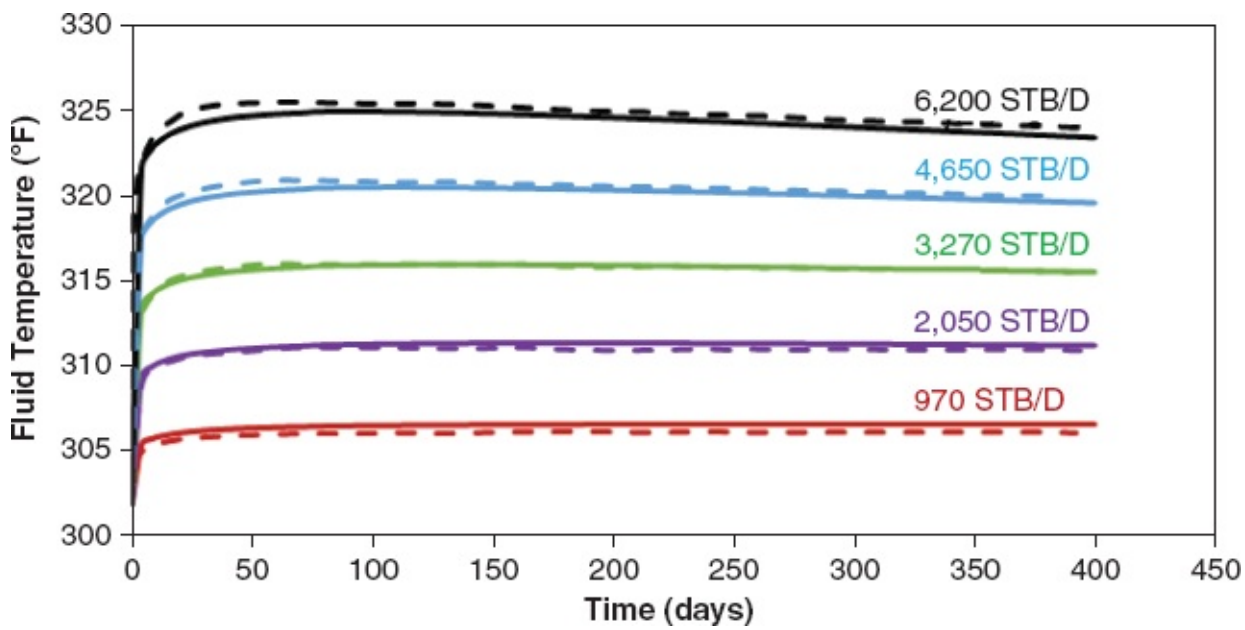

Fig. 7.43—Results of the analytical model compared with the numerical model of App (2010).

Summary

This chapter has attempted to capture some of the common coupled fluid flow and heat-transfer problems encountered in field operations. To that end, BHP estimation in geothermal wells, water injection in wells during transient testing of unconventional

formations, and issues pertaining to off-bottom gauges in deepwater completions are explored. Appropriate modeling approaches demonstrated solutions to these practical problems.

Thereafter, we tackled flow rate computations with single-temperature measurements and distributed-temperature measurements in the borehole. The ability to estimate rate, independent of conventional measurements, provides redundancy and instills a great deal of confidence while interpreting pressure transients. In this context, both direct and indirect verification of computed rates are shown. We also observed that the J-T effect plays a very important role in that its inversion at higher rates limits our ability to infer rates. Similar to gas/oil flow modeling, the accuracy of input data far outweighs the model's sophistication while converting WHP to BHP in geothermal wells. The last section revisits the J-T effect in the context of oil production from overpressured, low-conductivity formations. Accounting for viscosity variation with temperature and pressure in the analytical approach results in solutions that are comparable to those of a numerical model.

Nomenclature

a = thermal parameter defined by Eq. 7-B-21, ft/hr

A = cross-section area for flow, ft^2

B_o = formation volume factor, RB/STB

c_p = specific heat capacity of fluid, Btu/lbm-°F

c_{pf} = formation specific heat capacity, Btu/lbm-°F

c_{po} = oil specific heat capacity, Btu/lbm-°F

c_{pw} = water specific heat capacity, Btu/lbm-°F

c_t = total system compressibility, 1/psi

c_w = water compressibility, 1/psi

C_J = Joule-Thomson coefficient, (°F)/(lbf/ft^2)

f = friction factor, dimensionless

$f(T)$ = fluid temperature function defined by Eq. 7-A-4, ft

g = gravitational acceleration, ft/sec^2

g_c = conversion factor, 32.17 (lbm-ft)/(lbf-sec^2)

g_G = geothermal gradient, °F/ft

h = formation thickness, ft

h_c = heat-transfer coefficient, Btu/hr-ft^2-°F

H = enthalpy, lbm-ft^2/hr^2

J = ft-lbf to Btu conversion factor, dimensionless

k = formation permeability, md

k_a = thermal conductivity of annular fluid, Btu/hr-ft-°F

k_e = thermal conductivity of formation, Btu/hr-ft-°F

L = total wellbore measured depth, ft

L_j = measured (from wellhead) depth of section j of wellbore, ft

L_R = relaxation parameter defined by Eq. 6.20, ft^{-1}

m = mass of fluid, lbm

M_g = molecular weight of the free gas, lbm/lbm mol

p = pressure, psi

p_i = initial reservoir pressure, psi

P_e = Péclet number (= ur/α), dimensionless

p_{wf} = flowing-fluid pressure at well bottom, psi

q or q_o = volumetric oil rate, STB/D

q_g = volumetric gas rate, scf/D

$\vec{q}$ = conductive heat transport, Btu/hr-ft^2

Q = heat-transfer rate per unit length of wellbore, Btu/hr-ft

$\dot{Q}$ = net heat transfer rate between the system and surroundings, Btu/hr-ft^2

r = radius, ft

r_e = external reservoir radius, ft

r_t = tubing radius, ft

r_W = wellbore radius, ft

s = mechanical skin, dimensionless

S = saturation

S_o = oil saturation

S_w = water saturation

t = producing time, hours

t_D = dimensionless time, hours

T_D = dimensionless temperature

T or T_f = fluid temperature, °F

T_c = calculated fluid temperature, °F

T_e = earth or formation temperature, °F

T_{ei} = undisturbed earth or formation temperature, °F

T_{eij} = undisturbed earth or formation temperature at L, °F

T_{fc} = computed fluid temperature, °F

T_{fm} = measured fluid temperature, °F

T_i = initial reservoir temperature, °F

T_s = temperature of over- and underburden formations, °F

T_{wf} = flowing-fluid temperature at well bottom, °F

$\vec{u}$ = reservoir fluid superficial velocity, ft/hr

u_r = reservoir fluid local velocity in radial direction, ft/hr

U = overall-heat-transfer coefficient, Btu/hr-ft^2-°F

v = fluid velocity, ft/hr

v_{sg} = superficial gas velocity, ft/sec

v_{sL} = superficial liquid velocity, ft/sec

v_m = velocity of gas/liquid mixture, ft/sec

v_∞ = rise velocity of gas bubbles, ft/sec

$\overline{v}_\infty$ = average rise velocity of gas bubbles, ft/sec

$v_{\infty b}$ = rise velocity of small gas bubbles (in bubbly flow), ft/sec

$v_{\infty T}$ = rise velocity of Taylor bubbles, ft/sec

V = fluid specific volume (= 1/p), ft^3/lbm

w = mass rate, lbm/hr

x = gas mass fraction (quality), dimensionless

z = variable wellbore measured depth from surface, ft

Z = gas compressibility factor, dimensionless

α = well inclination (to horizontal) angle, degrees

δ = liquid-film thickness, ft

$\underline{\delta}$ = dimensionless thickness of the liquid film (= δ/d)

γ_o = oil gravity, °API

γ_g = gas gravity (air = 1), dimensionless

λ = reservoir thermal conductivity, Btu/hr-ft-°F

μ = viscosity, cp

μ_g = gas viscosity, cp

μ_L = liquid viscosity, cp

ρ = fluid density, lbm/ft^3

ρ_o = oil density, lbm/ft^3

ρ_w = water density, lbm/ft^3

ρ_e = earth or formation density, lbm/ft^3

ϕ = lumped parameter defined by Eq. 7-A-6, °F/ft

ϕ = reservoir porosity

σ = standard deviation of pressure, psi

ε = friction roughness factor, in.

σ = surface tension, lbm/sec^2

θ = well inclination with horizontal, degrees

$\vec{\tau}$ = stress, lbf/ft^2

ψ = lumped parameter defined by Eq. 7-A-5, °F/ft

σ_o = Thomson throttling coefficient of oil = $-c_p C_J$, Btu/lbm-psi

σ_w = Thomson throttling coefficient of water, Btu/lbm-psi

Subscripts

A	=	acceleration
cv	=	control volume
e	=	earth (formation)
ei	=	initial earth condition (for temperature)
$eiwh$	=	initial earth at wellhead condition (for temperature)
f	=	fluid
fwh	=	fluid at wellhead
F	=	friction
g	=	gas
H	=	hydrostatic
i	=	initial
j	=	spatial coordinate
L	=	liquid
wh	=	wellhead

Appendix 7-A

Flow Rate Estimation From Temperature Data

We used the model for steady flowing-fluid temperature in a complex well developed by Hasan et al. (2009) to handle changing tubular configurations, geothermal gradients, and water depth. The model, shown schematically in **Fig. 7-A-1,** develops the following expression for fluid temperature at a depth position of *j* + 1 in terms of that at j.

$$T_f = T_{ei} + \frac{1 - e^{(z-z_j)L_R}}{L_R}\psi + e^{(z-z_j)L_R}\left(T_{f_j} - T_{eij}\right) \quad \text{(7-A-1)}$$

Izgec et al. (2010) outlined the basis of this computational approach in which the fluid temperature depends on L_R, which, in turn, depends on mass rate w. The operating expression for the usual case of a wellbore surrounded by formation is

$$w \equiv \frac{2\pi r_{to} U_{to}}{c_p}\left[\frac{k_e}{k_e + \left(r_{to} U_{to} T_D\right)}\right]\frac{1}{L_R} = \frac{2\pi r_{to} U_{to}}{c_p}\left[\frac{k_e}{k_e + \left(r_{to} U_{to} T_D\right)}\right] f(T) \quad \text{(7-A-2)}$$

For the submerged section of an offshore well, we have

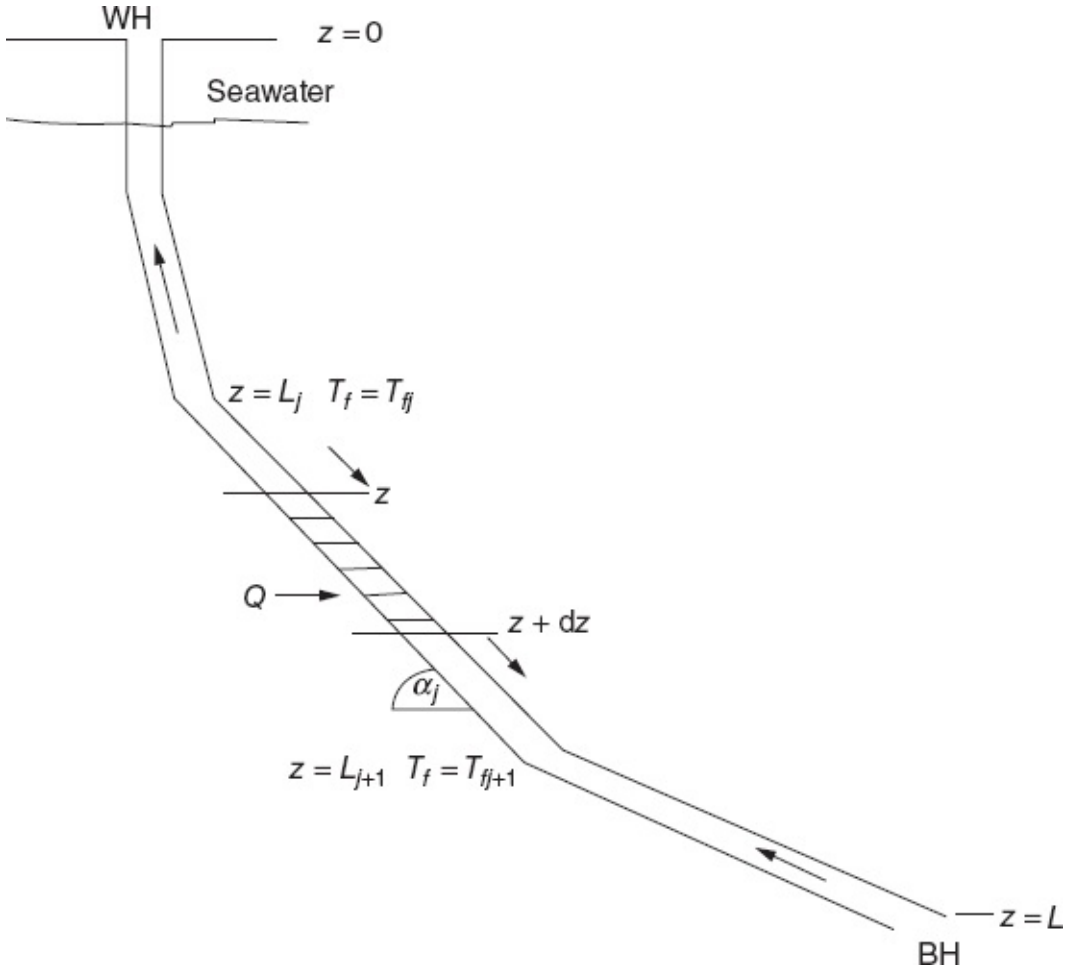

Fig. 7-A-1—Elements of the heat-transfer model.

$$w = \frac{2\pi r_{to} U_{to}}{c_P} f(T), \qquad (7\text{-A-3})$$

where

$$f(T) = \frac{\left(T_f - T_{ei}\right) - e^{(z-z_j)L_R}\left(T_{f_j} - T_{eij}\right)}{\left[1 - e^{(z-z_j)L_R}\right]\psi}. \qquad (7\text{-A-4})$$

In Eq. 7-A-4,

$$\psi = \left(g_G \sin\alpha + \phi - \frac{g\sin\alpha}{c_p}\right), \qquad (7\text{-A-5})$$

and

$$\phi c_p = v\frac{\mathrm{d}v}{\mathrm{d}z} - C_J c_p \frac{\mathrm{d}p}{\mathrm{d}z}, \qquad (7\text{-A-6})$$

where C_J is the J-T coefficient.

7-A.1 Solution Approach. Eqs. 7-A-2 and 7-A-3 show that flow rate is nonlinearly dependent on fluid temperature, thereby precluding any direct solution of rate from WHT. Therefore, we used an iterative procedure by guessing a rate followed by calculating fluid temperature using a top-down approach with known wellhead temperature (WHT). The calculated bottomhole temperature (BHTc) is compared against the known BHT value. The magnitude and direction of the error (BHT – BHTc) is used to guess a better value of the rate. The process is repeated until the error is within a preassigned tolerance.

7-A.2 Methodology for Multiple T_f Data. In this study, the depth-dependent fluid temperature data were available for multiple flow rates. Using the approach outlined in the previous section for all these data points would have been inefficient. Therefore, we used an iterative procedure that consisted of guessing a rate, followed by calculating the fluid temperature throughout the wellbore. The calculated temperature (T_c) is compared with the known fluid temperature T_f at various depths. The magnitude and direction of the error ($T_f - T_c$) is used to guess a better value of the rate. We used an optimization procedure to calculate the best value of rate, given the fluid temperature data at various locations in the well. In this optimization, higher weights were used for errors at shallower depths because of the greater solution accuracy as a result of increased temperature difference ($T_f - T_{ei}$). The procedure also allowed us to optimize parameters that are known with some degree of uncertainties, such as cement conductivity, pipe roughness, and the like. These parameters, however, were not varied for different rates or for different wells in the same field.

Appendix 7-B

Depth-Dependent Fluid Temperature With Superposition

The process of producing hot reservoir fluid results in heating up the near-wellbore region, thereby decreasing the heat-transfer rate with time even when the production rate remains constant. To account for this changing heat flow during steady production, the superposition principle is used. Superposition of heat flow modeling follows an approach similar to that used for modeling pressure transients in variable-rate situations. However, modeling depth-dependent heat flow is more complicated because heat transfer varies with both time and depth.

7-B.1 Pseudosteady-State Fluid Temperature. Let us consider a new well that produces fluids at a constant rate—that is, at a steady state for a time t_n. To estimate the fluid temperature at time t_n, we divide the total time into n periods (not necessarily equal)—$(t_1 - 0)$, $(t_2 - t_1)$, $(t_3 - t_2)$, …, $(t_{n-1} - t_n)$—as shown in **Fig. 7-B-1.**

For each period, the heat exchange between the formation and tubing fluid can be related in terms of the dimensionless temperature T_D and for the first time period can be written as

$$Q_1 = -\frac{2\pi k_e}{T_D(t_D)}\left(T_{wb} - T_{ei}\right)_1, \qquad (7\text{-B-1})$$

where t_D (dimensionless time = $\alpha t/r_{wb}^2$) is used to calculate dimensionless temperature T_D as follows using Eq. 6.10, reproduced below for convenience.

$$T_D = \ln\left[e^{-0.2t_D} + \left(1.5 - 0.3719e^{-t_D}\right)\sqrt{t_D}\right]. \qquad (6.10)$$

Note in Eq. 7-B-1 that temperatures (T_{wb} and T_{ei}) are functions of well depth and that T_D (t_{Dn}) is the value of the dimensionless temperature function for a dimensionless producing time of t_{Dn}. In this particular case, the independent variable is in the parenthesis for the dependent variable. In all other situations, the general expression $y(x)$ implies y is multiplied by x, *not* that y is a function of x. When y is a function of x, we simply write y and assume that the reader will understand the variability of y with respect to x (and any other variable, such as t) from the context.

Let us recast Eq. 7-B-1 in the temperature-difference form as

$$T_{ei} - T_{wb,1} = \frac{Q_1 T_D\left(t_{Dn}\right)}{2\pi k_e} \quad \text{(7-B-2)}$$

The heat flow rate Q_2 during the second timestep, $t_2 - t_1$, is represented by adding another constant heat source to the well at time > t_1, whose magnitude is equal to $Q_2 - Q_1$. The wellbore/formation interface temperature at this step, $T_{wb,2}$, is then the sum of these two heat sources, which is given by

$$T_{ei} - T_{wb,2} = \frac{Q_1 T_D\left(t_{Dn}\right) + \left(Q_2 - Q_1\right) T_D\left(t_{D,n} - t_{D1}\right)}{2\pi k_e} \quad \text{(7-B-3)}$$

Similarly, the third period can be represented by three sources of heat, and so on. Therefore, for the nth period, we have

$$T_{ei} - T_{wb,n} = \frac{\sum_n}{2\pi k_e}, \quad \text{(7-B-4)}$$

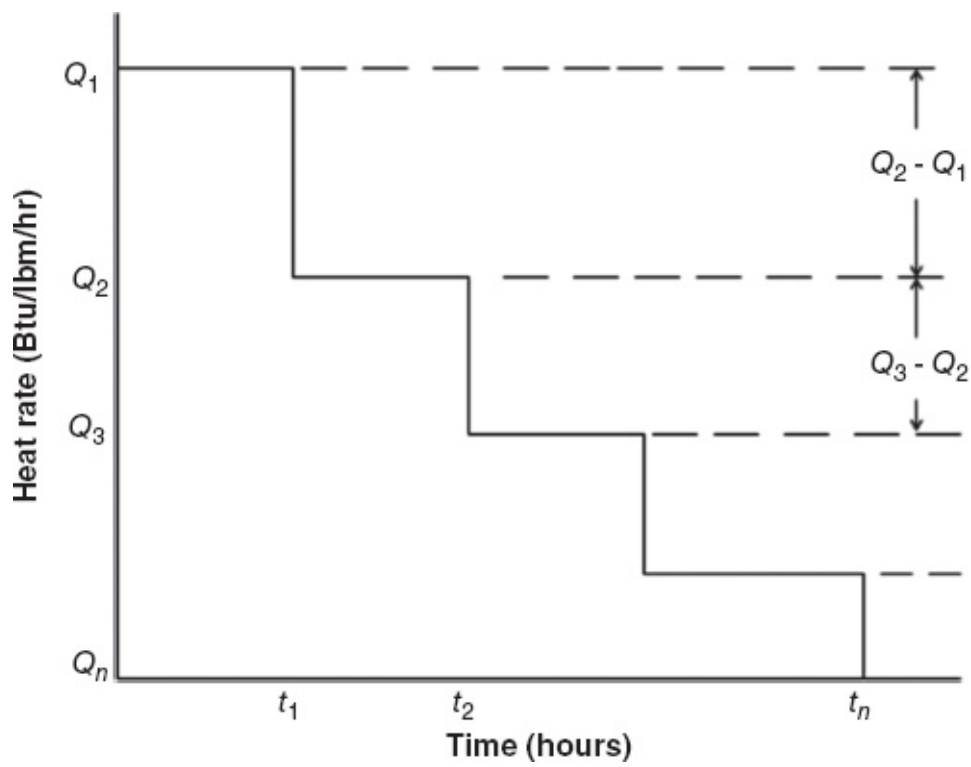

Fig. 7-B-1—Schematic of the superposition principle.

where

$$\sum_n = \sum_{i=1}^{n} \left(Q_i - Q_{i-1}\right) T_D\left(t_{D,n} - t_{D,i-1}\right) \quad \text{(7-B-5)}$$

and both Q_0 and T_{D0} are zero.

Let us emphasize that T_D $(t_{D,n} - t_{D,i-1})$ in Eq. 7-B-5 and similar expressions in other

equations represent the value of the dimensionless temperature T_D corresponding to the dimensionless time, T_D ($t_{D,n}$ – $t_{D,i-1}$). The flowing wellbore fluid temperature is obtained from an energy balance between the wellbore fluid and the surrounding formation at the time of interest, t_n. The rate of heat transfer from the wellbore fluid to the wellbore/formation interface, in terms of the overall-heat-transfer coefficient for the wellbore, can be written as

$$Q_n = -2\pi r U \left(T_f - T_{wb}\right)_n \qquad \text{(7-B-6)}$$

and

$$T_{wb,n} = T_{f,n} + \frac{Q_n}{2\pi r U} \qquad \text{(7-B-7)}$$

Substituting this expression for $T_{wb,n}$ into Eq. 7-B-3, we get

$$T_{ei} - T_{f,n} = \frac{Q_n}{2\pi r U} + \frac{\left(Q_n - Q_{n-1}\right) T_D \left(t_{D,n} - t_{D,n-1}\right)}{2\pi k_e} + \frac{\sum_{n-1}}{2\pi k_e}, \qquad \text{(7-B-8)}$$

where Σ_{n-1} is defined the same way as Eq. 7-B-5 for n–1 elements. Energy balance on the flowing fluid for a differential depth, dz, gives

$$\frac{\mathrm{d}T_f}{\mathrm{d}z} = \frac{1}{c_p}\left(-\frac{Q_n}{w} + \frac{g\ \sin\alpha}{g_c J} - \frac{v}{g_c J}\frac{\mathrm{d}v}{\mathrm{d}z}\right) + C_J \frac{\mathrm{d}p}{\mathrm{d}z} \qquad \text{(7-B-9)}$$

Substituting Eq. 7-B-8 into Eq. 7-B-9 and rearranging,

$$\frac{\mathrm{d}T_{f,n}}{\mathrm{d}z} = -L_R T_{ei} + L_R\left(T_{f,n}\right) - \frac{g\ \sin\theta}{g_c J c_p} + \phi + \xi, \qquad \text{(7-B-10)}$$

where

$$T_D\left(t_D - t_{D,n-1}\right)\frac{L_{Rn} Q_{n-1}}{2\pi k_e} + \frac{L_{Rn}}{2\pi k_e}\sum_{n-1}, \qquad \text{(7-B-11)}$$

$$\phi = C_j \frac{\mathrm{d}p}{\mathrm{d}z} - \frac{v\dfrac{\mathrm{d}v}{\mathrm{d}z}}{g_c\, J\, c_p}, \qquad \text{(7-B-12)}$$

and

$$L_{Rn} = \frac{2\pi}{c_p w}\left\{\frac{r_t U_t k_e}{k_e + \left[r_t U_t T_D\left(t_{D,n} - t_{D,n-1}\right)\right]}\right\}. \qquad \text{(7-B-13)}$$

Note that when superposition is neglected, L_{Rn} defined by Eq. 7-B-13 reduces to the

L_R given by Eq. 7.2 in the text. We can rewrite Eq. 7-B-10 as

$$\frac{dT_{f,n}}{dz} = \frac{dT_{fws}}{dz} + \xi, \quad \text{(7-B-14)}$$

where T_{fws} is the fluid temperature estimated without superposition. Assuming that ξ is invariant, the linear differential equation, Eq. 7-B-14, is solved as

$$T_f = T_{ei} + \frac{\left[1 - e^{(z-L)L_R}\right]}{L_R}(\psi + \xi), \quad \text{(7-B-15)}$$

where

$$\psi = g_G \sin\theta + \phi + \frac{g \sin\alpha}{g_c J c_p} \quad \text{(7-B-16)}$$

7-B.2 Transient Fluid Temperature. When superposition in depth is considered, we assume that fluid flow transients subside quickly and that flow rate *w* is independent of well depth. However, as mentioned in Section 7.2.2, temperature transients take significant time before they stabilize. In Chapter 9, fluid temperature estimation during such thermal transients is presented in detail and an analytical expression developed. Here, we show the applicability of that analytical expression when heat superposition is also accounted for. An energy balance indicates that any heat received from or lost to the formation would change the fluid temperature with time and depth. In terms of fluid internal energy, fluid enthalpy (*H*), fluid mass rate (*w*), and fluid mass in the control volume (*m*), the energy balance equation can be expressed as

$$Q = \frac{d}{dt}\left[mc_p T_f (1 + C_T)\right] - \frac{d}{dz}\left[w\left(H + \frac{1}{2}v^2 + g\ z\ \sin\alpha\right)\right] \quad \text{(7-B-17)}$$

The term C_T represents the heat-storage effect of the tubulars and cement sheaths in the wellbore. The heat received from (or lost to) the formation, *Q*, is

$$Q = -\frac{2\pi k_e}{T_D(t_D)}(T_{wb} - T_{ei}) \quad \text{(7-B-18)}$$

As we discussed, the requirement of constant *Q* may be made by subdividing the time in consideration to discrete temporal steps. Analogous to the derivation of Eq. 7-B-9, we obtained the following differential equation for fluid temperature as a function of time and depth:

$$dT_f / dz = \frac{wc_p L_R}{mc_p(1 + C_T)}(T_{ei} - T_f) + \frac{wc_p}{mc_p(1 + C_T)}\left(1 - e^{(z-L)L_R}\right)(\psi + \xi) \quad \text{(7-B-19)}$$

In Eq. 7-B-19, ξ is given by an expression similar to that in Eq. 7-B-11. Assuming ξ

and ψ to be constant, we arrive at the following expression for fluid temperature:

$$T_f = T_{ei} + \left(T_{fi} - T_{ei}\right)e^{-at} + \frac{\left(1 - e^{-at}\right)}{L_R}\left[1 - e^{(z-L)L_R}\right]\left(\psi + \xi\right), \quad \text{(7-B-20)}$$

where

$$a = \frac{wc_p L_R}{mc_p\left(1 + C_T\right)} \quad \text{(7-B-21)}$$

Appendix 7-C

Flow Rate Estimation for Slug and Closed-Chamber Tests

We present the derivations for the slug-test and closed-chamber-test models. Most of the design equations used for both tests are similar. The differences in approach, where they arise, are mentioned as well. The approach involves an iterative process in two separate steps. We assume that the reservoir inflow will create a piston-like displacement of any fluid already present in the wellbore. The wellbore is assumed to be vertical. Inclinations can easily be integrated into the pressure-drop model if required. **Fig. 7-C-1** presents the simple vertical well model. Referring to Fig. 7-C-1, the flowing pressure at the well bottom, p_{wf}, can be expressed in terms of pressure at the top of the gas chamber, in addition to the static pressure exerted by the gas in the chamber and that exerted by any existing water and reservoir fluid in the system.

While pressure exerted by the gas in the chamber is purely static, pressures exerted by the water and reservoir fluid must also account for the frictional and acceleration pressure loss experienced by a moving fluid column. Therefore, we can write

$$p_{wf} = p_g + p_w + p_{rf} \quad (7.4)$$

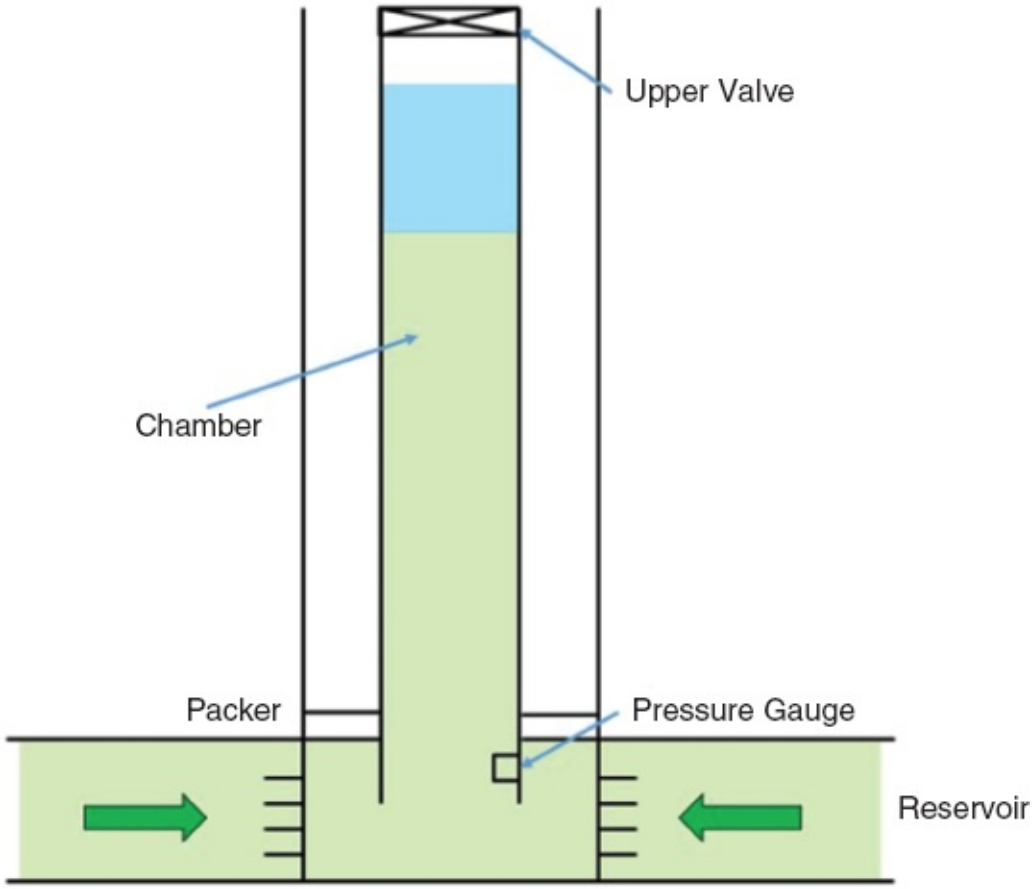

Fig. 7-C-1—Wellbore schematic in closed-chamber testing.

The difference between gas chamber bottom and top pressures is attributable only to static head. Thus the gas chamber bottom pressure, p_g, can be obtained from the chamber top pressure, p_{gi}, in terms of the chamber height, Δz_g, gas specific gravity, γ_g, and temperature, T, as

$$p_g = p_{gi} \exp\left(\frac{29\gamma_g \Delta z_g}{1545(T+460)Z}\right) \quad \text{(7-C-1)}$$

When gas column height is large, Δz_g can be subdivided into number of sections to estimate gas chamber bottom temperature more accurately. To estimate the pressure exerted by the water and reservoir fluid columns, p_w and p_{rf}, we must account for static, friction, and acceleration heads because the wellbore fluid columns move covering a distance of Δz_g. Therefore, Eq. 7-C-2 will apply to these two terms. These two terms of Eq. 7.4 are calculated in the same manner for both the slug and closed-chamber tests, as shown:

$$p = \left[\left(\frac{dp}{dz}\right)_H + \left(\frac{dp}{dz}\right)_F + \left(\frac{dp}{dz}\right)_A\right]\Delta z \quad \text{(7-C-2)}$$

The Z-factor is calculated using the Dranchuk and Abou-Kassem (1975)

correlation. Once the BHP is calculated, we make an initial guess for the producing rate based on the infinite-acting radial flow assumption for transient fluid flow in the formation as

$$q=\frac{kh\left(p_{wf}-p_i\right)}{70.6B\mu E_i\left(-\frac{948\phi\mu c_t r_w^2}{kt}\right)} \quad \text{(7-C-3)}$$

At very small times, we recommend that the exponential-integral function E_i be used, rather than its logarithmic approximation. On the basis of influx rates and time intervals, one can calculate cumulative inflow that accounts for the increase in fluid-column height in the wellbore. Simple material balance for the heights of the fluid in the wellbore and the gas chamber can be worked out according to the applicability of the appropriate system, slug or closed chamber. The entire process requires two levels of iterations. That is because the pressure depends on the fluid heights, they in turn depend on reservoir inflow, and this influx depends on the BHP itself.

Once the material balance of wellbore fluids is established, the reservoir inflow is calculated using Eqs. 7.5 through 7.7, as shown in Section 7.2.4 and repeated here:

$$p_{wf}=p_i-q_n m'\left\{\sum_{j=1}^{n}\left[\left(\frac{q_j-q_{j-1}}{q_n}\right)log\left(t_n-t_{j-1}\right)\right]+A\right\}, \quad (7.5)$$

where

$$m'=\frac{162.6\mu}{kh} \quad (7.6)$$

and

$$A=\log\frac{k}{\phi\mu c_t r_w^2}-3.23+0.869s \quad (7.7)$$

We then use both the p_{wf} calculated using Eqs. 7.4 and 7.5 and put them through the generalized reduced-gradient nonlinear optimization algorithm, which minimizes the difference between the two values by finding a local value for the flow rate that satisfies both pressure equations. Because Eq. 7.5 incorporates the superposition in time of different flow rates, the minimization algorithm provides an efficient way for accurate estimation of flow rate. This way, both pressure and flow rate are calculated on the basis of the physical mechanism of the system and a test design can be obtained for various design input variables.

Note that heat-transfer calculations are not handled explicitly because of short-duration (in terms of minutes to a few hours) fluid influx; the consequent fluid property changes are not expected to have significant impact on computational results in most settings. Nonetheless, one can pursue a methodology similar to that described in

Appendix 7-D to account for transient temperature effect on fluid properties.

Appendix 7-D

Transient Temperature Model During Water Injection

As mentioned earlier, Chapter 9 develops an analytical solution for producing-fluid temperature as a function of time and depth. The solution presented here follows the same approach to estimate transient fluid temperature during *injection*. Setting up a general energy balance for a control volume at depth *z* from surface with a wellbore differential length of d*z*, we obtain

$$Q = \frac{\mathrm{d}(mE)_{cv}}{\mathrm{d}t} + \frac{\mathrm{d}(m'E')_{w}}{\mathrm{d}t} + \frac{\mathrm{d}}{\mathrm{d}z}\left[w\left(H + \frac{1}{2}v^2 - gz\sin\alpha \right)\right] \quad \text{(7-D-1)}$$

In Eq. 7-D-1, the first two terms on the right side represent change in internal energy of the fluid and the tubing/casing/annuli material. In terms of temperature and pressure, we obtain

$$\frac{\mathrm{d}T_f}{\mathrm{d}t} = a\left(T_{ei} - T_f\right) + ae^{-zL_R}\left(T_{fwh} - T_{eiwh}\right) - \frac{a\psi}{L_R}\left(1 - e^{-zL_R}\right), \quad \text{(7-D-2)}$$

where

$$a = \frac{wc_pL_R}{mc_p\left(1 + C_T\right)}, \quad \text{(7-D-3)}$$

$$\phi = -\frac{v}{c_pJg_c}\frac{\mathrm{d}v}{\mathrm{d}z} + C_J\frac{\mathrm{d}p}{\mathrm{d}z}, \quad \text{(7-D-4)}$$

and

$$\psi = g_G\sin\alpha + \phi - \frac{g\sin\alpha}{c_pJg_c} \quad \text{(7-D-5)}$$

The solution for Eq. 7-D-2 with a constant L_R and initial condition of $T_f = T_{ei}$ at $t = 0$ is

$$T_f = T_{ei} - \frac{\psi}{L_R}\left(1 - e^{-zL_R}\right)\left(1 - e^{-at}\right) + e^{-zL_R}\left(T_{fwh} - T_{eiwh}\right)\left(1 - e^{-at}\right) \quad \text{(7-D-6)}$$

Eq. 7-D-6 can be used for estimating fluid temperature profile at any time during injection. The steady-state injection temperature profile, T_{fo}, can be obtained by using $t = \infty$ in Eq. 7-D-6 as

$$T_{fo} = T_{ei} - \frac{\Psi}{L_R}\left(1 - e^{-zL_R}\right) + \left(T_{fwh} - T_{eiwh}\right) e^{-zL_R} \quad \text{(7-D-7)}$$

However, if the injection period is short and the variation of L_R with t needs to be accounted for, one can approximate $L'_R = \left[2\pi k_e / \left(T_D c_p\right)\right] = a''/\sqrt{t}$. With those assumptions, Eq. 7-D-7 has the following solution:

$$T_f = T_{ei} + \left(T_{fo} - T_{ei} - \frac{b}{a'^2}\right) e^{-2a'\sqrt{t}} + \frac{b}{2a'^2} - \frac{b\sqrt{t}}{a'} \quad \text{(7-D-8)}$$

To estimate the shut-in fluid temperature as a function of time, when flow rate w is zero, we use only the first two terms on the right of Eq. 7-D-1, leading to

$$Q = \frac{\mathrm{d}(mE)_{cv}}{\mathrm{d}t} + \frac{\mathrm{d}(m'E')_w}{\mathrm{d}t} \quad \text{(7-D-9)}$$

The heat received from the formation Q is written as

$$Q \equiv c_P\left(T_{ei} - T_f\right) L'_R \quad \text{(7-D-10)}$$

The alternative relaxation distance parameter, L'_R (which omits flow rate, w), is given by

$$L'_R = \frac{2\pi}{c_P}\left[\frac{rUk_e}{k_e + \left(rUT_D\right)}\right], \quad \text{(7-D-11)}$$

where L'_R is equivalent to wL'_R for injection. As Chapter 9 shows, the temperature rise of the cement/tubular material at any time may be taken to be a multiple of the rise in the fluid temperature. In that case, we may write the first term of the right side of Eq. 7-D-1 in terms of fluid mass per unit depth, m, as

$$\frac{\mathrm{d}}{\mathrm{d}t}\left(mE + m'E'\right) = \frac{\mathrm{d}}{\mathrm{d}t}\left[mc_P T_f\left(1 + C_T\right)\right]. \quad \text{(7-D-12)}$$

Combining Eqs. 7-D-9 through 7-D-12, we obtain the following first-order, linear differential equation for fluid temperature in time and space:

$$\frac{\mathrm{d}T_f}{\mathrm{d}t} = \frac{L'_R}{m\left(1 + C_T\right)}\left(T_{ei} - T_f\right) \quad \text{(7-D-13)}$$

Eq. 7-D-13 was solved by Hasan et al. (2005) assuming L'_R to be constant. The approach appears to work, perhaps because Hasan et al. (2005) allowed L'_R in the integrated expression to vary with time. However, as Eq. 7-D-11 shows, L'_R depends on T_D, which depends on time, especially at early times. Incorporating early time variation in L'_R on production time, using the following expression for T_D that applies to

dimensionless shut-in periods of $t_D < 1.5$, as shown earlier in Eq. 6.9 in Chapter 6:

$$T_D = 1.1282\sqrt{t_D}\left(1 - 0.3\sqrt{t_D}\right) \approx 1.1282\sqrt{t_D}, \quad \text{(7-D-14)}$$

where $t_D = \alpha t/r_{wb}^2$. When k_e is small, one may approximate L'_R as

$$L'_R = \frac{2\pi k_e}{c_p 1.1282\sqrt{t_D}} = \frac{5.57\,k_e}{c_p\sqrt{t_D}} = \frac{5.57\,k_e r_{wb}}{c_p\sqrt{\alpha t}} = a''/\sqrt{t} \quad \text{(7-D-15)}$$

With these assumptions, Eq. 7-D-13 has the following solution:

$$T_f = T_{ei} + \left(T_{fo} - T_{ei}\right)e^{-a'\sqrt{t}} \quad \text{(7-D-16)}$$

7-D.1 Fluid Temperature Computation. For this vertical well, g_G = 0.01526°F/ft; hence, T_{ei} = 70 + 0.01526 z. For initial fluid temperature before shut-in, we use Eq. 7-D-17, the steady-state injection temperature (with L_R/ψ = 76.1977, L_R = 0.0001834),

$$T_{fo} = T_{ei} - 76.198\left(1 - e^{-0.0001834z}\right) + (40 - 70)\,e^{-0.0001834z} \quad \text{(7-D-17)}$$

Fluid temperature as a function of depth and time after well shut-in is obtained from Eq. 7-D-16 (with thermal diffusivity α = 0.04 and wellbore radius r_{wb} = 0.5 ft) as

$$T_f = \left(T_{fo} - T_{ei}\right)e^{-1.91915\sqrt{t_D}} + T_{ei} \quad \text{(7-D-18)}$$

7-D.2 Fluid Pressure Computation. To obtain the BHP from the WHP, only static head ρgh needs to be calculated; that is, $p_{i+1} = p_i + \rho gh$. Density of a liquid, however, depends on both pressure and temperature and is usually computed using the following expression:

$$\rho = \rho_o e^{c_w \Delta P - \beta \cdot \Delta T}, \quad \text{(7-D-19)}$$

where ρ_o is the fluid density at standard conditions; fluid compressibility $c_w \equiv -(1/\rho)(\partial\rho/\partial p)_T$, and expansivity $\beta \equiv (1/\rho)(\partial\rho/\partial T)_p$. These fluid properties themselves are weak functions of pressure and temperature. We used the following expressions for both fluid compressibility and expansivity (with p in psi and T_f in °F).

$$c_w = \left(a + bT_f + cT_f^2\right)10^{-6}, \quad \text{(7-D-20)}$$

where

$$\begin{aligned} a &= 3.8546 - 0.000134p \\ b &= -0.01052 + 4.77\times10^{-7}p \\ c &= 3.9267\times10^{-5} - 8.8\times10^{-10}p \end{aligned} \quad \text{(7-D-21)}$$

and

$$\beta = \left(2\times10^{-9}T_f^2 + 1.9\times10^{-6}T_f - 7.64\times10^{-5}\right) \quad \text{(7-D-22)}$$

To accomplish the pressure-traverse computation at any timestep, the wellbore is divided into a number of discrete depth steps for computation of fluid temperature at each depth location. Thereafter, c_w and β are calculated allowing estimation of ρ. Pressure at the next depth location is then calculated from density using Eq. 7-D-19. The process is then repeated until the well bottom is reached for a given timestep.

Appendix 7-E

Example Bottomhole Pressure Calculations for a Geothermal Well

In this appendix, we show stepwise calculations in two flow regimes for the KEI-22 well, reported by Garg et al. (2004a, b). Slug flow occurs in the lower section of the well, whereas annular flow is dominant in the upper section. For two-phase flow calculations, we show the use of a few selected models. The KE1-22 well produces geothermal fluids from 2,957-ft MD with 8.819-in.-inner-diameter tubing. The well is deviated 2.87° from the vertical, thereby making TVD of 2,953 ft.

The well delivers 0.198×10^6 lbm/hr of hot water at the well bottom with an enthalpy of 427.8 Btu/lbm. The following values of fluid properties, obtained from interpolation of steam tables, and other parameters are computed at the well bottom, where the pressure is 477.4 psia.

Saturated Steam/Water Property Values

h_g = 1,205.3 Btu/lbm

ρ_L = 51.03 lbm/ft^3

μ_L = 0.144 cp

h_L = 444 Btu/lbm

ρ_g = 1.02 lbm/ft^3

μ_g = 0.013 cp

σ = 28.8 dynes/cm = 0.0635 lbm/sec^2

d = 8.819 in.

$q_{ms} = 0.198 \times 10^6$ lbm/hr

$$x = (h - h_L)/(h_g - h_L)$$
$$= (427.8 - 444)/(1205 - 444)$$
$$= -0.0213$$
$$A_x = 0.424 \text{ ft}^2$$

Thus, we have single-phase flow of hot water at the well bottom. The total pressure gradient, almost entirely owing to the static head (0.3543 psi/ft), is 0.3550 psi/ft. With this pressure gradient, we compute a fluid pressure of 419.1 psia at 164 ft above the well bottom. Heat loss over this section is minimal, and fluid enthalpy is calculated to

be 427.3 Btu/lbm; the fluid is still single-phase water. Similar pressure-gradient computation leads to a pressure of 371.9 psi at the next location, at a depth of 2,957 ft. At this point, the enthalpy is calculated to be 426.6 Btu/lbm. The saturated liquid enthalpy at 371.9 psi being 415.9 Btu/lbm, we compute the following steam quality and velocity:

$$x = (426.6 - 405.7)/(1204.6 - 415.9)$$
$$= 0.0136$$
$$q_g = q_{ms}\, x/r_g$$
$$= 0.198 \times 10^6 \times 0.0136/0.79/3600$$
$$= 0.941 \text{ ft}^3/\text{sec}$$
$$v_{sg} = q_g/A_x = 2.218 \text{ ft/sec}$$
$$v_{sL} = q_L/A_x = 2.455 \text{ ft/sec}$$

7-E.1 Slug Flow Regime. Here, slug flow regime is calculated for the homogeneous, Ansari et al., and Hasan-Kabir models.

***The Homogeneous Model*.**
Gas volume fraction = v_{sg} / v_m = 0.491
Mixture density, $\rho_m = (0.491\ \rho_g) + (0.509)(\rho_L)$ = 26.96 lbm/ft^3
Mixture viscosity, $\mu_m = x\ \mu_g + (1 - x)\mu_L$ = (0.0136) (0.0166) + (0.9864)(0.12) = 0.12 cp
$\text{Re}_m = v_m\ \rho_m\ d/\mu_m$ = 1,200,139

Using the Chen (1979) correlation, the friction factor is estimated to be

$$f = \frac{4}{\left[4 \log\left(\frac{\varepsilon/d}{3.7065} - \frac{5.0452}{\text{Re}} \log A\right)\right]^2} = 0.01345.$$

A pipe roughness factor of 0.00984 in. was used, resulting in a value of 0.000112 for ε/d.
– $(dp/dz)_F = f_m v_m^2 \rho_m /(2d)/144$ = 0.0012 psi/ft
– $(dp/dz)_H = \rho_m\ g \sin\theta$ = 2.445 psf/ft = 0.1872 psi/ft
– $(dp/dz)_A = \rho_m\ v_m\ (dv_m/dz)$ = 0.00012 psi/ft
– dp/dz = 0.1885 psi/ft total pressure gradient at 2,957 ft

***The Ansari et al. (1994) Model*.** The v_{sg} needed for transition from bubbly to slug flow is 1.30 ft/sec (Eq. 3.7), whereas the v_m needed for transition to churn flow (Eq. 3.10 and 3.11) is 11.44 ft/sec. The flow pattern is therefore slug. The computational approach for in-situ volume fraction and pressure gradient using the Ansari et al. model can be found elsewhere (Hasan and Kabir 2007); we summarize the important results here:

Gas volume fraction, f_g = 0.328
Mixture density, ρ_m = 35.35 lbm/ft^3
– $(dp/dz)_F$ = 0.00159 psi/ft
– $(dp/dz)_H = \rho_m\, g \sin\theta$ = 0.2455 psi/ft
– $(dp/dz)_A = \rho_m\, v_m\, (dv/dz)$ = 0.00012 psi/ft
– dp/dz = 0.2471 psi/ft total pressure gradient at 2,957 ft

***The Hasan-Kabir Model*.** For slug flow, we have these values:

$v_{\infty T}$ = 1.765 ft/sec, v_∞ = 0.6952 ft/sec, $\overline{v}_\infty$ = 1.6235 ft/sec
Gas volume fraction, f_g = [2.218/(1.2 × 4.672 + 1.6235)] = 0.3067
Mixture density, ρ_m = 36.43 lbm/ft^3
– $(dp/dz)_F = f_m v_m^2 \rho_m /(2d)/144$ = 0.0015 psi/ft
– $(dp/dz)_H = \rho_m\, g \sin\theta$ = 2.445 psf/ft = 0.2529 psi/ft
– $(dp/dz)_A = \rho_m\, v_m\, (dv/dz)$ = 0.00012 psi/ft
– dp/dz = 0.2545 psi/ft total pressure gradient at 2,957 ft

As with many geothermal wells, our calculations show that most of this well (from wellhead down to 2,100 ft) experiences annular two-phase flow. In the following, we show sample calculations for a location 337 ft below the wellhead.

7-E.2 Annular Flow Regime. This section presents the annular flow computed for the homogeneous, Hasan-Kabir, and Ansari et al. models.

***The Homogeneous Model*.** The model computed pressure at 337 ft below wellhead = 182.7 psia. The values are these:

ρ_L = 54.83 lbm/ft^3, ρ_g = 0.400 lbm/ft^3
x = (915.6 – 789.2)/(2782.7 – 789.2) = 0.063
$v_{sg} = q_g/A_x = q_{ms}\, x/\rho_g\, A_x$ = 20.044 ft/sec
$v_{sL} = q_L/A_x$ = 2.222 ft/sec

Gas volume fraction = v_{sg} / v_m = 0.900
Mixture density, $\rho_m = (0.9\, \rho_g) + (0.1)(\rho_L)$ = 5.833 lbm/ft^3
– $(dp/dz)_F = f_m v_m^2 \rho_m /(2d)/144$ = 0.00577 psi/ft
– $(dp/dz)_H = \rho_m\, g \sin\theta$ = 2.445 psf/ft = 0.0405 psi/ft
– $(dp/dz)_A = \rho_m\, v_m\, (dv_m/dz)$ = 0.0002 psi/ft
– dp/dz = 0.0465 psi/ft total pressure gradient

***The Hasan-Kabir Model*.** The Hasan-Kabir model computed pressure at 337 ft below wellhead = 142.8 psia. The values are

ρ_L = 55.57 lbm/ft^3, ρ_g = 0.315 lbm/ft^3
x = (920.95 – 738.6)/(2782.7 – 738.6) = 0.063
$v_{sg} = q_g/A_x = q_{ms}\, x/\rho_g\, A_x$ = 20.044 ft/sec

$v_{sL} = q_L/A_x = 2.222$ ft/sec

The minimum v_{sg} needed for transition to annular flow is given by Eq. 3.12.

$$v_{sg} > 3.1\left[g\sigma\left(\rho_L - \rho_g\right)/\rho_g^2\right]^{1/4}$$

$$= 3.1\ [32.2 \times 0.0936(55.57 - 0.315)/0.315^2]^{1/4}$$
$$= 19.83 \text{ ft/sec}$$

Therefore, we have annular two-phase flow. For fully developed annular flow, we use Eq. 3.12 with $C_o = 1.0$ and $v_\infty = 0.0$. However, because actual v_{sg} is close to the transition value, $C_o = 1.018$ (calculated using an exponential expression). Accordingly, the values are these:

Gas volume fraction, $f_g = [20.044/(20.044 + 2.222)] = 0.927$
Mixture density, $\rho_m = 4.329$ lbm/ft^3
– $(dp/dz)_F = f_m v_m^2 \rho_m /(2d)/144 = 0.0122$ psi/ft
– $(dp/dz)_H = \rho_m\ g \sin\theta = 0.0301$ psi/ft
– $(dp/dz)_A = \rho_m\ v_m\ (dv_m/dz) = 0.0004$ psi/ft
– $dp/dz = 0.0427$ psi/ft total pressure gradient

The Ansari et al. Model. The Ansari et al. (1994) model computed pressure at 337 ft below the wellhead = 184.17 psia. The values are these:

$\rho_L = 54.81$ lbm/ft^3, $\rho_g = 0.4027$ lbm/ft^3
$x = (933.1 - 809.7)/(2786.3 - 809.7) = 0.0624$
$v_{sg} = q_g/A_x = q_{ms}\ x/\rho_g\ A_x = 20.138$ ft/sec
$v_{sL} = q_L/A_x = 2.222$ ft/sec

The computational approach for in-situ volume fraction and pressure gradient in annular flow using the Ansari et al. model can be found elsewhere (Hasan and Kabir 2007); we summarize the important results here:

Dimensionless film thickness, $\delta = \delta/d = 0.07348$

$f_g = 1 - 4\underline{\delta} = 0.706$

Film friction factor, $f_f = f_{sm}(1 + 300\underline{\delta}) = 0.264$
– $(dp/dz)_F = f_f v_c^2 \rho_c /[2d(1 - 2\underline{\delta})]/144 = 0.0276$ psi/ft
– $(dp/dz)_H = \rho_m\ g \sin\theta = 0.0054$ psi/ft
– $(dp/dz)_A = \rho_m\ v_m\ (dv_m/dz) = 0.0001$ psi/ft
– $dp/dz = 0.0331$ psi/ft total pressure gradient

Appendix 7-F

Comprehensive Energy Balance for Transient Temperature in Oil Reservoirs

A principle for estimation of fluid temperature distribution in the reservoir is the conservation of energy in the system, which includes reservoir fluid and rock. Conservation of mass for reservoir fluids is also incorporated in this study to achieve a comprehensive energy balance equation of the system. The general form of thermal energy balance, in terms of the equation of change for internal energy, was presented in Eq. 7.15. This equation can also be written in terms of enthalpy, temperature, and pressure. In other words, Eq. 7.15 can be rewritten in the following form:

$$\frac{\partial}{\partial t}\rho H - \frac{\partial p}{\partial t} = -(\nabla \cdot \rho H \bar{u}) + \nabla \cdot p\bar{u} - (\nabla \cdot \bar{q}) - (\bar{\tau} : \nabla \bar{u}) - p(\nabla \cdot \bar{u}) + \dot{Q} \quad \text{(7-F-1)}$$

Our reservoir system is a 1D radial system for which the double-dot product can be represented by Newton's law of viscosity, $-(\bar{\tau} : \nabla \bar{u}) = 2\mu\left(\frac{\partial u_r}{\partial r}\right)^2$, and heat conduction can be represented by $-\nabla \cdot \bar{q} = \frac{1}{r}\frac{\partial}{\partial r}\left(\lambda r \frac{\partial T}{\partial r}\right)$; therefore, Eq. 7-F-1 can be written as

$$\frac{\partial}{\partial t}\rho H + \frac{1}{r}\frac{\partial}{\partial r}(r\rho H u_r) = \frac{1}{r}\frac{\partial}{\partial r}\left(\lambda r \frac{\partial T}{\partial r}\right) + 2\mu\left(\frac{\partial u_r}{\partial r}\right)^2 + \frac{Dp}{Dt} + \dot{Q} \quad \text{(7-F-2)}$$

Al-Hadhrami et al. (2003) examined the viscous dissipation term in the energy balance equation in Cartesian coordinates. Following their work, we approximate the viscous term for our 1D radial flow in porous media with $-u_r \frac{\partial p}{\partial r}$. Eq. 7-F-2 then becomes

$$\frac{\partial}{\partial t}\rho H + \frac{1}{r}\frac{\partial}{\partial r}(r\rho \hat{H} u_r) = \frac{1}{r}\frac{\partial}{\partial r}\left(\lambda r \frac{\partial T}{\partial r}\right) - u_r \frac{\partial p}{\partial r} + \frac{Dp}{Dt} + \dot{Q} \quad \text{(7-F-3)}$$

Applying mass conservation in a 1D radial system, $\frac{\partial p}{\partial t} + \frac{1}{r}\frac{\partial}{\partial r}(r\rho u_r) = 0$, Eq. 7-F-3 can be rewritten as

$$\rho \frac{\partial H}{\partial t} = \frac{1}{r}\frac{\partial}{\partial r}\left(\lambda r \frac{\partial T}{\partial r}\right) + \frac{\partial p}{\partial t} + \dot{Q} \quad \text{(7-F-4)}$$

Enthalpy of the reservoir rock depends only on its temperature, which is given by

$$dH_f = c_{pf} dT \quad \text{(7-F-5)}$$

However, the enthalpy of a fluid depends on both its temperature and its pressure; that is,

$$dH = \left(\frac{\partial H}{\partial T}\right)_p dT + \left(\frac{\partial H}{\partial p}\right)_T dp = c_p dT - C_J c_p dp \quad \text{(7-F-6)}$$

In Eq. 7-F-6, c_p is the oil specific heat and C_J is the J-T coefficient. Enthalpy of reservoir oil can be expressed by Eq. 7-F-6 as

$$dH_o = c_{po} dT + \sigma_o dp, \quad \text{(7-F-7)}$$

where σ_o represents the product $-C_J c_p$. A similar expression for connate water can be written.

We write enthalpy in terms of pressure and temperature for each reservoir component—namely, oil, connate water, and formation rock—and combine all parameters into Eq. 7-F-4 to obtain

$$\begin{aligned}&\left[\phi s_o \rho_o c_{po} + \phi s_w \rho_w c_{pw} + (1-0)\rho_s c_{pf}\right]\frac{\partial T}{\partial r} + \rho_o u_r c_{po}\frac{\partial T}{\partial r} + \rho_o u_r c_{po}\frac{\partial p}{\partial r}\\ &+\left[\phi s_o \rho_o \sigma_o + \phi s_w \rho_w \sigma_w - 1\right]\frac{\partial p}{\partial r} = \frac{1}{r}\frac{\partial}{\partial r}\left[\lambda r \frac{\partial T}{\partial r}\right] + \dot{Q}\end{aligned} \quad \text{(7-F-8)}$$

Eq. 7-F-8 is the comprehensive energy balance equation for our system. The first two terms on the left side of Eq. 7-F-8 represent a change of energy because of temperature transient and convective transport, respectively. The third term is energy change attributable to the J-T effect, whereas the fourth term represents energy change from the pressure transient in the reservoir. The first term on the right side of Eq. 7-F-8 is energy change from radial heat conduction, and the last term represents the rate of heat transfer across the system boundary (to overand underburden formations).

Eq. 7-F-8 is fundamentally the same as the final form of thermal energy balance equation presented by App (2010). This equation is also the basis for our analytical model to evaluate the flowing-fluid temperature distribution in the reservoir.

Analytical Solution for Reservoir Flowing-Fluid Temperature Estimation. A comprehensive energy balance equation for the system with a consideration of heat transfer between the system and surroundings is given by Eq. 7-F-8. On the basis of our general assumptions, radial heat conduction during constant-rate production is negligible. In addition, the $\partial p/\partial t$ term is assumed to be minimal and can be omitted. Therefore, Eq. 7-F-8 becomes

$$\left[\phi s_o \rho_o c_{po} + \phi s_w \rho_w c_{pw} + (1-\phi)\rho_s c_{pf}\right]\frac{\partial T}{\partial r} + \rho_o u_r c_{po}\frac{\partial T}{\partial r} + \rho_o u_r c_{po}\frac{\partial p}{\partial r} = \dot{Q} \quad \text{(7-F-9)}$$

We rewrite velocity u_r in terms of flow rate as $q/(2\pi rh)$ and rewrite the $\partial p/\partial r$ in terms of flow rate as $-(\mu q)/(2\pi rhk)$. Also, we replace q with $-q$ because flow occurs in the negative r direction during production. Therefore, Eq. 7-F-9 becomes

$$\left[\phi s_o \rho_o c_{po} + \phi s_w \rho_w c_{pw} + (1-\phi)\rho_s c_{pf}\right]\frac{\partial T}{\partial r} - \frac{q p_o c_{po}}{2\pi rh}\frac{\partial T}{\partial r} - \frac{\mu q^2 \rho_o \sigma_o}{(2\pi rh)^2 k} = \dot{Q} \quad \text{(7-F-10)}$$

Solution Neglecting $\dot{Q}$. If we neglect heat loss to the over- and underburden and use lumped parameters A, B, and C, Eq. 7-F-10 is simplified to

$$Ar^2\frac{\partial T}{\partial t} - Br\frac{\partial T}{\partial r} - C = 0 \quad \text{(7-F-11)}$$

Eq. 7-F-11 is a first-order, partial-differential equation in which fluid temperature T is a function of radial distance from wellbore into the reservoir r and producing time t. Initially, fluid temperature in the reservoir is constant at T_i, giving the following initial condition:

$$T(r, t=0) = T_i \quad \text{(7-F-12)}$$

Eq. 7-F-11 can be solved by the method of characteristics. The final form of an analytical solution for the flowing-fluid temperature without considering heat transfer to surroundings is presented in the following:

$$T(r,t) = T_i - \frac{C}{2B}\ln\left(\frac{r^2 A}{\left|r^2 A + 2Bt\right|}\right), \quad \text{(7-F-13)}$$

where

$$A = \left[\phi s_o \rho_o c_{po} + \phi s_w \rho_w c_{pw} + (1-\phi)\rho_s c_{pf}\right]\left(\frac{2\pi h}{q}\right), \quad \text{(7-F-14)}$$

$$B = \rho_o c_{po}, \quad \text{(7-F-15)}$$

and

$$C = \frac{q\rho_o \sigma_o \mu}{2\pi hk}. \quad \text{(7-F-16)}$$

Note that parameters A, B, and C are constant for a particular reservoir and are reported in the main text in Eqs. 7.21, 7.22, and 7.23, respectively. Details of derivation for this solution are found in Chevarunotai et al. (2015).

Solution Including $\dot{Q}$. The net input rate of energy between reservoir and under- and overburden formations, $\dot{Q}$, is related to the formation undisturbed temperature in a complex manner. We are approximating this term following App's (2010) approach

using Newton's law of cooling, giving $\dot{Q} = -\frac{2h_c(T - T_s)}{h}$. Therefore, the complete energy balance equation of the system becomes

$$\left[\phi s_o \rho_o c_{po} + \phi s_w \rho_w c_{pw} + (1-\phi)\rho_s c_{pf}\right]\frac{\partial T}{\partial r} - \frac{q\rho_o c_{po}}{2\pi rh}\frac{\partial T}{\partial r} - \frac{\mu q^2 \rho_o \sigma_o}{(2\pi rh)^2 k} = -\frac{2h_c\left[T - T_s\right]}{h} \quad \text{(7-F-17)}$$

Multiplying both sides of Eq. 7-F-17 by $\frac{2\pi r^2 h}{q}$, we can write

$$Ar^2\frac{\partial T}{\partial t} - Br\frac{\partial T}{\partial r} - C = -\frac{4\pi r^2 h_c}{q}T + \frac{4\pi r^2 h_c}{q}T_s, \quad \text{(7-F-18)}$$

where constants *A, B*, and *C* are as defined before.

We assume that the heat-transfer coefficient h_c is constant. In this study, the heat-transfer coefficient presented in App's paper was used. In addition, we assume that the surrounding temperature remains at its initial condition throughout the production period even after heat transfer takes place. Eq. 7-F-19 can then be written as

$$Ar^2\frac{\partial T}{\partial t} - Br\frac{\partial T}{\partial r} - C = -Dr^2 T + Er^2. \quad \text{(7-F-19)}$$

We apply the method of characteristics with the initial condition $T(r, t = 0) = T_i$ to solve Eq. 7-F-19. The final form of the analytical solution for flowing-fluid temperature in the reservoir with a consideration of energy transfer between the system and surroundings can be expressed as

$$T(r,t) = T_i + \frac{C}{2B}e^{\frac{H(Ar^2+2Bt)}{2B}}Ei\left[-\frac{H(Ar^2+2Bt)}{2B}\right] - \frac{C}{2B}e^{\left(\frac{HAr^2}{2B}\right)}Ei\left(-\frac{HAr^2}{2B}\right). \quad \text{(7-F-20)}$$

Definitions of all constant parameters—that is, *A, B, C, D, E*, and *H*—are presented by the following expressions:

$$A = \left[\phi s_o \rho_o c_{po} + \phi s_w \rho_w c_{pw} + (1-\phi)\rho_s c_{pf}\right]\left(\frac{2\pi h}{q}\right), \quad \text{(7-F-21)}$$

$$B = \rho_o c_{po}, \quad \text{(7-F-22)}$$

$$C = \frac{q\rho_o \sigma_o \mu}{2\pi hk}, \quad \text{(7-F-23)}$$

$$D = \frac{4h_c\pi}{q}, \quad \text{(7-F-24)}$$

$$E = \frac{4h_c\pi}{q}T_i, \quad \text{(7-F-25)}$$

and

$$H = \frac{D}{A} \qquad (7\text{-F-}26)$$

Appendix 7-G

Input Data for Model Validation

In this appendix, reservoir rock and fluid properties from an actual well and reservoir are used to test the model. These field data are the same as those presented in App (2010), wherein the solutions were generated with a numerical model.

Table 7-G-1 shows static (rock) properties of the reservoir, which are considered as a base case in this study. We assume that the reservoir is homogeneous and that these parameters remain constant throughout the production period. **Table 7-G-2** presents the reservoir fluid properties. Only single-phase oil flow occurs in the formation, without any associated gas or water production.

Another critical fluid property in flowing-fluid temperature and well productivity calculation is oil viscosity. Data from laboratory measurements for this particular reservoir were also presented in App (2010). **Fig. 7-G-1** presents the oil viscosity as a function of pressure and temperature, which is used for model validation.

An important assumption in our model is that conductive heat flow for our problem is negligible. App and Yoshioka (2013) have shown that the effect of formation thermal conductivity can be represented by the Péclet number. Relating fluid velocity *u* to production rate *q*, they expressed P_e as follows:

$$P_e = \frac{ur}{\alpha} = \frac{q\rho_o c_{po}}{2\pi h\lambda} \quad \text{(7-G-1)}$$

Their work showed that when $0.1 > P_e > 3$, the effect of P_e is negligible, and therefore the effect of formation thermal conductivity *l* on fluid temperature change from expansion is also negligible. The calculations for P_e for our lowest production rate of 970 STB/D are

$$q = 970\frac{\text{STB}}{D} \times \left(\frac{5.615\frac{\text{ft}^3}{\text{STB}}}{24\frac{\text{hr}}{D}} \right) = 227\frac{\text{ft}^3}{\text{hr}}, \quad \text{(7-G-2)}$$

Parameters	Value
k, md	20
φ, %	25
h, ft	100
p_i psia	21,000
p_b, psia	7,000

C_t, psi^{-1}	$3 \cdot 10^{-6}$
T_i, °F	302
r_w, ft	0.41
r_e, ft	4,000
S_{wi}, %	15
h_c, Btu/hr·ft·^{2}°F	0.92

Table 7-G-1—Reservoir static parameters (App 2010).

Parameter (units)	Value
B_o, bbl/STB	1.05
ρ_o, lbm/ft^3	51.19
C_{po}, Btu/lbm/°F	0.53
σ_o, °F/psi	–0.0055
ρ_w, lbm/ft^3	63.68
C_{pw}, Btu/lbm/°F	1.0
σ_w, °F/psi	–0.0024
ρ_f, lbm/ft^3	165.43
C_{pf}, Btu/lbm/°F	0.20
λ, Btu/hr ft °F	1.73
μ, cp	2.0

Table 7-G-2—Reservoir fluid parameters (App 2010).

and

$$\mathrm{P}_e = \frac{q\rho c_p}{2\pi h\lambda} = \frac{227\dfrac{\mathrm{ft}^3}{\mathrm{hr}} \times 51.19\dfrac{\mathrm{lbm}}{\mathrm{ft}^3} \times 0.53\dfrac{\mathrm{Btu}}{\mathrm{lbm}\ ^\circ\mathrm{F}}}{2\pi \times 100\ \mathrm{ft} \times 1.73\left(\dfrac{\mathrm{BTU}}{\mathrm{hr}\ ^\circ\mathrm{F\ ft}}\right)} = 5.6 \qquad (7\text{-G-}3)$$

Similarly, for our highest production rate of 6,200 STB/D, P_e = 36.3. Thus, for the cases considered in this study, omitting thermal conductivity of the formation does not introduce any significant error. We note that for most deepwater assets, economic production rates are expected to be high enough to result in correspondingly high Péclet numbers. As a consequence, the underlying assumptions made while deriving the analytical formulation of this coupled fluid/heat flow problem appear reasonable.

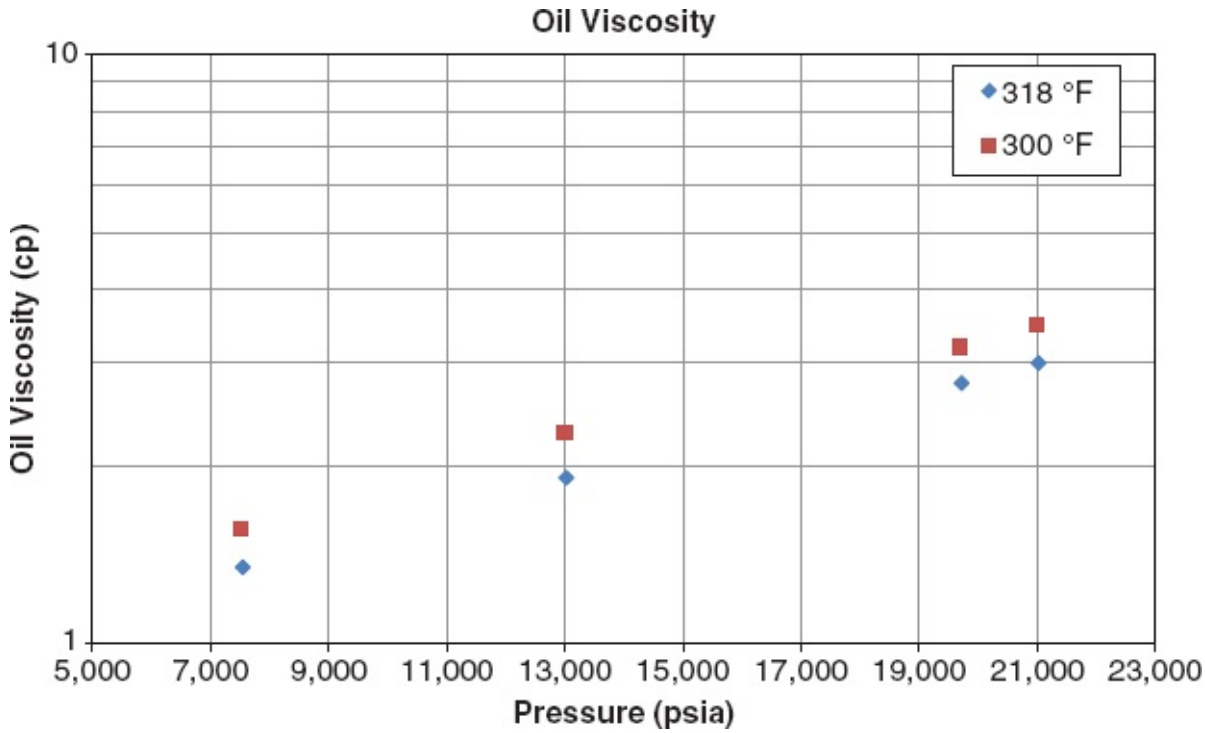

Fig. 7-G-1—Oil viscosity as a function of pressure and temperature (App 2010).

Chapter 8

Wellbore Temperature Profiles in Multiple Strings

8.1 Introduction

Ordinarily, solutions of most fluid flow and heat flow problems in a wellbore deal with unidirectional fluid flow in a single production string. Chapter 6 presents working equations for estimating fluid temperature in such systems. However, oil production often involves more than the traditional single-string scenario. Economic necessity dictates coproduction of fluids through the annulus and tubing, through two independent strings, and injection down one string and production up the other in the same wellbore. The heat-transfer issue becomes complicated when production through seawater and air occurs in an offshore environment. These and other complex configurations demand knowledge of temperature and pressure profiles for optimization of production and/or injection in each string.

In subsequent chapters, we discuss a number of complex heat-transfer issues. For example, modeling unsteadystate heat transfer during transient testing of gas and oil wells, presented in Chapter 9, aids understanding of wellbore phenomena, leading to improved test interpretation and design. Similarly, temperature estimation during steady fluid circulation through tubing/annulus in drilling and during gas injection through an annulus into tubing in gas lift is discussed in Chapter 11, Section 11.2, and Chapter 12, Section 12.2. Chapter 12, Section 12.3, presents other heat-transfer issues as they pertain to petroleum production.

Estimating fluid temperature in bundled tubes can be demanding in deepwater producing environments, where considerable heat transfer may occur. To address some of the plausible scenarios, in this chapter we present analytic solutions for temperature profiles when flow occurs simultaneously in multiple strings. Our motivation stems from the difficulty of using in complex systems the systems analysis (Hagedorn and Brown 1965; Brown and Lea 1985; Kabir et al. 1998; among others) —as discussed in Chapter 12, Section 12.1—that was originally intended for single-string completions. That is because the unknown fluid temperature profiles may have significant bearing on the fluid properties and, in turn, on pressure-drop computation. Besides pursuing issues related to systems analysis, we hope to present building blocks for interpreting temperature logs, which can pose significant challenges because of complex heat-transfer issues in systems with multiple strings.

Very few researchers have dealt with analysis of energy exchange among fluids in multiple conduits in a single wellbore. Hight et al. (1992) discussed parallel tubing in the wellbore to convey steam and hot water for injection in steamflooding. As

expected, they found that parallel tubing conserved more heat than did single tubing, but they presented no heat-transfer model. More recently, Stone et al. (2014) presented a thermal model developed for steam-assisted-gravity-drainage application that can handle multiple tubing strings in a well. The model uses an involved numerical scheme to account for heat transfer among fluids in various conduits. Eq. 6.19 is used for heat transfer between the wellbore and the formation.

In the next section, we present physical models for three different configurations: (1) production through tubing and annulus, (2) production through two tubing strings, and (3) production and injection through two tubing strings in a common wellbore. Note that the annular fluid in production through tubing and annulus is forced convection, discussed in Section 8.2. In contrast, when production and/or production/injection occurs through two tubing strings, as discussed in Sections 8.3 and 8.4, the annular fluid remains static, allowing only natural convective heat transfer. Mathematical models developed for these flow problems reflect differing modes of heat transfer in the annulus.

Despite the apparent difference, the three situations are similar in some respects. For example, heat exchange between the formation and the annular fluid is represented by the same expression for the three cases and is similar to the one used in Chapter 6 (Eq. 6.19): $Q = wc_{pa}(T_{ei} - T_a)L_R$. These models, however, differ from the basic model of Chapter 6 because the fluid temperature in an additional conduit must be modeled by setting up an energy balance involving the fluid. This additional equation leads to the second-order governing differential equation, as opposed to the first-order equation for a single conduit, presented in Chapter 6. Let us discuss these three cases in detail.

8.2 Production Through the Tubing and Annulus

8.2.1 Mathematical Model. To segregate fluids, production from geologically contrasting horizons often occurs through two separate completions. **Fig. 8.1** schematically shows that the primary production occurs through the tubing, while a secondary production is up the annulus. The energy balance for a differential fluid element in the annulus involves heat transfer to the annular fluid from the formation, $Q = wc_{pa}(T_{ei} - T_a)L_R$ (Eq. 6.19) and from the annular fluid to the tubing fluid, Q_{ta}; enthalpy change in the annular fluid; and energy related to fluid static and kinetic heads. Thus, the energy balance based on a unit flow rate for the annulus fluid contained in a differential element, dz, is given by:

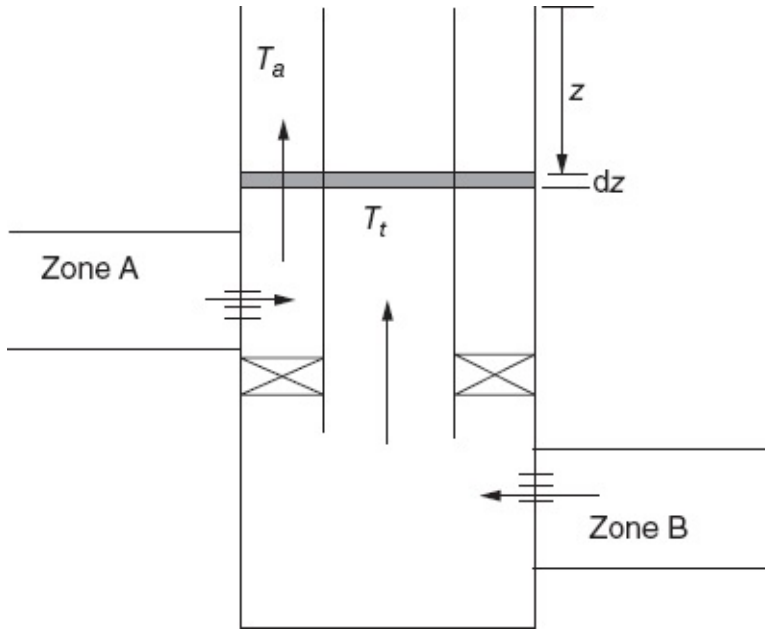

Fig. 8.1—Production through tubing and annulus.

$$H_a\big|_{z+\mathrm{d}z} + \frac{(L-z-\mathrm{d}z)g\sin\alpha}{Jg_c} + \frac{v^2\big|_{z+\mathrm{d}z}}{2Jg_c} + \frac{Q}{w_a}\mathrm{d}z = H\big|_z + \frac{(L-z)g\sin\alpha}{Jg_c} + \frac{v^2\big|_z}{2Jg_c} + \frac{Q_{ta}}{w_a}\mathrm{d}z, \quad (8.1a)$$

as stated in Hasan and Kabir (1994a) and Alves et al. (1992). Rearranging, we obtain

$$\frac{Q_{ta}-Q}{w_a} = \frac{\mathrm{d}H_a}{\mathrm{d}z} - \frac{g\sin\alpha}{g_cJ} + \frac{v_a}{g_cJ}\frac{\mathrm{d}v_a}{\mathrm{d}z}. \quad (8.1b)$$

Note the similarities between Eq. 8.1b and its counterpart for production through a single conduit, Eq. 6.13. Eq. 8.1b relates two unknowns—tubing and annulus fluid temperatures—represented by the two heat-transfer terms, Q and Q_{ta}. Therefore, the solution of Eq. 8.1b requires an additional relationship, which is obtained by relating annular and tubing fluid temperatures with a coefficient representing heat transfer between the two fluids. Heat transferred from the annular fluid to the tubing fluid is related to the temperature difference between the fluids in two conduits and to the heat-transfer coefficient for the system. On a per-unit-length basis, this heat-transfer rate is given by

$$Q_{ta} = 2\pi r_t U_t\left(T_a - T_t\right) = \frac{c_{pa}}{B_a}\left(T_a - T_t\right), \quad (8.2)$$

where

$$B_a = \frac{w_a c_{pa}}{2\pi r_t U_t}. \quad (8.3)$$

By combining Eqs. 8.1b, 8.2, and 6.20 and expressing enthalpy change in terms of changes in temperature and pressure, $dH = c_p dT - C_j c_p dp$ (Eq. 6.14), we obtain

$$c_{pa}\frac{dT}{dz} - \frac{C_J c_{pa}}{J}\frac{dT}{dz} - \frac{g\sin\alpha}{g_c J} + \frac{v}{g_c J}\frac{dv}{dz} = -L_R c_{pa}\left(T_{ei} - T_a\right) + \frac{c_{pa}}{B_a}\left(T_t - T_a\right),$$

or

$$c_{pa}\frac{dT}{dz} + D_a = -L_R c_{pa}\left(T_{ei} - T_a\right) + \frac{c_{pa}}{B_a}\left(T_t - T_a\right). \quad (8.4)$$

We use D_a to combine those terms having a small total contribution in Eq. 8.4 and values that remain relatively constant throughout the length of the wellbore. The term D_a in Eq. 8.4 is given by

$$D_a = -\frac{C_J c_{pa}}{J}\frac{dT}{dz} - \frac{g\sin\alpha}{g_c J} + \frac{v}{g_c J}\frac{dv}{dz} \quad (8.5)$$

The energy balance for the tubing fluid may be similarly written as

$$c_{pt}\frac{dT}{dz} + D_t = \frac{w_a c_{pa}}{w_t B_a}\left(T_t - T_a\right), \quad (8.6)$$

where D_t, is the term analogous to D_a for the tubing fluid.

Eq. 8.6 can be used to write T_a in terms of T_t for substitution in Eq. 8.4 as

$$T_a = T_t - B'\frac{dT_t}{dz} - B'\frac{D_t}{c_{pt}}, \quad (8.7)$$

where

$$B' = \frac{w_t c_{pt}}{2\pi r_t U_t}. \quad (8.8)$$

Combining Eqs. 8.4 and 8.7, we derive the governing differential equation for fluid temperature, which we can write as

$$-\frac{B'}{L_R}\frac{d^2T_t}{dz^2} + B''\frac{dT_t}{dz} - T_t + T_{es} + g_G z\sin\alpha + D' = 0, \quad (8.9)$$

where

$$B'' = B' + \frac{B'}{BL_R} + \frac{1}{L_R} \quad (8.10)$$

and

$$D' = B'\frac{D_t}{c_{pt}} + B'\frac{D_t}{c_{pt}}\frac{1}{B_a L_R} - \frac{D_a}{L_R c_{pa}}. \quad (8.11)$$

Eq. 8.9 is a second-order differential equation that becomes linear and solvable if D' is constant. The solution of Eq. 8.9 is similar to that of the gas lift problem (Hasan and Kabir 1996) (Chapter 12, Section 12.2). The solution leads to the expressions for the temperature of the annular and tubing fluids above Zone A, which are written as

$$T_t = \alpha e^{\lambda_1 z} + \beta e^{\lambda_2 z} + g_G z \sin\alpha + B'' g_G \sin\alpha + T_{es} + D' \quad (8.12)$$

and

$$T_a = (1-\lambda_1 B')\alpha e^{\lambda_1 z} + (1-\lambda_2 B')\beta e^{\lambda_2 z} + g_G \sin\alpha (B'' - B') + g_G z \sin\alpha + T_{es} + D' \quad (8.13)$$

Section 8-A.1, in Appendix 8-A, presents the expressions for various parameters. Note that tubing fluid temperature below Zone A can be estimated with Eq. 6.29.

Field Example 8.1—Well A28. Well A28 produces up the tubing and tubing/casing annulus. Field measurements were made in the tubing string during flowing condition at various depths, called stations. At each station, 15 minutes was allowed for thermal equilibration to occur between the external temperature probe with its surrounding fluids. Section 8-A.4, in Appendix 8-A, presents relevant field data needed for computation.

***Solution*. Fig. 8.2** shows that Eq. 8.12, represented by the solid line, reproduces the measured tubing fluid temperature within engineering accuracy. The temperature difference between the tubing and annulus is small because flow in both strings promotes heat transfer. Note that production of annular fluid causes higher dissipation of heat because of forced convection than would be the case if the annular fluid were stationary, as shown by the dashed line in Fig. 8.2 (static annulus). The temperature difference between the two cases is rather large, strongly indicating the need for rigorous modeling.

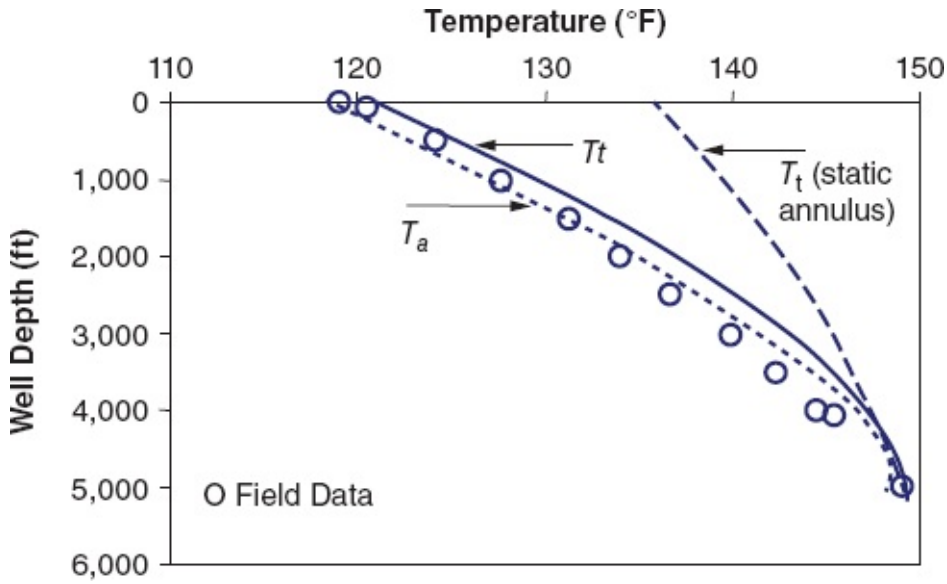

Fig. 8.2—Matching field data during tubing/annulus flow, Well A28.

8.3 Production Through Two Tubing Strings

8.3.1 Mathematical Model. Fig. 8.3 shows a schematic for the case where two tubing strings are used to produce from two separate zones with stationary fluid in the annulus. We let subscript *ls* denote the long string, producing from the deeper horizon (Zone B), and subscript *ss* stands for the short string, producing from the shallower horizon (Zone A). In writing the energy balance for this case, we have denoted Q_2 as the energy entering the short string from the annulus, while Q_1 is the energy entering the annulus from the long string. Heat gained from the annulus to the formation is designated Q_3. The energy balance for the annulus is then written as

$$Q_2 = Q_1 + Q_3. \qquad (8.14)$$

These energy-transfer terms—Q_1, Q_2, and Q_3—can be expressed in terms of temperature-difference driving forces and heat-transfer coefficients as

$$Q_1 = 2\pi r_1 U_1 \left(T_{ls} - T_a\right), \qquad (8.15)$$

$$Q_2 = 2\pi r_2 U_2 \left(T_a - T_{ss}\right), \qquad (8.16)$$

and

$$Q_3 = w_{ls} c_{pls} \left(T_{ei} - T_a\right) L_R. \qquad (8.17)$$

Energy balance for the annular fluid, given by Eq. 8.14, may then be rewritten as

$$\left(T_{ls} - T_a\right)\left(2\pi r_{ls} U_{ls}\right) = \left(T_a - T_{ss}\right)\left(2\pi r_{ss} U_{ss}\right) + \left(T_a - T_{ei}\right)\left(w_{ls} c_{pls} L_R\right) \qquad (8.18)$$

Energy balance for the long string is given by

$$\frac{dT_{ls}}{dz} = (T_{ls} - T_a)\frac{2\pi r_{ls} U_{ls}}{c_{pls} w_{ls}} + \frac{g \sin\alpha}{c_{pls}} + \phi_{ls} \quad (8.19)$$

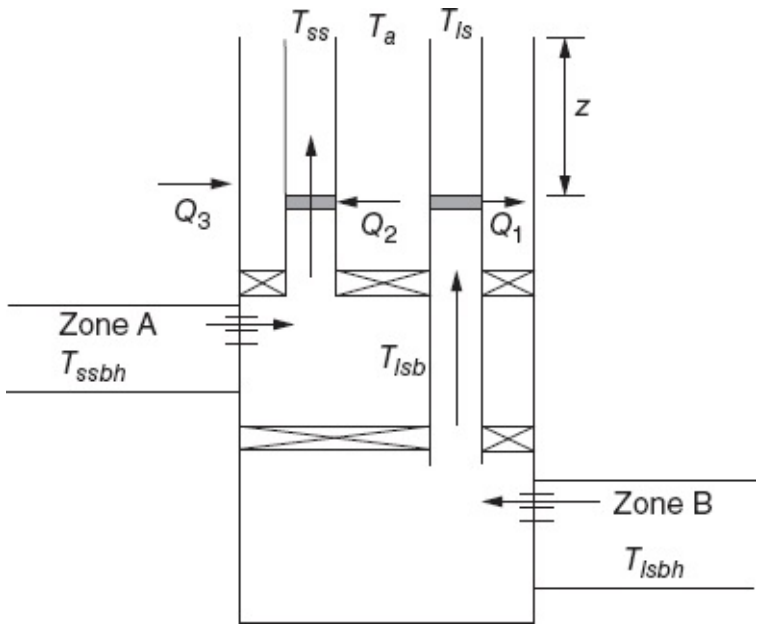

Fig. 8.3—Production through two tubing strings.

Similarly, for the short string, the energy balance is

$$\frac{dT_{ss}}{dz} = (T_a - T_{ss})\frac{2\pi r_{ss} U_{ss}}{c_{pss} w_{ss}} + \frac{g \sin\alpha}{c_{pss}} + \phi_{ss}, \quad (8.20)$$

where parameters f_{ls} and f_{ss} are defined as

$$\phi_{ls} = \left[C_{Jls}\left(\frac{dp}{dz}\right)_{ls} - \frac{v_{ls}}{c_{pls}}\frac{dv_{ls}}{dz} \right] \quad (8.21)$$

and

$$\phi_{ss} = \left[C_{Jss}\left(\frac{dp}{dz}\right)_{ss} - \frac{v_{ss}}{c_{pss}}\frac{dv_{ss}}{dz} \right] \quad (8.22)$$

Eqs. 8.18 through 8.20 have three unknowns: T_{ls}, T_{ss}, and T_a. Therefore, they can be solved if ϕ_{ls} and ϕ_{ss} are considered constants. These equations are rewritten in the following forms using parameters a_1, a_2, … a_7, which are defined in Appendix 8-A.

$$a_1 T_{ls} + a_2 T_a + a_3 T_{ss} + a_4 (L - z) + a_5 = 0, \quad (8.23)$$

$$\frac{dT_{ls}}{dz} = -a_6(T_{ls} - T_a) + \phi_{ls} + \frac{g\sin\alpha}{c_{pls}}, \quad (8.24)$$

and

$$\frac{dT_{ss}}{dz} = a_7(T_{ss} - T_a) + \phi_{ss} + \frac{g\sin\alpha}{c_{pss}} \quad (8.25)$$

The general solutions for temperature in the long and short strings are given by

$$T_{ls} = c_1 e^{\lambda_{ls} z} + c_2 e^{\lambda_{ss} z} + \frac{b_4}{b_3} z + \frac{b_3 b_5 - b_2 b_4}{b_3^2} \quad (8.26)$$

and

$$T_{ss} = d_1 c_1 e^{\lambda_{ls} z} + d_2 c_2 e^{\lambda_{ss} z} + d_3 z + d_4 \quad (8.27)$$

The expression for the annular fluid temperature is given by

$$T_a = d_1 c_1 e^{\lambda_{ls} z}\left(1 - \frac{w_{ss} c_{pss} \lambda_{ls}}{2\pi r_{ss} U_{ss}}\right) + d_3 z + d_4 + d_2 c_2 e^{\lambda_{ss} z}\left(1 - \frac{w_{ss} c_{pss} \lambda_{ss}}{2\pi r_{ss} U_{ss}}\right) + \frac{w_{ss} c_{pss}}{2\pi r_{ss} U_{ss}}(\phi_{ss} - d_3) \quad (8.28)$$

Appendix 8-A, Section 8-A.2, presents the parameters of Eqs. 8.26 through 8.28.

Field Example 8.2—Well C39. Fluids are produced up two separate tubing strings in Well C39. Relevant data are presented in Appendix 8-A, Section 8-A.4. We attempted to reproduce the temperature profile recorded in the long string.

***Solution*.** Fig. 8.4 exhibits Eq. 8.13 in the solid line, mimicking the long-string fluid temperature data very well. As in the previous case, the temperature difference between the tubing fluid and annular fluid is small. However, unlike the previous case, a temperature difference of approximately 8°F occurs at the wellhead when the short string remains idle, suggesting the lesser dominance of annular fluid in controlling the convective heat transfer. Producing through the short string and keeping the long string idle produces a temperature trace quite similar to that in the short string.

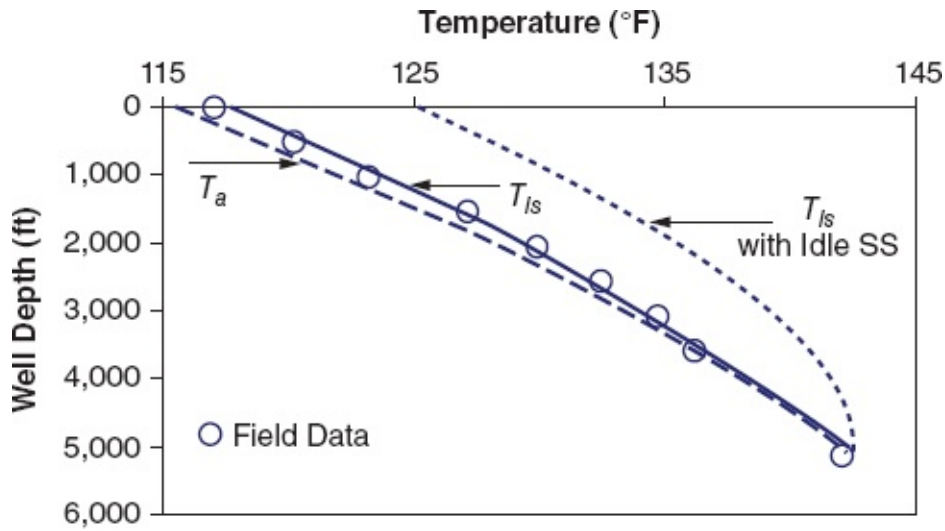

Fig. 8.4—Matching field data during flow up two independent strings, Well C39.

8.4 Production and Injection Through a Common Wellbore

8.4.1 Mathematical Model. When simultaneous production and injection occurs through the same wellbore, questions arise as to whether cold-water injection will promote formation of hydrates during gas production or of paraffin during oil production. **Fig. 8.5** shows a schematic for the dual injection/production scheme. In this case, a fluid is injected into a deeper horizon (long string or *ls*) while production occurs through a shallower interval (short string or *ss*) through two independent strings.

The governing differential equations, in this case, obtained from energy balances, are the same as those for the last case. Thus, Eqs. 8.18, 8.19, and 8.20 apply to the state of production and injection through two strings as well. Solutions for these equations are also the same; that is, Eqs. 8.26 through 8.28 represent fluid temperatures of the conduits in this case. However, differences in the flow direction here compared with the previous case result in a slight difference in boundary conditions for the two cases, which leads to somewhat different expressions for the various parameters in the temperature equations. These differences are clearly noted in Section 8-A.3 in Appendix 8-A.

Illustrative Example—Injection/Production Scenario. We present a synthetic case to show the variation in temperature profiles when simultaneous injection/production occurs through two strings in the same wellbore. Here, cold water is injected at 10,000 ft, while oil production occurs from an interval of 8,000 ft. The kinks in the annular and injected-fluid temperatures at 8,000 ft are a direct reflection of the abrupt fluid entry. Input parameters are detailed in Appendix 8-A.

Solution. **Fig. 8.6** shows that the injected fluid assumes a much lower temperature profile in the absence of oil production, thereby suggesting poor heat convection in the annulus. In other words, whereas the phase behavior of the

producing fluid may be favorable during simultaneous operation, problems may arise during startup if contingency plans are not made. These types of computations during completion design are needed to avoid potential production/operation problems.

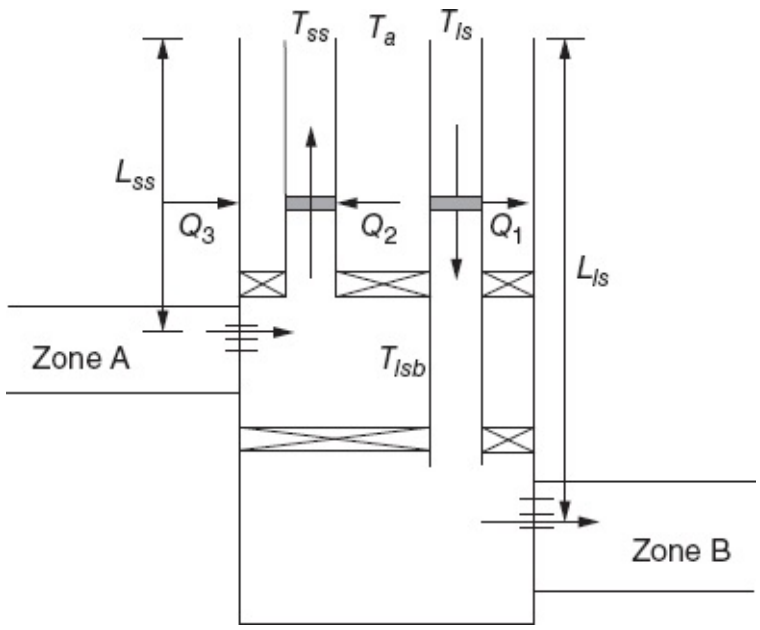

Fig. 8.5—Production and injection through two independent strings.

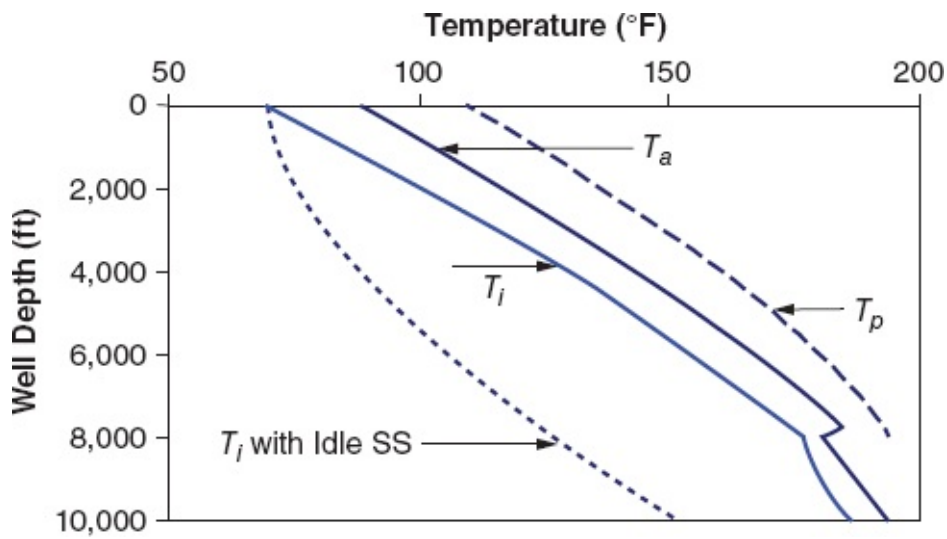

Fig. 8.6—Temperature profiles during a production/injection scenario.

Summary

In this chapter, we have discussed how temperature profiles could be computed in three scenarios involving multiple strings. Solutions for each case, including those presented here, are needed to aid completion design, perform systems analysis, and evaluate temperature logs.

Complications arise when production or production/injection occurs through two strings in the same wellbore. For example, we learned that heat loss is promoted in

the tubing string when simultaneous production occurs in both the tubing and the tubing/casing annulus. Consequently, the tubular fluid experiences lower temperature than the static annular fluid situation. In contrast, the static annular fluid controls heat exchange with its surrounding formation when production in two independent production strings is involved. Therefore, production or shut-in of the short string has a marginal impact on the temperature profile in the long string and vice versa. When cold water is injected in one of the two strings, the temperature profile in the production string may be altered significantly, which may promote problems with precipitation of solids such as hydrates, paraffins, and asphaltenes. In Chapter 12, we discuss how asphaltenes and paraffin may be combated, as well as issues related to systems analysis.

Nomenclature

a_1, a_2, a_3 = parameters defined by Eq. 8-A-11 through Eq. 8-A-13, Btu/hr-ft-°F

a_4 = parameter defined by Eq. 8-A-14, Btu/hr-ft^2

a_5 = parameter defined by Eq. 8-A-15, Btu/hr-ft

a_6, a_7 = parameters defined by Eqs. 8-A-16 and Eq. 8-A-17, 1/ft

b_1 = $-a_2$, Btu/hr-ft-°F

b_2 = parameter defined by Eq. 8-A-19, Btu/hr-ft^2-°F

b_3 = parameter defined by Eq. 8-A-20, Btu/hr-ft^3-°F

b_4 = parameter defined by Eq. 8-A-21, Btu/hr-ft^4

b_5 = parameter defined by Eq. 8-A-22, Btu/hr-ft

B' = parameter defined by Eq. 8.8, ft

B'' = parameter defined by Eq. 8.10, ft

c_p = heat capacity of fluids, Btu/lbm-°F

C_j = Joule-Thomson coefficient, °F/psi

g = gravitational acceleration, ft/sec^2

g_G = geothermal temperature gradient, °F/ft

D_a = parameter defined by Eq. 8.5, Btu/lbm-ft

D_t = parameter defined by Eq. 8.6, Btu/lbm-ft

D' = parameter defined by Eq. 8.11, °F

H = fluid enthalpy, Btu/lbm

J = ft-lbf to Btu conversion factor, dimensionless

k_e = earth or formation conductivity, Btu/hr-ft-°F

L = well length, ft

L_R = relaxation distance parameter, 1/ft

p = pressure, psi

q = volumetric oil flow rate, STB/D

Q = heat flow rate per unit length from or to the formation, Btu/hr-ft

r = radius of flow string, L

T = fluid or formation temperature, °F

T_D = dimensionless temperature (= $2\pi k_e \Delta T/Q$)

U = overall-heat-transfer coefficient for a string, Btu/hr-ft^2-°F

v = fluid velocity, ft/sec

w = mass flow rate, lbm/sec

z = variable well depth from surface, ft

α = parameter used in Eq. 8.12, °F

β = parameter used in Eq. 8.12, °F

ϕ = parameter used in Eq. 8.20, °F/ft

λ = parameter defined by Eqs. 8-A-1 and 8-A-2

Subscripts

a	=	annulus
bh	=	bottomhole
es	=	earth static
ls	=	long string
ss	=	short string
t	=	tubing

Appendix 8-A

Working Equations for Multiple-String Completions

8-A.1 Production Through Tubing and Annulus. Eq. 8.9 is a second-order linear differential equation the solution of which is given by Eqs. 8.12 and 8.13. The constants of Eqs. 8.12 and 8.13 are given by

$$\lambda_{ls} = \frac{L_R B''}{2B'} - \frac{L_R B''}{2B'}\sqrt{1-\frac{4B'}{L_R B''^2}}, \qquad (8\text{-A-1})$$

$$\lambda_{ss} = \frac{L_R B''}{2B'} + \frac{L_R B''}{2B'}\sqrt{1-\frac{4B'}{L_R B''^2}}, \qquad (8\text{-A-2})$$

$$\alpha = \frac{(1-\lambda_{ss}B')\left(T_{tbh} - T_{es} - g_G L_{ss}\sin\alpha - B'' g_G \sin\alpha\right)}{B'(\lambda_{ls}-\lambda_{ss})\exp(\lambda_{ls}L_{ss})} - \frac{T_{abh} - T_{es} - g_G L_{ss}\sin\alpha - (B''-B')g_G\sin\alpha}{B'(\lambda_{ls}-\lambda_{ss})\exp(\lambda_{ls}L_{ss})}, \qquad (8\text{-A-3})$$

$$\beta = -\frac{(1-\lambda_{ls}B')\left(T_{tbh} - T_{es} - g_G L_{ss}\sin\alpha - B'' g_G \sin\alpha\right)}{B'(\lambda_{ls}-\lambda_{ss})\exp(\lambda_2 L_{ss})} + \frac{T_{abh} - T_{es} - g_G L_{ss}\sin\alpha - (B''-B')g_G\sin\alpha}{B'(\lambda_{ls}-\lambda_{ss})\exp(\lambda_{ss}L_{ss})}, \qquad (8\text{-A-4})$$

$$L_R \equiv \frac{2\pi}{c_{Pa}w_a}\left[\frac{r_{to}U_{to}k_e}{k_e + \left(r_{to}U_{to}T_D\right)}\right], \qquad (8\text{-A-5})$$

$$B_a = \frac{w_a c_{pa}}{2\pi r_t U_t}, \qquad (8\text{-A-6})$$

$$B' = \frac{w_t c_{pt}}{2\pi r_t U_t}, \qquad (8\text{-A-7})$$

and

$$B'' = B' + \frac{B'}{L_R B} + \frac{1}{L_R}. \quad (8\text{-A-}8)$$

8-A.2 Production Through Two Tubing Strings. The relaxation length, L_{Ra}, has the same form as L_R defined by Eq. 8-A-5. However, the total-heat-transfer coefficient should be calculated from the annulus instead from the tubing, giving

$$\frac{1}{U_a} = \frac{r_{wb}\ln(r_{caseo}/r_{casein})}{k_{case}} + \frac{r_{wb}\ln(r_{cemt}/r_{caseo})}{k_{cemt}}, \quad (8\text{-A-}9)$$

and

$$L_R \equiv \frac{2\pi}{c_{Pls}w_{ls}}\left[\frac{r_{wb}U_a k_e}{k_e + \left(r_{wb}U_a T_D\right)}\right] \quad (8\text{-A-}10)$$

The parameters in the governing differential equations, Eqs. 8.23 through 8.25, are

$$a_1 = 2\pi r_{ls}U_{ls}, \quad (8\text{-A-}11)$$

$$a_2 = -\left(2\pi r_{ls}U_{ls} + 2\pi r_{ss}U_{ss} + L_R w_{ls}c_{pls}\right), \quad (8\text{-A-}12)$$

$$a_3 = 2\pi r_{ss}U_{ss}, \quad (8\text{-A-}13)$$

$$a_4 = -L_R w_{ls}c_{pls}g_G \sin\alpha, \quad (8\text{-A-}14)$$

$$a_5 = L_R T_{lsbh}w_{ls}c_{pls}, \quad (8\text{-A-}15)$$

$$a_6 = -\frac{2\pi r_{ls}U_{ls}}{c_{ls}w_{ls}}, \quad (8\text{-A-}16)$$

and

$$a_7 = -\frac{2\pi r_{ss}U_{ss}}{c_{ss}w_{ss}}. \quad (8\text{-A-}17)$$

Omitting the tedious derivation, we present the final differential equation for T_{ls} as

$$b_1\frac{d^2T_{ls}}{dz^2} + b_2\frac{dT_{ls}}{dz} + b_3T_{ls} = b_4 z + b_5, \quad (8\text{-A-}18)$$

where parameters $b_1 = -a_2$, and b_2, b_3, b_4, and b_5 are defined as

$$b_2 = a_7(a_2 + a_3) - a_6(a_1 + a_2), \quad (8\text{-A-}19)$$

$$b_3 = a_6 a_7 (a_1 + a_2 + a_3), \quad (8\text{-A-}20)$$

$$b_4 = a_4 a_6 a_7, \quad (8\text{-A-}21)$$

and

$$b_5 = a_3 a_7 \phi_{ls} + a_3 a_6 \phi_{ss} - a_4 a_6 + a_7(a_2 \phi_{ls} - a_5 a_6) - a_4 a_6 a_7 L. \quad (8\text{-A-}22)$$

The particular solution for Eq. 8-A-18 is

$$T_{lp} = \frac{b_4}{b_3} z + \frac{b_3 b_5 - b_2 b_4}{b_3^2}. \quad (8\text{-A-}23)$$

The general solution becomes

$$T_{ls} = c_1 e^{\lambda_{ls} z} + c_2 e^{\lambda_{ss} z} + \frac{b_4}{b_3} z + \frac{b_3 b_5 - b_2 b_4}{b_3^2}, \quad (8\text{-A-}24)$$

where

$$\lambda_{ls} = \frac{-b_2 + \sqrt{b_2^2 - 4 b_1 b_3}}{2 b_1}, \quad (8\text{-A-}25)$$

and

$$\lambda_{ss} = \frac{-b_2 - \sqrt{b_2^2 - 4 b_1 b_3}}{2 b_1}. \quad (8\text{-A-}26)$$

By substituting Eq. 8-A-24 into Eqs. 8-A-12 and 8-A-13 and eliminating T_a, one can obtain the final expression for T_{ss} as

$$T_{ss} = d_1 c_1 e^{\lambda_{ls} z} + d_2 c_2 e^{\lambda_{ss} z} + d_3 z + d_4, \quad (8\text{-A-}27)$$

where

$$d_1 = -\left(\frac{a_2 \lambda_{ls}}{a_3 a_6} + \frac{a_1 + a_2}{a_3} \right), \quad (8\text{-A-}28)$$

$$d_2 = -\left(\frac{a_2 \lambda_{ss}}{a_3 a_6} + \frac{a_1 + a_2}{a_3} \right), \quad (8\text{-A-}29)$$

$$d_3 = +\frac{a_4}{a_3} - \frac{a_1 + a_2}{a_3}\frac{b_4}{b_3}, \qquad (8\text{-A-}30)$$

and

$$d_4 = \frac{a_2\phi_1 - a_5 a_6 - a_4 a_6 L}{a_3 a_6} - \frac{a_2 b_4}{a_6 a_3 b_3} - \frac{a_1 + a_2}{a_3}\frac{b_3 b_5 - b_2 b_4}{b_3^2} \qquad (8\text{-A-}31)$$

The integration constants, c_1 and c_2, are evaluated from known bottomhole temperatures. Thus, $z = L_{ss}$, and $T_{ss} = T_{ssbh}$. We use Eq. 6.29 to estimate the longer string's fluid temperature, $T_{ls} = T_{lsb}$, at the same depth, $z = L_{ss}$. These two boundary conditions are used in Eqs. 8-A-24 and 8-A-27 to derive the following expressions for calculating c_1 and c_2:

$$c_1 e^{\lambda_1 L_{ss}}(d_2 - d_1) = d_2 T_{lsbh} - T_{ssbh} + d_4 - \frac{d_2 b_4 L_{ss}}{b_3} + d_3 L_{ss} - \frac{d_2}{b_3^2}\left(b_3 b_5 - b_2 b_4\right) \qquad (8\text{-A-}32)$$

and

$$c_2 e^{\lambda_2 L_{ss}}(d_1 - d_2) = d_1 T_{lsb} - T_{ssbh} + d_4 - \frac{d_1 b_4 L_{ss}}{b_3} + d_3 L_{ss} - \frac{d_1}{b_3^2}\left(b_3 b_5 - b_2 b_4\right) \qquad (8\text{-A-}33)$$

8-A.3 Production and Injection Through Common Wellbores. As stated earlier in the text, the governing differential equations, Eqs. 8.23 through 8.25, and the expressions for fluid temperatures, Eqs.8.26 through 8.28, also apply to the case of production and injection through two tubing strings. In this case, however, the integration constants c_1 and c_2 are different because of different boundary conditions. Unlike in the previous case, we now know the inlet temperature of the injected fluid in the long string. Thus, using the boundary conditions at $z = 0$, $T_{ls} = T_{lsi}$, $z = L_{ss}$, and $T_{ss} = T_{ssbh}$, we obtain

$$T_{lsi} = c_1 + c_2 + \frac{b_3 b_5 - b_2 b_4}{b_3^2} \qquad (8\text{-A-}34)$$

and

$$T_{ssbh} = d_1 c_1 e^{\lambda_1 L_{ss}} + d_2 c_2 e^{\lambda_2 L_{ss}} + d_3 L_{ss} + d_4. \qquad (8\text{-A-}35)$$

The solutions for c_1 and c_2 are given by

$$c_1 = \frac{d_2 e^{\lambda_{ss} L_{ss}} \left(T_{lsi} - \frac{b_3 b_5 - b_2 b_4}{b_3^2} \right) - T_{ssbh} + d_3 L_{ss} + d_4}{d_2 \exp(\lambda_{ss} L_{ss}) - d_1 \exp(\lambda_{ls} L_{ss})} \quad \text{(8-A-36)}$$

and

$$c_2 = \frac{d_1 e^{\lambda_{ss} L_{ss}} \left(T_{lsi} - \frac{b_3 b_5 - b_2 b_4}{b_3^2} \right) - T_{ssbh} + d_3 L_{ss} + d_4}{d_1 \exp(\lambda_{ls} L_{ss}) - d_2 \exp(\lambda_{ss} L_{ss})} \quad \text{(8-A-37)}$$

8-A.4 Input Parameters for Field Examples 8.1 and 8.2. Table 8-A-1 shows the input parameters for Well A28 and Well C39, which are the two field examples presented in this chapter.

Parameters	Well A28	Well C39
Producing rates (*LS*/*SS*), STB/D	4,088/352	2,698/1,138
Gas/oil ratio (LS/SS), scf/STB	489/489	449/449
Oil density (LS/SS), lbm/ft^3	54/54	57/57
Gas gravity (LS/SS), (air = 1)	0.85/0.85	0.85/0.85
Cement sheath diameter, in	16.0	16.0
Length of strings (*LS*/*SS*), ft	5,194/4,984	5,151/4,984
Casing inner diameter, in.	10.0	10.0
Tubing inner diameter (*LS*/*SS*), in.	3.0	3.0
Geothermal gradient, °F/ft	0.012	0.012
Tubular thermal conductivity, Btu/hr-ft-°F	30.0	30.0
Formation thermal conductivity, Btu/hr-ft-°F	3.33	3.33
Tubular fluid thermal conductivity, Btu/hr-ft-°F	0.07	0.07
Cement thermal conductivity, Btu/hr-ft-°F	0.38	0.38
Formation density, lbm/ft^3	135.0	135.0
Formation heat capacity, Btu/lbm-°F	0.625	0.625
Pipe roughness, ft	0.000018	0.000018
Reservoir pressure, psi	2,011	2,147

Table 8-A-1—Input parameters for field examples.

Chapter 9

Transient Fluid and Heat Flows In Wellbores

9.1 Introduction

When production of fluids occurs from moderate- to high-temperature (> 300°F) reservoirs, considerable heat exchange takes place between the fluid and its surroundings. This flow condition is further exacerbated in an offshore, deepwater producing environment as fluids are transported through segments of cold seawater and air in the riser. Whereas Chapter 6 deals with the steady-state fluid flow, which is accompanied by unsteady-state heat flow, here we consider modeling of unsteady-state fluid flow and heat flow processes.

Transient flows of mass, momentum, and energy occur whenever the coupled wellbore/reservoir system is perturbed either by design or inadvertently. By perturbation, we mean changes in volumetric flow rates. Multipoint drawdown and buildup tests are cases in point. These transport processes are also coupled such that change in one influences the other two. For example, temperature change in the wellbore fluid affects fluid density and viscosity, which changes pressure gradient. This pressure change will, in turn, influence fluid flow.

Although transient tests are obvious candidates for rigorous treatment, we will show that a fully transient wellbore/reservoir simulator is useful for a variety of production operation applications. Some of these examples include computing dynamic productivity and injectivity indices, performing fully transient systems or Nodal™ analysis, and designing or interpreting temperature logs. Estimation of flowing bottomhole pressure and then flow rates and volume during a well blowout is another example in which the transient simulation becomes essential. Transient simulations are also required for designing and maintaining flowlines, equipment, and facilities, particularly in an offshore environment. However, pressure-transient analysis is beyond the scope of this book.

A few simulators have been reported in the literature to study transient flow problems in a coupled wellbore/reservoir system. They can be categorized into two groups. One approach considers an isothermal wellbore and the other deals with the general case of nonisothermal flow problems. Models of Winterfeld (1989) and Almehaideb et al. (1989) fall into the first category. Unless we address onshore production from shallow reservoirs, near-isothermal boreholes are difficult to find. The second category involves the implicit coupling of wellbore with reservoir for nonisothermal flow problems. Miller (1980) first reported fully implicit numerical coupling of the wellbore and the reservoir for geothermal wells. Subsequently, Su and

Lee (1995) and Stone et al. (2002), among others, also offered models handling coupled nonisothermal flow problems. In this modeling approach, the energy equation is solved in addition to the mass and momentum equations for two-phase gas/liquid flow. More recently, wellbore models offered by Pourafshary et al. (2009) and Livescu et al. (2010) have a direct coupling with numerical reservoirs models for handling nonisothermal flow problems. The model offered by Bahonar et al. (2011a, b) removes some of the limiting assumptions of its predecessors, such as that of Livescu et al. (2010), wherein a constant overall-heat-transfer coefficient for the wellbore is assumed. We note that the semianalytical wellbore/reservoir model of Fan et al. (2000) is limiting in that it is intended as a buildup test, preceded by a longduration flow period to attain thermal equilibrium.

In this chapter, we present a hybrid approach to couple the wellbore with the reservoir. The wellbore, which solves the mass, momentum, and energy equations, is numerical; the reservoir, where single-phase fluid flow occurs, is analytical. This approach reduces computational time significantly. Some of the other advantages of this approach include easy simulation inputs and desktop or laptop computation. Ramey (1962) was the first to show the usefulness of this coupling procedure while modeling the steady-state steam injection process. The last section of this chapter presents a simplified coupled analytical modeling approach to explore the possibilities of surface-pressure conversion to downhole conditions in well testing.

Here, we briefly describe wellbore/reservoir simulators for modeling single-phase gas, single-phase oil, and two-phase gas/oil flow problems. Much of the material presented here is drawn from the studies of Hasan and Kabir (1994a) and Hasan et al. (1997, 1998, 2005).

9.2 Modeling Single-Phase Gas Flow

9.2.1 Model Formulation. Mass, momentum, and energy balances, along with gas pressure/volume/temperature (PVT), are used to generate the constitutive equations. **Fig. 9.1** sketches the basis of these balances for a control volume of unit length within the wellbore.

Material Balance. The mass balance equation for a differential depth, d*z*, of the well, in terms of wellbore fluid density, ρ, fluid velocity, v, and cross-sectional flow area, A, is written as

$$\frac{\partial(A\rho)}{\partial t}+\frac{\partial}{\partial z}(A\rho v)=0 \qquad (9.1)$$

***Momentum Balance*.** The momentum balance equation is given by

$$\frac{\partial v}{\partial t}+v\frac{\partial v}{\partial z}=-\frac{1}{\rho}\frac{\partial p}{\partial z}+g\sin\alpha-\frac{2fv^2}{d_t} \qquad (9.2)$$

Energy Balance. The energy balance is written by noting the conductive heat loss to the formation, and the convective energy transport into and out of the control volume of unit length. In terms of fluid internal energy E, fluid enthalpy H, fluid mass flow rate w, fluid mass in the control volume m, and the internal energy and mass of the wellbore system—the tubulars and cement sheaths combined $(m'E)_w$—the energy balance equation, as shown in Fig. 9.1, gives

$$Q = \frac{\mathrm{d}(mE)_{cv}}{\mathrm{d}t} + \frac{\mathrm{d}(m'E)_w}{\mathrm{d}t} - \frac{\mathrm{d}}{\mathrm{d}z}\left[w\left(H + \frac{1}{2}v^2 - gz\sin\alpha\right)\right] \quad (9.3)$$

The second term on the right side of Eq. 9.3 represents the energy absorbed or released by the tubulars and cement sheaths in the wellbore. Omitting this term can lead to serious error because it accounts for a significant fraction of the total energy exchange between the wellbore and the formation. In our simulations, we noted an anomalously sharp increase at early times in computed wellbore fluid temperatures during drawdowns and a decrease during buildups when this term was neglected.

The heat lost to (or received from) the formation, Q, is given by Hasan and Kabir (1994a) as

$$Q \equiv \rho v c_p \left(T_{ei} - T_f\right) L_R \quad (6.19)$$

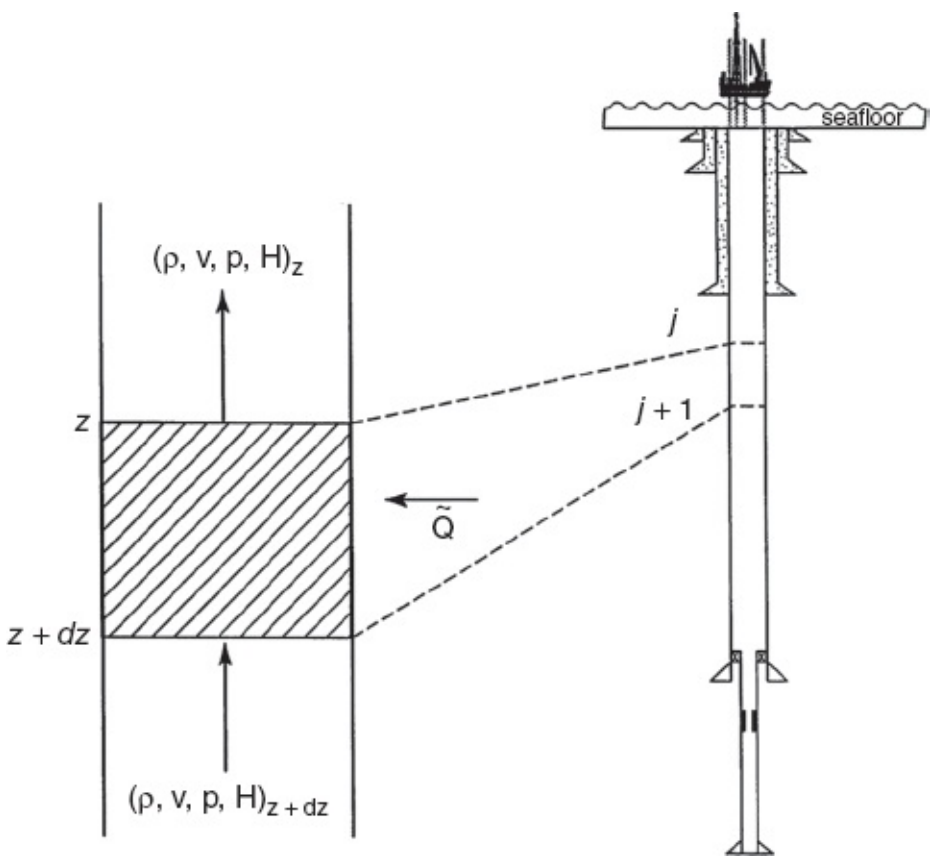

Fig. 9.1—Schematic of mass, momentum, and energy balances.

In Eq. 6.19, the product ρv represents mass flow rate and L_R is the relaxation distance parameter, which is the inverse of the parameter A defined in Chapter 6 and is given by

$$L_R = \frac{2\pi}{c_p w}\left[\frac{r_{to}U_{to}k_e}{k_e + \left(r_{to}U_{to}T_D\right)}\right] \qquad (6.20)$$

The dimensionless temperature-distribution function T_D was defined in Chapter 6 and is reproduced here for convenience.

$$T_D = \ln\left[e^{(-0.2t_D)} + \left(1.5 - 0.3719e^{-t_D}\right)\sqrt{t_D}\right] \qquad (6.10)$$

Dimensionless time is given by $t_D = \alpha t/r_w^2$, where the thermal diffusivity α equals $k_e/\rho_e c_e$. Eq. 6.19 is valid only when heat loss from the wellbore is constant. In general, energy exchange between the fluid and formation gradually changes with time because of the steady change in the formation temperature surrounding the wellbore. The superposition principle can be used to account for changes in both heat and mass flow rate with time. However, our experience shows that most flow problems do not require that rigor, given the marginal gain in accuracy and excessive computation time.

Change in fluid enthalpy is related to changes in fluid temperature and pressure, which is written as

$$\frac{dH}{dz} = -C_J c_p \frac{dp}{dz} + c_p \frac{dT_f}{dz}, \qquad (6.14)$$

where c_p is the heat capacity at constant pressure and C_j is the Joule-Thomson (J-T) coefficient. Methods to estimate the J-T coefficient for gases, liquids, and two-phase mixtures have been discussed in Chapter 6, Section 6.4.2. For a real gas, C_J is given by

$$C_J = \frac{1}{c_p}\left\{\frac{1}{\rho_g}\left[-\frac{T}{Z}\left(\frac{\partial Z}{\partial T}\right)_p\right]\right\} \qquad (6.39)$$

Eq. 9.3 is rewritten by replacing the internal energy of the gas in the control volume with gas enthalpy, H, and gas pressure and volume, noting that mass per unit well length m equals $A\rho$.

$$\begin{aligned} Q = {} & A\rho\frac{\partial H}{\partial t} + \frac{\partial\left(m'cT_f\right)}{\partial t} - A\rho R\frac{\partial\left(ZT_f\right)}{\partial t} \\ & + A\left(H - \frac{ZRT_f}{M}\right)\frac{\partial\rho}{\partial t} - \frac{d}{dz}\left[\left(A\rho v\right)\left(H + \frac{v^2}{2} - gz\sin\alpha\right)\right] \end{aligned} \qquad (9.4)$$

where c represents the weighted-average specific heat of the wellbore cement/tubular material. Note that Eq. 9.4 allows for changes in the flow cross-sectional area in the well. Modeling the heat absorbed or released by the annular fluid, tubulars, and cement sheath is important. However, to account for the individual heat capacity and transient temperature of each element of the wellbore becomes prohibitively time consuming. We suggest the use of a weighted-average temperature of the fluid/cement/tubular material and assume that at any given time, the temperature rise of this composite system is a fraction of the rise in the fluid temperature. This approximation simplifies to the

$$p = \frac{Z\rho R T_f}{M} \qquad (9.5)$$

mathematical formulation and saves computation time without significantly affecting accuracy, as our field experience shows.

Note that in arriving at Eq. 9.4, we used the gas law to replace pressure p by temperature T_f, where M represents the molecular weight of the gas.

Wellbore Fluid Temperature. The development of the finite-difference form of Eq. 9.4, using j to denote the spatial coordinate, is shown in Appendix 9-A, Section 9-A.1. The final form of wellbore fluid temperature as a function of time and depth is

$$\left(T_f\right)_j^{l+1} = \frac{(\sigma_j^l / A) - \psi_j^l + \left[\rho v T_{ei} c_p (L_R)\right]_j^{l+1} + \xi_j^l (T_f)_j^l \omega_j^l}{\left(\rho v c_p L_R\right)_j^{l+1} + \xi_j^l - \lambda_j^l} \qquad (9.6)$$

Expressions for the various terms, σ, ψ, ξ, λ, and ω, are given in Appendix 9-A, Section 9-A.1.

The relaxation parameter L_R in Eq. 9.6 is normally defined by Eq. 6.20, which accounts for conductive heat transport in the formation. However, in an offshore facility, a portion of the wellbore is exposed to convective heat transport of seawater and ambient air in the riser. Exposure of this nature may significantly affect the wellhead fluid temperature. As discussed in Chapter 6, Eq. 9.6 may be used as long as L_R is defined properly to account for these convective effects as

$$L_{Rc} = \frac{2\pi r_{to} U_{toc}}{c_p w}, \qquad (9.7)$$

where the overall-heat-transfer coefficient U_{toc} accounts for the convective heat transfer outside the flow string and those for the wellbore system. In Appendix 6-A, we show how the overall-heat-transfer coefficients, U and U_{toc}, are calculated for various situations.

Sandface Flow Rate. The diffusivity equation for single-phase flow in a homogeneous reservoir is given by

$$\frac{\partial p_{pn}}{\partial t} = \frac{k}{\phi \mu c} \frac{1}{r} \frac{\partial}{\partial r}\left(r \frac{\partial p_{pn}}{\partial r} \right) \quad (9.8)$$

The numerical solution of the formation flow equation (Eq. 9.8) is often time consuming. We used an analytical solution for the case of constant production rate, which is written as

$$p_i - p_w = m^* q \left(p_D + s \right) \quad (9.9)$$

The reservoir influence function or model p_D for a cylindrical source well may be expressed in terms of the dimensionless time analogous to Eq. 6.10. Alternatively, one may use Laplace space solutions to retain generality. Note that for pressure transients, dimensionless time is given by $t_D = \beta_m t/r_w^2$, where the momentum diffusivity β_m equals $2.64 \times 10^{-4} k/\phi \mu c_t$ in field units.

Fluid influx into the wellbore changes rapidly at early times during either drawdown or buildup. Superposition in time is used to account for the variation in influx rate q with time. The resulting expression for bottomhole flow rate at a time step l+1 in terms of flow rates at earlier times is

$$q_n = q_{n-1} + \frac{p_i - p_{wn}}{m^* \left[p_D \left(t_{Dn} - t_{D\,n-1} \right) + s + Dq_n \right]} - \frac{\sum_{i=1}^{n-1} (q_i - q_{i-1}) \left[p_D \left(t_{Dn} - t_{i-1} \right) + s + Dq_i \right]}{p_D (t_D - t_{n-1}) + s + Dq_n}, \quad (9.10)$$

where $t_{D0} = 0$ and $q_o = 0$. For a nonequilibrium initial condition, $p_i = p_{wf1}$, q_1 is the prevailing flow rate, and $D_{qi} = |D(q_1 - q_{i-1})|$. Note that the Dq term represents the skin associated with non-Darcy flow. Eq. 9.10 is general, and so any reservoir model p_D can be inserted for a given system, such as double-porosity, composite, or fractured.

9.2.2 Sensitivity Study: Single-Phase Gas Example. In this section, we discuss the results of a simulated case generated by the model. This vertical well has a depth of 10,000 ft with a bottomhole temperature of 300°F.

Fig. 9.2 shows the wellbore fluid density and temperature profiles corresponding to a production rate of 5 MMscf/D. **Fig. 9.3** shows similar results during the subsequent well shut-in. The nonlinear and time-dependent nature of these profiles is noteworthy. These profiles underscore the importance of accounting for thermal effects whenever conversion of wellhead pressure (WHP) to bottomhole pressure (BHP) is desired.

Fig. 9.4 presents the wellhead temperature (WHT) transients from the last two simulations. Note the gradual rise in the wellhead fluid temperature during drawdown and the subsequent gentle decline during well shut-in. Also shown in the figure are profiles generated by neglecting the heat absorption or rejection by the wellbore

system, comprising tubulars, annular fluid, and the cement sheath. Note the sharp increase in WHT at early times during drawdown and a similar sharp decrease during shut-in compared to the base case. Differences between the two WHT signatures are analogous to differences observed for either the BHP or WHP when the wellbore fluid storage is included or excluded during a transient test. Because of this analogy, we term this phenomenon associated with the WHT "thermal storage."

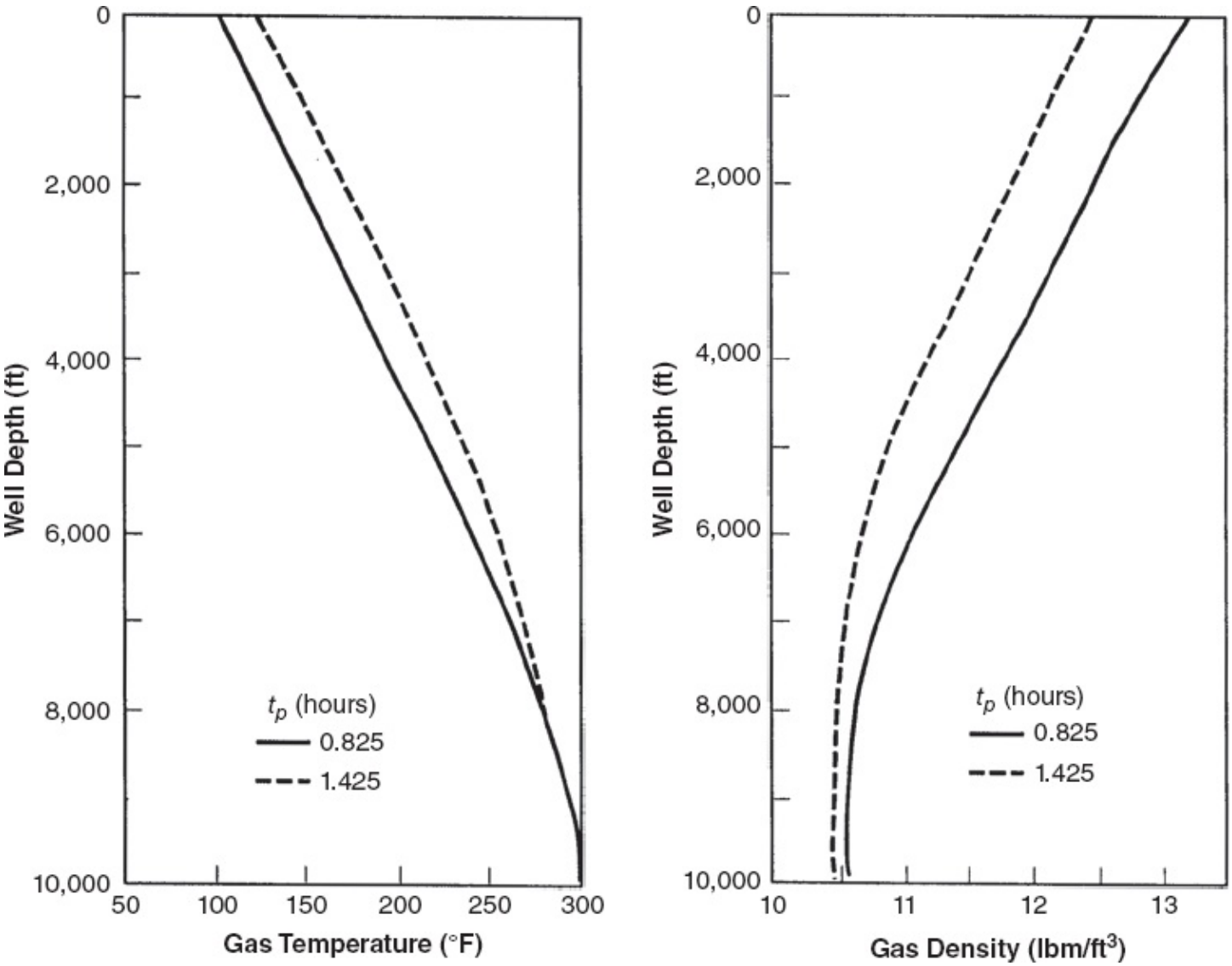

Fig. 9.2—Wellbore temperature and density profiles during gas flow.

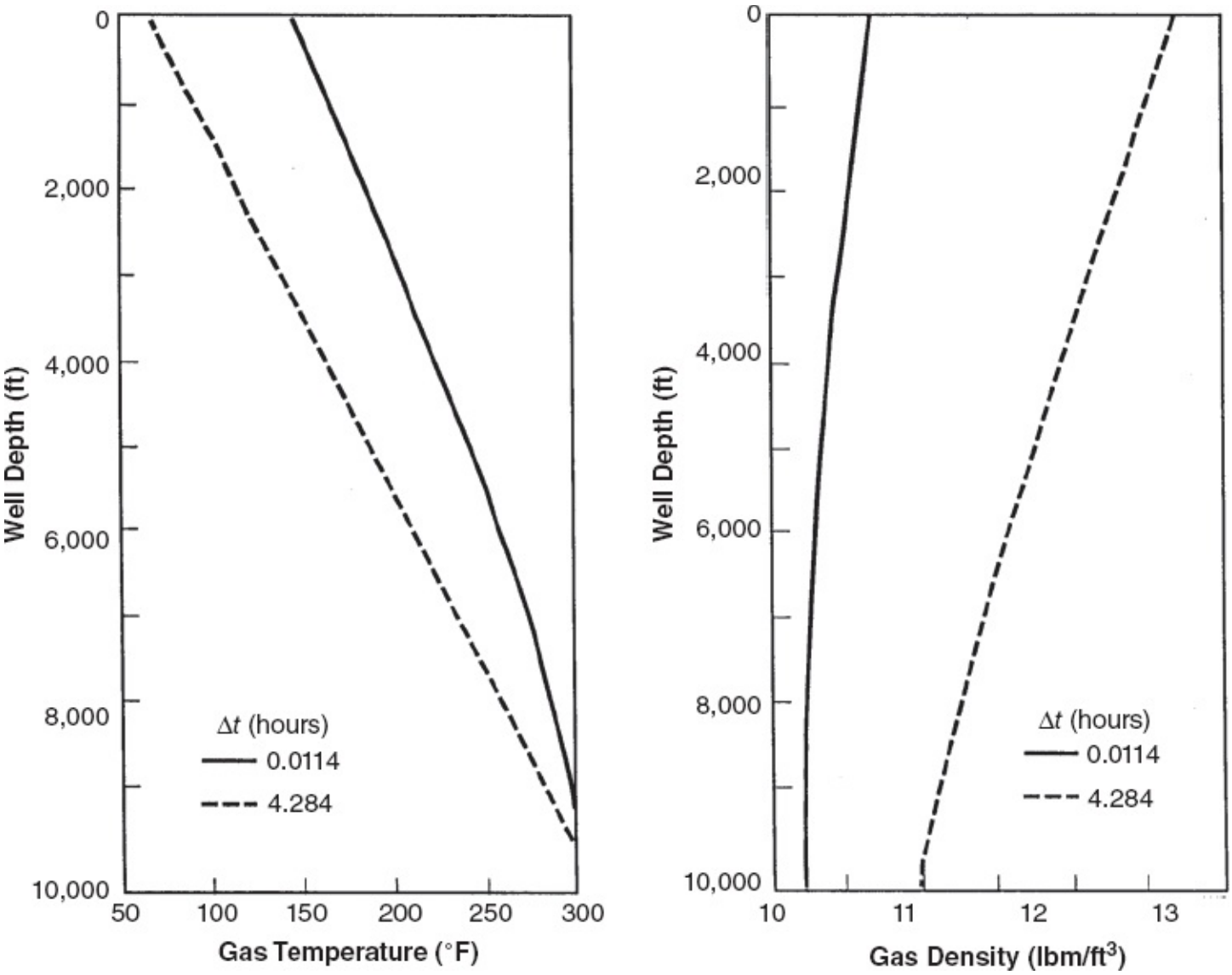

Fig. 9.3—Wellbore temperature and density profiles during well shut-in.

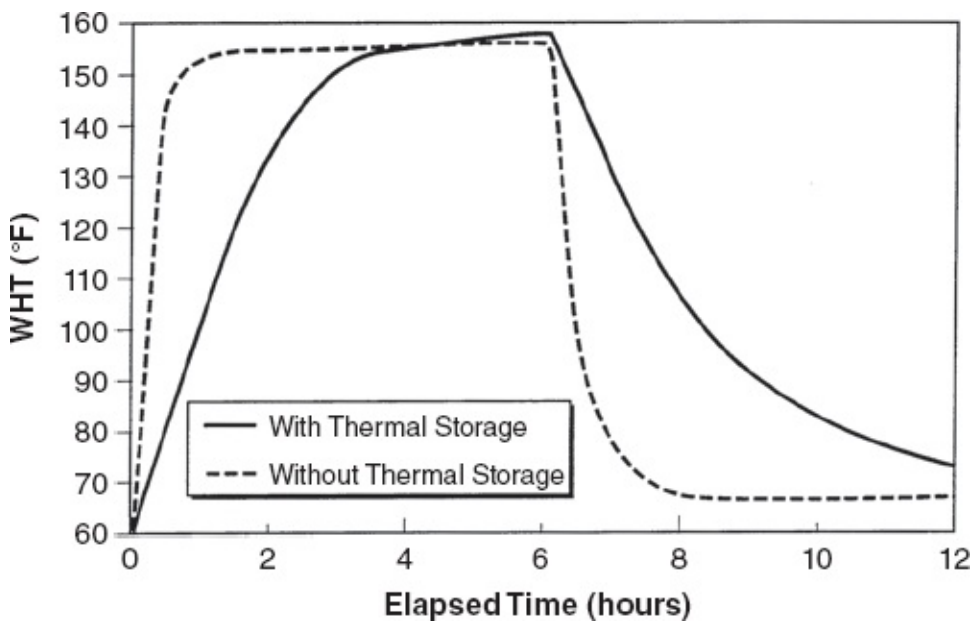

Fig. 9.4—Occurrence of thermal storage during flow and shut-in tests.

By thermal storage, we mean the ability of the wellbore system to store or release heat, thereby causing delay for the WHT to attain an equilibrium value when the production rate is held constant. In any real system, the tubulars will provide significant storage of heat, thereby causing any analysis to be erroneous that neglects thermal storage. Note that the phenomenon of thermal storage is not limited to the wellbore system; any physical body in thermal contact with another body at a different temperature may experience it. Temperature-logging tools provide another example of this phenomenon. We discuss that particular thermal storage situation in Chapter 11, Section 11.3.

To study the effect of the production rate on the transient behavior of pressure and temperature, we simulated both drawdown and buildup tests for three flow rates. **Fig. 9.5** shows the WHPs and WHTs corresponding to rates of 2.5, 5.0, and 7.5 MMscf/D. Increase in WHT with rate is a direct consequence of increased associated total fluid energy (*wH*). Simulations of this nature are prerequisite to the design of both subsurface and surface equipment and facilities to handle high WHTs. This point is made clear by evaluating a real case, as examined next.

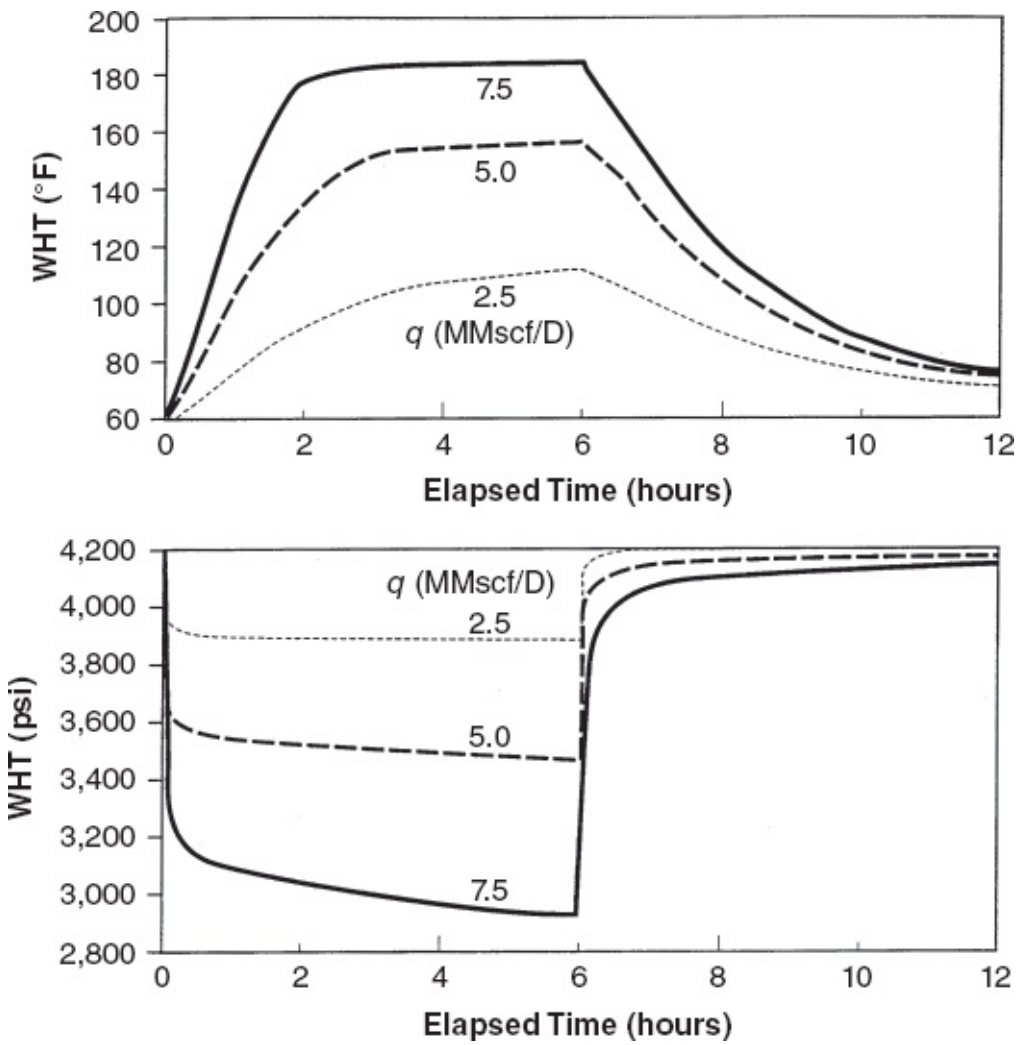

Fig. 9.5—Flow rate governs WHP and WHT.

In this actual scenario, the operator was interested in learning about the WHTs because at certain temperatures, CO2-induced corrosion becomes very pronounced. While a steady-state simulator yields only the final equilibrium WHT value, severity and duration of the critical temperature range experienced can be discerned only by using a transient simulator. Knowledge of WHTs and subsequent cooling during the pipeline transport of this sour-gas/condensate mixture dictates the metallurgy requirements of the entire system. Besides, the transient output (fluid composition and temperature) of this simulation is necessary for the input of the transient pipeline simulation. We now discuss the results of these simulations.

Fig. 9.6 shows the subsea WHT transients for various flow rates for the deviated (approximately 45°) well case. Note that the temperature plateau occurs at different times because of the thermal storage effect. At the lowest rate, such as 50 MMscf/D, thermal storage lasts longer because of correspondingly lower associated fluid energy. In other words, a low mass rate will take longer to heat up tubulars and attain temperature equilibrium. The corresponding pressures at the well bottom (BHP) and wellhead (WHP) are shown in **Fig. 9.7.**

Figs. 9.8 and 9.9 show the WHT and WHP/BHP plots, respectively, for a vertical-well case. The WHT values in this case are considerably higher than in its deviated-well counterpart. For example, we observe a 29°F higher equilibrium WHT when the rate is 100 MMscf/D. The rationale for this observation is that the gas must traverse an additional well length of approximately 8,000 ft in the deviated-well case, thereby losing more heat than in the vertical-well situation.

Simulations were also made for the platform-well scenario by adding approximately 1,000 ft of seawater and air segments to the subsea completion model. These simulation runs show that the gas experiences marginal cooling because of low residence time in the riser (seabed-to-rigfloor) section. For instance, at the lowest rate of 50 MMscf/D, an element of gas is exposed for less than 3 minutes in the riser. Consequently, a decrease of approximately 2°F is observed for the equilibrium WHT. For the same reason, a WHT decrease of less than 1°F is observed when the rate is 150 MMscf/D. Note, however, that these simulations presupposed a constant ambient air temperature of 75°F during each flow period.

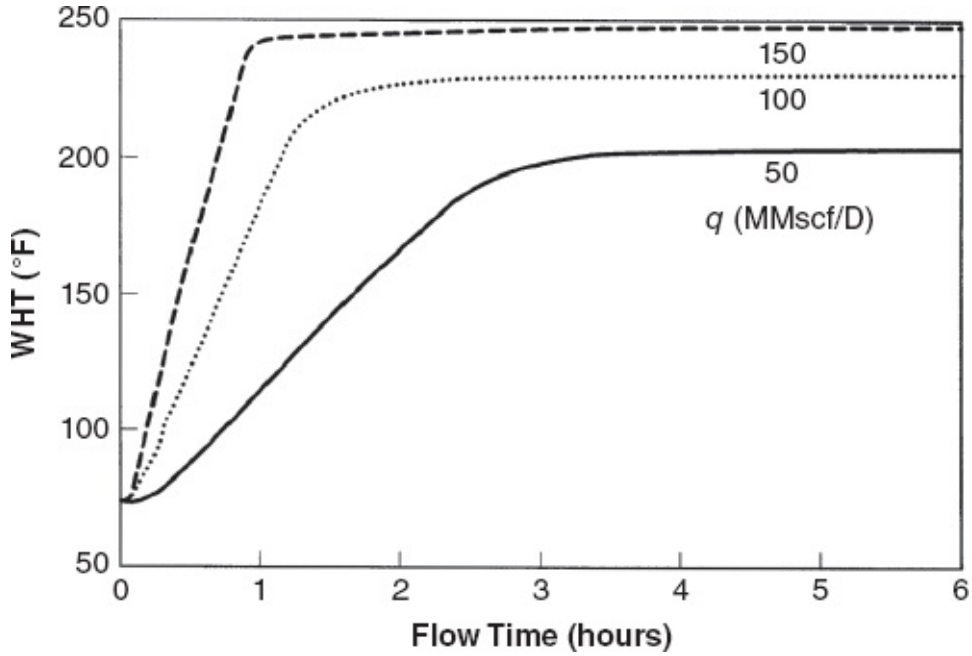

Fig. 9.6—Subsea WHT depends on the production rate.

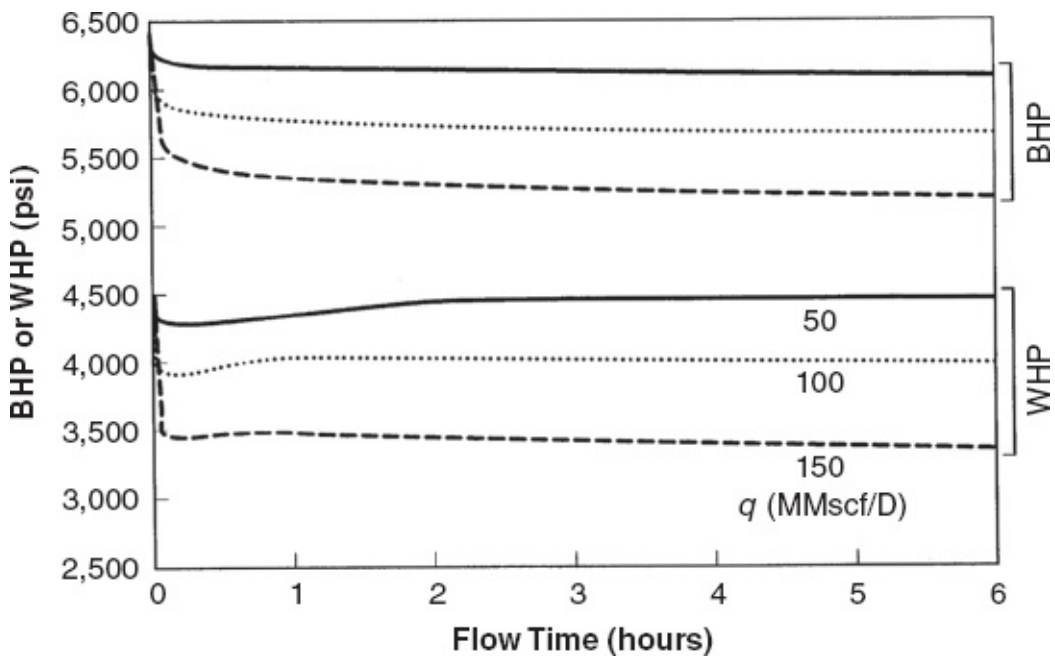

Fig. 9.7—Low rates exhibit longer WHP distortion owing to thermal storage.

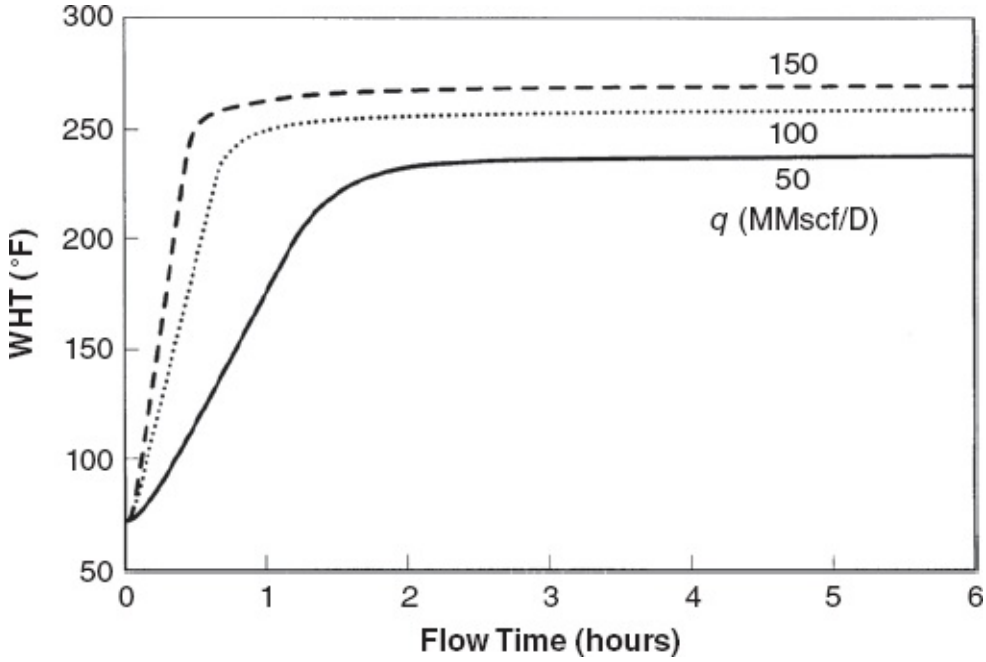

Fig. 9.8—Gas in a vertical well retains more heat because of shorter residence time.

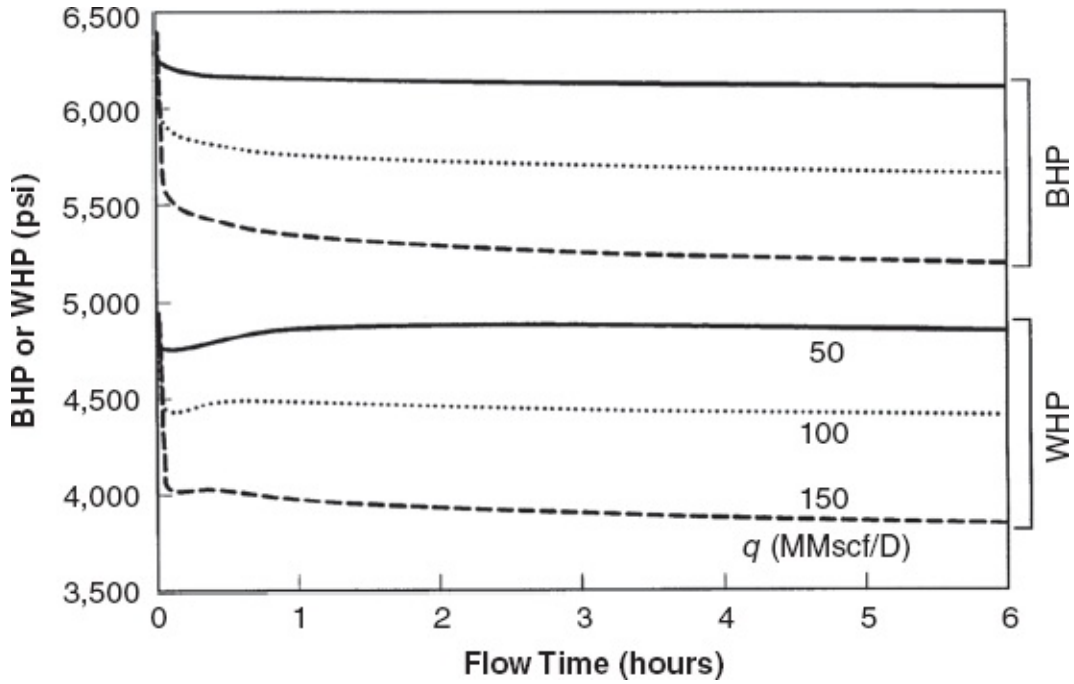

Fig. 9.9—Higher pressures are experienced in a vertical well.

On the basis of these calculations, the operator considered drilling longer well lengths to produce gas at relatively low temperatures at the subsea completion. In this way, corrosion hazards were thought to be minimized. The annular fluid offers significant resistance to heat flow, making its conductivity an important determinant of the WHT. Then, from a metallurgical design standpoint, fluid WHTs dictate the makeup of surface equipment and flowlines. In the next section, we discuss how the conductivity of annular fluid influences the WHT.

9.3 Modeling Single-Phase Oil Flow

9.3.1 Model Formulation. Formulation of a single-phase oil flow model is analogous to that for the gas model described earlier in this chapter. The resulting expression for flowing-fluid temperature is reported in Appendix 9-A, Section 9-A.2; Hasan et al. (1997) details this formulation.

9.3.2 Sensitivity Study: Single-Phase Oil Example. We explore the sensitivity of certain essential parameters on the transient behavior of pressure and temperature at both the wellhead and the well bottom in an oil well. **Table 9.1** presents the wellbore/reservoir data used to generate the synthetic cases.

Reservoir pressure, psia	7,000
Well depth, ft	10,000
Tubing inner diameter, in.	2.75
Tubing outer diameter, in.	3.5
Casing inner diameter, in.	8.9
Casing outer diameter, in.	9.375
Pipe roughness, ft	1.8×10^{-4}
Production rate, STB/D	2,000
Formation permeability, md	500
Formation thickness, ft	100
Formation porosity, fraction	0.2
Oil gravity, °API	28
Gas gravity (air = 1)	0.75
Total system compressibility, 1/psi	8×10^{-5}
Damaged skin	0
Reservoir temperature, °F	220
Geothermal gradient, °F/ft	0.015
Formation thermal conductivity, Btu/ft-°F-hr	2.5
Formation density, lbm/ft^3	165
Formation heat capacity, Btu/lbm-°F	0.625
Tubing/casing material thermal conductivity, Btu/ft-°F-hr	30
Annular fluid thermal conductivity, Btu/ft-°F-hr	0.2
Cement thermal conductivity, Btu/ft-°F-hr	0.38
Cement sheath diameter to 270 ft, in.	30
Cement sheath diameter from 270 ft to total depth, in.	20

Table 9.1—Well, reservoir, and fluid data.

Fig. 9.10 shows the effect of the producing rate on WHP, WHT, and BHP. Increasing WHT with a higher rate is a result of increased associated fluid enthalpy. While the BHP shows the expected smooth trend, the early-time WHP suggests otherwise. This behavior is a direct consequence of thermal storage, precipitated by storage (during drawdown) or release (during buildup) of thermal energy by tubulars, cement sheaths, and annular fluid. Fig. 9.11 compares the derivative curves generated for buildup using WHP data. One observes that the WHPs associated with decreasing flow rate exhibit larger thermal-storage distortion, as indicated by the increasing departure of the derivative signature from the flat response, which signifies lack of storage. Low rates simply take a longer time to promote heat exchange between the fluids and their surroundings, thereby contributing to distortion. Therefore, Fig. 9.11 underscores an important point—namely, that one cannot simply add the hydrostatic head to the WHP for computing the BHP without a proper accounting of fluid temperature variation with time and depth, as **Figs. 9.12 and 9.13** testify. Figs. 9.12 and 9.13 show these profiles for drawdown as well as buildup cases. Note the increasing WHT with an increasing production rate because of the associated fluid energy.

Similarly, for the same volumetric rate, energy increases with increasing fluid density (decreasing API gravity), as shown in **Fig. 9.14.** Therefore, the total mass rate dictates the WHT behavior.

Questions may arise about the effect of initial formation temperature distribution on WHP because fluid circulation during drilling and completion can potentially distort the virgin geothermal gradient in the wellbore vicinity. Experience with transient fluid circulation modeling, as discussed in Chapter 11, Section 11.1, shows that fluid temperatures in the annulus (formation/drillpipe) and tubing (drillpipe) are not very sensitive to various heat-transfer parameters, including those at surface and subsurface. Moreover, the entire formation essentially acts as an infinite heat source or sink. Therefore, the initial-formation temperature profile is not distorted to any appreciable degree owing to fluid circulation.

We performed some simulations nonetheless to address the distorted geothermal gradient issue. **Fig. 9.15** shows the transient WHT corresponding to various geothermal gradient values. The underlying thought is to simulate cases assuming fluid circulation before testing caused enough cooling to distort the geothermal gradient itself. As expected, very little difference in WHPs occurs, as **Fig. 9.16** shows, with no differences in BHPs. Although this simulation approach does not mimic reality, the approach represents the worst possible scenario. Therefore, the aspect of near-wellbore cooling appears unimportant.

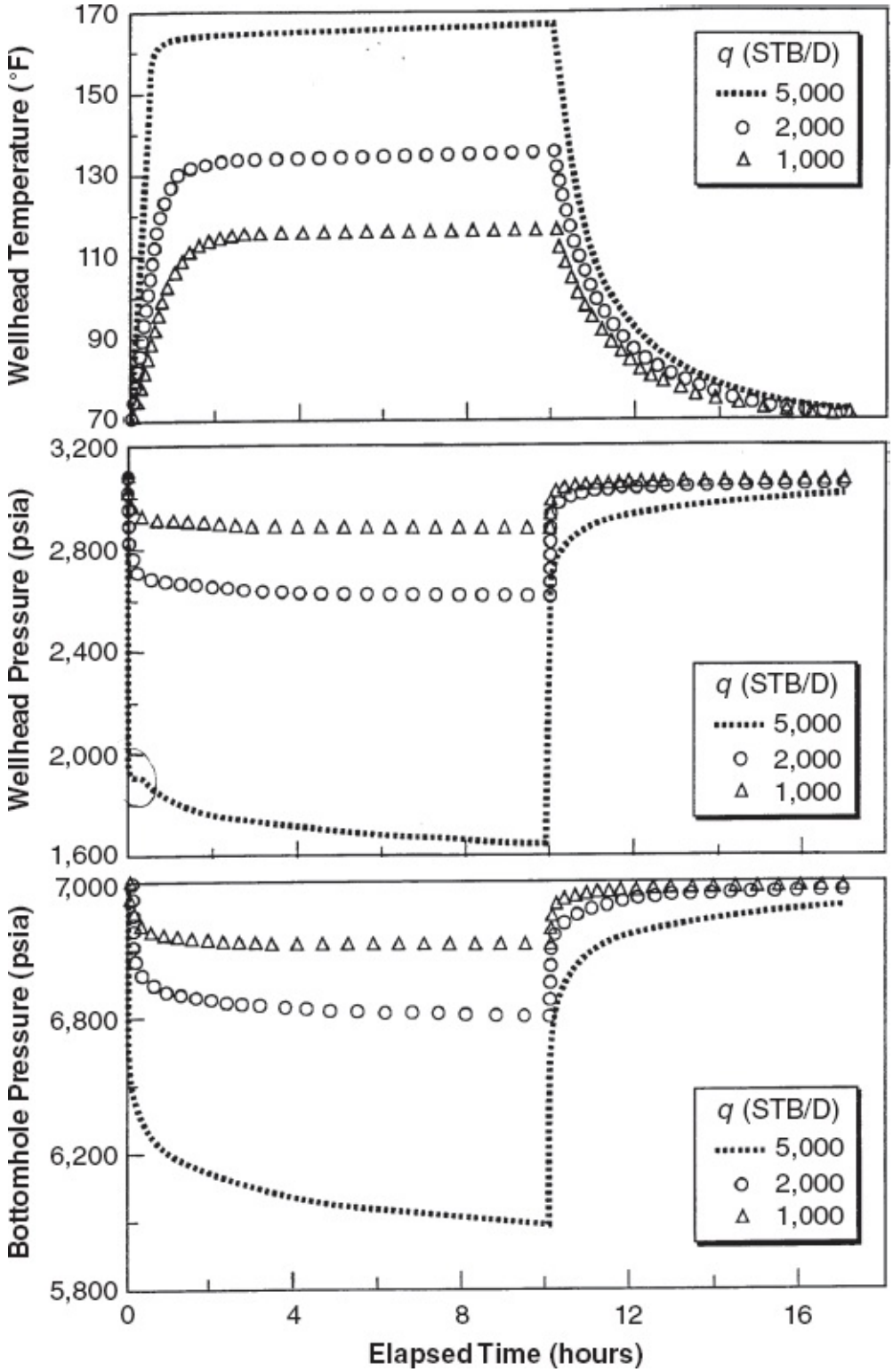

Fig. 9.10—Increasing rate causes higher WHTs.

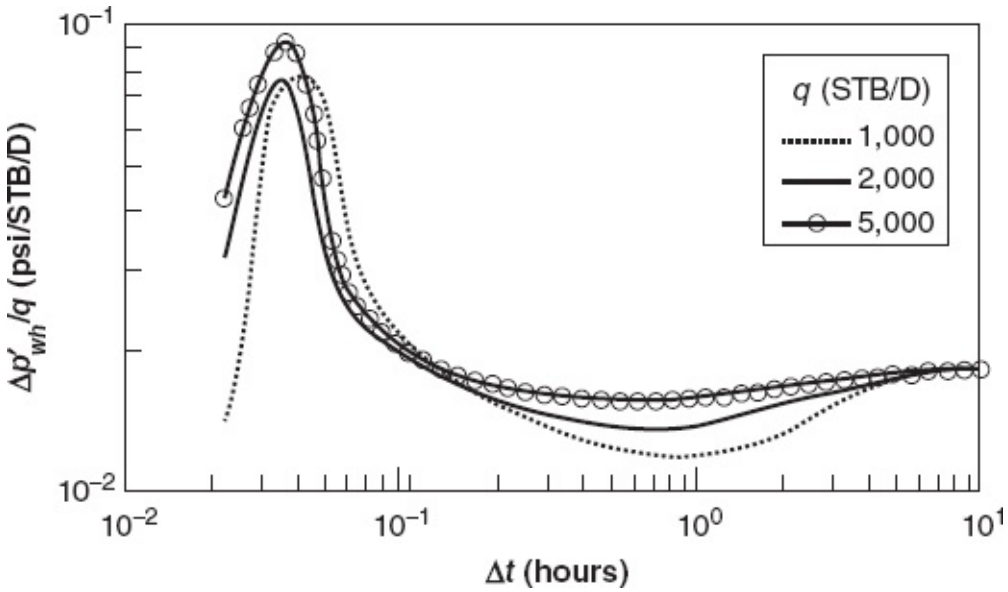

Fig. 9.11—Buildup WHP behavior shows flow-rate-dependent thermal storage distortion.

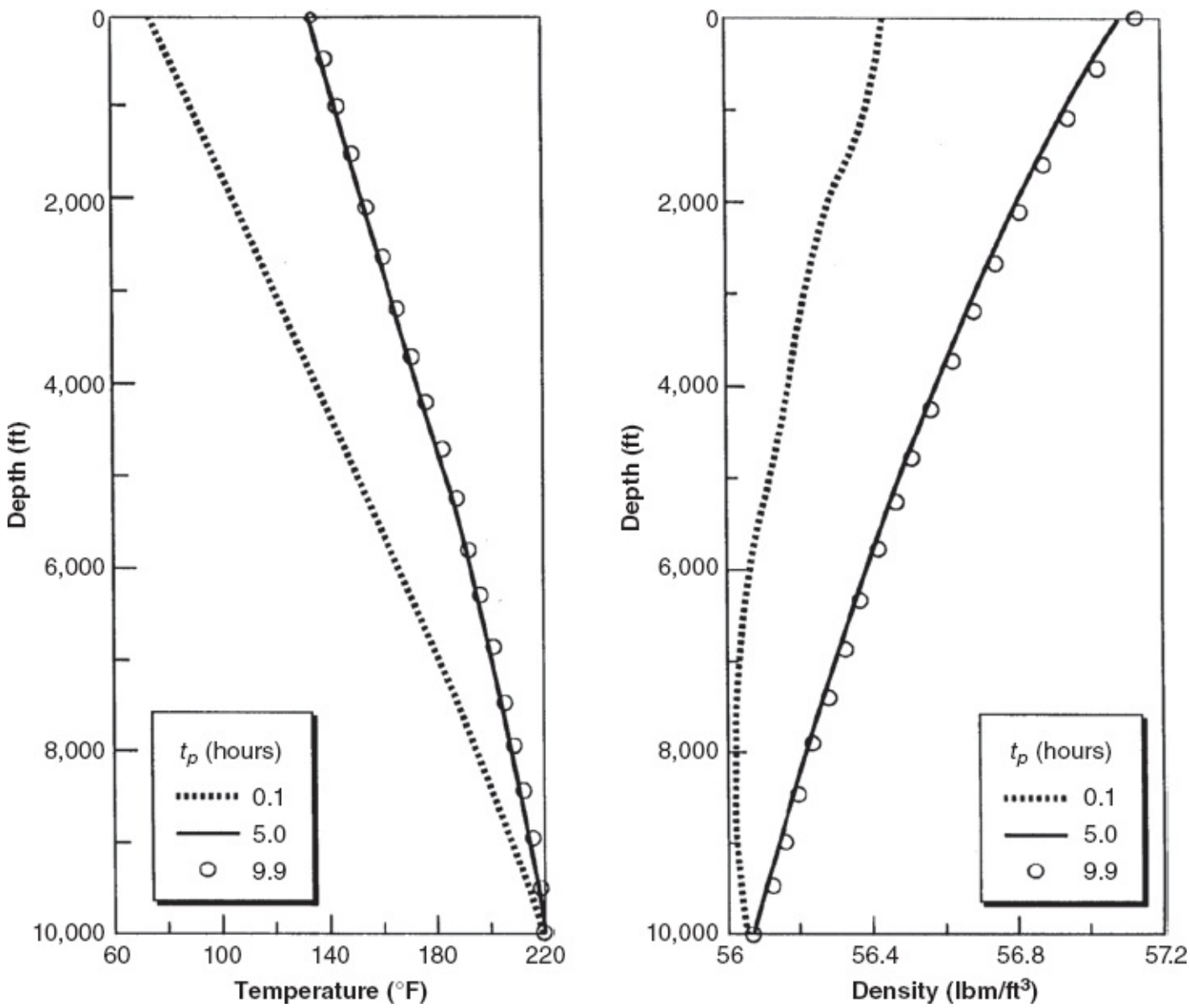

Fig. 9.12—Wellbore density and temperature profiles during single-phase oil flow.

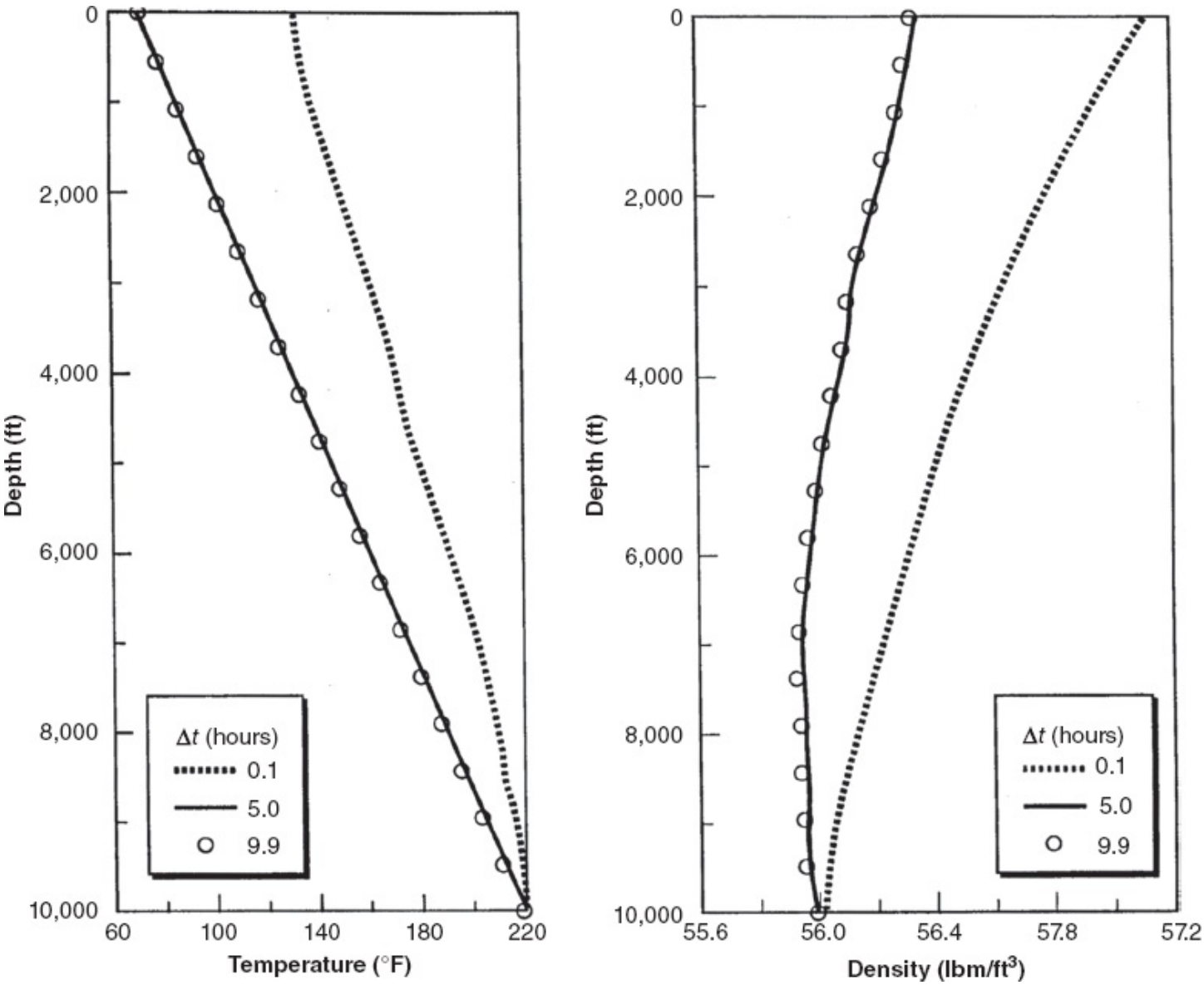

Fig. 9.13—Wellbore density and temperature profiles during well shut-in.

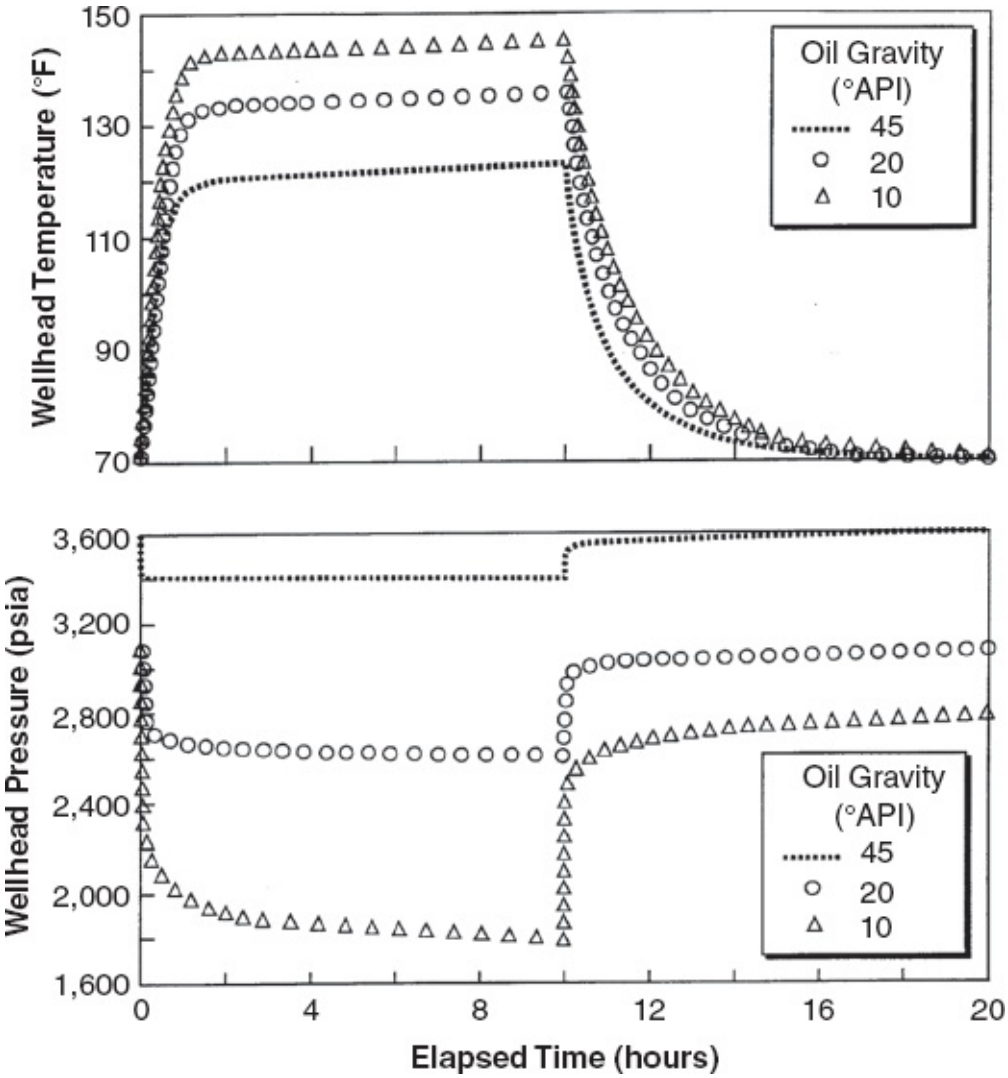

Fig. 9.14—WHT increases with increasing oil density.

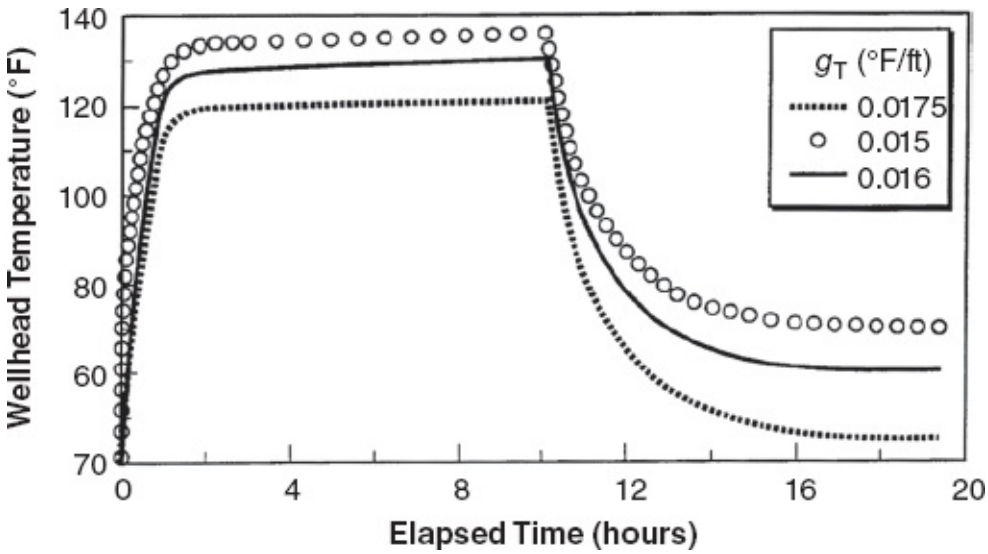

Fig. 9.15—Geothermal gradient influences WHT.

High WHT can potentially increase the project development cost by raising the

metallurgy requirements of tubulars, flowlines, and surface facilities. This problem is compounded further when corrosion considerations arise because of sour crudes. Predictably, this approach provides a vehicle for addressing the issue at the project's inception. For example, one can explore consequences of using water-based mud instead of oil-based mud to establish the anticipated WHT. **Fig. 9.17** shows that oil-based mud, having low thermal conductivity, is inefficient in losing heat to the surroundings. Consequently, high WHTs are reported. Although not germane to this discussion, retaining wellbore heat is highly desirable when either steam is injected or geothermal fluids are produced.

If high WHT is a concern and oil-based mud must be used because of corrosion considerations, a viable option of losing heat to the surroundings lies in drilling a deviated well. **Fig. 9.18** shows how well deviation increases fluid residence time, thus leading to a cooler WHT for wells of the same true vertical depth.

In an offshore producing environment, besides using water-based or higher-conductive mud, fluid cooling may be augmented by the presence of seawater. **Fig. 9.19** shows that unlike in the case of a gas well, significant cooling occurs in an offshore oil well. The reason for greater heat loss in oil wells than gas wells is the higher residence time because of the lower velocity experienced in oil wells. Note the temperature reversal occurring soon after the flow initiation when the water depth exceeds 2,000 ft. Production of cold fluid is responsible for this seemingly anomalous temperature response. Accordingly, **Fig. 9.20** indicates a shorter thermal-storage distortion period during buildups for the same reason. Note that this beneficial cooling effect starts to diminish with an increasing production rate, leading to an optimal withdrawal rate when temperature considerations are important.

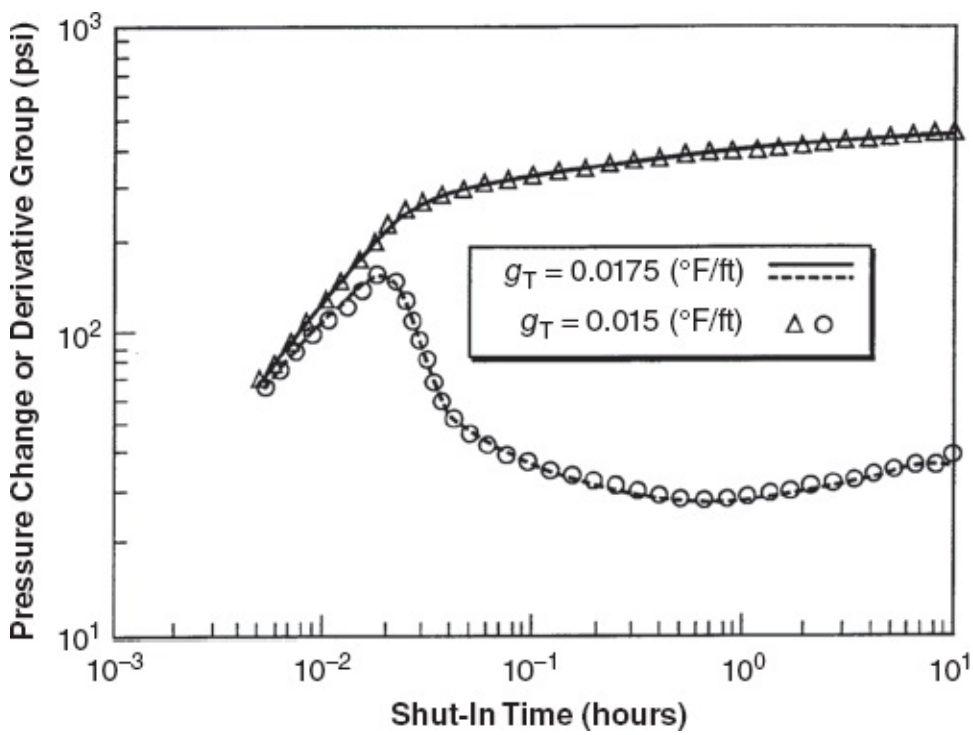

Fig. 9.16—Minor difference occurs in WHP response with changes in geothermal gradient.

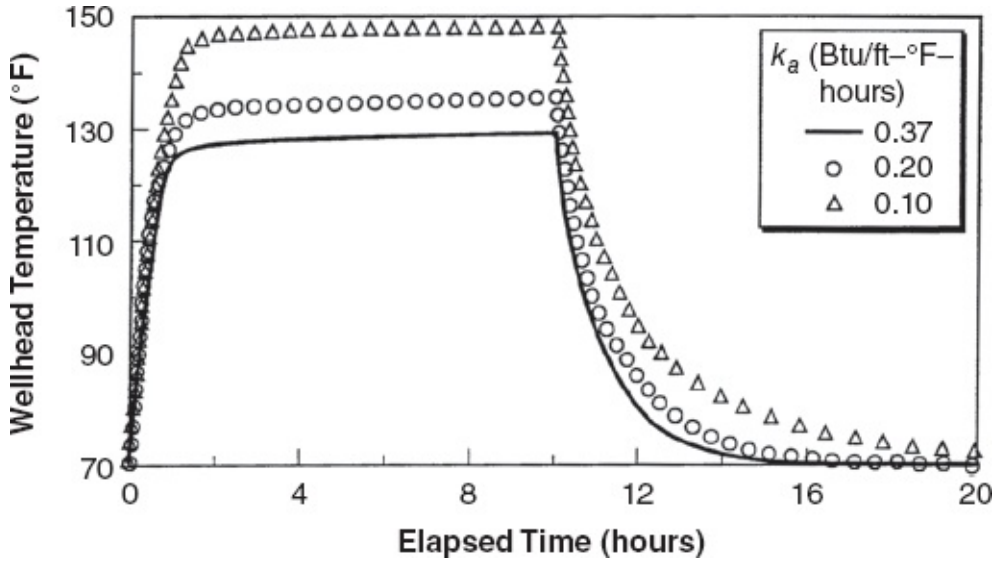

Fig. 9.17—Annular fluid conductivity influences WHT response.

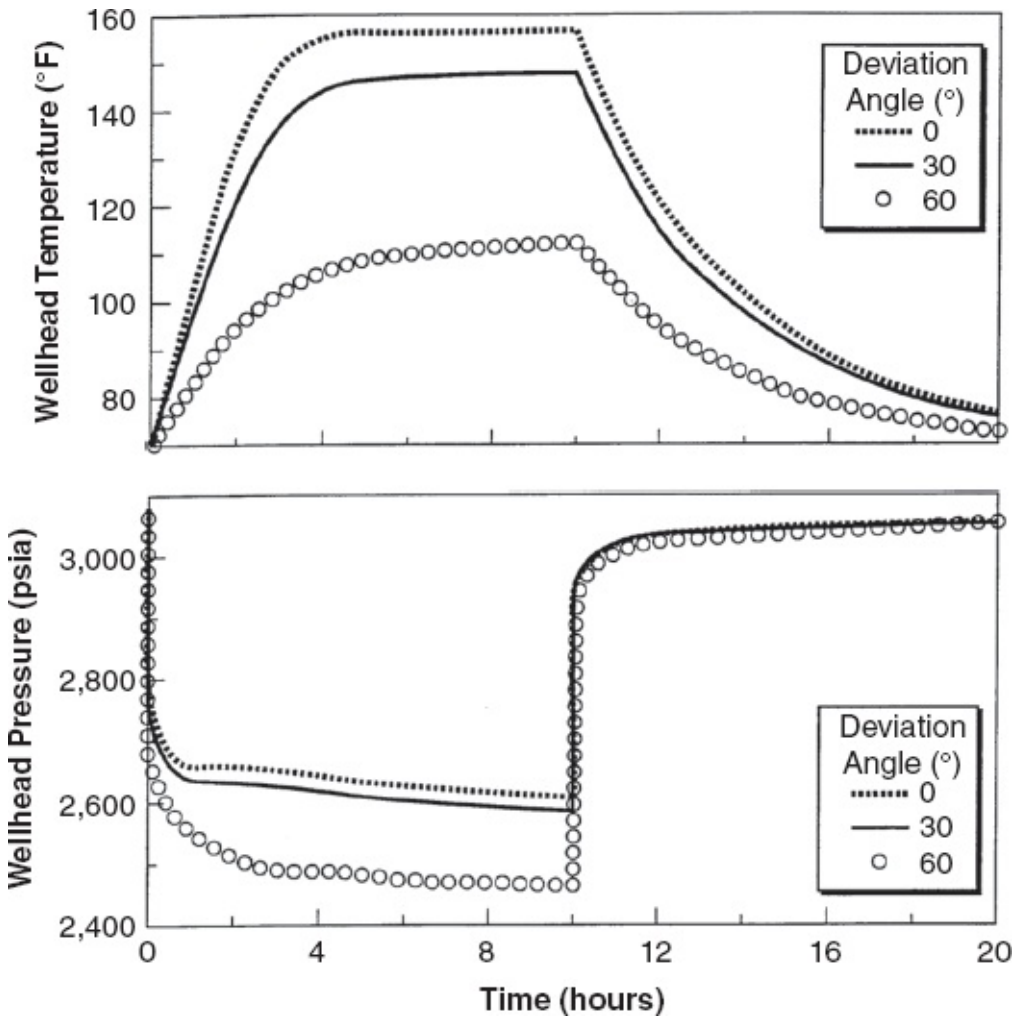

Fig. 9.18—Well deviation can potentially reduce WHT.

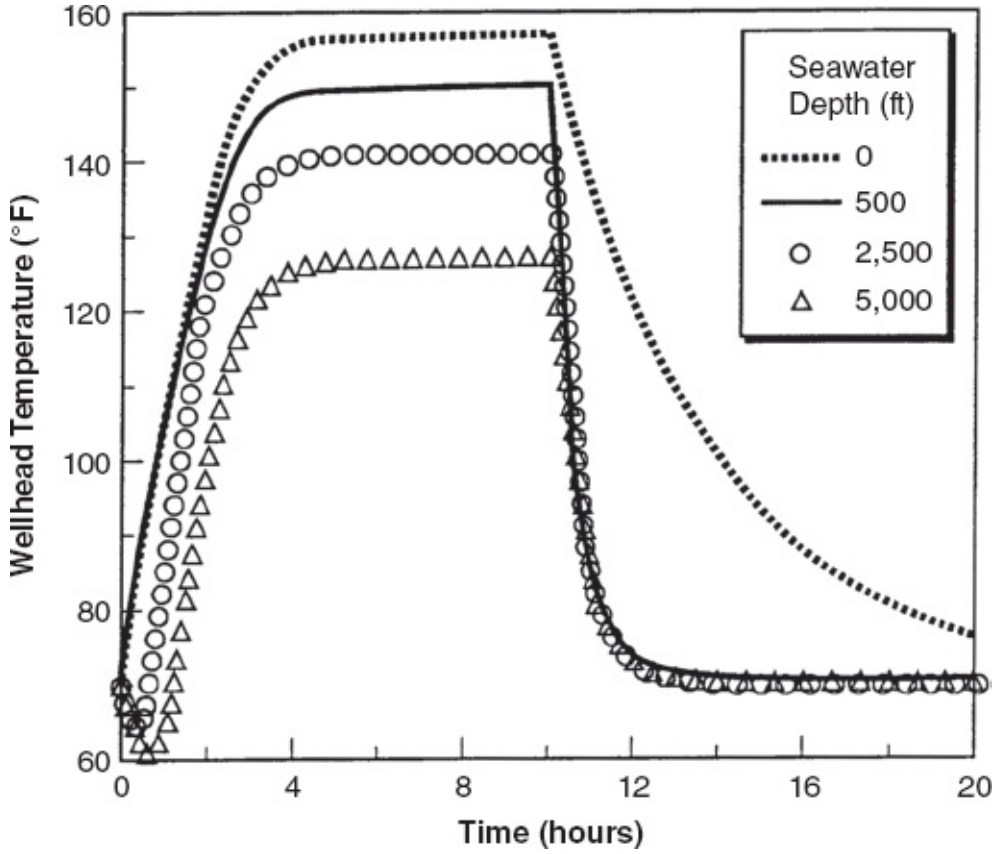

Fig. 9.19—Significant fluid cooling occurs with increasing seawater depth.

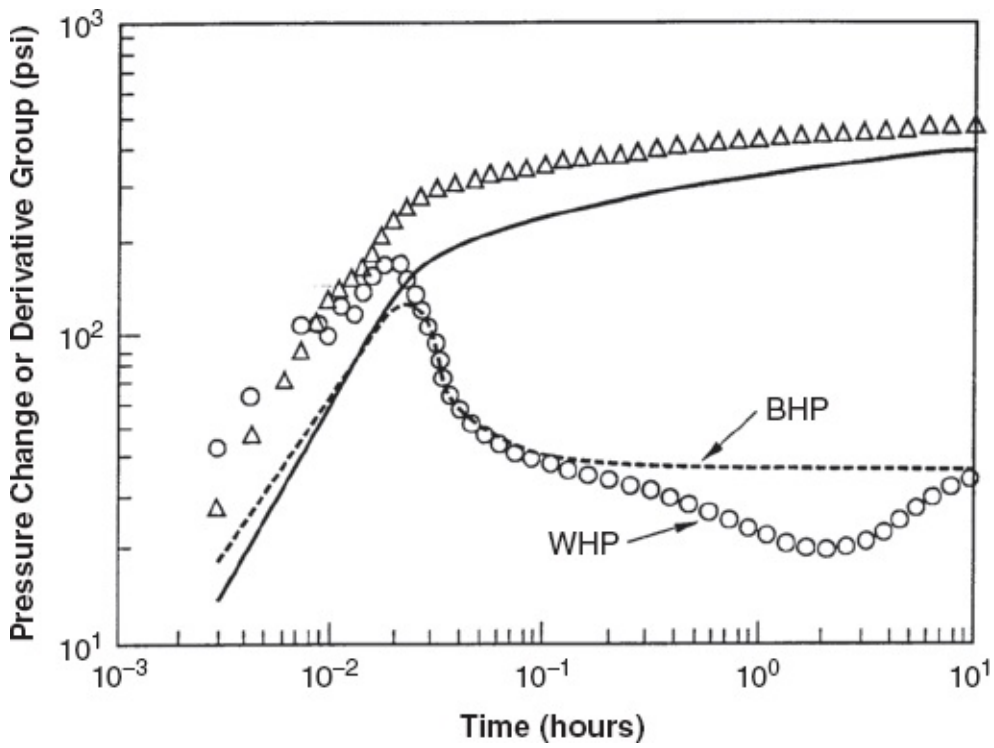

Fig. 9.20—Thermal storage distorts WHP response in 5,000-ft water.

9.4 Modeling Two-Phase Gas/Oil Flow

9.4.1 Model Formulation. Formulation of the two-phase gas/oil flow model is analogous to that of the gas and oil models described earlier in this chapter. The resulting expression for flowing two-phase fluid temperature is reported in Appendix 9-A, Section 9-A.3; Hasan et al. (1998) present the details of this formulation.

9.4.2 Sensitivity Study. **Fig. 9.21** shows that an increase in the gas/oil ratio (GOR) decreases the WHT. Higher turbulence with increased gas causes greater heat transfer for the high-GOR cases. The corresponding increase in WHPs is caused by an increase in wellbore gas volume with the attendant decrease in static-head loss. Consequently, we observe a progressively diminishing change in WHP (shut-in minus flowing wellhead pressure for a given GOR) because of increasing compressibility of the wellbore fluid. This observation also suggests that reliable reverse simulation to translate wellhead p and T measurements to downhole pressures will be more difficult to perform because the WHP response is dampened by the fluid compressibility.

Perhaps the preceding discussion is better understood by examining the wellbore fluid characteristics during the flow and shut-in conditions for the base case. **Fig. 9.22** shows the fluid temperature profiles at various drawdown and buildup times. As shown, the early-time (0.1-hour) drawdown and the late-time (10-hour) buildup have a similar linear character. The implication is that the wellbore has not exchanged significant heat with the formation. Conversely, the late-time (10-hour) drawdown and the early-time (0.1-hour) buildup exhibit a similar nonlinear response, suggesting considerable heat transfer. We can gain insight by examining the wellbore in-situ gas volume fraction and density profiles. **Fig. 9.23** shows the gradual progression of these two entities during a drawdown test. As expected, the gas occupies an increasingly larger space in the flow string with an increasing production time, until a steady flow rate is attained at the surface, beyond the storage period. Storage is induced by both compressible fluid and heat flows.

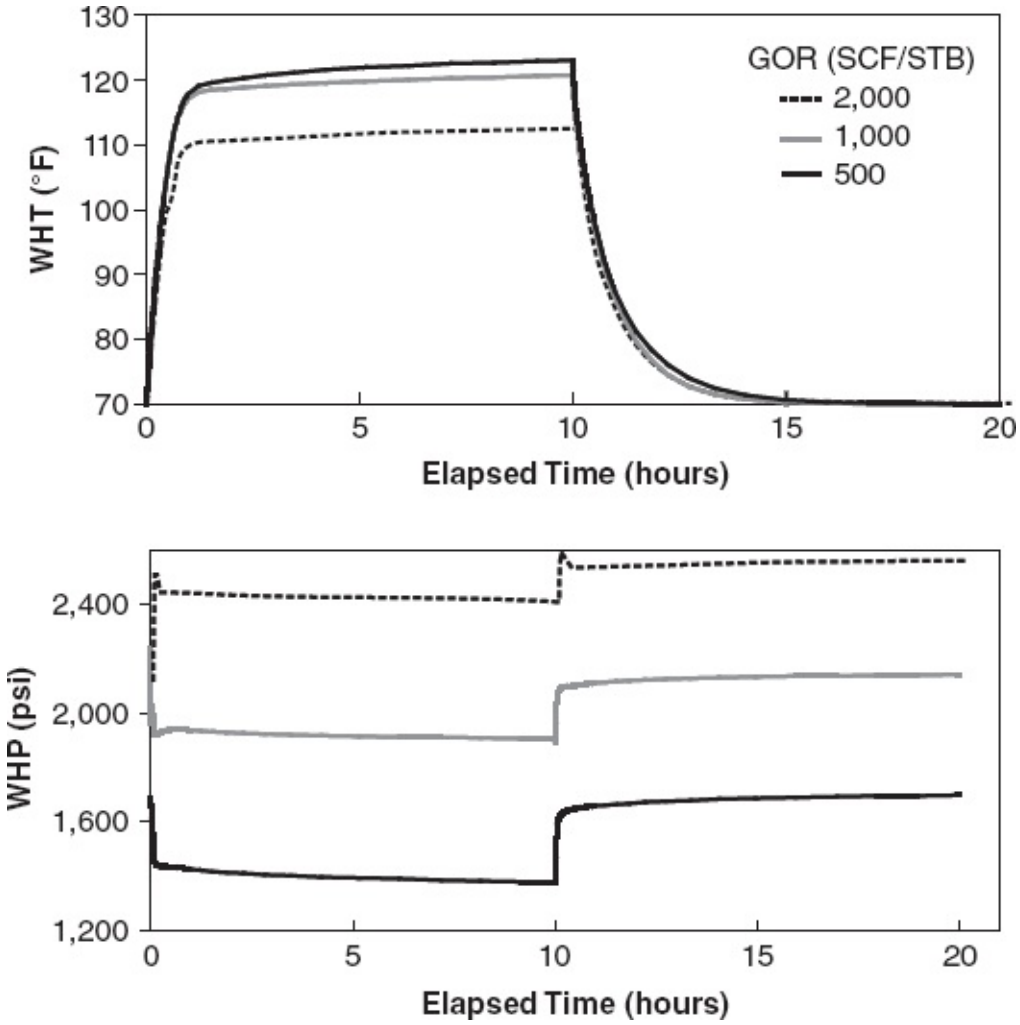

Fig. 9.21—Increasing GOR causes lowering of WHT but a rise in WHP.

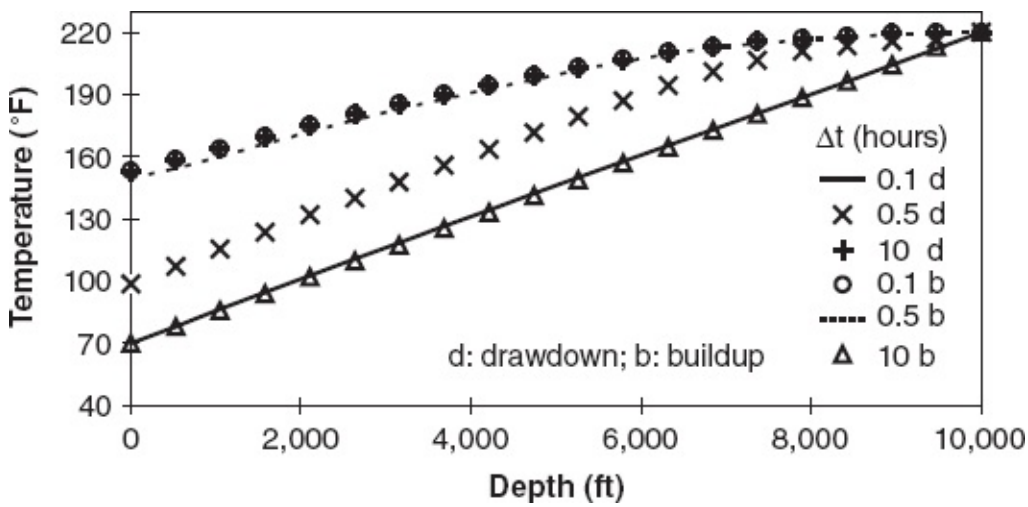

Fig. 9.22—Wellbore temperature profiles during two-phase transient tests.

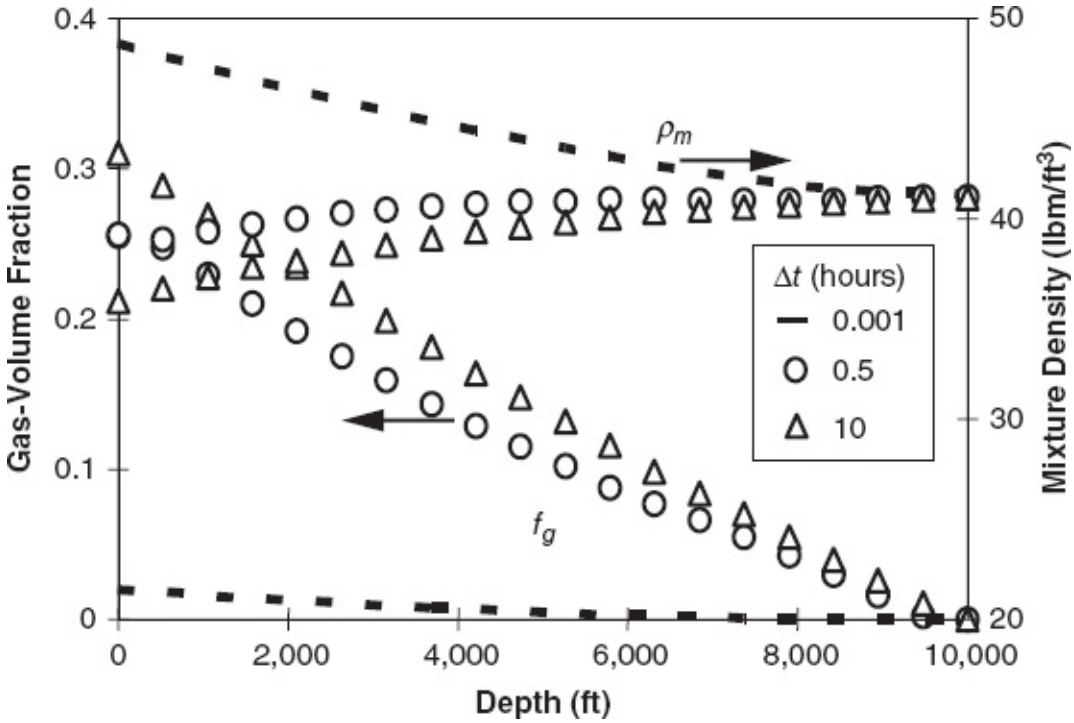

Fig. 9.23—Changing gas volume and mixture density during a buildup test.

One implication of this observation is that any in-situ measurements, temperature for instance, made during the transient wellbore flow period can potentially lead to misdiagnosis of downhole flow problems. Duration of this transient period may last from a few minutes to several days, depending on the formation and wellbore characteristics. For example, shallow wellbores in high-transmissivity reservoirs will exhibit a very short wellbore-induced transient period. In contrast, deep wells in tight reservoirs may take several days before stabilizing, from the standpoint of both heat and fluid flows.

As one may surmise intuitively, the heat and fluid storage problem are more acute for two-phase flow because of the added phase and its distribution in the wellbore. Complications stem from depth- and time-dependent mixture density profiles. In a two-phase flow situation, in-situ gas volume and thermal effects both contribute to the non-linearity of the wellbore mixture density profile. In contrast, for single-phase flow, only thermal effects influence the depth-dependent fluid density and, hence, the wellbore pressure at any point in the fluid column.

Transient pressure/temperature behavior in environments where enhanced heat exchange takes place provides some interesting observations. A deviated offshore well is a case in point, as illustrated by **Fig. 9.24.** Here, the well deviation causes increased heat exchange because of increased residence time for the same vertical depth in the deviated segment, leading to cooler WHT. As **Fig. 9.25** shows, an increasing submerged well length causes significant cooling, especially when the well is opened for flow after attaining thermal equilibrium with the surroundings.

We can surmise that one cannot easily translate the WHP into BHP. The solution of this problem is difficult even when single-phase oil flow occurs. Complications arising

from changing gas volume and temperature effects can limit our ability to translate WHP values into BHP values when we treat a two-phase mixture. Any notion of using WHP for deliverability calculations must be approached cautiously because of the transient nature of the flow problem. This statement is true even when a stable surface rate has been attained. We explore this point further when we discuss systems analysis in Chapter 12, Section 12.2.

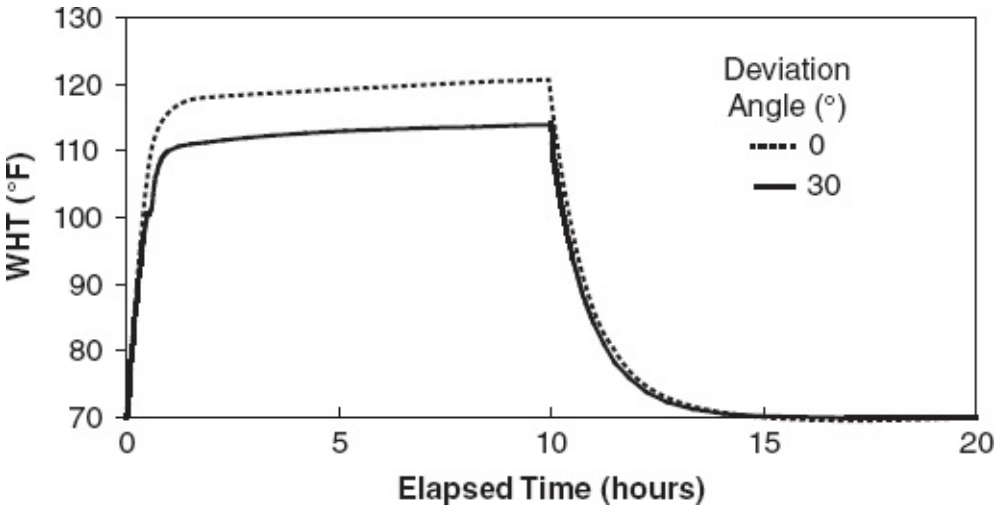

Fig. 9.24—Well deviation causes reduced WHT.

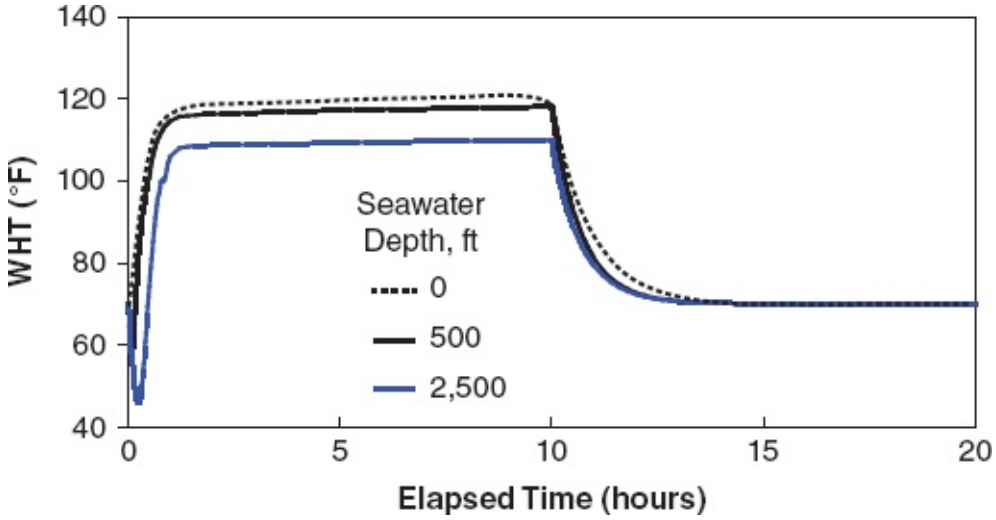

Fig. 9.25—Increased water depth causes reduced WHT.

9.5 Analytical Wellbore Transient Temperature Modeling

As mentioned before, the time-dependent and coupled nature of the three transport processes has led us and other researchers to solve the governing differential equations numerically. Previous sections discussed numerical models for probing various transient wellbore flow problems. In this section, we present a simplified analytical approach by conserving mass, momentum, and energy in the wellbore to capture physical phenomena. The simplification is achieved on the basis that mass

and momentum transients die much faster than temperature transients. Hasan et al. (2005) assumed that mass rate becomes constant instantly after a rate change, which allows the transport processes to be decoupled; thus one needs to contend only with the energy balance equation. This assumption of constant mass rate was also later made by Guo et al. (2006) and Spindler (2011). Guo et al. offered solutions for fluid transportation in pipelines for startup (similar to drawdown) and rate change (including buildup) situations. By including kinetic and potential energies and neglecting the J-T effect, their solution is not directly applicable to wellbores. Spindler used the same approach, detailed below, but added an expression for heat conduction along the wellbore. This addition made the mathematical formulation more rigorous, but it also made the final analytical expression much more cumbersome. Spindler concluded that heat conduction along the wellbore did not result in significantly different solutions, especially for practical wellbore conditions.

The intrinsic idea for developing an analytical expression for fluid temperature is to explore the feasibility of converting WHP to bottomhole condition in transient testing involving flow and shut-in conditions. This section captures the essence of the study that Hasan et al. (2005) presented.

The following expressions for the wellbore fluid temperature, T_f, are developed in Appendix 9-B by conserving energy while conserving momentum iteratively. For mass conservation, the steady-state assumption is used. The resulting T_f expressions are

$$T_f = T_{eibh} - g_G(L-z)\sin\alpha + \frac{\left(1-e^{-at}\right)}{L_R}\left[1-e^{(z-L)L_R}\right]\psi \qquad (9.11)$$

for drawdown and

$$T_f = \left(T_{fo} - T_{ei}\right)e^{-a't} + T_{eibh} - g_G(L-z)\sin\alpha \qquad (9.12)$$

for buildup. In Eqs. 9.11 and 9.12, the system constants a and a' and the lumped parameter ψ are defined in Appendix 9-B. Information on variation of T_f with well depth and time is critical to performing pressure-traverse calculations with the mechanical energy balance equation.

Let us show an example application of the proposed model, reported earlier in Hasan et al. (2005). **Fig. 9.26** presents the WHP and WHT measurements. **Fig. 9.27** shows WHTs that are evaluated in accord with the proposed top-down computational algorithm. Overall, Eqs. 9.11 and 9.12 suggest that an acceptable match is at hand for all transients. Previously, WHTs were predicted with a forward numerical simulator.

Fig. 9.28 shows that the converted BHPs agrees well with those measured downhole. Accurate estimation of T_f has a profound bearing on the match quality. To further examine the solution quality, for the first drawdown we graphed both sets of data on a semilog paper, shown in **Fig. 9.29.** Both the early- and late-time match appear good, and the analysis yields the same values of the parameters. The middle

time mismatch is rooted in our assumption of steady-state dT_f/dz for a transientflow problem. This assumption necessitated derivation of simple analytical solutions. This assumption becomes closer to reality with increasing time.

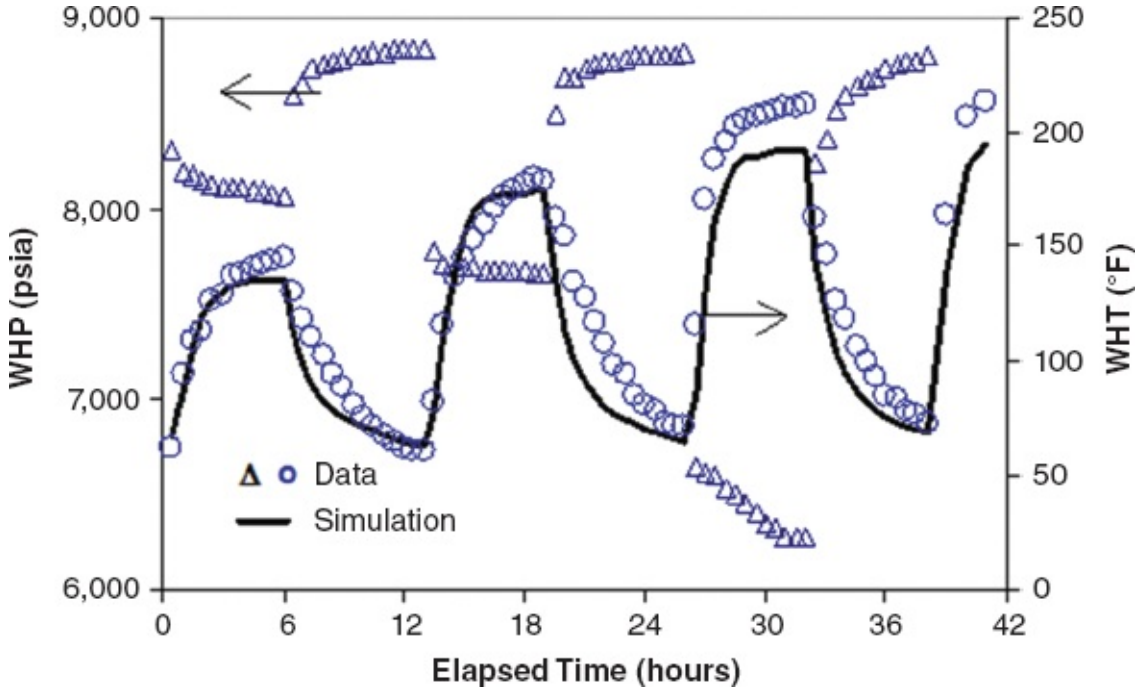

Fig. 9.26—Measured WHP/WHT history for the modified-isochronal period, Example 1.

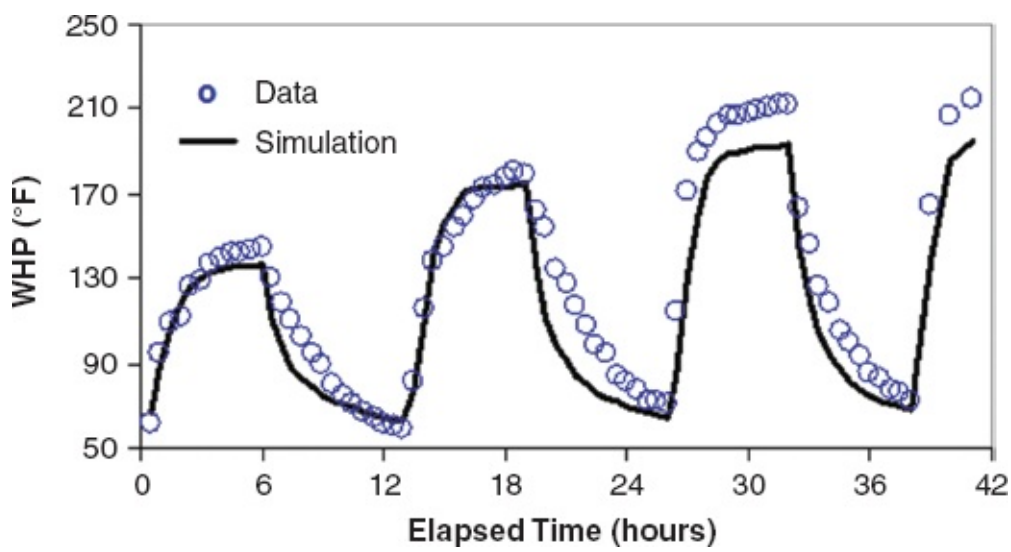

Fig. 9.27—Matching the WHT profile, Example 1.

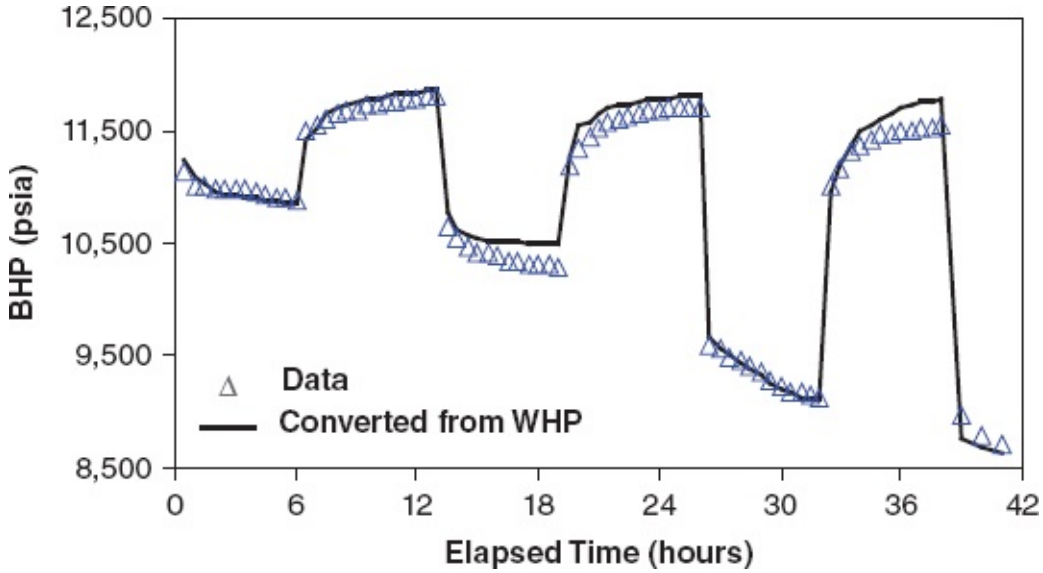

Fig. 9.28—Matching the BHP history, Example 1.

Tests in high-permeability reservoirs present pressure-conversion (WHT to BHP) challenges, as elaborated by Hasan et al. (2005). This issue primarily arises because of low fidelity in pressure response in high-transmissivity systems, especially at early times. In fact, a systematic design-of-experiments study with the forward simulator illuminated this point when both formation conductivity (*kh*) and flow rate turned out to be the most influential independent variables on the dependent-variable semilog slope.

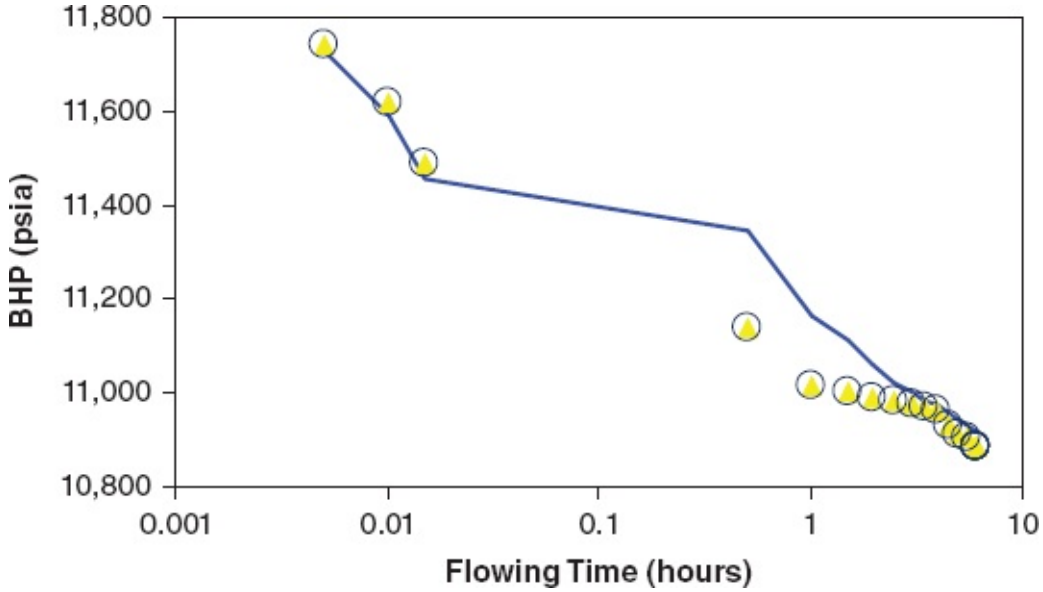

Fig. 9.29—Computed BHP compares favorably with measured values, Drawdown 1, Example 1.

Summary

In this chapter, we showed the development of rigorous wellbore/reservoir simulators to compute transient pressure and temperature at any point in the wellbore. Large

wellbore-temperature differences cause severe distortion of transient WHP response even when single-phase liquid production occurs. Duration of this distortion period is system specific, however. Results of various computations also show that the nonlinear nature of the wellbore density profile makes simple WHP conversion to BHP a difficult proposition, regardless of the nature of the wellbore fluid.

As expected, general heat-transfer characteristics of all fluids are quite similar. Whereas single-phase oil retains most of the heat relative to gas while ascending the well, a gas/oil mixture's performance lies between that of each of the two single-phase fluids. Heat transfer, in terms of importance, is governed by the conductivity of the annular fluid, the well length and its deviation, and the geothermal gradient itself.

These simulators serve a multitude of needs. For instance, we can design a mud system from a heat-loss standpoint. We can also compute WHTs associated with flow rates so that surface equipment and facilities can be designed properly; and when corrosion considerations are important, we can assist flowline design. The cooling of production fluids in the seawater segment is rather marginal unless deepwater wells of more than 2,000 ft are considered.

Nomenclature

A = flow cross-sectional area, ft^2
B = formation volume factor, RB/STB
C_p = heat capacity of fluids, Btu/lbm-°F
C' = weighted-average heat capacity of tubulars, Btu/lbm-°F
C_t = total system compressibility, 1/psi
C_J = Joule-Thomson coefficient, °F/psi
C_o = velocity profile correction factor, dimensionless
d = pipe diameter, ft
D = non-Darcy flow coefficient, darcies/scf or darcies/STB
E = internal energy, Btu/lbm
f = friction factor, dimensionless
f_g = in-situ gas volume fraction, dimensionless
f_L = liquid holdup, dimensionless
g = gravitational acceleration, ft/sec^2
g_c = conversion factor, 32.17 (lbm-ft)/lbf-sec^2
g_T = geothermal temperature gradient, °F/ft
H = enthalpy, Btu/lbm
h = formation thickness, ft
j = depth index for discretization, dimensionless
J = conversion factor, 778 (ft-lbf/Btu)
K = formation permeability, md

K_e = earth or formation conductivity, Btu/hr-ft-°F

I = time coordinate for discretization, dimensionless

L = cell length, L

m = mass in a control volume, m

M = molecular weight, lbm/lbm mol

L_R = inverse relaxation distance, 1/ft

p = pressure, psia

p_i = initial reservoir pressure, psia

p_w = wellbore pressure, psia

p_{pn} = normalized pseudopressure, psia

Δp = pressure drop, psi

q = volumetric gas or oil flow rate, MMscf/D or STB/D

Q = heat flow rate per unit length from or to the formation, Btu/hr-ft

r = radial distance, ft

r_w = radial distance, ft

R = universal gas-law constant, psia-ft^3/lbm mol-°R

s = skin factor, dimensionless

V = cell volume, ft^3

t = time, hours

t_D = dimensionless time (= 2.64×10^{-4}kt/

t_P = production time, hours

Δt = shut-in time, hours

T = temperature, °F

T_D = dimensionless temperature

T_f = fluid temperature in the wellbore, °F

U = overall-heat-transfer coefficient, Btu/hr-ft^2-°F

v = velocity, ft/sec

w = mass rate of fluid, lbm/hr

x = mass fraction of gas, dimensionless

z = variable well depth from surface, ft

Z = gas-law deviation factor, dimensionless

α = well angle from horizontal, degrees

β = expansivity of fluid [= $-1/\rho\ (d\rho/dT)_p$], 1/°F

β_m = momentum diffusivity (= $2.64 \times 10^{-4}\ k/\phi\mu c_t$)

ϕ = formation porosity, dimensionless

ρ = density, lbm/ft^3

μ = oil viscosity, cp

λ = lumped parameter defined by Eq. 9-A-6, Btu/hr-ft-°F

ψ = lumped parameter defined by Eq. 9-A-7, Btu/hr-ft

ξ = lumped parameter defined by Eq. 9-A-8, Btu/hr-ft-°F

ω = lumped parameter defined by Eq. 9-A-9, Btu/hr-ft

Subscripts

c	=	convective
cv	=	control volume
D	=	dimensionless
e	=	earth
ei	=	earth initial
f	=	fluid
g	=	gas
L	=	liquid
m	=	mixture
n	=	indicator for last timestep in discretization
o	=	outside
∞	=	terminal
i	=	initial
j	=	cell index or spatial coordinate
to	=	tubing outside
toc	=	tubing outside, convective
w	=	well

Superscripts

l	=	timestep index
′	=	average property

Appendix 9-A

Finite-Difference Equations for Wellbore Fluid Temperature

9-A.1 Single-Phase Gas Flow. Using j and l to denote the spatial and time coordinates respectively, the finitedifference form of Eq. 9.4 is

$$\frac{\rho v}{A}\left\{c_p L_R\left[(T_{ei})_j-(T_f)_j^{l+1}\right]+\sigma_j^l\right\}=\rho_j^l\frac{\Delta H}{\Delta t}-\rho_j^l R\frac{\Delta(ZT_f)}{\Delta t}+\left[H_j^l-R\frac{Z(T_f)_j^l}{M}\right]\left(\frac{\rho_j^{l+1}-\rho_j^l}{\Delta t}\right)$$
$$-\frac{(w)_{j+1}^l}{A\Delta z}\left[H^l+\frac{(v^l)^2}{2}-gz\sin\alpha\right]_{j+1}+\frac{(w)_{j-1}^l}{A\Delta z}\left[H^l+\frac{(v^l)^2}{2}-gz\sin\alpha\right]_{j-1}, \quad \text{(9-A-1)}$$

where

$$\Delta H=-C_J c_p^l R\left[(Z\rho T_f)_j^{l+1}-(Z\rho T_f)_j^l\right]+c_p^l\left[(T_f)_j^{l+1}-(T_f)_j^l\right]/M \quad \text{(9-A-2)}$$

and

$$\Delta\left[Z(T_f)\right]=Z_j^{l+1}(T_f)_j^{l+1}-Z_j^l(T_f)_j^l. \quad \text{(9-A-3)}$$

Eqs. 9-A-1 and 9-A-2 do not show any conversion factors that might be needed to retain unit consistency. For example, T_f in these equations is in °R, whereas the measurements are reported in °F. The left side of Eq. 9-A-1 may be written in the following form with Eqs. 9-A-2 and 9-A-3.

We can now write an explicit expression for $(T_f)_j^{l+1}$ as

$$\rho_j^l c_p^l\frac{(T_f)_j^{l+1}-(T_f)_j^l}{\Delta t}-\frac{C_J c_p^l(p_j^{l+1}-p_j^l)}{\Delta t}-R\rho_j^l\frac{Z_j^{l+1}(T_f)_j^{l+1}-Z_j^l(T_f)_j^l}{\Delta t}+\psi_j^l$$
$$=\xi_j^l\left[(T_f)_j^{l+1}-(T_f)_j^l\right]-\lambda_j^l T_{f\,j}^{l+1}-\omega_j^l+\psi_j^l \quad \text{(9-A-4)}$$

$$\left(T_f\right)_j^{l+1}=\frac{(\sigma_j^l/A)-\psi_j^l+\left(\rho v T_{ei}c_p L_R\right)_j^{l+1}+\xi_j^l(T_f)_j^l+\omega_j^l}{\left(\rho v c_p L_R\right)_j^{l+1}+\xi_j^l-\lambda_j^l}, \quad \text{(9-A-5)}$$

which is the same as Eq. 9.6. In Eq. 9-A-5,

$$\lambda_j^l = \frac{R\rho_j^l Z_j^{l+1}}{\Delta t}\left(1 + C_J c_p^l \rho_j^{l+1}\right), \qquad (9\text{-A-6})$$

$$\psi_j^l = \left(H_j^l - \frac{p_j^l}{\rho_j^l}\right)\left(\frac{\rho_j^{l+1} - \rho_j^l}{\Delta t}\right) - \frac{(w)_{j+1}^l}{A\Delta z}\left[H^l + \frac{\left(v^l\right)^2}{2} - gz\sin\alpha\right]_{j+1} + \frac{(w)_{j-1}^l}{A\Delta z}\left[H^l + \frac{\left(v^l\right)^2}{2} - gz\sin\alpha\right]_{j-1}, \qquad (9\text{-A-7})$$

$$\xi_j^l = \frac{c_p^l \rho_p^l}{\Delta t}, \qquad (9\text{-A-8})$$

and

$$\omega_j^l = \frac{RC_J c_p^l \left(\rho_p^l\right)^2 Z_j^l (T_f)_j^l}{\Delta t} + \frac{R\rho_j^l Z_j^l (T_f)_j^l}{\Delta t}. \qquad (9\text{-A-9})$$

9-A.2 Single-Phase Oil Flow. The development of the finite-difference equations for the case of oil wells is similar to that for gas wells described in the previous subsection. We present only the final expression for the fluid temperature here; the details are found in Hasan et al. (1997).

$$\left(T_f\right)_j^{l+1} = \frac{(\sigma_j^l / A) - \psi_j^l + \left(\rho v T_{ei} c_p L_R\right)_j^{l+1} + \xi_j^l (T_f)_j^l + \omega_j^l}{\left(\rho v c_p L_R\right)_j^{l+1} + \xi_j^l}. \qquad (9\text{-A-10})$$

In Eq. 9-A-10, as in Eq. 9-A-5, ψ_j is given by Eq. 9-A-7. However, other parameters of Eq. 9-A-10 are somewhat different from their counterparts in Section 9-A.1. Therefore,

$$\psi_j^l = \left(H_j^l - \frac{p_j^l}{\rho_j^l}\right)\left(\frac{\rho_j^{l+1} - \rho_j^l}{\Delta t}\right) + \rho_j^l\left[\frac{(p/\rho)_j^{l+1} - (p/\rho)_j^l}{\Delta t}\right] - \frac{(w)_{j+1}^l}{A\Delta z}\left[H^l + \frac{\left(v^l\right)^2}{2} - gz\sin\alpha\right]_{j+1} + \frac{(w)_{j-1}^l}{A\Delta z}\left[H^l + \frac{\left(v^l\right)^2}{2} - gz\sin\alpha\right]_{j-1}, \qquad (9\text{-A-11})$$

and

$$\omega_j^l = \frac{\left[1 - \beta(T_f)_j^l\right]\left(p_j^{l+1} - p_j^{l+1}\right)}{\Delta t}. \qquad (9\text{-A-12})$$

9-A.3 Two-Phase Gas/Oil Flow. The development of the finite-difference equations

for the case of two-phase flow is like that for gas or oil wells described in previous subsections of this appendix. We present only the final expression for the fluid temperature here; the details are found in Hasan et al. (1998).

The final finite-difference form of the energy balance equation in terms of the fluid temperature is given by

$$\left(T_f\right)_j^{l+1} = \frac{(\sigma_j^l / A) - \psi_j^l + \left(\rho v T_{ei} c_p L_R\right)_j^{l+1}}{\left(\rho v c_p L_R\right)_j^{l+1} + \phi_j^l + \gamma_j^l (c_{pg})_j^l} + \frac{\phi_j^l (T_f)_j^l + \Gamma_j^l - \eta_j^l + \gamma_j^l (c_{pg})_j^l (T_f)_j^l}{\left(\rho v c_p L_R\right)_j^{l+1} + \phi_j^l + \gamma_j^l (c_{pg})_j^l}, \quad \text{(9-A-13)}$$

where

$$\psi_j^l = \left(H_j^l - \frac{p_j^l}{\rho_j^l J}\right)\frac{(\rho_j^{l+1} - \rho_j^l)}{\Delta t} - \frac{(\rho v)_{j+1}^l}{\Delta z}\left[H^l + \frac{1}{2}(v^l)^2 - gz\right]_{j+1} + \frac{(\rho v)_j^l}{\Delta z}\left[H^l + \frac{1}{2}(v^l)^2 - gz\right]_j, \quad \text{(9-A-14)}$$

$$\xi_j^l = \frac{c_p^l \rho_j^l}{\Delta t} + \frac{\rho' c'}{\Delta t}, \quad \text{(9-A-15)}$$

$$\gamma_j^l = \frac{\rho_j^l x_j^l}{\Delta t}, \quad \text{(9-A-16)}$$

$$\phi_j^l = \rho_j^l (1 - x_j^l)\frac{(c_{pl})_j^l}{\Delta t} + \frac{\rho' c'}{\Delta t}, \quad \text{(9-A-17)}$$

$$\eta_j^l = \rho_j^l (H_{gj}^l - H_{lj}^l)\frac{x_j^{l+1} - x_j^l}{\Delta t}, \quad \text{(9-A-18)}$$

and

$$\Gamma_j^l = \frac{\rho_j^l \left[1 - x_j^l c_{pgj}^l C_{Jgj}^l - (1 - x_j^l) c_{plj}^l C_{Jlj}^l\right](p_j^{l+1} - p_j^l)}{\Delta t} \quad \text{(9-A-19)}$$

Eqs. 9-A-13 through 9-A-19 lead to a tridiagonal matrix, which is solved by using the two-step Gaussian elimination method.

Appendix 9-B

Derivation of Analytical Transient Fluid Temperature Models

In many situations, the effects of changes in pressure and flow rates on heat transfer are minimal, and so decoupling the transport processes presents a valid approach to modeling. In this section, we present models for transient wellbore heat transfer, decoupled from momentum and mass transport, during initiation and cessation of production. The resulting analytical expressions for fluid temperature as a function of well depth and time would be a valuable tool for designing and analyzing well tests. The model developed has been validated using field data and results from rigorous numerical simulations. We first present the model for initiation of fluid production (drawdown); the shut-in (buildup) case is presented thereafter. We also discuss modeling transient fluid temperature during fluid injection.

9-B.1 Drawdown. Fig. 6.4 is reproduced below because it sketches the basis for the unsteady-state energy balance for a control volume of unit length within the wellbore. The well is inclined by an angle α with horizontal. The energy balance equation is written by noting the conductive heat loss to the formation, as well as the convective energy transport into and out of the control volume of unit length. In terms of fluid internal energy E, fluid enthalpy H, fluid mass rate w, fluid mass in the control volume m, and internal energy and mass of the wellbore system $(m'E')_w$, the energy balance equation can be expressed as

$$Q = \frac{\partial (mE)_{cv}}{\partial t} + \frac{\partial (m'E)_w}{\partial t} - \frac{\partial}{\partial z}\left[w\left(H + \frac{1}{2}v^2 - gz\sin\alpha \right)\right] \quad \text{(9-B-1)}$$

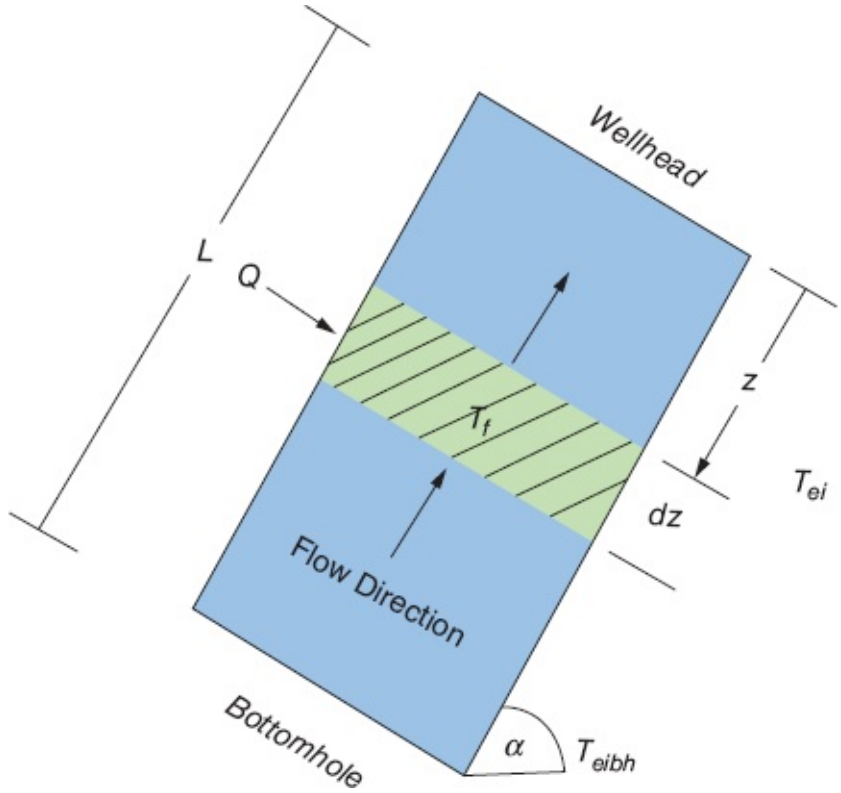

Fig. 6.4—Energy balance for wellbore fluid.

For dimensional consistency, the conversion factors g_c and J are needed in Eq. 9-B-1 for oilfield units (these factors are defined in the Nomenclature). Eq. 9-B-1 is similar to Eq. 6.13, which describes the energy balance for steady production. Unsteady-state production, represented by Eq. 9-B-1, also includes change in energy with time of the control volume material. The second term on the right side of Eq. 9-B-1 represents the energy absorbed by or released from the tubulars and cement sheaths in the wellbore. Omitting this term can lead to serious errors because it accounts for a significant fraction of the total energy exchange between the wellbore and the formation. Hasan et al. (1997, 1998) noted an anomalously sharp increase at early times in computed wellbore fluid temperature during drawdowns and a decrease during buildups when this term was neglected.

The heat received from (or lost to) the formation, Q, is given by Eq. 6.19.

$$Q \equiv -L_R w c_p \left(T_f - T_{ei}\right) \quad \text{(6.19)}$$

In Eq. 6.19, L_R is the relaxation-distance parameter that has been discussed extensively in Chapter 6 and reproduced earlier in this chapter.

During the early period of a drawdown, the mass flow rate w varies with depth even for single-phase fluid flow; that is, $d(wH)/dz \neq w(dH/dz)$. However, a steady rate in fluid flow is attained much more rapidly than stabilization of fluid temperature. For this analysis, we assume that w is independent of well depth. Therefore, the last term of Eq. 9-B-1 is rewritten as

$$\frac{\partial}{\partial z}\left[w\left(H+\frac{1}{2}v^2-gz\sin\alpha\right)\right]=w\frac{\partial}{\partial z}\left[\left(H+\frac{1}{2}v^2-gz\sin\alpha\right)\right]$$
$$=w\left[\left(c_p\frac{\partial T_f}{\partial z}-C_J c_p\frac{\partial p}{\partial z}+v\frac{\partial v}{\partial z}-gz\sin\alpha\right)\right] \quad \text{(9-B-2)}$$

Eq. 9-B-1 is rewritten by replacing the internal energy of the fluid in the control volume with fluid enthalpy, *H*, and fluid pressure and volume, noting that *m* = *Ar*. As Hasan et al. (2005) noted, the temperature rise of the cement/tubular material at any time may be taken to be a fraction of the rise in the fluid temperature. In that case, we may write

$$m'E'=C_T\times mE, \quad \text{(9-B-3)}$$

and the first term on the right side of Eq. 9-B-1 can be written as

$$\frac{\mathrm{d}}{\mathrm{d}t}(mE+m'E')=\frac{\mathrm{d}}{\mathrm{d}t}\left[m\,c_P T_f\left(1+C_T\right)\right] \quad \text{(9-B-4)}$$

Note that the thermal-storage parameter c_T (= *m'E'/mE)* represents the capacity of the wellbore to store or release heat, involving multiple fluid mass and their heat capacities. Therefore, the value of c_T will vary from well to well. For the field examples, we noted that c_T was 3.0 for drawdowns and 2.0 for buildups.

Combining the J-T effect and kinetic energy contribution into a single term ϕ, we rewrite Eq. 9-B-2 as a first-order linear differential equation for fluid temperature in time, shown in Eq. 9-B-5.

$$\frac{\mathrm{d}T_f}{\mathrm{d}t}=\frac{wc_pL_R}{mc_p\left(1+C_T\right)}\left(T_{ei}-T_f\right)+\frac{wc_p}{mc_p\left(1+C_T\right)}\left(\frac{\partial T_f}{\partial z}-\phi-g\sin\alpha\right) \quad \text{(9-B-5)}$$

In Eq. 9-A-5, $\phi=C_J c_p\frac{\partial p}{\partial z}-v\frac{\partial v}{\partial z}$, as given by Eq. 6.27. Note that T_{ei} depends on well depth and that *z* is positive in the downward direction: $T_{ei} = T_{eibh} - g_G\ (L - z)$,sin$\alpha$. Therefore, Eq. 9-B-5 expresses T_f as a function of time and well depth. For steady flow in a deep well, fluid temperature change with well depth, ($\mathrm{d}T_f/\mathrm{d}z$), equals the formation geothermal gradient, g_G sinα. However, under ordinary conditions, the term $\mathrm{d}T_f/\mathrm{d}z$ is slightly depth dependent, as is evident in the following steady-state temperature expressions developed in Chapter 6:

$$\frac{\mathrm{d}T_f}{\mathrm{d}z}=\pm L_R(T_f-T_{ei})+\frac{g\sin\alpha}{c_pJg_c}+\phi, \quad \text{(6.26)}$$

$$T_f = T_{ei} + \frac{1-e^{(z-L)L_R}}{L_R}\left(g_G \sin\alpha + \phi + \frac{g\sin\alpha}{c_p}\right) \qquad (6.29)$$
$$= T_{ei} + \frac{1-e^{-zL_R}}{L_R}\psi$$

where

$$\psi = g_G \sin\alpha + \phi + \frac{g\sin\alpha}{c_p} \qquad (9\text{-B-}6)$$

An expression for dT_f/dz at steady-state can be obtained by substituting T_f from Eq. 6.29 in Eq. 6.26, giving

$$\left[\frac{dT_f}{dz} = \psi\left(1-e^{(z-L)L_R}\right) + \frac{g_G \sin\alpha}{c_p} + \phi\right] \qquad (9\text{-B-}7)$$

Assuming that Eq. 9-B-7 may be used for (dT_f/dz) for the transient model, we rewrite Eq. 9-B-5 as follows:

$$\frac{dT_f}{dt} = \frac{wc_pL_R}{mc_p(1+C_T)}\left(T_{ei}-T_f\right) + \frac{wc_p}{mc_p(1+C_T)}\psi\left[1-e^{(z-L)L_R}\right] \qquad (9\text{-B-}8)$$

We use the following lumped parameters:

$$a = \frac{wc_pL_R}{mc_p(1+C_T)}$$
$$b = \frac{wc_p\psi}{mc_p(1+C_T)}\left(1-e^{-zL_R}\right) \qquad (9\text{-B-}9)$$

We write the general solution for Eq. 9-B-8 as

$$T_f = ICe^{-at} + T_{ei} + \frac{b}{a} \qquad (9\text{-B-}10)$$

To obtain the integration constant *IC*, we need to use fluid temperature at initial drawdown in Eq. 9-B-10. Sometimes, the fluid initial temperature at any depth in the wellbore may equal the surrounding earth temperature, T_{ei}. However, this may not always be the case, especially if the prior shut-in was of short duration. Given this reality, we use T_{fi} as the initial fluid temperature; that is, the initial condition is given by $T_f = T_{fi}$ when $t = 0$. Therefore,

$$T_{fi} = IC + T_{ei} + \frac{b}{a}; \text{ that is, } IC = \left(T_{fi}-T_{ei}\right) - \frac{b}{a} \qquad (9\text{-B-}11a)$$

$$T_f = -\frac{b}{a}e^{-at} + \left(T_{fi} - T_{ei}\right)e^{-at} + T_{ei} + \frac{b}{a} \quad \text{(9-B-11b)}$$

Using Eq. 9-B-9, the *b*/*a* ratio leads to the following expression:

$$\frac{b}{a} = \frac{\left[1 - e^{(z-L)L_R}\right]\psi}{L_R} \quad \text{(9-B-12)}$$

and

$$\begin{aligned} T_f &= T_{ei} + \left(T_{fi} - T_{ei}\right)e^{-at} + \frac{\left(1 - e^{-at}\right)}{L_R}\left[1 - e^{(z-L)L_R}\right]\psi \\ &= T_{ei} + \left(T_{fi} - T_{ei}\right)e^{-at} + \frac{b}{a}\left(1 - e^{-at}\right) \end{aligned} \quad \text{(9-B-13)}$$

Note that for very large values of time *t*, when e^{-at} approaches zero, the expression for wellbore fluid transient temperature, T_f (given by Eq. 9-B-13), becomes the same as the steady-state expression, given by Eq. 6.29. Eq. 9-B-13 gives the wellhead transient temperature when $z = 0$ and $T_{ei} = T_{eiwh}$ is used.

9-B.2 Shut-In Tests. Following well shut-in at the surface, afterflow at the sandface can persist for some time. However, as in drawdown, we assume that rate variation with well depth rapidly becomes negligible. With wellhead shut-in, *w* is zero, and the general energy balance equation (Eq. 9-B-1) simplifies to

$$Q = \frac{\mathrm{d}(mE)_{cv}}{\mathrm{d}t} + \frac{\mathrm{d}(m'E')_w}{\mathrm{d}t} \quad \text{(9-B-14)}$$

The heat received from (or lost to) the formation, Q, is written as

$$Q \equiv c_p\left(T_{ei} - T_f\right)L'_R \quad \text{(9-B-15)}$$

The alternative relaxation-distance parameter, L_R' (which omits flow rate *w*) is given by

$$L'_R = \frac{2\pi}{c_P}\left[\frac{r_{to}U_{to}k_e}{k_e + \left(r_{to}U_{to}T_D\right)}\right] \quad \text{(9-B-16)}$$

That is, L'_R is equivalent to wL_R for drawdown. Following the approach used for drawdown, we combine Eqs. 9-B-14, 9-B-15, and 9-B-16 with Eq. 9-B-4 to obtain the following first-order linear differential equation for fluid temperature in time and space:

$$\frac{\mathrm{d}T_f}{\mathrm{d}t} = \frac{L'_R}{m\left(1 + C_T\right)}\left(T_{ei} - T_f\right), \quad \text{(9-B-17)}$$

with the solution

$$T_f = ICe^{-a't} + T_{ei} \quad \text{(9-B-18)}$$

where the lumped parameter, a'—similar to a, defined by Eq. 9-B-9—is defined by

$$a' = \frac{L'_R}{m(1+C_T)} \quad \text{(9-B-19)}$$

Using the initial condition, $T_f = T_{fo}$ (fluid temperature just before shut-in), when $t = 0$, we obtain the fluid temperature expression for shut-in, which is given by

$$T_f = (T_{fo} - T_{ei})e^{-a't} + T_{ei} \quad \text{(9-B-20)}$$

Note that the relationship for T_{ei} in Eqs. 9-B-13 and 9-B-20 is $T_{ei} = T_{eibh} - (L-z)g_G$, sin$\alpha$.

The robustness of the assumption leading to the development of Eqs. 9-B-13 and 9-B-20—that is, the assumption of Eq. 9-B-7 for the transient flow problem at hand—remains in question. Figs. 9.27 and 9.28 answer that question by comparing the two solutions—rigorous (Kabir et al. 1996b) and analytical—for Example 1. We note a good agreement between the two solutions, which is probably adequate for most field applications.

Chapter 10

Applications of Transient Heat Flows in Assessing Well Integrity

10.1 Introduction

Chapter 9 addressed wellbore fluid flow situations involving single- and two-phase fluids. The attendant heat transfer is implicit in these formulations. This chapter explores applications of some of those principles concerning well integrity and safety considerations. Specifically, we discuss (1) annular pressure buildup (APB) arising from induced heat transfer because of fluid flow in the tubing string, (2) sustained casing pressure (SCP) from fluid influx into the annulus by way of leakage through poor cement bond and/or corroded tubing, and (3) liquid influx into the annulus through the gas lift valve upon depressurization of the annular gas.. In all cases, we present a brief account of the appropriate modeling considerations and field examples illustrating how safety issues can be quantified and mitigated to stay within safe, operable limits.

10.2 Annular Pressure Buildup

10.2.1 Introduction. Fluid production in a typical production string may conceivably affect pressures in both production and surface casings. Generally speaking, only the shallowest casings are cemented to the top, whereas the others, cemented at the bottom, contain mostly drilling fluid. Producing fluids in the tubing string transmit heat to the liquid-filled annuli, thereby triggering pressure increase. APB is not just associated with fluid production; fluid circulation during drilling may also induce the same, as reported by Pattillo et al. (2006). Accessible wellheads in typical land and offshore dry-tree wells allow the operator to monitor and bleed off annuli as needed. However, subsea wells present serious logistical difficulties for managing APB. Predictably, the stakes are high in high-pressure/high-temperature wells and those that are completed in a deepwater environment, where intervention costs are prohibitive. High flow rates exacerbate the APB issue because of the associated high energy that the fluids bring to the surface.

Consequences of APB are increased stresses on tubulars, which in the limit may cause well failure. Reduced production to alleviate annulus fluid temperature and pressure rise is, of course, economically unattractive. Given this reality, multistring casing designs have been proposed by Halal and Mitchell (1994) and Adams and MacEachran (1994), among others. Methods for APB mitigation have been proposed

using reduced heat transport with vacuum-insulated tubing (Azzola et al. 2007; Ellis et al. 2004), induced compressible fluids with nitrogen foam spacers (Vargo et al. 2003; Loder et al. 2003), and water-based spacer fluid containing emulsified methyl methacrylate monomer (Bloys et al. 2008). More recently, Sathuvalli et al. (2016) discussed the design basis and reliability of currently used mitigation techniques and also evaluated various options that have the potential to work as mitigation techniques.

Understanding the underlying mechanisms of APB is essential for developing any mitigation approach. To that end, Adams and MacEachran (1994) and Oudeman and Bacarreza (1995) have identified three mechanisms responsible for APB: fluid expansion, fluid influx or efflux, and tubing buckling. Mechanistic modeling of APB is currently performed with a well-known commercial package, which relies on numerical modeling of the wellbore heat-transfer process. This section presents two semianalytical approaches involving semisteady-state and transient formulations. These models offer the potential for ongoing management of annular pressures. In their current form, these tools are limited to handling annular pressure increase resulting from fluid expansion. Issues with tubular buckling are not handled, but fluid influx or efflux is accounted for in discrete steps. Details of the models can be found in Hasan et al. (2010a).

10.2.1 Annular Pressure Buildup Modeling Approach. The fluid trapped in an enclosed annulus can experience significant pressure increase when it receives heat from the producing fluids in the tubing string and is unable to expand. In other words, a mass of fluid when confined in a rigid space experiences volume increase because of fluid temperature rise. The volume change is counteracted by the pressure increase to compress the fluid. Therefore, we can write, $(\beta)(\Delta T) = (k)\,\Delta p$, where k is the coefficient of isothermal compressibility and β is the coefficient of isobaric thermal expansion, as shown in Eqs. 10.1 and 10.2.

$$\beta \equiv -\frac{1}{\rho}\left(\frac{\partial \rho}{\partial T}\right)_p \qquad (10.1)$$

$$\kappa \equiv \frac{1}{\rho}\left(\frac{\partial \rho}{\partial p}\right)_T \qquad (10.2)$$

In a rare event, extreme pressure rise may cause buckling of the tubulars, leading to change in volume available for the fluid to expand. In addition, fluid may enter or leave the annular space. These considerations led Oudeman and Bacarreza (1995) and Oudeman and Kerem (2006) to write the following expression using the three components contributing to the annular pressure increase from heating:

$$\Delta p = \frac{\beta}{\kappa}\Delta T - \frac{1}{\kappa V_a}\Delta V_a + \frac{1}{\kappa V_l}\Delta V_l, \qquad (10.3)$$

where V_l is the volume of annular liquid and V_a is the annular volume. The first term in Eq. 10.3 implies liquid expansion; the second term accounts for volume change in the annulus owing to tubular buckling, which is usually negligible; and the third term includes liquid influx (ΔV_l, positive) or efflux (ΔV_1 negative) in the annulus. Because the first term—the liquid expansion—is by far the most dominant in a sealed annulus, accounting for more than 80% of pressure increase in most cases, our modeling approaches center around this term. In the following, we briefly describe the two methods for estimating APB (Hasan et al. 2010a). In both methods, only the first term in the Oudeman-Bacarreza model is used and integrated over the entire wellbore.

Semisteady-State Approach. In the semisteady-state approach, the fluid temperature in the tubing is assumed to be at pseudosteady state, allowing Eq. 6.29 to be used for estimating the flowing-fluid temperature. With this assumption in mind, consider an annulus of unit depth containing fluid of mass M per unit length, with heat content Mc_{pi}. We use subscript 1 for the annulus closest to the tubing (production casing), 2 for the annulus next to it, and so on. **Fig. 10.1** depicts a typical well sketch with multiple annuli. In the following, the energy balance is modeled for Annulus 1; however, this approach has been extended for multiple annuli but skipped here for brevity. Heat accumulation in the first annulus equals heat exiting the tubing fluid minus heat going out from the annulus. Heat going out from annulus into the formation is given by Eq. 10.4, which is similar to Eq. 6.19:

$$Q = -L_{R1}\left(T_1 - T_{ei}\right), \qquad (10.4)$$

where, similar to Eq. 6.20,

$$L_{R1} \equiv 2\pi\left[\frac{r_{1o}U_{1e}k_e}{k_e + \left(r_{1o}U_{1e}T_D\right)}\right] \qquad (10.5)$$

Note that because Eq. 10.4, in combination with Eq. 10.5, expresses heat exchange between the formation and a static fluid; that is, flow rate $w = 0$, the wc_p term does not appear in these equations.

In Eq. 10.5, T_D is the dimensionless temperature function introduced in Chapter 6, defined by Eq. 6.7 and calculated using Eq. 6.10. Also, in Eq. 10.5, U_{1e} represents the overall coefficient for heat transfer from the first annular fluid to the wellbore/formation interface. Note that U_{1e} is estimated by inverting the sum of the resistances offered by all the elements and is given by

$$\frac{1}{U_{1e}} = \frac{r_{to}}{r_{1o}h_1} + \frac{r_{to}\ln\left(r_{\text{ins}}/r_1\right)}{k_{\text{ins}}} + \frac{r_{to}\ln\left(r_{1o}/r_{1i}\right)}{k_1} + \frac{r_{to}}{r_{2i}h_{a2}} + \frac{r_{to}\ln\left(r_{2o}/r_{2i}\right)}{k_{c2}} \qquad (10.6)$$

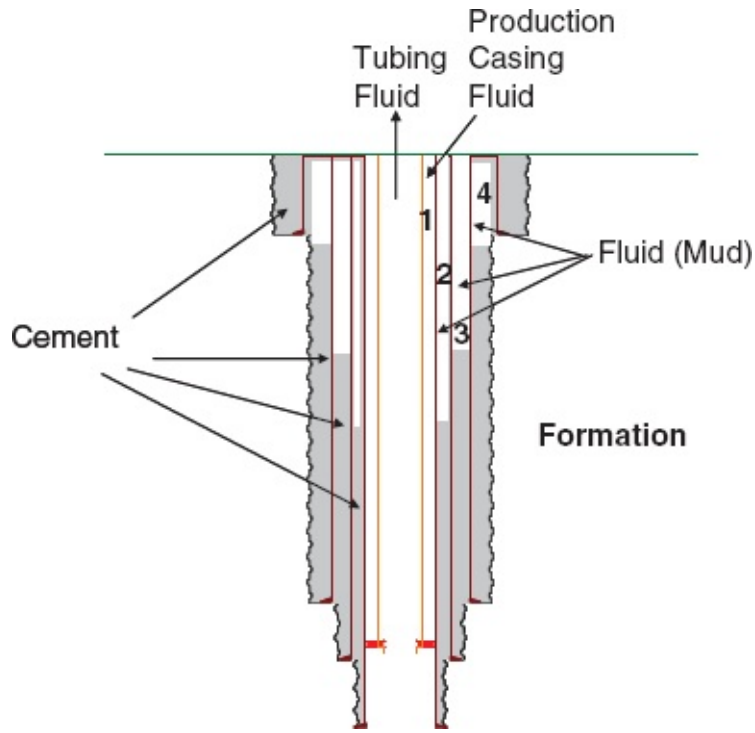

Fig. 10.1—Well sketch showing various concentric annuli in a typical well construction.

Eq. 10.6 is a general expression similar to Eq. 6.22. However, not all elements, such as tubing insulation represented by the second term of the right side, may be present in a given wellbore. Note that all overall-heat-transfer coefficients in this section are expressed in terms of tubing outside diameter. Heat entering from the tubing fluid into the annulus is given by

$$Q_{ta} = (\pi d_{1o}) U_{1t} (T_f - T_1) \quad (10.7)$$

Therefore, heat accumulation in annulus 1, $Mc_{p1}(\mathrm{d}T_1/\mathrm{d}t)$, is that given by Eq. 10.7 minus that given by Eq. 10.4.

$$Mc_{p1}(\mathrm{d}T_1/\mathrm{d}t) = (\pi d_{1o}) U_{1i} (T - T_1) - L_{R1}(T_1 - T_{ei}) \quad (10.8)$$

In Eqs. 10.7 and 10.8, U_{1t} is the coefficient for heat transfer between the tubing and the first annular fluid. In terms of annulus and tubing fluid heat-transfer coefficients h_1 and h_t and tubing conductivity k_t, U_{1t} is given by

$$\frac{1}{U_{1t}} = \frac{r_{to}}{r_{1o} h_1} + \frac{r_{to} \ln\left(r_{to}/r_{ti}\right)}{k_t} + \frac{1}{h_t} \quad (10.9)$$

Eq. 10.9 is solved semi-analytically to obtain annular fluid temperature in the production casing or the first annulus. Using the same approach leads to solutions for subsequent annuli. This model is semisteady-state because we presuppose steady-state flow of oil in the flow string, but transient heat flow in the annuli and formation. Details of model development and calculation procedures are provided in Appendix

10-A. We reaffirm that the model neglects the second and third terms of Eq. 10.3.

***Transient Approach*.** The procedure described above relies on tubing fluid temperature T_f reaching pseudosteady state. If the heat flow in the tubing is in a transient state, we can still use the same method to estimate APB if we use the transient temperature expression for tubing fluid developed in Chapter 9. Further improvement in the model can be achieved by accounting for the gradual heating of the near-wellbore region of the formation. The details of such a procedure are presented in Appendix 10-B.

10.2.2 Example Applications. ***Synthetic Example*.** Let us illustrate how temperature propagation occurs radially, leading to APB. Consider a 14,000-ft vertical well producing single-phase oil with multiple casing strings, such as the one shown in Fig. 10.1. As expected, the fluid temperature at the tubinghead is considerably higher than the initial temperature of 70°F as a result of the energy that the fluid brings to surface. As **Fig. 10.2a** shows, the tubinghead temperature stabilizes at 200°F after approximately 24 hours of production. The associated heat transport in the radial direction also causes temperature increase in different annuli. Annulus 1 represents the fluid temperature in the production casing; and at the wellhead, it is approximately 138°F. This increase in temperature from 70 to 138°F is the cause of pressure rise in the annulus.

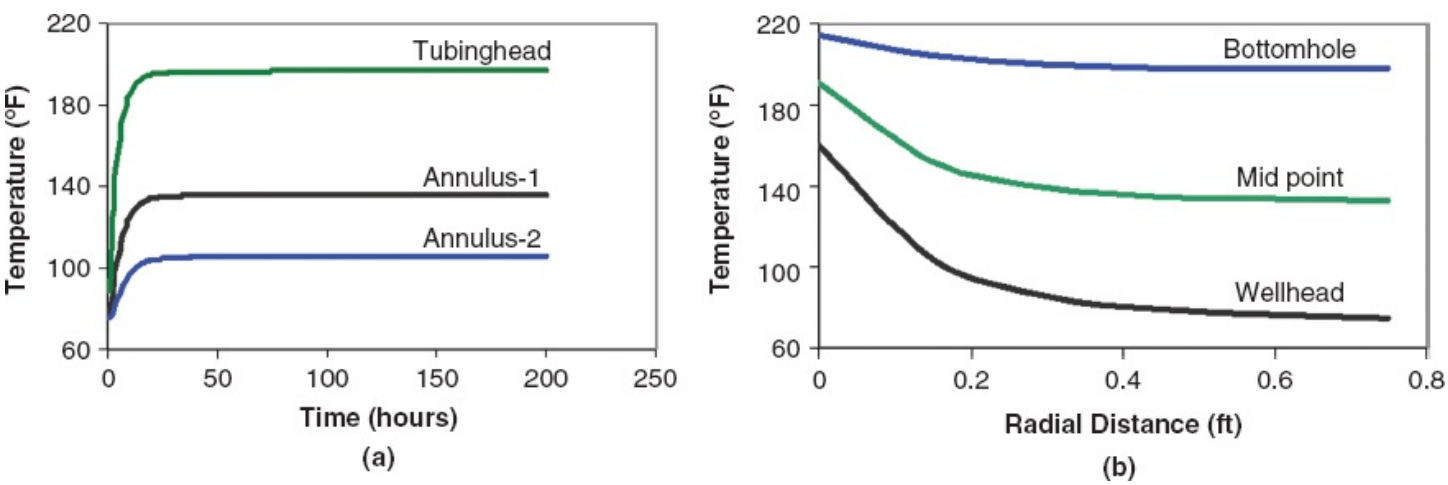

Fig. 10.2—Time-dependent temperature trace in various annuli at surface (a) and radial temperature at various points in the wellbore (b).

After 24 hours of production, the corresponding energy dissipation in the radial direction is as shown in Fig. 10.2b. In the proximity of the well bottom, minimal changes in temperature occur as we trace it in the reservoir. The gradual decrease in temperature is more pronounced in the midsection and is maximum at the wellhead. As the tubinghead temperature profile suggests, most of the temperature drop is locally confined; that is, it remains within the production casing. These computations were performed with the transient model, described in the previous subsection. **Table 10.1** presents the relevant data used to generate Fig. 10.2.

Field Example. High-rate single-phase oil production occurs from a 12,000-ft well in an onshore field in central Asia. First, in 2002 and 2005, we modeled this well behavior with the semisteady-state approach for pressure increase. Pressure buildup was observed in the 7-in. production casing owing to heating of annular fluid by the producing fluid in the tubing string. As **Fig. 10.3a** shows, the rise in annulus pressure is directly related to increase in flow rate. With increased rate, the available energy for heat transfer increases proportionately, leading to increased annular pressure. Fig. 10.3b makes this point amply clear. Because the fluid cannot expand in the annular confined space, its low compressibility manifests in terms of increased pressure with increased temperature, resulting in the APB behavior.

Fig. 10.4 shows the match of the semisteady-state model response with the wellhead temperature in the tubing. In Fig. 10.4 the green triangles show tubinghead temperature and the pink circles represent tubinghead pressures. Note that the early-time mismatch is a result of starting production in a cold well when in actuality the well had been in production for some time. However, this mismatch did not impede the model's ability to match the annular pressure rise, as the pressure match indicates.

In 2005, some annular liquid was bled off to relieve pressure. As a consequence, higher producing rate was restored while the annulus pressure decreased, as **Fig. 10.5a** exhibits. This bleed-off volume was not reported, however. When we used a bleed-off volume of 79 gal of known compressibility, the model was able to reproduce the annular pressure decline quite accurately. Fig. 10.5b displays this pressure and the temperature match.

Although the semisteady-state model provided encouraging results, we used the transient model to compare with results obtained earlier for the well. As **Fig. 10.6a** shows, the issue with prediction of higher wellhead temperature was improved significantly with the transient formulation. The quality of APB prediction is comparable, as Fig. 10.6b demonstrates. Note that the late-time pressures reflect bleeding of 79 gal of annular fluid.

q, STB/D	3,000	T_{ei}, °F	222	k_t, Btu/hr-ft-°F	30
L, ft	14,000	k_e, Btu/hr-ft-°F	1.5	k_c, Btu/hr-ft-°F	30
k, md	700	c_{pe}, Btu/lbm-°F	0.625	k_a, Btu/hr-ft-°F	0.1
h, ft	500	g_t, °F/ft	0.011	k_f, Btu/hr-ft-°F	0.34
ϕ, fraction	0.2	Tubing outer diameter, in.	3.5	α_d, hr/ft^2	0.04
°API	25	Tubing inner diameter, in.	2.992		

Table 10.1—Input data for generating the synthetic example.

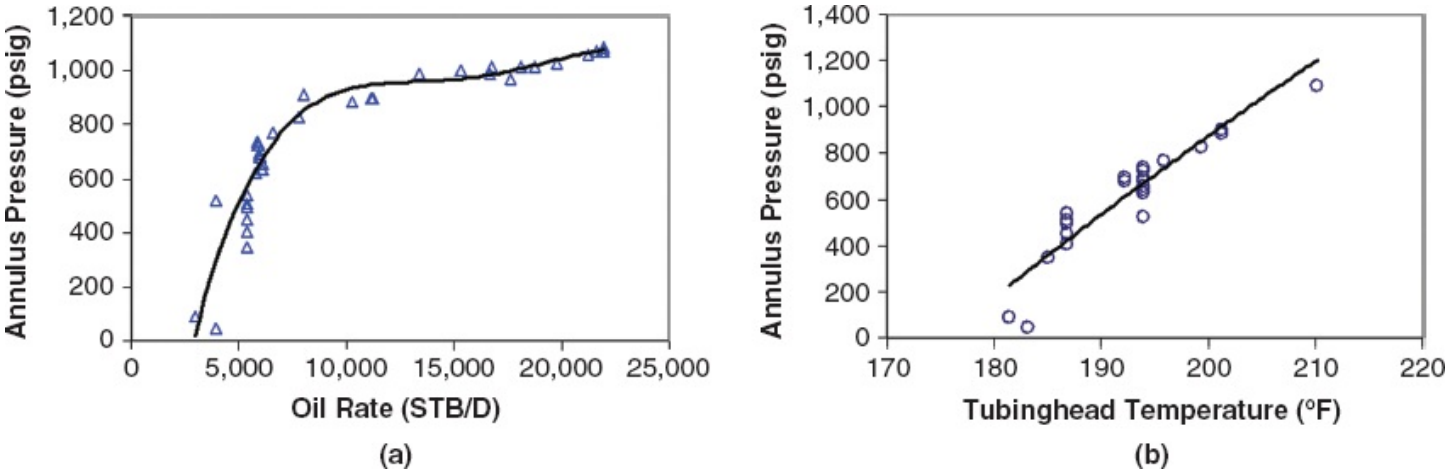

Fig. 10.3—Increasing production rate causes increased heat transfer, leading to APB (a); increase in annulus pressure is directly related to increase in tubinghead temperature (b).

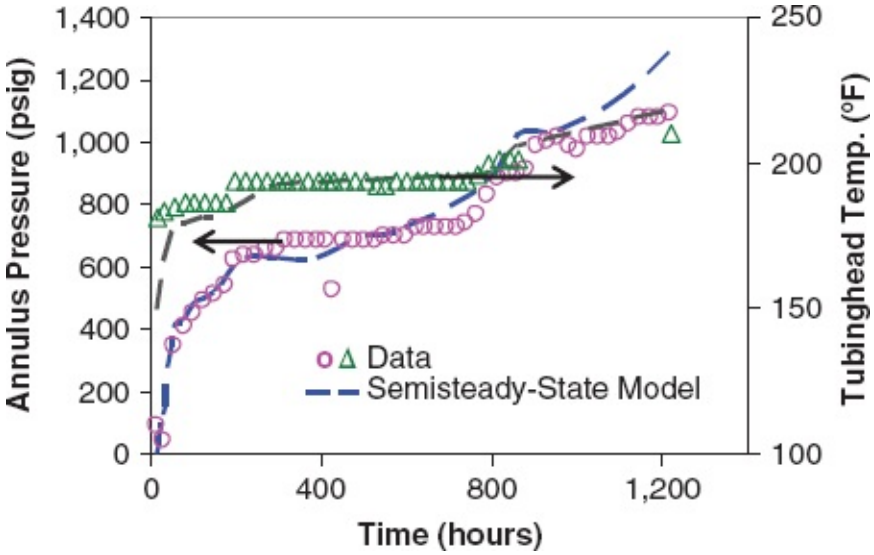

Fig. 10.4—Matching tubinghead temperature and APB in early life.

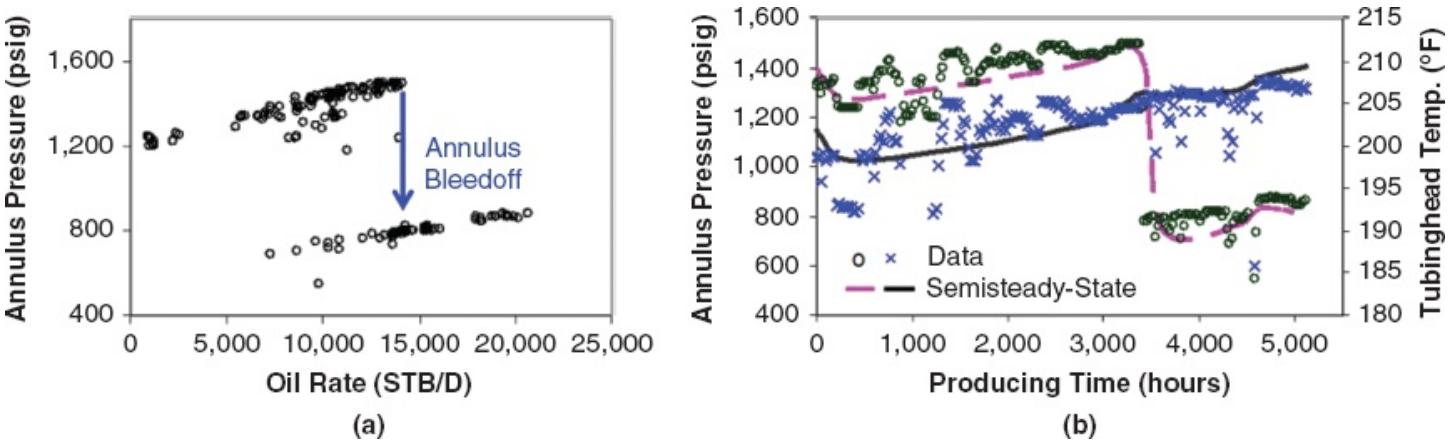

Fig. 10.5—Annulus pressure bleedoff leads to restoration of high producing rates in 2006 (a); matching tubinghead temperature and APB (b).

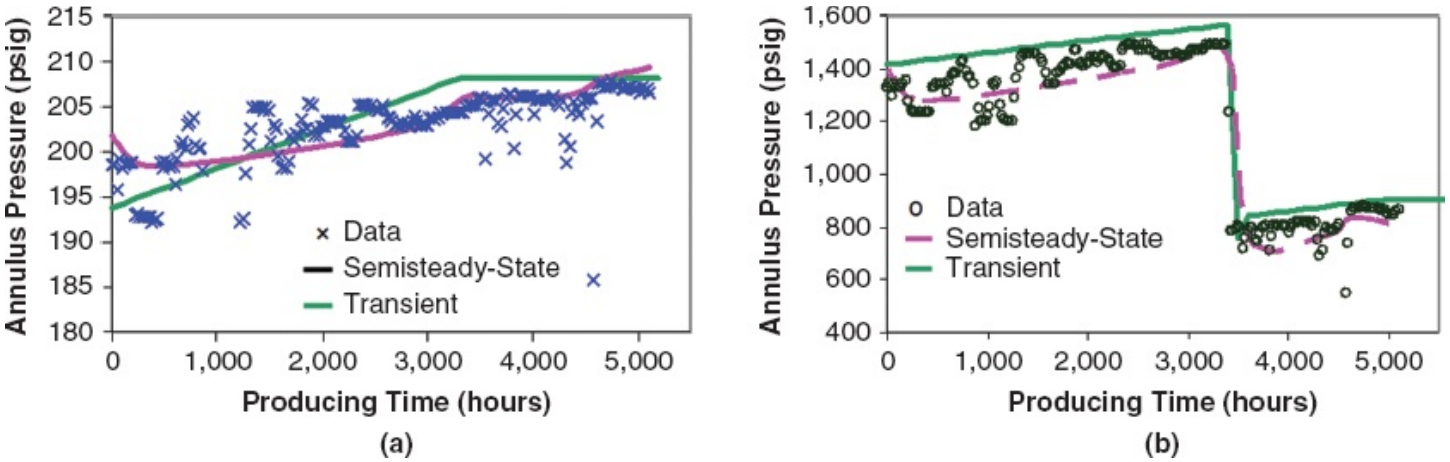

Fig. 10.6—Comparing tubinghead temperature predictions (a) and APB predictions (b) in 2006.

10.2.3 Lessons Learned. Increased drilling in deep waters makes prediction and management of APB imperative simply because accessibility of various annuli is limited. The two analytical models presented in this section provide methods for estimating APB. Real-time monitoring of pressure and temperature in various annuli and use of proposed models make day-to-day management of APB much more viable in land-based operations than in deep water. However, such measurements are infeasible in subsea wells; only Annulus-A is monitored (*API RP 90 2006*). Regardless of the number of annuli, a calibrated model provides clues about the maximum allowable rate commensurate with the system's mechanical integrity. Moreover, the model can guide an engineer on the bleed volume needed to improve the operable range of production rate; Fig. 10.7 illustrates such an example. The field example shows that both models allow easy application to managing APB en route to preserving well integrity. In so doing, the field example intrinsically addresses low assurance and real-time production management.

Of the two approaches presented, the semisteady-state model is simpler than its transient counterpart and, therefore, lends itself to rapid implementation. However, this simplicity is a trade-off in that it is not designed to handle transient rates associated with any production scenario. In contrast, the transient model is more complex, but it is capable of properly representing early-time transient behavior, as indicated by the synthetic and field examples. Consequently, the transient model is capable of providing early warnings for anomalous rise in APB and would allow ample time for mitigation. Perhaps more important, one can assess the maximum producing rate at the current condition and after a certain volume of annular fluid has been bled off.

10.3 Sustained Casing Pressure in an Annulus

10.3.1 Introduction. In contrast to APB discussed in the previous section, physical hydrocarbon leaks cause pressure increase in the annular string. In this situation, well

integrity issues merit a different treatment. Because SCP detection triggers well intervention and subsequent well shut-in or loss of production for a finite period, a strong incentive exists for periodic well integrity assessment.

Many field operators have adopted safety measures that have evolved with time. For instance, Anders et al. (2008) chronicled various well integrity operations at the Prudhoe Bay Field in Alaska. Particularly, wells were designed to handle acceptable limits of 2,000 psig in Annulus-A, 1,000 psig in Annulus-B, and 500 psig in the subsequent annuli. In this context, the American Petroleum Institute (API) recommends a bleed-off and buildup test when the annulus pressure exceeds 100 psig (*API RP 90 2006*).

Besides the operations and the consequent regulations in the US, issues with casing integrity have been reported in other settings. For instance, a systematic well integrity study by Watson and Bachu (2009) revealed that over 64% of 20,725 wells in a test area in Alberta, Canada, suffered from leakage through the surface-casing vent. Poorly cemented casing was cited as the major contributor to the leaks. Vignes and Aadnoy (2010) explored the well integrity issues of Norway's offshore setting involving 406 wells. Their findings suggested that 18% of the wells have had integrity failures, issues, or uncertainties; of these, 7% were shut in because of well integrity concerns.

In addition to concerns about integrity in producing wells are concerns about quantifying the CO_2-leakage rate during CO_2 sequestration. This leakage issue has gained considerable interest lately because of possible CO_2 emission into the environment. The studies of D'Alesio et al. (2011), Loizzo et al. (2011), Tao et al. (2012, 2014), and Huerta et al. (2009) examine this subject.

For casings that are filled with cemented and mud sections, a numerical solution approach was developed by Xu and Wojtanowicz (2001) and Xu (2002). These two studies explored the effects of parameters that are usually unknown for most wells. Following up on the recent studies of Rocha-Valadez et al. (2014a, 2014b), this section presents an analytical solution to the Xu (2002) model for gas migrating up the annulus through the cement sheath and the liquid column. The algebraic expressions for the casing pressure rise (Annulus-A) and the gas-seepage rate with time are readily adaptable for spreadsheet calculations. The model validation step with five sets of field data showed that the long shut-in time can be minimized significantly, given the solution quality achieved with earlytime response.

10.3.2 Sustained Casing Pressure Modeling Approach. The model as sketched in Fig. 10.7 shows a gas cap of length L_g, a mud column of length L_f, and a cemented section of height L_c. The formation gas seeps through the cement and percolates up the mud column into the gas cap, compressing the mud column and accumulating at the top because of buoyancy. This model's implicit assumption is that the well produces at a stable rate to ensure that flow rate fluctuations do not induce any heattransfer effects that influence the outcome of the SCP test.

At the beginning of the test, the casing is fully opened and the pressure is bled to a

certain initial pressure, p_o. The instant the Annulus-A casinghead valve is closed, the gas bubbles will percolate up the mud column. We assumed the gas leaking through the cement will move up the mud column and displace the same amount of gas from the top of the mud column and into the gas cap. In that sense, one can presuppose that the gas emerging out of the cement will affect the gas cap instantaneously. The gas cap volume will increase with time because of the slight compressibility of the mud, and the mud column length will decrease slowly with time. However, because the mud is enclosed in the annulus, the mass of the mud remains constant; therefore, the pressure exerted by the mud column will remain constant.

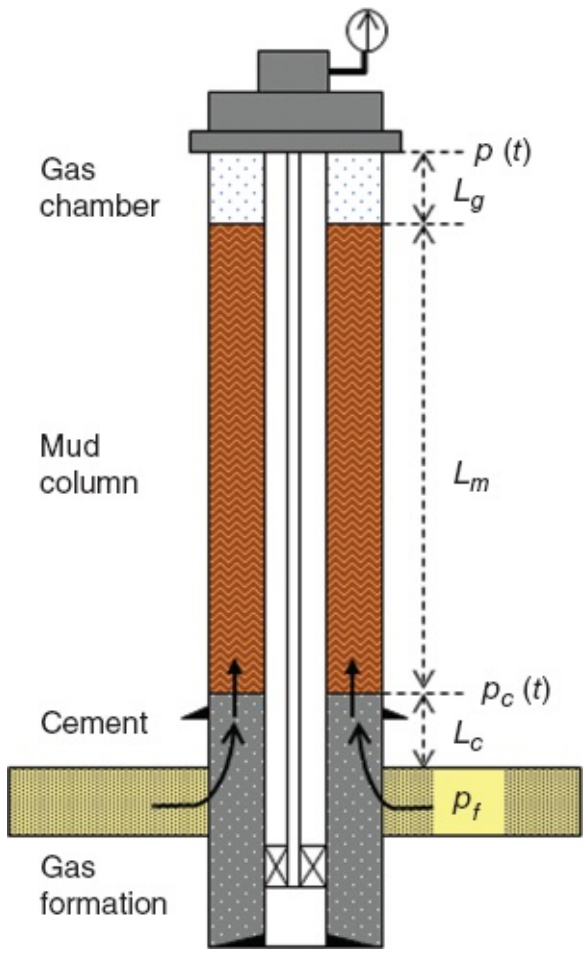

Fig. 10.7—Schematic of the cement/mud annular system.

An expression for gas flow rate q through the cement has been derived from first principles in Appendix 10-C. Here, we present that expression in field units as

$$q = \frac{0.003164\ kA_A T_{sc}}{L_c \mu_f Z_f p_{sc} T_f}\left(p_f^2 - p_c^2\right), \qquad (10.10)$$

where q is in scf/D, k is cement permeability in md, μ is gas viscosity in cp, and p_f and p_c are formation pressure and pressure on top of the cement in psia. In Eq. 10.10, p_{sc} and T_{sc} represent pressure and temperature at standard conditions (14.7 psia and

520 °R), T is the temperature in °R at the cement top, and μ_ρ T_f, and Z_f are the viscosity, temperature, and Z-factor of the gas at formation conditions. We use the gas law, $n = pV/(ZRT)$, to relate the number of moles of gas n in the gas cap to its pressure p, volume V, and temperature T. The change in the gas-cap volume is accounted for by the compressibility of the mud column. Appendix 10-C shows the steps leading to the differential equation governing the transient behavior of casing pressure, which is presented here:

$$\frac{\mathrm{d}p}{\mathrm{d}t} = \frac{\dfrac{0.003164kAT_{wh}}{L_c\mu_i Z_i T}\left[p_f^2 - (p + 0.052\rho_m L_m)^2\right]}{V_i + c_m V_m p\left(1 + \dfrac{1}{1 + c_m p}\right)} \quad \ldots\ldots (10.11)$$

Note that in Eq. 10.11 and in subsequent expressions, L_m is the true vertical length of the annular mud column, exerting a pressure of $0.052\rho_m L_m$ psi when the mud density ρ_m is expressed in lbm/gal. The analytical solution of Eq. 10.11 is expressed by the following equation in terms of the independent variable, t:

$$t = \frac{\left[(\alpha - 1)V_i - \alpha\beta V_m\right]\tanh^{-1}\left(\dfrac{p + b}{p_f}\right)}{p_f d(\alpha - 1)} + \frac{c_m V_m\left\{2\ln\left(1 + c_m p\right) + (2 - \alpha)\ln\left[p_f^2 - (p + b)^2\right]\right\}}{2d(\alpha - 1)} \quad \ldots\ldots (10.12)$$

For ease of arriving at a solution, Eq. 10.12 is written in terms of an independent time variable rather than the customary dependent variable. Appendix 10-C defines the parameters b, d, α, and β. Besides estimating the annular pressure rise and the attendant gas influx rate, one can calculate the cement-seepage factor k_s, which is akin to permeability. The analytical model developed in Appendix 10-C allows for rapid seepage factor estimation for a given data set. Because the pressure vs. time expression is nonlinear, we used the generalized reduced gradient (GRG) method (Lasdon et al. 1978) to estimate the k_s.

One advantage of the analytical form of the solution is that the maximum attainable casinghead pressure $p_{\max}$ can be estimated corresponding to the long periods of shut-in ($t \rightarrow \infty$). This task is completed by noting that $p_{\max}$ must occur when $\mathrm{d}p/\mathrm{d}t$, given by Eq. 10.11, equals zero. In other words,

$$\frac{0.003164kAT_{wh}}{L_c\mu_i Z_i T}\left[p_f^2 - (p_{\max} + 0.052\rho_m L_m)^2\right] \rightarrow 0$$

$$p_{\max} + 0.052\rho_m L_m \rightarrow p_f \quad \ldots\ldots (10.13)$$

Eq. 10.13 makes intuitive sense because when the sum of casinghead pressure and the pressure exerted by the mud column (= $0.052\rho_m L_m$) equals the formation pressure p_f, there is no pressure differential available for gas to seep into the annulus; that is, the maximum casing pressure has been attained.

10.3.3 Model Validation With Field Examples. This section presents the analysis of two sets of wells: oil wells and gas wells. The two oil-producing wells were discussed initially by Xu and Wojtanowicz (2001) and Xu (2002), and more recently by Huerta et al. (2009). In addition, Huerta et al. (2009) and Tao et al. (2012) probed the application of the same model in gas wells to test the well integrity issues in the context of possible CO_2 sequestration.

Analysis of Oil Wells. **Fig. 10.8** presents history matching of data collected over 300 days and forecasting for Well 23, reported earlier in Xu (2002). Only cement-seepage factor adjustment and initial gas cap height were sought to obtain this match. We assumed that formation pressure p_f, cemented length L_c, and total well depth L are known with reasonable confidence. The relevant input parameters are shown in **Table 10.2,** and the computational results are presented in **Table 10.3.**

Note that the volumetric rate of gas that permeates the cement is inversely proportional to the seepage factor. There are two reasons for the significant differences between the k values calculated by our model and those reported by Xu. The primary reason is the imprudent use of the cement-top pressure, p_c (5,347 psig at t = 0), instead of the standard pressure p_{sc}, to convert the gas-seepage rate into molar rate in Eq. 10.10. The secondary reason, which contributes less than 2% of the difference, is the way the mud column height and the hydrostatic pressure are treated. In the proposed method, the hydrostatic pressure of the mud column is considered to be constant throughout, which is consistent with APB analysis induced by heat transfer.

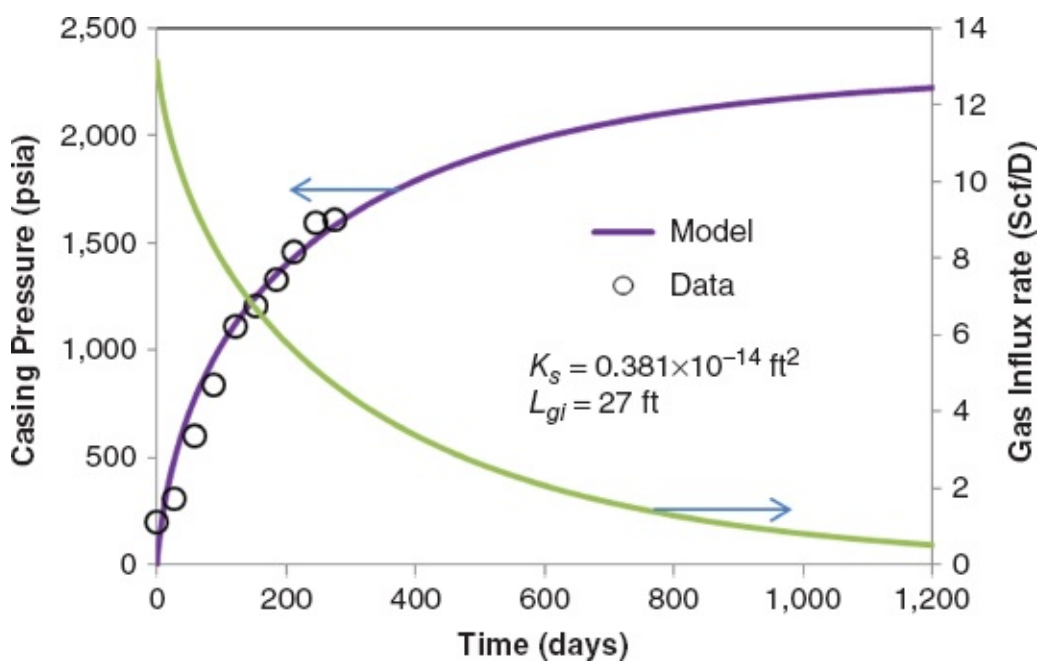

Fig. 10.8—Modeling SCP data and future prediction for Well 23.

	Well 23	Well 24
T_{wb}, °R	575	552
T, °R	630	584
T_{wh}, °R	520	520
T_{sc}, °R	491.7	491.7
D_1, ft	0.829	0.829
D_2, ft	0.583	0.635
L_c, ft	1,821	3,217
Initial L_m, ft	8,273	6,433
ρ, lbm/gal	10	16
μ_g, cp	0.02	0.015
P_{sc}, psia	14.7	14.7
Z-factor	0.86	0.92

Table 10.2—Input parameters for Wells 23 and 24.

	Well 23			Well 24		
Model Parameters	Xu (2002)	Huerta et al.(2009)	This Study	Xu (2002)	Huerta et al. (2009)	This Study
f, psia	6,600	6515	6,600	6,362	6,330	6,362
Initial L_g, ft	27	–	27	0	–	0
C_m, psi^{-1}	4.0E-6	–	4.0E-6	1.5E-6	–	1.5E-6
k, md	**0.001**	**0.403**	**0.358**	**0.003**	**0.94**	**1.496**
k_s, ft^2			**0.38×10^{-14}**			**1.59×10^{-14}**

Table 10.3—Study results for Wells 23 and 24.

Fig. 10.9 presents the results of Well 24, in which near-stabilization of pressure occurs in 33 days, as signified by the low gas influx rate. This example is also taken from Xu (2002).

Besides the seepage factor, given the uncertainty in reservoir pressure and the initial gas column height, a systematic study can illuminate the range of solutions obtained with multivariate regression analyses. We examined three cases by increasing the number of unknown variables in the parameter optimization process: (1) seepage factor (k_s); (2) seepage factor and the initial gas column length (L_{gi}); and (3) three variables, k_s, L_{gi}, and formation pressure (p_f). As **Table 10.4** and **Fig. 10.10** illustrate, increasing the number of optimized unknowns did not change the solution

outcome markedly for Well 24. This finding was reassuring, given the uncertainty in any field data.

Let us explore the notion of partial history matching, followed by future projection to minimize the test duration. **Fig. 10.11a** examines the sensitivity of k_s estimated from the limited data. We used the casinghead pressure vs. time data from Well 24 and estimated a series of k_s values using the first n_d number of data, where n_d = 3, 5, 7, and so on. Fig. 10.11b shows the error in various estimations assuming that the value obtained using all data is the best solution. This figure shows counterintuitive results; prediction accuracy does not increase with the number of data points used to obtain k_s (except for n_d = 3). This example illustrates that performing a pressure test for a week is comparable to performing such a test over a few months.

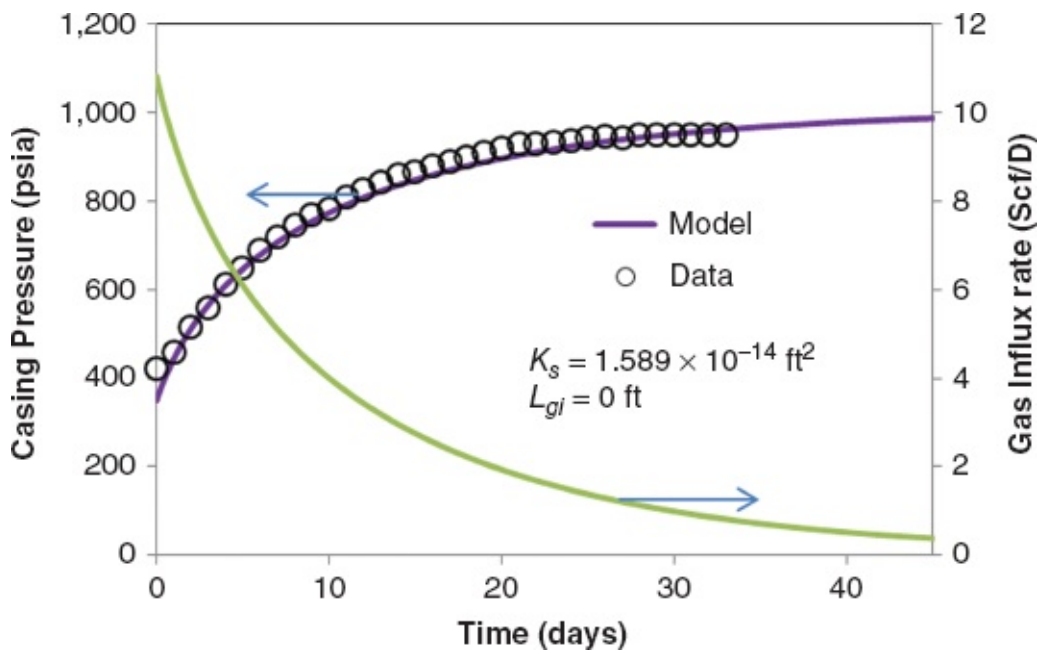

Fig. 10.9—Modeling SCP data and future prediction for Well 24.

Case Number	k (md)	k_s (ft^2)	p_f (psia)	L_{gi} (ft)	Mean Square Error
1	1.490	1.583E-14	6,362	0	2.620
2	1.867	1.983E-14	6,332	0	1.675
3	2.579	2.740E-14	6,325	3	1.515

Table 10.4—Multivariate regression analysis.

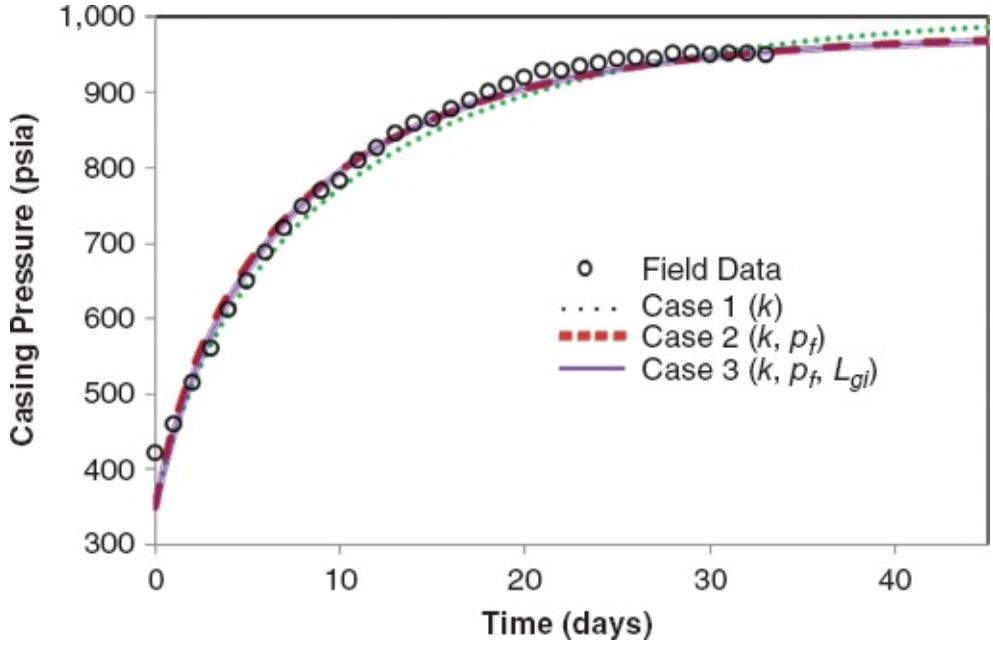

Fig. 10.10—SCP modeling with parameters derived from multivariate regression, Well 24.

Analysis of Gas Wells. In principle, the same SCP model should apply to any well, at least as a first approximation of the physical facts. The well integrity issue becomes a requirement, particularly where the environmental stakes are high, such as in a CO_2 sequestration project. Containment of the injected fluid within a given geologic horizon is of paramount importance during sequestration. For example, Aschehoug and Kabir (2013) have shown that fault breach occurred during CO_2 sequestration into a saline aquifer. Supercritical CO_2 lowering the formation fracture gradient and encountering the unsuspected geologic confinement were cited as possible reasons for the fault breach.

Given the reservoir and/or well integrity issue, Huerta et al. (2009) and Tao et al. (2014) have used the SCP model in potential observation wells in gas reservoirs. The following three figures are examples from those studies. **Fig. 10.12** is taken from Buildup 4 of Case Study 1, as reported by Huerta et al. (2009). A high-quality match of the data with our model estimates is evident. **Fig. 10.13** shows the results of Case Study 2 (by the same authors) and provides some clues about continuous gas influx over 200 days.

Fig. 10.14, taken from Tao et al. (2014), shows that the initial gas rate is two orders of magnitude lower than those of all the examples discussed thus far. This low rate is because of the seepage permeability of 0.01 md, which compares favorably with that of 0.012 md, reported earlier by Tao et al. (2014). The gas rate estimation appears to provide significant insights into the leakage rate, which may, in turn, be used to establish regulatory guidelines that are anchored in realistic data.

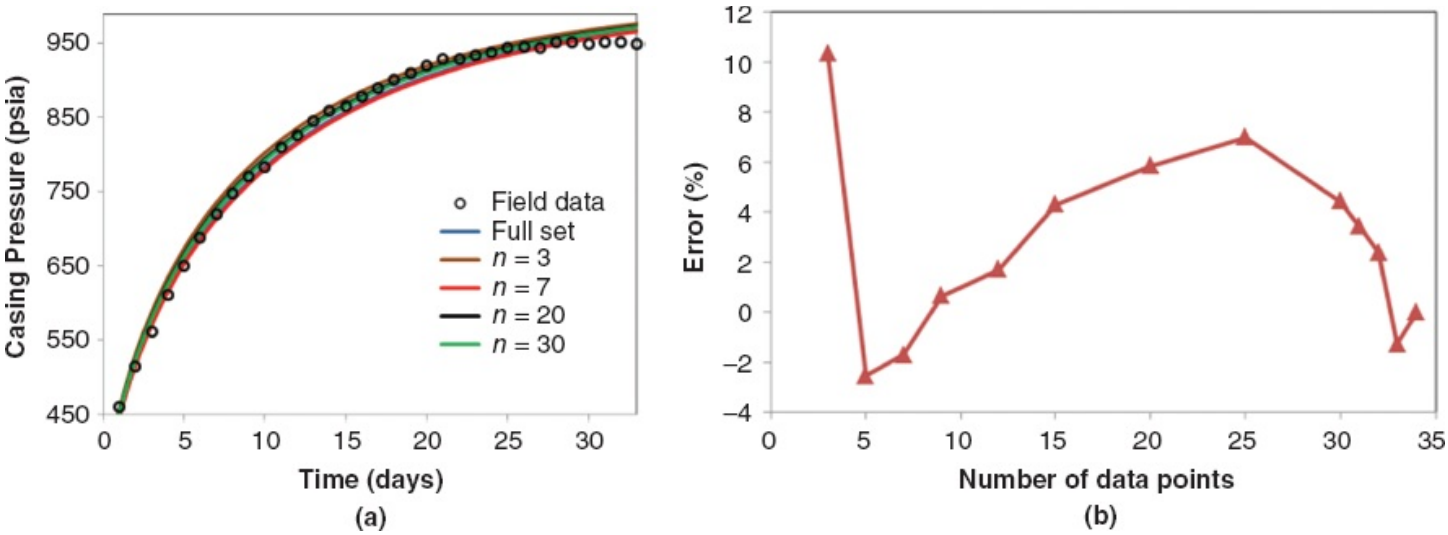

Fig. 10.11—Pressure profiles from estimated *k* values with limited data (a) and percent error in *k* values estimated from limited data (b), Well 24.

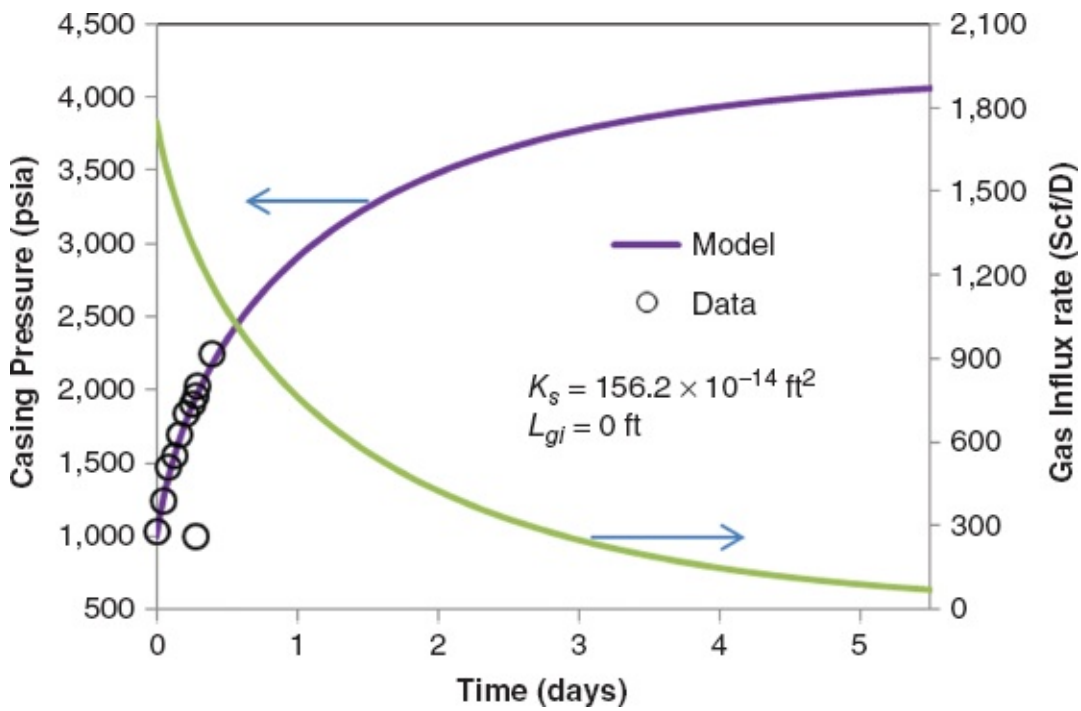

Fig. 10.12—Huetal et al. (2009) with: Huerta, N.J., Checkai, D.A., and Bryant, S.L. (2009).

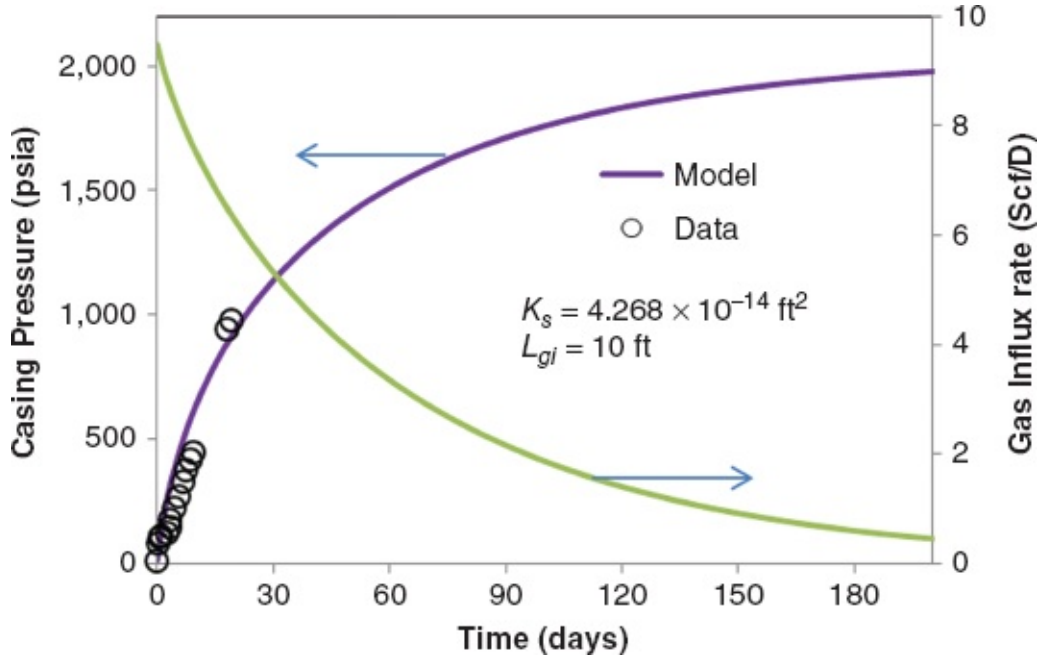

Fig. 10.13—SCP modeling of field data, Case Study 2, Huerta et al. (2009).

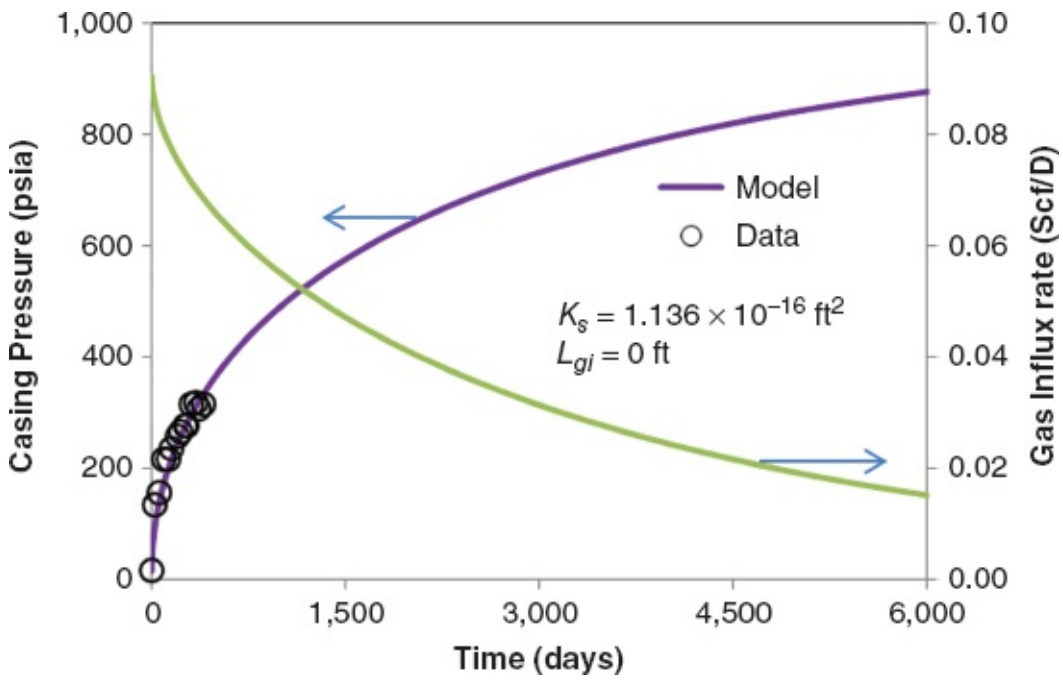

Fig. 10.14—SCP modeling of field data, Tao et al. (2010) data.

	Case 1		Case 2		Case from Tao et al. (2014)	
Model Parameters	Huerta et al. (2009)	This Study	Huerta et al. (2009)	This Study	Tao et al. (2014)	This Study
p_f, psia	12,041	12,041	3,200.7	3,200.7	1,860	1,860
Initial L_{gi}, ft	0	0	10	10	0	0
c_m, psi^{-1}	3.0E-6	3.0E-6	6.5E-6	6.5E-6	4.0E-6	4.0E-6
k, md	**140**	**147.08**	**4.0**	**4.01**	**0.012**	**0.0114**

k_S, ft^2	**156.21E-14**	**4.268E-14**	**1.136E-16**

Table 10.5—Study results of gas wells from Huerta et al. (2009) and Tao et al. (2014).

The SCP profiles obtained with the proposed solution are in good agreement with field data. **Table 10.5** displays estimated parameters obtained with the analytical model and those reported by Huerta et al. (2009) and Tao et al. (2014). In particular, permeability values compare quite favorably.

10.3.4 Lessons Learned. This section presents an analytical solution to the Xu (2002) numerical formulation for studying SCP. There are several advantages of an analytical solution presented here. First, the time to reach a certain pressure can be estimated rapidly without any information from the previous timestep. Second, this problem can be solved by a single-step calculation rather than requiring an iterative approach. Third, the gas rate estimation quantifies the leakage rate or the cumulative production over a certain time period. The fluid properties are evaluated on the basis of a constant geothermal gradient for the annular fluid. However, improved heat-transfer modeling can be performed for a known system for which tubular flow rates and relevant information are known.

The analytical solution presented here offers significant insights into the leakage rate, which may be used to establish regulatory guidelines. The model's ease of use and its ability to estimate the seepage constant and stabilized casing pressure at each timestep allow shortening of the SCP test duration, thereby reducing the test burden. In this context, we also found that the analytical approach corroborated the results obtained by others in four out of five examples.

10.4 Integrity Testing of Gas Lift Valves

10.4.1 Introduction. The use of gas lift technology dates back to the 1940s. Recently, Decker (2008) provided some insights into modern design and use of injection-pressure-operated gas lift valves. Accurate models are also available for calculating critical flow rate across Venturi valves, especially for high-pressure gas lift systems, as proposed by Almeida (2011). Given the widespread use of gas lift as an artificial lift mechanism, integrity of gas lift valves (GLVs) is of great interest to the industry. Accordingly, some operators (Xu et al. 2012; Carlsen et al. 2010) have taken proactive measures to ensure GLV safety beyond those suggested by the API recommended practices (API 1999, 2008, 2010). To improve well safety, Gilbertson et al. (2013) offered a passive, thermally actuated safety valve for offshore wells.

The use of artificial-intelligence agents, such as the one described by Stephenson et al. (2010) to diagnose the lift system, has significantly helped manage data gathering and interpretation, as well as subsequent actions. Models have also been

offered to design and analyze flow instability; the studies of Poblano et al. (2005), Blick et al. (1988), and Asheim (1988) are cases in point. More recently, Garcia (2013), Eikrem et al. (2008), and others have offered stability analysis when cyclic variations in pressure and production rates occur, resulting in significant disturbances to the downstream processing facility.

Inherent risks of gas lift operations, involving a large inventory of gas and high operating pressures, dictate that detection and quantification of leaks in GLVs are imperative. Prevention of uncontrolled release of hydrocarbons forms the backbone of barrier philosophy in modern well construction and operation. Quoting Norwegian guidelines, Carlsen et al. (2010) stated that “well barriers are envelopes of one or several dependent well barrier elements preventing fluids or gases from flowing unintentionally from the formation into another formation or to surface.” They cited several reasons for GLV failures, including flow cutting in sealing seats because of well unloading of completion fluids, valve-spring fatigue failure, damage during installation, erosion during multiphase or wet-gas injection, and damage to the valve seat from chattering in a low-pressure-drop situation.

Gilbertson et al. (2013) developed a thermally actuated GLV for offshore wells to add redundancy to well systems and significantly increase well safety. This valve avoids the use of either active control or passive pressure-induced actuation, a component of current valve systems. By modeling heat transfer and laboratory prototype construction, they showed that this safety valve is applicable to wells with at least 13°C temperature difference across the valve.

To assess the well integrity risk, Dethlefs and Chastain (2012) reported formulation of a qualitative model. Their modeling approach of risk assessment entails comparison between well barrier failure-mode scenarios and qualitatively assesses well barrier failure risk for every segment of a well. This risk assessment approach may be applied to a given well, a group of similar wells, or an entire well portfolio in a field. Citing long-standing operational experiences in Prudhoe Bay, Alaska, Julian et al. (2014) suggested that the barrier-qualified GLVs now meet performance metrics.

Properly operating GLVs allow annular gas to flow into the tubing and prevent any backflow. However, erosion, corrosion, and other effects may cause a GLV to leak, thereby posing a serious safety issue. Suspected leaking GLVs are often retrieved for inspection to address safety issues. Proactive testing is a way to minimize costly interventions. Accordingly, nonintrusive test procedures have emerged. For example, tests entailing monitoring of annular pressure-transient response can establish a GLV’s integrity while avoiding valve retrieval for inspection.

This section presents a forward model that assists GLV test design. The model recommends drawing down the annular gas to develop a positive pressure differential to allow fluid flow from the tubing into the annulus through the suspected GLV. This drawdown is followed by a pressure-buildup test. These pressure-transient tests allow determining the integrity and extent of GLV damage. The forward model also allows estimating the time needed for each segment of the transient test sequence, thereby helping to schedule such tests at a certain operational frequency.

10.4.2 Modeling Approach for Gas Lift Valve Testing. The basis of the proposed test methodology is depicted in **Fig. 10.15.** As Fig. 10.15a shows, even if the GLV has a leak, liquid from the tubing will not flow into the annulus if there is no pressure differential. If a positive pressure differential is created across a faulty GLV by venting some of the annular gas, liquid from tubing will flow into the annulus, as Fig. 10.15b indicates. If the valve at the casinghead is closed after a period of venting, liquid coming in from the tubing will then compress the gas in the annulus, resulting in pressure increase with shut-in time; Figs. 10.15c and 10.15d illustrate this point. The rate of casing pressure rise can then be analyzed to obtain a quantitative measure of GLV damage.

This methodology recommends venting through an appropriate choke such that sonic velocity occurs, allowing venting rate to be known (Fig. 10.15b). To avoid a casing integrity issue arising from excessive pressure differential, venting is terminated when the casinghead pressure reaches a certain level, p_{risk} (Fig. 10.15c). Obviously, if the initial annular pressure was not high enough, venting would cease when casinghead pressure nears atmospheric pressure (or venting line pressure), as shown in Fig. 10.15d.

The test methodology and model formulation are described in the subsequent subsections. However, to provide a perspective, we present how the gathered data can be used to determine the extent of GLV damage if any. When a GLV is damaged and fluid flows through it from the tubing into the annulus, we may visualize the flow process as one through an orifice, with ε representing the fraction of the total open cross-sectional area of the valve. In this context, ε may be viewed as a damage coefficient, meaning that a value of ε = 0% represents a fault-free GLV, whereas ε = 100% implies a wide-open GLV check valve.

Fig. 10.16 shows pressure or liquid level (dependent variable) rise in the annulus as a function of time for various valve damage coefficient values, ε. The solid lines represent simulated values of the dependent variable for various degrees of GLV damage. The open circles show data from an actual test. Fig. 10.16, therefore, indicates that this GLV is faulty, and approximately 35% of the check valve area is “open.”

The test methodology consists of opening the casinghead valve and drawing down the annular gas, followed by a pressure-buildup test, conducted by closing the casinghead valve. The methodology relies on calculating the mass of a known volume of gas in the annulus using the gas law and gas pressure and temperature.

For a buildup test when gas mass does not change with time, rate of change of casinghead pressure is used to calculate the rate of change in gas volume, which is equal to the liquid ingress rate through the GLV. For a drawdown test, the rate at which gas is escaping the annulus needs to be known to set up a proper material balance to calculate liquid ingress rate into the annulus. We recommend the use of a flow-prover at the casinghead so that critical velocity is attained for the exiting gas, allowing estimation of its rate. Note that the inside-outside-pressure ratio for the annular gas is so high that attaining critical gas velocity through any choke will easily

be attained.

The pressure differential across the GLV affects the flow from the tubing into the annulus. Because any gas in the tubing fluid moves up quickly to the wellhead after well shut-in, we assume that only liquid flows from the tubing into the annulus through a faulty GLV. In addition, we note that given the compressible wellbore fluid, after the tubinghead is closed, fluid will still flow (afterflow) from the reservoir into the well. The afterflow will either raise the tubinghead pressure or flow across the GLV into the annulus. If the tubinghead pressure remains essentially constant, all the fluid afterflow from the reservoir enters the annulus through the faulty GLV.

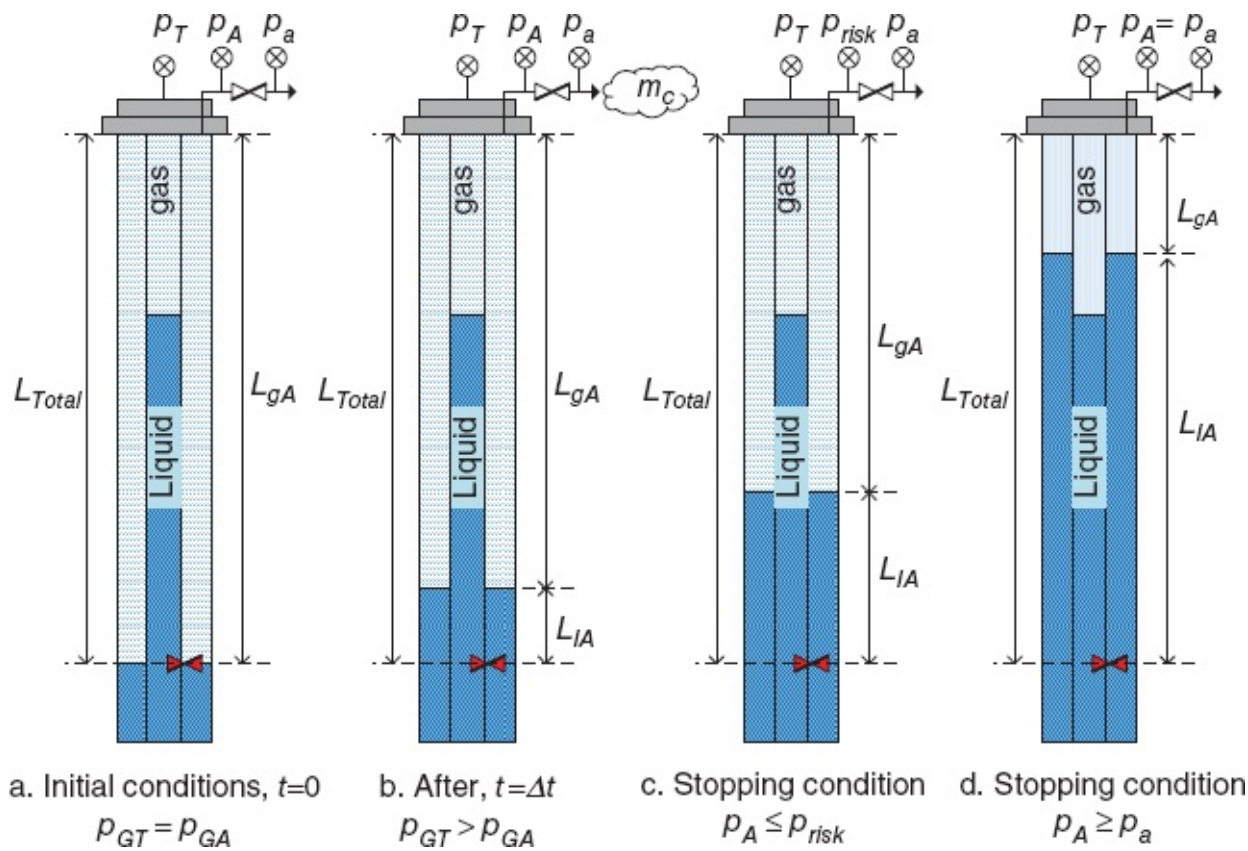

Fig. 10.15—Changes in liquid level in the system because of flow through the GLV during drawdown, followed by a buildup test.

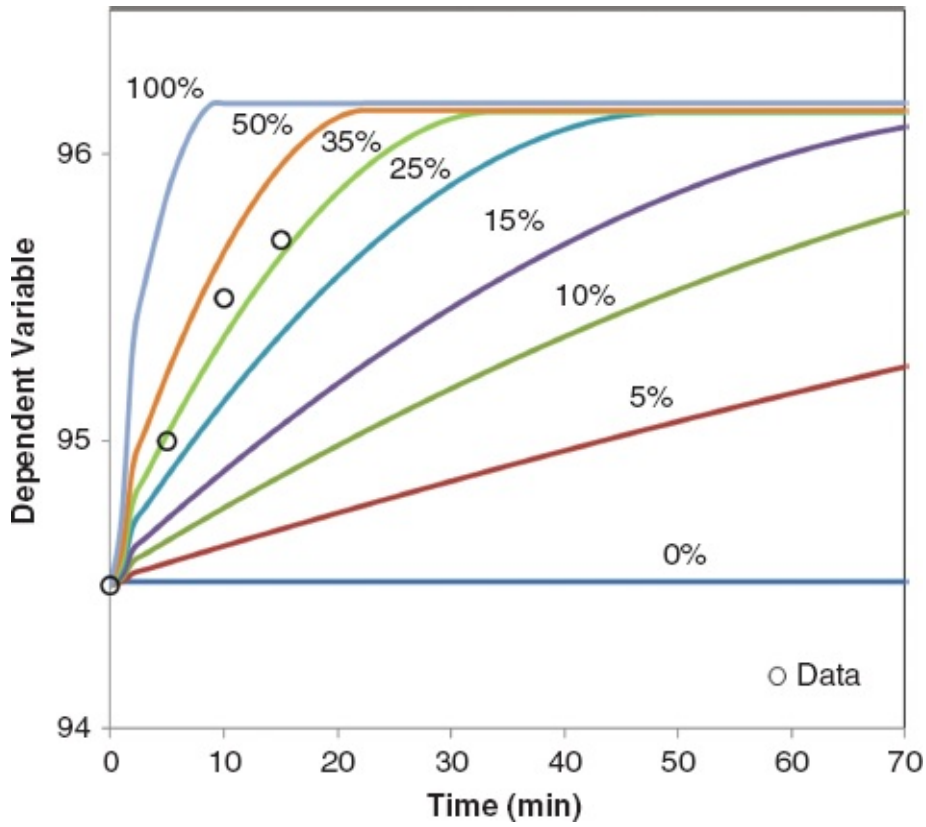

Fig. 10.16—Profiles of dependent variable (pressure or liquid level) for several ε values.

Note that the approach just described can be used in conjunction with the acoustic well sounding (AWS) data acquisition to provide more confidence in the estimates. The steps for the test procedure are enumerated below:

1. Begin the test by turning off gas injection and closing the tubinghead valve. Allow some time for the gas bubbles in the tubing to escape before shutting in the valve. We assume that the pressure in the annulus and that in the tubing at GLV depth will essentially be the same.
2. Initiate the drawdown test by opening the casinghead valve and letting gas flow through a choke (of known size) so that the critical sonic velocity is attained, thereby allowing estimation of the exiting gas flow rate.
3. Terminate the drawdown test when the annular pressure reaches 60% (p_{risk}) of its original value to maintain a safe operating pressure. The shortest possible time to reach p_{risk} is calculated using the known gas rate and assuming that no liquid inflow from the tubing occurs into the annulus; that is, GLV damage coefficient is assumed to be zero. This step ensures sufficient pressure differential across the GLV for the buildup test that follows.
4. Begin the buildup test by monitoring the annular wellhead pressure after closing the casinghead valve (Step 3). Perform pertinent gas compression calculations and liquid influx estimation.
5. Compare the pressure profile from the drawdown and/or buildup test with

theoretical pressure isopleths, described later. The match obtained with the test data and theoretical pressure isopleths allows estimation of the damage coefficient, ε, which is a reflection of the extent of GLV damage.

10.4.3 Model Formulation. The test begins when pressure in the tubing and pressure in the annulus across the GLV are equal. If there is a leak in the GLV, the liquid originally in the tubing, will enter into the annulus upon depletion of the annular gas because of the pressure differential. Our experience with a number of such tests indicates that the wellhead tubing pressure p_T remains practically constant even when liquid moves from the annulus into the tubing. This response is not surprising because the compressible tubular fluid column masks any subtle perturbation created downhole. The operating envelope of the tubinghead pressure during the complete test period (drawdown, buildup, and AWS measurements) remained within 415 ± 15 psi for Well 1; 418 ± 15 psi for Well 2; and 1,474 ± 30 psi for Well 3; varying only around 2% from the average value.

We have observed that if a leak exists, the liquid column above the GLV depth in the tubing remains unchanged, implying that the liquid entering the annulus originates from the formation. Therefore, the tubing pressure at GLV depth can be assumed constant. We also assume that the flow of gas from the annulus through a choke into a flowline will occur at the critical rate. Critical gas flow conditions exist when the inlet-outlet-pressure ratio is approximately 1.7, which is likely to be satisfied during these tests. Our model is based on mass and volume balance of the annular gas and liquid, as well as estimation of hydrostatic pressures exerted by the gas and liquid columns.

***Mass Balance*.** The mass conservation for the liquid and the gas in the system are represented by Eqs. 10.14 and 10.15 below.

Mass of liquid in the annulus:

$$m_{lA} = \rho_l L_{lAo} A_A + \int \dot{m}_l \, \mathrm{d}t = \rho_l L_{lA} A_A \qquad (10.14)$$

Mass of gas in the annulus:

$$m_{gA} = m_{gAo} - \int \dot{m}_g \mathrm{d}t \qquad (10.15)$$

In Eqs 10.14 and 10.15, m represents mass, $\dot{m}$ is mass rate, L represents length above GLV. The subscripts A, l, g, and o in Eqs. 10.14 and 10.15 represent annulus, liquid, gas, and values at initial conditions, respectively.

The initial mass of gas in the annulus is calculated using the gas law. However, because the pressure in the annulus varies significantly over the well depth, we discretize the annulus into n_c sections and calculate the mass and pressure in each section iteratively. Eq. 10.15 is therefore rewritten in a form that sums the mass of gas in each cell as

$$m_{gA} = \sum_{i=0}^{n_c} \frac{29\gamma_g \left(L_{gA,i+1} - L_{gA,i}\right) A_A \left(p_{gA,i} + p_{gA,i+1}\right)}{2\bar{Z}_i R\bar{T}_i} - \int \dot{m}_g \mathrm{d}t \quad (10.16)$$

Eqs. 10.14 and 10.16 represent the mass balance of each component of the system and are valid at any given time. The overbar on Z and T in Eq. 10.16 represents cell average values. To obtain the initial gas mass in the annulus, we use Eq. 10.16 by treating the entire length above the GLV as being gas. At any other time, because of liquid ingress from the tubing, the lengths of the liquid and gas columns add up to the same total length, L_T. Thus,

$$L_T = L_{gA} + L_{lA} \quad (10.17)$$

Hydrostatic Pressure. The density of a gas can be related to its pressure and temperature by $\boldsymbol{\rho} = (pM)/(ZRT)$. Therefore, the hydrostatic pressure, dp, of a gas column of vertical height dz is given by the following equation:

$$\mathrm{d}p = \rho \mathrm{d}z = \frac{pM}{ZRT} \mathrm{d}z, \quad (10.18)$$

where $M = 29\gamma_g$ is the molecular weight of the gas, and γ_g is the specific gravity of gas with respect to air. Note that dz is the vertical depth that can be related to measured depth L, as $\mathrm{d}z = \mathrm{d}L\ (\cos\theta)$, where θ is the deviation angle from the vertical. Eq. 10.18 may easily be integrated over a short depth using average temperature and Z-factor for the depth, yielding

$$p_2 = p_1 \exp\left[\frac{29\gamma_g \left(z_2 - z_1\right)}{R\bar{Z}\bar{T}}\right] \quad (10.19)$$

We compute the annular gas pressure from the known pressure at the casinghead and march downward in n steps to the gas/liquid interface. Therefore, the gas pressure at this position, p_{GA}, in terms of the hydrostatic pressure of the liquid and gas columns is given by

$$p_{GA} = \rho_L z_{lA} g + \sum_{i=0}^{n} p_{gA,i} \exp\left[\frac{29 g \gamma_g \left(z_{gA,i+1} - z_{gA,i}\right)}{\bar{Z}_i R\bar{T}_i}\right] \quad (10.20)$$

We use the same iterative solutions approach to estimate the mass of gas in the annulus, m_{gA}, at each timestep. However, there is an added complexity for computations for $t > 0$ because the length of the gas column changes with time as liquid enters the annulus from the tubing. Because p_{GA} depends on liquid level above it and on the liquid influx rate, which itself depends on p_{GA}, the computation becomes iterative. We need to solve for mass of gas remaining in the annulus, represented by Eq. 10.21, simultaneously with Eq. 10.20 for annular pressure at the GLV to obtain

p_{GA}, z_{LA}, and m_{GA}.

$$m_{GA} = \sum_{i=0}^{n_c} \frac{29\gamma_g \left(L_{gA,i+1} - L_{gA,i}\right) A_A \left(p_{gA,i} + p_{gA,i+1}\right)}{2\bar{Z}_i R\bar{T}_i} \quad (10.21)$$

Computational Scheme. One of the objectives of this model is to allow for estimating the time t_{60} needed for the annular pressure to go down to 60% of its initial value p_{risk} through a known (critical) rate of gas drawdown. The idea is to allow annular pressure to decrease to a minimum allowable annular wellhead pressure. If annular wellhead pressure decreases beyond p_{risk}, the risk of damaging the casing becomes a possibility. The time at which p_{risk} is reached will vary according to the damage coefficient of the GLV. To obtain a conservative estimate of t_{60}, we assume that the damage coefficient is zero; that is, the GLV is intact ($\varepsilon = 0$). The liquid flow rate $\dot{m}_l$ through the GLV is calculated using the following general expression for flow through orifices:

$$\dot{m}_l = \varepsilon A \sqrt{2\rho_l \left(p_{GT} - p_{GA}\right)} \quad (10.22)$$

Because pressure is a continuous variable and the methodology proposed discretizes this variable, the annular pressure at the GLV depth should use an average pressure between the previous timestep and the current one—that is, $(p_{GA,i} + p_{GA,i-1})/2$.

The magnitude of pressures at the casinghead is much higher than the outside pressure where gas is discharged, thereby making the gas flow from the casinghead critical. Therefore, we calculate the casinghead gas flow rate $\dot{m}_g$ by using the following critical flow equation:

$$\dot{m}_g = C_o A \sqrt{\rho_g p_A \left(\frac{2}{\lambda+1}\right)^{\frac{\lambda+1}{\lambda-1}}} \quad (10.23)$$

In Eq. 10.23, C_o is the valve's orifice discharge coefficient; A is its cross-sectional area; and ρ_g, λ, and p_A are the gas density, gas specific heat ratio, and gas pressure at the casinghead. All these properties are known from the top-down calculation and should be used at each timestep.

Next, we discuss the computational scheme used. At initial conditions, pressure equilibrium exists and there is no flow through the GLV. At these conditions the pressure at GLV depth in both annulus and tubing can be established. The procedure to calculate the mass and pressure of the gas column is as follows.

1. We assume that initially there is no liquid above the GLV in the annulus; thus, the length of the gas column is the same as the depth of the GLV, $L_{gA} = L_T$. Because the casinghead initial pressure p_A is known, we estimate the pressure at GLV depth p_{GA} and the total mass of annular gas m_{gA} using Eqs.

10.20 and 10.21.

2. With the known annular initial mass, we proceed to estimate these quantities at later times, allowing for gas bleedoff. The reduction in the amount of annular gas, with consequent pressure reduction, allows liquid to flow from the tubing into the annulus through a faulty GLV. This and several important stages of the test are sketched in **Figs.** 10.15 and **10.17** for drawdown and buildup tests, respectively.

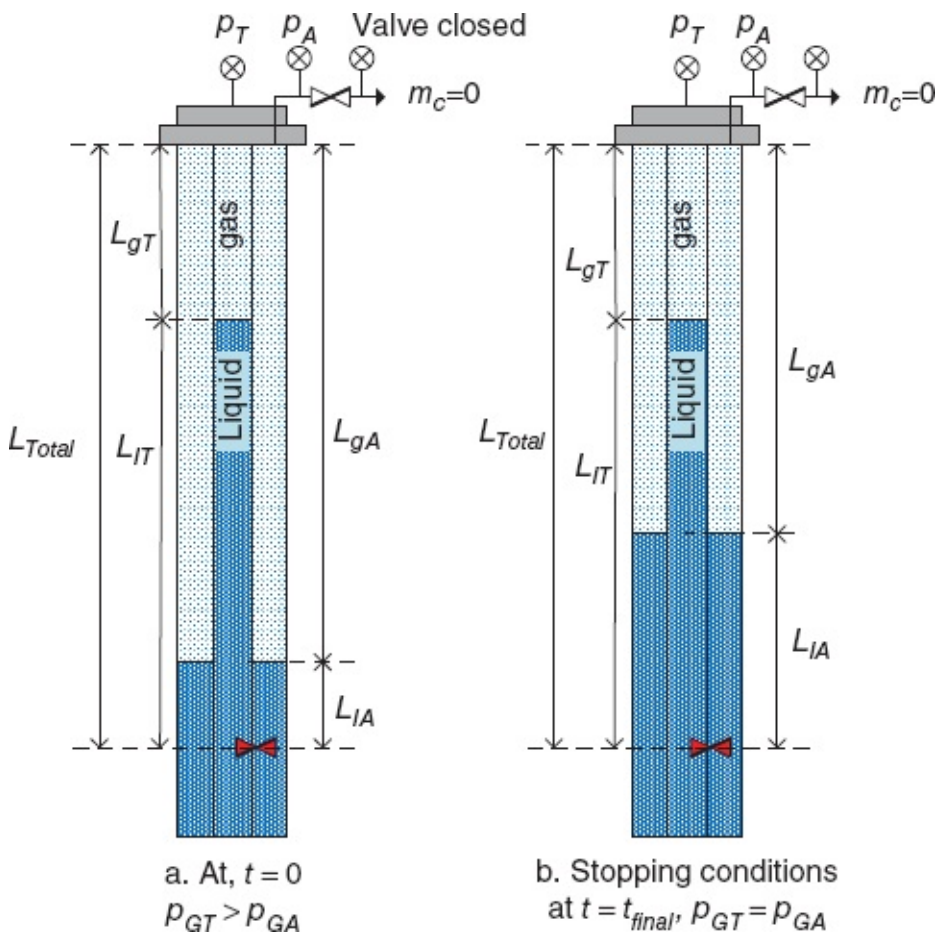

Fig. 10.17—Changes occurring in the system because of flow through GLV during the buildup test.

The damage coefficient can range from $0 \geq \varepsilon \geq \varepsilon_{max}$. We used $\varepsilon = 0$ to calculate t_{60}. For a damaged GLV when liquid coming in from the tubing will support the annulus pressure, t_{60} calculated this way will lead to lesser drawdown, leading to a safer test environment.

The procedure to estimate time needed for 40% annulus pressure reduction is as follows.

1. Estimate the mass of gas in the annulus after a given timestep Δt for a $\varepsilon = 0$.
2. For the next timestep, use an initial p_A value, smaller than in the previous timestep. Verify that p_A satisfies gas properties for mass $m_{gA} = pV/(29\gamma_g RT)$ and length of gas chamber L_{gA}.

3. Repeat Steps 1 and 2 until convergence is achieved.
4. Estimate new p_{GA} using Eq. 10.20 along with $z_{\text{Total}} = z_{gA} + z_A$ and use Eq. 10.21 to estimate the amount of mass of liquid that entered the annular section.
5. Use density of the oil (ρ_L) and geometry of the annulus to estimate the height occupied by liquid (L_{lA} and z_{lA}).
6. Calculate the change in gas and liquid columns with Eqs. 10.16 and 10.17, and use as input for the next timestep.
7. Repeat Steps 2 through 6 until $t = t_{\text{final}}$, $p_A = p_{\text{risk}}$ or $p_A = 0$ psig.

The procedure for a buildup test is same as that for a drawdown test, except that the gas mass, m_{gA}, remains constant during the entire test.

10.4.4 Model Validation. We compared our simulated pressure vs. time profiles from a buildup test with those performed in three gas lift wells using AWS data. The data acquired during the drawdown tests could not be used to validate the model because the bleed-off rate for gas discharge remained unmeasured. The gas discharge rate is a required parameter in our model and is the reason for recommending a flowmeter at the casinghead for drawdown tests.

We used the liquid level measured by AWS and annular pressure data at the beginning of the buildup test as initial conditions; the proposed model was used thereafter to track all changes. The initial conditions of Wells 1, 2, and 3 are given in **Table 10.6.**

We simulated pressure buildup over a time for several GLV damage coefficients and compared the estimated values with the pressure reported from the field tests. **Figs. 10.18 and 10.19** show the pressure contours for these buildup tests. In these figures, open circles represent data and solid lines represent annular pressure calculated using various ε values. For all these wells, the GLV aperture was 0.5-in. inner diameter.

Fig. 10.18a shows that the pressure buildup for Well 1 is similar to the profile resulting from an orifice of 35% of the cross-sectional area of the GLV. A 35% damaged area would be the equivalent to having a completely open valve with a diameter of 0.3 in. or 7.25 mm. Fig. 10.18b represents the pressure response for Well 2. The data indicated a damage of 60% for the GLV, equivalent to having an orifice of 0.39 in., almost 80% of the original diameter. The severity of the calculated leak matches the field test using AWS for this well.

	p_A, psi	Liquid Level, ft	p_{GT}, psi
Well 1	1,370.6	6,747.7	2,371.4
Well 2	1,472.1	6,332.0	2,644.0
Well 3	1,083.4	5,143.4	2,339.5

Table 10.6—Initial well conditions for buildup tests.

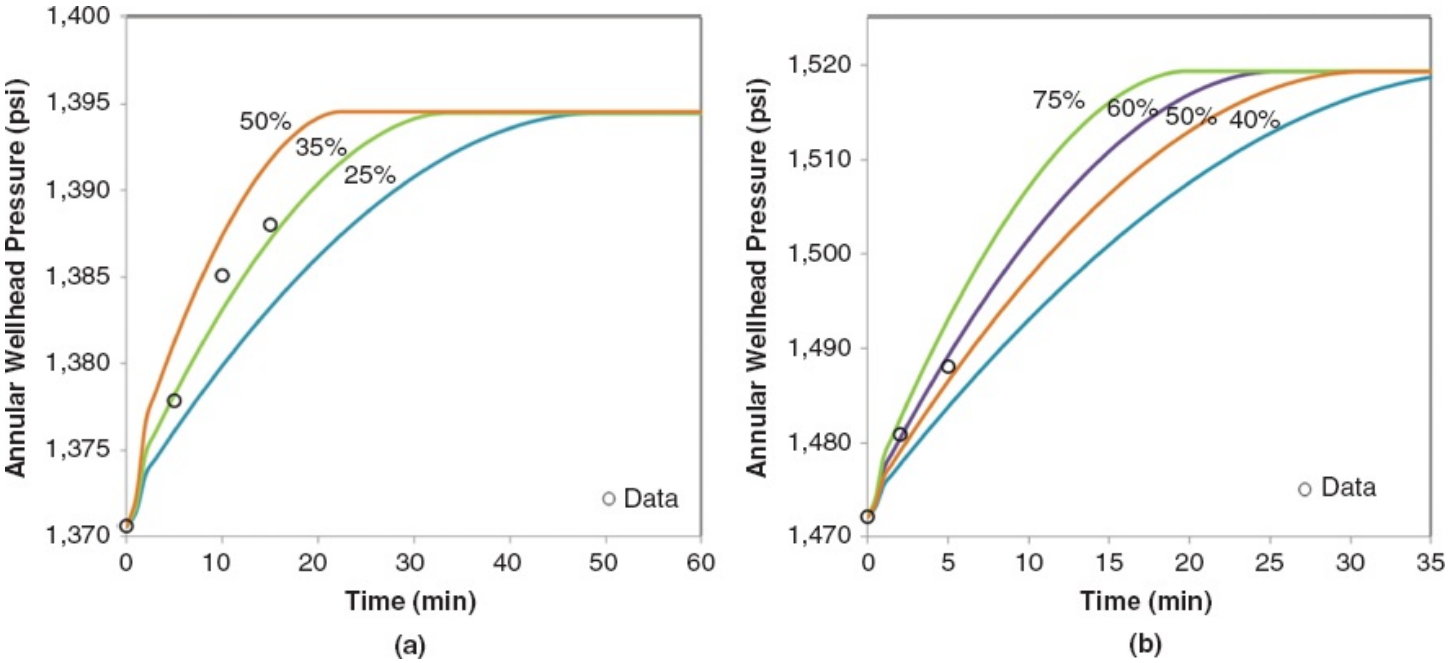

Fig. 10.18—Comparison of pressure profiles during buildup tests, Well 1 (a) and Well 2 (b).

Fig. 10.19 showing the test results for Well 3 suggests essentially no pressure increase for the entire duration of the test. The pressure rise of less than 1.5 psi (magnified by the small range of the *y*-axis) could have resulted from temperature or other operational fluctuations. This test is an indication that if a leak exists, it is minimal.

The flow rate estimations for all wells for various damage coefficient values are presented in **Table 10.7.** A comparison of the best fit, according to the pressure profile contours, is given in **Table 10.8.** In Table 10.7, the damage coefficients in bold correspond to the profile that had the best match to the reported pressure data.

Well 1 and Well 3 flow rate estimates match well with estimates reported in field measurements. This test helped us conclude that a leak exists in Well 1 with a 35% GLV damage. The difference in Well 3 test data and model estimation most likely corresponds to temperature fluctuations or noise in the equipment. We conclude that there is probably no leak in the GLV of this well. In contrast, Well 2 shows a severe leak that represents a damage flow area of 60%. The difference between our estimate and the measured data can be related to the fact that the test was terminated because of severe liquid leak after just 5 minutes of testing, allowing insufficient time for a proper test. On the basis of the performance of these tests, we recommend buildup times of at least 15 minutes.

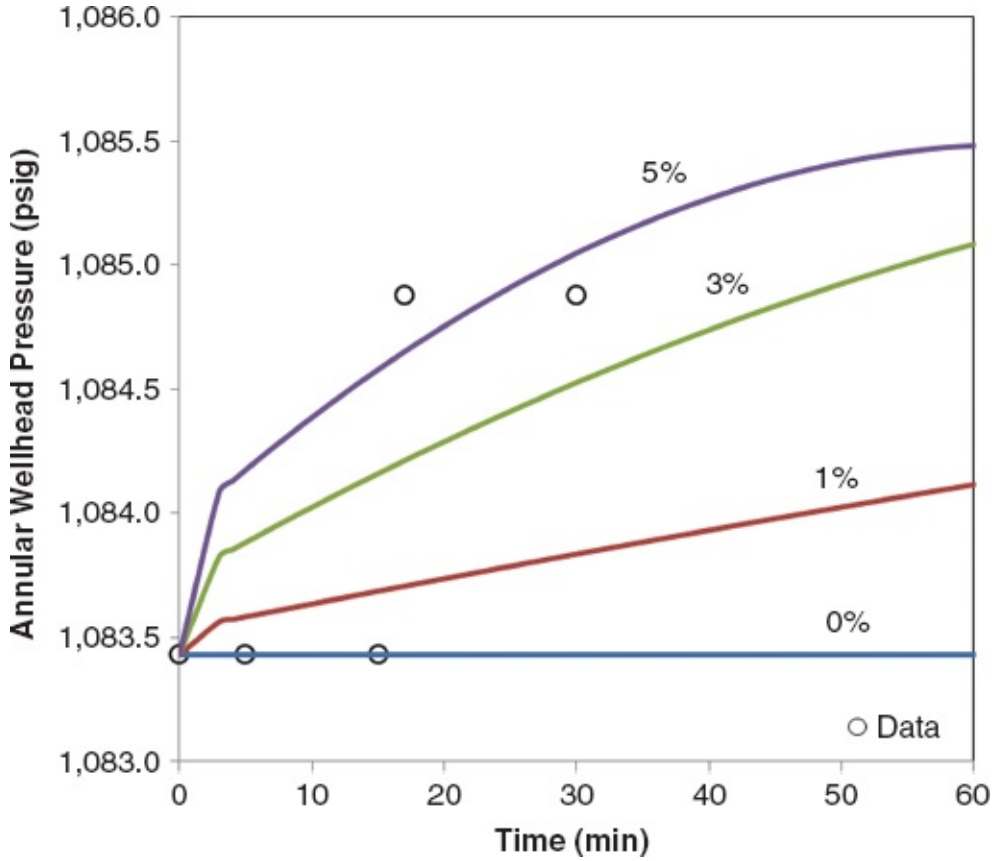

Fig. 10.19—Comparison of pressure profiles during buildup tests, Well 3.

WELL 1			WELL 2			WELL 3		
ε (%)	Test Duration (minutes)	Flow Rate (RB/D)	ε (%)	Test Duration (minutes)	Flow Rate (RB/D)	ε (%)	Test Duration (minutes)	Flow Rate (RB/D)
5	15	100	0	–	0.0	0	–	0.0
10	15	192	25	5	657	1	60	5
15	15	277	40	5	102	**3**	**60**	12
25	15	424	50	5	1,239	5	60	13
35	**15**	539	**60**	**5**	1,467	25	12	69
50	15	645	75	5	1,770	50	4	112
100	8	982	100	5	2,212	100	3	213

Table 10.7—Estimated flow rates for several GLV damage coefficients in three wells.

Well	Modeled Flow Rate (RB/D)	Field Estimated Flow Rate (RB/D)	Modeled ε (%)
1	539	540	35
2	1,467.3	1,218	60
3	0–12	<1	0–3

Table 10.8—Comparison of flow rates from this model and acoustic well sounding (AWS) measurement.

10.4.5 Case Studies. Two case studies are presented in this section. The first one shows the general application of the test procedure for a vertical well. In this case, we assume that only initial conditions are known and that there are no data to compare with the simulated values. This case study shows how the simulated pressure and liquidlevel profiles can be examined to assess actual data.

The second case is based on Well 1, for which we have the most complete set of data. Data from the buildup test from this well have already been used to validate the model. In this section, we show the full simulated pressure profiles for the drawdown and buildup tests, as well as choke size needed to achieve a pressure profile comparable to that shown in the reported data.

Case 1. Case Study 1 involves the application of the forward model in a vertical well that avoids the need for an AWS test. This vertical well contains the GLV at a depth of 8,740 ft. We assume that at the beginning of the drawdown test, the liquid level is just below the GLV. The mass of gas in the annulus is tracked during the test and serves as input for the subsequent buildup test, wherein flow rates are calculated to assess the GLV damage.

For this well, the initial wellhead annular pressure p_A is 1,727 psig, the initial liquid-level depth L_{lA} is 8,740 ft, and calculated pressure at GLV depth p_{gA} is 2,312 psig. These input parameters return an initial amount of annular gas of 493 Mscf. From that point forward, the gas is released through a 0.375-in.-inner-diameter choke with a discharge coefficient C_o = 0.61 under the critical flow condition. The drawdown continues until the pressure reaches 60% of the original p_A, which is approximately 1,037 psig in this case. **Table 10.9** shows important parameters for the well at the end of the drawdown test, which also serves as the initial condition for the buildup test.

Note that Table 10.9 shows simulation results for 144 minutes of drawdown for all ε values. This is the t_{60} (minimum allowable annular wellhead pressure) only for $\varepsilon = 0$ (a faultless GLV); for all other ε values, the annular pressure drop will be less than 60% after 144 minutes of drawdown, resulting in safer conduct of the GLV test. **Figs. 10.20 and 10.21** show the variation in pressures at the casinghead p_A and at the GLV depth p_{gA} with time. In each figure, the left side corresponds to the drawdown segment of the test and the right side corresponds to the buildup test.

During a GLV test, the casinghead pressure vs. time data for the drawdown and buildup tests can be plotted and compared, as in Fig. 10.21, against the simulated values. Matching field data will help in obtaining an ε value, which is a measure of valve damage. Alternatively, the *preliminary* results from a drawdown test can be used to design a better and shorter buildup test. Also, a drawdown test that indicates severe leak in a GLV can be used to terminate the test because valve retrieval and replacement has become obvious.

Case 2. Well 1 was selected for the Case 2 study because it has the most complete set of data. Unfortunately, the gas rate exiting the annulus was not measured nor was the choke size at the casinghead reported. However, the high

inside-outside-pressure ratio allows us to presume that critical flow was achieved. The simulated results are based on critical flow for a choke valve with a diameter such that the initial conditions for the buildup test at the end of the drawdown test were matched. The initial p_A was 1,748 psig, and the faulty GLV was located at a depth of 8,286 ft, giving a pressure in the annulus at GLV depth p_{GA} of approximately 2,400 psig. This result is similar to the estimated p_{GT} obtained with AWS data, as reported in Table 10.6. This outcome reaffirms that the initial hydrostatic equilibrium assumption is reasonable. The data reported in the test are shown in **Table 10.10.** We note that there are some discrepancies between the end time for drawdown and start time for buildup tests in the reported data.

ε (%)	Test Time (minutes)	p_A (psi)	p_{gA} (psi)	Final m_{ga} (Mscf)	Final Liquid Level (ft)
0	144	1,039	1,369	274	8,740
5	144	1,067	1,555	271	8,345
10	144	1,093	1,712	268	8,012
15	144	1,115	1,843	266	7,737
25	144	1,148	2,033	262	7,338
50	144	1,181	2,229	257	6,923
100	144	1,190	2,291	255	6,784

Table 10.9—Parameters at the end of Drawdown Test 1.

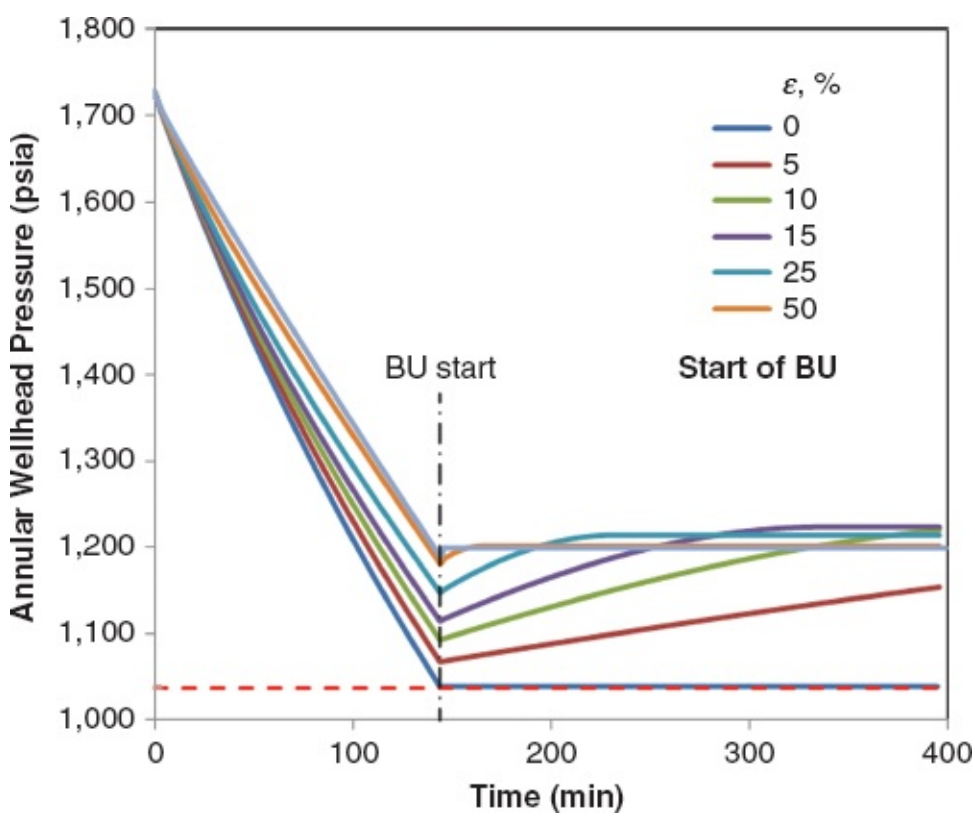

Fig. 10.20—Annular wellhead pressure profile for full GLV test. BU = buildup.

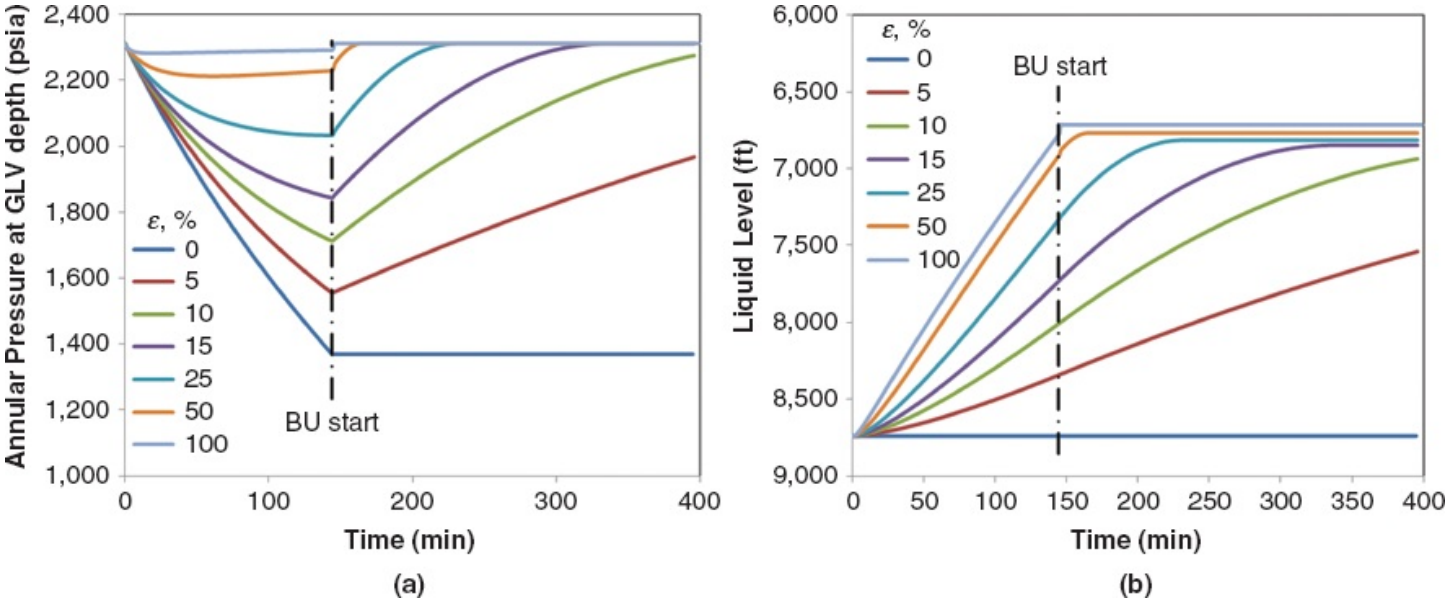

Fig. 10.21—Annular pressure profile at GLV depth (a) and liquid-level profile (b) for full GLV test.

	Processed Data			
	Relative Time (min)	p_T (psi)	p_A (psi)	Liquid Level (ft)
Drawdown period	0	407	1,748	–
	5	402	1,717	–
	15	413	1,700	–
	30	410	1,666	–
	60	407	1,629	–
	120	400	1,542	–
	180	405	1,460	–
	240	403	1,382	–
Buildup period	245	–	1,370	6,748
	250	407	1,378	–
	255	409	1,385	–
	260	409	1,388	–

Table 10.10—Data used for GLV leak estimation.

Using data in Table 10.10, we computed the casinghead pressure for the drawdown test followed by the buildup test. **Fig. 10.22** suggests good agreement between the model estimates (solid line) and data (open circles). **Fig. 10.23** shows the liquid-level profile when the two tests are performed successively. Fig. 10.23 plots the liquid-level estimation from pressure data using the methodology shown by Rocha-Valadez et al. (2016).

We think that critical flow conditions prevailed during the AWS test for Well 1; the model's ability to match data using the critical gas discharge rate instills confidence in

solution quality. As mentioned earlier, given the magnitude of the pressure ratio between the annulus and the flowline, critical flow is likely to occur. Finally, given specific parameters and variability between valves, such as the flow coefficient, we cannot be sure that a valve of 0.225-in. inner diameter was used. However, we have shown that given the pertinent information, the process of bleeding off a well followed by pressure-buildup test can be modeled and the damage to a gas lift valve evaluated.

10.4.6 Lessons Learned. On the basis of the field tests discussed in this section, improvements in test procedures can be made because the integrity test demands the creation of pressure differential across the GLV. Accordingly, a 10 to 40% pressure drawdown for the annulus may be required for the test to create sufficient perturbation. Let us elaborate on the test procedure and simplified analysis steps that can be enacted for efficiency that is less intrusive than those discussed here.

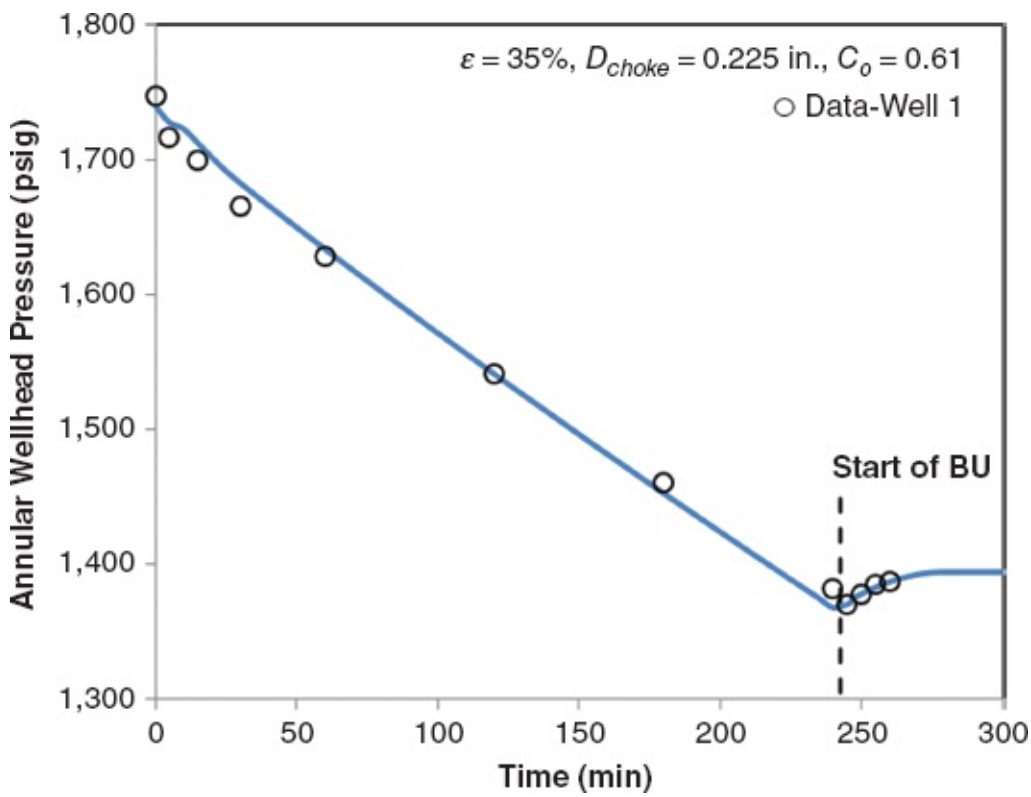

Fig. 10.22—Wellhead pressure trace generated with proposed model mimics field data, Well-1.

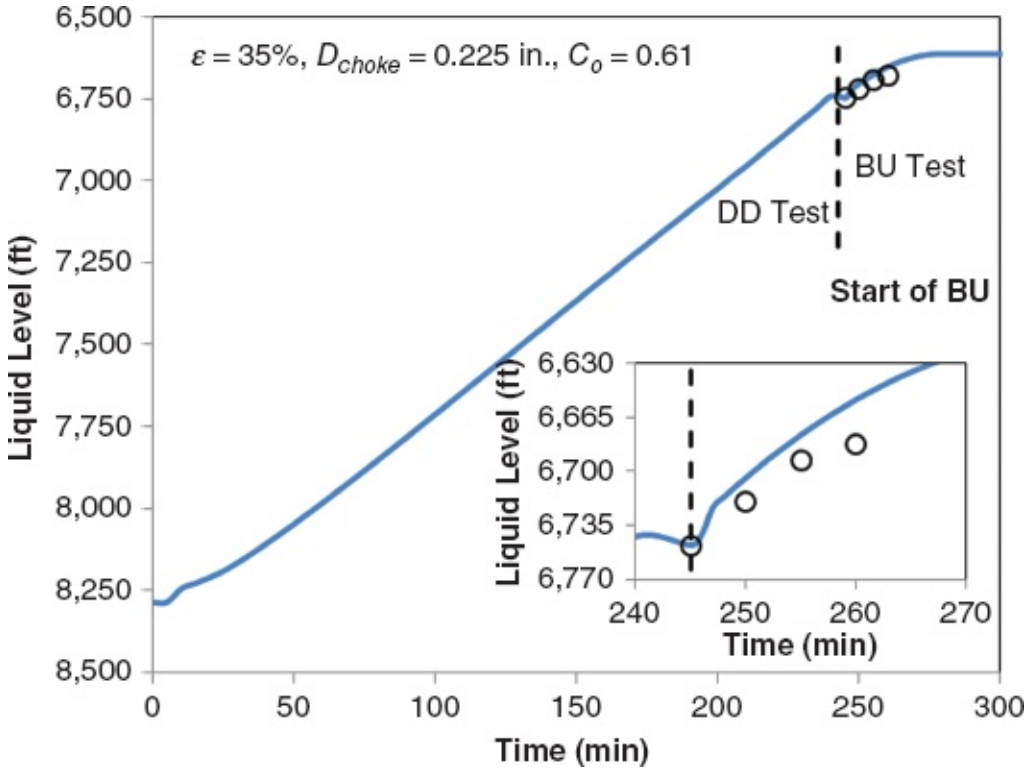

Fig. 10.23—Liquid-level profile with proposed methodology with two different thermodynamic models. DD = drawdown.

Ideally, the test entails three simple steps:

1. After the cessation of gas injection, allow a few minutes so that the injected gas has had time to escape the tubing.
2. Shut in the tubing and bleed off the annular gas so that the casinghead pressure is approximately 60% of the initial pressure. Monitor the pressure and rate with time. While a constant rate is not essential for the method to work, a near-constant rate makes the analysis more robust.
3. Shut in the annulus and monitor pressure evolution with time.

This section presents a forward model that allows test design and quantifies the degree of leakage across the GLV following the test. The system-response curves involving annular pressure change and/or liquid level as a function of time constitute the type curves corresponding to various degrees of GLV damage, reflecting the severity of the leak. This tool serves dual purposes; that is, it lends itself to test design and to the interpretation of test data. In fact, data from three wells demonstrated the modeling approach. In these tests, leak severity ranged from zero to 60%. Assessing leak severity may help prioritize the valve replacement schedule in a given asset.

Summary

This chapter presented three items related to well integrity and safety issues in different settings. First, we showed that the wellhead fluid temperature in the tubing string is directly correlated with APB; the model helped establish the magnitude of rate reduction en route to alleviating APB. Second, modeling SCP resulting from the influx of gas into the annulus can be achieved with a simple analytical expression, which leads to the projection of future performance with limited field data. Third, the integrity of GLVs can be quantified easily with simple drawdown and buildup tests of the annular gas on cessation of gas injection and shut-in of tubing.

Nomenclature

A = GLV bellow cross-sectional area, ft^2

A = parameter defined by Eq. 10-A-3a, °F/hr

A_A = annular cross-sectional area, ft^2

A_T = tubular cross-sectional area, ft^2

b = parameter defined by Eq. C-14, psi

B = parameter defined by Eq. 10-A-3b, hr^{-1}

c_m = mud compressibility, psi^{-1}

c_p = heat capacity, Btu/lbm-°F

C_o = orifice discharge coefficient, dimensionless

C_J = Joule-Thomson coefficient of fluid, ft-°F-sec^2/lbm

C_T = thermal storage coefficient, dimensionless

d = parameter defined by Eq. C-14, scf-D^{-1}-psi^{-2}

d = diameter, ft

d = inside (or equivalent) pipe (annulus) diameter, ft

D_1 = outer diameter of annulus, ft

D_2 = inner diameter of annulus, ft

f = friction factor, dimensionless

g = acceleration because of gravity, ft/sec^2

g_c = conversion factor, dimensionless

g_G = geothermal gradient, °F/ft

G = cumulative gas volume, MMscf

G_i = initial gas volume, MMscf

h = convective heat-transfer coefficient, Btu/°F-hr

h_1, h_t, = convective heat-transfer coefficients for the Annulus 1 and tubing fluid, Btu/°F-hr

J = conversion factor, 778 ft-lbf/Btu

J_1 = Bessel function of order 1

l = length of annular gas column or liquid column depth, ft

L_o = initial length of annular gas column, ft

k_a = thermal conductivity of annular fluid, Btu/hr-ft-°F

k_{cem} = cement permeability to gas, md

k_s = cement-seepage factor, ft^2

L_c = length of cement column, ft

L_g = gas column length, ft

L_{gi} = initial gas column length, ft

L = length of flow string, ft

L_m = length of mud column, ft

L_{R1} = relaxation-length parameter (Eq. 10.5), Btu/ft-hr-°F

L_{gA} = measured depth of gas column in the annulus, ft

L_{lA} = measured depth of liquid column in the annulus, ft

L_T = total measured depth from casinghead to GLV, ft

m = mass of gas in the annulus, lbm

m_{gA} = mass of gas in the annulus at any given time, lbm

m_{lA} = mass of liquid in the annulus at any give time, lbm

$\dot{m}_c$ = mass flow of gas from choke flow on wellhead, scf/hr

$\dot{m}_l$ = mass flow rate of liquid through GLV, lbm/hr

M = mass per unit depth, lbm/ft

n = moles of gas in the annulus, lbm mol

n_c = number of cells for calculation to liquid level, dimensionless

n_d = number of data points, dimensionless

p = fluid pressure, psia

p_1, p_2 = pressure at location 1 or 2, psia

p_a = pressure of choke flow outlet (=14.7), psia

p_A = annular wellhead pressure, psi

p_c = cement-top pressure, psia

p_f = formation pressure, psia

p_{GA} = annulus pressure at GLV depth, psi

p_{GT} = tubing pressure at GLV depth, psi

p_{risk} = minimum allowable annular wellhead pressure, psi

p_{max} = maximum casinghead pressure, psia

p_o = Initial casinghead pressure, psia

p_{sc} = standard condition pressure (=14.7), psia

p_T = tubing wellhead pressure, psi

q = gas rate, scf/D

q_{sc} = gas rate at the cement top, scf/D

Q = heat-transfer rate per unit length of wellbore, Btu/hr-ft

Q_{ta} = heat-transfer rate from tubing to production annulus per unit length of wellbore, Btu/hr-ft

r = radius, ft

R = gas constant, psi-ft^3/lbm mol-°R

t = producing time, hours

T = fluid temperature, °F

T_{ei} = undisturbed earth or formation temperature at any depth, °F

T_C = heat transmissivity in center cell, in Eq. 10-B-7, Btu/°F-hr

T_E = heat transmissivity in east cell, in Eq. 10-B-3, Btu/°F-hr

T_w = heat transmissivity in west cell, in Eq. 10-B-5, Btu/°F-hr

T_{sc} = standard condition temperature (=419.7), °R

T_{wb} = average wellbore temperature, °R

U = overall-heat-transfer coefficient for annular fluid, Btu/hr-°F-ft^2

U_{1e} = overall coefficient for heat transfer from first annular fluid to wellbore/formation interface, Btu/hr-°F-ft^2

U_{1t} = overall coefficient for heat transfer from first annular fluid to tubing fluid, Btu/hr-°F-ft^2

$\overline{T}$ = average fluid temperature, °R

V = fluid volume, ft^3

V_l = volume of annular liquid, ft^3

V_a = annular volume, ft^3

V_i = initial gas chamber volume in Eq. 10-C-12, ft^3

V_m = mud volume in Eq. 10-C-9, ft^3

z = depth coordinate, ft

z_{gA} = true vertical depth of gas column in the annulus, ft

z_{lA} = true depth of liquid column in the annulus, ft

z_{Total} = total true vertical depth from casinghead to GLV, ft

Z = gas-law deviation factor, dimensionless

$\overline{Z}$ = average gas-law deviation factor, dimensionless

Z_f = gas-law deviation factor at formation condition, dimensionless

α_d = diffusivity of heat, hr/ft^2

α = well inclination (to horizontal) angle, degrees

α = parameter defined by Eq. 10-C-16, dimensionless

β = parameter defined by Eq. 10-C-16, dimensionless

β = coefficient of isothermal compressibility, 1/psi

κ = coefficient of thermal expansion, 1/°F

ε = GLV damage coefficient or fraction of valve area open because of damage, dimensionless

γ_g = gas specific gravity (with respect to air, = molecular weight ratio of gas to air), dimensionless

λ = gas polytrophic constant, dimensionless

λ = heat capacity ratio, dimensionless

ρ_f = fluid density, lbm/ft^3

μ_g = gas viscosity, cp

ρ_m = mud density, lbm/gal

k = coefficient of isothermal compressibility, l/psi

ρ = density, lbm/ft^3

ρ_{gA} = density of gas in annulus, lbm/ft^3

ρ_l = density of liquid, lbm/ft^3

θ = well deviation (from vertical) angle, degrees

Subscripts

a	=	annulus
c	=	convective
c	=	casing
c_i	=	casing inside
c_o	=	casing outside
e	=	earth (formation)
f	=	formation condition
f	=	produced fluid
i	=	inside
i	=	*i*th annulus
o	=	outside
r	=	radiative
t	=	tubing
t_o	=	tubing outside
t_i	=	tubing inside
1	=	first or production annulus

Appendix 10-A

Annular Pressure Buildup Formulation in Multiple Annuli

For a well to experience APB, two conditions are prerequisite. First, a sealed annulus or annuli must exist. In general, a drilled formation is isolated in a cased well. Cement is circulated above the formation, and the top of cement occurs inside the annulus of the previous casing. When the wellhead is sealed, an isolated volume of liquid is created or trapped. Second, a temperature increase resulting from either production or drilling operations must take place. When the fluid is heated, it begins to expand and can produce a substantial increase in pressure, which can be compounded if more than one annulus is isolated. APB can also occur when a producing well is shut in for a significant time and well cooldown results. In this case, the pressure changes are negative.

Let us develop an expression for annular fluid temperature as a function of time. This relationship is then used in the expression for the annular pressure buildup. Eq. 10.8 presents a differential equation relating changes in annular fluid temperature T_1 in terms of tubing fluid temperature T_f and heat-transfer parameters. That expression is reproduced below.

$$Mc_{p1}(\mathrm{d}T_1/\mathrm{d}t) = (\pi d_{1o})U_{1i}(T_f - T_1) - L_{R1}(T_1 - T_{ei}) \quad (10.8)$$

Eq. 10.8 is rewritten as

$$Mc_{p1}\frac{\mathrm{d}T_1}{\mathrm{d}t} = \left(\pi d_{ti}U_{1i}T_f + L_{R1}T_{ei}\right) - T_1\left(L_{R1} + \pi d_{ti}U_{1i}\right) \quad (10\text{-A-}1)$$

Eq. 10-A-1 may be written as

$$\frac{\mathrm{d}T_1}{\mathrm{d}t} = A - BT_1, \quad (10\text{-A-}2)$$

where

$$A = \left(\frac{\pi d_{ti}U_1T_f + L_{R1}T_{ei}}{Mc_{p1}}\right) \quad (10\text{-A-}3a)$$

and

$$B = \frac{L_{R1} + \pi d_{ti} U_1}{M c_{p1}} \quad \text{(10-A-3b)}$$

As Eq. 10-A-3a shows, A varies slightly with fluid temperature. However, if we assume A to be constant, Eq. 10-A-2 can be expressed as a first-order linear differential equation, $dy/y = -B dt$, where $y = A - BT_1$. Integrating between time $t = 0$ to t, when y changes from y_o to y, we can write

$$y \equiv A - BT_1 = y_o e^{-Bt} = (A - BT_{1o})\, e^{-Bt} \quad \text{(10-A-4)}$$

Let us consider the case of constant production through the tubing and assume that tubing fluid temperature rises quickly (compared to annular mud temperature) to a near-steady-state value. Therefore, T_f is assumed to remain constant with time. When $t = 0$, annular fluid temperature T_{ao} equals T_{ei} in most cases. However, using $T_{ao} = T_{ei} + \delta$ (where δ is a small positive number reflecting the T_{ao} value after T_f has equilibrated) is more prudent. Eq. 10-A-4 is recast as follows:

$$T_1 = (A/B) - [(A/B) - T_{1o}]\, e^{-Bt} \quad \text{(10-A-5)}$$

Note that because

$$A / B = \left(\frac{\pi d_{a1} U_{a1} T_f + L_{R1} T_{ei}}{\pi d_{a1} U_{a1} + L_{R1}} \right), \quad \text{(10-A-6)}$$

the value of A/B lies between T_f and T_{ei}. Eq. 10-A-5 is used for the annular fluid temperature responsible for the annular pressure rise expression as developed below.

Basically, the pressure at a specific depth in a trapped column of liquid is determined by the average annulus temperature, the volume of annulus, and the amount of fluid trapped. The following expression for a change in pressure in a contained annulus can be written by recalling Eq. 10.3 of the text,

$$\Delta p = \frac{\beta}{\kappa} \Delta T - \frac{1}{\kappa V_a} \Delta V_a + \frac{1}{\kappa V_l} \Delta V_l, \quad \text{(10-A-7)}$$

where β is the coefficient of thermal expansion of annular fluid, κ is the coefficient of isothermal compressibility, V_l is the volume of annular liquid, and V_a is the annular volume. Eq. 10-A-1 suggests that three terms contribute to annular pressure buildup:

- Thermal expansion, which results in an increase in pressure when the annular volume does not increase sufficiently to accommodate this expansion
- Change of annular volume by thermal expansion, ballooning, or compression of the casings
- Change in the amount of the fluid in the annulus caused by either liquid leakoff

to formation or fluid influx into the annulus

In a sealed annulus, the first term, thermal expansion, is dominant. The second term, change in annular volume, is a downward correction to the first term. For a perfectly sealed annulus, the last term is eliminated because the amount of liquid remains constant with time. Because the first term or the liquid expansion is by far the most dominant in a sealed annulus, accounting for over 80% of pressure increase in most cases, our modeling approach centers around this term. For the thermal expansion term to dominate APB, the two conditions need to apply: (1) no liquid is lost or added to the annulus, and (2) the walls of annulus are nearly rigid, a condition that is satisfied when the casings are cemented to the surface. We note that Halal and Mitchell (1994) include this effect, whereas Sathuvalli et al. (2005) quantify the effect of elastic cement and wellbore.

Therefore, Eq. 10-A-1 simplifies to the following expression in the absence of leakoff and changes in annular volume.

$$\Delta p = \frac{\beta}{\kappa_T} \Delta T \qquad \text{(10-A-8)}$$

The contribution to APB is governed by the ratio of isobaric thermal expansion and the isothermal compressibility of the fluid. Thermodynamically, fluid volume (or density) can be expressed as a function of pressure and temperature as follows:

$$\mathrm{d}\rho = \left(\frac{\partial \rho}{\partial T}\right)_p \mathrm{d}T + \left(\frac{\partial \rho}{\partial p}\right)_T \mathrm{d}p \qquad \text{(10-A-9)}$$

When density is constant, dρ= 0, and we have

$$\left(\frac{\partial \rho}{\partial T}\right)_p \partial T = \left(-\frac{\partial \rho}{\partial p}\right)_T \partial p. \qquad \text{(10-A-10)}$$

Using the definitions of coefficient of thermal expansion and coefficient of isothermal compressibility, Eq. 10-A-4 can be rearranged for pressure as

$$\beta \equiv -(1/\rho)(\partial \rho / \partial T)_p, \qquad \text{(10-A-11)}$$

$$\kappa \equiv -(1/\rho)(\partial \rho / \partial P)_T, \qquad \text{(10-A-12)}$$

and

$$\mathrm{d}p = -\frac{(\partial \rho / \partial T)_p}{(\partial \rho / \partial p)_T} \partial T = (\beta / \kappa) \partial T \qquad \text{(10-A-13)}$$

Along with the annular fluid temperature, fluid properties (β and k) will change with

depth. For example, near the well bottom, the annular fluid temperature is high; further, the temperature increase around that region with producing time, and hence Δp, is likely to be small. However, near the wellhead, the annular fluid temperature is initially low and may rise substantially over the production period. Fig. 10.2 illustrates this point. Therefore, direct use of Eq. 10-A-7 will give inaccurate results. To account for changes in volume of the trapped fluid as a function depth, we followed a different procedure, as explained next.

The annular temperature profile is first calculated using Eq. 10-A-6. Then we use the first term on the right-hand side of Eq. 10-A-9 to calculate a pseudovolume increase ΔV_t for a small section of the annulus by discretizing the wellbore; that is, $\Delta V_t = (M/\rho) \int \beta \, dT = -\int (M/\rho^2)(\partial\rho/\partial T)_p \, \Delta T$. In this formulation, M is the mass of fluid per unit length of annulus and (M/ρ) represents the fluid volume per unit length in the section. The integral is evaluated by summing up over the entire wellbore, meaning $\Sigma V_t = -\Sigma \, (M/\rho^2) \, (\partial p/\partial T)_p \, \Delta T$. Thereafter, we use this calculated value of ΔV_t in the second term of Eq. 10-A-9 to obtain a total pressure rise; that is, $\Delta V_t = (M/\rho) \int k \, dp = \int (M/\rho^2) \, (\partial\rho/\partial\rho)_T \, dp = \Sigma \, (M/\rho^2) \, (\partial\rho/\partial\rho)_T \, \Delta p$. We can apply this approach to each unit length of the annulus when

$$\partial p = -\frac{(\partial V/\partial T)_p}{(\partial V/\partial p)_T}\partial T = (\beta/\kappa)\partial T = \frac{\Sigma\left(M/\rho^2\right)(\partial\rho/\partial T)_p \, \partial T}{\Sigma\left(M/\rho^2\right)(\partial\rho/\partial P)_T} \quad \text{(10-A-14)}$$

Mass of fluid M per unit length of annulus is calculated from fluid volume and density. In other words, $M = \pi \, \rho(d^2_{1o} - d^2_{1i})$, where d_{1o} and d_{1i} are the outside and inside diameters of Annulus 1, respectively.

Appendix 10-B

Solution of Transient Formulation for Annular Pressure Buildup

The wellbore is represented by cylindrical grids in the *z*-direction to calculate heat and mass flow during production and shut-in. The heat flow from tubing fluid into the formation can be accounted for by generating radial grids around each cylindrical element and solving the conduction equation, assuming axial conduction to be negligible.

The radial grids around the wellbore are generated logarithmically, as shown in **Fig. 10-B-1.** Heat conduction in an unsteady-state radial system may be evaluated by completing an energy balance for a volume element. Using Fourier's law of heat conduction for volume element i, the final form of the equation is given by

$$2k_{i-1}\pi r_{i-1}h\frac{T_{i-1}^{n+1}-T_{i}^{n+1}}{\Delta r_i}+2k_i\pi r_i h\frac{T_{i+1}^{n+1}-T_{i}^{n+1}}{\Delta r_{i+1}}=c_p\rho\pi\Delta r^2 h\frac{T_i^{n+1}-T_i^{n}}{\Delta t} \quad \text{(10-B-1)}$$

In Eq. 10-B-1, the first term represents the heat flux into a volume element, the second term implies the heat flux out, the last term on the right side suggests the heat accumulation term, and *h* represents the height of the computational element. Defining,

$$T_W=\frac{2k_{i-1}\pi r_{i-1}h}{\Delta r_i}, \quad \text{(10-B-2)}$$

$$T_E=\frac{2k_i\pi r_i h}{\Delta r_{i+1}}, \quad \text{(10-B-3)}$$

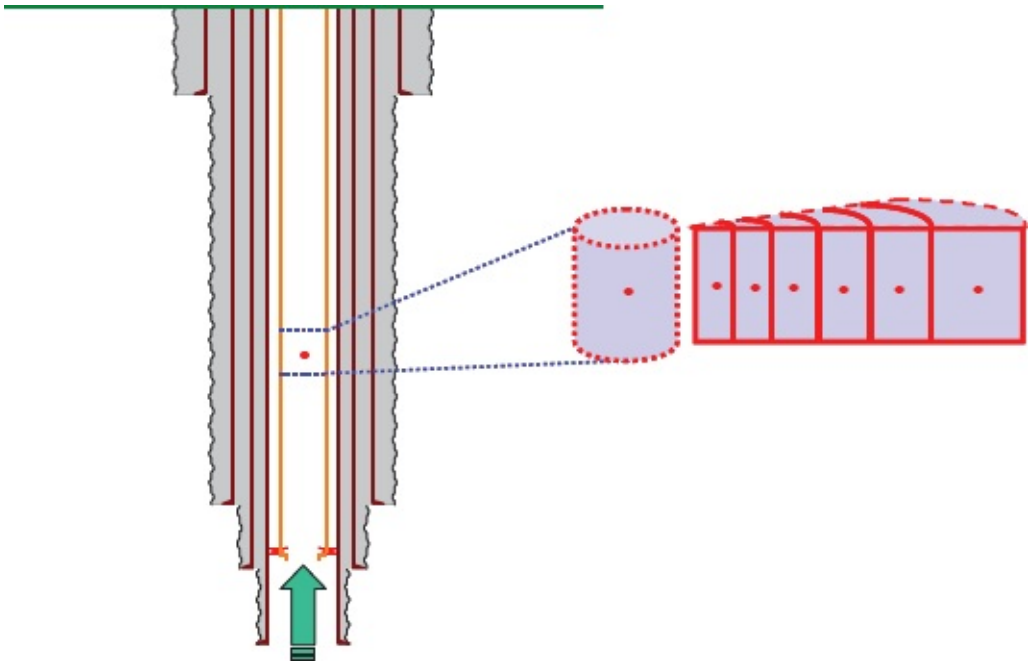

Fig. 10-B-1– Radial grids for heat-transfer and pressure-drop calculations.

$$\lambda = c_p \rho \pi \Delta r^2 h, \qquad (10\text{-B-}4)$$

and

$$T_W\left(T_{i-1}^{n+1} - T_i^{n+1}\right) + T_E\left(T_{i+1}^{n+1} - T_i^{n+1}\right) = \lambda \frac{T_i^{n+1} - T_i^n}{t}. \qquad (10\text{-B-}5)$$

With manipulation, the matrix form is given by

$$T_W T_{i-1}^{n+1} - \left(T_W - T_E + \frac{\lambda}{t}\right) T_i^{n+1} - T_E T_{i+1}^{n+1} = -\frac{\lambda}{t} T_i^n \qquad (10\text{-B-}6)$$

Defining,

$$T_C = \left(T_W - T_E + \frac{\lambda}{\Delta t}\right). \qquad (10\text{-B-}7)$$

and

$$T_W T_{i-1}^{n+1} - T_C T_i^{n+1} - T_E T_{i+1}^{n+1} = -\frac{\lambda}{t} T_i^n. \qquad (10\text{-B-}8)$$

This equation is implicit, which means it can be solved in matrix form. For a cylindrical wellbore element with four radial grids, the matrix from is given by

$$\begin{vmatrix} 1 & & & \\ T_W & T_C & T_E & \\ & T_W & T_C & T_E \\ & & T_W & T_C \end{vmatrix} \bullet \begin{vmatrix} T_1^{n+1} \\ T_2^{n+1} \\ T_3^{n+1} \\ T_4^{n+1} \end{vmatrix} = -\frac{\lambda}{\Delta t} \begin{vmatrix} T_t^n \\ T_2^n \\ T_3^n \\ T_4^n \end{vmatrix} \quad \text{(10-B-9)}$$

The first temperature value on the right side is specified and provided by the analytical temperature solution given in Eq. 10-A-5.

Perhaps a comment on how to select the size of the time increment in the right-hand side of Eq. 10-B-9 will be useful. The size will depend on the term T_D. Note that one of the most vexing stages of a numerical procedure is the selection of a physically meaningful time increment.

Appendix 10-C

Sustained Casing Pressure Model Derivation and Analytical Solution

10-C.1 Gas Influx Rate. Poorly designed cement slurry and/or lack of bonding of cement to casing or formation will allow gas to seep through into the annulus. Although flow through channels that develop in the presence or absence of well-bonded cement may not be the same, Darcy's law can be used effectively to model such gas flow. Darcy's law allows us to write the following expression relating pressure gradient to fluid velocity (or rate):

$$\frac{dp}{dz} = \frac{\mu v}{k_s} = \frac{\mu q}{A k_s} \quad \text{(10-C-1)}$$

In Eq. 10-C-1, k_s is the seepage factor for flow and is analogous to permeability. Because that seepage through the cement sheath may not be quite the same as flow through porous media, in the equation we have used k_s, instead of k. However, because the intended readership of this work is much more familiar with the term "permeability" and the symbol k, the rest of our work uses this symbol. The conversion factor for k in md to k_s in ft^2 is 1.06235×10^{-14}. In flowing through the cement column, the gas velocity (or flow rate) will change with cement depth, z. To account for that change, the in-situ flow rate q can be substituted in terms of q_{sc}, the flow rate at standard pressure p_{sc}, standard temperature T_{sc}, in-situ pressure p, and temperature T. These substitutions allow one to rewrite Eq. 10-C-1 as follows:

$$q_{sc} = \frac{k A_A T_{sc}}{\mu Z T p_{sc}} p \frac{dp}{dz} \quad \text{(10-C-2)}$$

As the gas flows through the cement column, changes in gas temperature, viscosity, and Z-factor are likely to be small and expected to be well-represented by the average values evaluated at the formation condition, T_f, μ_f and Z_f. Under these assumptions, integration of Eq. 10-C-2 leads to the following relationship between the gas-seepage rate q_{sc}, the formation pressure p_f, and pressure at the top of cement p_c:

$$q_{sc} = \frac{k A_A T_{sc}}{2 L_c \mu_f Z_f p_{sc} T_f} \left(p_f^2 - p_c^2 \right) \quad \text{(10-C-3)}$$

In oilfield units, Eq. 10-C-3 is rewritten as

$$q = \frac{0.003164 k A_A T_{sc}}{L_c \mu_f Z_f p_{sc} T_f}\left(p_f^2 - p_c^2\right) \quad \text{(10-C-4)}$$

Eq. 10-C-4 was used by Xu (2002) and others without showing its origin.

10-C.2 Governing Equation and Solution for Sustained Casing Pressure. Using the gas law, $n = pV/(ZRT)$, and neglecting the variation of gas deviation factor (Z) with time, the molar rate of gas into the casinghead can be written as

$$\frac{\mathrm{d}n}{\mathrm{d}t} = \frac{1}{ZRT_{wh}}\left(V\frac{\mathrm{d}p}{\mathrm{d}t} + p\frac{\mathrm{d}V}{\mathrm{d}t}\right) \quad \text{(10-C-5)}$$

The gas accumulation rate, dn/dt, can also be related to the volumetric flow rate, q, at standard condition, sc, by

$$\frac{\mathrm{d}n}{\mathrm{d}t} = \frac{q_{sc} p_{sc}}{ZRT_{sc}} \quad \text{(10-C-6)}$$

Because the rate equation is written in terms of gas rate at standard conditions, Eq. 10-C-6 has standard pressure, p_{sc}, in the numerator. Xu (2002) used pressure at the top of the cement (bottom of the mud column), p_c, which may be less than accurate. Eqs. 10-C-5 and 10-C-6 are combined to obtain the following expression for the change of pressure with time:

$$\left(\frac{q_{sc} p_{sc}}{ZRT_{sc}}\right) = \frac{1}{ZRT_{wh}}\left(V\frac{\mathrm{d}p}{\mathrm{d}t} + p\frac{\mathrm{d}V}{\mathrm{d}t}\right) \quad \text{(10-C-7)}$$

Because the change in the length of the mud column is compensated by the change in mud density, the pressure exerted by the mud column is constant. In other words, the pressure increase at the cement top will be attributed solely to the gas chamber pressure increase, as follows:

$$p_c = p + 0.052\rho_m L_m \quad \text{(10-C-8)}$$

Note that the gas cap volume increases with time as the mud column is compressed. The change in mud volume is given by

$$\mathrm{d}V = c_m\left(V_m \mathrm{d}p + p\mathrm{d}V_m\right), \quad \text{(10-C-9)}$$

and the variation of gas volume with respect to time can be written as

$$\frac{\mathrm{d}V}{\mathrm{d}t} = c_m\left(V_m\frac{\mathrm{d}p}{\mathrm{d}t} + p\frac{\mathrm{d}V_m}{\mathrm{d}t}\right) \quad \text{(10-C-10)}$$

Because the change of the mud volume represents the equal and opposite change of the gas cap volume, the second term on the right-hand side of Eq. 10-C-10, [p

(dV_m/dt)], can be written as [$-p$ (dV/dt)]. This step allows rearrangement of Eq. 10-C-10 in explicit form for (dV/dt) as

$$\frac{dV}{dt}=\left(\frac{c_m V_m}{1+c_m p}\right)\frac{dp}{dt} \qquad \text{(10-C-11)}$$

Substituting Eqs. 10-C-4, 10-C-9, and 10-C-11 into Eq. 10-C-7, the following equations are obtained:

$$\frac{0.003164kA_A T_{sc}}{L_c\mu_i Z_i p_{sc} T}\frac{p_{sc}}{ZRT_{sc}}\left(p_f^2-p_c^2\right)=\frac{1}{ZRT_{wh}}\left[V\frac{dp}{dt}+p\frac{dV}{dt}\right]$$

$$\frac{0.003164kA_A T_{wh}}{L_c\mu_i Z_i T}\left(p_f^2-p_c^2\right)=\left[\left(V_i+c_m V_m p\right)\frac{dp}{dt}+p\frac{dV}{dt}\right]$$

$$\frac{0.003164kA_A T_{wh}}{L_c\mu_i Z_i T}\left(p_f^2-p_c^2\right)=\left[\left(V_i+c_m V_m p\right)\frac{dp}{dt}+p\left(\frac{c_m V_m}{1+c_m p}\right)\frac{dp}{dt}\right]$$

$$\frac{0.003164kA_A T_{wh}}{L_c\mu_i Z_i T}\left(p_f^2-p_c^2\right)=\left[V_i+c_m V_m p\left(1+\frac{1}{1+c_m p}\right)\right]\frac{dp}{dt} \qquad \text{(10-C-12)}$$

Substitution and regrouping leads to the differential equation governing the transient behavior of casing pressure. Thus,

$$\frac{dp}{dt}=\frac{\dfrac{0.003164kA_A T_{wh}}{L_c\mu_i Z_i T}\left[p_f^2-(p+0.052\rho_m L_m)^2\right]}{V_i+c_m V_m p\left(1+\dfrac{1}{1+c_m p}\right)} \qquad \text{(10-C-13)}$$

For simplification, we group constants in the following form:

$$b=0.052\rho_m L_m; \quad d=\frac{0.003164kA_A T_{wh}}{L_c\mu_f Z_f P_{sc} T_f} \qquad \text{(10-C-14)}$$

We note again that in Eq. 10-C-14, as in Eq. 10-C-8, L_m is the true vertical depth of the mud column. Using these lumped parameters and separating the variables allow us to solve Eq. 10-C-13 as follows:

$$t=\frac{\left[(\alpha-1)V_i-\alpha\beta V_m\right]\tanh^{-1}\left(\dfrac{p+b}{p_f}\right)}{p_f d(\alpha-1)}+\frac{c_m V_m\left\{2\ln\left(1+c_m p\right)+(2-\alpha)\ln\left[p_f^2-(p+b)^2\right]\right\}}{2d(\alpha-1)}, \qquad \text{(10-C-15)}$$

where α and β represent the following groups of constants:

$$\alpha = 2bc_m - b^2c_m^2 + c_m^2 p_f^2, \beta = bc_m - 1 \quad \text{(10-C-16)}$$

The time *t* to reach a certain pressure *p* can be obtained by evaluating Eq. 10-C-14:

$$t = t(p) - t(p_o) \quad \text{(10-C-17)}$$

Chapter 11

Drilling Operations

This chapter addresses several heat-transfer topics that originate from well drilling, meaning in openhole situations. In most cases, simple analytical expressions derived from governing differential equations enable estimation of fluid and/or formation temperatures. These topics include (1) fluid circulation temperature under various boundary conditions, both at the surface and downhole; and (2) static formation temperature in the open and cased-hole situations. Thereafter, we present coupled wellbore/reservoir models for estimating flow rates and cumulative fluid loss in an uncontrolled well involving both oil and gas wells.

11.1 Fluid Circulation Temperature

11.1.1 Introduction. In drilling operations, the knowledge of accurate temperature with circulating time has a direct bearing on drilling fluid density and rheology. Beyond the design of drilling fluids itself, temperature plays a significant role in many aspects of the well and related engineering. Some of these relevant areas include determination of thermal stresses on tubulars, particularly in permafrost or high-temperature regions; design of cementing programs; logging-tool design; and log interpretation. The estimation of fluid temperature becomes critical for high-temperature and geothermal reservoirs, in which significant heat exchange occurs. In these reservoirs, problems compound when dealing with temperature-sensitive fluid properties such as a non-Newtonian fluid.

Similar to drilling, production and well control or dynamic kill operations also demand accurate computations of fluid circulation rates and flowing-fluid temperature. Fluid temperature, as a function of both depth and elapsed time, dictates the intrinsic fluid properties of density and viscosity and, in turn, the pressure drop or the maximum allowable pumping rate. Offshore wells present another dimension to the heat-transfer problem in that heat exchange through the seawater and air must be incorporated.

A few reliable predictive tools exist for drilling fluid temperature estimation. For instance, the popular American Petroleum Institute thickening-time schedule for cementing operations is unreliable because it often over- or underestimates the true temperature. Although direct temperature measurements can be made at a given depth during certain operations, we cannot overemphasize the need for computing temperature profiles for the entire wellbore by simulating the transient processes. Note that the earlier analytical models proposed by Edwardson et al. (1962) and Tragesser et al. (1967) are unsuitable as a generalized computational tool because

they require a detailed knowledge of the drilling history.

Two approaches, numerical and analytical, have emerged for estimating the circulating-fluid temperature. The numerical approach requires a solution of the governing finite-difference equations dealing with the unsteady-state heat-transfer problem. Raymond (1969) proposed the first numerical model for computing circulating-fluid temperatures during unsteady- and pseudosteady-state conditions. Subsequently, many improvements were offered by others (Keller et al. 1973; Wooley 1980; and Beirute 1991).

In the second approach, the analytical solutions present system geometry of lesser complexity—that is, in the absence of multiple casing strings. For example, Holmes and Swift (1970) obtained a solution for steady-state heat transfer in both the conduits and the formation. Subsequently, Kabir et al. (1996c), Hasan et al. (1996a), and Hasan and Kabir (1994a) presented formulations for forward- and reverse-circulation cases. This chapter presents simple but realistic analytical models that allow calculation of the inlet/outlet mud temperatures with time with fluid circulation in and out of a tank. These models are also capable of tracking temperature profile for the entire borehole.

11.1.2 Constant Tank Fluid Temperature. In flowing down the drillstring and back up the annulus (forward circulation), or down the annulus and up the drillstring (reverse circulation), the circulating fluid generally exchanges heat with the formation and the tubing fluid. Therefore, the heat-transfer rate for the fluid in the annulus depends on the formation and the drillpipe fluid temperatures. A schematic for the reverse-circulation case is shown in **Fig. 11.1.** Kabir et al. (1996c) derived the following equations for the drillstring (T_t) and annulus (T_a) fluid temperatures by completing an energy balance for a fluid element that Appendix 11-A details.

$$\frac{B}{L_R}\frac{\mathrm{d}^2T_t}{\mathrm{d}z^2} \pm B\frac{\mathrm{d}T_t}{\mathrm{d}z} - T_t + T_{es} + g_G z \sin\alpha = 0. \qquad (11.1)$$

and

$$T_a = T_t \mp B\frac{\mathrm{d}T_t}{\mathrm{d}z}\ , \qquad (11.2)$$

where

$$L_R = \frac{2}{c_{fl}w}\left(\frac{r_c U_a k_e}{k_e + r_c U_a T_D}\right), \qquad (11.3)$$

and

$$B = \frac{wc_{fl}}{2\pi r_t U_t}. \qquad (11.4)$$

Note that the upper signs (+ in Eq. 11.1, − in Eq. 11.2) apply to the reverse-circulation case, and the lower signs apply to the forward-circulation case. Solutions for the two flow directions differ because of the boundary conditions. We reproduce the solution from Hasan and Kabir (1994a), which is written as

$$T_t = \alpha e^{\lambda_1 z} + \beta e^{\lambda_2 z} + g_G z \sin\alpha \pm B g_G + T_{es}, \quad (11.5)$$

$$T_a = (1 \mp B\lambda_1)\alpha e^{\lambda_1 z} + (1 \mp B\lambda_2)\beta e^{\lambda_2 z} + g_G z \sin\alpha + T_{es} \quad (11.6)$$

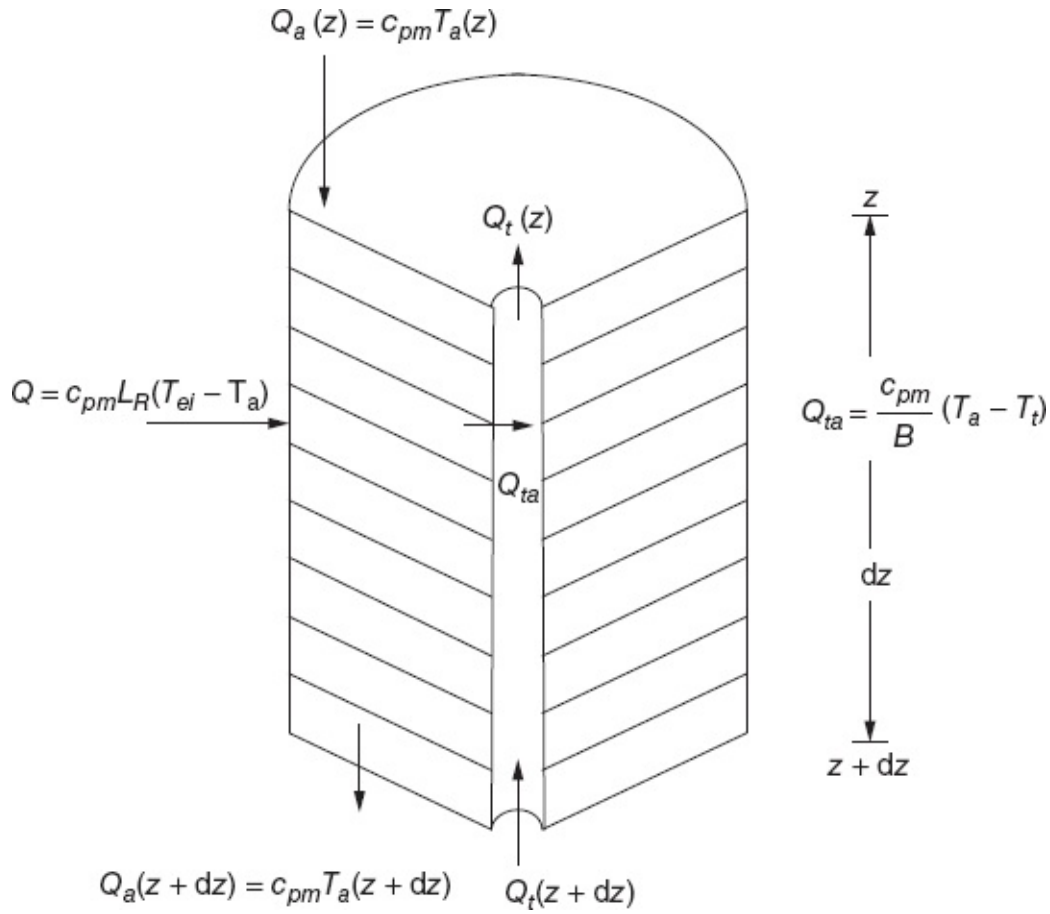

Fig. 11.1—Schematic of the heat-transfer model.

Again, the upper signs (+ in Eq. 11.5, - in Eq. 11.6) apply to reverse flow, and the lower ones apply to the forward flow situation. The constants, α β, λ_1, and λ_2, are dependent on boundary conditions and thermal properties, which are presented in Appendix 11-A. **Fig. 11.2** shows how the flow direction influences the temperature profiles.

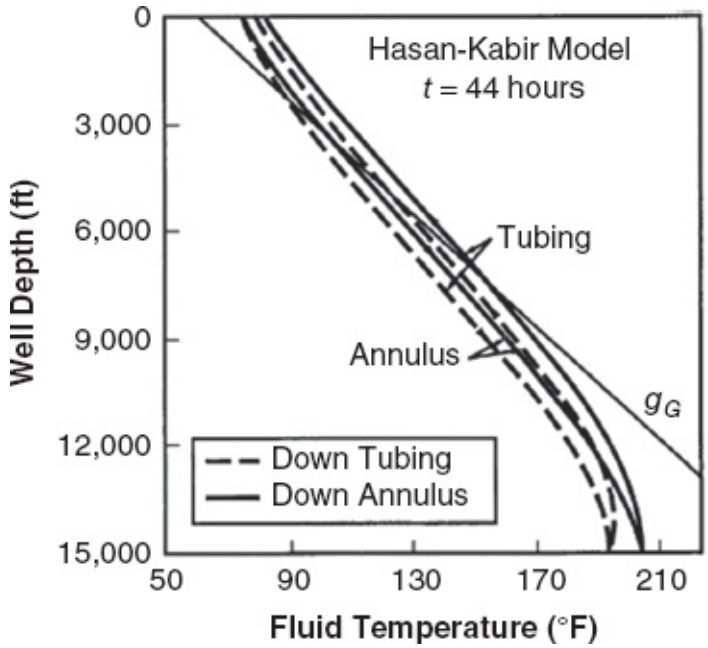

Fig. 11.2—Influence of flow direction on a fluid temperature profile. Solid curves are for flow down the annulus, while broken curves are for flow down the drillpipe.

11.1.3 Variable Tank Fluid Temperature. The solutions presented previously presupposed that the circulating-fluid inlet temperature is constant (either T_{ai} or T_{ti}). Fluid circulating through tubing (or a drillpipe) and a tubing/casing (or tubing/formation) annulus exchanges heat with the formation, which is usually at a higher temperature than the flowing fluid. Therefore, the fluid exiting the wellbore and entering the tank is at a temperature greater than the average value. Adding this hotter fluid gradually raises the tank fluid temperature with time. In other words, the wellbore acts as a heat exchanger supplying heat to the tank from the formation. However, as the tank temperature increases, heat loss from the tank to the surrounding air also increases. The tank temperature finally approaches a steady value when the heat gained from the circulating fluid (from formation) equals the heat lost to the ambient air.

The transient energy balance for the tank may be made by noting the energy gain from the hot wellbore fluid and heat loss to the surrounding air. First, consider the case of forward circulation through a rectangular tank, as depicted in **Fig. 11.3.** Here, the fluid is at an initial temperature, T_o, which is often equal to the ambient air temperature, T_{air}. The energy balance comprises three elements: first, the energy is added to the tank by the entering circulating fluid at a temperature of T_{ae} (exit temperature of the annular fluid); second, the energy is lost by the fluid exiting the tank (and entering the wellbore) at a temperature of T_{ti}; third, the heat is lost to the ambient air. In other words,

$$wc_{fl}\left(T_{ae}-T_{ti}\right)-U(ab)Uab\left(T_{ae}-T_{ti}\right)=(abh)\rho_{fl}c_{fl}\frac{\mathrm{d}T_{ti}}{\mathrm{d}t},$$

or

$$\frac{dT_{ti}}{dt} + \Omega T_{ti} = Y, \quad (11.7)$$

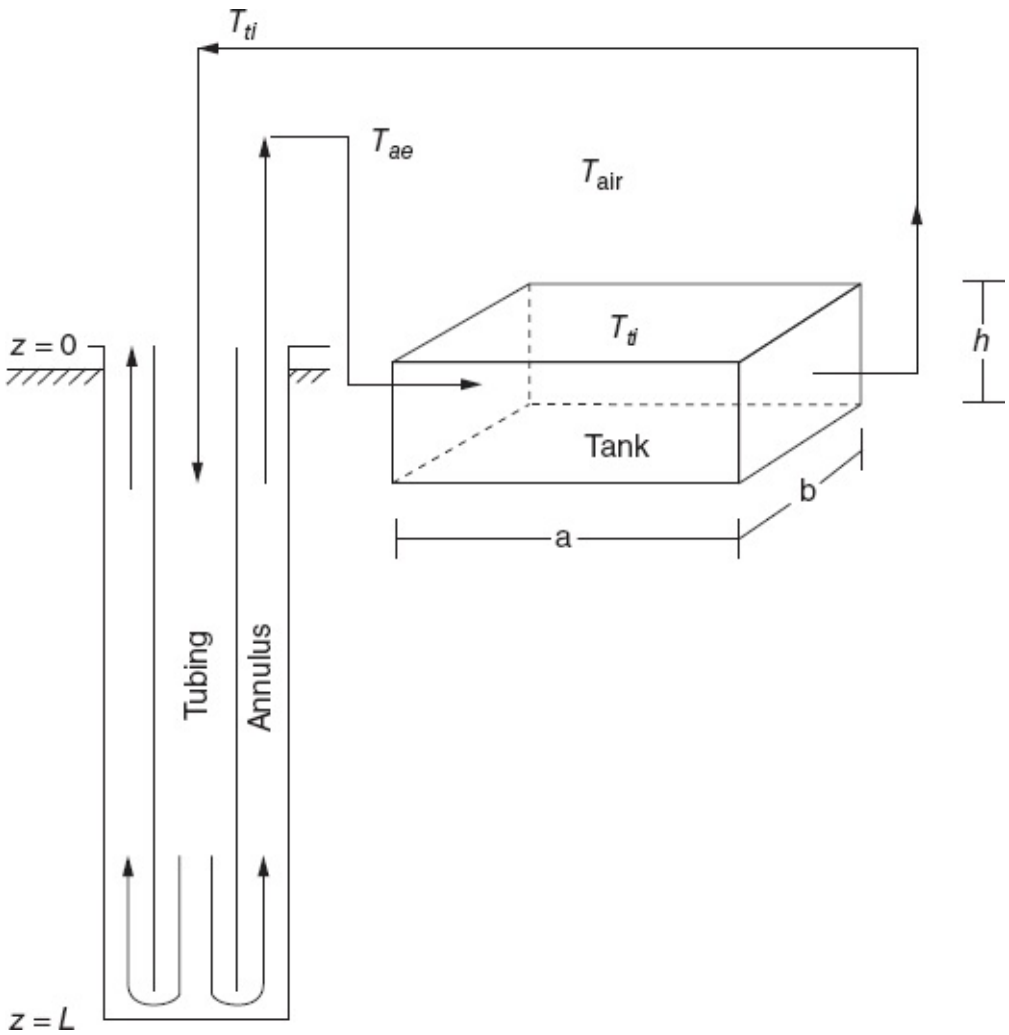

Fig. 11.3—Schematic of the mud circulation model.

where

$$\Omega = \frac{w + (Uab / c_{fl})}{abh\rho_{fl}} \quad (11.8)$$

and

$$Y = \frac{wT_{ae} + U(ab)T_{air} / c_{fl}}{abh\rho_{fl}}. \quad (11.9)$$

Eq. 11.7 is a linear differential equation, which yields a solution with the boundary condition ($T_{ti} = T_{air}$ at $t = 0$) and is written as

$$T_{ti} = \frac{Y}{\Omega} + \left(T_{air} - \frac{Y}{\Omega}\right)e^{-\Omega t}. \quad (11.10)$$

Note that in arriving at the expression (Eq. 11.10) for tank temperature variation with time, we assumed that Y is a constant, although it contains term T_{ae}, the annular fluid exit temperature. As the tank temperature increases, T_{ae} will also increase gradually with time. However, assuming T_{ae} to be constant is still reasonable because the variation in the value of T_{ae} with time is small and because the term wT_{ae} is generally much smaller than the term $UabT_{air}$. A simplified expression for Eq. 11.10 (Hasan and Kabir 1990a) may be written as

$$T_{ti} = T_{ae} + (T_o - T_{ae})e^{-\Omega t}. \quad (11.11)$$

Eq. 11.11 shows that the tank fluid temperature asymptotically approaches the terminal exit-fluid temperature. This expression also holds when reverse circulation occurs, with wT_{ae} being replaced by wT_{te} in all appropriate equations.

11.1.4 Variable Heat Flux at Formation/Wellbore Interface. In contrast to fluid flow, heat flow occurs throughout the length of the wellbore and not just at the perforated intervals. Therefore, the variable heat flux is considered along the entire wellbore/formation interface.

Expressions for fluid temperature in the tubing and annulus, given by Eqs. 11.5 and 11.6, include the exponents λ_1 and λ_2, which are dependent on the relaxation distance L_R. The development of the expression for L_R, given by Eq. 11.3, involves the solution of the thermal-diffusivity equation. One boundary condition in the solution includes constant heat flux at the wellbore/formation interface, as given in Ramey (1962) and Hasan and Kabir (1994a). However, with increased circulation time, the wellbore fluid temperature tends to approach that of its immediate surroundings, thereby decreasing the heat-transfer rate with time and invalidating this boundary condition. The superposition principle can account for this changing heat flux, as shown in Hasan and Kabir (1994a) and discussed in Appendix 11-B. The governing differential equation then becomes

$$\frac{B}{L_{Rn}}\frac{d^2T_t}{dz^2} \pm B\frac{dT_t}{dz} - T_t + T_{es} + g_G z \sin\alpha + \omega_{1'} - \omega_{2'} = 0. \quad (11.12)$$

Unlike Eq. 11.1, Eq. 11.12 includes terms involving heat flux, which must be linear in well depth z for the differential equation to be linear and yield an analytic solution. If each heat flux is represented by a linear equation, solutions to Eq. 11.12 are given by

$$T_t = \alpha e^{\lambda_1 z} + \beta e^{\lambda_2 z} + \Lambda z \pm B\Lambda + T_{es} + \omega_1 - \omega_2 \quad (11.13)$$

and

$$T_a = (1 \mp B\lambda_1)\alpha e^{\lambda_1 z} + (1 \mp B\lambda_2)\beta e^{\lambda_2 z} + \Lambda z + T_{es} + \omega_1 - \omega_2 \quad (11.14)$$

The constants Λ, α, β, λ_1, λ_2, ω_1, and ω_2 are reported in Appendix 11-B.

11.1.5 Fluid Temperature Inversion. One interesting aspect of studying the forward-circulation behavior is that the maximum temperature occurs in the annulus away from the bottom of the borehole. Here, we present a simple analytic expression for the depth at which the maximum fluid temperature occurs and offer a physical explanation of this phenomenon.

By differentiating Eq. 11.6 with respect to well depth z and setting it equal to zero, we obtain

$$\frac{dT_a}{dz} = 0 = (1+\lambda_1 B)\alpha\lambda_1 e^{\lambda_1 z} + (1+\lambda_2 B)\beta\lambda_2 e^{\lambda_2 z} + g_G, \quad (11.15)$$

or

$$e^{\lambda_1 z_{Tmax}} = -\frac{g_G}{(1+\lambda_1 B)\alpha\lambda_1} - \frac{(1+\lambda_2 B)\beta\lambda_2 e^{\lambda_2 z_{Tmax}}}{(1+\lambda_2 B)\beta\lambda_1}. \quad (11.16)$$

Because z_{Tmax} is implicit in Eq. 11.16, a trial-and-error solution is required. Alternatively, one can also differentiate the temperature profile numerically to find z_{Tmax}, as shown later.

The temperature inversion is precipitated by heat flow equilibrium attained by the fluid as it ascends the annulus. In forward circulation, the drillpipe fluid temperature continues to rise on receiving heat from the annular fluid, reaching a maximum at the bottom of the hole. This high-temperature fluid then flows up the annulus. The annular fluid, being at a temperature lower than the formation temperature, receives heat from the formation. Initially, this gain in heat is larger than the heat lost to the fluid in the drillpipe, with a consequent net increase in enthalpy and temperature as the fluid rises the annulus. However, the rate of heat gain diminishes as the annular fluid encounters cooler formation with decreasing depth, while the annular fluid loses heat to the relatively colder tubing fluid. At some depth away from the bottom of the hole, the net heat gained by the fluid equals the net heat loss, and the maximum fluid temperature is reached.

Fig. 11.4 helps to understand the preceding discussion. As the rate of heat transfer between the wellbore and the formation diminishes with increasing circulation time, the temperature profiles in both conduits approach the geothermal temperature, showing a cooling effect. Fig. 11.4 shows only the annular temperature profiles. Although temperature inversion is apparent for each curve on Fig. 11.4, the depth at which the maximum temperature occurs is best amplified on a derivative graph. **Fig. 11.5** displays the same depth (13,776 ft or 4199 m) for all the curves when the derivative goes to zero. Note that the derivative was taken with respect to the logarithm of depth to retain the same units for the x-axis (°F or °C) and facilitate plotting on the same graph. **Fig. 11.6** shows such a combined plot, in which the derivative was taken by using the central-difference scheme. We also observe

maxima on the derivative.

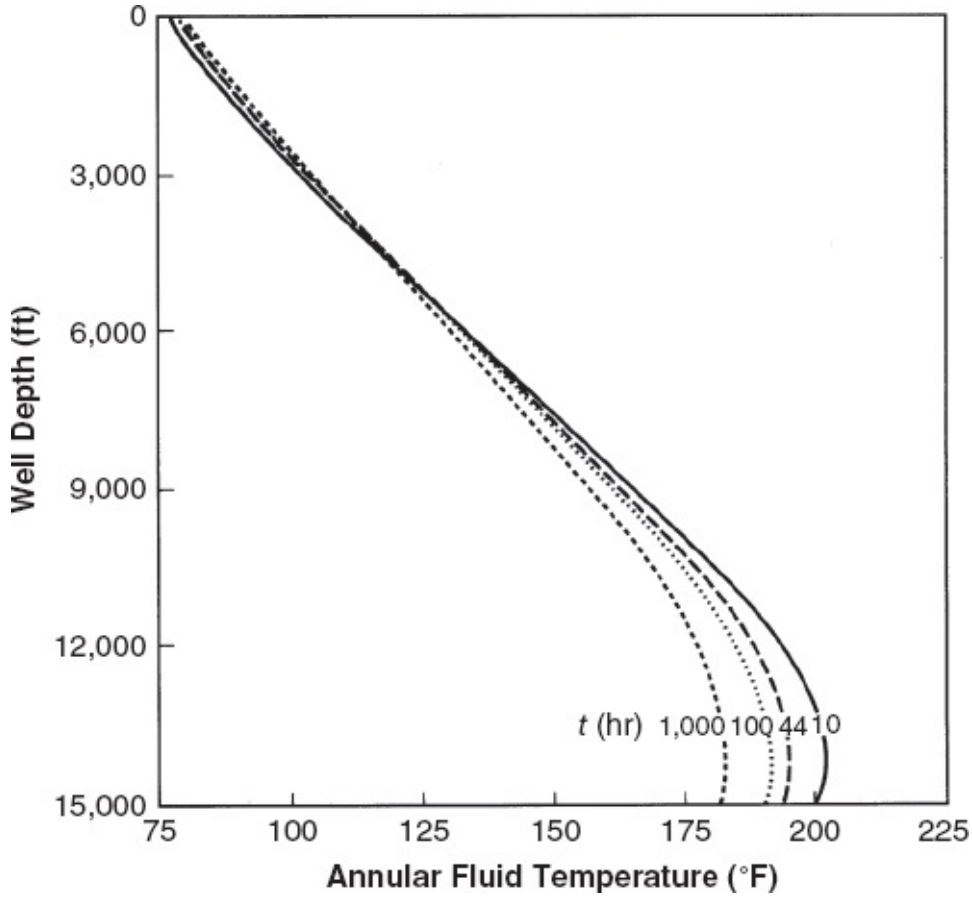

Fig. 11.4—Effect of circulation time on an annular temperature profile.

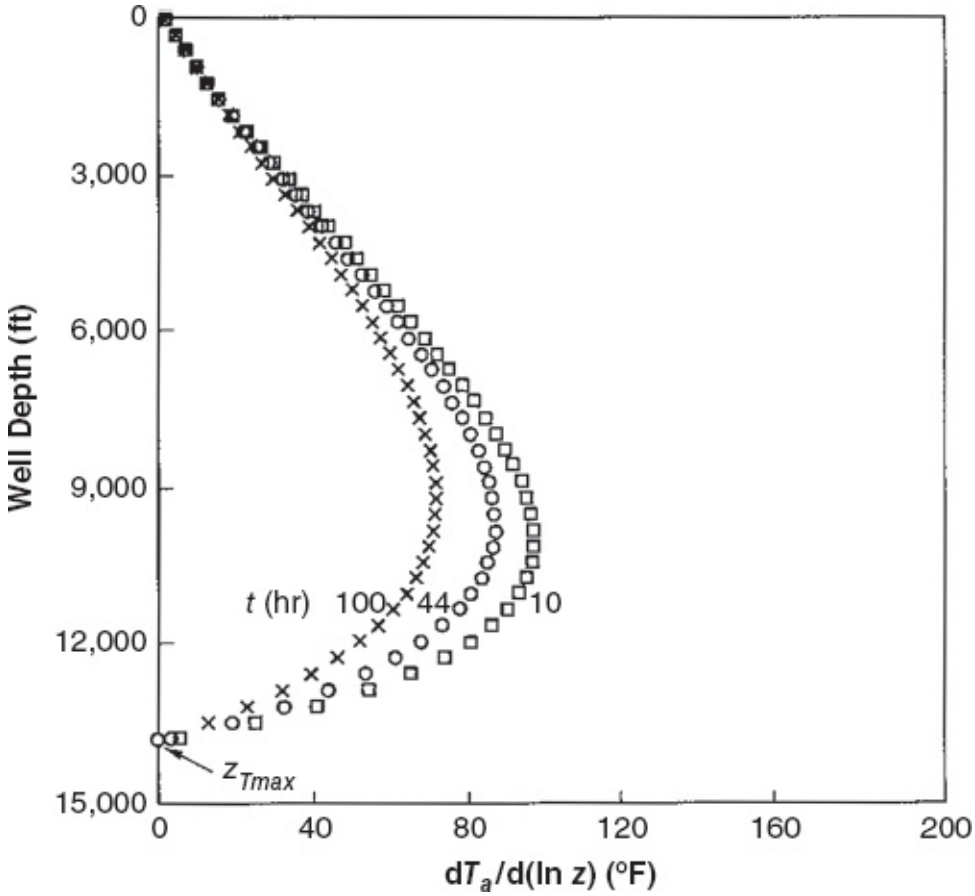

Fig. 11.5—Temperature derivative aids locating the temperature maxima.

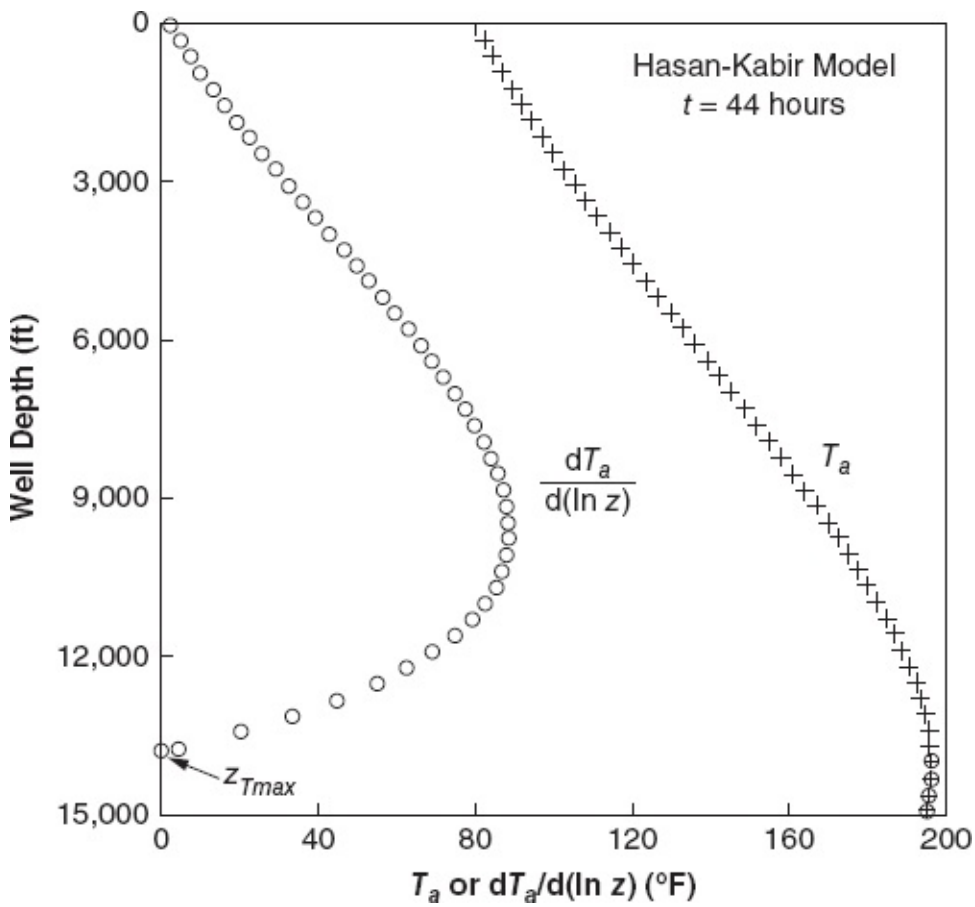

Fig. 11.6—Combined fluid temperature and its derivative show the temperature maxima.

11.1.6 Influence of Parameters on Circulation Temperature. We explored the effects of tank fluid temperature variation and heat flux variation at the wellbore/formation interface on the circulating-fluid temperature using the Holmes and Swift (1970) data set, given in **Table 11.1.** The tank, as shown in Fig. 11.3, has the dimension of 100 × 10 × 5 ft^3.

***Tank Temperature Variation*. Fig. 11.7** shows the fluid temperature profile obtained after approximately 44 hours (44.14 hours) of circulation. Here, the annular inlet temperature of the fluid is assumed to be constant at 75°F, compared to that when the inlet temperature is allowed to increase with time, as indicated by Eq. 11.10. The difference in the two profiles—that is, the more than 25% increase in the wellhead fluid temperature—emphasizes the importance of accounting for such variations in temperature-sensitive applications.

Well depth, ft	15,000
Drillstem outer diameter, in.	$6\frac{5}{8}$
Drill-bit size, in.	$8\frac{3}{8}$
Circulation rate, bbl/hr	300
Inlet mud temperature, °F	75
Mud viscosity, lbm (ft-hr)	110
Mud thermal conductivity, Btu/(ft-°F-hr)	1
Mud specific heat, Btu/(lbm-°F)	0.4
Mud density, lbm/gal	10
Formation thermal conductivity, Btu/(ft-°F-hr)	1.3
Formation specific heat, Btu/(lbm-°F)	0.2
Formation density, lbm/ft^3	165
Surface earth temperature, °F	59.5
Geothermal gradient, °F/ft	0.0127

Table 11.1—Well and mud data from Holmes and Swift (1970).

Fig. 11.8 shows the variations of tank fluid temperature and temperature of the exiting annular fluid with time for two different initial temperatures, 35°F and 75°F. As indicated by Eq. 11.10, the tank temperature initially increases rapidly with time and then gradually levels off in both cases. The increase in tank fluid temperature causes a gradual increase in the annular fluid exit temperature, which is also shown in Fig. 11.8. An interesting feature of Fig. 11.8 is the progressive decline in the difference between the annular fluid exit temperature and the tubing fluid inlet temperature with increasing time. We can explain this decrease in the temperature difference in the following manner: as the wellbore fluid temperature increases, the temperature difference driving heat flow from the formation to the wellbore decreases. Therefore,

the net energy gain for the fluid gradually decreases with time, leading to an ever-decreasing temperature difference of the two streams at the wellhead.

As Eq. 11.10 implies, many variables influence the rise in the tank's fluid temperature. Parameters that are likely to have the largest effect are initial tank temperature, area of the tank exposed to the air (heat-transfer area = *ab*), heat-transfer coefficient between the tank and the air (which can change dramatically with wind velocity), and tank volume. The sensitivity of the calculated tank and annular exit temperatures to these variables is displayed in **Figs. 11.9 through 11.12.** Note that in these figures, we report tank and annular fluid exit temperatures at the end of 44 hours of circulation.

Fig. 11.9 shows that the initial tank temperature does not appear to affect the tank's fluid temperature after 44 hours of circulation: the large initial difference of 40°F between the two cases reduces to only 5.5°F. This observation implies that the heat transported from the formation and lost to the ambient air has a more pronounced effect than the initial tank temperature for establishing the equilibrium inlet and exit temperatures. Fig. 11.10 also shows a similar trend showing that the tank temperature at the end of 44 hours is 5°F lower when the tank area is four times larger. The increased heat loss from a larger surface area causes the lower temperature. Fig. 11.11 similarly shows a lower tank temperature for the case when the heat-transfer coefficient is larger. The effect of tank volume, which is displayed in Fig. 11.12, is small. Reduction of tank volume by 400% shows an increase of only 2.1°F in tank temperature, after 44 hours of circulation.

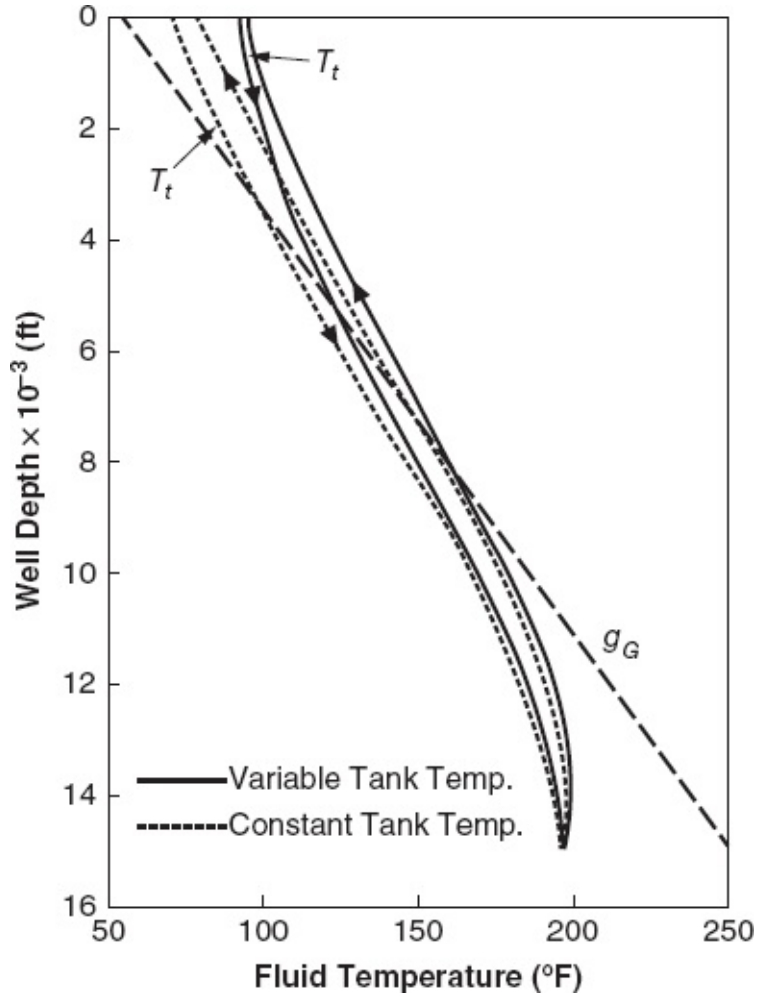

Fig. 11.7—Fluid temperature profiles for the variable inlet-temperature model.

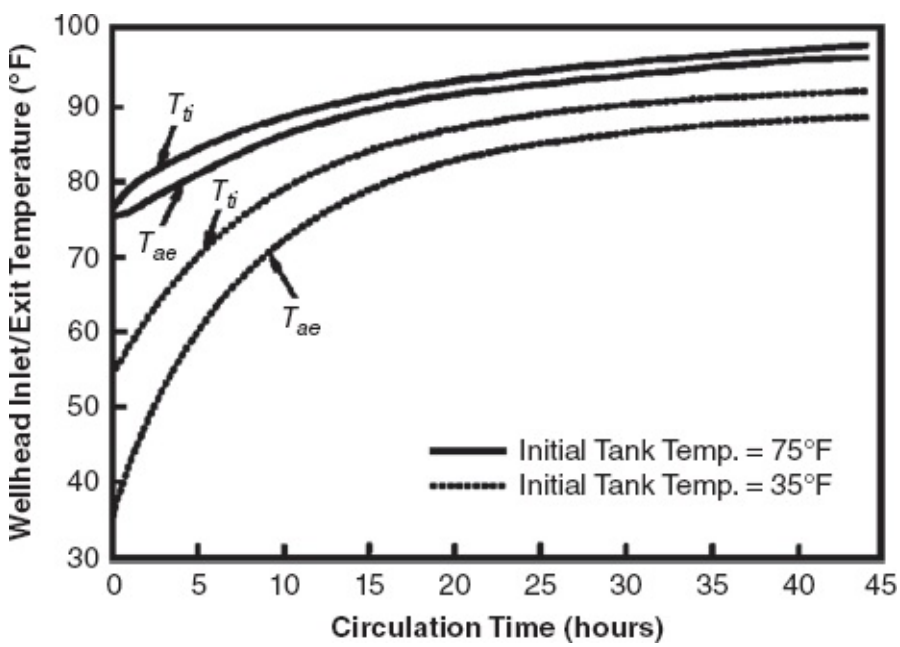

Fig. 11.8—Effect of circulation time on the wellhead fluid inlet/exit temperature.

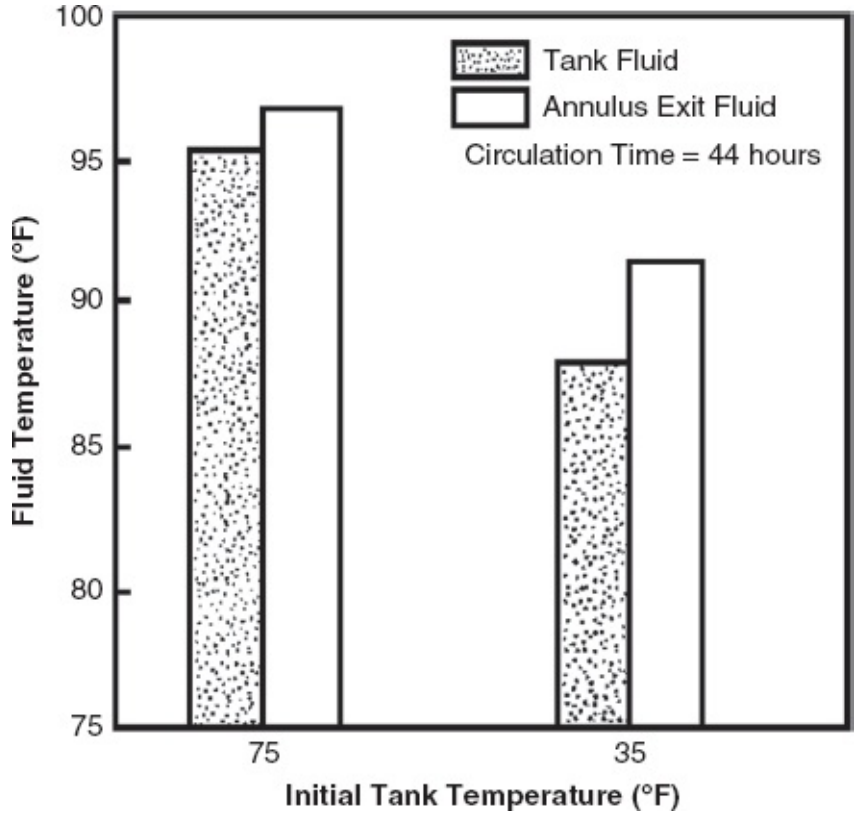

Fig. 11.9—Influence of initial tank fluid temperature on the final fluid temperatures.

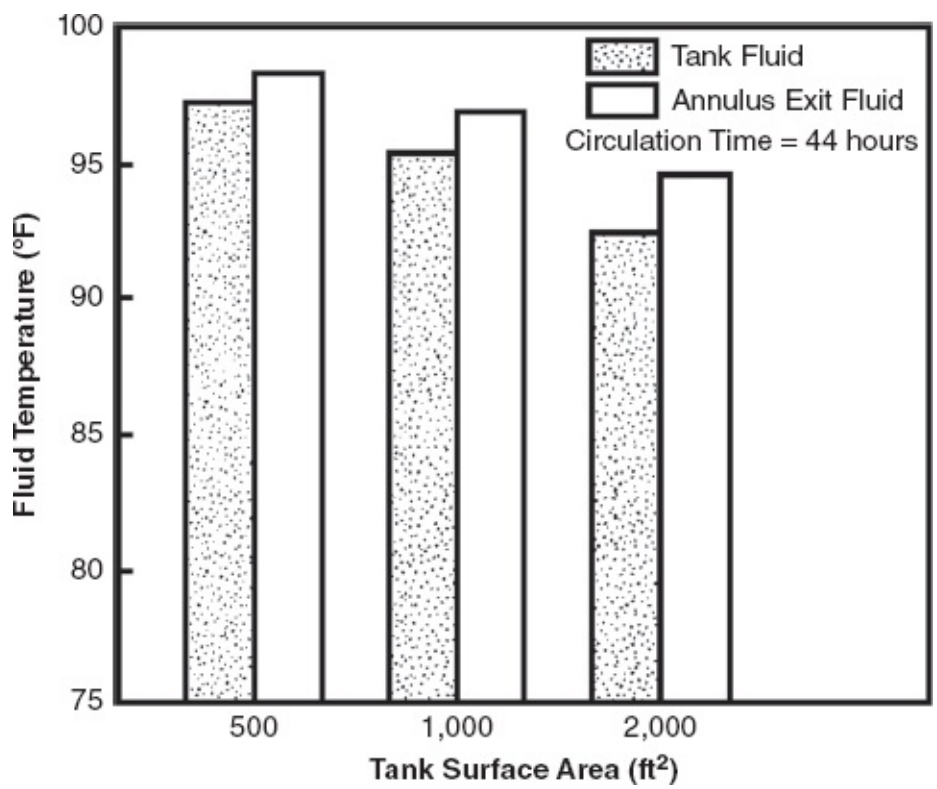

Fig. 11.10—Final fluid temperatures are insensitive to the heattransfer area.

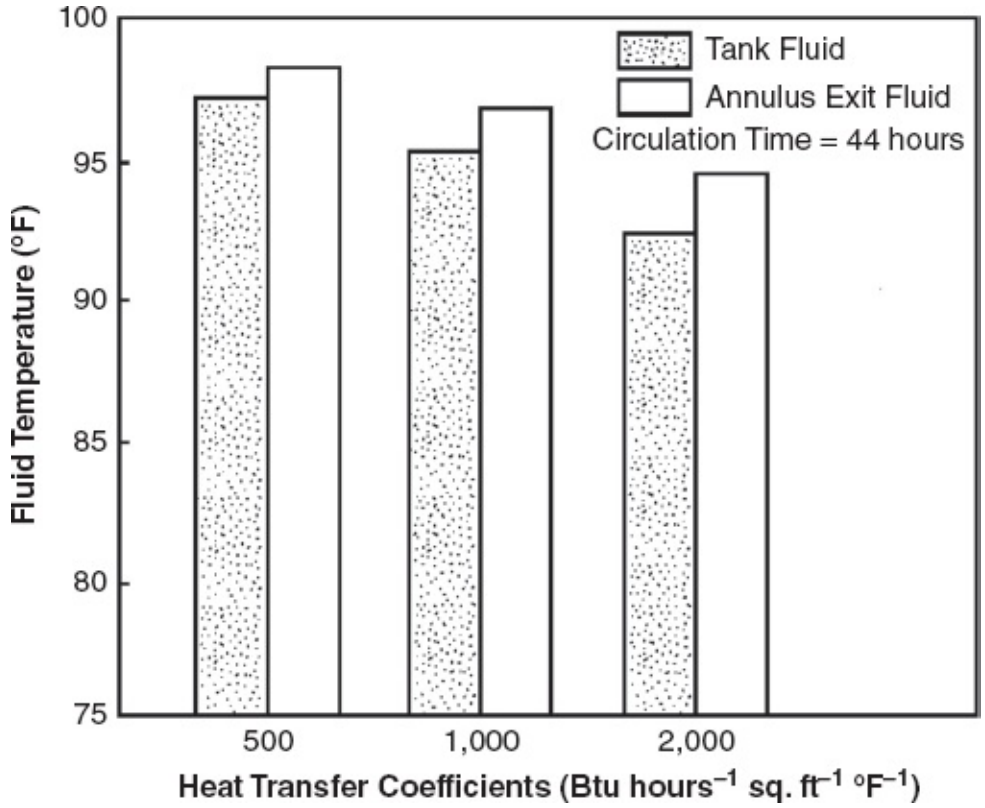

Fig. 11.11—Final fluid temperatures are insensitive to heat-transfer coefficients.

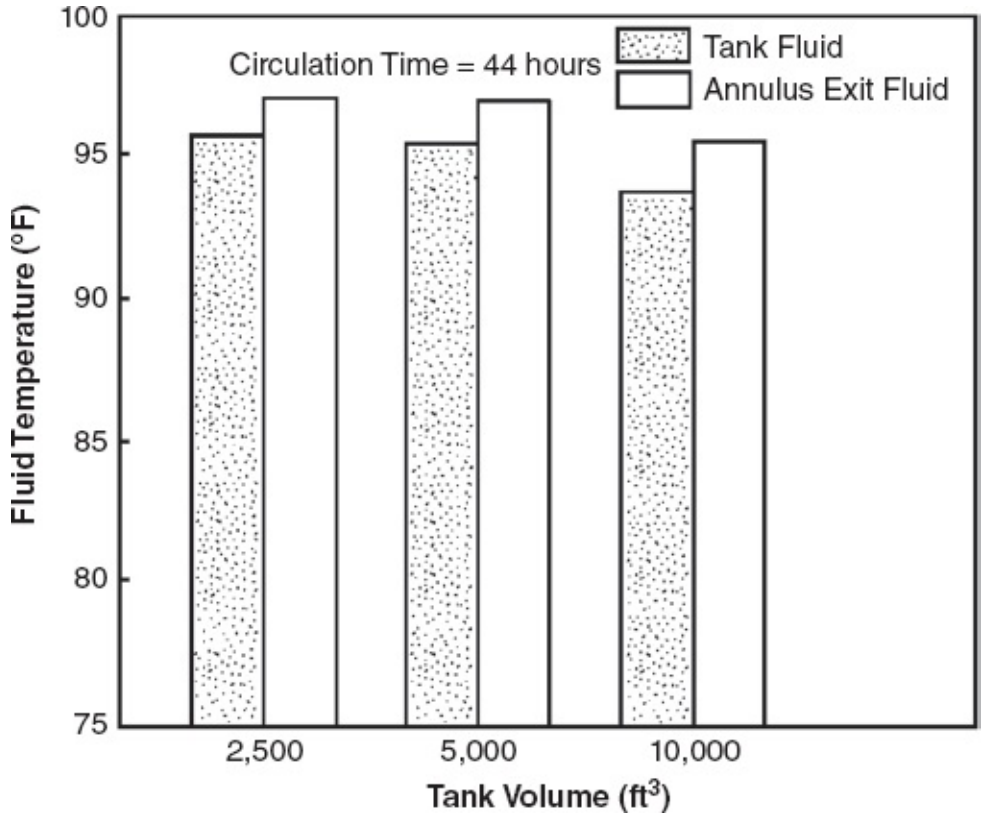

Fig. 11.12—Final fluid temperatures are insensitive to the tank volume.

***Heat-Flux Variation*.** The base case illustrated in the last subsection is used here

to show the effect of variable heat flux on circulating-fluid temperature. In these applications, we used a constant wellbore inlet temperature of 75°F: that is, a constant tank temperature. **Fig. 11.13** shows the temperature profile for the case of forward flow after 44 hours of circulation. The bottomhole temperature, for the case that accounts for variable heat flux, is approximately 7°F (approximately 3.5%) higher than when heat flux is assumed constant. The difference would be more pronounced in deeper wells with higher temperature differentials between the wellhead and the bottom of the hole. Note that the two profiles are quite similar near the wellhead, and the difference becomes significant only near the bottom. **Fig. 11.14** shows a similar case for the reverse-circulation case. Here, the variable heat flux appears to have negligible effect on the estimated temperature in both conduits.

***Field Example 11.1*.** To illustrate application of the model discussed (Eqs. 11.10 or 11.11), we used the data of Davies et al. (1994) for both cases. They reported wellhead or inlet fluid temperature with inlet flow rate variations in Case 1. For simplicity, we attempted to reproduce most of the measured data beyond the initial 100 minutes into the circulation. Because detailed reporting of individual parameters was lacking, we estimated the constants Ω and Y with Eqs. 11.8 and 11.9, respectively.

***Solution*.** To perform this calculation, we observed that the tank fluid temperatures at the start of the first (3 bbl/min) and the second (7 bbl/min) circulation rates were 30° and 32.5°C, respectively. For the second circulation period, the fluid attained an asymptotic value, T_{ae} = 46°C. A simple optimization procedure led to a Ω value of 0.025 for the second period. Because Ω is directly proportional to the circulation rate w, one obtains Ω of 0.01071 (= 0.025 × 3/7) for the first circulation period. In this way, we obtain the lumped parameters of the model, leading to a very satisfactory match, as shown in **Fig. 11.15.**

We did a similar analysis for Case 2. Here, we considered the late-time data only. The reported data show a constant value of 18°C at the inlet for approximately 2 hours before rising sharply to 40°C. This initial temperature transient reflects the travel time the fluid requires to return to the surface in this 16,400-ft well. Because the model presupposes steady-state circulation rates, mismatch results at early times. However, good agreement results beyond 1 hour of circulation, as **Fig. 11.16** illustrates. **Fig. 11.17** exhibits the quality of match obtained in the entire borehole. Although the overall trend has been captured by simulation, a more desirable agreement eludes us. This discrepancy is expected to occur because measurements were made after the cessation of circulation, whereas the model computes temperature during circulation. Consequently, we expected generally higher measured temperature, especially at shallower depths, as the wellbore fluid gained heat from the formation. Note that good agreement of the inlet or tank temperature implies good agreement in the downhole dynamic temperature.

11.1.7 Discussion. Many variables significantly affect wellbore temperature distribution during fluid circulation. These variables include fluid heat capacity and

density, inlet temperature, geothermal gradient, formation thermal conductivity, well depth, and circulation time and rate. In Section 11.1, we presented simple algebraic solutions, involving all these variables as input parameters, which are adaptable for simple spreadsheet calculations.

From a heat-transfer viewpoint, a wellbore with a uniform hydraulic radius is quite adequate and thus allowance for multiple casing strings and a string of drill collars is unnecessary. Therefore, the inability to easily include multiple casing strings is not a limitation of the analytical approach presented here. Although not discussed explicitly, various T_D models can be used (in Eq. 11.3) en route to solving the temperature equations. However, our preference is to use the model presented by Hasan and Kabir (1994a) because it encompasses the entire time domain of interest.

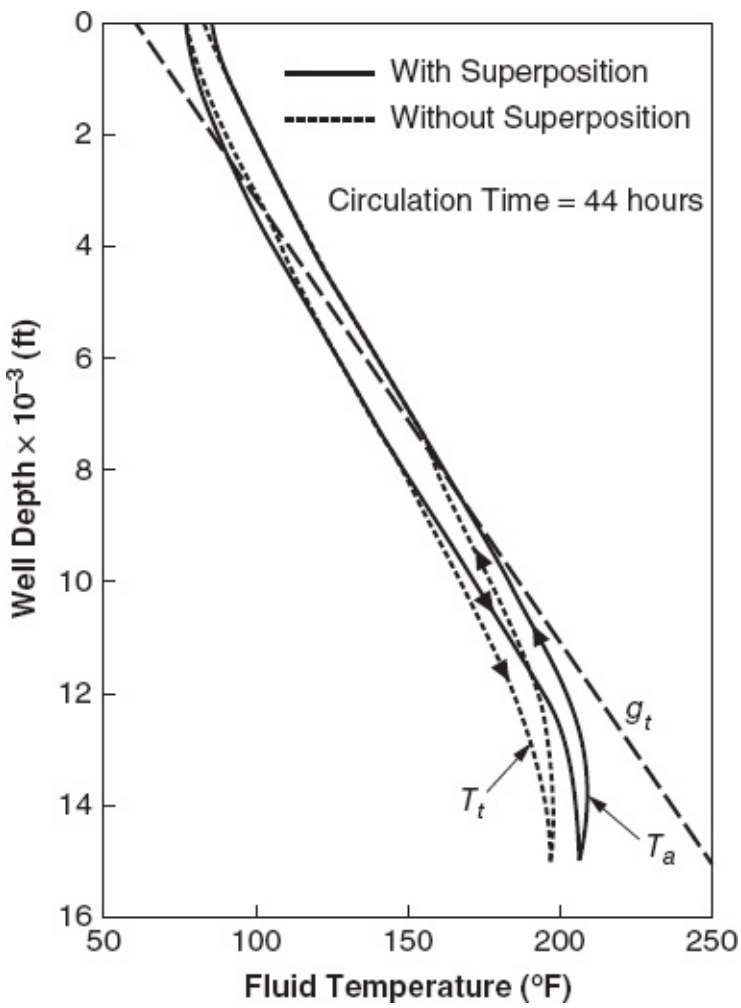

Fig. 11.13—Pronounced temperature-superposition effect during forward circulation.

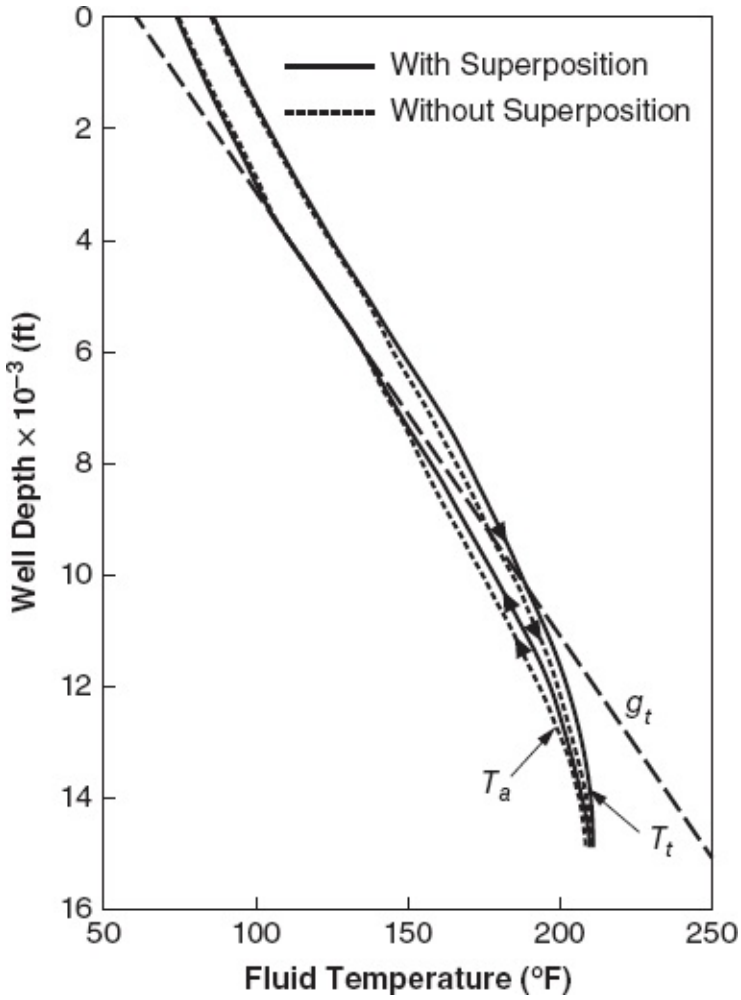

Fig. 11.14—Minimal temperature-superposition effect during reverse circulation.

11.1.8 Fluid Circulation Temperature Summary. In Section 11.1, we discussed two approaches for computing fluid temperature profiles as a function of time during fluid circulation in both conduits. Both the forward- and the reverse-circulation cases are considered in the formulations. In the first approach, we showed how the variable inlet fluid temperature could be modeled; in the second, we account for variable heat flux, leading to a fully transient model. Specifically, on the basis of our computational results and field testing, we observed that

- Increasing the inlet fluid temperature results in a much higher exit temperature than obtained for the constant inlet temperature case.
- A cold tank gains considerable heat with increasing circulation time—heat-transfer parameters, such as the tank's cross-sectional area, volume, and heat-transfer coefficient, appear to have a marginal impact on fluid temperature profiles if we allow for a long circulation time.
- A somewhat higher temperature is attained at the bottom of the hole when the variable heat flux is accounted for throughout the wellbore for the forward-circulation case; however, no significant temperature difference occurs for the reverse-circulation situation—perhaps the variable heat flux boundary condition

is of limited importance for the flow problem at hand.

- Field examples demonstrate the usefulness of the proposed model, and in particular we showed that the tank fluid and downhole temperatures could be computed accurately even without precise knowledge of various heat-transfer parameters.

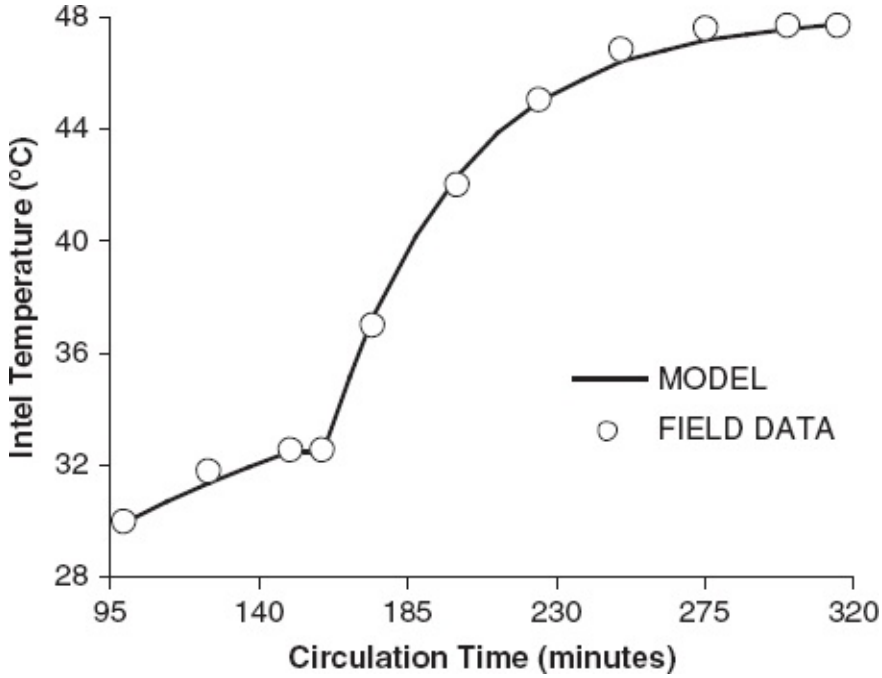

Fig. 11.15—Matching inlet fluid temperature, Davies et al. (1994) Case-1 data.

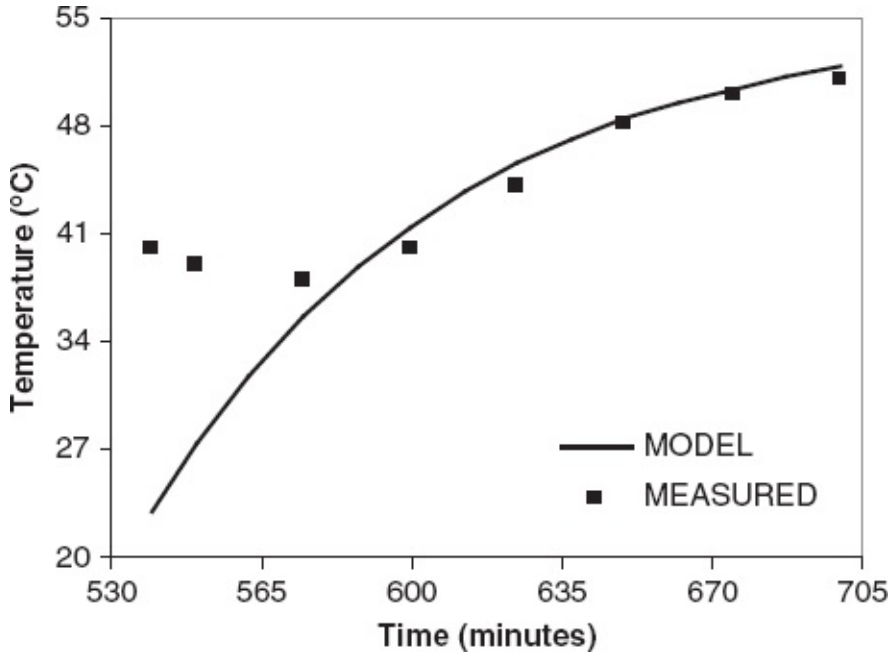

Fig. 11.16—Matching inlet fluid temperature, Davies et al. (1994) Case-2 data.

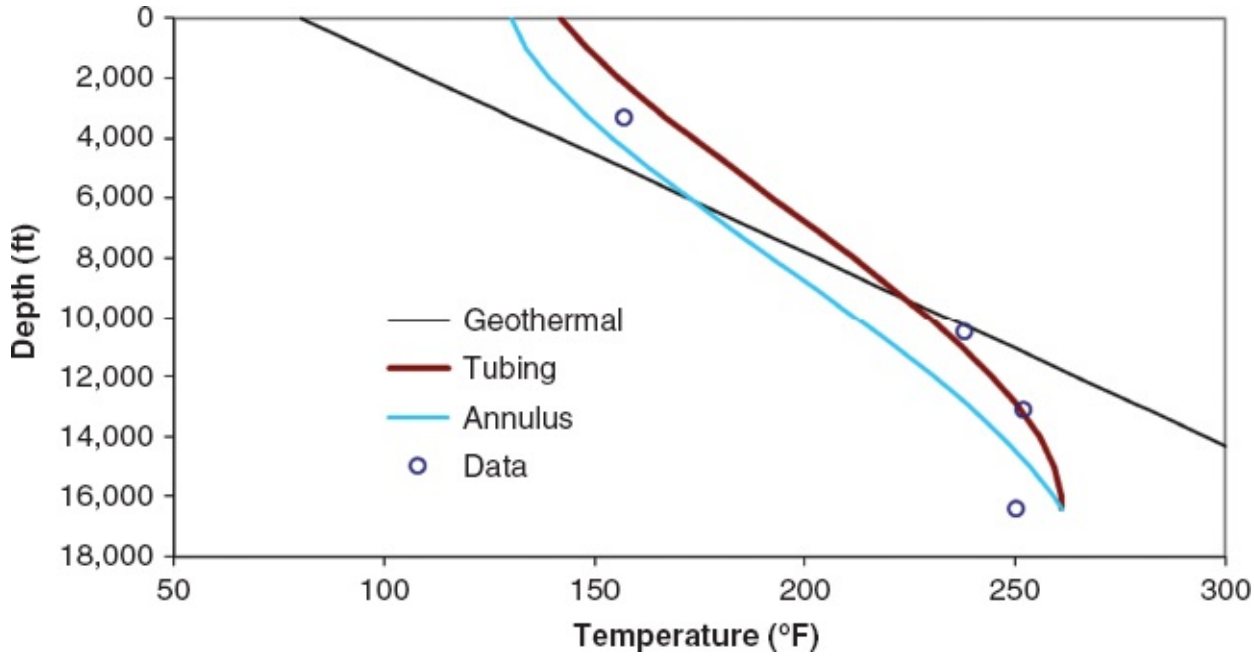

Fig. 11.17—Matching downhole fluid temperature, Davies et al. (1994) Case-2 data.

11.2 Static Formation Temperature

11.2.1. Introduction. Geothermal gradient is a cornerstone to many engineering analyses. An accurate estimation of the static formation temperature (T_{ei}) is required for designing cementing programs, for evaluating formation water resistivity for openhole log analysis, for exploration mapping and casedhole temperature logging, and for estimating heat content in geothermal reservoirs. Formation temperature is also critically important when transient simulations are made using a coupled wellbore/reservoir simulator, as discussed in Chapter 9. Stakes increase when well tests are interpreted using both pressure and temperature transients. Yet, systematic methods to arrive at such a gradient in most field evaluation are ad hoc at best. In many instances, the sources for temperature data are logs and/or formation testers in an openhole environment, and drillstem tests in casedhole situations. Formation testers and drillstem tests provide the necessary ingredients by way of transient testing at a certain depth. But the same is not necessarily true for openhole logs unless multiple passes are made to collect time-dependent temperature data for extrapolation. In this study, we probed the use of distributed temperature sensors in estimating static and dynamic temperature gradients.

These needs have prompted many to estimate T_{ei} from stagnant fluid temperature in open- and casedhole situations. Mud circulated during drilling causes considerable cooling of the formation around the well. Therefore, temperatures recorded after the cessation of mud circulation are always lower than the static formation temperature. Conversely, producing fluid generally causes significant heating of the formation around the wellbore. Depending on the contrast between the mud/fluid and formation temperatures and thermal characteristics of the reservoir, several days or weeks may be required to attain complete thermal equilibrium between the wellbore fluid and the

formation. Such long waits are usually economically prohibitive. Therefore, practicality demands discerning T_{ei} from transient temperature data after the cessation of mud circulation or fluid production. In this process, effects of thermal disturbances, introduced earlier by the mud/fluid, must be addressed. In the following subsections, we first discuss approaches used to estimate T_{ei} in an openhole situation after mud circulation has ceased. The approach for stagnant fluid in cased holes is discussed thereafter.

Two approaches have emerged for estimating T_{ei} in an openhole situation. In the first approach, forward simulation is attempted by accounting for changes in mud composition, inlet temperature of mud, circulation rate, and rock physical properties for the entire borehole. Methods of Edwardson et al. (1962), Holmes and Swift (1970), and Wooley (1980), among others, are cases in point.

In the second approach, inverse solution is sought of the measured mud-temperature transient data, gathered at the bottom section of the borehole, which is analogous to pressure-transient analysis. This approach is convenient because of its simplicity and is rooted in the line-source solution proposed by Bullard (1947). In the petroleum literature, Dowdle and Cobb (1975) popularized this method in an analogy to Horner's (1951) method of analyzing pressure-transient data. In this approach, the circulation time is presumed long enough for the logarithmic approximation of the *Ei* (exponential integral) function to be valid. Unfortunately, the line-source assumption is usually much less appropriate for thermal transients than for pressure transients. In other words, this popular method has limitations. Circumventing those limitations, solutions of different complexity offered by Cao et al. (1988) and Shen and Beck (1986) are now available. We present some simplified approaches for evaluating T_{ei} in this section.

All these methods presuppose that the data are free of errors. Actually, a gauge carrier can store or release heat just as the tubulars and cement sheath do. This heat storage leads to distortion of early-time temperature data. Of course, this storage issue is far less problematic in an openhole situation than in a cased hole. We will show that when temperature data are gathered during pressure-transient testing in a cased borehole, they lend themselves to proper analysis. A pragmatic approach of data gathering and data analysis, after the diagnosis and exclusion of storage-free data, will be presented.

11.2.2. Analysis of Openhole Data. A simple model, reported by Hasan and Kabir (1994a), is used for estimating the static formation temperature T_{ei} from openhole temperature logs. **Fig. 11.18** presents a schematic of the temperature measurements made in an open hole after mud circulation. This model, based on an unsteady-state energy balance, is given in Appendix 11-C. The analysis leads to the following expression for the mud temperature T_{ws}, in terms of the static formation temperature T_{ei} and a time function $F(t_D)$:

$$T_{ws} = T_{ei} - C_o^{*} F(t_D). \qquad (11.17)$$

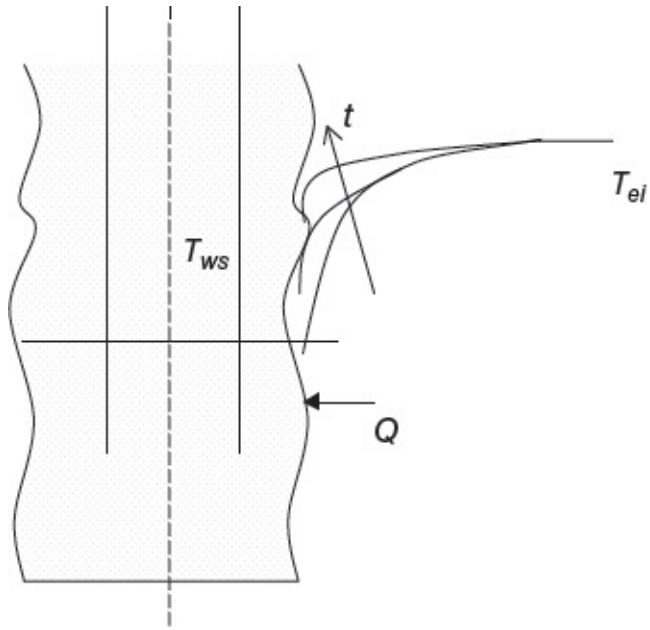

Fig. 11.18—Schematic of temperature rise after mud circulation.

In Eq. 11.17, also shown in Appendix 11-C as Eq. 11-C-16, C_o'' depends on the temperature difference between the mud initial temperature and formation temperature; that is, $C_o'' = (T_{ei} - T_{wso})e^m$, where. $F(t_D)$ in Eq. 11.17 is composed of various functions of dimensionless time, t_D (= $k_m t_p/\rho\, c_m r_w^2$, where m represents mud) and is presented in Appendix 11-C.

Eq. 11.17 is valid only as long as t_D is less than 1.5, which corresponds to approximately 6 real hours for a typical formation. Note that the formulation includes both conductive and convective heat-transfer mechanisms. Another assumption made in deriving Eq. 11.17 is that the formation temperature distribution remains undisturbed during mud circulation. In reality, however, mud circulation causes a general decrease in the formation temperature around the wellbore. Therefore, the assumption is untenable in general, and it is only approximately true if the mud circulation time is short.

Method One: Rigorous Approach. To account for the effect of mud circulation on the formation temperature distribution, we can apply the superposition principle. Here, for a total dimensionless mud circulation time t_{pD}, Eq. 11.18 applies with t_{pD} replacing t_D. We write the following expression for the mud temperature for a period of Δt_D because of the cessation of circulation.

$$T_{ws} = T_{ei} - C_o''\left[F\left(t_{pD} + \Delta t_D\right) - F\left(\Delta t_D\right)\right]. \quad (11.18)$$

The analysis just presented assumes that all heat flowing from the reservoir is absorbed by the mud in the wellbore. This is untrue because some of the heat goes to gradually raising the near-wellbore formation temperature as the equilibrium is approached. The continuous decay of heat gain (or loss) from the formation to the

mud poses some theoretical problems with any method for estimating T_{ei}. However, note that the heat-transfer rate following mud circulation is negligible compared with that during mud circulation. Thus, Eq. 11.18 is likely to be quite sound for most practical cases.

Eq. 11.18 suggests that a plot of T_{ws} vs. $F(t_{pD} + \Delta t_D) - F(\Delta t_D)$ should result in a straight line, with the intercept yielding the static formation temperature. To evaluate $F(t_{pD} + \Delta t_D)$ and $F(\Delta t_D)$ for use in Eq. 11.18, estimates of three constants—C_1, C_2, and a—are needed; these constants may be calculated with Eqs. 11-C-13, 11-C-14, and 11-C-21 from Appendix 11-C, when appropriate property values for the mud and formation are known. The estimation of free convective heat-transfer coefficient U for the wellbore mud presents a challenge. However, reasonably accurate values may be calculated from available correlations. When data are sketchy, Eq. 11-C-16, in Appendix 11-C, may still be applied with initial guesses for the constants, C_1 and C_2, and a regression analysis would yield values of T_{ei} and C_o". Mud temperatures can then be computed with standard deviation. This procedure can be repeated for a set of values of the constants. The values of the constants exhibiting the lowest standard deviation are then selected as the final solution.

Method Two: Exponential Approach. One approximation results if we assume parameter L'_R, given by Eq. 11-C-6, is a constant. This would be true for a combination of small values of t_D and low heat-transfer coefficient for the mud. In such a case, integrating Eq. 11-C-5 between $t = 0$ (T_{ei}) to $t = t$ (T_{ws}) yields

$$T_{ws} = T_{ei} - (T_{ei} - T_{wso})\, e^{-tL'_R}. \qquad (11.19)$$

Eq. 11.19 shows that a plot of mud temperature against $e^{-tL'_R}$ should result in a straight line with the intercept yielding the static formation temperature. Use of superposition to account for mud circulation before shut-in does not change the form of Eq. 11.19 because of the exponential nature of the equation. Therefore, with superposition,

$$T_{ws} = T_{ei} - (T_{ei} - T_{wso})\left(e^{-tL'_R} - 1\right) e^{-L'_R \Delta t}. \qquad (11.20)$$

Note that the initial mud temperature, T_{wso}, need not be known; it may be estimated from the slope of the curve. However, the procedure requires an estimate of L'_R. When data are unavailable, an optimization procedure may be used.

Method Three: Log-Linear Approximation. Noting the similarities between the differential equations for temperature and pressure distribution in the formation, Dowdle and Cobb (1975) suggested that the transient response of fluid temperature in the wellbore may be used to estimate T_{ei}, analogous to estimating initial reservoir pressure from a pressure-buildup analysis. If the mud has been circulating long enough, the logarithmic approximation to formation temperature distribution would apply, and the Ramey (1962) $f(t)$ function and the dimensionless temperature function,

T_D, are both approximated by Eq. 11-C-8. If we further assume that $T_{wb} = T_{ws}$, the defining equation for T_D may then be written in terms of T_{ws} as

$$T_{ws} = T_{ei} - BT_D, \qquad (11.21)$$

where

$$B = \frac{MQ}{2\pi k_e}. \qquad (11.22)$$

Therefore, for a total dimensionless mud circulation time, t_{pD}, we can combine Eqs. 11.22 and 11-C-8 to write

$$T_{ws} = T_{ei} - B(0.406 + 0.5\ln t_D). \qquad (11.23)$$

Note that the second bracketed term of Eq. 11-C-8 has been omitted simply because the equation becomes the line-source approximation or the Ramey (1962) $f(t)$ function at large times, as discussed by Cao et al. (1988).

Applying the superposition principle, we may write the expression for the mud temperature for a period of Δt_D after the cessation of circulation as

$$\begin{aligned} T_{ws} - T_{ei} &= -B\left(T_{pD} + \Delta T_D\right) + \Delta T_D \\ &= -0.5B\ln\left(\frac{t_p + \Delta t}{\Delta t}\right) \end{aligned} \qquad (11.24)$$

Therefore, a plot of the mud temperature against log of time ratio, $(t_p + \Delta t)/\Delta t$, should be linear. The intercept at $(t_p + \Delta t)/\Delta t = 1.0$ (that is, at very large At) of such a line should yield T_{ei}. We note that the method presupposes heat exchange between the formation and wellbore to be zero after the mud circulation has ceased. While this assumption is reasonable at very long circulation times, it may be untenable at intermediate times when significant heat transfer may occur.

In addition to the assumption of instantaneous cessation of heat flow with mud circulation, the method uses the log-linear approximation of Ramey's $f(t)$ solution, which is acceptable only at long times. In most cases of newly drilled holes, mud circulation is discontinued almost immediately after drilling. The data reported by Dowdle and Cobb (1975) show typical circulation time between 1 to 10 hours. For typical formation and fluid properties, such circulation times are equivalent to the dimensionless production time, t_{pD}, between 0.25 and 2.5 hours. Unfortunately, the log-linear approximation is invalid for such short periods. In addition, note that we have assumed a rather high heat-transfer coefficient for the mud, so the mud temperature at the wellbore center T_w may be assumed to be equal to the temperature at the interface of the wellbore and the formation, T_{wb}. This assumption is not robust for high-viscosity muds because of low convective heat transfer.

Method Four: Square-Root-of-Time Approximation. Another approach that

relies on the principle of superposition uses Eq. 11-C-16. But instead of using the log-linear approximation for T_D, we use Eq. 11-C-7, which represents dimensionless temperature T_D as a function of $\sqrt{t_D}$. Assuming, as in the last case, $T_{wb} = T_{ws}$, we obtain

$$T_{ei} - T_{ws} = B\left[T_D\left(t_{pD} + \Delta t_D\right) - T_D\left(\Delta t_D\right)\right]. \quad (11.25)$$

Rewriting Eq. 11.25,

$$T_{ws} = T_{ei} - 1.1282\, BF'\left(t_D\right), \quad (11.26)$$

where

$$F'(t_D) = \left(\sqrt{t_{pD} + \Delta t_D}\right)\left(1 - 0.3\sqrt{t_{pD} + \Delta t_D}\right) - \sqrt{t_{pD}}\left(1 - 0.3\sqrt{t_{pD}}\right). \quad (11.27)$$

A plot of T_{ws}, against the term in parentheses in Eq. 11.26, should yield a straight line with T_{ei} as the intercept and −1.1282 B as the slope. The major drawback of this approach is that it is applicable only to very-early-time data. Application of this approach to the data reported in **Tables 11.2 and 11.3** resulted in unrealistic numbers, except for the first data point in each set. The method is recommended only for dimensionless time less than 1.5, which translates to approximately 8 hours in a typical system.

Data Source	Methods				
	Time (Hours)	**Mud Temp. (°C)**	**Log-Linear Eq. 11.24**	**Rigorous Eq. 11.18**	**Exponential Eq. 11.20**
Shen-Beck synthetic data with T_{ei} = 80°C	2.5	56.6	55.5	57.2	57.55
	5.0	61.3	62.4	61.0	60.85
	7.5	64.3	65.4	63.9	63.65
	10.0	66.6	67.2	66.2	66.01
	15.0	69.6	69.2	69.6	69.69
	20.0	71.7	70.3	72.2	73.32
Computed static temperature,°C			74.1	78.6	78.9

Table 11.2—Comparison of static temperature computation, synthetic data.

Data Source	Methods				
	Time (hours)	**Measured Mud Temp. (°F)**	**Log-Linear Eq. 11.24**	**Rigorous Eq. 11.18**	**Exponential Eq. 11.20**
Dowdle and Cobb (1975), Set One	5.10	99	98.9	99.4	99.4

	10.30	106	105.7	104.8	104.7
	14.48	107	108.0	107.9	107.8
	18.12	110	109.2	109.9	109.9
Computed static temperature, °F			114.8	117.2	117.4
Dowdle and Cobb (1975), Set Two	8.25	241	241.7	242.1	242.1
	11.00	257	255.2	254.4	254.2
	13.50	262	263.1	263.5	263.5
Computed static temperature, °F			303.4	315.1	313.9
Roux et al. (1980), Set One	7.0	286	286.7	287.1	287.0
	11.0	308	305.6	304.8	304.9
	13.5	312	313.7	314.1	314
Computed static temperature, °F			364.0	382.0	363.2
Roux et al. (1980), Set Two	14.3	183	182.5	182.8	182.6
	22.3	194	195.2	194.6	194.9
	29.3	202	201.0	201.6	201.3
Computed static temperature, °F			221.6	213.2	212.1

Table 11.3—Comparison of static temperature computation, field data.

Although use of Eq. 11-C-7 is inherent in formulation of Eqs. 11-C-10 and 11.26, there is an important difference between the two equations. The development of Eq. 11-C-10 involved a treatment of the convolution integral, which is analogous to the pressure/rate problem solved in well testing. Thus, Eq. 11-C-10 is rigorous for the heat flow problem in question. On the other hand, the formulation of Eq. 11.26 circumvents the convolution operation, thereby limiting its application to early-time data, $t_D < 1.5$.

Example Application 11.1—Synthetic Example 1. We used the Shen and Beck (1986) synthetic data to verify the model just presented. Thereafter, oilwell data of Dowdle and Cobb (1975) and geothermal well data of Roux et al. (1980) illustrate applications of the recommended approach. Both exponential and log-linear approximations were also considered in these analyses.

***Solution*.** To generate their data, Shen and Beck (1986) used a constant temperature wellbore model, without convective heat transfer. Most of the property values were available, which were used to calculate constants C_1 and C_2. The overall-heat-transfer coefficient U in our model was approximated with $U = k_m/r_w$. The results are shown in Table 11.2 and **Fig. 11.19.** We must emphasize that the model used by Shen and Beck to generate the data in Table 11.2 assumes only conductive heat transfer in the mud. Therefore, Eq. 11.17 will not agree completely with these

synthetic data. We think that convective heat transfer in mud is a more accurate representation of reality, especially when large temperature differentials exist between the inlet mud and the formation; geothermal and high-temperature reservoirs are cases in point. However, the excellent agreement between the model and data, as shown in Table 11.2 and Fig. 11.18, indicates that differences in one particular aspect of modeling are not critical for this situation. **Figs. 11.20 and 11.21** show how T_{ei} values were obtained with the simple graphical technique.

Note that the exponential approximation performed very well in this case. The underlying assumption of the exponential approximation is that L_R' is time invariant, which is true if the $1/rU$ term dominates the T_D/k_e term in Eq. 11-C-6. Because T_D increases slowly with t_D, the approximation works reasonably well, as it did in this case. A U value of 1 Btu-hr^{-1}-ft^{-2}-°F^{-1} was used along with an average value of T_D of unity to compute L_R'. As expected, the log-linear approximation performed less satisfactorily because the early-time data were used for extrapolation. Indeed, the T_{ei} value was lower than the true solution by as much as 6°C.

Approximately half the data in Table 11.2 involved dimensionless times larger than 1.5, for which the proposed solution is not strictly applicable. Nonetheless, the agreement of the method's predictions is quite encouraging. The physical explanation lies in the convolution approach as used here at early times when most heat transfer occurs. At late time, the inaccuracy of Eq. 11-C-7, in Appendix 11-C, is not necessarily magnified because the heat-transfer rate diminishes. The primary application of this model is to early-time data when other available methods are of doubtful validity.

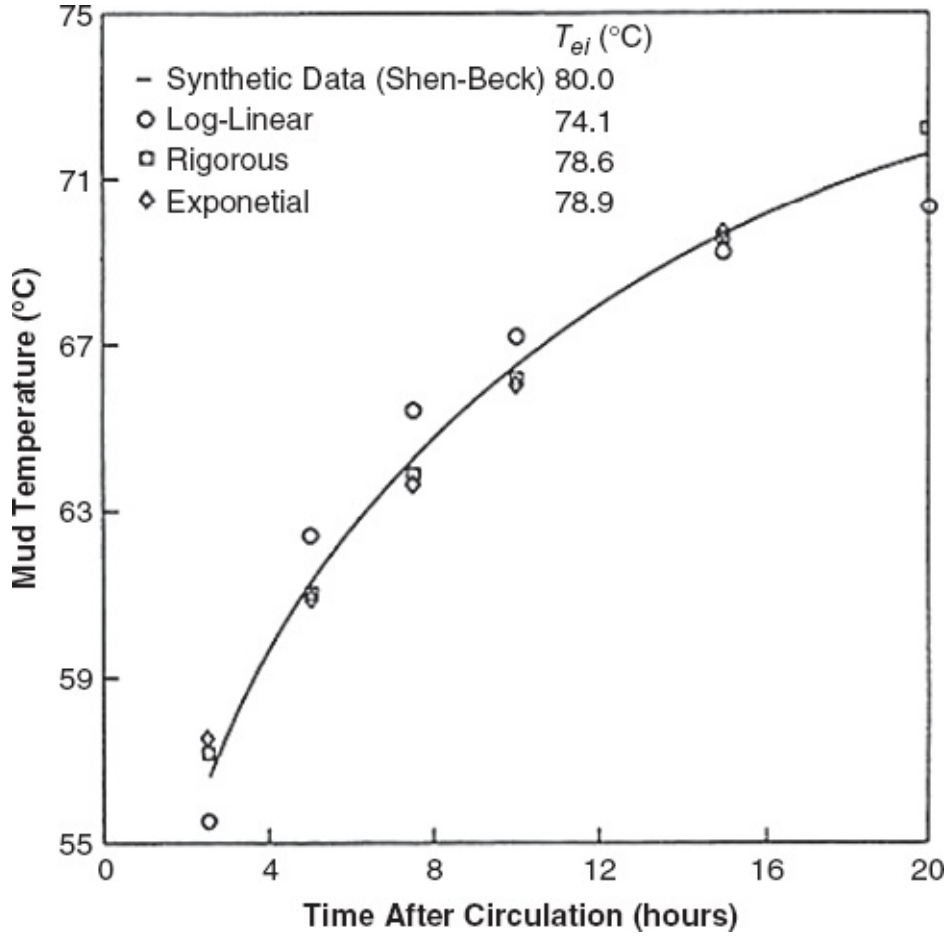

Fig. 11.19—Comparison of different methods with synthetic data.

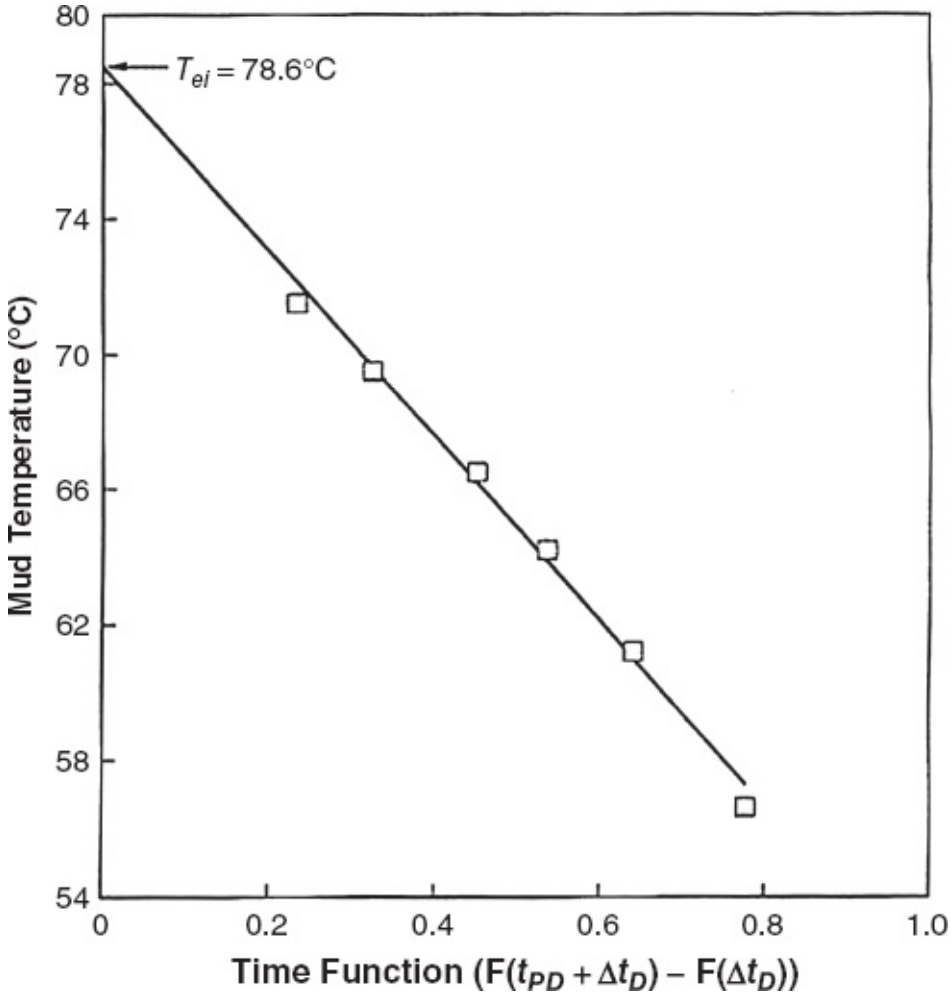

Fig. 11.20—Estimating static formation temperature (rigorous method).

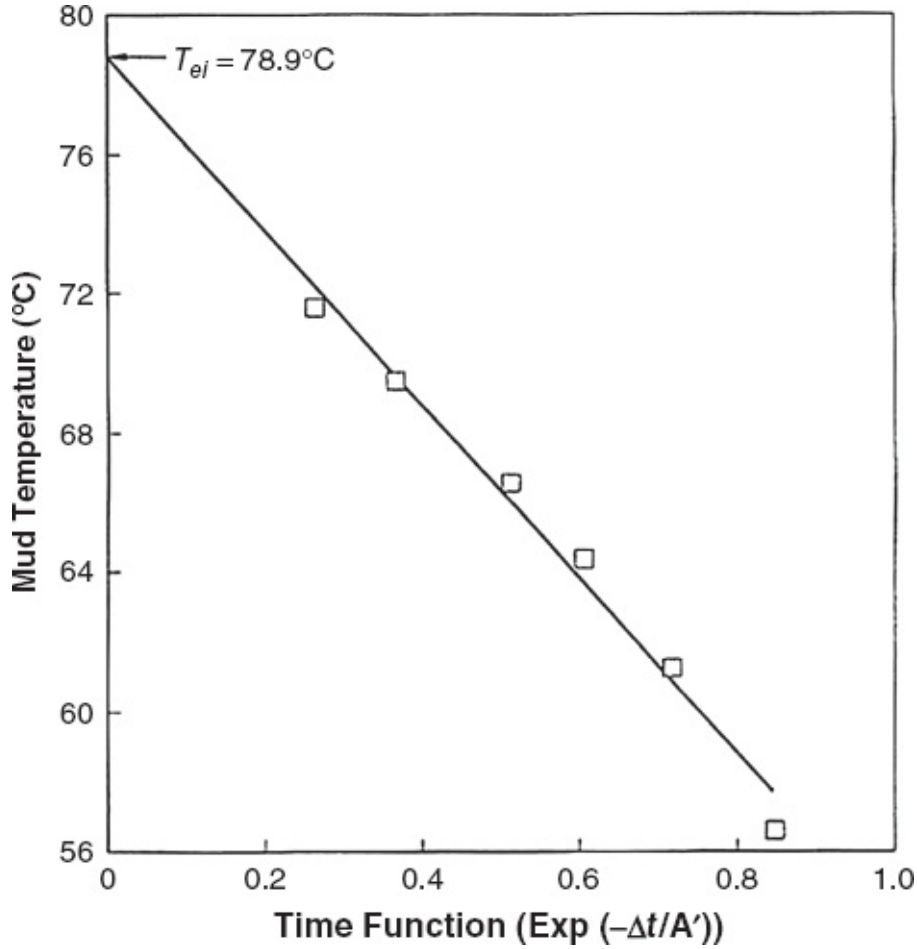

Fig. 11.21—Estimating static formation temperature (exponential method).

Example Application 11.2—Field Example 1. Field data reported by Dowdle and Cobb (1975) and by Roux et al. (1980) were used to verify the model and also to compare the results with other approximate solutions. Because of lack of various property values for the mud and formation, we supposed the mud to have the properties of water and a U of 1 Btu-hr^{-1}-ft^{-2}-°F^{-1}. The rock was assumed to have a conductivity of 1.4 Btu-hr^{-1}-ft^{-1}-°F^{-1} and a thermal diffusivity of 0.04 hr-ft^{-2}. These property values, with the exception being k_e, did not influence the solution outcome in a significant way. Table 11.3 and **Fig. 11.22** show good agreement between the model results and the data.

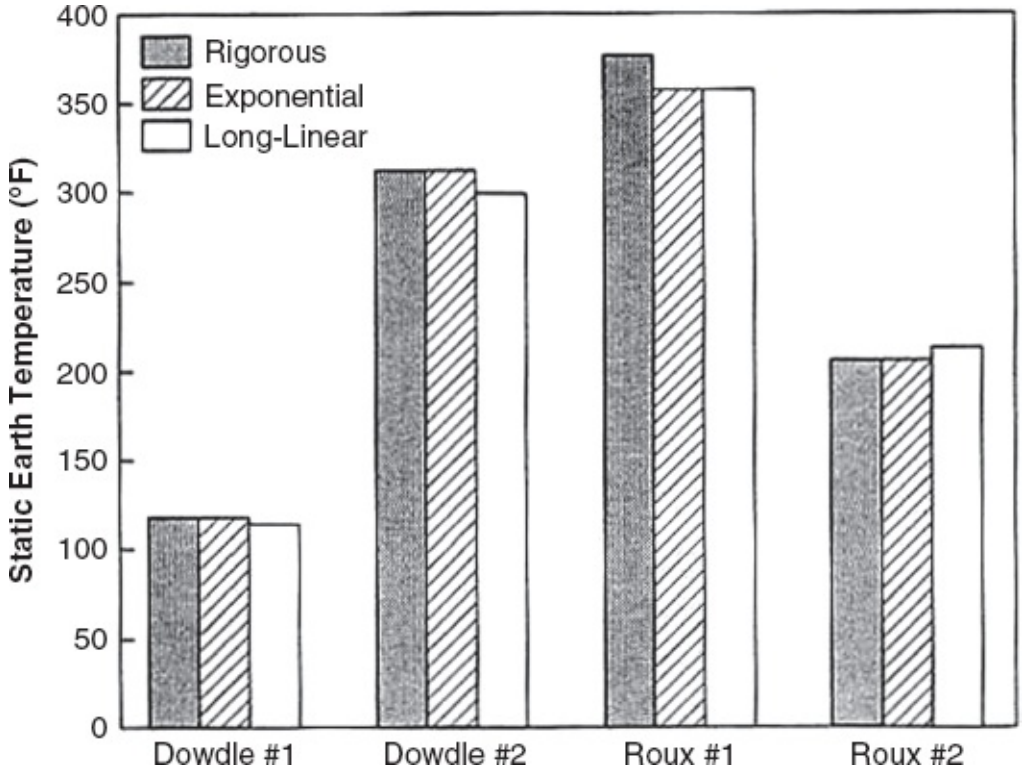

Fig. 11.22—Comparison of static formation temperature evaluated by various methods.

***Solution*.** Because the true formation temperatures are unknown in these field data sets, absolute accuracy of the rigorous approach (Eq. 11.18) cannot be attested. However, model validation suggests that Eq. 11.18 should yield results very close to the true values. Inspection of Table 11.3 suggests that the log-linear approximation underestimates the true solution, with the exception of the last data set. This general underestimation of Eq. 11.24 was also noted by Roux et al. (1980) and by Shen and Beck (1986). A similar trend also persists for the exponential approach, as given by Eq. 11.20.

We point out that the results, obtained for the Dowdle-Cobb and exponential approximation methods, which are presented in Tables 11.2 and 11.3, reflect the mud temperature values obtained following a regression analysis of the data. So, the reasonable agreement between these results is not surprising. In contrast, the temperature values were computed with the appropriate values for the mud-formation systems in the case of the proposed methods, Eqs. 11.18 and 11.20.

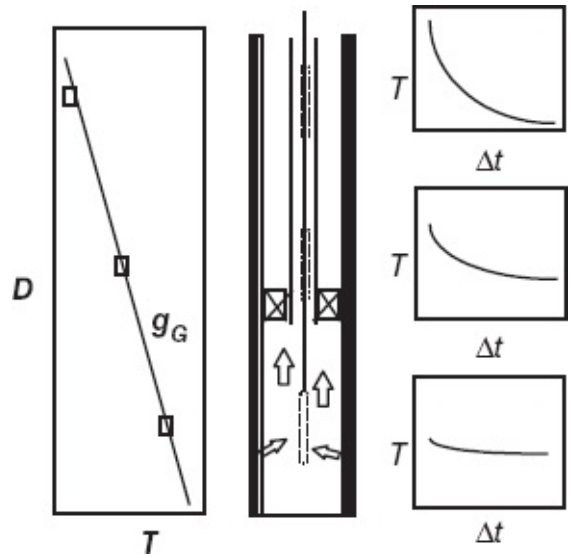

Fig. 11.23—Schematic of temperature transients at various well depths.

11.2.3 Analysis of Casedhole Data. Problems common to application of all the analytic methods previously discussed revolve around the quality and the quantity of data collected in an openhole situation. In other words, sparse data gathering with each logging trip makes any method difficult to apply. In contrast, when data are gathered in a casedhole environment, such as during pressure-transient testing, continuous data gathering over longer duration makes analysis less challenging.

Fig. 11.23 schematically illustrates how the temperature perturbation is related to gauge location during shut-in testing in an oil well. Shallower depths increase the temperature contrast between the fluid and its surroundings, leading to pronounced temperature excursions. Heating of liquid or cooling of gas, collectively known as Joule-Thomson (J-T) effects, can also lead to large temperature perturbations even if the probe is located at the producing interval. The severity of temperature contrast depends directly on the degree of pressure drawdown involved. In this context, a damaged well in a formation with very high flow capacity can induce a large pressure drop with attendant large temperature change.

Next, we present the semianalytic, rectangular hyperbola method for obtaining T_{ei}. The method is verified by using synthetic data, and its application is shown by using field data. We also illustrate how discrete T_{ei} data can be pieced together to obtain a region's geothermal gradient.

Hyperbola Method. As shown elsewhere (Kabir et al. 1997), the temperature decay equation during a pressure-buildup test can be approximated by a rectangular hyperbola during the infinite-acting period. The hyperbola equation is given by

$$(T_{ws} - a')(b' + \Delta t) = c', \quad (11.28)$$

where

$$a' = T_{ei} - \frac{m_t}{1.151}(\ln \alpha' - 2), \quad (11.29)$$

$$b' = \frac{t_p}{(\alpha' + 1)}, \quad (11.30)$$

$$c' = -\frac{4 m_t t_p}{2.303(\alpha + 1)}, \quad (11.31)$$

$$m_t = C_J \frac{162.6 q B \mu}{kh}, \quad (11.32)$$

$$C_J = \left(\frac{\partial T}{\partial p}\right)_H = -\frac{0.185}{\rho c_h}; \quad (11.33)$$

and α′ is a system parameter. Eq. 11.28 representing infinite-acting reservoir behavior is always applicable when dealing with temperature transients because the radius of investigation is only a few feet. We explore this point further while discussing field examples. Note that Eq. 11.28 may also be written as $T_{ws} = a' + c'/(b' + \Delta t)$. Therefore, when Δt approaches infinity, T_{ws} approaches a', the hyperbola's asymptote. Therefore, the parameter a' represents the reservoir temperature at infinite shutin time; that is, $a' = T_{ei}$, the static reservoir temperature.

Example Application 11.3—Synthetic Example 2. As shown in Table 11.2, we used the synthetic data of Shen and Beck (1986), generated after mud circulation, to compute T_{ei}. Because the data contained no thermal storage, as exemplified by the plateau on the derivative graph of Fig. 11.24, all six data points were included in these analyses. Fig. 11.25 presents the hyperbola and its derivative fitting the data. Although the results of the three methods used previously were close to the true value of 176°F (80°C), the hyperbola analysis gives an answer that is closest to the true value.

Also shown in Fig. 11.24 is the radius of investigation, r_i. We can write a relation for r_i by recognizing the analogy between pressure and thermal diffusion processes as

$$r_i = \sqrt{\frac{4 k_e \Delta t}{\rho_e c_e}}. \quad (11.34)$$

Typical parameter values used for the r_i computation for all examples include k_e = 1.8 Btu/(ft-hr-°F), p_e = 165 lbm/ft^3, and c_e = 0.22 Btu/(lbm-°F).

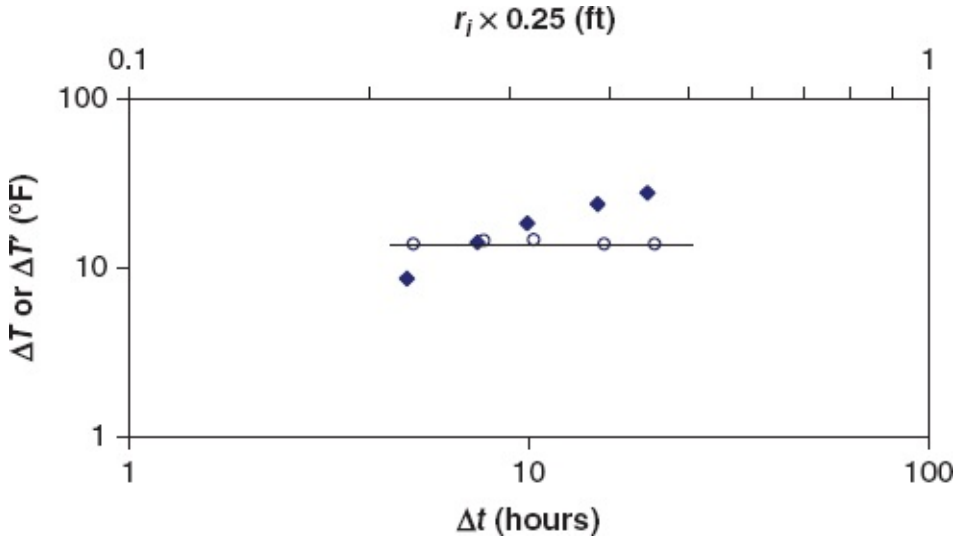

Fig. 11.24—Diagnosis of storage-free Shen-Beck synthetic data (after Shen and Beck 1986).

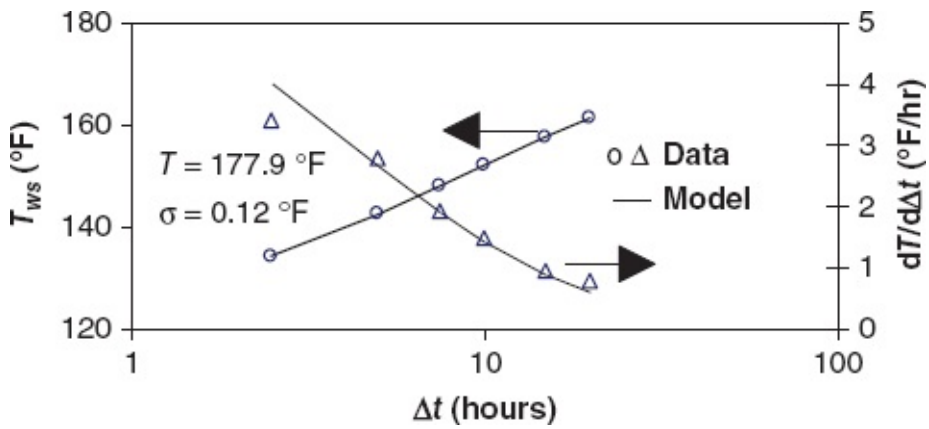

Fig. 11.25—Hyperbola analysis yields T_e, for synthetic data.

Given that in the modern era most wells are tested in a casedhole situation, analysis of transient temperature data allows estimation of T_{ei} at a given depth. The following section shows how data analysis in thermal-storage-dominated scenarios is feasible for individual wells completed in different intervals, leading to estimation of a region's geothermal gradient.

11.2.4 Establishing Geothermal Gradient. This segment presents two field studies in which geothermal gradients were established after analyzing transient temperature data in the casedhole environment in two different settings. The first setting is Kuwait, where analysis of 52 tests comprising several oil fields enabled establishing the geothermal gradient. Australia's deepwater Equus gas fields constituted the second setting, wherein distributed temperature measurements along the entire wellbore were available.

Case 1. In this segment we present two field examples in which data were gathered from two different wells in the same general area but completed in different geologic horizons. In the first example, **Fig. 11.26** presents the diagnostic log-log

graph of temperature data gathered some 2,500 ft above the midpoint of perforations in an 11,000-ft oil well. Unlike the previous synthetic example, one observes the dominating influence of thermal storage here. A derivative plateau barely appears toward the end of the test. **Fig. 11.27a** presents the semilog analysis yielding a T_{ei} value of 214.5°F with a least-squares coefficient of 0.94. In contrast, the hyperbola analysis shows a good fit beyond 15 hours, as Fig. 11.27b shows. The hyperbola-derived value of 215.1°F is in good agreement with that of the semilog analysis. However, much greater confidence can be placed on the T_{ei} value computed by the hyperbola approach because of its ability to treat a much larger data span.

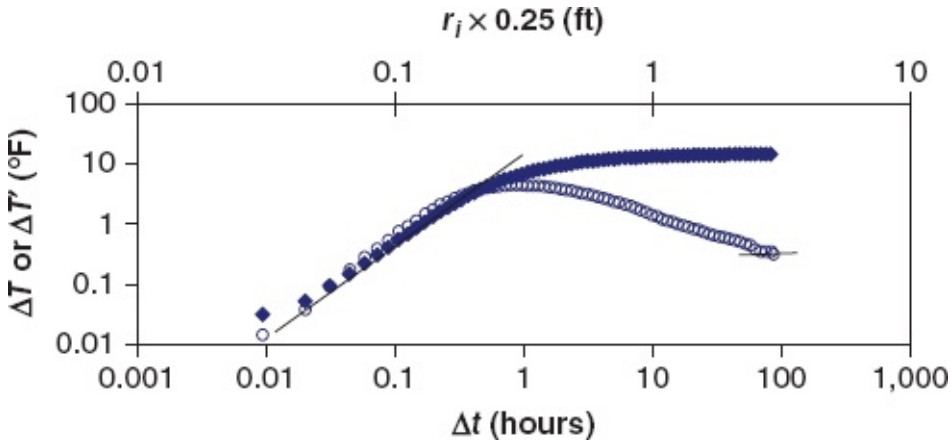

Fig. 11.26—Log-log diagnosis shows storage domination in off-bottom measurements.

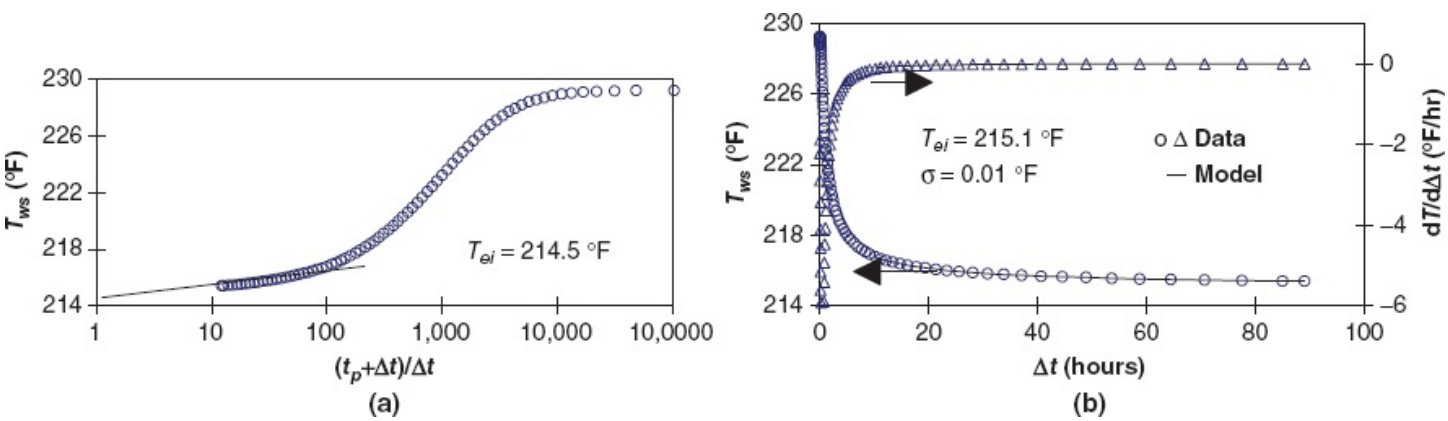

Fig. 11.27—Semilog analysis straightens a small data segment (a); hyperbola analysis fits large data span (b).

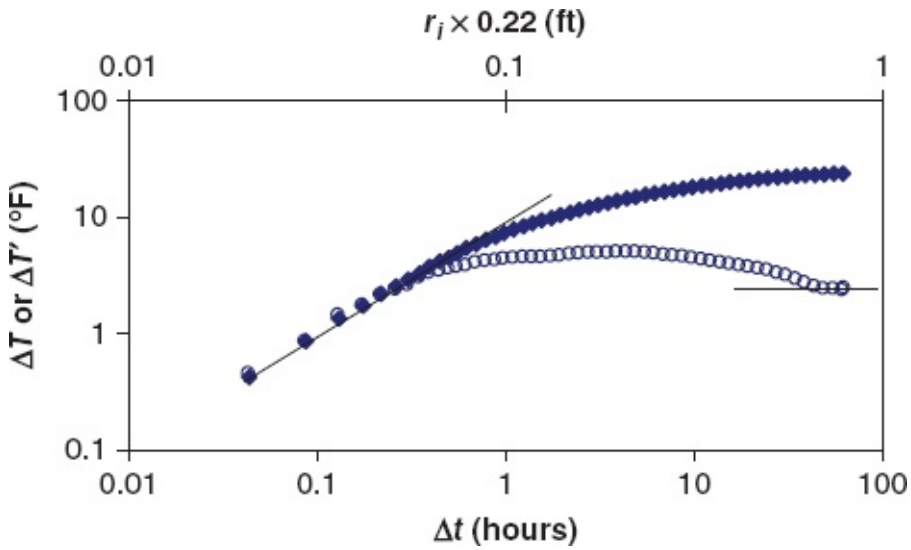

Fig. 11.28—Log-log diagnosis of a test with large J-T heating effects.

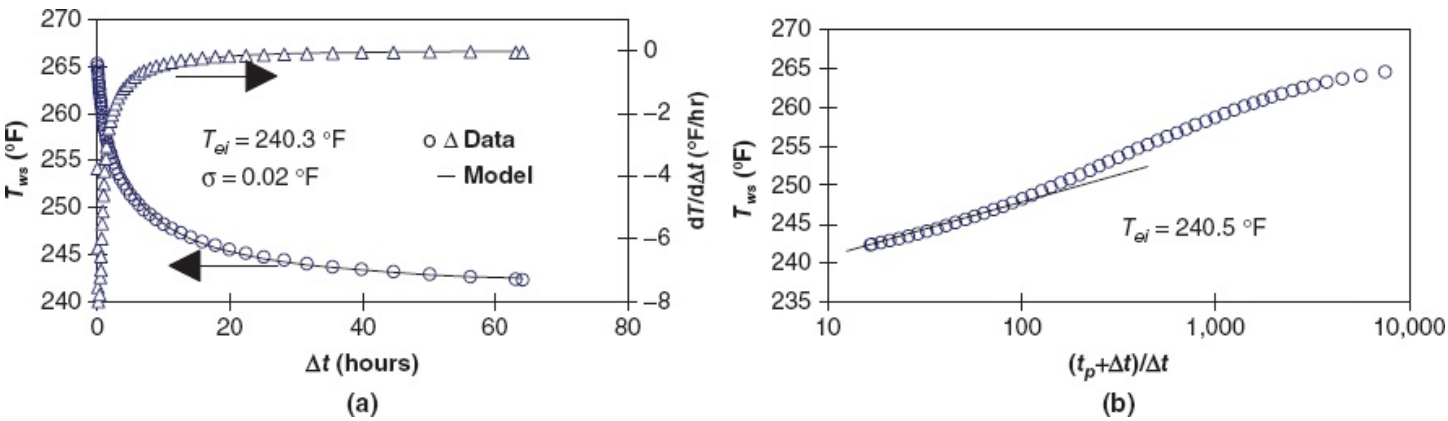

Fig. 11.29—Hyperbola analysis yields reliable by T_{ei} fitting over large data span (a), and semilog analysis corroborates hyperbola-derived T_{ei} (b).

The J-T heating of oil is associated with the degree of drawdown involved. In this second example, where the test experienced some 5,800-psi drawdown at the sandface because of high skin damage, a large attendant temperature change also occurred. **Fig. 11.28,** representing the diagnostic graph, shows a total temperature change of approximately 23°F, although the gauge was located at the perforations. In this case, thermal effects are caused by the J-T effects and not by the borehole gauge location. **Figs. 29a and 29b** present the hyperbola and semilog analyses, respectively, showing good agreement with each other.

Transient temperature data, collected during pressure-buildup tests in different producing horizons, can be used to construct a region's geothermal gradient, g_G. The examples just presented, constituted 2 of the 52 tests that enabled establishing g_G. **Fig. 11.30** presents the geothermal gradient obtained. As discussed by Kabir et al. (1997), the transient analysis approach is superior to approaches using the openhole and cased-borehole data, gathered during various logging operations, unless enough time is allowed for thermal equilibration to occur between the borehole fluids and

formation. We verified this geothermal gradient by measuring borehole temperatures in a well shut in for nearly a year. Here, the measurements were made at each station stop for 15 minutes. **Fig. 11.31** presents these data, corroborating the g_G obtained by the transient method.

Case 2. The Case 2 example comes from the Equus field (Kabir et al. 2014) and was presented earlier, in Chapter 7, while discussing application of temperature data in rate estimation. Here, we show the use of shut-in temperature data collected at various depths during pressure-transient testing to estimate the static formation temperature profile.

A nearly 100-hr shut-in period during a buildup provided us with an opportunity to obtain the static formation temperature (T_{ei}) at each depth in this well. **Fig. 11.32** depicts temperature falloff response at three different depths on the diagnostic log-log graph. The lower curve at each depth represents the derivative signature, which exhibits stabilization or presence of an infinite-acting period. This diagnosis allowed us to treat the infinite-acting data and beyond for curve-fitting with the rectangular-hyperbola approach. **Fig. 11.33** typifies the quality of fit at a given depth with the rectangular-hyperbola approach.

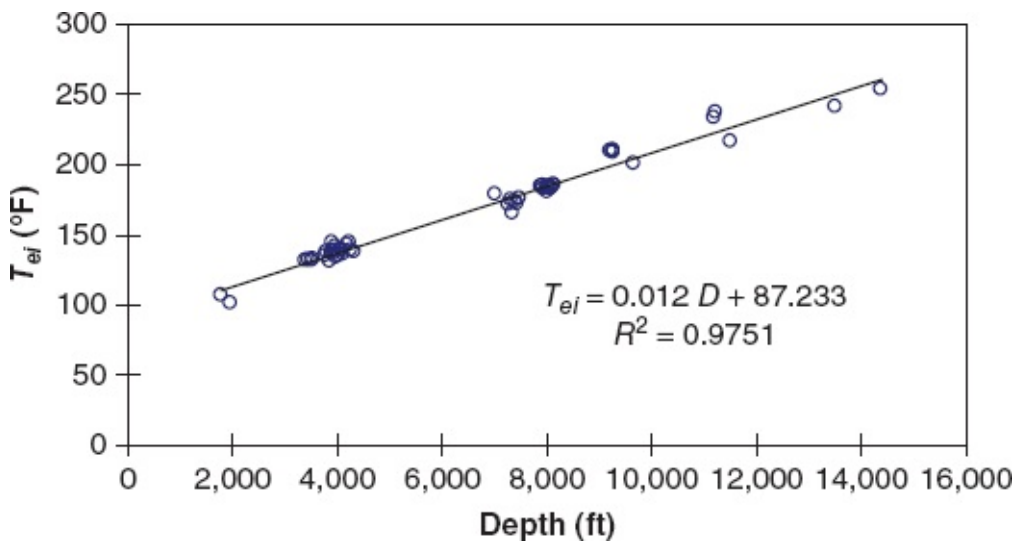

Fig. 11.30—Estimating g_G using transient-test data.

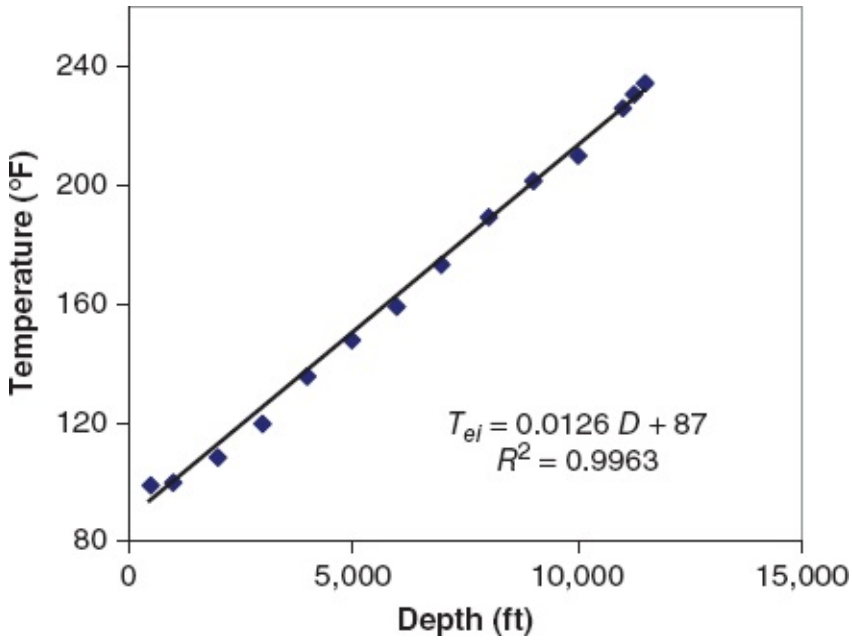

Fig. 11.31—Estimating g_G using static test data.

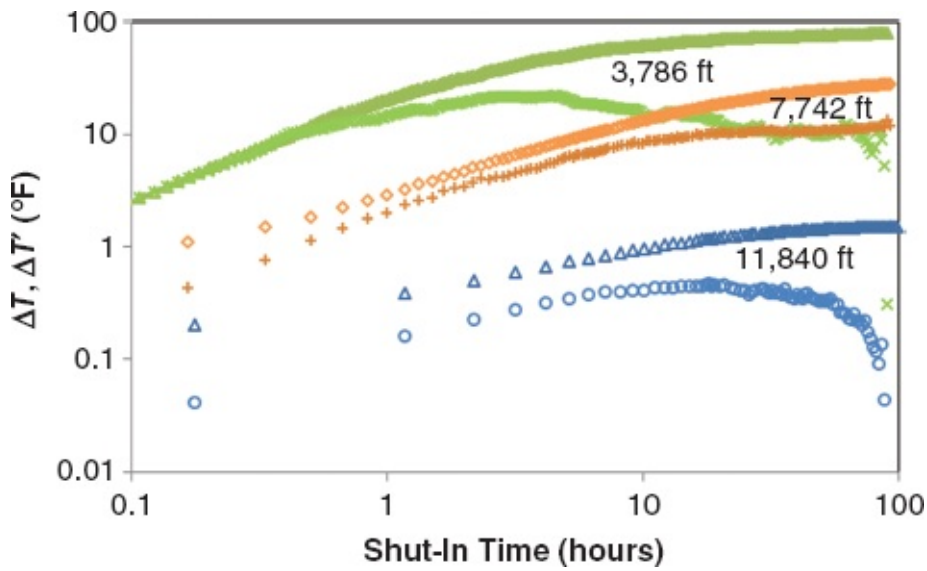

Fig. 11.32—Log-log signatures of temperature decay during well shut-in at various depths.

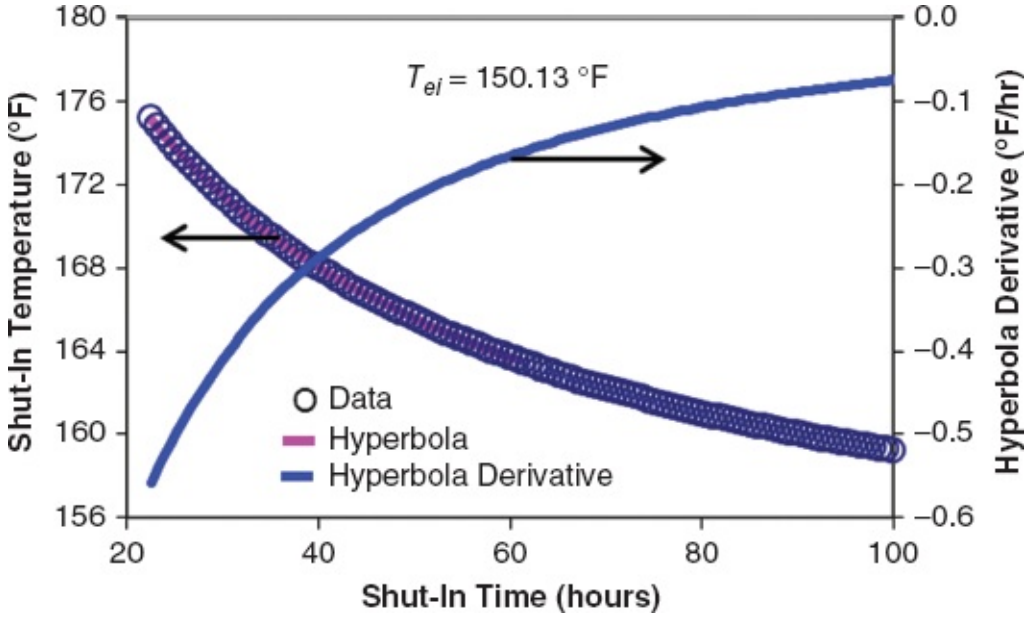

Fig. 11.33—Estimating formation temperature at 7,742 ft with rectangular-hyperbola analysis.

After conducting a systematic temperature falloff analysis on all four wells at various depths, two static gradient signatures emerged, with a steeper geothermal gradient indicated beneath 9,200 ft, as **Fig. 11.34** shows. The two static gradients are 0.0247 °F/ft for the shallower horizon and 0.015 °F/ft for the deeper horizon. Note that the top of the shallower gradient line is close to the mudline and therefore cannot be extrapolated to a shallower depth. The change from one gradient to the other occurs at an approximate depth of 9,200 ft, which is a major stratigraphic boundary occurring at the Jurassic/Triassic interface. Without the benefit of this rich data set and appropriate analysis, granularity in the gradient could have been missed. Ordinarily, temperature sensors in openhole logs have neither the necessary residence time nor the resolution to allow accurate estimation of the static formation temperature.

11.2.5 Discussion. The first approach for interpreting openhole data attempts to capture both heat-transfer mechanisms—conduction and convection—while formulating the working equations for estimating T_{ei}. We note that convective heat transfer can play a significant role when large contrast exists between the inlet mud and the formation temperatures. Both geothermal and high-temperature hydrocarbon reservoirs are cases in point. Previous studies in this area appear to have neglected this important heat-transfer mechanism.

If we were to consider the conductive-heat-transfer mode alone, the formulation would be much simplified even when the superposition effects were considered, as shown by Shen and Beck (1986). In this context, theoretical difficulty of using the superposition principle is noteworthy. For example, from a heat-transfer viewpoint, the complex process of drilling and mud circulating is not analogous to that of fluid flow, in which measurable quantities of fluid may be withdrawn or injected into the

formation. Therefore, the superposition theorem, as used here, is approximate at best. Note also that the model considers conductive and convective heat transfer in the borehole only and that conductive heat transfer occurs in the formation. In other words, the filtrate that invades the formation is assumed not to carry any heat.

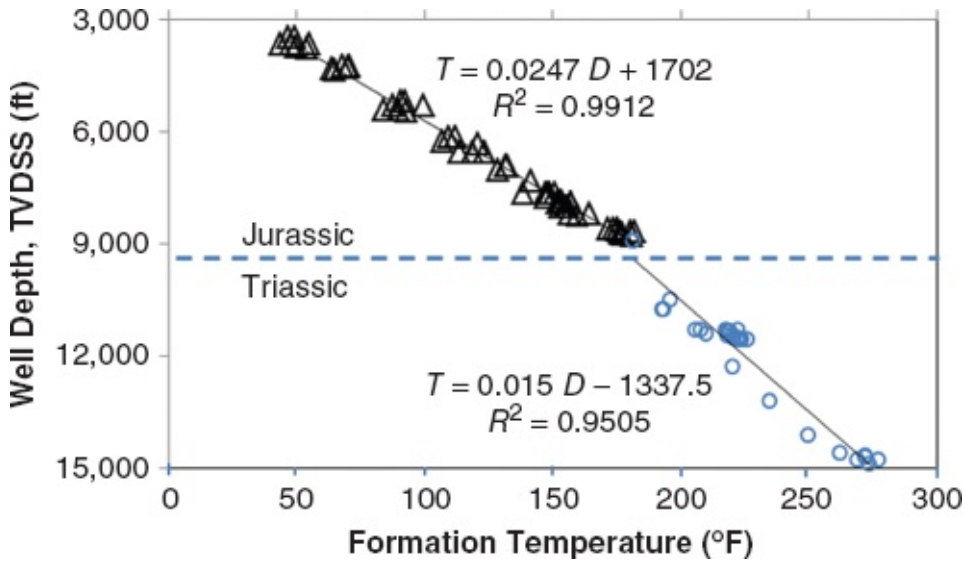

Fig. 11.34—Estimating geothermal gradient with estimated formation temperatures at various depths.

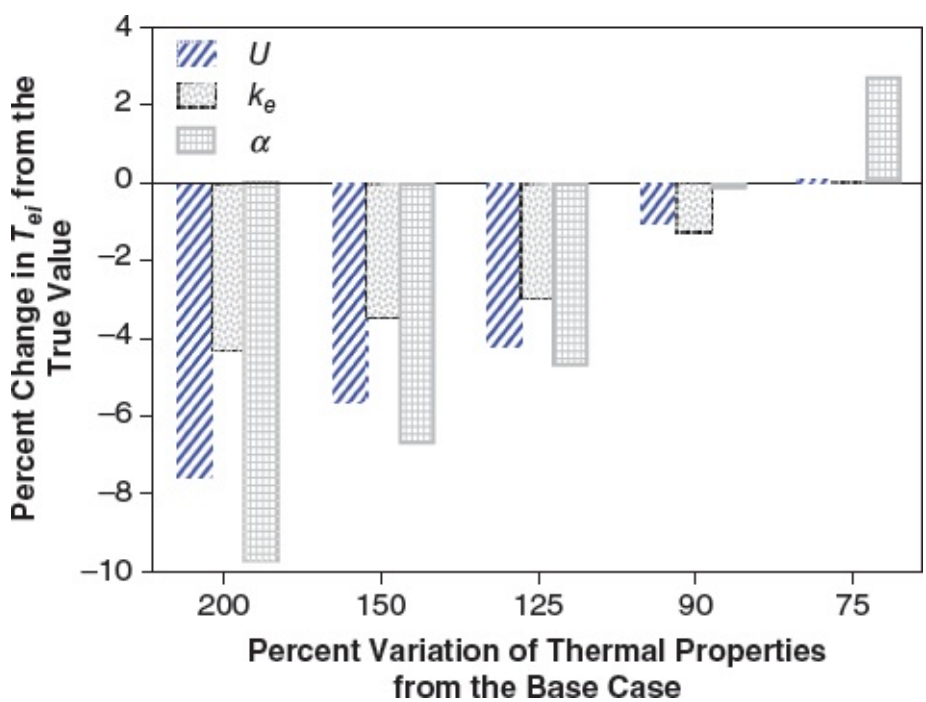

Fig. 11.35—Sensitivity of three parameters on T_{ei} estimation.

Despite these apparent restrictions, the first method presents a simple tool for analyzing field data even when mud and formation properties are not well-defined. The method also avoids making some of the assumptions made in the existing techniques. For example, assumptions of a line-source well and its logarithmic

approximation are not always tenable in a heat-transfer problem of this nature. Use of the cylindrical source well avoids the problem of treating the early-time data. The algebraic simplifications, given in Appendix 11-C, lead to solutions in different time domains.

The main advantage of the first method is that T_{ei} can be estimated reliably from very-early-time data. Consequently, considerable rig time can be saved because waiting periods can be minimized to a large degree. We point out that the traditional practice of gathering transient temperature data during each discrete logging trip with different tools is not conducive to ensuring data quality because of the physical operation. Collection of continuous temperature data with minimal disturbances ensures unambiguous interpretation.

Methods based on sparse openhole data are still reliable even when questions arise about the availability or accuracy of values for various heat-transfer parameters. Experience suggests that modeling of the physical process is far more important than the absolute values of these parameters. **Fig. 11.35** illustrates this point by showing large variations of the overall-heat-transfer coefficient U, formation thermal conductivity k_e, and thermal diffusivity α. We observe that the error in the T_{ei} solution is no greater than 10% of the true value even under extreme circumstances.

In contrast to a drilling environment, continuous temperature data can be gathered routinely during a pressuretransient test. Thus, open- or casedhole drillstem tests or production tests offer excellent opportunities to collect this information. Note that maximum perturbations are created when (1) large J-T heating or cooling is associated with large pressure drawdowns and (2) measurements are made away from the midpoint of a producing interval. In a cased borehole, the early-time data are generally distorted by thermal storage effects.

An important point to reiterate is the thermal-storage phenomenon, first mentioned in Chapter 9. Thermal storage arises because depending on the fluid type and well-operating condition, tubulars, cement sheath, and the gauge carrier all have the ability to store or release heat. Slow thermal equilibrium at any depth of measurement raises questions about the validity of routine cased-borehole temperature surveys to diagnose flow problems. For instance, attempting to diagnose tubular leaks by temperature logs may run into serious problems unless large volumes of flow are associated with the leaks. That is because significant cooling or heating is required to monitor measurable temperature difference. For the same reason, subtle problems may remain clouded by a probe's inability to respond to the temperature change, given the time allowed at each station stop or when the tool is run at a certain speed.

We illustrate this point by presenting **Fig. 11.36,** which shows temperature and pressure data measured before and after a pressure-buildup test. While pressure attains rapid equilibrium at each station, shown by solid stairsteps, the same is not true for temperature during the flowing and static gradient surveys. Smearing of the temperature profile, regardless of the wellbore flow condition, is a direct consequence of the tool-induced thermal storage. The probe's casing sheath largely contributes to this measurement distortion. In other words, true fluid temperature at a

given depth cannot be discerned directly from raw measurements; clearly, interpretation is required. One way of reducing thermal-storage distortion is to use probes that are in direct contact with wellbore fluids.

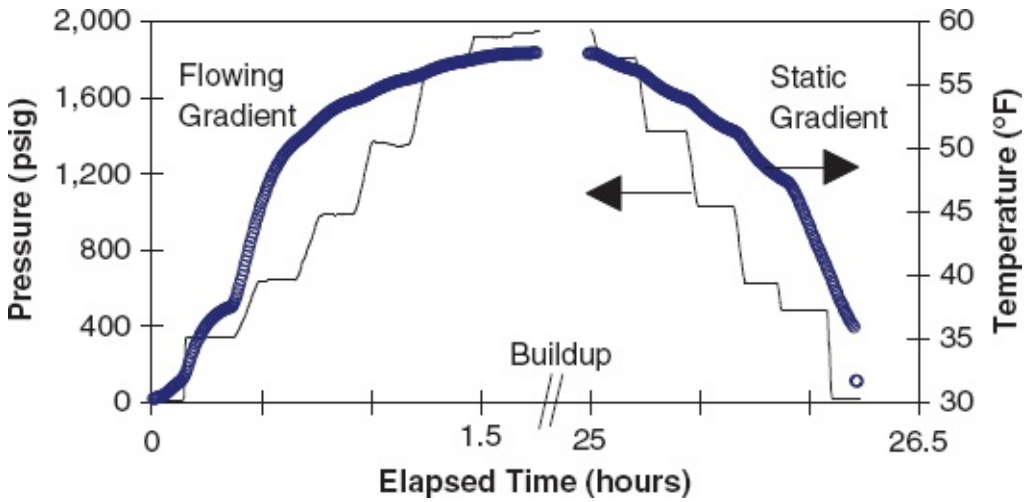

Fig. 11.36—Tool-induced temperature distortion in gradient surveys.

11.2.6 Static Formation Temperature Summary. We presented two approaches, reflecting open- and casedhole data sources, for estimating the undisturbed formation temperature, T_{ei}. In the first approach, an algebraic equivalence of the cylindrical source well solution at early times (t_D < 1.5) is used. Both conductive and convective heat-transfer mechanisms are considered in this formulation. Also in the first approach, a rigorous method and its various simplifications, representing different time domains, are presented. In all cases, a simple graphical analysis is possible. The first approach is validated by using synthetic data and verified by using published field data obtained from both oil and geothermal wells.

In the second approach, a semitheoretical method is shown to yield reliable T_{ei} when temperature data are collected with pressure data during a transient test in a casedhole environment. Here, we identified thermal storage as exhibited by the gauge carrier, tubulars, and cement sheath. Despite this storage, the data are amenable to rectangular hyperbola analysis, aided by its derivative counterpart. Finally, we show how discrete T_{ei} values, collected from different horizons, can be used to develop a region's geothermal gradient.

11.3 Well Blowout

11.3.1 Introduction. Unrestricted or uncontrolled flow of pressurized fluids from a pipe or a well is commonly termed "blowout." Well blowout has been a concern for the industry from the very inception of drilling. In fact, papers on this topic date back to the 1930s.The main concerns with blowout of an oil well are the danger of gas/oil combustion, leading to possible damages to equipment and wellhead, jeopardizing

personnel safety, and resulting in serious environmental effects of the expelled fluids. In addition, loss of significant hydrocarbon volumes can adversely affect project economics in certain settings, such as the expensive deepwater environment.

Danenberger (1993) compiled a list of 87 blowouts that occurred during 1971 and 1991 on the outer continental shelf of the US. These blowout incidents accounted for 1 of every 246 wells drilled and were mostly attributable to shallow gas influxes. The vast majority (84%) of these blowouts lasted less than a week. While compiling blowout data over a wider time horizon in the US Gulf Coast area from 1960 to 1993, Skalle and Podio (1998) and Skalle et al. (1999) reported that 800 blowouts had occurred. They attributed two main reasons for blowout: formation pressure higher than expected, and excessive mud weight during circulation or downward movement of the string leading to fractures, loss of circulation, and kick. Most relevant studies address kick detection and blowout control; a few deal with dynamic-kill operations to regain well control. Clark and Perkins (1981) presented a comprehensive study on blowout, using as their basis steady-state two-phase flow calculations. Unsteady-state modeling for well control was reported by Fan et al. (1996), whereas Hasan et al. (2000) addressed the dynamic aspects of blowout in the context of oil wells. Many have documented the containment of blowout through well-kill operations. Miller and Clements (1972) outlined reservoir engineering methods to contain blowout in Bay Marchand in the Gulf of Mexico. Among other, Lehner and Williamson (1974), Warriner and Cassity (1988), and Kouba et al. (1993) have explored theoretical analysis of controlling blowout through relief wells by water injection. Lewis (1978) reported successful control of blowout for the West Cameron field.

The primary mechanism governing a blowout well is the rapid, near-surface liberation and subsequent expansion of large amounts of dissolved gas. Increased free gas results in higher mixture velocity with consequent increase in the total pressure gradient owing to higher friction and kinetic energy losses. The reduced fluid pressure leads to lower fluid density and further increase in velocity and pressure loss. As the fluids accelerate to the surface, the available flowing pressure limits their speeds and corresponding flow rates. If fluid pressure becomes sufficiently low, the velocities of the fluids will reach the critical (sonic, choking) velocity of the mixture. Under this condition, the pressure at the wellhead is termed “critical discharge pressure.”

For a number of reasons, the blowout rate can be less than the critical value. For example, surface restrictions at the wellhead or relatively low reservoir potential can lead to a blowout in which the fluid velocity is below its critical value. In this case, the wellhead pressure will stabilize at a value lower than the critical pressure, and the sonic discharge velocity will not be reached. This section attempts to assess the coupled nature of transient fluid flow in the reservoir and the combined fluid and heat flows in the wellbore. To that end, a coupled reservoir/wellbore analytical model is first presented for gas wells (Liu et al. 2015), followed by a fully transient wellbore/reservoir flow model (Hasan et al. 2000). Thereafter, we present a case study focusing on the Macondo oil spill event that occurred in the Gulf of Mexico in

2010 (Liu et al. 2017). In both cases, published rate calculations are reproduced for model validations.

11.3.2 Gas-Well Blowout Modeling. To understand the blowout mechanism, we consider the blowout model in three segments: the reservoir, the wellbore, and their interactions. In the following, we discuss a simple approach to capturing the physics of flow in all segments.

***Reservoir Model*.** In the reservoir model, the material balance in the reservoir is considered to calculate the average reservoir pressure so that the average reservoir properties can be properly addressed. For the reservoir containing solely gas, $\overline{p}/z$ is computed considering cumulative production:

$$\frac{\overline{p}}{z}=\frac{G_i-G(\overline{p})}{G_i}\frac{p_i}{z_i} \qquad (11.35)$$

***Wellbore Model*.** During the blowout event, a large amount of formation fluid flows from the reservoir to the bottom of the hole. Because of the high pressure deep in the wellbore, the velocities are relatively low. The upward movement of fluid will reduce the pressure, and the velocity of formation fluid will increase until it reaches sonic velocity, a result of the thermodynamics limitation. The existence of sonic velocity rarely occurs for single-phase oil well blowout because the large hydrostatic pressure gradient does not allow such high velocity; neither does it generally happen for offshore wells because the pressure difference between the wellhead and the bottom of the hole is not significant enough. However, for onshore gas wells and oil/gas wells, the sonic velocity becomes a critical factor that needs to be considered. It is important to calculate sonic velocities of different phases under various wellhead conditions. Sonic velocity of gas is derived from the thermodynamic knowledge of ideal-gas behavior, offered by Kieffer (1977), as

$$c=\left(\gamma\frac{R}{M}T\right)^{0.5} \qquad (11.36)$$

In a blowout, various scenarios may play out, given the unknown nature of formation conductivity, reservoir pressure, and fluid properties. For overpressured reservoirs, the diameter of the flow conduit will largely dictate the wellbore pressure gradient. In small volumetric reservoirs, the wellhead pressure may gradually decrease to a point at which the flow becomes marginal. In all situations, wellhead pressure controls the blowout behavior. Because the sonic velocity of fluid is determined by the temperature in Eq. 11.36, evaluation of this entity is critical. Accordingly, we adopted the method of Hasan and Kabir (2012) in this section and presented previously in Chapter 6. The wellbore fluid temperature can be calculated as follows:

$$T_f = T_{ei} + \frac{1 - e^{(z_w - L)L_R}}{L_R}\left(g_G \sin\alpha + \phi + \frac{g \sin\alpha}{c_p J g_c}\right), \quad (6.29)$$

where

$$\phi = \frac{v}{c_p J g_c}\frac{dv}{dz} - C_J \frac{dp}{dz}. \quad (6.27)$$

Understanding Heat-Transfer Components. **Fig. 11.37** shows the temperature profile in the wellbore when chocked flow rate is achieved at the wellhead. Two interesting phenomena emerge from this figure. First, the fluid temperature starts to decrease as it moves up from the bottomhole and quickly declines near the wellhead. Second, the wellhead temperature increases over time, although the blowout rate may decline during the blowout event because of reservoir depletion. These observations can be explained by examining Eqs. 6.28 and 6.27. In fact, Eq. 6.28 combines the two important heat-transfer components involving kinetic energy loss (KE) and J-T effects.

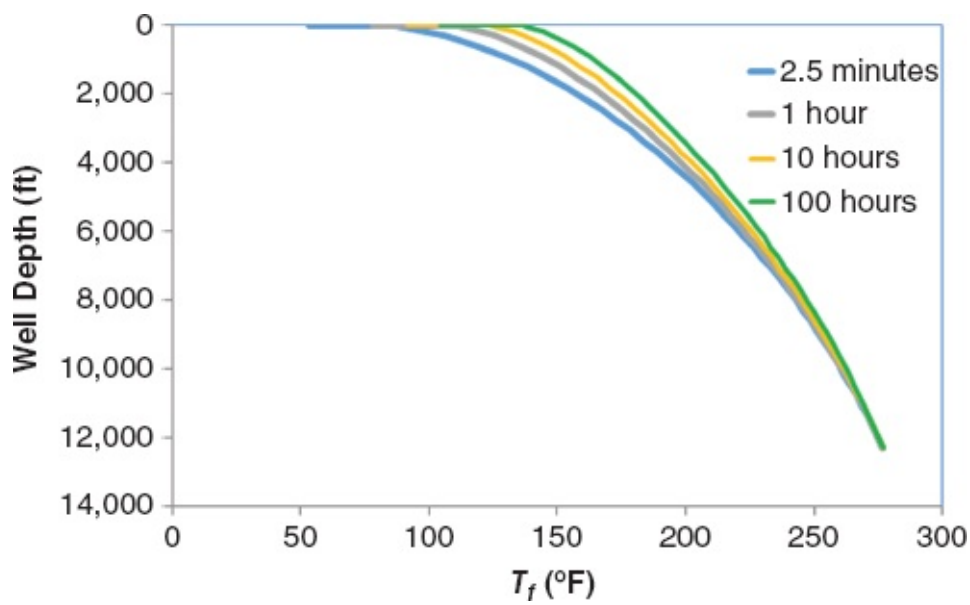

Fig. 11.37—Fluid temperature in wellbore after 2.5 minutes during a blowout event.

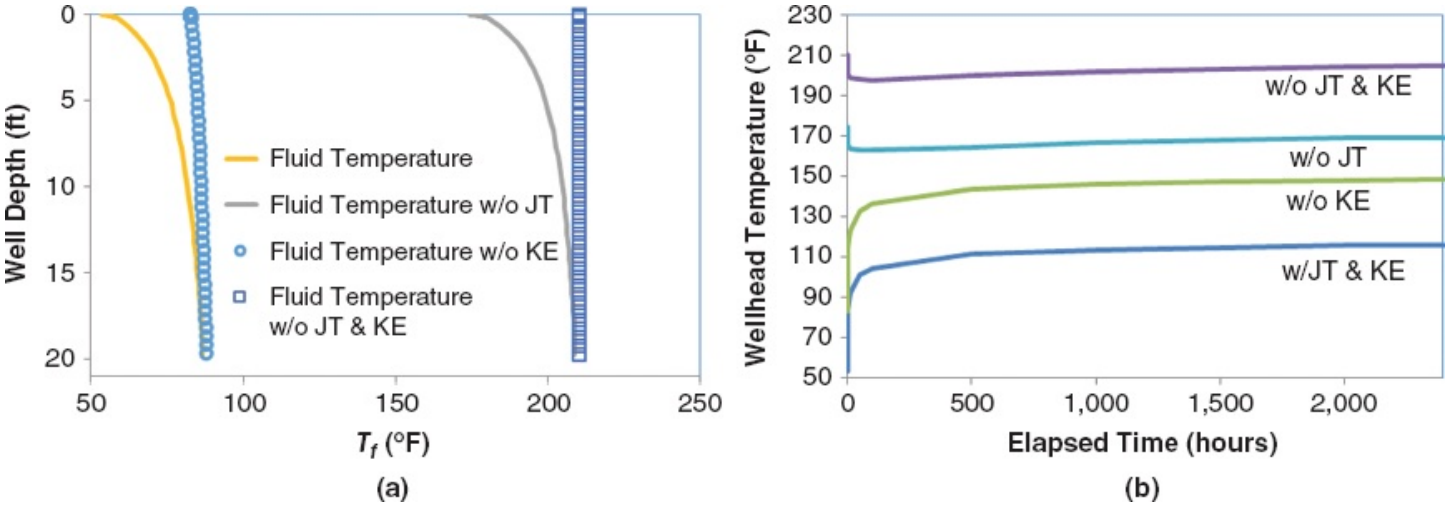

Fig. 11.38—Wellbore fluid temperature profiles by considering different heat-transfer components: (a) after 2.5 minutes near wellhead and (b) evolution with time at wellhead.

Fig. 11.38a shows how these two components affect the behavior of heat transfer in blowout events with and without considerations of KE and/or J-T near the wellhead in a given situation. The contributions of KE and J-T effects are significant near the wellhead. The figure illustrates the fluid temperature profile in the wellbore starting from 20 ft below the wellhead for four cases: with J-T and KE, with J-T but without KE, with KE but without J-T, and without JE and KE. When the rate approaches the chocked flow condition at wellhead (potential blowout scenario), the gas will experience extreme expansion, resulting in significant increase in pressure gradient. This phenomenon leads to the increase in KE contribution (vdv/dz) in Eq. 6.27 at the expense of internal energy, thereby explaining the rapid decrease of fluid temperature near the wellhead. As Fig. 11.38a shows, absence of KE will precipitate minimal changes in the wellhead fluid temperature. To summarize, KE contributes to the fluid temperature change near the wellhead, whereas J-T affects the fluid temperature in the entire wellbore.

Fig. 11.38b illustrates how KE and J-T effects can affect the evolution of fluid temperature in a blowout scenario. When the KE term is neglected, the temperature is higher compared to the one considering KE but has a similar trend. The blowout rate declines with the increase in temperature. If the J-T effect is not taken into account, the blowout rate and temperature decrease at the same time. The fluid temperature at wellhead will change minimally if neither of these two important heat-transfer components is considered.

Reservoir/Wellbore Coupling. The phenomenon of blowout is similar to high-rate production, except that the rate of blowout keeps changing over time. As a result, it is possible to apply the flow equations of a drawdown test in our blowout model by neglecting the superposition in time. Following the Matthews and Russell (1967) approach, we considered both the early-time transient and the late-time pseudosteady-state flow for a gas well in a bounded circular reservoir in this study, which is written as

$$p_{wf} = p_i - \frac{1422qT}{kh}\left\{\frac{2t_{Dw}}{r_{eD}^2} + \ln r_{eD} - \frac{3}{4} + s + q_D + 2\sum_{n=1}^{\infty}\frac{\exp(-a_n^2 t_{Dw})J_1^2(a_n r_{eD})}{a_n^2[J_1^2(a_n r_{eD}) - J_1^2(a_n)]}\right\}, \quad (11.37)$$

where

$$r_{eD} = \frac{r_e}{r_w}, \quad (11.38)$$

$$t_{Dw} = \frac{kt}{\phi\mu c_t r_w^2}, \quad (11.39)$$

and the a_n values are the root of

$$J_1(a_n r_{eD})Y_1(a_n) - J_1(a_n)Y_1(a_n r_{eD}) = 0. \quad (11.40)$$

The roots of Eq. 11.37 increase monotonically as n goes to infinity. Therefore, the summation term is significant compared with other terms at early time. However, the summation term becomes less important as time progresses, thereby indicating that the transition between early time and late time is occurring. At late time, the summation term becomes negligible. Stated differently, the pressure difference between $\bar{p}$ and p_{wf} bears a linear relationship with flow rate during the pseudosteady-state flow period when the effects of all the boundaries have been felt at the wellbore. The advantage of Eq. 11.37 is that it avoids the discontinuity between the two flow periods of interest, transient and pseudosteady-state. Note that the computational approach accounts for the μc_t, variation with pressure (or pseudopressure) in Eq. 11.37.

As discussed, the blowout model as presented includes both reservoir and wellbore and their interactions. Because the analytical modules for the reservoir and the wellbore are well-established, we considered the constant-rate drawdown test case for gas production. **Fig. 11.39** indicates a good agreement with the results of a commercial package for the reservoir response. As expected, a smooth transition occurs between the two flow periods: the early-time transient period that ends near 10,000 hours, followed by late-time pseudosteady-state period.

Model Validation With Field Examples. First, we used the results of Oudeman (2010) to validate the blowout model. These data were obtained from the results of well testing of a small, tight offshore gas reservoir in the North Sea. This gas well was drilled underbalanced, and a series of well tests were performed. This example presented a great opportunity to verify the blowout model because of the high flow rates associated with testing. Different wellhead pressures during the testing may be construed as blowouts at various water depths. Given the wellhead and reservoir pressures, computations of blowout rate and bottomhole flowing pressure become feasible. **Fig. 11.40** shows the comparison of the calculated and measured rates. In general, the calculated rates match the measured rates fairly well; poor flow stabilization in the wellbore may have contributed to the scatter in Fig. 11.40.

We also verified this blowout model with the results of the model presented by Kikani et al. (1996), describing a blowout episode of an onshore sour-gas well in Germany. **Table 11.4** presents the field data reported by Kikani et al. After adjusting the permeability to approximately 2 md instead of 4.3 md, the model reached good agreement with the previous solution, as shown in **Fig. 11.41.** In this case, the sonic velocity is present throughout the duration of blowout, given the reason discussed in the previous subsection.

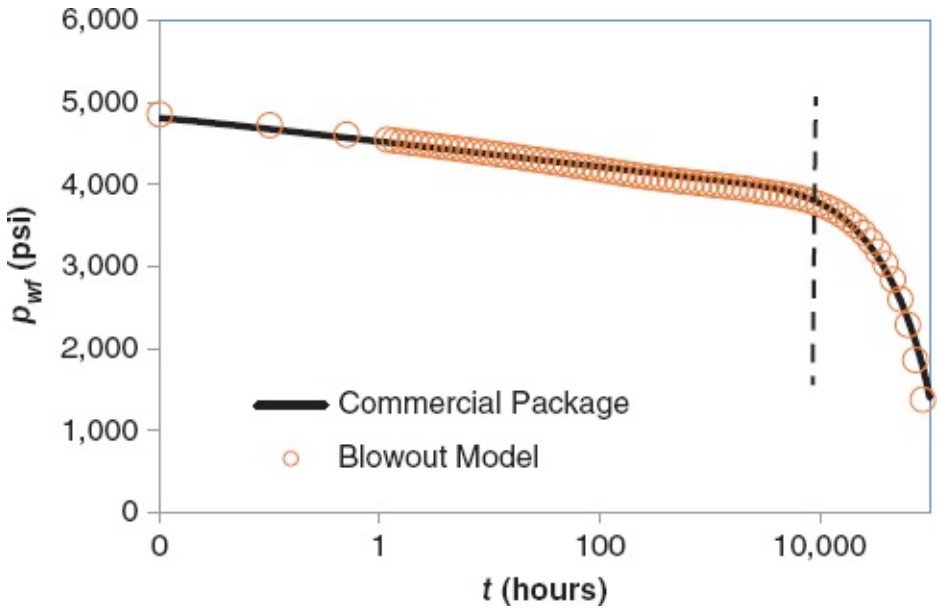

Fig. 11.39—Constant-rate drawdown test in a gas reservoir.

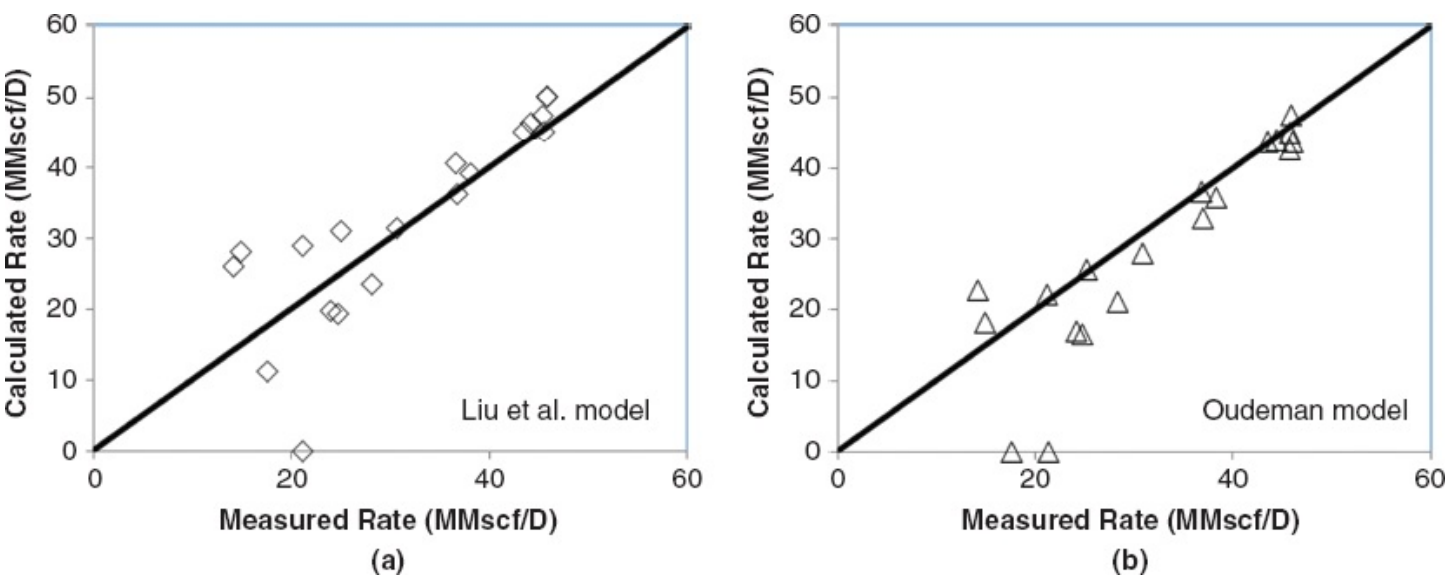

Fig. 11.40—Comparison of measured and calculated blowout rates by two models, (a) Liu et al. (2015) and (b) Oudeman (2010).

Parameters	Value
Well depth, ft	12,300

Reservoir depth, ft	12,456
Net thickness, ft	100
Porosity	0.149
Water saturation	0.15
Reservoir pressure, psia	5,985
Reservoir temperature, °F	276.8
Gas gravity	0.83
H_2S concentration	0.2869
Tubing inner radius, ft	0.25
Drainage radius, ft	3,280
Skin	-2.5
Non-Darcy coefficient, D/Mscf	2.57E-05
Permeability, md	4.3

Table 11.4—Data presented in the field example of Kikani et al. (1996).

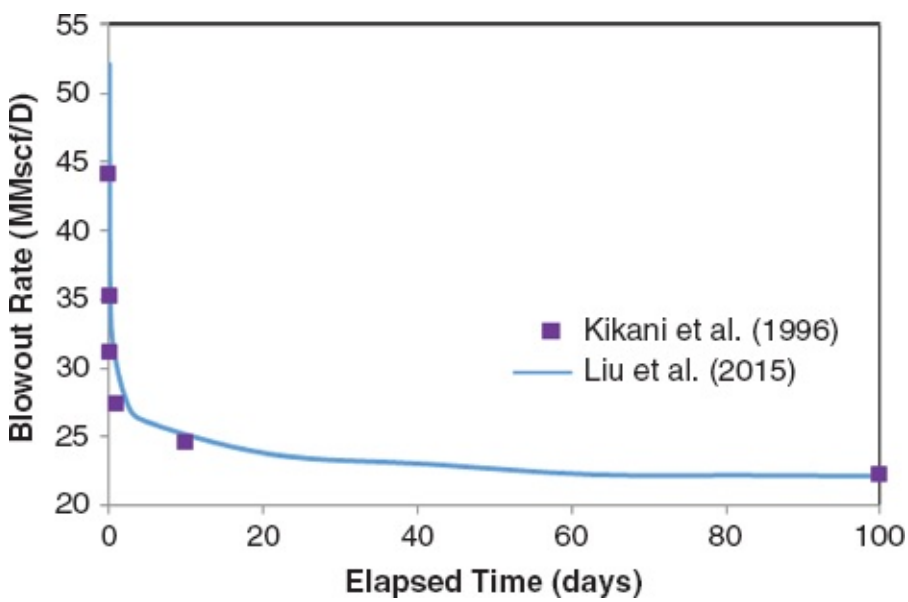

Fig. 11.41—Comparison of models performance with Kikani et al. data (1996).

***Understanding Variables AffectingTotal Discharge*.** Fig. 11.41 shows the results of the blowout evolution based on field data. However, many of the reservoir variables cannot be measured accurately and may have large uncertainties in an actual setting. This aspect is especially true for exploratory wells. We adopted a probabilistic simulation approach in this section so that we can fully understand how the reservoir parameters affect a blowout. As **Table 11.5** shows, four independent variables were considered in three levels within certain bounds of uncertainty. **Fig. 11.42** is generated by using different levels of selected variables, showing the low-, medium-, and high-level cases. To calculate production loss, we assumed that the blowout lasted for 300 days

Table 11.5 is also used in folded Plackett-Burman (Wolff 2010) design of experiments to quantify the significance of each variable. This statistical design captures both nonlinearities and interactions between the independent variables. Cumulative production loss during a 100-day blowout constituted the dependent variable. **Fig. 11.43** presents the Pareto chart of this analysis. Permeability and formation thickness turned out to be the most significant variables. The vertical line defines the results within the 95% confidence interval.

	Low	Medium	High
Formation thickness, ft	50	100	150
Initial reservoir pressure, psia	5,387	5,985	6,584
Reservoir radius, ft	2,952	3,280	3,608
Permeability, md	1	2.3	5

Table 11.5—Reservoir parameters with uncertainties for blowout model performance.

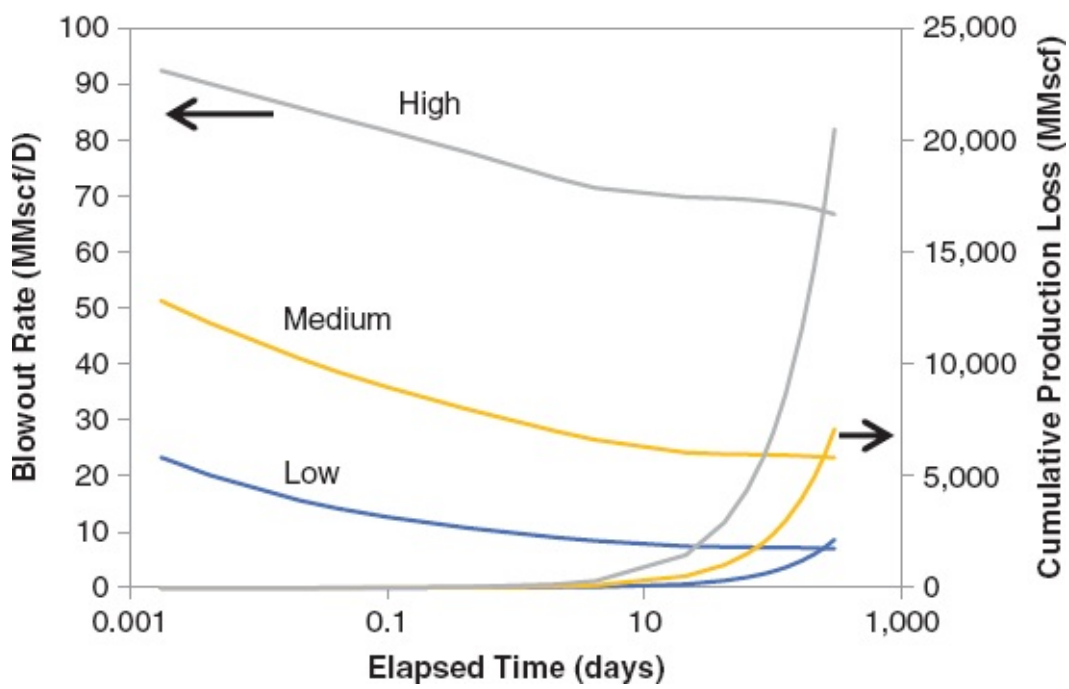

Fig. 11.42—Probabilistic blowout behavior for the Kikani et al. (1996) case.

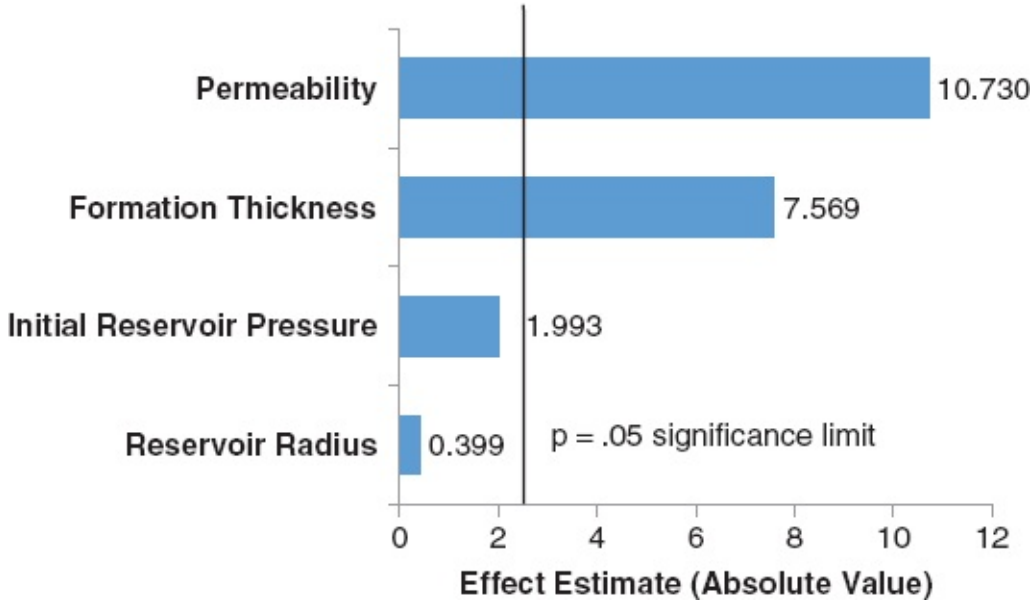

Fig. 11.43—Pareto chart for the folded Plackett-Burman design.

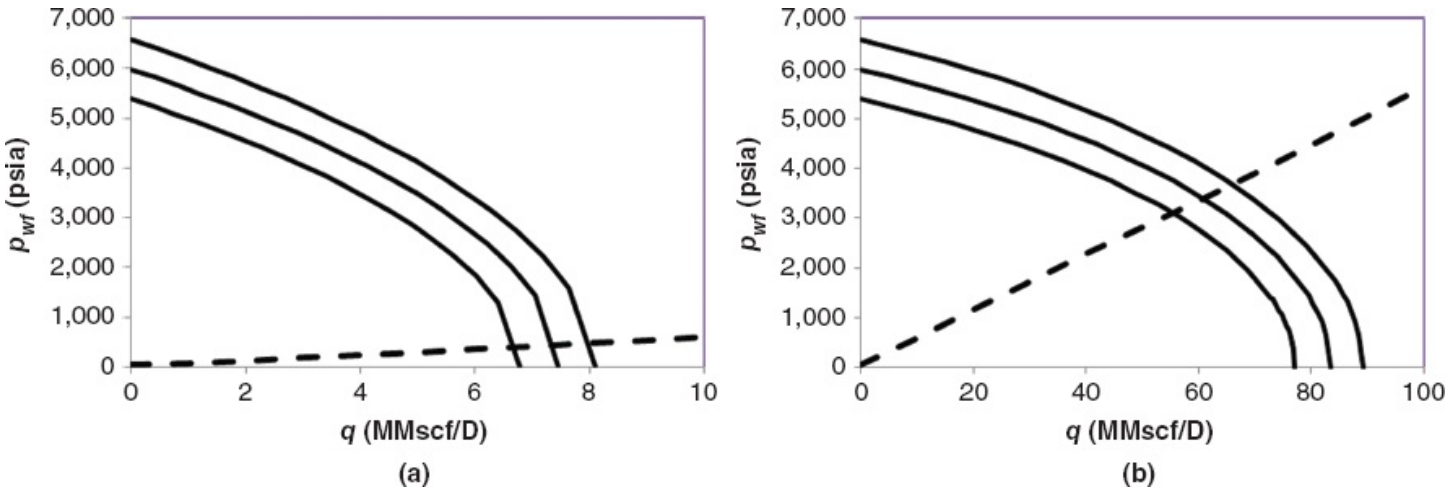

Fig. 11.44—TPC and IPR curves in 1-md (a) and 5-md permeability reservoir (b).

Note that the sonic velocity cannot be sustained for a certain combination of variables. This item can be explored by studying the tubing performance curve (TPC) and inflow performance relationship (IPR) curves. **Fig. 11.44a** displays the TPC and IPR curves for a 1-md permeability reservoir. The solid lines represent the IPR curves at different levels of reservoir pressure, and the dashed line represents the TPC at constant wellhead pressure, close to atmospheric. Note that nonlinearity of TPC is minimal because of the low wellhead pressure. The operating points are between 6 and 8 MMscf/D. However, the choked flow rate of gas in this field example at standard conditions is approximately 19.8 MMscf/D. This rate indicates that for a low-permeability reservoir, the sonic velocity cannot be reached even when the wellhead pressure approaches atmospheric condition. In contrast, Fig. 11.44b presents the TPC and IPR curves for a 5-md permeability reservoir. The operating points are

between 50 and 70 MMscf/D, indicating that chocked flow rate will be reached.

The linear behavior of TPC in Fig. 11.44b may raise questions. The underlying reason for this phenomenon is the pressure loss resulting from acceleration at low wellhead pressure. When the wellhead pressure is high, the dominating term in pressure loss is the frictional component, which leads to the nonlinear behavior at low rates. However, when low wellhead pressure is precipitated by blowout, the gas velocity increases dramatically, leading to considerable pressure loss because of the acceleration term. Consequently, linear pressure-loss behavior at high rates emerges, as shown in **Fig. 11.45.**

11.3.3 Oilwell Blowout Modeling. As discussed in the previous subsection, the critical (sonic) velocity represents the maximum speed fluids may attain. The reason for this limitation lies in the inability of rarefaction wave fronts—the pulse traveling down the wellbore—to propagate in a direction counter to that of the flow. In other words, the sonic velocity of these downstream-traveling pressure pulses is balanced exactly by that of the upstream-traveling fluids. If critical flow is reached, it must stabilize such that the sonic condition is established at the wellhead while subsonic flow occurs below the wellhead.

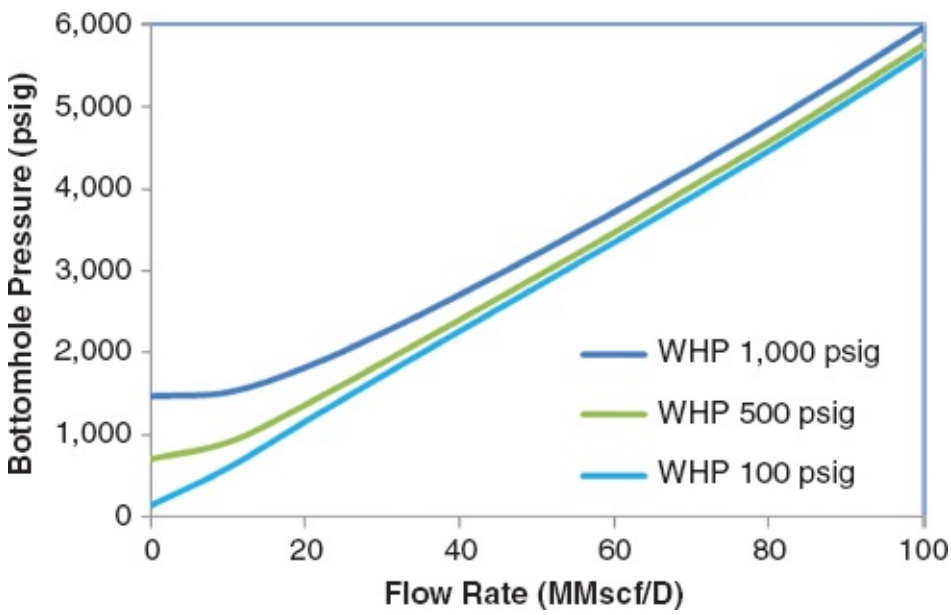

Fig. 11.45—Domination of acceleration term causes the linear behavior in TPC at high rates. WHP = wellhead pressure.

Analysis of oilwell blowout is complicated by the need to consider the sonic velocity of a two-phase mixture. Sonic velocities in two-phase systems are typically much lower than those in single-phase flows of the individual components. Wallis (1969, 25) developed a model for two-phase sonic velocity in one-dimensional steady-state homogeneous equilibrium flow.

In this text, we adopted the model proposed by Wallis (1969, 50), which is based on the analysis of one-dimensional steady homogeneous flow. According to this model, the critical or sonic velocity v_c for a two-phase system depends on the sonic velocities of the two phases, v_{cL} and v_{cg}, and their in-situ volume fractions, f_L and f_g, as

$$\frac{1}{v_c^2}=\left[f_L\rho_L+(1-f_L)\rho_g\right]\left(\frac{f_L}{\rho_L v_{cL}^2}+\frac{1-f_L}{\rho_g v_{cg}^2}\right). \quad (11.41)$$

The sonic velocities of the individual phases can be estimated from the partial derivative of pressure with respect to density at constant entropy with the expressions

$$v_L^2=\left(\frac{\partial p}{\partial \rho_L}\right)_S \text{ and } v_g^2=\left(\frac{\partial p}{\partial \rho_g}\right)_S. \quad (11.42)$$

Expressions for these partial derivatives depend on the pressure/volume/temperature behavior of the fluids and are available in many thermodynamics texts.

During critical flow in an oil well, there may be a two-phase supersonic flow above the wellhead. To analyze the interaction between discharge jet and atmosphere, the flow conditions at the end of the supersonic jet must be determined. We will not present any such analysis; the interested reader is referred to the work of Seubold and Shirie (1967).

Computation of Blowout Rate. When control of a well is lost, leading to blowout, critical flow is generally established at the wellhead at near-atmospheric pressure. With the reservoir properties and the wellhead pressures known, the problem becomes one of computing a flow rate for which the total pressure drop in the formation and the wellbore equals reservoir pressure minus the wellhead pressure. Transient pressure loss in the wellbore and in the formation depends on flow rates, which may evolve in a complex manner given flow restrictions and flow path.

We use the same approach described in the preceding subsection for gas wells. The material-balance relationship in the reservoir model to calculate the average-reservoir pressure follows the relation

$$p_{av}=p_i-\frac{0.234qBt}{\phi c_t h(\pi r_e^2)}. \quad (11.43)$$

Although transient flow will be prevalent at a blowout's inception, steady flow in wellbore is expected to dominate over a very short time span. Hasan et al. (2000), among others, have proposed transient solution for the wellbore flow problem. However, our preferred solution approach entails treating the reservoir flow as transient, followed by boundary-dominated flow, but with the wellbore flow remaining at steady state. The convenience of this simplified coupled modeling approach is

rooted in our objective assessment of the total discharged volume by incorporating uncertainties in both the reservoir and fluid properties and by managing risks in wellbore flow barriers.

***Estimating Mixture and Sonic Velocity*.** We present an example of a blowout oil well. Table 11.6 presents the synthetic data set, originally published by Clark and Perkins (1981). Table 11.7 lists the relevant data and parameters used in our simulator, and Table 11.8 reports the final calculated results.

Reservoir pressure, psia	4,300
Bottomhole pressure, psia	1,420
Well depth, ft	8,800
Tubing inner diameter, in.	5.5
Gas/oil ratio, Scf/STB	800
Productivity index, STB/D-psi	3.5
Critical flow rate, STB/D	10,000
Critical wellhead pressure, psia	29

Table 11.6—Well, reservoir, and fluid data for the example problem.

Pipe roughness, ft	0.00002
Formation permeability, md	212
Formation thickness, ft	100
Formation porosity, fraction	0.26
Skin factor	21.1
Oil gravity, °API	30
Reservoir temperature, °F	138.7
Geothermal gradient, °F/ft	0.015
Formation thermal conductivity, Btu/(ft-°F-hr)	3.33
Formation density, lbm/ft^3	135
Formation heat capacity, Btu/(lbm-°F)	0.625
Tubing/casing material thermal conductivity, Btu/(ft-°F-hr)	30
Annular fluid thermal conductivity, Btu/(ft-°F-hr)	0.2
Annulus fluid thermal conductivity, Btu/(ft-°F-hr)	0.1
Cement thermal conductivity, Btu/(ft-°F-hr)	0.38

Table 11.7—Additional data used in two-phase flow simulation.

Possible lowest bottomhole pressure, psia	1,480.5	1,420
Possible lowest wellhead pressure, psia	28.5	29

Terminal blowout rate, STB/D	10,000	10,000

Table 11.8—Major simulation results.

In our modeling, flow in the reservoir is that of single-phase oil, however, pressure drop causes two-phase flow in the wellbore. The two-phase flow model of Hasan et al. (2010) was used for estimating liquid holdup and pressure drop in the wellbore. Our computed mixture velocity at the wellhead condition is 396.5 ft/sec, quite close to the theoretical sonic velocity of 405 ft/sec. Because the theoretical sonic velocity is still higher than the calculated mixture velocity, we continued computation with a slightly higher production rate. However, near the wellhead, the program computed negative pressure at this flow rate, and the computation was terminated. Thus, the simulator calculates a blowout rate of approximately 10,000 STB/D. **Fig. 11.46** presents the evolution of sonic and mixture velocities at the wellhead condition of one of the cases we considered here.

We expect the theoretical sonic velocity to be higher than the actual maximum velocity attainable in the well because the sonic velocity is computed assuming isentropic expansion. One issue with the assumption of isentropic expansion is that all mechanical losses, such as frictional losses, are negligible, which is untenable in practice. For instance, with increases in GOR, the assumption of isentropic expansion becomes progressively worse because of higher expected frictional loss. Our simulations at various GOR values clearly bear out this fact—namely, that the higher the GOR, the greater the difference between sonic velocity and computed maximum attainable velocity.

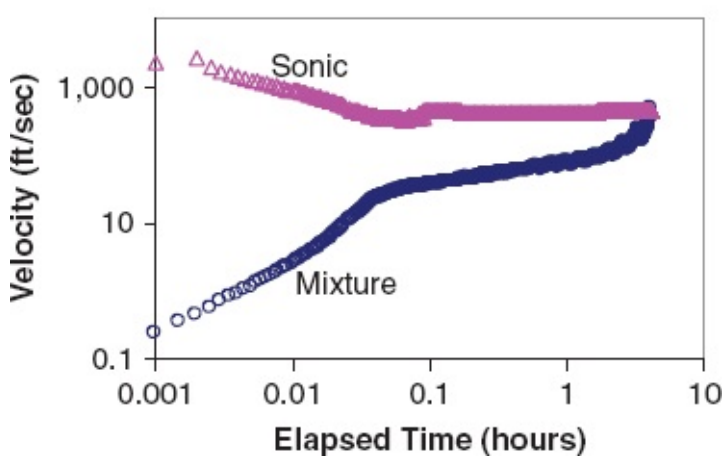

Fig. 11.46—Evolution of sonic and mixture velocities during blowout, example problem.

Validation of Wellbore & Reservoir Model. This subsection attempts to validate some of the model results that are available in the public domain. Specifically, flow in the wellbore and the reservoir are explored to provide confidence in solution quality before embarking on performance predictions for the total system in a probabilistic frame.

The results of the wellbore flow model of Hasan et al. (2010b), discussed in Chapter 5, are compared with those reported by Clark and Perkins (1981) in a 5.5-in. tubing for an oil rate of 10,000 STB/D for GOR of 800 scf/STB. **Fig. 11.47** compares the two solutions with good agreement, although Clark and Perkins had used the Orkiszewski (1967) correlation to handle two-phase flow modeling in wellbore. This convergence of results is reassuring despite the difference in flow-modeling approaches.

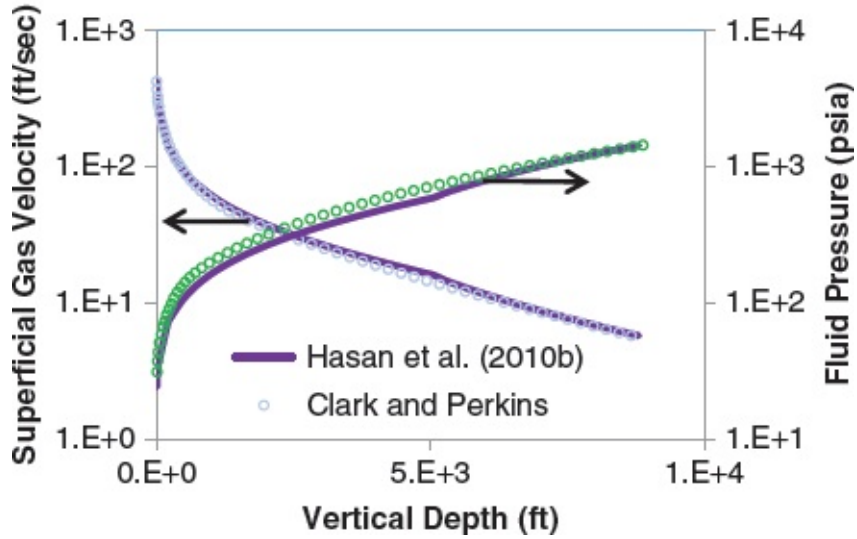

Fig. 11.47—Model validation for flow in wellbore.

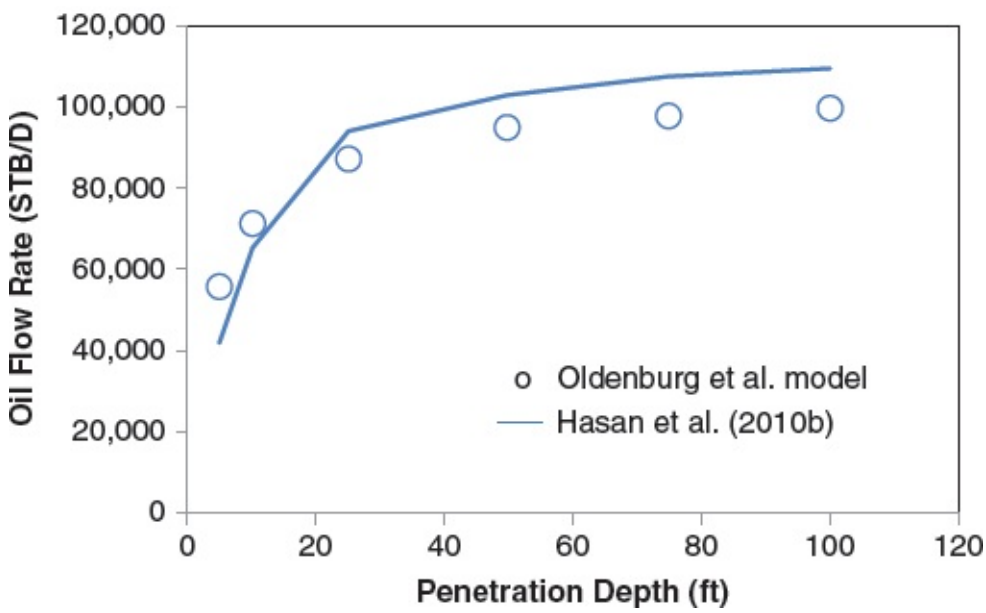

Fig. 11.48—Model validation for flow in reservoir.

Next, we pursued validation of our simplified reservoir model with the results of a numerical model obtained by Oldenburg et al. (2012). This comparison shows the performance of a partially penetrated well, which is an unknown entity in any blowout

situation. We used the Odeh (1968) partial-penetration skin model to mimic the flow impediment. **Fig. 11.48** compares the results of two modeling approaches in decent agreement. The oil rate attained stability in about 10 days, which represents the end of each simulation run.

Understanding System Response and Exploring Uncertainty in Input Parameters. This section explores the characteristics of the wellbore model response while probing the uncertainty in reservoir parameters with respect to flow rates. **Fig. 11.49a** presents the wellhead flow rate profiles corresponding to three permeability values, whereas **Fig. 11.49b** shows their corresponding reservoir-pressure profiles. As expected, the maximum discharge rate is strongly influenced by the formation permeability.

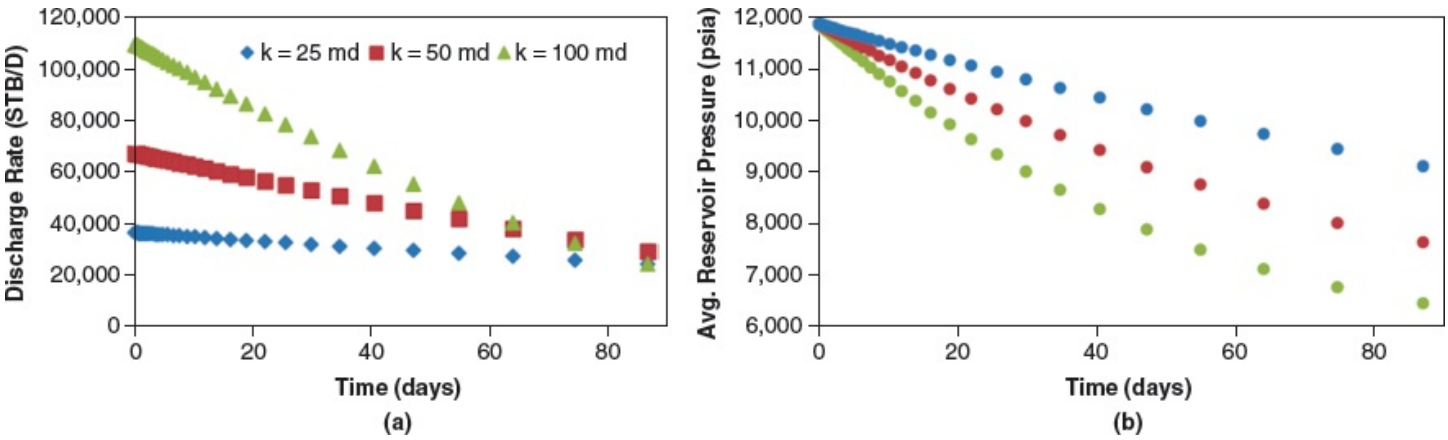

Fig. 11.49—Discharge rate (a) and corresponding average-reservoir pressure (b) for three different permeability reservoirs.

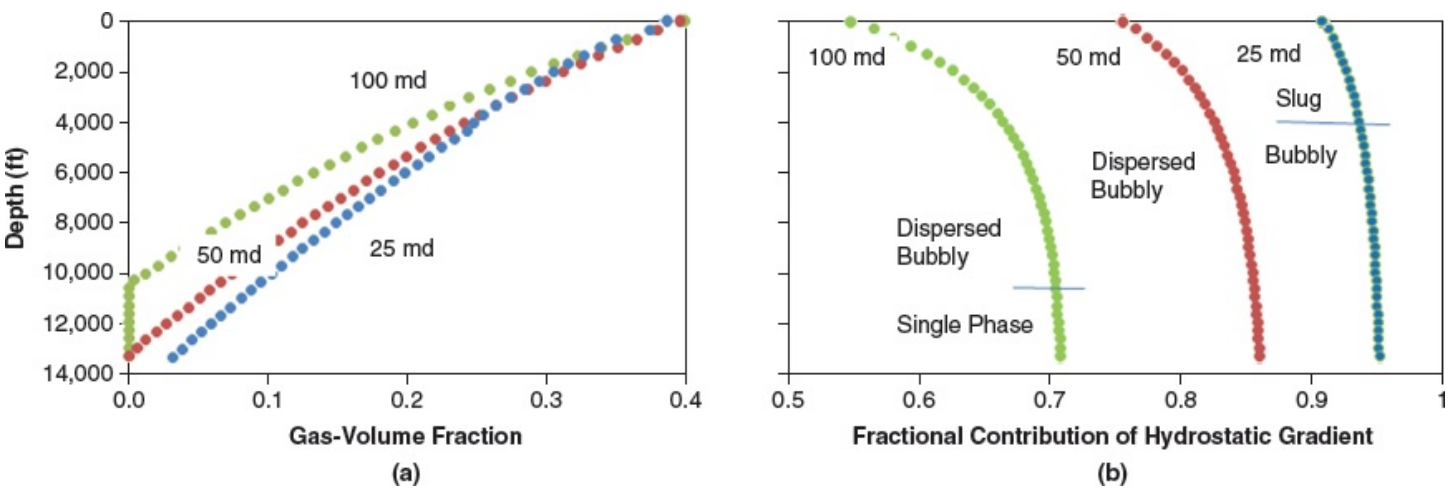

Fig. 11.50—Gas-volume fraction (a) and corresponding contribution of hydrostatic pressure gradient (b) for three different permeability reservoirs.

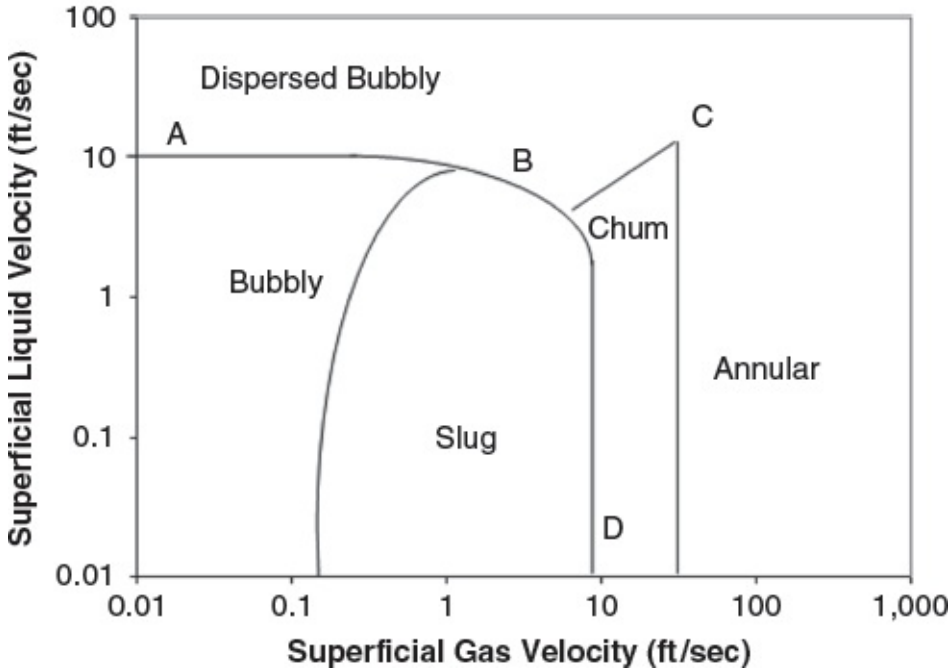

Fig. 11.51—Flow-pattern map at standard conditions.

For these wellhead rates, **Figs. 11.50a and 11.50b** display the gas-volume fraction and contribution of the hydrostatic gradient in this 14,000-ft wellbore at approximately 2 hours into blowout. For the highest rate in 100-md formation, single-phase oil flow occurs over 2,000 ft near the well bottom. But, given the high oil-superficial velocity, dispersed bubbly flow predominates in the remainder of the wellbore. Dominance of dispersed bubbly flow is also apparent in the 50-md formation. However, low flow rates associated with 25-md reservoir involving large drawdowns precipitate bubbly and slug flows. For an overall understanding of flow regimes, **Fig. 11.51,** shown earlier as Fig. 3.7a, presents a flow-pattern map at standard conditions.

Fig. 11.52 provides some perspective on the reservoir flow response in all three cases discussed above. In all situations, the log-log diagnostic plot (Blasingame et al. 1991), used routinely in rate-transient analysis, can provide clues about the influence of the boundary-dominated flow (BDF). As expected, the 100-md case exhibits the largest response, and the opposite is true for the 25-md case. Such a diagnosis after ascertaining a range of possible flow rates in a given situation can help narrow down the reservoir's connected pore volume. Note that the reservoir volume, along with intrinsic rock properties, will play a large role in contributing to the overall discharged volume.

Let us explore the question surrounding the discharged volume in a probabilistic frame for a simple case. In this example, we considered permeability, skin, initial reservoir pressure, and reservoir radius as independent variables as shown in Table 11.7. Discharged volume constituted the dependent variable. Using the folded-Plackett-Burman statistical design of experiments, as suggested by Wolff (2010), we

made 17 runs to generate the Pareto chart, as shown in **Fig. 11.53.** Although all four independent variables are significant because they exceed 95% confidence, reservoir permeability appears to be the most important variable within the range of selected values. This exercise preludes the Macondo case study that we analyze next.

Variables	Low	Medium	High
Permeability, md	25	100	224
Skin	0	3	6
Initial Reservoir Press, psia	9,485	11,856	14,227
Reservoir Radius, ft	3,648	4,560	5,472

Table 11.7—Range of independent variables in initial study.

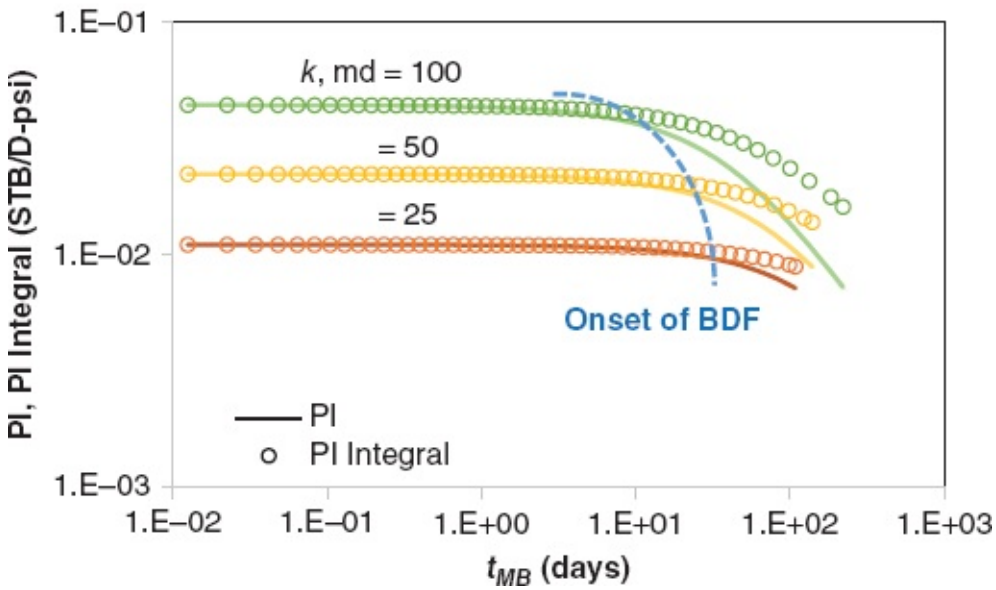

Fig. 11.52—Separation of two curves identify the boundary-dominated flow (BDF) in reservoir.

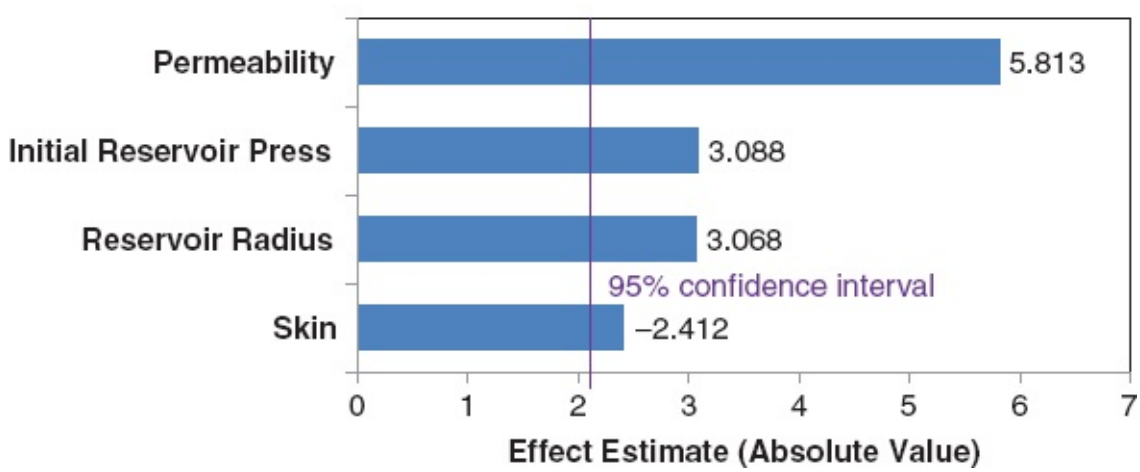

Fig. 11.53—Pareto chart for the four-variable study.

***Assessing Risk and Uncertainty for the Macondo Case Study*.** This subsection explores the range of scenarios with discharge rate and other significant independent variables. **Fig. 11.54** presents some of the potential blowout scenarios and their assessment. Each blowout scenario has a unique probability depending on the assumptions of the probability distribution and availability of regional data in a given situation. The sum of probabilities associated with each scenario equals unity. Here, we explore the Macondo case given the body of information that is available in the open literature.

As shown in the preceding section, the dynamic blowout rate and the resulting total discharged volume can be estimated for each potential blowout scenario. The product summation of the total amount of discharged volume and the corresponding probability yields the well-specific blowout risk. This approach leads to barrier effectiveness and risk-reduction studies.

As Fig. 11.54 indicates, the status of blowout preventer or BOP is unknown in a given situation. **Fig. 11.55** underscores the importance of this flow barrier in fluid's flow path using the proposed modeling approach. The initial discharge rate of 104.76 MSTB/D compares well with the Oldenburg et al. (2012) estimation of 105 MSTB/D and that of BP's reported internal value of 100 MSTB/D. In contrast, when the BOP restriction triggers 850 psia backpressure, the initial rate reduces to 95.3 MSTB/D. As a consequence, the cumulative discharged volume decreases to 5 MMSTB, from 5.73 MMSTB when no such restriction applies. Given its potential impact, we included the barrier effect in our design of experiments study to generate realistic scenarios.

Fluid's PVT characteristics may potentially have a large impact on flow performance. To address this issue, PVT properties were generated with an equation-of-state model after due consideration of regional fluids at comparable burial depths in the Gulf of Mexico. Appendix 11-D presents the compositions of three fluids used in this study to mimic the range of possible fluids. This appendix also shows the principal fluid properties that contributed to the generation of dynamic flow simulation results by using the coupled wellbore/reservoir model discussed above.

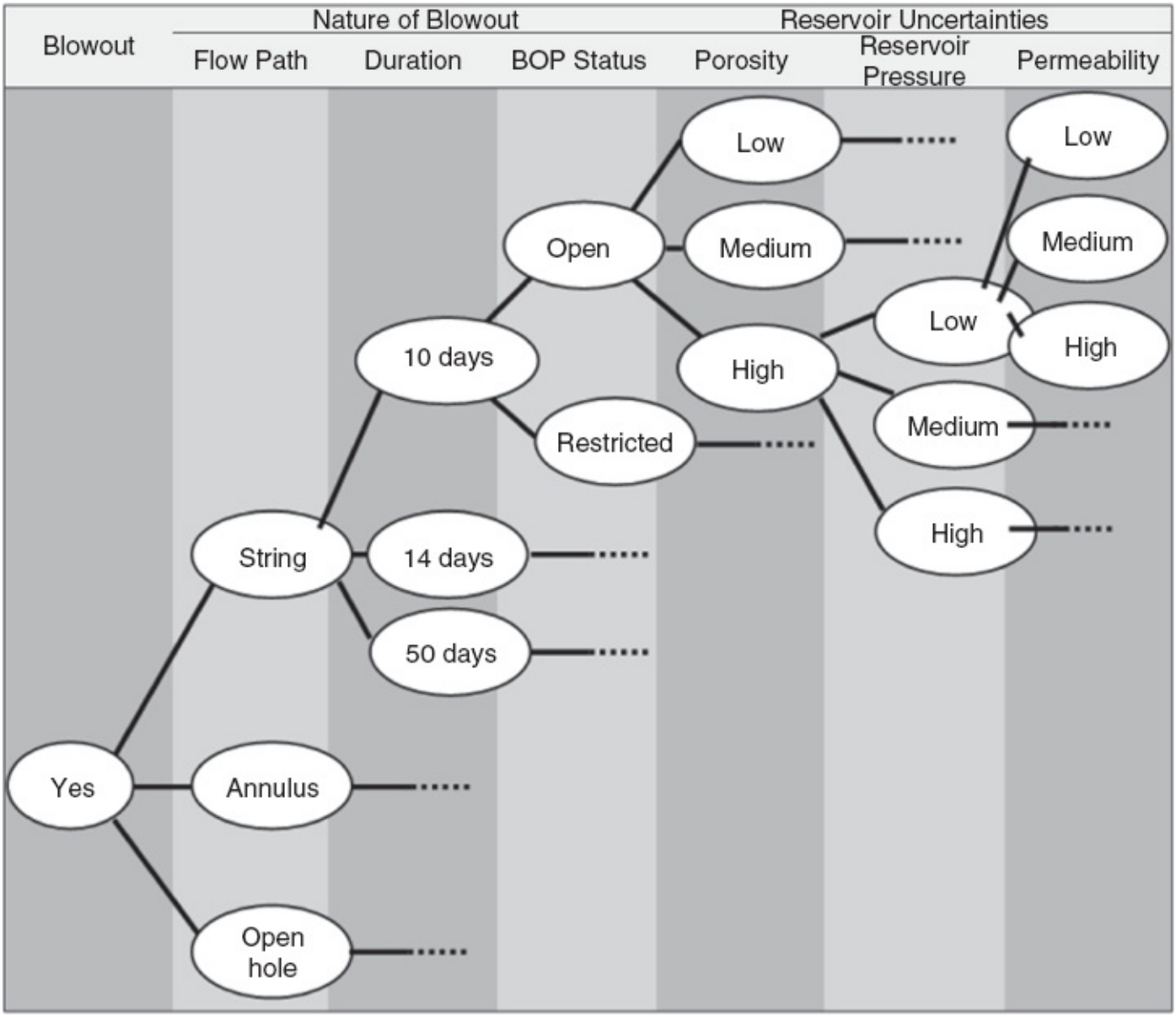

Fig. 11.54—Risk and uncertainty assessment in a blowout scenario.

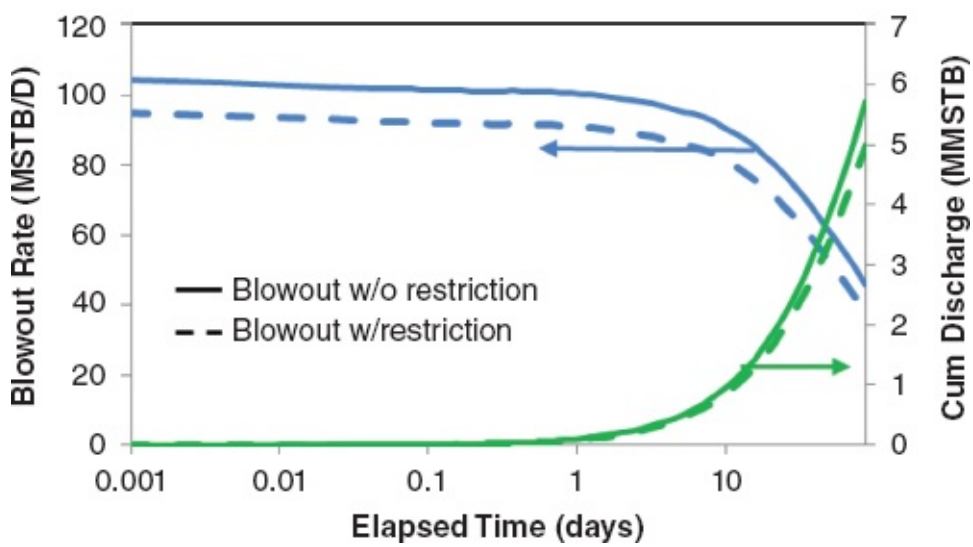

Fig. 11.55—Influence of BOP on blowout rate and cumulative discharge.

Table 11.8 presents the range of five independent variables considered in the Macondo case study. The Oldenburg et al. (2012) study provided the source of most of these parameters. For example, information about reservoir pressure and permeability came directly from their study. However, regional data dictated the range of GOR and the related PVT properties by way of Peng-Robinson's equation-of-state modeling, and the same is true for reservoir size. Given the arbitrary and large pressure range selected for BOP restriction in Oldenburg et al. (2012), we chose to work with a smaller pressure interval.

Fig. 11.56 shows the corresponding Pareto chart for the dependent variable discharged volume. As in the previous case, all five variables appear consequential. On a Pareto chart, the x-axis represents the student's *t*-values and the y-axis the independent variables. Details can be found in a statistics textbook, such as Montgomery (2012).

Variable	Low	Medium	High
GOR, scf/STB	2,804	3,313	4,009
Reservoir pressure, psia	9,975	10,640	11,305
Reservoir radius, ft	3,500	4,500	5,500
Permeability, md	100	300	500
BOP restriction, psia	514	949	1,384

Table 11.8-Range of independent variables in the Macondo case study.

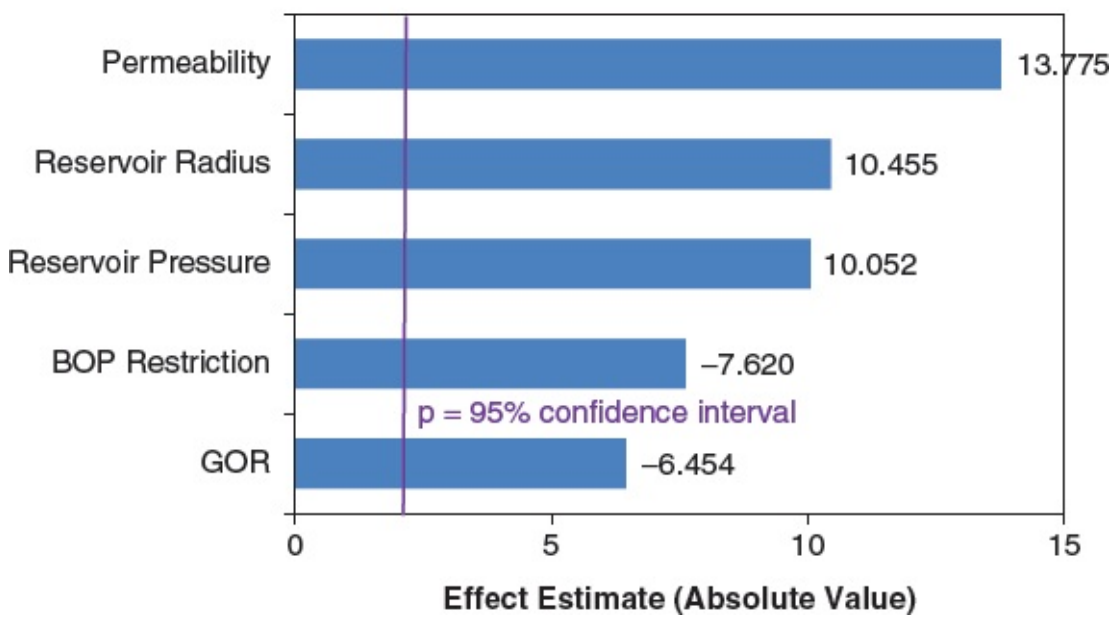

Fig. 11.56—Pareto chart for the five-variable Macondo case study.

Let us point out that a negative value associated with a variable suggests that its increase has an adverse impact on the dependent variable discharged volume; whereas, the opposite is true for a positive value. In other words, Fig. 11.56 suggests that discharged volume increases with increasing values of reservoir permeability, connected pore-volume associated with a well (reservoir radius), and reservoir pressure. Decreasing the BOP restriction and GOR will also contribute to larger discharged volume due to lower flow resistance in the wellbore.

Unlike Monte Carlo simulations, use of the folded-Plackett-Burman approach significantly reduces the number of simulation runs needed to generate objective solutions. **Fig. 11.57a** presents the cumulative-distribution function (CDF) for just 17 runs. By eliminating the first and last data points, a decent CDF profile emerged, as Fig. 11.57b shows. The most probable or p-50 case suggests a total discharge volume of 3.75 MMSTB, with an uncertainty range of 2.91 and 4.73 MMSTB. As stated earlier, these values compare well with those single-value assessment of the operators (3.5 MMSTB), and that of the US government (4.9 MMSTB) reported by McNutt et al. (2011).

11.3.4 Blowout Summary. Blowout is an unsteady-state, uncontrolled flow process. In general terms, the maximum or critical rate is reached after the initiation of a blowout. Thereafter, rate decline occurs owing to constant pressure production. As shown, even steady-state wellbore modeling can capture the essence of well behavior in case of gas wells. The linear tubing performance response because of the acceleration term's dominance, is worthy of note. For oil wells, several wellbore/reservoir parameters govern the magnitude of blowout rate and the time to reach this maximum rate. The statistical design of experiments helped ascertain the range of spilled volume assessed by others in the Macondo case study. The overall pattern of consensus among independent assessors using different tools and methodologies instills confidence in the solution approach presented here. Determining critical uncertainties concerning blowout risk can guide operators in allocating appropriate resources to important flow barriers, thereby allowing for a better approach to mitigate blowout-related risks.

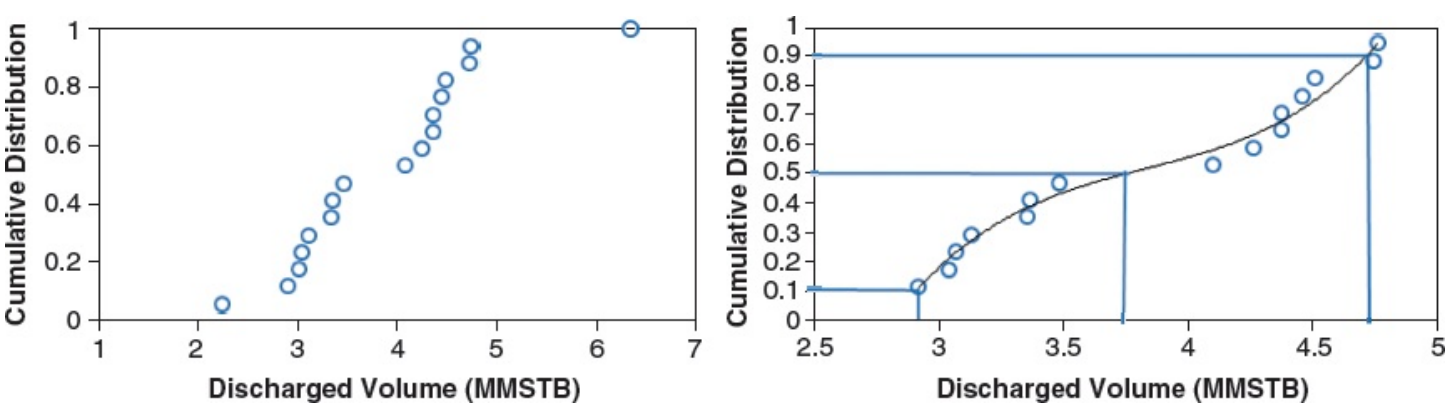

Fig. 11.57—CDF of the folded-Plackett-Burman study (a) and its simplification (b) for ascertaining possible scenarios in Macondo.

Summary

This chapter dealt with issues that pertain to drilling operations. The first two sections discussed unsteady-state heat-transfer models that are associated with steady fluid circulation. Measurements of borehole temperature made after the cessation of circulation lead to estimating the undisturbed formation temperature. We also showed how the temperature data, collected in conjunction with pressure-buildup tests in cased boreholes, can yield formation temperature en route to establishing a region's geothermal gradient.

The last section explored the application of two wellbore/reservoir coupled modeling approaches in the context of well blowout. In both cases, reservoir fluid flow occurred in unsteady-state mode. In the first method, steady-state fluid flow coupled with unsteady-state heat-transfer modeling in the wellbore suggested that replication of published data is feasible in the context of gas wells. When unsteady-state fluid and heat flows in the wellbore together with unsteady-state reservoir fluid influx occur, the influence of various independent variables on total discharge can be learned in the context of two-phase gas/oil flow in the wellbore. Regardless of a model's complexity, the use of a coupled wellbore/reservoir model helps one to understand the issues surrounding the loss of reservoir fluids. The modeling approaches outlined here allow one to assess the appropriate steps that can be taken to minimize fluid loss in the event of such an occurrence.

Nomenclature

a = length of mud tank, ft

a' = asymptote of rectangular hyperbola, °F

a_n = series roots of Eq. 11.37

b = width of mud tank, ft

b' = parameter of rectangular hyperbola, °F

B = parameter defined by Eq. 11.4, ft

c' = parameter of rectangular hyperbola, °F -hr

c_e = specific heat of earth or formation, Btu/(lbm-°F)

c_{fl} = specific heat of fluid, Btu/(lbm-°F)

c_h = specific heat of fluid, Btu/(lbm-°F)

c_{pm} = specific heat of mud, Btu/(lbm-°F)

c_t = total compressibility, 1/psi

C''_o = constant defined by Eq. 11-C-20, dimensionless

C_o = constant defined by Eq. 11-C-10, dimensionless

C_1 = constant defined by Eq. 11-C-13, dimensionless

C_2 = constant defined by Eq. 11-C-14, dimensionless

C_3 = constant defined by Eq. 11-C-15, dimensionless

C_4 = constant defined by Eq. 11-C-22, dimensionless

c_j = Joule-Thomson coefficient, °F/psi

d = diameter, ft

$f_1(t_D)$ = function defined by Eq. 11-C-17, dimensionless

$f_2(t_D)$ = function defined by Eq. 11-C-18, dimensionless

$f_3(t_D))$ = function defined by Eq. 11-C-19, dimensionless

f_g = volumetric in-situ gas fraction

f_L = volumetric in-situ liquid fraction

$F(t_D)$ = function used in Eq. 11.18, defined by Eq. 11-C-16, dimensionless

F' = function used in Eq. 11.26, defined by Eq. 11.27, dimensionless

g_G = geothermal gradient, °F/ft

h = mud tank height, ft

I = integral defined by Eq. 11-C-12

J_1 = Bessel function of the first kind

k = formation permeability, md

K_e = earth or formation thermal conductivity, Btu/(hr-ft- °F)

k_h = formation thermal conductivity, Btu/(hr-ft-°F)

k_m = thermal conductivity of mud, Btu/(hr-ft-°F)

L = total vertical well depth, ft

L'_R = parameter used in Eqs. 11.19 and 11.20, 1/hr

L_R = relaxation length, ft^{-1}

L_{Rn} = relaxation length with superposition taken into account, ft^{-1}

m_t = semilog slope, °F/~

M = mass of fluid in a 1-ft length of well, lbm

p = pressure at any point in the well, psia

p_i = initial reservoir pressure, psia

p_{wf} = flowing bottomhole pressure, psia

p_{wh} = flowing wellhead pressure, psia

q = liquid or gas flow rate, STB/D or MMscf/D

q_{bo} = blowout rate, STB/D

q_{wf} = flow rate at sandface, STB/D

q_{wh} = flow rate at wellhead, STB/D

Q = heat flow rate per unit well length, Btu/(hr-ft)

Q_a = convective heat flow in the annulus, Btu/hr

Q_t = convective heat flow in the tubing, Btu/hr

Q_{ta} = rate of heat flow from the annulus to the tubing per unit depth, Btu/hr-ft

r_w = wellbore radius, ft

r_i = radius of investigation, ft

r_c = casing radius, ft

r_{eD} = dimensionless reservoir radius (= r_e/r_w)

t, t_p = fluid circulation or production time, hours

t_D = dimensionless circulation time (=$k_h t_p/\rho\ c_h r_w^2$)

t_{Dw} = dimensionless producing time (=$kt/ø\ \mu c_t r_w{}^2$)

T = fluid temperature at any point in the well, °F

T_a = annular fluid temperature, °F

T_{as} = annular fluid temperature at surface, °F

T_{ae} = annular fluid exit temperature, °F

T_{ai} = annular fluid inlet temperature, °F

T_{air} = air temperature, °F

T_{as} = annular fluid temperature at surface, °F

T_D = dimensionless temperature [= $2\pi k_e(T_{wb} - T_{ei})/q_F$]

T_{ei} = static formation temperature at well bottom, °F

T_{es} = static formation temperature at surface, °F

T_t = tubing/drillpipe fluid temperature, °F

T_{ti} = fluid temperature entering wellbore, °F

T_w,T_{wb} = wellbore temperature, °F

T_{ws} = sandface shut-in temperature, °F

T_{wso} = initial wellbore temperature, °F

U = overall-heat-transfer coefficient, Btu/(hr-ft^2-°F)

U_a = overall-heat-transfer coefficient for annulus, Btu/(hr-ft^2-°F)

U_t = overall-heat-transfer coefficient for tubing, Btu/(hr-ft^2-°F)

v_e = critical velocity of two-phase mixture, ft/sec

v_{eg} = critical velocity of gas, ft/sec

v_{cL} = critical velocity of liquid, ft/sec

v_m = in-situ velocity of gas/oil mixture, ft/sec

w = mass flow rate of fluid, lbm/hr

x = mass fraction of gas, dimensionless

Y = parameter defined by Eq. 11.9, °F

Y_1 = Bessel function of the second kind

z = any vertical depth, ft

$Z_{T\max}$ = depth at which maximum temperature occurs, ft

α = heat diffusivity of formation (= $k_e/c_e\rho_e$), ft^2/hr

α' = constant used in Eqs. 11.5 and 11.6, °F

β = constant used in Eqs. 11.5 and 11.6, °F

Δt = shut-in time, hours

= dimensionless shut-in time

Δ_{td}

Δ_T = shut-in temperature difference, °F

Δ_T' = superposition-time derivative of AT, °F

λ_1 λ_2 = exponents used in Eqs. 11.5 and 11.6, ft−1

Λ = parameter used in Eqs. 11.13 and 11.14, °F/ft

μ = fluid viscosity, cp

ρe = bulk density of earth or formation, lbm/ft3

ρ_{fl} = density of fluid, lbm/ft3

ρ_g = gas density, lbm/ft3

ρ_L = liquid density, lbm/ft3

Φ = porosity, fraction

σ = standard deviation, °F

ω_1, ω_2. = lumped parameters used in Eqs. 11.13 and 11.14, °F, defined by Eq. 11-B-4 and 11-B-5

Ω = parameter defined by Eq. 11.8, dimensionless

Subscripts

c = casing

i = time index for superposition

m = fluid mixture

n = last timestep for superposition

S = entropy

t = tubing

w = wall of tubulars

Appendix 11-A

Models Related to Drilling Operations

11-A.1 Constants for Reverse-Circulation Models. Using Fig. 11.1, which shows flow down the annulus and up the drillpipe, we can develop an energy balance for the annulus and tubing fluid during mud circulation. The annular fluid gains Q amount of heat per unit length of the wellbore from the formation and loses Q_{ta} heat to the tubing fluid. For a differential section, then,

$$Q_a\big|_{z+dz} - Q_a\big|_z = Q - Q_{ta}. \qquad (11\text{-A-}1)$$

Ignoring the effect of pressure on mud enthalpy, we can rewrite Eq. 11-A-1 in terms of mud heat capacity and temperature as follows:

$$wc_{fl}\left(T_a\big|_{z+\mathrm{d}z} - T_a\big|_z\right) = \left(Q - Q_{ta}\right)\mathrm{d}z. \qquad (11\text{-A-}2)$$

In differential form, Eq. 11-A-2 is transformed into

$$wc_{fl}\frac{\mathrm{d}T_a}{\mathrm{d}z} = \left(Q - Q_{ta}\right). \qquad (11\text{-A-}3)$$

Note that Eq. 11-A-3 assumes that drilling adds a negligible number of cuttings to the fluid and does not change its specific heat; that is, the fluid flow rate w and its specific heat c_{fl} remain the same in both the drillstring and the annulus. Heat flowing from the formation, Q—analogous to Eq. 6.19—is given in terms of annulus fluid temperature, T_a, by

$$Q = -L_R wc_{fl}\left(T_a - T_{ei}\right). \qquad (11\text{-A-}4)$$

Heat flowing from the annulus to the tubing, Q_{ta}, is

$$Q_{ta} = -\frac{wc_{fl}}{B}\left(T_a - T_t\right), \qquad (11\text{-A-}5)$$

where

$$B = -\frac{wc_{fl}}{2\pi r_t U_t}. \qquad (11\text{-A-}6)$$

An expression for tubing fluid temperature, T_t, can be derived by setting up an energy balance for this fluid in the way that Eq. 11-A-2 was developed. Convective heat transfer within the tubing fluid must be balanced by heat transfer between the tubing

and annulus fluid. Thus,

$$\frac{dT_t}{dz} = \frac{(T_t - T_a)}{B}. \qquad (11\text{-A-}7)$$

Eqs. 11-A-1 through 11-A-7 are combined to arrive at Eq. 11.1, a second-order linear differential equation for tubing fluid temperature during reverse circulation.

$$\frac{B}{L_R}\frac{d^2T_t}{dz^2} \pm B\frac{dT_t}{dz} - T_t + T_{es} + g_G z \sin\alpha = 0. \qquad (11.1)$$

For the two boundary conditions needed to solve Eq. 11.1, we use the known wellhead annulus fluid temperature, $T_a = T_{ai}$, and assume that circulating-fluid temperatures for the tubing and annulus at the bottom are equal; that is, $T_t = T_a$ when z = well bottom. Integrating Eq. 11.1 with these boundary conditions, we obtain

$$T_t = \alpha e^{\lambda_1 z} + \beta e^{\lambda_2 z} + g_G z \sin\alpha \pm B g_G + T_{es}, \qquad (11.5)$$

and

$$T_a = (1 \mp B\lambda_1)\alpha e^{\lambda_1 z} + (1 \mp B\lambda_2)\beta e^{\lambda_2 z} + g_G z \sin\alpha + T_{es} \qquad (11.6)$$

Expressions for the various parameters are

$$\alpha = \frac{(T_{ti} T_{es} + B\,\Lambda + |\omega_2 \omega_1|_{z=0})\,\lambda_2 e^{\lambda_2 L} + |\Lambda|_{z=L}}{\lambda_1 e^{\lambda_1 L}\ \lambda_2\ e^{\lambda_2 L}}, \qquad (11\text{-A-}8)$$

$$\beta = \frac{(T_{ai} - T_{es})\ \lambda_1 e^{\lambda_1 L} + g_G(1 - \lambda_1 B)}{\lambda_1\ e^{\lambda_1 L}(1 - \lambda_2 B) - \lambda_2\ e^{\lambda_2 L}(1 - \lambda_1 B)}, \qquad (11\text{-A-}9)$$

$$\lambda_1 = -\frac{L_R}{2} + \frac{L_R}{2}\sqrt{1 + 4(r_c U_a T_D + k_e)\frac{r_t U_t}{r_c U_a k_e}}, \qquad (11\text{-A-}10)$$

and

$$\lambda_2 = -\frac{L_R}{2} - \frac{L_R}{2}\sqrt{1 + 4(r_c U_a T_D + k_e)\frac{r_t U_t}{r_c U_a k_e}}. \qquad (11\text{-A-}11)$$

11-A.2 Constants for Forward-Circulation Models. The constants for the forward-circulation case are somewhat different from those for reverse circulation and are given by the expressions

$$\alpha = \frac{(T_{ti} - T_{es} + B g_G)\ \lambda_2 e^{\lambda_2 L} + g_G}{\lambda_1 e^{\lambda_1 L} - \lambda_2\ e^{\lambda_2 L}}, \qquad (11\text{-A-}12)$$

$$\beta = \frac{(T_{ai} - T_{es} + Bg_G)\ \lambda_1 e^{\lambda_1 L} + g_G}{\lambda_1\ e^{\lambda_1 L} - \lambda_2\ e^{\lambda_2 L}}, \quad \text{(11-A-13)}$$

$$\lambda_1 = \frac{L_R}{2} + \frac{L_R}{2}\sqrt{1 + 4(\ r_c U_a T_D + k_e\ )\ \frac{r_t U_t}{r_c U_a k_e}}, \quad \text{(11-A-14)}$$

and

$$\lambda_2 = \frac{L_R}{2} - \frac{L_R}{2}\sqrt{1 + 4(\ r_c U_a T_D + k_e)\ \frac{r_t U_t}{r_c U_a k_e}}. \quad \text{(11-A-15)}$$

Appendix 11-B

Constants for the Variable Heat-Flux Model

The superposition principle accounts for the variable heat flow rate. To do so, the entire production period is divided into small timesteps. Variables having subscript *i* refer to any given time period, and those with *n* suggest the last time period. The solutions for the tubing- and annular-fluid temperatures are the same as those for the constant heat flux; that is, Eqs. 11.5 and 11.6 apply. However, the expressions for the constants are different. For the case of reverse circulation, the constants are given by

$$\alpha = \frac{(T_{ti} - T_{es} + B\Lambda + |\omega_2 - \omega_1|_{z=0})\ \lambda_2 e^{\lambda_2 L} + |\Lambda|_{z=L}}{\lambda_1 e^{\lambda_1 L} - \lambda_2\ e^{\lambda_2 L}}, \quad \text{(11-B-1)}$$

$$\beta = \frac{(T_{ai} - T_{es} + B\Lambda + |\omega_2 - \omega_1|_{z=0})\ \lambda_1 e^{\lambda_1 L} + |\Lambda|_{z=L}}{\lambda_1 e^{\lambda_1 L} - \lambda_2\ e^{\lambda_2 L}}, \quad \text{(11-B-2)}$$

$$\Lambda = g_G + \frac{F_{n-1}}{2\pi\ k_e} - \frac{1}{2\pi\ k_e} \sum_{i=1}^{n-1} (F_i - F_{i-1})\, T_D\,(t_{D,n} - t_{D,i-1}), \quad \text{(11-B-3)}$$

$$\omega_1 = \frac{Q_{n-1}}{2\pi k_e} T_D(t_{D,n} - t_{D,n-1}), \quad \text{(11-B-4)}$$

and

$$\omega_2 = \frac{1}{2\pi k_e} \sum_{i=1}^{n-1} \left(Q_i - Q_{i-1}\right) T_D(t_{D,n} - t_{D,n-1}), \quad \text{(11-B-5)}$$

where *F* is the change in heat flux (*Q*) per unit well depth (*z*), and the subscripts *i* and *n* are values of the variable for the *i*th and *n*th (last) superposition time.

The constants, *α* and *β*, for the forward-circulation case are somewhat different than those for reverse circulation and are given by the expressions

$$\alpha = \frac{(T_{ti}\ T_{es} + B\,\Lambda + |\omega_2 \omega_1|_{z=0})\ \lambda_2 e^{\lambda_2 L} + |\Lambda|_{z=L}}{\lambda_1 e^{\lambda_1 L}\ \lambda_2\ e^{\lambda_2 L}} \quad \text{(11-B-6)}$$

and

$$\beta = \frac{(T_{ai} - T_{es} + |\omega_2 - \omega_1|_{z=0})\ \lambda_1 e^{\lambda_1 L} + |\Lambda|_{z=L}(1-\lambda_1 B)}{\lambda_1\ e^{\lambda_1 L}(1-\lambda_2 B) - \lambda_2\ e^{\lambda_2 L}(1-\lambda_1 B)} \quad \text{(11-B-7)}$$

The expressions for λ_1 and λ_2 remain the same as in Eqs. 11-A-10 and 11-A-11 for the reverse-circulation case and Eqs. 11-A-14 and 11-A-15 for the forward-circulation case.

Appendix 11-C

Transient Heat Transfer From Mud to Formation

Our analysis is made on the basis of 1 ft of well, containing mass (M) of mud at a temperature T_{ws}. The heat loss per unit time, per unit length of wellbore, is given by

$$Q = M c_p \frac{dT_{ws}}{dt} \quad \text{(11-C-1)}$$

Eq. 11-C-1 shows that heat gained by (or lost from) the mud is a direct consequence of its change in temperature. Because the mud temperature, T_{ws}, will gradually approach the static formation temperature, T_{ei}, the driving force and, hence, the heat-transfer rate, Q, decrease with time. Therefore, T_{ws} is also a function of time. In addition, for any finite well diameter, the mud temperature will vary from the well center to the wall because the mud has ceased to circulate. Here, we have assumed that the mud temperature available is that at the center of the wellbore.

Applying Fourier's law of heat conduction, we can also relate the rate of heat gain to the temperature difference between the well center and the wall, $T_{ws} - T_{wb}$, and the overall-heat-transfer coefficient for the wellbore, U, as

$$Q = -2\pi r U (T_{ws} - T_{wb}). \quad \text{(11-C-2)}$$

Note that, in this case, mud is the only element of resistance to heat transfer in the well. Therefore, here U represents free convection in the wellbore; that is, $U = h$.

Similarly, we can relate heat transfer to the temperature difference between the well wall, T_{wb}, (at well/formation interface) and the undisturbed formation temperature, T_{ei}, as

$$Q = -2\pi k_e \frac{(T_{wb} - T_{ei})}{T_D}, \quad \text{(11-C-3)}$$

where T_D represents the solution of the thermal diffusivity equation obtained by using the cylindrical-source well (Hasan and Kabir 1994b).>

Combining Eqs. 11-C-2 and 11-C-3,

$$Q = -2\pi \left(\frac{r U k_e}{k_e + r U T_D} \right) (T_{ws} - T_{ei}). \quad \text{(11-C-4)}$$

Combining Eqs. 11-C-1 and 11-C-4, we obtain the differential equation for the

variation of mud temperature with time. Thus,

$$\frac{dT_{ws}}{dt} = -\left(\frac{2\pi}{Mc_p}\right)\left(\frac{rUk_e}{k_e + rUT_D}\right)(T_{ws} - T_{ei}) \qquad (11\text{-}C\text{-}5)$$
$$= -L_R'(T_{ws} - T_{ei})$$

where the relaxation-time parameter, L_R', is given by

$$L_R' \equiv \left(\frac{2\pi}{Mc_p}\right)\left(\frac{rUk_e}{k_e + rUT_D}\right), \qquad (11\text{-}C\text{-}6)$$

which is similar to the relaxation parameter L_R discussed in Chapter 6 that relates wellbore flowing-fluid temperature to formation temperature.

As discussed in Chapter 6, T_D in Eq. 11-C-6 may be approximated by the equations

$$T_D = 1.1282\sqrt{t_D}\left(1 - 0.3\sqrt{t_D}\right), \text{for } t_D < 1.5, \qquad (11\text{-}C\text{-}7)$$

$$T_D = (0.4063 + 0.5\ln t_D)\left(1 + \frac{0.6}{t_D}\right), \text{for } t_D > 1.5 \qquad (11\text{-}C\text{-}8)$$

Eq. 11-C-5 may be rearranged and integrated to yield

$$-\ln(T_{ei} - T_{ws}) = C_o + \left(\frac{2\pi}{Mc_p}\right)(rUk_e)\int\frac{dt}{(k_e + rUT_D)}, \qquad (11\text{-}C\text{-}9)$$

where the constant of integration C_o indicates the initial temperature difference between the mud and the formation. Noting that the value of the integral is zero at t = 0, and denoting the initial mud temperature by T_{wso}, we may write

$$C_o = -\ln(T_{ei} - T_{wso}) \qquad (11\text{-}C\text{-}10)$$

Eq. 11-C-10 will be difficult to integrate with T_D, given by Eq. 11-C-8. Even if such operations were possible, the final form will probably be too complex to be useful for graphical analysis. However, for most cases of mud circulation, the elapsed time is small and Eq. 11-C-7 is perhaps adequate. In those circumstances, we can rewrite Eq. 11-C-9 as

$$-\ln(T_{ei} - T_{ws}) =$$
$$C_o + \left(\frac{2\pi}{wc_{pm}}\right)(rUk_e)\left(\frac{r^2}{a}\right)\int\frac{dT_D}{k_e + rU\left[1.1282\sqrt{t_D}\left(1 - 0.3\sqrt{t_D}\right)\right]}, \qquad (11\text{-}C\text{-}11)$$
$$= C_o - C_1 I$$

where

$$I = \int \frac{dT_D}{1 + C_2\sqrt{t_D} - C_3 t_D}, \qquad (11\text{-}C\text{-}12)$$

$$C_1 = \left(\frac{2\pi}{Mc_p}\right)(rU)\left(\frac{r^2}{\alpha}\right), \qquad (11\text{-}C\text{-}13)$$

$$C_2 = 1.1282\left(\frac{rU}{k_e}\right), \qquad (11\text{-}C\text{-}14)$$

and

$$C_3 = 0.3385\left(\frac{rU}{k_e}\right) = 0.3\,C_2 \qquad (11\text{-}C\text{-}15)$$

The integral, *I*, was evaluated by using partial fractions (Hasan and Kabir 1994b), giving the solution

$$T_{ws} = T_{ei} - C_o'' \left\{ \frac{\left[\dfrac{f_1(t_D)}{f_2(t_D)}\right]^{\left(\frac{5.555}{aC_2}\right)}}{f_3(t_D)^{\left(\frac{3.333}{C_2}\right)}} \right\}^{-C_1}, \qquad (11\text{-}C\text{-}16)$$

$$= T_{ei} - C_o'' F(t_D)$$

where

$$f_1(t_D) = a + \sqrt{t_D} - 1.667, \qquad (11\text{-}C\text{-}17)$$

$$f_2(t_D) = a - \sqrt{t_D} + 1.667, \qquad (11\text{-}C\text{-}18)$$

$$f_3(t_D) = 1 + C_2\sqrt{t_D} - 0.3\,C_2 t_D, \qquad (11\text{-}C\text{-}19)$$

$$C_o'' = (T_{ei} - T_{wso})C_4, \qquad (11\text{-}C\text{-}20)$$

$$a = \left[\left(\frac{C_2^2}{4C_3^2}\right) + \left(\frac{1}{C_3}\right)\right]^{0.5} = \left[2.777 + \left(\frac{3.3333}{C_2}\right)\right]^{0.5}. \qquad (11\text{-}C\text{-}21)$$

and

$$C_4 = \frac{a - 1.667^{\frac{5.555C_1}{aC_2}}}{a + 1.667}, \qquad (11\text{-}C\text{-}22)$$

Appendix 11-D

Oil PVT Properties for Estimating Maximum Discharge

Table 11-D-1 presents compositional analysis of three fluids for generating fluid properties needed for probabilistic analysis. Note that these fluids represent those that are of comparable burial depth and in general proximity to Macondo. Table 11-D-2 shows the generated PVT properties for three oil types needed for flow simulations in both reservoir and wellbore.

Separator	Component	Oil-1	Oil-2	Oil-3
	N2	0.187	0.187	0.187
	CO2	0.461	0.461	0.461
	C1	73.06098	71.16893	69.27689
	C2	5.821	5.821	5.821
	C3	4.142	4.142	4.142
	iC4	0.908	0.908	0.908
	nC4	2.034	2.034	2.034
	iC5	0.795	0.795	0.795
	nC5	0.941	0.941	0.941
	C6	1.511	1.511	1.511
	C7-10	3.4964	4.148865	4.801328
	C11-14	2.265387	2.688132	3.110876
	C15-19	2.017568	2.394068	2.770566
	C20-29	1.647187	1.954569	2.261951
	C30+	0.712479	0.845435	0.978391
	Total	100	100	100
	C7+	10.13902	12.03107	13.92311
4-Stage	GOR, scf/STB	4009	3313	2804

Table 11-D.1—Compositional analysis of three fluids.

Oil Type	p, psia	Bo, RB/STB	μo, cp
Oil-1	7,655	2.60616	0.11
	8,253	2.56669	0.117
	9,015	2.52259	0.126

	11,015	2.43088	0.151
	13,015	2.36246	0.177
	15,015	2.30897	0.203
	17,507	2.25633	0.236
	19,015	2.22993	0.257
	20,015	2.21419	0.27
Oil-2	7,210	2.74501	0.097
	7,515	2.71997	0.1
	8,253	2.66581	0.109
	9,015	2.6177	0.117
	11,015	2.51807	0.14
	13,015	2.44409	0.165
	15,015	2.38646	0.189
	17,507	2.32989	0.221
	19,015	2.30158	0.24
	20,015	2.28473	0.253
Oil-3	6,784	2.49136	0.109
	6,887	2.48368	0.11
	7,015	2.4744	0.112
	7,065	2.47084	0.112
	7,515	2.44059	0.118
	8,253	2.39677	0.128
	9,015	2.3576	0.139
	11,015	2.27577	0.167
	13,015	2.21442	0.196
	15,015	2.16628	0.226
	17,507	2.11876	0.263
	19,015	2.09488	0.286
	20,015	2.08063	0.301

Table 11-D.2—PVT properties of fluids.

Chapter 12

Production Operations and Flow Assurance

12.1 Systems Analysis

This chapter explores combining various aspects of flow in wellbores with that in the reservoir to gain a holistic understanding of the coupled system. Accordingly, we will explore systems analysis with flow-after-flow tests, temperature profiles in gas lift wells, steam/water flow and surface metering, and wellbore solids deposition. In doing so, we will provide two field examples that probe flow assurance issues with coupled wellbore, reservoir, and surface-network models.

12.1.1 Introduction. The systems or Nodal™ analysis as practiced today is rooted in Gilbert's (1954) pioneering work. Studies of Mach et al. (1979), Brown (1984), and Brown and Lea (1985) laid the foundation of modern systems analysis. In conventional systems analysis, a steady-state two-phase model is used to simulate the wellbore flow behavior, and Vogel's (1968) empirical correlation or its variations describe the reservoir's inflow performance. This approach has served the industry quite well. Many texts (Beggs 1991; Brill and Mukherjee 1999; Economides et al. 2012) have elucidated this approach, and so we will not repeat it here. Instead, we provide some insights that will improve flow simulation in both the reservoir and the wellbore.

This section also explores how surface and downhole data gathering can be coordinated and the systems analysis can be performed at the same time, leading to superior understanding of the behavior of a coupled wellbore/reservoir system. Finally, we introduce the concept of seamless systems analysis, which allows one to model elements of the wellbore and reservoir as an integrated system, rather than in discrete nodes.

12.1.2 Conventional Systems Analysis. Ordinarily, systems analysis relies on forward steady-state, two-phase flow calculation from such input parameters as wellhead pressure and temperature, tubular inner diameter (ID), flow rates of each phase, and the like. If measured downhole pressure and/or rate data are available, the pressure traverse is matched before projecting well behavior at other wellhead choke settings. While this approach is practiced routinely, attention to details often reveals some of the uncertainties associated with the analysis and the potential pitfalls. Problems compound in systems in which pressure drops in the reservoir and wellbore are of the same order of magnitude.

Let us examine some of the uncertainties associated with any systems analysis. While matching performance of a production test, change in gas/oil ratio (GOR) is perhaps the most popular of them all. Modest changes in GOR are often justified because of the inherent errors associated with rate measurements, for gas in particular. Use of a standard pressure/volume/temperature (PVT) correlation is another source of error. In particular, if the oil's bubblepoint pressure occurs in the wellbore, matching this pressure is of great significance before successfully mimicking the entire pressure profile. Other sources of error stem from unstable wellhead rates, assumptions of linear wellbore fluid temperature profiles, and computations from the top down rather than the bottom up, among others. Besides wellbore flow simulation, flow in the reservoir can introduce a great deal of uncertainty. Presence of non-Darcy flow, flow contributions from other layers at larger drawdowns, and disproportionate volumes of gas or water at larger drawdowns are some of the problems one may encounter.

What is disconcerting is that matching wellhead pressure or a wellbore pressure profile for a given rate is no guarantee that the well will behave any better at other rates. In other words, calibration does not ensure superior performance projection, which runs counter to conventional wisdom. This point is made amply clear when we examine **Fig. 12.1.** Here, a match was obtained at a p_{wh} of 529 psia with the Hagedorn and Brown (1965) correlation. With decreased p_{wh} or increased choke settings, the mismatch becomes quite apparent.

This mismatch problem is further highlighted by **Fig. 12.2,** showing another field example. In these two figures, the equations describing flow in the reservoir have the following forms.

$$\text{Forchheimer equation: } \Delta p = \overline{p} - p_{wf} = a_t q + bq^2 \quad (12.1)$$

$$\text{Backpressure or Fetkovich equation: } q = C(\Delta p)^n \quad (12.2)$$

The Darcy equation has the same form as Eq. 12.2 but without the exponent n. Note that in the examples shown, we used Δp instead of Δp^2 because of single-phase flow in the reservoir.

We surmise that the logical explanation for seemingly unpredictable behavior, with different choke settings, is rooted in two-phase flow modeling in the wellbore. That is, a correlation may represent a given flow condition better than others yet may do an unsatisfactory job in mimicking the pressure behavior when flow patterns change under different choke settings. Let us explore practical implications of the uncertainty of the p_{wf} calculation from wellhead data.

Often, engineers estimate p_{wf} en route to computing inflow performance relationship (IPR) when direct measurements are unavailable. While this practice is acceptable in systems in which large reservoir pressure drop occurs because of unfavorable flow characteristics (Chambers et al. 2001), problems arise for systems where pressure drops in the formation and wellbore are comparable. Let us illustrate

this point with a case study. Wellbore pressure-drop calculations on some 109 wells in a multidarcy reservoir show that among other correlations, the widely used Hagedorn and Brown (1965) correlation yields the lowest average error of 3.17%. **Fig. 12.3** compares the measured p_{wf} with calculated values. By all measures, this error is very low. Yet, its implication may be quite serious. For instance, **Table 12.1** exemplifies the problem by showing the error analysis for a single well, assuming just 3% error. For wells not conforming to the 3% error band, the absolute error in the productivity index J_p will be much higher. The main problem stems from the error in the p_{wf} calculation (±50 psi), which is on the same order as the Δp (≈ 91 psi) itself. Uncertainty in $\overline{p}$ is, of course, another source for error.

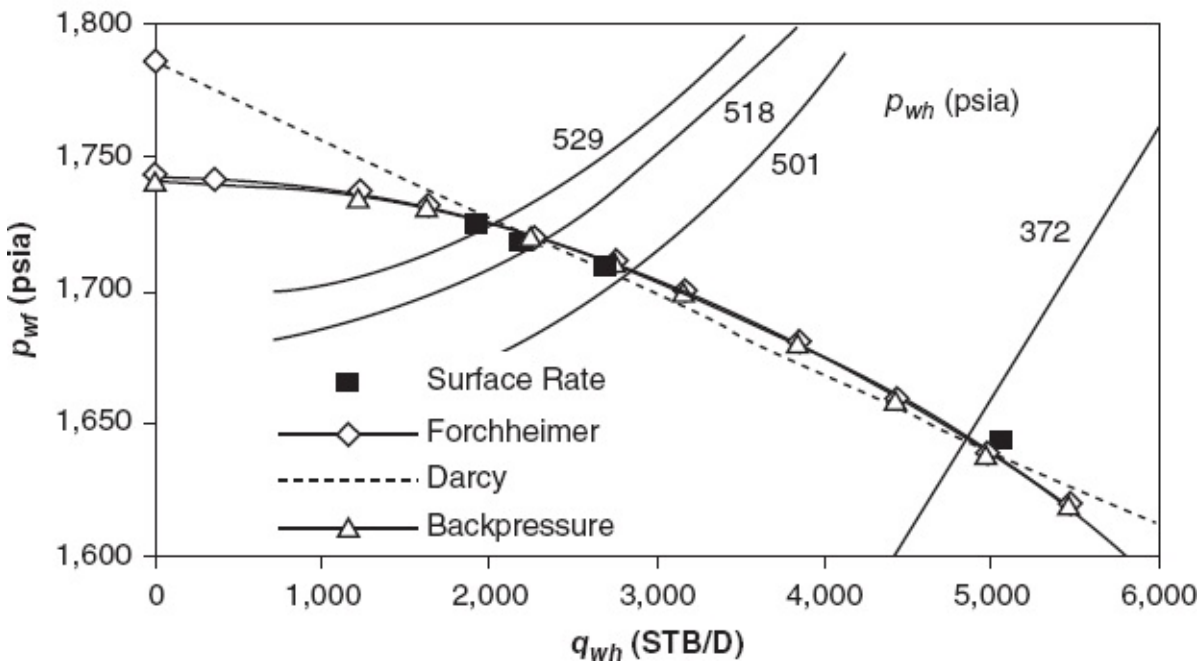

Fig. 12.1—Systems analysis for Well B-OF8.

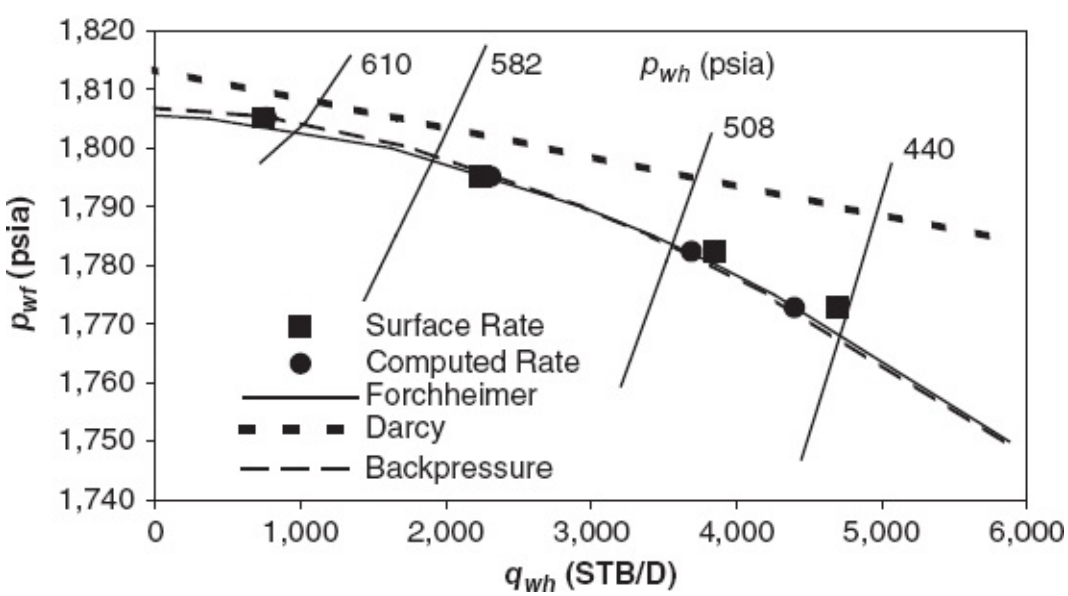

Fig. 12.2—Systems analysis for Well B-FN9.

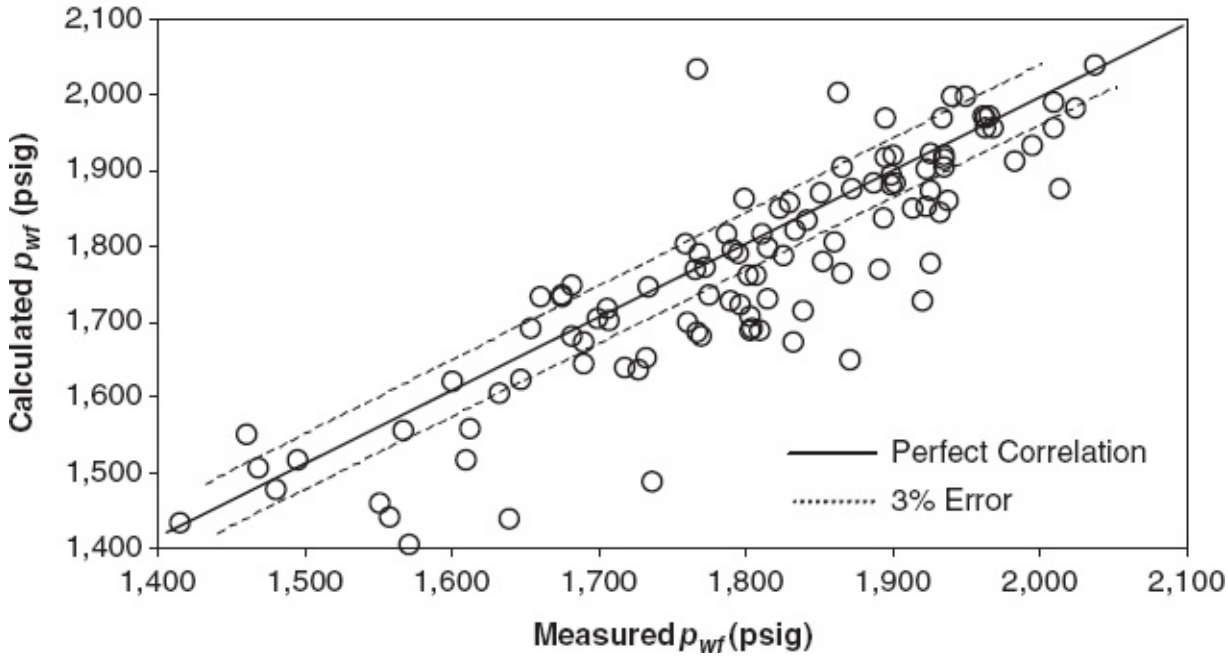

Fig. 12.3—Comparison of measured and computed p_{wf}.

	Measured	P_{wf} Error (-3%)	P_{wf} Error (3%)
$\overline{p}$ psig	1,841	1,841	1,841
P_{wf}, psig	1,738	1,685.86	1,790.14
Δp, psi	103	155.14	50.86
q, STB/D	4,956	4,956	4,956
J_p, STB/D-psi	48.12	31.945	97.44
Error in J_p, %	0	-33.6	102.5

Table 12.1—Error analysis of J_p, Well D-78.

12.1.3 Establishing Reservoir Flow Behavior With Pressure-Rate Data. As stated earlier, the conventional systems analysis relies on the use of Vogel's (1968) method for computing a well's IPR. Once the bubblepoint pressure is established, the method requires measuring or inferring flowing bottomhole pressure for the corresponding wellhead rate to establish IPR during pseudosteady- or steady-state flow in the reservoir. Below the bubblepoint pressure, the Vogel-type expression is given by

$$\frac{q}{q_m} = 1 - 0.2\frac{p_{wf}}{\overline{p}} - 0.8\left(\frac{p_{wf}}{\overline{p}}\right)^2 \quad (12.3)$$

Ordinarily, one rate suffices to describe the IPR once q_m is evaluated from Eq. 12.3

for a corresponding $p_{wf} - q$ data set, with known system $\bar{p}$. Howeer, this method presupposes that flow in the reservoir obeys Darcy's law. In other words, presence of non-Darcy flow can potentially introduce large errors in systems analysis.

Historically, non-Darcy flow has been associated with gas wells. However, a number of studies have shown that non-Darcy flow can occur in oil reservoirs. We will now explore the approach that establishes the Darcy or non-Darcy characteristic of the reservoir flow behavior using transient testing. Although a multirate transient test can be conducted in a standalone mode, data gathering can often occur in conjunction with production logging.

Conventional practices of systems analysis, transient testing, and flow profiling generally lack coordination to maximize information gathering. Although production logs are run routinely to diagnose wellbore flow problems, their full potential often goes unexplored. Ordinarily, flow and shut-in passes are recorded to discern flow contributions from completion intervals. Because various choke settings cause changes in rates, stationary measurements of transient pressure and rate data have the potential for yielding reservoir parameters for a single zone or a layered-reservoir system. Tests can be conducted so that flow profiling and transient downhole pressure/rate data gathering is completed in a single operation. Kabir et al. (1998) present details of the test procedure.

Field Example 12.1. This example comes from Kabir et al. (1998). The well was flowing on a 36/64-in. choke, and the test was carefully performed to avoid altering the pseudosteady-state flow condition. Flowing gradient data were gathered en route to reaching the desired depth by running flowing passes across perforations at various tool speeds. Thereafter, the tool string was set within the tubing, and all transient test data were gathered by keeping the entire production-logging tool string within the tubing.

***Solution*. Fig. 12.4** presents the test history without the 2-hour buildup at the end of the 4-hour flow-after-flow period for clarity. Note that Kabir et al. (2012a) provided theoretical justification of the flow-after-flow test and offered a pragmatic approach to analyzing field data. Also shown in Fig. 12.4 is the computed rate history, generated after diagnosing the model and estimating its parameters. Measurements of both surface and sandface rates allowed calibration of inline spinner, used for collecting sandface rates. **Fig. 12.5** presents a calibration curve reflecting the expected linear trend of two independent measurements. This calibration line was used to convert the spinner response to volumetric surface rate recorded at discrete time intervals, as shown in Fig. 12.4.

Model diagnosis entails constructing the log-log pressure/convolution-derivative graph of all transients, shown in **Fig. 12.6.** Despite the use of quality spinner data, scatter is quite evident. However, the buildup signature, shown by the solid line, presents the customary radial-flow response. Separation of pressure curves is a strong indication of rate-dependent skin, however.

Fig. 12.7, presenting the same data on a semilog graph, clearly indicates separation of various flow period data with progressively higher rates. Data for the

first flow period do not conform to the expected positive-slope trend. Scrutiny of absolute rates suggests that the well was not in a very stable flowing condition at the 24/64-in. choke setting, thereby explaining the discrepancy.

The analysis of individual transients, shown in Fig. 12.7, allowed separation of static from dynamic or non-Darcy skin. **Fig. 12.8** presents the total skin-rate analysis. Interestingly enough, the conventional buildup analysis estimates the total composite skin, shown in **Fig. 12.9.** In the absence of multirate tests, diagnosing non-Darcy skin becomes a nearly impossible proposition.

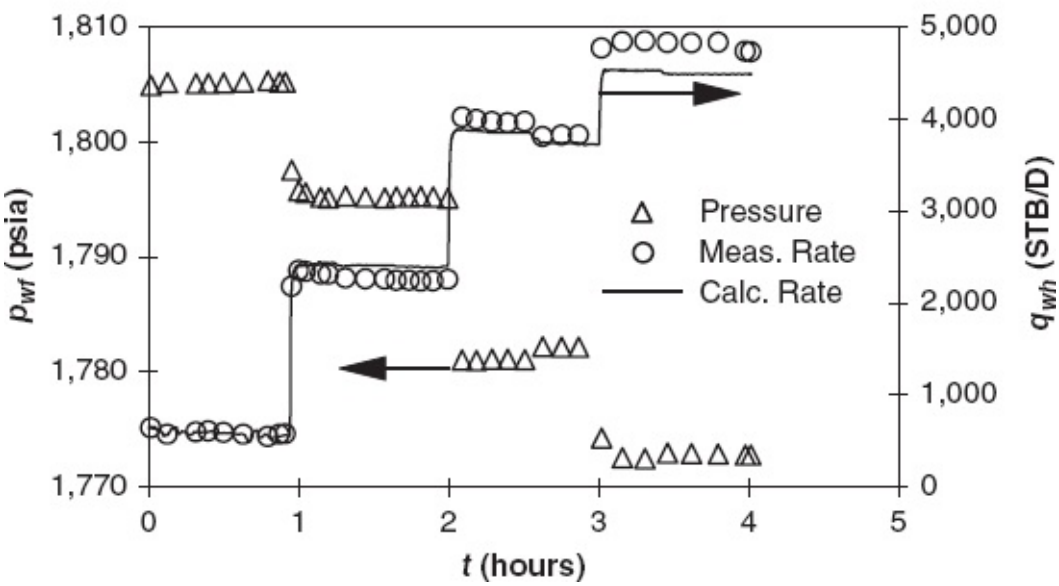

Fig. 12.4—Test history, Well B-148.

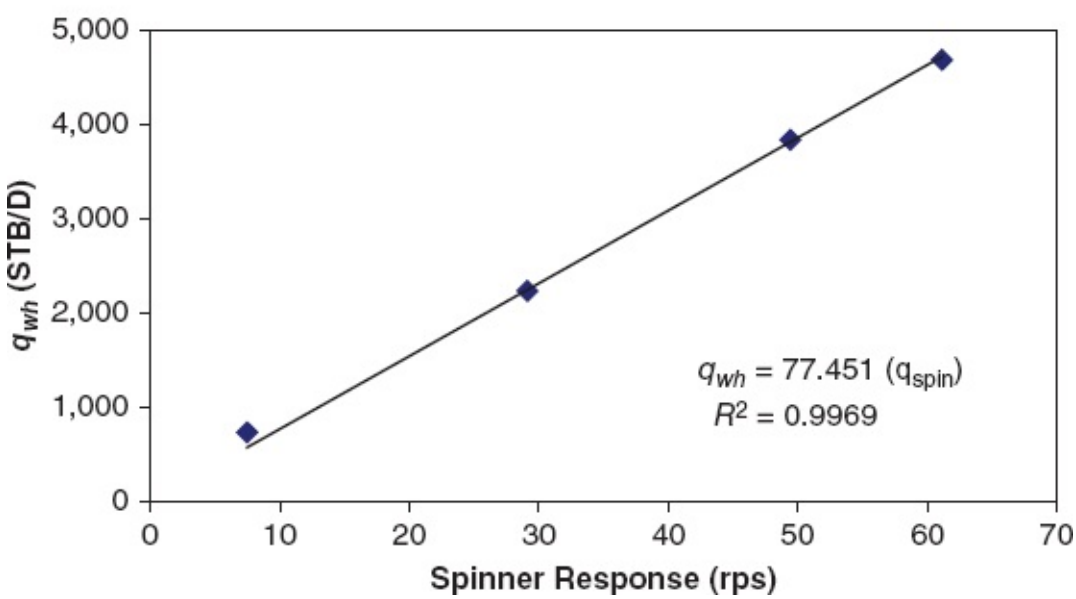

Fig. 12.5—Calibration of inline spinner response.

To check the results of the multirate analysis, we constructed a graph in accord

with Eq. 12-A-4 in Appendix12-A. Appendix 12-A presents the details of the pressure and rate superposition equations used in this example. **Fig. 12.10** corroborates the quality of computed rates. We estimated that at the highest drawdown, corresponding to the fourth flow period, additional production of approximately 300 STB/D occurred from the upper completion interval, shown in **Fig. 12.11.** Actually, there was evidence of some flow from the upper interval, which has flow characteristics inferior to those of the main interval, even at 2,811 STB/D of total production. With this body of information, one can attempt to ascertain the flow properties of the tighter upper layer by using the layered-reservoir analysis.

Field Example 12.1 demonstrates how transient data can be collected and analyzed for estimating reservoir parameters. Once parameters are estimated, characterizing a reservoir's inflow performance becomes the next logical step. As shown in Fig. 12.1, the IPR can be generated using three methods: the straightline method, assuming Darcy flow above the bubblepoint, and the Forchheimer and backpressure analyses for non-Darcy flow. Note that the average pressure calculation of 1,807 psia from the non-Darcy analysis corroborates that estimated from the semilog analysis (Fig. 12.9), thereby lending credence to the non-Darcy flow parameter estimation.

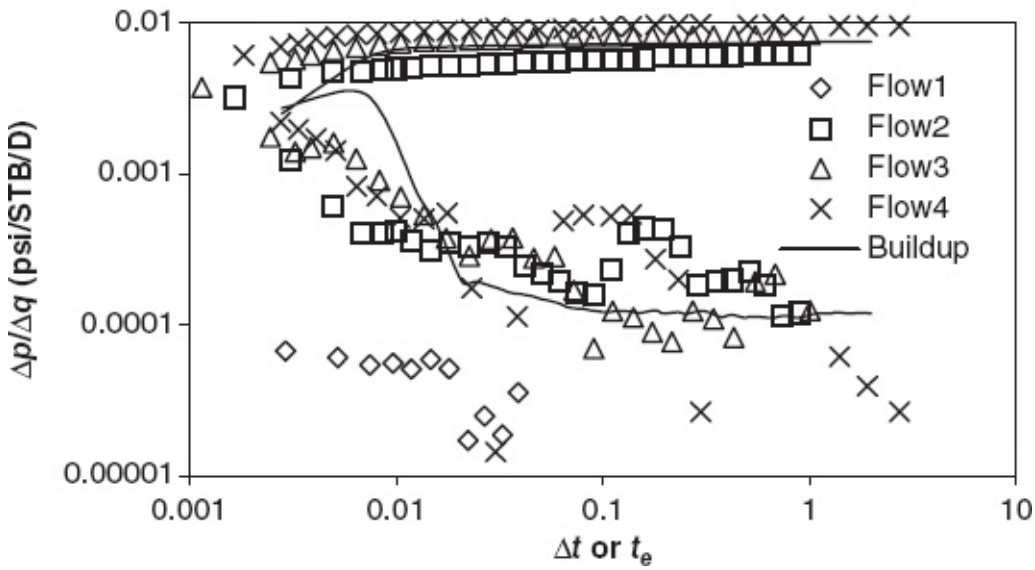

Fig. 12.6—Log-log diagnosis of all transients.

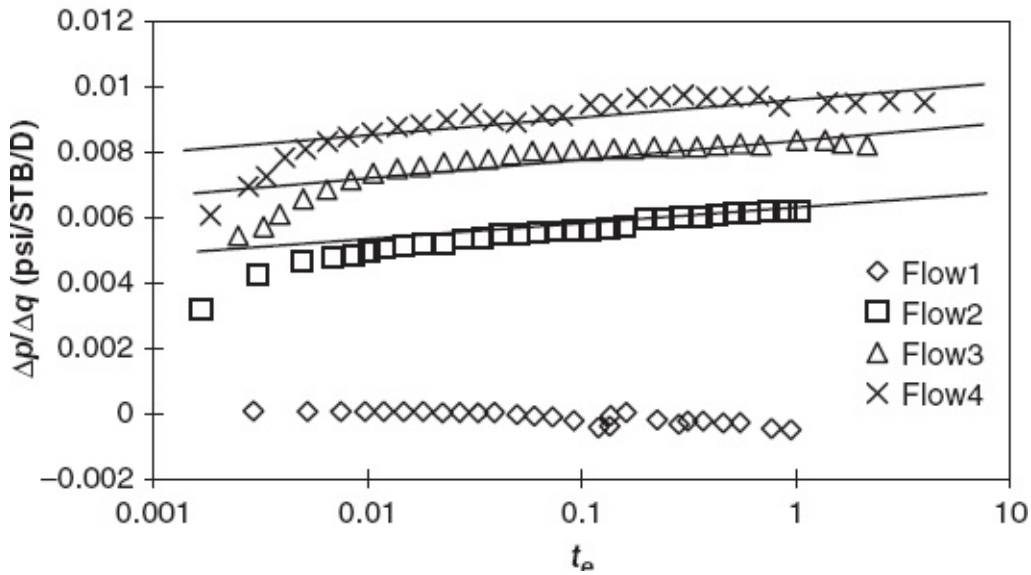

Fig. 12.7—Semilog analysis separates skin components.

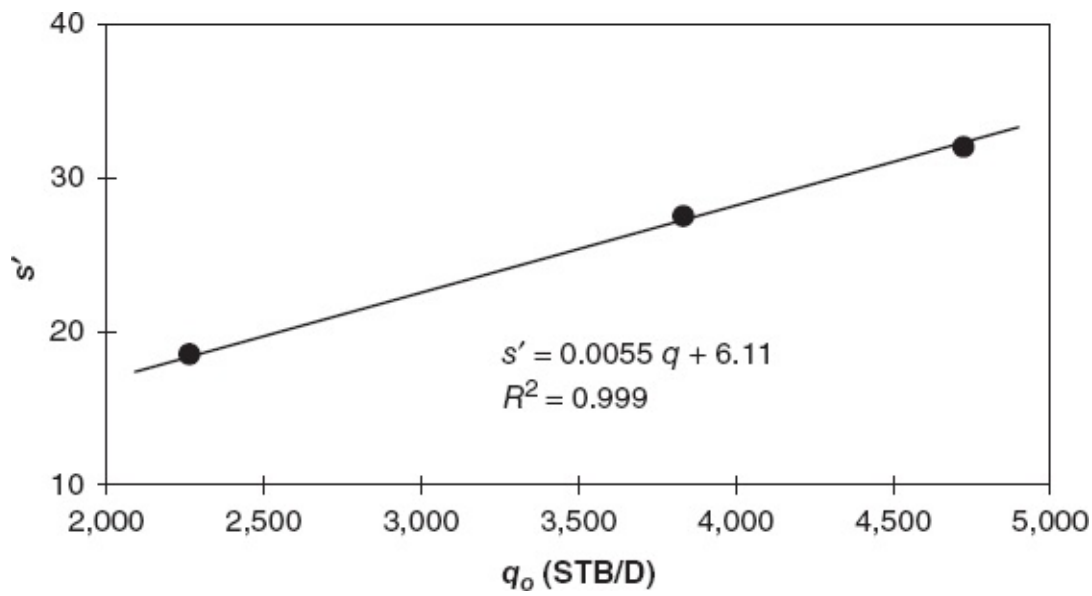

Fig. 12.8—Skin analysis shows significant non-Darcy effect.

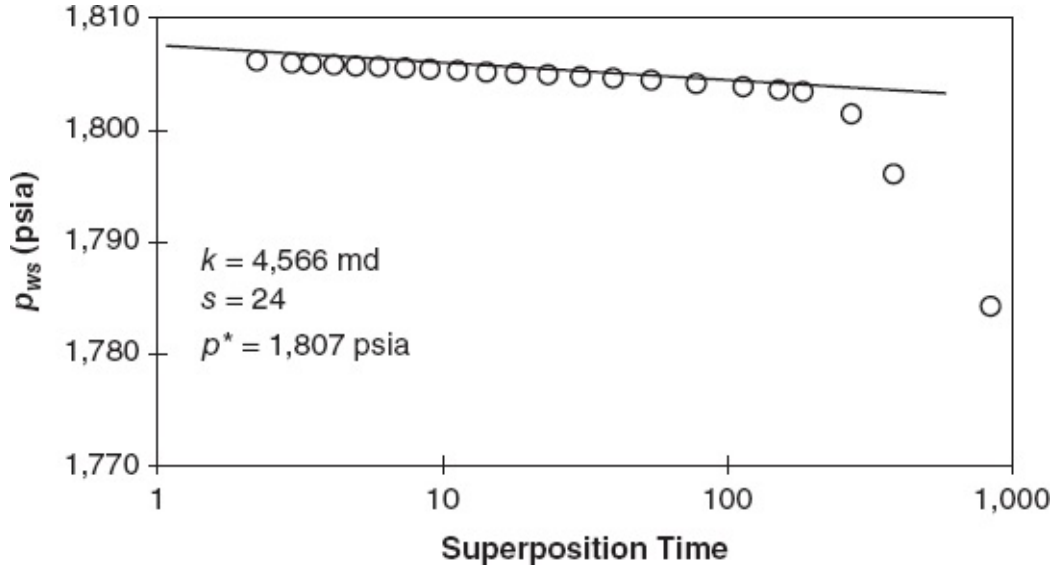

Fig. 12.9—Semilog analysis of buildup data.

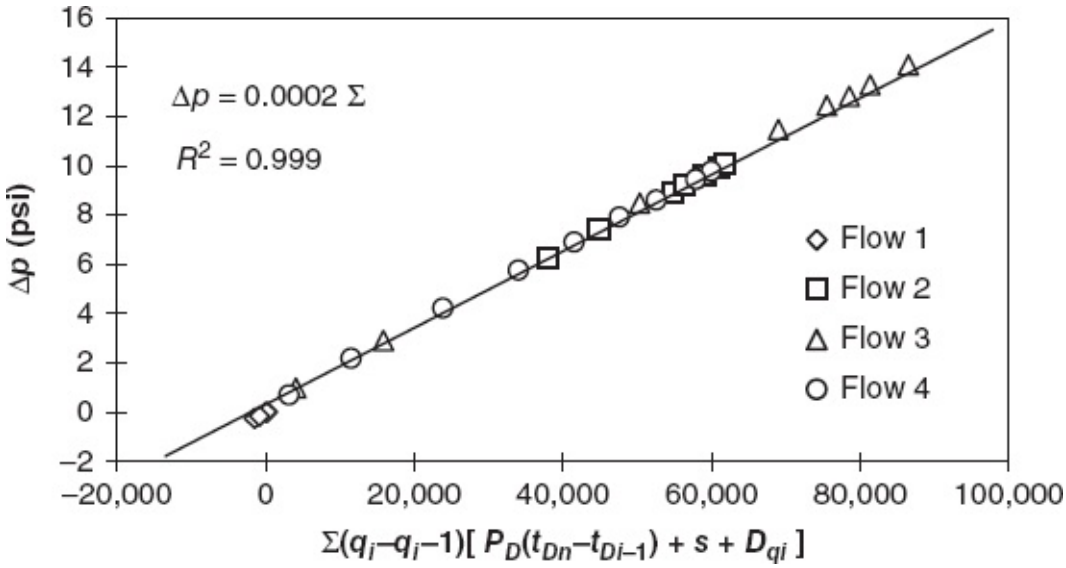

Fig. 12.10—Validation of computed rates.

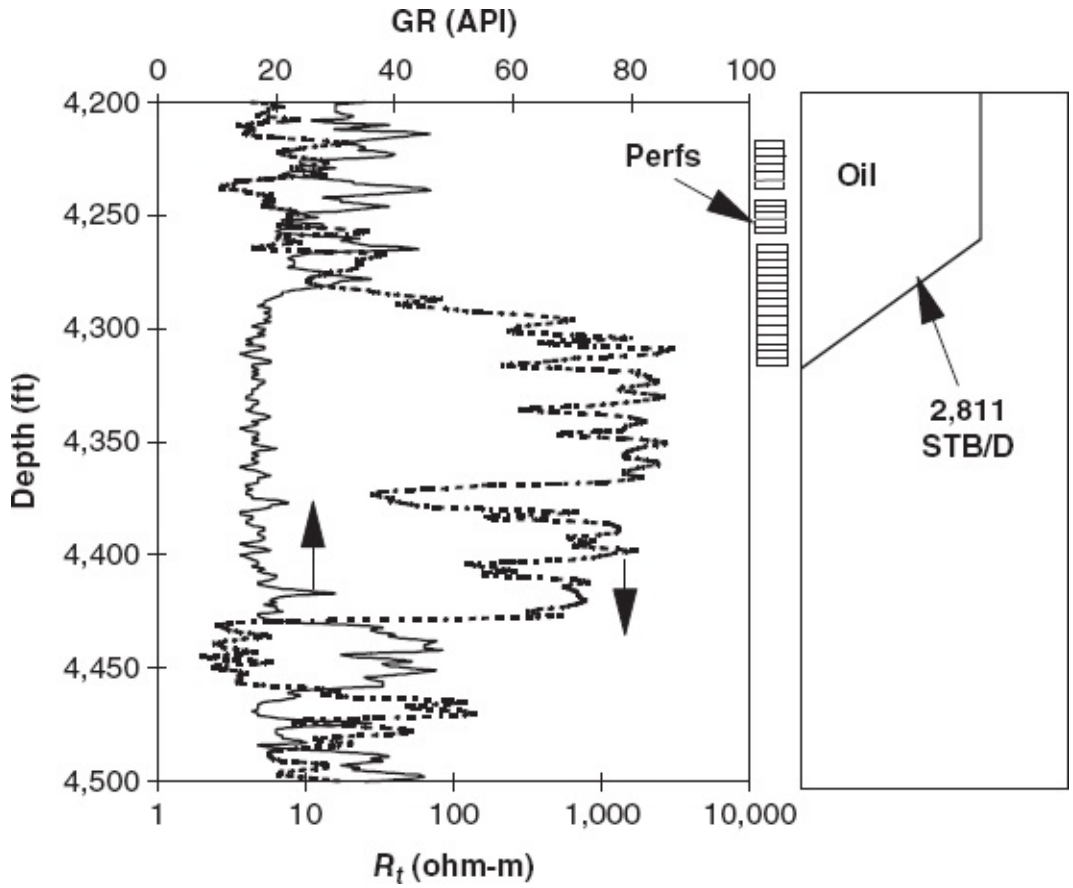

Fig. 12.11—Openhole and production log traces, Well B-OF8.

12.1.4 Seamless Systems Analysis. As shown in Figs. 12.1 and 12.2, individual nodes (across which pressure drop occurs), such as the reservoir and the wellbore, require separate analysis in a conventional systems analysis. That is, the final output at the wellhead is determined by the intersection of the IPR with the tubing performance curve at a given wellhead pressure. Other nodes, such as completion and surface and downhole chokes, may be added to the analysis if desired. In other words, various nodes can be pieced together to make up the complete system. Note that because of steady-state flow simulation at each node, rate instability or any transient process cannot be captured. We now present the notion of seamless systems analysis.

In this systems analysis approach, various nodes of reservoir, completion, and wellbore are treated as parts of a contiguous unit. This treatment is possible when we use a coupled transient wellbore/reservoir simulator, such as discussed in Chapter 9. The advantage of this approach is that various, everyday unsteady-state flow situations can be addressed to obtain a realistic picture of the well's ability to handle a given situation. Some of these examples include, among others, flow instability, triggered by reduced choke size; complex heat flow problems, induced by simultaneous flow in both tubing and annulus or in offshore wells; and wellbore unloading upon well shut-in. Conventional systems analysis is clearly not designed to handle these and other transient problems.

Field Example 12.2. The advantages of seamless systems analysis is emphasized by the following field example involving the reservoir and wellbore described earlier. Forward simulations were performed using the estimated reservoir parameters (k, s, $\bar{p}$, D) and the well description to match the observed wellbore data, collected during flow and shut-in conditions. **Fig. 12.12** shows the match of wellbore pressure profiles during both flow and shut-in conditions. On the other hand, **Fig. 12.13** presents the fluid temperature and density profiles during the flowing condition. No adjustments of input parameters were made to achieve the matches.

In these transient simulations, we observed the dominating influence of bubbly and slug flows. To perform these simulations, Hasan et al. (1998) modified the simulator, as discussed in Chapter 9, to include non-Darcy flow effects. Because data from only one flow period were available, we were able to match data from that flow period. However, the ability to reproduce the pressure behavior during shut-in condition lends confidence in the modeling approach.

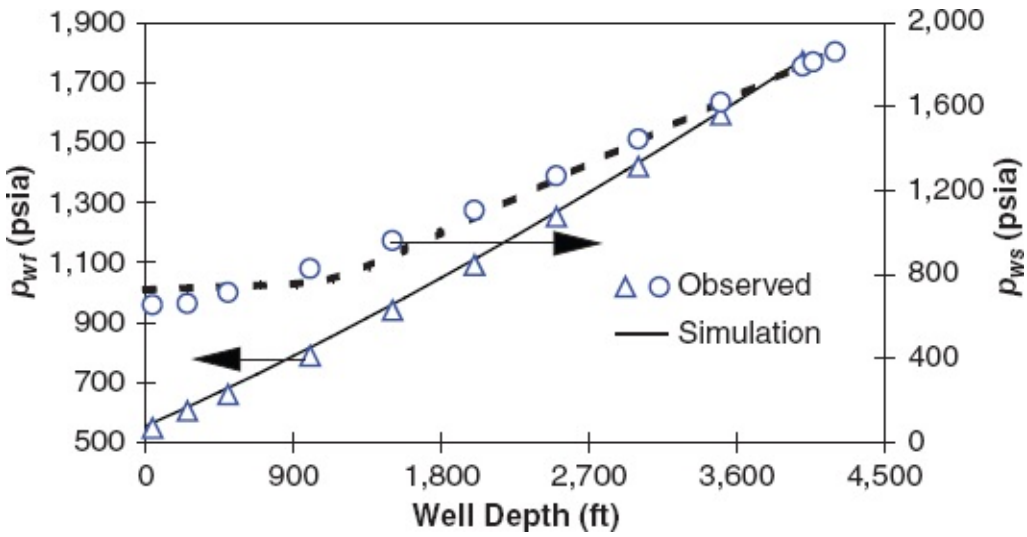

Fig. 12.12—Matching pressure profiles during flow and shut-in cases.

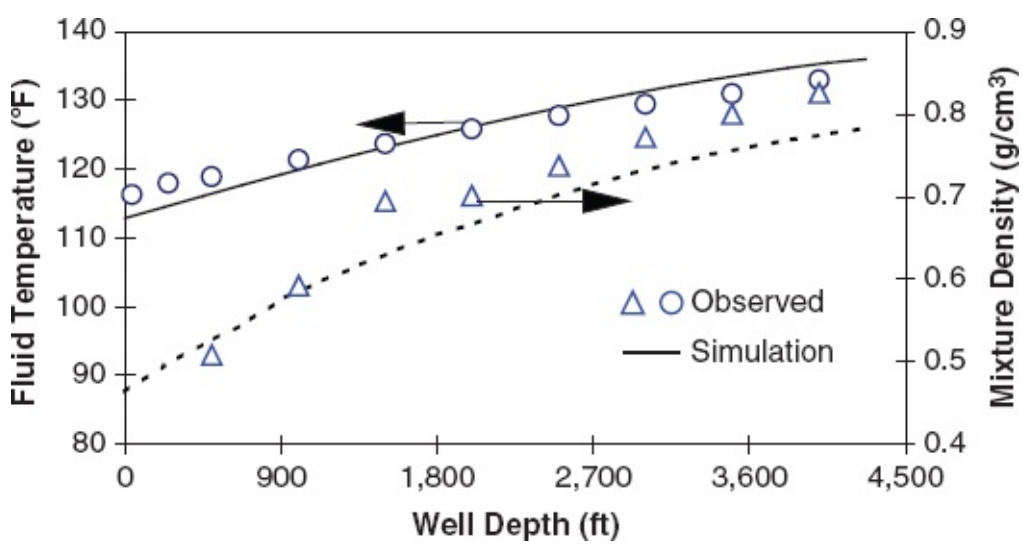

Fig. 12.13—Matching fluid temperature and density profiles.

We present one other field example in which complex heat transfer occurs because of simultaneous production in the tubing and in the tubing/casing annulus. In this case, we present just the steady-state flow simulation in the wellbore to underscore the need for an appropriate heat-transfer model to solve a given problem.

This well produces up the tubing and annulus. Field measurements were made in the tubing string during flowing condition at various depths, called stations. At each station, 15 minutes was allowed for thermal equilibration to occur between the external temperature probe and its surrounding fluids.

***Solution*. Fig. 12.14** shows that the model, discussed in Chapter 8 and represented by the solid line, successfully reproduces the measured tubing fluid temperature within engineering accuracy. The temperature difference between the tubing and the annulus is small because flow in both strings promotes heat transfer. Note that the production of annular fluid causes higher dissipation of heat because of forced convection than would be the case had the annular fluid been stationary. The dotted line captures the trend for this hypothetical case of no production through the annulus. Also shown in Fig. 12.14 is the match of pressure data with the two-phase flow models of Ansari et al. (1994) and Hasan and Kabir (1992).

As Fig. 12.14 shows, both the Hasan-Kabir and Ansari et al. models performed well in reproducing the field data. In fact, these two models produced indistinguishable traces. That is because most of the string is dominated by the bubbly flow pattern, straddled by single-phase flow toward the bottom and slug flow at the top. As shown by Ansari et al., these two models perform similarly in the bubbly flow regime.

12.1.5 Systems Analysis Summary. Conventional systems analysis as practiced today is intended for steadystate flow. Although it works well for common usage, problems arise when heat flow becomes complex owing to completion and/or when non-Darcy flow occurs in the reservoir. In Section 12.1, we presented a method for collecting and analyzing transient data for generating an appropriate IPR for a well. Thereafter, we presented the notion of seamless systems analysis, which requires the use of a transient wellbore/reservoir simulator. In this approach, complex fluid and heat flow situations can be handled for either unsteady-state or steady-state flow in a rigorous fashion.

12.2 Temperature Profiles In Gas Lift Wells

12.2.1 Introduction. In a continuous-flow gas lift operation, gas is injected down the annulus into the tubing near the top of perforations to aerate the liquid column, thereby providing the necessary stimulus for fluid flow. Because the volumetric gas rate is dependent on both pressure and temperature at the depth of injection, accurate knowledge of these entities cannot be overemphasized for an efficient lift. In particular, the behavior of the nitrogen gas, charged in the dome, is critically

dependent on the temperature estimation for optimal performance of the bellows-charged gas lift valves.

Gas lift technology has evolved and matured over the years since the pioneering studies of Poettmann-Carpenter (1952) and Bertuzzi et al. (1953). This lift technique ranks second to sucker-rod pumping, given the number of installations around the world. The main design criterion revolves around minimizing the energy—that is, compressor horsepower. For gas injection at a certain depth for maximum lift, systematic approaches have emerged (Kanu et al. 1981; Brown et al. 1982; Mach et al. 1983) for optimizing gas lift design. Rapid development has also been made in the design of various types of gas lift valves (Brown et al. 1982; Winkler 1987, Chap. 5), such as pressure-controlled, fluid-controlled, and throttled valves. In particular, wireline-retrievability of these valves has made this lift technique most attractive, especially in offshore wells.

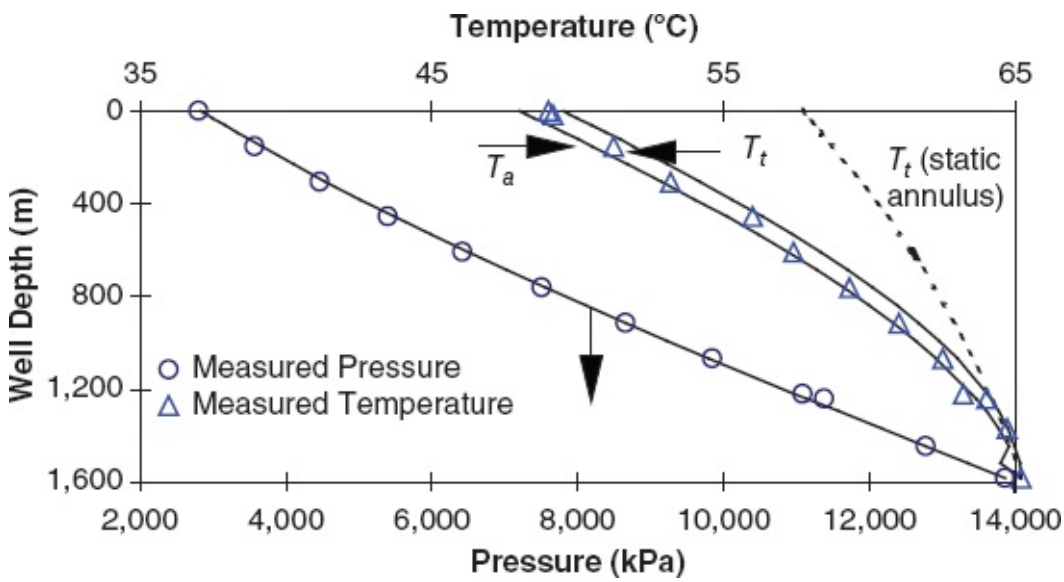

Fig. 12.14—Matching wellbore temperature and pressure data, Well A28.

To design a gas lift system from the viewpoints of fluid flow and valve mechanics, an accurate knowledge of fluid temperature in both strings is very desirable. Empirical methods (Kirkpatrick 1959; Shiu and Beggs 1980) are available for computing temperature profiles in the tubing while assuming a linear temperature profile in the annulus experiencing gas injection. Usually, these methods are not always reliable because of their empirical basis. Methods discussed earlier in Chapter 6, Section 6.4, apply to self-flowing wells and are not directly applicable here because the gas temperature in the annulus needs estimating.

In this section, we present a mechanistic model to compute temperature profiles for fluids in both conduits of a vertical or a deviated well. The coupled tubing/annulus/formation heat flow problem is solved so that simultaneous solutions are obtained as a function of elapsed time and well depth. Unsteady heat transfer is considered in the formation, while steady heat transfer is assumed in the conduits.

This material is abstracted from Hasan and Kabir (1996).

12.2.2 Mathematical Model. During a continuous-flow gas lift operation, the gas is injected down the annulus to aerate the liquid to be lifted up the tubing. The physical situation, as shown schematically in **Fig. 12.15,** is quite similar to the case of production through tubing and annulus described in Chapter 8. We may write energy balance (Hasan and Kabir 1996) for the annular gas contained in a differential element dz in terms of heat transferred from the formation to the fluid Q and from the annulus fluid to the tubing fluid Q_{ta}, fluid enthalpy H, and its potential and kinetic energies as

$$H_a(z)+\frac{(L-z)g\sin\alpha}{g_cJ}+\frac{v^2(z)}{g_cJ}+\frac{Q}{w_a}\mathrm{d}z = H_a(z+\mathrm{d}z)+\frac{(\mathrm{L}-z-\mathrm{d}z)g\sin\alpha}{g_cJ}+\frac{v^2(z+\mathrm{d}z)}{g_cJ}+\frac{Q_{ta}}{w_a}\mathrm{d}z \quad \ldots\ldots (12.4)$$

Rewriting Eq. 12.4,

$$\frac{\mathrm{d}H_a}{\mathrm{d}z}-\frac{g\sin\alpha}{g_cJ}+\frac{v_a}{g_cJ}\frac{\mathrm{d}v_a}{\mathrm{d}z}=\frac{Q-Q_{ta}}{w} \quad \ldots\ldots (12.5)$$

In Eq. 12.5, as in Eq. 6.19, Q is the heat transferred from the formation to the annular fluid, given by

$$Q=w_ac_{pa}L_R\left(T_{ei}-T_a\right) \quad \ldots\ldots (12.6)$$

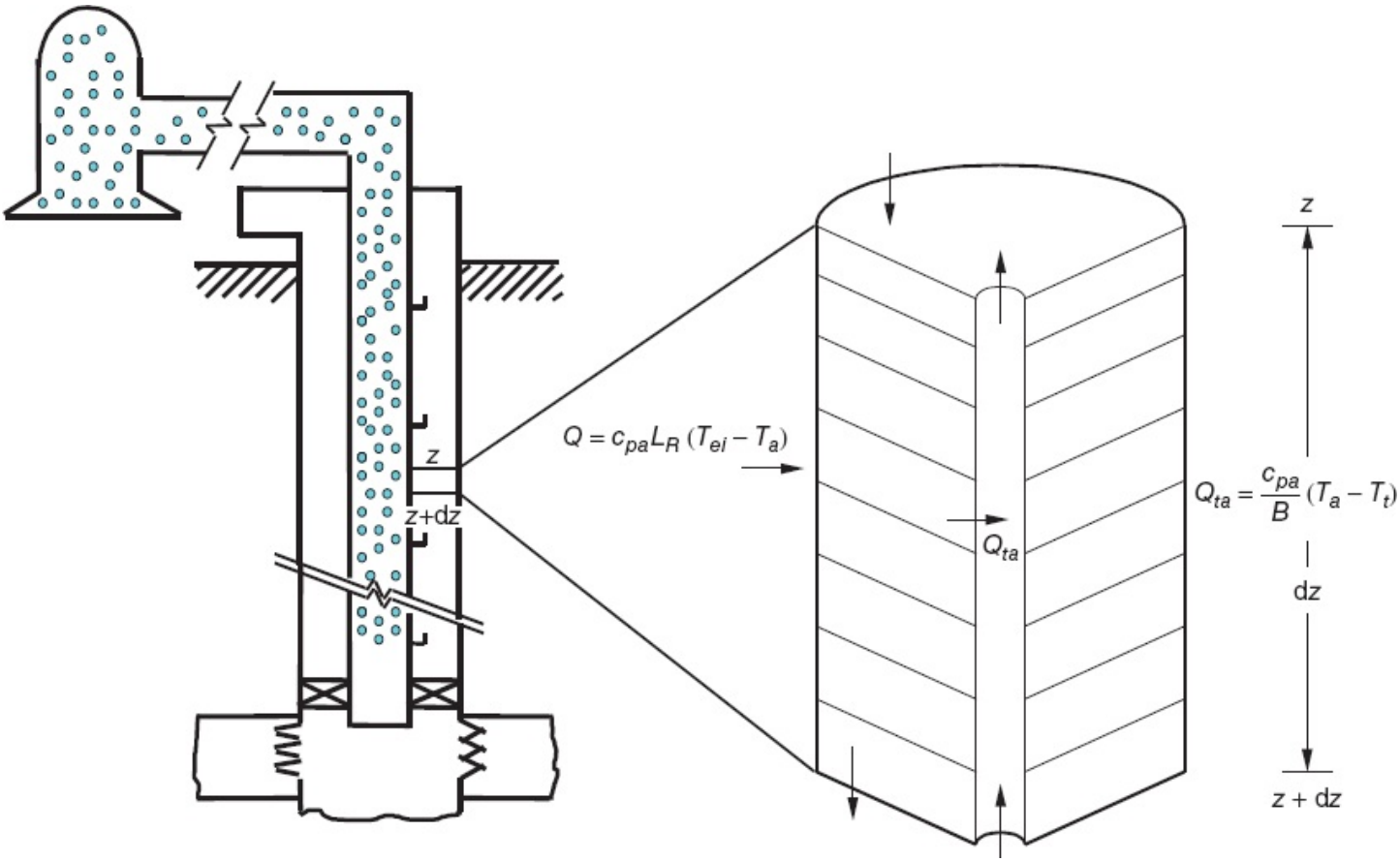

Fig. 12.15—Schematic of heat balance for tubulars and formation in a gas lift well.

Heat transferred from the annular fluid to that in the tubing, Q_{ta}, is given by Eq. 12.7 (see Eq. 8.2) as

$$Q_{ta} = \frac{w_a c_{pa}}{B}\left(T_a - T_t\right), \qquad (12.7)$$

where

$$B = \frac{w_a c_{pa}}{2\pi r_t U_t} \qquad (12.8)$$

Combining Eqs. 12.5 through 12.8 and expressing enthalpy change in terms of changes in temperature and pressure, such that $dH = c_p dT - C_J\, C_p dp$ (as in Eq. 6.14, where C_J is the Joule-Thomson, or J-T, coefficient), we obtain

$$c_{pa}\frac{\mathrm{d}T_a}{\mathrm{d}z} - \frac{C_J c_{ga}}{J}\frac{\mathrm{d}p}{\mathrm{d}z} - \frac{g\sin\alpha}{g_c J} + \frac{v_a}{g_c J}\frac{\mathrm{d}v_a}{\mathrm{d}z} = c_{pa}L_R(T_{ei} - T_a) + \frac{c_{pa}}{B}(T_t - T_a) \qquad (12.9)$$

Following the arguments we made in Chapter 8, we combine the insignificant terms as D_a and obtain

$$c_{pa}\frac{\mathrm{d}T}{\mathrm{d}z}+D_a=-L_R c_{pa}\left(T_{ei}-T_a\right)+\frac{c_{pa}}{B}\left(T_t-T_a\right), \quad (12.10)$$

where

$$D_a=-\frac{C_J c_{pa}}{J}\frac{\mathrm{d}T}{\mathrm{d}z}-\frac{g\sin\alpha}{g_c J}+\frac{v}{g_c J}\frac{\mathrm{d}v}{\mathrm{d}z} \quad (12.11)$$

Following Hasan and Kabir (1996), an energy balance for the tubular two-phase mixture yields

$$c_{pa}\frac{\mathrm{d}T_a}{\mathrm{d}z}-\frac{C_J c_{pt}}{J}\frac{\mathrm{d}p}{\mathrm{d}z}-\frac{g\sin\alpha}{g_c J}+\frac{v_t}{g_c J}\frac{\mathrm{d}v_t}{\mathrm{d}z} = \frac{w_a c_{pa}}{w_t B}(T_t-T_a) \quad (12.12)$$

In other words,

$$c_{pt}\frac{\mathrm{d}T}{\mathrm{d}z}+D_t=\frac{w_a c_{pa}}{w_t B}\left(T_t-T_a\right), \quad (12.13)$$

where D_t, is the term analogous to D_a for the tubing fluid.

Combining Eqs. 12.10 and 12.13 and simplifying and defining $B' = B\ w_t/w_a$, as detailed by Hasan and Kabir (1996), we obtain

$$\frac{B'}{L_R}\frac{\mathrm{d}^2T_t}{\mathrm{d}z^2}+B''\frac{\mathrm{d}T_t}{\mathrm{d}z}-T_t+T_{es}+g_G z\sin\alpha+D'=0, \quad (12.14)$$

where

$$B''=B'+\frac{B'}{L_R B}-\frac{1}{L_R}, \quad (12.15)$$

and

$$D'=B'\frac{D_t}{c_{pt}}+\frac{D_t}{c_{pt}}\frac{B'}{L_R B}-\frac{D_a}{L_R c_{pa}} \quad (12.16)$$

The term D, comprising D_a, D_t, and other terms, is quite small and may be neglected. For example, D_a, the second term with (dp/dz) of the annular gas, is usually very small in all cases. The kinetic term in the high annulus pressure environment turns out to be negative and tends to balance the potential energy term. For instance, for injection of methane at surface conditions of 100°F and 1,000 psi, the sum of the kinetic and potential energy terms amounts to 0.001496 Btu/lbm-ft. By contrast, the first term (c_{pa} dT_a/dz) has a value of 0.221 Btu/lbm-ft. Similar arguments for simplification also apply to Eq. 12.12. The final solutions of Eq. 12.14 are

presented here, and more details are shown in Appendix12-B.

$$T_t = \alpha e^{\lambda_1 z} + \beta e^{\lambda_2 z} + g_G z \sin\alpha + B'' g_G + T_{es} + D', \quad (12.17)$$

and

$$\begin{aligned} T_a &= T_t - B' \frac{dT_t}{dz} \\ &= (1-\lambda_1 B')\alpha e^{\lambda_1 z} + (1-\lambda_2 B')\beta e^{\lambda_2 z} \\ &\quad + g_G(B'' - B') + g_G z \sin\alpha + T_{es} \end{aligned} \quad (12.18)$$

These expressions for the annular and tubing fluid temperatures are exactly the same as those for the case of production through the annulus and tubing, as shown in Chapter 8 (Eqs. 8.12 and 8.13). However, because the annular fluid flows in a direction opposite to that in the tubing, unlike the case shown in Chapter 8, the expressions for the various parameters are different.

12.2.3 Factors Affecting Temperature Profiles. In this section, we explore the sensitivity of overall-heat-transfer coefficients and production/injection rates on fluid temperature profiles during steady-state gas lift operation in vertical wells.

Heat-Transfer Coefficient. *Example One*. Consider a vertical well with an oil rate of 9,286 STB/D and a gas injection of 10% of the total mass in the tubing string. To reflect the low heat-transfer coefficient for flowing gas in the annulus, let us assign a value of 4 Btu/(hr-ft-°F) for U_a (for heat transfer between formation and annulus) and 10 Btu/(hr-ft-°F) for U_t, (for heat transfer between the annulus and the tubing). **Table 12.2** presents all the relevant data for this example and the two other examples that we discuss.

Temperature profiles so calculated are shown in **Fig. 12.16.** The figure shows that the fluid temperature remains high throughout the length of the tubing. This high tubing fluid temperature (T_t) is precipitated by the annular gas, which reduces the overall-heat-transfer coefficient, thereby permitting the produced fluid mixture to retain most of its high entering enthalpy. As a consequence of high T_t and low overall-heat-transfer rate, the annular gas also is generally at a high temperature, except in the area close to the wellhead.

Parameter	Examples 1 and 2	Example 3
Total well depth, ft	15,000	4,500
Casing diameter, ft	0.35	0.35
Tubing diameter, ft	0.23	0.23
Mass fraction of gas In the tubing	0.10	0.676
Formation density, lbm/ft^3	165	165
Formation heat capacity, Btu/(lbm-°F)	0.20	0.20
Producing time, hours	44	44

Specific heat of oil, Btu/(lbm-°F)	0.4	1.0
Specific heat of gas, Btu/(lbm-°F)	0.25	0.25
Tubing overall-heat-transfer coefficient, Btu/(hr-°F -ft)	10.0	5.0
Annular overall-heat-transfer coefficient, Btu/(hr-°F -ft)	4.0	2.0
Earth thermal conductivity, Btu/(hr-°F -ft)	1.3	1.3
Geothermal gradient, °F/ft	0.0127	0.012
Bottomhole earth temperature, °F	250	124
Surface earth temperature, °F	59.5	60
Surface gas inlet temperature, °F	75	75

Table 12.2—Well, formation, and fluid data of synthetic examples.

Figs. 12.16 and 12.17 show the effect of changing heat-transfer coefficients for the annulus and tubing. As expected, Fig. 12.17 shows that when U_a and U_t are both reduced by 50%, the tubing fluid temperature, and to some extent the annular gas temperature (T_a), becomes somewhat higher than shown in Fig. 12.16. However, the U_t value also makes the temperature difference between the tubing and annulus larger. **Fig. 12.18** has U_a = 4 and U_t = 20 Btu/(hr- ft- °F). The higher value of U_t causes T_a to approach T_t more closely.

The impact of low gas injection rate on temperature profiles is explored by keeping the same production rate of 9,286 STB/D, but with a gas injection rate of only 5% of the total mass. **Fig. 12.19** shows that the temperature profiles are similar to those shown in Fig. 12.16 except that they are slightly higher. The T_a is now closer to T_t because of a lower mass rate in the annulus, leading to a sharper rise near the wellhead because of increased heat transfer from the tubing fluid.

***Flow Rate*.** Conduit fluid temperatures, given by Eqs. 12.17 and 12.18, are influenced by flow rate because the parameters L_R, B, B', B'', λ_1, and λ_2 used in these expressions are strong functions of rate. This influence of flow rate is apparent in **Fig. 12.20,** which shows that a decrease in annular injection rate results in an increase in both T_a and T_t. In particular, the values of λ_1 and λ_2 (Eqs. 12-B-4 and 12-B-5 in Appendix 12-B) are much smaller at low rates than at higher rates. Because $e^{\lambda z}$ may be expressed as $1+\lambda z$ for low values of λz, expressions for the tubing and annular fluid temperatures may be simplified to the form

$$T_t = \alpha + B'' g_G + T_{es} + (\alpha \lambda_1 + g_G) z \sin\alpha \qquad (12.19)$$

and

$$T_a = (1-\lambda_1 B')\alpha + (B''-B') g_T + T_{ew} + [(1-\lambda_1 B')\alpha\lambda_1 + g_G] z \sin\alpha \qquad (12.20)$$

Thus, T_t and T_a become linear with z at shallower depths, with slopes represented by the terms in the parentheses of Eqs. 12.19 and 12.20. Because λ_1 and λ_2 are small,

the values of these slopes are extremely close to g_G, and T_t and T_a are lines parallel to the geothermal gradient.

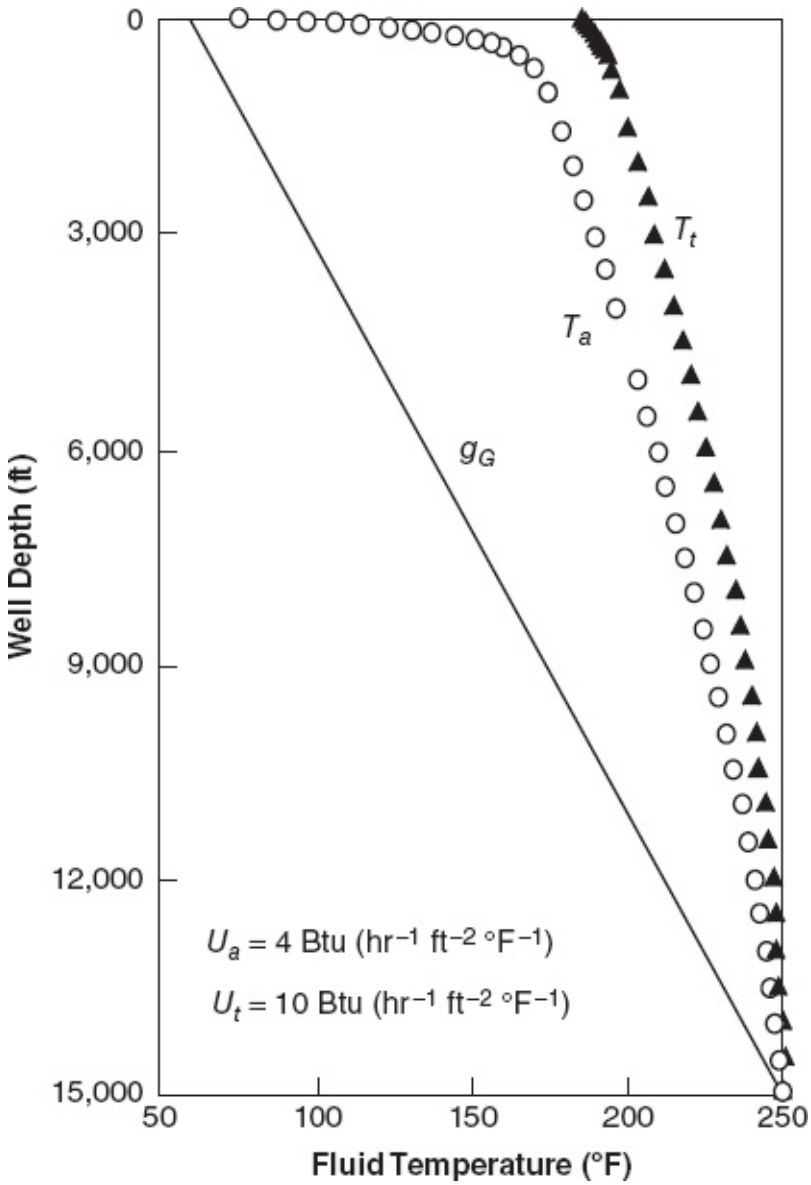

Fig. 12.16—Fluid temperature profiles for moderate U_a and U_t values.

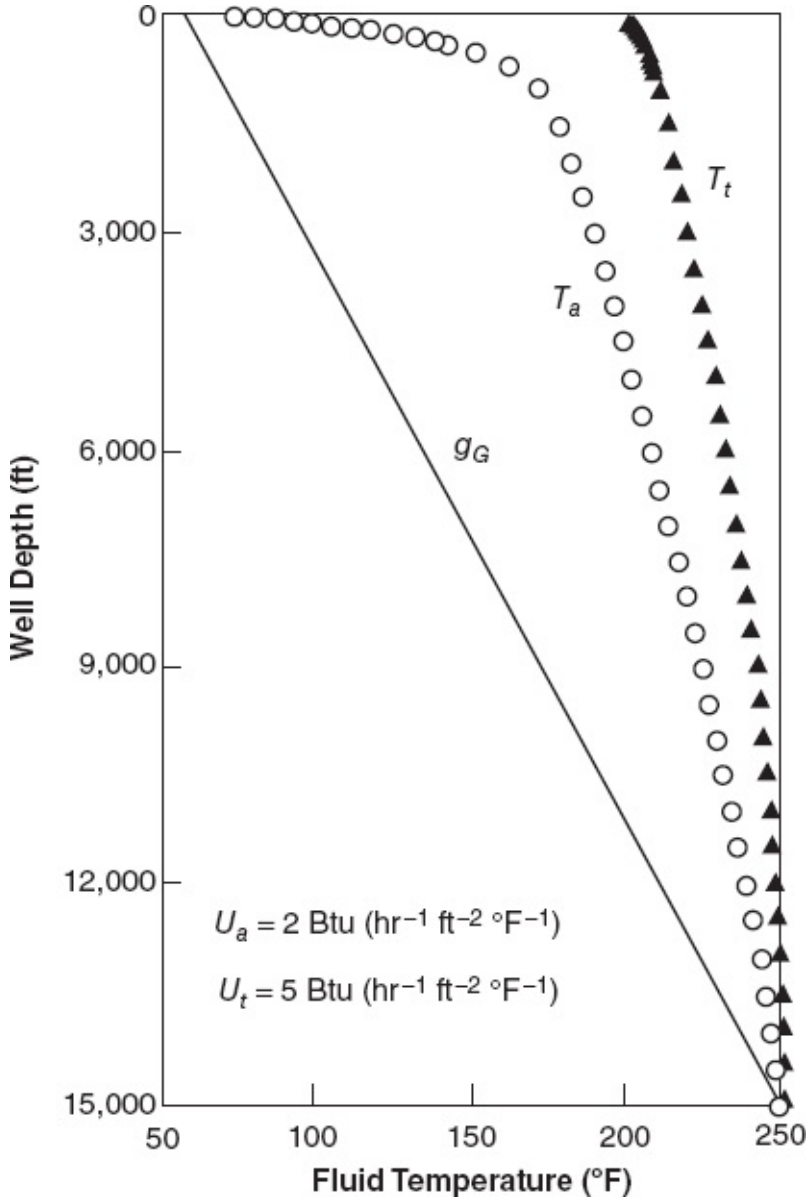

Fig. 12.17—Fluid temperature profiles for low U_a and U_t values.

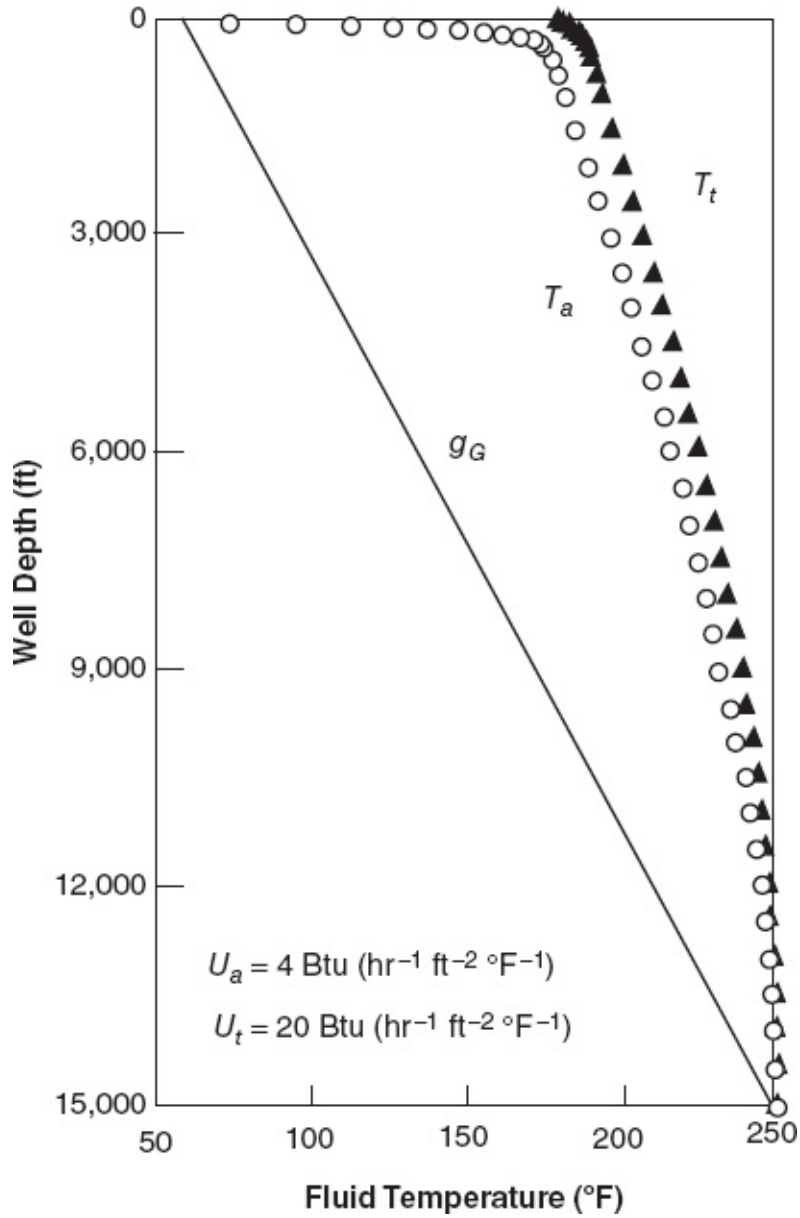

Fig. 12.18—Fluid temperature profiles for high U_t values.

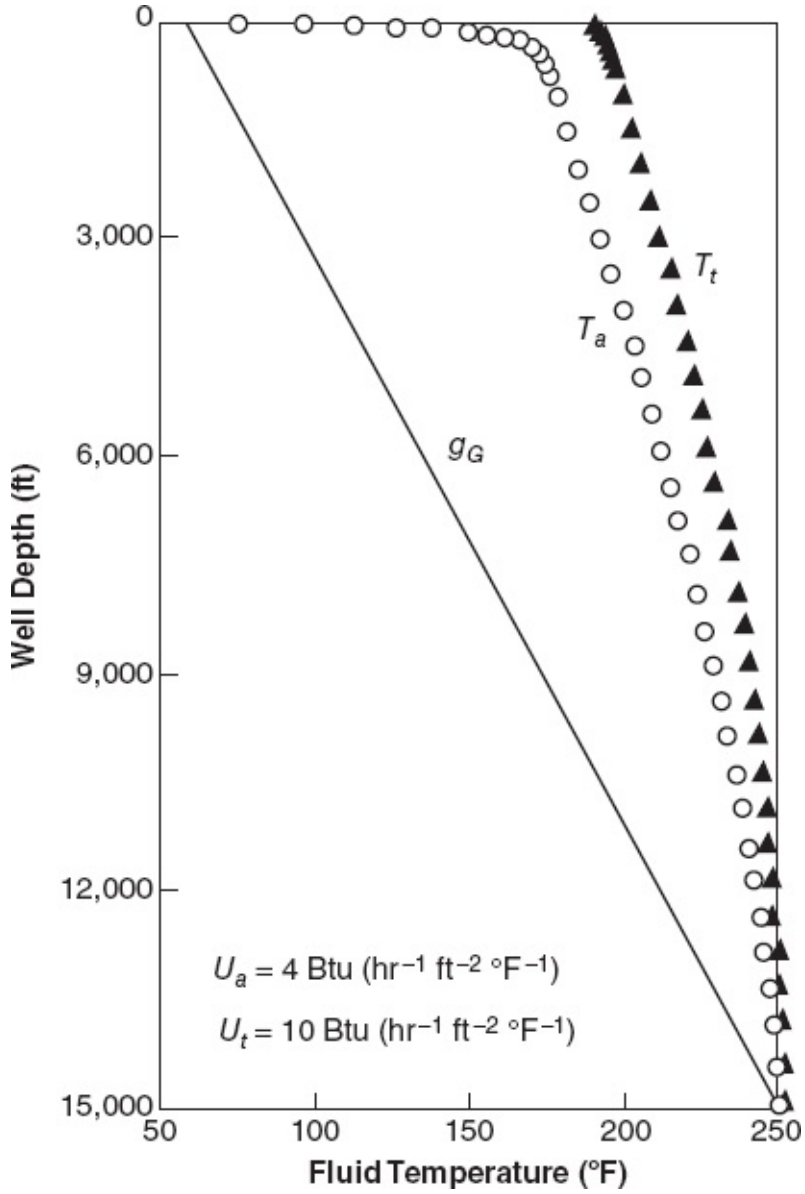

Fig. 12.19—influence of low mass fraction of gas on fluid temperature profiles.

Example Two. Fig. 12.20 shows the temperature profile for a gas lift operation with 431 STB/D of oil production rate. The gas injection rate was kept at 10% of the total mass produced. Table 12.2 presents the pertinent parameters. Both T_t and T_a profiles in Fig. 12.20 appear to be parallel to the geothermal temperature for the entire well. An exception occurs very close to the bottom of the hole, where λz is no longer small because of large z. Small values of α, β, λ_1, and λ cause the slopes of these lines to be approximately equal to the geothermal gradient, and ultimately T_a and T_t, profiles become close to each other.

Example Three. No field data of T_a profiles have been reported because of the obvious difficulty of such measurements. Nonetheless, we selected a case reported by Bertuzzi et al. (1953) to capture the essence of a field example. Whereas the flow rates and tubular dimensions are used verbatim, the heat-transfer coefficients are assumed values. Again, Table 12.2 presents all the pertinent data.

The sensitivity of different T_D models (Ramey 1962; Chiu and Thakur 1991) on fluid temperature profiles is shown in **Fig. 12.21.** As discussed by Hasan and Kabir (1994a), different inner-boundary conditions of the two models result in some difference in the T_a profile, which shows the maximum temperature change. However, no perceptible difference exists for the T_t profile because the wellhead and bottomhole temperature difference is minimal. Although this figure is generated after only 1 hour into the injection period, a similar trend persists for larger times.

Fig. 12.22 illustrates that the temperature profiles do change with injection time, particularly in the annulus. The significance of the highly nonlinear T_a (t) profile is that the characteristics of the transfer valves, located at shallower depths, can be fine-tuned for the optimal performance. Therefore, the model allows one to take advantage of annular temperature computation as a function of both time and depth.

One readily observes that the temperature profiles have different starting points at the well bottom, unlike those shown earlier. Larger mass of gas and shorter well depth translate to a cooler annular fluid than is evident in the previous cases, in which heat-transfer characteristics remain unchanged.

Field Examples 12.3. We present two field examples to show application of the model discussed here. These examples are taken from the published work of Kanu (1981). The pressure-traverse match is shown in **Fig. 12.23** for the Thompson Well. This match was obtained by using the Hasan-Kabir two-phase model discussed in Chapter 3. As shown, large discontinuity in the in-situ gas volume fraction occurs at 2,500 ft, where the lift gas is introduced through the annulus. Predictably, the high producing gas/liquid ratio (GLR) of 550 scf/STB caused excessive pressure drop toward the wellhead. As Kanu reported, when the GLR was reduced to 221 scf/STB, a 58% gain in total liquid productivity was realized.

***Solution*.** The corresponding tubing temperature profile, both measured and computed, is shown in **Fig. 12.24.** Results of the Shiu-Beggs (SB) correlation (Shiu and Beggs 1980) are also included in this figure. The measured pressure and temperature profiles are both in good agreement with the model presented here. However, the same is not true for the SB correlation. As expected, the computed temperature profile, obtained from the proposed model, is quite different at shallower depths in the annulus. **Table 12.3** presents all the parameters used to compute the pressure and temperature traverses.

For the O'Connor Well, we reproduced the flowing tubing pressure traverse quite well, as **Fig. 12.25** suggests. **Fig. 12.26** shows that good agreement in temperature occurs at shallower depths, where two-phase flow is prevalent. However, the match suffers below the point of gas injection. Two possible reasons exist for this mismatch. Either the geothermal gradient is different below the point of gas injection or the short-duration station stops did not allow the thermometer to equilibrate with the fluid temperature. Despite this difficulty, both pressure and temperature profiles were reproduced with acceptable accuracy above the point of gas injection, which leads one to achieve proper design or adjustments of gas lift valves for optimal

performance. Again, we observed a large discrepancy between the SB correlation and the measured values. All the parameters used to compute the pressure and temperature profiles are presented in Table 12.3.

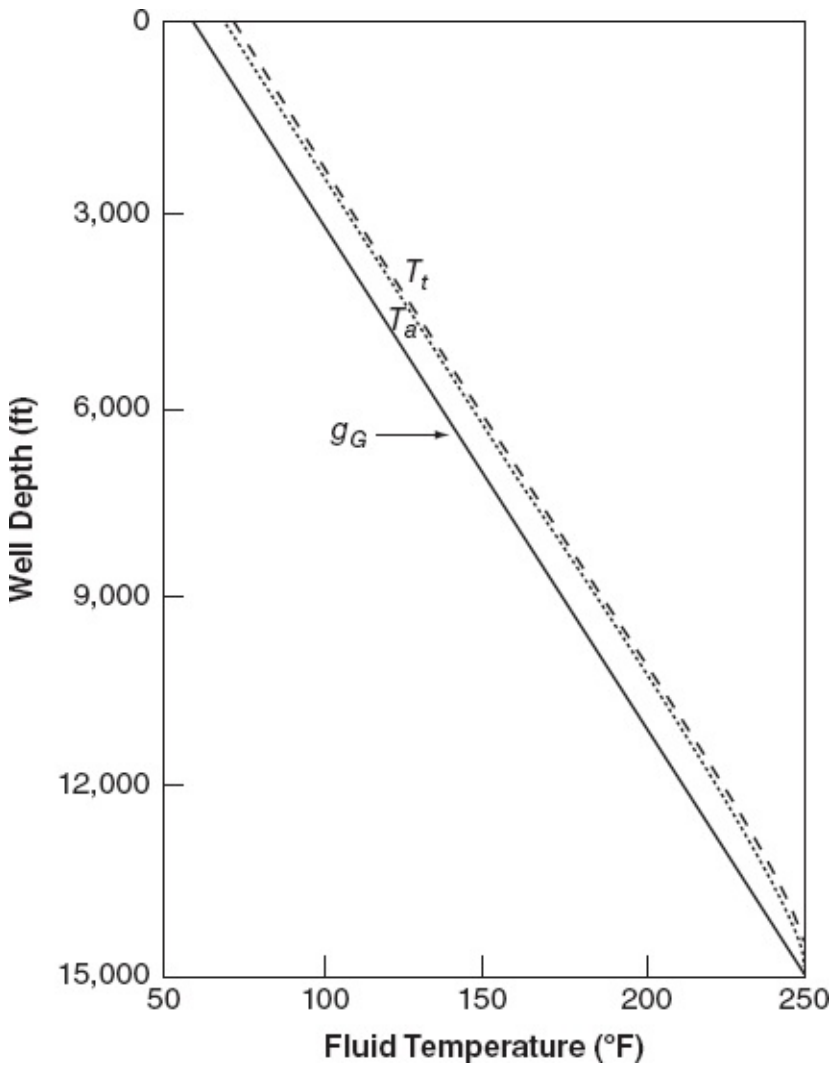

Fig. 12.20—Influence of low oil rate on fluid temperature profiles.

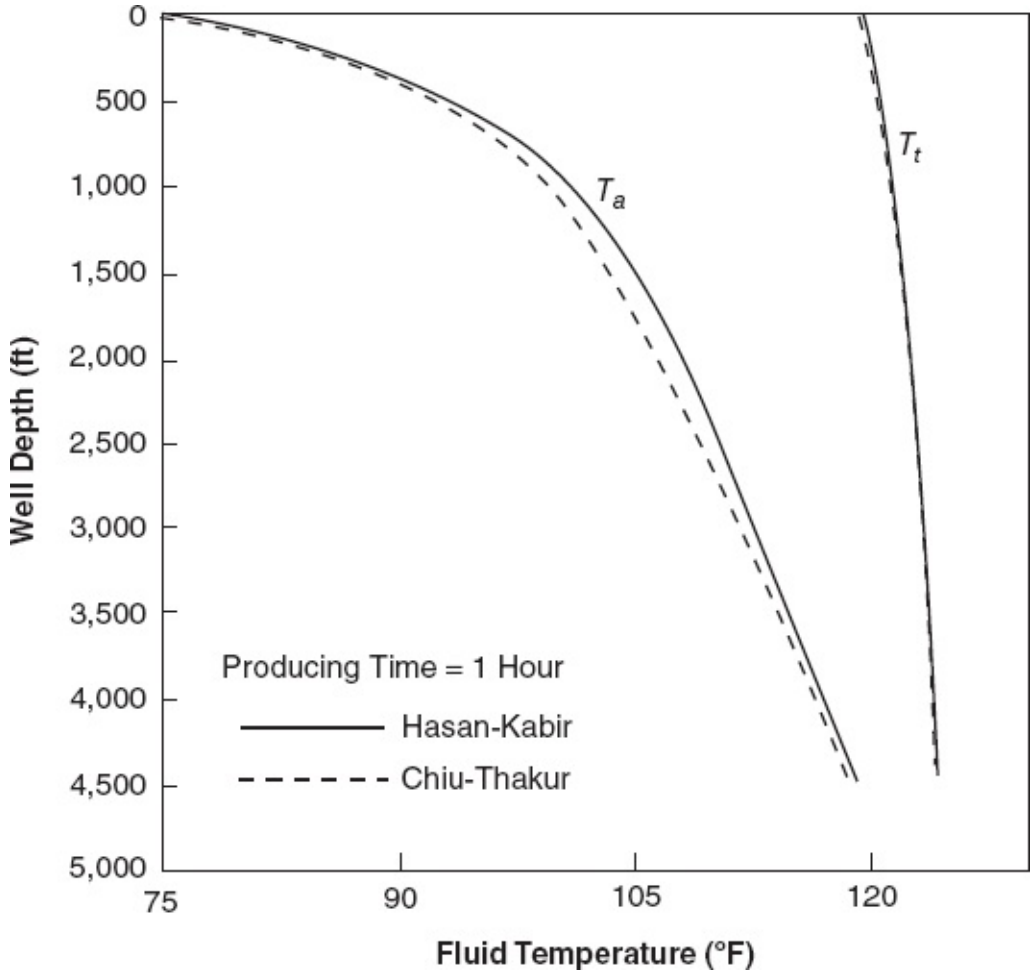

Fig. 12.21—Impact of T_D models on fluid temperature profiles.

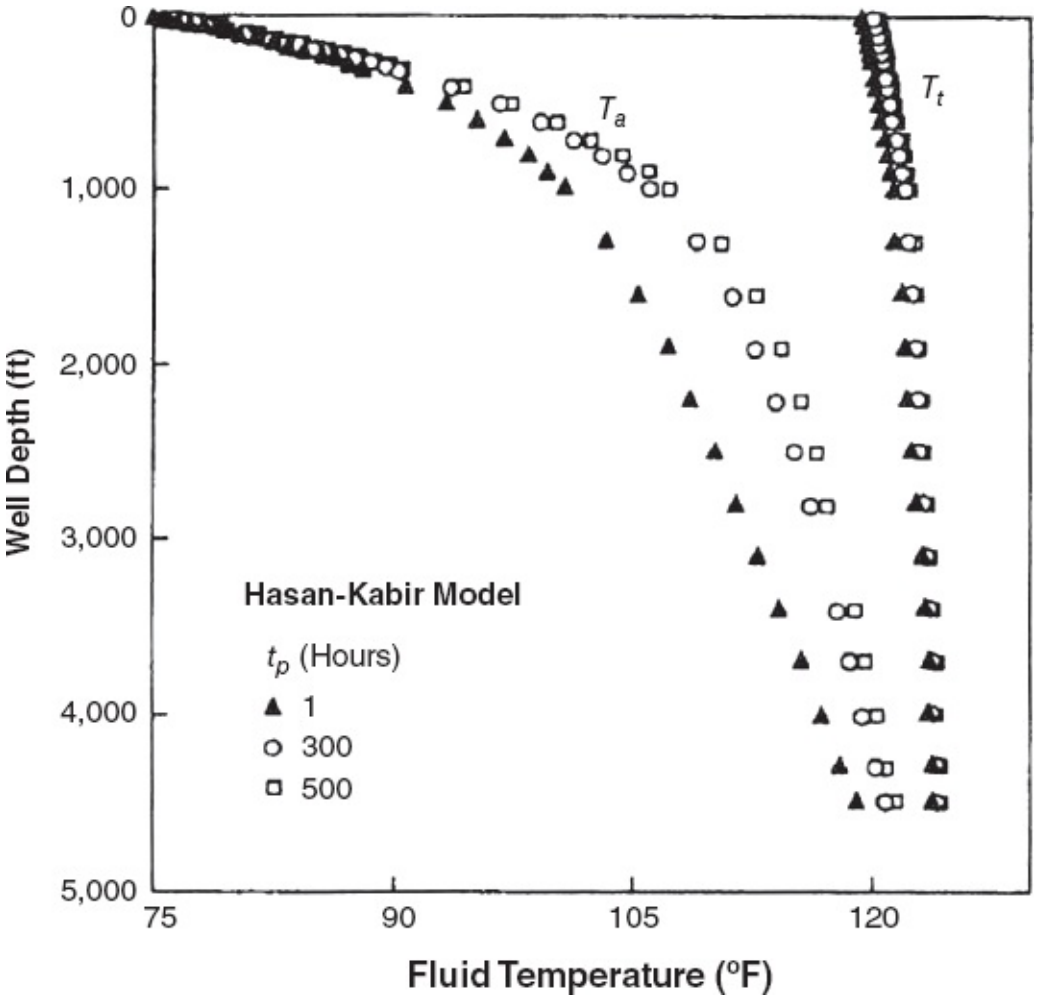

Fig. 12.22—Influence of producing time on fluid temperature profiles.

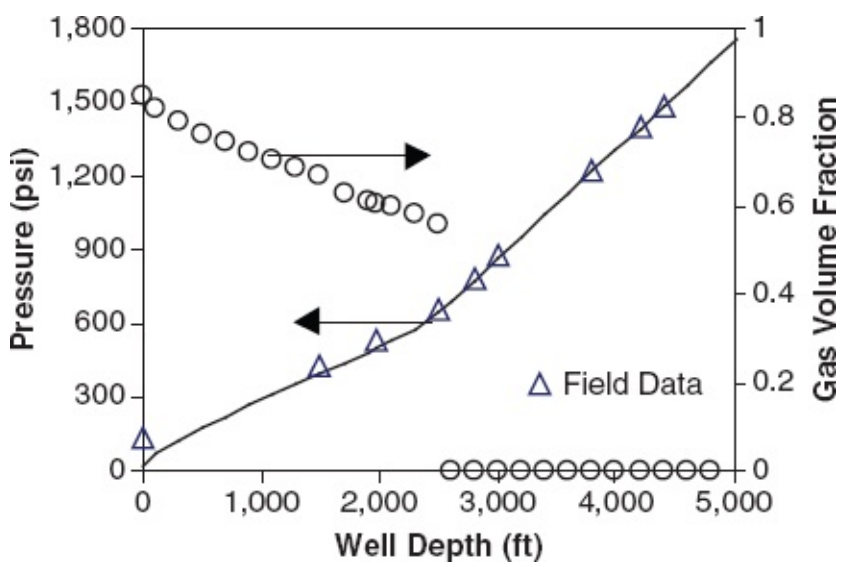

Fig. 12.23—Matching tubing pressure with two-phase model, Thompson Well.

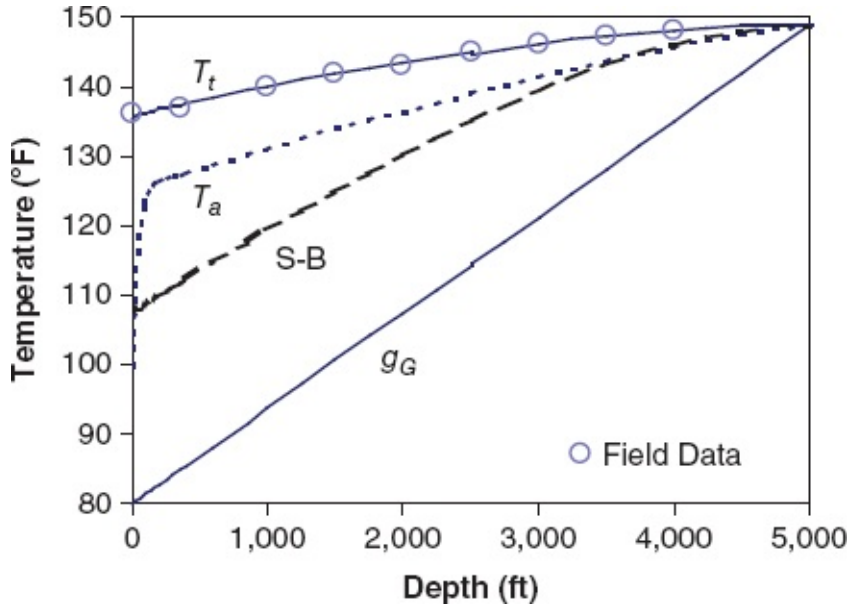

Fig. 12.24—Matching tubing temperature with Eq. 12.17, Thompson Well.

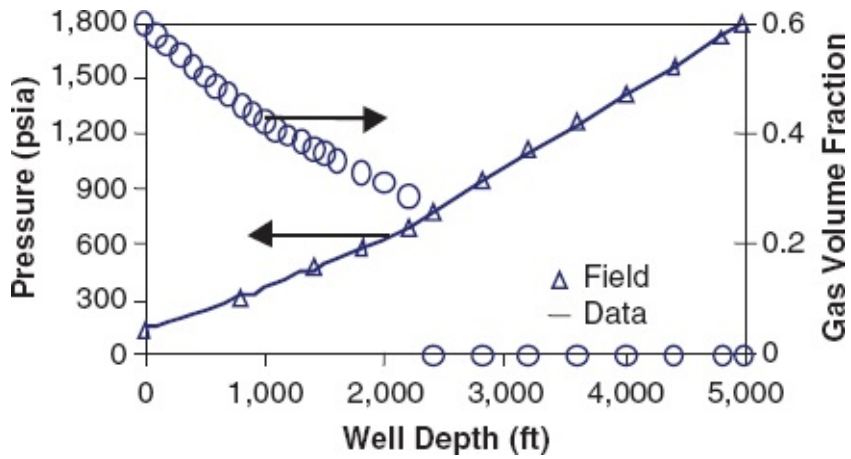

Fig. 12.25—Matching tubing pressure with two-phase model, O'Connor Well.

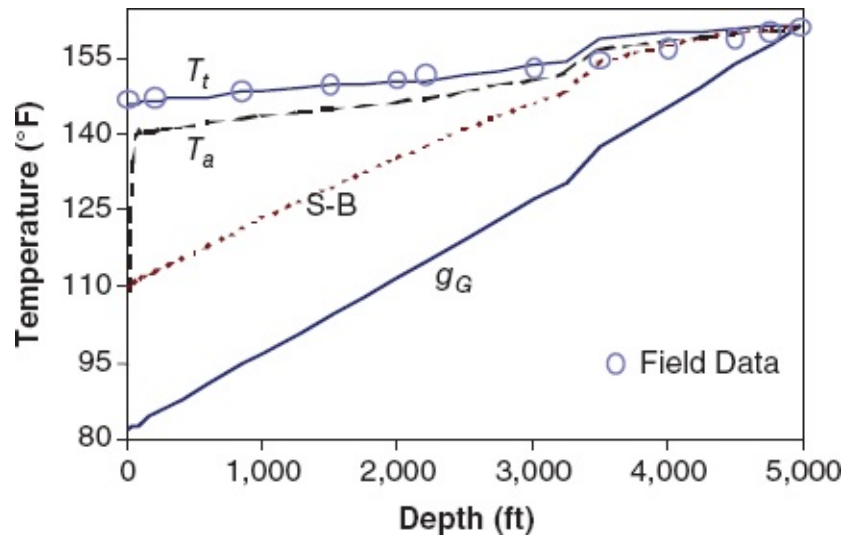

Fig. 12.26—Matching tubing temperature with Eq. 12.17, O'Connor Well.

Parameters	*O'Connor Well*	*Thompson Well*
Total well depth, ft	4,979	5,019
Depth of gas injection, ft	2,209	2,400
Casing ID, in.	5.0	7.0
Tubing outer diameter, in.	2.5	2.875
Oil + water flow rate, STB/D	3,660	2,080
Mass fraction of gas In the tubing	0.0225	0.0681
Gas/liquid ratio, scf/STB	158	550
Oil + water °API gravity	26	10.3
Gas gravity (air = 1)	0.60	0.61
Specific heat of liquid, Btu/(lbm-°F)	1.0	1.0
Specific heat of gas, Btu/(lbm-°F)	0.25	0.25
Tubing overall-heat-transfer coefficient, Btu/(hr-°F-ft)	10.0	10.0
Annular overall-heat-transfer coefficient, Btu/(hr-°F-ft)	1.0	4.0
Earth thermal conductivity, Btu/(hr-°F-ft)	1.30	1.30
Geothermal gradient, °F/ft	0.0159	0.0137
Bottomhole earth temperature, °F	161	149
Surface earth temperature, °F	82	80
Surface gas inlet temperature, °F	100	100

Table 12.3—Well, formation, and fluid data of field examples.

Note that the low-gas/liquid-ratio (GLR) situations in both cases do not result in large separation of the two temperature profiles at the existing conditions. As Kanu (1981) indicated, adjustments in the GLR were required to improve the gas lift performance in both wells. Therefore, one must perform the temperature and pressure analysis again with the new GLR values to ensure that valve adjustments are made for the revised operating conditions.

Discussion. The intent of this section is to introduce the reader to a mechanistic approach for computing fluid temperature profiles in both conduits. Therefore, by definition, we addressed a narrow issue that pertains to the design and operation of a gas lift operation. We hope that this piece of technology can be plugged into a comprehensive software package to facilitate design calculations.

Knowledge of accurate fluid temperature profiles in both flow conduits is critical for gas lift operations. With the introduction of mechanistic models (Acuna et al. 1992; Sagar et al. 1992) for valve mechanics and flow through such valves, the importance of fluid temperature modeling has become more relevant than ever before. Here, the model formulation considers steady gas injection at the lowermost valve; that is, the transfer valves required for flow initiation are not considered in this analysis. However, the model presented by Tang et al. (1999) shows how the dynamic unloading process can be modeled rigorously. Their model adapts many elements of the heat-transfer model discussed here and also the countercurrent flow model discussed in Chapter 4.

In this section, we presented expressions for fluid temperature in both tubing and annulus by analyzing energy transport between the tubular fluids and the formation. Note that the final form of the fluid temperature expressions (Eqs. 12.14 and 12.15) does not contain the well deviation term in an explicit fashion; rather, it manifests itself in terms of geothermal gradient g_G.

Pressure profile calculations in the annulus, though not shown, indicate that the pressure gradient, dp/dz, is essentially linear, although we are dealing with highly nonlinear temperature profiles. Only density inversion will cause a nonlinear pressure profile. Thus, the current practice for calculating the annular gas pressure remains unchanged. However, the pressure gradient for a deviated wellbore will differ greatly from that for a vertical wellbore.

12.2.4 Temperature Profiles in Gas Lift Wells Summary. This section discussed a mechanistic approach to compute flowing-fluid temperature profiles in both conduits simultaneously for a continuous-flow gas lift operation. While formulating, we assumed unsteady heat flow in the formation, but steady heat flow in the conduits. This model can treat either a vertical or a deviated wellbore. The solution is presented in simplified algebraic form for easy implementation in any existing computer model handling gas lift issues. A limited sensitivity study shows that nonlinearity in the annular gas temperature profile is dependent on the mass fraction of gas (GOR) injected into the tubing, well depth, heat-transfer coefficients, and magnitudes of flow rates in both conduits.

12.3 Wellbore Steam/Water Flow and Surface Metering

12.3.1 Steam Injection. Previous discussion on heat transfer in Chapters 5 and 6 pertains to flow of noncondensable fluids in wellbores, which was pioneered by Ramey (1962). In a steamflood project, superheated or saturated steam is injected into oil-bearing formations to reduce oil viscosity, thereby improving the recovery. Injection of condensable steam into a single horizon as described by Satter (1965), Pacheco and Farouq Ali (1972), Farouq Ali (1981), and Griston and Willhite (1987) is a common occurrence. Concentric injection down the common wellbore can also occur in more than one sand interval, according to Griston and Willhite (1987), for efficient heat management. **Fig. 12.27** schematically shows the two injection schemes.

As steam travels downward in the wellbore, it loses energy to the surrounding formation. This heat loss may result in condensation with consequent reduction in steam quality and enthalpy. During phase change, the temperature of a single-component fluid depends solely on its pressure. Increases in pressure with depth occur owing to the static head of steam. This increased steam pressure will result in a rise of temperature, although heat is lost to the formation.

In this section, we present a computational scheme for steady-state flow. For

simplicity, we treat the traditional single-string injection scheme, which is based on the material presented in Chapter 5. Although not shown, one can easily adapt the model presented in Chapter 6 to deal with the concentric injection case.

Mathematical Model. Unlike the earlier treatment of heat-transfer problems in Chapters 6 and 7, which did not involve occurrence of phase change, simultaneous solution of the momentum balance and energy balance equations is required for the problem at hand. For convenience, we reproduce the energy balance equation, Eq. 5.13 from Chapter 5, as

$$\frac{dH}{dz} - \frac{g \sin\alpha}{g_c J} + \frac{v}{g_c J}\frac{dv}{dz} = \mp \frac{Q}{w} \qquad (12.21)$$

For steady flow systems, the pressure gradient, d*p*/d*z*, is balanced by the static head, $\rho g \sin\theta$, the friction head, $\rho f v^2/2d$, and the kinetic head, $(\rho v)(dv/dz)$. Therefore, the momentum balance equation becomes

$$-\frac{dp}{dz} = -\rho g \sin\alpha + \frac{f\rho v^2}{2d} + \rho v \frac{dv}{dz} \qquad (12.22)$$

Here, the friction factor, *f*, must account for flow of a two-phase mixture. For mixture density, we need to use the appropriate expression, given by

$$\rho_m = f_L \rho_L + (1 - f_L)\rho_g \qquad (12.23)$$

One can use either the Hasan model (1995), discussed in Chapter 4 and 5, or the Beggs and Brill correlation (1973) for the computation of liquid holdup and pressure drop in downward two-phase flow. Note that the Griston and Willhite (1987) model for concentric steam injection involves simultaneous solution of four partial-differential equations, two each for two conduits, using a numerical scheme.

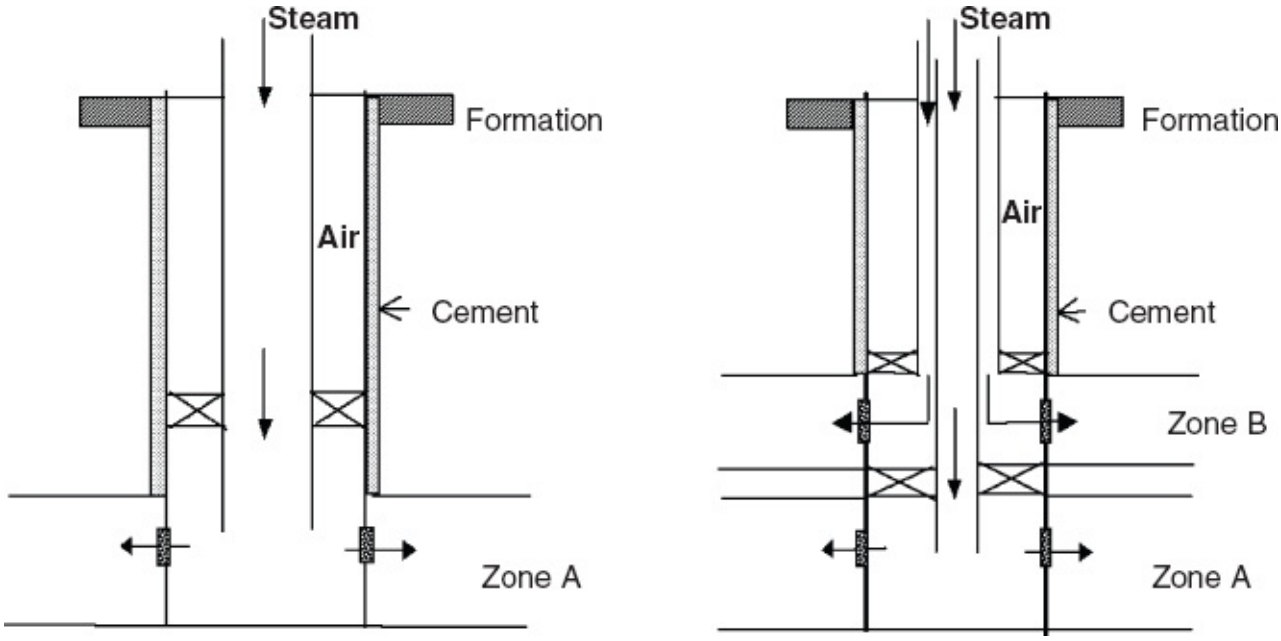

Fig. 12.27—Schematic of single and concentric steam injection systems.

Example Application. Superheated steam at the rate of 120,000 STB/D (1331.4 lbm/hr) at 1,000°F and 500 psia is being injected into a 6,000-ft vertical well. The pertinent data are these:

q_t	=	120,000 STB/D
d_{ti}	=	2.441 in.
d_{ci}	=	5.989 in.
T_{es}	=	75°F
k_e	=	1
k_t	=	26
T_{ts}	=	1,000°F
d_{to}	=	2.875 in.
d_{co}	=	6.625 in.
T_{eb}	=	141°F
k_{cem}	=	4.021
k_c	=	26
p_{ts}	=	500 psia
d_{ins}	=	3.5 in.
t_p	=	8.75 hours
α_h	=	0.0458 ft^2/hr
k_a	=	0.1 Btu/(hr-ft°F)
k_{ins}	=	0.135 Btu/(hr-ft°F)

H = 1520.3 Btu/lbm

***Solution*.** Using these data, we calculate an overall-heat-transfer coefficient, U, of 0.80 Btu/(hr-ft^2-°F) and a relaxation parameter, L_R, of 3.45×10^{-4} ft^{-1} at the wellhead. Note that because of the high temperature involved in this case, we have allowed for radiative heat transport. In addition, for this case, the U and L_R values vary significantly with well depth. Therefore, the problem demands a solution using a numerical scheme.

Accordingly, we divided the wellbore into 100 parts, each 60 ft long. Computation was initiated at the wellhead. Assuming that steam temperature and the value of L_R remain the same for the 60-ft interval, we calculated that the steam will lose 26,122 Btu/hr of heat in this section. Use of the energy balance equation then gives a steam enthalpy of 1,500.7 Btu/lbm at 60 ft below the wellhead. At 500 psia, with this value of enthalpy, the steam is still superheated, and we estimated its temperature at 981°F.

Next, we use the momentum balance equation (Eq. 12.21) to estimate a pressure of 500.3 psi for the steam at this point. Because steam enthalpy depends slightly on pressure as well as temperature, we recalculate the steam temperature at this point. This value then allows us to estimate an average temperature for this section, and we refine our heat loss estimate on the basis of that value. Usually, a single iteration suffices.

Repeating this calculation procedure by traversing the well in the downward direction, we found that at a depth of 1,440 ft, the steam enthalpy becomes 1,199.4 Btu/lbm, and steam pressure is 507.64 psia. Steam quality of 0.991 at this condition indicated slight condensation and the start of two-phase flow. While calculations involving the energy balance equation hereafter remain the same, the pressure-drop estimation procedure must account for a two-phase mixture flowing in the downward direction. As mentioned earlier, we used the Hasan (1995) model discussed earlier in Chapter 4, Section 4.4, to estimate the pressure drop.

The iterative procedure becomes somewhat more complicated in the remaining wellbore as a result of two-phase flow. As long as the vapor and liquid phases coexist, the fluid temperature depends only on its pressure and not on the extent of heat loss or its enthalpy. However, the mass fraction of steam (quality) depends on its enthalpy, H, the saturation liquid enthalpy, H_l^{sat}, and the heat of vaporization, H_{lg}, as shown in Eq. 12.24.

$$x = \frac{H - H_l^{sat}}{H_{lg}} \qquad (12.24)$$

Saturation enthalpy and heat of vaporization depend on system pressure. Therefore, the calculation procedure involves first estimating the fluid pressure using the momentum- balance equation. This step requires an estimated average value for quality (x) to allow computation of fluid density and frictional loss. The estimated

pressure is used to calculate the fluid temperature and steam/water property values. Thereafter, the energy balance equation is used to estimate heat loss, fluid enthalpy, and quality. With the new value of quality, the interval (60 ft, in this case) pressure drop is recalculated. Usually, two iterations lead to good estimates of fluid temperature, pressure, and quality.

Fig. 12.28 shows the calculated values of temperature and steam quality along with the values reported by Satter (1965). We note a very good agreement between the two methods.

12.3.2 Metering Steam Flow Rate and Quality. Steam injection often requires steam flow rate and quality measurements. These measurements are also critical in producing hot water and wet steam from geothermal wells. Metering of two-phase flow of oil and gas using chokes was described in Chapter 5. In this section, we present methods to meter steam/water flow. Steam/water flow through restrictions differs from that of gas/oil flow in two ways. First, significant evaporation that occurs during flow of steam and water resulting from depressurization through an orifice poses additional difficulties in relating pressure drop to flow rates. Second, GLR provides an estimate of the gas rate, given total flow rate (such as from Eq. 5.23) during gas/oil flow. Unfortunately, steam flow rate needs to be separately obtained from additional data during steam/water flow. In addition, the interaction and slip between the steam and water phases may have to be accounted for through modeling or empiricism.

As discussed in Chapter 5, Eq. 5.18, which is applicable to single-phase flow, can be used for flow of two-phase mixtures by invoking some simplifying assumptions regarding the mixture density at the constriction. The pressure drop is then related to the total flow rate and the quality (gas mass fraction). However, we must obtain another independent expression relating rate and phase fraction.

Critical flow of steam and water yields the desired relationship between flow rate and quality. An expression for the maximum (critical or sonic) velocity attainable in pipe flow can be derived from thermodynamic considerations of isentropic expansion of single-phase systems with uniform density. However, for two-phase systems, some assumptions regarding the flowing density and its rate of change are needed to obtain a critical flow relationship. A number of theoretical models have been proposed relating steam/water critical flow with system variables. These models usually involve writing the momentum and energy balance equations for each phase and making an assumption regarding the rate of change of pressure or the slip ratio of phases at critical flow. Usually, however, the assumptions made in these models cannot be verified, and the resulting expressions are quite complicated.

James (1962, 1965) proposed an empirical equation relating the combined mass flux of steam and water at critical flow conditions to the lip (critical) pressure and stagnation enthalpy. He validated his equation using a large set of data with a wide range of parameters. Subsequently, Hasan (1990) developed modifications of the James equation, allowing the critical flow correlation to be used for geothermal wells

containing dissolved substances, such as carbon dioxide (CO_2) and salts.

Because of its simplicity, James' equation for critical flow of wet steam has become extremely popular in the geothermal industry. In conjunction with his correlation for flow through orifices, James' critical flow correlation is often used for computing geothermal wellbore discharge characteristics. The industry practice is to use an orifice at the well's upstream and attach a James tube, which has a smaller diameter than the well itself, to obtain critical flow. Such a combination of an orifice meter and James tube is schematically shown in **Fig. 12.29.** Data gathered are the pressure drop across the orifice and the pressure at the lip of the James tube. Because pressure changes rapidly during critical flow, positioning the pressure tap is critical. The standard location is one-quarter inch from the exit of the tube, as suggested by James. The two equations, one for flow through orifices and the other for critical flow, are solved simultaneously for mass flux and quality, using an iterative procedure.

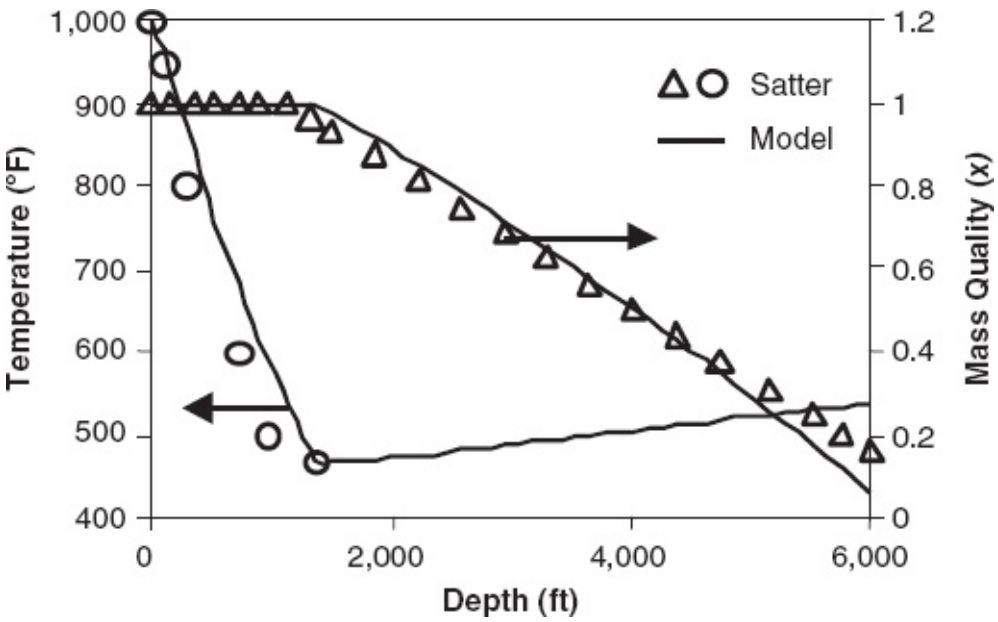

Fig. 12.28—Comparison of temperature and mass quality of steam with data reported by Satter (1965).

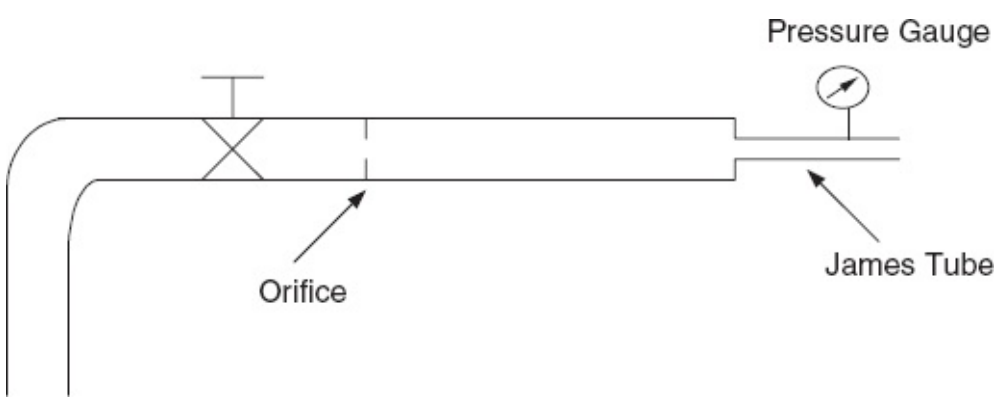

Fig. 12.29—Schematic of a combination of an orifice meter and James tube for metering steam flow in geothermal wells.

James rewrote Eq. 5.18 in terms of mass flux (mass rate/area) at the orifice throat, G_o, in terms of the density, ρ, the pressure drop across the orifice, Δp (= $p_2 - p_1$), and the throat/pipe diameter ratio, $\beta\,(=\sqrt{(A_2/A_1)})$, as follows

$$G_o = Y\,C_D\,\frac{\sqrt{2g_c\Delta p\rho_m}}{\sqrt{(1-\beta^4)}} \qquad (12.25)$$

At high Reynolds numbers, typical of these applications, the value of the orifice discharge coefficient, C_D, is usually 0.61. Note that expansion factor Y has a value of unity for single-phase liquid flow. For two-phase flow, the expression developed for single-phase gases may be used without sacrificing much accuracy.

Attempts were made to use homogeneous mixture density, given by

$$\frac{1}{\rho_m} = \frac{x}{\rho_g} + \frac{1-x}{\rho_L} \qquad (12.26)$$

However, use of Eq. 12.26 was not been particularly successful in correlating two-phase orifice-meter data. This experience led James to propose the following expression for calculating the throat mixture density for use in Eq. 12.26.

$$\frac{1}{\rho_m} = \frac{x^{1.5}}{\rho_g} + \frac{1-x^{1.5}}{\rho_L} \qquad (12.27)$$

Two-Phase Critical Flow Relationship for Steam/Water. As mentioned earlier, theoretical relationships for critical flow are quite complicated and are not necessarily accurate for steam/water flow. The empirical correlation proposed by James (1962, 1965) shows excellent agreement with available steam/water data and has become the industry standard for geothermal wells. The correlation relates the lip critical pressure, p_c, and stagnation enthalpy, H_c, to the critical mass flow rate at the exit of the James tube, G_c, as

$$G_c = 11{,}400\,p_c^{0.96}/H_c^{1.102} \qquad (12.28)$$

The critical mass flux at the exit of a James tube of diameter D_c is related to the mass flux at the orifice throat of diameter D_o through the continuity equation,

$$G_o = G_c(d_c/d_o)^2 \qquad (12.29)$$

Eq 12.28 is dimensional, with units of pressure p_c in psia, enthalpy H_c in Btu/lbm, and mass flux G_c in lbm/ft^2-sec. The stagnation enthalpy H_c refers to the enthalpy at the critical condition and the kinetic energy of the fluid. However, if the process is assumed adiabatic and enthalpy is evaluated at the upstream pressure tap of the

orifice meter where pressure is high and kinetic energy is low, the kinetic energy may be neglected. This simplification allows the stagnation enthalpy to be related to steam quality at the throat by the expression

$$H_c = x\,H_L + (1 - x)\,H_L \qquad (12.30)$$

The liquid and vapor enthalpies, H_L and H_g, are saturation enthalpies corresponding to the pressure at the orifice throat.

James (1962) showed excellent agreement between Eq. 12.28 and field data when steam quality was known. When flow rate and quality are both unknowns, Eqs. 12.25 and 12.28 (in conjunction with Eqs. 12.27 and 12.29) can be solved simultaneously for G_o and x, when data for the pressure drop across the orifice and the critical lip pressure are available. However, when both G_o and x must be computed from these equations, solution accuracy deteriorates significantly for high-quality (x > 40%) systems. Hasan (1991) noted that the use of a rigorous model for Δp across the orifice, rather than Eqs. 12.25 and 12.26, does not significantly improve accuracy. Reasons for this inaccuracy at high quality are related to the coupled nature of data gathering—that is, of orifice meter and critical flow—rather than the uncertainty stemming from individual correlations themselves.

Chien and Schrodt (1995) developed a similar method of using an orifice in series with a critical flow meter to measure steam flow rate. They used the James correlation (Eq. 12.27) for flow through the orifice and the King and Crocker (1967, p. 59) equation for critical flow. They reported excellent agreement between their estimates and their model. The model's superior performance owes largely to the optimized parameters that they had developed using field data in orifice and critical flow correlations. However, for making a priori estimates, the method proposed by James appears preferable.

12.3.3 Pressure Drop in Fittings. Pressure change, occurring when two-phase fluid flows through sudden enlargements and contractions, such as expanders, reducers, and orifices, depends on the area ratio, R_A (= final area/initial area = A_2/A_1), as well as other parameters. We recommend the following expression for estimating permanent pressure gain during two-phase flow through a sudden enlargement.

$$p_2 - p_1 = \frac{G_1^2\,(1-x)^2}{R_A \rho_l}\left(1 - \frac{1}{R_A}\right)\left(1 + \frac{C}{X} + \frac{1}{X^2}\right) \qquad (12.31)$$

where C and X are given by

$$C = \left[\lambda + (C_2 - \lambda)\sqrt{\rho_g / (\rho_l - \rho_g)}\right]\left[\sqrt{\rho_g / \rho_l} + \sqrt{\rho_l / \rho_g}\right] \qquad (12.32)$$

and

$$X = \frac{1-x}{x}\sqrt{\rho_g / \rho_L}\,, \qquad (12.33)$$

with λ = 1.0 and C_2 = 0.5 as suggested by Chisholm (1967a). Note that the area ratio, $R_A = A_2/A_1$, is greater than unity in this case.

For sudden contraction, we recommend a homogeneous flow approach, as suggested by Collier (1981, 86–94) for estimating two-phase pressure loss, which is written as

$$p_1 - p_2 = \frac{G_2^2}{\rho_l}\left[\left(1 - R_A{}^2\right) + \left(\frac{1}{C_c} - 1\right)^2\right]\left[1 + \frac{x(\rho_l - \rho_g)}{\rho_g}\right] \qquad (12.34)$$

The value of C_c, which depends on the area ratio, R_A (R_A < 1 for contractions), can be approximated by 0.598 + 0.13 (R_A − 0.2) using the data given by Collier (1981).

In single-phase flow, the pressure loss in valves is generally expressed as the loss that would be experienced in an equivalent length of the straight pipe (Perry 1950, p. 389). For example, for a globe valve, the pressure drop is that which would occur in the straight pipe of length 300*d*, where *d* is the pipe diameter. Chisholm (1967a) suggested that the equivalent-pipe-length approach be used for estimating two-phase pressure loss in valves and bends. Thus, for any such fitting, the pressure loss is given by

$$(\Delta p)_{\text{fit}} = d\left(L_e\right)_{\text{fit}}\left(\mathrm{d}p/\mathrm{d}z\right), \qquad (12.35)$$

where the equivalent length $(L_e)_{\text{fit}}$ is the empirically determined value for the particular fitting. We recommend the Lockhart and Martinelli (1949) method for calculating the two-phase pressure gradient, (d*p*/d*z*), in Eq. 12.35 because the L_e values recommended by Chisholm (1967a) for various fittings were developed using the same method of (d*p*/d*z*) calculation. Therefore, following the method outlined in Chapter 2,

$$(\Delta p)_{\text{fit}} = d\left(L_e\right)_{\text{fit}}\left[\frac{fG^2(1-x)^2}{2\rho_L d}\right]\left(1 + \frac{C}{X} + \frac{1}{X^2}\right) \qquad (12.36)$$

Eq. 2.30, repeated next and slightly different from Eq. 12.33, is used for calculating the Lockhart-Martinelli parameter, *X*.

$$X = \frac{1-x}{x}\sqrt{\rho_g / \rho_L}\left(\frac{\mu_L}{\mu_g}\right)^{0.1} \qquad (12.37)$$

Chisholm (1967a) also suggested that for high-pressure systems (p > 30 atm), the

parameter C in Eq. 12.36 be calculated with Eq. 12.32. To account for the effect of mass flux on the parameter C in straight pipes, Chisholm (1968) suggested that in Eq. 12.32, the value of λ is 1.0 and that $C_2 = G/G^*$, where the reference mass flux G^* is 307 lbm/ft^2-sec (= 1,500 kg/m^2.s). For all fittings, he recommends that the value of λ be 1.0. The value of C_2 varies with the fitting; in **Table 12.4,** we reproduce the recommended values of these parameters for various fittings.

	C_2	$L_e = L/d$	X	Pressure Drop
Straight pipe	G/G^*	1	Eq. 12.33	Eq. 12.36
45° Elbow/bend	3	15	Eq. 12.37	Eq. 12.36
90° Elbow/bend	3	32	Eq. 12.37	Eq. 12.36
180° Elbow	3	75	Eq. 12.37	Eq. 12.36
Tee	1.75	90	Eq. 12.37	Eq. 12.36
Gate valve (open)	1.2	7	Eq. 12.37	Eq. 12.36
Globe valve (open)	2.3	300	Eq. 12.37	Eq. 12.36
Disk water meter	1	400	Eq. 12.37	Eq. 12.36
Reducer/contraction	0.5		Eq. 12.37	Eq. 12.34
Expander	0.5		Eq. 12.37	Eq. 12.31

Table 12.4—Equivalent length and other factors for pipes and fittings.

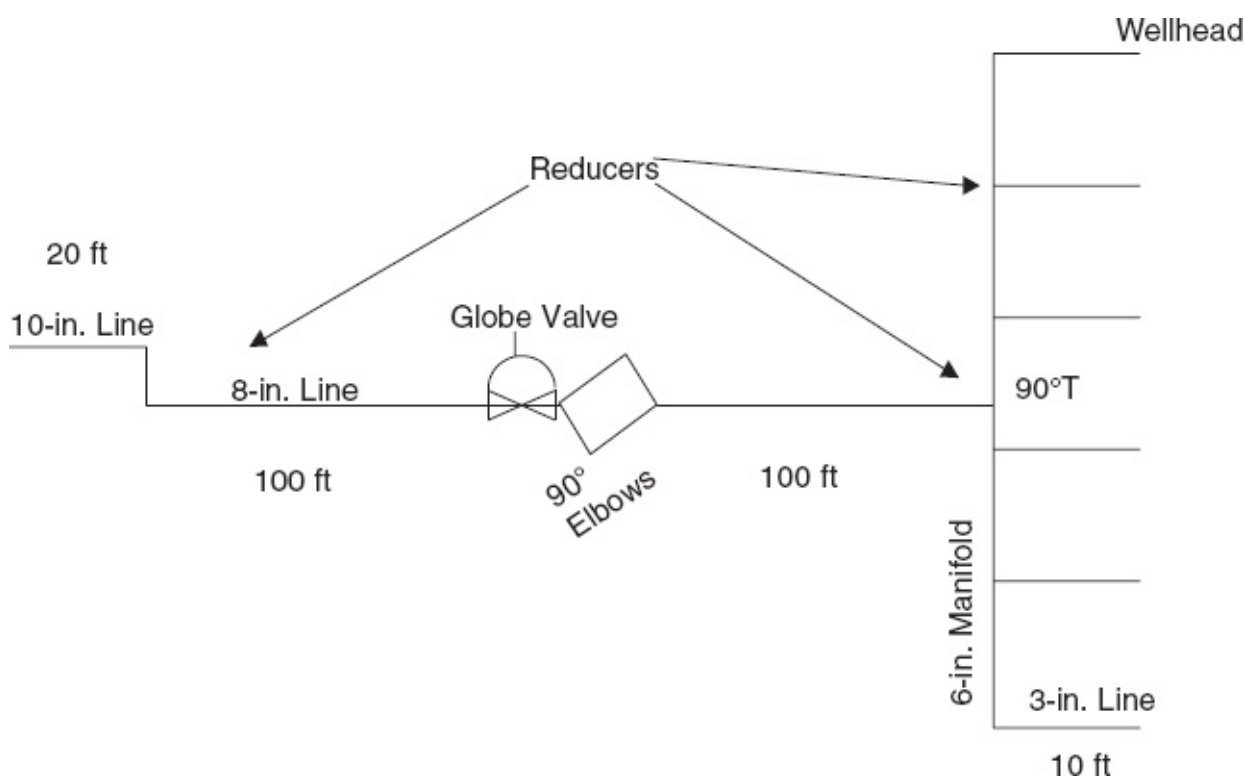

Fig. 12.30—Schematic of a steam injection manifold.

Field Example 12.4. Here, we present a calculation procedure for various fittings using a simplified version of an actual field problem. Note that the flowlines are all horizontal.

A 10-in. line supplies steam to a system of six steam injection wells, as shown in **Fig. 12.30.** The flow rate is 660,790 lbm/D/well water equivalent or 45.89 lbm/sec. The steam pressure at the main is 1,500 psia, and the quality is 80%. There is a 90° bend in the 10-in. line, which is 20 ft from the boiler, and another 90° bend after 5 ft. At this point, the 10-in. line connects to an 8-in. line with a 10 × 8 reducer. This 8-in. line continues for 100 ft, at which point there is a fully open globe valve. After the valve, there are four 45° elbows. The 8-in. line continues after that for another 100 ft.

The 8-in. line then connects to a 6-in. manifold by means of a T-joint and an 8 × 6 reducer. The 6-in. manifold supplies the wet steam to six 3-in. lines, connected by means of 6 × 3 reducers. These 3-in. lines are 10-ft long and are each connected to a vertical injection well.

Calculate the pressure and quality at the wellhead and at various points in the network.

The following values of saturated steam properties are available from any steam table.

p = 1,500 psia T^{sat} = 596.2°F x = 0.80 d_{main} = 0.8233 ft

Enthalpies, Btu/lbm: H_g = 1,169.2

H_L = 611.7

$H_m = x\,H_g + (1 - x)$

H_L = 1,057.7

Densities, lbm/ft^3:

ρ_g = 3.6137

ρ_L = 42.6

Viscosities, cp: μ_g = 0.02052 μ_L = 0.08589

Friction factor specific to the flowlines: $f_L/4 = 0.0035 + 0.264/\mathrm{Re}_L^{0.42}$

Solution. The following solutions apply.

For a 10-in. line (20 ft long),

G_{mi} = (mass flow rate/area) = 84.135 lbm/ft^2-sec,

$X = [(1 - x)/x]\,(\rho_g/\rho_i)^{0.5}\,(\mu_L/\mu_g)^{00.1} = 0.0965$,

$C = \{\lambda + (C_2 - \lambda)[(\rho_L - \rho_g)/\rho_L]^{1/2}\}[(\rho_g/\rho_L)^{1/2} + (\rho_L/\rho_g)^{1/2}] = 13.1608$,

$\varnothing_L{}^2 = 1 + C/X + 1/X^2 = 244.71$,

$\mathrm{Re}_L = (dG/\mu_L) = 1.216 \times 10^6$, and $f_L/4 = 0.0035 + 0.264/\mathrm{Re}_L^{0.42} = 0.0042$,

$(dp/dz)_L = f_L G_m{}^2(1 - x)^2/[2(\rho_L)(g_c)(d)] = 2.0984 \times 10^{-3}$ psf/ft,

and

$-(\Delta p)_F = (\mathrm{dp/dz})_L\, L\varnothing_L{}^2 = 20(2.0984 \times 10^{-3})(244.71) = 10.27$ psf = 0.071 psi.

For a 90° bend,

$X = [(1 - x)/x]\ (\rho_g\ \rho_l)^{0.5} = 0.0729$,

$C = \{1 + (3 - 1)[(\rho_L - \rho_g)/\rho_l^{1/2}\}[(\rho_g/\rho_L)^{1/2} + (\rho_L/\rho_g)^{1/2}] = 10.851$,

$\varnothing_L^2 = 1 + C/X + 1/X^2 = 337.9$,

and

$-(\Delta p) = (dp/dz)_L\ \varnothing_L^2\ (L_e)\ d$

$= (2.0984 \times 10^{-3})(337.9)(32 \times 0.8233) = 18.96$ psf = 0.1317 psi.

For a 10 × 8 contraction,

Area ratio $R_A = (8/10)^2 = 0.64$, and $G_2 = G_{mi}/0.64 = 84.135/0.64 = 131.46$ lbm/ft^2-sec,

$C_e = 0.598 + 0.13\ (R_A - 0.2) = 0.655$, and $1/C_e = 1.526$,

(Eq. 12.34, first term) $(131.46)^2[(1 - 0.64^2) + (1.526 - 1)^2]/(2 \times 42.6)/(32.2) = 5.468$ psf,

(Eq. 12.34, second term) $1 + [0.7999(42.6 - 3.613)]/\ 3.613 = 9.633$,

and

$-(\Delta p) = 5.468 \times 9.633 = 52.67$ psf = 0.366 psi.

For a globe valve on the 8-in. line,

$G_2 = 131.46$ lbm/ft^2-sec,

$\mathrm{Re}_L = (dG/\mu_L) = 1.519 \times 10^6$, and $f_L/4 = 0.0035 + 0.264/\ \mathrm{Re}_L^{0.42} = 0.00417$,

$(dp/dz)_L = f_L G_2^2/(1 - x)^2/[2(\rho_L)(g_c)(d)] = 6.384 \times 10^{-3}$ psf/ft,

$X = [(1 - x)/x]\ (\rho_g/\rho_l)^{0.5} = 0.0733$,

$C = \{1 + (2.3 - 1)\ [(\rho_L - \rho_g)/\rho_L]^{1/2}\}[(\rho_g/\rho_L)"^2 + (\rho_L/\rho_g)^{1/2}] = 8.362$,

$\varnothing_L^2 = 1+ C/X + 1/X^2 = 301.2$,

and

$-(\Delta p) = (dp/dz)_L\ \varnothing_L^2\ (L_e)\ d$

$= (6.384 \times 10^{-3})\ (301.2)(300)(8/12) = 384.3$ psf = 2.669 psi.

For a 45° elbow on the 8-in. line,

$\mathrm{Re}_L = (dG/\mu_L) = 1.518 \times 10^6$, and $f_L/4 = 0.0035 + 0.264/\ \mathrm{Re}_L^{0.42} = 0.00417$,

$(dp/dz)_L = f_L\ G_2^2(1 - x)^2/[2(\rho_L)(g_c)(d)] = 6.377 \times 10^{-3}$ psf/ft,

$X = [(1 - x)/x]\ (\rho_g/\rho_l)^{0.5} = 0.0732$,

$C = \{1 + (3 - 1)\ [(\rho_L - \rho_g)/\rho_L^{1/2}\}[(\rho_g/\rho_L)^{1/2} + (\rho_L/\rho_g)^{1/2}] = 10.871$,

$\varnothing_L^2 = 1+ C/X + 1/X^2 = 336.2$,

and

$-(\Delta p) = (dp/dz)_L\ \varnothing_L^2\ (L_e)\ d$

$= (6.377 \times 10^{-3})\ (336.2)(15)(8/12) = 21.441$ psf = 0.1489 psi.

For a T-joint on the 8-in. line,

$Re_L = (dG/\mu_L) = 1.518 \times 10^6$, and $f_L/4 = 0.0035 + 0.264/Re_L^{0.42} = 0.00417$,

$(dp/dz)_L = f_L\, G_2^2/(1 - x)^2/[2(\rho_L)(g_c)(d)] = 6.387 \times 10^{-3}$ psf/ft,

$X = [(1 - x)/x]\,(\rho_g/\rho_l)^{0.5} = 0.0732$,

$C = \{1 + (1.75 - 1)\,[(\rho_L - \rho_g)/\rho_L]^{1/2}\}[(\rho_g/\rho_l)^{1/2} + (\rho_L/\rho_g)^{1/2}] = 6.4123$,

$\varnothing_L^2 = 1 + C/X + 1/X^2 = 275$,

and

$-(\Delta p) = (dp/dz)_L\, \varnothing_L^2\, (L_e)\, d$

$= (6.387 \times 10^{-3})\,(275)(90)(8/12) = 105.4$ psf $= 0.7321$ psi.

For a 6 × 8 expansion,

Area ratio $R_A = (8/6)^2 = 1.7778$, $1/\beta = 0.75$, and $G_2 = 131.46$ lbm/ft^2-sec,

$X = [(1 - x)/x]\,(\rho_g/\rho_l)^{0.5} = 0.0731$,

$C = \{1 + (0.5 - 1)\,[(\rho_L - \rho_g)/\rho_L]^{1/2}\}[(\rho_g/\rho_L)^{1/2} + (\rho_L/\rho_g)^{1/2}] = 1.9487$,

(Eq. 12.31, first term) $(131.46)^2(1 - 0.7987)^2(1 - 0.5625)/1.7778/42.6/32.2 = 0.3972$ psf,

(Eq. 12.31, second term) $1 + C/X + 1/X^2 = 214.5$,

and

$(\Delta p) = 0.3972 \times 214.5 = 85.1929$ psf $= 0.592$-psi increase in pressure.

Analysis of Field Example 12.4. **Table 12.5** shows calculated pressure drop for the particular fitting/segment as well as cumulative pressure drop up to the point. The cumulative distance is shown from the steam entrance point at the boiler. Note the significant pressure drop caused by the globe valve when it is open. The next highest single-item pressure drop, 1.487 psi, occurs in the 8 × 6 reducer. The pressure drop at this reducer is much higher than that in the 10 × 8 reducer because the mass flux in the 6-in. line is almost twice as much as that in the 10-in. line. A reduced crosssectional area causes this high pressure loss as the pressure drop varies directly as the square of the mass flux. The pressure loss in the 6 × 3 reducer is also high, but not as high as the loss in the 8 × 6 reducer. That is because even though the flow area is lower in the 3-in. line, the total rate of fluid flow, which is distributed over the six wells, is also lower.

12.3.4 Wellbore Steam/Water Flow and Surface Metering Summary. In this section, we presented some elements of steam/water two-phase flow during saturated steam injection and surface metering. The intrinsic idea was to show application of fluid and heat flow principles developed in earlier chapters to areas where heat transfer is accompanied by phase change. Results show that the fundamental principles hold in any fluid and heat flow situation.

Description	Segment Length (ft)	No. of Items	Cumulative Distance (ft)	Pressure (psia)	Item Δp (psi)	Cumulative Δp (psi)

p_L			0	1,500.00	0	0
10-in. Pipe	20		20	1,499.93	0.0692	0.0692
90º Bend		2	20	1,499.67	0.2634	0.33255
10-in. Pipe	5		25	1,499.65	0.0173	0.34985
10 × 8 Reducer		1	25	1,499.28	0.3658	0.71563
8-in. Pipe	100		125	1,498.61	0.6781	1.39372
Globe valve		1	125	1,495.94	2.6694	4.06311
45º Elbow		4	125	1,495.34	0.5956	4.65867
8-in. Pipe	100		225	1,494.66	0.6804	5.33905
Tee		1	225	1,493.93	0.7321	5.47949
8 × 6 Reducer		1	225	1,492.44	1.4866	6.96611
6 × 8 Expander		1	225	1,493.03	-0.5916	4.74743
6 × 3 Reducer		1	225	1,492.78	0.8122	7.77835
3-in. Pipe	10		235	1,492.75	0.0961	7.87449
p_{wh}				1,492.75		

Table 12.5—Pressure drop in various items of the example problem.

12.4 Combating Wellbore Solids Deposition

12.4.1 Introduction. In oilfield operations, unwanted flow restrictions frequently occur in the fluid production chain, from perforations to a gathering center. Potential causes for the development of these restrictions are numerous, including thermal stress, mechanical failures, stuck pigs, and vapor locks. However, most blockage-related damage is caused by the formation of compounds that adhere to the walls of the production string. Asphaltene and paraffin deposition and hydrate formation are primary examples of such sticky problems that cost the industry millions of dollars in lost production and cleaning operations. Leontaritis and Mansoori (1988) present a comprehensive review of various field experiences arising from asphaltenes. **Fig. 12.31** shows a field example of asphaltene deposition onto a 2.992-in.-ID tubing wall. Besides experiencing declining productivity with increasing deposition thickness, assigning a friction factor becomes a daunting task.

Some studies showed novel ways of locating and characterizing wellbore blockages, such as those offered by Hasan et al. (1996b) and Massinon (1988), among others. Unfortunately, treating problems arising from paraffin, asphaltene, or hydrate deposition still relies largely on pumping aromatic solvents to the suspected location in a flow string. Asphaltenes are ordinarily treated with aromatic solvents such as toluene or xylene or with deasphalted oil. As the name implies, deasphalted oil is devoid of asphaltenes and therefore acts as a potent solvent. On the other hand, remedial measures for paraffins involve treatment with hot oil, use of

mechanical scrapers, and injection of chemical inhibitors and microbes. Regardless of the method used, these measures are expensive and are usually undertaken after the problem surfaces.

In this section, we focus on preventive or proactive measures by examining phase behavior as well as fluid and heat flow characteristics in a producing string. In other words, we examine the viability of measures, such as well design and altering flow characteristics, by exploring the underlying physics. Here, we address issues pertaining to asphaltenes and paraffins; hydrates are not explicitly considered. Much of the material discussed earlier in Chapter 8, Section 8.2, and Chapter 12, Section 12.1, will be used to tackle this problem. The study of Kabir et al. (2001a) forms the backbone of this section.

12.4.2 Fluid/Solid Thermodynamic Behavior. Understanding thermodynamic behavior of fluids forms the basis for most remedial measures. This element is particularly true for the solution approach discussed here. Most investigators focused on separate studies of each solid component—that is, asphaltene, wax or paraffin, and hydrate. However, in many oils, all these solids can potentially occur and may present problems depending on the fluids' state (pressure and temperature) in the flow string. Jamaluddin et al. (2003) presented a unified approach to combining all three solids envelopes, as shown in **Fig. 12.32.**

Paraffins. Paraffins or waxes are high-molecular-weight, high-carbon-number (30–75) *n*-paraffins that can present significant challenges when transported from reservoir conditions to any other condition. Wax crystallizes at a higher temperature than its deposition temperature. This temperature is also known as the cloudpoint. Comparison of extensive laboratory measurements with field data showed that the wax crystallization temperature values obtained from dead oils were in good agreement with those measured in flowing wellbores. Hammami and Raines (1999) speculated that the laminar or transitional flow was probably conducive to crystallization of wax and its subsequent deposition.

Monger-McClure et al. (1999) showed that thermodynamic models' ability to estimate the cloudpoint temperature and subsequent deposition achieved moderate success in modeling wax deposition. However, over the years, significant progress has been made in understanding deposition kinetics of paraffins, as studies of Burger et al. (1981), Weingarten and Euchner (1988), Singh et al. (2000), among others, suggest. In particular, Singh et al. (2000) provided insights into the deposition mechanism and subsequent growth of the wax deposit with time. They showed that deposition growth is a result of counterdiffusion, in which the wax molecules diffuse into the deposit, and oil molecules diffuse out.

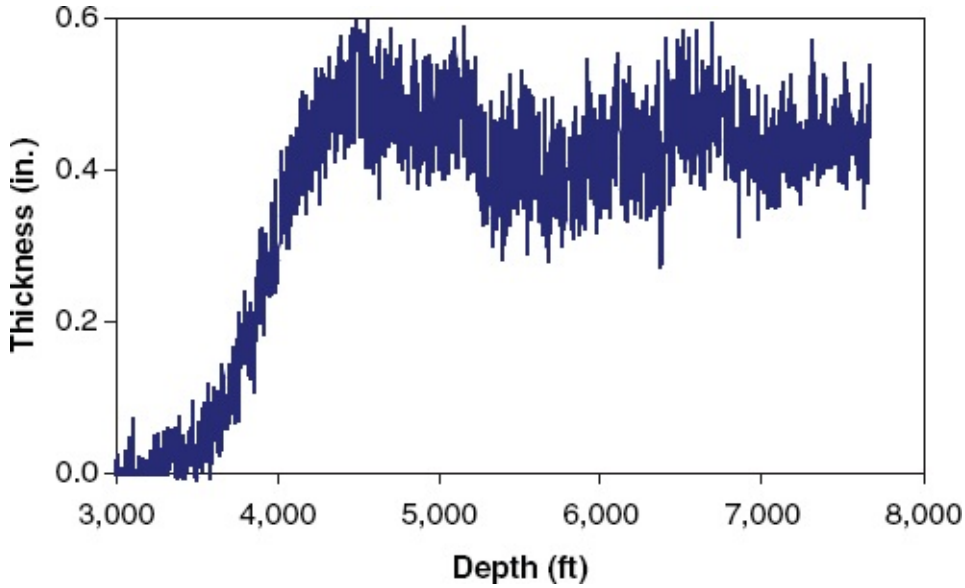

Fig. 12.31—Asphaltene deposition in a producing well.

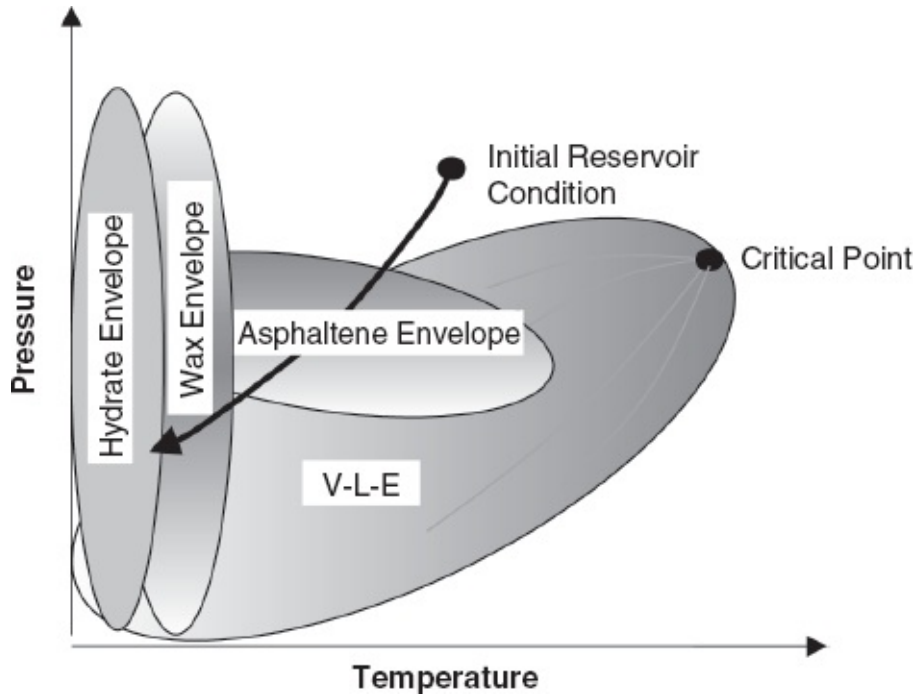

Fig. 12.32—Phase behavior of fluids showing solids envelopes (after Jamaluddin et al. 2003). V-L-E is vapor-liquid equilibrium.

Fig. 12.33 shows a qualitative paraffin phase envelope and a well sketch. Our approach of addressing this issue is to avoid crossing the paraffin phase envelope while expanding the fluid from downhole, *X*, to surface, *Z*, as shown in Fig. 12.33. As the oil expands up the wellbore to reach point *Z* at the wellhead, it experiences decline in pressure and temperature. In so doing, the liquid oil phase, *L*, enters the liquid/gas (*L* + *G*) region before crossing the solid envelope (*L* + *S* + *G*), thereby triggering flocculation of paraffins. The proposed treatment involves circulating a hot fluid in the annulus and/or insulating the production string. Thermodynamically

speaking, paraffins are strongly temperature dependent; consequently, they are amenable to thermal treatment.

Asphaltenes. Asphaltenes, defined as *n*-pentane insoluble fraction of crude oil, are polar molecules, which aggregate through orbital association, hydrogen bonding, and acid-based interactions. The growth of aggregates is limited by the presence of resins in solution. Various asphaltene-solubility studies have been reported, and a number of models to compute asphaltene flocculation or onset condition are available. Studies by Leontaritis and Mansoori (1987), MacMillan et al. (1995), Pan and Firoozabadi (2000), and Nghiem and Coombe (1997) are cases in point.

In general, asphaltene onset depends on the existing pressure and temperature at any point in the wellbore. Asphaltene onset condition does not imply deposition onto the wall, however. Unlike paraffins, deposition kinetics for asphaltenes is not well-understood. Nonetheless, variation of oil composition in the wellbore requires that asphaltene flocculation envelope (AFE) be established for a given oil before solution is sought. Note that we prefer the term AFE over ADE, which implies asphaltene deposition envelope, simply because flocculation is not necessarily deposition.

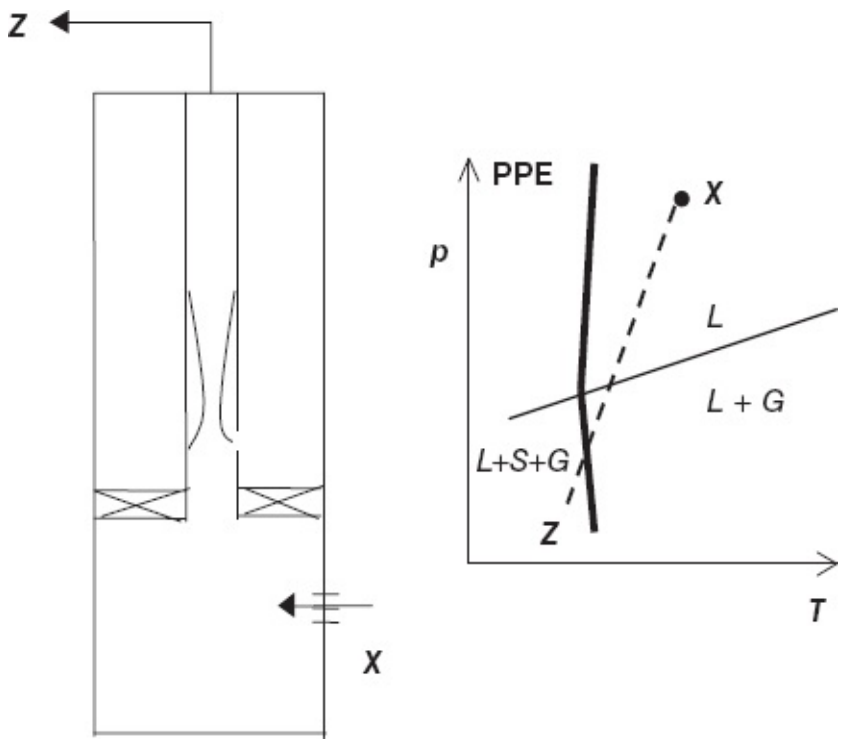

Fig. 12.33—Paraffin phase envelope (PPE) offers the possibility of profile alteration.

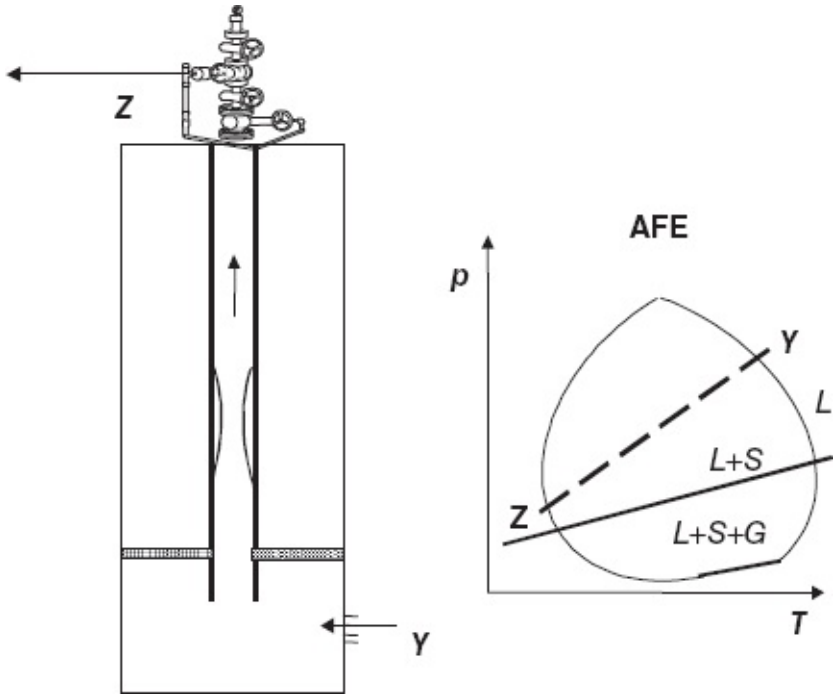

Fig. 12.34—Asphaltene flocculation envelope (AFE) provides clues about asphaltene deposition.

Fig. 12.34 shows a qualitative AFE diagram and a well schematic. Unlike Fig. 12.33, the liquid oil phase, *L*, enters the liquid/solid (*L*+*S*) region within the phase envelope, thereby triggering flocculation of asphaltenes. Below the saturation line (in solid), gas evolution will occur either near the wellhead or in the flowline. At very low pressure and temperature—that is, outside the AFE—asphaltenes are resolubilized in the liquid. Notwithstanding our lack of understanding of kinetics of deposition, we presuppose that deposition occurs when the oil remains within the phase envelope.

Our approach to mitigating the asphaltene deposition problem is to inject solvent directly at the suspected depth of deposition. When the asphaltene phase envelope was originally advanced (Leontaritis and Mansoori 1987), occurrence of oil to the left side of the phase envelope, the same side of *Z*, was thought to be a possibility. However, experimental studies tend to show the occurrence of asphaltic oil to the right side of AFE—that is, *Y*– is more common than thought previously. The study of Jamaluddin et al. (2003) is a case in point.

12.4.3 Fluid Circulation Model. This section probes the elements of a fluid circulation model. **Fig. 12.35** shows a schematic of the physical model. Either single-phase oil or a two-phase mixture of oil and gas is produced up the tubing. The circulating string carrying a cooling fluid is injected into the annulus at a depth L_j. This string may have insulation to minimize energy exchange before actual injection.

Developing expressions for fluid temperature in the tubing, the annulus, and the circulating string requires setting up balances for heat transfer among these fluids. The energy balances are set up for the fluids in the control volume as shown in Fig. 12.35. Note that the *z*-coordinate represents well length, not depth, and that *z* is

positive in the upward direction. We let subscript *f* denote the fluid in the production string, whereas subscripts *w* and *a* stand for the circulating and annular fluid, respectively.

We derived the differential equations for the tubing fluid, circulating fluid, and annular fluid, respectively, as shown in Appendix 12-C, and these are written as

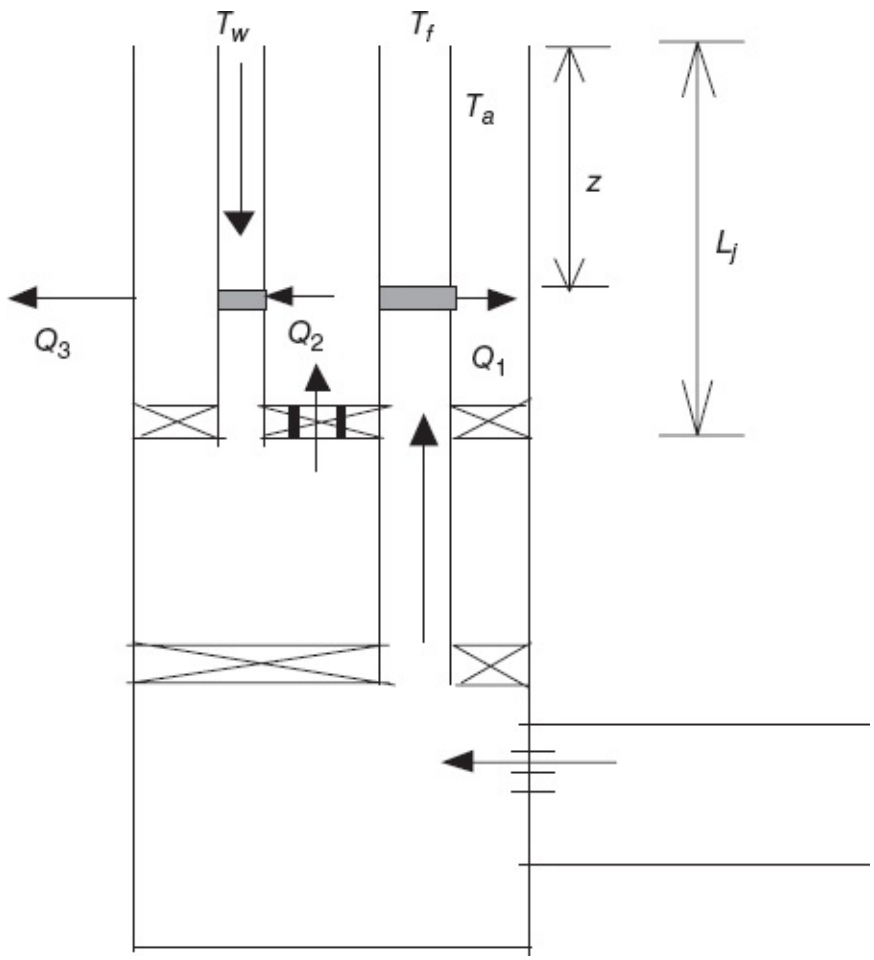

Fig. 12.35—Schematic of the fluid circulation system.

$$\frac{dT_f}{dz} = -L_{R1}\left(T_f - T_a\right) + \phi_f, \quad (12.38)$$

$$\frac{dT_w}{dz} = -L_{R2}(T_a - T_w) + \phi_w, \quad (12.39)$$

and

$$\frac{dT_a}{dz} = \frac{T_f - T_a}{A_1}\frac{c_f}{c_a} - \frac{T_a - T_w}{A_2}\frac{c_w}{c_a} - \frac{T_a - T_{ei}}{A_3} + \phi_a . \quad (12.40)$$

Simultaneous solutions of Eqs. 12.38, 12.39, and 12.40 should give the expressions

for fluid temperatures in the three conduits of the system. Unfortunately, combining these three equations results in a third-order differential equation, which does not lend itself to analytic treatment. Therefore, we offer a numerical solution to this problem in Appendix 12-C.

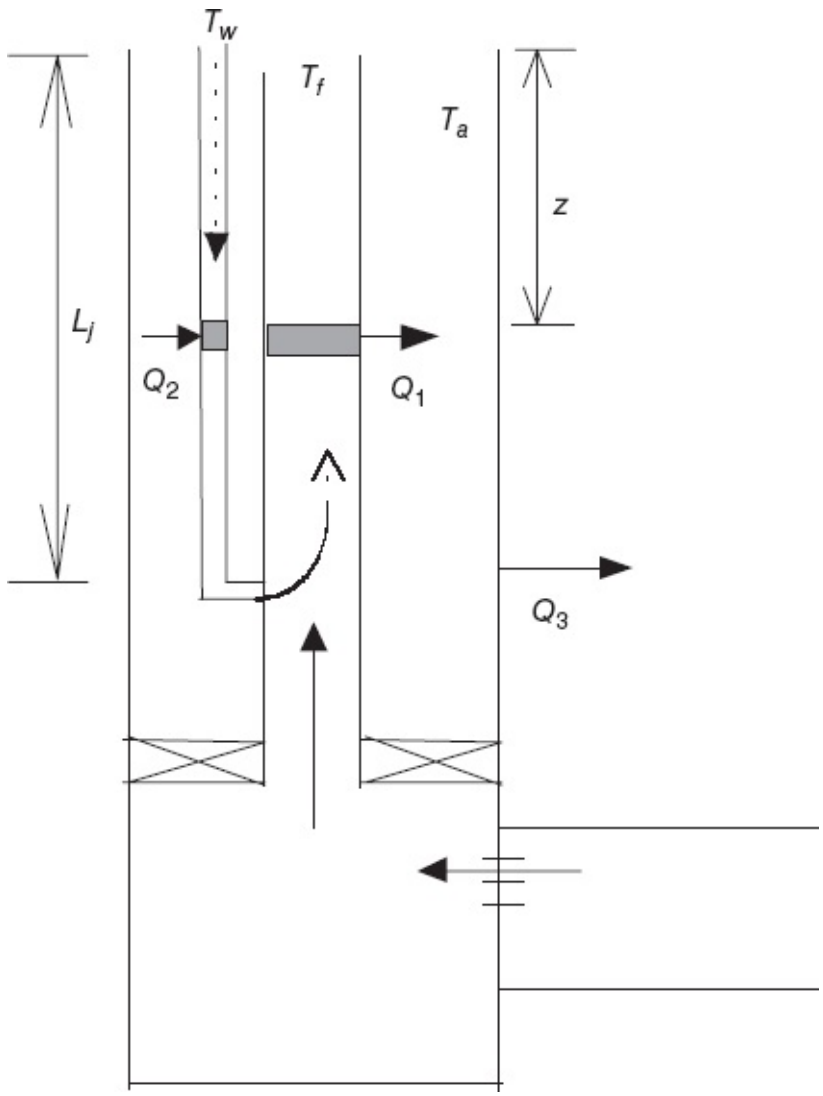

Fig. 12.36—Schematic of the solvent injection system.

12.4.4 Solvent Injection Model. Solvent injection is often invoked in a variety of operations. **Fig. 12.36** presents a schematic of the model when a solvent is injected directly into the producing string at a distance L_j from the surface, after being conveyed through a chemical injection line. We wish to compute temperature profiles in all three conduits so that the solvent's potency at a given pressure and temperature can be aligned with the asphaltene or paraffin deposits within the tubing. In other words, knowledge of the temperature profiles at the well operating condition leads us to optimal design of the injection line.

Energy balances for the fluids in the three conduits in this case are similar to that of fluid circulation in the annulus. For produced and injected fluids, Eqs. 12.38 and 12.39 from the previous case apply here. However, direct injection increases the fluid

rate in the tubing above the point of injection, thereby requiring a slight modification in the definition of the relaxation parameter, L_{RI}, as

$$L_{R1} = \frac{2\pi r_{to} U_1}{c_w w_w + c_f w_f} \quad (12.41)$$

The relaxation parameters L_{R2} and L_{R3} are the same as those defined in Eqs. 12-C-13 and 12-C-16. Another difference in this case is that the annular fluid is not subjected to forced convection. For the annulus, the heat gain from the tubing fluid equals the heat loss to the injection string and the formation. In other words,

$$L_{R1}(T_f - T_a)(w_f c_f) = L_{R2}(T_a - T_w)(w_w c_w) + L_{R3}(T_a - T_{ei})(w_a c_a) \quad (12.42)$$

The overall-heat-transfer coefficient U_{to} needed to compute L_{R3} in Eq. 12-C-16 is slightly different in this case because of lack of forced convection in the annulus. Note that U_{to} can be calculated from the following expression:

$$\frac{1}{U_{to}} = \frac{r_{to}\ln(r_{co}/r_{ci})}{k_c} + \frac{r_{to}\ln(r_{cmo}/r_{cmi})}{k_{cm}} + \frac{r_{to}}{r_{ci}h_a} \quad (12.43)$$

The annular fluid may experience natural convective heat transport because of the temperature difference between the inner and outer wall of the annulus. The estimation procedure for the heat-transfer coefficient for the annular fluid, h_a, may be made using the procedure discussed in Chapter 6.

This model is robust enough for applications in offshore environments. In an offshore riser, direct heat transfer occurs between the production string and the seawater. We modified the expression for U_{to} to account for this altered heat-transfer scenario. Chapter 6 captures this modification.

Eqs. 12.38, 12.39, and 12.42 may be combined to form a second-order linear differential equation, which can be solved analytically for three unknowns: T_f, T_w, and T_a. We present the solutions by omitting the tedious derivation.

$$T_f = \alpha_1 e^{\lambda_1 z} + \alpha_2 e^{\lambda_2 z} + (\beta_4/\beta_3)z + \beta_5/\beta_3 - (\beta_2\beta_4/\beta_3^2), \quad (12.44)$$

$$T_a = \omega_1\alpha_1 e^{\lambda_1 z}(1 - A_2\lambda_1) + \omega_2\alpha_2 e^{\lambda_2 z}(1 - A_2\lambda_2) + \omega_3 z + \omega_4 - A_2(\varphi_w + \omega_3), \quad (12.45)$$

and

$$T_w = \omega_1\alpha_1 e^{\lambda_1 z} + \omega_2\alpha_2 e^{\lambda_2 z} + \omega_3 z + \omega_4. \quad (12.46)$$

Constants of Eqs. 12.44 through 12.46 are given in Appendix 12-C.

12.4.5 Application of Models. ***Paraffin Control Using Fluid Circulation*.** As discussed earlier, paraffininduced plugging can occur in wellbores or flowlines. **Fig. 12.37** shows significant plugging in a flowline. Hot-oil treatment is a popular way of addressing wellbore paraffin problems despite its potential for formation damage (Barker 1989; Mansure and Barker 1993). Let us explore the feasibility of mitigating the same in a deepwater environment where well intervention is prohibitive. Cooling of fluids in the riser simply adds another dimension to the deposition problem. The measures studied include retaining fluids' energy by insulating the flow string and supplementing energy at the seafloor by circulating a fluid.

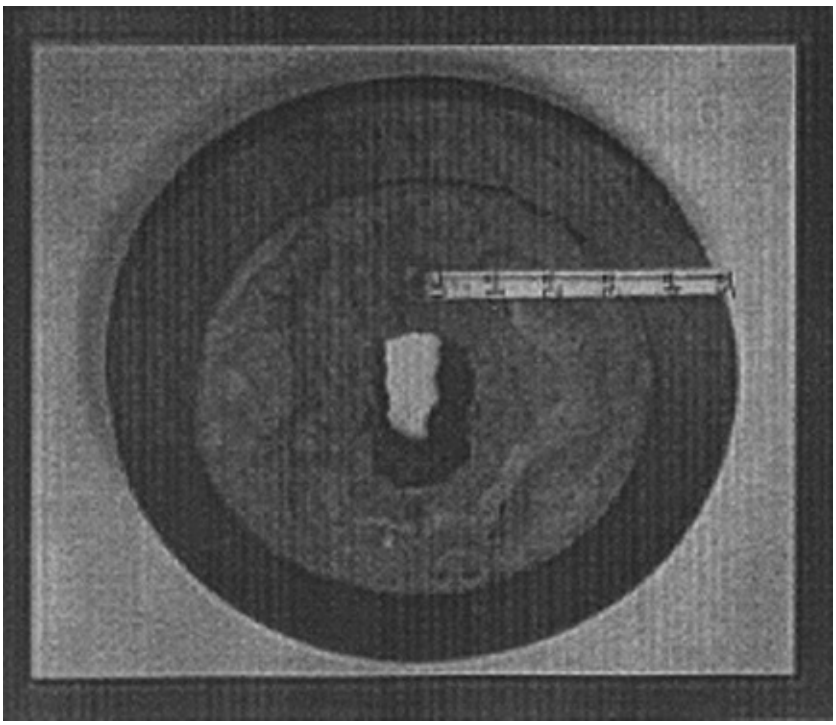

Fig. 12.37—Paraffin-plugged flowline (after Singh et al. 2000).

Let us probe the underlying issue at hand. **Fig. 12.38** shows that higher temperature at the wellhead is tied to higher rates. The rationale is rather straightforward: Fluids will retain higher energy at higher rates, a point made earlier in Chapter 9. In addition, the residence time in the riser declines with higher rates, thereby augmenting energy conservation. Economics dictates high-rate production in any offshore environment, let alone in deep water. Fig. 12.38 shows that rates must be maintained above 5,000 STB/D to avoid potential wax precipitation at 190°F in this example.

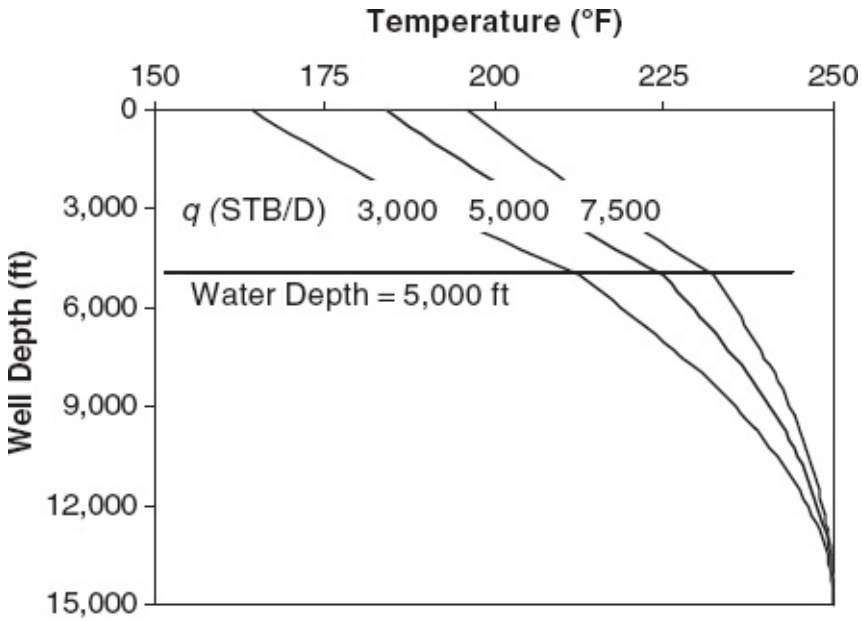

Fig. 12.38—Higher rate retains higher fluid temperature at the wellhead.

When fluid is circulated down to the seafloor of a riser's annulus, the fluids' energy retention is enhanced, but only in presence of insulation. As **Fig. 12.39** shows, an increasing fluid circulation rate helps retain increased energy in the presence of insulation. In this case, the energy retention plateaus at a circulation rate of approximately 1,000 STB/D when production occurs at 5,000 STB/D. However, **Fig. 12.40** suggests that heat retention is quite efficient when fluid (preferably produced oil) is circulated down to the seafloor for augmenting energy retention. In the absence of insulation and/or fluid circulation, heat transfer is dominated by the temperature gradient of the seawater. As **Fig. 12.41** shows, excessive heat loss in a bare riser will be conducive to solids deposition because of significant lowering of fluid temperature. At low temperatures, hydrates add to the solids problem.

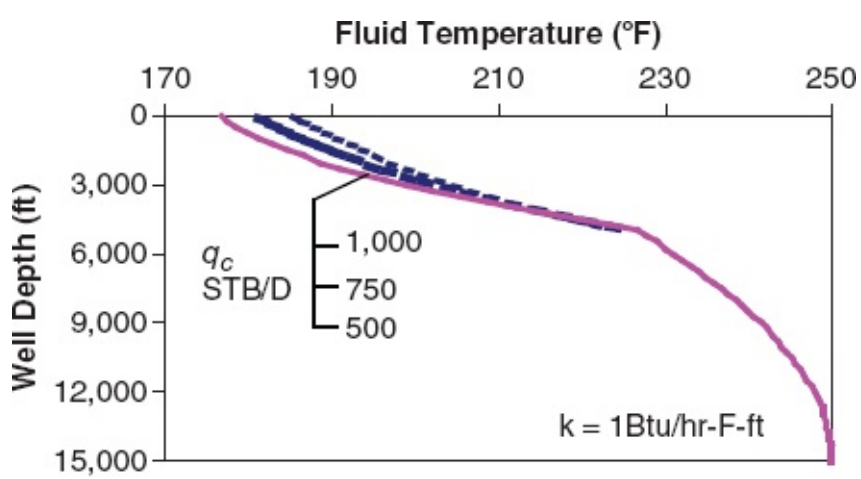

Fig. 12.39—Increasing circulation rate helps retain fluid energy.

To explore the question of well intervention, we used a transient simulator to study

the time taken for temperature to decay at the wellhead (Hasan et al. 1998). **Fig. 12.42** exhibits the decay trends with and without insulating the flow string. Insulation does help at the shallowest water depth of 2,500 ft. However, at greater depths, no advantage can be realized simply because the seawater acts as an overwhelming heat sink. Figs. 12.40 and 12.41 both suggest that any notion of seafloor processing of fluids must consider heated pipelines for flow assurance.

***Asphaltene Control Using Fluid Injection*.** As stated before, many kinds of aromatic solvents can be injected into tubing to remove asphaltene plugs. Ordinarily, the solvent is banked by spacer fluids, such as diesel, and pumped directly into the tubing, thereby displacing the produced fluid back into the formation. This form of displacement is known as bullheading. Use of deasphalted oil (Jamaluddin et al. 1996; Kabir and Jamaluddin 2002) has shown promise in mitigating asphaltene deposition, as illustrated by **Fig. 12.43.** A soak period of over 24 hours was used in this case. Note that several months had elapsed between the two measurements, during which production continued to occur. This operating condition explains further deposition higher up (< 4,000 ft) in the string, which remained untreated. The appeal for deasphalted oil stems from the fact that it is less expensive than other solvents and is environmentally friendly, unlike the routinely used solvents.

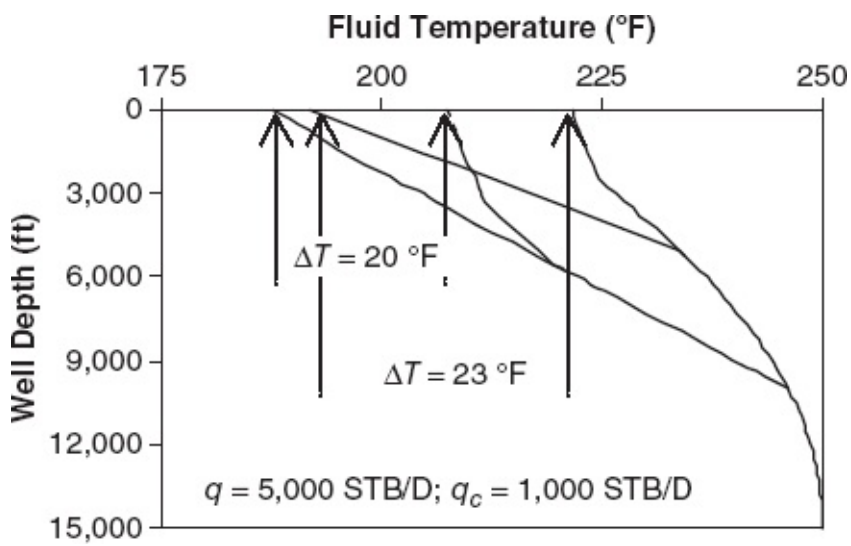

Fig. 12.40—Both fluid circulation and tubing insulation retain high wellhead fluid temperature.

One problem with the traditional bullheading treatment is that well intervention is required, which implies loss of production. In the novel approach discussed earlier, we wish to inject either deasphalted oil or a suitable solvent into the production string through a chemical injection line, as shown in Fig. 12.36. This approach is intrinsically different in that no well shut-in is required, and this measure can be undertaken proactively. Let us now discuss some results of the model presented earlier.

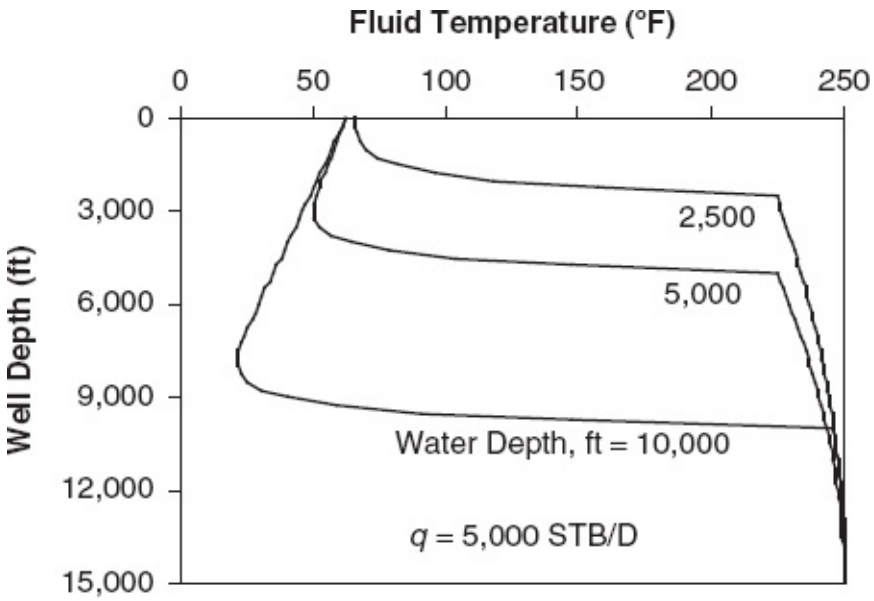

Fig. 12.41—Energy dissipation along a bare producing string.

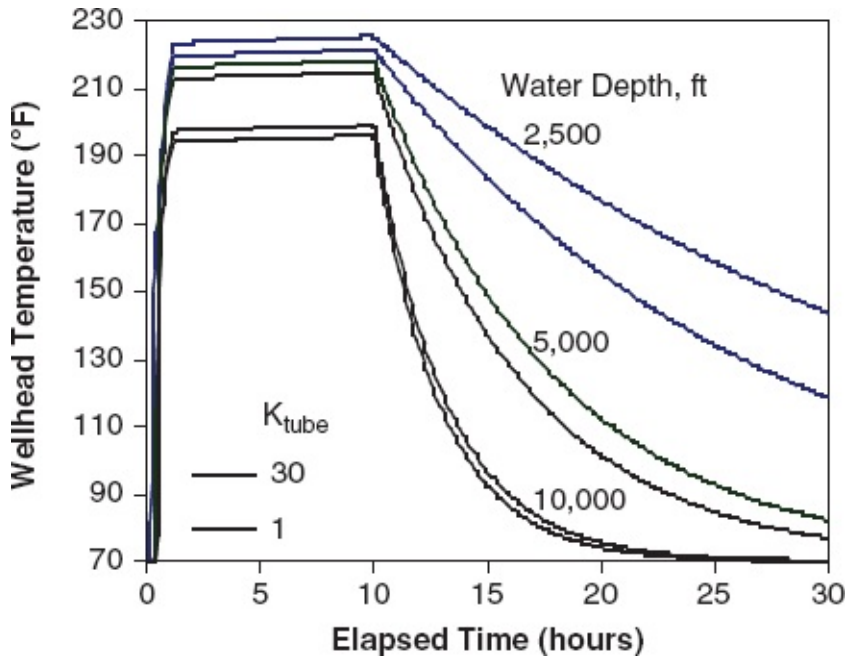

Fig. 12.42—Effect of insulation diminishes with increasing water depth.

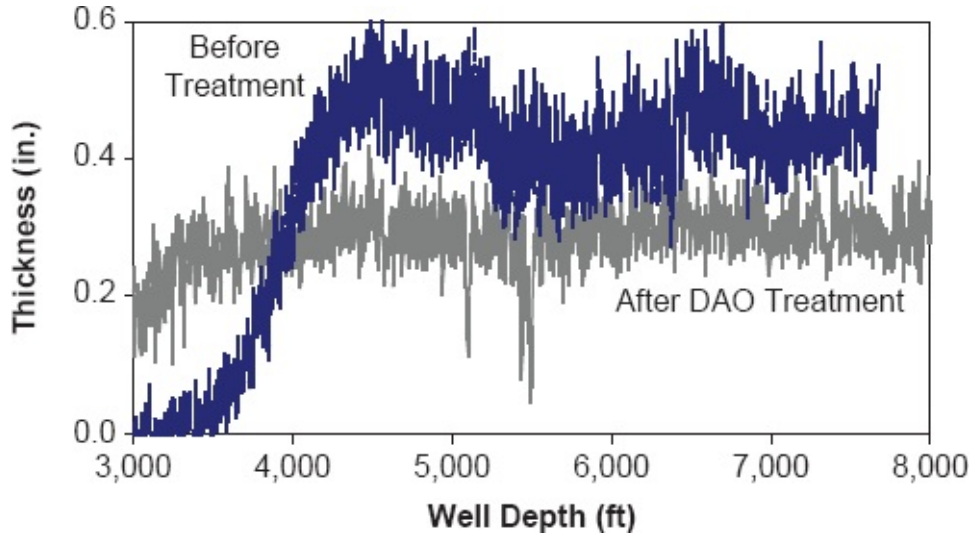

Fig. 12.43—Caliper measurements show the effectiveness of deasphalted-oil (DAO) treatment.

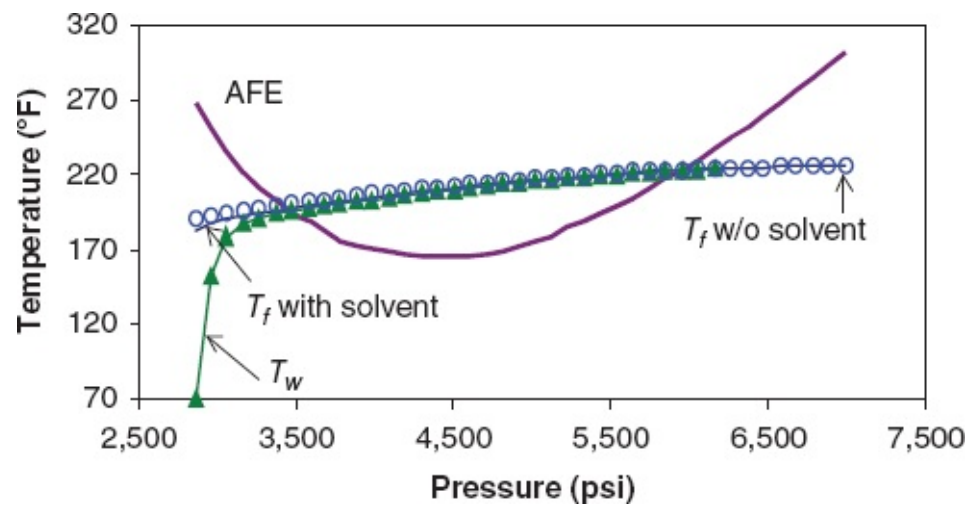

Fig. 12.44—Fluid temperature profiles with or without solvent injection.

Fig. 12.44 presents the pressure/temperature (*p*/*T*) trace for direct injection of 200 STB/D of deasphalted oil into the tubing that is producing at 5,000 STB/D. The solvent is transported to a depth of 8,000 ft from the wellhead using a 0.5-in.-ID, 0.75-in.-outer-diameter string. Other well and fluid property data are the same as those shown in **Table 12.6.**

Fig. 12.44 shows that the temperature of the solvent quickly approaches that of the produced fluid as it is transported down the circulation string. Note that the addition of the solvent somewhat reduces the temperature of the produced fluid. The main purpose of this model is to have the ability to compute the *p*/*T* trace and observe how the addition of solvent can help mitigate the problem at hand. For instance, to ensure efficient treatment, the flow rate may be significantly reduced. This action, in turn, will reduce the temperature profile itself, leading to a favorable condition during treatment.

Well depth, ft	10,000
Production string ID, in.	2.75
Production string OD, in.	3.25
Circulating-string ID, in.	2.75
Circulating-string OD, in.	3.25
Production casing ID, in.	10
Production casing OD, in.	11.5
Pipe roughness, in.	1.8×10^{-5}
Production rate, STB/D	2,000
Circulating-fluid (water) rate, STB/D	200
Formation permeability, md	25
Formation thickness, ft	50
Formation porosity	0.293
Bottomhole temperature, °F	225
Geothermal gradient, °F/ft	0.0155
Formation thermal conductivity, Btu/(ft-°F-hr)	3.33
Formation density, lbm/ft^3	135
Formation heat capacity, Btu/(lbm-°F)	0.625
Production tubing/casing material thermal conductivity, Btu/(ft-°F-hr)	30
Circulating-string thermal conductivity (with insulation), Btu/(ft-°F-hr)	0.1
Circulating-fluid inlet (wellhead) temperature, °F	70
Annular fluid thermal conductivity, Btu/(ft-°F-hr)	0.3
Cement thermal conductivity, Btu/(ft-°F-hr)	0.38
Cement diameter to 500 ft, in.	30
Cement diameter from 500 ft to bottom of hole, in.	24

Table 12.6—Well, fluid, and transport property data. OD = outer diameter; ID = inner diameter.

12.4.6 Combating Wellbore Solids Summary. This section presented proactive approaches to mitigating paraffin and asphaltene deposition in production strings. The first approach involves fluid circulation, leading to alteration of the *p*/*T* trace of the produced fluid to avoid intersecting the solid envelope. Specifically, mitigation of paraffins in deepwater situations was attempted. As exploration of deepwater prospects matures, flow assurance becomes the cornerstone to their development. For instance, seafloor processing of all fluid streams is being actively investigated. As the results of this study show, ever-increasing riser length will pose considerable challenges to conventional production systems. Electrical heating of flowlines and riser is another option that is factored in while designing flow assurance. Nonetheless, models presented here may be used as the starting point for designing conventional as well as deepwater production strings.

For remediation of asphaltenes, practical solutions involve direct solvent injection into the production string when the reservoir fluid is in an unfavorable state relative to

the AFE. Computational results shed light on the temperature profiles of the injection and production fluids. The model also allows one to adjust production rate, thereby permitting optimization of the solvent injection rate in relation to the AFE. Both approaches are conceptual and, therefore, need field verification. Highlights of this section are given here:

- Flowing temperature profile of a producing fluid may be altered by circulating a fluid in the annulus. When the altered temperature profile avoids intersecting the equilibrium solid envelope, deposition of solids is minimized. Low circulation rates are efficient for heat removal while mitigating asphaltene deposition.
- Intermittent or continuous injection of chemicals, such as deasphalted oil, may provide the desired result when alteration of the fluid temperature profile becomes infeasible.
- High-rate production coupled with fluid circulation and/or tubing insulation appears attractive for controlling wax deposition.

12.4.7 Integrated Methods for Flow Assurance. This section attempts to encapsulate the elements discussed above for deliverability of hydrocarbons to surface by considering reservoir, wellbore, and surface network for a given project. To that end, two field examples demonstrate the importance of integrated methods for assessing risks of flow impediments. The first example deals with a holistic approach to handling various aspects of flow assurance for a number of gas/condensate reservoirs. The second example combines the steady-state fluid flow and heat-transfer characteristics along with asphaltene thermodynamic considerations, leading to assessments of risks involved in commingling gas and oil reservoirs in a deepwater setting.

***Example 1: Coupled Wellbore/Reservoir/Surface Network Modeling*.** Previous chapters have addressed various aspects of fluid flow and the associated heat transfer in wellbores and flowlines transporting hydrocarbons from reservoirs to the surface facility. This case study underscores various flow assurance and the attendant elements with a holistic modeling approach involving flow from reservoirs to the sales meter.

This study entails production from a number of gas/condensate reservoirs. Specifically, probabilistic production forecasting with a compositional coupled wellbore/reservoir/surface (CWRS) network model was sought for nine reservoirs involved in delivering gas supply to a liquefied natural gas plant in Nigeria. Our main objective was to use an economic indicator to select optimal design of two main pipelines, each transporting 200 and 300 MMscf/D from the two production platforms, located 15 and 5 km, respectively, from the processing platform. Kabir et al. (2007) reports details of this study.

Because of the complex coupling of the multiple reservoirs, hydraulics in the well

and network models, economics, and uncertainty, we felt that a physical model was required to investigate the overall project uncertainty. One key focus was on the selection of gathering-system pipeline diameters because we presupposed that the selection could have a large impact on the project through deliverability. Specifically, the project requirement dictated that the 5-km F-flowline delivers at 300 MMscf/D and the 15-km O-flowline delivers 200 MMscf/D for a total feed of 500 MMscf/D to a liquefied natural gas plant. Of course, the attendant condensate with yields ranging from 45 to 135 STB/MMscf, drawn from nine reservoirs, added complexity to the design. **Fig. 12.45** schematically shows the reservoirs and wellbores in the material balance, wellbore, and network model.

There are nine “tank” material balance models feeding the network. Each tank had uncertainty distributions for the original gas-in-place and condensate/gas ratio provided by the subsurface team. The well capital and operating costs were also uncertain. With nine reservoirs coupled in the network flow model, there are complex relationships between the production and net present value (NPV) and the subsurface and surface uncertainties.

As shown in **Fig. 12.46,** the CWRS network model is integrated with a detailed economics spreadsheet model. The integrated framework software is executed iteratively with a sampling of values of the uncertainty parameters and is described elsewhere (Cullick et al. 2004). Multiple, dynamic iterations can be made by sampling algorithms, including Monte Carlo (MC) or Latin hypercube (LH) sampling. In this evaluation, we sought to optimize the pipe diameter of both the F- and O-flowlines, subject to an economic parameter, such as the differential discounted profitability index (DPI). The DPI is simply the ratio of net present value (NPV) to discounted capital investment. Each candidate pipe diameter varied from 16 to 22 in. in increments of 2 in.

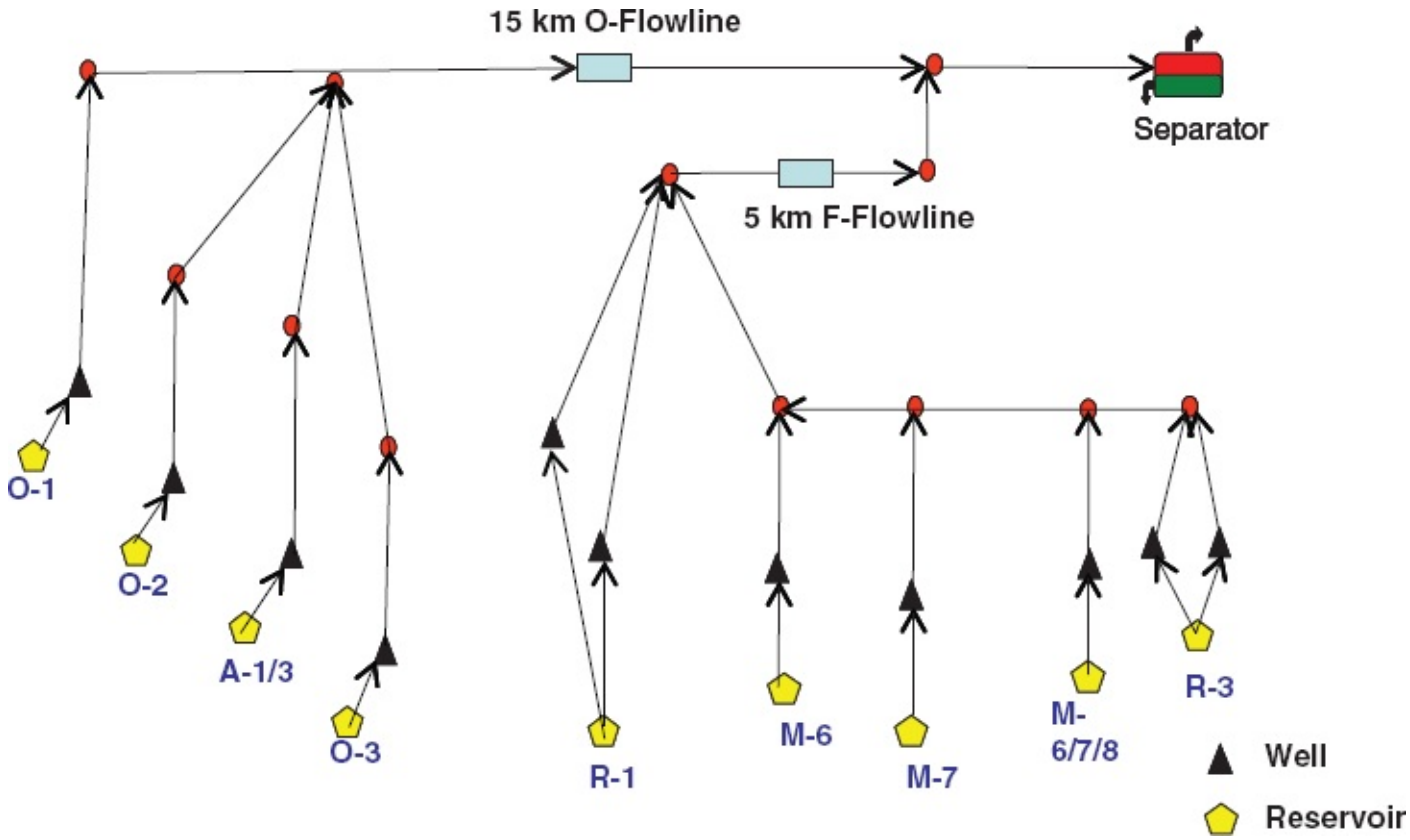

Fig. 12.45—Schematic of a CWRS model for the nine-reservoir flow problem.

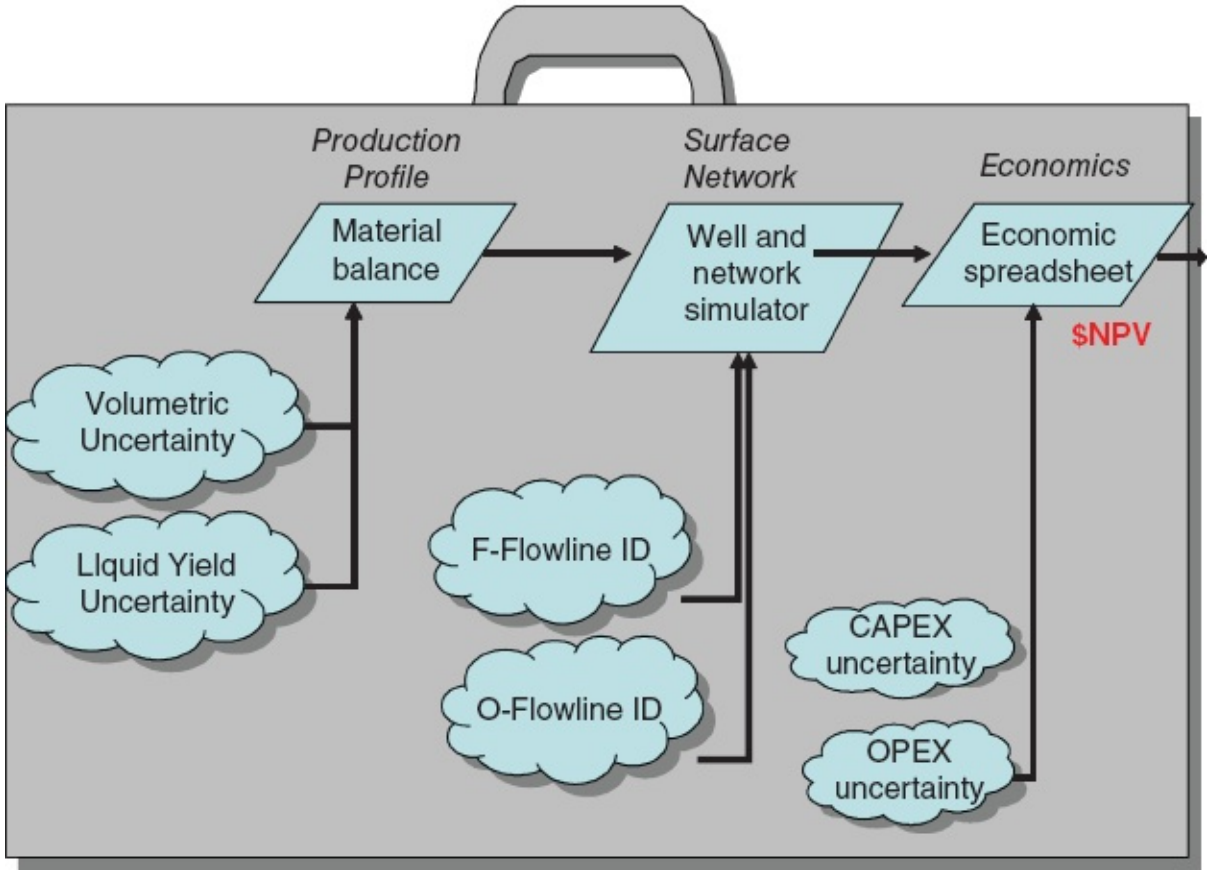

Fig. 12.46—Schematic showing various uncertainty elements modeled for the flowline scenario evaluation.

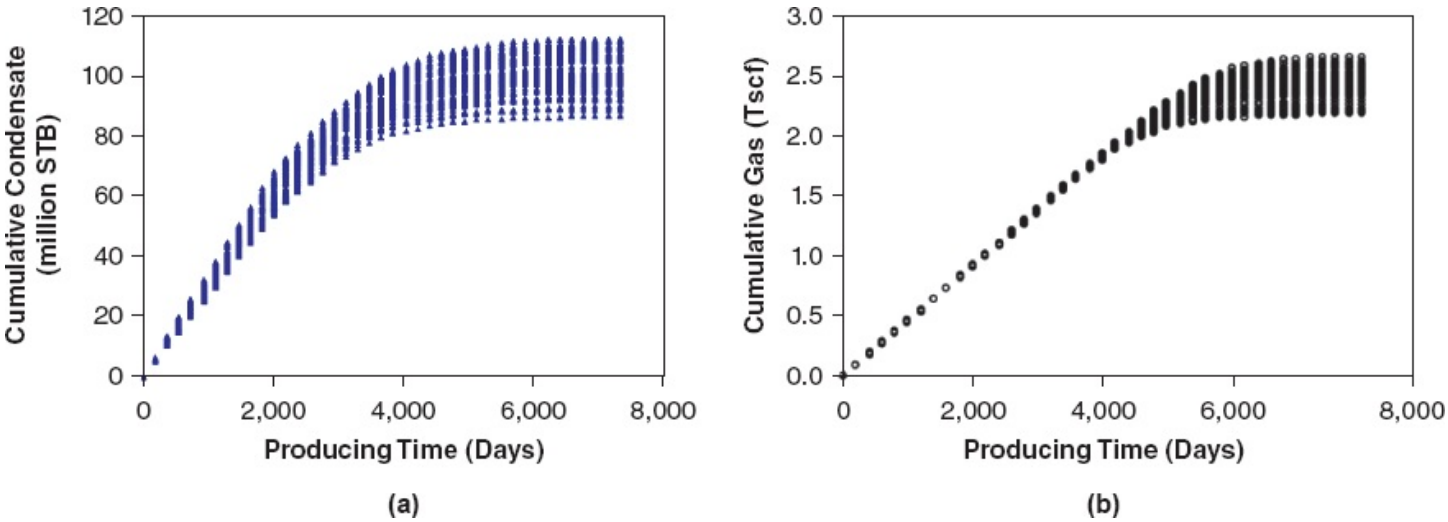

Fig. 12.47—Uncertainty spread in cumulative condensate (a) and gas (b) production (after Kabir et al. 2007).

Our analysis, not reported here, showed that DPI or its difference with a base model is a much more discriminating tool than the NPV. That is because the cost of a flowline of different dimensions in this approximately USD 2 billion project is relatively small. Note that we compared both DPI and NPV or their differences with a base model. We found that the DPI was more discriminating because it tended to give less variation within each distribution and more variation between the different distributions for each value of I_D, the global index representing both pipe diameters.

Condensate yield and in-place gas volume constituted the two subsurface uncertainties, while CAPEX (capital expenditures) and OPEX (operating expenditures) made up the economic uncertainties. **Fig. 12.47** shows how uncertainties in the two subsurface variables manifest themselves. As Fig. 12.47a shows, uncertainty in liquid yield shows a range of condensate production from the project's very early life, and the spread grows with the project's maturity. In contrast, Fig. 12.47b shows that the gas can be delivered for 4,000 days without the uncertainty of the original gas in place affecting the rate decline. This finding suggests that while the gas deliverability is assured for project's success, collection and analysis of reservoir fluids can only narrow the uncertainty range with respect to liquids, which has a profound impact on project economics.

Probing Corrosion and Erosion Issues. This segment of the study investigated the impact of uncertainty in input variables on the production forecast for systems consisting of multiple gas/condensate reservoirs, honoring wellbore and CO_2 production constraints. Production complexity arises because of the interactions through a common flowline system. The CWRS model facilitated investigation of uncertainty for the fully coupled system under multiple gathering pipeline scenarios.

In this study, we focused on discerning pipe diameter, given the uncertainty in subsurface and economic variables. Separate studies on corrosion showed that the

flowlines will last approximately 30 years with wet gas (vapor of condensation only) and CO_2 concentration not exceeding 4.5% at inlet fluid temperature of 198°F. To meet the CO_2 production constraint of 2.5% in the total gas stream, we invoked an optimizer in the network simulator to facilitate blending of streams with various CO_2 content. In general, the CO_2 content in reservoir fluids exhibited linear increase with formation depth. This CO_2 specification met the surface facility's requirements for the scrubbing unit.

Flow assurance from the erosional-velocity standpoint was explored before arriving at the minimum diameter of 16 in. **Fig. 12.48** depicts that both flowlines meet the American Petroleum Institute 14E requirements. Erosion implies removal of material from a solid surface by fluids (and solids) because of mechanical forces. Generally, a correlation factor, called *C*-factor, below 100 is considered safe for continuous operation without any solids production. However, Salama (2000) showed that the *C* value can be as high as 400 for solid-free, noncorrosive fluids and 300 for solid-free, corrosive fluids. Note that sand production is not expected to occur from the reservoirs in question because of burial depths exceeding 10,000 ft. One potential issue with large-diameter flowlines is the frequency of pigging owing to accumulation of liquids in the low sections of an undulating terrain. In other words, when larger-than-required pipe diameter is used in the flowlines, increase in OPEX may occur; however, this aspect remained unexplored in this study.

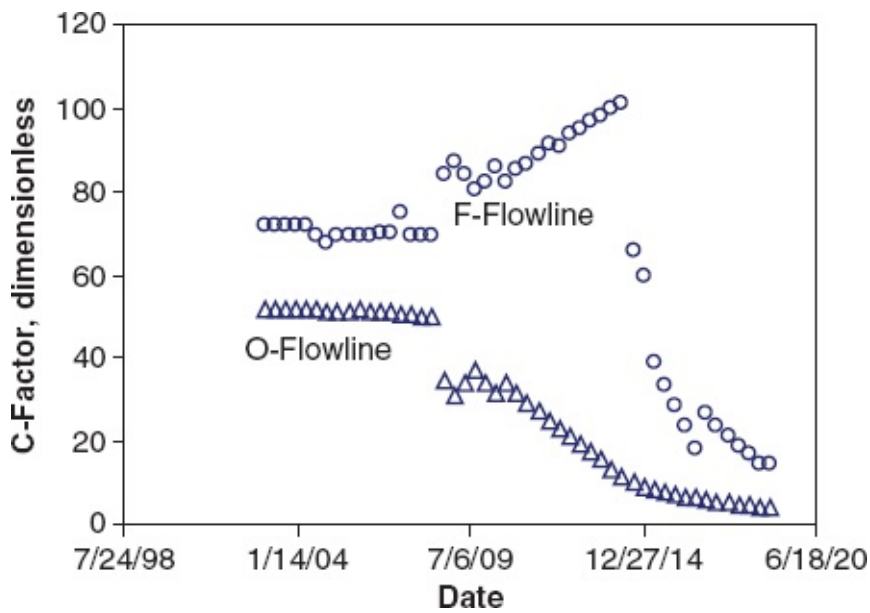

Fig. 12.48—Changes in C-factor with time for 16-in.-ID pipe.

Example 2: Impact of Flow Assurance in the Development of a Deepwater Prospect. The size of the range of the potential reserves recovery drives initial CAPEX, and reservoir appraisal is limited in marginal fields. Reducing the number of flowlines by commingling streams from several wells or manifolds can decrease capital and operational costs, but may pose problems for incompatible fluid streams.

In other words, the mixture of two reservoir fluids can potentially precipitate asphaltene at their commingling point. This problem may occur when fluids of very different densities are mixed. For example, when a condensate is mixed with black oil, problems may result. With the decrease of density of the entire liquid phase, the crude oil solubility parameter decreases and the asphaltenes aggregate. As the field production matures, oil crossflow from the higher-pressure oil zone into the lower-pressure gas reservoir may lead to precipitation and plugging of the gas sand.

Gonzalez et al. (2007) presented a case study describing the impact of flow assurance considerations in a deepwater Gulf of Mexico development project. The paper was based on experimental measurements of asphaltene and wax precipitation of a hydrocarbon fluid when contacted with gas condensate from another zone. The evaluation was performed using multiphase flow behavior in an integrated asset modeling that provides system deliverability predictions through the project's lifetime, coupled with asphaltene and wax thermodynamic models. The perturbed-chain statistical associating fluid theory (PC-SAFT) equation-of-state model (Chapman et al. 1990) is the thermodynamic tool used to predict asphaltene precipitation. Wax deposition is predicted using a solid solution model as implemented in a commercial software package.

***Combined Fluid-Flow/Heat-Transfer Modeling*.** In this field example, separated oil and gas/condensate reservoirs were located at approximately 22,700 and 21,900 ft of depth and had initial reservoir pressures of 16,990 and 15,740 psia, respectively. The option of downhole commingling of oil and condensates with a downhole valve was considered in the field development plan. **Fig. 12.49** illustrates the system's CWRS model.

The study showed that the oil reservoir is expected to deplete 6,000 psia during the first 5 years of production. At the point of commingling, pressure can be maintained approximately constant by using a one-way downhole valve, which controls the amount of produced gas. At the same time, an in-situ downhole gas lift operation can be achieved to enhance oil deliverability.

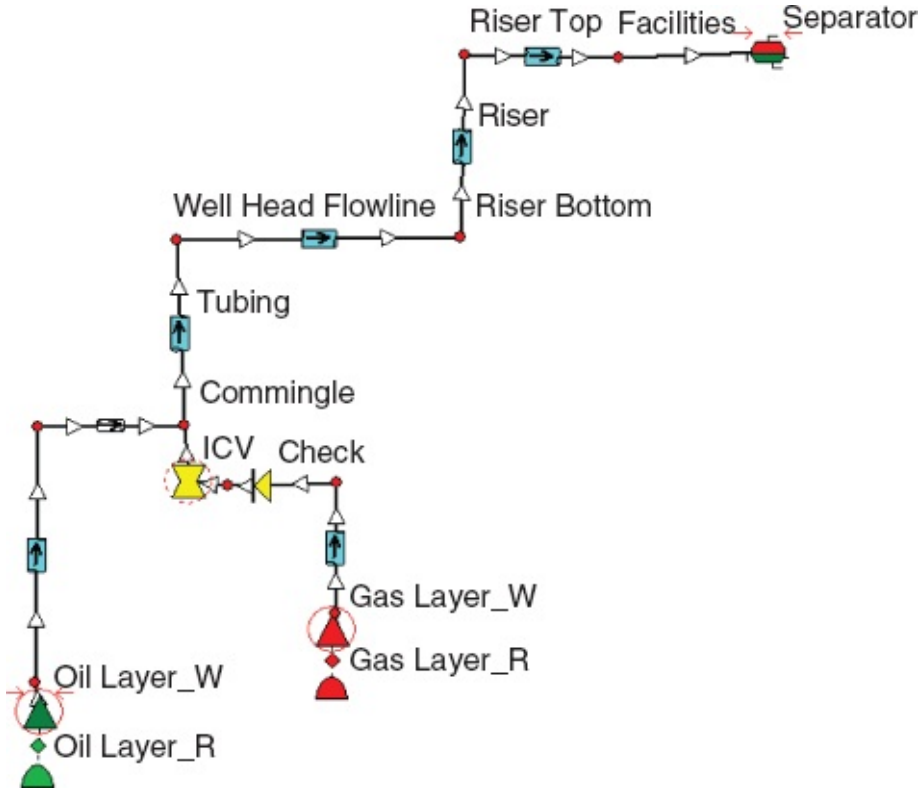

Fig. 12.49—CWRS model schematic (after Gonzalez et al. 2007).

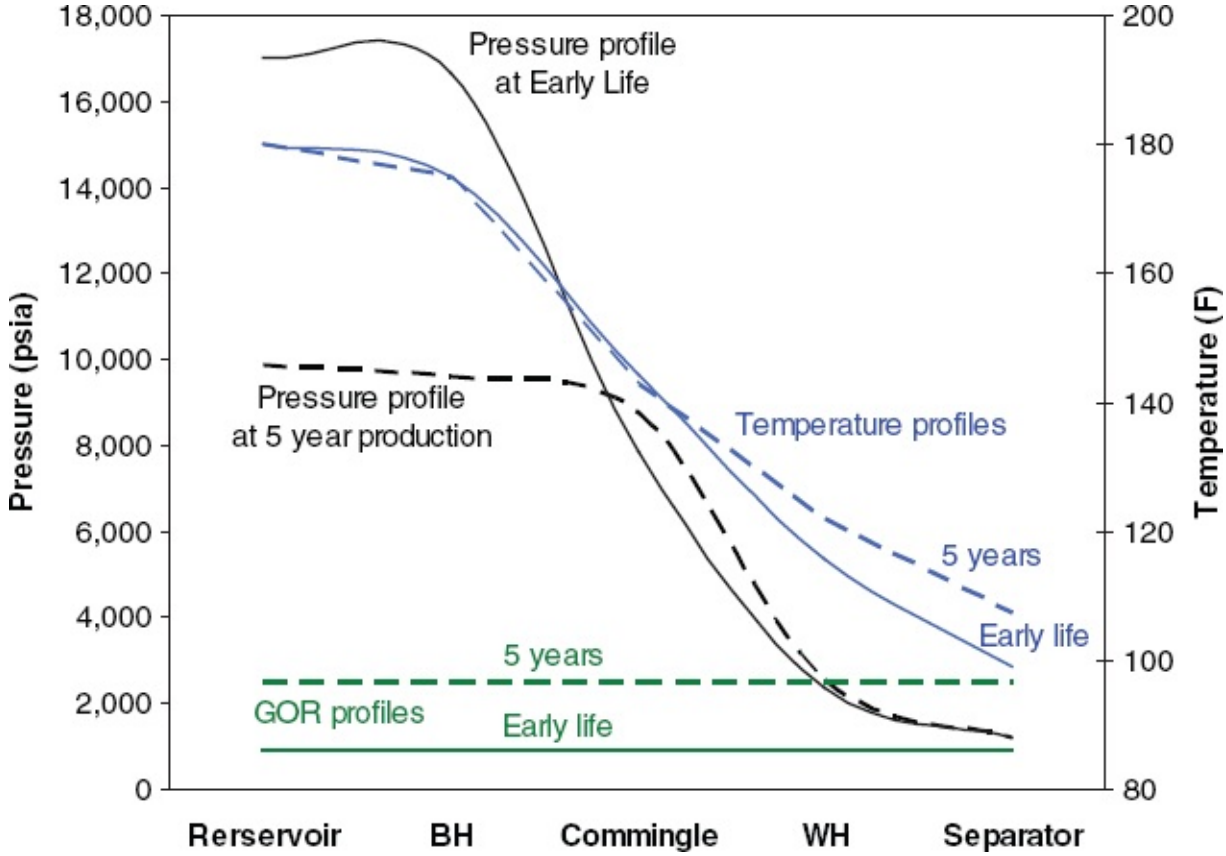

Fig. 12.50—Predicted pressure, temperature, and GOR profiles: early life (continuous lines) and after 5 years of production (dash lines) (after Gonzalez et al. 2007).

Significant temperature changes were not expected during the same production period. Note that GOR acted as an indicator of compositional changes. As shown in **Fig. 12.50,** GOR at the point of commingling increased with the maturity of field production.

Another critical flow assurance variable is the downhole internal control valve (ICV) design. As determined by the CWRS, the ICV needs to operate at a 0.15-in. opening to control the gas flow for most of the life of the project. The pressure losses reached up to 7,000 psig across this ICV early in the life of the project. The J-T effect explains the change in temperature of the commingled fluid as a result of gas expansion across the ICV. The CWRS predicted that the temperature drop is approximately 26°F early in the life of the project and increased to 30°F after 5 years. **Fig. 12.51** shows the evolving nature of ICV pressure and temperature profiles.

Measurements to evaluate asphaltene and wax precipitation include PVT analysis, saturates/aromatics/resins/asphaltenes (SARA) analysis, wax content, wax-appearance temperature (WAT), high-temperature gas chromatography, high-pressure/high-temperature onset determination, and gas titration using near-infrared technique. The example fluid was a highly oil-based-mud (OBM) contaminated reservoir fluid of 36 °API gravity with a characteristic GOR of 852 scf/STB with a bubblepoint of 3,427 psi at 184°F. The commingling was simulated in the laboratory by mixing the fluid with a synthetic gas with a composition similar to that of the actual gas/condensate fluid located in the upper layer. The onset of asphaltene precipitation for the reservoir black-oil fluid (oil layer) was measured by pressure depletion starting from 15,000 psi and at a reservoir temperature of 184°F using fixed-wavelength near-infrared particle-size analysis and high-pressure microscopy technique, as discussed

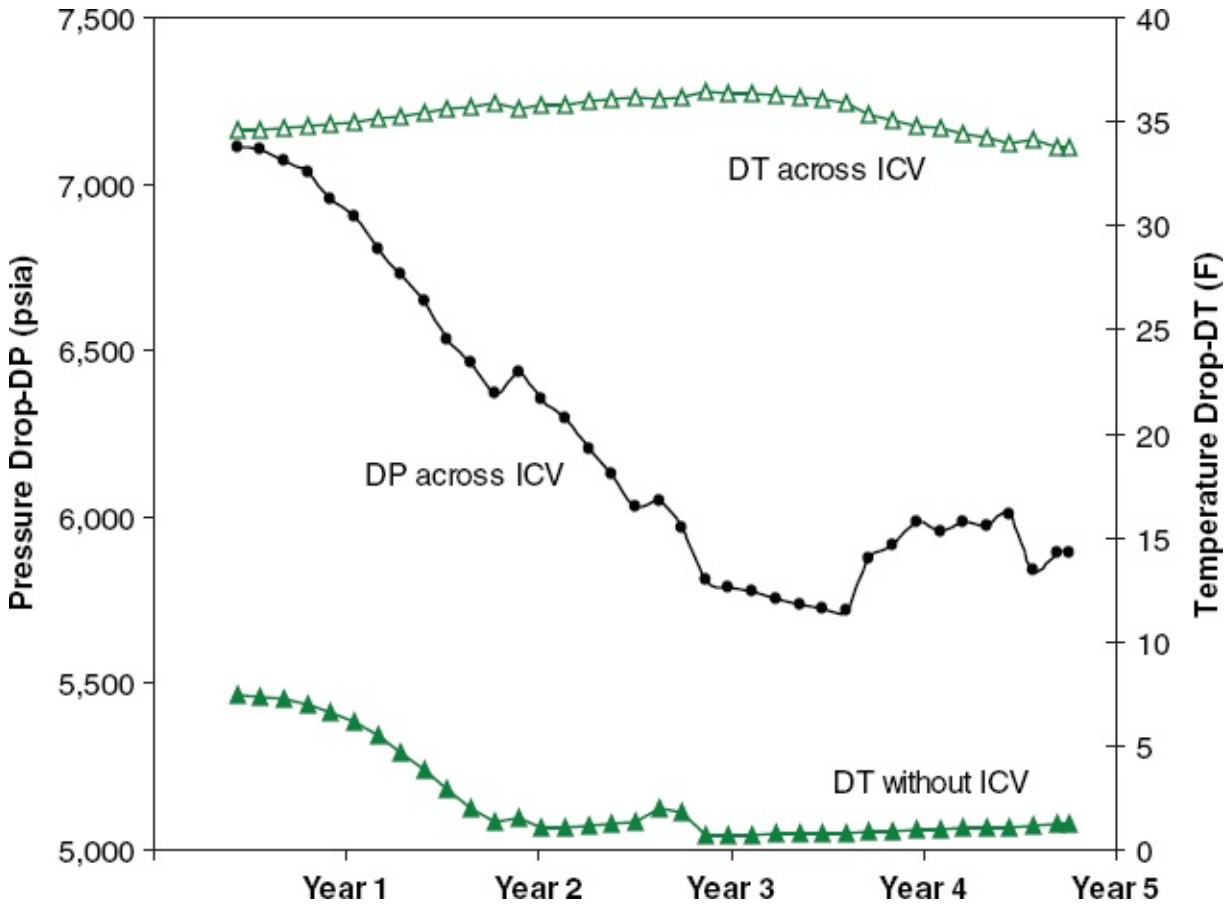

Fig. 12.51—Pressure- and temperature-drop calculation across the downhole valve controlling the gas zone rates using CWRS (after Gonzalez et al. 2007).

by Jamaluddin et al. (2002).

The PC-SAFT equation-of-state compositional model predicted the asphaltene precipitation tendencies during production. The detailed modeling principles and assumptions can be found in Ting et al. (2003) and Gonzalez et al. (2005). A brief step-by-step calculation protocol is given below.

- Identification of the thermodynamic asphaltene phase boundaries using the PC-SAFT precipitation model for the reservoir oil.
- Calculation of the fluid properties and phase behavior after mathematical OBM decontamination.
- Evaluation of the asphaltene stability regions resulting from reservoir fluid contact with gas/condensate at different concentrations.

The equation-of-state parameters are calculated for each of the seven components and pseudocomponents of the OBM-contaminated sample using SARA, GOR, PVT data, and compositional information. The reservoir fluid is contaminated with 20 wt% (live basis) of OBM that has carbon number peaks from C_{10} to C_{21}. The asphaltene parameters are tuned to meet the onset of asphaltene precipitation of 7,000 ± 100 psig measured by depressurization at 184°F.

Fig. 12.52, showing the simulation results, indicated that the black-oil reservoir fluid presents a high tendency to precipitate asphaltene during primary depletion. In other words, asphaltenes will become unstable and start to precipitate at a pressure of 10,700 psia at the reservoir temperature of 184°F. Further reduction in temperature will aggravate the precipitation condition. Asphaltene precipitation in commingled fluids is dependent on compositional changes that arise from the relative proportions of the mixing fluids. Asphaltene might separate from the solution by titration of a gas/condensate fluid into a relatively unstable crude oil. An increase in the precipitation onset occurred as gas and condensate commingled to the system. The mixture GOR increased rapidly from 1,133 scf/STB as the gas/condensate titrated with the crude oil.

Wax phase boundaries were modeled with a solid-solution model, as outlined by Zuo et at. (2001). Wax modeling included C_{30}+ composition and normal paraffin distribution from high-temperature gas chromatography. The simulation results indicated the WAT for stock-tank oil was 71°F and decreased with increasing pressure as a result of gas solubility. Above the bubblepoint, WAT increased with increasing pressure caused by the liquid compressibility effect.

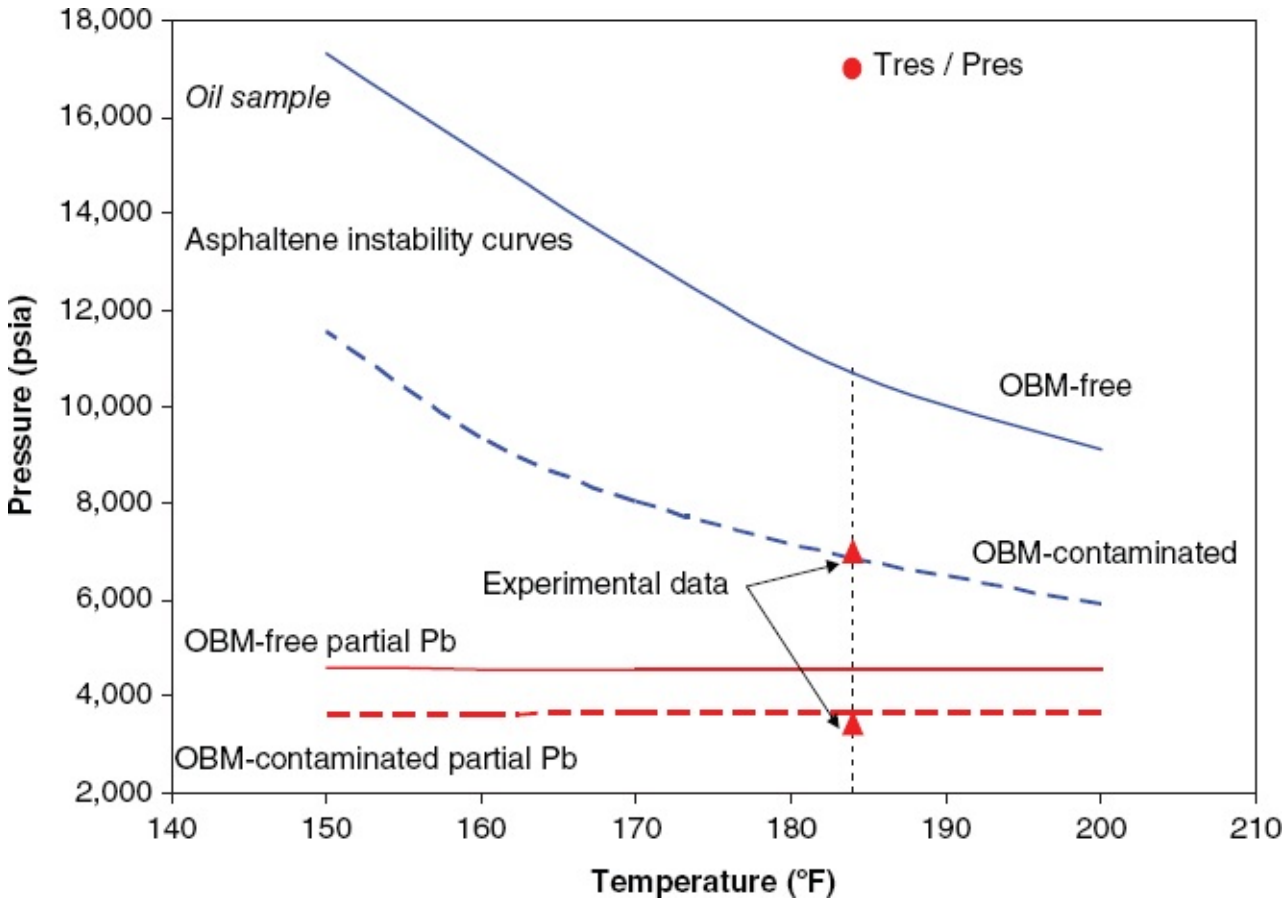

Fig. 12.52—Asphaltene precipitation behavior of the contaminated reservoir fluid (after Gonzalez et al. 2007).

The lessons learned by combining a CWRS model with an asphaltene and a wax

thermodynamic model enable realistic flow assurance predictions. That is primarily because the coupled modeling provides a vehicle for estimating solid formation resulting from variations in pressure, temperature, and composition during a project's life. Experimental and simulation results indicated that the lower black-oil layer is unstable with respect to solid formation. Asphaltenes are expected to precipitate during primary depletion of this layer; therefore, installation of an asphaltene inhibitor line is recommended. The addition of gas and condensate at any ratio is expected to severely aggravate the asphaltene precipitation condition. In addition, commingled production from both zones has a high potential for crossflow, which can induce formation plugging.

The prudent approach is to plan this field's development on the basis of production that is sequential/intermittent. If commingled production is inevitable, the installation of an ICV is mandatory from the viewpoints of flow assurance and reservoir management. That way one can control the amount of gas that mixes with the oil, thereby mitigating the asphaltene precipitation tendency and improving the oil lift performance. The mechanical design will have to withstand a high pressure drop early in the project's life. Wax precipitation can be avoided if the temperature along the system remains above 105°F. Adequate insulation can ensure arrival temperatures above WAT for all production conditions during the field's producing life.

Summary

This chapter treated applications of four elements of production operations as practiced in the field. Our main objective was to show how the principles learned earlier can be used to solve everyday field problems. That is why complete treatment of any element was not attempted.

As expected, many problems are intertwined. For instance, a transient fluid and heat flow simulator, discussed in Chapter 9, became useful in dealing with seamless systems analysis. Similarly, principles of heat flow, discussed in Chapter 6, were instrumental in developing working models for fluid temperatures in gas lift operation, in geothermal production and steam injection, and in combating the solids problem. We also demonstrated that the drift-flux approach, used successfully in modeling gas/oil flow, is equally applicable to flow of steam and water in both upward and downward directions. Finally, we showed two field examples illuminating flow assurance issues being handled with a coupled wellbore, reservoir, and surface network model.

Nomenclature

a_t = linear coefficient in the Forchheimer deliverability equation, STB/D-psi

A = cross-sectional area for flow, ft^2

b = nonlinear coefficient in deliverability equation, $(STB/D)^2$-psi

B = constant defined by Eq. 12.8, ft

B' = constant (= B_t/w_a) used in Eq. 12.14, ft

B'' = constant defined by Eq. 12.15, ft

C_a = annular fluid heat capacity, Btu/(lbm-°F)

c_e = formation heat capacity, Btu/(lbm-°F)

c_f, c_{flt} = specific heat of tubing fluid, Btu/(lbm-°F)

C_{ga} = specific heat of annular gas, Btu/(lbm-°F)

C_p = specific heat of fluid, Btu/(lbm-°F)

C_{pa} = specific heat of annular gas, Btu/(lbm-°F)

C_{pt} = specific heat of tubing fluid, Btu/(lbm-°F)

C_w = circulating-fluid heat capacity, Btu/(lbm-°F)

C = coefficient in backpressure deliverability equation, STB/D-psi

C_c = contraction coefficient used in Eq. 12.34, dimensionless

C_J = Joule-Thomson coefficient, °F/psi

d = diameter, ft

D = non-Darcy flow coefficient, STB/D

D'' = constant defined by Eq. 12.16, °F

D_a = constant defined by Eq. 12.11, Btu/lbm-ft

D_t = constant analogous to D_a for tubing fluid, Btu/(lbm-ft)

f = friction factor, dimensionless

f_L = liquid holdup, dimensionless

g = gravitational acceleration, ft/sec^2

g_c = conversion factor, dimensionless

g_G = geothermal gradient, °F/ft

G = mass flux (mass flow rate/unit area), lbm/(hr-ft^2)

h = formation thickness, ft

h_a = forced convection heat-transfer coefficient, Btu/(°F-hr-ft)

h_c = natural convection heat-transfer coefficient, Btu/(°F-hr-ft)

H, H_f = fluid enthalpy, Btu/lbm

J = conversion factor, dimensionless

J_p = productivity index, STB/D-psi

k = formation permeability, md

k_c = casing material conductivity, Btu/(hr-ft-°F)

k_{cm} = cement conductivity, Btu/(hr-ft-°F)

K_e = earth or formation thermal conductivity, Btu/(hr-ft-°F)

L_e = equivalent length factor, dimensionless

L_R = relaxation length parameter, ft^{-1}

m^* = kh/(141^), md-ft/cp

p = pressure, psi

p^* = Horner's extrapolated pressure, psia

p_D = dimensionless pressure (=Δp/141.2qBμ)

p_i = initial reservoir pressure, psia

P_{ws} = shut-in bottomhole pressure, psia

p_{wf} = flowing bottomhole or wellhead pressure, psia

q, q_{wh} = oil rate at wellhead, STB/D

q_c = liquid circulation rate, STB/D

q_m = maximum or open flow potential, STB/D

q_{sf} = sandface oil rate, STB/D

q_t = total (gas + liquid) volumetric fluid flow rate, STB/D

Q = heat flow from formation to annular fluid per unit well length, Btu/(hr-ft)

Q_{ta} = heat flow from annular fluid to tubing fluid per unit well length, Btu/(hr-ft)

r_c, r_w = wellbore radius, ft

r_{co} = outside casing radius, in.

r_{jo} = outside injection tubular radius, in.

r_t = tubing radius, ft

r_{ti} = inside tubing radius, in.

r_{to} = outside tubing radius, in.

R_a = area ratio (= A_2/A_1), dimensionless

R_t = formation resistivity, ohm.m

s = damaged or static skin, dimensionless

$s¢$ = total skin (= s + Dq), dimensionless

t = producing time, hours

t_D = dimensionless production or injection time (= $2.64 \times 10^{-4} kt/øμc_t r_w^2$)

t_e = effective superposition time, hours

t_p = production time, hours

T = temperature, °F

T_a = annular fluid temperature, °F

T_{ai} = annular fluid temperature at surface, °F

T_D = dimensionless temperature [= $2\pi k_e(T_{wb} - T_{ei})/q_F$]

T_{ei} = formation static temperature at bottom of hole, °F

T_{es} = formation static temperature at surface, °F

T_f = tubing fluid temperature, °F

T_t = tubing fluid temperature, °F

T_{tp} = particular solution of tubing fluid temperature, °F

T_w = circulating water or fluid temperature, °F

= wellbore/formation interface temperature, °F

T_{wb}

U = overall-heat-transfer coefficient, Btu/(hr-ft^2-°F)

U_1 = overall-heat-transfer coefficient for tubing fluid, Btu/(hr-°F-ft)

U_{tc} = overall-heat-transfer coefficient for tubular in seawater, Btu/(hr-°F-ft)

U_{to} = overall-heat-transfer coefficient for annular fluid, Btu/(hr-°F-ft)

v, v_f = fluid velocity, ft/sec

W, W_f = mass rate of tubing fluid, lbm/hr

w_w = mass rate of circulating fluid, lbm/hr

x = mass fraction of gas in the tubing fluid mixture, dimensionless

X = Lockhart/Martinelli parameter, dimensionless

z = vertical well depth, ft

Z = gas-law deviation factor, dimensionless

a = constant used in Eq. 12.17, defined by Eq. 12-B-10, °F

a = well inclination angle from horizontal, degrees

α_h = heat diffusivity of formation (= $k_e/c_e\rho_e$), ft^2/hr

β = constant used in Eq. 12.18, defined by Eq. 12-B-11, °F

Δp = pressure drop, psi

Δq = rate change, STB/D

Δ_t = shut-in time, hours

λ_1, λ_2 = constants used in Eq. 12.18, defined by Eqs. 12-B-4 and 12-B-5, °F

μ = oil viscosity, cp

ρ = density, lbm/ft^3

ρ_e = bulk density of earth or formation, lbm/ft^3

$\varnothing$ = porosity, fraction

ω = lumped parameters, defined by Eqs. 12-C-53 through 12-C-56

Subscripts

1 = inlet state

2 = outlet state

a = annulus

bh = bottomhole

c = casing

cem = cement

ci = casing inside

co = casing outside

e = earth

es = earth static

fit = fitting

g	=	gas
i	=	index for summation
ins	=	insulation
j	=	depth index
L	=	liquid
n	=	nth time index
t	=	tubing
ti	=	tubing inside
to	=	tubing outside
ts	=	tubing saturated
w	=	circulating string

Appendix 12-A

Derivation of Superposition Equations

Considering rate-dependent skin, we can write the generalized expression for a constant-rate test as

$$p_i - p_{wf} = m^* q\left[p_D\ (t_D)\ + s + Dq\right], \qquad (12\text{-A-1})$$

where $p_D(t_D)$ is the reservoir model, s is the static skin, and D is the rate-dependent or non-Darcy skin parameter.

For a two-rate test, one obtains the expression by applying the principle of superposition in time, which is written as

$$\begin{aligned} p_i - p_{wf2} = {} & m^* q_1\left[p_D(t_{D1}) + s + Dq_1\right] \\ & + m^*(q_2 - q_1)\left[p_D(t_{D2} - t_{D1}) + s + Dq_2\right] \end{aligned} \qquad (12\text{-A-2})$$

For the nth period in a multirate test, we can write

$$\begin{aligned} p_i - p_{wfn} = {} & m^* q_1\left[p_D(t_{D1}) + s + Dq_1\right] \\ & + m^*(q_2 - q_1)\left[p_D(t_{D2} - t_{D1}) + s + Dq_2\right] \\ & + \cdots + m^*(q_n - q_{n-1})\left[p_D(t_{Dn} - t_{Dn-1}) + s + Dq_n\right] \end{aligned}, \qquad (12\text{-A-3})$$

or

$$p_i - p_{wfn} = m^* \left\{ \sum_{i=1}^{n} (q_i - q_{i-1})\left[p_D\ (t_{Dn} - t_{Di-1}) + s + Dq_i\right] \right\}, \qquad (12\text{-A-4})$$

where $t_{D0} = 0$ and $q_0 = 0$. For a nonequilibrium initial condition, $p_i = p_{wfl}$; q_1 is the prevailing flow rate, and Dq, = |D(q1 - qi-1)|.

Assuming a constant flow rate after timestep k and a buildup that starts at timestep n + 1, we can write the expression for buildup at time t_m as

$$
\begin{aligned}
p_i - p_{wm} = m^*\{ & q_1\left[p_D(t_{Dm}) + s + Dq_1\right] + (q_2 - q_1) \\
& \times\left[p_D(t_{Dm} - t_{D1}) + s + Dq_2\right] + \cdots + (q_k - q_{k-1}) \\
& \times\left[p_D(t_{Dm} - t_{Dk-1}) + s + Dq_k\right] + \cdots + (q_{n+1} - q_n) \\
& \times\left[p_D(t_{Dm} - t_{Dn}) + s + Dq_{n+1}\right] + \cdots + (q_m - q_{m-1}) \\
& \times\left[p_D(t_{Dm} - t_{Dm-1}) + s + Dq_m\right]\} \\
= m^* & \sum_{i=1}^{k}(q_i - q_{i-1})[p_D(t_{Dm} - t_{Di-1}) + s + Dq_i] \\
+ m^* & \sum_{j=n+1}^{m}(q_j - q_{j-1})[p_D(t_{Dm} - t_{Dj-1}) + s + Dq_j]
\end{aligned}
\qquad \text{(12-A-5)}
$$

To obtain an expression for rate, Eq. 12-A-4 is rearranged to obtain

$$
q_n = q_{n-1} + \frac{p_i - p_{wn}}{m^*\left[p_D(t_{Dn} - t_{D\,n-1}) + s + Dq_n\right]} - \frac{\sum_{i=1}^{n-1}(q_i - q_{i-1})\left[p_D(t_{Dn} - t_{i-1}) + s + Dq_i\right]}{p_D(t_D - t_{n-1}) + s + Dq_n}
\qquad \text{(12-A-6)}
$$

Similarly, Eq. 12-A-5 can be rearranged to obtain the expression for afterflow rate during buildup, which is written as

$$
q_m = q_{m-1} + \frac{p_i - p_{wm}}{m^*\left[p_D(t_{Dm} - t_{D\,m-1}) + s + Dq_m\right]} - \frac{\sum_{i=1}^{k}(q_i - q_{i-1})\left[p_D(t_{Dm} - t_{Di-1}) + s + Dq_i\right]}{p_D(t_{Dm} - t_{m-1}) + s + Dq_m} - \frac{\sum_{j=n+1}^{m-1}(q_j - q_{j-1})\left[p_D(t_{Dm} - t_{Dj-1}) + s + Dq_j\right]}{p_D(t_{Dm} - t_{m-1}) + s + Dq_m}
\qquad \text{(12-A-7)}
$$

Appendix 12-B

Solution of Equation 12.14 in Gas Lift

At the wellhead, the gas injection temperature, T_{ai}, is known and forms one boundary condition for Eq. 12.14 ($T_a = T_{ai}$ when $z = 0$). The bottomhole condition takes into account the formation fluid entering the production string and mixing with the injected gas. The tubing fluid temperature at the bottom of the hole can be obtained from a simple energy balance, given by

$$T_{tbh} = \frac{w_t - w_a}{w_t} c_{pt} T_{ebh} + \frac{w_a}{w_t} c_{pa} T_{abh} \quad \text{(12-B-1)}$$

The particular solution to Eq. 12.14 is

$$T_{tp} = g_G z + T_{ew} + B'' g_G \quad \text{(12-B-2)}$$

The characteristic polynomial equation for the complementary solution becomes

$$p(\lambda) = AB'\lambda^2 - B''\lambda - 1 = 0, \quad \text{(12-B-3)}$$

with the two roots

$$\lambda_1 = -\frac{B''}{2AB'} + \frac{B''}{2AB'}\sqrt{1 + \frac{4AB'}{B''^2}} \quad \text{(12-B-4)}$$

and

$$\lambda_2 = -\frac{B''}{2AB'} - \frac{B''}{2AB'}\sqrt{1 + \frac{4AB'}{B''^2}} \quad \text{(12-B-5)}$$

The complete solution, obtained by adding the particular and the complementary solutions, is

$$T_t = \alpha e^{\lambda_1 z} + \beta e^{\lambda_2 z} + g_G z \sin\alpha + B'' g_G + T_{es} \quad \text{(12-B-6)}$$

and

$$
\begin{aligned}
T_a &= T_t - B'\frac{\mathrm{d}T_t}{\mathrm{d}z} \\
&= (1-\lambda_1 B')\alpha e^{\lambda_1 z} + (1-\lambda_2 B')\beta e^{\lambda_2 z} \\
&\quad + g_G(B''-B') + g_G z + T_{es}
\end{aligned}
\qquad \text{(12-B-7)}
$$

To obtain constants α and β, we apply the first boundary condition to Eq. 12-B-7.

$$
\begin{aligned}
T_a &= T_{ai} = (1-\lambda_1 B')\alpha \\
&\quad + (1-\lambda_2 B')\beta + g_G(B''-B') + T_{es}
\end{aligned}
\qquad \text{(12-B-8)}
$$

By applying the second boundary condition and using T_{tbh} from Eq. 12-B-1 in Eq. 12-B-6, we obtain

$$
T_{tbh} = \alpha e^{\lambda_1 L} + \beta e^{\lambda_2 L} + g_G L + B'' g_G + T_{es} \qquad \text{(12-B-9)}
$$

Therefore,

$$
\alpha = \frac{T_{tbh} - T_{es} - \beta e^{\lambda_2 L} - g_G L - B'' g_G}{e^{\lambda_1 L}} \qquad \text{(12-B-10)}
$$

By substituting this expression for α into Eq. 12-B-8 and rearranging, we obtain

$$
\begin{aligned}
\beta &= \frac{(T_{ai} - T_{ew})e^{\lambda_1 L} + (1-\lambda_1 B')(g_G L \sin\theta + B'' g_G + T_{es} - T_{tbh})}{e^{\lambda_1 L}(1-\lambda_2 B') - e^{\lambda_2 L}(1-\lambda_1 B')} \\
&\quad - \frac{g_G e^{\lambda_1 L}(B''-B')}{e^{\lambda_1 L}(1-\lambda_2 B') - e^{\lambda_2 L}(1-\lambda_1 B')}
\end{aligned}
\qquad \text{(12-B-11)}
$$

Appendix 12-C

Solids Deposition Models

12-C.1 Development of the Fluid Circulation Model. ***Tubular Fluid*.** During steady-state flow, tubing fluid loses energy to the surrounding annular fluid, which causes a decrease in the tubing fluid's enthalpy, kinetic energy, and/or potential energy. Therefore, we can write

$$Q_1 = w_f\left(\frac{dH_f}{dz} + v_f\frac{dv_f}{dz} + g\sin\alpha\right), \quad \text{(12-C-1)}$$

where w_f is the fluid mass flow rate, H_f is fluid enthalpy, v_f is fluid velocity, and α is the inclination angle of the wellbore with respect to horizontal. Enthalpy can be expressed as a function of pressure and temperature by

$$\frac{dH_f}{dz} = c_f\frac{dT_f}{dz} - C_J c_f\frac{dp}{dz}, \quad \text{(12-C-2)}$$

where c_f is the heat capacity at constant pressure and C_j [= $(-1/c_f)(\partial H/\partial p)_T$] is the J-T coefficient of the fluid in the producing string. Combining Eqs. 12-C-1 and 12-C-2, we have

$$Q_1 = w_f\left(c_f\frac{dT_f}{dz} - C_J c_f\frac{dp}{dz} + v_f\frac{dv_f}{dz} + g\sin\alpha\right) \quad \text{(12-C-3)}$$

The heat loss to (or gain from) the annulus per unit length of tubing Q_1 can be expressed in terms of a heat-transfer coefficient U_1 and the temperature difference, $T_f - T_a$ as

$$Q_1 = U_1(2\pi r_{to})(T_f - T_a) \quad \text{(12-C-4)}$$

The heat-transfer coefficient U_1 depends on the convective heat-transfer coefficient h_{to} of the tubing fluid and the thermal conductivity of the tubing wall, given by

$$\frac{1}{U_1} = \frac{r_{to}\ln(r_{to}/r_{ti})}{k_t} + \frac{r_{to}}{r_{ti}h_{to}} + \frac{1}{h_a} \quad \text{(12-C-5)}$$

We define relaxation parameter L_{Rl} in terms of U_1 as

$$L_{R1} = U_1\frac{2\pi r_{to}}{w_f c_f} \quad \text{(12-C-6)}$$

By combining Eq. 12-C-6 with Eq. 12-C-3 and simplifying, we obtain an expression for the tubing and annular fluid temperatures, written as

$$\frac{dT_f}{dz} = L_{R1}\left(T_f - T_a\right) + \phi_f, \quad \text{(12-C-7)}$$

where

$$\phi_f = C_J \frac{dp}{dz} - \frac{v}{c_f}\frac{dv}{dz} - \frac{g\sin\alpha}{c_f} \quad \text{(12-C-8)}$$

For single-phase liquid flow, the J-T coefficient is negligible, as is the change in kinetic energy. Therefore, the parameter ϕ_f for liquid flow is equal to $g \sin\alpha/c_f$.

Circulating Fluid. Differential equations governing the temperatures of the fluid (water) in the circulating string, T_w, are derived in a manner similar to the derivation shown for the tubing fluid. Heat transferred from the annular fluid to the circulating fluid, Q_2, is given by expressions similar to Eqs. 12-C-3 and 12-C-4. Thus, temperature of water in the circulating string flowing in the downward direction is governed by

$$\frac{dT_w}{dz} = (2\pi r_{jo} U_2)(T_a - T_w)/(w_w c_w) + \phi_w, \quad \text{(12-C-9)}$$

where

$$\frac{1}{U_2} = \frac{r_{jo}\ln(r_{jo}/r_{ji})}{k_j} + \frac{r_{jo}}{r_{ji}h_{jo}} + \frac{1}{h_a} \quad \text{(12-C-10)}$$

Using the relaxation parameter, $L_{R2} = (U_2)(2\pi r_{jo})/(w_w c_w)$, we obtain

$$\frac{dT_w}{dz} = L_{R2}(T_a - T_w) + \phi_w \quad \text{(12-C-11)}$$

In Eq. 12-C-11, the parameters ϕ_w, and L_{R2} are given by

$$\phi_w = C_J \frac{dp}{dz} - \frac{v}{c_w}\frac{dv}{dz} - \frac{g\sin\alpha}{c_w} \quad \text{(12-C-12)}$$

and

$$L_{R2} = \frac{2\pi r_{to}}{w_w c_w\left[\frac{r_{jo}\ln(r_{jo}/r_{ji})}{k_j} + \frac{r_{jo}}{r_{ji}h_{jo}} + \frac{1}{h_a}\right]} \quad \text{(12-C-13)}$$

Annular Fluid. The fluid in the annulus moves upward and exchanges energy with the fluid flowing inside the production tubing and that in the circulating string. In

addition, the annular fluid exchanges energy with the surrounding formation. We can write the energy balance equation as

$$Q_1 - Q_2 - Q_3 = -w_a\left(\frac{\mathrm{d}H_a}{\mathrm{d}z} + v_a\frac{\mathrm{d}v_a}{\mathrm{d}z} + g\sin\alpha\right) \quad \text{(12-C-14)}$$

Following the treatment presented in Chapter 6, we can write the expression for heat lost by the annular fluid to the formation, per unit length of the well, as

$$Q_3 = c_a w_a L_{R3}\left(T_a - T_{ei}\right), \quad \text{(12-C-15)}$$

where L_{R3} is given by

$$L_{R3} = \frac{2\pi r_{to} U_{to} k_e}{c_a w_a\left(k_e + r_{to} U_{to} T_D\right)} \quad \text{(12-C-16)}$$

In Eq. 12-C-16, T_D is the dimensionless temperature distribution function and is discussed by Hasan and Kabir (1994a) and in Chapter 6. The overall-heat-transfer coefficient U_{to} used in Eq. 12-C-16 is given by

$$\frac{1}{U_{to}} = \frac{r_{to}\ln(r_{co}/r_{ci})}{k_c} + \frac{r_{to}\ln(r_{cmo}/r_{cmi})}{k_{cm}} + \frac{r_{to}}{r_{ci}h_a}, \quad \text{(12-C-17)}$$

where h_a is the forced convection heat-transfer coefficient for the annular fluid. In offshore wells, where casing is exposed to cold seawater, the expression for L_{R3} changes to

$$L_{R3} = \frac{2\pi r_{to} U_{tc}}{c_a w_a} \quad \text{(12-C-18)}$$

In Eq. 12-C-18, the overall-heat-transfer coefficient accounting for the effect of seawater cooling, U_{tc}, is given by

$$\frac{1}{U_{tc}} = \frac{r_{to}\ln(r_{co}/r_{ci})}{k_c} + \frac{r_{to}}{r_{co}h_c} + \frac{r_{to}}{r_{ci}h_a} \quad \text{(12-C-19)}$$

Natural current will make forced convection the most likely mode of heat transfer in offshore operations. We suggest the use of the Fishenden and Saunders (1950) correlation for flow across long vertical pipes, which is

$$h_c = 0.26\left(k_c/d_{co}\right)^{0.6}\left(d_{co}v_c\rho_c/\mu_c\right)\left(c_c\mu_c/k_c\right)^{0.3} \quad \text{(12-C-20)}$$

Subscript *c* in Eq. 12-C-20 indicates properties for seawater. Similar to Eqs. 12-C-7 and 12-C-11, the governing differential equation for the annular fluid is written as

$$\frac{dT_a}{dz} = -L_{R1}\left(T_f - T_a\right)\frac{c_f}{c_a} + L_{R2}\left(T_a - T_w\right)\frac{c_w}{c_a} + L_{R3}\left(T_a - T_{ei}\right) + \phi_a \quad \text{(12-C-21)}$$

where

$$\phi_a = C_J\frac{dp}{dz} - \frac{v}{c_a}\frac{dv}{dz} - \frac{g\sin\alpha}{c_a} \quad \text{(12-C-22)}$$

Note that simultaneous solution of Eqs. 12-C-7, 12-C-11, and 12-C-21 should give the expressions for fluid temperatures in the three conduits of the system. The resulting third-order differential equation does not lend itself to analytic solution. The numerical solution procedure is discussed in the next subsection. In this derivation, we assumed that the inlet temperature of the circulating fluid remains constant. In case one wishes to circulate the fluid using a surface tank, the tank fluid temperature will asymptotically approach the final annular fluid exit temperature in a manner similar to that described for mud circulation, discussed in Chapter 11, Section 11.1.3.

12-C.2 Solution of Fluid Circulation Model. The known wellhead injection fluid temperature forms one of the boundary conditions. At the point of injection, the annular fluid temperature is the same as the injection fluid temperature; that is, $T_{aj} = T_{wj}$ is the second boundary condition. The tubing fluid temperature at $z = L_j$ can be estimated from the known bottomhole temperature using the method presented in Chapter 5 and forms the last boundary condition needed to solve the system of equations.

We introduce the fractional parameter ξ to write the difference equations in terms of the value of the variable (temperatures) at the jth node and the (j + 1)th node. Therefore, the difference equation for the tubing fluid temperature from Eq. 12.40 is given by

$$\frac{T_{fj+1} - T_{fj}}{\Delta z} = -\frac{1}{A_1}\left[\xi(T_{fj} - T_{aj}) + (1-\xi)(T_{fj+1} - T_{aj+1}) + \right]\phi_{fj}. \quad \text{(12-C-23)}$$

Similarly, for the fluid in the circulating string, we have

$$-\frac{T_{wj+1} - T_{wj}}{\Delta z} = \frac{1}{A_2}\left[\xi\left(T_{aj} - T_{wj}\right) + \left(1-\xi\right)\left(T_{aj+1} - T_{wj+1}\right)\right] - \phi_{wj}, \quad \text{(12-C-24)}$$

and, for the annular fluid

$$\frac{T_{aj+1}-T_{aj}}{\Delta z}=\frac{c_f}{A_1c_a}\left[\xi(T_{fj}-T_{aj})+(1-\xi)(T_{fj+1}-T_{aj+1})\right]$$
$$-\frac{c_w}{A_2c_a}\left[\xi(T_{aj}-T_{wj})+(1-\xi)(T_{aj+1}-T_{wj+1})\right] \quad (12\text{-}C\text{-}25)$$
$$-\frac{1}{A_3}\left[\xi T_{aj}+(1-\xi)T_{aj+1}-T_{ej}\right]+\phi_{aj}$$

We rearrange Eqs. 12-C-23 through 12-C-25 by moving the variables T_{fj+1}, T_{wj+1}, and T_{aj+1} to the right side of the equation and obtain the expressions

$$b_1T_{fj+1}+b_2T_{aj+1}=b_3, \quad (12\text{-}C\text{-}26)$$

$$C_1T_{aj+1}+C_2T_{wj+1}=C_3, \quad (12\text{-}C\text{-}27)$$

and

$$d_1T_{fj+1}+d_2T_{aj+1}+d_3T_{wj+1}=d_4 \quad (12\text{-}C\text{-}28)$$

Further rearrangement gives the expressions for fluid temperatures in the three conduits at the $(j + 1)^{th}$ node in terms of temperature at the jth node and other parameters, which are

$$T_{fj+1}=\frac{b_3C_1d_3+b_2C_2d_4-C_2d_2b_3-b_2C_3d_3}{b_1C_1d_3+b_2C_2d_1-C_2d_2b_1}, \quad (12\text{-}C\text{-}29)$$

$$T_{aj+1}=\frac{b_1C_3d_3+b_3C_2d_1-C_2d_4b_1}{b_1C_1d_3+b_2C_2d_1-C_2d_2b_1}, \quad (12\text{-}C\text{-}30)$$

and

$$T_{wj+1}=\frac{b_1C_1d_4+b_2C_3d_1-b_3C_1d_1-b_1C_3d_2}{b_1C_1d_3+b_2C_2d_1-C_2d_2b_1} \quad (12\text{-}C\text{-}31)$$

The parameters used in Eqs. 12-C-29 through 12-C-31 are

$$b_1=1+\frac{\Delta z}{A_1}(1-\xi), \quad (12\text{-}C\text{-}32)$$

$$b_2=-\frac{\Delta z}{A_1}(1-\xi), \quad (12\text{-}C\text{-}33)$$

$$b_3=-\frac{\Delta z}{A_1}\xi(T_{fj}-T_{aj})+T_{fj}+\phi_j, \quad (12\text{-}C\text{-}34)$$

$$C_1=\frac{\Delta z}{A_2}(1-\xi), \quad (12\text{-}C\text{-}35)$$

$$C_2=1-\frac{\Delta z}{A_2}(1-\xi), \quad (12\text{-}C\text{-}36)$$

$$C_3 = -\frac{\Delta z}{A_2}\xi(T_{aj}T_{wj}) + T_{wj}, \quad \text{(12-C-37)}$$

$$d_1 = \frac{\Delta z c_f}{A_1 c_a}(1-\xi), \quad \text{(12-C-38)}$$

$$d_2 = -\left[1 + \frac{\Delta z c_f}{A_1 c_a}(1-\xi) + \frac{\Delta z c_w}{A_2 c_a}(1-\xi) + \frac{\Delta z}{A_3}(1-\xi)\right], \quad \text{(12-C-39)}$$

$$d_3 = \frac{\Delta z c_w}{A_2 c_a}(1-\xi), \quad \text{(12-C-40)}$$

and

$$\begin{aligned} d_4 = {} & L_{R2}\Delta z \frac{c_w \xi}{c_a}(T_{aj} - T_{wj}) + L_{R1}\Delta z \frac{c_f \xi}{c_a}(T_{fj} - T_{aj}) \\ & + L_{R3}\Delta z \xi T_{aj} - L_{R3}\Delta z T_{eij} + T_{aj} + \phi_{aj}\Delta z \end{aligned} \quad \text{(12-C-41)}$$

12-C.3 Constants of the Solvent Injection Model. In Eqs. 9.44 through 9.46, α_1 and α_2 are the constants of integration that require two boundary conditions. The circulating-fluid temperature at the wellhead, T_{ww}, and the fluid temperature at the point of injection, T_{ff}, constitute the two boundary conditions. Substituting $T_w = T_{ww}$ at L and $T_f = T_{ff}$ at L_j in Eq. 12.46, we obtain

$$T_{ff} = \alpha_1 e^{\lambda_1 L_j} + \alpha_2 e^{\lambda_2 L_j} + \frac{\beta_4}{\beta_3}L_j + \frac{\beta_3\beta_5 - \beta_2\beta_4}{\beta_3^2} \quad \text{(12-C-42)}$$

and

$$T_{ww} = \omega_1\alpha_1 + \omega_2\alpha_2 + \omega_4 \quad \text{(12-C-43)}$$

Therefore, α_1 and α_2 are given by

$$\alpha_1 = \frac{e^{\lambda_2 L_j}\left(T_{ww} - \omega_4\right) - \omega_2\left(T_{ff} - \frac{\beta_4}{\beta_3}L_j - \frac{\beta_3\beta_5 - \beta_2\beta_4}{\beta_3^2}\right)}{\omega_1 e^{\lambda_2 L_j} - \omega_2 e^{\lambda_1 L_j}} \quad \text{(12-C-44)}$$

and

$$\alpha_2 = \frac{\omega_1\left(T_{ff} - \frac{\beta_4}{\beta_3}L_j - \frac{\beta_3\beta_5 - \beta_2\beta_4}{\beta_3^2}\right) - e^{\lambda_1 L_j}\left(T_{ww} - \omega_4\right)}{\omega_1 e^{\lambda_2 L_j} - \omega_2 e^{\lambda_1 L_j}} \quad \text{(12-C-45)}$$

The parameters βi (i = 1, 2…5) are defined by the expressions

$$\beta_1 = 2\pi r_{io}U_1 + 2\pi r_{jo}U_2 + L_{R3}w_a c_a, \quad \text{(12-C-46)}$$

$$\beta_2 = (4\pi^2 r_{to} r_{jo} U_1 U_2)\left(\frac{1}{w_w c_w} - \frac{1}{w_f c_f}\right) - L_{R3} 2\pi w_a c_a \left(\frac{r_{to} U_1}{w_f c_f} - \frac{r_{jo} U_2}{w_w c_w}\right), \quad (12\text{-C-}47)$$

$$\beta_3 = \frac{4\pi^2 r_{to} r_{jo} U_2 U_1 w_a c_a L_{R3}}{w_f w_w c_f c_w}, \quad (12\text{-C-}48)$$

$$\beta_4 = -\frac{4\pi^2 r_{to} r_{jo} U_1 U_2 w_a c_a L_{R3} g_G \sin\theta}{w_f w_w c_f c_w}, \quad (12\text{-C-}49)$$

and

$$\beta_5 = \frac{2\pi r_{jo} U_2 \phi_f}{w_w c_w}\left(2\pi r_{to} U_1 + L_{R3} w_a c_a\right) - \frac{2\pi r_{to} U_1}{w_f c_f}(2\pi r_{jo} U_2 \phi_w - w_a c_a L_{R3} g_G \sin\alpha) - \frac{2\pi r_{to} U_1}{w_f c_f}\left[\frac{2\pi r_{jo} U_2 w_a c_a (T_{bh} - L g_G \sin\alpha) L_{R3}}{w_w c_w}\right] \quad (12\text{-C-}50)$$

Note that λ_1 and λ_2 are given by

$$\lambda_1 = \frac{-\beta_2 + \sqrt{\beta_2^2 - 4\beta_1\beta_3}}{2\beta_1} \quad (12\text{-C-}51)$$

and

$$\lambda_2 = \frac{-\beta_2 - \sqrt{\beta_2^2 - 4\beta_1\beta_3}}{2\beta_1} \quad (12\text{-C-}52)$$

The parameters for ω_i are

$$\omega_1 = -\frac{\left(2\pi r_{to} U_1 + 2\pi r_{jo} U_2 + L_{R3} w_a c_a\right) w_f c_f \lambda_1}{4\pi^2 r_{to} r_{jo} U_1 U_2} + \frac{2\pi r_{jo} U_2 + L_{R3} w_a c_a}{2\pi r_{jo} U_2}, \quad (12\text{-C-}53)$$

$$\omega_2 = -\frac{\left(2\pi r_{to} U_1 + 2\pi r_{jo} U_2 + L_{R3} w_a c_a\right) w_f c_f \lambda_2}{4\pi^2 r_{to} r_{jo} U_1 U_2} + \frac{2\pi r_{jo} U_2 + L_{R3} w_a c_a}{2\pi r_{jo} U_2}, \quad (12\text{-C-}54)$$

$$\omega_3 = \frac{2\pi r_{jo}U_2 + L_{R3}w_a c_a}{2\pi r_{jo}U_2}\frac{\beta_4}{\beta_3} - \frac{L_{R3}g_G \sin\alpha\, w_a c_a}{2\pi r_{jo}U_2} \quad \text{(12-C-55)}$$

and

$$\omega_4 = -\frac{2\pi r_{to}U_1 + 2\pi r_{jo}U_2 + L_{R2}w_a c_a}{4\pi^2 r_{to}r_{jo}U_1U_2}\frac{w_f c_f \beta_4}{\beta_3} - \frac{2\pi r_{jo}U_1 T_{bh} L_{R3}w_a c_a}{4\pi^2 r_{to}r_{jo}U_1U_2} - \frac{Lg_G \sin\alpha\, L_{R3}w_a c_a}{2\pi r_{jo}U_2} + \frac{w_f c_f \phi_1\left(2\pi r_{to}U_1 + 2\pi r_{jo}U_2 + L_{R3}w_a c_a\right)}{4\pi^2 r_{to}r_{jo}U_1U_2} + \frac{2\pi r_{jo}U_2 + L_{R3}w_a c_a}{2\pi r_{jo}U_2}\frac{\beta_3\beta_5 - \beta_2\beta_4}{\beta_3^2} \quad \text{(12-C-56)}$$

Chapter 13

Production Logging

13.1 Introduction

Production logs have the potential for providing an array of valuable information about the well or near-wellbore formation throughout the life of a well. This array of information includes well performance evaluation, workover and completion evaluation, and reservoir performance monitoring.

Conventional production logging as practiced today traces its origin to the introduction of temperature logs by Schlumberger et al. (1937) and, subsequently, to the use of other sensors by Wade et al. (1965). Over the past five decades, continuous enhancement of sensor resolution paved the way for improved downhole diagnosis. One cornerstone to the early success lay in the ability to run multiple sensors in one run, although surface transmission of only one sensor response at a time was permitted early on, as reported by Meunier et al. (1971). Approximately a decade later, simultaneous transmission of signals from all sensors to the surface became possible (Anderson et al. 1980). Advances in data-gathering techniques and instrumentation continue to this day. At the same time, our understanding of the mechanics of gas/liquid and liquid/liquid flows in conduits of various orientations, as discussed in Chapter 4, has also matured over the years. Despite these advances, integration of mechanistic models with sensor responses has lagged behind. For instance, a holdup model may be used, but without an explicit usage of the flow pattern map associated with it. We also observe that the traditional approach of station-based analysis, dealing with a few data points, often does not explain anomalous flow behavior. Stated differently, one wonders whether a certain sensor response is induced by the complex flow behavior, poor sensor resolution, logging speed, or a combination thereof.

Modern production logging encompasses many sensors and techniques, including spinner flowmeter logging, temperature logging, radioactive tracer logging, noise logging, and cement quality logging, among others. In accordance with the focus of this book on fluid flow and heat transfer, this chapter only presents interpretations of spinner flowmeter and temperature log responses. For a detailed treatment of conventional topics, the reader is referred to other work, notably to McKinley (1982) and the SPE monograph by Hill (1990). More recently, Chapter 17 of the dynamic data analysis digital book of Houzé et al. (2016) presented a detailed overview of tools, their responses, and quantitative interpretation of different signals.

In this chapter, we discuss a rigorous depth-indexed analysis of flowmeter response. Thereafter, we address how flow-pattern-based mechanistic models, discussed in Chapters 3 and 4, can be integrated with log responses to gain superior

understanding of flow mechanics and improved interpretation. Although the illustrative field examples involve oil/water flow, the principle can be extended to all flow situations. Much of the material presented here is abstracted from studies by Hoadley et al. (2001) and Kabir et al. (2001b), which consider examples from Kuwait's Burgan field. Thereafter, we discuss certain aspects of temperature logging.

13.2 Spinner Flowmeter Production Log Interpretation

Spinners are impellers that are placed in the well to rotate as fluid moves past them. The rotational speed, being dependent on flow rate, allows rate measurement. A centralized tool is likely to "read" the fluid velocity at the center of the well and may need to be corrected to obtain the "channel average" velocity, given that $v_{center} = v_{max} = C_o v_m$. Therefore, production rate q equals Av_f/C_o. Note that borehole rugosity may introduce uncertainty in crosssectional flow area A in an openhole situation.

Ideally, spinner rotation revolutions per second (rps) will be directly proportional to in-situ fluid velocity. However, mechanical friction and viscous effects make the spinner response deviate significantly from linearity at low flow rates, as indicated in **Fig. 13.1**.

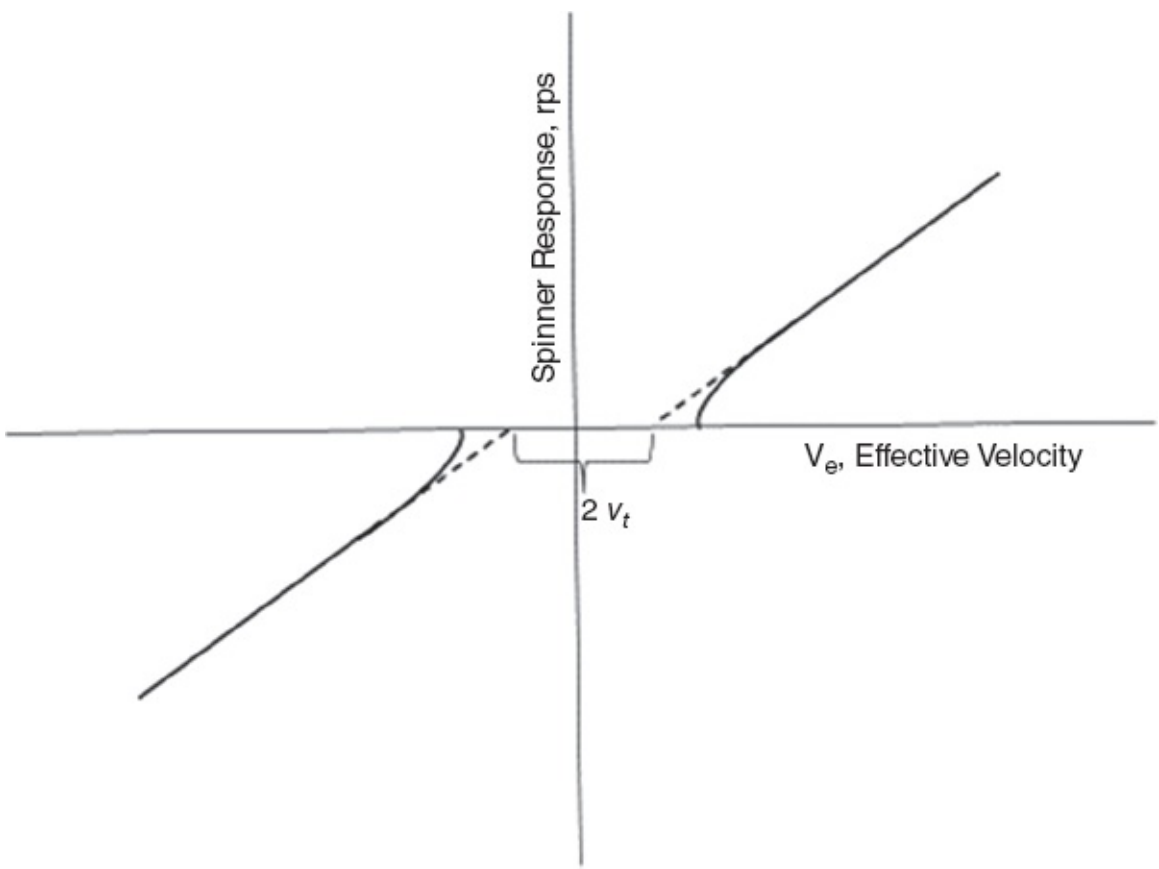

Fig. 13.1—Typical spinner response, in revolutions per second (rps).

Spinners are also conveyed by a cable to specific locations in the wellbore and may have a relative velocity with respect to the well. For example, a descending

spinner in a producing well will measure an effective velocity v_e equal to the tool (cable) velocity v_T plus the fluid velocity v_f ; that is,

$$v_e = v_f + v_T \quad (13.1)$$

Tool velocity v_T is considered positive in the direction opposite to fluid flow. For example, in an injection well, an upward-moving tool will have positive velocity.

As Fig. 13.1 shows, spinner response is linear with effective velocity v_e for large values of v_e. The linear spinner responses have somewhat different slope values for positive and negative spinner responses. At low effective velocities, the actual spinner response, indicated by the solid line, will drop. At very low values of v_e, the spinner will stop rotating (because of mechanical friction) even though true effective velocity is nonzero. To properly interpret spinner data, the linear portions of the positive and negative spinner responses are extrapolated and their *x*-axis intercepts are noted. The average value of these two intercepts is termed "spinner threshold velocity," v_t. Therefore, threshold velocity is the hypothetical minimum effective velocity needed for a spinner to rotate.

Fig. 13.1 also shows that by varying cable speed, data can be gathered that will allow dynamic calibration of the flowmeter. Data gathered at high effective positive and negative velocities will allow one to draw regression lines and obtain slopes and intercepts that can be used to calculate fluid velocity and, therefore, production rates.

13.2.1 Conventional Approach. The idealized spinner response owing to fluid influx at different tool velocities is illustrated by the synthetic Example A, shown in **Fig. 13.2.** Between the sets of perforations, spinner revolutions ideally remain constant. An increase in spinner response signifies fluid entry, whereas a decreased response suggests loss of fluid because of leak or injection into the formation. For each pass at a constant cable speed, a depth-dependent spinner profile or spinner response will develop. Ideally, each response will be parallel to the other responses. These data can be analyzed to quantify the amount of fluid produced, injected, or crossflowed within the wellbore.

Dynamic spinner response must account for mechanical, viscous, and cable speed effects. We note again that effective velocity in these analyses represents the relative velocity between the fluid and the cable and is given by $v_e = v_f + v_T$.

We may express the reported spinner response or frequency *f* as follows:

$$f = m_p(v_e - v_t) \text{ when } v_e > v_T \text{ and } f = m_n(v_e - v_t) \text{ when } v_e < v_T,$$

or

$$f = m_p(v_f + v_T - v_t) \text{ when } v_e > v_T \text{ and } f = m_n(v_f + v_T - v_t) \text{ when } v_e < v_T \quad (13.2)$$

Therefore, spinner vs. cable speed data from any position between two producing or injecting zones can be used to obtain the applicable slopes, m_p and m_n, and threshold

velocity v_t. The slopes and threshold velocity can then be used to calculate the actual fluid velocity and, therefore, the production/injection rate for that interval.

As shown in **Fig. 13.3,** at each depth A, B, C, and D, a linear regression of the data yields a slope and an *x*-axis intercept. Fluid density, viscosity, and the spinner bearing friction affect the slope and the position of the line in the calibration plot. However, with constant fluid properties, the lines will be theoretically parallel to one another between the 100 and 0% flow intervals, as illustrated in Fig. 13.3. Here, Depth D represents the no-flow interval below all perforations, and Depth A represents the maximum flow above all fluid entry from the formation.

Typically, log presentation includes static and dynamic spinner calibration plots. The static calibration may be derived from logging passes below all contributing perforations or a sump area in the well during flowing conditions or from passes over the entire interval during well shut-in. In contrast, the dynamic calibration plot is usually generated from the data collected during flowing conditions at specific depth intervals above the sump. The selection of depth intervals is arbitrary and ordinarily left to the discretion of the on-site log analyst.

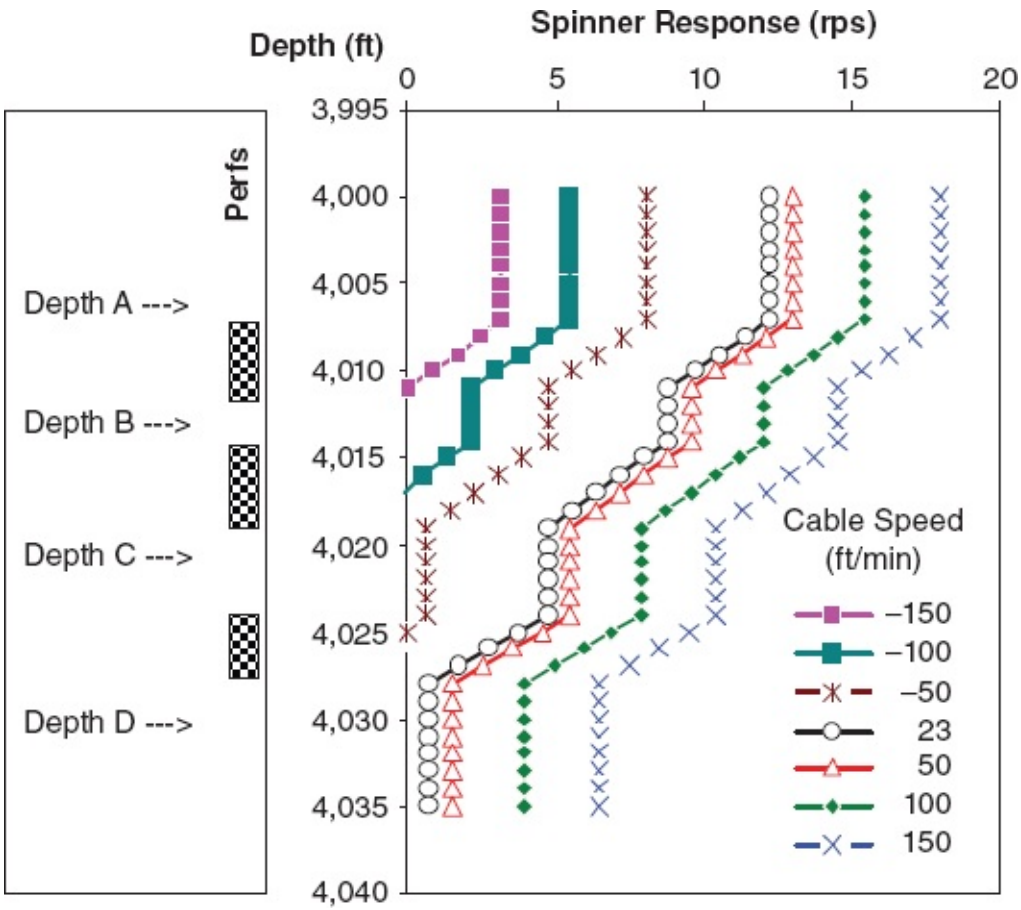

Fig. 13.2—Production spinner, Example A.

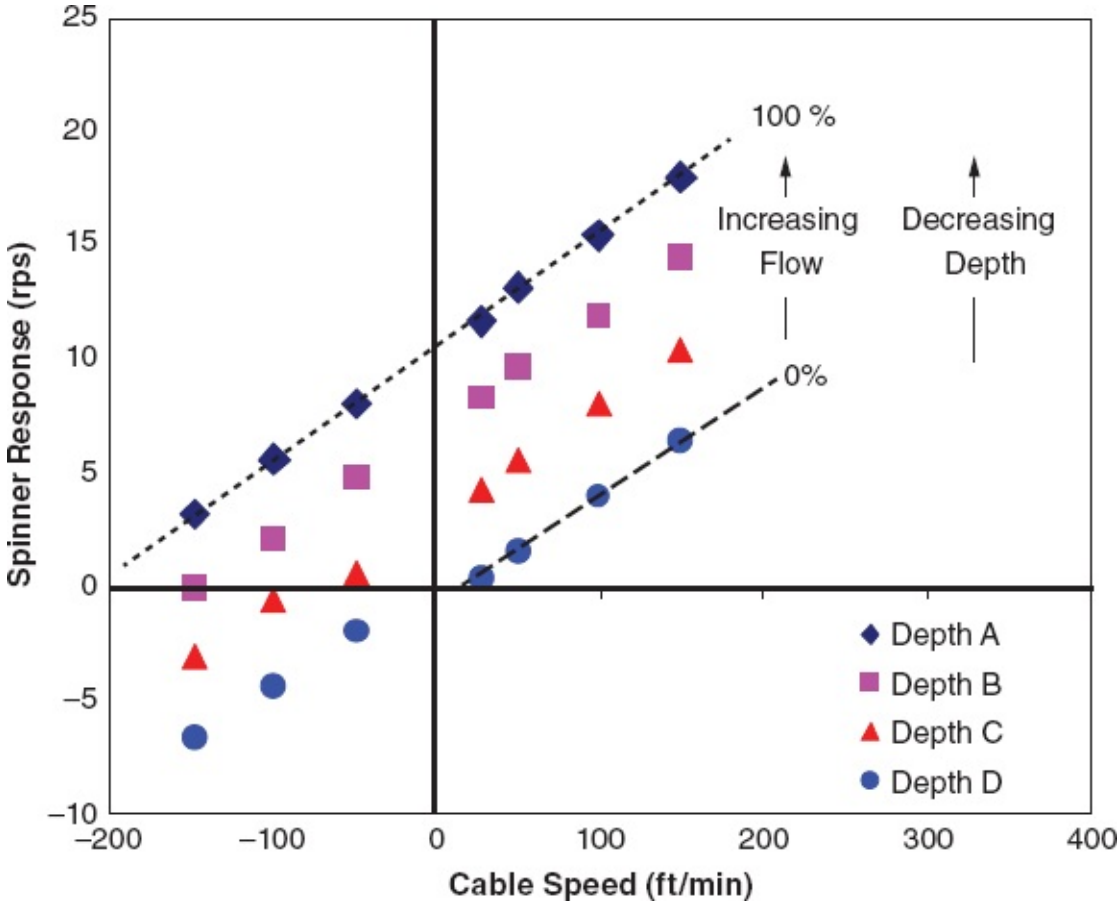

Fig. 13.3—Combined static and dynamic spinner calibration plot.

13.2.2 Depth-Indexed Analysis. Production log interpretation can be improved by generating depth-indexed flowmeter response quality traces (FRQT). The FRQT basically consist of three tracks that present the statistics in terms of the *x*-axis intercept, the slope's correlation coefficient, and the slope of the line at each depth. Performing a regression analysis of spinner velocity vs. cable velocity generates the spinner calibration response statistics at every depth or at small intervals. This analysis is a significant departure from the norm, which relies on the use of a spinner response chart for a small group of selected intervals.

Using FRQT, an analyst can identify logging intervals that are appropriate for interpretation. For instance, poor correlation coefficients shed light on the behavior of fluids in the wellbore, reflecting turbulence or jetting effects, changes in fluid viscosity at the new entry point, and abrupt changes in cable speed. This approach allows us to distinguish poor data quality from true system response.

In Example A, data were evaluated at four depth intervals. This method provides an indication of the flow rate change only between intervals and not over the complete logged interval. Performing a linear regression on a continuous basis at small discrete intervals, through the logged section, yields additional information on flow behavior. For instance, the subtle spinner changes that occur during the logging passes are easier to recognize. If all logging passes at constant cable speeds result in parallel spinner response curves, as presented in Fig. 13.2, then the slopes and correlation

coefficients will remain constant. Plotting this information in **Fig. 13.4** replaces the traditional plot in Fig. 13.2. That is because generating a conventional single calibration plot for all discrete depth intervals will produce an illegible graph. Fig. 13.4 improves display of the data, which, in turn, may improve confidence in the interpretation.

The spinner response at each depth is consistent with the tool velocity, provided that the correlation coefficient is unity and at least two tool passes are available. The relative fluid velocity is the same for each pass at a given depth. To obtain meaningful correlation coefficients, a minimum of four passes at different logging speeds, preferably in increments of 30 ft/min, is recommended. Correlation coefficients less than unity may be a result of many factors that are discussed later.

Evaluating the slope of the line at each discrete depth while considering the correlation coefficient can assist in interpretation. Changing slopes throughout the complete log interval may indicate changing fluid properties or possibly poor data correlations. For the entire log section, checking the trends and values of the FRQT; reviewing the collected pressure, temperature, and specific gravity data; and knowing the characteristics of the produced fluids may help explain the anomalous response.

We find the *x*-axis intercept and, hence, the rate to be highly dependent on the slope. When both the correlation coefficient and the slope are continuously changing, the calculated rates from the *x*-axis intercept may vary significantly. Consequently, interpretation becomes difficult. In these cases, one may identify certain intervals from the revised spinner calibration plot that best represent flow in the well. Other alternatives include increasing the interval by considering several discrete intervals together or smoothing anomalous and severe data spikes. Regenerating the revised spinner calibration plot will determine the effectiveness of the selected approach.

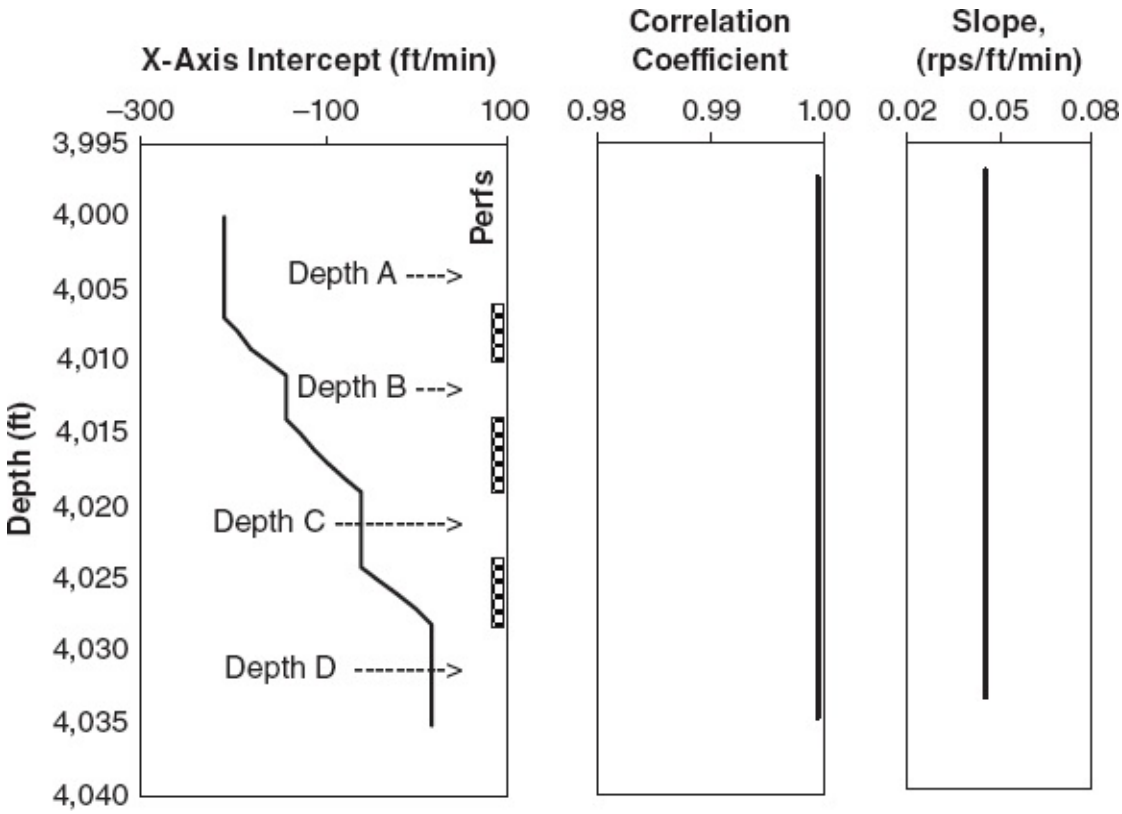

Fig. 13.4—FRQT calibration plot.

Similarly, the individual spinner response curves for each cable speed can be normalized to overlay each other, as illustrated in **Fig. 13.5.** In the static or no-flow interval as shown, the spinner response should be zero.

Now, consider the case in which the spinner response curves are not parallel to each other over the logged section, as shown in **Fig. 13.6** for Example B. Possible dynamic attributes, such as inclined segregated flow, changing flow regimes, significant slip velocities, perforation flow eddies, poor depth control, or spinner mechanical deficiencies, may result in incongruous spinner curves. Repeat logging using the same production log tools may not improve interpretation. However, understanding the wellbore flow mechanics and reservoir performance may provide insights into the nature of the problem.

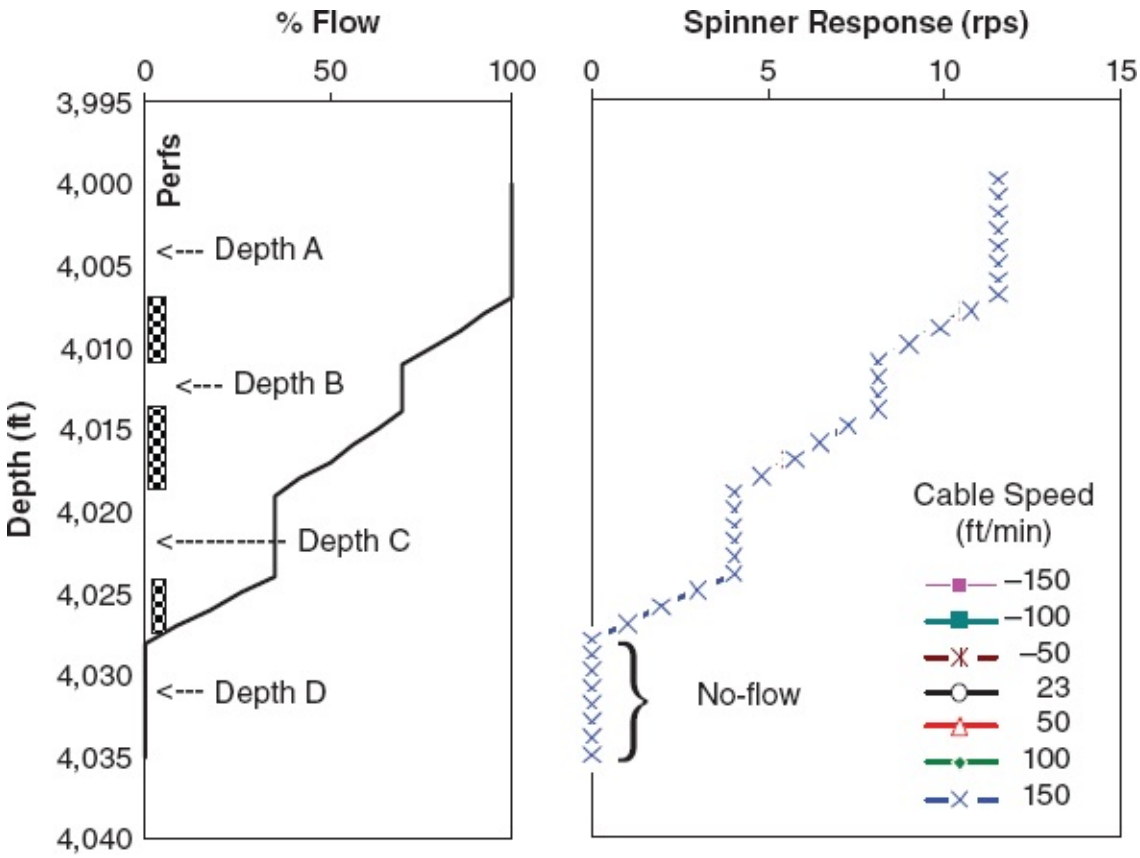

Fig. 13.5—Spinner response overlay.

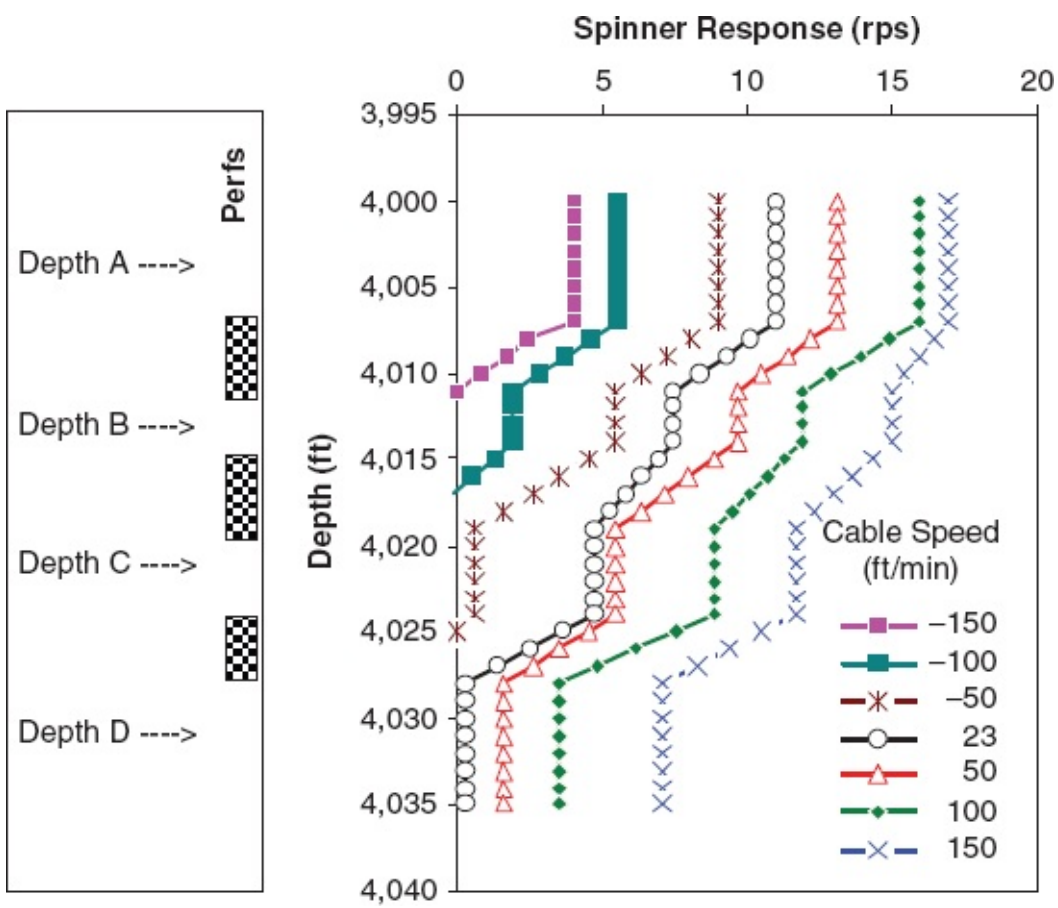

Fig. 13.6—Production spinner, Example B.

Fig. 13.7 shows the revised spinner calibration plot generated from the synthetic data in Example B. Note the apparent degradation in the correlation coefficient and an increasing variation in values of slope or spinner rotation. The FRQT provides a qualitative indication that flow measurement and, therefore, interpretation require careful attention.

Although the spinner response curves are parallel between the perforation sets, the correlation coefficients are less than unity. Because the slopes vary, selecting the appropriate *x*-axis intercept is difficult. This observation implies that the rate determination has some associated errors.

Fig. 13.8 presents the overlay of spinner response curves and the fluid contribution profile. By comparing Figs. 13.5 and 13.8, we note with interest that interpretation of the percentage flow contribution profile did not change significantly between Example A and Example B. This is so because the 100% flow rate occurs at the minimum *x*-axis intercept and the minimum flow rate occurs near zero on the *x*-axis intercept. Because the *x*-axis intercept profiles are similar in both cases, the calculated percentage flow yields profiles that are nearly the same.

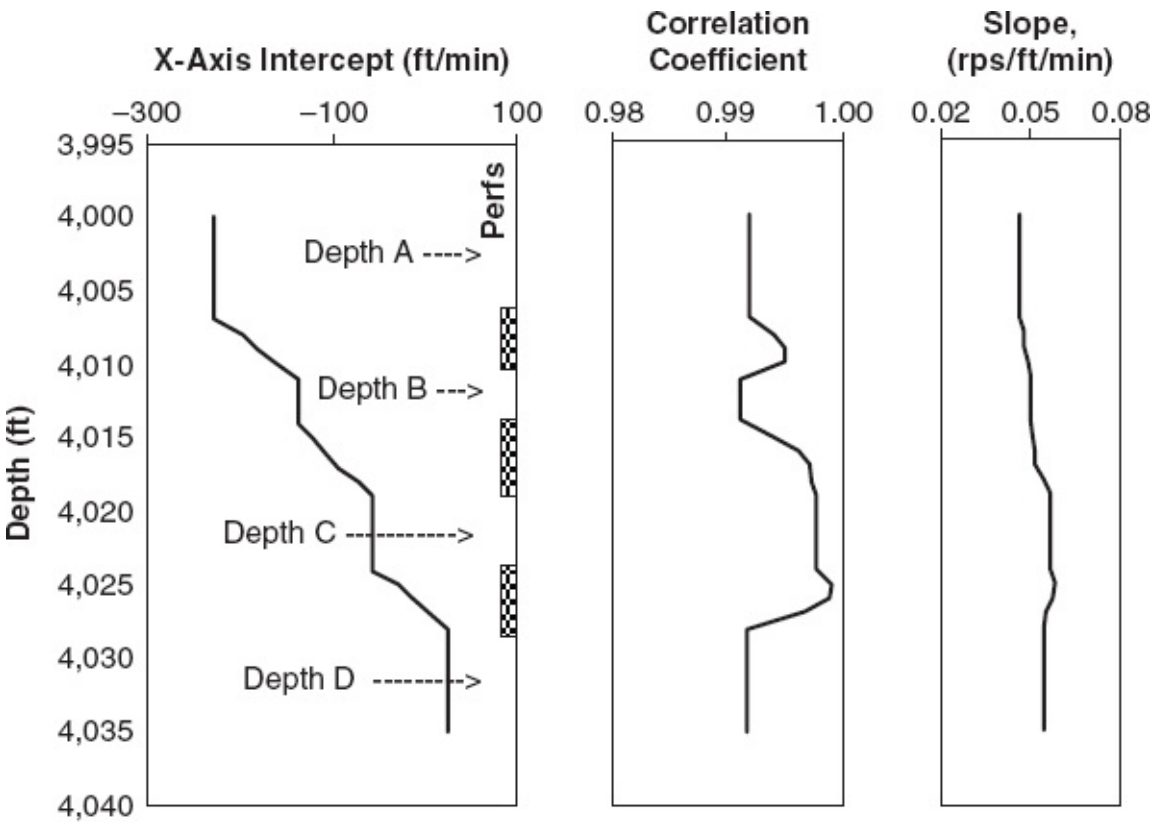

Fig. 13.7—FRQT calibration plot.

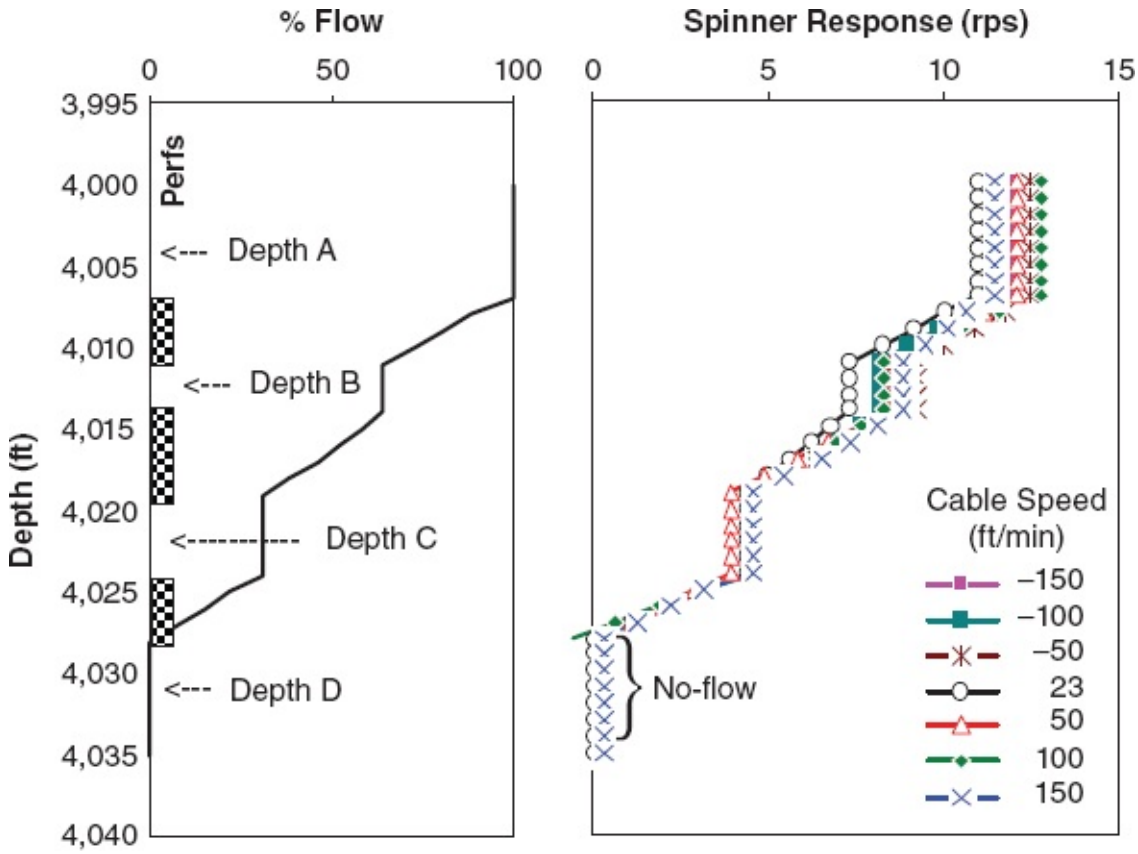

Fig. 13.8—Spinner response overlay.

In some instances, logging programs forego the shut-in passes when a dead area or sump is available in a flowing well. Log interpreters use this assumed static interval to calibrate the no-flow spinner response. Useful pressure, temperature, and density information is sacrificed and, as a result, comparisons cannot be made between flowing and static conditions. Often, subtle temperature and density differences between these conditions can help identify flow behind pipe or bottom flow in the well. In addition, false indication of formation fluid densities can occur when heavier drilling fluids, used in well-kill operations, segregate out in the sump interval. Without the shut-in pressure data, the static reservoir pressure and, hence, the drawdown can only be estimated. As a result, systems performance analysis may not provide the desired accuracy. By having both flowing and shut-in passes, even when sumps exist, corroborative information from various sensors can provide additional insights to improve interpretation.

13.2.3 Field Examples. This subsection presents two field examples—Well A-22 and Well B-235—that demonstrate spinner response interpretation and the usefulness of the FRQT traces.

Well A-22. A production log was run in Well A-22 to identify the water entry point and any potentially leaking squeezed perforations. From a pulsed neutron capture (PNC) log run several years earlier, the oil/water contact was found to be 16 ft below the open perforations. The oil/water contact conceivably had risen into the squeezed

perforations and could have been partially leaking. This perceived oil/water contact movement accounted for the increasing water production after PNC logging operations were completed. During the production-logging operation, portable separator testing showed that the well was producing at 1,274 STB/D with a 54% water cut.

In **Fig. 13.9,** four different cable speeds in the downward direction are presented in the flowing condition for this well. The line pattern is parallel except near the top, above 4,500 ft. The significant change in spinner rotation for each line consistently occurs across the interval of open perforations, 4,588–4,611 ft. The darkened set of squeezed perforations above and below the open perforations do not appear to be leaking.

Here, shut-in passes were not taken because the sump was considered to be of insufficient length, thereby minimizing the deferred production. After generating the spinner calibration plot from below the point of fluid entry at 4,611 ft, we note that the static threshold intercept is approximately 2.13 ft/min, as illustrated in **Fig. 13.10.** This value is realistic and is well within the range of values typically observed in many cases during static conditions and is interpreted as no-flow condition.

An anomalous spike develops owing to the spinner rotation inconsistency, as seen near the top of the 33-ft/min pass in Fig. 13.9. Data collected above this point should not be considered in the rate calculation because they will suggest additional fluid entry with possible crossflow. The correlation coefficient values in Fig. 13.10 support this notion. Values closer to unity suggest better data consistency between passes. Correspondingly, the changing slope causes the x-intercept and, therefore, the rate calculation to change. Interpretation of data above 4,500 ft is cautioned. Note that the slope values increase slightly above the sump zone. This observation may possibly be attributed to a combination of tool friction effects, in addition to viscosity and density difference between the formation water and the produced fluids.

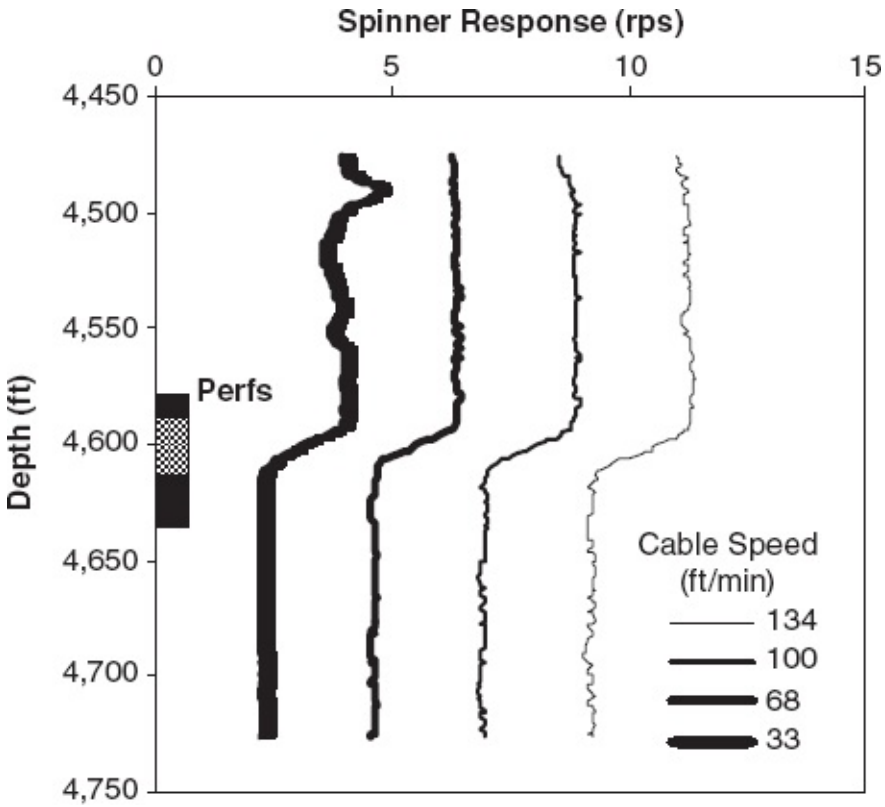

Fig. 13.9—Spinner response at different cable speeds.

Developing a frequency plot for the correlation coefficient over the entire logged section for the up passes and down passes, as shown in **Fig. 13.11,** provides an indication of consistency of the correlation. Clearly, approximately 95% of the data in both cases have a correlation better than 0.998. This observation is significant considering that there are more than 250 individual-depth regression analyses for this well at four different logging speeds. The degradation in the down-flowing pass occurs because of the anomalous spike in the spinner response. Static pass correlations are not presented because they were unavailable.

Plotting other data such as specific gravity, temperature, and pressure can provide additional support for this conclusion. In **Fig. 13.12,** the temperature and specific gravity plots indicate major fluid entry just below 4,600 ft, whereas a noticeable change in temperature or specific gravity is not observed above 4,500 ft. This suite of data supports the notion that there is no fluid entry near the top of the logged interval. Although not shown, the same conclusion was drawn from the up-pass interpretation.

The flowing bottomhole pressure of 1,960 psia is above the bubblepoint pressure, which is estimated at approximately 1,600 psia. The producing mixture specific gravity values are not significantly lowered and, therefore, do not reflect gas evolution.

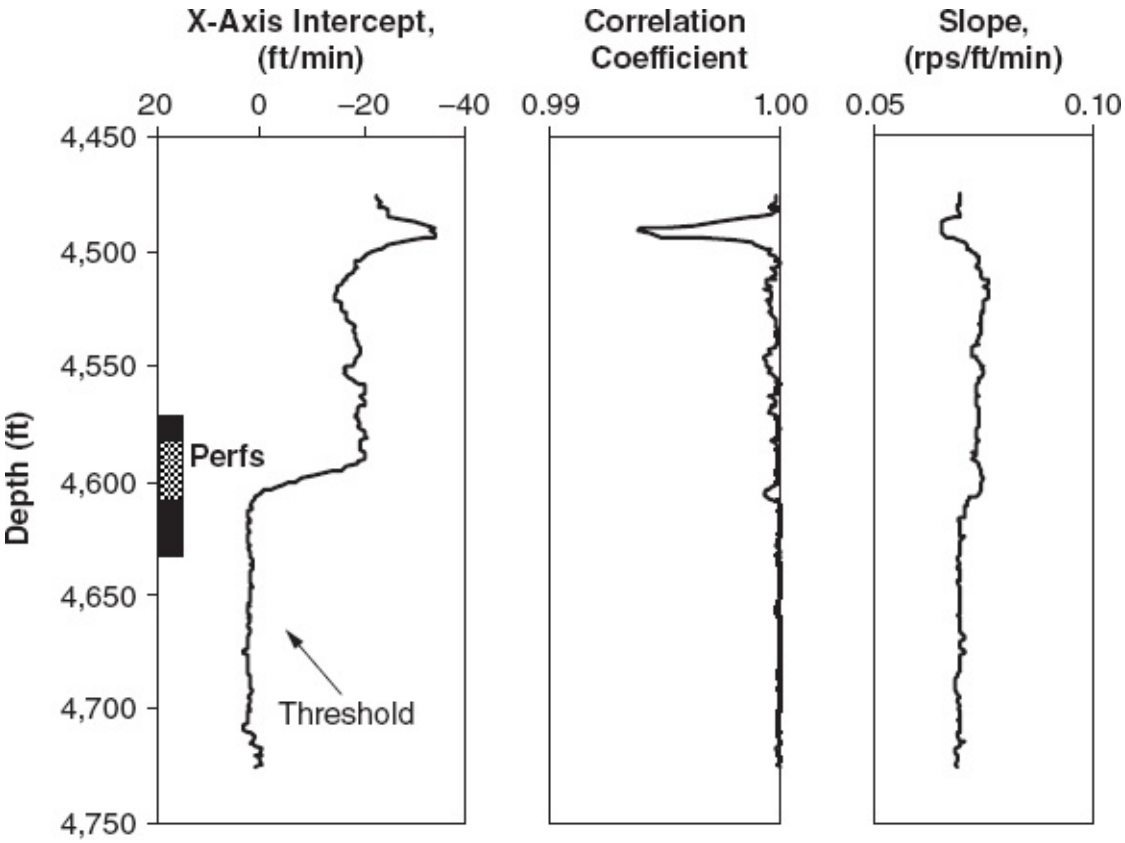

Fig. 13.10—FRQT spinner calibration plot.

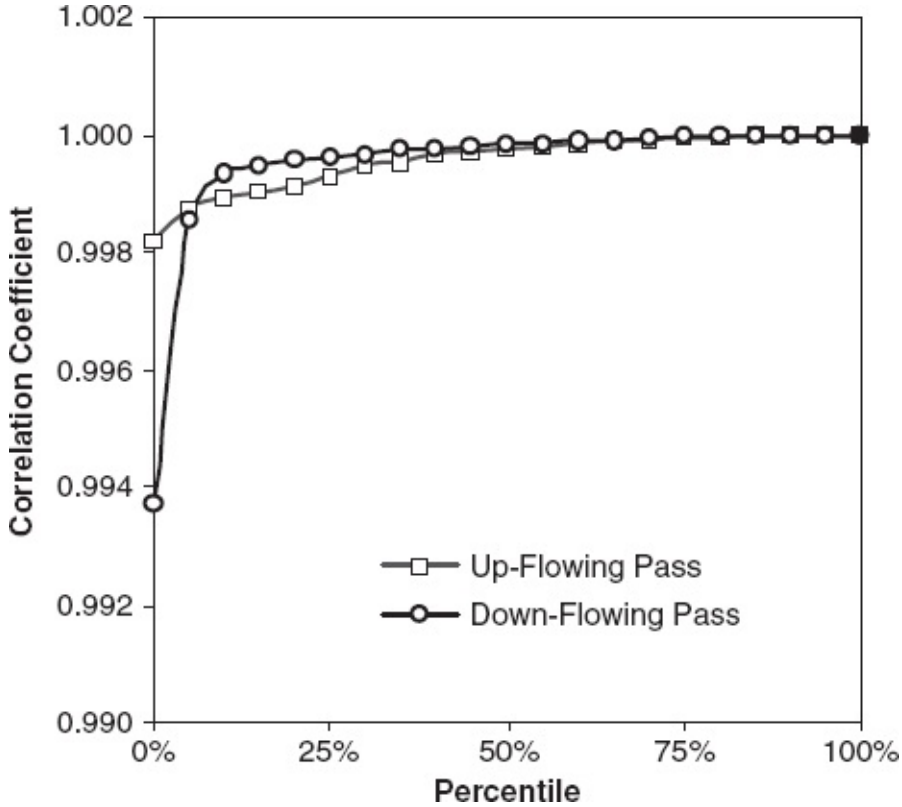

Fig. 13.11—Correlation coefficient frequency.

Knowing the geothermal gradient, as discussed in Section 8.2, and the water specific gravity, we can conclude that below 4,600 ft, the geothermal gradient exists and the formation water has segregated into the sump. However, static passes would have provided additional data for comparison and thereby revealed conclusively whether any fluid was channeling behind pipe from below the bottom perforations.

Although not presented, the flow profile interpretation for the up/down passes is similar, with the exception of the interval above 4,500 ft, where the anomaly is not repeated. Discounting the spinner rotation spike in **Fig. 13.13,** the maximum or 100% flow is observed just above the open perforations. Accounting for the cable speeds, the upward spinner response overlay is generated to normalize the spinner rotation. Using the corresponding spinner data, the calculated surface rates of approximately 1,325 STB/D from the downhole spinner rotation are similar to the independently measured field surface rates of 1,274 STB/D. Corroborating the rate measurements from various sources can be beneficial, particularly when the flow rates are less than 1,000 STB/D. If a continuous flowmeter inside the tubing is available, use should be made of it to substantiate the rate measurements.

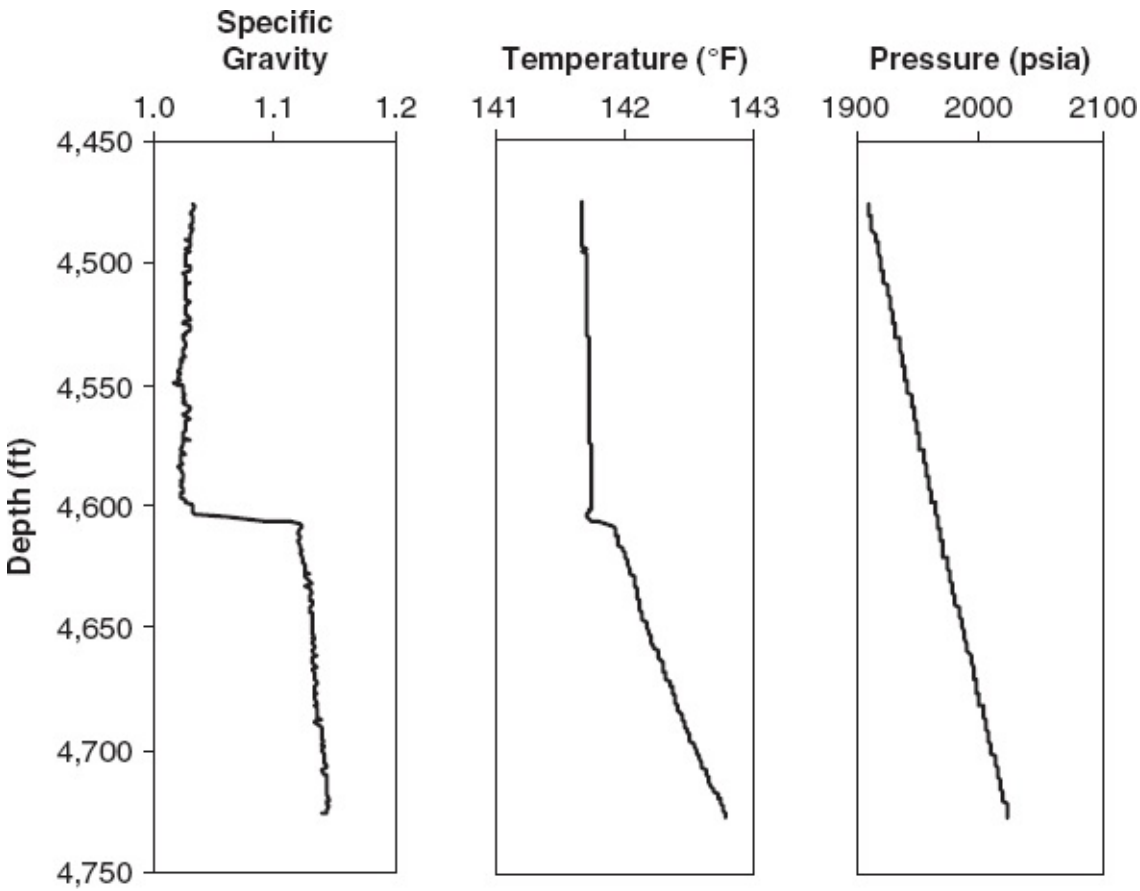

Fig. 13.12—Specific gravity, temperature, and pressure.

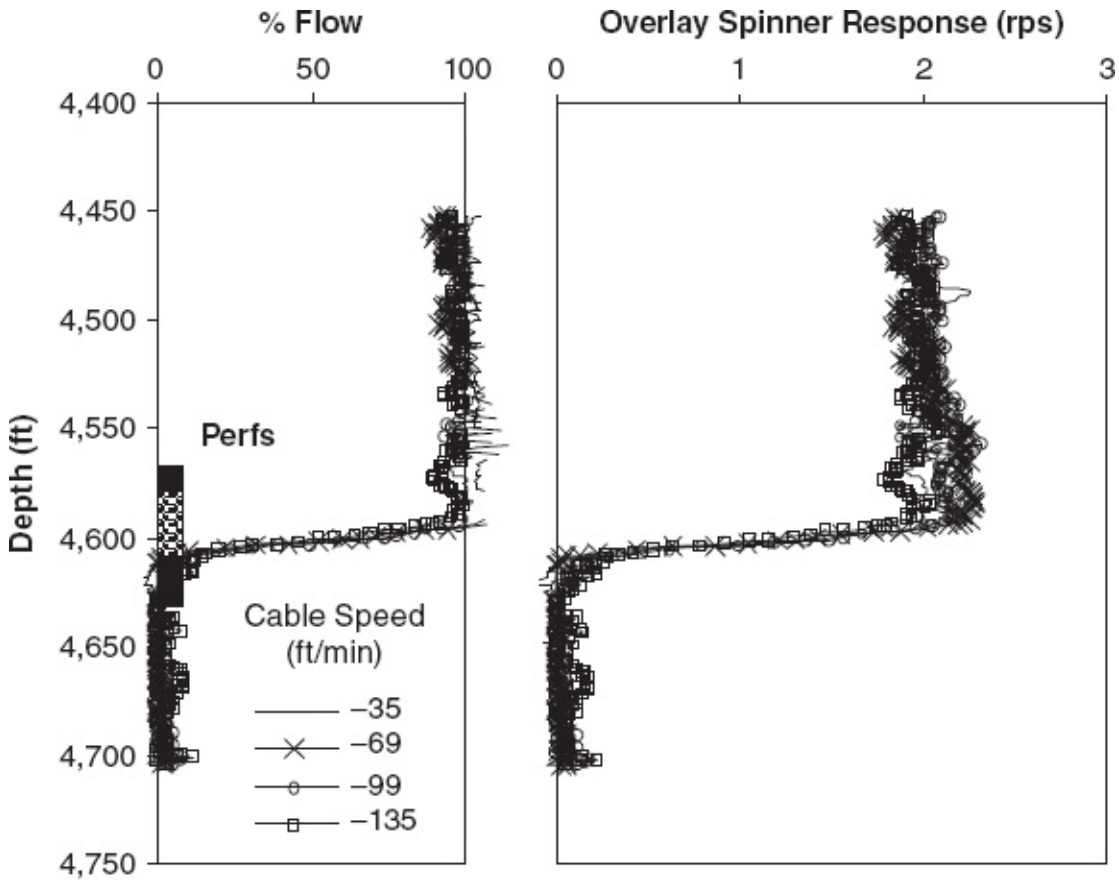

Fig. 13.13—Spinner response overlay.

In **Fig. 13.14,** the total and water rates for the up pass are shown. Assuming the water specific gravity to be 1.13 and the oil gravity to be 0.77, the calculated surface water cut from the measured mixture specific gravity yields a value ranging between 47 and 62%, depending on the slip model used. The flow regime map and the slip model are discussed in detail in the next section.

On the basis of the results of the interpretation, the well was plugged back at a later date when the increasing water cut had finally killed the well and prevented flow. A through-tubing bridge plug was set at 4,580 ft and cement was dumped on top, up to 4,573 ft. New perforations were added just above the plugback depth that resulted in dry-oil production of 950 STB/D.

Well B-235. When the water cut reached approximately 30%, the well was logged with a memory productionlogging tool to identify the water source. Because there were two sets of perforations within a large sand body, the lower set was suspected as the main water contributor. This sand profile is presented in **Fig. 13.15.** This graph also includes the down-pass spinner response profile at different cable speeds to illustrate the congruent nature of the lines, as well as to provide a preliminary indication of the flow contribution over the perforated interval.

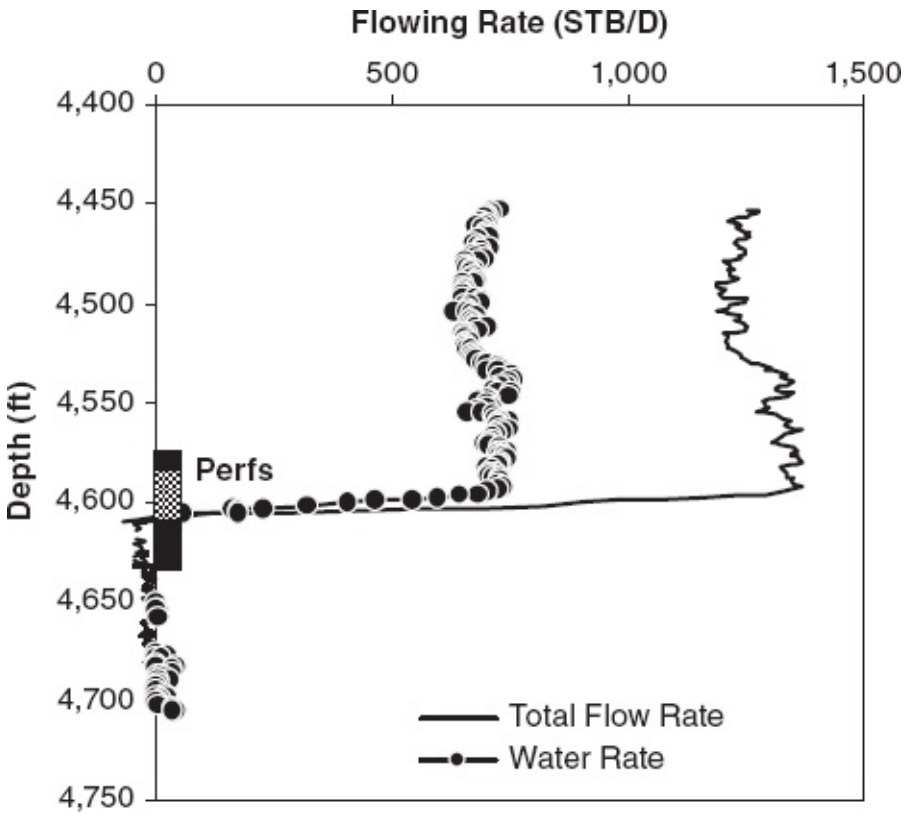

Fig. 13.14—Spinner interpretation.

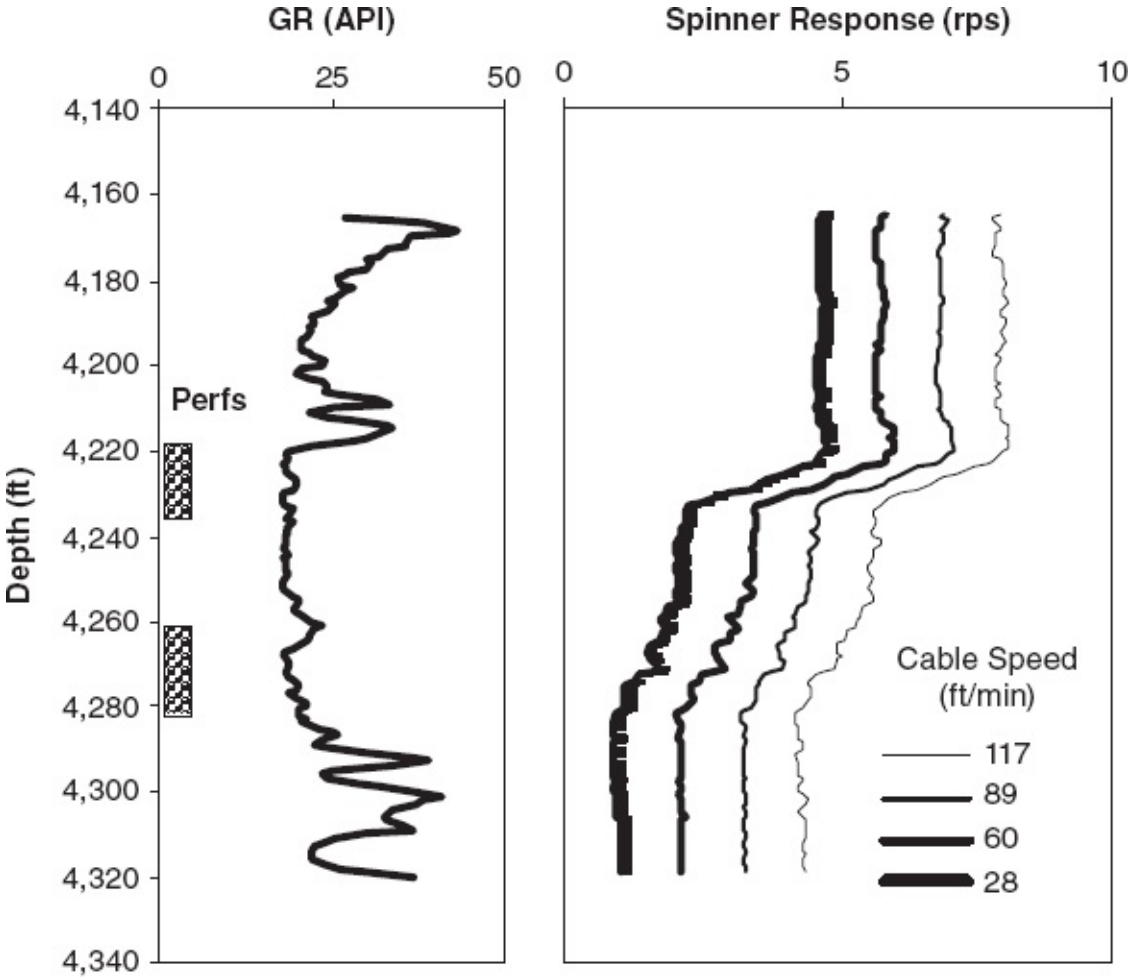

Fig. 13.15—Spinner response at different cable speeds.

For this well, the survey included both static and flowing passes in memory mode. **Fig. 13.16** combines flowing and static FRQT spinner calibration plots for comparison. The *x*-axis intercept in the static condition is approximately zero. Because the two curves overlie each other below the bottom perforations, a sump is clearly indicated. When the two curves separate, fluid entry is observed near the bottom perforation set. Significant separation occurs over the upper perforation set, where the majority of the well's production occurs.

The slope values over the discrete intervals are fairly realistic and constant for the entire logged interval for both the static and the flowing conditions. In addition, the values of the correlation coefficients are close to unity, indicating favorable interpretable data over the entire interval. This is discussed in more detail with the frequency plots presented later.

In **Fig. 13.17,** density and temperature data suggest a static sump below the bottom perforation interval. After the well was shut in, the fluids segregated, leaving oil above the water-filled sump. As a result, the temperature shows a cooling effect as the water migrates downward from higher up in the wellbore. When the flow resumed, separation occurred between the curves in each track. The flowing density data show two distinct changes over the perforated intervals. Similarly, the temperature curve also reflects two points of fluid entry in the wellbore.

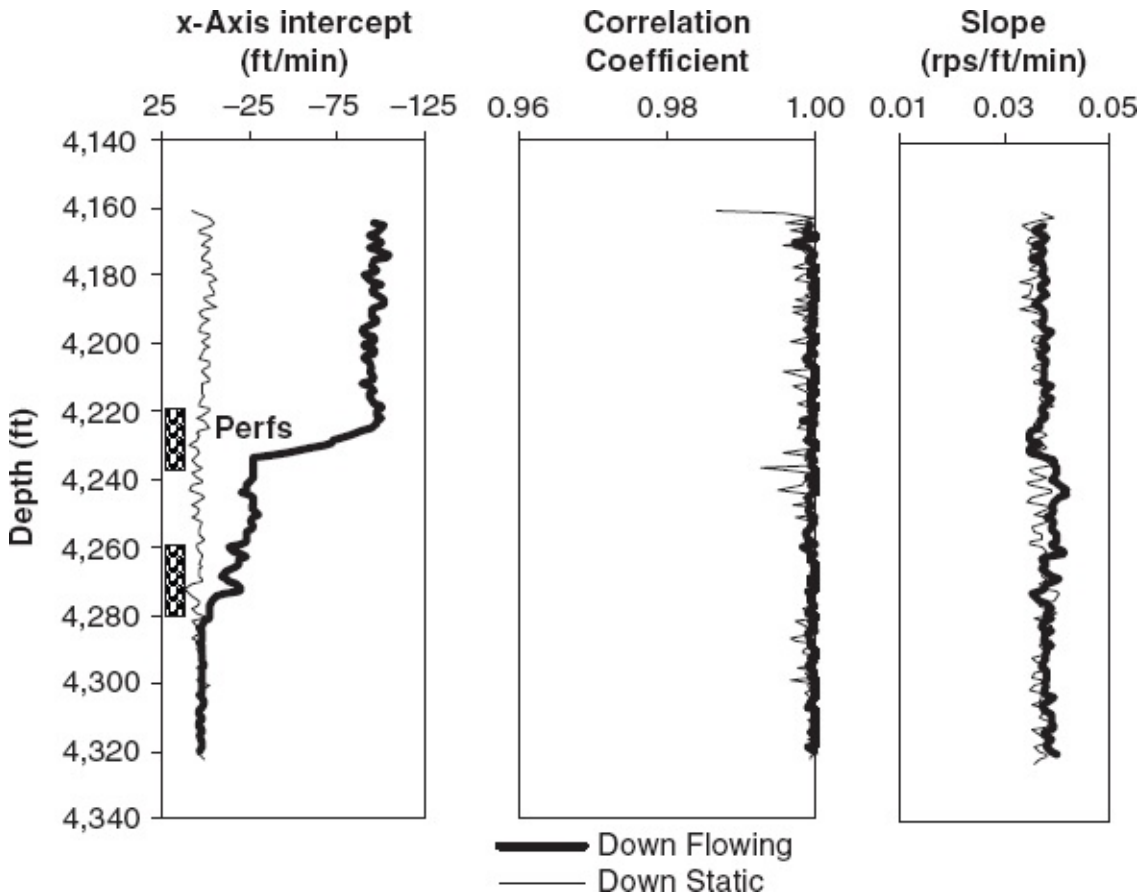

Fig. 13.16—FRQT spinner calibration plot.

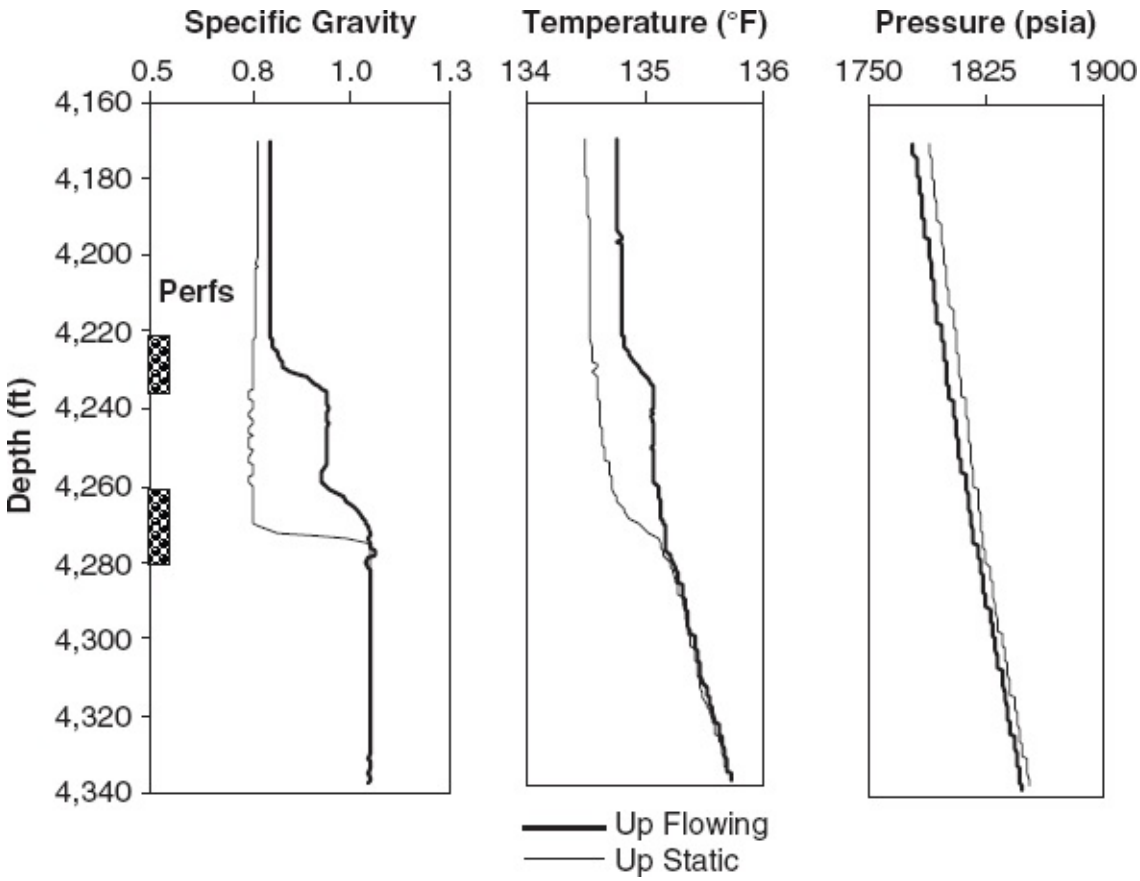

Fig. 13.17—Specific gravity, temperature, and pressure.

In **Fig. 13.18,** the spinner response overlay confirms the profile suggested from earlier graphs. Both the static and the flowing passes overlie each other respectively. On the basis of the downward cable speeds, the curves were shifted accordingly. The static passes are aligned along the y-axis, indicating static conditions. Approximately 30% of the flow originates from the bottom set of perforations, and the remaining 70% from the top set.

For the up passes, there are sections in the individual spinner response traces that are slightly nonparallel. The resulting FRQT display in **Fig. 13.19** indicates that between 4,225 and 4,275 ft, the up-pass flowing correlation coefficient drops to 0.98 with a spike to approximately 0.92. Although the latter correlation is fairly good, it suggests that the data and spinner response passes need reviewing to confirm that they are parallel for the entiredata set. Further, in the same graph, the slope values over the interval change slightly, possibly affecting the intercept values and, hence, the rate.

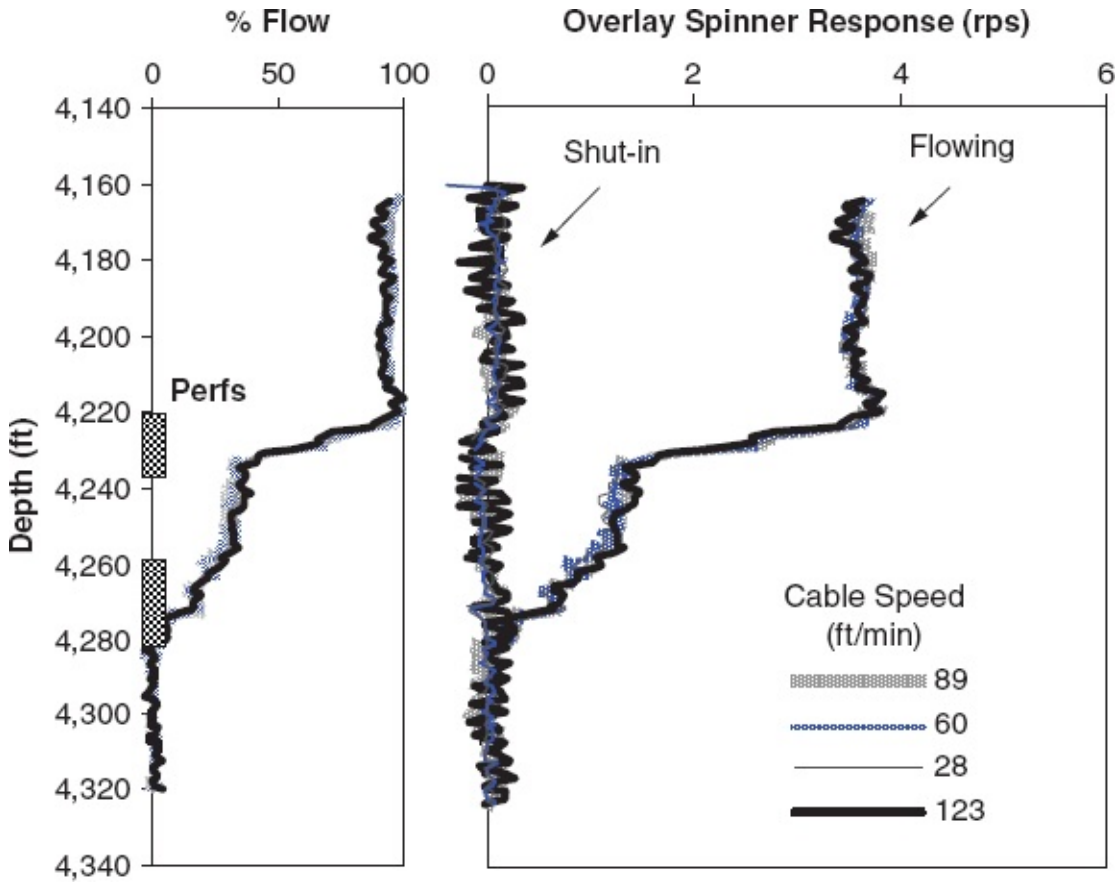

Fig. 13.18—Spinner response overlay.

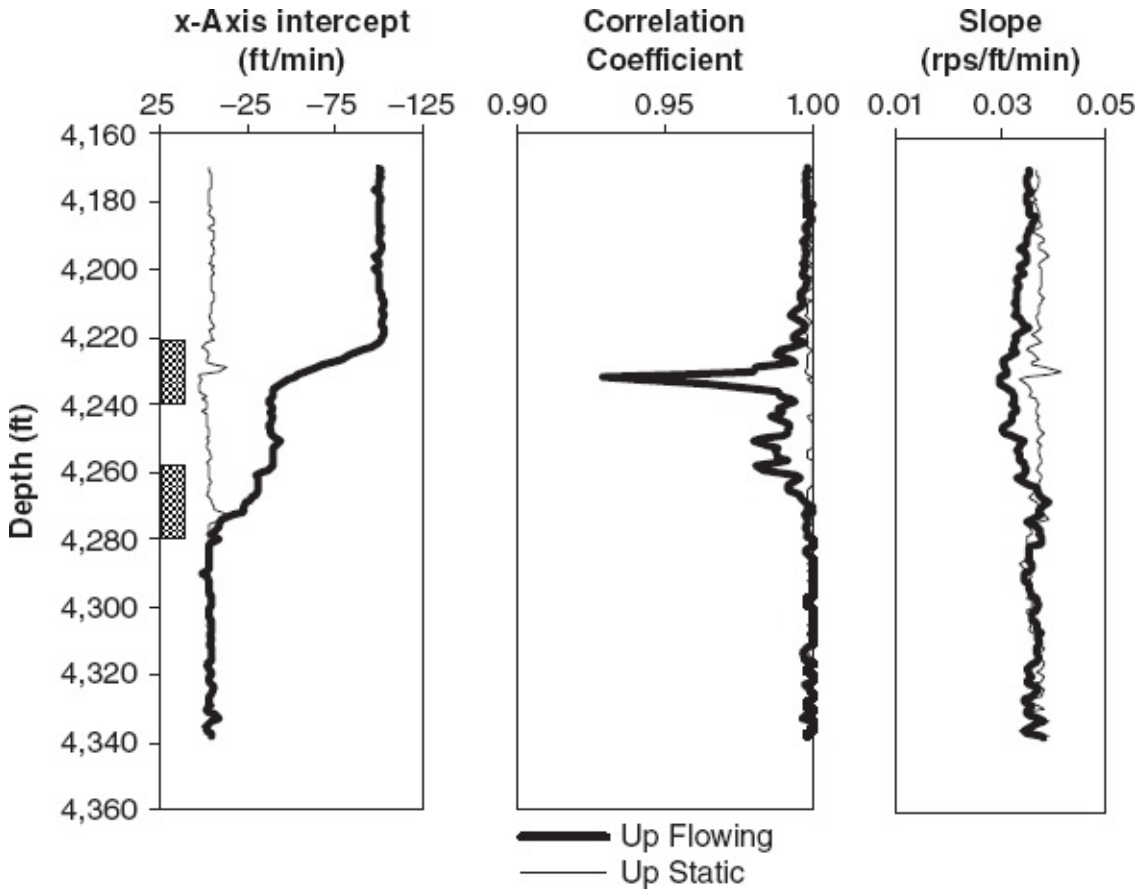

Fig. 13.19—FRQT spinner calibration plot.

For the static conditions, the FRQT plots for the up pass and down pass, in flowing as well as shut-in conditions, still yield basically the same interpretation. However, more confidence can be placed on the down-pass interpretation. **Fig. 13.20,** displaying the frequency plot, mirrors this reality. Here, we observe that the correlation coefficients for down passes are closer to unity than for up passes.

Similarily, the frequency plot for the slope in **Fig. 13.21** shows consistency in the shut-in passes in both directions. This behavior is expected because the spinner tool should encounter the same nonmoving fluid profile over the logged section. The flowing passes yield different slopes; however, the downflowing pass has a smaller range of values and is, overall, closer to the static slope values.

The production rate measured downhole using the spinner tool and converted to surface condition matches the surface portable separator measurement within engineering accuracy. For instance, the spinner tool rate of 4,075 STB/D, shown in **Fig. 13.22,** compares favorably with 4,293 STB/D, measured by a surface separator. The calculated water cuts from the different slip models yield values between zero and 21%, whereas the surface sample shakeout varied from 24 to 30%.

A PNC log was run, and the oil/water contact was verified in the middle of the bottom perforations at 4,270 ft. On the basis of the results of production log interpretation and the PNC log, the well was recommended for a plugback, thereby isolating the bottom set of perforations. Closing the lower set will eliminate the unnecessary water production. Subsequently, a through-tubing bridge plug was set at 4,250 ft and cement was dumped on top up to 4,240 ft. As a result, the well is producing approximately 4,900 STB/D with no water cut, thereby stressing the usefulness of the FRQT. Increased confidence in the interpretation of production log data was thus gained.

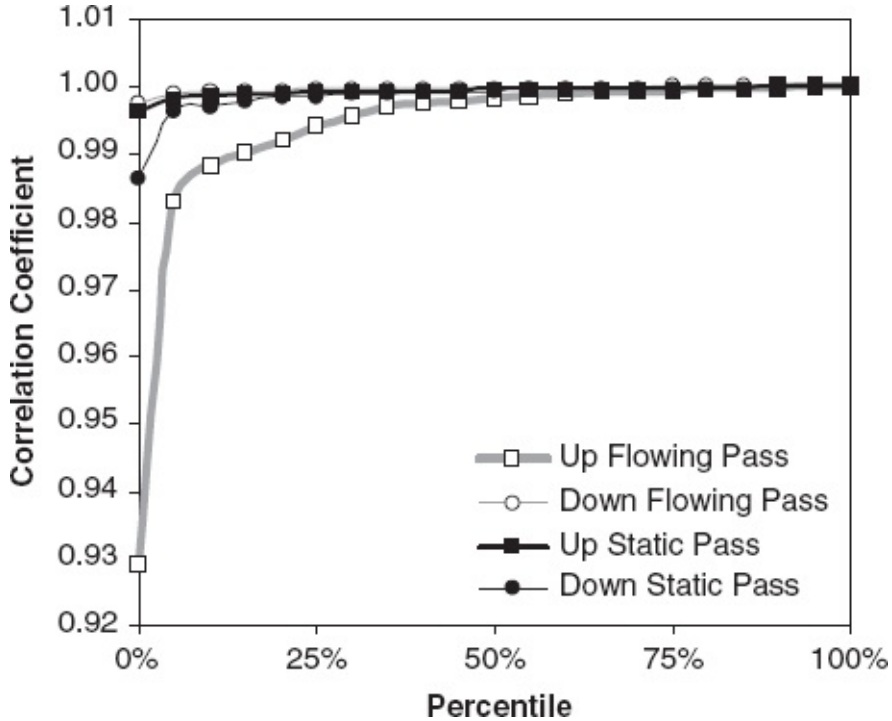

Fig. 13.20—Correlation coefficient frequency.

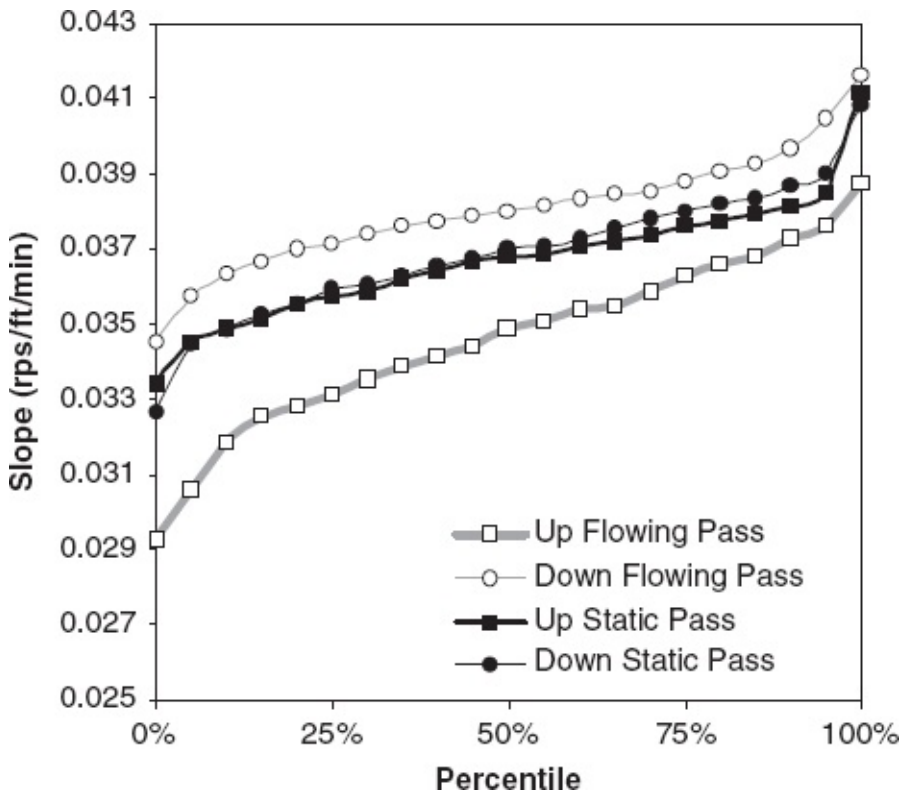

Fig. 13.21—Spinner response slope frequency.

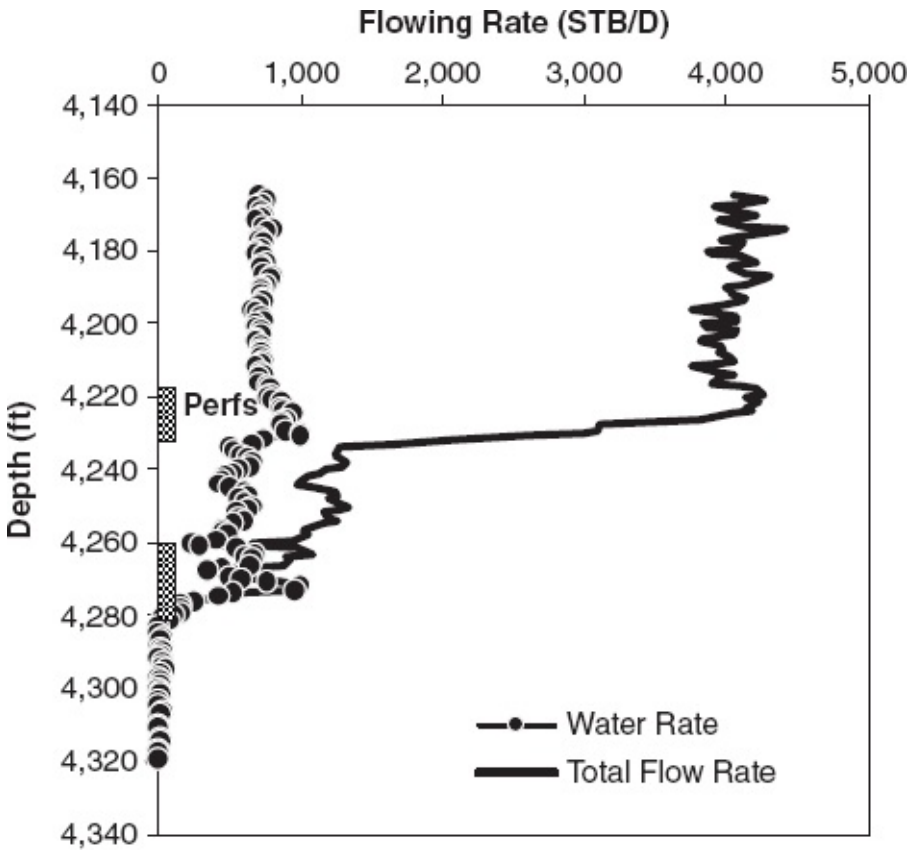

Fig. 13.22—Spinner interpretation.

13.3 Flow Pattern Maps for Production Log Analysis

Traditional interpretation procedures do not normally make explicit use of the flow pattern maps; instead, they establish slip velocity at each station using an empirical correlation. For example, Choquette (1975) correlated slip velocity with density difference between the two phases, with water holdup as the parameter. Although this approach has served the industry quite well, we will discuss an alternative method that provides insights into the mechanics of flow and its impact on the flowmeter response.

We illustrate some of these points with field examples. In all cases, we used the Flores et al. (1999) map, as adapted by Hasan and Kabir (1999) and their holdup model.

13.3.1 Field Examples. This section focuses on four wells to illustrate the alternative method: Well A-55, Well B-235, Well A-22, and Well B-175.

Well A-55. In Well A-55, the fluid entry occurs through a single interval over 4,500–4,510 ft. We graphed the individual phase velocities in **Fig. 13.23.** As shown by the triangles, increases in oil velocity with shallower depth cause most of the flow to occur in the churn flow regime. The chaotic nature of flow, associated with the churn flow pattern, triggers an oscillatory response of the flowmeter, shown in circles. The secondary y-axis, representing the depth, shows the flowmeter response.

Fig. 13.24 displays the raw spinner response curves for up passes. The oscillatory response is evident at all cable speeds, thereby confirming the notion that the churning motion of fluids caused this unusual behavior. This type of flow behavior remained unexplained in the past. Clearly, the flow pattern map helped us identify the root cause of this anomalous response.

An analyst often assigns a single value for the velocity-profile correction factor for all production zones. However, this practice may lead to serious errors in production log analysis because the correction factor, which is the inverse of the flow parameter C_o, depends on the local Reynolds number. As we discussed in Chapters 3 and 4, the value of the flow parameter depends on the bubble concentration profile and the mixture velocity profile. Indeed, Govier and Aziz (2008) presented an elegant analysis for rigorous calculation of C_o when the velocity and concentration profiles are available. In practice, such rigor is unwarranted, given the uncertainties involved in the data. Assuming that the bubbles flow mostly through the channel center simplifies the C_o computation because the mixture velocity profile can be expressed readily as a function of fluid Reynolds number. The essence of this discussion is that the use of a single value for the velocity profile correction factor is often incorrect because changes in flow velocity occur with fluid entry. **Fig. 13.25** illustrates this point for the A-55 well. We used this depth-dependent correction factor to compute velocity of each phase, thereby avoiding any prior assumption in all examples presented here.

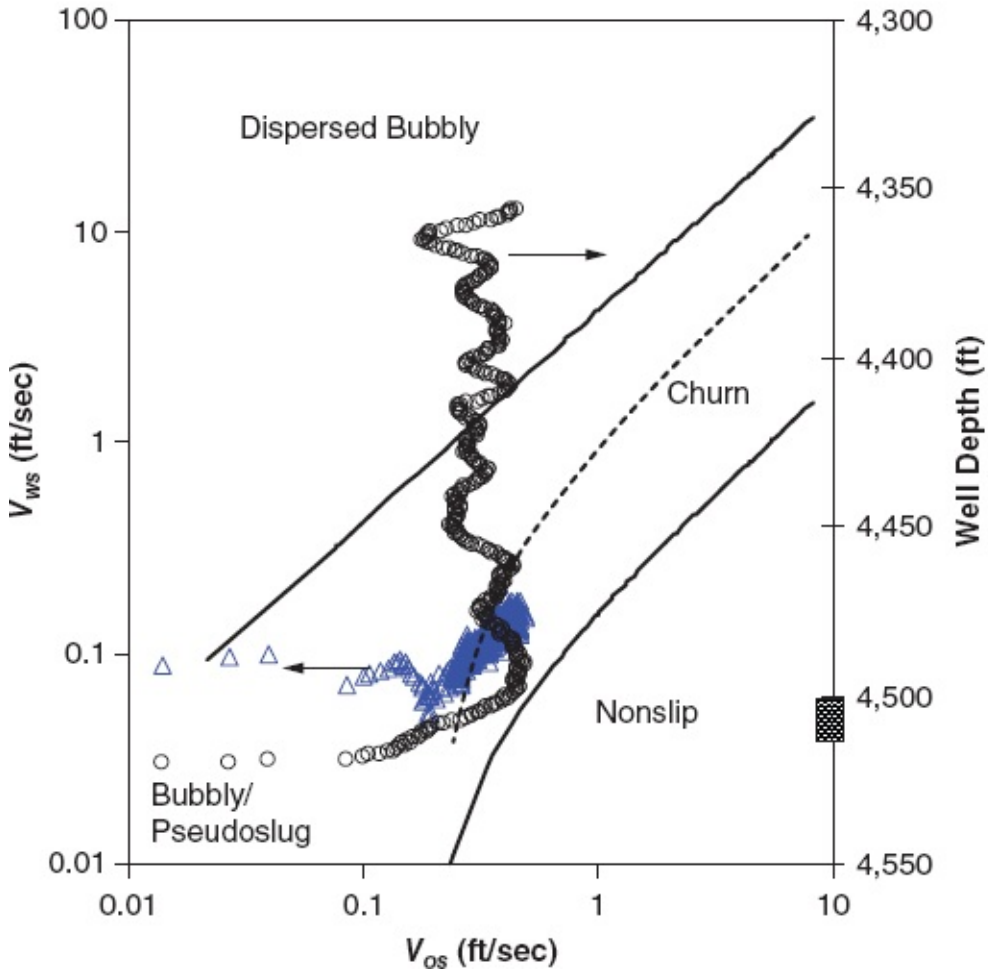

Fig. 13.23—Churn flow affects flowmeter response, Well A-55.

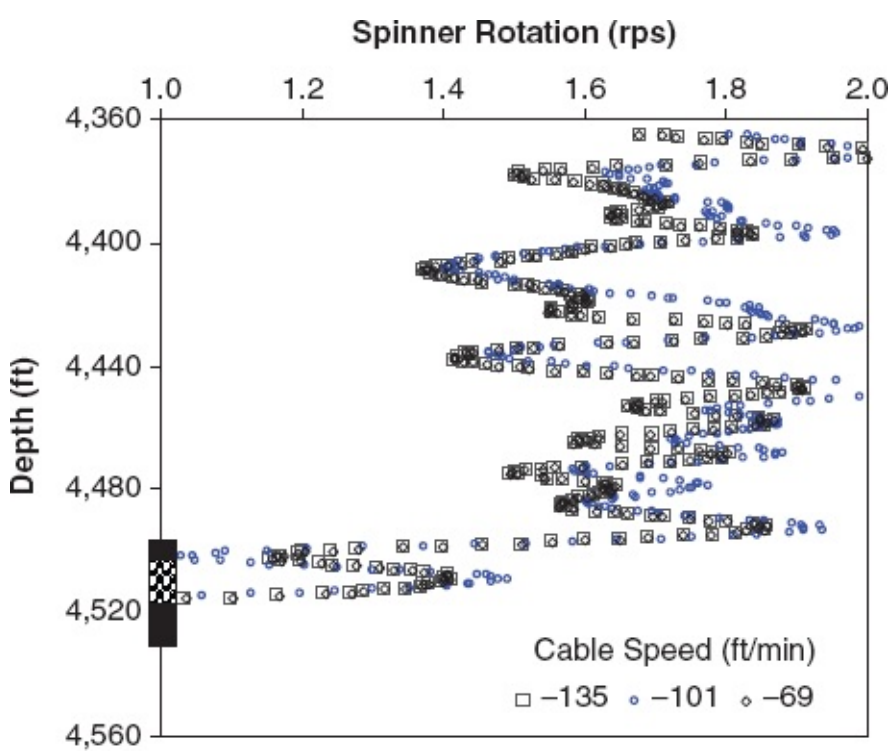

Fig. 13.24—Up-pass spinner overlay shows consistent trend, Well A-55.

Well B-235. The B-235 well was discussed earlier in the preceding section. Fluid entry occurs through two sets of perforations in this well, as depicted in **Fig. 13.26.** Bubbly and pseudoslug flows dominate the entry from the bottom set (4,260–4,280 ft), while homogeneous flow (zero slip) is prevalent above the top set (4,220–4,235 ft) of perforations. Increased oil influx from the upper interval leads to a no-slip situation; that is, $H_w < 0.30$. The smooth response of the flowmeter is not surprising. That is because gentle flow is observed in the laboratory for these two flow patterns. Note that transition through the churn flow pattern occurs over short vertical distance; therefore, it does not present any problem, as in the previous case.

To shed light on sensor response, we compared the measured holdup with holdup computed from two models (Hasan and Kabir 1999; Flores et al. 1998) in **Fig. 13.27.** Overall, the agreement between measurement and models is quite good. However, both models tend to overestimate the holdup following the fluid entry. We suspect that the flowmeter had difficulties in responding to the turbulent eddies. That is because sharp excursions to the right occur only for the velocity-based sensor (model-derived values), but not for the density-based sensor (data). In other words, inaccuracies in flow measurements precipitate this mismatch.

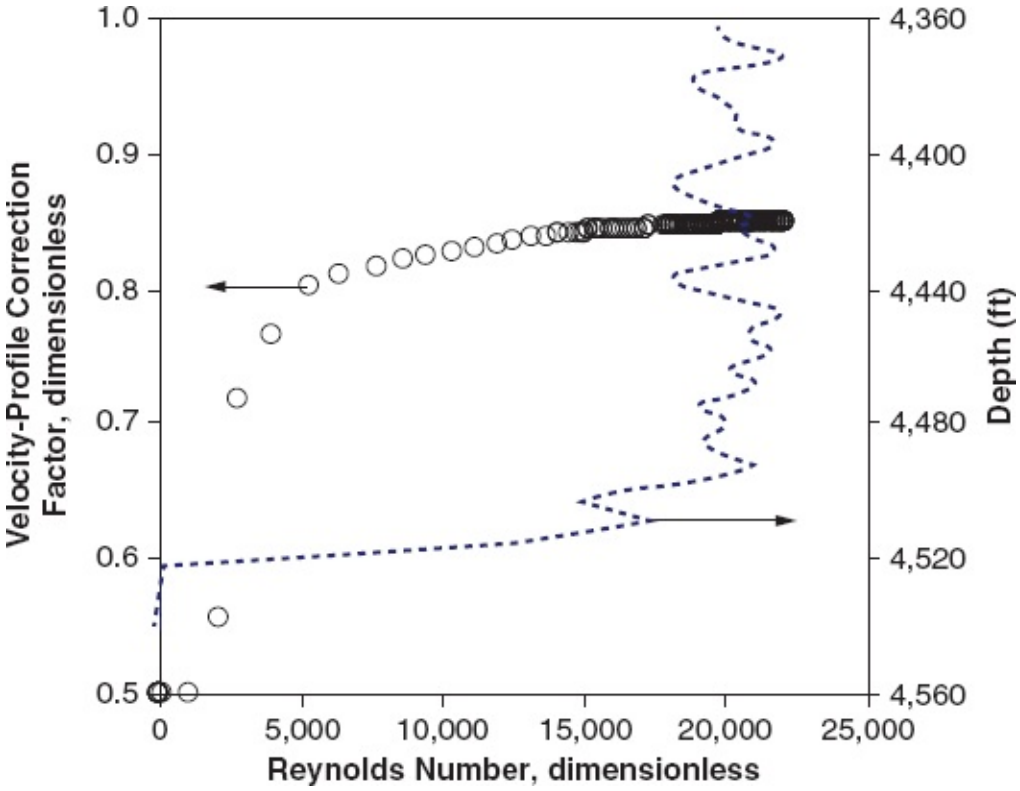

Fig. 13.25—Depth-dependent velocity-profile correction factor, Well A-55.

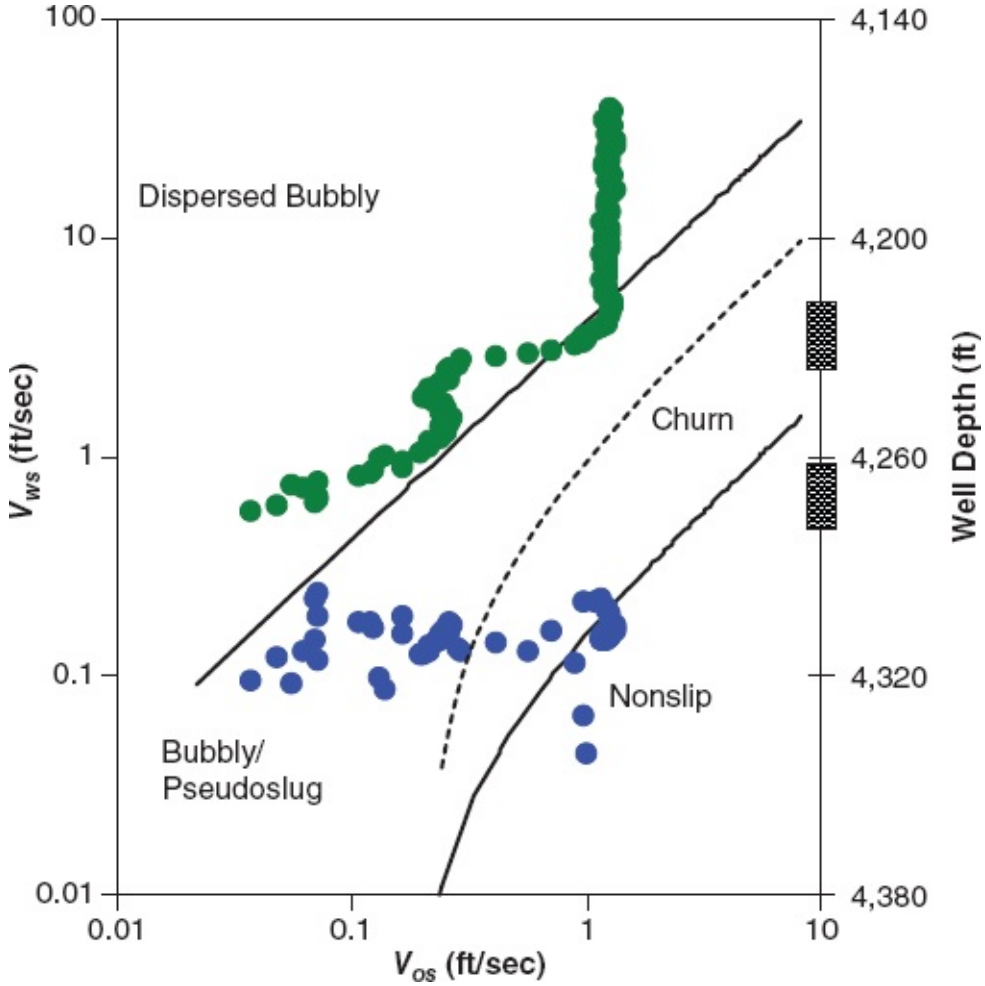

Fig. 13.26—Flowmeter response insensitive to flow regimes, Well B-235.

Well A-22. Well A-22 was also discussed in the preceding section. Here, the velocity of the fluid entry occurring through a single interval (4,570–4,610 ft) is low enough to cause bubbly flow only. **Fig. 13.28** illustrates this point. The higher velocity associated with the up pass presents an unambiguous flowmeter trace. In contrast, the down pass exhibits a spike at the top because of spinner resolution at a low velocity. This point is made clear by the overlay of down-pass spinner response, as shown in **Fig. 13.29.** Only the data corresponding to the lowest cable speed (33 ft/min), which is the trace in question, depart from the norm. Therefore, in this case, flow-pattern-induced problems can safely be ruled out. As we stressed in the preceding section, one must examine all traces for quality control before including them in flow interpretation.

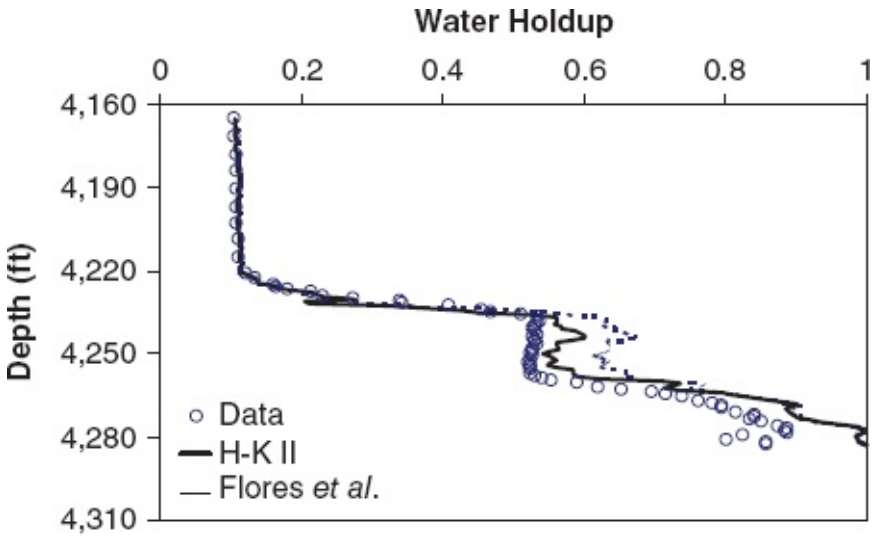

Fig. 13.27—Comparison of holdup calculations, Well B-235.

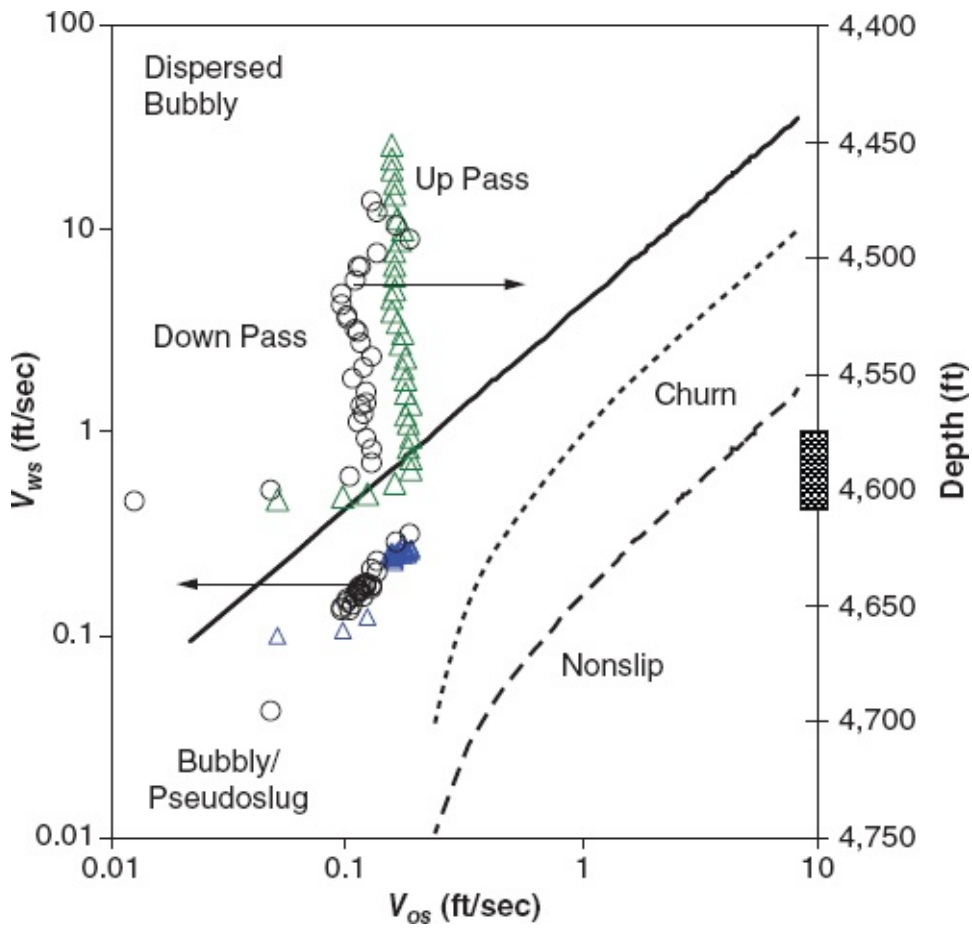

Fig. 13.28—Flowmeter response insensitive to bubbly flow, Well A-22.

Well B-175. In the Well B-175 example, we illustrate the goodness of model-derived water holdup results with those obtained from two independent measurements. **Fig. 13.30** shows that the bubbly/pseudoslug flow pattern is observed in this well. Comparisons of holdup calculations are made with those obtained from differential manometer-type tool and the bubble-imaging sensor. **Fig.**

13.31 compares the performance of the Hasan-Kabir (1999) model with two independent measurements.

The general overestimation by the imaging sensor is explained by the presence of four low-frequency resistivity probes mounted around the tool's periphery—that is, near the casing wall. Consequently, fewer bubbles are observed by the probes because the bubbles have a tendency to flow through the center of the channel. In other words, positioning of the probes leads us to observe a disproportionately higher volume of the continuous phase, which is water. Thus, in a vertical wellbore, we should expect to observe a somewhat higher H_w value if water is the continuous phase. Conversely, we would observe a lower H_w value than that measured by a centralized manometer-type tool if oil is the continuous phase. Bear in mind that neither the water-cut measurement at surface nor the in-situ density measurement has enough precision for a perfect agreement of all three traces. Nonetheless, the agreement shown here is rather reassuring.

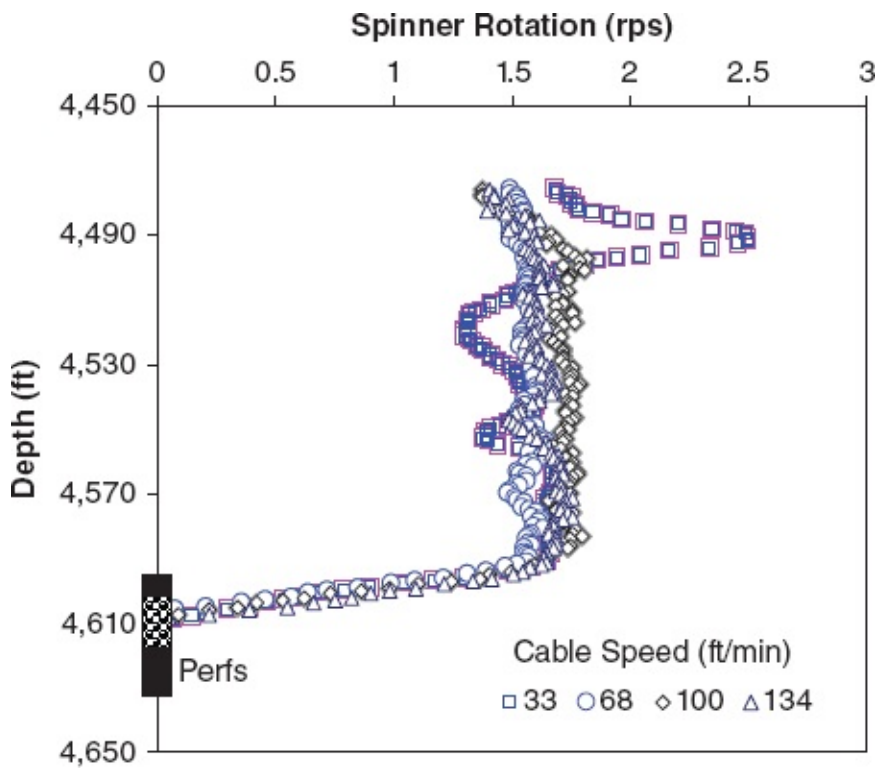

Fig. 13.29—Down-pass spinner overlay identifies the problem pass, Well A-22.

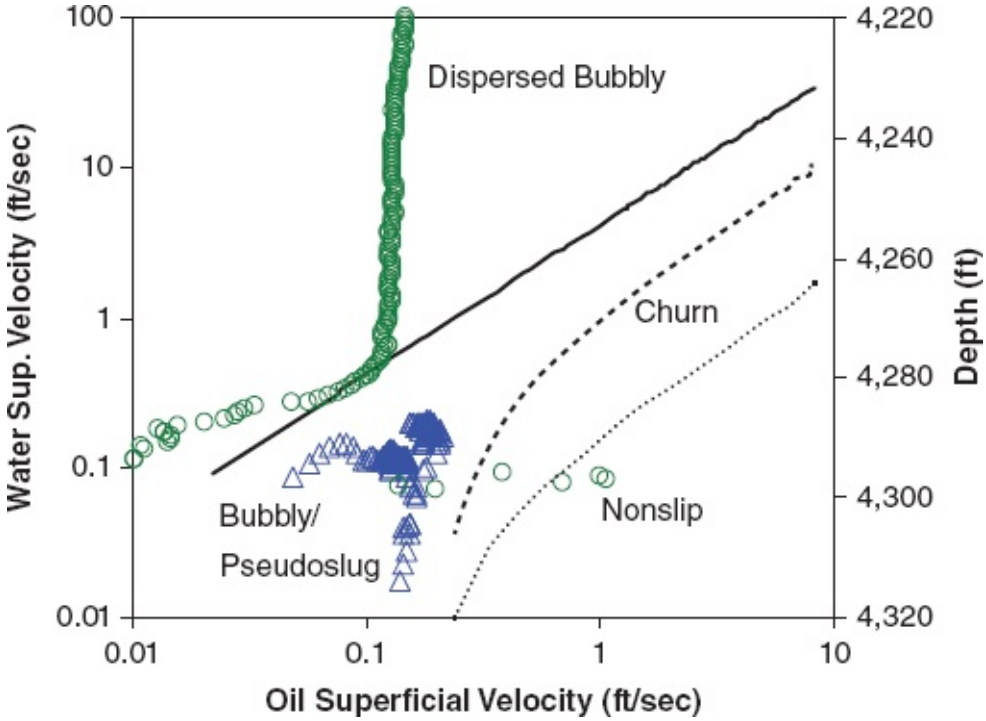

Fig. 13.30—Flowmeter response insensitive to bubbly flow, Well B-175.

13.4 Rate Estimation From Temperature Surveys

We showed in Chapter 7 that the dependence of flowing-fluid temperature on flow rate can be used to estimate flow rate when temperature is known. In this section, we show how the rigorous temperature expression is simplified under specific circumstances during temperature logging to obtain rate. The differential (Eq. 6.26) and integral (Eq. 6.29) expressions for the flowing-fluid temperature in a simple producing well are reproduced below.

$$\frac{dT_f}{dz} = \pm L_R(T_f - T_{ei}) + \frac{g\sin\alpha}{c_p J g_c} + \phi \qquad (6.26)$$

and

$$T_f = T_{ei} + \frac{1 - e^{(z-L)L_R}}{L_R}\left(g_G \sin\alpha + \phi + \frac{g\sin\alpha}{c_p J g_c}\right), \qquad (6.29)$$

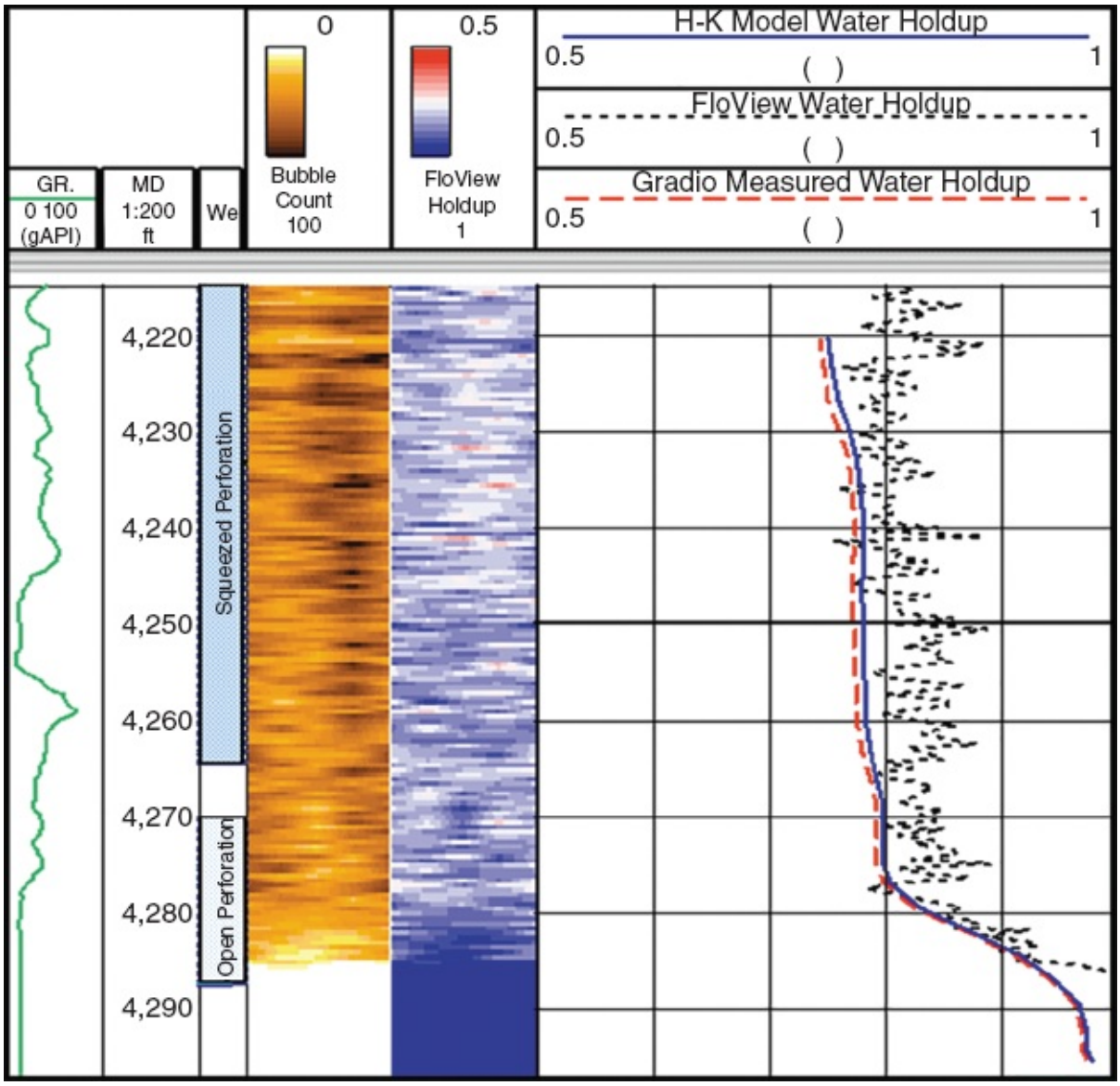

Fig. 13.31—Comparison of measured and computed holdup, Well B-175.

where

$$\phi = -\frac{v}{c_p J g_c}\frac{\mathrm{d}v}{\mathrm{d}z} + C_J \frac{\mathrm{d}p}{\mathrm{d}z} \qquad (6.27)$$

and

$$L_R \equiv \frac{2\pi}{c_P w}\left[\frac{r_{to} U_{to} k_e}{k_e + \left(r_{to} U_{to} T_D\right)}\right] \qquad (6.20)$$

Therefore, in long producing wells at shallow depths, when $(z - L) \rightarrow -\infty$, the fluid temperature profile becomes asymptotic and the difference between fluid and formation temperatures becomes constant. This constant temperature difference, T_f –

T_{ei}, is related to L_R, which is in turn related to the mass flow rate w or the desired flow rate. Rewriting Eq. 6.33 for *shallow depths*, we have

$$T_f - T_{ei} = \frac{1}{L_R}\left(g_G \sin\alpha + \phi + \frac{g \sin\alpha}{c_p J g_c}\right) \quad (13.3)$$

Eq. 13.3 is particularly useful for estimating zonal contributions because estimated L_R from various zones will essentially be proportional to production rates; that is,

$$\frac{L_{R1}}{L_{R2}} = \frac{w_2}{w_1} = \frac{\left(T_f - T_{ei}\right)_1}{\left(T_f - T_{ei}\right)_2} \quad (13.4)$$

Similarly, for many single-phase oil production scenarios, when $\phi \approx -g \sin\alpha$, Eq. 13.3 simplifies to

$$L_R = \frac{(T_f - T_{ei})}{\left(\mathrm{d}T_f / \mathrm{d}z\right)} \quad (13.5)$$

Measured fluid and formation temperature profiles can be used with Eq. 13.5 to estimate L_R, which allows rate estimation. Similar to Eq. 13.3, Eq. 13.5 is useful for estimating zonal contributions. Combining Eqs. 13.4 and 13.5, we have

$$\frac{L_{R1}}{L_{R2}} = \frac{w_2}{w_1} = \left(\frac{T_f - T_{ei}}{\mathrm{d}T_f / \mathrm{d}z}\right)_1 \Bigg/ \left(\frac{T_f - T_{ei}}{\mathrm{d}T_f / \mathrm{d}z}\right)_2 \quad (13.6)$$

The expressions for the flow rate in terms of temperature discussed above use various simplifying assumptions, which may not be robust in many practical cases, and so more-rigorous computations using Eq. 6.33 may be required.

13.4.1 Distributed-Flow Profiling. In most cases, temperature logs are run to assess flow contributions from different intervals. However, in some cases wells may be instrumented to offer distributed temperature data in the wellbore. When such data are available, energy balance can be applied to estimate zonal fluid contribution. In its simplest form, the analysis can be construed as that of the “mixing cup” approach. Consider **Fig. 13.32** depicting fluid entry at w_2 lbm/hr from a production horizon and mingling with the fluids from down below (w_1). By neglecting changes in all other forms of energy except heat, we can write

$$w_1 c_{p1} T_{f1} + w_2 c_{p2} T_{f2} = \left(w_1 + w_2\right) c_p T_f, \quad (13.7)$$

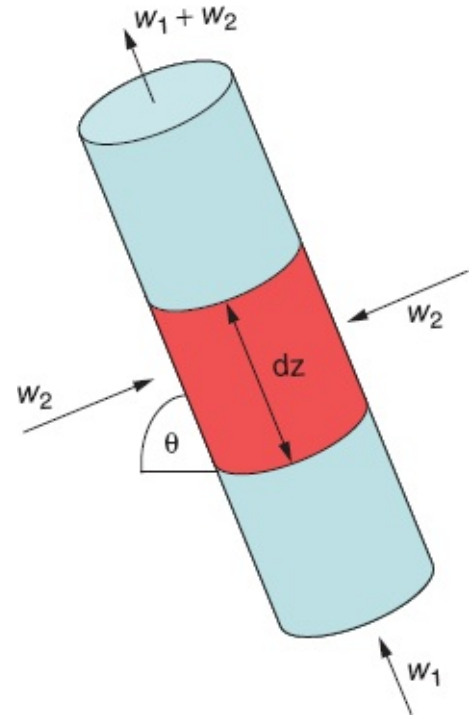

Fig. 13.32—Wellbore schematic for energy balance across a production zone.

where c_p and T_f are the specific heat and temperature of the mixed fluid. If the specific heat values of the reservoir fluid and the wellbore fluid are the same, Eq. 13.7 can be simplified to the following expression:

$$\frac{w_1}{w_2} = \frac{c_{p2}\left(T_f - T_{f2}\right)}{c_{p1}\left(T_f - T_{f1}\right)} \quad \text{(13.8)}$$

For more-rigorous computations, changes in all forms of energy must be accounted for. Wang et al. (2008) and Kabir et al. (2012b) presented such a rigorous model with the following differential equation for the producing horizon of interest.

$$\frac{\mathrm{d}T_f}{\mathrm{d}z} + \frac{(1-\lambda)}{\lambda}\frac{(T_f - T_{fe})}{\mathrm{d}z} = \frac{L_R}{\lambda}(T_{ei} - T_f) + \left(\frac{g\sin\alpha}{Jg_c C_p} + \phi\right), \quad \text{(13.9)}$$

where λ is the fraction of total production from zone 1, given as

$$\lambda = \frac{w_1}{w_1 + w_2} \quad \text{(13.10)}$$

Eq. 13.9 is solved for the rate for a given fluid temperature with the finite-difference method. As discussed in Chapter 7, when multiple temperature data are available, an iterative process may be needed to minimize error in estimating temperature for a given rate. Note that the solution requires evaluation of the Joule-Thomson coefficient, which is given by

$$C_J = \frac{1}{c_P}\left[\frac{xT}{Z\rho_g}\left(\frac{\partial Z}{\partial T}\right)_P - (1-x)(1-T\beta)/\rho_L\right] \quad (13.11)$$

In Eq. 13.11, β is liquid volume expansion factor and x is the mass fraction of gas in the two-phase mixture.

13.4.2 Field Examples. This subsection presents two field examples to illustrate application of the model just discussed. The first one involves oil/water flow, and the second one involves a dry-gas flow problem.

Oil/Water Field Example. This oil/water example was originally presented by Ouyang and Belanger (2006) and was subsequently analyzed by Wang et al. (2008) and Kabir et al. (2012b). For simplicity, we use the data presented by the original authors. **Fig. 13.33** depicts the production contributions from three horizons, with water entering from the bottom interval only. We used the homogeneous two-phase flow analysis for the entire-wellbore approach, with the bottom-up computation starting at 2,000 ft. Because we are interested in estimating the total flow rate from the zones, the coupled fluid and heat flow modeling from the top of perforations became the starting point. In this case, modeling of homogeneous flow is justified because the oil volume fraction is approximately 0.7 (Chapter 4, Section 4.4.4).

Following the model setup, we estimated the fluid temperature profile and attained a good agreement with the simulated data. **Fig. 13.34** shows the match and presents the main results of the entire-wellbore approach. Note that we obtained a total liquid rate of 3,006 STB/D, which is in close agreement with the reported value of 3,000 STB/D.

Gas-Well Field Example. This field example comes from a dry-gas reservoir. Data were collected with a conventional production logging run. Using the procedure described earlier, a good quality match was attained with the Wang et al. (2008) and Kabir et al. (2012b) models, as **Fig. 13.35** indicates. Approximately 80% of the production occurs from the top of the formation, while the remaining percentage comes from the bottom part of this highly heterogeneous carbonate reservoir. This high-quality match instills confidence in the solution obtained.

13.5 Discussion

Specifying the logging data requirements and suitably presenting the information are important aspects of making an appropriate production log interpretation. If data are not analyzed over the entire log section, some significant well behavior may be overlooked. In particular, turbulence within the wellbore, jetting through perforations, flow channeling from below, changes in fluid properties, and mechanical problems of a spinner tool may not be evident from limited and specific-depth interpretations. In some instances, poor spinner response can be identified and prevented from influencing the prodcution log interpretation. As illustrated in the first field example, we could have incorrectly interpreted the anomalous spinner response spike as crossflow

or flow contribution.

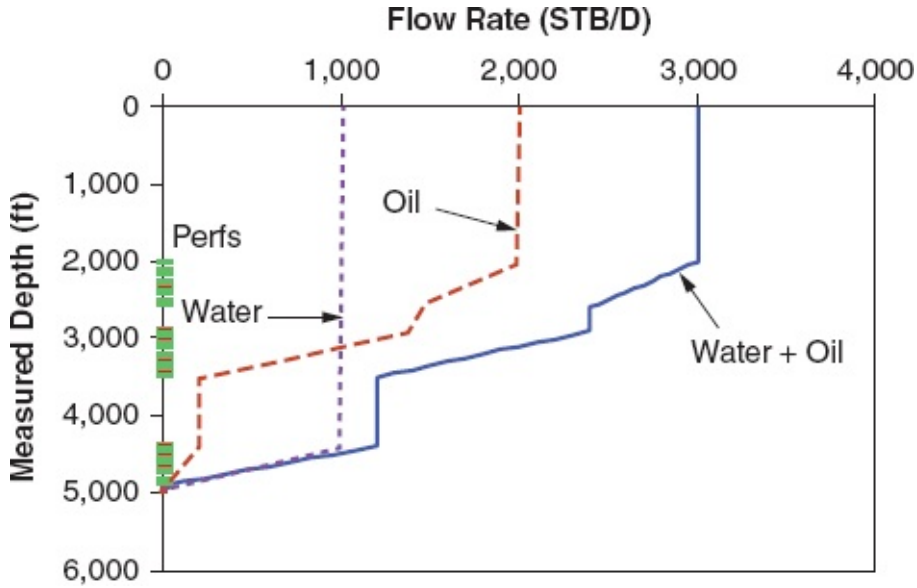

Fig. 13.33—Flow contributions from different horizons are indicated.

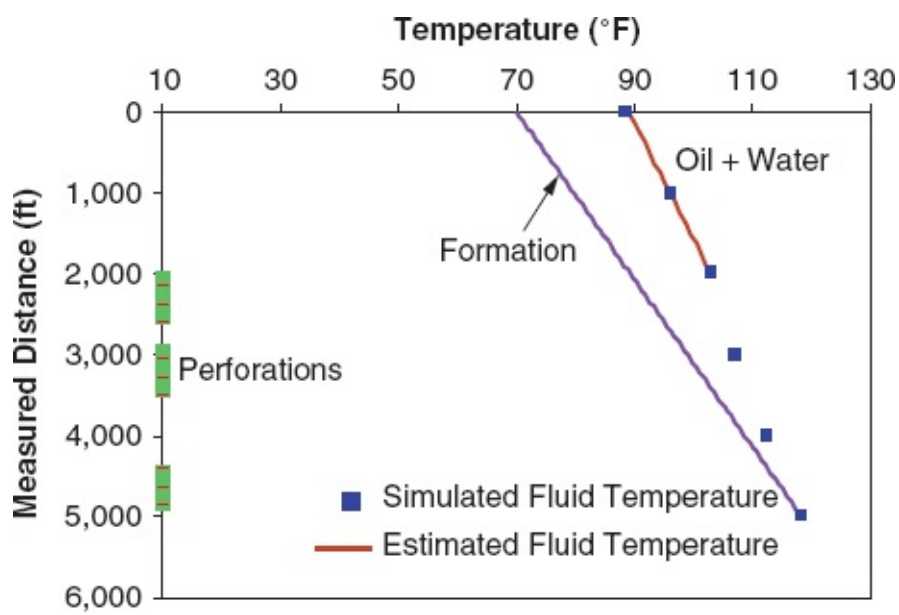

Fig. 13.34—Matching the original fluid temperature profile en route to rate estimation.

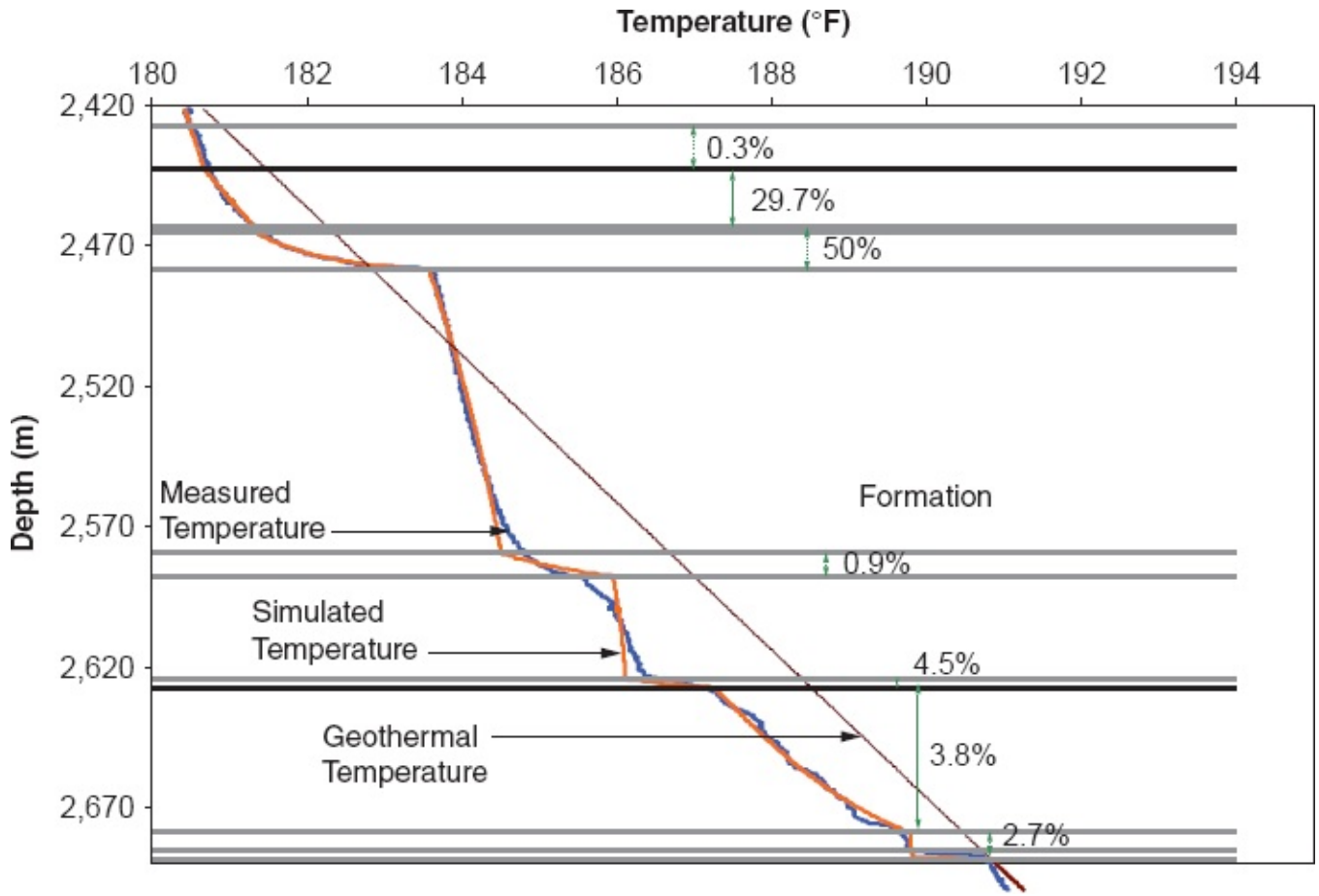

Fig. 13.35—Matching distributed temperature, gas-well field example.

By generating the FRQT display instead of the traditional calibration plot, an improved assessment of the flow profile may be achieved through increased understanding. Reviewing specific data over the intervals of lower correlation coefficients and changing spinner response slopes can help discern poor data quality from a well's inherent producing characteristics. Through repeated application of this procedure, an analyst can quickly perform a quality check of the log, as well as gain an improved understanding of the well and field performance characteristics.

The use of flow-pattern-based models—that is, those of Flores et al. (1999) and Hasan and Kabir (1999)—allows understanding of flow regimes prevalent in downhole conditions. For instance, one can conceivably adjust flow conditions to minimize churn flow while logging. We have also identified that smooth holdup response may be derived from a manometer-type tool. However, when the same information is obtained from a flowmeter using a two-phase flow model, overestimation may occur because of the uncertainties in the tool response in the wake of fluid entry. The basic idea is to collect unambiguous information, which can be aided by on-site usage of a flow pattern map and holdup computation. The imaging sensor is a welcome addition to the production logging tool inventory. One must, however, understand the measurement principle before making a comparison with the standard tool response.

Summary

In this chapter, we presented two elements to improve understanding of tool response and flow mechanics in production log interpretation. The first element involves the use of a systematic procedure, called the FRQT analysis. This approach makes use of the full suite of data in that the continuous-depth spinner calibration plot can identify intervals over which data are suspect and require exclusion from interpretation. We recommend simultaneous plotting of data from static passes, constituting the baseline, and flowing passes. In other words, presenting density, pressure, and temperature of both passes on the same graph facilitates and confirms production log interpretation. The frequency plots of spinner response slopes and correlation coefficients provide a measure of data quality and consistency.

The second element revolves around integrating flow pattern maps in production log interpretation. Use of a flow pattern map helps one discern fluid entry points, which in turn reveal much information about the prevailing flow regimes, show any anomaly in flowmeter response, and, above all, provide insights into mechanics of flow. For instance, holdup derived from the density-based sensor will have a different response from holdup derived from the velocity-based sensor. Finally, we presented an approach for estimating flow rates from temperature logs; the reader can gain further insights from Chapter 7.

Nomenclature

C_o = flow distribution parameter, dimensionless

C_j = Joule-Thomson coefficient, °F/psi

C_p = fluid specific heat at constant pressure, Btu/lbm-°F

f = spinner response, rev/sec

g = gravitational acceleration, ft/sec^2

g_c = conversion factor, 32.17 (lbm-ft)/lbf-sec^2

g_G = geothermal gradient, °F/ft

J = conversion factor, 778 (ft-lbf)/Btu

k_e = conductivity of earth or formation, Btu/hr-ft-°F

L = total vertical well depth, ft

L_R = relaxation-distance parameter, 1/ft

m_n = negative spinner response slope, rev/ft

m_p = positive spinner response slope, rev/ft

p = pressure, psia

q = liquid flow rate, STB/D

r_{to} = tubing outside radius, ft

T_D = dimensionless temperature, dimensionless

T_{ei} = static formation temperature, °F

T_f = fluid temperature, °F

U = overall-heat-transfer coefficient, Btu/hr-ft^2-°F

v = fluid velocity related to temp logs (Eq. 6.27), ft/sec

v_e = effective (fluid) velocity = $v_e = v_f + v_T$, ft/sec

v_f = fluid velocity, ft/sec

v_o = in-situ oil velocity, ft/sec

v = superficial oil velocity, ft/sec

v_t = threshold velocity, ft/sec

v_T = tool velocity, ft/sec

v_{ws} = superficial water velocity, ft/sec

w = mass flow rate of fluid, lbm/hr

z = depth coordinate, ft

α = well inclination from horizontal, degrees

Φ = lumped parameter defined by Eq. 6.27, °F/ft

λ = fraction of total production (Eq. 13.10), dimensionless

γ = specific gravity

Subscripts

1, 2 = depth location

References

Achong, I. 1961. Revised Bean Performance Formula for Lake Maracaibo Wells. Shell International Report (October 1961).

Acuna, H. G., Schmidt, Z., and Doty, D. R. 1992. Modeling of Gas Rates Through 1-in., Nitrogen-Charged Gas-Lift Valves. Presented at the SPE Annual Technical Conference and Exhibition, Washington, DC, 4–7 October. SPE-24839-MS. https://doi.org/10.2118/24839-MS.

Acuña, J. A. and Arcedera, B. A. 2005. Two-Phase Flow Behavior and Spinner Data Analysis in Geothermal Wells. *Proc*., Thirtieth Workshop on Geothermal Reservoir Engineering, Stanford University, Stanford, California, 31 January–2 February. SGP–TR–176.

Adams, A. J. and MacEachran, A. 1994. Impact on Casing Design of Thermal Expansion of Fluids in Confined Annuli. *SPE Drill & Compl* **9** (3): 210–216. SPE-21911-PA. https://doi.org/10.2118/21911-PA.

Aggour, M. A. and Al-Yousef, H. Y. 1996. Vertical Multiphase Flow Correlations for High Production Rates and Large Tubulars. *SPE Prod & Fac* **11** (1): 41–48. SPE-28465-PA. https://doi.org/10.2118/28465-PA.

Alamu, M. B. 2012. Gas-Well Liquid Loading Probed With Advanced Instrumentation. *SPE J.* **17** (1): 251–270. SPE-153724-PA. https://doi.org/10.2118/153724-PA.

Al-Hadhrami, A. K., Elliott, L., and Ingham, D. B. 2003. A New Model for Viscous Dissipation in Porous Media Across a Range of Permeability Values. *Transport in Porous Media* **53** (1): 117–122. https://doi.org/10.1023/A:1023557332542.

Almehaideb, R. A., Aziz, K., and Pedrosa, O. A. 1989. A Reservoir/Wellbore Model for Multiphase Injection and Pressure Transient Analysis. Presented at the SPE Middle East Oil Show, Manama, Bahrain, UAE, 11–14 March. SPE-17941-MS. https://doi.org/10.2118/17941-MS.

Almeida, A. R. 2011. A Model to Calculate the Theoretical Critical Flow Rate Through Venturi Gas Lift Valves. *SPE J.* **16** (1): 134–147. SPE-126184-PA. https://doi.org/10.2118/126184-PA.

Al-Safran, E. M. and Kelkar, M. 2009. Prediction of Two-Phase Flow Boundary and Mass-Flow Rates Across Chokes. *SPE Prod & Oper* **24** (2): 249–256. SPE-109243-PA. https://doi.org/10.2118/109243-PA.

Alves, I. N., Alhanati, F. J. S., and Shoham, O. 1992. A Unified Model for Predicting Flowing Temperature Distribution in Wellbores and Pipelines. *SPE Prod Eng* **7** (4): 363–367. SPE-20632-PA. https://doi.org/10.2118/20632-PA.

Ameen, M. M. 1992. *Unified Model for Two-Phase Flow and Heat Transfer in Wellbores*. MS thesis, University of North Dakota, Grand Forks, North Dakota (1992).

Anders, J. L., Cismoski, D. A., Daniel, R. J. et al. 2008. Prudhoe Bay Well P2 15 Surface Casing Collapse. Presented at the SPE Annual Technical Conference and Exhibition, Denver, 21–24 September. SPE-116771-MS. https://doi.org/10.2118/116771-MS.

Anderson, R. A., Smolen, J. J., Laverdiere, L. et al. 1980. A Production Logging Tool With Simultaneous Measurements. *J Pet Technol* **32** (2): 191–198. SPE-7447-PA. https://doi.org/10.2118/7447-PA.

Ansari, A. M., Sylvester, N. D., Sarica, C. et al. 1994. A Comprehensive Mechanistic Model for Upward Two-Phase Flow in Wellbores. *SPE Prod & Fac* **9** (2): 143–151. *Trans*., AIME, **297.** SPE-20630-PA. https://doi.org/10.2118/20630-PA.

API RP 11V5, Operation, Maintenance, Surveillance, and Troubleshooting of Gas-Lift Installations, second edition. 1999. Washington, DC: API. http://www.engineer.documents.org/4842-API-RP-11V7-pdf.html.

API RP 11V5, Operation, Maintenance, Surveillance, and Troubleshooting of Gas-Lift Installations, third edition. 2008. Washington, DC: API.

API RP 19G2, Flow-Control Devices for Side-Pocket Mandrels. 2010. Washington, DC: API.

API RP 90, Annular Casing Pressure Management for Offshore Wells, first edition. 2006. Washington, DC: API. http://docs.regulations.justia.com/entries/2009-07-31/E9-17874.pdf.

App, J. F. 2010. Nonisothermal and Productivity Behavior of High-Pressure Reservoirs. *SPE J.* **15** (1): 50–63. SPE-114705-PA. https://doi.org/10.2118/114705-PA.

App, J. F. and Yoshioka, K. 2013. Impact of Reservoir Permeability on Flowing Sandface Temperatures: Dimensionless Analysis. *SPE J.* **18** (4): 685–694. SPE-146951-PA.

Aschehoug, M. and Kabir, C. S. 2013. Real-Time Evaluation of Carbon Dioxide Production and Sequestration in a Gas Field. *SPE Res Eval & Eng* **16** (2): 134–143. SPE-163149-PA.

Asheim, H. 1986. MONA: An Accurate Two Phase Well Flow Model Based on Phase Slippage. *SPE Prod Eng* **1** (3):

221–230. SPE-12989-PA. https://doi.org/10.2118/12989-PA.

Asheim, H. 1988. Criteria for Gas-Lift Stability. *J Pet Technol* **40** (11): 1452–1456. SPE-16468-PA. https://doi.org/10.2118/16468-PA.

Asheim, H., Kolnes, J., and Oudeman, P. 1992. A Flow Resistance Correlation for Completed Wellbore. *J Pet Sci & Eng* **8** (2): 97–104. https://doi.org/10.1016/0920-4105(92)90048-6.

Aziz, K., Govier, G. W. and Fogarasi, M. 1972. Pressure Drop in Wells Producing Oil and Gas. *J Can Pet Technol* **11** (3): 38. PETSOC-72-03-04. https://doi.org/10.2118/72-03-04.

Azzola, J. H., Tselepidakis, D., Patillo, P. D. et al. 2007. Application of Vacuum-Insulated Tubing to Mitigate Annular Pressure Buildup. *SPE Drill & Compl* **22** (1): 46–51. SPE-90232-PA.

Bahonar, M., Azaiez, J., and Chen, Z. 2011a. Transient Nonisothermal Fully Coupled Wellbore/Reservoir Model for Gas Well Testing, Part 1: Modelling. *J Can Pet Technol* **50** (9–10): 37–50. SPE-149617-PA. https://doi.org/10.2118/149617-PA.

Bahonar, M., Azaiez, J., and Chen, Z. 2011b. Transient Nonisothermal Fully Coupled Wellbore/Reservoir Model for Gas Well Testing, Part 2: Applications. *J Can Pet Technol* **50** (9–10): 51–70. SPE-149618-PA. https://doi.org/10.2118/149618-PA.

Baker, O. 1954. Design of Pipe Lines for Simultaneous Flow of Oil and Gas. *Oil & Gas J* **53** (26 July): 185.

Baker, O. and Swerdloff, W. 1956. Finding Surface Tension of Hydrocarbon Liquids. *Oil & Gas J* (2 January): 125. Barker, K. M. 1989. Formation Damage Related to Hot Oiling. *SPE Prod Eng* **4** (4): 371–375. SPE-16230-PA.

Barnea, D. 1986. Transition From Annular Flow and From Dispersed Bubble Flow Unified Models for the Whole Range of Pipe Inclinations. *Int J Multiphase Flow* **12** (5): 733–744. https://doi.org/10.1016/0301-9322(86)90048-0.

Barnea, D. 1987. A Unified Model for Predicting Flow-Pattern Transitions for the Whole Range of Pipe Inclination. *Int J Multiphase Flow* **13** (1): 1–12. https://doi.org/10.1016/0301-9322(87)90002-4.

Barnea, D., Shoham, O., Taitel, Y. 1985. Gas-Liquid Flow in Inclined Tubes: Flow Pattern Transition for Upward Flow. *Chem Eng Sci* **40** (1): 131–291. https://doi.org/10.1016/0009-2509(85)85053-3.

Baxendell, P. B. and Thomas, R. 1961. The Calculation of Pressure Gradient in High Rate Flowing Wells. *J Pet Technol* **13** (10): 1023–1028; *Trans*., AIME, **222**. SPE-2-PA. https://doi.org/10.2118/2-PA.

Beggs, H. D. 1972. *An Experimental Study of Two Phase Flow in Inclined Pipes*. PhD dissertation, University of Tulsa, Oklahoma (1972).

Beggs, H. D. 1991. *Production Optimization Using Nodal Analysis*, Chaps. 3 & 4. Tulsa: OGCI.

Beggs, H. D. and Brill, J. P. 1973. A Study of Two-Phase Flow in Inclined Pipes. *J Pet Technol* **25** (5): 607–617. SPE-4007-PA. https://doi.org/10.2118/4007-PA.

Beggs, H. D. and Robinson, J. R. 1975. Estimating the Viscosity of Crude Oil Systems. *J Pet Technol* **27** (9): 1140–1141. SPE-5434-PA. https://doi.org/10.2118/5434-PA.

Beiranvand, M. S. and Khorzoughi, M. B. 2012. Introducing a New Correlation for Multiphase Flow Through Surface Chokes With Newly Incorporated Parameters. *SPE Prod & Oper* **27** (4): 422–428. SPE-158649-PA. https://doi.org/10.2118/158649-PA.

Beirute, R. M. 1991. A Circulating and Shut-In Well Temperature Profile Simulator. *J Pet Technol* **43** (9): 1140–1146. SPE-17591-PA. https://doi.org/10.2118/17591-PA.

Belfroid, S., Schieferli, W., Alberts, G. et al. 2008. Predicting Onset and Dynamic Behavior of Liquid Loading Gas Wells. Presented at the SPE Annual Technical Conference and Exhibition, Denver, 21–24 September. SPE-115567-MS. https://doi.org/10.2118/115567-MS.

Bendiksen, K. H. 1984. An Experimental Investigation of the Motion of Long Bubbles in Inclined Tubes. *Int J Multiphase Flow* **10** (4): 467–483. https://doi.org/10.1016/0301-9322(84)90057-0.

Bendiksen, K. H., Maines, D., Moe, R. et al. 1991. The Dynamic Two-Fluid Model OLGA: Theory and Application. *SPE Prod Eng* **6** (3): 171–180. SPE-19451-PA. https://doi.org/10.2118/19451-PA.

Bertuzzi, A. F., Welchon, J. K., and Poettmann, F. H. 1953. Description and Analysis of an Efficient Continuous-Flow Gas-Lift Installation. *J Pet Technol* **5** (11): 271–278; *Trans.*, AIME **198:** 271. https://doi.org/10.2118/953271-G.

Bird, J. M. 1954. Interpretation of Temperature Logs in Water-and Gas-Injection Wells and Gas-Producing Wells. *Drill & Prod Prac* (1954): 187–195.

Bird, R. B., Stewart, W. E., and Lightfoot, E. N. 2002. *Transport Phenomena*, second edition, 55. New York: Wiley.

Blalock, H. M., Jr. 1972. *Social Statistics*, second edition. New York: McGraw-Hill.

Blasingame, T. A., McCray, T. L., and Lee, W. J. 1991. Decline Curve Analysis for Variable Pressure Drop/Variable Flowrate Systems. Presented at the SPE Gas Technology Symposium, Houston, 22–24 January. SPE-21513-MS. https://doi.org/10.2118/21513-MS.

Blick, E. F., Enga, P. N., and Lin, P. C. 1988. Theoretical Stability Analysis of Flowing Oil Wells and Gas Lift Wells.

SPE Prod Eng **3** (4): 508–514. SPE-15022-PA. https://doi.org/10.2118/15022-PA.

Bloys, B. Gonzalez, M. E., Lofton, J. et al. 2008. Trapped Annular Pressure Mitigation: Trapped Annular Pressure—A Spacer Fluid That Shrinks. Presented at the IADC/SPE Drilling Conference, Orlando, Florida, USA, 4–6 March. SPE-112872-MS. https://doi.org/10.2118/112872-MS.

Bonnecaze, R. H., Erskine, W., and Greskovich, E. J. 1971. Holdup and Pressure Drop for Two-Phase Slug Flow in Inclined Pipelines. *AIChE J* **17** (5): 1109–1113. https://doi.org/10.1002/aic.690170516.

Brauner, N. and Barnea, D. 1986. Slug/Churn Transition in Upward Gas-Liquid Flow. *Chem Eng Sci* **41** (1): 159–163. https://doi.org/10.1016/0009-2509(86)85209-5.

Brill, J. P. and Mukherjee, H. 1999. *Multiphase Flow in Wells*, Vol. 17. Richardson, Texas: Monograph Series, Society of Petroleum Engineers.

Brodie, A. D., Allan, J. C., and Hill, G. 1995. Operating Experience With ESP's and Permanent Downhole Flowmeters in Wytch Farm Extended-Reach Wells. *J Pet Technol* **47** (10): 902–906. SPE-28528-PA. https://doi.org/10.2118/28528-PA.

Brown, K. E. 1984. *Technology of Artificial Lift Methods, Volume 4: Production Optimization of Oil and Gas Wells by Nodal Systems Analysis*. Tulsa: PennWell.

Brown, K. E. and Lea, J. F. 1985. Nodal Systems Analysis of Oil and Gas Wells. *J Pet Technol* **37** (10): 1751–1763. SPE-14714-PA. https://doi.org/10.2118/14714-PA.

Brown, K. E., Mach, J., and Proano, E. A. 1982. Application of Systems Analysis Techniques in Optimizing Gas Lift Installations. *J Energ Resour Technol* **104** (2): 157–161. https://doi.org/10.1115/1.3230393.

Bullard, E. C. 1947. The Time Necessary for a Bore Hole to Attain Temperature Equilibrium. *Monthly Notices, Geophys J R Astron Soc, Geophys Suppl* **5** (5): 127–130.

Burger, E. D., Perkins, T. K., and Striegler, J. H. 1981. Studies of Wax Deposition in the Trans Alaska Pipeline. *J Pet Technol* **33** (6): 1075–1088. SPE-8788-PA. https://doi.org/10.2118/8788-PA.

Busaidi, K. and Bhaskaran, H. 2003. Multiphase Flow Meters: Experience and Assessment in PDO. Presented at the SPE Annual Technical Conference and Exhibition, Denver, 1–4 October. SPE-84505-MS. https://doi.org/10.2118/84505-MS.

Caetano, E. F., Shoham, O., and Brill, J. P. 1992a. Upward Vertical Two-Phase Flow Through an Annulus, Part I: Single-Phase Friction Factor, Taylor Bubble Rise Velocity and Flow Pattern Prediction. *J Energ Resour Technol* **114** (1): 1–13. https://doi.org/10.1115/1.2905917.

Caetano, E. F., Shoham, O., and Brill, J. P. 1992b. Upward Vertical Two-Phase Flow Through an Annulus, Part II: Modeling Bubble, Slug, and Annular Flow. *J Energy Resour Technol* **114** (1): 14–30. https://doi.org/10.1115/1.2905916.

Cao, S., Lerche, I., and Hermanrud, C. 1988. Formation Temperature Estimation by Inversion of Borehole Measurements. *Geophysics* **53** (7): 979–988. https://doi.org/10.1190/1.1442534.

Carlsen, J. A., Stokka, O., and Kleppa, E. 2010. Taking the Gas Lift Valves to a New Level of Reliability. Presented at the Offshore Technology Conference, Houston, 3–6 May. OTC-20820-MS. https://doi.org/10.4043/20820-MS. Carslaw, H. S. and Jaeger, J. C. 1986. *Conduction of Heat in Solids*, second edition. London: Oxford University Press.

Cavalcanti, P., Falcone, G., and Barrufet, M. 2014. Upward Gas-Liquid Flow in Concentric and Eccentric Annular Spaces. Presented at the SPE Latin American and Caribbean Petroleum Engineering Conference, Maracaibo, Venezuela, 21–23 May. SPE-169303-MS. https://doi.org/10.2118/169303-MS.

Chambers, K. T., Hallager, W. S., Kabir, C. S. et al. 2001. Characterization of a Carbonate Reservoir Using Pressure-Transient Tests and Production Logs: Tengiz Field, Kazakhstan. *SPE Res Eval & Eng* **4** (4): 250–259. SPE-72598-PA. https://doi.org/10.2118/72598-PA.

Chapman, W. G., Gubbins, K. E., Jackson, G. et al. 1990. New Reference Equation of State for Associating Liquids. *Ind Eng Chem Res* **29** (8): 1709–1721. https://doi.org/10.1021/ie00104a021.

Chen, N. H. 1979. An Explicit Equation for Friction Factor in Pipe. *Ind Eng Chem Fund* **18** (3): 296–297. *https://doi.org/10.1021/i160071a019*.

Chevarunotai, N. 2014. *Analytical Model for Flowing-Fluid Temperature Distribution in Single-Phase Oil Reservoir Accounting for Joule-Thomson Effect*. MS Thesis, Petroleum Engineering Department, Texas A&M University, College Station, Texas.

Chevarunotai, N., Hasan, A. R., and Kabir, C. S. 2015. Transient Flowing-Fluid Temperature Modeling in Oil Reservoirs for Flow Associated with Large Drawdowns. Presented at the SPE Annual Technical Conference and Exhibition, Houston, 28–30 September. https://doi.org/10.2118/175008-MS.

Chien, S.-F. and Schrodt, J. L. G. 1995. Determination of Steam Quality and Flow Rate Using Pressure Data From

an Orifice Meter and a Critical Flowmeter. *SPE Prod & Fac* **10** (2): 76–81. SPE-24832-PA. https://doi.org/10.2118/24832-PA.

Chisholm, D. 1967a. Pressure Losses in Bends and Tees During Steam-Water Flow. NEL Report No. 318, National Engineering Laboratory, Great Britain.

Chisholm, D. 1967b. A Theoretical Basis for the Lockhart-Martinelli Correlation for Two-Phase Flow. *Int J Heat & Mass Transfer* **10** (12): 1767–1778. https://doi.org/10.1016/0017-9310(67)90047-6.

Chisholm, D. 1968. The Influence of Mass Velocity on Friction Pressure Gradients During Steam-Water Flow. *Proc*., Thermodynamic and Fluid Mechanics Group Convention, Institute of Mechanical Engineers. Bristol, England, UK. Vol. 182, Part 3H, pp. 336–341.

Chiu, K. and Thakur, S. C. 1991. Modeling of Wellbore Heat Losses in Directional Wells Under Changing Injection Conditions. Presented at the SPE Annual Technical Conference and Exhibition, Dallas, 6–9 October. SPE-22870-MS. https://doi.org/10.2118/22870-MS.

Choquette, S. P. 1975. *Vertical Two-Phase Flow Systems and Interpretation of the Flowmeter and the Gradiomanometer Production Log Interpretation*. MS thesis, Stanford University, Stanford, California.

Cicchitti, A., Lombardi, C., Silvestri, G. et al. 1960. Two-Phase Cooling Experiments: Pressure Drop, Heat Transfer and Burnout Measurements. *Energia Nucleare* **7** (6): 407–425.

Clark, A. R. and Perkins, T. K. 1981. Wellbore and Near-Surface Hydraulics of a Blown-Out Oil Well. *J Pet Technol* **33** (11): 2181–2188. SPE-9257-PA. https://doi.org/10.2118/9257-PA.

Coleman, S. B., Hartley, B. C., McCurdy, D. G. et al. 1991a. A New Look at Predicting Gas-Well Load-Up. *J Pet Technol* **43** (3): 329–333. SPE-20280-PA. https://doi.org/10.2118/20280-PA.

Coleman, S. B., Hartley B. C., McCurdy, D. G. et al. 1991b. Understanding Gas-Well Load-Up Behavior. *J Pet Technol* **43** (3): 334–338. SPE-20281-PA. https://doi.org/10.2118/20281-PA.

Collier, J. G. 1981. *Convective Boiling and Condensation*, second edition. New York: McGraw-Hill.

Crawford, T. J., Weinberger, C. B., and Weisman, J. 1986a. Two-Phase Flow Patterns and Void Fractions in Downward Flow, Part I: Steady-State Flow Patterns. *Int J Multiphase Flow* **11** (6): 761–782. https://doi.org/10.1016/0301-9322(85)90023-0.

Crawford, T. J., Weinberger, C. B., and Weisman, J. 1986b. Two-Phase Flow Patterns and Void Fractions in Downward Flow, Part II: Void Fractions and Transient Flow Patterns. *Int J Multiphase Flow* **12** (2): 219–236. https://doi.org/10.1016/0301-9322(86)90027-3.

Cullender, M. H. and Smith, R. V. 1956. Practical Solutions of Gas-Flow Equation for Wells and Pipelines With Large Temperature Gradients. *Trans*., AIME **207:** 281–287. SPE-696-G. https://doi.org/10.2118/696-G.

Cullick, A. S., Heath, D., Narayanan, K. et al. 2004. Optimizing Multiple-Field Scheduling and Production Strategy With Reduced Risk. *J Pet Technol* **56** (11): 77–83. SPE-88991-JPT. https://doi.org/10.2118/88991-JPT.

Curtis, M. R. and Witterholt, E. J. 1973. Use of the Temperature Log for Determining Flow Rates in Producing Wells. Presented at the SPE Annual Fall Meeting, Las Vegas, Nevada, 1–3 October. SPE-4637-MS. https://doi.org/10.2118/4637-MS.

D'Alesio, P., Poloni, R., Valente, P. et al. 2011. Well-Integrity Assessment and Assurance: The Operational Approach for Three CO^{2}-Storage Fields in Italy. *SPE Prod & Oper* **26** (2): 140–148. SPE-133056-PA. https://doi.org/10.2118/133056-PA.

Danenberger, E. P. 1993. Outer Continental Shelf Drilling Blowouts, 1971–1991. Presented at the Offshore Technology Conference, Houston, 3–6 May. OTC-7248-MS. https://doi.org/10.4043/7248-MS.

Davies, R. M. and Taylor, G. 1949. The Mechanics of Large Bubbles Rising Through Extended Liquids and Through Liquids in Tubes. *Proc., Royal Astr Soc London*, Series A, **200:** 375–390. No. A1062.

Davies, S. N., Gunningham, M. M., Bittleston, S. H. et al. 1994. Field Studies of Circulating Temperatures Under Cementing Conditions. *SPE Drill & Compl* **9** (1): 12–16. SPE-21973-PA. https://doi.org/10.2118/21973-PA.

Dawkrajai, P., Lake, L. W., Yoshioka, K. et al. 2006. Detection of Water or Gas Entries in Horizontal Wells From Temperature Profiles. Presented at the SPE/DOE Symposium on Improved Oil Recovery, Tulsa, 22–26 April. SPE-100050-MS. https://doi.org/10.2118/100050-MS.

Decker, K. L. 2008. IPO Gas Lift Design With Valve Performance. *SPE Prod & Oper* **23** (4): 464–467. SPE-109694-PA. https://doi.org/10.2118/109694-PA.

De Nevers, N. 2004. *Fluid Mechanics for Chemical Engineers*, third edition. New York: McGraw – Hill.

Dethlefs, J. and Chastain, B. 2012. Assessing Well-Integrity Risk: A Qualitative Model. *SPE Drill & Compl* **27** (2): 294–302. SPE-142854-PA. https://doi.org/10.2118/142854-PA.

Dikken, B. J. 1990. Pressure Drop in Horizontal Wells and Its Effect on Production Performance. *J Pet Technol* **42** (11): 1426–1433. SPE-19824-PA. https://doi.org/10.2118/19824-PA.

Dittus, F. W. and Boelter, L. M. K. 1930. Heat Transfer in Automobile Radiators of the Tubular Type. *Univ Calif Pub Eng* **2** (13): 443–461; reprinted in *Int Comm Heat Mass Transfer* **12** (1985): 3–22.

Dowdle, W. L. and Cobb, W. M. 1975. Static Formation Temperature From Well Logs: An Empirical Method. *J Pet Technol* **27** (11): 1326–1330. SPE-5036-PA. https://doi.org/10.2118/5036-PA.

Dranchuk, P. M. and Abou-Kassem, J. H. 1975. Calculation of *Z* Factors for Natural Gases Using Equations of State. *J Can Pet Technol* **14** (3): 34–36. PETSOC-75-03-03. https://doi.org/10.2118/75-03-03.

Dropkin, D. and Sommerscales, E. 1965. Heat Transfer by Natural Convection in Liquids Confined by Two Parallel Plates Inclined at Various Angels With Respect to the Horizontal. *J Heat Transfer*, *Trans*., ASME, Series C, **87:** 77.

Dukler, A. E., Wicks, M., and Cleveland, R. G. 1964. Frictional Pressure Drop in Two-Phase Flow, Part A: A Comparison of Existing Correlations for Pressure Loss and Holdup. *AIChE J* **10** (1): 38–43. https://doi.org/10.1002/aic.690100117.

Duns, H., Jr. and Ros, N. C. J. 1963. Vertical Flow of Gas and Liquid Mixtures in Wells. *Proc*., Sixth World Petroleum Congress, 6, Tokyo, 19–26 June. Section 2, Paper 22-PD, 451–465.

Duru, O. O. and Horne, R. N. 2010. Modeling Reservoir Temperature Transients and Reservoir-Parameter Constrained to the Model. *SPE Res Eval & Eng* **13** (6): 873–883. SPE-115791-PA. https://doi.org/10.2118/115791-PA.

Economides, M. J., Hill, A. D., Ehlig-Economides, C. et al. 2012. *Petroleum Production Systems*, second edition. Upper Saddle River, New Jersey: Prentice-Hall.

Edwardson, M. J., Girner, H. M., Parkinson, H. R. et al. 1962. Calculation of Formation Temperature Disturbances Caused by Mud Circulation. *J Pet Technol* **14** (4): 416–426; *Trans*., AIME, **225**. SPE-124-PA. https://doi.org/10.2118/124-PA.

Eikrem, G. O., Aamo, O. M., and Foss, B. A. 2008. On Instability in Gas-Lift Wells and Schemes for Stabilization by Automatic Control. *SPE Prod & Oper* **23** (1): 268–279. SPE-101502-PA. https://doi.org/10.2118/101502-PA.

Ellis, R. C., Fritchie, D. G., Jr., Gibson, D. H. et al. 2004. Marlin Failure Analysis and Redesign, Part 2: Redesign. *SPE Drill & Compl* **19** (2): 112–119. SPE-88838-PA. https://doi.org/10.2118/88838-PA.

Fan, L., Lee, W. J., and Spivey, J. P. 2000. Semi-Analytical Model for Thermal Effect on Gas Well Pressure-Buildup Tests. *SPE Res Eval & Eng* **3** (6): 480–491. SPE-68020-PA. https://doi.org/10.2118/68020-PA.

Fan, J., Shi, T.-H., and Lian, Z.-G. 1996. A Dynamic Model and Simulation for Killing of Empty Hole Blowout. Presented at the 1996 Asia Pacific Oil and Gas Conference and Exhibition, Perth, Australia, 12–14 October. SPE-49963-MS. https://doi.org/10.2118/49963-MS.

Fancher, G. H. and Brown, K. E. 1963. Prediction of Pressure Gradients for Multiphase Flow in Tubing. *SPE J.* **3** (1): 59–69; *Trans*., AIME, **228.** SPE-440-PA. https://doi.org/10.2118/440-PA.

Farouq Ali, S. M. 1981. A Comprehensive Wellbore Steam/Water Flow Model for Steam Injection and Geothermal Applications. *SPE J.* **21** (5): 527–534. SPE-7966-PA. https://doi.org/10.2118/7966-PA.

Fernandes, R. C., Semiat, R., and Dukler, A. E. 1983. Hydrodynamic Model for Gas-Liquid Slug Flow in Vertical Tubes. *AIChE J* **29** (6): 981–989. *https://doi.org/10.1002/aic.690290617*.

Firouzi, M., Towler, B. F., and Rufford, T. E. 2015. Mechanistic Modeling of Counter-Current Slug Flow in Vertical Annuli. Presented at the Asia Pacific Unconventional Resources Conference & Exhibition, Brisbane, Australia, 9–11 November. SPE-176885-MS. https://doi.org/10.2118/176885-MS.

Fishenden, M. and Saunders, O. A. 1950. *An Introduction to Heat Transfer*, first edition. London: Oxford University Press.

Flores, J. G., Chen, X. T., Sarica, C. et al. 1999. Characterization of Oil-Water Flow Patterns in Vertical and Deviated Wells. *SPE Prod & Fac* **14** (2): 94–101. SPE-56108-PA. https://doi.org/10.2118/56108-PA.

Flores, J. G., Sarica, C., Chen, T. X., et al. 1998. Investigation of Holdup and Pressure Drop Behavior for Oil-Water Flow in Vertical and Deviated Wells. *J Energ Resour Technol* **120** (1): 8–14. https://doi.org/10.1115/1.2795016.

Fortunati, F. 1972. Two-Phase Flow through Wellhead Chokes. Paper SPE-3742-MS presented at the SPE European Spring Meeting, 16-18 May, Amsterdam, the Netherlands. SPE-3742-MS. https://doi.org/10.2118/3742-MS.

Garcia, A. P. 2013. Stability Analysis and Stabilization of Gas Lift Systems. Paper presented at the 22nd International Congress of Mechanical Engineering, Ribeirao Preto, SP, Brazil, 3–7 November.

Garg, S. K., Pritchett, J. W., and Alexander, J. H. 2004a. Development of New Geothermal Wellbore Holdup Correlations Using Flowing Well Data. Report INEEL/EXT–04–01760 prepared for Idaho National Engineering and Environmental Laboratory. Idaho Falls, ID. http://www.osti.gov/geothermal/servlets/purl/893490.

Garg, S. K., Pritchett, J. W., and Alexander, J. H. 2004b. A New Liquid Hold-Up Correlation for Geothermal Wells.

Geothermics **33** (6): 795–817. http://www.sciencedirect.com/science/article/pii/S0375650504000513.

Gebhart, B. 1971. *Heat Transfer*, second edition. New York: McGraw-Hill.

Ghanbari, A., Farshad, F. F., and Reike, H. H. 2011. Newly Developed Friction Factor Correlation for Pipe Flow and Flow Assurance. *J Chem Eng & Material Sci* **2** (6): 83–86. http://www.academicjournals.org/journal/JCEMS/article-abstract/43BC5B11677.

Gilbert, W. E. 1954. Flowing and Gas-Lift Well Performance. Presented in New York City, 1 January. *Drill and Prod Prac* API-54-126.

Gilbertson, E., Hover, F., and Freeman, B. 2013. A Thermally Actuated Gas-Lift Safety Valve. *SPE Prod & Oper* **28** (1): 77–84. SPE-161930-PA. https://doi.org/10.2118/161930-PA.

Godbey, J. K. and Dimon, C. A. 1977. The Automatic Liquid Level Monitor for Pumping Wells. *J Pet Technol* **29** (8): 1019–1024. SPE-6039-PA. https://doi.org/10.2118/6039-PA.

Gomez, L. E., Shoham, O., Schmidt, Z. et al. 2000. Unified Mechanistic Model for Steady-State Two-Phase Flow: Horizontal to Vertical Upward Flow. *SPE J.* **5** (3): 339–350. SPE-65705-PA. https://doi.org/10.2118/65705-PA.

Gonzalez, D. L., Ting, D. P., Hirasaki, G. J. et al. 2005. Prediction of Asphaltene Instability Under Gas Injection With the PC-SAFT Equation of State. *Energ Fuel* **19** (4): 1230–1234. https://doi.org/10.1021/ef049782y.

Gonzalez, D., Hirasaki, G. J., Jamaluddin, A. K. M. et al. 2007. Impact of Flow Assurance in the Development of a Deepwater Prospect. Presented at the SPE Annual Technical Conference and Exhibition, Anaheim, California, USA, 11–14 November. SPE-110833-MS. https://doi.org/10.2118/110833-MS.

Govier, G. W. and Aziz, K. 2008. *The Flow of Complex Mixtures in Pipes*, second edition. Richardson, Texas: Society of Petroleum Engineers.

Govier, G. W. and Fogarasi, M. 1975. Pressure Drop in Wells Producing Gas and Condensate. *J Can Pet Technol* **14** (4): 28. PETSOC-75-04-03. https://doi.org/10.2118/75-04-03.

Goyal, K. P., Miller, C. W., and Lippmann, M. J. 1980. Effect of Measured Wellhead Parameters and Well Scaling on the Computed Downhole Conditions in Cerro Prieto Wells. Presented at the Sixth Annual Workshop on Geothermal Reservoir Engineering, Stanford University, Stanford, California, USA, 16–18 December. LBL-11835.

Gregory, G. A. 1974. Comments on the Prediction of Liquid Holdup for Gas-Liquid Flow in Inclined Pipes. *Can J Chem Eng* **52** (4): 463–467. https://doi.org/10.1002/cjce.5450520405.

Gregory, G. A. 1975. Comparison of Methods for Comments on the Prediction of Liquid Holdup for Upward Gas-Liquid Flow in Inclined Pipes. *Can J Chem Eng* **53** (4): 384–388. https://doi.org/10.1002/cjce.5450530405.

Gregory, G. A. and Scott, D. S. 1969. Correlation of Liquid Slug Velocity and Frequency in Horizontal Cocurrent Gas-Liquid Slug Flow. *AIChE J* **15** (6): 933–935. https://doi.org/10.1002/aic.690150623.

Griston, S. and Willhite, G. P. 1987. Numerical Model for Evaluating Concentric Steam Injection Wells. Presented at the SPE California Regional Meeting, Ventura, California, 8–10 April. SPE-16337-MS. https://doi.org/10.2118/16337-MS.

Grolmes, M. A. and Leung, J. C. 1985. Code Method for Evaluating Integrated Relief Phenomena. *Chem Eng Progress* **81** (8): 47–52.

Gunn, D. J. and Darling, C. W. W. 1963. Fluid Flow and Energy Losses in Non Circular Conduits. *Trans., Inst Chem Eng* **41:** 163.

Guo, B., Duan, S., and Ghalambor, A. 2006. A Simple Model for Predicting Heat Loss and Temperature Profiles in Insulated Pipelines. *SPE Prod & Oper* **21** (1): 107–113. SPE-86983-PA. https://doi.org/10.2118/86983-PA.

Hagedorn, A. R. and Brown, K. E. 1965. Experimental Study of Pressure Gradients Occurring During Continuous Two-Phase Flow in Small-Diameter Conduits. *J Pet Technol* **17** (4): 475–484. *Trans*., AIME, **234.** SPE-940-PA. https://doi.org/10.2118/940-PA.

Hagoort, J. 2004. Ramey's Wellbore Heat Transmission Revisited. *SPE J.* **9** (4): 465–474. SPE-87305-PA. https://doi.org/10.2118/87305-PA.

Halal, A. S. and Mitchell, R. F. 1994. Casing Design for Trapped Annular Pressure Buildup. *SPE Drill & Compl* **9** (2): 107–114. SPE-25694-PA. https://doi.org/10.2118/25694-PA.

Hammami, A. and Raines, M. A. 1999. Paraffin Deposition From Crude Oils: Comparison of Laboratory Results With Field Data. *SPE J.* **4** (1): 9–18. SPE-54021-PA. https://doi.org/10.2118/54021-PA.

Harmathy, T. Z. 1960. Velocity of Large Drops and Bubbles in Media of Infinite or Restricted Extent. *AIChE J* **6** (2): 281–288. https://doi.org/10.1002/aic.690060222.

Hasan, A. R. 1988. Void Fraction in Bubbly, Slug, and Churn Flow in Vertical Two-Phase Up-Flow. *Chem Eng Comm* **66** (1): 101–111. https://doi.org/10.1080/00986448808940263.

Hasan, A. R. 1990. Modifications of James Correlation for Predicting Mass Flux and Steam Quality in Geothermal Wells Containing Dissolved Gases and Solids. *Chem Eng Comm* **97** (1): 1–7.

https://doi.org/10.1080/00986449008911500.

Hasan, A. R. 1991. Simultaneous Measurement of Mass Flux and Steam Quality in Geothermal

Wells Using Homogeneous and Separated Flow Models. *Chem Eng Comm* **105** (1): 185–199. https://doi.org/10.1080/00986449108911525.

Hasan, A. R. 1995. Void Fraction in Bubbly and Slug Flow in Downward Two-Phase Flow in Vertical and Inclined Systems. *SPE Prod & Fac* **10** (3): 172–176. SPE-26522-PA. https://doi.org/10.2118/26522-PA.

Hasan, A. R., Izgec, B., and Kabir, C. S. 2010a. Sustaining Production by Managing Annular-Pressure Buildup. *SPE Prod & Oper* **25** (2): 195–203. SPE-120778-PA. https://doi.org/10.2118/120778-PA.

Hasan, A. R. and Kabir, C. S. 1988a. Predicting Multiphase Flow Behavior in a Deviated Well. *SPE Prod Eng* **3** (4): 474–482. SPE-15449-PA. https://doi.org/10.2118/15449-PA.

Hasan, A. R. and Kabir, C. S. 1988b. A Study of Multiphase Flow Behavior in Vertical Wells. *SPE Prod Eng* **3** (2): 263–272; *Trans*., AIME, **285.** SPE-15138-PA. https://doi.org/10.2118/15138-PA.

Hasan, A. R. and Kabir, C. S. 1990a. Determination of Static Reservoir Temperature From Transient Data Following Mud Circulation. *SPE Drill & Compl* **9** (1): 17–24. SPE-24085-PA. https://doi.org/10.2118/24085-PA.

Hasan, A. R. and Kabir, C. S. 1990b. A New Model for Two-Phase Oil/Water Flow: Production Log Interpretation and Tubular Calculations. *SPE Prod Eng* **5** (2): 193–199; *Trans*., AIME, **287.** SPE-18216-PA. https://doi.org/10.2118/18216-PA.

Hasan, A. R. and Kabir, C. S. 1992. Two-Phase Flow in Vertical and Inclined Annuli. *Int J Multiphase Flow* **18** (2): 279–293. https://doi.org/10.1016/0301-9322(92)90089-Y.

Hasan, A. R. and Kabir, C. S. 1994a. Aspects of Wellbore Heat Transfer During Two-Phase Flow. *SPE Prod & Fac* **9** (3): 211–216. SPE-22948-PA. https://doi.org/10.2118/22948-PA.

Hasan, A. R. and Kabir, C. S. 1994b. Determination of Static Reservoir Temperature Determination From Transient Data After Mud Circulation. *SPE Drill & Compl* **9** (3): 211–216. SPE-24085-PA. https://doi.org/10.2118/24085-PA.

Hasan, A. R. and Kabir, C. S. 1996. A Mechanistic Model for Computing Fluid Temperature Profiles in Gas-Lift Wells. *SPE Prod & Fac* **11** (3): 179–185. SPE-26098-PA. https://doi.org/10.2118/26098-PA.

Hasan, A. R. and Kabir, C. S. 1999. A Simplified Model for Oil/Water Flow in Vertical and Deviated Wellbores. *SPE Prod & Fac* **14** (1): 56–62. SPE-54131-PA. https://doi.org/10.2118/54131-PA.

Hasan, A. R. and Kabir, C. S. 2007. A Simple Model for Annular Two-Phase Flow in Wellbores. *SPE Prod & Oper* **22** (2): 168–175. SPE-95523-PA. https://doi.org/10.2118/95523-PA.

Hasan, A. R. and Kabir, C. S. 2010: Modeling Two-Phase Fluid and Heat Flows in Geothermal Wells. *J Pet Sci & Eng* **71** (1–2): 77–86. https://doi.org/10.1016/j.petrol.2010.01.008.

Hasan, A. R., Kabir, C. S. 2012. Wellbore Heat-Transfer Modeling and Applications. *J Pet Sci & Eng* **86–87** (May) 127–136. https://doi.org/10.1016/j.petrol.2012.03.021.

Hasan, A. R., Kabir, C. S., and Ameen, M. M. 1996a. A Fluid Circulating Temperature Model for Workover Operations. *SPE J.* **1** (2): 133–144. SPE-27848-PA. https://doi.org/10.2118/27848-PA.

Hasan, A. R., Kabir, C. S., and Lin, D. 2000. Modeling Wellbore Dynamics During Oil Well Blowout. Presented at the International Oil and Gas Conference and Exhibition, Beijing, 7–10 November. SPE-64644-MS. https://doi.org/10.2118/64644-MS.

Hasan, A. R., Kabir, C. S., and Lin, D. 2005. Analytic Wellbore Model for Transient Gas-Well Testing. *SPE Form Eval* **8** (3): 240–247. SPE-84288-PA. https://doi.org/10.2118/84288-PA.

Hasan, A. R., Kabir, C. S., and Rahman, R. 1988. Predicting Liquid Gradient in a Pumping-Well Annulus. *SPE Prod Eng* **3** (1): 113–120; *Trans*., AIME, **285.** SPE-13638-PA. https://doi.org/10.2118/13638-PA.

Hasan, A. R., Kabir, C. S., and Sayarpour, M. 2010b. Simplified Two-Phase Flow Modeling in Wellbores. *J Pet Sci & Eng* **72** (1–2): 42–49. https://doi.org/10.1016/j.petrol.2010.02.007.

Hasan, A. R., Kabir, C. S., and Srinivasan, S. 1994. Countercurrent Bubble and Slug Flows in a Vertical System. *Chem Eng Sci* **49** (16): 2567–2574. https://doi.org/10.1016/0009-2509(94)E0084-4.

Hasan, A. R., Kabir, C. S., and Wang, X. 1997. Development and Application of a Wellbore/Reservoir Simulator for Testing Oil Wells. *SPE Form Eval* **12** (3): 182–188. SPE-29892-PA. https://doi.org/10.2118/29892-PA.

Hasan, A. R., Kabir, C. S., and Wang, X. 1998. Wellbore Two-Phase Flow and Heat Transfer During Transient Testing. *SPE J.* **3** (2): 174–180. SPE-38946-PA. https://doi.org/10.2118/38946-PA.

Hasan, A. R., Kabir, C. S., and Wang, X. 2009. A Robust Steady-State Model for Flowing-Fluid Temperature in Complex Wells. *SPE Prod & Oper* **24** (2): 269–276. SPE-109765-PA. https://doi.org/10.2118/109765-PA.

Hasan, A. R., Kouba, G. E., and Wang. X. 1996b. Transient Analysis to Locate and Characterize Plugs in Gas Wells. Presented at the SPE Annual Technical Conference and Exhibition, Denver, 5–9 October. SPE-36553-MS. https://doi.org/10.2118/36553-MS.

Hasan, A. R. and Rhodes, E. 1984. Effect of Mass Flux and System Pressure on Two-Phase Friction Multiplier. *Chem Eng Comm* **27** (3–4): 209–229. https://doi.org/10.1080/00986448408940502.

Hashmi, G. M., Kabir, C. S., and Hasan, A. R. 2015. Estimating Reliable Gas Rate With Transient-Temperature Modeling for Interpreting Early-Time Cleanup Data During Transient Testing. *J Pet Sci & Eng* **133** (September): 285–295. https://doi.org/10.1016/j.petrol.2015.06.001.

Hashmi, G. M., Kabir, C. S., and Hasan, A. R. 2016. Design and Interpretation of Transient Tests at Well's Inception. *J Pet Sci & Eng* **145** (June): 573–584. https://doi.org/10.1016/j.petrol.2016.06.035.

Henstock, W. H. and Hanratty, T. J. 1976. The Interfacial Drag and the Height of the Wall Layer in Annular Flow. *AIChE J* **22** (6): 990–1000. https://doi.org/10.1002/aic.690220607.

Hewitt, G. F. and Hall-Taylor, N. S. 1970. *Annular Two Phase Flow*. Oxford: Pergamon Press.

Hewitt, G. F. and Jayanti, S. 1993. To Churn or Not to Churn. *Int J Multiphase Flow* **19** (3): 527–529. https://doi.org/10.1016/0301-9322(93)90065-3.

Hewitt, G. F. and Roberts, D. N. 1969. Studies of Two-Phase Flow Patterns by Simultaneous X-Ray and Flash Photography. AERE-M 2159, HMSO. UKAEA Robert No. AERE-R 4022, HMSO, London.

Hight, M. A., Redus, C. L., and Lehrmann, J. K. 1992. Evaluation of Dual-Injection Methods for Multiple-Zone Steamflooding. *SPE Res Eng* **7** (1): 45–51. SPE-18811-PA. https://doi.org/10.2118/18811-PA.

Hill, A. D. 1990. *Production Logging: Theoretical and Interpretative Elements*, Vol. 14. Richardson, Texas: Monograph Series, Society of Petroleum Engineers.

Hoadley, S. F., Kabir, C. S., and Kamal, D. 2001. Continuous Depth-Indexed Analysis of Production-Log Data in Oil-Water Flow. Presented at the SPE Middle East Oil Show, Bahrain, UAE, 17–20 March. SPE-68079-MS. https://doi.org/10.2118/68079-MS.

Holmes, C. S. and Swift, S. C. 1970. Calculations of Circulating Mud Temperatures. *J Pet Technol* **22** (6): 670–674. SPE-2318-PA. https://doi.org/10.2118/2318-PA.

Horner, D. R. 1951. Pressure Build-Up in Wells. *Proc*., Third World Petroleum Congress, The Hague (1951), Section 2, 503; *Pressure Analysis Methods*, Reprint Series Vol. 9, p. 25. Richardson, Texas: Society of Petroleum Engineers (1967).

Houzé, O., Viturat, D., and Fjaere, O. S. 2016. Dynamic Data Analysis, v. 5.10.01, Chap. 17. http://www.kappaeng.com/documents/flip/dda51001/#.

Huerta, N. J., Checkai, D. A., and Bryant, S. L. 2009. Utilizing Sustained Casing Pressure Analog to Provide Parameters to Study CO^2 Leakage Rates Along a Wellbore. Presented at the SPE International Conference on CO^2 Capture, Storage, and Utilization, San Diego, California, USA, 2–4 November. SPE-126700-MS. https://doi.org/10.2118/126700-MS.

Hughmark, G. A. 1963. Pressure Drop in Horizontal and Vertical Cocurrent Gas-Liquid Flow. *Industrial Eng Chem Fund* **2** (4): 315–320. https://doi.org/10.1021/i160008a014.

Hughmark, G. A. 1965. Holdup and Heat Transfer in Horizontal Slug Gas-Liquid Flow. *Chem Eng Sci* **20** (12): 1007–1010. https://doi.org/10.1016/0009-2509(65)80101-4.

Idsinga, W., Todreas, N., and Bowring, R. 1977. An Assessment of Two-Phase Pressure Drop Correlations for Steam-Water Systems. *Int J Multiphase Flow* **3** (5): 401–413. https://doi.org/10.1016/0301-9322(77) 90019-2.

Ihara, M. and Kikuyama, K. 1994. Flow in Horizontal Wellbores With Influx Through Porous Walls. Presented at the SPE Annual Technical Conference and Exhibition, New Orleans, 25–28 September. SPE-28485-MS. https://doi.org/10.2118/28485-MS.

Ismadi, D., Kabir, C. S., and Hasan, A. R. 2012. The Use of Combined Static- and Dynamic-Material-Balance Methods With Real-Time Surveillance Data in Volumetric Gas Reservoirs. *SPE Res Eval & Eng* **15** (3): 351–360. SPE-145798-PA. https://doi.org/10.2118/145798-PA.

Ismadi, D., Suthichoti, P. and Kabir, C. S. 2010. Understanding Well Performance With Surveillance Data. *J Pet Sci & Eng* **74** (1): 99–106. https://doi.org/10.1016/j.petrol.2010.08.015.

Izgec, B., Cribbs, M. E., Pace, S. V. et al. 2009. Placement of Permanent Downhole-Pressure Sensors in Reservoir Surveillance. *SPE Prod & Oper* **24** (1): 87–95. SPE-107268-PA. https://doi.org/10.2118/107268-PA.

Izgec, B., Hasan, A. R., Lin, D. et al. 2010. Flow-Rate Estimation From Wellhead Pressure and Temperature Data. *SPE Prod & Oper* **25** (1): 31–39. SPE-115790-PA. https://doi.org/10.2118/115790-PA.

Izgec, B., Kabir, C. S., Zhu, D. et al. 2007. Transient Fluid and Heat Flow Modeling in Coupled Wellbore/Reservoir Systems. *SPE Res Eval & Eng* **10** (3): 294–301. SPE-102070-PA. https://doi.org/10.2118/102070-PA.

Jamaluddin, A. K. M., Creek, J., Kabir, C. S. et al. 2002. Laboratory Techniques to Measure Thermodynamic Asphaltene Instability. *J Can Pet Technol* **41** (7): 44–52. PETSOC-02-07-04. https://doi.org/10.2118/02-07-04.

Jamaluddin, A. K. M., Nighswander, J. N., and Joshi, N. 2003. A Systematic Approach for Characterizing

Hydrocarbon Solids. *SPE J.* **8** (3): 304–213. SPE-86573-PA. https://doi.org/10.2118/86573-PA.

Jamaluddin, A. K. M., Nozarko, T. W., Sills, S. et al. 1996. Deasphalted Oil: A Natural Asphaltene Solvent. *SPE Prod & Fac* **11** (12): 58. SPE-28994-PA. https://doi.org/10.2118/28994-PA.

James, R. 1962. Steam-Water Critical Flow Through Pipes. *Proc Inst Mech Engrs* **176** (26): 741–748.

James, R. 1965. Metering of Steam-Water Two-Phase Flow by Sharp-Edged Orifices. *Proc Inst Mech Engrs* **180** (1): 549–572.

Jayanti, S. and Hewitt, G. F. 1992. Prediction of the Slug-to-Churn Flow Transition in Vertical Two-Phase Flow. *Int J Multiphase Flow* **18** (6): 847–860. https://doi.org/10.1016/0301-9322(92)90063-M.

Johnson, D., Sierra, J., Kaura, J. et al. 2006. Successful Flow Profiling of Gas Wells Using Distributed Temperature Sensing Data. Presented at the SPE Annual Technical Conference and Exhibition, San Antonio, Texas, USA, 24–27 September. SPE-103097-MS. https://doi.org/10.2118/103097-MS.

Julian, J. Y., Jackson, J. C., and White, T. M. 2014. A History of Gas Lift Valve and Gas Lift Mandrel Damage and Subsequent Retrofit Gas Lift Straddle Installation in Alaska. Presented at the SPE/ICoTA Coiled Tubing and Well Intervention Conference and Exhibition, The Woodlands, Texas, USA, 25–26 March. SPE-168304-MS. https://doi.org/10.2118/168304-MS.

Kabir, C. S., Del Signore, A. G., Hasan, A. R. et al. 1997. Establishing Geothermal Gradient Using a New Static-Temperature Analysis Method. Presented at the SPE Annual Technical Conference and Exhibition, San Antonio, Texas, USA, 5–8 October. SPE-38667-MS. https://doi.org/10.2118/38667-MS.

Kabir, C. S., Elgmati, M., and Reza, Z. 2012a. Estimating Drainage-Area Pressure With Flow-After-Flow Testing. *SPE Res Eval & Eng* **15** (5): 571–583. SPE-146049-PA. https://doi.org/10.2118/146049-PA.

Kabir, C. S., Gorell, S. B., Portillo, M. E. et al. 2007. Decision Making With Uncertainty While Developing Multiple Gas/Condensate Reservoirs: Well Count and Pipeline Optimization. *SPE Res Eval & Eng* **10** (3): 251–259. SPE-95528-PA. https://doi.org/10.2118/95528-PA.

Kabir, C. S., Hasan, A. R., Jordan, D. L. et al. 1996a. A Wellbore/Reservoir Simulator for Testing Gas Wells in High-Temperature Reservoirs. *SPE Form Eval* **11** (2): 128–134. SPE-28402-PA. https://doi.org/10.2118/28402-PA.

Kabir, C. S., Hasan, A. R., Lin, D. et al. 2001a. An Approach to Mitigating Wellbore Solids Deposition. Presented at the SPE Annual Technical Conference and Exhibition, New Orleans, 30 September–3 October. SPE-71558-MS. https://doi.org/10.2118/71558-MS.

Kabir, C. S., Hoadley, S. F., Al-Dashti, Q. et al. 1998. Combined Production Logging, Transient Testing, and Well-Performance Analysis. Presented at the SPE Annual Technical Conference and Exhibition, New Orleans, 27–30 September. SPE-48965-MS. https://doi.org/10.2118/48965-MS.

Kabir, C. S., Hoadley, S. F., and Kamal, D. 2001b. Use of Flow-Pattern-Based Models for Interpreting Oil-Water Flow in Production Logging. Presented at the SPE Middle East Oil Show, Bahrain, UAE, 17–20 March. SPE-68468-MS. https://doi.org/10.2118/68468-MS.

Kabir, C. S. and Hasan, A. R. 1998. Does Gauge Placement Matter in Downhole Transient-Data Acquisition? *SPE Res Eval & Eng* **1** (1): 64–68. SPE-36527-PA. https://doi.org/10.2118/36527-PA.

Kabir, C. S. and Hasan, A. R. 1990. Performance of a Two-Phase Gas/Liquid Model in Vertical Wells. *J Pet Sci & Eng* **4** (3): 273–289. https://doi.org/10.1016/0920-4105(90)90016-V.

Kabir, C. S. and Hasan, A. R. 1994. Two-Phase Flow Correlations as Applied to Pumping Well Testing. *J Energy Resour Technol* **116** (2): 121–128. https://doi.org/10.1115/1.2906016.

Kabir, C. S. and Hasan, A. R. 2006. Simplified Wellbore Flow Modeling in Gas-Condensate Systems. *SPE Prod & Oper* **21** (1): 89–97. SPE-89754-PA. https://doi.org/10.2118/89754-PA.

Kabir, C. S., Hasan, A. R., Kouba, G. E. et al. 1996b. Determining Circulating Fluid Temperature in Drilling, Workover, and Well Control Operations. *SPE Drill & Compl* **11** (2): 74–79. SPE-24581-PA. https://doi.org/10.2118/24581-PA.

Kabir, C. S. and Izgec, B. 2009. Diagnosis of Reservoir Compartmentalization From Measured Pressure/Rate Data During Primary Depletion. *J Pet Sci & Eng* **69** (3–4): 271–281. https://doi.org/10.1016/j.petrol.2009.09.007.

Kabir, C. S., Izgec, B., Hasan, A. R. et al. 2012b. Computing Flow Profiles And Total Flow Rate With Temperature Surveys in Gas Wells. *J Nat Gas Sci & Eng* **4** (January): 1–7.

Kabir, C. S. and Jamaluddin, A. K. M. 2002. Asphaltene Characterization and Mitigation in South Kuwait's Marrat Reservoir. *SPE Prod & Fac* **17** (4): 251–258. SPE-80285-PA. https://doi.org/10.2118/80285-PA.

Kabir, C. S., Yi, X., Jakymec, M. et al. 2014. Interpreting Distributed-Temperature Measurements in Deepwater Gas-Well Testing: Estimation of Static and Dynamic Thermal Gradients, and Flow Rates. *SPE Prod & Oper* **29** (2): 97–104. SPE-166333-PA. https://doi.org/10.2118/166333-PA.

Kanu, E. P. 1981. Systems Analysis Hikes Well Performance. *Pet Engineer Int* (May): 96.

Kanu, E. P., Mach, J., and Brown, K. E. 1981. Economic Approach to Oil Production and Gas Allocation in Continuous Gas Lift. *J Pet Technol* **33** (10): 1887–1892. SPE-9084-PA. https://doi.org/10.2118/9084-PA.

Kaya, A. S., Sarica, C., and Brill, J. P. 2001. Mechanistic Modeling of Two-Phase Flow in Deviated Wells. *SPE Prod & Fac* **16** (3): 156–165. SPE-72998-PA. https://doi.org/10.2118/72998-PA.

Kelessidis, V. C. and Dukler, A. E. 1989. Modeling Flow Pattern Transitions for Upward Gas-Liquid Flow in Vertical Concentric and Eccentric Annuli. *Int J Multiphase Flow* **15** (2): 173–191. https://doi.org/10.1016/0301-9322(89)90069-4.

Keller, H. H., Couch, E. J., and Berry, P. M. 1973. Temperature Distribution in Circulating Mud Columns. *SPE J.* **13** (1): 23–30. SPE-3605-PA. https://doi.org/10.2118/3605-PA.

Kieffer, S. W. 1977. Sound Speed in Liquid-Gas Mixtures: Water-Air and Water-Steam. *J Geophys Res* **82** (20): 2895–2904. https://doi.org/10.1029/JB082i020p02895.

Kikani, J., Schwartz, H., and Graute, J. 1996. A Method for Blowout Rate Prediction for Sour Gas Wells: Oldenburg Fields, Germany. *SPE Res Eng* **11** (3): 158–162. 35582-PA. https://doi.org/10.2118/35582-PA.

King, R. C. and Crocker, S. 1967. *Pipe Handbook*, fifth edition, Chap. 3. New York: McGraw-Hill.

Kirkpatrick, C. V. 1959. Advances in Gas-Lift Technology. *API Drill & Prod. Prac API-59-024*. New York: API.

Kouba, G. E., MacDougall, G. R., and Schumacher, B. W. 1993. Advances in Dynamic-Kill Calculations for Blowout Wells. *SPE Drill & Compl* **8** (93): 189–194. SPE-22559-PA. https://doi.org/10.2118/22559-PA.

Kouba, G. E., Wang, S., Gomez, L. et al. 2006. Review of the State-of-the-Art Gas-Liquid Cylindrical Cyclone (GLCC) Technology: Field Applications. Presented at the SPE International Oil & Gas Conference and Exhibition, Beijing, 5–7 December. SPE-104256-MS. https://doi.org/10.2118/104256-MS.

Kragas, T. K., van der Spek, A., and Al-Hashmi, K. M. 2002. Field Trial of a Downhole, Fiber Optic, Two-Phase Flowmeter in PDO's Nimr Field. Presented at the SPE European Petroleum Conference, Aberdeen, 29–31 October. SPE-78306-MS. https://doi.org/10.2118/78306-MS.

Kragas, T. K., Johansen, E. S., Hassanali, H., et al. 2003. Installation and Data Analysis of a Downhole, Fiber Optic Flowmeter at Mahogany Field, Offshore Trinidad. Presented at the SPE Latin American and Caribbean Petroleum Engineering Conference, Port-of-Spain, Trinidad and Tobago, 27–30 April. SPE-81018-MS. https://doi.org/10.2118/81018-MS.

Lage, A. C. V. M. and Time, R. W. 2002. An Experimental and Theoretical Investigation of Upward Two-Phase Flow in Annuli. *SPE J.* **7** (3): 325–336. SPE-79512-PA. https://doi.org/10.2118/79512-PA.

Lasdon, L. S., Waren, A. D., Jain, A. et al. 1978. Design and Testing of a Generalized Reduced Gradient Code for Nonlinear Programming. *ACM Trans on Math Software* **4** (1): 34–50. https://doi.org/10.1145/355769.355773.

Lau, C. W. 1972. *Bubbly and Slug Flow Pressure Drop in an Inclined Pipe*. SB thesis, Massachusetts Institute of Technology, Cambridge, Massachusetts.

Lauwerier, H. A. 1955. The Transport of Heat in an Oil Layer Caused by Injection of Hot Fluid. *Appl Sci Res*, Section A.5, p. 145.

Lehner, F. and Williamson, A. S. 1974. Gas-Blowout Control by Water Injection Through Relief Wells: A Theoretical Analysis. *SPE J.* **14** (4): 321–329. SPE-3963-PA. https://doi.org/10.2118/3963-PA.

Leontaritis, K. J. and Mansoori, G. A. 1987. Asphaltene Flocculation During Oil Production and Processing: A Thermodynamic-Colloidal Model. Presented at the SPE International Symposium on Oil Field Chemistry, San Antonio, Texas, USA, 4–6 February. SPE-16258-MS. https://doi.org/10.2118/16258-MS.

Leontaritis, K. J. and Mansoori, G. A. 1988. Asphaltene Deposition: A Survey of Field Experiences and Research Approaches. *J Pet Sci & Eng* **1** (3): 229–239. https://doi.org/10.1016/0920-4105(88)90013-7.

Lewis, J. B. 1978. New Uses of Existing Technology for Controlling Blowouts: Chronology of a Blowout Offshore Louisiana. *J Pet Technol* **30** (10): 1473–1480. SPE-6909-PA. https://doi.org/10.2118/6909-PA.

Lesem, I. B., Greytok, F., Marotta, F. et al. 1957. A Method of Calculating the Distribution of Temperature in Flowing Gas Wells. *Trans, AIME* **210:** 169–176. SPE-767-G.

Li, M., Li, S. I., and Sun, L. T. 2002. New View on Continuous-Removal Liquids From Gas Wells. *SPE Prod & Fac* **17** (1): 42–46. SPE-75455-PA. https://doi.org/10.2118/75455-PA.

Limpasurat, A., Valko, P. P., and Falcone, G. 2015. A New Concept of Wellbore-Boundary Condition for Modeling Liquid Loading in Gas Wells. *SPE J.* **20** (3): 550–564. SPE-166199-PA. https://doi.org/10.2118/166199-PA.

Liu, R., Kabir, C. S., Mannan, M. S., and Hasan, A. R. 2017. Estimating Total Discharged Volume in Uncontrolled Oil Wells. *J Pet Sci & Eng* **156** (July): 373-380. https://doi.org/10.1016/j.petrol.2017.06.018.

Liu, K. T., Canfield, D. R., and Conley, J. T. 1988. Application of a Mass Flowmeter for Allocation Measurement of Crude Oil Production. *SPE Prod Eng* **3** (4): 633–636. SPE-15394-PA. https://doi.org/10.2118/15394-PA.

Liu, R., Hasan, A. R., and Mannan, M. S. 2015. Flow Rate and Total Discharge Estimations in Gas-Well Blowouts. *J*

Nat Gas Sci & Eng **26** (September): 438–445. https://doi.org/10.1016/j.jngse.2015.06.006.

Livescu, S., Durlofsky, L., and Aziz, K. 2010. A Semianalytical Thermal Multiphase Wellbore-Flow Model for Use in Reservoir Simulation. *SPE J.* **15** (3): 794–804. SPE-115796-PA. https://doi.org/10.2118/115796-PA.

Lockhart, R. W. and Martinelli, R. C. 1949. Proposed Correlation of Data for Isothermal Two-Phase Two Component Flow in Pipes. *Chem Eng Prog* **45** (1): 39–48.

Loder, T., Evans, J. H., and Griffith, J. E. 2003. Prediction of and Effective Preventative Solution for Annular Fluid Pressure Buildup on Subsea Completed Wells—Case Study. Presented at the SPE Annual Technical Conference and Exhibition, Denver, 5–8 October. SPE-84270-MS. https://doi.org/10.2118/84270-MS.

Loizzo, M. Akemu, A., Jammes, L. et al. 2011. Quantifying the Risk of CO2 Leakage Through Wellbores. *SPE Drill & Compl* **26** (3): 324–331. SPE-139635-PA. https://doi.org/10.2118/139635-PA.

Luo, S., Kelkar, M., Pereyra, E. et al. 2014. A New Comprehensive Model for Predicting Liquid Loading in Gas Wells. *SPE Prod & Oper* **29** (4) 337–349. SPE-172501-PA. https://doi.org/10.2118/172501-PA.

Mach, J., Proano, E., and Brown, K. E. 1979. A Nodal Approach for Applying Systems Analysis to the Flowing and Artificial Lift Oil or Gas Well. Unsolicited, paper available from SPE, Richardson, Texas. SPE-8025-MS.

Mach, J. M., Proano, E. A., Mukherjee, H. et al. 1983. A New Concept in Continuous-Flow Gas-Lift Design. *SPE J.* **23** (6): 885–891. SPE-8026-PA. https://doi.org/10.2118/8026-PA.

MacMillan, D. J., Tackett, J. E. Jr., Jessee, M. A. et al. 1995. A Unified Approach to Asphaltene Precipitation: Laboratory Measurement and Modeling. *J Pet Technol* **47** (9): 788–793. SPE-28990-PA. https://doi.org/10.2118/28990-PA.

Mandhane, J. M., Gregory, G. A., and Aziz, K. 1974. A Flow Pattern Map for Gas-Liquid Flow in Horizontal Pipes. *Int J Multiphase Flow* **1** (4): 537–553. https://doi.org/10.1016/0301-9322(74)90006-8.

Mansure, A. J. and Barker, K. M. 1993. Insights Into Good Hot Oiling Practices. Presented at the SPE Production Operations Symposium, Oklahoma City, Oklahoma, USA, 21–23 March. SPE-25484-MS. https://doi.org/10.2118/25484-MS.

Mao, Z. S. and Dukler, A. E. 1993. The Myth of Churn Flow? *Int J Multiphase Flow* **19** (2): 377–383. https://doi.org/10.1016/0301-9322(93)90010-R.

Massinon, R. V. J. 1988. A Real-Time Transient Hydraulic Model for Leak Detection and Batch Tracking on a Liquid Pipeline System. Presented at the CIM Annual Technical Meeting, Calgary, 12–16 June. PETSOC-88-39-93. https://doi.org/10.2118/88-39-93.

Mattar, L. and Gregory, G. A. 1974. Air-Oil Slug Flow in an Upward Inclined Pipe, I: Slug Velocity, Holdup and Pressure Gradient. *J Can Pet Technol* **13** (1): 69–76. PETSOC-74-01-07. https://doi.org/10.2118/74-01-07.

Matthews, C. S. and Russell, D. G. 1967. *Pressure Buildup and Flow Tests in Wells,* Vol. 1, 11. Richardson, Texas: Monograph Series, Society of Petroleum Engineers.

McAdams, W. H., Wood, W. K., and Bryan, R. L. 1942. Vaporization Inside Horizontal Tubes, Part II: Benzene-Oil Mixtures. *Trans.*, ASME **64** (3): 193–200.

McCain, W. D. Jr., and Alexander, R. A. 1992. Sampling Gas-Condensate Wells. *SPE Res Eng* **7** (3): 358–362. SPE-19729-PA. https://doi.org/10.2118/19729-PA.

McKinley, R. M. 1982. Production Logging. Presented at the SPE International Petroleum Exhibition and Technical Symposium, Beijing, 17–24 March. SPE-10035-MS. https://doi.org/10.2118/10035-MS.

McNutt, M, Camilli, R., Guthrie, G. et al. 2011. Assessment of Flow Rate Estimates for the Deepwater Horizon/Macondo Well Oil Spill. Flow Rate Technical Group report to the National Incident Command, Interagency Solutions Group, March 10, 2011. http://large.stanford.edu/courses/2011/ph240/mina1/docs/FRTG-final-report3_10_11-final-pdf.pdf.

Meunier, D., Tixier, M. P., and Bonnet, J. L. 1971. The Production Combination Tool: A New System for Production Monitoring. *J Pet Technol* **23** (5): 603–613. SPE-2957-PA. https://doi.org/10.2118/2957-PA. Miller, C. W. 1980. Wellbore Storage Effect in Geothermal Wells. *SPE J.* **20** (6): 555–566. SPE-8203-PA. https://doi.org/10.2118/8203-PA.

Miller, R. T. and Clements, R. L. 1972. Reservoir Engineering Techniques Used To Predict Blowout Control During the Bay Marchand Fire. *J Pet Technol* **24** (3): 234–240. SPE-3630-PA. https://doi.org/10.2118/3630-PA.

Monger-McClure, T. G., Tackett, J. E., and Merrill, L. S. 1999. Comparisons of Cloud Point Measurement and Paraffin Prediction Methods. *SPE Prod & Fac* **14** (1): 4–16. SPE-54519-PA. https://doi.org/10.2118/54519-PA.

Montgomery, D. C. 2012. *Design and Analysis of Experiments*, eighth edition. New York City: John Wiley & Sons.

Moody, L. F. 1944. Friction Factors for Pipe Flow. *Trans*., ASME **66** (8): 671–684.

Moses, P. L. 1986. Engineering Applications of Phase Behavior of Crude Oil and Condensate Systems. *J Pet Technol* **38** (7): 715–723. SPE-15835-PA. https://doi.org/10.2118/15835-PA.

Mukherjee, H. and Brill, J. P. 1983. Liquid Holdup Correlations for Inclined Two-Phase Flow. *J Pet Technol* **25** (5): 1003–1008. SPE-10923-PA. https://doi.org/10.2118/10923-PA.

Nghiem, L. X. and Coombe, D. A. 1997. Modeling Asphaltene Precipitation During Primary Depletion. *SPE J.* **2** (2): 170–176. SPE-36106-PA. https://doi.org/10.2118/36106-PA.

Nicolas, Y. and Witterholt, E. J. 1972. Measurement of Multiphase Fluid Flow. Presented at the SPE Annual Fall Meeting, San Antonio, Texas, 8–11 October. SPE-4023-MS. https://doi.org/10.2118/4023-MS.

Nojabeei, B., Hasan, A.R., and Kabir, C.S. 2014. Modelling Wellbore Transient Fluid Temperature and Pressure During Diagnostic Fracture-Injection Testing in Unconventional Reservoirs. J Can Pet Technol 53 (3): 161–167. https://doi.org/10.2118/166120-PA.

Novy, R. A. 1995. Pressure Drops in Horizontal Wells: When Can They Be Ignored? *SPE Res Eng* **10** (1): 29–35. SPE-24941-PA. https://doi.org/10.2118/24941-PA.

Odeh, A. S. 1968. Steady-State Flow Capacity of Wells With Limited Entry to Flow. *SPE J.* **8** (1): 43–51. SPE-1797-PA. https://doi.org/10.2118/1797-PA.

Oglesby, K. D., Mehdizadeh, P., and Rodger, G. J. 2006. Portable Multiphase Production Tester for High-Water-Cut Wells. Presented at the SPE Annual Technical Conference and Exhibition, San Antonio, Texas, USA, 24–27 September. SPE-103087-MS. https://doi.org/10.2118/103087-MS.

Oldenburg, C. M., Freifeld, B. M., Pruess, K. et al. 2012. Numerical Simulations of the Macondo Well Blowout Reveal Strong Control of Oil Flow by Reservoir Permeability and Exsolution of Gas. *Proc National Academy Sci* **109** (50): 20254–20259. https://doi.org/10.1073/pnas.1105165108.

Orkiszewski, J. 1967. Predicting Two-Phase Pressure Drops in Vertical Pipe. *J Pet Technol* **19** (6): 829–838; *Trans*., AIME, **240.** SPE-1546-PA. https://doi.org/10.2118/1546-PA.

Oudeman, P. 2010. Validation of Blowout-Rate Calculations for Subsea Wells. *SPE Drill & Compl* **25** (3): 282–289. SPE-115019-PA. https://doi.org/10.2118/115019-PA.

Oudeman, P. and Bacarreza, L. J. 1995. Field Trial Results of Annular Pressure Behavior in a High-Pressure/High-Temperature Well. *SPE Drill & Compl* **10** (2): 84–88. SPE-26738-PA. https://doi.org/10.2118/26738-PA.

Oudeman, P. and Kerem, M. 2006. Transient Behavior of Annular Pressure Buildup in HP/HT Wells. *SPE Drill & Compl* **21** (4): 234–241. SPE-88735-PA. https://doi.org/10.2118/88735-PA.

Ouyang, L.-B., Arbabi, S., and Aziz, K. 1998. General Wellbore Flow Models for Horizontal, Vertical, and Slanted Wells. *SPE J.* **3** (2): 124–133. SPE-36608-PA. https://doi.org/10.2118/36608-PA.

Ouyang, L.-B. and Aziz, K. 2000. A New Homogeneous Model for Gas-Liquid Flow in Horizontal Wells. *J Pet Sci & Eng* **27** (3–4): 119–128. https://doi.org/10.1016/S0920-4105(00)00053-X.

Ouyang, L.-B. and Belanger, D. 2006. Flow Profiling by Distributed Temperature Sensor (DTS) System: Expectation and Reality. *SPE Prod & Oper* **21** (2): 269–281. SPE-90541-PA. https://doi.org/10.2118/90541-PA.

Pacheco, E. F. and Farouq Ali, S. M. 1972. Wellbore Heat Losses and Pressure Drop in Steam Injection. *J Pet Technol* **24** (2): 139–144. SPE-3428-PA. https://doi.org/10.2118/3428-PA.

Pan, H. and Firoozabadi, A. 2000. Thermodynamic Micellization Model for Asphaltene Precipitation From Reservoir Crudes at High Pressures and Temperatures. *SPE Prod & Fac* **15** (1): 58–65. SPE-60842-PA. https://doi.org/10.2118/60842-PA.

Papadimitriou, D. A. and Shoham, O. 1991. A Mechanistic Model for Annulus Bottomhole Pressures in Pumping Wells. Presented at the SPE Production Operation Symposium, Oklahoma City, Oklahoma, USA, 7–9 April. SPE-21669-MS. https://doi.org/10.2118/21669-MS.

Patel, R. 1988. *Multiphase Flow in Vertical and Inclined Annuli*. MS thesis, University of North Dakota, Grand Forks, North Dakota.

Patillo, P. D., Cocales, B. W., and Morey, S. C. 2006. Analysis of an Annular Pressure Buildup Failure During Drill Ahead. *SPE Drill & Compl* **21** (4): 242–247. SPE-89775-PA. https://doi.org/10.2118/89775-PA.

Peffer, J. W., Miller, M. A., and Hill, A. D. 1988. An Improved Method for Calculating Bottomhole Pressures in Flowing Gas Wells With Liquid Present. *SPE Prod Eng* **3** (4): 643–655. SPE-15655-PA. https://doi.org/10.2118/15655-PA.

Perkins, T. K. 1993. Critical and Subcritical Flow of Multiphase Mixtures Through Chokes. *SPE Drill & Compl* **8** (4): 271–276. SPE-20633-PA. https://doi.org/10.2118/20633-PA.

Perry, J. H. 1950. *Chemical Engineering Handbook,* third edition. New York: McGraw-Hill.

Pilehvari, A. A. 1981. Experimental Study of Critical Two-Phase Flow Through Wellhead Chokes. University of Tulsa Fluid Flow Projects Report, Tulsa, Oklahoma.

Pinguet, B. G., Roux, G., and Hopman, N. 2006. Field Experience in Multiphase Gas-Well Testing: The Benefit of the Combination of Venturi and Multienergy Gamma Ray. Presented at the SPE Annual Technical Conference and

Exhibition, San Antonio, Texas, USA, 24–27 September. SPE-103087-MS.

Plackett, R. L. and Burman, J. P. 1946. The Design of Optimum Multifactorial Experiments. *Biometrika* **33** (4): 305–325. Cambridge, England, UK: Cambridge University Press. http://www.jstor.org/stable/2332195?origin=JSTOR-pdf.

Poblano, E., Camacho, R., and Fairuzov, Y. V. 2005. Stability Analysis of Continuous-Flow Gas Lift Wells. *SPE Prod & Fac* **20** (1): 70–79. SPE-77732-PA. https://doi.org/10.2118/77732-PA.

Poettmann, F. H. and Carpenter, P. G. 1952. The Multiphase Flow of Gas, Oil, and Water Through Vertical Flow Strings. New York: API. *Drill & Prod Prac* API-52-257.

Pourafshary, P., Varavei, A., Sepehrnoori, K. et al. 2009. A Compositional Wellbore/Reservoir Simulator to Model Multiphase Flow and Temperature Distribution. *J Pet Sci & Eng* **69** (1–2): 40–52. https://doi.org/10.1016/j.petrol.2009.02.012.

Prosper User's Manual. 2015. Edinburgh, Scotland, UK: Petroleum Experts.

Pucknell, J. K., Mason, J. N. E., and Vervest, E. G. 1993. An Evaluation of Recent Mechanistic Models of Multiphase Flow for Predicting Pressure Drops in Oil and Gas Wells. Presented at the Offshore European Conference, Aberdeen, 7–10 September. SPE-26682-MS. https://doi.org/10.2118/26682-MS.

Radovicich, N. A. and Moissis, R. 1962. The Transition From Two-Phase Bubble Flow to Slug Flow. Report No. 7-7673-22, Dept. of Mech. Eng., MIT, Cambridge, Massachusetts.

Rahman, R. 1984. *Void Fraction During Gas Flow Through a Stagnant Liquid Column in Annular Geometry*. MS thesis, University of North Dakota, Grand Forks, North Dakota.

Ramey, H. J., Jr. 1962. Wellbore Heat Transmission. *J Pet Technol* **14** (4): 427–435; *Trans*., AIME, **225.** SPE-96-PA. https://doi.org/10.2118/96-PA.

Raymond, L. R. 1969. Temperature Distribution in a Circulating Drilling Fluid. *J Pet Technol* **21** (3): 333–341. SPE-2320-PA. https://doi.org/10.2118/2320-PA.

Retnanto, A., Weimer, B., Kontha, I. N. H. et al. 2001. Production Optimization Using Multiphase Well Testing: A Case Study From East Kalimantan, Indonesia. Presented at the SPE Annual Technical Conference and Exhibition, New Orleans, 30 September–3 October. SPE-71556-MS. https://doi.org/10.2118/71556-MS.

Riza, M. F., Hasan, A. R., and Kabir, C. S. 2016. A Pragmatic Approach to Understanding Liquid Loading in Gas Wells. *SPE Prod & Oper* **31** (3): 185–196. SPE-170583-PA. https://doi.org/10.2118/170583-PA.

Rocha-Valadez, T., Hasan, A. R., Mannan, M. S. et al. 2015. Assessing Integrity of the Gas-Lift Valves By Analyzing Annular-Pressure-Transient Response. *J Pet Sci & Eng* **133** (September): 177–183. https://doi.org/10.1016/j.petrol.2015.05.002.

Rocha-Valadez, T., Hasan, A. R., Mannan, M. S. et al. 2016. Design and Analysis of Leak-Testing Methodology for Gas Lift Valves. *SPE Prod & Oper* **31** (2): 176–184. SPE-179724-PA. https://doi.org/10.2118/179724-PA.

Rocha-Valadez, T., Hasan, A. R., Mannan, M. S. et al. 2014a. Assessing Wellbore Integrity in Sustained-Casing-Pressure Annulus. *SPE Drill & Compl* **29** (1): 131–138. SPE-169814-PA. https://doi.org/10.2118/169814-PA.

Rocha-Valadez, T., Metzger, R. A., Hasan, A. R. et al. 2014b. Inherently Safer Sustained Casing Pressure Testing for Well Integrity Evaluation. *J Loss Prev Proc Industr* **29**: 209–215. https://doi.org/10.1016/j.jlp.2014.02.012.

Romero, J. and Touboul, E. 1998. Temperature Prediction for Deepwater Wells: A Field Validated Methodology. Presented at the SPE Annual Technical Conference and Exhibition, New Orleans, 27–30 September. SPE-49056-MS. https://doi.org/10.2118/49056-MS.

Ros, N. C. J. 1960. An Analysis of Critical Simultaneous Gas/Liquid Flow Through a Restriction and Its Application to Flow Metering. *Appl Sci Res*, Section A, **9:** 374–389.

Roux, B., Sanyal, S. K., and Brown, S. L. 1980. An Improved Approach to Estimating True Reservoir Temperature From Transient Temperature Data. Presented at the SPE California Regional Meeting, Los Angeles, California, USA, 9–11 April. SPE-8888-MS. https://doi.org/10.2118/8888-MS.

Sachdeva, R., Schmidt, Z., Brill, J. P. et al. 1986. Two-Phase Flow Through Chokes. Presented at the SPE Annual Technical Conference and Exhibition, New Orleans, 5–8 October. SPE-15657-MS. https://doi.org/10.2118/15657-MS.

Sadatomi, M., Sato, Y., and Saruwatari, S. 1982. Two-Phase Flow in Vertical Noncircular Channels. *Int J Multiphase Flow* **8** (6): 641–655. https://doi.org/10.1016/0301-9322(82)90068-4.

Sagar, R. K., Dotty, D. R., and Schmidt, Z. 1991. Predicting Temperature Profiles in a Flowing Well. *SPE Prod Eng* **6** (4): 441–448. SPE-19702-PA. https://doi.org/10.2118/19702-PA.

Sagar, R. K., Schmidt, Z., Doty, D. R. et al. 1992. A Mechanistic Model of a Nitrogen-Charged, Pressure-Operated Gas Lift Valve. Presented at the SPE Annual Technical Conference and Exhibition, Washington, DC, 4–7 October. SPE-24838-MS. https://doi.org/10.2118/24838-MS.

Salama, M. M. 2000. An Alternative to API 14E Erosional Velocity Limits for Sand-Laden Fluids. *J Energ Resour Technol* **122** (2): 71–77. https://doi.org/10.1115/1.483167.

Sarica, C., Yuan, G., Sutton, R. P. et al. 2013. An Experimental Study on Liquid Loading of Vertical and Deviated Gas Wells. Presented at the SPE Production and Operations Symposium, Oklahoma City, Oklahoma, USA, 23–26 March. SPE-164516-MS. https://doi.org/10.2118/164516-MS.

Sathuvalli, U. B., Payne, M. L., Pattillo, P. D. et al. 2005. Development of a Screening System to Identify Deepwater Wells at Risk for Annular Pressure Buildup. Presented at the SPE/IADC Drilling Conference, Amsterdam, The Netherlands, 23–25 February. SPE-92954-MS. https://doi.org/10.2118/92594-MS.

Sathuvalli, U. B., Piko, R. M., Gonzalez, R. A. et al. 2016. Design and Performance of Annular Pressure Buildup (APB) Mitigation Techniques. Presented at the IADC/SPE Drilling Conference and Exhibition, Fort Worth, Texas, USA, 1–3 March. SPE-178886-MS. https://doi.org/10.2118/178886-MS.

Satter, A. 1965. Heat Losses During Flow of Steam Down a Wellbore. *J Pet Technol* **17** (7): 845–851; *Trans*., AIME, **234.** SPE-1071-PA. https://doi.org/10.2118/1071-PA.

Schlumberger, M., Doll, H. G., and Perebinossoff, A. A. 1937. Temperature Measurements in Oil Wells. *J Inst Pet Technologists* **23:** 159.

Schmidt, Z. 1977. *Experimental Study of Two-Phase Flow in a Pipeline Riser Pipe System*. PhD dissertation, University of Tulsa, Oklahoma.

Schuller, R. B., Munaweera, S. J., Selmer-Olsen, S. et al. 2006. Critical and Subcritical Oil/Gas/Water Mass Flow Rate Experiments and Predictions for Chokes. *SPE Prod & Oper* **21** (3): 372–380. SPE-88813-PA. https://doi.org/10.2118/88813-PA.

Scott, S. L. and Kouba, G. E. 1990. Advances in Slug Flow Characterization for Horizontal and Slightly Inclined Pipelines. Presented at the SPE Annual Technical Conference and Exhibition, New Orleans, 23–26 September. SPE-20628-MS. https://doi.org/10.2118/20628-MS.

Seubold, J. G. and Shirie, J. W. 1967. Length of the Supersonic Core in High-Speed Jets. *AIAA J* **5** (11): 2062–2064. https://doi.org/10.2514/3.4369.

Shah, Y. T., Stiegel, G. J., and Sharma, M. M. 1978. Backmixing in Gas-Liquid Reactors. *AIChE J* **24** (3): 369–400. https://doi.org/10.1002/aic.690240302.

Shen, P. Y. and Beck, A. E. 1986. Stabilization of Bottomhole Temperature With Finite Circulation Time and Fluid Flow. *Geophys J R Astron Soc* **86** (1): 63–90.

Sheriff, N. 1966. Experimental Investigation of Natural Convection in Single and Multiple Vertical Annuli With High Pressure Carbon Dioxide. *Proc*., Third International Heat Transfer Conference, Houston, Texas. Vol. 2, p.132.

Shi, H., Holmes, J. A., Durlofsky, L. J. et al. 2005a. Drift-Flux Modeling of Two-Phase Flow in Wellbores. *SPE J.* **10** (1): 24–33. SPE-84228-PA. https://doi.org/10.2118/84228-PA.

Shi, H., Holmes, J. A., Durlofsky, L. J. et al. 2005b. Drift-Flux Parameters for Three-Phase Steady-State Flow in Wellbores. *SPE J.* **10** (2): 130–137. SPE-89836-PA. https://doi.org/10.2118/89836-PA.

Shiu, K. S. and Beggs, H. D.1980. Predicting Temperatures in Flowing Oil Wells. *J Energ Resour Technol* **102** (1): 2–11. https://doi.org/10.1115/1.3227845.

Shoham, O. 1982*. Flow Pattern Transition and Characterization in Gas-Liquid Two-Phase Flow in Inclined Pipes*. PhD dissertation, University of Tel Aviv, Tel Aviv, Israel.

Shoham, O. 2006. *Mechanistic Modeling of Gas-Liquid Two-Phase Flow in Pipes*, 153. Richardson, Texas: Society of Petroleum Engineers.

Singh, G. and Griffith, P. 1969. Determination of the Pressure Drop Optimum Pipe Size for a Two-Phase Slug Flow in an Inclined Pipe. *J Eng Industry* **92** (4): 717–726; *Trans*., ASME, **92.** https://doi.org/10.1115/1.3427837.

Singh, P., Venkatesan, R., Fogler, H. S. et al. 2000. Formation and Aging of Incipient Thin Film Wax-Oil Gels. *AIChE J* **46** (5): 1059–1074. https://doi.org/10.1002/aic.690460517.

Skalle, P., Jinjun, H., and Podio, A. L. 1999. Killing Methods and Consequences of 1120 Gulf Coast Blowouts During 1960–1996. Presented at the SPE Latin America and Caribbean Petroleum Engineering Conference, Caracas, Venezuela, 21–23 April. SPE-53974-MS. https://doi.org/10.2118/53974-MS.

Skalle, P. and Podio, A. L. 1999. Trends Extracted From 800 Gulf Coast Blowouts During 1960–1996. Presented at the IADC/SPE Drilling Conference, Dallas, 3–6 March. SPE-39354-MS. https://doi.org/10.2118/39354-MS.

Soliman, M. Y. 1986. Analysis of Buildup Test With Short Producing Time. *SPE Form Eval* **1** (4): 363–371. https://doi.org/10.2118/11083-PA.

Spindler, R. P. 2011. Analytical Models for Wellbore-Temperature Distribution. *SPE J.* **16** (1): 125–133. SPE-140135-PA. https://doi.org/10.2118/140135-PA.

Standing, M. B. 1981. *Volumetric and Phase Behavior of Oil Field Hydrocarbon Systems*, ninth edition. Richardson,

Texas: Society of Petroleum Engineers.

Stephenson, G., Molotkov, R., De Guzman, N. et al. 2010. Real-Time Diagnostics of Gas Lift Systems Using Intelligent Agents: A Case Study. *SPE Prod & Oper* **25** (1): 111–123. SPE-124926-PA. https://doi.org/10.2118/124926-PA.

Stone, T. W., Bennett, J., Law, D. H.-S. et al. 2002. Thermal Simulation With Multisegment Wells. *SPE Res Eval & Eng* **5** (3): 206–218. SPE-78131-PA. https://doi.org/10.2118/78131-PA.

Stone, T. W., Brown, G., Guyaguler, B. et al. 2014. Practical Control of SAGD Wells With Dual-Tubing Strings. *J Can Pet Technol* **53** (1): 32–47. SPE-149352-PA. https://doi.org/10.2118/149352-PA.

Su, H. J. and Lee, S. H. 1995. Modeling Transient Wellbore Behavior in Horizontal Wells. Presented at the SPE International Meeting on Petroleum Engineering, Beijing, 14–17 November. SPE-29961-MS. https://doi.org/10.2118/29961-MS.

Sutton, R. P., Cox, S. A., Lea, J. F. et al. 2010. Guidelines for the Proper Application of Critical Velocity Calculations. *SPE Prod & Oper* **25** (2): 182–194. SPE-120625-PA. https://doi.org/10.2118/120625-PA.

Sylvester, N. D. 1987. A Mechanistic Model for Two-Phase Vertical Slug Flow in Pipes. *J Energ Resour Technol* **109** (4): 206–213. https://doi.org/10.1115/1.3231348.

Taitel, Y. and Barnea, D. 1983. Counter Current Gas-Liquid Vertical Flow: Model for Flow Pattern and Pressure Drop. *Int J Multiphase Flow* **9** (6): 637–647. https://doi.org/10.1016/0301-9322(83)90113-1.

Taitel, Y., Barnea, D., and Dukler, A. E. 1980. Modeling Flow Pattern Transitions for Steady Upward Gas-Liquid Flow in Vertical Tubes. *AIChE J* **26** (3): 345–354. https://doi.org/10.1002/aic.690260304.

Taitel, Y. and Dukler, A. E. 1976. A Model for Predicting Flow Regime Transitions in Horizontal and Near Horizontal Gas-Liquid Flow. *AIChE J* **22** (5): 47–55. https://doi.org/10.1002/aic.690220105.

Taitel, Y., Lee, N., and Dukler, A. E. 1978. Transient Gas-Liquid Flow in Horizontal Pipes: Modeling the Flow Pattern Transitions. *AIChE J* **24** (5): 920–934. https://doi.org/10.1002/aic.690240518.

Tanaka, S. and Nishi, K. 1988. Computer Code of Two-Phase Plow in Geothermal Wells Producing Water and/or Water-Carbon Dioxide Mixtures. *Proc*., Thirteenth Workshop on Geothermal Reservoir Engineering, Stanford University, Stanford, California, 19–21 January. SGP-TR-113.

Tang, Y., Schmidt, Z., Blais, R. N. et al. 1999. Transient Dynamic Characteristics of the Gas-Lift Unloading Process. *SPE J.* **4** (3): 268–278. SPE-57659-PA. https://doi.org/10.2118/57659-PA.

Tao, Q., Bryant, S. L., Meckel, T. A. et al. 2012. Wellbore Leakage Model for Above-Zone Monitoring at Cranfield, MS. Presented at the Carbon Management Technology Conference, Orlando, Florida, USA 7–9 February. CMTC-151516-MS. https://doi.org/10.7122/151516-MS.

Tao, Q., Checkai, D., Huerta, N. et al. 2014. Estimating CO2 Fluxes Along Leaky Wellbores. *SPE J.* **19** (2): 227–238. SPE-135483-PA. https://doi.org/10.2118/135483-PA.

Thomson, W. and Joule, J. P. 1853. On the Thermal Effects of Fluids in Motion (Part 1). *Phil Trans., Royal Astr Soc London* **143:** 357–366.

Tibold, M. P., Simonian, S., Chawla, M. et al. 2000. Well Testing With a Permanent Monitoring System. Presented at the SPE Annual Technical Conference and Exhibition, Dallas, 1–4 October. SPE-63079-MS. https://doi.org/10.2118/63079-MS.

Ting, P. D., Hirasaki, G., and Chapman, W. 2003. Modeling of Asphaltene Phase Behavior With the SAFT Equation of State. *Pet Sci & Technol* **21** (3–4): 647–661. https://doi.org/10.1081/LFT-120018544.

Tragesser, A. F., Crawford, P. B., and Crawford, H. R. 1967. A Method for Calculating Circulating Temperatures. *J Pet Technol* **19** (11): 1507–1512. SPE-1484-PA. https://doi.org/10.2118/1484-PA.

Turner, R. G., Hubbard, M. G., and Dukler, A. E. 1969. Analysis and Prediction of Minimum Flow Rate for the Continuous Removal of Liquids From Gas Wells. *J Pet Technol* **21** (11): 1475–1482; *Trans*., AIME, **246.** SPE-2198-PA. https://doi.org/10.2118/2198-PA.

Upadhyay, R. N., Hartz, J. D., Gulati, M. S. 1977. Comparison of Calculated and Observed Pressure Drops in Geothermal Wells Producing Steam–Water Mixtures. Presented at the SPE Annual Technical Conference and Exhibition, Denver, 9–12 October. SPE-6766-MS. https://doi.org/10.2118/6766-MS.

User's Manual for *API 14B, SSCSV Sizing Computer Program*, second edition, Appendix B, 38, P2-E. 1978. Washington, DC: API.

van Everdingen, A.F. and Hurst, W. 1949. The Application of the Laplace Transformation to Flow Problems in Reservoirs. *J Pet Technol* **1** (12): 305–324. *Trans.,* AIME, **186.** SPE-949305-G. https://doi.org/10.2118/949305-G.

Vargo, R. F., Jr., Payne, M., Faul, R. et al. 2003. Practical and Successful Prevention of Annular Pressure Buildup on the Marlin Project. *SPE Drill & Compl* **18** (3): 228–234. SPE-85113-PA. https://doi.org/10.2118/85113-PA.

Veeken, K., Hu, B., and Schiferli, W. 2010. Gas-Well Liquid-Loading-Field-Data Analysis and Multiphase-Flow

Modeling. *SPE Prod & Oper* **25** (3): 275–284. SPE-123657-PA. https://doi.org/10.2118/123657-PA.

Vignes, B. and Aadnøy, B. 2010. Well-Integrity Issues Offshore Norway. *SPE Prod & Oper* **25** (2): 145–150. SPE-112535-PA. https://doi.org/10.2118/112535-PA.

Vogel, J. V. 1968. Inflow Performance Relationships for Solution-Gas Drive Wells. *J Pet Technol* **20** (1): 83–92; *Trans*., AIME, **243.** SPE-1476-PA. https://doi.org/10.2118/1476-PA.

Wade, R. T. Cantrell, R. C., Poupon, A. et al. 1965. Production Logging: The Key to Optimum Well Performance. *J Pet Technol* **17** (2): 137–144. SPE-944-PA. https://doi.org/10.2118/944-PA.

Wallis, G. B. 1969. *One-Dimensional Two-Phase Flow*. New York: McGraw-Hill. https://doi.org/10.1002/aic.690160603.

Waltrich, P. J., Falcone, G. and Barbosa, J. R. 2013. Axial Development of Annular, Churn, and Slug, Flows in a Long Vertical Tube. *Int J Multiphase Flow* **57:** 38–48. https://doi.org/10.1016/j.ijmultiphaseflow.2013.06.008.

Wang, S., Zhang, H.-Q., Sarica, C. et al. 2013. Experimental Study of High-Viscosity Oil/Water/Gas Three-Phase Flow in Horizontal and Upward Vertical Pipes. *SPE Prod & Oper* **28** (3): 306–316. SPE-163148-PA. https://doi.org/10.2118/163148-PA.

Wang, S., Zhang, H.-Q., Sarica, C. et al. 2014. A Mechanistic Slug-Liquid-Holdup Model for Different Oil Viscosities and Pipe-Inclination Angles. *SPE Prod & Oper* **29** (4): 329–336. SPE-171563-PA. https://doi.org/10.2118/171563-PA.

Wang, X., Lee, J., Thigpen, B. et al. 2008. Modeling Flow Profile Using Distributed Temperature Sensor (DTS) System. Presented at the SPE Intelligent Energy Conference and Exhibition, Amsterdam, The Netherlands, 25–27 February. SPE-111790-MS. https://doi.org/10.2118/111790-MS.

Warren, P. B., Al-Dusari, K. H., Zabihi, M. et al. 2003. Field-Testing a Compact Multiphase Flow Meter: Offshore Saudi Arabia. Presented at the SPE Middle East Oil Show and Conference, Bahrain, UAE, 5–8 April. SPE-81560-MS. https://doi.org/10.2118/81560-MS.

Warren, P. B., Hussain, S., and Ghamdi, S. 2001. Background and Operational Experience of Multiphase Metering in the Safaniya Field: Offshore Saudi Arabia. Presented at the SPE Annual Technical Conference and Exhibition, New Orleans, 30 September–3 October. SPE-71534-MS. https://doi.org/10.2118/71534-MS.

Warriner, R. A. and Cassity, T. G. 1988. Relief-Well Requirements to Kill a High-Rate Gas Blowout From a Deepwater Reservoir. *J Pet Technol* **40** (12): 1602–1608. SPE-16131-PA. https://doi.org/10.2118/16131-PA.

Watson, T. L. and Bachu, S. 2009. Evaluation of the Potential for Gas and CO2 Leakage Along Wellbores. *SPE Drill & Compl* **24** (1): 115–126. SPE-106817-PA. https://doi.org/10.2118/106817-PA.

Webster, M., Richardson, S. M., Gabard-Cuoq, C. et al. 2006. Well Surveillance With a Permanent Downhole Multiphase Flowmeter. *SPE Prod & Oper* **21** (3): 388–393. SPE-90024-PA. https://doi.org/10.2118/90024-PA.

Weingarten, J. S. and Euchner, J. A. 1988. Methods for Predicting Wax Precipitation and Deposition. *SPE Prod Eng* **3** (1): 121–126. SPE-15654-PA. https://doi.org/10.2118/15654-PA.

Weisman, J. and Kang, S. Y. 1981. Flow Pattern Transitions in Vertical and Upwardly Inclined Lines. *Int J Multiphase Flow* **7** (3): 271–291. https://doi.org/10.1016/0301-9322(81)90022-7.

Van't Westende, J. M. C., Kemp, H. K., Belt, R. J. et al. 2008. On the Role of Droplets in Cocurrent Annular and Churn-Annular Pipe Flow. *Int J Multiphase Flow* **33** (5): 595–615. https://doi.org/10.1016/j.ijmultiphaseflow.2006.12.006.

Whalley, P. and Hewitt, G. F. 1978. The Correlation of Liquid Entrainment Fraction and Entrainment Rate in Annular Two-Phase Flow. UKAEA Report, AERE-R9187, Harwell, Oxfordshire, England, UK.

Willhite, G. P. 1967. Overall Heat Transfer Coefficients in Steam and Hot Water Injection Wells. *J Pet Technol* **19** (5): 607–615. SPE-1449-PA. https://doi.org/10.2118/1449-PA.

Winkler, H. W. 1992. *Petroleum Engineering Handbook*, ed. H. B. Bradley. Richardson, Texas: Society of Petroleum Engineers.

Winterfeld, P. H. 1989. Simulation of Pressure Buildup in a Multiphase Wellbore/Reservoir System. *SPE Form Eval* **4** (2): 247–252. SPE-15534-PA. https://doi.org/10.2118/15534-PA.

Wolff, M. 2010. Probabilistic Subsurface Forecasting What Do We Really Know? *J Pet Technol* **62** (5): 86–92. SPE-118550-JPT. https://doi.org/10.2118/118550-JPT.

Wooley, G. R. 1980. Computing Downhole Temperatures in Circulation, Injection, and Production Wells. *J Pet Technol* **32** (9): 1509–1522. SPE-8441-PA. https://doi.org/10.2118/8441-PA.

Xiao, J. J., Shoham, O., and Brill, J. P. 1990. A Comprehensive Mechanistic Model for Two-Phase Flow in Pipelines. Presented at the SPE Annual Technical Conference and Exhibition, New Orleans, 23–26 September. SPE-20631-MS. https://doi.org/10.2118/20631-MS.

Xu, J., Scott, S. L., Mabry, W. et al. 2012. High Reliability Gas-Lift Flow Control Device Technology and

Erosion/Endurance Tests. Presented at the SPE Annual Technical Conference and Exhibition, San Antonio, Texas, USA, 8–10 October. SPE-159848-MS. https://doi.org/10.2118/159848-MS.

Xu, R. 2002. *Analysis of Diagnostic Testing of Sustained Casing Pressure in Wells*. PhD dissertation, Louisiana State University, Baton Rouge, Louisiana.

Xu, R. and Wojtanowicz, A. K. 2001. Diagnosis of Sustained Casing Pressure from Bleed-Off/Buildup Testing Patterns. Presented at the SPE Production Operations Symposium, Oklahoma City, Oklahoma, USA, 24–27 March. SPE-67194-MS. https://doi.org/10.2118/67194-MS.

Yoshioka, K., Zhu, D., Hill, A. D. et al. 2005. A Comprehensive Model of Temperature Behavior in a Horizontal Well. Presented at the SPE Annual Technical Conference and Exhibition, Dallas, 9–12 October. SPE-95656-MS. https://doi.org/10.2118/95656-MS.

Yoshioka, K., Zhu, D., Hill, A. D. et al. 2006. Detection of Water or Gas Entries in Horizontal Wells From Temperature Profiles. Presented at the SPE Europec/EAGE Annual Conference and Exhibition, Vienna, Austria, 12–15 June. SPE-100209-MS. https://doi.org/10.2118/100209-MS.

Yu, T., Zhang, H., Li, M. et al. 2010. A Mechanistic Model for Gas/Liquid Flow in Upward Vertical Annuli. *SPE Prod & Oper* **25** (3): 285–295. SPE-124181-PA. https://doi.org/10.2118/124181-PA.

Yuan, H. J., Sarica, C., and Brill, J. P. 1999. Effect of Perforation Density on Single-Phase Liquid Flow Behavior in Horizontal Wells. *SPE Prod Fac* **14** (3): 203–209. SPE-57395-PA. https://doi.org/10.2118/57395-PA.

Zahradnik, J. and Kast Nek, F. 1979. Gas Holdup in Uniformly Aerated Bubble Column Reactors. *Chem Eng Comm* **3** (4–5): 413–429. https://doi.org/10.1080/0098644790893587.

Zhang, H.-Q. and Sarica, C. 2006. Unified Modeling of Gas/Oil/Water Pipe Flow: Basic Approaches and Preliminary Validation. *SPE Proj Fac & Const* **1** (2): 1–7. SPE-95749-PA. https://doi.org/10.2118/95749-PA.

Zhang, H.-Q., Wang, Q., Sarica, C. et al. 2003a. Unified Model for Gas-Liquid Pipe Flow via Slug Dynamics, Part 1: Model Development. *J Energ Resour Technol* **125** (4): 266–273. https://doi.org/10.1115/1.1615246.

Zhang, H.-Q., Wang, Q., Sarica, C. et al. 2003b. Unified Model for Gas-Liquid Pipe Flow via Slug Dynamics, Part 2: Model Validation. *J Energ Resour Technol* **125** (4): 274–283. https://doi.org/10.1115/1.1615618.

Zhou, T. A. 2017. Comprehensive Study of Modeling Multiphase Flow Through Chokes. MS Thesis, Texas A&M University, College Station, Texas.

Zuber, N. and Findlay, J. 1965. Average Volumetric Concentration in Two-Phase Flow Systems. *J Heat Transfer* **87** (4): 453–468. https://doi.org/10.1115/1.3689137.

Zuo, J. Y., Zhang, D. D. and Ng, H.-J. 2001. An Improved Thermodynamic Model for Wax Precipitation From Petroleum Fluids. *Chem Eng Sci* **56** (24): 6941–6947. https://doi.org/10.1016/S0009-2509(01)00338-4.

INDEX

A

acoustic well sounding (AWS), 238, 242, 243
Alamu criteria, 101
allocation algorithms, 135
analytical transient fluid temperature models, 213–215
    derivation of, 220–223
    drawdown, 220–222
    shut-in tests, 223
annular flow, 5–6, 53
annular flow regime, 177–178
Ansari et al. model, 178
    Hasan-Kabir model, 178
    homogeneous model, 177–178
annular fluid conductivity, 209
annular fluid temperature, 189
annular pressure, 225, 226, 228, 237, 239–241, 243, 244
annular pressure buildup (APB), 225–229
    modeling approach, 226–227
    in multiple annuli, 249–251
    semisteady-state approach, 226–227
    transient approach, 227
    transient formulation for, 252–253
annular temperature, 251, 317
    circulation time effect, 261
annulus pressure bleedoff, 229
Ansari et al. model, 44–45, 62, 98–99, 178
artificial-intelligence agents, 236
artificial lift, 9, 101, 144, 236
asphaltene flocculation envelope (AFE), 330–331, 335
asphaltenes, 329, 341
    control, fluid injection, 333–335
average rise velocity, 35

B

Beggs and Brill correlation, 54–56, 61–63, 74, 321
Blasius equation, 3, 34, 68
Blasius-type equation, 67
bleed-off volume, 228
bottomhole pressure (BHP), 92, 144, 145, 152–154, 164, 172, 200, 203, 205, 212, 215, 362
bottomhole-pressure calculations, uncertainty, 94–95
    condensate gravity range, 94–95
    gauges, absolute accuracy, 94
    liquid rate or condensate/gas ratio trend, 94

separator efficiency, 94
wall roughness, 95
bottomhole temperature (BHT), 154, 156, 167, 194
boundary-dominated flow (BDF), 291, 292
bubble rise velocity, 52, 57
bubble terminal rise velocity, 73
bubbly flow, 31, 57–59
bubbly-to-slug transition, 28
buoyancy force, 52, 68

C

capital expenditures (CAPEX), 337
casedhole data analysis, 274–276
example application, 275–276
hyperbola method, 274–275
casinghead gas flow rate, 240
C-factor, 338
channel average velocity, 355
churn flow, 53, 61, 74, 369
circulation temperature, parameters influence, 262–266
heat-flux variation, 265–266
tank temperature variation, 262–265
cleanup period, 146, 147
closed-chamber model, 145
closed-chamber tests, 171–172
cocurrent bubbly flow, 87
Coleman et al. data set, 103
complex heat-transfer issues, 185
complex wells, temperature, 123–126
comprehensive energy balance, 162, 170. *See also* energy balance
transient temperature, in oil reservoirs, 179–181
condensate/gas ratio (CGR), 94, 104
conductive heat transfer, 131–132
constant-rate drawdown test, 284
constant tank fluid temperature, 258–259
continuity equation, 324
convective heat-transfer coefficient, 131–133
conventional systems analysis, 305–307, 312
conversion factors, 221
Coriolis principle, 135
correction factor, 56
correlation coefficient frequency, 362
correlation coefficients, 358, 376
countercurrent two-phase flow, 78–79
coupled system, 305
coupled wellbore/reservoir/surface (CWRS) network model, 336–339, 341
critical discharge pressure, 281

critical gas velocity, 40
critical superficial gas velocity, 100
critical velocity, 99, 100, 237
cumulative-distribution function (CDF), 294

D

damage coefficient, 240–242
Darcy equation, 306
Darcy flow, 310
deasphalted-oil (DAO) treatment, 334
density, 311
density inversion, 320
depth-dependent fluid temperature, 167–170
depth-dependent measurements, 137, 140
depth-dependent temperature response, 137
depth-indexed analysis, 355, 358–361
    Well A-22, 358–364
    Well B-235, 364–368
design of experiments (DoE), 104
deviated wells flow, 49–64
    holdup and pressure drop, empirical correlations, 53–56
    holdup and pressure drop, mechanistic models, 56–64
    pattern transition criteria, 50–53
    upwardly inclined systems, flow patterns, 49–50
diagnostic fracture injection testing, 153–155
differential reservoir volumes, 152
diffusivity equation, 114–115
    solution for, 115–117
discounted profitability index (DPI), 337
dispersed bubbly flow, 29, 34, 53
distributed temperature, gas-well field, 376
distributed temperature sensing (DTS), 135
downhole fluid temperature, 267
downhole gauge placement configurations, 148
down-pass spinner overlay, 372
downward two-phase flow, 76–78
drift-flux approach, 77
drift velocity, 70
drilling operations, 257–295
    circulation temperature, parameters influence, 262–266
    constant tank fluid temperature, 258–259
    fluid circulation temperature, 257
    fluid temperature inversion, 260–262
    reverse-circulation models, 297–298
    static formation temperature, 268–281
    variable heat flux, formation/wellbore interface, 260
    variable tank fluid temperature, 259–260

well blowout, 281–295
Duns-Ros correlation, 16–17
dynamic spinner response, 356
dynamic unloading process, 320

E

earth temperature, 120
eccentricity (E), 6
effective velocity, 356
electrical heating, of flowlines, 335
energy balance, 114, 117, 120, 186–188, 198–199, 220, 223, 322
wellbore fluid, 117–120
energy dissipation, 228, 334
energy exchange, 185, 199
energy retention, 333
energy transfer, 188
energy transport, 156–157
enthalpy, 322, 348. *See also* fluid enthalpy
enthalpy change, 186
entrainment, 40
Eotvos number, 58
error estimation, flow rate, 138
exponential approach, 269–270

F

Fetkovich equation, 306
field data modeling, 146–147
film friction factor, 40–41
finite-difference equations, 217–219
single-phase gas flow, 217–218
single-phase oil flow, 218
two-phase gas/oil flow, 218–219
flow-after-flow test, 308
flow and shut-in conditions, 311
flow assurance, 305–353
flow assurance, integrated methods for, 336–341
combined fluid-flow/heat-transfer modeling, 338–341
corrosion and erosion issues, probing, 338
deepwater prospect development, 338
flow behavior modeling, 49
flowing-fluid temperature, 115, 121, 126, 320
flowmeter response, 370, 371
flowmeter response quality traces (FRQT), 358, 360, 365–367, 376
flowmeters, 135
flow parameter, 57, 58
flow pattern, 10
flow pattern and transition criteria, 61

flow pattern delineation, 25–32
flow pattern maps, 25–27
flow pattern transition criteria, 27–32
flow pattern maps, 50–52, 54, 55, 291, 368–372
Well A-22, 370–371
Well A-55, 368–369
Well B-175, 371–372
Well B-235, 369–370
flow pattern maps and transition criteria, 65–69
intermittent and dispersed bubbly flow, 68–69
smooth and wavy stratified flows, 68
stratified and intermittent or annular flow, 66–68
flow patterns, horizontal flow, 64–65
annular flow, 65
dispersed bubbly flow, 65
plug (or elongated bubbly) flow, 64
slug flow, 64–65
stratified smooth flow, 64
stratified wavy flow, 64
flow pattern transition criteria, 27–32
annular flow, transition, 30–31
bubbly flow/slug flow transition, 27–29
in oil well, 31
pattern transition computation approach, 31
slug to churn flow transition, 29–30
flow period, 139
flow rate, 316–320
flow rate estimation
flow initiation, Well's inception, 143–145
methodology, multiple T_t data, 167
from multistation temperature data, 137–138
slug and closed-chamber tests, 171–172
solution approach, 167
from temperature data, 166–167
with temperature data, 136–137
with unsteady-state temperature data, 138–142
flow rates, 124
flow test, 146
fluid circulation model, 266, 331, 348–352
annular fluid, 349–350
circulating fluid, 349
development of, 348–350
solution of, 350–352
tubular fluid, 348–349
fluid circulation temperature, 257
fluid cooling, 208, 210
fluid density, 2, 17, 25, 39, 40, 132, 175, 198
fluid enthalpy, 157, 162, 170, 176, 198, 199, 205

fluid heat loss, 121
fluid mass flow rate, 2
fluids, compositional analysis, 303–304
fluid/solid thermodynamic behavior, 329–331
fluid temperature, 136, 170, 185, 187, 263, 265, 283, 311, 334, 375
fluid temperature distribution, 161
fluid temperature inversion, 260–262
fluid velocity, 355, 358
fluid volume, 250, 251. *See also* density
folded-Plackett-Burman approach, 294
Forchheimer equation, 306
formation heat conductivity, 4
formation temperature, 115, 279
formation temperature distribution, 114–117
    diffusivity equation, 114–117
frictional pressure gradient, 55
friction factor, 3, 321
friction factor geometry parameter, 6
Froude number, 50, 54, 56

G

gas/condensate wells, two-phase flow, 91–99
    bottomhole-pressure calculations, uncertainty, 94–95
    computational approach and field applications, 92–93
    homogeneous modeling approach justification, 95–96
gas discharge rate, 241
gas lift, 346–347
gas lift technology, 312
gas lift valves (GLVs) integrity testing, 236–246
    case studies, 243–245
    computational scheme, 240–241
    hydrostatic pressure, 239
    mass balance, 239
    methodology, 237
    model formulation, 238–241
    modeling approach for, 237–238
    model validation, 241–243
gas lift wells, temperature profiles in, 312–321
gas/liquid cylindrical cyclone (GLCC) technology, 135
gas/liquid flow, modeling approach, 85–87
    model parameter values, 86
    pattern transition, computational approach for, 87
    pattern transition criteria, 86–87
    pattern transition smoothing, 87
    volume fraction, 85
gas/liquid-ratio (GLR), 14, 318, 320, 322
gas/oil ratio (GOR), 60, 90, 210, 211, 289, 293, 305, 339, 340

gas velocity, 61
gas volume fraction, 11–12, 32, 44, 61, 62, 135, 212, 291
gas-well blowout modeling, 282–287
    heat-transfer components, 282–283
    model validation, field examples, 284–285
    reservoir model, 282
    reservoir/wellbore coupling, 283–284
    variables affecting total discharge, 286–287
    wellbore model, 282
gas wells, drawdown and buildup responses in, 150–151
gas wells, liquid loading, 99–105
    diagnostic approach application, 102–103
    liquid-loading mechanism, 99–102
    parameters influencing, 104
geothermal gradient, 208, 276–279, 320, 363
geothermal well model, 155–160
    analysis of field data, 157–160
    bottomhole pressure calculations, 176–178
    modeling approach, 156–157
GLV leak estimation, 244
Gomez model, 89
Govier-Fogarasi data set, 97
Grashof number, 125
Gray correlation, 98

H

Hagedorn-Brown (H-B) correlation, 17–20, 42, 88, 89
Harmathy correlation, 37, 74, 78, 80
Harmathy equation, 28
Hasan-Kabir (H-K) model, 43, 44, 56, 61, 88, 89, 91, 159, 318
Hasan model, 321, 322
heat conduction, 252
heat energy, 117
heat flow equilibrium, 261
heat flow modeling superposition, 168
heat loss to formation, 118–119
heat of vaporization, 157, 322
heat-transfer calculations, 158–160
heat-transfer coefficients, 129–133, 188, 263, 265, 315–316, 348
    conduction, 129–130
    conductive/convective heat transfer, cylindrical geometry, 131–132
    convection, 131–132
    forced convection, 132
    natural convection, 132–133
    radiation, 129
heat-transfer model, 258
heat-transfer model elements, 166

heat-transfer principle, 114
heat-transfer rate, 186, 258
heat transport
    field applications, 135–183
    flow rate estimation, 135–145
history-matching effort, temperature profiles, 137
history-matching time-lapse temperature profiles, 138
history-matching transient-temperature profiles, 140, 141
holdup and pressure drop
    empirical correlations, 53–56
    mechanistic models, 56–64
    in near-horizontal flow, 69–72
homogeneous flow models, 12–14, 20, 73
homogeneous liquid, 60
homogeneous modeling approach justification
    Ansari et al. model, comparison, 96
    Gray correlation, comparison, 95–96
horizontal flow pattern map, 69
horizontal pipes and wells flow, 64–74
    flow pattern maps and transition criteria, 65–69
    flow patterns in, 64–65
    holdup and pressure drop, in near-horizontal flow, 69–72
horizontal wells flow, 6–7
    pressure drop in, 6
Hughmark correlation, 71
hydrostatic pressure, 239
hydrostatic pressure gradient, 291
hyperbola method, 274–275

I

individual transition criteria, 52–53
infinite-acting radial flow model, 144
inflow performance relationship (IPR), 287, 306, 309, 311, 312
initial tank fluid temperature, 264
injection-pressure-operated gas lift valves, 236
injection wells, fluid temperature, 123
inlet fluid temperature, 267
inline spinner response, 308
in-situ core velocity, 40
in-situ fluid velocities, 10, 355
in-situ gas velocity, 32, 33, 36, 77
in-situ gas volume fraction, 95
in-situ oil fraction, 80
insulation effect, water depth, 334
internal control valve (ICV) design, 339, 341
isobaric thermal expansion, 226
isothermal compressibility, 226, 251

iterative-solution technique, 157

J

James correlation, 324
James equation, 323
Joule-Thomson (J-T) effect, 113, 121–123, 135, 137, 138, 142–143, 153, 161, 162, 164, 180, 199, 213, 277, 280, 282, 283, 314, 339, 348

K

kinetic energy (KE), 2, 63, 72, 105, 114, 122, 221, 281–283, 324
Kutadelaze number, 50

L

Latin hypercube (LH) sampling, 336
liquid-film flow reversal principle, 99
liquid holdup, 11–12
liquid holdup and pressure drop, 32–41
    annular flow, 39–41
    bubbly flow, 32–35
    churn flow, 39
    slug flow, 35–39
liquid holdup, bubbly flow, 32–34
    flow parameter, 33–34
    terminal rise velocity, 33
liquid-level profile, 245
liquid-loading mechanism, 99–102
    critical liquid-loading velocity model, 99–101
    well performance with simulated data, 101–102
liquid saturation enthalpy, 157
Lockhart-Martinelli (L-M) approach, 14–16, 20, 31, 67–69, 96, 325
log-linear approximation, 270
loss of fidelity, 137
low oil rate, fluid temperature, 318

M

mass balance, 198, 239
mass flux, 10–11, 324
mass fraction, 10–11
mass velocity, 11
material balance, 198
mathematical model
    common wellbore, production and injection, 190–191
    tubing and annulus, production, 186–188
    two tubing strings, production, 188–189
mechanical energy balance, 1–2
mixture density, 12, 13, 212

mixture friction factor, 13, 14, 55
mixture velocity, 29, 34, 39, 101
model parameter values, 86
model validation, input data for, 182–183
momentum balance equation, 1, 198, 321, 322
momentum conservation, 1–2
momentum transport, 156
Monte Carlo (MC) sampling, 336
Moody friction factor, 3, 5–7, 12, 70
Moody friction factor chart, 4
mud circulation model, 259
mud temperature, 270
multiphase choke correlations, flow rates, 105–109
    modeling approach, 105–106
    models, application, 108–109
    two-phase flow through chokes, 106–108
multiphase flow, 9–21
    concepts and definitions, 10–12
    deviated wells flow, 49–64
    flow pattern delineation, 25–32
    gas/condensate wells, two-phase flow, 91–99
    gas/liquid flow, modeling approach, 85–87
    gas wells, liquid loading, 99–105
    homogeneous flow models, 13–14
    horizontal pipes and wells flow, 64–74
    liquid holdup and pressure drop, 32–41
    method of analysis, 12–13
    multiphase choke correlations, 105–109
    nonconventional situations, modeling flow, 74–81
    oil wells, two-phase flow, 88–91
    separated flow models, 14–21
    vertical cocurrent systems, flow patterns, 23–24
    wellbores, flow patterns, 24–25
multiple-string completions
    bottomhole temperatures, 194
    common wellbores, production and injection, 195
    input parameters, 195
    tubing and annulus, production, 192
    two tubing strings, production, 193–194
    working equations for, 192–195
multistation temperature, 140

N

natural convective fluid, 131
near-horizontal flow, holdup and pressure drop, 69–72
    annular flow, 71–72
    dispersed bubbly flow, 71

intermittent flow, 70–71
stratified wavy/smooth flow, 69–70
net present value (NPV), 336, 337
Newton-Raphson method, 37
nonconventional situations, modeling flow, 74–81
countercurrent two-phase flow, 78–79
downward two-phase flow, 76–78
oil/water two-phase flow, 79–81
two-phase flow, in annulus, 74–76
non-Darcy flow effects, 305, 307, 309–312
nonisothermal systems flow, 4
nonlinear temperature profiles, 320
Nusselt number, 132

O

O'Connor Well, 318, 319
off-bottom gauges, 146–155
model validation, field example, 146–155
oil-based-mud (OBM) contamination, 339, 340
oil gravity (API), 19, 94, 95, 97, 109, 236
oil PVT properties, maximum discharge, 303–304
oil reservoirs with large drawdowns
analytical model, 161–162
model validation with field example, 162–164
transient temperature in, 160–164
oil/water two-phase flow, 79–81
oil well blowout modeling, 287–294
blowout rate computation, 288
mixture and sonic velocity, 288–289
risk and uncertainty, Macondo case study, 292–294
system response and uncertainty, input parameters, 290–292
wellbore & reservoir model validation, 289–290
oil wells, buildup response in, 150
oil wells, drawdown response, 148–150
oil wells, two-phase flow, 88–91
six models, comparative study, 88–89
uncertainty analysis, 89–90
openhole data analysis, 269–274
example application, 272–274
exponential approach, 269–270
log-linear approximation, 270
rigorous approach, 269
square-root-of-time approximation, 270–272
operating expenditures (OPEX), 337, 338
Oudeman-Bacarreza model, 226
overall-heat-transfer coefficient (U_t), 91, 118, 125, 126, 156, 169, 197, 200, 227, 272, 280, 322, 332, 350

P

paraffin control, fluid circulation, 332–333
Pareto chart, 90, 91, 104, 149, 151, 286, 292
    five-variable Macondo case study, 294
pattern transition, computational approach for, 87
pattern transition criteria, 50–53, 86–87
    flow pattern maps, 50–52
    individual transition criteria, 52–53
pattern transition smoothing, 87
Péclet numbers, 161, 163
Peng-Robinson's equation-of-state modeling, 293
permanent downhole gauge, optimal location, 147–148
perturbed-chain statistical associating fluid theory (PC-SAFT) equation-of-state model, 338, 340
phase redistribution modeling, 49
pipe-diameter effect, 28
pipe-surface roughness, 6
Plackett-Burman design, 286
Poettmann-Carpenter correlation, 14
Prandtl number, 132
pressure buildup, 228
pressure-buildup test, 76
pressure-computation algorithm, 154
pressure drop, 322, 325–328
pressure-drop calculations, 157–158
pressure gradient, 19–21, 34, 38–39, 41, 44, 59–63, 72, 76, 80, 85, 176
pressure response, 146–155
pressure-transient tests, 113, 236
pressure-traverse calculations, 63, 157–158, 160
pressure/volume/temperature (PVT) model, 91, 292, 305
probabilistic blowout behavior, 286
production logging, 355–376
    flow pattern maps for, 368–372
    rate estimation, temperature surveys, 372–375
    spinner flowmeter production log interpretation, 355–368
production-logging tool string, 308
production loss, 286
production operations, 305–353
production rate, 367
production system, 9
productivity index (PI), 104
pseudo-Reynolds number, 14
pseudoslugs, 79
pseudosteady-state fluid temperature, 168–170
pulsed neutron capture (PNC), 361

R

radial flow, 149, 150

radiative-heat-transfer coefficient, 129
rate inversion, 142–143
real-time production management, 230
rectangular-hyperbola analysis, 279
relative roughness, 5
relaxation parameter, 174, 200, 223, 322, 332, 348
reservoir flow behavior, pressure-rate, 307–310
reservoir flowing-fluid temperature
    analytical solution for, 180
    solution including Q, 181
    solution neglecting Q, 180–181
reservoir model, 144
reservoir-pressure, 290
reverse-circulation models, 297–298
Reynolds numbers, 3, 68, 70, 71, 80, 96, 125, 132, 324
rigorous approach, 269
risk and uncertainty assessment, blowout, 293
roughness ratio, 157

S

sandface flow rate, 200
saturates/aromatics/resins/asphaltenes (SARA) analysis, 339
saturation enthalpies, 322, 324
seamless systems analysis, 305, 311–312
second-order linear differential equation, 332
separated flow models, 14–21
    Duns-Ros correlation, 16–17
    Hagedorn-Brown method, 17–19
    Lockhart-Martinelli correlation, 14–16
Shen-Beck synthetic data, 275
Shiu-Beggs (SB) correlation, 318
shut-in fluid temperature, 174
shut-in tests, 146, 223
simplified annular flow model, 41
simplified film flow reversal model, 100
single-phase flow, 1–4, 312
    mechanical energy balance, 1–2
    pressure gradient components, 2–4
single-phase gas flow
    finite-difference equations, 217–218
    J-T effect, 122
    model formulation, 198–200
    producing-fluid temperature, 121
    single-phase gas example, sensitivity study, 200–204
single-phase liquid flow
    J-T effect, 122
    producing-fluid temperature, 120–121

single-phase oil flow
finite-difference equations, 218
model formulation, 204
single-phase oil example, sensitivity study, 204–210
slip, 11–12
slug and closed-chamber tests, 144
slug flow model, 35–39, 57, 59, 144–145
slug flow regime, 177
Ansari et al. (1994) model, 177
Hasan-Kabir model, 177
homogeneous model, 177
slug tests, 171–172
solids deposition models, 348–353
fluid circulation model, 348–352
solvent injection model, 352–353
solvent injection model, 332
constants of, 352–353
sonic velocity, 237, 282, 284, 287, 288
spinner flowmeter production log interpretation, 355–368
conventional approach, 356–358
depth-indexed analysis, 358–361
spinner response slope frequency, 359, 360, 363, 364, 366, 367, 376
spinner threshold velocity, 356
spinner velocity vs. cable velocity, 358
square-root-of-time approximation, 270–272
stagnation enthalpy, 324
static and dynamic spinner calibration plots, 357
static formation temperature, 268–281
casedhole data analysis, 274–276
geothermal gradient, establishing, 276–279
openhole data analysis, 269–274
steady-state flow simulation, 113, 312, 320
steady-state heat transfer, 118
steady-state injection temperature profile, 173
steady-state two-phase model, 305
steam injection, 321–322
example application, 322
mathematical model, 321–322
steam quality, 322
Stefan-Boltzmann constant, 129
sucker-rod pumping, 312
superficial core fluid velocity, 40
superficial gas velocity, 87
superficial liquid velocity, 100
superficial velocity, 10, 25, 77
superposition equations, 344–345
superposition principle, 169
surface metering, 321–328

sustained casing pressure model
derivation and analytical solution, 254–256
gas influx rate, 254
governing equation and solution for, 255–256
systems analysis, 305–312
for well B-FN9, 306
for well B-OF8, 306

T

Taylor bubble rise velocity, 28, 38, 53, 57–59, 63, 71, 73, 75, 79
Taylor bubbles, 24, 29, 35–37, 50, 56, 57, 86
temperature distribution, 114, 199
temperature maxima, 262
temperature perturbation, 274
temperature profiles, in gas lift wells, 312–321
factors affecting, 315–320
mathematical model, 313–315
temperature sensors, 140
temperature-superposition effect, 266
temperature surveys, rate estimation, 372–375
distributed-flow profiling, 374
gas-well field example, 375
oil/water field example, 374–375
temperature transients, 136
temporary downhole gauge system, 148
terminal rise velocity, 28, 32
thermal diffusivity, 114, 199, 260
thermal effects, 146–155
thermal energy balance, 162, 179
thermal expansion, 250, 251
thermal storage parameter, 221
thermal stress failure, 114
Thompson Well, 318
throat mixture density, 324
time dependent temperature gradient, 155, 227
tool velocity, 358
transient fluid and heat flows, 197–223
transient fluid temperature, 170
transient heat flows
annular pressure buildup, 225–229
applications of, 225–246
example applications, 227–229
gas lift valves integrity testing, 236–246
sustained casing pressure, annulus, 230–236
transient heat transfer, 300–302
transient pressure loss, 288
transient pressure/temperature behavior, 212

transient simulations, 197
transient temperature, in oil reservoirs, 179–181
transient temperature model, 140, 277, 280
    fluid pressure computation, 175
    fluid temperature computation, 174–175
    in oil reservoirs with large drawdowns, 160–164
    water injection, 173–175
tubing fluid temperature, 346
tubinghead temperature, 228, 229
tubing performance curve (TPC), 287
tubing pressure, 319
tubing temperature, 319
turbulent flow, 3
two-phase flow, in annulus, 74–76
two-phase flow through chokes, 106–108
    empirical correlations, 107–108
    thermodynamic modeling, 106–107
two-phase flow velocity, 73
two-phase friction factor, 14, 55
two-phase gas/oil flow
    finite-difference equations, 218–219
    model formulation, 210
    sensitivity study, 210–213
two-phase Reynolds number, 14
two-phase viscosity, 17

U

unsteady heat flow, 320
up-pass spinner overlay, 369

V

valve damage coefficient, 237
valve mechanics, 320
variable heat flux, formation/wellbore interface, 260
variable heat flux model, 268, 299
variable tank fluid temperature, 259–260
Veeken et al. data set, 103
velocity-profile correction factor, 368, 370
velocity strings, 101
venturi-type flowmeters, 135
venturi valves, 236
vertical cocurrent systems, flow patterns, 23–24
    annular flow, 24
    bubbly flow, 23
    churn flow, 24
    slug flow, 24
vertical well produces, 43–45

viscous dissipation, 179
volume fraction, 10–11, 85
volumetric expansion coefficient, 73

W

water/gas ratio (WGR), 104
water injection wells, 153–155
wave propagation velocity, 68
wax-appearance temperature (WAT), 339, 341
wax phase boundaries, 340
Weisman-Kang correlation, 51
well blowout, 281–295
    gas-well blowout modeling, 282–287
    oilwell blowout modeling, 287–294
wellbore fluid, energy balance, 117–120
    heat loss to formation, 118–119
    heat transport, offshore riser, 119–120
    overall-heat-transfer coefficient, 118
    relaxation parameter, 119
wellbore fluid temperature, 113, 120–126, 199–200, 282
    complex wells, temperature, 123–126
    fluid temperature, in injection wells, 123
    Joule-Thomson coefficient, 121–123
    producing-fluid temperature, 120–121
    single-phase gas flow, 121
    single-phase liquid flow, 120–121
wellbore/formation interface temperature, 168
wellbore heat-transfer coefficient, 4
wellbore heat transport, 113–133
    formation temperature distribution, 114–117
    wellbore fluid, energy balance, 117–120
    wellbore fluid temperature, 120–126
wellbore pressure gradient, 282
wellbore/reservoir coupling, 144
wellbore/reservoir modeling, 146
wellbores, flow patterns, 24–25
wellbore solids deposition, combating, 329–341
    application of models, 332–335
    asphaltene control, fluid injection, 333–335
    flow assurance, integrated methods for, 336–341
    fluid circulation model, 331
    fluid/solid thermodynamic behavior, 329–331
    paraffin control, fluid circulation, 332–333
    solvent injection model, 332
wellbore steam/water flow, 321–328
    pressure drop, fittings, 325–328
    steam flow rate metering and quality, 322–324

steam injection, 321–322
two-phase critical flow relationship, 324
wellbore temperature model, 161
wellbore temperature profiles, 136
common wellbore, production and injection, 190–191
injection/production scenario, 190–191
in multiple strings, 185–191
tubing and annulus, production, 186–187
two tubing strings, production, 188–189
Well A28, 187–188
Well C39, 189–190
well deviation factor, 86
wellhead-and bottomhole-pressure conversion, 153–155
wellhead fluid inlet/exit temperature, circulation time effect, 264
wellhead pressure (WHP), 92, 147, 152, 153, 159, 160, 200, 202, 203, 205, 211–213, 215
wellhead pressure conversion, 151–153
in shut-in and flowing conditions, 151–153
wellhead temperature (WHT), 142, 143, 147, 167, 200, 202–205, 208, 210, 212–215
well integrity, assessing, 225–246
wireline-retrievability, valves, 312

Z

Z-factor, 172